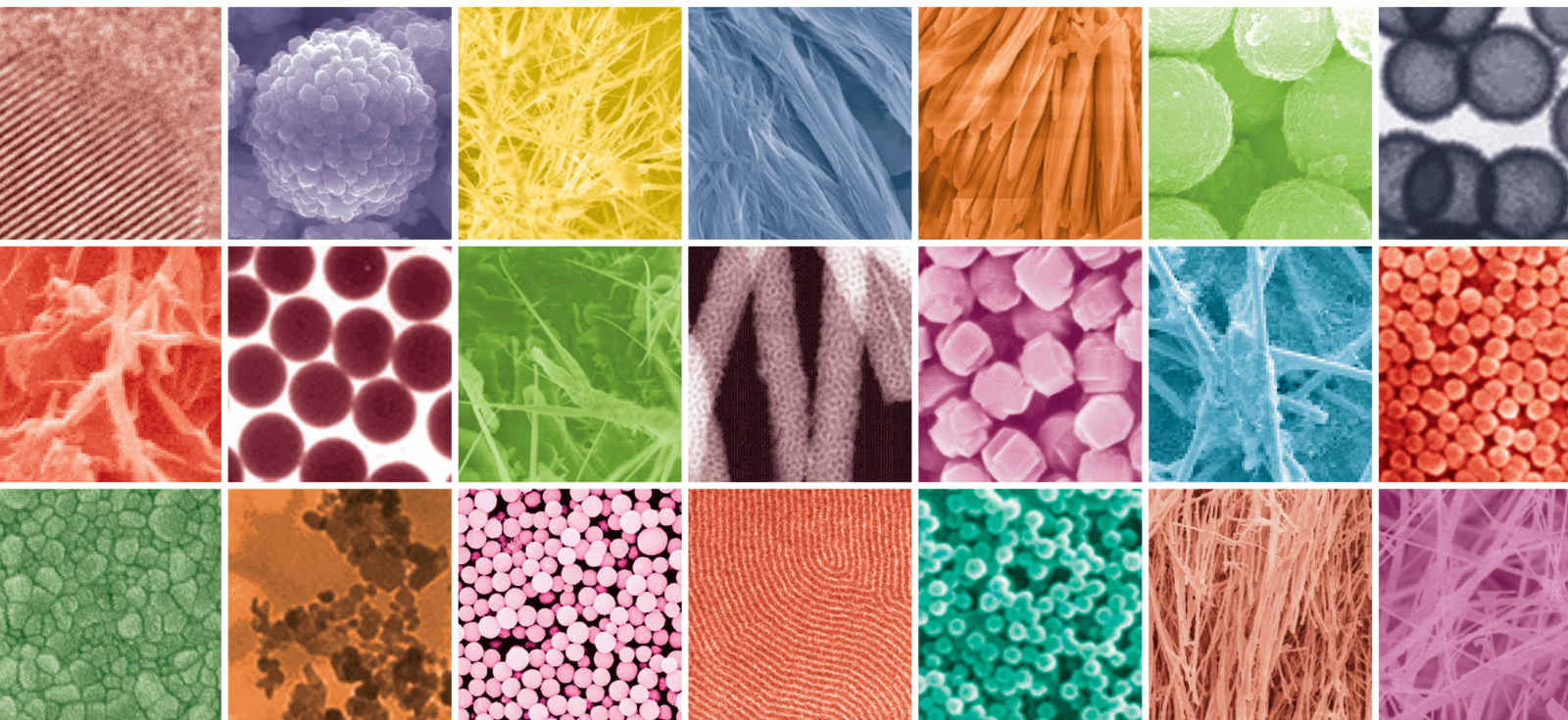


# Classical and Fractional-Order Derivative Approaches in Hybrid Nanofluids

Lead Guest Editor: Taza Gul

Guest Editors: Anwar Saeed and Amir Khan





---

# **Classical and Fractional-Order Derivative Approaches in Hybrid Nanofluids**

Journal of Nanomaterials

---

**Classical and Fractional-Order  
Derivative Approaches in Hybrid  
Nanofluids**

Lead Guest Editor: Taza Gul

Guest Editors: Anwar Saeed and Amir Khan



---




Copyright © 2023 Hindawi Limited. All rights reserved.

This is a special issue published in "Journal of Nanomaterials." All articles are open access articles distributed under the Creative Commons Attribution License, which permits unrestricted use, distribution, and reproduction in any medium, provided the original work is properly cited.




# Chief Editor

Stefano Bellucci , Italy

















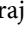
















## Associate Editors

Ilaria Armentano, Italy  
Stefano Bellucci , Italy  
Paulo Cesar Morais , Brazil  
William Yu , USA

## Academic Editors

Buzuayehu Abebe, Ethiopia  
Domenico Acierno , Italy  
Sergio-Miguel Acuña-Nelson , Chile  
Katerina Aifantis, USA  
Omer Alawi , Malaysia  
Nageh K. Allam , USA  
Muhammad Wahab Amjad , USA  
Martin Andersson, Sweden  
Hassan Azzazy , Egypt  
Ümit Ağbulut , Turkey  
Vincenzo Baglio , Italy  
Lavinia Balan , France  
Nasser Barakat , Egypt  
Thierry Baron , France  
Carlos Gregorio Barreras-Urbina, Mexico  
Andrew R. Barron , USA  
Enrico Bergamaschi , Italy  
Sergio Bietti , Italy  
Raghvendra A. Bohara, India  
Mohamed Bououdina , Saudi Arabia  
Victor M. Castaño , Mexico  
Albano Cavaleiro , Portugal  
Kondareddy Cherukula , USA  
Shafiul Chowdhury, USA  
Yu-Lun Chueh , Taiwan  
Elisabetta Comini , Italy  
David Cornu, France  
Miguel A. Correa-Duarte , Spain  
P. Davide Cozzoli , Italy  
Anuja Datta , India  
Loretta L. Del Mercato, Italy  
Yong Ding , USA  
Kaliannan Durairaj , Republic of Korea  
Ana Espinosa , France  
Claude Estournès , France  
Giuliana Faggio , Italy  
Andrea Falqui , Saudi Arabia

Matteo Ferroni , Italy  
Chong Leong Gan , Taiwan  
Siddhartha Ghosh, Singapore  
Filippo Giubileo , Italy  
Iaroslav Gnilitzkiy, Ukraine  
Hassanien Gomaa , Egypt  
Fabien Grasset , Japan  
Jean M. Greneche, France  
Kimberly Hamad-Schifferli, USA  
Simo-Pekka Hannula, Finland  
Michael Harris , USA  
Hadi Hashemi Gahruei , Iran  
Yasuhiko Hayashi , Japan  
Michael Z. Hu , USA  
Zhengwei Huang , China  
Zafar Iqbal, USA  
Balachandran Jeyadevan , Japan  
Xin Ju , China  
Antonios Kellarakis , United Kingdom  
Mohan Kumar Kesarla Kesarla , Mexico  
Ali Khorsand Zak , Iran  
Avvaru Praveen Kumar , Ethiopia  
Prashant Kumar , United Kingdom  
Jui-Yang Lai , Taiwan  
Saravanan Lakshmanan, India  
Meiyong Liao , Japan  
Shijun Liao , China  
Silvia Licocchia , Italy  
Zainovia Lockman, Malaysia  
Jim Low , Australia  
Rajesh Kumar Manavalan , Russia  
Yingji Mao , China  
Ivan Marri , Italy  
Laura Martinez Maestro , United Kingdom  
Sanjay R. Mathur, Germany  
Tony McNally, United Kingdom  
Pier Gianni Medaglia , Italy  
Paul Munroe, Australia  
Jae-Min Myoung, Republic of Korea  
Rajesh R. Naik, USA  
Albert Nasibulin , Russia  
Ngoc Thinh Nguyen , Vietnam  
Hai Nguyen Tran , Vietnam  
Hiromasa Nishikiori , Japan

Sherine Obare , USA  
Abdelwahab Omri , Canada  
Dillip K. Panda, USA  
Sakthivel Pandurengan , India  
Dr. Asisa Kumar Panigrahy, India  
Mazeyar Parvinzadeh Gashti , Canada  
Edward A. Payzant , USA  
Alessandro Pegoretti , Italy  
Oscar Perales-Pérez, Puerto Rico  
Anand Babu Perumal , China  
Suresh Perumal , India  
Thathan Premkumar , Republic of Korea  
Helena Prima-García, Spain  
Alexander Pyatenko, Japan  
Xiaoliang Qi , China  
Haisheng Qian , China  
Baskaran Rangasamy , Zambia  
Soumyendu Roy , India  
Fedlu Kedir Sabir , Ethiopia  
Lucien Saviot , France  
Shu Seki , Japan  
Senthil Kumaran Selvaraj , India  
Donglu Shi , USA  
Muhammad Hussnain Siddique , Pakistan  
Bhanu P. Singh , India  
Jagpreet Singh , India  
Jagpreet Singh, India  
Surinder Singh, USA  
Thangjam Ibomcha Singh , Republic of Korea  
Korea  
Vidya Nand Singh, India  
Vladimir Sivakov, Germany  
Tushar Sonar, Russia  
Pingan Song , Australia  
Adolfo Speghini , Italy  
Kishore Sridharan , India  
Marinella Striccoli , Italy  
Andreas Stylianou , Cyprus  
Fengqiang Sun , China  
Ashok K. Sundramoorthy , India  
Bo Tan, Canada  
Leander Tapfer , Italy  
Dr. T. Sathish Thanikodi , India  
Arun Thirumurugan , Chile  
Roshan Thotagamuge , Sri Lanka

Valeri P. Tolstoy , Russia  
Muhammet S. Toprak , Sweden  
Achim Trampert, Germany  
Tamer Uyar , USA  
Cristian Vacacela Gomez , Ecuador  
Luca Valentini, Italy  
Viet Van Pham , Vietnam  
Antonio Vassallo , Italy  
Ester Vazquez , Spain  
Ajayan Vinu, Australia  
Ruibing Wang , Macau  
Magnus Willander , Sweden  
Guosong Wu, China  
Ping Xiao, United Kingdom  
Zhi Li Xiao , USA  
Yingchao Yang , USA  
Hui Yao , China  
Dong Kee Yi , Republic of Korea  
Jianbo Yin , China  
Hesham MH Zakaly , Russia  
Michele Zappalorto , Italy  
Mauro Zarrelli , Italy  
Osman Ahmed Zeleke, Ethiopia  
Wenhui Zeng , USA  
Renyun Zhang , Sweden

# Contents

## **Retracted: The Mathematical Analysis of the New Fractional Order Ebola Model**

Journal of Nanomaterials




Retraction (1 page), Article ID 9854956, Volume 2023 (2023)

## **Corrigendum to “Thermal Transport in Radiative Nanofluids by Considering the Influence of Convective Heat Condition”**

Adnan , Waqas Ashraf, Abdulaziz H. Alghtani, Ilyas Khan , and M. Andualem 





Corrigendum (1 page), Article ID 9791071, Volume 2023 (2023)

## **Effect of Joule Heating and Thermal Radiation of MHD Boundary Layer Oldroyd-B Nanofluid Flow with Heat Transfer over a Porous Stretching Sheet by Finite Element Method**

Hakeem Ullah , Mehreen Fiza , Kamal Khan, Shamaila Batool, S. M. Ghufuran, and Seham M. Al-Mekhlafi 


Research Article (11 pages), Article ID 7373631, Volume 2022 (2022)

## **Aggregation Effects on Entropy Generation Analysis for Nanofluid Flow over a Wedge with Thermal Radiation: A Numerical Investigation**

Rabia Rehman , Hafiz Abdul Wahab , Nawa Alshammari , Umar Khan, and Ilyas Khan 

Research Article (10 pages), Article ID 3992590, Volume 2022 (2022)

## **[Retracted] The Mathematical Analysis of the New Fractional Order Ebola Model**

Faiz Muhammad Khan, Amjad Ali, Ebenezer Bonyah , and Zia Ullah Khan





Research Article (12 pages), Article ID 4912859, Volume 2022 (2022)

## **Melting Heat Transition in a Spinning Flow of Silver-Magnesium Oxide/Engine Oil Hybrid Nanofluid Using Parametric Estimation**

Muhammad Bilal, Taza Gul , Abir Mouldi, Safyan Mukhtar, Wajdi Alghamdi , Souhail Mohamed Bouzgarrou, and Nosheen Feroz

Research Article (13 pages), Article ID 2891315, Volume 2022 (2022)

## **Entropy Generation Analysis for MHD Flow of Hybrid Nanofluids over a Curved Stretching Surface with Shape Effects**

Basharat Ullah , Umar Khan, Hafiz Abdul Wahab , Ilyas Khan , and Md. Nur Alam 



Research Article (10 pages), Article ID 8929985, Volume 2022 (2022)

## **Heat Transfer Analysis on Carboxymethyl Cellulose Water-Based Cross Hybrid Nanofluid Flow with Entropy Generation**

F. Ali , K. Loganathan , S. Eswaramoorthi , K. Prabu, A. Zaib , and Dinesh Kumar Chaudhary 



Research Article (11 pages), Article ID 5252918, Volume 2022 (2022)

## **A Novel Analysis of Generalized Perturbed Zakharov–Kuznetsov Equation of Fractional-Order Arising in Dusty Plasma by Natural Transform Decomposition Method**

Sharifah E. Alhazmi, Shaimaa A. M. Abdelmohsen, Maryam Ahmed Alyami, Aatif Ali , and Joshua Kiddy K. Asamoah 




Research Article (15 pages), Article ID 7036825, Volume 2022 (2022)

**Cooling a Hot Semiannulus with Constant Heat Flux by Using  $\text{Fe}_3\text{O}_4$ -Water Nanofluid and a Magnetic Field: Natural Convection Mechanism**

Zhengqiang Yang, S. M. Bouzgarrou, Riadh Marzouki, Fatma Aouaini, M. A. El-Shorbagy , Mahidzal Dahari, Said Anwar Shah, and D. L. Suthar 






Research Article (9 pages), Article ID 4761989, Volume 2022 (2022)

**Heat Transfer Analysis of the MHD Stagnation Point Flow of a Non-Newtonian Tangent Hyperbolic Hybrid Nanofluid past a Non-Isothermal Flat Plate with Thermal Radiation Effect**

Abdullah Dawar , Saeed Islam , Ahmed Alshehri, Ebenezer Bonyah , and Zahir Shah

Research Article (12 pages), Article ID 4903486, Volume 2022 (2022)

**Electro-Magnetohydrodynamic Fractional-Order Fluid Flow with New Similarity Transformations**

Fuad S. Al-Duais , Saeed Ahmed Asiri , Anwar Saeed , Jihen Majdoubi, Mohammad Mahtab Alam , and Taza Gul 



Research Article (9 pages), Article ID 5198968, Volume 2022 (2022)

**Darcy-Forchheimer 3D Flow of Glycerin-Based Carbon Nanotubes on a Riga Plate with Nonlinear Thermal Radiation and Cattaneo-Christov Heat Flux**

S. Eswaramoorthi , K. Loganathan , Reema Jain, and Sonam Gyeltshen 


Research Article (20 pages), Article ID 5286921, Volume 2022 (2022)

**Analysis of Natural Convection in Nanofluid Flow through a Channel with Source/Sink Effect**

Imran Siddique , Kashif Sadiq, Fahd Jarad , Mohammed K. Al Mesfer, Mohd Danish, and Sonia Yaqoob





Research Article (9 pages), Article ID 2738398, Volume 2022 (2022)

**Nonlinear Convective  $\text{SiO}_2$  and  $\text{TiO}_2$  Hybrid Nanofluid Flow over an Inclined Stretched Surface**

Shrish, Said Anwar Shah, Abir Mouldi, and Ndolane Sene 




Research Article (11 pages), Article ID 6237698, Volume 2022 (2022)

**Analytical Assessment of MHD Flow of Nanoliquid Subject to Thermal Radiation and Brownian Effect**

Haroon Ur Rasheed , Ebenezer Bonyah , Soumaya Gouadria, Waris Khan , Ahmed Alshehri , and Raees Khan






Research Article (13 pages), Article ID 2680489, Volume 2022 (2022)

**Rheological Model for Generalized Energy and Mass Transfer through Hybrid Nanofluid Flow Comprised of Magnetized Cobalt Ferrite Nanoparticles**

Fahad S. Al-Mubaddel, F. M. Allehiany, Taher A. Nofal, Mohammad Mahtab Alam , Aatif Ali , and Joshua Kiddy K. Asamoah 

Research Article (11 pages), Article ID 7120982, Volume 2022 (2022)

**New Iterative Method for Solving a Coupled System of Fractional-Order Drinfeld–Sokolov–Wilson (FDSW) and Fractional Shallow Water (FSW) Equations**


Nasir Ali , Mansour F. Yassen, Saeed Ahmed Asiri , Rashid Nawaz , Laiq Zada, Mohammad Mahtab Alam , and Ndolane Sene 

Research Article (13 pages), Article ID 8370107, Volume 2022 (2022)





## Contents

### **Fractional Analysis of Dissipative Viscous Fluid Flow with Mixed Convection and Variable Viscosity**

Abir Mouldi, Riadh Marzouki, Mohamed Hechmi El Ouni, and Abdul Bariq 

Research Article (14 pages), Article ID 4848864, Volume 2022 (2022)

### **Impact of Ferromagnetic Nanoparticles Submerged in Chemically Reactive Viscoelastic Fluid Transport Influenced by Double Magnetic Dipole**

N. Kousar , Taher A. Nofal, W. Tahir, S. M. Bilal, and Ndolane Sene 

Research Article (12 pages), Article ID 2558419, Volume 2022 (2022)

### **Analytical and Numerical Analysis of the Squeezed Unsteady MHD Nanofluid Flow in the Presence of Thermal Radiation**

Hakeem Ullah , Muhammad Arif Khan, Mehreen Fiza, Kashif Ullah, Muhammad Ayaz, and Seham M. Al-Mekhlafi 





Research Article (14 pages), Article ID 1668206, Volume 2022 (2022)

### **Analytical Approximate Solution of the Fractional Order Biological Population Model by Using Natural Transform**

Nasir Ali, Rashid Nawaz , Laiq Zada , Abir Mouldi, Souhail Mohamed Bouzgarrou, and Ndolane Sene 

Research Article (12 pages), Article ID 6703086, Volume 2022 (2022)

### **Evaluating the Higher-Order Slip Consequence in Bioconvection Nanofluid Flow Configured by a Variable Thick Surface of Disk**

Hassan Waqas , Sumeira Yasmin, Nesreen Althobaiti, Ebenezer Bonyah , Ahmed Alshehri , and Zahir Shah 


Research Article (13 pages), Article ID 2766317, Volume 2022 (2022)

### **Numerical Investigation of Fractional-Order Kawahara and Modified Kawahara Equations by a Semianalytical Method**

Weaam Alhejaili, Sharifah E. Alhazmi, Rashid Nawaz , Aatif Ali , Joshua Kiddy Kwasi Asamoah , and Laiq Zada

Research Article (9 pages), Article ID 1985572, Volume 2022 (2022)

### **Heat and Mass Transfer of the Darcy-Forchheimer Casson Hybrid Nanofluid Flow due to an Extending Curved Surface**

Gohar, Tahir Saeed Khan, Ndolane Sene , Abir Mouldi, and Ameni Brahmia

Research Article (12 pages), Article ID 3979168, Volume 2022 (2022)

### **Numerical Study of the Flow of Two Radiative Nanofluids with Marangoni Convection Embedded in Porous Medium**

Ravi Gupta , Manish Gaur , Qasem Al-Mdallal , Sunil Dutt Purohit , and Daya Lal Suthar 



Research Article (7 pages), Article ID 7880488, Volume 2022 (2022)

**Thermal Transport in Radiative Nanofluids by Considering the Influence of Convective Heat Condition**

Adnan , Waqas Ashraf, Abdulaziz H. Alghtani, Ilyas Khan , and M. Andualem 


Research Article (11 pages), Article ID 1854381, Volume 2022 (2022)

**Theoretical Analysis of Cu-H<sub>2</sub>O, Al<sub>2</sub>O<sub>3</sub>-H<sub>2</sub>O, and TiO<sub>2</sub>-H<sub>2</sub>O Nanofluid Flow Past a Rotating Disk with Velocity Slip and Convective Conditions**

Abdullah Dawar, Ebenezer Bonyah , Saeed Islam , Ahmed Alshehri, and Zahir Shah

Research Article (10 pages), Article ID 5471813, Volume 2021 (2021)

**Couple Stress Hybrid Nanofluid Flow through a Converging-Diverging Channel**

Malik Zaka Ullah, Dina Abuzaid, M. Asma, and Abdul Bariq 

Research Article (13 pages), Article ID 2355258, Volume 2021 (2021)

**Numerical Investigation of Chemical Schnakenberg Mathematical Model**

Faiz Muhammad Khan, Amjad Ali, Nawaf Hamadneh , Abdullah, and Md Nur Alam 

Research Article (8 pages), Article ID 9152972, Volume 2021 (2021)

**Impact of Ramped Concentration and Temperature on MHD Casson Nanofluid Flow through a Vertical Channel**

Kashif Sadiq, Imran Siddique , Rifaqat Ali , and Fahd Jarad 

Research Article (17 pages), Article ID 3743876, Volume 2021 (2021)

## *Retraction*

# **Retracted: The Mathematical Analysis of the New Fractional Order Ebola Model**

### **Journal of Nanomaterials**

Received 20 June 2023; Accepted 20 June 2023; Published 21 June 2023

Copyright © 2023 Journal of Nanomaterials. This is an open access article distributed under the Creative Commons Attribution License, which permits unrestricted use, distribution, and reproduction in any medium, provided the original work is properly cited.

This article has been retracted by Hindawi following an investigation undertaken by the publisher [1]. This investigation has uncovered evidence of one or more of the following indicators of systematic manipulation of the publication process:

1. Discrepancies in scope
2. Discrepancies in the description of the research reported
3. Discrepancies between the availability of data and the research described
4. Inappropriate citations
5. Incoherent, meaningless and/or irrelevant content included in the article
6. Peer-review manipulation

The presence of these indicators undermines our confidence in the integrity of the article's content and we cannot, therefore, vouch for its reliability. Please note that this notice is intended solely to alert readers that the content of this article is unreliable. We have not investigated whether authors were aware of or involved in the systematic manipulation of the publication process.

Wiley and Hindawi regrets that the usual quality checks did not identify these issues before publication and have since put additional measures in place to safeguard research integrity.

We wish to credit our own Research Integrity and Research Publishing teams and anonymous and named external researchers and research integrity experts for contributing to this investigation.

The corresponding author, as the representative of all authors, has been given the opportunity to register their agreement or disagreement to this retraction. We have kept a record of any response received.

### **References**

- [1] F. M. Khan, A. Ali, E. Bonyah, and Z. U. Khan, "The Mathematical Analysis of the New Fractional Order Ebola Model," *Journal of Nanomaterials*, vol. 2022, Article ID 4912859, 12 pages, 2022.

## Corrigendum

# Corrigendum to “Thermal Transport in Radiative Nanofluids by Considering the Influence of Convective Heat Condition”

**Adnan <sup>1</sup>, Waqas Ashraf,<sup>2</sup> Abdulaziz H. Alghtani,<sup>3</sup> Ilyas Khan <sup>4</sup>, and M. Andualem <sup>5</sup>**

<sup>1</sup>Department of Mathematics, Mohi-ud-Din Islamic University, Nerian Sharif, AJ&K 12080, Pakistan

<sup>2</sup>Department of Applied Mathematics and Statistics (AM&S), Institute of Space Technology (IST), Islamabad 44000, Pakistan

<sup>3</sup>Mechanical Engineering Department at Taif University, P.O. Box 11099, Taif 21944, Saudi Arabia

<sup>4</sup>Department of Mathematics, College of Science Al-Zulfi, Majmaah University, Al-Majmaah 11952, Saudi Arabia

<sup>5</sup>Department of Mathematics, Bonga University, Bonga, Ethiopia

Correspondence should be addressed to Adnan; [adnan\\_abbasi89@yahoo.com](mailto:adnan_abbasi89@yahoo.com)  
and M. Andualem; [mulugetaandualem4@gmail.com](mailto:mulugetaandualem4@gmail.com)

Received 9 August 2022; Accepted 9 August 2022; Published 4 April 2023

Copyright © 2023 Adnan et al. This is an open access article distributed under the Creative Commons Attribution License, which permits unrestricted use, distribution, and reproduction in any medium, provided the original work is properly cited.

In the article titled “Thermal Transport in Radiative Nanofluids by Considering the Influence of Convective Heat Condition” [1], the authors want to add the acknowledgement statement as follows: “The research was supported by the Taif University Researchers Supporting Project number (TURSP-2020/349), Taif University, Taif, Saudi Arabia.”

## References

- [1] Adnan, W. Ashraf, A. H. Alghtani, I. Khan, and M. Andualem, “Thermal Transport in Radiative Nanofluids by Considering the Influence of Convective Heat Condition,” *Journal of Nanomaterials*, vol. 2022, Article ID 1854381, 11 pages, 2022.

## Research Article

# Effect of Joule Heating and Thermal Radiation of MHD Boundary Layer Oldroyd-B Nanofluid Flow with Heat Transfer over a Porous Stretching Sheet by Finite Element Method

Hakeem Ullah <sup>1</sup>, Mehreen Fiza <sup>1</sup>, Kamal Khan,<sup>1</sup> Shamaila Batool,<sup>2</sup> S. M. Ghufuran,<sup>1</sup> and Seham M. Al-Mekhlafi <sup>3</sup>

<sup>1</sup>Department of Mathematics, Abdul Wali Khan University, Mardan, Khyber Pakhtunkhwa, Pakistan 23200

<sup>2</sup>Institute of Numerical Sciences, Kohat University of Science and Technology, Kohat, Pakistan

<sup>3</sup>Department of Mathematics, Sana'a University, Yemen

Correspondence should be addressed to Seham M. Al-Mekhlafi; [smdk100@gmail.com](mailto:smdk100@gmail.com)

Received 11 January 2022; Revised 21 August 2022; Accepted 7 September 2022; Published 3 October 2022

Academic Editor: Taza Gul

Copyright © 2022 Hakeem Ullah et al. This is an open access article distributed under the Creative Commons Attribution License, which permits unrestricted use, distribution, and reproduction in any medium, provided the original work is properly cited.

In this study, an incompressible two-dimensional Oldroyd-B nanofluid steady flow past a stretching sheet considering the outcomes of magneto-hydrodynamics (MHD) and porous medium with magnetic, electrical, and thermal radiation effects is investigated. Using a similarity transformation, the governing equations in the form of partial differential equations (PDEs) are converted into a nonlinear ordinary differential equations (ODEs) system. The acquired system is numerically solved by the finite element method (FEM). The effects of physical parameters like Deborah numbers " $\beta_1$ " and " $\beta_2$ ", Brownian motion " $N_b$ ", thermophoresis parameter " $N_t$ ", Prandtl parameter "Pr", Lewis number " $L_e$ ", thermal conductivity " $k$ ", dynamic viscosity " $\mu$ ", magnetic and electric effects as " $M$ " and " $E_1$ ", and thermal radiation effect "Rd" on the flow are studied in detail. For higher  $N_b$  values, regional Nusselt numbers are increasing in magnitude. The local Sherwood number's size rises for high  $N_b$  numbers.

## 1. Introduction

The fluid which obeys the Newton's law of viscosity is known as the Newtonian fluid, whereas the non-Newtonian fluid is recognized as to be the satisfaction of the Newton's law of viscosity [1, 2]. The non-Newtonian fluid dragged the attraction of the researchers due to its significant applications in industrial and engineering such as mud drilling, plastic polymers, optical fiber, metal cooling and wire of polymer plates, damping agent in braking devices, and protective devices [3–5]. Sakiadis introduced the concept of flow due to a stretching sheet [6]. Scientists used this concept to develop the new results to various fluids [7–19]. Magyar and Keller extended this concept by using it as the exponential stretching sheet [20]. The boundary layer flow (BLF) of an incompressible fluid over a stretching sheet and the viscoelastic fluids is used commonly in engineering and industrial developments. The field has attracted

researchers in the last few decades. In industries, BLF is used like wrapping thermal, cooling plates, condensation of thin film, fiber glass, heat exchangers, plastic processing, cosmetics, geology composites, paint flow, adhesives, tower generators, accelerators, electrostatic filters, and droplet filters [3, 4, 5]. By immersing them in quiescent liquids, many metal processes need to cool continuously such as fibers. The BLF is used by many scientists. The BLF based on the exponential stretching is studied by Bidin and Nazar who study the BLF due to exponential stretching sheet with thermal radiations [21]. This experiment is further extended with the partial slip effect by Mukhopadhyay and Gorla [22]. Singh and Agarwal [23] study the thermal radiation effect of the boundary layer flow with exponential stretching. The BLF and heat transfer HT over a moving surface are studied by Tsou et al. and Elbashareshy [24, 25]. Choi proposed the concept of nanofluid in 1995 [26]. The nanofluid has many industrial and engineering applications like heat

exchangers, engine radiators, and cooling processes [27, 28]. Khan et al. [29, 30] investigated the BLF of a nanofluid in a porous material. The thermal effect of the nanofluid flow of the boundary layer on the moving surface in various conditions was presented by Olanrewaju et al. [31], Crane [7], Koo and Kleinstreuer [32], and Khan et al. [29, 33]. The porous material containing the pores and the skeletal portion of the material is known as a matrix. The pores are filled by a fluid under consideration. Fiza et al. studied the nanofluid flows in a porous medium with viscoelastic properties [34]. The recent development in the study of nanofluid by considering various physical effects can be seen in [29, 33–59]. From the literature survey, it is clear that the effect of Joule heating and thermal radiation of MHD boundary layer Oldroyd-B nanofluid flow with heat transfer over a porous stretching sheet is not studied. This article is aimed at studying the effect of Joule heating and thermal radiation of MHD boundary layer Oldroyd-B nanofluid flow with heat transfer over a porous stretching sheet by a numerical computation method known as finite element method (FEM). The basic fundamental equations Navier-Stokes equations and continuity are used for the mathematical formulations. After using the similarity transformation, the formulation in the form of PDEs is converted into ODEs. The FEM is used for the solution of the modeled problem [60–63]. The physical parameters are discussed with the help of graphs and tables. Organisation of the paper is as follows: Section 1 is dedicated to introduction, Section 2 to problem formulation, Section 3 to solution techniques, Section 4 to results and discussions, and Section 5 to conclusions.

## 2. Problem Formulation [57]

Consider the nanofluid motion of an incompressible two-dimensional Oldroyd-B across a stretching sheet. Nanoparticles are saturated when the sheet is stretched at  $y = 0$ , and the flow is originated at  $y > 0$ . The fluid is electrically conducted in the existence of magnetic field  $\vec{B} = (0, B_0, 0)$  and electric field  $\vec{E} = (0, 0, -E_0)$  which follow the Ohm's law  $\vec{J} = \sigma(\vec{E} + \vec{V} \times \vec{B})$ . The sheet is stretched linearly  $u(x) = ax$ , where " $a > 0$ " and the sheet is considered as porous. The sheet velocity is taken parallel to the flow. The induced magnetic field and Hall current effects are disregarded due to the minute magnetic field. The governing equations are as follows:

$$\begin{aligned} u_x + v_y &= 0, \\ uu_x + vv_y + A_1(u^2u_{xx} + v^2u_{yy} + 2uvu_{xy}) \\ &= v(u_{yy} + A_2uu_{xyy} + vu_{yyy} - u_xu_{yy} - u_yv_{yy}) \\ &\quad + \frac{\sigma}{\rho}(E_0B_0 - B_0^2u) - \frac{v}{k}u, \\ uF_x + vF_y &= \alpha(F_{xx} + F_{yy}) + \tau\{D_B(C_xF_x + C_yF_y) \\ &\quad + \left(\frac{D_t}{F_\infty}\right)[(F_x)^2 + (F_y)^2] + \frac{\sigma}{\rho}(uB_0 - E_0)^2 - \frac{\partial q_r}{\partial y}, \\ uC_x + vC_y &= D_B(C_{xx} + C_{yy}) \\ &\quad + \left(\frac{D_F}{F_\infty}\right)(F_{xx} + F_{yy}) \cdot D_B(C_{xx} + C_{yy}) + \left(\frac{D_F}{F_\infty}\right)(F_{xx} + F_{yy}). \end{aligned} \quad (1)$$

Here  $u, v$  represent the velocity components, fluid density  $\rho$ , kinematic viscosity  $\nu$ , electrical conductivity  $\sigma$ ,  $A_1/A_2$  the relaxation/retardation parameters, the thermal diffusivity  $\alpha$ , the temperature  $T$ , the concentration  $C$ ,  $D_B$  the Brownian diffusions,  $D_T$  the thermophoretic diffusion coefficient, and  $\tau = (\rho c)_p/(\rho c)_f$  the nanoparticle to fluid heat capacity.  $\rho_p$  represents the density of the particle,  $\vec{J}$  is the Joule current,  $\sigma$  is the electrical conductivity, and  $\vec{V}$  is the velocity field of the flow. If  $Y \rightarrow \infty$ , then the values of  $F$  and  $C$  are, respectively,  $F_\infty$  and  $C_\infty$  as shown in Figure 1.

$q_r$  represents the radioactive heat fluctuation that is proposed by Rosseland approximation like as follows:

$$q_r = -\frac{16\varphi}{3K} \frac{\partial T^4}{\partial y}, \quad (2)$$

where  $K$  represents the mean absorption coefficient and  $\varphi$  denotes the Stefan Boltzmann constant. By Taylor series equation, we obtain the following:

$$T^4 = T_0^4 + 4T_0^3(T - T_0)^2 + \dots \quad (3)$$

On ignoring higher-order terms, we have the following:

$$T^4 = 4TT_0^3 - 3T_0^4. \quad (4)$$

Inserting Equation (10) in Equation (8), it reduced to the form of the following:

$$\frac{\partial q_r}{\partial y} = -\frac{16T_C^3\varphi}{3K} \frac{\partial^2 T}{\partial y^2}. \quad (5)$$

The boundary conditions are as follows:

$$\begin{aligned} u(x) &= ax, v = 0, C = C_0, F = F_0, y \rightarrow 0, \\ u(\infty) &= 0, v(\infty) = 0, C = C_\infty, F = F_\infty, y \rightarrow \infty. \end{aligned} \quad (6)$$

Using the similarity transformation,

$$\begin{aligned} \psi &= (av)^{1/2}x F(\eta), \\ \theta(\eta) &= \frac{F - F_\infty}{F_w - F_\infty}, \\ \phi(\eta) &= \frac{C - C_\infty}{C_w - C_\infty}, \\ \eta &= \sqrt{\frac{a}{\nu}}y. \end{aligned} \quad (7)$$

Using the stream function as  $u = \partial\psi/\partial y$  and  $v = -\partial\psi/\partial x$ , we get the following:

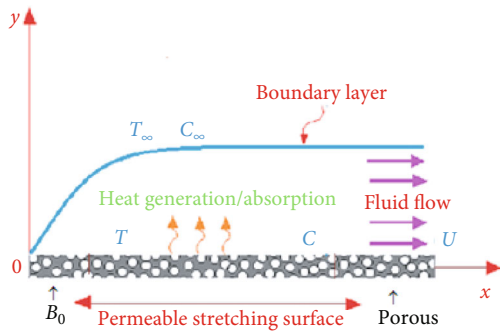


FIGURE 1: Schematic diagram of the flow.

$$f''' - f'^2 + ff'' + \beta_1 (f^2 f''' - 2ff'f'') + \beta_2 (ff'''' - (f'')^2) + M^2 (E_1 - f') - \kappa (f') = 0, \quad (8)$$

$$\left(1 + \frac{4}{5} \text{Rd}\right) \theta'' + \text{Pr} \left( \theta \theta' + N_b (\theta' \phi') + N_t (\theta')^2 \right) + M^2 \text{Pr} (f' - E_1)^2 = 0, \quad (9)$$

$$\phi'' + L_e \text{Pr} (f \phi') + \frac{N_t}{N_b} \theta'' = 0, \quad (10)$$

with

$$f(0) = 0, f'(0) = 1, f'(\infty) = 0, f''(\infty) = 0, \quad (11)$$

$$\theta(0) = 1, \theta(\infty) = 0, \quad (12)$$

$$\phi(0) = 1, \phi(\infty) = 0, \quad (13)$$

where  $\beta_1 = aA_1$ ,  $\beta_2 = aA_2$  are the Deborah numbers,  $\text{Pr} = \nu/\alpha$ , is the Prandtl number,  $N_b = (\rho c)_p D_B (C_w - C_\infty) / \nu (\rho c)_p$  and  $N_t = (\rho c)_p D_T (T_w - T_\infty) / \nu (\rho c)_p$  are the Brownian and thermophoresis parameters, respectively, and  $L_e = \alpha/D_B$  is the Lewis number.

Also,

$$\text{Nu}_x = \frac{xq_w}{\alpha(T_w - T_\infty)}, \quad (14)$$

$$\text{Sh}_x = \frac{xq_m}{D_B(C_w - C_\infty)}, \quad (15)$$

where  $q_w = -\alpha(\partial T/\partial y)_{y=0}$ ,  $q_m = -D_B(\partial C/\partial y)_{y=0}$  are the heat and mass flux, respectively.

The dimensionless form of Equation (14) is given as follows:

$$\begin{aligned} \text{Re}_x^{-1/2} \text{Nu}_x &= -\theta'(0), \\ \text{Re}_x^{-1/2} \text{Sh}_x &= -\phi'(0), \end{aligned} \quad (16)$$

where  $\text{Re}_x = u_w(x)x/\nu$  is the Reynolds local,  $\kappa = \nu/k$  is the porosity parameter,  $M^2 = \sigma B_0^2/\rho a$  is the magnetic variable, and the electric parameter is  $E_1 = E_0/B_0 a x$ .

### 3. Finite Element Method

The FEM is a powerful method to evaluate the nonlinear differential equations and can be used to engineering problems such as fluid mechanics, biomathematics, physics, and channel process [49–51].

The important steps of FEM are as follows:

- (1) Discretization into finite elements of the infinite domain
- (2) Generation of component equations
- (3) Gathering component equations
- (4) Imposing boundary conditions
- (5) Evaluation of gathered equations

Iterative approach can be applied in the last step.

A grid sophistication experiment is performed via dividing the domain in consecutive grids sized  $81 \times 81$ ,  $101 \times 101$  and  $121 \times 121$  in  $z$  direction. Four functions are to be assessed at each node, and assembly of element equations, we get 404 nonlinear equations. An iterative scheme is acquired for solving the system introduced by BCs. If the relative difference among the sequential iteration is fewer than  $10^{-6}$ , so the solution is considered as convergent. The code is run for various grid sizes and observed that the solution is free of the grid. The effect of the step size for step  $h = 0.01$  is verified by achieving an excellent agreement for different profiles.

### 4. Results and Discussion

**4.1. Figures Discussions.** The nonlinear system of ODEs (Equations (8)–(13)) constrained by boundary conditions (Equations (11)–(13)) is assessed numerically by FEM. Figures 2–22 describe the actions of emerging parameters like Prandtl parameter  $\text{Pr}$ , relaxation time constant  $\beta_1$ , retardation time constant  $\beta_2$ , Brownian parameter  $N_b$ , Lewis number  $L_e$ , thermophoresis parameter  $N_t$ , and porosity parameter  $\kappa$  on velocity profile  $f'(\eta)$ , mass fraction function  $\phi(\eta)$ , and temperature profile  $\theta(\eta)$ . Figures 2–4 represent the effect of  $\beta_1$  on  $f'(\eta)$ ,  $\theta(\eta)$ , and  $\phi(\eta)$ .  $\beta_1$  which is a function of relaxation time  $A_1$  assists the flow due to the viscoelastic characteristics of fluids. The BL thickness and the velocity profile  $f'(\eta)$  increased by increasing the values of  $\beta_1$ . Also by the increase of  $\beta_1$ , both  $\theta(\eta)$  and  $\phi(\eta)$  of the mass fraction increase. The effects of  $\beta_2$  on  $f'(\eta)$ ,  $\theta(\eta)$ , and  $\phi(\eta)$  are given in Figures 5–7. Since the retardation time of the fluid increases the fluid movement, so as a result,  $f'(\eta)$ ,  $\theta(\eta)$ , and  $\phi(\eta)$  increases by increasing  $\beta_2$ . The effect of the porosity number for the velocity profile is given in Figure 8. It is noticed that by increasing the porosity parameter, the velocity profile decreases. Since in the porous medium, there exist

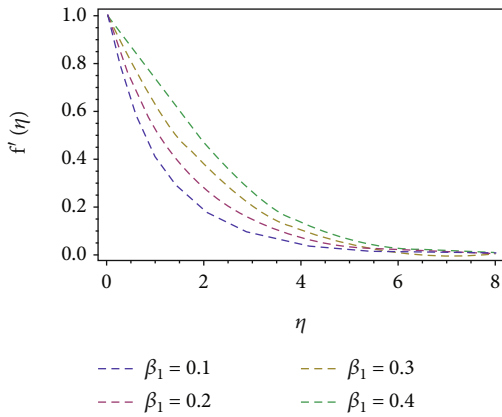


FIGURE 2:  $f'(\eta)$  versus  $\beta_1$ .

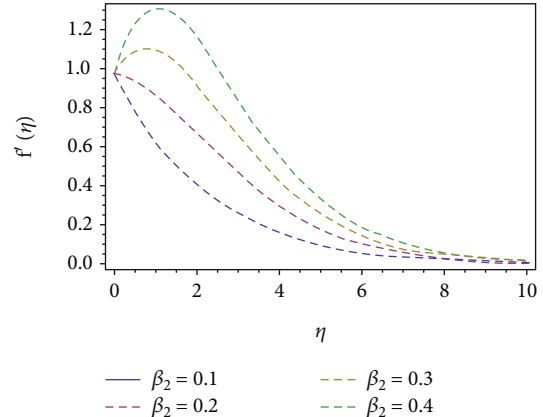


FIGURE 5:  $f'(\eta)$  versus  $\beta_2$ .

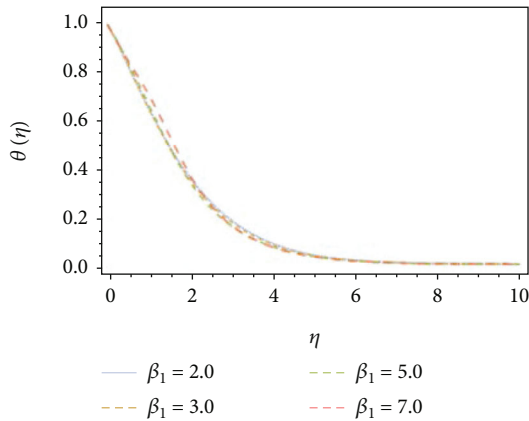


FIGURE 3:  $\theta(\eta)$  versus  $\beta_1$ .

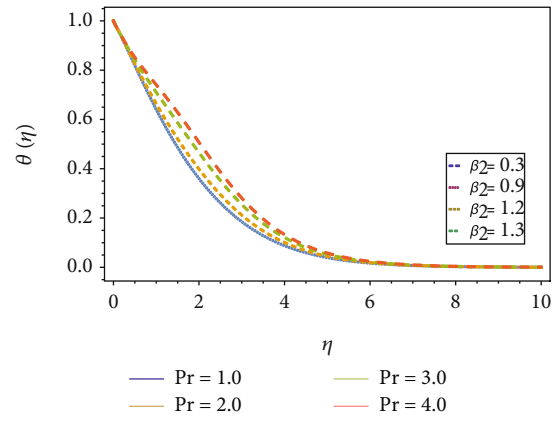


FIGURE 6:  $\theta(\eta)$  versus  $\beta_2$ .

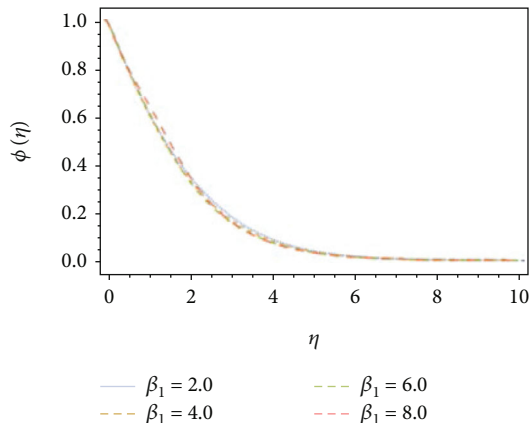


FIGURE 4:  $\phi(\eta)$  versus  $\beta_1$ .

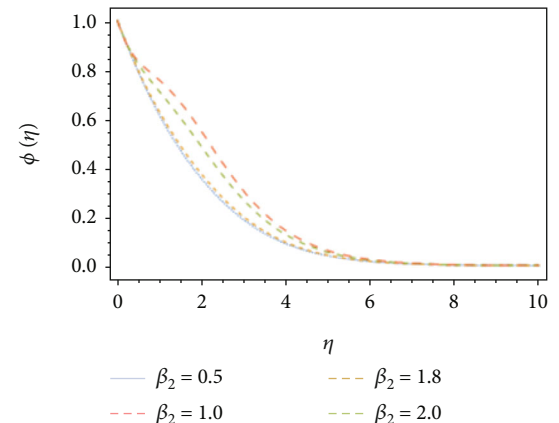


FIGURE 7:  $\phi(\eta)$  versus  $\beta_2$ .

the porous holes and these holes reduce the velocity profile. The Lewis numbers are plotted for the temperature and concentrations profiles in Figures 9 and 10. An increase in the Lewis value caused to increase  $\theta(\eta)$  and  $\phi(\eta)$ . The impacts on mass fraction function  $\phi(\eta)$  of Brownian motion and

temperature profile  $\theta(\eta)$  and thermophoresis parameters are displayed in Figures 11, 12, 13, and 14, respectively. By increasing the values of  $N_b$ , the temperature profile increases while the concentration profile first decreases near the boundary and then increases as can be seen in Figures 11



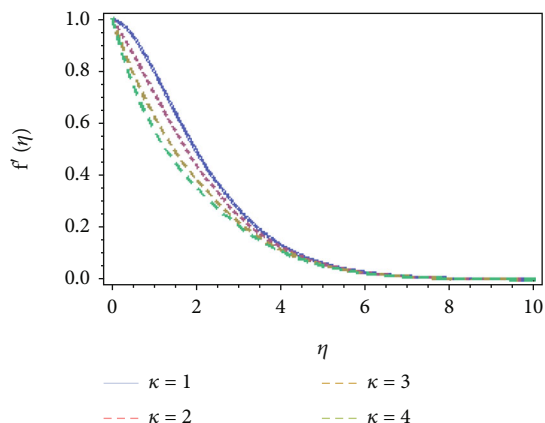


FIGURE 8:  $f'(\eta)$  versus  $k$ .

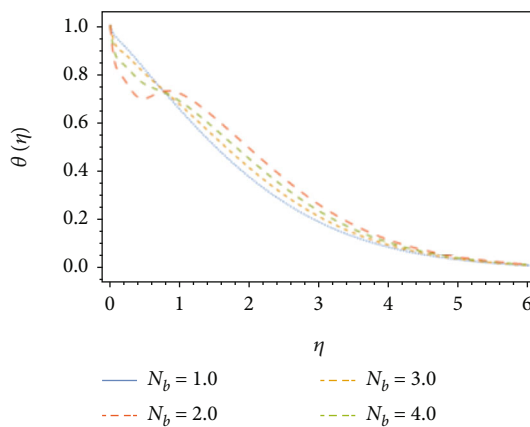


FIGURE 11:  $f'(\eta)$  versus  $N_b$ .

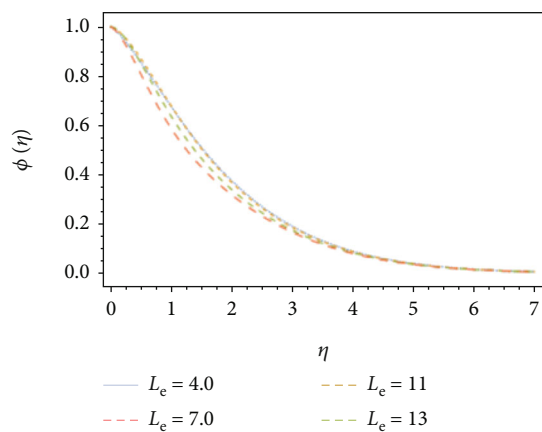


FIGURE 9:  $\theta(\eta)$  versus  $L_e$ .

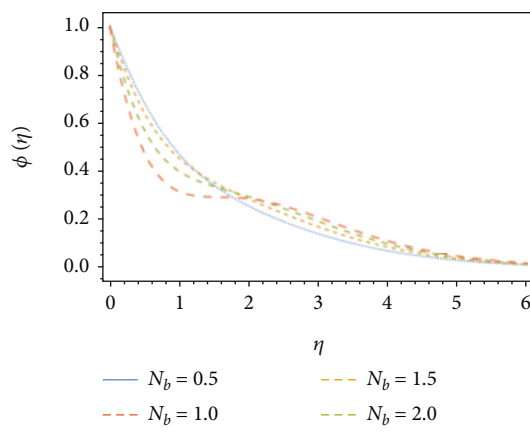


FIGURE 12:  $\phi(\eta)$  versus  $N_b$ .

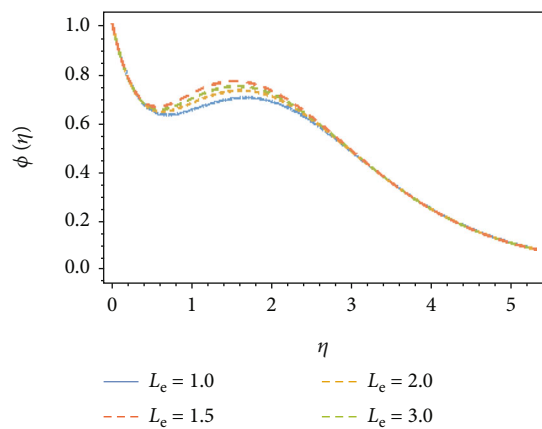


FIGURE 10:  $\phi(\eta)$  versus  $L_e$ .

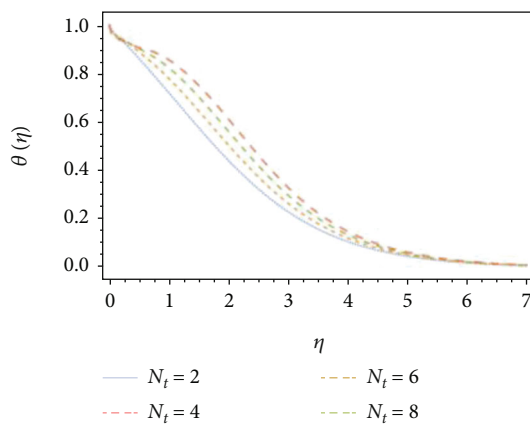


FIGURE 13:  $\theta(\eta)$  versus  $N_t$ .

and 12; for the effect of  $N_t$ , it is noticed that by uplifting  $N_t$ , the temperature profile increases while the concentration profiles decrease can be seen in Figures 13 and 14. The effects of the Prandtl number on the temperature and concentration profiles are presented in Figures 15 and 16.

Higher values of Prandtl numbers caused to decrease the temperature and concentration profiles. It is due to the fact that the Pr has an inverse relation with  $\alpha$ , increasing Pr is basically to reduce the value of  $\alpha$  which turn to reduce the elastic collision of the nanoparticles caused to reduce the

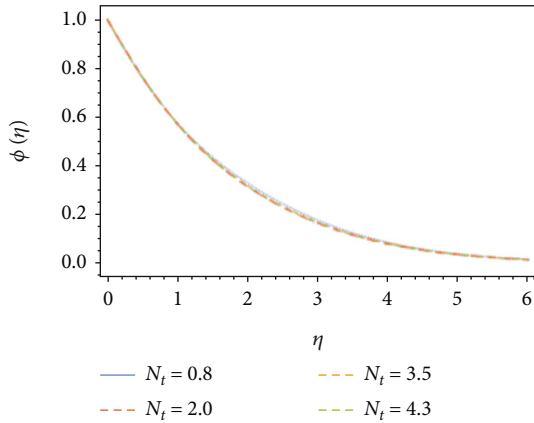


FIGURE 14:  $\phi(\eta)$  versus  $N_t$ .

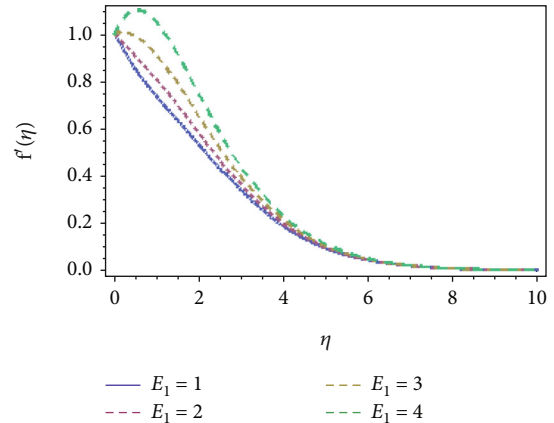


FIGURE 17:  $f'(\eta)$  versus  $E_1$ .

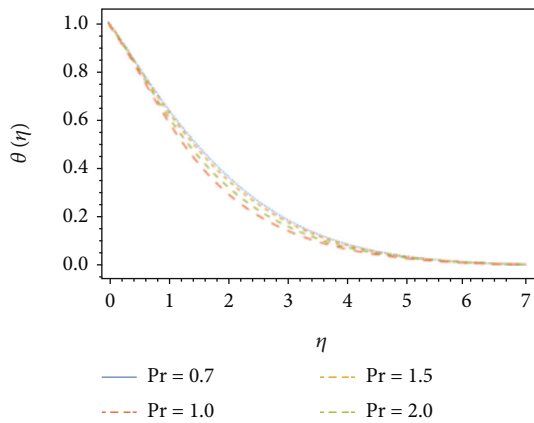


FIGURE 15:  $\theta(\eta)$  versus Pr.

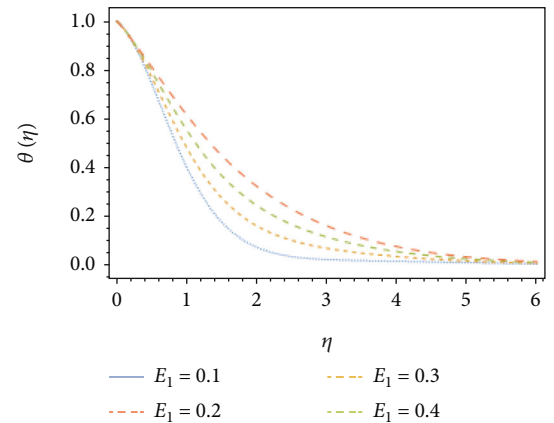


FIGURE 18:  $\theta(\eta)$  versus  $E_1$ .

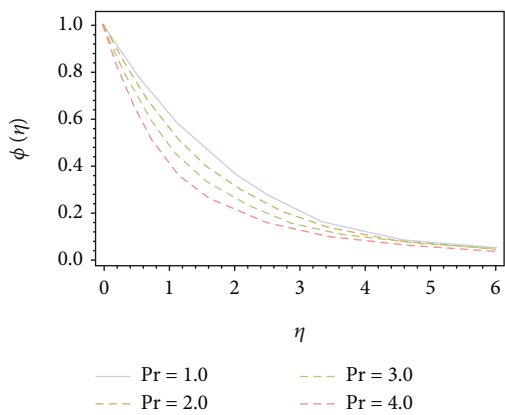


FIGURE 16:  $\phi(\eta)$  versus Pr.

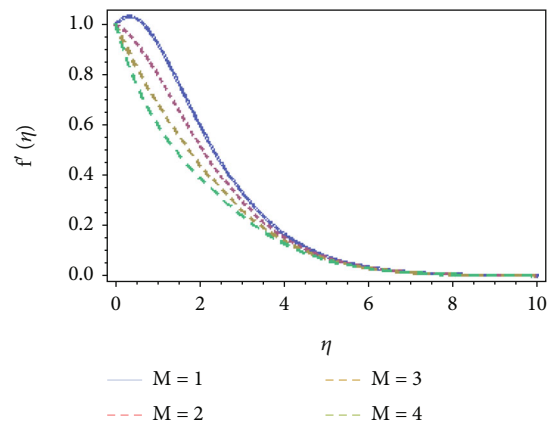


FIGURE 19:  $f'(\eta)$  versus  $M$ .

profiles of concentration and temperature. The effects of the electric field  $E_1$  on the velocity and temperature profiles are given in Figures 17 and 18, respectively. Increase in  $E_1$  causes to increase the profiles of temperature and velocity. Also, the effects of the magnetic field on velocity and tem-

perature profiles are given in Figures 19 and 20. Increase in magnetic field causes to decrease the velocity profile, whereas by increasing the magnetic field decreases the temperature profile. The magnetic field is put in perpendicular to the flow and it resisted the flow; thus, the velocity profile

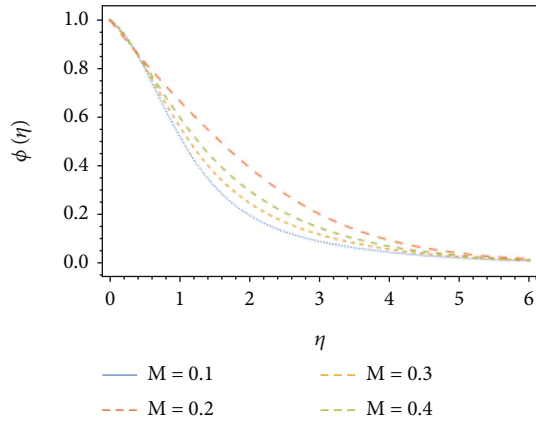


FIGURE 20:  $\theta(\eta)$  versus  $M$ .

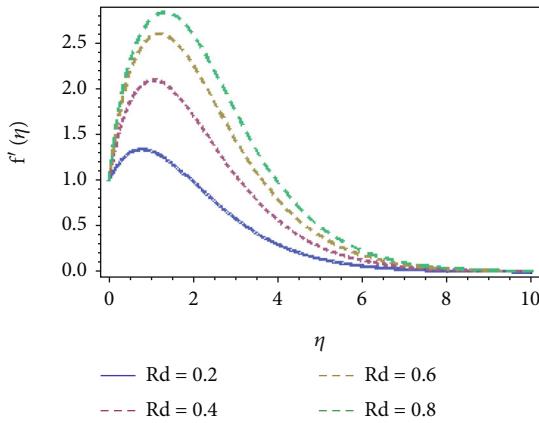


FIGURE 21:  $f'(\eta)$  versus  $Rd$ .

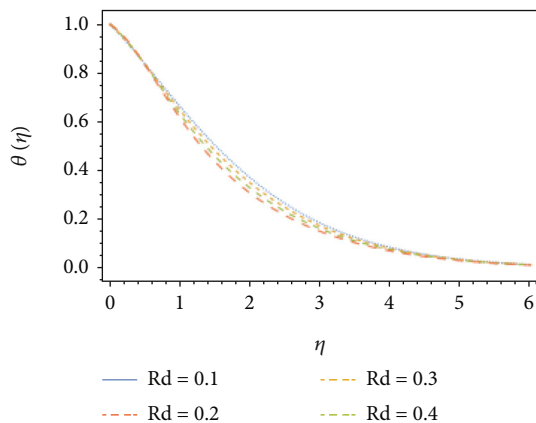


FIGURE 22:  $\theta(\eta)$  versus  $Rd$ .

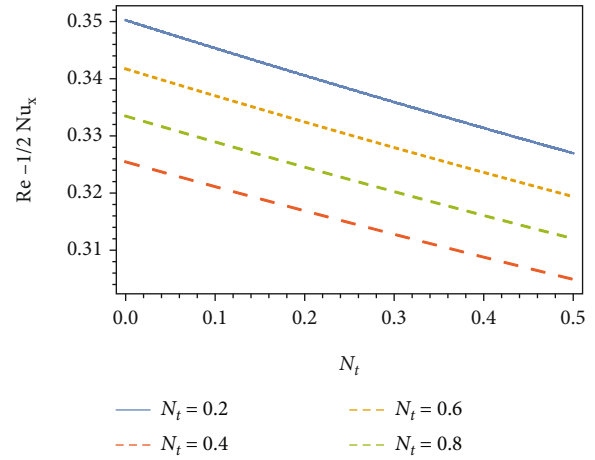


FIGURE 23: Nusselt number versus  $N_t$ .

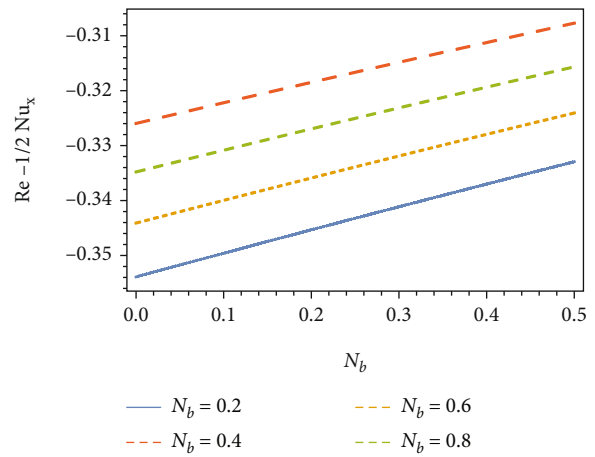


FIGURE 24: Nusselt number versus  $N_b$ .

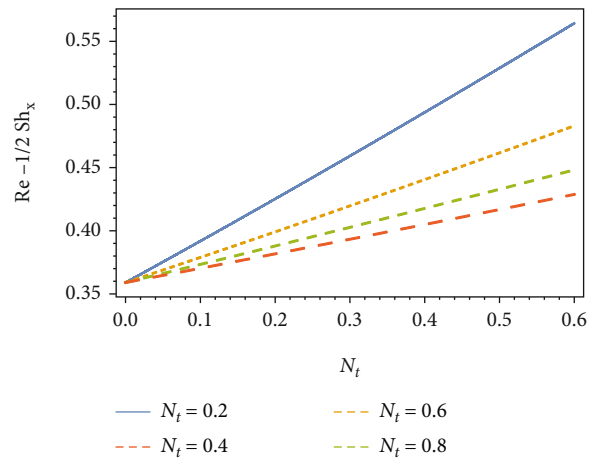


FIGURE 25: Sherwood number versus  $N_t$ .

reduced. The effect of the thermal radiations on the velocity and temperature field is given in Figures 21 and 22. Increase in thermal radiation caused to increase/decrease the velocity and temperature profiles. Results on the Sherwood number

of the Brownian parameter, the Nusselt number, and thermophoresis parameter are given in Figures 23–26. It is noticed that the Nusselt number falls by rising  $N_t$ , whereas

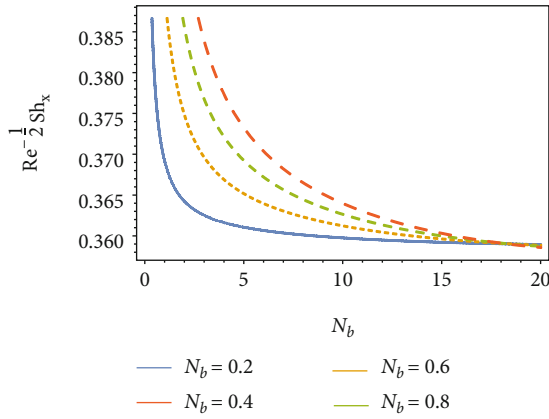


FIGURE 26: Sherwood number versus  $N_b$ .

TABLE 1: Numerical values of the local Nusselt number  $Re^{-1/2}Nu_x$ .

$N_b/N_t$	0.2	0.4	0.6	0.8
0.1	0.345332	0.337005	0.328932	0.321109
0.2	0.340533	0.332416	0.324528	0.316885
0.3	0.335903	0.327949	0.320241	0.312776
0.4	0.331372	0.323636	0.316071	0.308779
0.5	0.326962	0.319368	0.312013	0.304892

TABLE 2: Numerical values of the local Nusselt number  $Re^{-1/2}Nu_x$ .

$N_t/N_b$	0.2	0.4	0.6	0.8
0.1	-0.344720	-0.335351	-0.326466	-0.318049
0.2	-0.340555	-0.331372	-0.322668	-0.314424
0.3	-0.336454	-0.327456	-0.318931	-0.310857
0.4	-0.332416	-0.323620	-0.315252	-0.307347
0.5	-0.328441	-0.319805	-0.311629	-0.303894

TABLE 3: Numerical values of the Sherwood number  $Re^{-1/2}Sh_x$ .

$N_b/N_t$	0.2	0.4	0.6	0.8
0.1	0.555100	0.759519	0.970036	1.186100
0.2	0.457804	0.560222	0.665774	0.773986
0.3	0.425221	0.493763	0.564315	0.636564
0.4	0.408919	0.460513	0.513555	0.567815
0.5	0.399130	0.440547	0.483077	0.526535

the Nusselt number rises by rising  $N_b$  as given in Figures 23 and 24. The effects of  $N_t$  and  $N_b$  on the Sherwood number are given in Figures 25 and 26.

4.2. *Tables Discussions.* In Tables 1–4, an increase in  $N_t$  caused to reduce the Sherwood numbers and an increase

TABLE 4: Numerical values of the Sherwood number  $Re^{-1/2}Sh_x$ .

$N_t/N_b$	0.2	0.4	0.6	0.8
0.1	0.407924	0.383741	0.375666	0.359017
0.2	0.457804	0.408919	0.392597	0.371618
0.3	0.5085591	0.434520	0.409789	0.384416
0.4	0.560222	0.460513	0.427223	0.410539
0.5	0.612637	0.486868	0.444879	0.423837

TABLE 5: Comparison of local Nusselt results in the absence of non-Newtonian and nanoparticle parameters.

Re	Wang [64]	Present
0.7	0.4539	0.4539
2	0.9114	0.9114
7	1.8954	1.8954
20	3.3539	3.3539
70	6.4622	6.4622

in  $N_b$  caused to rise the Sherwood number. The Nusselt number decreases whenever the  $Pr$  is less than  $L_e$  and increases when the  $Pr$  is greater than  $L_e$  for  $N_b$  and  $N_t$ . However, the Sherwood number decreases with the rise of  $N_b$  and  $N_t$  for both the cases when the  $Pr$  is greater or less than  $L_e$ . Lastly, low thermal conductivity is caused by a high Prandtl fluid which decreases conductivity, resulting in an increase in sheet surface heat transfer. In the absence of non-Newtonian parameters  $\beta_1$  and  $\beta_2$ , it is observed that the effect of both temperature and concentration profiles of nanoparticles brings the falling action. Consequently, as  $Pr$  grows, the thickness of the boundary layer shrinks. Table 5 shows a comparison of our results to the results presented by Jawad and Saeed [58]. In the absence of the nanoparticles and non-Newtonian parameters, our results are identical to the Jawad and Saeed results. This comparison shows the accuracy and validity of our method.

## 5. Conclusion

The Oldroyd-B nanofluid model was presented across a stretched sheet for this investigation. The quantitative analysis of the impacts of thermophoresis parameter, elastic parameter, and Brownian motion on heat and flow transfer is studied here. Below are the key features of the study.

- (1) For the mass fraction, temperature, and speed functions,  $\beta_1$  and  $\beta_2$  impacts have the opposite behavior. Such anomalies arise only because of the influence of  $\beta_1$  and  $\beta_2$  viscoelastic parameters
- (2) Prandtl's actions are the same for both the temperature and mass fraction functions. As  $Pr$  is the link

among visual and dynamic viscosity, at greater Pr levels, the temperature profile remains under control

- (3) Similar effects of  $N_b$  and  $N_t$  are seen on the temperature profile as both  $N_b$  and  $N_t$  increase the temperature
- (4) For higher  $N_b$  values, regional Nusselt numbers are increasing in magnitude
- (5) The local Sherwood number's size rises for high  $N_b$  numbers
- (6) The electric field increasement increases the velocity and temperature profile, whereas the thermal radiation has reverse results
- (7) The increases in magnetic field resist the flow, and so the velocity profile get decreases while it assists the temperature profile
- (8) On increasing  $\beta$  and porosity parameters, the velocity distribution decreases
- (9) Increase in the Pr thermal boundary-layer thickness and contraction profiles is noticed to decrease
- (10) Increase in the Lewis number causes to decrease the profiles of velocity, temperature, and concentration

## Abbreviations

### Nomenclature

$\tilde{B}$ :	Magnetic field ( $\text{NmA}^{-1}$ )
$C$ :	Fluid concentration
$c_p$ :	Specific heat ( $\text{J/kgK}$ )
$\beta$ :	Non-Newtonian paramter
$\tilde{E}$ :	Electric field intensity ( $\text{NC}^{-1}$ )
$J_w$ :	Mass flux
$\alpha_1, \alpha_2, \beta_1, \beta_2, \beta_3$ :	Material constants
$A_1, A_2, A_3$ :	Kinematic tensors
$k$ :	Thermal conductivity ( $\text{Wm}^{-1}\text{K}^{-1}$ )
$M$ :	Magnetic parameter
$n_e$ :	Number density of electron
$O$ :	Origin
$P$ :	Fluid pressure (Pa)
Pr:	Prandtl number
$Q_w$ :	Heat flux ( $\text{Wm}^{-2}$ )
$q_r$ :	Radioactive heat flux (J)
Re:	Viscosity parameter
S:	Cauchy stress tensor
$t_e$ :	Flow time (s)
T:	Fluid temperature (K)
$u, v, w$ :	Velocity components ( $\text{ms}^{-1}$ )
$x, y, z$ :	Coordinates
$t$ :	Time.

### Greek Letters

$\alpha$ : Thermal diffusivity ( $\text{m}^2\text{s}^{-1}$ )

$\hat{\kappa}$ : Vertex viscosity (mPa)  
 $\mu$ : Dynamic viscosity (mPa)  
 $\nu$ : Kinematic coefficient of viscosity  
 $\rho_f$ : Base fluid density ( $\text{kgm}^{-3}$ )  
 $\rho_b$ : Density of the particles ( $\text{kgm}^{-3}$ ).

## Data Availability

The data is available in the paper.

## Conflicts of Interest

The authors declare that they have no conflicts of interest.

## References

- [1] M. C. Potter and D. C. Wiggert, *Schaum's outline of Fluid mechanics*, McGraw-Hill Education, 1996.
- [2] F. M. White, *Viscose Fluid Flow*, McGraw-Hill, Inc, 1992.
- [3] T. Altan, S. I. Oh, and G. Gegel, *Metal forming fundamentals and applications*, Metal Park: American Society of Metals, 1979.
- [4] E. G. Fisher, *Extrusion of Plastics*, Wiley, New York, 1976.
- [5] Z. Tadmor and I. Klein, *Engineering Principles of Plastic Ting Extrusion, Polymer Science and Engineering Series*, Van Nostrand Reinhold, New York, 1970.
- [6] B. C. Sakiadis, "Boundary-layer behavior on continuous solid surfaces: III. The boundary layer on a continuous cylindrical surface," *Journal of the Taiwan Institute of Chemical Engineers*, vol. 7, no. 3, pp. 467–472, 1961.
- [7] L. J. Crane, "Flow past a stretching plate," *Zeitschrift für Angewandte Mathematik und Physik*, vol. 21, no. 4, pp. 645–647, 1970.
- [8] P. S. Gupta and A. S. Gupta, "Heat and mass transfer on a stretching sheet with suction or blowing," *The Canadian journal of chemical engineering*, vol. 55, no. 6, pp. 744–746, 1977.
- [9] M. I. Char, "Heat transfer of a continuous, stretching surface with suction or blowing," *Journal of Mathematical Analysis and Applications*, vol. 135, no. 2, pp. 568–580, 1988.
- [10] M. Turkyilmazoglu and I. Pop, "Exact analytical solutions for the flow and heat transfer near the stagnation point on a stretching/shrinking sheet in a Jeffrey fluid," *International Journal of Heat and Mass Transfer*, vol. 57, no. 1, pp. 82–88, 2013.
- [11] S. Nadeem, S. Zaheer, and T. Fang, "Effects of thermal radiation on the boundary layer flow of a Jeffrey fluid over an exponentially stretching surface," *NumerAlgorith*, vol. 57, no. 2, article 187205, pp. 187–205, 2011.
- [12] T. Hayat, M. Awais, S. Asghar, and A. A. Hendi, "Analytic solution for the magnetohydrodynamic rotating flow of Jeffrey fluid in a channel," *Journal of fluids engineering*, vol. 133, no. 6, article 0612017, 2011.
- [13] M. Qasim, "Heat and mass transfer in a Jeffrey fluid over a stretching sheet with heat source/sink," *Alexandria Engineering Journal*, vol. 52, no. 4, pp. 571–575, 2013.
- [14] S. Nadeem, R. U. Haq, and Z. H. Khan, "Numerical solution of non-Newtonian nanofluid flow over a stretching sheet," *Applied Nanoscience*, vol. 4, no. 5, pp. 625–631, 2014.

- [15] T. Hayat, M. Awais, and S. Obaidat, "Three-dimensional flow of a Jeffrey fluid over a linearly stretching sheet," *Communications in Nonlinear Science and Numerical Simulation*, vol. 17, no. 2, pp. 699–707, 2012.
- [16] P. S. Narayana and D. H. Babu, "Numerical study of MHD heat and mass transfer of Jeffrey fluid over a stretching sheet with chemical reaction and thermal radiation," *Journal of the Taiwan Institute of Chemical Engineers*, vol. 59, p. 18, 2016.
- [17] P. V. S. Narayana, "Effects of variable permeability and radiation absorption on magnetohydrodynamic (MHD) mixed convective flow in a vertical wavy channel with traveling thermal waves," *Propulsion and Power Research*, vol. 4, no. 3, pp. 150–160, 2015.
- [18] P. S. Narayana, B. Venkateswarlu, and B. Devika, "Chemical reaction and heat source effects on MHD oscillatory flow in an irregular channel," *Ain Shams Engineering Journal*, vol. 7, no. 4, pp. 1079–1088, 2016.
- [19] B. Venkateswarlu and P. V. Narayana, "MHD visco-elastic fluid flow over a continuously moving vertical surface with chemical reaction," *Walailak Journal of Science and Technology (WJST)*, vol. 12, no. 9, pp. 775–783, 2015.
- [20] E. Magyari and B. Keller, "Heat and mass transfer in the boundary layers on an exponentially stretching continuous surface," *Journal of Physics D: Applied Physics*, vol. 32, no. 5, pp. 577–585, 1999.
- [21] B. Bidin and R. Nazar, "Numerical solution of boundary layer flow over an exponentially stretching sheet with thermal radiation," *European journal of scientific research*, vol. 33, pp. 710–717, 2009.
- [22] S. Mukhopadhyay and R. S. R. Gorla, "Effects of partial slip on boundary layer flow past a permeable exponential stretching sheet in presence of thermal radiation," *Heat and Mass Transfer*, vol. 48, no. 10, pp. 1773–1781, 2012.
- [23] V. Singh and S. Agarwal, "MHD flow and heat transfer for Maxwell fluid over an exponentially stretching sheet with variable thermal conductivity in porous medium," *Thermal Science*, vol. 18, article 599615, suppl.2, pp. 599–615, 2014.
- [24] F. K. Tsou, E. M. Sparrow, and R. J. Goldstein, "Flow and heat transfer in the boundary layer on a continuous moving surface," *International Journal of Heat and Mass Transfer*, vol. 10, no. 2, pp. 219–235, 1967.
- [25] E. M. A. Elbashareshy, "Heat Transfer over an Exponentially Stretching Continuous Surface with Suction," *Archives of Mechanics*, vol. 53, no. 6, pp. 643–651, 2001.
- [26] S. U. S. Choi and J. A. Eastman, "Enhancing thermal conductivity of fluids with nanoparticles," in *Development and applications of non-Newtonian flows*, D. A. Siginer and H. P. Wang, Eds., p. 9910, ASME, 1995.
- [27] L. Godson, B. Raja, D. M. Lal, and S. E. Wongwises, "Enhancement of heat transfer using nanofluids: an overview," *Renewable and sustainable energy*, vol. 14, no. 2, article 629641, pp. 629–641, 2010.
- [28] S. M. Sebdani, M. Mahmoodi, and S. M. Hashemi, "Effect of nanofluid variable properties on mixed convection in a square cavity," vol. 52, pp. 112–126, 2012.
- [29] W. A. Khan and I. Pop, "Boundary-layer flow of a nanofluid past a stretching sheet," *International Journal of Heat and Mass Transfer*, vol. 53, no. 11–12, pp. 2477–2483, 2010.
- [30] W. A. Khan and A. Aziz, "Double-diffusive natural convective boundary layer flow in a porous medium saturated with a nanofluid over a vertical plate: Prescribed surface heat, solute and nanoparticle fluxes," *International Journal of Thermal Sciences*, vol. 50, no. 11, pp. 2154–2160, 2011.
- [31] P. O. Olanrewaju, A. Olanrewaju, and A. O. Adesanya, "Boundary layer flow of nanofluids over a moving surface in a flowing fluid in the presence of radiation," *International Journal of Applied Science and Technology*, vol. 2, 2012.
- [32] J. Koo and C. Kleinstreuer, "Laminar nanofluid flow in micro-heat-sinks," *International Journal of Heat and Mass Transfer*, vol. 48, no. 13, article 26522661, pp. 2652–2661, 2005.
- [33] S. K. Khan, M. S. Abel, and R. M. Sonth, "Visco-elastic MHD flow, heat and mass transfer over a porous stretching sheet with dissipation of energy and stress work," *Heat and Mass Transfer*, vol. 40, no. 1–2, pp. 47–57, 2003.
- [34] M. Fiza, H. Ullah, and S. Islam, "Three dimensional MHD rotating flow of viscoelastic nanofluid in porous medium between two parallel plates," *Journal of Porous Media*, vol. 23, pp. 715–729, 2020.
- [35] D. A. Nield and A. V. Kuznetsov, "The Cheng-Minkowycz problem for natural convective boundary-layer flow in a porous medium saturated by a nanofluid," *International Journal of Heat and Mass Transfer*, vol. 52, no. 25–26, pp. 5792–5795, 2009.
- [36] M. A. A. Hamad and M. Ferdows, "Similarity solutions to viscous flow and heat transfer of nanofluid over nonlinearly stretching sheet," *Applied Mathematics and Mechanics*, vol. 33, no. 7, article 923930, pp. 923–930, 2012.
- [37] M. A. Hamad and M. Ferdows, "Similarity solution of boundary layer stagnation-point flow towards a heated porous stretching sheet saturated with a nanofluid with heat absorption/generation and suction/blowing: a lie group analysis," *Communications in Nonlinear Science and Numerical Simulation*, vol. 17, no. 1, pp. 132–140, 2012.
- [38] N. S. Akbar, S. Nadeem, T. Hayat, and A. A. Hendi, "Peristaltic flow of a nanofluid in a non-uniform tube," *Heat and Mass Transfer*, vol. 48, no. 3, pp. 451–459, 2012.
- [39] N. S. Akbar, S. Nadeem, T. Hayat, and A. A. Hendi, "Peristaltic flow of a nanofluid with slip effects," *Meccanica*, vol. 47, no. 5, pp. 1283–1294, 2012.
- [40] A. N. Akbar and S. Nadeem, "Peristaltic flow of a Phan-Thien-Tanner nanofluid in a diverging tube," *Heat Transfer Asian Research*, vol. 41, no. 1, pp. 10–22, 2012.
- [41] R. Ellahi, T. Hayat, F. M. Mahomed, and A. Zeeshan, "Exact solutions of flows of an Oldroyd 8-constant fluid with nonlinear slip conditions," vol. 65, no. 12, pp. 1081–1086, 2010.
- [42] R. Ellahi, M. Raza, and K. Vafai, "Series solutions of non-Newtonian nanofluids with Reynolds' model and Vogel's model by means of the homotopy analysis method," *Mathematical and Computer Modelling*, vol. 55, no. 7–8, pp. 1876–1891, 2012.
- [43] A. Zeeshan, R. Ellahi, A. M. Siddiqui, and H. U. Rahman, "An investigation of porosity and magnetohydrodynamic flow of non-Newtonian nanofluid in coaxial cylinders," *International Journal of Physical Sciences*, vol. 7, no. 9, pp. 1353–1361, 2012.
- [44] O. D. Makinde, W. A. Khan, and Z. H. Khan, "Buoyancy effects on MHD stagnation point flow and heat transfer of a nanofluid past a convectively heated stretching/shrinking sheet," *International Journal of Heat and Mass Transfer*, vol. 62, pp. 526–533, 2013.
- [45] H. Ullah, I. Khan, M. Fiza et al., "MHD boundary layer over a stretching sheet: a new stochastic method," *Mathematical*

- Problems in Engineering*, vol. 2021, Article ID 9924593, 26 pages, 2021.
- [46] I. Khan, H. Ullah, H. AlSalman et al., "Falkner Skan equatin with heat transfer: A new stochastic numerical approach," *Mathematical Problems in Engineering*, vol. 2021, Article ID 3921481, 17 pages, 2021.
- [47] H. Bilal, H. Ullah, S. Islam et al., "A Levenberg-Marquardt backpropagation method for unsteady squeezing flow of heat and mass transfer behaviour between parallel plates," *Advances in Mechanical Engineering*, vol. 13, no. 10, 2021.
- [48] R. A. Khan, H. Ullah, M. A. Raja, M. A. Khan, S. Islam, and M. Shoaib, "Heat transfer between two porous parallel plates of steady nano fludis with Brownian and thermophoretic effects: a new stochastic numerical approach," *International Communications in Heat and Mass Transfer*, vol. 126, article 105436, 2021.
- [49] H. Ullah, I. Khan, H. AlSalman et al., "Levenberg–Marquardt backpropagation for numerical treatment of micropolar flow in a porous channel with mass injection," *Complexity*, vol. 2021, Article ID 5337589, 12 pages, 2021.
- [50] H. Ullah, M. Shoaib, R. A. Khan, M. A. Z. Raja, and S. Nisar, "Heat transfer impacts on Maxwell nanofluid flow over a vertical moving surface with MHD using stochastic numerical technique via artificial neural networks," *Coatings*, vol. 11, p. 1483, 2021.
- [51] H. Ullah, R. A. Khan, M. Fiza, S. Islam, and S. M. Al-Mekhlafi, "Comparative evaluation of the optimal auxiliary function method and numerical method to explore the heat transfer between two parallel porous plates of steady nanofluids with Brownian and thermophoretic influences," *Mathematical Problems in Engineering*, vol. 2022, Article ID 7975101, 16 pages, 2022.
- [52] H. Ullah, H. Khan, M. Fiza, K. Ullah, S. Islam, and S. M. al-Mekhlafi, "Comparative analysis of the effect of Joule heating and slip velocity on unsteady squeezing nanofluid flow," *Mathematical Problems in Engineering*, vol. 2022, Article ID 8452862, 10 pages, 2022.
- [53] H. Ullah, M. Arif, M. Fiza, M. Ayaz, K. Ullah, and S. Makhlafi, "Analytical and numerical analysis of the squeezed unsteady MHD nanofluid flow in the presence of thermal radiation," *Journal of Nanomaterials*, vol. 2022, Article ID 1668206, 14 pages, 2022.
- [54] A. Tassaddiq, S. Khan, M. Bilal et al., "Heat and mass transfer together with hybrid nanofluid flow over a rotating disk," *AIP Advances*, vol. 10, no. 5, article 055317, 2020.
- [55] W. Khan, M. Idress, T. Gul, M. A. Khan, and E. Bonyah, "Three non-Newtonian fluids flow considering thin film over an unsteady stretching surface with variable fluid properties," *Advances in Mechanical Engineering*, vol. 10, no. 10, 2018.
- [56] T. Gul, S. Islam, R. A. Shah, A. Khalid, I. Khan, and S. Shafie, "Unsteady MHD thin film flow of an Oldroyd-B fluid over an oscillating inclined belt," *PloS one*, vol. 10, no. 7, article e0126698, 2015.
- [57] M. Bilal, A. Saeed, T. Gul, I. Ali, W. Kumam, and P. Kumam, "Numerical approximation of microorganisms hybrid nanofluid flow induced by a wavy fluctuating spinning disc," *Coatings*, vol. 11, no. 9, p. 1032, 2021.
- [58] M. Jawad, A. Saeed, and T. Gul, "Entropy generation for MHD Maxwell nanofluid flow past a porous and stretching surface with Dufour and Soret effects," *Brazilian Journal of Physics*, vol. 51, no. 3, pp. 469–480, 2021.
- [59] T. Gul, R. S. Gul, W. Noman et al., "CNTs-nanofluid flow in a rotating system between the gap of a disk and cone," *Physica Scripta*, vol. 95, no. 12, article 125202, 2020.
- [60] K. J. Bathe, *Finite Element Procedures*, Prentice-Hall, New Jersey, USA, 1996.
- [61] J. N. Reddy, *An Introduction to the Finite Element Method*, McGraw-Hill, New York, 1985.
- [62] J. J. Connor and C. A. Brebbia, *Finite Element Techniques for Fluid Flow*, Butterworths, London, 1976.
- [63] S. Nadeem, R. Haq, N. S. Akbar, C. Lee, and Z. H. Khan, "Numerical Study of Boundary layer flow and heat transfer of Oldroyd-B nanofluid towards a stretching sheet," *Plos One*, vol. 8, no. 8, article e69811, 2013.
- [64] C. Y. Wang, "Free convection on a vertical stretching surface," *Journal of Applied Mathematics and Mechanics*, vol. 69, no. 11, pp. 418–420, 1989.

## Research Article

# Aggregation Effects on Entropy Generation Analysis for Nanofluid Flow over a Wedge with Thermal Radiation: A Numerical Investigation

Rabia Rehman <sup>1</sup>, Hafiz Abdul Wahab <sup>1</sup>, Nawa Alshammari <sup>2</sup>, Umar Khan,<sup>1</sup>  
and Ilyas Khan <sup>3</sup>

<sup>1</sup>Department of Mathematics and Statistics, Hazara University, Mansehra, Pakistan

<sup>2</sup>Department of Basic Sciences, College of Science and Theoretical Studies, Saudi Electronic University, Riyadh 11673, Saudi Arabia

<sup>3</sup>Department of Mathematics, College of Science Al-Zulfi, Majmaah University, Al-Majmaah 11952, Saudi Arabia

Correspondence should be addressed to Rabia Rehman; rabiarehman635@gmail.com

Received 18 October 2021; Revised 28 May 2022; Accepted 8 August 2022; Published 24 September 2022

Academic Editor: Anwar Saeed

Copyright © 2022 Rabia Rehman et al. This is an open access article distributed under the Creative Commons Attribution License, which permits unrestricted use, distribution, and reproduction in any medium, provided the original work is properly cited.

The current study investigated the formation of entropy in a nanofluid flow in a wedge with thermal radiation and convective boundary conditions. Nanoparticle aggregation is also taken into consideration. The rate of heat transmission of a water-based aggregated fluid over a wedge has been investigated due to the effects of thermal radiation. A set of nonlinear differential equations governs the flow process, and these are numerically solved using a helpful approach called the Runge-Kutta-Fehlberg scheme. This method starts by breaking down the equations into a collection of first-order equations. The RK method then solves those equations. The effects on flow and heat transmission are studied using graphical analysis. Entropy generation and Bejan number changes are also graphically displayed, and the results are discussed in detail. These equations' answers were also incorporated into a dimensionless entropy generating equation. According to the findings, raising the radiation parameter and decreasing boundary convection minimize entropy generation, while nanoparticles boost entropy production.

## 1. Introduction

The “nanofluid” is characterized by conventional nanofluid papers as the scattering of solid nanoparticles, rods, and pipes in the standard heat transfer flow, for instance, water, lubricating oil, ethane-1,2 diols, and petrol. Many scholars have investigated the degree to which thermophysical characteristics of nanofluid boost heat dissipation by their scale, shape, concentrating, etc. The hollow cylindrical nanostructures are carbon nanofluids, whose walls are constructed from dense carbon sheets. (CNTs) are known as walled single nanotubes and wall-mounted nanotubes. CNTs have usually lots of processing and biomedical applications while the most critical function of nanotubes in fluid dynamics is the control of heat transfer to fluids [1]. In various engineering and science fields, the theory for boundary layers plays an important role. The boundary layer flow of a single-walled carbon nanotube nanofluid approaching three non-

linear thin isothermal needles of paraboloid, cone, and cylinder shapes with convective boundary conditions is predicted in [2] using an artificial neural network (ANN). Under the phenomenon of zero heat and mass flux, a single and dual phase technique is employed to build the management model. In ref [3], the role of Casson carbon nanotubes in boundary layer flow is being studied, having implications for both single-walled and multiwalled CNTs. The rate of heat transmission is examined under convective conditions. Various studies of nanofluid boundary layer motion around a wedge have been found in the literature. Khan and Pop [4] numerically analyzed the flow of the nanofluid limit layer through a wedge. The thermal radiation, viscose dissipation, and chemical reactions of MHD boundary layer nanofluid flow by the wedge were investigated by Pandey and Kumar [5]. Flows past a wedge could be used in polymer processing, crude oil extraction, the flow of molten metals over ramped surfaces, liquid metal flows in heat exchangers, the throwing



of chilled air through AC panels, nuclear power plants, designing flaps on aeroplane wings for increased lift, drag, and maneuverability, modeling of warships and submarines, and a variety of other scientific and engineering fields. Many scholars have recently shown a strong interest in studying fluid flow past a wedge surface.

The irreversibility of simple heat transfer methods is assessed using the Second Thermodynamics Law. Entropic generation is studied to understand the connection between thermal energy and other energy types that influence process matter. Malvandi et al. [6] are investigating the formation of entropy in nanofluid on a flat plate.

In recent decades, the issue of MHD and nanofluid has become more industrial. Initially, the magnetic field's influence on the convection of natural heat transfer was investigated by Sparrow and Cess. The hydromagnetic flow and heat transport through the stretching layer have been investigated by Chakrabarti and Gupta [7]. Casson nanofluids, which belong to the class of non-Newtonian fluids, have rheological properties in the shear stress-strain relationship. These are routinely used in several processes in engineering and technology [8].

More than one paper was then flooded and extensively discussed in the field of nanofluid science. The transmission of heat with fluid particulate suspension was documented under Saeed et al. [9]. At the melting heat transfer to the boundary nanofluid fluid layer stagnation point on to the stretching shrinking sheet, Kumar and Bandari [10] were recently noted. Features of double stratification on stagnation point flow of Walter's B nanoliquid driven through Riga surface are examined in [11]. Via solutal stratification, radiation, and thermal effects, heat and mass phenomena are examined.

The limit layer flow was observed by Yacob et al. [12] past a deteriorating/decreasing surface in nanofluid under an external, consistent shear flow with a convective surface border status. The MHD-forced layer flow of  $\text{Al}_2\text{O}_3 - \text{H}_2\text{O}$  nanofluid over a flat, motionless plate with convective surface configuration was observed [13].

The intensive nanofluid study has undergone significant advances and is applied to various surfaces, sizes, and conditions by numerous researchers. The MHD convection and thermal transfer over the inclined cylinder were investigated by Dhanai et al. [14] for velocity and thermal slip effects:  $\text{Al}_2\text{O}_3 - \text{H}_2\text{O}$ . Nanofluid force convection in a nanoparticle was observed by the Malvandi and Ganji [15].

The study of 3D flows is mentioned in comparison to two-dimensional flows. The physical question is better known. The 3D boundary layer flow caused by the extension layer was addressed by Wang [16]. Different types of papers were suggested for 3D flow accordingly. The three-dimensional nanofluid flow model with the use for solar energy was explored by Ahmad Khan et al. [17]. Some recent demonstration on flow in circular rings and circular cylinder can be seen in [18, 19].

At its general three-dimensional stagnation, Bachok et al. [20] investigate the flow and heat transfer of nanofluid. The 3D hydromagnetic point flow of stagnation to a heat generating layer was addressed by Attia [21]. Mansur and

Ishak [22] depicted the nanofluid three-dimensional fluid flow and thermal transmission across a permeable, convective boundary layer.

Khan et al. [23] convected exponentially expanded layers to computer analysis of the 3D nanofluid flow. Hayat et al. [24] have been studying 3D magneto-hydrodynamic nanofluid flow with slip speed and nonlinear thermal radiation. The role of nanoparticle aggregation kinetics in thermal conductivity is experimentally recognized by Prasher [25]. Chen et al. [26] recorded entropy characteristics to include titanium particles. They used the nanoparticle aggregation mechanism to predict thermal conductivity. Zhou and Keller [27] used ZnO to describe the effect of the fractal component of the nanoparticle aggregation. They showed the effect of pH on the phenomenon of aggregation. Mahanthesh et al. [28] investigated the kinematics of nanoparticle aggregation by using modified models for thermal conductivity and dynamic viscosity developed by Maxwell-Bruggeman and Krieger-Dougherty. Sedighi and Mohebbi [29] have investigated the thermal conductivity and basic heat characteristics of nanolithic aggregations by adding nanoparticles. Heris et al. [30] conducted an inspection on ZnO nanolubricants. The development of nanoparticle aggregation in the base fluid was demonstrated by the correlation of Krieger and Dougherty. Chen et al. [31] conducted a comprehensive study on impact of the nanoparticle aggregation on the nanofluid's radiative properties. The increment of viscosity nanoparticle aggregation was reported by He et al. [32].

In physics and engineering challenges, heat transmission is crucial. The influence of Newtonian heating on nanofluid flow over a nonlinear permeable stretching/shrinking sheet towards the stagnation point is investigated in this work. In the heat transfer process, entropy generation analysis also plays a vibrant role. Entropic scrutiny is focused on irreversibility of the thermal system. Any thermal and heat transfer equipment, including the heat exchanger and heat sink, shall obey the irreversibility. The source of irreversibility should be established and to some degree minimized. Mustafa et al. [33] investigated the generation of entropy by nanofluid flow in the vertical microchannel. They found that the number of grass increases the rate of entropy. A porous  $\text{Al}_2\text{O}_3$ /water fluid phase has been shown by Makinde and Egunjobi [34]. They found that the nanoparticle concentration in Bejan increased.

The thermal characteristics that define the physical situation have often been challenged by scientists and inventors. Ibanez et al. investigated entropy generation using the separate flow model in a nanofluid-driven microchannel. The MHD nanofluid stream over L-shaped ribs was examined by Torabi et al. [35]. Toghraie et al. [36] use the spectral quasilinearization (SQLM) approach to solve the complex differential equations that govern nonlinear mixed convective heat transfer of a Williamson fluid down a vertical microchannel. They demonstrated that the boundary conditions of convection heating at the microchannel walls cause the most entropy formation.

The present article addresses the entropy generation of internal layer flow and MWCNT-containing nanofluid thermal transmission. In this research project, the uniqueness

and impact of nanoparticles, convective surfaces, and heat radiation are calculated. The solutions are obtained by numerical calculation. In both situations, the physical effects of nanofluid flow, i.e., (i) without aggregating the nanoparticles and (ii) with nanoparticles, are examined.

The main objectives of this work are as follows.

- (i) The characteristics of flow and thermal field are interpreted and missing by filming with nanofluid aggregation
- (ii) Examine the heat transfer phenomenon root of irreversibility
- (iii) Find out which physical factor contributes to the generation of entropy
- (iv) Find out how entropy production can be minimized by manipulating flow parameters

## 2. Description of the Model

Consider a two-dimension, laminar, steady, incompressible nanofluids of viscous flow through a wedge in a stream of water-based nanofluid containing multiwall CNT (see Figure 1). The set of Cartesian coordinates is used in the problem under consideration. The lower surface of the wedge is supposed to be heated by convection from a hot fluid at a temperature  $T_f$  that yields the heat transfer coefficient  $h_f$ . The nanoparticles and the base fluid (water) are also considered to be in equilibrium, with no slip between them.

The equations that govern the nanofluid model over wedge geometry was described in the following form [37]:

$$\begin{aligned} \frac{\partial u}{\partial x} + \frac{\partial v}{\partial y} &= 0, \\ u \frac{\partial u}{\partial x} + v \frac{\partial u}{\partial y} &= U_\infty \frac{\partial U_e}{\partial x} + \frac{\mu_{nf}}{\rho_{nf}} \frac{\partial^2 u}{\partial y^2}, \\ u \frac{\partial T}{\partial x} + v \frac{\partial T}{\partial y} &= \alpha_{nf} \frac{\partial^2 T}{\partial y^2} + \frac{\mu_{nf}}{(\rho C_p)_{nf}} \left( \frac{\partial u}{\partial y} \right)^2 - \frac{1}{(\rho C_p)_{nf}} \frac{\partial q_r}{\partial y}, \end{aligned} \quad (1)$$

where  $u$  and  $v$  represent the components of velocity in the  $x$  and  $y$  direction of the fluid flows, respectively. The coordinate system and problem geometry are described in Figure 1.  $T$  represents the temperature of nanofluid. Furthermore,  $\mu_{nf}$  and  $\rho_{nf}$  are the dynamic nanofluids viscosity and density, and  $\sigma_{nf}$  is the thermal diffusivity of the nanofluid.

### 2.1. Thermal Physical Characteristics of Nanofluids

**2.1.1. The Conventional Model without Aggregation (Case 1).** The productive hybrid nanofluid density  $\rho_{nf}$  and capacity of

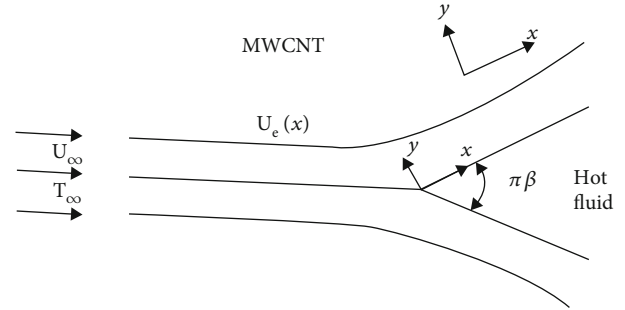


FIGURE 1: Physical model of the problem.

heat  $((\rho C_p)_{nf})$  are defined by

$$(\rho C_p)_{nf} = (1 - \phi)(\rho C_p)_f + \phi(\rho C_p)_s, \quad \rho_{nf} = (1 - \phi)\rho_f + \phi\rho_s, \quad (2)$$

where  $\phi$  is a nanofluid fixed volume fraction. The nanofluid dynamic viscosity is calculated as [38]

$$\frac{\mu_{nf}}{\mu_f} = \frac{1}{(1 - \phi)^{2.5}}. \quad (3)$$

The effective nanofluid thermal conductivity is determined by

$$\frac{k_{nf}}{k_f} = \frac{k_s + 2k_f - 2\phi(k_f - k_s)}{k_s + 2k_f + \phi(k_f - k_s)}, \quad (4)$$

where  $k_{nf}$  is the nanofluid thermal conductivity, and  $k_f$  is the thermal conductivity of base fluid. Recommended boundary conditions are implemented through the disk as

$$\begin{aligned} u = 0, v = 0, -k_{nf} \frac{\partial T}{\partial y} &= h_f (T_f - T), \text{ at } y = 0, \\ u = U_e(x) = U_\infty x^m, v = 0, T &= T_\infty, \text{ at } y \rightarrow \infty. \end{aligned} \quad (5)$$

**2.1.2. The Conventional Model with Aggregation (Case 2).** The fluid model, for example, Brinkman, Einstein, and Maxwell, depends only on the fraction of the nanoparticle volume. The nanofluid's normalized shear viscosity does not depend on the temperature. The model of aggregation clarifies these features. In addition, nanofluid thermal conductivity is higher with experimental results than with common fluid models. This difference is explained by the neglected effect of nanoparticles [9, 10]. Therefore, consideration of the film aggregation of nanoparticles is necessary to explore the ratio of thermal conductivity. Thermophysical properties of base fluid and

nanoparticles are given in Table 1.

$$\begin{aligned}\rho_{nf} &= (1 - \phi_a)\rho_f + \phi_a\rho_s, \\ \frac{\mu_{nf}}{\mu_f} &= \left(1 - \frac{\phi_a}{\phi_m}\right)^{[\eta]\phi_m}, \\ (\rho C_p)_{nf} &= (1 - \phi_a)(\rho C_p)_f + \phi_a(\rho C_p)_s, \\ \frac{k_{nf}}{k_f} &= \frac{k_a + 2k_f - 2\phi_a(k_f - k_a)}{k_a + 2k_f + \phi_a(k_f - k_a)},\end{aligned}\quad (6)$$

where  $\phi_m$  is an extreme fraction of the volume,  $[\eta]$  is an Einstein coefficient, and  $\phi_a$  is an effective fraction of the volume of the aggregates.

$$\phi_a = \phi \left(\frac{r_a}{r_p}\right)^{3-D}. \quad (7)$$

Experimental values are very well agreed with the commonly accepted values  $D = 1.8$ ,  $(r_a/r_p) = 3.34$ ,  $\phi_m = 0.605$ , and  $[\eta] = 2.5$ . Nanoparticle aggregation is included in the thermal conductivity deduction by Bruggeman:

$$\begin{aligned}\frac{k_{nf}}{k_f} &= \frac{1}{4} \left\{ (3\phi_m - 1) \frac{k_s}{k_f} + (3(1 - \phi_m) - 1) \right. \\ &\quad \left. + \left[ \left( (3\phi_{in} - 1) \frac{k_s}{k_f} + (3(1 - \phi_{in}) - 1) \right)^2 + 8 \frac{k_s}{k_f} \right] \right\}, \\ \phi_{in} &= \left(\frac{r_a}{r_p}\right)^{D-3}.\end{aligned}\quad (8)$$

By using similarity transformations,

$$\eta = \left(\frac{(m+1)U_\epsilon(x)}{2v_{bf}x}\right)^{1/2}, \quad y, u = U_\epsilon(x)f'(\eta),$$

$$\theta(\eta) = \frac{(T - T_\infty)}{(T_w - T_\infty)}, \quad v = \left(\frac{(m+1)v_{bf}U_\epsilon(x)}{2x}\right)^{1/2} \left[ f + \left(\frac{m-1}{m+1}\right)\eta f'(\eta) \right]. \quad (9)$$

Substituting values to get

$$f'''' + (1 - \phi)^{2.5} \left(1 - \phi + \phi \frac{\rho_{nf}}{\rho_f}\right) \left[ ff'' + \frac{(2m)}{(m+1)} (1 - f'^2) \right] = 0, \quad (10)$$

$$\left(\frac{k_{nf}}{k_f} + \frac{4}{3Nr}\right)\theta'' + \left(1 - \phi + \phi \rho_{nf}/\rho_f\right) \text{Pr} f \theta' + \frac{\text{Br}}{(1 - \phi)^{2.5}} f'^2 = 0, \quad (11)$$

where  $N_r$  is the radiation parameter, and  $\text{Br} = \text{Pr} \cdot \text{Ec}$  (where  $\text{Ec}$  represents the Eckert number) is the Brinkman number.  $\text{Bi}$  is the surface convection parameter,  $\text{Pr} = \nu_f/\alpha_f$  is the Prandtl number, and primes signify derivative w.r.t  $\eta$ . The modified BCs transform into

$$f(0) = 0, f'(0) = 0, \theta'(0) = -\text{Bi}(1 - \theta(0)), \quad (12)$$

$$f'(\eta) = 1, \theta(\eta) = 0 \text{ as } (\eta) \rightarrow \infty. \quad (13)$$

**2.2. Entropy Generation.** Entropy generation includes the existing irreversibility of the physical phenomenon. The term entropy is used

$$S_g = \frac{k_{nf}}{T_\infty^2} \left[ \left(\frac{\partial T}{\partial y}\right)^2 + \frac{16\sigma^* T_\infty^2}{3k_{bf}k^*} \left(\frac{\partial T}{\partial y}\right)^2 \right] + \frac{\mu_{nf}}{T_\infty} \left(\frac{\partial u}{\partial y}\right)^2 = 0. \quad (14)$$

The nondimensional entropy generation is given by

$$N_s = \frac{S_g}{S_{g0}} = \left(\frac{m+1}{2}\right) \text{Re}_x \left[ \frac{k_{nf}}{k_{bf}} \left(1 + \frac{4}{3Nr}\right) \theta'^2 + \frac{\text{Br}}{\Omega(1 - \phi)^{2.5}} (f'')^2 \right], \quad (15)$$

where  $S_{g0} = (k_{bf}\Delta T^2/T_\infty^2 x^2)$  is the characteristic entropy generation rate, and  $\Omega^{-1} = T_\infty/\Delta T$  is the dimensionless temperature difference.

Table 2 shows the comparison between results of previous publications [39, 40] and some of our results with a perfect agreement.

We are introducing the Bejan number ( $\text{Be}$ ) as the ratio between entropy and total entropy output induced by heat transfer.

$$\text{Be} = \frac{\text{Entropy generation due to heat transfer}}{\text{Total entropy generation}}. \quad (16)$$

If  $\text{Be} = 1$  dominates irreversibility in heat transfers, while  $\text{Be} = 0$  dominates irreversibility as a result of fluid friction,  $\text{Be} = 1/2$  dominates when fluid rubbing, and heat transfers are irreversible.

**2.2.1. Mathematical Analysis.** Equations (10) and (11) relative to equation (12) are combined with nonlinear DEs to be numerically solved by Runge-Kutta-Fehlberg scheme for differential values of physical parameters. In order to obtain the numerical approaches, the governing nonlinear ODEs (10) and (11) and BCs (12) transformed to a number of simultaneous DEs of the first order.

TABLE 1: Thermal physical characteristics of H<sub>2</sub>O and MWCNT [31].

Physical properties	$\rho \left(\frac{\text{kg}}{\text{m}^3}\right)$	$C_p \left(\frac{\text{J}}{\text{kg K}}\right)$	$k \left(\frac{\text{W}}{\text{m K}}\right)$
Pure water (H <sub>2</sub> O)	997.0	4179	0.613
MWCNT	1600	796	3000

TABLE 2: Comparison between present result and Ref [39, 40].

$m$	Yih [36]	White [37]	Present
0	0.4696	0.4696	0.4696
$\frac{1}{11}$	0.6550	0.6550	0.6550
$\frac{1}{5}$	0.8021	0.8021	0.8021
$\frac{1}{3}$	0.9276	0.9276	0.9277

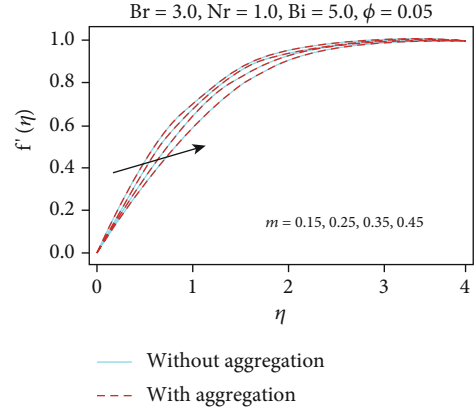


FIGURE 4: Impact of  $m$  parameter on  $f'(\eta)$ .

### 3. Interpretations of the Results

In the presence of thermal radiation, the numerical results for entropy production inside the nanofluid border layer over the wedge are graphically represented. The results show extraordinary agreement and therefore trust us to use the current code. For certain values of ( $Bi$ ),  $m$ ,  $Nr$ ,  $Br$ , and  $\phi$ , the nonlinear ordinary differential equations (10) and (11) subject to boundary condition (12) is numerically solved. Many kinds of nanoparticles are considered that are the fluid of base Cu, CuO, Al<sub>2</sub>O<sub>3</sub>, and H<sub>2</sub>O. Let us take into account of the value ( $Pr$ ) of 6.2 for the current analysis.

The impact of  $Bi$  for the velocity component  $f'(\eta)$  and the field of temperature,  $\theta(\eta)$ , respectively, are shown in Figures 2 and 3. Biot number is a dimensional quantity comparing relative external and internal resistance transmission. The heated fluid heats up the lower surface of the stretch sheet as  $Bi$  rises, causing convective heat to be transferred. As a result of the rise in the number of Biot, the temperature increases. Eventually, it increases the thickness of the thermal boundaries. It is important to note that the inclusion of nanoparticle aggregation leads to an enhanced temperature profile.

For velocity components  $f'(\eta)$  and the distribution of the temperature field  $\theta(\eta)$ , respectively, the effects of the  $m$  parameter are shown in Figures 4 and 5. The findings are very much in agreement. The  $f'(\eta)$  values are reduced and for the larger  $m$ ,  $\theta(\eta)$  increases. Physically, the increment in  $\theta(\eta)$  is due to the resistive force that occurs from the magnetic field. The Lorentz force, which is induced by the magnetic field, is the physical reason behind this. Figures 6 and 7 display the effect of  $Nr$  on  $f'(\eta)$  and  $\theta(\eta)$  temperature.  $f'(\eta)$  decreases and increases the thickness of thermal boundary layer as  $Nr$  increases. Figures 8 and 9 show that with the rise in  $\phi$ , both the velocity profile  $f'(\eta)$  and the distribution of the temperature field  $\theta(\eta)$  increase. Physically, this is due to increased dynamic viscosity and increased momentum diffusion. The increase in the thermal conductivity of the nanoliquid is attributable to the existence of more nanoparticles. The fluid close to the nanoparticles forms a nanolayer

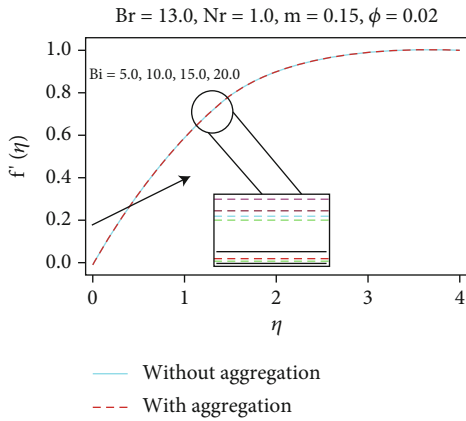


FIGURE 2: Impact of  $Bi$  parameter on  $f'(\eta)$ .

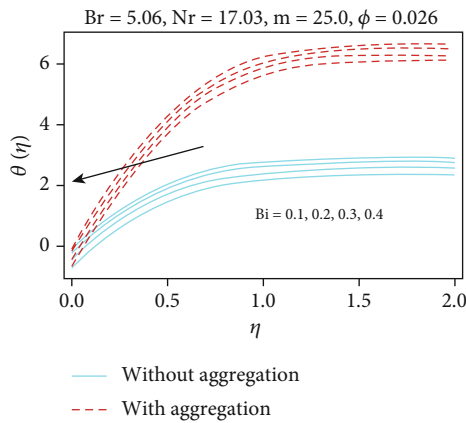


FIGURE 3: Impact of  $Bi$  parameter on  $\theta(\eta)$ .

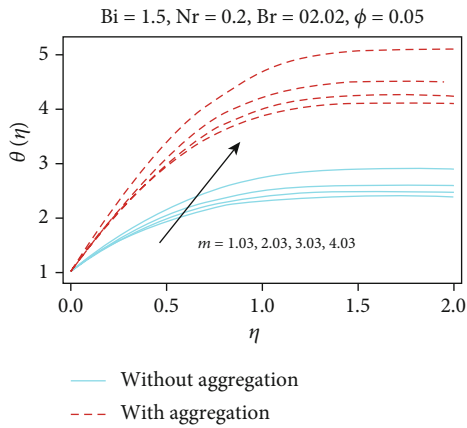


FIGURE 5: Impact of  $m$  parameter on  $\theta(\eta)$ .

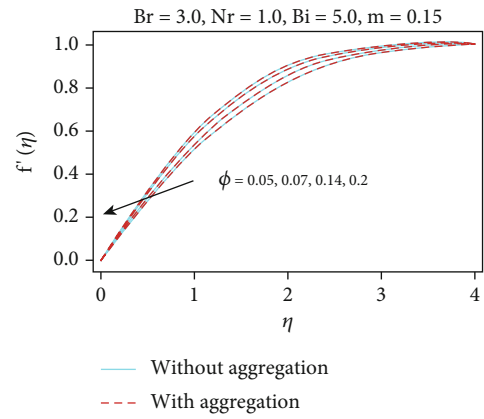


FIGURE 8: Impact of  $\phi$  parameter on  $f'(\eta)$ .

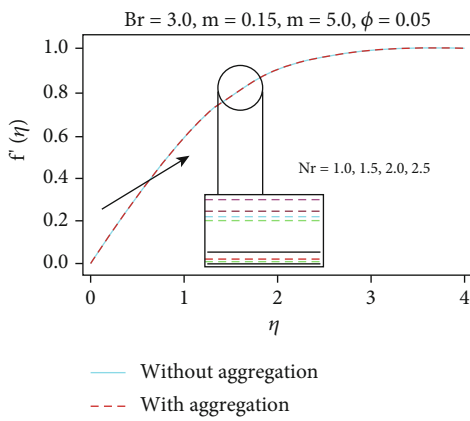


FIGURE 6: Impact of  $Nr$  parameter on  $f'(\eta)$ .

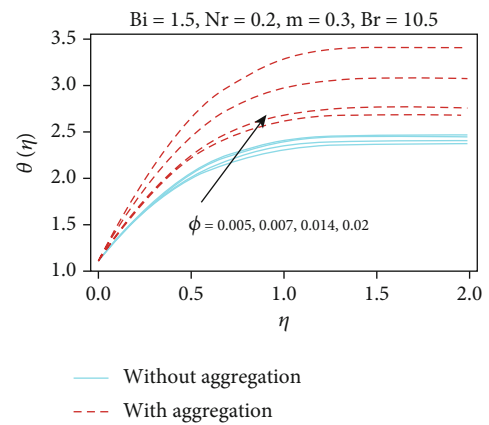


FIGURE 9: Impact of  $\phi$  parameter on  $\theta(\eta)$ .

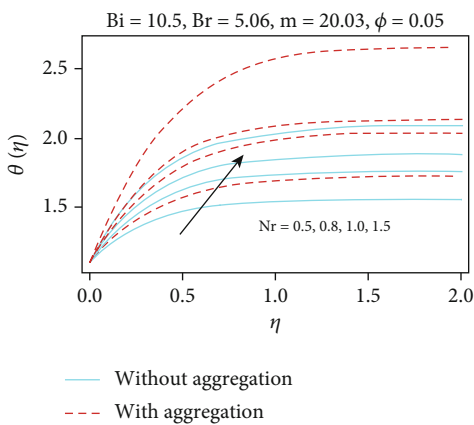


FIGURE 7: Impact of  $Nr$  parameter on  $\theta(\eta)$ .

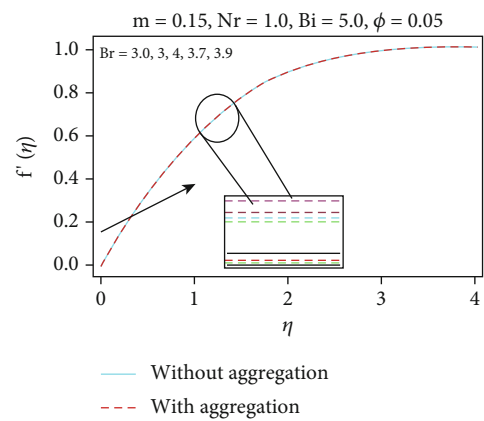


FIGURE 10: Impact of  $Br$  parameter on  $f'(\eta)$ .

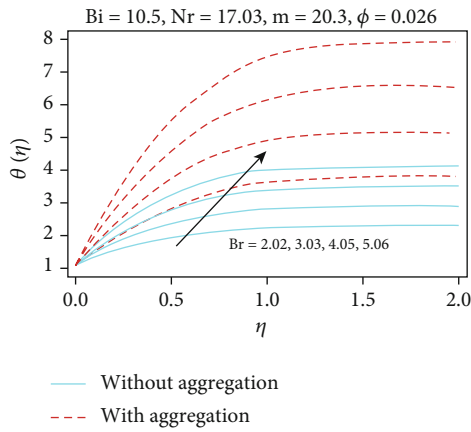


FIGURE 11: Effect of Br on  $\theta(\eta)$ .

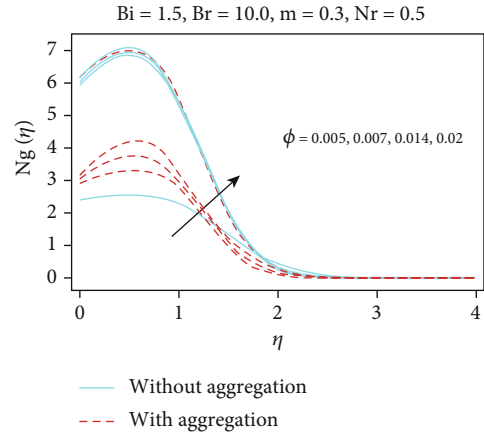


FIGURE 14: Impact of  $\phi$  parameter on  $Ng(\eta)$ .

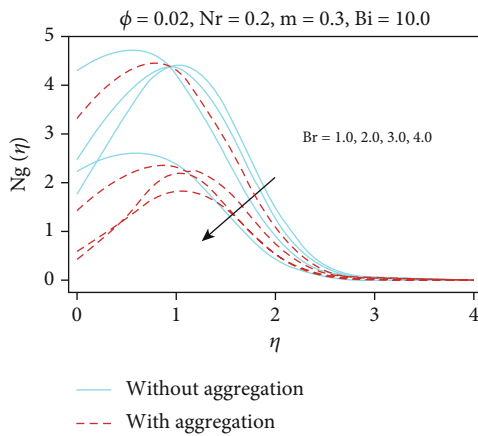


FIGURE 12: Effect of Bi parameter on  $Ng(\eta)$ .

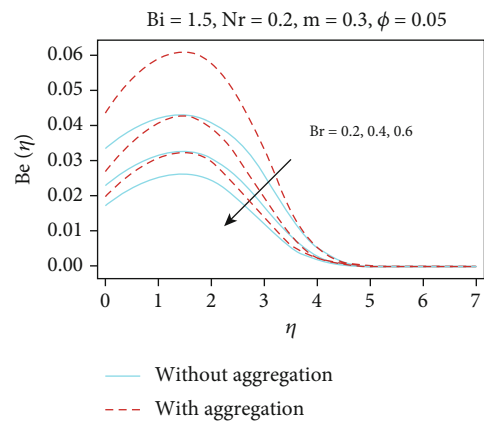


FIGURE 15: Impact of Br parameter on  $Be(\eta)$ .

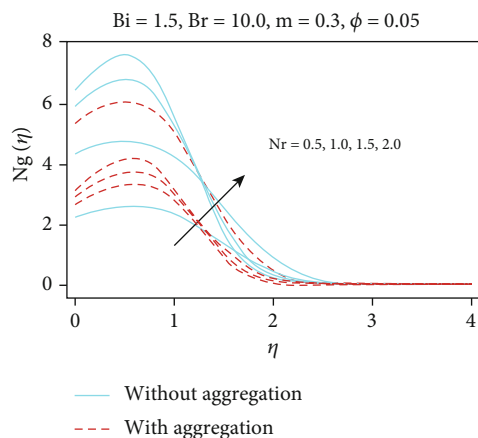


FIGURE 13: Impact of Nr parameter on  $Ng(\eta)$ .

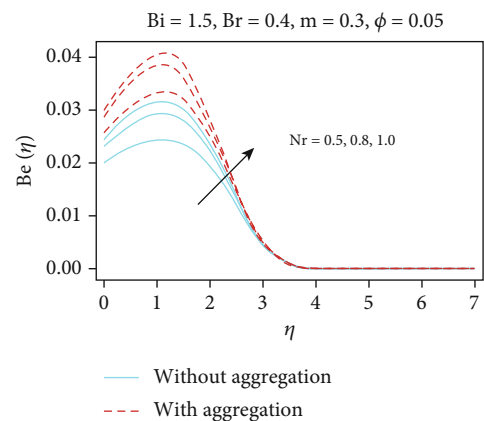


FIGURE 16: Impact of Nr parameter on  $Be(\eta)$ .

since the nanoparticles are formed and serve as a bridge between the particles and the fluid aggregates. The density of the nanolayer plays an important part in improving thermal conductivity. This nanolayer plays an important role in the transmission of heat from solid to nearby liquid.

Br effects are shown in Figures 10 and 11 for  $f'(\eta)$  and  $\theta(\eta)$ . It seems that  $f'(\eta)$  decreases, and the thermal limit thickness increases with Br. The effect of Bi, Nr, and  $\phi$  nanoparticles on  $Ng(\eta)$  is shown in Figures 12–14. It is evident that with higher  $\phi$ ,  $Ng(\eta)$  decreases and Bi increases. Increased

radiation parameters in  $Ng(\eta)$  and  $Nr$  continue to increase the entropy generation. This action of entropy generation is motivated by a reduction in the radiation absorption rate. Therefore, the best way to reduce entropy production is to increase the radiation parameter. It is illustrated that the nanoparticle aggregation model has a lower entropy generation.

The Bejan number for parameters  $\phi$ ,  $Nr$ , and  $Br$  is shown in Figures 15 and 16. The  $Be(\eta)$  curve tends to increase until the maximum value is reached first and then begins to decrease unless the value is zero. It is observed that the number of Bejan increases to increase the value of  $Nr$ . The maximum value of  $Be(\eta)$  is increased with greater  $Nr$  and decreased with  $\phi$  and  $Br$ . It is known from these graphs that the number of Bejan is greater for the aggregation model.

#### 4. Conclusions

This study develops a mathematical expression for the entropy processing and heat transfer studies of MWCNT-containing incompressible nanofluids under the conditions of convective conditions and nanofluid thermal radiation. A cinematic aggregation model for the analysis of nanoliquid flow is considered. The significance of the different speed profile parameters, thermal profile, entropy generation, and the number of Bejan is considered. The following fundamental conclusions are drawn from the current study:

- (i) The increase in volume  $\phi$  and Biot  $Bi$  fraction increases thickness of temperature but decreases the radiation parameter
- (ii) It is noted that the aggregation model has a higher temperature profile than traditional models
- (iii) Entropy production increases in nanofluid for a wider volume fraction of nanoparticles
- (iv) The entropy production is reduced in the aggregation model of nanoparticles
- (v) The reduction of entropy can be achieved by increasing the radiation parameter and reducing crossborder convection
- (vi) Nanofluid entropy production increases for higher volume fraction values
- (vii) The number Bejan is increased with the radiation parameter and the number Biot
- (viii) It has been emphasized that a model of aggregation of nanoparticles shows a higher number Bejan

#### Nomenclature

$u$ :	Component of velocity in the $x$ direction
$v$ :	Component of velocity in the $y$ direction
$\mu$ :	Dynamic viscosity
$\nu$ :	Kinematics viscosity
$Re$ :	Local Reynolds number

$T$ :	Surface temperatures
$T_{\infty}$ :	Environmental temperatures
$(\rho Cp)_{nf}$ :	Nanofluid heat power
$\rho_{nf}$ :	Density of nanofluid
$\rho_s$ :	Density of solid particle
$\phi$ :	Volume fraction of nanoparticles
$k_f$ :	Conductivity of the base fluid
$\theta$ :	Dimensionless temperature
$\eta$ :	Dimensionless variable
$Nu$ :	Nusselt number
$Pr$ :	Prandtl number
$q_r$ :	Rosseland approximation
$Ec$ :	Eckert number
$N$ :	Radiation parameter
$Ng$ :	Entropy generation
$Be$ :	Bejan number
$\Omega$ :	Thermal difference parameter
$k_a$ :	Thermal conductivity of the aggregates
$\phi_a$ :	Volume fraction of nanoparticle aggregates
$\phi_m$ :	Maximum volume fraction of nanoparticles
$r_a, r_p$ :	Radii of aggregates and nanoparticles.

#### Data Availability

No data were used in the presented work.

#### Conflicts of Interest

The authors declare that there is no financial/competing interest regarding to this work.

#### References

- [1] Y. Ding, H. Alias, D. Wen, and R. A. Williams, "Heat transfer of aqueous suspensions of carbon nanotubes (CNT nanofluids)," *International Journal of Heat and Mass Transfer*, vol. 49, no. 1-2, pp. 240–250, 2006.
- [2] A. Shafiq, A. B. Çolak, and T. Naz Sindhu, "Designing artificial neural network of nanoparticle diameter and solid–fluid interfacial layer on single-walled carbon nanotubes/ethylene glycol nanofluid flow on thin slendering needles," *International Journal for Numerical Methods in Fluids*, vol. 93, no. 12, pp. 3384–3404, 2021.
- [3] A. Shafiq, T. N. Sindhu, and Q. M. Al-Mdallal, "A sensitivity study on carbon nanotubes significance in Darcy–Forchheimer flow towards a rotating disk by response surface methodology," *Scientific Reports*, vol. 11, no. 1, pp. 1–26, 2021.
- [4] W. A. Khan and I. Pop, "Boundary layer flow past a wedge moving in a nanofluid," *Mathematical Problems in Engineering*, vol. 2013, Article ID 637285, 7 pages, 2013.
- [5] A. K. Pandey and M. Kumar, "Chemical reaction and thermal radiation effects on boundary layer flow of nanofluid over a wedge with viscous and Ohmic dissipation," *St. Petersburg Polytechnical University, Journal of Physics and Mathematics*, vol. 3, pp. 322–332, 2017.
- [6] A. Malvandi, D. D. Ganji, F. Hedayati, and E. Yousefi Bar, "An analytical study on entropy generation of nanofluids over a flat plate," *Journal of Alexandria Engineering*, vol. 52, no. 4, pp. 595–604, 2013.

- [7] A. Chakrabarti and A. S. Gupta, "Hydromagnetic flow and heat transfer over a stretching sheet," *Quarterly Journal of Mechanics and Applied Mathematics*, vol. 37, pp. 73–78, 1979.
- [8] M. Bilal, A. Saeed, T. Gul, I. Ali, W. Kumam, and P. Kumam, "Numerical approximation of microorganisms hybrid nanofluid flow induced by a wavy fluctuating spinning disc," *Coatings*, vol. 11, no. 9, p. 1032, 2021.
- [9] A. Saeed, P. Kumam, T. Gul, W. Alghamdi, W. Kumam, and A. Khan, "Darcy–Forchheimer couple stress hybrid nanofluids flow with variable fluid properties," *Scientific Reports*, vol. 11, no. 1, pp. 1–13, 2021.
- [10] A. Saeed, P. Kumam, S. Nasir, T. Gul, and W. Kumam, "Non-linear convective flow of the thin film nanofluid over an inclined stretching surface," *Scientific Reports*, vol. 11, no. 1, pp. 1–15, 2021.
- [11] A. Shafiq, F. Mebarek-Oudina, T. N. Sindhu, and A. Abidi, "A study of dual stratification on stagnation point Walters' B nanofluid flow via radiative Riga plate: a statistical approach," *The European Physical Journal Plus*, vol. 136, no. 4, pp. 1–24, 2021.
- [12] N. A. Yacob, A. Ishak, I. Pop, and K. Vajravelu, "Boundary layer flow past a stretching/shrinking surface beneath an external uniform shear flow with a convective surface boundary condition in a nanofluid," *Nanoscale Research Letters*, vol. 6, no. 1, p. 314, 2011.
- [13] J. Bouslimi, M. A. Abdelhafez, A. M. Abd-Alla, S. M. Abo-Dahab, and K. H. Mahmoud, "MHD mixed convection nanofluid flow over convectively heated nonlinear due to an extending surface with Soret effect," *Complexity*, vol. 2021, Article ID 5592024, 20 pages, 2021.
- [14] R. Dhanai, P. Rana, and L. Kumar, "MHD mixed convection nanofluid flow and heat transfer over an inclined cylinder due to velocity and thermal slip effects: Buongiorno's model," *Powder Technology*, vol. 288, pp. 140–150, 2016.
- [15] A. Malvandi and D. D. Ganji, "Effects of nanoparticle migration on force convection of alumina/water nanofluid in a cooled parallel-plate channel," *Advanced Powder Technology*, vol. 25, no. 4, pp. 1369–1375, 2014.
- [16] C. Wang, "The three-dimensional flow due to a stretching flat surface," *Physics of Fluids*, vol. 27, no. 8, pp. 1915–1917, 1984.
- [17] J. A. Khan, M. Mustafa, T. Hayat, M. A. Farooq, A. Alsaedi, and S. Liao, "On model for three-dimensional flow of nanofluid: an application to solar energy," *Journal of Molecular Liquids*, vol. 194, pp. 41–47, 2014.
- [18] A. A. Memon, M. A. Memon, K. Bhatti, K. Nonlaopon, and I. Khan, "Simulation of non-isothermal turbulent flows through circular rings of steel," *CMC-Computers Materials & Continua*, vol. 70, no. 3, pp. 4341–4355, 2022.
- [19] A. A. Memon, M. A. Memon, K. Bhatti, T. A. Alkanhal, I. Khan, and A. Khan, "Analysis of power law fluids and the heat distribution on a facing surface of a circular cylinder embedded in rectangular channel fixed with screen: a finite element's analysis," *IEEE Access*, vol. 9, pp. 74719–74728, 2021.
- [20] N. Bachok, A. Ishak, R. Nazar, and I. Pop, "Flow and heat transfer at a general three-dimensional stagnation point in a nanofluid," *Physics B*, vol. 405, no. 24, pp. 4914–4918, 2010.
- [21] H. A. Attia, "Steady three-dimensional hydromagnetic stagnation point flow towards a stretching sheet with heat generation," *Italian Journal of Pure and Applied Mathematics*, vol. 27, pp. 9–18, 2010.
- [22] S. Mansur and A. Ishak, "Three-dimensional flow and heat transfer of a nanofluid past a permeable stretching sheet with a convective boundary condition," *AIP Conf. Proc.*, vol. 1614, pp. 906–912, 2014.
- [23] J. A. Khan, M. Mustafa, T. Hayat, and A. Alsaedi, "Numerical study on three-dimensional flow of nanofluid past a convectively heated exponentially stretching sheet," *Canadian Journal of Physics*, vol. 93, no. 10, pp. 1131–1137, 2015.
- [24] T. Hayat, M. Imtiaz, A. Alsaedi, and M. A. Kutbi, "MHD three-dimensional flow of nanofluid with velocity slip and nonlinear thermal radiation," *Journal of Magnetism and Magnetic Materials*, vol. 396, pp. 31–37, 2015.
- [25] R. Prasher, P. E. Phelan, and P. Bhattacharya, "Effect of aggregation kinetics on the thermal conductivity of nanoscale colloidal solutions (nanofluid)," *Nano Letters*, vol. 6, no. 7, pp. 1529–1534, 2006.
- [26] H. Chen, Y. Ding, Y. He, and C. Tan, "Rheological behaviour of ethylene glycol based titania nanofluids," *Chemical Physics Letters*, vol. 444, no. 4–6, pp. 333–337, 2007.
- [27] D. Zhou and A. A. Keller, "Role of morphology in the aggregation kinetics of ZnO nanoparticles," *Water Research*, vol. 44, no. 9, pp. 2948–2956, 2010.
- [28] B. Mahanthesh, N. Srikantha, and J. Mackolil, "A study on heat transfer in three-dimensional nonlinear convective boundary layer flow of nanomaterial considering the aggregation of nanoparticles," *Heat Transfer*, vol. 51, no. 1, pp. 891–908, 2022.
- [29] M. Sedighi and A. Mohebbi, "Investigation of nanoparticle aggregation effect on thermal properties of nanofluid by a combined equilibrium and non-equilibrium molecular dynamics simulation," *Journal of Molecular Liquids*, vol. 197, pp. 14–22, 2014.
- [30] S. Z. Heris, M. A. Razbani, P. Estelle, and O. Mahian, "Rheological behavior of zinc oxide nanolubricants," *Journal of Dispersion Science and Technology*, vol. 36, no. 8, pp. 1073–1079, 2015.
- [31] J. Chen, C. Y. Zhao, and B. X. Wang, "Effect of nanoparticle aggregation on the thermal radiation properties of nanofluids: an experimental and theoretical study," *International Journal of Heat and Mass Transfer*, vol. 154, article 119690, 2020.
- [32] Y. He, Y. Jin, H. Chen, Y. Ding, D. Cang, and H. Lu, "Heat transfer and flow behaviour of aqueous suspensions of TiO<sub>2</sub> nanoparticles (nanofluids) flowing upward through a vertical pipe," *International Journal of Heat and Mass Transfer*, vol. 50, no. 11–12, pp. 2272–2281, 2007.
- [33] I. Mustafa, T. Javed, A. Ghaffari, and H. Khalil, "Enhancement in heat and mass transfer over a permeable sheet with Newtonian heating effects on nanofluid: multiple solutions using spectral method and stability analysis," *Pramana*, vol. 93, no. 4, pp. 1–13, 2019.
- [34] O. D. Makinde and A. S. Eegunjobi, "Entropy generation in a couple stress fluid flow through a vertical channel filled with saturated porous media," *Entropy*, vol. 15, no. 12, pp. 4589–4606, 2013.
- [35] M. Torabi, S. M. Ghiaasiaan, and G. P. Peterson, "The effect of Al<sub>2</sub>O<sub>3</sub>-water nanofluid on the heat transfer and entropy generation of laminar forced convection through isotropic porous media," *International Journal of Heat and Mass Transfer*, vol. 111, pp. 804–816, 2017.
- [36] D. Toghraie, M. Mahmoudi, O. A. Akbari, F. Pourfattah, and M. Heydari, "The effect of using water/CuO nanofluid and L-shaped porous ribs on the performance evaluation criterion of microchannels," *Journal of Thermal Analysis and Calorimetry*, vol. 135, no. 4, pp. 145–159, 2018.



- [37] B. Mahanthesh, C. Srinivas Reddy, N. Srikantha, and G. Lorenzini, "Entropy generation analysis of radiative heat transfer in Williamson fluid flowing in a microchannel with nonlinear mixed convection and joule heating," *Proceedings of the Institution of Mechanical Engineers, Part E: Journal of Process Mechanical Engineering*, 2022.
- [38] A. Zeeshan, M. Hassan, R. Ellahi, and M. Nawaz, "Shape effect of nanosize particles in unsteady mixed convection flow of nanofluid over disk with entropy generation," *Proceedings of the Institution of Mechanical Engineers, Part E: Journal of Process Mechanical Engineering*, vol. 231, no. 4, pp. 871–879, 2016.
- [39] D. Lu, Z. Li, M. Ramzan, A. Shafee, and J. D. Chung, "Unsteady squeezing carbon nanotubes based nano-liquid flow with Cattaneo-Christov heat flux and homogeneous-heterogeneous reactions," *Applied Nanoscience*, vol. 9, no. 2, pp. 169–178, 2019.
- [40] K. A. Yih, "Uniform suction/blowing effect on forced convection about a wedge: uniform heat flux," *Acta Mechanica*, vol. 128, no. 3-4, pp. 173–181, 1998.

## Retraction

# Retracted: The Mathematical Analysis of the New Fractional Order Ebola Model

### Journal of Nanomaterials

Received 20 June 2023; Accepted 20 June 2023; Published 21 June 2023

Copyright © 2023 Journal of Nanomaterials. This is an open access article distributed under the Creative Commons Attribution License, which permits unrestricted use, distribution, and reproduction in any medium, provided the original work is properly cited.

This article has been retracted by Hindawi following an investigation undertaken by the publisher [1]. This investigation has uncovered evidence of one or more of the following indicators of systematic manipulation of the publication process:

1. Discrepancies in scope
2. Discrepancies in the description of the research reported
3. Discrepancies between the availability of data and the research described
4. Inappropriate citations
5. Incoherent, meaningless and/or irrelevant content included in the article
6. Peer-review manipulation

The presence of these indicators undermines our confidence in the integrity of the article's content and we cannot, therefore, vouch for its reliability. Please note that this notice is intended solely to alert readers that the content of this article is unreliable. We have not investigated whether authors were aware of or involved in the systematic manipulation of the publication process.

Wiley and Hindawi regrets that the usual quality checks did not identify these issues before publication and have since put additional measures in place to safeguard research integrity.

We wish to credit our own Research Integrity and Research Publishing teams and anonymous and named external researchers and research integrity experts for contributing to this investigation.

The corresponding author, as the representative of all authors, has been given the opportunity to register their agreement or disagreement to this retraction. We have kept a record of any response received.

### References

- [1] F. M. Khan, A. Ali, E. Bonyah, and Z. U. Khan, "The Mathematical Analysis of the New Fractional Order Ebola Model," *Journal of Nanomaterials*, vol. 2022, Article ID 4912859, 12 pages, 2022.

## Research Article

# The Mathematical Analysis of the New Fractional Order Ebola Model

Faiz Muhammad Khan,<sup>1</sup> Amjad Ali,<sup>1</sup> Ebenezer Bonyah <sup>2</sup> and Zia Ullah Khan<sup>1</sup>

<sup>1</sup>Department of Mathematics and Statistics, University of Swat, Khyber Pakhtunkhwa, Pakistan

<sup>2</sup>Department of Mathematics Education, Akenen Appiah Menka University of Skills Training and Entrepreneurial Development, (Kumasi Campus), Ghana

Correspondence should be addressed to Ebenezer Bonyah; [ebonyah@aamusted.edu.gh](mailto:ebonyah@aamusted.edu.gh)

Received 11 October 2021; Accepted 25 May 2022; Published 25 June 2022

Academic Editor: Mohammad Rahimi-Gorji

Copyright © 2022 Faiz Muhammad Khan et al. This is an open access article distributed under the Creative Commons Attribution License, which permits unrestricted use, distribution, and reproduction in any medium, provided the original work is properly cited.

This research study focuses on the analytical behavior and numerical computation of the fractional order Ebola model. In this study we have calculated the conditions for the existence, uniqueness, and stability of the solution with the help of the fixed point results. In addition to this, we calculated the numerical solution of the fractional order smoke model with the help two-step fractional Adam's Bashforth method using the Caputo's fractional derivative of order  $\mu$ . Furthermore, the results obtained for different orders of the fractional derivative  $\mu$  have been shown graphically with the help of Matlab.

## 1. Introduction

The concept of fractional calculus (FC) was raised in seven century from famous correspondence between Leibniz and L'Hôpital. In the consequences of aforementioned correspondence, Leibniz wrote a letter to Guillaume de L'Hôpital that what will be the half order derivative of dependent variable  $y$  w.r.t  $x$ , i.e.  $d^{1/2}x/dy^{1/2}$ . In the response, he wrote that this will bear some useful consequence in near future. Later on, it was traced that fractional calculus was introduced by Abel in one of his papers, where the author discussed the idea of fractional-order derivatives (FOD), fractional-order integration (FOI), and the mutual inverse relationship between them [1]. In 1832, one of the greatest French mathematicians (of his era) Liouville presented the definitions for the fractional derivative and fractional integration named as Riemann-Liouville fractional derivative and integration [2]. Later, on in 1890, Heaviside practically used the fractional differential operator in electrical transmission line analysis circa [3]. Recently, the researchers of the 19th and 20th century have made their significant contributions to introduce new definitions of fractional differential

and integral operators and in the study of the practical applications of FC [4].

In modern era, the uses of FC in various engineering problems have been raised [5–7] 2014). For instance, FC has various applications in different diffusion phenomenon including heat transfer, gaseous exchange, and water transfer through permeable materials [8–11]. Bagley and Torvik presented FC as an instrument for displaying tissue viscoelasticity during the 1980s (Uchaikin, 2013). Study of intricacy gives another view to a few genuine wonders which appeared to be odd, and during the most recent years, new strategies have been utilized to separate secret properties of complex frameworks [12]. Further, a variety of FC tools have been widely used in several complex phenomena [13–15]. In some circumstances, FC has been perceived for taking care of issues in viscoelasticity, electrochemistry, and dispersion [16–19]. A few analysts featured FC as a tool for examination of complex phenomenon by bringing the techniques of FC and its applications to a more extensive crowd [20, 21].

The technique by which a real world problem is described in mathematical concepts or language is known as mathematical modeling [22]. Mathematical modeling of

infectious diseases has been the main focus for the scientists and researchers over the last two decades. Mathematical modelers used to model the infectious diseases in the form of mathematical models consist of classical differential equations (CDEs). Recently, the researchers have diverted their focus to model the diseases in the form of fractional differential equations (FDEs) which has the potential to describe the real world phenomena more accurate and considered reliable as compared to the conventional derivatives. FDEs are global in nature, more realistic, and give great degree of freedom to modelers as compared to the CDEs. Modeling via FDEs has produced highly influential results in the investigation of transmission of the infectious diseases models [23, 24].

In the year 1976, a flare-up occurred in African nation of the Democratic Republic of Congo (DRC), which was then termed after the name of the lake “Ebola” flows near to the DRC. The infection has five sorts, four out of these five spread illnesses in people. The infection use to attack on the immune system which then cause internal bleeding and affect each organ of the individuals. This terrifying infection spread by contacting directly with the tainted individuals either via body fluids or direct skin contact. The infection can also be pass through connection with the creatures like monkeys, etc. Nonetheless, the infection cannot be transmit through air and food. Later on, in 2013, the infection arose in Guck-duo and Guinea, where 28,616 casualties were reported, and out of these casualties, 11,310 lost their lives. Today, where the advanced world is confronting another pandemic flare-up as COVID-19, the investigation of such irresistible sicknesses is still a center of focus for the researchers [25].

## 2. Model Formulation

In this section of the article, we have presented the formulation of the model, which we will be studying in this paper. For this, we have considered a population and divided it into five different compartments with some assumptions. The assumptions considered for the formulation of the model are stated below

- (i)  $\mathbb{S}$ : the first class of the model has been named as susceptible class. This class contains individuals who have no symptoms or any infection of the disease but can be attacked by the virus
- (ii)  $\mathbb{E}$ : the second class of the population has been named as exposed class. This class contains individuals who have been attacked by the virus but not yet shown the symptoms of the infection or not yet infectious
- (iii)  $\mathbb{I}$ : this is the third class of the population containing individuals who have been attacked by the virus and are being able to transfer the disease to not yet attacked individuals of the populations
- (iv)  $\mathbb{V}$ : this class has been named as vaccinated class containing those individuals of the susceptible class who have been vaccinated against the virus

- (v)  $\mathbb{R}$ : this class is the recovered class which contains those individuals who have survived the disease

The transition or transfer among the compartments has been considered in the following manner

- (i)  $\mathbb{S} \xrightarrow{\tau} \mathbb{E}$ : an individual of the population  $\mathbb{S}$  move to the population  $\mathbb{E}$  through the rate  $\tau_1$
- (ii)  $\mathbb{S} \xrightarrow{\beta} \mathbb{I}$ : an individual of the class  $\mathbb{S}$  joins the class  $\mathbb{I}$  with the rate  $\beta$  after getting infectious
- (iii)  $\mathbb{S} \xrightarrow{\psi} \mathbb{V}$ : the given parameter is used for the rate of the vaccination which transfer an individual from  $\mathbb{S}$  to  $\mathbb{V}$
- (iv)  $\mathbb{I} \xrightarrow{\xi} \mathbb{R}$ : the rate of transfer of the individuals from  $\mathbb{I}$  to  $\mathbb{R}$  after surviving the disease

$$\begin{aligned} \frac{d\mathbb{S}}{dt} &= \Lambda - d_0\mathbb{S}(t) - \tau_1\mathbb{S}(t)\mathbb{E}(t) - \beta\mathbb{S}(t)\mathbb{I}(t) - \psi\mathbb{S}(t) \\ \frac{d\mathbb{E}}{dt} &= \tau_1\mathbb{S}(t)\mathbb{E}(t) - (d_0 + d_1 + \kappa)\mathbb{E}(t) \\ \frac{d\mathbb{I}}{dt} &= \beta\mathbb{S}(t)\mathbb{I}(t) + \kappa\mathbb{E}(t) - \xi\mathbb{I}(t) - (d_0 + d_2)\mathbb{I}(t) \\ \frac{d\mathbb{V}}{dt} &= \psi\mathbb{S}(t) - d_0\mathbb{V}(t) \\ \frac{d\mathbb{R}}{dt} &= \xi\mathbb{I}(t) - d_0\mathbb{R}(t) \end{aligned} \quad (1)$$

And the corresponding fractional form of the system (1) is

$$\begin{aligned} {}^c D^\mu \mathbb{S}(t) &= \Lambda - d_0\mathbb{S}(t) - \tau\mathbb{S}(t)\mathbb{E}(t) - \beta\mathbb{S}(t)\mathbb{I}(t) - \psi\mathbb{S}(t) \\ {}^c D^\mu \mathbb{E}(t) &= \tau\mathbb{S}(t)\mathbb{E}(t) - (d_0 + d_1 + \kappa)\mathbb{E}(t) \\ {}^c D^\mu \mathbb{I}(t) &= \beta\mathbb{S}(t)\mathbb{I}(t) + \kappa\mathbb{E}(t) - \xi\mathbb{I}(t) - (d_0 + d_2)\mathbb{I}(t) \\ {}^c D^\mu \mathbb{V}(t) &= \psi\mathbb{S}(t) - d_0\mathbb{V}(t) \\ {}^c D^\mu \mathbb{R}(t) &= \xi\mathbb{I}(t) - d_0\mathbb{R}(t) \end{aligned} \quad (2)$$

The paper has been organized as follows: the first section of the paper contains introduction. The second section has been restricted to the formulation of the model, while the third section has been devoted to the preliminaries. The fourth section of the paper contains the existence and uniqueness of the solution of the model. The fifth section of the paper includes the stability of the solution, while the sixth section contains qualitative study where we formulated the disease free, disease endemic, and basic reproduction number  $R_0$  and then test the stability of the  $R_0$  locally with the help of theorems. In the seventh section, we have formulated the numerical solution of the model via Adam's

Bashforth scheme, and the eighth section contains the numerical simulation of the results obtained in the section seventh. At last, we have concluded our work in the conclusion section.

### 3. Preliminaries

In this section of the present article, we provide some basic definitions, theorems, and results that will be used and fruitful in understanding the rest of the article.

*Definition 1.* (see [26]). The Caputo’s fractional differential operator of any arbitrary order  $\mu > 0$  is defined as

$${}^c D^\mu \theta(t) = \frac{1}{\Gamma(n-\mu)} \int_0^t f(s, \theta(s))^n (t-s)^{n-\mu-1} ds. \quad (3)$$

**Lemma 2.** (see [27]). “The following result holds for fractional differential equations

$$I^\mu [{}^c D^\mu \theta(t)] = \theta(t) + \alpha_0 + \alpha_1 t + \alpha_2 t^2 + \dots + \alpha_{m-1} t^{m-1}, \quad (4)$$

for arbitrary  $\alpha_i \in R, i = 0, 1, 2, 3, \dots, m-1$ , where  $m = [\mu] + 1$  and  $[\mu]$  symbolizes the integer part of  $\mu$ ”.

**Lemma 3.** (see [28]). Let  $\theta \in AC^n[0, T], \mu > 0$ , and  $n = [\mu]$ , then the following result holds

$$I^\mu [{}^c D^\mu \theta(\vartheta)] = \theta(\vartheta) - \sum_{j=0}^{n-1} \frac{D^j \theta(a)}{j!} (t-a)^j. \quad (5)$$

**Lemma 4.** (see [28]). In view of Lemma 3, the solution of  $\mathbb{D}^\mu \theta(t) = y(t), n-1 < \mu < n$  is given by

$$\theta(t) = I^\mu y(t) + c_0 + c_1 t + c_2 t^2 + \dots + c_{n-1} t^{n-1}, \quad (6)$$

where  $c_j \in R$ .

*Definition 5.* (see [26]). Suppose we have Caputo’s fractional differential equation of order  $\mu$

$${}^c D^\mu \theta(t) = f(t, \theta(t)), \quad (7)$$

then the solution is given as

$$\begin{aligned} \theta(t_{n+}) &= \theta(t_n) + \frac{f(t_n, \theta_n)}{h\Gamma(\mu)} \left\{ \frac{2h}{\mu} t_{n+1}^\mu - \frac{t_{n+1}^{\mu+1}}{\mu+1} + \frac{h}{\mu} t_n^\mu - \frac{t_n^{\mu+1}}{\mu} \right\} \\ &\quad + \frac{f(t_{n-1}, \theta_{n-1})}{h\Gamma(\mu)} \left\{ \frac{h}{\mu} t_{n+1}^\mu - \frac{t_{n+1}^{\mu+1}}{\mu+1} + \frac{t_n^\mu}{\mu+1} \right\} + R_n^\mu(t), \end{aligned} \quad (8)$$

where  $R_n^\mu(t)$  represent the remainder term. For the study of convergence and uniqueness of the solution of the scheme, we refer to ([26]).

**Theorem 6.** (see [29]). “Let  $X$  be a Banach space and  $\mathfrak{P} : X \rightarrow X$  is compact and continuous, if the set,

$$E = \{\theta \in X : \theta = m\mathfrak{P}\theta, m \in (0, 1)\}, \quad (9)$$

is bounded, then  $\mathfrak{P}$  has a unique fixed point.”

### 4. Existence of the Solution

In this section of the paper, we construct the conditions for the existence and uniqueness of the solution, and to get the desired results, we construct the following function.

$$\begin{cases} \vartheta_1(t, \mathbb{S}, \mathbb{E}, \mathbb{I}, \mathbb{V}, \mathbb{R}) = \Lambda - d_0 \mathbb{S}(t) - \tau \mathbb{S}(t) \mathbb{E}(t) - \beta \mathbb{S}(t) \mathbb{I}(t) - \psi \mathbb{S}(t), \\ \vartheta_2(t, \mathbb{S}, \mathbb{E}, \mathbb{I}, \mathbb{V}, \mathbb{R}) = \tau \mathbb{S}(t) \mathbb{E}(t) - (d_0 + d_1 + \kappa) \mathbb{E}(t), \\ \vartheta_3(t, \mathbb{S}, \mathbb{E}, \mathbb{I}, \mathbb{V}, \mathbb{R}) = \beta \mathbb{S}(t) \mathbb{I}(t) + \kappa \mathbb{E}(t) - \xi \mathbb{I}(t) - (d_0 + d_2) \mathbb{I}(t), \\ \vartheta_4(t, \mathbb{S}, \mathbb{E}, \mathbb{I}, \mathbb{V}, \mathbb{R}) = \psi \mathbb{S}(t) - d_0 \mathbb{V}(t), \\ \vartheta_5(t, \mathbb{S}, \mathbb{E}, \mathbb{I}, \mathbb{V}, \mathbb{R}) = \xi \mathbb{I}(t) - d_0 \mathbb{R}(t). \end{cases} \quad (10)$$

Suppose that the considered space  $C[0, T] = \mathbb{B}$  be a Banach space with norm

$$\|\theta(t)\| = \sup_{t \in [0, T]} [|\mathbb{S}(t)| + |\mathbb{E}(t)| + |\mathbb{I}(t)| + |\mathbb{V}(t)| + |\mathbb{R}(t)|], \quad (11)$$

where

$$\theta(t) = \begin{cases} \mathbb{S}(t) \\ \mathbb{E}(t) \\ \mathbb{I}(t) \\ \mathbb{V}(t) \\ \mathbb{R}(t) \end{cases}, \theta_0(t) = \begin{cases} \mathbb{S}^0 \\ \mathbb{E}^0 \\ \mathbb{I}^0 \\ \mathbb{V}^0 \\ \mathbb{R}^0 \end{cases}, \mathfrak{Z}(t, \theta(t)) = \begin{cases} \vartheta_1(t, \mathbb{S}, \mathbb{E}, \mathbb{I}, \mathbb{V}, \mathbb{R}) \\ \vartheta_2(t, \mathbb{S}, \mathbb{E}, \mathbb{I}, \mathbb{V}, \mathbb{R}) \\ \vartheta_3(t, \mathbb{S}, \mathbb{E}, \mathbb{I}, \mathbb{V}, \mathbb{R}) \\ \vartheta_4(t, \mathbb{S}, \mathbb{E}, \mathbb{I}, \mathbb{V}, \mathbb{R}) \\ \vartheta_5(t, \mathbb{S}, \mathbb{E}, \mathbb{I}, \mathbb{V}, \mathbb{R}) \end{cases}. \quad (12)$$

With the help of (12), the system (1) can be written in as

$$\begin{aligned} {}^c D^\mu \theta(t) &= \mathfrak{Z}(t, \theta(t)), t \in [0, T], \\ \theta(0) &= \theta_0, \end{aligned} \quad (13)$$

By Lemma 2, equation (13) converts into the following form

$$\theta(t) = \theta_0 + \int_0^t \frac{(t-s)^{\mu-1}}{\Gamma(\mu)} \mathfrak{Z}(s, \theta(s)) ds, t \in J = [0, T]. \quad (14)$$

To prove the existence of the solution, we make the following assumptions:

(P1)  $\exists$  constants  $K_1^*, M_1^* \geq 0$

$$|\mathfrak{Z}(t, \theta(t))| \leq K_1^* |\theta|^q + M_1^*. \quad (15)$$

(P2)  $\exists L_* > 0$ ,  $\ni$  for each  $\theta, \bar{\theta}$

$$\left| \mathfrak{Z}(t, \theta) - \mathfrak{Z}(t, \bar{\theta}) \right| \leq L_* \left\| \theta - \bar{\theta} \right\|. \quad (16)$$

And let  $\mathfrak{P} : \mathbb{B} \rightarrow \mathbb{B}$  be an operator as

$$\mathfrak{P}\theta(t) = \theta_0 + \int_0^t \frac{(t-s)^{\mu-1}}{\Gamma(\mu)} \mathfrak{Z}(s, \theta(s)) ds. \quad (17)$$

**Theorem 7.** *When the assumptions (P1) and (P2) are true, it verifies that the problem (13) has at least of one fixed point which also implies that the problem of our study has also at least one solution.*

*Proof.* Furthermore we proceed as.  $\square$

*Step 1.* First, we have to show that  $\mathfrak{P}$  is continuous. To acquire the results, we suppose that  $\mathfrak{Z}_j$  is continuous for  $j = 1, 2, 3, 4, 5, 6$ . Which implies that  $\mathfrak{Z}(s, \theta(s))$  is also continuous. Assume  $\theta_n, \theta \in X \ni \theta_n \rightarrow \theta$ , we must have  $\mathfrak{P}\theta_n \rightarrow \mathfrak{P}\theta$ .

For this, we consider

$$\begin{aligned} \|\mathfrak{P}\theta_n - \mathfrak{P}\theta\| &= \max_{t \in J=[0, T]} \left| \int_0^t \frac{(t-s)^{\mu-1}}{\Gamma(\mu)} \mathfrak{Z}_n(s, \theta_n(s)) ds \right. \\ &\quad \left. - \frac{1}{\Gamma(\mu)} \int_0^t (t-s)^{\mu-1} \mathfrak{Z}(s, \theta(s)) ds \right| \\ &\leq \max_{t \in J=[0, T]} \int_0^t \frac{(t-s)^{\mu-1}}{\Gamma(\mu)} \left| \mathfrak{Z}_n(s, \theta_n(s)) - \mathfrak{Z}(s, \theta(s)) \right| \\ &\quad \cdot ds \leq \frac{T^\mu}{\Gamma(\mu+1)} \|\mathfrak{Z}_n - \mathfrak{Z}\| \rightarrow 0 \text{ as } n \rightarrow \infty. \end{aligned} \quad (18)$$

As  $\mathfrak{Z}$  is continuous, therefore  $\mathfrak{P}\theta_n \rightarrow \mathfrak{P}\theta$ , yields that  $\mathfrak{P}$  is continuous.

*Step 2.* Now, to prove that  $\mathfrak{P}$  is bounded for any  $\theta \in \mathbb{X}$ , we make of the supposition that  $\mathfrak{P}$  satisfies the growth condition:

$$\begin{aligned} \|\mathfrak{P}\theta\| &= \max_{t \in [0, T]} \left| \theta_0 + \frac{1}{\Gamma(\mu)} \int_0^t (t-s)^{\mu-1} \mathfrak{Z}(s, \theta(s)) ds \right| \\ &\leq |\theta_0| + \max_{t \in [0, T]} \frac{1}{\Gamma(\mu)} \int_0^t (t-s)^{\mu-1} \|\mathfrak{Z}(s, \theta(s))\| ds, \quad (19) \\ &\leq |\theta_0| + \frac{T^\mu}{\Gamma(\mu+1)} [K_1^* \|\theta\|^q + M_1^*]. \end{aligned}$$

Here, we assume a  $\mathcal{S}$ , the subset of  $\mathbb{X}$  with the property of boundedness, and we need to prove that  $\mathfrak{P}(\mathcal{S})$  is also bounded. To reach our destination, we assume that for any  $\theta \in \mathcal{S}$ , now as  $\mathcal{S}$  is bounded, so  $\exists K_q \geq 0 \ni$

$$\|\theta\| \leq K_q, \forall \theta \in \mathcal{S}. \quad (20)$$

Further, for any  $\theta \in \mathcal{S}$  by using the growth condition, we have

$$\begin{aligned} \|\mathfrak{P}\theta\| &\leq |\theta_0| + \frac{T^\mu}{\Gamma(\mu+1)} [K_1^* \|\theta\|^q + M_1^*] \\ &\leq |\theta_0| + \frac{T^\mu}{\Gamma(\mu+1)} [K_1^* K_q^q + M_1^*]. \end{aligned} \quad (21)$$

Therefore,  $\mathfrak{P}(\mathcal{S})$  is bounded.

*Step 3.* Here, we attempt to prove that the operator we defined is equicontinuous, for this we assume that  $t_2 \leq t_1 \in J = [0, T]$ , then

$$\begin{aligned} |\mathfrak{P}\theta(t_1) - \mathfrak{P}\theta(t_2)| &= \left| \frac{1}{\Gamma(\mu)} \int_0^{t_1} (t_1-s)^{\mu-1} \mathfrak{Z}(s, \theta(s)) ds \right. \\ &\quad \left. - \frac{1}{\Gamma(\mu)} \int_0^{t_2} (t_2-s)^{\mu-1} \mathfrak{Z}(s, \theta(s)) ds \right| \\ &\leq \left| \frac{1}{\Gamma(\mu)} \int_0^{t_1} (t_1-s)^{\mu-1} - \frac{1}{\Gamma(\mu)} \int_0^{t_2} (t_2-s)^{\mu-1} \right| \\ &\quad \cdot |\mathfrak{Z}(s, \theta(s))| ds, \\ &\leq \frac{T^\mu}{\Gamma(\mu+1)} [K_1^* \|\theta\|^q + M_1^*] |t_1 - t_2|. \end{aligned} \quad (22)$$

By taking advantage of Arzelà-Ascoli theorem, we can say that  $\mathfrak{P}(\mathcal{S})$  is relative compact.

*Step 4.* In this step, we need to prove that the set defined below is bounded

$$E = \{\theta \in X : \theta = m\mathfrak{P}\theta, \quad m \in (0, 1)\}. \quad (23)$$

To prove this, we suppose that  $\theta \in E$ ,  $\ni$  for each  $t \in J$ , where  $J = [0, T]$  we have

$$\|\theta\| = m \|\mathfrak{P}\theta\| \leq m \left[ |\theta_0| + \frac{T^\mu}{\Gamma(\mu+1)} [K_1^* \|\theta\|^q + M_1^*] \right]. \quad (24)$$

From here, we can claim that the set defined above is bounded. By using Schaefer's FPT, the operator we defined, i.e.,  $\mathfrak{P}$  has atleast one fixed point, and hence, the model we studied in this paper has at least one solution.

**Theorem 8.** *The problem (13) is unique solution, if  $T^\mu K_1^* / \Gamma(\mu+1) < 1$ .*

*Proof.* Let  $\theta, \bar{\theta} \in X$ , then

$$\begin{aligned} \|\mathfrak{P}\theta - \mathfrak{P}\bar{\theta}\| &\leq \max_{t \in J=[0, T]} \int_0^t \frac{(t-s)^{\mu-1}}{\Gamma(\mu)} \left| \mathfrak{F}(s, \theta(s)) - \mathfrak{F}(s, \bar{\theta}(s)) \right| ds, \\ &\leq \frac{T^\mu L_{\mathfrak{F}}}{\Gamma(\mu+1)} \|\theta - \bar{\theta}\|. \end{aligned} \quad (25)$$

□

Hence, we can say that the fixed point is unique, and therefore, our solution is unique.

## 5. Stability Results

To prove that the solution of the considered model is stable, we use the concept of Ulam and Ulam Hyer stability. To get the desired results we proceed as

Assume  $\mathcal{L} : \mathbb{X} \rightarrow X$  be an operator which satisfy

$$\theta = \mathcal{L}(\theta), \text{ where } \theta \in X. \quad (26)$$

*Definition 9.* (see [27]). Equation (26) has UH-stability, if for  $\varsigma_1 > 0$  and assume any solution  $\theta \in \mathcal{L}$  for the inequality given by

$$\|\theta - \mathcal{L}\theta\| \leq \varsigma_1, \forall t \in J = [0, T], \quad (27)$$

and the unique solution  $\bar{\theta}$  for (25) with  $C_q^* > 0$ , such that

$$\|\bar{\theta} - \theta\| \leq C_q^* \varsigma_1, \forall t \in [0, T]. \quad (28)$$

*Definition 5.2.* “If  $\exists \vartheta \in C(R, R)$  with  $\vartheta(0) = 0$ ,” for unique result  $\bar{\theta}$  and any solution of equation (26)  $\ni$

$$\|\bar{\theta} - \theta\| \leq \vartheta(\varsigma_1), \quad (29)$$

then equation (26) has GUH-stability.

*Remark 10.* (see [27]). “If  $\exists \zeta_1^{**}(t) \in C([0, T], R)$ , then  $\bar{\theta} \in X$  satisfies (27) if

- (i)  $|\zeta_1^{**}(t)| \leq \varsigma_1, \forall t \in [0, T]$
- (ii)  $\mathcal{L}\bar{\theta}(t) = \bar{\theta} + \zeta_1^{**}(t), \forall t \in [0, T]$ ”

For further analysis, we suppose that the following is the solution of the perturbed problem of (13)

$$\begin{cases} {}^C D_{+0}^\mu \theta(t) = \mathfrak{F}(t, \theta(t)) + \zeta_1^{**}(t), \\ \theta(0) = \theta_0. \end{cases} \quad (30)$$

**Lemma 11.** *The result stated below holds true for equation (30),*

$$|\theta(t) - \mathfrak{P}\theta(t)| \leq a\varsigma_1, \text{ where } a = \frac{T^\mu}{\Gamma(\mu+1)} \quad (31)$$

**Theorem 12.** *By making use of Lemma 11, the solution of the problem (13) is UH-stable as well as GUH-stable, if  $T^\mu L_\omega / \Gamma(\mu+1) < 1$ .*

*Proof.* Assume  $\theta, \bar{\theta} \in X$  be any and unique solutions, respectively, problem (13), then

$$\begin{aligned} |\theta(t) - \bar{\theta}(t)| &= |\theta(t) - \mathfrak{P}\bar{\theta}(t)|, \leq |\theta(t) - \mathfrak{P}\theta(t)| \\ &+ |\mathfrak{P}\theta(t) - \mathfrak{P}\bar{\theta}(t)|, \leq a\varsigma_1 \\ &+ \frac{T^\mu L_\theta}{\Gamma(\mu+1)} |\theta(t) - \bar{\theta}(t)|, \\ &\leq \frac{a\varsigma_1}{1 - T^\mu L_\theta / \Gamma(\mu+1)}. \end{aligned} \quad (32)$$

From here, we claim that the solution of (13) is UH and GUH stability if

$$Y(\varsigma_1) = \frac{a\varsigma_1}{1 - T^\mu L_\theta / \Gamma(\mu+1)}. \quad (33)$$

Such that  $Y(0) = 0$ . □

*Definition 13.* The UHR-Stability of (26) is ensured for  $g^* \in C([0, T], R)$ , if for  $\varsigma_1 > 0$  and assume  $\theta \in X$  be any solution of the inequality expressed by

$$\|\theta - H\theta\| \leq g(t)\varsigma_1. \quad (34)$$

$\exists$  a unique solution  $\bar{\theta}$  of (26) with  $\mathcal{K}'_q > 0$

$$\|\bar{\theta} - \theta\| \leq \mathcal{K}'_q g^*(t)\varsigma_1, \quad \forall t \in [0, T]. \quad (35)$$

*Definition 14.* (see [27]). “For  $g^* \in C[0, T], R$ ], if  $\exists \mathcal{K}'_{q,g}$  and for  $\varsigma_1 > 0$ , consider that  $\theta$  be any solution of (34) and  $\bar{\theta}$  be any solution of (26)  $\ni$

$$\|\bar{\theta} - \theta\| \leq \mathcal{K}'_{q,g} g^*(t), \forall t \in J = [0, T], \quad (36)$$

then equation (26) is generalized UHR stable.”

*Remark 15.* If  $\exists \zeta_1^{**}(t) \in C(J, R)$ , then for  $\bar{\theta} \in X$  (27) holds, if

- (i)  $|\zeta_1^{**}(t)| \leq \varsigma_1 \omega(t), \forall t \in J$
- (ii)  $\mathcal{L}\bar{\theta}(t) = \bar{\theta} + \zeta_1^{**}(t), \forall t \in J$

**Lemma 16.** *The stated result below holds true for (30)*

$$|\theta(t) - \mathfrak{P}\theta(t)| \leq a\omega(t)\varsigma_1, \quad a = \frac{T^\mu}{\Gamma(\mu+1)} \quad (37)$$

*Proof.* The proof has been left for the readers. □

**Theorem 17.** *With the help of Lemma 16, our solution is Ulam and Generalized Ulam stable if  $T^\mu L_\theta/\Gamma(\mu+1) < 1$ .*

*Proof.* Assume  $\theta, \bar{\theta} \in X$  be two solutions such that  $\theta$  is any and any and  $\bar{\theta}$  is the unique solution of our problem, then

$$\begin{aligned} |\theta(t) - \bar{\theta}(t)| &= |\theta(t) - \mathfrak{P}\bar{\theta}(t)|, \leq |\theta(t) - \mathfrak{P}\theta(t)| \\ &+ |\mathfrak{P}\theta(t) - \mathfrak{P}\bar{\theta}(t)|, \leq a\omega(t)\varsigma_1 + \frac{T^\mu L_\theta}{\Gamma(\mu+1)} \\ &\cdot |\theta(t) - \bar{\theta}(t)|, \leq \frac{a\omega(t)\varsigma_1}{1 - T^\mu L_\theta/\Gamma(\mu+1)}. \end{aligned} \quad (38)$$

□

Hence, the solution possesses both type of the stabilities.

## 6. Qualitative Study

In this section of the article, we present disease free equilibrium, disease endemic equilibrium, the basic reproduction number  $R_0$ , and the local asymptotical stability of the  $R_0$ . To proceed, we first find the disease free equilibrium and disease endemic equilibrium of the model. The disease free equilibrium is given as  $S^0 = (\Lambda/d_0 + \psi, 0, 0, 0, 0)$ , while the endemic equilibrium is given below.

**6.1. Endemic Equilibrium.** The endemic equilibrium of the model is given as

$$\begin{aligned} S^* &= \frac{d_0 + d_1 + \kappa}{\tau}, \\ E^* &= \frac{1}{\tau\kappa} (\tau(\xi + d_0 + d_2) - \beta(d_0 + d_1 + \kappa))I^*, \\ I^* &= \left( \frac{\Lambda\tau}{d_0 + d_1 - \kappa} - (d_0 + \psi) \right) \left( \frac{\kappa}{\tau(\xi + d_0 + d_2) - \beta(d_0 + d_1 + \kappa) - \kappa\beta} \right), \\ V^* &= \frac{\psi}{d_0} \left( \frac{d_0 + d_1 - \kappa}{\tau} \right), \\ R^* &= \frac{\xi}{d_0} R^*. \end{aligned} \quad (39)$$

**6.2. The Basic Reproduction Number.** To find  $R_0$ , we construct two vectors such as

$$\mathcal{F} = \begin{bmatrix} f_1 \\ f_2 \end{bmatrix} = \begin{bmatrix} \tau\mathcal{S}(t)\mathbb{E}(t) \\ \beta\mathcal{S}(t)\mathbb{I}(t) \end{bmatrix}, \quad (40)$$

$$\mathcal{V} = \begin{bmatrix} v_1 \\ v_2 \end{bmatrix} = \begin{bmatrix} (d_0 + d_1 + \kappa)\mathbb{E}(t) \\ (\xi + d_0 + d_2)\mathbb{I}(t) - \kappa\mathbb{E}(t) \end{bmatrix}. \quad (41)$$

Now, we present the Jacobian of both the matrix, i.e.,

$$J_{\mathcal{F}} = \begin{bmatrix} \tau\mathcal{S}(t) & 0 \\ 0 & \beta\mathcal{S}(t) \end{bmatrix}, \quad (42)$$

$$J_{\mathcal{V}} = \begin{bmatrix} d_0 + d_1 + \kappa & 0 \\ -\kappa & \xi + d_0 + d_2 \end{bmatrix}. \quad (43)$$

with

$$(J_{\mathcal{V}})^{-1} = \begin{bmatrix} \frac{1}{d_0 + d_1 + \kappa} & 0 \\ \frac{\kappa}{(\xi + d_0 + d_2)(d_0 + d_1 + \kappa)} & \frac{1}{\xi + d_0 + d_2} \end{bmatrix}. \quad (44)$$

Now, to find the next generation matrix (NGM), we find the product of  $J_{\mathcal{F}}$  and  $(J_{\mathcal{V}})^{-1}$ , i.e.,

$$\text{NGM} = \begin{bmatrix} \frac{\tau\mathcal{S}(t)}{d_0 + d_1 + \kappa} & 0 \\ \frac{\beta\mathcal{S}(t)\kappa}{(\xi + d_0 + d_2)(d_0 + d_1 + \kappa)} & \frac{\beta\mathcal{S}(t)}{\xi + d_0 + d_2} \end{bmatrix}. \quad (45)$$

Clearly, the eigen values are (say)  $\lambda_1$  and  $\lambda_2$  which are given as  $\lambda_1 = \tau\mathcal{S}(t)/d_0 + d_1 + \kappa$  and  $\lambda_2 = \beta\mathcal{S}(t)/\xi + d_0 + d_2$ . Therefore, the basic reproduction number  $R_0 = \max(\lambda_1, \lambda_2)$ .

**Theorem 18.** *The basic reproduction number  $R_0$  is locally asymptotically stable at the disease free equilibrium point that is stable if  $R_0 < 1$ .*

*Proof.* For this purpose, we construct the following Jacobian.

$$A_j = \begin{bmatrix} -(d_0 + \psi) & -\tau\mathcal{S}^0 & -\beta\mathcal{S}^0 & 0 & 0 \\ 0 & \tau\mathcal{S}^0 - (d_0 + d_1 + \kappa) & 0 & 0 & 0 \\ \beta\mathcal{S}^0 & \kappa & -\xi - (d_0 + d_2) & 0 & 0 \\ \psi & 0 & 0 & -d_0 & 0 \\ 0 & 0 & \xi & 0 & -d_0 \end{bmatrix}. \quad (46)$$

Now, let the eigen values are (say)  $\lambda_1, \lambda_2, \lambda_3, \lambda_4, \lambda_5$ . Clearly  $\lambda_1 = \lambda_2 = -d_0$ ,  $\lambda_3 = \tau\mathcal{S}^0 - (d_0 + d_1 + \kappa)$ ,  $\lambda_4 = -(d_0 + \psi)$ , and  $\lambda_5 = -\beta^2\mathcal{S}^2 - (d_0 + \psi)(\xi + d_0 + d_2)$ . From  $\lambda_3$ , we have  $\tau\mathcal{S}^0/d_0 + d_1 + \kappa < 1$ , and from  $\lambda_5$ , we have  $d_0 + \psi/\beta\mathcal{S}^0 < \beta\mathcal{S}^0/\xi + d_0 + d - 2 < 1$ . Therefore,  $R_0 = \max(\lambda_3, \lambda_5) < 1$  and hence is locally asymptotically stable at the disease free equilibrium point. □

**Theorem 6.2.** *The basic reproduction number  $R_0$  is locally asymptotically stable at the endemic equilibrium point if  $R_0 > 1$ .*



*Proof.* The proof of this result can be obtained on the same manner as the proof in [30].  $\square$

### 7. Numerical Solution

This section of the article is devoted to the numerical solution of the considered model. For this, we will use the well-known two-step fractional order Adam's Bashforth method. The considered model is given as

$$\begin{aligned}
 {}^c D^\mu \mathbb{S}(t) &= \Lambda - d_0 \mathbb{S}(t) - \tau \mathbb{S}(t) \mathbb{E}(t) - \beta \mathbb{S}(t) \mathbb{I}(t) - \psi \mathbb{S}(t), \\
 {}^c D^\mu \mathbb{E}(t) &= \tau \mathbb{S}(t) \mathbb{E}(t) - (d_0 + d_1) \mathbb{E}(t), \\
 {}^c D^\mu \mathbb{I}(t) &= \beta \mathbb{S}(t) \mathbb{I}(t) + \kappa \mathbb{E}(t) - \varkappa \mathbb{I}(t) - (d_0 + d_2) \mathbb{I}(t), \\
 {}^c D^\mu \mathbb{V}(t) &= \psi \mathbb{S}(t) - d_0 \mathbb{V}(t), \\
 {}^c D^\mu \mathbb{R}(t) &= \varkappa \mathbb{I}(t) - d_0 \mathbb{R}(t).
 \end{aligned}
 \tag{47}$$

To obtain the desired results, we apply the fundamental theorem of fractional calculus to system (3) gives

$$\begin{aligned}
 \mathbb{S}(t) &= \mathbb{S}(0) + \frac{1}{\Gamma(\mu)} \int_0^t \mathcal{A}_1(\beta, \mathbb{S}(\beta))(t - \beta)^{\mu-1} d\beta, \\
 \mathbb{E}(t) &= \mathbb{E}(0) + \frac{1}{\Gamma(\mu)} \int_0^t \mathcal{A}_2(\beta, \mathbb{E}(\beta))(t - \beta)^{\mu-1} d\beta, \\
 \mathbb{I}(t) &= \mathbb{I}(0) + \frac{1}{\Gamma(\mu)} \int_0^t \mathcal{A}_3(\beta, \mathbb{I}(\beta))(t - \beta)^{\mu-1} d\beta, \\
 \mathbb{V}(t) &= \mathbb{V}(0) + \frac{1}{\Gamma(\mu)} \int_0^t \mathcal{A}_4(\beta, \mathbb{V}(\beta))(t - \beta)^{\mu-1} d\beta, \\
 \mathbb{R}(t) &= \mathbb{R}(0) + \frac{1}{\Gamma(\mu)} \int_0^t \mathcal{A}_5(\beta, \mathbb{R}(\beta))(t - \beta)^{\mu-1} d\beta.
 \end{aligned}
 \tag{48}$$

The unknown terms  $\mathcal{A}_1, \mathcal{A}_2, \mathcal{A}_3, \mathcal{A}_4, \mathcal{A}_5$  are given below. Now, for  $t = t_{n+1}$ , we get

$$\begin{aligned}
 \mathbb{S}(t_{n+1}) &= \mathbb{S}(0) + \frac{1}{\Gamma(\mu)} \int_0^{t_{n+1}} \mathcal{A}_1(t, \mathbb{S}(t))(t_{n+1} - t)^{\mu-1} dt, \\
 \mathbb{E}(t_{n+1}) &= \mathbb{E}(0) + \frac{1}{\Gamma(\mu)} \int_0^{t_{n+1}} \mathcal{A}_2(t, \mathbb{E}(t))(t_{n+1} - t)^{\mu-1} dt, \\
 \mathbb{I}(t_{n+1}) &= \mathbb{I}(0) + \frac{1}{\Gamma(\mu)} \int_0^{t_{n+1}} \mathcal{A}_3(t, \mathbb{I}(t))(t_{n+1} - t)^{\mu-1} dt, \\
 \mathbb{V}(t_{n+1}) &= \mathbb{V}(0) + \frac{1}{\Gamma(\mu)} \int_0^{t_{n+1}} \mathcal{A}_4(t, \mathbb{V}(t))(t_{n+1} - t)^{\mu-1} dt, \\
 \mathbb{R}(t_{n+1}) &= \mathbb{R}(0) + \frac{1}{\Gamma(\mu)} \int_0^{t_{n+1}} \mathcal{A}_5(t, \mathbb{R}(t))(t_{n+1} - t)^{\mu-1} dt.
 \end{aligned}
 \tag{49}$$

For  $t = t_n$ , we get the following

$$\begin{aligned}
 \mathbb{S}(t_n) &= \mathbb{S}(0) + \frac{1}{\Gamma(\mu)} \int_0^{t_n} \mathcal{A}_1(t, \mathbb{S}(t))(t_n - t)^{\mu-1} dt, \\
 \mathbb{E}(t_n) &= \mathbb{E}(0) + \frac{1}{\Gamma(\mu)} \int_0^{t_n} \mathcal{A}_2(t, \mathbb{E}(t))(t_n - t)^{\mu-1} dt, \\
 \mathbb{I}(t_n) &= \mathbb{I}(0) + \frac{1}{\Gamma(\mu)} \int_0^{t_n} \mathcal{A}_3(t, \mathbb{I}(t))(t_n - t)^{\mu-1} dt, \\
 \mathbb{V}(t_n) &= \mathbb{V}(0) + \frac{1}{\Gamma(\mu)} \int_0^{t_n} \mathcal{A}_4(t, \mathbb{V}(t))(t_n - t)^{\mu-1} dt, \\
 \mathbb{R}(t_n) &= \mathbb{R}(0) + \frac{1}{\Gamma(\mu)} \int_0^{t_n} \mathcal{A}_5(t, \mathbb{R}(t))(t_n - t)^{\mu-1} dt.
 \end{aligned}
 \tag{50}$$

By  $\mathbb{S}(t_{n+1}) - \mathbb{S}(t_n)$ ,  $\mathbb{E}(t_{n+1}) - \mathbb{E}(t_n)$ ,  $\mathbb{I}(t_{n+1}) - \mathbb{I}(t_n)$ ,  $\mathbb{V}(t_{n+1}) - \mathbb{V}(t_n)$ , and  $\mathbb{R}(t_{n+1}) - \mathbb{R}(t_n)$  in (49) and (50), we obtain

$$\begin{aligned}
 \mathbb{S}(t_{n+1}) &= \mathbb{S}(t_n) + \mathfrak{A}_{\mu,1}^1 + \mathfrak{A}_{\eta,2}^1, \\
 \mathbb{E}(t_{n+1}) &= \mathbb{E}(t_n) + \mathfrak{A}_{\mu,1}^2 + \mathfrak{A}_{\eta,2}^2, \\
 \mathbb{I}(t_{n+1}) &= \mathbb{I}(t_n) + \mathfrak{A}_{\mu,1}^3 + \mathfrak{A}_{\eta,2}^3, \\
 \mathbb{V}(t_{n+1}) &= \mathbb{V}(t_n) + \mathfrak{A}_{\mu,1}^4 + \mathfrak{A}_{\eta,2}^4, \\
 \mathbb{R}(t_{n+1}) &= \mathbb{R}(t_n) + \mathfrak{A}_{\mu,1}^5 + \mathfrak{A}_{\eta,2}^5,
 \end{aligned}
 \tag{51}$$

where

$$\begin{aligned}
 \mathfrak{A}_{\mu,1}^1 &= \frac{1}{\Gamma(\mu)} \int_0^{t_{n+1}} \mathcal{A}_1(t, \mathbb{S}(t))(t_{n+1} - t)^{\mu-1} dt, \\
 \mathfrak{A}_{\mu,1}^2 &= \frac{1}{\Gamma(\mu)} \int_0^{t_{n+1}} \mathcal{A}_2(t, \mathbb{E}(t))(t_{n+1} - t)^{\mu-1} dt, \\
 \mathfrak{A}_{\mu,1}^3 &= \frac{1}{\Gamma(\mu)} \int_0^{t_{n+1}} \mathcal{A}_3(t, \mathbb{I}(t))(t_{n+1} - t)^{\mu-1} dt, \\
 \mathfrak{A}_{\mu,1}^4 &= \frac{1}{\Gamma(\mu)} \int_0^{t_{n+1}} \mathcal{A}_4(t, \mathbb{V}(t))(t_{n+1} - t)^{\mu-1} dt, \\
 \mathfrak{A}_{\mu,1}^5 &= \frac{1}{\Gamma(\mu)} \int_0^{t_{n+1}} \mathcal{A}_5(t, \mathbb{R}(t))(t_{n+1} - t)^{\mu-1} dt. \\
 \mathfrak{A}_{\mu,2}^1 &= \frac{1}{\Gamma(\mu)} \int_0^{t_n} \mathcal{A}_1(t, \mathbb{S}(t))(t_n - t)^{\mu-1} dt, \\
 \mathfrak{A}_{\mu,2}^2 &= \frac{1}{\Gamma(\mu)} \int_0^{t_n} \mathcal{A}_2(t, \mathbb{E}(t))(t_n - t)^{\mu-1} dt, \\
 \mathfrak{A}_{\mu,2}^3 &= \frac{1}{\Gamma(\mu)} \int_0^{t_n} \mathcal{A}_3(t, \mathbb{I}(t))(t_n - t)^{\mu-1} dt, \\
 \mathfrak{A}_{\mu,2}^4 &= \frac{1}{\Gamma(\mu)} \int_0^{t_n} \mathcal{A}_4(t, \mathbb{V}(t))(t_n - t)^{\mu-1} dt, \\
 \mathfrak{A}_{\mu,2}^5 &= \frac{1}{\Gamma(\mu)} \int_0^{t_n} \mathcal{A}_5(t, \mathbb{R}(t))(t_n - t)^{\mu-1} dt.
 \end{aligned}
 \tag{52}$$

$$\begin{aligned}
 \mathfrak{A}_{\mu,2}^1 &= \frac{1}{\Gamma(\mu)} \int_0^{t_n} \mathcal{A}_1(t, \mathbb{S}(t))(t_n - t)^{\mu-1} dt, \\
 \mathfrak{A}_{\mu,2}^2 &= \frac{1}{\Gamma(\mu)} \int_0^{t_n} \mathcal{A}_2(t, \mathbb{E}(t))(t_n - t)^{\mu-1} dt, \\
 \mathfrak{A}_{\mu,2}^3 &= \frac{1}{\Gamma(\mu)} \int_0^{t_n} \mathcal{A}_3(t, \mathbb{I}(t))(t_n - t)^{\mu-1} dt, \\
 \mathfrak{A}_{\mu,2}^4 &= \frac{1}{\Gamma(\mu)} \int_0^{t_n} \mathcal{A}_4(t, \mathbb{V}(t))(t_n - t)^{\mu-1} dt, \\
 \mathfrak{A}_{\mu,2}^5 &= \frac{1}{\Gamma(\mu)} \int_0^{t_n} \mathcal{A}_5(t, \mathbb{R}(t))(t_n - t)^{\mu-1} dt.
 \end{aligned}
 \tag{53}$$

TABLE 1: The physical interpretation and numerical values of the parameters.

Parameters	Physical description	Numerical value	Source
$\Lambda$	The birth rate	0.4	Assumed
$d_0$	Natural death rate	0.7	Assumed
$d_1$	Disease death rate in $\mathbb{E}(t)$	0.075	Assumed
$d_2$	Disease death rate in $\mathbb{I}(t)$	0.35	Assumed
$\tau$	The contact rate of $\mathbb{S}(t)$ and $\mathbb{E}(t)$	0.14280	Assumed
$\kappa$	The transference rate from $\mathbb{E}(t)$ to $\mathbb{I}(t)$	0.048	Assumed
$\beta$	The contact rate of $\mathbb{S}(t)$ and $\mathbb{I}(t)$	0.35	Assumed
$\xi$	Recovery rate	0.53	Assumed
$\psi$	Vaccination rate	0.00493	Assumed

By approximating  $A_{\mu,1}^1, A_{\mu,2}^1, A_{\mu,1}^2, A_{\mu,2}^2, A_{\mu,1}^3, A_{\mu,2}^3, A_{\mu,1}^4, A_{\mu,2}^4, A_{\mu,1}^5, A_{\mu,2}^5$  with the help of Lagrange's polynomials and the plugging back in (51), we get the following solution

$$\begin{aligned} \mathbb{S}(t_{n+1}) = & \mathbb{S}(t_n) + \frac{\mathcal{A}_1(t_n, \mathbb{S}(t_n))}{\hbar\Gamma(\mu)} \left\{ \frac{2\hbar}{\mu} t_{n+1}^\mu - \frac{t_{n+1}^{\mu+1}}{\mu+1} + \frac{\hbar}{\mu} t_n^\mu - \frac{t_n^{\mu+1}}{\mu} \right\} \\ & + \frac{\mathcal{A}_1(t_{n-1}, \mathbb{S}_{n-1})}{\hbar\Gamma(\mu)} \left\{ \frac{\hbar}{\mu} t_{n+1}^\mu - \frac{t_{n+1}^{\mu+1}}{\mu+1} + \frac{t_n^\mu}{\mu+1} \right\} + \mathbb{R}_{1,n}^\mu(t), \end{aligned}$$

$$\begin{aligned} \mathbb{E}(t_{n+1}) = & \mathbb{E}(t_n) + \frac{\mathcal{A}_2(t_n, \mathbb{E}(t_n))}{\hbar\Gamma(\mu)} \left\{ \frac{2\hbar}{\mu} t_{n+1}^\mu - \frac{t_{n+1}^{\mu+1}}{\mu+1} + \frac{\hbar}{\mu} t_n^\mu - \frac{t_n^{\mu+1}}{\mu} \right\} \\ & + \frac{\mathcal{A}_2(t_{n-1}, \mathbb{E}_{n-1})}{\hbar\Gamma(\mu)} \left\{ \frac{\hbar}{\mu} t_{n+1}^\mu - \frac{t_{n+1}^{\mu+1}}{\mu+1} + \frac{t_n^\mu}{\mu+1} \right\} + \mathbb{R}_{2,n}^\mu(t), \end{aligned}$$

$$\begin{aligned} \mathbb{I}(t_{n+1}) = & \mathbb{I}(t_n) + \frac{\mathcal{A}_3(t_n, \mathbb{I}(t_n))}{\hbar\Gamma(\mu)} \left\{ \frac{2\hbar}{\mu} t_{n+1}^\mu - \frac{t_{n+1}^{\mu+1}}{\mu+1} + \frac{\hbar}{\mu} t_n^\mu - \frac{t_n^{\mu+1}}{\mu} \right\} \\ & + \frac{\mathcal{A}_3(t_{n-1}, \mathbb{I}_{n-1})}{\hbar\Gamma(\mu)} \left\{ \frac{\hbar}{\mu} t_{n+1}^\mu - \frac{t_{n+1}^{\mu+1}}{\mu+1} + \frac{t_n^\mu}{\mu+1} \right\} + \mathbb{R}_{3,n}^\mu(t), \end{aligned}$$

$$\begin{aligned} \mathbb{V}(t_{n+1}) = & \mathbb{V}(t_n) + \frac{\mathcal{A}_4(t_n, \mathbb{V}(t_n))}{\hbar\Gamma(\mu)} \left\{ \frac{2\hbar}{\mu} t_{n+1}^\mu - \frac{t_{n+1}^{\mu+1}}{\mu+1} + \frac{\hbar}{\mu} t_n^\mu - \frac{t_n^{\mu+1}}{\mu} \right\} \\ & + \frac{\mathcal{A}_4(t_{n-1}, \mathbb{V}_{n-1})}{\hbar\Gamma(\mu)} \left\{ \frac{\hbar}{\mu} t_{n+1}^\mu - \frac{t_{n+1}^{\mu+1}}{\mu+1} + \frac{t_n^\mu}{\mu+1} \right\} + \mathbb{R}_{4,n}^\mu(t), \end{aligned}$$

$$\begin{aligned} \mathbb{R}(t_{n+1}) = & \mathbb{R}(t_n) + \frac{\mathcal{A}_5(t_n, \mathbb{R}(t_n))}{\hbar\Gamma(\mu)} \left\{ \frac{2\hbar}{\mu} t_{n+1}^\mu - \frac{t_{n+1}^{\mu+1}}{\mu+1} + \frac{\hbar}{\mu} t_n^\mu - \frac{t_n^{\mu+1}}{\mu} \right\} \\ & + \frac{\mathcal{A}_5(t_{n-1}, \mathbb{R}_{n-1})}{\hbar\Gamma(\mu)} \left\{ \frac{\hbar}{\mu} t_{n+1}^\mu - \frac{t_{n+1}^{\mu+1}}{\mu+1} + \frac{t_n^\mu}{\mu+1} \right\} + \mathbb{R}_{5,n}^\mu(t), \end{aligned}$$

(54)

where

$$\mathcal{A}_1 = \Lambda - d_0\mathbb{S}(t) - \tau\mathbb{S}(t)\mathbb{E}(t) - \beta\mathbb{S}(t)\mathbb{I}(t) - \psi\mathbb{S}(t),$$

$$\mathcal{A}_2 = \tau\mathbb{S}(t)\mathbb{E}(t) - (d_0 + d_1 + \kappa)\mathbb{E}(t),$$

$$\mathcal{A}_3 = \beta\mathbb{S}(t)\mathbb{I}(t) + \kappa\mathbb{E}(t) - \xi\mathbb{I}(t) - (d_0 + d_2)\mathbb{I}(t),$$

$$\mathcal{A}_4 = \psi\mathbb{S}(t) - d_0\mathbb{V}(t),$$

$$\mathcal{A}_5 = \xi\mathbb{I}(t) - d_0\mathbb{R}(t).$$

(55)

And  $\mathbb{R}_{1,n}^\mu(t), \mathbb{R}_{2,n}^\mu(t), \mathbb{R}_{3,n}^\mu(t), \mathbb{R}_{4,n}^\mu(t),$  and  $\mathbb{R}_{5,n}^\mu(t)$  are the remainder's terms.

## 8. Numerical Simulation

In this section of the article, we present the graphical results of the solution obtained in (54). For this purpose we have simulated the results via Matlab by assigning the values given in (Table 1) to the parameters and classes of the model. The graphical results are shown in the following.

## 9. Discussion

Figure 1 describes the dynamics of susceptible population for different values of the order of fractional derivatives. Each curve tends to the equilibrium solution irrespective of the value of  $\mu$ . As we increase the value of  $\mu$ , the rate of convergence to the stated equilibrium increases. Figure 2 represents the behavior of  $\mathbb{E}(t)$  along the time direction, and the figure shows that for describing the slow evolution of disease, one might assume small values of  $\mu$ . Infection from the community could be rapidly eliminated by increasing the order of the derivative as shown in Figure 3. A similar conclusion could be drawn from Figures 4 and 5, i.e., to capture the realistic scenario of slowly spreading diseases, one must consider the tools of fractional order derivative while modeling such epidemics.

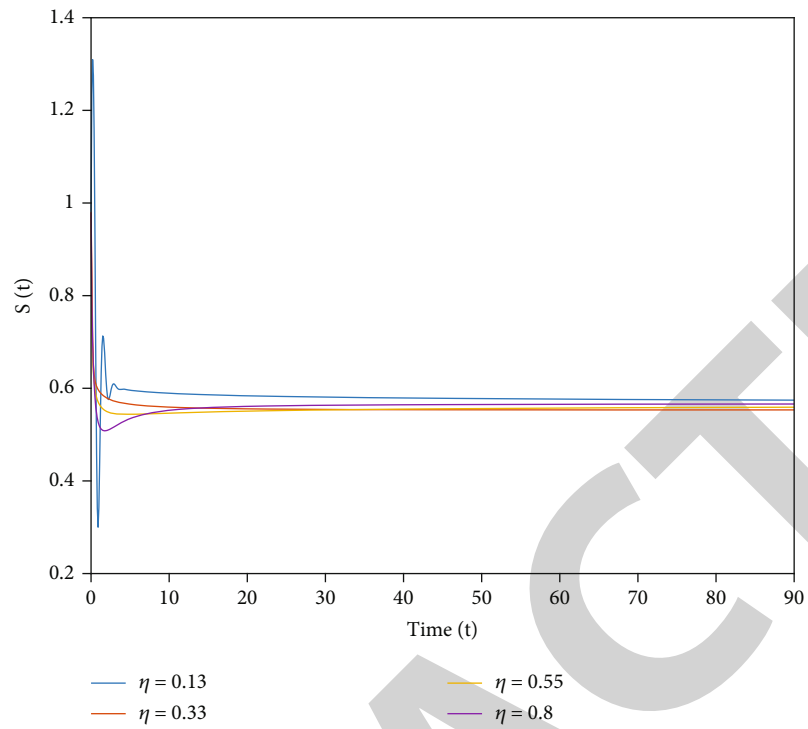


FIGURE 1: The behavior of susceptible population.

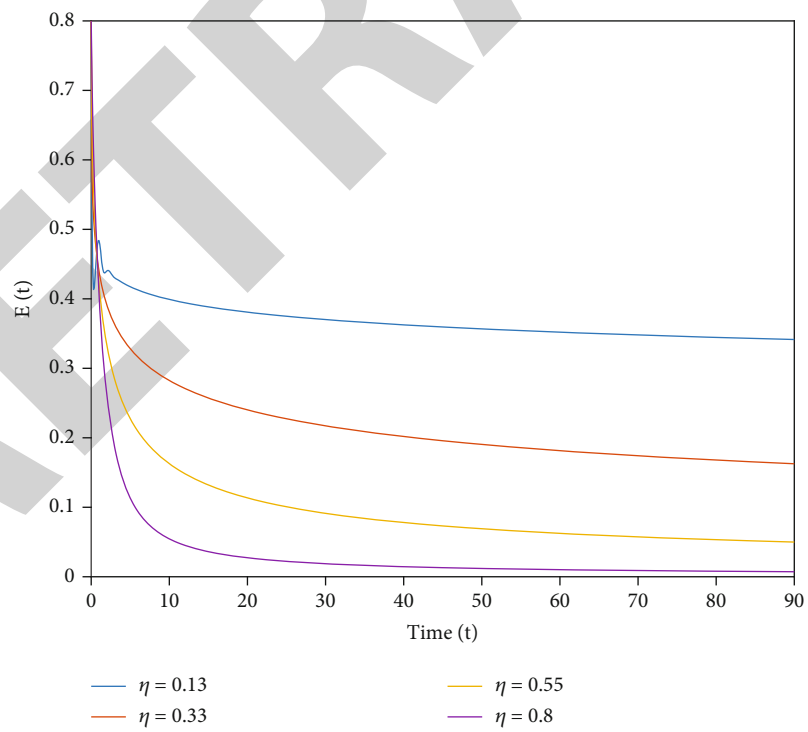


FIGURE 2: The behavior of exposed population.

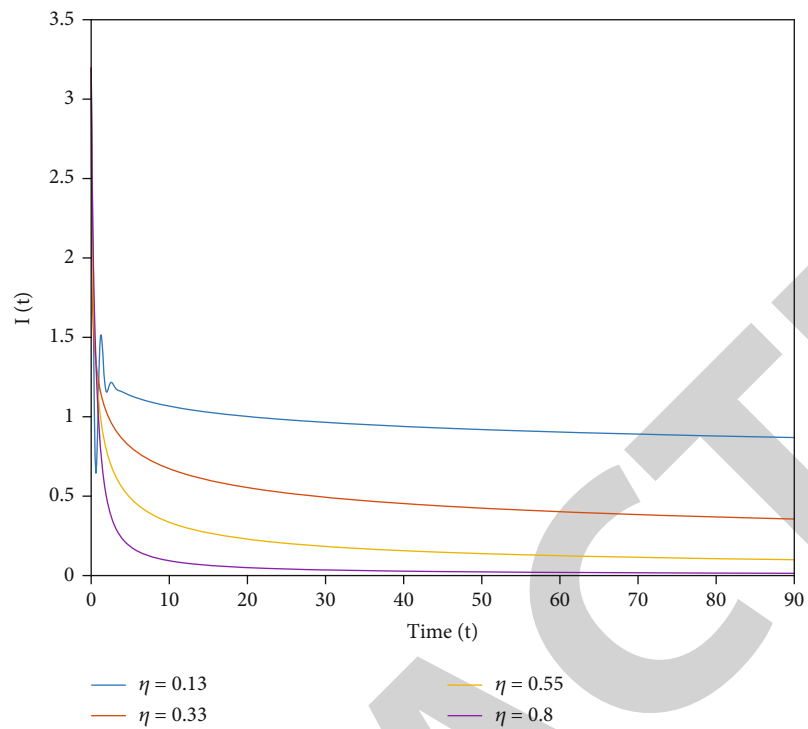


FIGURE 3: The behavior of infected population.

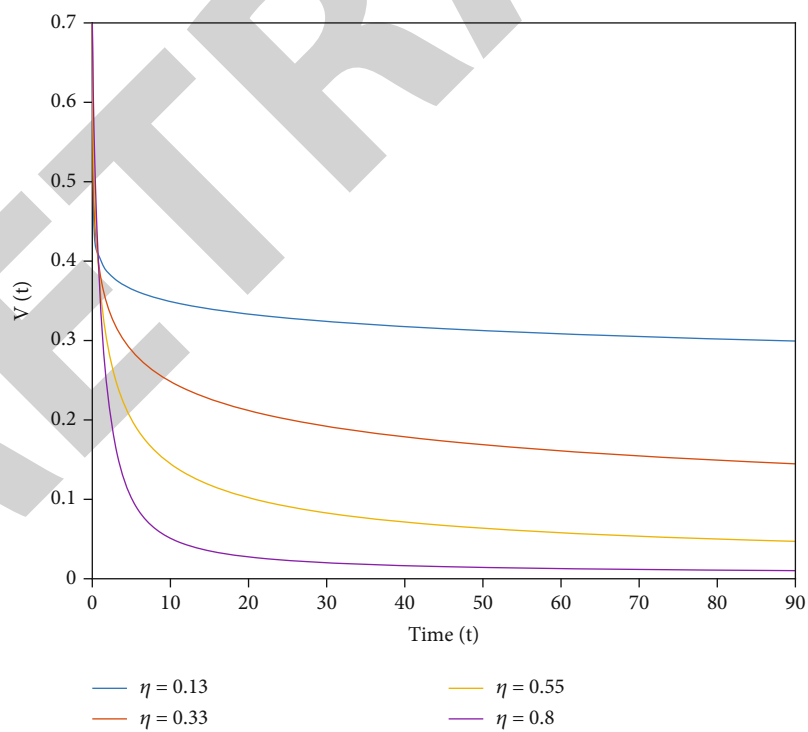


FIGURE 4: The behavior of vaccinated population.

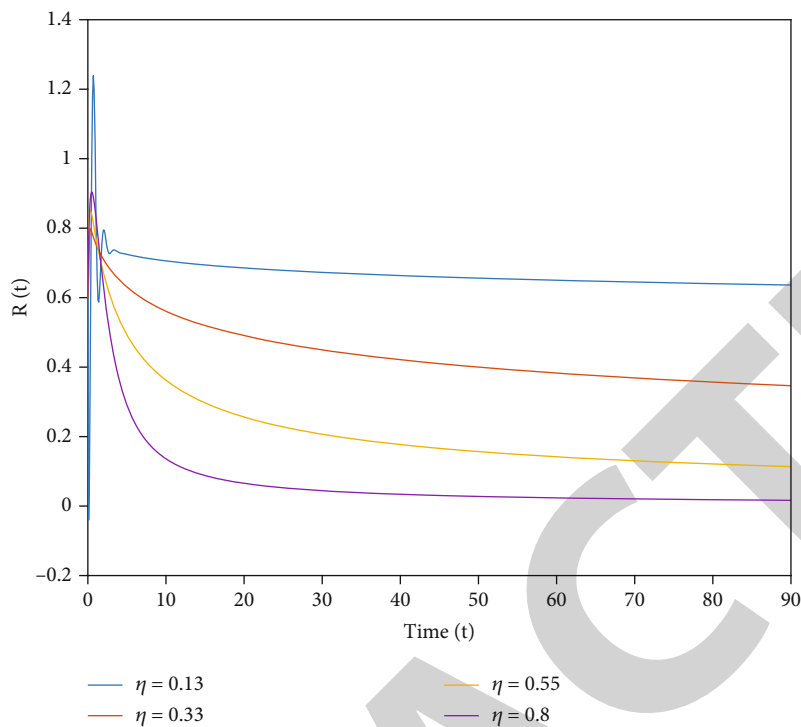


FIGURE 5: The behavior of recovered population.

## 10. Conclusion

In this paper, we have studied the fractional order Ebola model containing Caputo's fractional derivative of order  $\mu$ . The paper contains the study related to the existence of the solution performed by using theorems of fixed point theory for the existence of fixed point. In addition, we have proved that the solution of the system is unique as well as Ulam stable. Apart from this, we have found the numerical solution of the studied model with the help of two-point fractional order Adam's Bashforth method presented for the approximation of the fractional differential equations containing the Caputo's fractional derivative. In addition, we have visualized the results graphically with the help of Matlab. At last, we have discussed the dynamical behavior of the obtained solution for all classes of the said model.

## Data Availability

The data will be for public after the publication.

## Conflicts of Interest

The authors declare that they have no conflicts of interest.

## References

- [1] I. Podlubny, R. L. Magin, and I. Trymorush, "Niels Henrik Abel and the birth of fractional calculus," *Analysis*, vol. 20, no. 5, pp. 1068–1075, 2017.
- [2] S. Dugowson, *Les differentielles metaphysiques: histoire et philosophie de la generalisation de l' order de la derivation par*, Paris, 1994.
- [3] B. Ross, "The development of fractional calculus 1695-1900," *Historia Mathematica*, vol. 4, no. 1, pp. 75–89, 1977.
- [4] D. Valerio, J. T. Machado, and V. Kiryakova, "Some pioneers of the applications of fractional calculus," *Fractional Calculus and Applied Analysis*, vol. 17, no. 2, pp. 552–578, 2014.
- [5] B. J. West, *Fractional Calculus View of Complexity: Tomorrow's Science*, CRC Press, 1st edition, 2015.
- [6] R. R. Nighmanullin, R. A. Giniyatullin, and A. I. Skorinkin, "Membrane current series monitoring: essential reduction of data points to finite number of stable parameters," *Frontiers in Computational Neuroscience*, vol. 8, p. 120, 2014.
- [7] A. Sharma, S. Namsani, and J. K. Singh, "Molecular simulation of shale gas absorption and diffusion in inorganic nanopores," *Molecular Simulation*, vol. 415, no. 5-6, pp. 414–422, 2014.
- [8] R. Metzler, J. H. Jeon, A. G. Cherstvy, and E. Barkai, "Anomalous diffusion models and their properties: non-stationarity, non-ergodicity, and ageing at the centenary of single particle tracking," *Physical Chemistry Chemical Physics*, vol. 16, no. 44, pp. 24128–24164, 2014.
- [9] R. Garappa, "Grunwald-Letnikov operators for fractional relaxation in Havriliak-Negami models," *Communications in Nonlinear Science and Numerical Simulation*, vol. 38, pp. 178–191, 2016.
- [10] X. Yang, W. Chen, R. Xiao, and L. Ling, "A fractional model for time-variant non-Newtonian flow," *Thermal Science*, vol. 21, no. 1 Part A, p. 61, 2017.
- [11] V. Uchaikin, *Fractional derivatives for physicists and engineers. Volume I background and theory volume II applications (non-linear physical science) (2013th ed.)*, Springer, 2013.
- [12] D. A. Benson, S. W. Wheatcraft, and M. M. Meerschaert, "The fractional-order governing equation of Lévy motion," *Water Resources Research*, vol. 36, no. 6, pp. 1413–1423, 2000.

## Research Article

# Melting Heat Transition in a Spinning Flow of Silver-Magnesium Oxide/Engine Oil Hybrid Nanofluid Using Parametric Estimation

Muhammad Bilal,<sup>1</sup> Taza Gul ,<sup>1</sup> Abir Mouldi,<sup>2</sup> Safyan Mukhtar,<sup>3</sup> Wajdi Alghamdi ,<sup>4</sup> Souhail Mohamed Bouzgarrou,<sup>5</sup> and Nosheen Feroz<sup>6</sup>

<sup>1</sup>Department of Mathematics, City University of Science and Information Technology, Peshawar 25000, Pakistan

<sup>2</sup>Department of Industrial Engineering, College of Engineering, King Khalid University, Abha 61421, Saudi Arabia

<sup>3</sup>Department of Basic Sciences, Deanship of Preparatory Year, King Faisal University, Hafuf, Al Ahsa, Saudi Arabia

<sup>4</sup>Department of Information Technology, Faculty of Computing and Information Technology, King Abdulaziz University, Jeddah 80261, Saudi Arabia

<sup>5</sup>Department of Civil Engineering, Faculty of Engineering, Jazan University, Saudi Arabia

<sup>6</sup>Department of Mathematics, Bacha Khan University Charsadda, KP, Pakistan

Correspondence should be addressed to Taza Gul; tazagul@cusit.edu.pk

Received 7 November 2021; Revised 8 May 2022; Accepted 20 May 2022; Published 15 June 2022

Academic Editor: P. Davide Cozzoli

Copyright © 2022 Muhammad Bilal et al. This is an open access article distributed under the Creative Commons Attribution License, which permits unrestricted use, distribution, and reproduction in any medium, provided the original work is properly cited.

This study reports the three-dimensional (3D) flow of Ag-MgO hybrid nanofluid (HNF) over a spinning disc of flexible thickness in the presence of modified Fourier law. The HNF is contained of silver and magnetic nanoparticulate in the base fluid engine oil. The energy transition has been examined in the involvement of melting heat propagation. The highly nonlinear system of partial differential equations (PDEs) is processed by adopting the proper similarity conversions to attain the coupled ODE system. The obtained system of modeled equations is numerically solved by employing the Parametric Continuation Method (PCM). The nature of various constraints, as opposed to the velocities, energy, and mass transmission, is portrayed and described. In comparison to the simple nanofluid flow, the hybrid nanofluid flow's velocity and heat conduction are observed to have a significant influence. As a result, the functionality of the hybrid nanofluid is significantly superior to that of the conventional nanofluid. The positive variation in power-law exponent  $n$  and Reynold number  $Re$  significantly enhances the fluid velocity. The effect of both melting coefficient and thermal relaxation term reduces fluid temperature.

## 1. Introduction

In the analysis of HNF due to its substantial participation in engineering constraints and modern machinery, the examination of HNF flow over a turning disk with energy communication has taken significant interest [1, 2]. The well-recognized uses consist of electric control techniques, cocircling apparatus, aerodynamic systems, whirling machines, biochemical reactions, supercomputer management, and hydrothermal sectors [3]. Lv et al. [4] investigated the effects of magnetism and Hall potential on nanofluid flow across a revolving disc. Their target was to increase the level of heat dissipation for technological reasons. As per the conclusions,

the modification of CNTs in water is substantially more favorable than that of other nanoparticles due to their C-C interaction. Li et al. [5] employed the bvp4c packages to perform a percentage approximation for Darcy HNF flow over a pierced rotation disc with heat slip. Khan et al. [6] investigated the chemical reaction that influences Maxwell fluid flow over a diagonally gyrating oscillating disc with the magnetic flux during unstable motion. It should be observed that the energy transference ratio raises drastically when the disc radiation and rotation factors increase. The unsteady slip flow with entropy production over a revolving disc under the action of a ferromagnetic material was studied by Shuaib et al. [7] and Bilal et al. [8]. The slip factor

seems to be effective in regulating flow and heat characteristics. The Oldroyd-B fluid flow was investigated by Hafeez et al. [9] using a whirling disc. As the relaxation time factor is increased, the flow rate is spotted to diminish. The fluid potential spectrum is also lowered as the thermal relaxation phase develops. HNF flow through a swaying disc with sessile microbes and chemical reactions was discovered by Waqas et al. [10]. A concordance with previous research and a full simple geometric presentation for key variables aid the presented rebuttal. Tassaddiq et al. [11] created an HNF flow over an indefinite impermeable rotating disc. The role of magnetic flux was used to accurately analyze the positive rotation of nanofluid flow. Their primary project purpose was to raise public awareness about energy usage in scientific and technological contexts. The addition of ferric oxide  $Fe_3O_4$  nanoparticles enhances the heat transition rate considerably [12].

Nanofluids are a new type of solution that operates efficiently in heat exchanger when compared to traditional fluids. When the thermal sensitivity is high enough, nanocomposite can be used in a wide range of thermal processes, including freezing [13–17]. Nanofluid flow is used in a variety of applications, including heat converters, geothermal energy, heat pumps, metallurgy, climate control, the automobile sector, turbines, microelectronics, nuclear condenser networks, ships, medicine, and circuit condensation [18–21]. The vast demand for thermal energy in the era of development of science and technology cannot be met with widely utilized fluids. When similar base liquids were produced with the addition of tiny-sized particles, however, a substantial improvement in thermal properties was seen [22]. In the present analysis, we have utilized the MgO (magnesium oxide) and Ag (silver) nanomaterials in the base fluid. MgO is a chemical made up of  $Mg^{2+}$  and  $O^{2-}$  ions at 700–1500°C [23]. For metallurgical and electronic operations, MgO is more practical [24]. Similarly, Ag nanoparticulates' might be exploited to control bacterial movement in an array of products, involving dental work, injuries and wound therapy, surgery, and biomedical apparatus [25, 26]. Ahmadian et al. [27] investigate a 3D simulation of an unstable Ag-MgO HNF flow with heat conduction induced by a curvy spinning disc going up and downwards. With the dispersion of Ag-MgO nanocrystals, the HNF is created. The issue was solved using the PCM technique. The usage of Ag-MgO is thought to be more effective in overcoming poor energy transfer. Among metal and metal oxide, silver and magnesium oxide nanoparticles have been widely recorded to have broad-spectrum antibiotic assets [28]. Silver nanoparticles are the most widely utilized inorganic nanoparticles, having several applications in biomaterial detection and antibacterial activities [29]. Anuar et al. [30] used Ag and MgO nanocrystals in water to evaluate the energy distribution of a hybrid nanoliquid through an extending sheet with suction and buoyant force effects. The findings show that improving the quantity of Ag nanoparticles in HNF lowers the energy transference. Gangadhar et al. [31] arithmetically addressed the heat transport properties of a hybrid nanofluid mixture combining Au and MgO nanoparticulate. Hiba et al. [32] evaluated the thermal performance of HNF

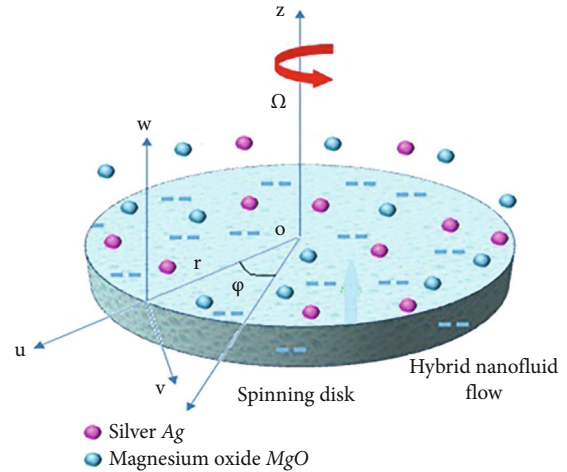


FIGURE 1: Spinning disk geometry.

including magnesium oxide and Silver and across a highly permeable hollow microplate under magnetic impact. Recently, several researchers have been reported on the study of hybrid nanofluid flow [33–36].

PCM tackles a lot of challenging nonlinear boundary value problems that other numerical techniques cannot solve. Convergence is subject to the relaxation variables and initial strategy for many problems that are generally addressed by traditional computational approaches [37–40]. The PCM's goal is to determine that the proposed methodology can be used to solve complex nonlinear problems related to industry [41]. Shuaib et al. [42] emphasized the 3D oscillating fluid and energy conductivity across the surface of an irregular elastic revolving disc. The fluid flow has been examined in the context of an external magnetism flux. The phenomena of an ionic fluid flow throughout a spinning disc were discovered by Shuaib et al. [43]. The Poisson's and Planck models were used to computing the molecular interactions. Dombovari et al. [44] investigated the robustness of nonlinear hydrological systems using a parametric continuation technique. They also looked into static bifurcation, which arises while addressing complex initial value systems with distinctive roots, and devised a method for efficiently determining the points of bifurcation. Ref. [45, 46] may be used to solve the stated challenge in the future.

The assessment was aimed at reporting the 3D flow of Ag- and MgO-based HNF over a spinning disk of flexible thickness. The HNF is synthesized with the composition of silver and magnetic nanomaterials in the engine oil. The energy transition is examined with the involvement of melting heat propagation. To evaluate the behaviors of the fluid flow, Tiwari and Das's model is employed. The nonlinear system of PDEs is processed through the proper similarity conversions to attain the coupled ODE system. The obtained system of modeled equations is numerically solved employing the Parametric Continuation Method (PCM). In the next section, the formulation, solution methodology, and results and discussion have been discussed in detail.

## 2. Mathematical Formulation

In this study, we considered the steady and incompressible flow of Ag-MgO hybrid nanoliquid over a gyrating disk of variable thickness  $z = a(1 + r^*)^{-m}$ , moving with fixed angular velocity  $\Omega$  about the  $z$ -axis. Here,  $u$ ,  $v$ , and  $w$  are the velocity component along  $r, \theta, z$  direction, respectively.  $T_\infty$  is the free stream temperature, and  $T_m$  is the temperature of the melting surface. Figure 1 reveals the flow mechanism over a spinning disk. The modeled equations can be rebound as [47–49]

$$\frac{\partial u}{\partial r} + \frac{u}{r} + \frac{\partial w}{\partial z} = 0, \quad (1)$$

$$u \frac{\partial u}{\partial r} + v \frac{\partial u}{\partial z} = \nu_{hnf} \frac{\partial^2 u}{\partial z^2} + \frac{v^2}{r} - \sigma_{hnf} B_0^2 u, \quad (2)$$

$$u \frac{\partial v}{\partial r} + w \frac{\partial v}{\partial z} = \nu_{hnf} \frac{\partial^2 v}{\partial z^2} - \frac{uv}{r} - \sigma_{hnf} B_0^2 v, \quad (3)$$

$$\begin{aligned} u \frac{\partial T}{\partial r} + w \frac{\partial T}{\partial z} &= \frac{k_{hnf}}{(\rho C_p)_{hnf}} \frac{\partial^2 T}{\partial z^2} - \lambda \\ &\cdot \left( u^2 \frac{\partial^2 T}{\partial r^2} - w^2 \frac{\partial^2 T}{\partial z^2} + \left( u \frac{\partial u}{\partial r} \frac{\partial T}{\partial r} + w \frac{\partial u}{\partial z} \frac{\partial T}{\partial r} \right), \right. \\ &\quad \left. + 2uw \frac{\partial^2 T}{\partial r \partial z} + \frac{\partial T}{\partial z} u \left( \frac{\partial w}{\partial r} + w \frac{\partial w}{\partial z} \right), \right) \end{aligned} \quad (4)$$

$$u \frac{\partial C}{\partial r} + v \frac{\partial C}{\partial z} = D_{hnf} \frac{\partial^2 C}{\partial z^2} - k(C - C_0). \quad (5)$$

Here,  $(u, v, w)$  exhibit the velocity element, and  $\nu_{hnf}$ ,  $k_{hnf}$  and  $(\rho C_p)_{hnf}$  reveal the kinematic viscosity, thermal conductivity, and volumetric heat capacity, respectively.

The boundary conditions are

$$u = 0, w = 0, v = r\Omega, T = T_\infty, C = C_\infty \text{ at } z = 0,$$

$$\begin{aligned} k_{hnf} \left( \frac{\partial T}{\partial z} \right)_{z=a(1-r^*)^{-m}} &= \rho_{hnf} (\lambda^* + C_s(T_m - T_0)) w(r, z), \\ u &\longrightarrow 0, v \longrightarrow 0, T \longrightarrow T_\infty, \\ C &\longrightarrow C_\infty \text{ when } z \longrightarrow \infty. \end{aligned} \quad (6)$$

Table 1 shows the thermophysical properties of nano-fluids and hybrid nanofluids in terms of viscosity, density, heat capacity and thermal conductivity.

Incorporating the following transformation in Equations (1)–(5) and (6)

$$\begin{aligned} u &= \Omega r F(\eta), v = \Omega r G(\eta), w = \frac{-R_0 \Omega (1 + r^*)^{-m}}{\left( R_0^2 \Omega \rho_f / \mu_f \right)^{1/n+1}} J(\eta), \theta(\eta) \\ &= \frac{T - T_m}{T_\infty - T_m}, \phi(\eta) = \frac{C - C_m}{C_\infty - C_m}, \\ \eta &= \frac{z}{R_0} (1 + r^*)^{-m} \left( \frac{R_0^2 \Omega \rho_f}{\mu_f} \right)^{1/n+1}, \end{aligned} \quad (7)$$

we get

$$J'(\eta) + 2F(\eta) + \eta m \varepsilon F'(\eta) = 0, \quad (8)$$

$$\begin{aligned} &\left( \frac{\mu_{hnf}}{\mu_f} \right) \text{Re}^{1-n/1+n} (1 + r^*)^{2m} F''(\eta) + \left( \frac{\rho_{hnf}}{\rho_f} \right) \\ &\cdot \left[ -F^2(\eta) - J(\eta)F'(\eta) + G^2(\eta) - \eta \varepsilon m F(\eta)F'(\eta) \right] = 0, \end{aligned} \quad (9)$$

$$\begin{aligned} &\left( \frac{\mu_{hnf}}{\mu_f} \right) \text{Re}^{1-n/1+n} (1 + r^*)^{2m} G''(\eta) + \left( \frac{\rho_{hnf}}{\rho_f} \right) \\ &\cdot \left[ -2G(\eta)F(\eta) - J(\eta)G'(\eta) - \eta m \varepsilon F(\eta)G'(\eta) \right] = 0, \end{aligned} \quad (10)$$

$$\begin{aligned} &\left( \frac{k_{hnf}}{k_f} \right) \left( \frac{\text{Re}^{1-n/1+n} (1 + r^*)^{2m}}{\text{Pr}} \right) \theta''(\eta) - \gamma \left( \frac{(\rho C_p)_{hnf}}{(\rho C_p)_f} \right) \\ &\cdot \left[ \begin{aligned} &m(m-1)\eta \varepsilon^2 F^2(\eta)\theta'(\eta) + \eta^2 m^2 \varepsilon^2 F(\eta)\theta''(\eta) \\ &+ J^2(\eta)\theta''(\eta) + \eta m \varepsilon F^2(\eta)\theta'(\eta) \\ &+ \eta^2 m^2 \varepsilon^2 F(\eta)F'(\eta)\theta'(\eta) + \eta m \varepsilon \theta'(\eta)J(\eta)F'(\eta) \\ &+ \eta m \varepsilon \theta'(\eta)J'(\eta)F(\eta) + J(\eta)J'(\eta)\theta(\eta) \end{aligned} \right] \\ &- \eta m \varepsilon \theta'(\eta)F(\eta) - J(\eta)\theta'(\eta) = 0, \end{aligned} \quad (11)$$

$$\begin{aligned} &\phi''(\eta) \alpha^2 (1 + r^*)^{-2m} - \frac{1}{\text{Sc}} d_1 \phi(\eta) \\ &+ \frac{1}{\text{Sc}} m a \varepsilon \eta (R_0 + 1) F(\eta) \phi(\eta) \\ &- \frac{1}{\text{Sc}} (1 + r^*)^{-m} a G(\eta) \phi(\eta) = 0. \end{aligned} \quad (12)$$



TABLE 1: The thermophysical properties of hybrid nanofluid and model [47].

	$\phi_{nf} = (\phi_{MgO} \text{ or } \phi_{Ag})$	$\phi_{hnf} = (\phi_{MgO} + \phi_{Ag})$
Viscosity $\mu$	$\frac{\mu_f(1 - \phi_{Au})}{\mu_f(1 - \phi_{Ag})}$	$\mu_f(1 - \phi_{hnf})^{2.5}$
Density $\rho$	$(1 - \phi_{Au})\rho_f + \phi_{Au}\rho_{Au}$ $(1 - \phi_{Ag})\rho_f + \phi_{Ag}\rho_{Ag}$	$(1 - \phi_{hnf})\rho_f + \phi_{MgO}\rho_{MgO} + \phi_{Ag}\rho_{Ag}$
Heat capacity $(\rho C_p)$	$(1 - \phi_{Au})(\rho C_p)_f + \phi_{Au}(\rho C_p)_{Au}$ $(1 - \phi_{Ag})(\rho C_p)_f + \phi_{Ag}(\rho C_p)_{Ag}$	$(1 - \phi_{hnf})(\rho C_p)_f + \phi_{MgO}(\rho C_p)_{MgO} + \phi_{Ag}(\rho C_p)_{Ag}$
Thermal conductivity $k$	$(k_{Au} + 2k_f - 2\phi_{Au}(k_f - k_{Au})/k_{Au} + 2k_f + 2\phi_{Au}(k_f - k_{Au}))k_f$ $(k_{Ag} + 2k_f - 2\phi_{Ag}(k_f - k_{Ag})/k_{Ag} + 2k_f + 2\phi_{Ag}(k_f - k_{Ag}))k_f$	$k_{Ag} + 2k_{nf} - 2\phi_{Ag}(k_{nf} - k_{Ag})/k_{Ag} + 2k_{nf} + 2\phi_{Ag}(k_{nf} - k_{Ag})$ $\times (k_{MgO} + 2k_f - 2\phi_{MgO}(k_f - k_{MgO})/k_{MgO} + 2k_f + 2\phi_{MgO}(k_f - k_{MgO}))k_f$
Diffusivity $\alpha$	$k_{nf}/(\rho C_p)_{nf}$	$k_{hnf}/(\rho C_p)_{hnf}$

The transform conditions are

$$\begin{aligned}
 F(\alpha) = 0, G(\alpha) = 1, \frac{k_{hnf}}{k_f} \text{Me Re}^{1-n/1+n} (1+r^*)^{2m} \theta'(\alpha) \\
 + \frac{\rho_{hnf}}{\rho_f} \text{Pr} J(\alpha) = 0, \theta(\alpha) = 1, \varphi(\alpha) = 1, \\
 F(\infty) = 0, \theta(\infty) = 0, \varphi(\infty) = 0, G(\infty) = 0.
 \end{aligned} \quad (13)$$

Here,  $\alpha$  is the disk thickness coefficient,  $\text{Re}$  is the Reynold number,  $\text{Me}$  is the melting constant,  $\varepsilon$  is the constant coefficient,  $r^*$  is the dimensionless radius parameter,  $\gamma$  is the thermal relaxation parameter, and  $\text{Pr}$  is the Prandtl number defined as [47]

$$\begin{aligned}
 \alpha &= \frac{a}{R_0} \left( \frac{R_0^2 \Omega \rho_f}{\mu_f} \right)^{1/n+1}, \text{Re} = \frac{R_0^2 \Omega \rho_f}{\mu_f}, \\
 \text{Me} &= \frac{(T_\infty - T_m) C_p}{C_s (T_m - T_0) + \lambda^*}, \varepsilon = \frac{r}{R_0 + r}, \\
 r^* &= \frac{r}{R_0}, \gamma = \Omega \lambda, \text{Pr} = \frac{\mu_f (C_p)_{nf}}{k_f},
 \end{aligned} \quad (14)$$

where  $F$ ,  $G$ , and  $J$  denote the radial, tangential, and axial velocities, and  $\phi, \theta$  show the dimensionless concentration and temperature. The deformations are expressed as

$$\begin{aligned}
 f(\xi) &= f(\eta - \alpha) = F(\eta), \\
 j(\xi) &= j(\eta - \alpha) = J(\eta), \\
 g(\xi) &= g(\eta - \alpha) = G(\eta), \\
 \theta(\xi) &= \theta(\eta - \alpha) = \theta(\eta), \\
 \varphi(\xi) &= \varphi(\eta - \alpha) = \varphi(\eta).
 \end{aligned} \quad (15)$$

Using Equation (15), Equations (7)–(12) take the form

$$J'(\xi) + \xi m \varepsilon f'(\xi) + \alpha m \varepsilon f'(\xi) + 2f(\xi) = 0, \quad (16)$$

$$\begin{aligned}
 \left( \frac{\mu_{hnf}}{\mu_f} \right) \text{Re}^{1-n/1+n} (1+r^*)^{2m} f''(\xi) + \left( \frac{\rho_{hnf}}{\rho_f} \right) \\
 \left[ -f^2(\xi) - j(\xi) f'(\xi) - \xi m \varepsilon f(\xi) f'(\xi) \right] \\
 + g^2(\xi) - \alpha m \varepsilon f(\xi) f'(\xi) \Big] = 0,
 \end{aligned} \quad (17)$$

$$\begin{aligned}
 \left( \frac{\mu_{hnf}}{\mu_f} \right) \text{Re}^{1-n/1+n} (1+r^*)^{2m} g''(\xi) + \left( \frac{\rho_{hnf}}{\rho_f} \right) \\
 \left[ -j(\xi) g'(\xi) - \xi m \varepsilon f(\xi) g'(\xi) \right] \\
 - 2g(\xi) f(\xi) - \alpha m \varepsilon f(\xi) g'(\xi) \Big] = 0,
 \end{aligned} \quad (18)$$

$$\begin{aligned}
 \left( \frac{k_{hnf}}{k_f} \right) \left( \frac{\text{Re}^{1-n/1+n} (1+r^*)^{2m}}{\text{Pr}} \right) \theta''(\xi) \\
 - (\xi + \alpha) m \varepsilon f(\xi) \theta'(\xi) - j(\xi) \theta'(\xi) - \gamma \left( \frac{\rho C_p}{\rho C_p} \right)_{hnf} \\
 \left[ \begin{aligned}
 &m(m-1)(\xi + \alpha) \varepsilon^2 f^2(\xi) \theta'(\xi) + (\xi + \alpha)^2 f(\xi) \theta''(\xi) \\
 &+ j^2(\xi) \theta''(\xi) + (\alpha + \xi) \varepsilon m f^2(\xi) \theta'(\xi) \\
 &+ (\xi + \alpha)^2 m^2 \varepsilon^2 f^2(\xi) f'(\xi) \theta(\xi) + (\xi + \alpha) m \varepsilon j(\xi) f'(\xi) \theta'(\xi) \\
 &+ (\xi + \alpha) m \varepsilon j'(\xi) f(\xi) \theta'(\xi) + j(\xi) j'(\xi) \theta(\xi)
 \end{aligned} \right],
 \end{aligned} \quad (19)$$

$$\begin{aligned}
 \varphi''(\xi) \alpha^2 (1+r^*)^{-2m} - \frac{1}{\text{Sc}} d_1 \varphi(\xi) \\
 + \frac{1}{\text{Sc}} m a \varepsilon \xi (R_0 + 1) f(\xi) \varphi(\xi) \\
 + \frac{1}{\text{Sc}} m a^2 \varepsilon (R_0 + 1) f(\xi) \varphi(\xi) \\
 - \frac{1}{\text{Sc}} (1+r^*)^{-m} a g(\xi) \varphi(\xi) = 0,
 \end{aligned} \quad (20)$$

$$\begin{aligned}
 f(0) = 0, g(0) = 1, \theta(0) = 1, \varphi(0) = 1, \\
 \frac{k_{hnf}}{k_f} \text{Me Re}^{1-n/1+n} (1+r^*)^{2m} \theta'(0) + \frac{\rho_{hnf}}{\rho_f} \text{Pr} j(0) = 0, \\
 f(\infty) = 0, g(\infty) = 0, \theta(\infty) = 0, \varphi(\infty) = 0.
 \end{aligned} \quad (21)$$

The skin friction is stated as

$$C_{fr} = \frac{\tau_{wr}}{\rho_f (R_0 \Omega)^2}, C_{f\theta} = \frac{\tau_{w\theta}}{\rho_f (R_0 \Omega)^2}. \quad (22)$$

Shear forces are

$$\tau_{wr} = \mu_{hnf} \frac{\partial u}{\partial z} \Big|_{z=(1+r^*)^{-m}}, \tau_{w\theta} = \mu_{hnf} \frac{\partial v}{\partial z} \Big|_{z=(1+r^*)^{-m}}. \quad (23)$$

The nondimensional form is

$$\begin{aligned}
 \text{Re}^{n/n+1} C_{fr} &= \left[ \frac{\mu_{hnf}}{\mu_f} (1+r^*)^m \right] r^* f'(0), \text{Re}^{n/n+1} C_{f\theta} \\
 &= \left[ \frac{\mu_{hnf}}{\mu_f} (1+r^*)^m \right] r^* g'(0).
 \end{aligned} \quad (24)$$

### 3. Numerical Solution

The basic steps of PCM are as follows: Step 1: simplifying Equations (16)–(20) to 1<sup>st</sup> order with the boundary conditions

$$\begin{aligned}
\chi_1 &= f(\xi), \chi_2 = f'(\xi), \chi_2' = \frac{B^* [2(\chi_1)^2 + \chi_2(\chi_5 + m(\xi + \alpha)\varepsilon\chi_1) - (\chi_3)^2]}{A^* (1 + r^*)^{2m} (\text{Re})^{1-n/1+n}}, \\
\chi_3 &= g(\xi), \chi_4 = g'(\xi), \chi_4' = \frac{B^* [2\chi_1\chi_3 + \chi_4(\chi_5 + m(\xi + \alpha)\varepsilon\chi_1) - \chi_5\chi_2]}{A^* (1 + r^*)^{2m} (\text{Re})^{1-n/1+n}}, \\
\chi_5 &= j(\xi), \chi_5' = -[-2\chi_1 + m(\xi + \alpha)\varepsilon(\chi_2)^2], \chi_6 = \theta(\xi), \chi_7 = \theta'(\xi), \\
\chi_7' &= \frac{D^* (\gamma Pr)^* \left[ \chi_5\chi_6\chi_5' + \chi_7 \begin{pmatrix} m(m-1)(\xi + \alpha)(\varepsilon\chi_1)^2 + m\varepsilon\chi_5\chi_1 + m \\ (\xi + \alpha)\varepsilon(\chi_1)^2 m^2(\xi + \alpha)^2 \varepsilon^2 \chi_1\chi_2 + m \\ (\xi + \alpha)\varepsilon\chi_5\chi_2 + m(\xi + \alpha)\varepsilon\chi_1\chi_5' - m\varepsilon\chi_1\chi_5 \end{pmatrix} \right] - m(\xi + \alpha)\varepsilon\chi_1\chi_7 + \chi_5\chi_7}{C^* C_1^* (1 + r^*)^{2m} (\text{Re})^{1-n/1+n} [(\chi_5)^2 + m^2(\xi + \alpha)^2 \varepsilon^2 (\chi_1)^2]}, \\
\chi_9' &= \frac{1/Sc d_1 \chi_8 + \chi_9 (-1/Sc m a \varepsilon \xi (R_0 + 1) \chi_1 - 1/Sc m a^2 \varepsilon (R_0 + 1) \chi_1 + 1/Sc (1 + r^*)^{-m} a \chi_3)}{\alpha^2 (1 + r^*)^{-2m}}, \\
\chi_1(0) &= 0, \chi_3(0) = 1, C^* C_1^* [(1 + r^*)^{2m} \text{Re}^{1-n/1+n} \text{Me}] \chi_7 + D^* \text{Pr}^* \chi_5 \chi_6 = 1, \\
\chi_1(\infty), \chi_3(\infty), \chi_6(\infty), \chi_8(\infty).
\end{aligned} \tag{25}$$

Step 2: introducing parameter  $p$

$$\begin{aligned}
\chi_1 &= f(\xi), \chi_2 = f'(\xi), \\
\chi_2' &= \frac{B^* [2(\chi_1)^2 + (\chi_2 - 1)p(\chi_5 + m(\xi + \alpha)\varepsilon\chi_1) - (\chi_3)^2]}{A^* (1 + r^*)^{2m} (\text{Re})^{1-n/1+n}}, \\
\chi_3 &= g(\xi), \chi_4 = g'(\xi), \\
\chi_4' &= \frac{B^* [2\chi_1\chi_3 + (\chi_4 - 1)p(\chi_5 + m(\xi + \alpha)\varepsilon\chi_1) - \chi_5\chi_2]}{A^* (1 + r^*)^{2m} (\text{Re})^{1-n/1+n}}, \\
\chi_5 &= j(\xi), \chi_5' = -[-2\chi_1 + (\chi_5 - 1)p - \chi_5 + m(\xi + \alpha)\varepsilon(\chi_2)^2], \\
\chi_6 &= \theta(\xi), \chi_7 = \theta'(\xi), \\
\chi_7' &= \frac{D^* (\gamma Pr)^* \left[ \chi_5\chi_6\chi_5' + (\chi_7 - 1)p \begin{pmatrix} m(m-1)(\xi + \alpha)(\varepsilon\chi_1)^2 + m\varepsilon\chi_5 \\ \chi_1 + (\xi + \alpha)m\varepsilon(\chi_1)^2 + m^2(\xi + \alpha)^2 \varepsilon^2 \chi_1\chi_2 + (\xi + \alpha)m\varepsilon\chi_5\chi_2 + \\ m(\xi + \alpha)\varepsilon\chi_1\chi_5' - m\varepsilon\chi_1\chi_5 \end{pmatrix} \right] - m(\xi + \alpha)\varepsilon\chi_1\chi_7 + \chi_5\chi_7}{C^* C_1^* (1 + r^*)^{2m} (\text{Re})^{1-n/1+n} [(\chi_5)^2 + m^2(\xi + \alpha)^2 \varepsilon^2 (\chi_1)^2]}, \\
\chi_9' &= \frac{1/Sc d_1 \chi_8 + (\chi_9 - 1)p(1/Sc - m a \varepsilon \xi (R_0 + 1) \chi_1 - 1/Sc m a^2 \varepsilon (R_0 + 1) \chi_1 + 1/Sc (1 + r^*)^{-m} a \chi_3)}{\alpha^2 (1 + r^*)^{-2m}}.
\end{aligned} \tag{26}$$

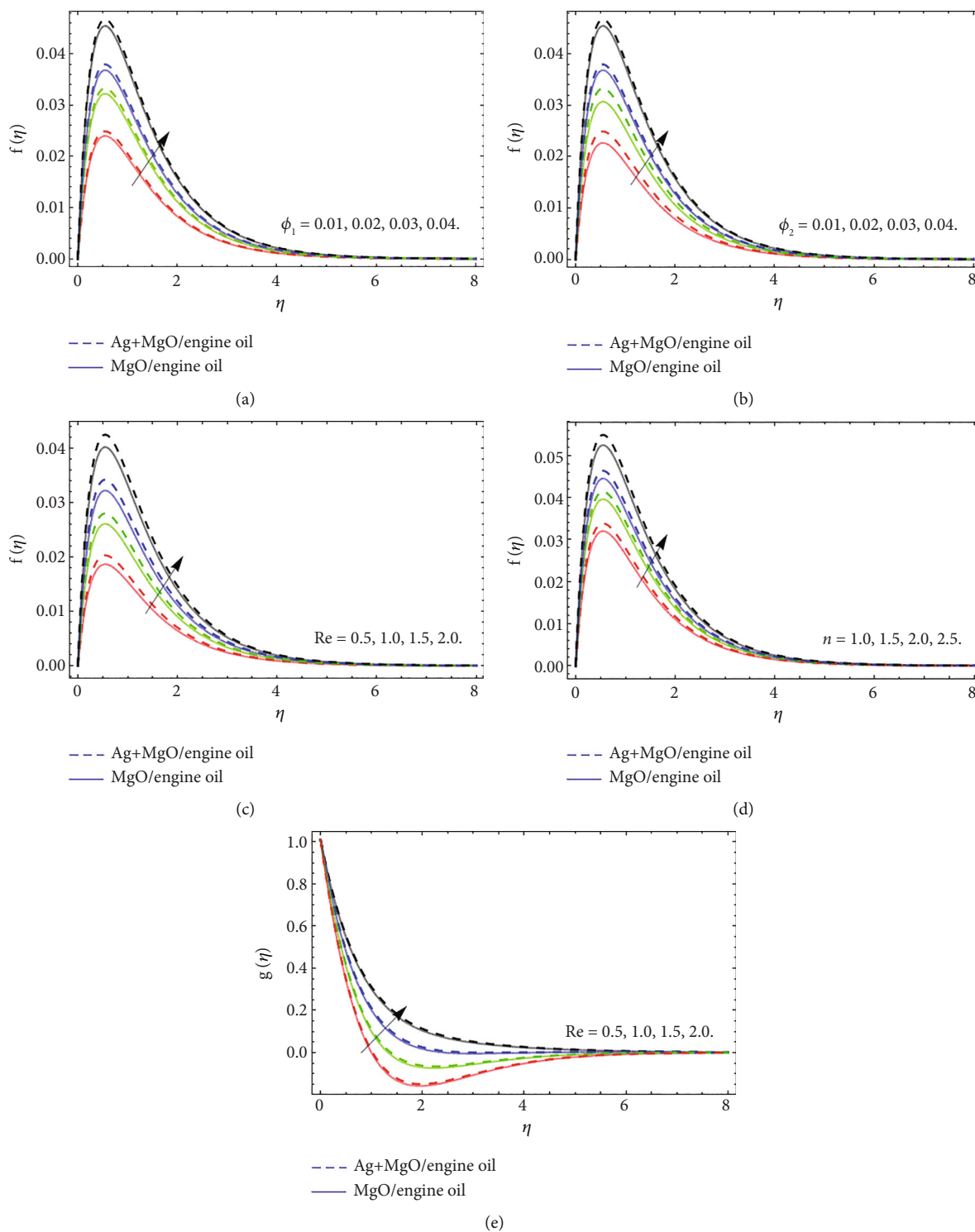


FIGURE 2: The nature of radial velocity  $f(\eta)$  and tangential velocity  $g(\eta)$  profiles versus (a) volume friction  $\phi_1$ , (b) volume friction  $\phi_2$ , (c) Reynold number  $Re$ , (d) power-law exponent  $n$ , and (e) Reynold number  $Re$ .

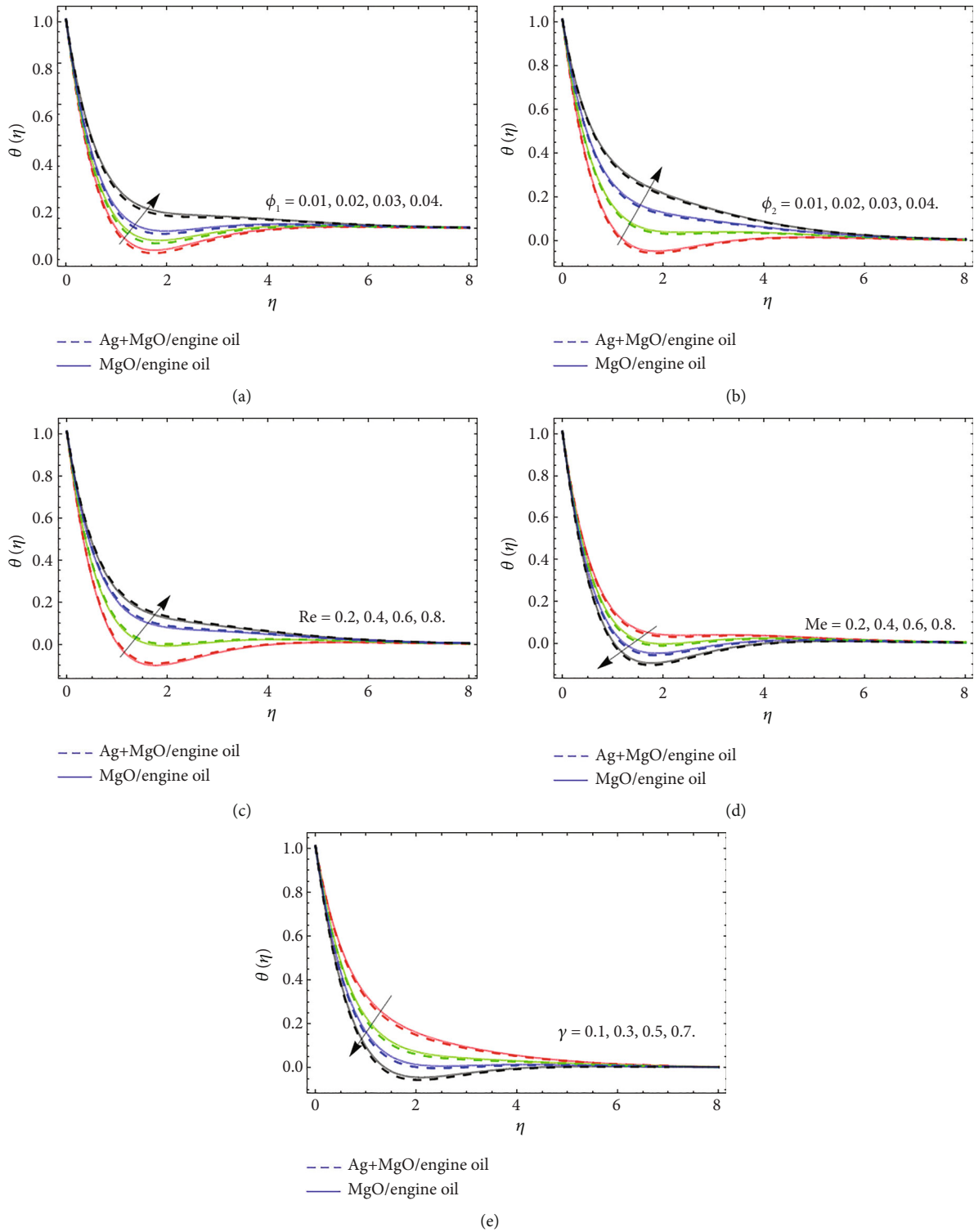


FIGURE 3: The energy outlines  $\theta(\eta)$  versus (a) volume friction  $\phi_1$ , (b) volume friction  $\phi_2$ , (c) Reynold number  $Re$ , (d) melting coefficient  $Me$ , and (e) thermal relaxation parameter  $\gamma$ , respectively.

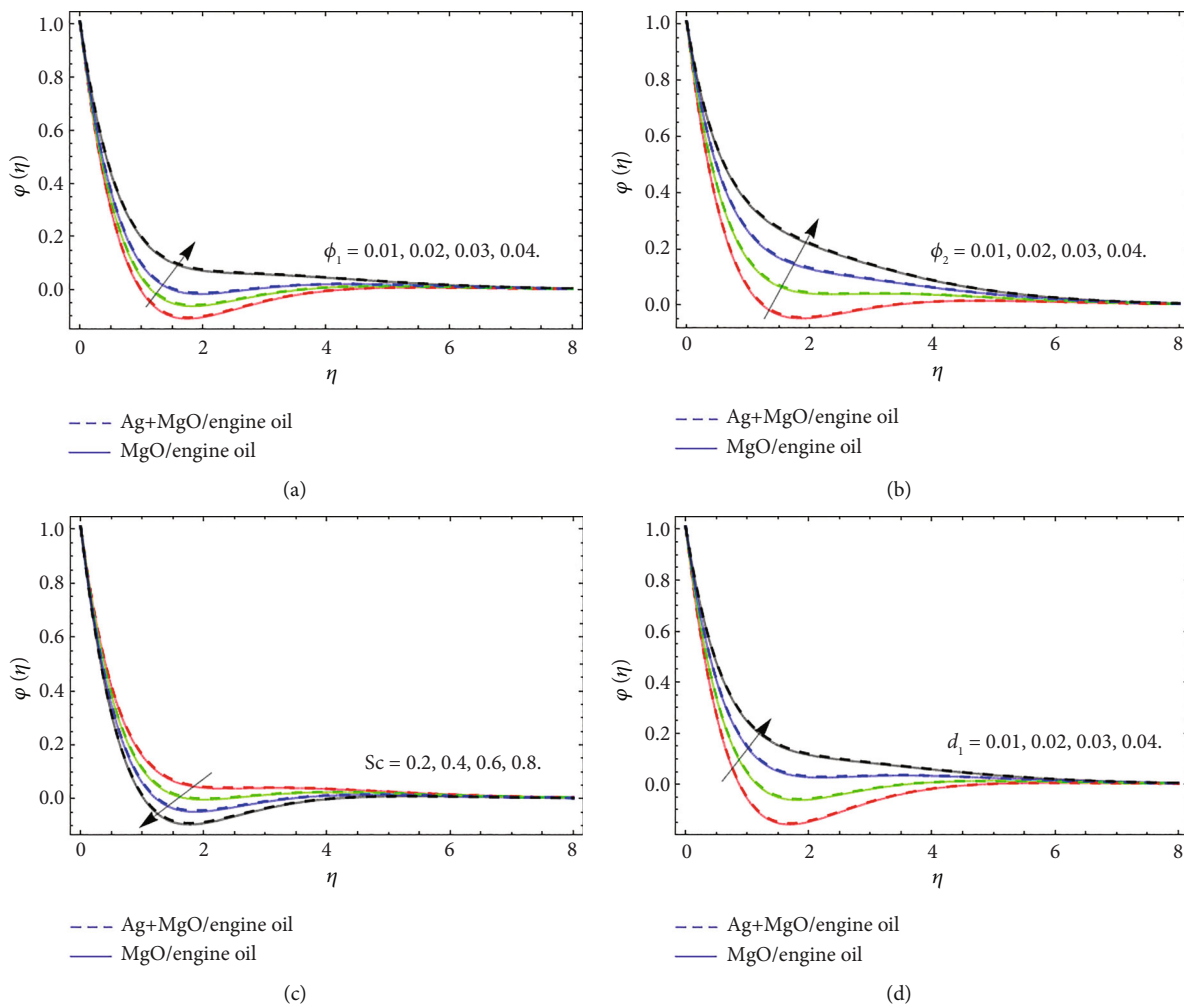


FIGURE 4: The nature of mass transition  $\varphi(\eta)$  versus (a) volume friction  $\varphi_1$ , (b) volume friction  $\varphi_2$ , (c) Schmidt number  $Sc$ , (d) chemical reaction  $d_1$ , respectively.

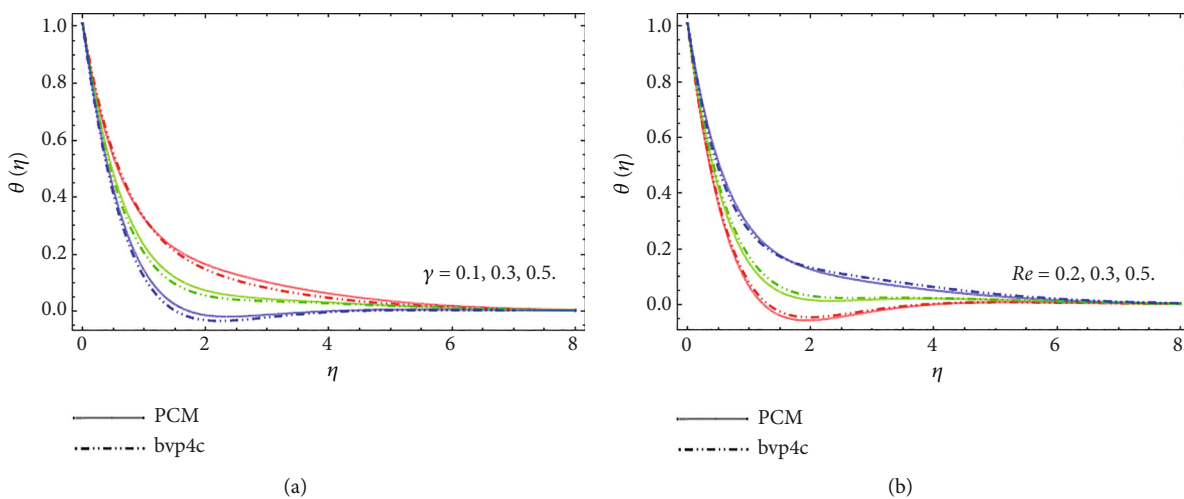


FIGURE 5: The comparison between PCM and Matlab built-in package bvp4c.

TABLE 2: The experimental values of Ag, MO, and engine oil [47].

	$\rho(\text{kg/m}^3)$	$C_p(\text{J/kg}\cdot\text{K})$	$k(\text{W/mK})$
Engine oil	884	1910	0.114
Magnesium oxide	3560	955	45
Silver	10,500	235	429

TABLE 3: Comparative analysis with the existing literature, when  $n = 1$  and  $\phi_{hnf} = 0..$ 

Order of approximations	$f'(0)$	$-g'(0)$
Present work	0.499321	0.500761
Zhang <i>et al.</i> [47]	0.497201	0.509623
Xun <i>et al.</i> [50]	0.410221	0.515911
Ming <i>et al.</i> [51]	0.410200	0.515901

TABLE 4: Statistical outcomes for skin friction ( $f'(0), -g'(0)$ ).

$m$	$\tau$	$Re$	$\phi_2$	$f'(0)$	$-g'(0)$
0.1	0.4	1.0	0.03	0.0474535	0.0702328
0.5	0.4	1.0	0.03	0.0554123	0.0739932
1.0	0.4	1.0	0.03	0.0664852	0.0815843
1.5	0.4	1.0	0.03	0.0791107	0.1130261
1.0	0.1	1.0	0.03	0.0664588	0.0817175
1.0	0.3	1.0	0.03	0.0664760	0.0716306
1.0	0.7	1.0	0.03	0.0664968	0.0815362
1.0	0.4	1.0	0.03	0.0665151	0.0814336
1.0	0.4	0.1	0.03	0.0629418	0.1161421
1.0	0.4	0.5	0.03	0.0685427	0.0857223
1.0	0.4	1.5	0.03	0.0656935	0.0792518
1.0	0.4	2.5	0.00	0.0644128	0.0764015
1.0	0.4	1.0	0.01	0.0726520	0.1136461
1.0	0.4	1.0	0.02	0.0705745	0.0893014
1.0	0.4	1.0	0.03	0.0686036	0.0852958
1.0	0.4	1.0	0.04	0.0667325	0.0815843

Step 3: apply the Cauchy principle and discretized Equation (26)

$$\frac{U^{i+1} - U^i}{\Delta\eta} = AU^{i+1}, \quad \frac{W^{i+1} - W^i}{\Delta\eta} = AW^{i+1}. \quad (27)$$

Finally, we get the iterative form as

$$U^{i+1} = (I - \Delta\eta A)^{-1} U^i, \quad W^{i+1} = (I - \Delta\eta A)^{-1} (W^i + \Delta\eta R). \quad (28)$$

#### 4. Results and Discussion

The discussion segment analyzed the compartment of velocity, energy, and mass-circulation as compared to the deviation of numerous physical parameters for hybrid nanoliquid consisting of Ag and magnetic nanoparticles.

TABLE 5: Arithmetic results for Nusselt number ( $k_{nf}/k_f\theta'(0), k_{hnf}/k_f\theta'(0)$ ).

Parameters		PCM	PCM	bvp4c	
Me	Re	$\phi_1, \phi_2$	$(k_{nf}/k_f)\theta'(0)$	$(k_{hnf}/k_f)\theta'(0)$	$(k_{hnf}/k_f)\theta'(0)$
0.1			0.0474535	0.0484531	0.0484340
0.5			0.0354123	0.0366122	0.0366031
1.0			0.0364852	0.0369853	0.0369542
1.5			0.0291107	0.0271407	0.0271268
	0.2		0.0564588	0.0554555	0.0554463
	0.3		0.0574760	0.0575961	0.0575870
	0.4		0.0578962	0.0589965	0.0589834
		0.01	0.0673420	0.0683460	0.0683352
		0.02	0.0683241	0.0693271	0.0693160
		0.03	0.0690324	0.0713142	0.0713021
		0.04	0.0723419	0.0743319	0.0743237

TABLE 6: Numerical outcomes for Sherwood number.

Sc	$d_1$	$\phi_1, \phi_2$	$(D_{nf}/D_f)\varphi'(0)$	$(D_{hnf}/D_f)\varphi'(0)$
0.2			0.0632328	0.0642322
0.4			0.062932	0.0639336
0.6			0.0615843	0.0614845
0.8			0.5930261	0.5910240
	0.1		0.0714336	0.0734331
	0.2		0.0761427	0.0771426
	0.3		0.0817223	0.0867224
	0.4		0.0822516	0.0882513
		0.01	0.0627612	0.0677635
		0.02	0.0638732	0.0728754
		0.03	0.6687450	0.7774504
		0.04	0.7026718	0.7906714

The default values used while solving the set of 1<sup>st</sup> order ODEs through PCM code are  $\phi_1 = \phi_2 = 0.01$ ,  $Re = 0.5$ ,  $n = 1.0$ ,  $Me = 0.2$ ,  $\gamma = 0.1$ ,  $Sc = 0.2$ ,  $d_1 = 0.01$  and  $\tau = 0.4$ .

**4.1. Velocity Profile.** Figures 2(a)–2(e) expose the nature of radial velocity  $f(\eta)$  and tangential velocity  $g(\eta)$  profiles versus volume friction  $\phi_1$ , volume friction  $\phi_2$ , Reynold number  $Re$ , power-law exponent  $n$ , and Reynold number  $Re$ . Figures 2(a) and 2(b) particularize that the velocity field rises with the growing values of volume friction of both silver and magnetic nanoparticles. Physically, the specific heat capacity of engine oil is much higher than silver and magnesium compounds that is why the increasing quantity of such nanomaterials reduces the average heat capacity of HNF and causes the elevation of fluid velocity. Figures 2(c) and 2(e) display the dominance of both radial  $f(\eta)$  and tangential velocity  $g(\eta)$  profiles against Reynold number  $Re$ . The upshot of Reynold's number increases the rotation of the disk, which accelerates the fluid particles and exercises their kinetic energy, which causes the improvement in the velocity

field. Similar behavior of radial velocity has been observed versus the increment of power-law exponent  $n$  in Figure 2 (d). The positive variation in the power-law exponent significantly enhances the fluid velocity in the radial direction.

**4.2. Energy Distribution Profile.** Figures 3(a)–3(e) illuminate the nature of energy transition  $\theta(\eta)$  versus volume friction  $\phi_1$ , volume friction  $\phi_2$ , Reynold number  $Re$ , melting coefficient, and thermal relaxation parameter  $\gamma$ , respectively. As discussed in Figure 2, the specific heat capacity of engine oil is much higher than silver and magnesium compounds that is why the increasing quantity of such nanomaterials reduces the average heat capacity of hybrid nanofluid and causes a rise in internal heat, which encourage both velocity and energy transmission rate. Figure 3(c) reports the Reynold number upshot on the energy profile. The number of rotations enhances with the variation of Reynold number that is why due to internal kinetic energy fluid temperature  $\theta(\eta)$  also enhances. The effect of both melting coefficient and thermal relaxation term  $\gamma$  reduces energy contour as shown in Figures 3(d) and 3(e). The specific heat capacity of fluid improves with the flourishing values of melting coefficient, as a result, energy transference enhances.

**4.3. Mass Transfer Profile.** Figures 4(a)–4(d) spot the nature of mass transition  $\varphi(\eta)$  versus volume friction  $\phi_1$ , volume friction  $\phi_2$ , Schmidt number  $Sc$ , and chemical reaction  $d_1$ , respectively. Mass transmission enhances with the rising quantity of nanoparticles, because, as we have discussed earlier, the rising values of volume friction parameters  $\phi_1$  and  $\phi_2$  significantly elevated the heat and fluid velocity that is why the mass transition also enhances their effects as shown in Figures 4(a) and 4(b). The upshot of the Schmidt number boosts the fluid kinetic viscosity, which results in the reduction of concentration profile  $\varphi(\eta)$  as illustrated in Figure 4(c). The energy transport rate is reduced by the chemical reaction variable, while the mass transport rate is increased. An increase in the intensity of  $d_1$  indicates that the species concentration interaction is less with the thermal boundary layer and more with the momentum Figure 4(d).

Figure 5 reports the comparative assessment of PCM technique with Matlab code `bvp4c`. From Figures 5(a) and 5(b), it can be clearly observed that both techniques show best settlement and PCM procedure is a reliable method. Table 2 describes the experimental values of Ag, MgO, and engine oil. Table 3 displays the comparative analysis of the current work with the existing literature, in which the present work revealed the best settlement with them. Table 4 presents the numerical results for skin friction. It has been observed that the drag force enhances along both radial and tangential direction with the variation of parameter  $m$  and  $\tau$  while reduces the effect of Reynold number. Table 5 communicates the numerical outcomes for Nusselt number versus melting coefficient, Reynold number, and both nanofluid and hybrid nanofluid. As comparative to the simple nanofluid, hybrid nanofluid energy transition rate is faster against volume friction coefficient  $\phi_1, \phi_2$ , respectively. Table 6 displays the Sherwood number versus volume friction parameter  $\phi_1, \phi_2$ , Schmidt number, and chemical reac-

tion  $d_1$  constant, respectively. The mass transference rate diminishes with the rising effect of Schmidt number while enhances against the increasing quantity of chemical reaction parameter and volume friction constants.

## 5. Conclusion

The 3D flow of Ag and MgO HNF past over a gyrating disk of varying thickness has been reported in the present estimation. The hybrid nanoliquid is synthesized by using silver, magnetic nanoparticulate, and engine oil. The energy transition consequences are examined in the involvement of melting heat propagation. The highly nonlinear system of PDEs is processed through the proper similarity conversions to attain the coupled ODE system. The obtained system of modeled equations is numerically solved through the PCM technique. The key points are rebound as follows:

- (i) The radial  $f(\eta)$  and tangential  $g(\eta)$  velocities and energy propagation enhance with the rising values of volume friction of both silver  $\phi_{1=Ag}$  and magnetic nanoparticulates  $\phi_{2=MgO}$
- (ii) The upshot of Reynold number  $Re$  improves the velocity and energy transition of fluid flow, due to an increase in the number of disk's rotation
- (iii) The positive variation in power-law exponent  $n$  significantly enhances the fluid velocity in the radial direction
- (iv) The increasing quantity of nanomaterials reduces the average heat capacity of hybrid nanofluid and causes a rise in internal heat, which encourages both velocity and heat transition rate
- (v) The effect of both melting coefficient and thermal relaxation term  $\gamma$  reduces fluid temperature

## Data Availability

The relevant data exist in the manuscript.

## Conflicts of Interest

The authors declare that they have no conflicts of interest.

## Authors' Contributions

Muhammad Bilal and Taza Gul contributed to the modeling and writing manuscript and conception or design of the work. Abir Mouldi, Safyan Mukhtar, Wajdi Alghamdi, Souhail Mohamed Bouzgarrou, and Nosheen Feroz contributed to the validation and critical revision of the article.

## Acknowledgments

The authors extend their appreciation to the Deanship of Scientific Research at King Khalid University for funding this work through Large Groups Project under grant number (RGP2./14/43).



## References

- [1] A. Ahmadian, M. Bilal, M. A. Khan, and M. I. Asjad, "The non-Newtonian Maxwell nanofluid flow between two parallel rotating disks under the effects of magnetic field," *Scientific Reports*, vol. 10, no. 1, pp. 1–14, 2020.
- [2] K. Anantha Kumar, V. Sugunamma, and N. Sandeep, "Influence of viscous dissipation on MHD flow of micropolar fluid over a slendering stretching surface with modified heat flux model," *Journal of Thermal Analysis and Calorimetry*, vol. 139, no. 6, pp. 3661–3674, 2020.
- [3] B. Ramadevi, K. Anantha Kumar, V. Sugunamma, J. V. Ramana Reddy, and N. Sandeep, "Magnetohydrodynamic mixed convective flow of micropolar fluid past a stretching surface using modified Fourier's heat flux model," *Journal of Thermal Analysis and Calorimetry*, vol. 139, no. 2, pp. 1379–1393, 2020.
- [4] Y. P. Lv, E. A. Algehyne, M. G. Alshehri et al., "Numerical approach towards gyrotactic microorganisms hybrid nanofluid flow with the hall current and magnetic field over a spinning disk," *Scientific Reports*, vol. 11, no. 1, pp. 1–13, 2021.
- [5] Y. X. Li, T. Muhammad, M. Bilal, M. A. Khan, A. Ahmadian, and B. A. Pansera, "Fractional simulation for Darcy-Forchheimer hybrid nanofluid flow with partial slip over a spinning disk," *Alexandria Engineering Journal*, vol. 60, no. 5, pp. 4787–4796, 2021.
- [6] M. Khan, J. Ahmed, and W. Ali, "Thermal analysis for radiative flow of magnetized Maxwell fluid over a vertically moving rotating disk," *Journal of Thermal Analysis and Calorimetry*, vol. 143, no. 6, pp. 4081–4094, 2021.
- [7] M. Shuaib, R. A. Shah, and M. Bilal, "Von-Karman rotating flow in variable magnetic field with variable physical properties," *Advances in Mechanical Engineering*, vol. 13, no. 2, 2021.
- [8] M. Bilal, A. Saeed, T. Gul, I. Ali, W. Kumam, and P. Kumam, "Numerical approximation of microorganisms hybrid nanofluid flow induced by a wavy fluctuating spinning disc," *Coatings*, vol. 11, no. 9, p. 1032, 2021.
- [9] A. Hafeez, M. Khan, and J. Ahmed, "Thermal aspects of chemically reactive Oldroyd-B fluid flow over a rotating disk with Cattaneo-Christov heat flux theory," *Journal of Thermal Analysis and Calorimetry*, vol. 144, no. 3, pp. 793–803, 2021.
- [10] H. Waqas, M. Imran, T. Muhammad, S. M. Sait, and R. Ellahi, "Numerical investigation on bioconvection flow of Oldroyd-B nanofluid with nonlinear thermal radiation and motile microorganisms over rotating disk," *Journal of Thermal Analysis & Calorimetry*, vol. 145, no. 2, pp. 523–539, 2021.
- [11] A. Tassaddiq, S. Khan, M. Bilal et al., "Heat and mass transfer together with hybrid nanofluid flow over a rotating disk," *AIP Advances*, vol. 10, no. 5, article 055317, 2020.
- [12] I. Tlili, N. Sandeep, M. G. Reddy, and H. A. Nabwey, "Effect of radiation on engine oil-TC4/NiCr mixture nanofluid flow over a revolving cone in mutable permeable medium," *Ain Shams Engineering Journal*, vol. 11, no. 4, pp. 1255–1263, 2020.
- [13] F. Jamil and H. M. Ali, "Applications of hybrid nanofluids in different fields," in *In Hybrid nanofluids for convection heat transfer*, Academic Press, 2020.
- [14] G. P. Ashwinkumar, S. P. Samrat, and N. Sandeep, "Convective heat transfer in MHD hybrid nanofluid flow over two different geometries," *International Communications in Heat and Mass Transfer*, vol. 127, p. 105563, 2021.
- [15] N. Joshi, A. K. Pandey, H. Upreti, and M. Kumar, "Mixed convection flow of magnetic hybrid nanofluid over a bidirectional porous surface with internal heat generation and a higher-order chemical reaction," *Heat Transfer*, vol. 50, no. 4, pp. 3661–3682, 2021.
- [16] H. Upreti, A. K. Pandey, and M. Kumar, "Thermophoresis and suction/injection roles on free convective MHD flow of Ag-kerosene oil nanofluid," *Journal of Computational Design and Engineering*, vol. 7, no. 3, pp. 386–396, 2020.
- [17] Y. M. Chu, U. Nazir, M. Sohail, M. M. Selim, and J. R. Lee, "Enhancement in thermal energy and solute particles using hybrid nanoparticles by engaging activation energy and chemical reaction over a parabolic surface via finite element approach," *Fractal and Fractional*, vol. 5, no. 3, p. 119, 2021.
- [18] C. Fisher, E. Rider, Z. Jun Han, S. Kumar, I. Levchenko, and K. K. Ostrikov, "Applications and nanotoxicity of carbon nanotubes and graphene in biomedicine," *Journal of Nanomaterials*, vol. 2012, 19 pages, 2012.
- [19] M. I. Asjad, M. Zahid, Y. M. Chu, and D. Baleanu, "Prabhakar fractional derivative and its applications in the transport phenomena containing nanoparticles," *Thermal Science*, vol. 25, no. 2, pp. 411–416, 2021.
- [20] K. Singh, A. K. Pandey, and M. Kumar, "Slip flow of micropolar fluid through a permeable wedge due to the effects of chemical reaction and heat source/sink with Hall and ion-slip currents: an analytic approach," *Propulsion and Power Research*, vol. 9, no. 3, pp. 289–303, 2020.
- [21] I. Ullah, "Heat transfer enhancement in Marangoni convection and nonlinear radiative flow of gasoline oil conveying boehmite alumina and aluminum alloy nanoparticles," *International Communications in Heat and Mass Transfer*, vol. 132, p. 105920, 2022.
- [22] X. Wang, L. Luo, J. Xiang et al., "A comprehensive review on the application of nanofluid in heat pipe based on the machine learning: theory, application and prediction," *Renewable and Sustainable Energy Reviews*, vol. 150, p. 111434, 2021.
- [23] A. U. Khan, A. U. Khan, B. Li et al., "Biosynthesis of silver capped magnesium oxide nanocomposite using *Olea cuspidata* leaf extract and their photocatalytic, antioxidant and antibacterial activity," *Photodiagnosis and Photodynamic Therapy*, vol. 33, p. 102153, 2021.
- [24] I. Ullah, "Activation energy with exothermic/endothermic reaction and Coriolis force effects on magnetized nanomaterials flow through Darcy-Forchheimer porous space with variable features," *Waves in Random and Complex Media*, vol. 2022, pp. 1–15, 2022.
- [25] H. Upreti, A. K. Pandey, and M. Kumar, "Assessment of entropy generation and heat transfer in three-dimensional hybrid nanofluids flow due to convective surface and base fluids," *Journal of Porous Media*, vol. 24, no. 3, pp. 35–50, 2021.
- [26] I. Ullah, R. Ullah, M. S. Alqarni, W. F. Xia, and T. Muhammad, "Combined heat source and zero mass flux features on magnetized nanofluid flow by radial disk with the applications of Coriolis force and activation energy," *International Communications in Heat and Mass Transfer*, vol. 126, p. 105416, 2021.
- [27] A. Ahmadian, M. Bilal, M. A. Khan, and M. I. Asjad, "Numerical analysis of thermal conductive hybrid nanofluid flow over the surface of a wavy spinning disk," *Scientific Reports*, vol. 10, no. 1, pp. 1–13, 2020.
- [28] E. A. Algehyne, M. Areshi, A. Saeed, M. Bilal, W. Kumam, and P. Kumam, "Numerical simulation of bioconvective Darcy Forchheimer nanofluid flow with energy transition over a permeable vertical plate," *Scientific Reports*, vol. 12, no. 1, pp. 1–12, 2022.

- [29] X. H. Zhang, A. Algehyne, M. Alshehri, M. Bilal, M. A. Khan, and T. Muhammad, "The parametric study of hybrid nanofluid flow with heat transition characteristics over a fluctuating spinning disk," *PLoS One*, vol. 16, no. 8, article e0254457, 2021.
- [30] N. S. Anuar, N. Bachok, and I. Pop, "Influence of buoyancy force on Ag-MgO/water hybrid nanofluid flow in an inclined permeable stretching/shrinking sheet," *International Communications in Heat and Mass Transfer*, vol. 123, p. 105236, 2021.
- [31] K. Gangadhar, R. E. Nayak, M. V. S. Rao, and T. Kannan, "Nodal/saddle stagnation point slip flow of an aqueous convectional magnesium oxide-gold hybrid nanofluid with viscous dissipation," *Arabian Journal for Science and Engineering*, vol. 46, no. 3, pp. 2701–2710, 2021.
- [32] B. Hiba, F. Redouane, W. Jamshed et al., "A novel case study of thermal and streamline analysis in a grooved enclosure filled with (Ag-MgO/Water) hybrid nanofluid: Galerkin FEM," *Case Studies in Thermal Engineering*, vol. 28, p. 101372, 2021.
- [33] K. Singh, A. K. Pandey, and M. Kumar, "Melting heat transfer assessment on magnetic nanofluid flow past a porous stretching cylinder," *Journal of the Egyptian Mathematical Society*, vol. 29, no. 1, pp. 1–14, 2021.
- [34] S. Rashid, S. Sultana, Y. Karaca, A. Khalid, and Y. M. Chu, "Some further extensions considering discrete proportional fractional operators," *Fractals*, vol. 30, no. 1, p. 2240026, 2022.
- [35] N. Joshi, H. Upreti, A. K. Pandey, and M. Kumar, "Heat and mass transfer assessment of magnetic hybrid nanofluid flow via bidirectional porous surface with volumetric heat generation," *International Journal of Applied and Computational Mathematics*, vol. 7, no. 3, pp. 1–17, 2021.
- [36] N. Joshi, H. Upreti, and A. K. Pandey, "MHD Darcy-Forchheimer Cu-Ag/H<sub>2</sub>O-C<sub>2</sub>H<sub>6</sub>O<sub>2</sub> hybrid nanofluid flow via a porous stretching sheet with suction/blowing and viscous dissipation," *International Journal For Computational Methods In Engineering Science And Mechanics*, vol. 2022, pp. 1–9, 2022.
- [37] K. Karthikeyan, P. Karthikeyan, H. M. Baskonus, K. Venkatachalam, and Y. M. Chu, "Almost sectorial operators on  $\Psi$ -Hilfer derivative fractional impulsive integro-differential equations," *Mathematical Methods in the Applied Sciences*, vol. 2022, 2021.
- [38] M. A. Abd El Salam, M. A. Ramadan, M. A. Nassar, P. Agarwal, and Y. M. Chu, "Matrix computational collocation approach based on rational Chebyshev functions for nonlinear differential equations," *Advances in Difference Equations*, vol. 2021, 17 pages, 2021.
- [39] Y. M. Chu, N. A. Shah, P. Agarwal, and J. D. Chung, "Analysis of fractional multi-dimensional Navier-Stokes equation," *Advances in Difference Equations*, vol. 2021, 18 pages, 2021.
- [40] X. Qiang, A. Mahboob, and Y. M. Chu, "Numerical approximation of fractional-order Volterra integrodifferential equation," *Journal of Function Spaces*, vol. 2020, 12 pages, 2020.
- [41] A. Patil, *A Modification and Application of Parametric Continuation Method to Variety of Nonlinear Boundary Value Problems in Applied Mechanics*, Rochester Institute of Technology, 2016.
- [42] M. Shuaib, R. A. Shah, and M. Bilal, "Variable thickness flow over a rotating disk under the influence of variable magnetic field: an application to parametric continuation method," *Advances in Mechanical Engineering*, vol. 12, no. 6, 2020.
- [43] M. Shuaib, R. A. Shah, I. Durrani, and M. Bilal, "Electrokinetic viscous rotating disk flow of Poisson-Nernst-Planck equation for ion transport," *Journal of Molecular Liquids*, vol. 313, p. 113412, 2020.
- [44] Z. Dombovari, A. Iglesias, T. G. Molnar et al., "Experimental observations on unsafe zones in milling processes," *Philosophical Transactions of the Royal Society A*, vol. 377, no. 2153, p. 20180125, 2019.
- [45] Y. M. Chu, U. Khan, A. Zaib, S. H. A. M. Shah, and M. Marin, "Numerical and computer simulations of cross-flow in the streamwise direction through a moving surface comprising the significant impacts of viscous dissipation and magnetic fields: stability analysis and dual solutions," *Mathematical Problems in Engineering*, vol. 2020, 11 pages, 2020.
- [46] S. B. Chen, H. Jahanshahi, O. A. Abba et al., "The effect of market confidence on a financial system from the perspective of fractional calculus: numerical investigation and circuit realization," *Chaos, Solitons & Fractals*, vol. 140, p. 110223, 2020.
- [47] Y. Zhang, N. Shahmir, M. Ramzan, H. Alotaibi, and H. M. Aljohani, "Upshot of melting heat transfer in a Von Karman rotating flow of gold-silver/engine oil hybrid nanofluid with Cattaneo-Christov heat flux," *Case Studies in Thermal Engineering*, vol. 26, p. 101149, 2021.
- [48] G. Taza and M. Zakaullah, "A thermal performance of the graphene oxide nanofluids flow in an upright channel through a permeable medium," *IEEE Access*, vol. 7, pp. 102345–102355, 2019.
- [49] T. Hayat, S. Qayyum, M. Imtiaz, and A. Alsaedi, "MHD flow and heat transfer between coaxial rotating stretchable disks in a thermally stratified medium," *PLoS One*, vol. 11, no. 5, article e0155899, 2016.
- [50] S. Xun, J. Zhao, L. Zheng, X. Chen, and X. Zhang, "Flow and heat transfer of Ostwald-de Waele fluid over a variable thickness rotating disk with index decreasing," *International Journal of Heat and Mass Transfer*, vol. 103, pp. 1214–1224, 2016.
- [51] C. Ming, L. Zheng, and X. Zhang, "Steady flow and heat transfer of the power-law fluid over a rotating disk," *International Communications in Heat and Mass Transfer*, vol. 38, no. 3, pp. 280–284, 2011.

## Research Article

# Entropy Generation Analysis for MHD Flow of Hybrid Nanofluids over a Curved Stretching Surface with Shape Effects

Basharat Ullah <sup>1</sup>, Umar Khan,<sup>1</sup> Hafiz Abdul Wahab <sup>1</sup>, Ilyas Khan <sup>2</sup>,  
and Md. Nur Alam <sup>3</sup>

<sup>1</sup>Department of Mathematics and Statistics, Hazara University, Mansehra 21120, Pakistan

<sup>2</sup>Department of Mathematics, College of Science, Al-Zulfi, Majmaah University, Al-Majmaah 11952, Saudi Arabia

<sup>3</sup>Department of Mathematics, Pabna University of Science & Technology, Pabna 6600, Bangladesh

Correspondence should be addressed to Hafiz Abdul Wahab; wahab@hu.edu.pk and Md. Nur Alam; nuralam.pstu23@gmail.com

Received 9 September 2021; Accepted 30 May 2022; Published 15 June 2022

Academic Editor: Iaroslav Gnilitzky

Copyright © 2022 Basharat Ullah et al. This is an open access article distributed under the Creative Commons Attribution License, which permits unrestricted use, distribution, and reproduction in any medium, provided the original work is properly cited.

The characteristic of magnetohydrodynamic flow of viscous fluids is explained here. The energy equation behavior is studied in the presence of heat, viscous dissipation, and joule heating. The major emphasis of this study is the physical behavior of the entropy optimization rate. Based on the implementation of curvilinear coordinates, the basic flow equations are established. Nonlinear partial differential expressions are reduced by appropriate transformation to the ordinary differential system. In the engineering and industrial processes, nanoparticles and their shape have practical consequences. For this reason, we give a detailed investigation of the shape impacts on the flow through the curved stretching surface of nanoparticles. The flow equations are reduced into a number of nonlinear differential equations which are solved numerically using a useful numerical approach called Runge-Kutta-4 (RK-4). The shooting method is first used to reduce the equations to a number of problems of first order, and then the RK-4 approach is used for solution. Impacts for entropy optimization, Bejan number, velocity, concentration, and temperature of several physical parameters are graphically studied.

## 1. Introduction

During the last few decades, extensive surfaces have been received by researchers. This is due to its extensive uses in mining, metallurgy, and engineering. In the production processes, sheet stretching has certain activities with respect to product characteristics. These applications are important in different real-life processes due to different stretching speeds such as rubber-plating flow generation, metal casting continuous, fiber spinning, paper products, glass blowing and fiber, wire drawing, and polymer sheeting. Due to viscous dissipation, the distribution of the temperature changes as a source of energy, which results in changes in the heat conductivity. Several researchers have recently been interested in developing and designing new cooling/heating equipment and machines.

In magnetohydrodynamic fluid flow, Rashidi et al. [1] highlight the impacts of thermal fluxes and the mixtures by means of a porous stretching sheet. Swain et al. [2] have investigated the heating transmission behaviors in a porous

medium for MHD flow in an exponentially expanding sheet. Thermal flux effects and Eid et al. [3] present magnetohydrodynamics in Carreau nanomaterials, which float a porous, nonlinear stretch sheet. Sheikholeslami et al. [4] analyzed the stretchable and forced surface flow of nanomaterials from MHD. The main results of the study demonstrate that radiation parameter improvement reduces the heat transfer rate. Imtiaz et al. [5] examine the effect of the chemical reaction to quartic autocatalysis in magnetohydrodynamic flow from a curved stretchable surface. Hayat et al. [6] analyzed viscous fluid MHD flow over a nonlinear curved, heat generation/absorption stretchable surface.

Usman et al. [7] demonstrate electromagnetic couple stress film flow of hybrid nanofluid over an unsteady rotating disc. Hayat et al. [8] examine the effect of thermal rays and chemical reactions on MHD convective flow through a curved stretching surface. Abbas et al. [9] investigate the flow of hydrodynamic nanomaterial by means of a curved thermal stretching field. The first step was taken to propose

an analytical model for the therapeutic efficiency of nanofluids. This model contains the concentration of nanoparticles and the thermal conductivity of the base fluid and nanoparticles.

Moreover, only spherical nanoparticle inclusions are required. Hamilton suggested a model for nonspherical nanoparticles to address this deficiency. Further studies are carried out in this area with a variety of models exploring nanoparticles sort [10–12], particulate form [13], particle size [14], and others. Furthermore, many scientists would also be interested in various heat transfer mechanisms, including Brownian particle motion [15], accumulation of particles [16, 17], and liquid layers [18].

While nanofluids can live up to the thermal efficiency thirst, researchers are still searching for different fluid forms. Hybrid nanofluids are hybrid nanofluid types with excellent thermal performance compared with nanofluids. These fluids were created by scattering into a base fluid two or more types of little particles inside the base fluid or composite nanostructures. This means that the homogeneous mixture of different products hardly could be imagined in a single substance, with the physicochemical properties [19]. The active role of hybrid nanofluids in the various applications of heat transfer is as follows: electronic cooling, automotive radiators, cooling generators, nuclear coolers, machining coolants, lubrications, solar heat, thermal storage, building heating, biomedical treatments, drug control, cooling, and protection. There are positive industrial characteristics, such as chemical stability and high thermal efficiency, which permit the efficient performance of nanofluids.

The measurement of entropy is used to explain the efficiency of many engineering and industrial systems. Various scientists and engineers therefore based their attention on the question of entropy. The sum of any sort of energy produced by a system or its surrounding irreversible processes is called entropy production. It is not necessary to use this energy for a successful operation. The second law of thermodynamics is used for entropy production. In contrast to the first law, Thermodynamics' second legislation is more effective. Irreversible processes include liquid flux due to resistance flux, diffusion, game heating, viscous fluid rubbing, chemical reaction, thermal radiation, etc. We regulated the entropy generation rate to boost the system's performance. The second law of thermodynamics states that entropy values must be null or larger within a system than 0. The entropy rate considering the porosity effect was discussed by Ajibade et al. [20]. The effects of entropy production caused by heat transmission over flat surfaces or stretching plates have examined by numerous researchers [21, 22], but few studies have found in the literature related to the investigation about rate of entropy production with thermal effects in the flow past stretching cylinders. Our current article theoretically examines transmission of thermal energy over a stretching cylinder using heat generation/absorption and Joule heating. Moreover, this work also investigates rate of entropy generation for the spinning flow system.

Entropy production eliminates the usable energy in the system in many engineering and industrial processes. In order to maximize energy in the system for efficient system operation, it is therefore imperative to evaluate the rate of

entropy generation in a system. Under the second thermodynamics theorem, all processes of flow and heat transfer undergo irreversible changes. The main cause of these irreversible changes is the lack of control during the processes. While steps to minimize these irreversible effects can be taken, all the energy lost cannot be recovered. The entropy of the system is increased by this process. This results in a standard metric for the investigation of the irreversibility effects of entropy generation rate. Bejan suggested this approach [23, 24]. Khan et al. [25] recently studied the entropy analysis in a curved tube.

This research is intended by means of a curved stretching surface to address entropy generation in MHD vincent fluid flow. Fluid velocity and temperature similarity solutions are obtained, and the reduced equation structure is numerically resolved by a Runge-Kutta shooting algorithm method. The effects of the various interesting variables are studied on the optimization of entropy, speed, number of Bejan, and temperature. The findings were subsequently described in graphical form along with a quantitative discussion about the embedded parameters.

## 2. Description of the Problem

Take a two-dimensional flow into a curved stretching sheet from an incompressible magnetohydrodynamic (MHD) viscous fluid. In a circle with radius  $R$ , the extension sheet is curved. The  $s$ -direction is perpendicular to the fluid motion direction along the stretching surface with the stretching velocity  $U_w(s) = as$  ( $a > 0$ ) and  $r$ -direction. In the  $r$  direction, the magnetic field ( $B_0$ ) is applied. The flow chart is shown in the Figure 1.

$$\frac{\partial}{\partial r}(r+R) + v + R \frac{\partial u}{\partial x} = 0, \quad (1)$$

$$\frac{u^2}{r+R} = \frac{1}{\rho_{\text{hnf}}} \frac{\partial H}{\partial r}, \quad (2)$$

$$\begin{aligned} v \frac{\partial u}{\partial r} + \frac{uR}{r+R} \frac{\partial u}{\partial s} + \frac{uv}{r+R} \\ = -\frac{1}{\rho_{\text{hnf}}} \frac{R}{r+R} \frac{\partial H}{\partial s} + v_{\text{hnf}} \left( \frac{\partial^2 u}{\partial r^2} + \frac{1}{r+R} \frac{\partial u}{\partial r} - \frac{u}{r+R} \right) \\ - \frac{\sigma B_0^2}{\rho_{\text{hnf}}} u, \end{aligned} \quad (3)$$

$$\begin{aligned} v \frac{\partial T}{\partial r} + u \frac{\partial T}{\partial s} \frac{R}{r+R} = \frac{\alpha_{\text{hnf}}}{(\rho c_p)_{\text{hnf}}} \left( \frac{\partial^2 T}{\partial r^2} + \frac{1}{r+R} \frac{\partial T}{\partial r} \right) \\ + \frac{\sigma B_0^2}{(\rho c_p)_{\text{hnf}}} u^2 + \frac{\mu_{\text{hnf}}}{(\rho c_p)_{\text{hnf}}} \\ \cdot \left( \left( \frac{\partial u}{\partial r} \right)^2 + \left( \frac{u}{r+R} \right)^2 \right) \\ + \frac{Q_0}{(\rho c_p)_{\text{hnf}}} (T - T_{\infty}). \end{aligned} \quad (4)$$

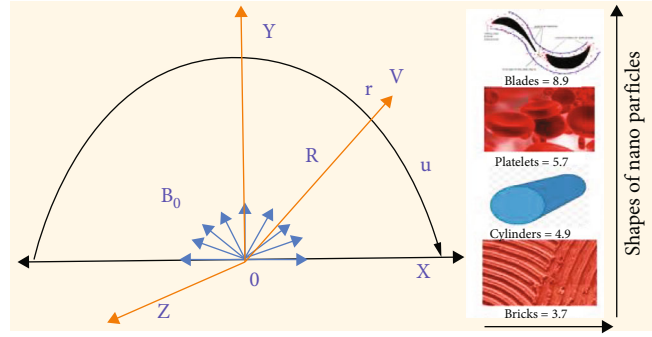


FIGURE 1: Geometry of problem.

TABLE 1: Thermophysical properties of nanofluid and hybrid nanofluid (see ref. [28]).

Properties	Nanofluid	Hybrid nanofluid
Density	$\rho_{nf} = (1 - \phi) + \phi_2 \rho_s$	$\rho_{hnf} = (1 - \phi_2) \left[ (1 - \phi_2) \rho_f + \phi_1 \rho_{s1} \right] + \phi_2 \rho_{s2}$
Heat capacity	$(\rho C_p)_{nf} = (1 - \phi) (\rho C_p)_f + \phi (\rho C_p)_s$	$(\rho_{cp})_{hnf} = (1 - \phi_2) \left[ (1 - \phi_1) (\rho_{cp})_f + \phi_1 (\rho_{cp})_{s1} \right] + \phi_2 (\rho_{cp})_{s2}$
Viscosity	$\mu_{nf} = \frac{\mu_f}{(1 - \phi)^{2.5}}$	$\mu_{hnf} = \frac{\mu_f}{(1 - \phi_1)^{2.5} (1 - \phi_2)^{2.5}}$
Thermal conductivity	$\frac{k_{nf}}{k_f} = \frac{k_s + (n - 1)k_f - (n - 1)\phi(k_f - k_s)}{k_s + (n - 1)k_f + \phi(k_f - k_s)}$	$\frac{k_{hnf}}{k_{bf}} = \frac{k_{s2} + (n - 1)k_{bf} - (n - 1)\phi_2(k_{bf} - k_{s2})}{k_{s2} + (n - 1)k_{bf} + \phi_2(k_{bf} - k_{s2})}$ where $k_{bf}/k_f = k_{s1} + (n - 1)\phi_1(k_f - k_{s1})/k_{s1} + (n - 1)k_f + \phi_1(k_f - k_{s1})$

$$u = U_w = as, v = 0, T = T_w = T_\infty \text{ at } r = 0, \quad (5)$$

$$u \rightarrow 0, \frac{\partial u}{\partial r} \rightarrow 0, T = T_\infty \text{ at } r \rightarrow \infty, \quad (6)$$

in which Eq. (1) reflects the preservation in the presence of transverse magnetic fields of mass, transverse, and axial components to preserve linear momentum in Eqs. (2) and (3), respectively. Furthermore, the energy equation defined in Eq. (4) will be used to analyze heat transfer. In addition,  $u$  and  $v$  denote  $s$ - and  $r$ -direction velocity components,  $H$  pressure,  $\rho_{hnf}$  hybrid nanofluid density,  $\nu$  kinematics viscosity,  $\mu$  dynamic viscosity,  $B_0$  strength of the magnetic field,  $\sigma$  electric conductivity,  $T$  and  $T_\infty$  surface temperatures and environmental temperatures, and  $Q_0$  heat generation, respectively. The transformation is used [26, 27]. Moreover, thermophysical properties of nanofluid and hybrid nanofluid, thermophysical properties of water, ethylene, and copper are displayed in Tables 1 and 2, respectively, which illustrate the effective property of  $Al_2O_3$ /water-based nanofluid and  $Cu/Al_2O_3$  hybrid nanofluid.

$$u = as f'(\zeta), v = -\frac{R}{r + R} \sqrt{av} f(\zeta), \theta(\zeta) = \frac{T - T_\infty}{T_w - T_\infty}, \quad (7)$$

$$H = \rho a^2 s^2 H(\zeta), \zeta = \sqrt{\frac{a}{\nu}} r.$$

The general relationship used to compute the density and specific heat for nanofluids (Brikman's model). The dynamic effective viscosity and the effective thermal conduc-

tivity are used by several researchers for many nanofluids and Maxwell's effective thermal conductivity model for two-phase mixtures.

Now, Eq. (1) is automatically verified, and Eqs. (2)–(4) are transformed to nondimensional ordinary differential equations as follows.

$$\left(\frac{1}{\psi_1}\right) H'(\zeta) = \frac{1}{\zeta + B} f'2, \quad (8)$$

$$\begin{aligned} \left(\frac{1}{\psi_1}\right) \frac{2B}{\zeta + B} H = & \left(\frac{1}{\psi_2}\right) \left( f'''' + \frac{1}{\zeta + B} f'' - \frac{B}{(\zeta + B)^2} f' \right. \\ & \left. - \frac{B}{\zeta + B} f'^2 \right) + \frac{B}{\zeta + B} f f'' \\ & + f f' \frac{B}{(\zeta + B)^2} - M f', \end{aligned} \quad (9)$$

$$\begin{aligned} & \frac{1}{\psi_3} \left( \theta'' + \frac{1}{\zeta + B} \theta' \right) \\ & + \frac{k_{hnf}}{k_{bf}} \left( MBr \left( f'^2 + \left(\frac{1}{\psi_4}\right) \left( f'^2 + \frac{1}{(\zeta + B)^2} f'^2 \right) \right) \right. \\ & \left. + Pr \frac{B}{\zeta + B} f \theta' \right) = 0, \end{aligned} \quad (10)$$

TABLE 2: Thermophysical properties of water, ethylene, and copper (see ref. [29]).

Properties	Water	Al <sub>2</sub> O <sub>3</sub>	Cu
$\rho \left( \frac{\text{kg}}{\text{m}^3} \right)$	997.0	3970	8933
$C_p \left( \frac{\text{J}}{\text{kgK}} \right)$	4180	765	385
$k \left( \frac{\text{W}}{\text{mK}} \right)$	0.6071	40	400

in which

$$\psi_1 = \frac{\rho_{\text{hnf}}}{\rho_f} = (1 - \phi_2) \left[ \left( (1 - \phi_1) + \phi_1 \frac{\rho_{s1}}{\rho_f} \right) \right] + \phi_2 \frac{\rho_{s2}}{\rho_f}, \quad (11)$$

$$\begin{aligned} \psi_2 &= \frac{v_f}{v_{\text{hnf}}} \\ &= (1 - \phi_1)^{2.5} (1 - \phi_2)^{2.5} \left\{ \left( (1 - \phi_2)(1 - \phi_1) + \phi_1 \frac{\rho_{s1}}{\rho_f} \right) \right\} \\ &\quad + \phi_2 \frac{\rho_{s2}}{\rho_f}, \end{aligned} \quad (12)$$

$$\begin{aligned} \psi_3 &= \frac{(\rho_{cp})_{\text{hnf}}}{(\rho_{cp})_f} \\ &= (1 - \phi_2) \left[ (1 - \phi_1) + \phi_1 \frac{(\rho_{cp})_{s1}}{(\rho_{cp})_f} \right] + \phi_2 \frac{(\rho_{cp})_{s2}}{(\rho_{cp})_f}, \end{aligned} \quad (13)$$

$$\begin{aligned} \psi_4 &= \frac{\mu_{\text{hnf}}}{(\rho_{cp})_{\text{hnf}}} \\ &= (1 - \phi_1)^{2.5} (1 - \phi_2)^{2.5} \left[ (1 - \phi_1) + \phi_1 \frac{(\rho_{cp})_{s1}}{(\rho_{cp})_f} \right] \\ &\quad + \phi_2 \frac{(\rho_{cp})_{s2}}{(\rho_{cp})_f}. \end{aligned} \quad (14)$$

Eliminating pressure  $H$  from Eqs. (8) and (9), we get

$$\begin{aligned} f^{iv} + \frac{2}{\zeta + B} f''' - \frac{1}{(\zeta + B)^2} f'' + \frac{1}{(\zeta + B)^3} f' \\ - (\psi_2) \left( \frac{B}{(\zeta + B)} f f'' + \frac{B}{(\zeta + B)} f f''' \right) - \frac{B}{(\zeta + B)^2} f'^2 \\ + \frac{B}{(\zeta + B)^2} f f'' - \frac{B}{(\zeta + B)^3} f f' - \frac{M}{\psi_1} \left( \frac{1}{(\zeta + B)} f' + f'' \right) = 0. \end{aligned} \quad (15)$$

The transformed boundary conditions are as follows:

$$f = 0, f' = 1, \theta = 1 \text{ at } \zeta = 0 \quad f' \rightarrow 0, f'' \rightarrow 0, \theta \rightarrow 0 \text{ as } \zeta \rightarrow \infty. \quad (16)$$

In the above relations,  $\text{Pr} = \nu_{\text{hnf}}/\alpha_{\text{hnf}}$  depicts the Prandtl number,  $M = (\sigma B_0^2/a\rho_{\text{hnf}})$  the Hartmann number,  $Ec = (a^2 s^2/(c_p)_{\text{hnf}}(T_w - T_\infty))$  the Eckert number,  $Br = (\text{Pr}Ec)$  the Brinkman number, and  $\beta = (Q_0/a(\rho c_p)_{\text{hnf}})$  the heat generation/absorption parameter, and  $B = \sqrt{a/\nu}$ ,  $R$ , is the curvature parameter.

**2.1. Skin Friction Coefficient and Local Nusselt Number.** The physical quantities of interest are skin friction coefficient  $C_f$  and local Nusselt number  $Nu_s$ , which are define as follows:

$$C_f = \frac{\tau_{rs}}{\rho_{\text{hnf}} u_w^2}, \quad Nu_s = \frac{sq_w}{k_{\text{hnf}}(T_w - T_\infty)}, \quad (17)$$

where the wall fraction  $\tau_{rs}$  and heat transfer  $q_w$  along the  $s$ -direction are define as follows:

$$\tau_{rs} = \mu_{\text{hnf}} \left( \frac{\partial u}{\partial r} - \frac{u}{r + R} \right) \Big|_{r=0}, \quad q_w = -k_{\text{hnf}} \left( \frac{\partial T}{\partial r} \right) \Big|_{r=0}. \quad (18)$$

In view of Eq. (7), expressions describe in Eq. (17) provide dimensionless skin friction and Nusselt as follows:

$$\left( \frac{Re_s}{2} \right)^{1/2} C_f = \frac{1}{(1 - \phi_2)} \left( f''(0) - \frac{1}{B} f'(0) \right), \quad (19)$$

$$\frac{L}{s} \left( \frac{Re_s}{2} \right)^{-1/2} Nu_s = -\frac{k_{\text{hnf}}'}{k_f} [\theta(0)], \quad (20)$$

where  $Re_s = \sqrt{a/\nu} s$  elucidates local Reynolds number.

**2.2. Entropy Generation Equation.** Measuring any sort of energy created in irreversible systems processes is referred to as the generation of entropy. Entropy generation is described in dimensional form:

$$S_G = \frac{k_{\text{hnf}}}{T_\infty^2} \left( \frac{\partial T}{\partial r} \right)^2 + \frac{\mu_{\text{hnf}}}{T_\infty} \left( \frac{\partial u}{\partial r} + \frac{u}{r + R} \right)^2 + \frac{\sigma B_0^2}{T_\infty} u^2. \quad (21)$$

Dimensionless version satisfies

$$N_G = \alpha_1 \theta'^2 + MBr f'^2 + Br \left( f'^2 + \frac{1}{(\zeta + B)^2} f'^2 + \frac{1}{\zeta + B} f' f'' \right). \quad (22)$$

Bejan number is expressed as follows:

$$\text{Be} = \frac{\text{Heat and mass transfer irreversibility}}{\text{Total Irreversibility}} \quad (23)$$

or

$$Be = \frac{\alpha_1 \theta'^2}{\alpha_1 \theta'^2 + MBrf'^2 + Br(f'^2 + (1/(\zeta + B))^2 f'^2 + (1/\zeta + B)f'f''')} \quad (24)$$

Here,  $N_G = (S_G T_\infty \nu / ak(T_w - T_\infty))$  denotes the entropy generation rate,  $\alpha_1 = (T_w - T_\infty / T_\infty)$  the temperature difference parameter, and  $Br = \mu_{\text{hnf}}(as)^2 / k(T_w - T_\infty)$  the Brinkman number.

For the sake of comparison, we have also solved the same problem by using the R-K-4 method (coupled with shooting technique), and the results are compared in Table 3. Both solutions show an excellent agreement with each other. These solutions are calculated for  $\beta = M = Br = 0.1$  and  $\phi_1 = \phi_2 = 0$ , and Prandtl number is taken to be 6.2.

### 3. Physical Description

In this section, we investigate the comportations of several interesting parameters for entropy optimization, velocity, number of Bejan, skin friction, and heat transfer rates.

**3.1. Velocity Profile.** For the velocity of different values, Figures 2–4 are shown. Changes of the axial velocity variable of dimensionless dimensions are shown in Figure 2, for  $B$ . The fluid velocity is also increased as the curvature parameter ( $B$ ) is increased. This means that when compared to the straight layer, the velocity of the curved layer is insufficient. This shift in velocity is much higher in shape.

The effect of  $M$  on velocity is plotted in Figure 3. Figure 3 shows that the parameter of  $M$  plays a role in this point. The explanation is that the fluid movement is due to the surface extension, and that any fluid change on the stretching surface helps decelerate the fluid flow. Moreover, it is apparent from this figure that for different form variables, the decrease in velocity occurs slightly greater.

Figure 4 is plotted to evaluate the effect on the velocity of varying shape variables of volumetric fractions  $\phi_2$ . From this figure, it is assumed that for shape variables, the velocity profile decreases in dominant.

**3.2. Temperature Profile.** The influences of  $B$ ,  $\beta$ ,  $Br$ ,  $M$  and  $\phi_2$  on  $\theta(\zeta)$  are plotted in Figures 5–9. The influence of these parameters on  $\theta(\zeta)$  is under discussion in the curved stretching surface. In addition, there are four distinct shape factors plotted for each graph. Figure 5 shows that ( $B$ ) has a decreasing  $\theta(\zeta)$  role to play. This is because the fluid acceleration is caused by surface stretching, and so any fluid ( $B$ ) change on the stretching surface causes the fluid to decelerate. Furthermore, it is evident from this figure that the decrease in range  $\theta(\zeta)$  is slightly more for different shape factors results.

Figure 6 is plotted to check the parameter ( $\beta$ ) for temperature effect. Through this calculation, it is discovered that the temperature increases with ( $\beta$ ). It is because the improvement in ( $\beta$ ) value strengthens the conduction effects and thereby increases the temperature. In the field outside

TABLE 3: Comparison between present result and ref. [25].

$M$	$B$	Ref [25]	Current result
0.2	0.8	6.975	6.9751
0.3		5.968	5.9683
0.4		5.123	5.1232
0.5	0.0	4.937	4.9371
	0.5	5.128	5.1283
	1.0	5.342	5.3422

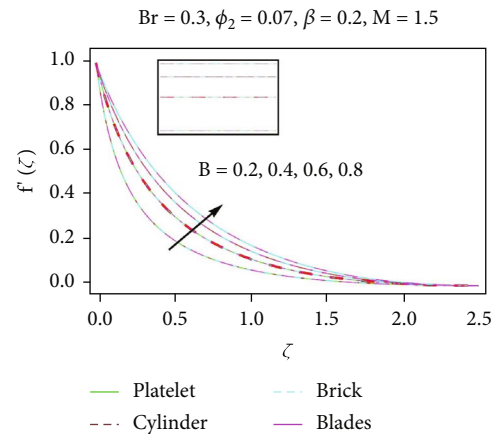


FIGURE 2: Impact of  $B$  on velocity.

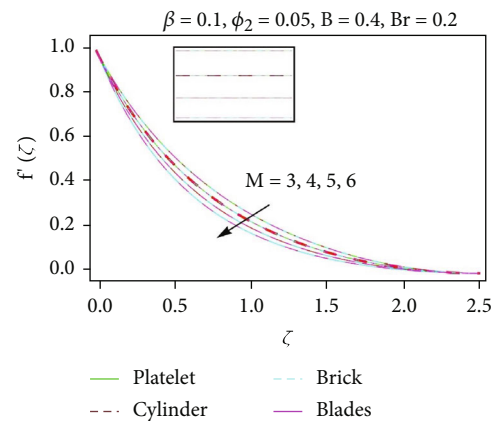


FIGURE 3: Impact of  $M$  on velocity.

the surface, the rise is prevalent and leads to the rising heat flux in the soil. Hybrid nanofluid-shape blade nanoparticles have the highest temperature and the lowest temperature of nanofluid nanoparticles formed by bricks. Furthermore, these effects are more massive than nanofluid in the case of hybrid nanofluids because hybrid nanofluid is more thermal than nanofluids.

Figure 7 indicates the effect of the parameter for the Brinkman number  $Br$ . From this figure, the parameter of heat generation is presumed to slowly affect the distribution of temperature. It is because it implies that the surface

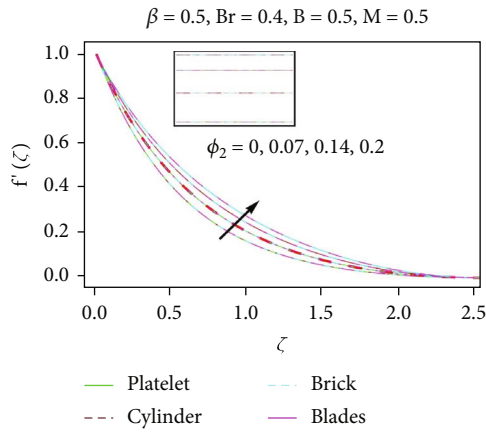


FIGURE 4: Impact of  $\phi_2$  on velocity.

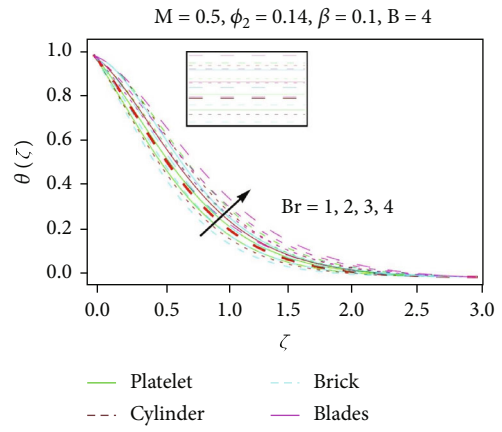


FIGURE 7: Impact of  $Br$  on temperature.

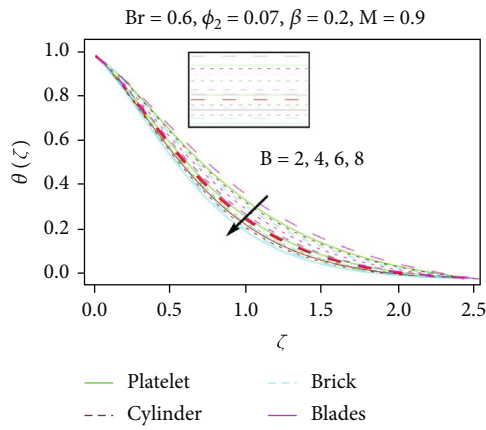


FIGURE 5: Impact of  $B$  on temperature.

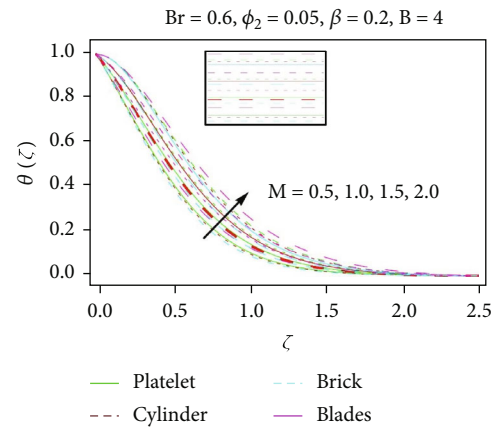


FIGURE 8: Impact of  $M$  on temperature.

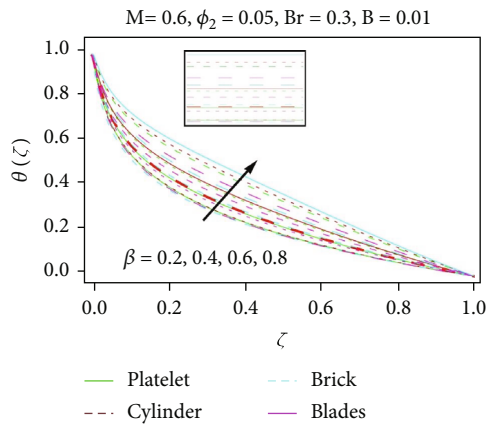


FIGURE 6: Impact of  $\beta$  on temperature.

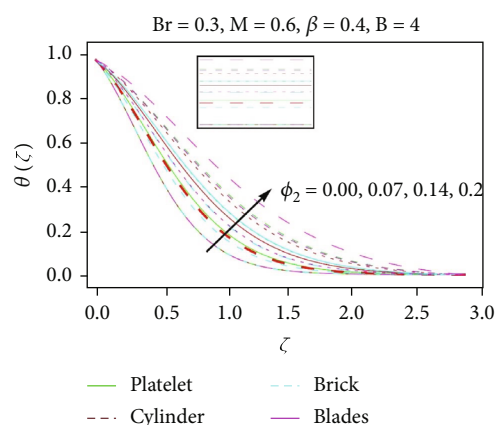


FIGURE 9: Impact of  $\phi_2$  on temperature.

temperature is above the ambient temperature, and more heat is transferred to the fluid from the ambient, which contributes to thermal boundary layer thickness and increasing temperature. In the case of hybrid nanofluid, this temperature rise is also assumed to predominate. The maximum temperature for blade-shaped nanofluid nanoparticles is

achieved; for brick-shaped nanofluid nanoparticles, the lowest temperature magnitude is noted.

The variance of the Hartmann number ( $M$ ) on  $\theta(\zeta)$  is shown in Figure 8. Here, we have found that higher ( $M$ ) values lead to an increase in  $\theta(\zeta)$  thickness and thermal boundaries. The implication is that the resistive force (force



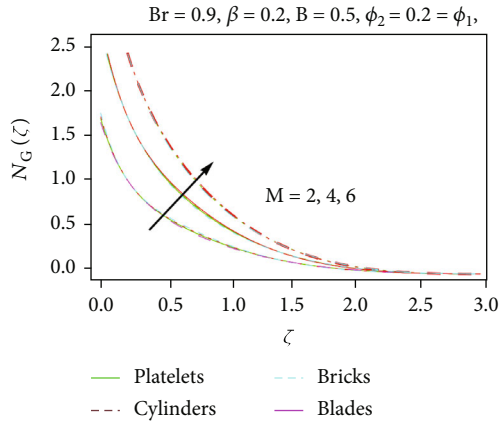


FIGURE 10: Impact of  $M$  on entropy generation.

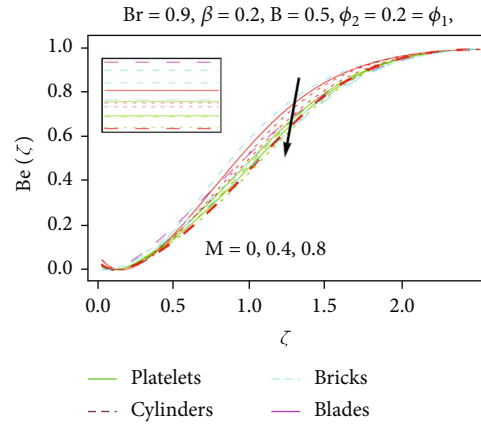


FIGURE 11: Impact of  $M$  on Bejan number.

Lorentz) increases with a higher value of  $M$  and therefore increases the temperature.

Figure 9 demonstrates the influence of volumetric fractions  $\phi_2$  on temperature. It is expected that the thickness of both the temperature and thermal boundary layer would grow with an increase of  $\phi_2$ . That is because  $\phi_2$  contributes to the deceleration of fluid flow and contributes indirectly to the magnitude of rising temperature. The temperature magnitude for hybrid nanofluids is also evident from this figure to be higher for the values of  $\phi_2$  than for the nanofluid value. In addition, hybrid nanofluid blade-shaped nanoparticles have a high temperature, and brick-shaped nanofluid nanoparticles have the lowest temperature.

**3.3. Entropy Generation.** Impacts on  $N_G$  and  $Be$  are examined in this section of a Hartmann number ( $M$ ), Brinkman number ( $Br$ ), and  $\phi_2$  volumetric fractions. Figures 10 and 11 illustrate the impact of Hartmann number ( $M$ ) on  $N_G$  and  $Be$ . Increased entropy generation ( $N_G$ ) in  $M$  is reported. Because of the fact that for higher ( $M$ ), the force of Lorentz creates greater resistance to fluid movement, and the entropy ( $N_G$ ) increases as expected. The Bejan number ( $Be$ ) was reduced compared to larger numbers ( $M$ ) of Hartmann.

The behavior of Brinkman number ( $Br$ ) on  $N_G$  and  $Be$  is illustrated in Figures 12 and 13. More ( $Br$ ) values are more entropy-generated ( $N_G$ ). In fact, the thermal conductivity decreases for higher estimates ( $Br$ ), and thus an increase is shown with the entropy optimization process. The counter effect is for ( $Br$ ) the Bejan number ( $Be$ ). The number of Bejan is the largest value if the number of Brinkman is zero and decreases accordingly ( $Br$ ).

Figures 14 and 15 are sketched for the impact of volumetric fractions  $\phi_2$  against ( $N_G$ ) and ( $Be$ ). It is noticed that the entropy of fluid increases for larger ( $N_G$ ) while Bejan number ( $Be$ ) reduces.

**3.4. Engineering Quantities.** In the final part of this section, Figures 16–19 are plotted to test the effect of different shape factor values in terms of variations of different embedded parameters on the local Nusselt number and skin friction. Numerous values of  $\phi_2$  were decorated with the horizontal

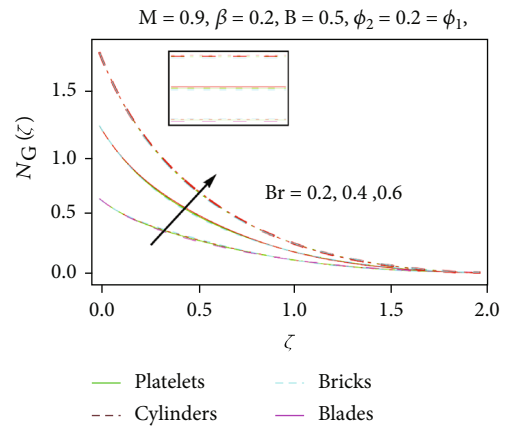


FIGURE 12: Impact of  $Br$  on entropy generation.

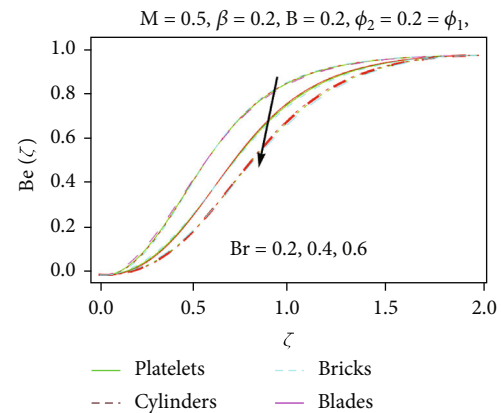


FIGURE 13: Impact of  $Br$  on Bejan number.

axis. From Figure 16, the case where the injection is paired with contraction, the parameter  $\beta$  increases the skin friction, while the parameter  $\phi_2$  shows a reversed behavior.

In addition, nanostructures formed by the blades possess high heat transmission. Figure 17 is plotted for the different values of  $M$ , which indicate the same corresponding analysis

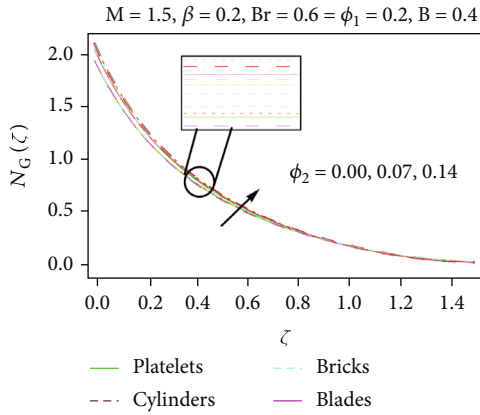


FIGURE 14: Impact of  $\phi_2$  on entropy generation.

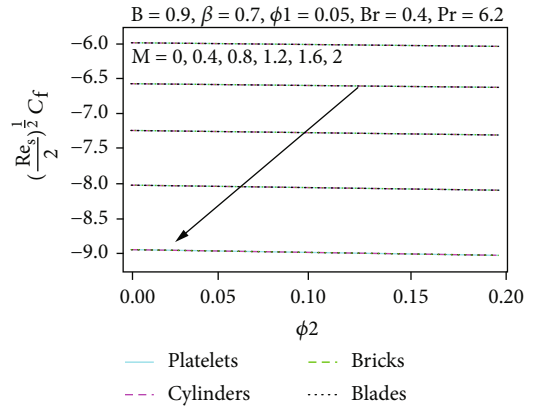


FIGURE 17: The variation of skin friction for varying  $\phi_2$  and  $M$ .

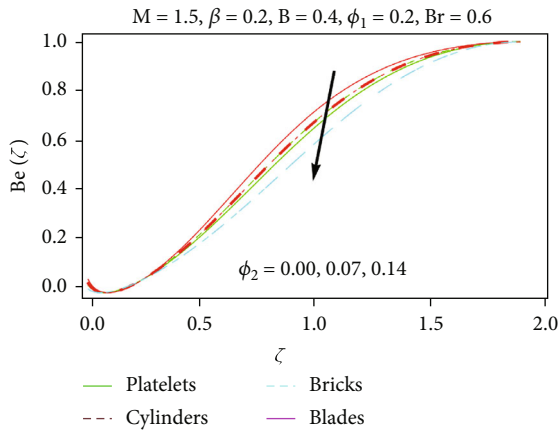


FIGURE 15: Impact of  $\phi_2$  on Bejan number.

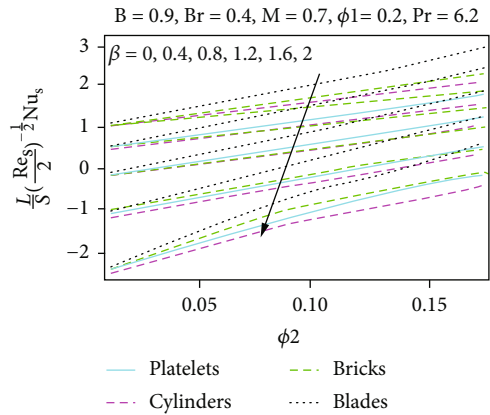


FIGURE 18: The variation of Nusselt number for varying  $\phi_2$  and  $\beta$ .

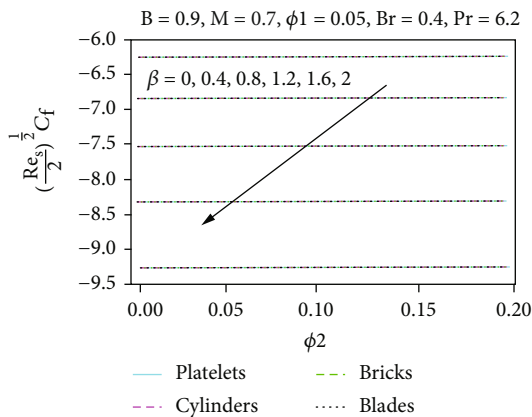


FIGURE 16: The variation of skin friction for varying  $\phi_2$  and  $\beta$ .

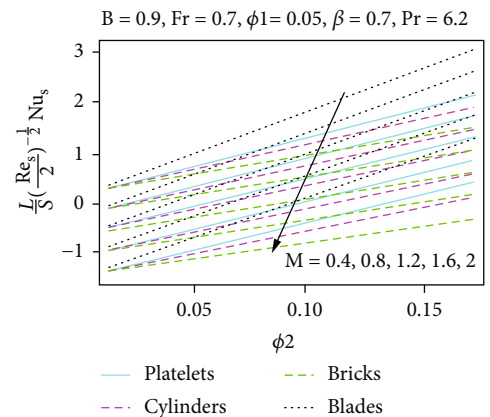


FIGURE 19: The variation of Nusselt number for varying  $\phi_2$  and  $M$ .

in Figure 16. Again, it has been found that nanocomposite-shaped blades are more capable of transferring heat than tiny particles formed by platelets, cylinders, or bricks.

Figures 18 and 19 show the effect  $\phi_2$ ,  $M$ , and  $\beta$  on the local heat transfer rate. Figure 18 shows that the local heat transfer rates decrease, as the value of  $\phi_2$  increases. For

blade-shaped nanoparticles, the rates are higher and against  $\beta$  are indicated.

The changes in the local number of Nusselt due to the increasing number of Hartmann ( $M$ ) are seen in Figure 19. It is found that nanoparticles formed by brick which decreases in the local heat transfer rate are lower than the others.

## 4. Conclusions

In this paper, the object of the present study is to analyze entropy generation with a curved stretcher surface of MHD flow of viscous fluids for several small particles. The findings of this study are concluded.

- (1) The velocity in the case of blade and brick small particles is noted to be rapidly increased
- (2) The fluid temperature increases quite slowly for platelet-shaped particles, and the rest of the nanoparticles show quit rapidly increases behavior
- (3) Enhancement in the curvature parameter increases the velocity profile, whereas the temperature profile diminishes
- (4) The heat generation parameter and Hartmann number contribute in lowering the magnitude of Nusselt number and increase in thermal radiation parameter and increase the magnitude of Nusselt number for both nano and hybrid nanofluids, respectively. Moreover, the magnitude of Nusselt number is slightly more in case of nanofluid as compare to hybrid nanofluid
- (5) Temperature and velocity profiles showed increasing activity in order to estimate the solid volume fraction
- (6) One of the essential sources of entropy production is a curved stretching sheet
- (7) For (Br) and ( $M$ ), NG shows the same results
- (8) For higher ( $M$ ) and (Br) numbers, (Be) is reduced

## Nomenclature

$u$ :	Component of velocity in the $x$ direction
$v$ :	Component of velocity in the $y$ direction
$\rho_{\text{hnf}}$ :	Density of hybrid nanofluid
$B_0$ :	Strength of the magnetic Field
$H$ :	Pressure
$\mu$ :	Dynamic viscosity
$\nu$ :	Kinematics viscosity
$\sigma$ :	Electric conductivity
$T$ :	Surface temperatures
$T_\infty$ :	Environmental temperatures
$Q_0$ :	Heat generation
$\rho_{\text{nf}}$ :	Density of nanofluid
$\rho_s$ :	Density of solid particle
$\phi_1, \phi_2$ :	Volume fraction of nanoparticles and hybrid nanoparticles
$k_f$ :	Conductivity of the base fluid
$\theta$ :	Dimensionless temperature
$m$ :	Shape factor of nanoparticles
$\zeta$ :	Dimensionless variable
$C_f$ :	Skin friction coefficient
Nu:	Nusselt number
Br:	Brinkman number
Ec:	Eckert number

$B$ :	Curvature parameter
Pr:	Prandtl number
$M$ :	Hartmann number
$N_G$ :	Entropy generation rate
$\alpha_1$ :	The temperature difference parameter
Be:	Bejan number.

## Data Availability

The study based on numerical technique and no data is used in findings of the study.

## Conflicts of Interest

The authors declare that they have no conflicts of interest.

## References

- [1] M. M. Rashidi, B. Rostami, N. Freidoonimehr, and S. Abbasbandy, "Free convective heat and mass transfer for MHD fluid flow over a permeable vertical stretching sheet in the presence of the radiation and buoyancy effects," *Ain Shams Engineering Journal*, vol. 5, no. 3, pp. 901–912, 2014.
- [2] I. Swain, S. Mishra, and H. Pattanayak, "Flow over Exponentially Stretching Sheet through Porous Medium with Heat Source/Sink," *Journal of Engineering*, vol. 2015, 7 pages, 2015.
- [3] M. Eid, K. Mahny, T. Muhammad, and M. Sheikholeslami, "Numerical treatment for Carreau nanofluid flow over a porous nonlinear stretching surface," *Results in physics*, vol. 8, pp. 1185–1193, 2018.
- [4] M. Sheikholeslami, M. Mustafa, and D. Domiri Ganji, "Effect of Lorentz forces on forced-convection nanofluid flow over a stretched surface," *Particuology*, vol. 26, pp. 108–113, 2015.
- [5] M. Imtiaz, T. Hayat, A. Alsaedi, and A. Hobiny, "Homogeneous-heterogeneous reactions in MHD flow due to an unsteady curved stretching surface," *Journal of Molecular Liquids*, vol. 221, pp. 245–253, 2016.
- [6] T. Hayat, R. Saif, R. Ellahi, T. Muhammad, and B. Ahmad, "Numerical study of boundary-layer flow due to a nonlinear curved stretching sheet with convective heat and mass conditions," *Results in physics*, vol. 7, pp. 2601–2606, 2017.
- [7] M. Usman, T. Gul, A. Khan, A. Alsubie, and M. Z. Ullah, "Electromagnetic couple stress film flow of hybrid nanofluid over an unsteady rotating disc," *International Communications in Heat and Mass Transfer*, vol. 127, article 105562, 2021.
- [8] T. Hayat, M. Rashid, M. Imtiaz, and A. Alsaedi, "MHD convective flow due to a curved surface with thermal radiation and chemical reaction," *Journal of Molecular Liquids*, vol. 225, pp. 482–489, 2017.
- [9] Z. Abbas, M. Naveed, and M. Sajid, "Hydromagnetic slip flow of nanofluid over a curved stretching surface with heat generation and thermal radiation," *Journal of Molecular Liquids*, vol. 215, pp. 756–762, 2016.
- [10] N. S. Khan, P. Kumam, and P. Thounthong, "Magnetic field promoted irreversible process of water based nanocomposites with heat and mass transfer flow," *Scientific Reports*, vol. 11, no. 1, pp. 1–25, 2021.
- [11] N. S. Khan, L. Ali, R. Ali, P. Kumam, and P. Thounthong, "A novel algorithm for the computation of systems containing different types of integral and integro differential equations," *Heat Transfer*, vol. 50, no. 4, pp. 3065–3078, 2021.

- [12] A. Saeed, M. Jawad, W. Alghamdi, S. Nasir, T. Gul, and P. Kumam, "Hybrid nanofluid flow through a spinning Darcy–Forchheimer porous space with thermal radiation," *Scientific reports*, vol. 11, no. 1, pp. 1–5, 2021.
- [13] M. Bilal, A. Saeed, M. M. Selim, T. Gul, I. Ali, and P. Kumam, "Comparative numerical analysis of Maxwell's time-dependent thermo-diffusive flow through a stretching cylinder," *Case Studies in Thermal Engineering*, vol. 27, p. 101301, 2021.
- [14] A. Saeed, W. Alghamdi, S. Mukhtar et al., "Darcy-Forchheimer hybrid nanofluid flow over a stretching curved surface with heat and mass transfer," *PLoS One*, vol. 16, no. 5, article e0249434, 2021.
- [15] P. Keblinski, J. Eastman, and D. Cahill, "Nanofluids for thermal transport," *Materials Today*, vol. 8, no. 6, pp. 36–44, 2005.
- [16] J. Buongiorno, "Convective transport in Nanofluids," *Journal of Heat Transfer*, vol. 128, no. 3, pp. 240–250, 2006.
- [17] N. S. Khan, P. Kumam, and P. Thounthong, "Computational approach to dynamic systems through similarity measure and homotopy analysis method for renewable energy," *Crystals*, vol. 10, no. 12, p. 1086, 2020.
- [18] H. Machrafi, G. Lebon, and C. S. Iorio, "Effect of volume-fraction dependent agglomeration of nanoparticles on the thermal conductivity of nanocomposites: applications to epoxy resins, filled by SiO<sub>2</sub>, AlN and MgO nanoparticles," *Composites Science and Technology*, vol. 130, pp. 78–87, 2016.
- [19] H. Machrafi and G. Lebon, "The role of several heat transfer mechanisms on the enhancement of thermal conductivity in nanofluids," *Continuum Mechanics and Thermodynamics*, vol. 28, no. 5, pp. 1461–1475, 2016.
- [20] J. Sarkar, P. Ghosh, and A. Adil, "A review on hybrid nanofluids: recent research, development and applications," *Renewable and Sustainable Energy Reviews*, vol. 43, pp. 164–177, 2015.
- [21] A. Ajibade, B. Jha, and A. Omame, "Entropy generation under the effect of suction/injection," *Applied Mathematical Modelling*, vol. 35, no. 9, pp. 4630–4646, 2011.
- [22] A. Khan, Z. Shah, E. Alzahrani, and S. Islam, "Entropy generation and thermal analysis for rotary motion of hydromagnetic Casson nanofluid past a rotating cylinder with joule heating effect," *International Communications in Heat and Mass Transfer*, vol. 119, p. 104979, 2020.
- [23] S. Islam, A. Khan, P. Kumam et al., "Radiative mixed convection flow of Maxwell nanofluid over a stretching cylinder with joule heating and heat source/sink effects," *Scientific Reports*, vol. 10, no. 1, pp. 1–18, 2020.
- [24] V. Narla, K. Prasad, and J. V. Murthy, "Second-law analysis of the peristaltic flow of an incompressible viscous fluid in a curved channel," *Journal of Engineering Physics and Thermophysics*, vol. 89, no. 2, pp. 441–448, 2016.
- [25] M. I. Khan, S. A. Khan, T. Hayat, S. Qayyum, and A. Alsaedi, "Entropy generation analysis in MHD flow of viscous fluid by a curved stretching surface with cubic autocatalysis chemical reaction," *The European Physical Journal Plus*, vol. 135, no. 2, p. 249, 2020.
- [26] M. Sheikholeslami, T. Hayat, and A. Alsaedi, "MHD free convection of Al<sub>2</sub>O<sub>3</sub>–water nanofluid considering thermal radiation: a numerical study," *International Journal of Heat and Mass Transfer*, vol. 96, pp. 513–524, 2016.
- [27] M. Sheikholeslami and M. M. Rashidi, "Non-uniform magnetic field effect on nanofluid hydrothermal treatment considering Brownian motion and thermophoresis effects," *Journal of the Brazilian Society of Mechanical Sciences and Engineering*, vol. 38, no. 4, pp. 1171–1184, 2016.
- [28] M. J. Nine, B. Munkhbayar, M. S. Rahman, H. Chung, and H. Jeong, "Highly productive synthesis process of well dispersed Cu<sub>2</sub>O and Cu/Cu<sub>2</sub>O nanoparticles and its thermal characterization," *Materials Chemistry and Physics*, vol. 141, no. 2–3, pp. 636–642, 2013.
- [29] R. Yan, J. R. Simpson, S. Bertolazzi et al., "Thermal conductivity of monolayer molybdenum disulfide obtained from temperature-dependent Raman spectroscopy," *ACS Nano*, vol. 8, no. 1, pp. 986–993, 2014.

## Research Article

# Heat Transfer Analysis on Carboxymethyl Cellulose Water-Based Cross Hybrid Nanofluid Flow with Entropy Generation

F. Ali <sup>1</sup>, K. Loganathan <sup>2,3</sup>, S. Eswaramoorthi <sup>4</sup>, K. Prabu,<sup>5</sup> A. Zaib <sup>1</sup>,  
and Dinesh Kumar Chaudhary <sup>6</sup>

<sup>1</sup>Department of Mathematical Sciences, Federal Urdu University of Arts, Sciences, & Technology, Gulshan-e-Iqbal, Karachi 75300, Pakistan

<sup>2</sup>Department of Mathematics and Statistics, Manipal University Jaipur, Jaipur, 303007 Rajasthan, India

<sup>3</sup>Research and Development Wing, Live4Research, Tiruppur, 638106 Tamilnadu, India

<sup>4</sup>Department of Mathematics, Dr. N.G.P. Arts and Science College, Coimbatore, Tamilnadu, India

<sup>5</sup>Department of Physics, Kongu Engineering College, Perundurai, Erode-638060, Tamilnadu, India

<sup>6</sup>Department of Physics, Amrit Campus, Tribhuvan University, Kathmandu, Nepal

Correspondence should be addressed to K. Loganathan; [loganathankaruppusamy304@gmail.com](mailto:loganathankaruppusamy304@gmail.com) and Dinesh Kumar Chaudhary; [din.2033@gmail.com](mailto:din.2033@gmail.com)

Received 25 December 2021; Revised 15 March 2022; Accepted 2 May 2022; Published 1 June 2022

Academic Editor: Anwar Saeed

Copyright © 2022 F. Ali et al. This is an open access article distributed under the Creative Commons Attribution License, which permits unrestricted use, distribution, and reproduction in any medium, provided the original work is properly cited.

The physical phenomena of convective flow of Cross fluid containing carboxymethyl cellulose water over a stretching sheet with convective heating were studied. Cross nanofluid containing  $\text{Al}_2\text{O}_3$ , Cu nanoparticles, and based fluid of CMC water is used. Entropy generation minimization is examined in the current analysis. The system of PDEs is altered into a set of ODEs through suitable conversion. Further, these equations are computed numerically through the MATLAB BVP4c technique. The behavior of governing parameters on the velocity, temperature, entropy generation, and Bejan number is plotted and reported via graphs. It is found that the larger value of unsteady variable reduced the velocity, thermal layer, and entropy production. Surface drag friction of the  $\text{Al}_2\text{O}_3$  and Cu and  $\text{Al}_2\text{O}_3 + \text{Cu}$  is enhanced with the more presence of unsteady parameter. Comparison of current results in a limiting case is obtained with earlier analysis and found an optimum agreement.

## 1. Introduction

Carboxymethyl cellulose (CMC) is a water-soluble cellulose derivative [1], and it has many flow properties due to its greater stability and high viscosity. The stability of nanoparticles in CMC escalates the fluid behavior. It is engaged to increase lubricating effects such as polymeric structures [2, 3]. These multifunction aspects of various cellulose derivatives have many industrial and technical applications. To recognize the fluid flow with CMC study, research have been studied [4–6]. Saqib et al. [7] described the natural convective flow of CMC with carbon nanotube using a fractional derivative approach. The effect of slip velocity and non-Newtonian nanofluid contained with 0.5% wt CMC water was discussed by Rahmati et al. [8]. Akinpelu et al. [9]

explored the thermophysical metal properties in CMC. MHD flow of Casson nanofluid under heat transfer in CMC over a solid sphere was developed by Alwawi et al. [10].

Nanotechnology has been progressively more fascinated by the researchers because of their efficiency in several industrial processes such as microelectronic, oil emulsion, and molecular emulsion. Nanotechnology has the ability in suspending nanoscale particles ( $1 \leq 100\text{nm}$ ) in ordinary fluids, like ethylene glycol, oil, and water. The origin of nanotechnology was initiated by Choi and Eastman [11] in 1995. After, Buongiorno [12] developed a mathematical model of heat transfer with the addition of Brownian motion and thermophoresis effects. Tiwari and Das [13] investigated to examine the solid volume fraction in nanofluids. Devi and Devi [14] reported the numerical simulation of hybrid

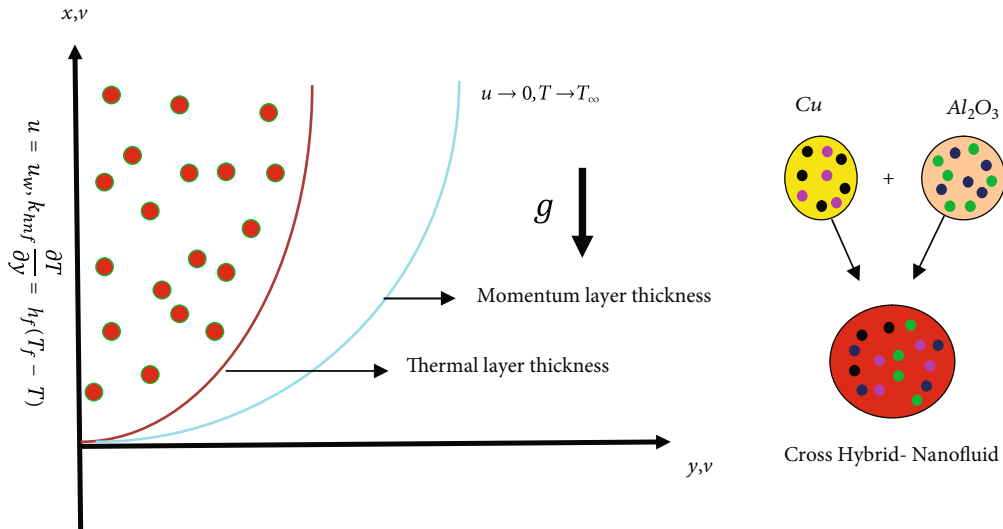


FIGURE 1: Geometry of problem.

nanofluid over a porous surface with suction. Afridi et al. [15] carried out the heat transfer analysis in hybrid nanofluid under fraction heating. The effect of second law analysis with hybrid nanofluid and viscous dissipation due to rotating disk was scrutinized by Farooq et al. [16]. Devi et al. [17, 18] revealed the heat transfer of hybrid nanofluid flow with two different base fluids. Gorla et al. [19] addressed the impact of heat sink/source in the hybrid nanofluid past the permeable surface. Chamkha et al. [20] analyzed the time-dependent flow of mixed convective hybrid nanofluid over half cavity. More recently, Zainal et al. [21] disclosed the unsteady 3-D MHD stagnation point flow of hybrid nanofluid using stability analysis. Few more cutting edge research reports are seen in Refs. [22–28].

The study of entropy optimization has broad features in the thermal engineering process such as heat pump, heat engine, solar power, and refrigerator. The improvement of the thermal system is enhanced due to the entropy production. The Bejan number [29] is a dimensionless quantity that represents overall entropy generation ratio of heat transmission and total entropy generation. Khana et al. [30] discussed the computational analysis of hybrid nanofluid with entropy generation due to rotating disk between parallel plates. Dawar et al. [31] surveyed the heat transfer analysis through SWCNTs/MWCNTs in entropy generation and activation energy over a moving wedge. The numerical study of second law analysis of nanofluid due to an inclined surface was discussed by Butt et al. [32]. Heat transfer in MHD third-grade nanofluid with convective condition and entropy generation over a stretching surface was encountered by Rashidi et al. [33]. The investigation of entropy production for the magnetic field, thermal radiation, and porous medium was reported by Makinde and Eegunjobi [34]. The impact of entropy generation on two permeable stretched surfaces was inspected by Khan et al. [35]. Afridi et al. [36] described the hybrid nanofluid flow over a thin needle with entropy generation. Reddy et al. [37] studied the entropy generation on Williamson nanofluid with thermal radiation and internal heat source over the lubricated surface.

The behavior of non-Newtonian fluid models, like second grade, power law, and Williamson, was investigated by many researchers in the past few years due to their vital role in engineering and industrial applications. However, these models cannot be recognized to analyze the behavior of fluid at higher and lower shear rates. To illustrate the behavior of fluid at a very low and high shear rate, the Cross fluid model has been introduced by Cross [38]. The Cross fluid model has optimum potential to trounce the challenges that are overlooked while the shear rate is highly accelerated or depreciated. Few recent developments under this direction are collected in [39, 40]. The effect of heat source/sink on Cross fluid with thermal radiation was studied by Nazeer et al. [41]. Sabir et al. [42] scrutinized the heat transfer phenomena through radiation and activation energy over an inclined sheet. Yao et al. [43] investigated the magnetic dipole effect for Cross fluid through spectroscopy. Khan et al. [44] interpreted the effect of thermal radiative and activation energy on Cross fluid near the stagnation point. Reddy and Ali [45] constructed the MHD Cross nanofluid under Cattaneo-Christov double diffusion theory over a vertical stretching sheet.

The abovementioned studies reveal the focus on the heat transport analysis of a CMC-nanofluid, but no authors examined the CMC-hybrid nanofluid in the presence of unsteady Cross fluid with the effect of mixed convection. So, the authors attempted to investigate the heat transfer analysis of CMC-based Cross hybrid nanofluid with convective heating. The system of PDEs is transformed into ODEs through the suitable transformation, and these ODEs are tackled through BVP4c for numerical solution. The entropy analysis is implemented in the present study. This combination is more useful in thermal and aerospace engineering.

## 2. Mathematical Formulation

Let us consider the unsteady incompressible mixed convective flow of Cross hybrid nanofluid over a stretching sheet with surface heating. Moreover, Cartesian coordinates have

TABLE 1: Thermophysical properties.

Physical properties	Specific heat capacity	Density	Thermal conductivity	Coefficient of thermal expansion
CMC-water (<0.4%)	4179	997.1	0.613	21
Al <sub>2</sub> O <sub>3</sub>	765	3970	40	0.85
Cu	531.8	6320	76.5	1.80
Dynamic viscosity	$\Pi_1$		$\frac{\mu_{\text{hnf}}}{\mu_f} = \frac{1}{(1 - \varphi_1 - \varphi_2)^{2.5}}$	
Density	$\Pi_2$		$\frac{\rho_{\text{hnf}}}{\rho_f} = (1 - \varphi_2) \left[ (1 - \varphi_1) + \frac{\varphi_1 \rho_{1s}}{\rho_f} \right] + \frac{\varphi_2 \rho_{2s}}{\rho_f}$	
Thermal expansion	$\Pi_3$		$\frac{(\rho\beta_T)_{\text{hnf}}}{(\rho\beta_T)_f} = (1 - \varphi_2) \left[ (1 - \varphi_1) + \frac{\varphi_1 (\rho\beta_T)_{1s}}{(\rho\beta_T)_f} \right] + \frac{\varphi_2 (\rho\beta_T)_{2s}}{(\rho\beta_T)_f}$	
Heat capacity	$\Pi_4$		$\frac{(\rho c_p)_{\text{hnf}}}{(\rho c_p)_f} = (1 - \varphi_2) \left[ (1 - \varphi_1) + \frac{\varphi_1 (\rho c_p)_{1s}}{(\rho c_p)_f} \right] + \frac{\varphi_2 (\rho c_p)_{2s}}{(\rho c_p)_f}$	
Thermal conductivity	$\Pi_5$		$\frac{k_{\text{hnf}}}{k_f} = \frac{k_{2s} + 2k_f - 2\varphi_2(k_f - k_{2s})}{k_{2s} + 2k_f + \varphi_2(k_f - k_{2s})} \times (k_{\text{nf}}) k_{\text{nf}} = \frac{k_{1s} + 2k_f - 2\varphi_1(k_f - k_{1s})}{k_{1s} + 2k_f + \varphi_1(k_f - k_{1s})}$	

been taken in the  $x$ -axis along the sheet, and  $y$ -axis is perpendicular to surface as seen in Figure 1. The radiation can only travel a distance within thick nanofluid; so, the Rosseland approximation is considered into account for radiative heat transfer.

Under the above assumptions, the flow model can be extract as follows:

$$\frac{\partial u}{\partial x} + \frac{\partial v}{\partial y} = 0, \quad (1)$$

$$\begin{aligned} \frac{\partial u}{\partial t} + u \frac{\partial u}{\partial x} + v \frac{\partial u}{\partial y} = \nu_{\text{hnf}} \frac{\partial}{\partial y} \left( \frac{\partial u / \partial y}{1 + \Gamma(\partial u / \partial y)^n} \right) \\ + \frac{g}{\rho_{\text{hnf}}} (\rho\beta_T)_{\text{hnf}} (T - T_{\infty}) = 0, \end{aligned} \quad (2)$$

$$\frac{\partial T}{\partial t} + u \frac{\partial T}{\partial x} + v \frac{\partial T}{\partial y} = \frac{k_{\text{hnf}}}{(\rho C_p)_{\text{hnf}}} \frac{\partial^2 T}{\partial y^2} - \frac{1}{(\rho C_p)_{\text{hnf}}} \frac{\partial q_r}{\partial y}. \quad (3)$$

The boundary constraints are applied as follows:

$$u = u_w(x, t), v = 0, -k_{\text{hnf}} \frac{\partial T}{\partial y} = h_f (T_f - T_{\infty}) \text{ at } y = 0, \quad (4)$$

$$u = u(x, t) = 0, T \longrightarrow T_{\infty} \text{ as } y \longrightarrow \infty.$$

Here,  $u$ ,  $v$ ,  $\mu_{\text{hnf}}$ ,  $\rho_{\text{hnf}}$ ,  $k_{\text{hnf}}$ ,  $(\rho C_p)_{\text{hnf}}$ , and  $q_r$  are horizontal velocity and vertical velocity, viscosity, density, thermal conductivity, specific heat capacity, and thermal radiative for hybridnanofluid, respectively.  $h_f$  is the heat transfer coefficient.

TABLE 2: Validation of current results of  $-\theta'(0)$  with Wakif [48] against Pr.

Pr	Wakif [48]	Current analysis
0.7	0.453916157	0.456051210134421
2.0	0.911357683	0.911321374513764
7.0	1.895403258	1.895381882154913
20	3.353904143	3.353886925689145
70	6.462199531	6.462184407558267

TABLE 3: Comparing of  $f''(0)$  for unsteady parameter  $\delta$  when  $n = \text{We} = \lambda = 0$ .

$\delta$	Ali and Zaib [49]	Current results
0.8	-1.261211	-1.260691
1.2	-1.377625	-1.377710

2.1. *Suitable Transformation for Unsteady Flow.* It is relevant to use the following appropriate transformation:

$$\begin{aligned} \eta = y \sqrt{\frac{a}{\nu_f(1 - \chi t)}}, u = \frac{ax}{(1 - \chi t)}, f'(\eta), \\ v = \sqrt{\frac{a\nu_f}{(1 - \chi t)}} f(\eta), \theta(\eta) = \frac{T - T_{\infty}}{T_f - T_{\infty}}. \end{aligned} \quad (5)$$

Using the suitable transformation described in Eq. (5), to Eq. (2), Eq. (3) altered into the following ordinary differential equations with respect to parameter  $\eta$ :

$$\begin{aligned} \Pi_1 \left[ \left( 1 + (1 - n) (\text{We} f'' )^n \right) f''' \right] + \Pi_2 \left[ f f'' - \delta \left( f' + \frac{\eta}{2} f'' \right) - (f')^2 \right] \\ \cdot \left( 1 + (\text{We} f'' )^n \right)^2 + \Pi_3 \lambda \theta \left( 1 + (\text{We} f'' )^n \right)^2 = 0, \end{aligned} \quad (6)$$

TABLE 4: Numerical outcomes of value of skin friction coefficient and local Nusselt number.

We	$\lambda$	$\delta$	Bi	Pr	Rd	$Re_x^{1/2} C_f$		
						Cu	$Al_2O_3$	Cu + $Al_2O_3$
1.5	0.9	0.1	0.2	6.2	0.5	2.7247	2.3915	5.1162
2.0			1.1420			1.1102	2.2522	
2.5			0.5355			0.5097	1.0452	
1.0	1.4	0.2	0.2	6.8	0.7	2.7469	2.4140	5.1609
1.1			1.1550			1.1226	2.2776	
1.2			0.5460			0.5102	1.0562	
1.0	1.5	0.3	0.2	7.2	0.9	2.7480	2.4339	5.1819
1.1			1.1643			1.1361	2.3004	
1.2			0.5507			0.5222	1.0729	

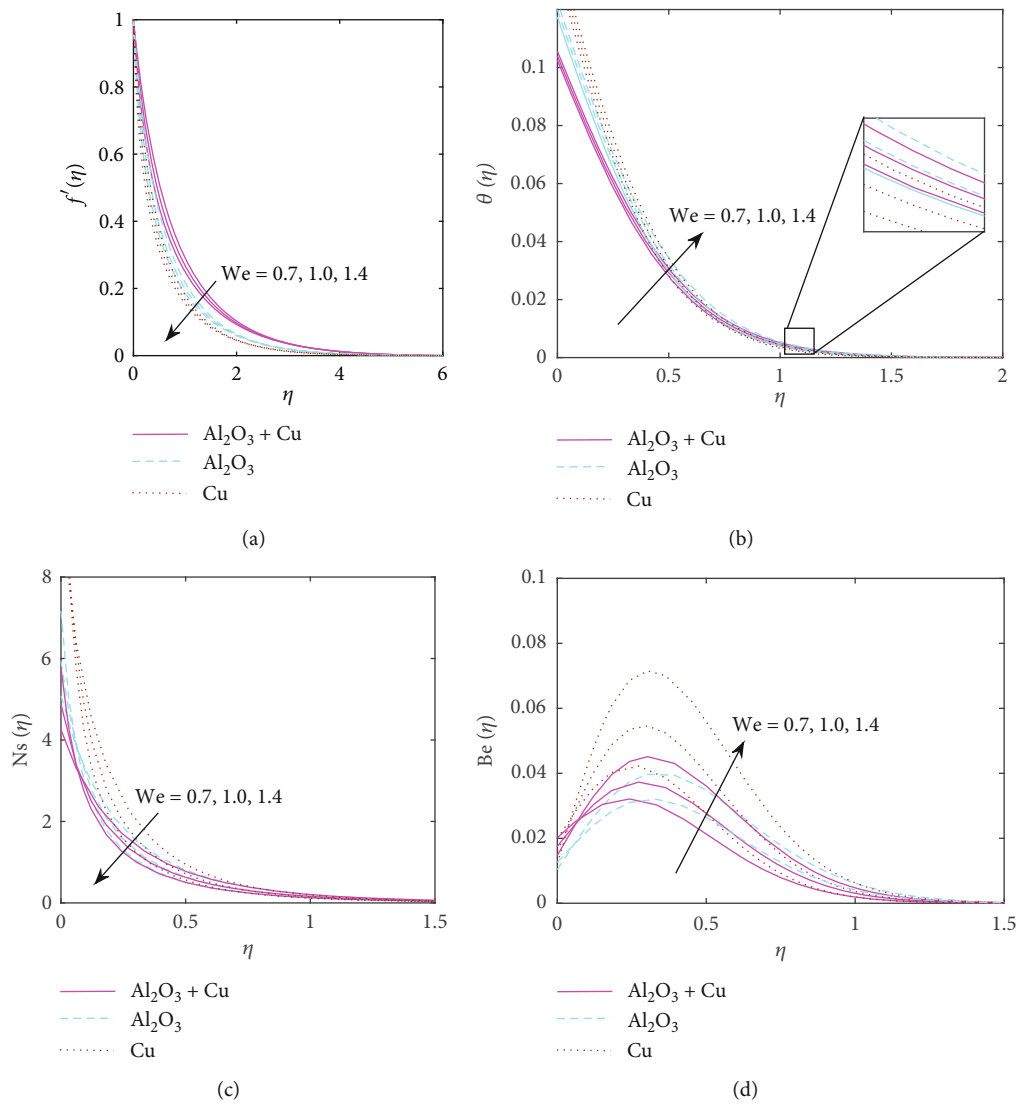


FIGURE 2: (a)–(d)  $f'(\eta)$ ,  $\theta(\eta)$ ,  $Ns(\eta)$ ,  $Be(\eta)$  versus We.



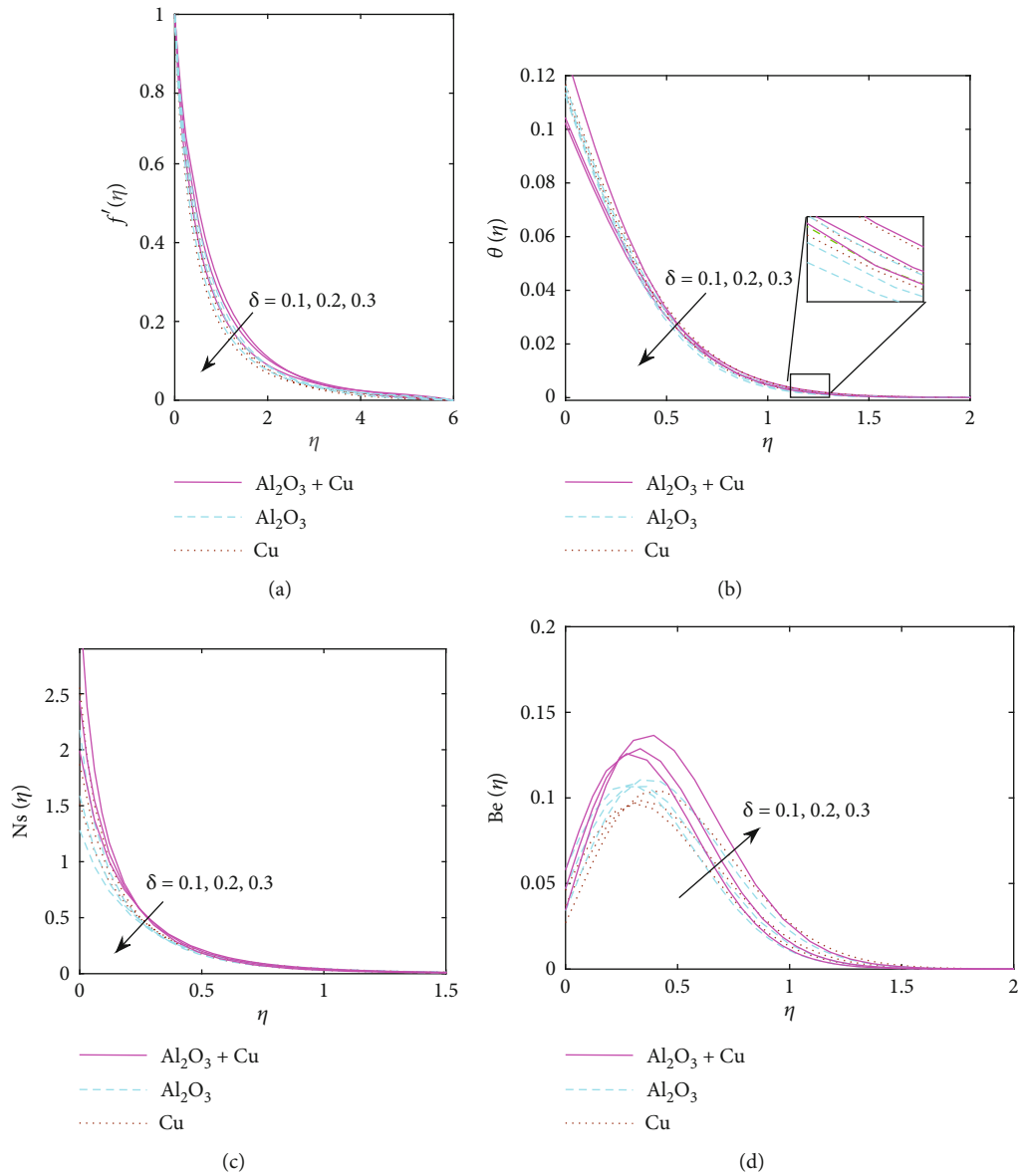


FIGURE 3: (a)–(d)  $f'(\eta), \theta(\eta), Ns(\eta), Be(\eta)$  versus  $\delta$ .

$$\theta''(1 + \Pi_4 Rd) - \frac{\Pi_3 \eta}{\Pi_4 2} \delta Pr \theta' + Pr \Pi_5 f \theta' = 0. \quad (7)$$

The transformation boundary conditions are stated as follows:

$$f(0) = 0, f'(0) = 1, \Pi_4 \theta'(0) = -Bi(1 - \theta(0)), f'(\infty) = 0, \theta(\infty) = 0. \quad (8)$$

Nondimensionless governing variables are Weissenberg number  $We(= \Gamma ax \sqrt{a/\nu})$ , unsteady parameter  $\delta(= c/a)$ , mixed convection  $\lambda(= Gr_x/Re_x^2)$ , Prandtl number  $Pr(= \mu_f (c_p)_x / k_f)$ , radiation parameter  $(Rd = (16\sigma^* T_\infty^3)/(kk^*))$ , the skin friction coefficient  $C_f$ , and the local Nusselt number which are presented by

$$C_f = \left( \frac{\tau_w}{\rho_f u_w^2} \right), Nu = \left( \frac{x q_w}{k_f (T_f - T_\infty)} \right). \quad (9)$$

Wall shear stress and heat flux are as follows:

$$\tau_w = \mu_{hnf} \left( \frac{\partial u}{\partial y} \right)_{y=0}, q_w = -k_{hnf} \left( \frac{\partial T}{\partial y} \right)_{y=0}. \quad (10)$$

In view of Eqs. (5) and (10), we get

$$Re_x^{1/2} C_f = \Pi_1 \left( \frac{f''(0)}{1 + (We f''(0))^n} \right)_{y=0}, Re_x^{-1/2} Nu_x = (\Pi_5 (1 + Rd) \theta'(0))_{y=0}. \quad (11)$$

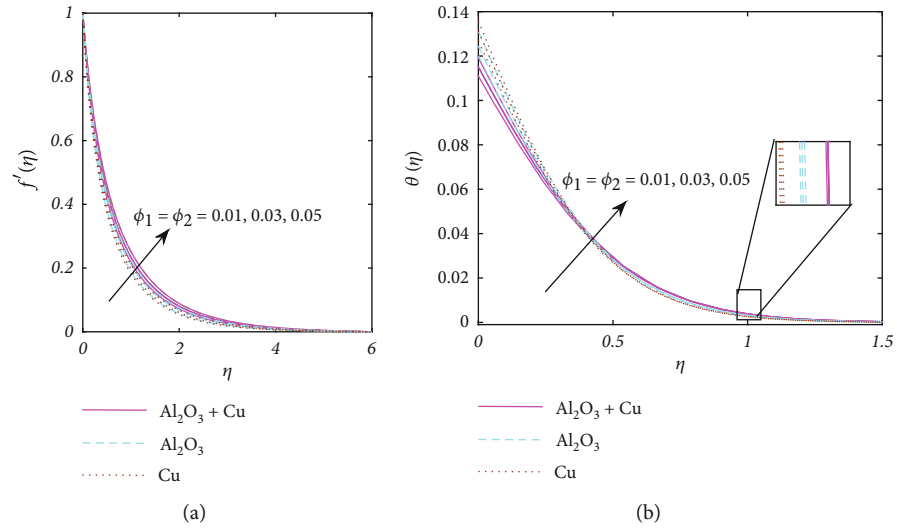


FIGURE 4: (a, b)  $f'(\eta), \theta(\eta)$  versus  $\phi_1, \phi_2$ .

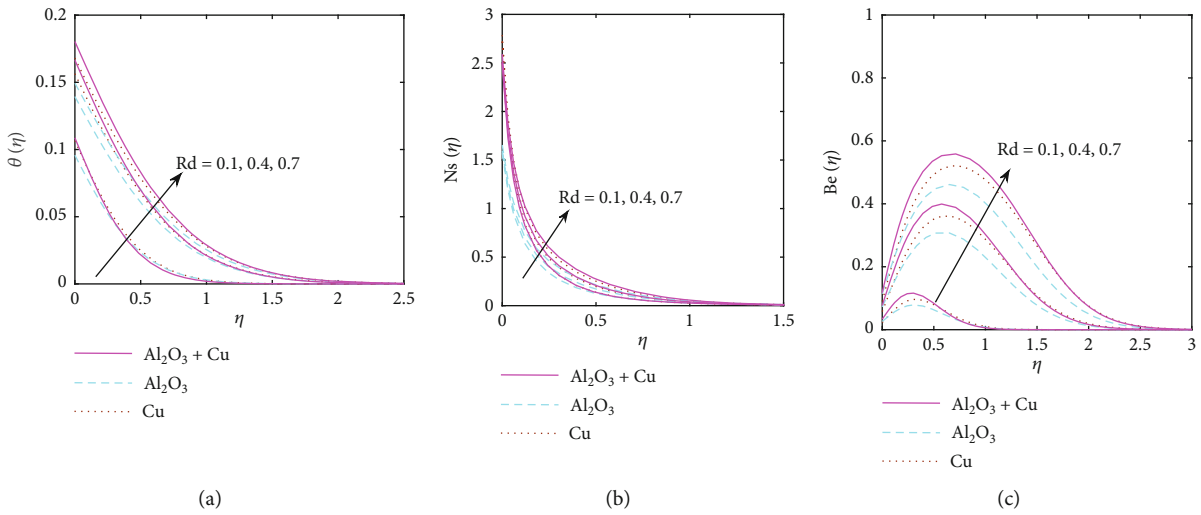


FIGURE 5: (a)-(c)  $\theta(\eta), Ns(\eta), Be(\eta)$  versus  $Rd$ .

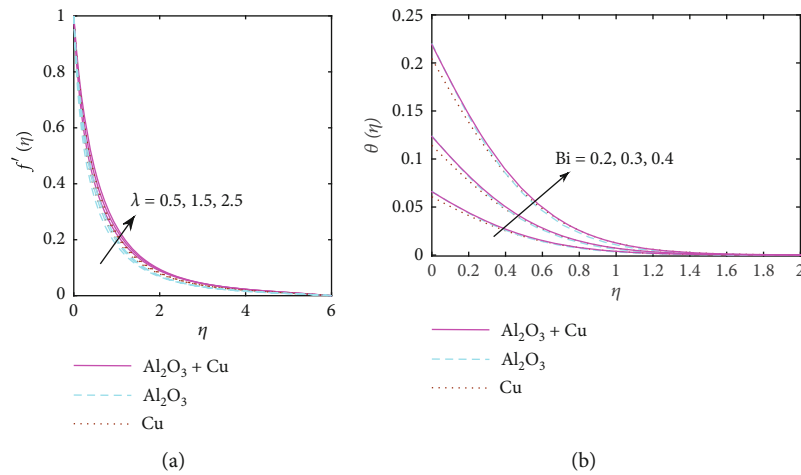


FIGURE 6: (a, b)  $f'(\eta)$  and  $\theta(\eta)$  versus  $\lambda$  and  $Bi$ .

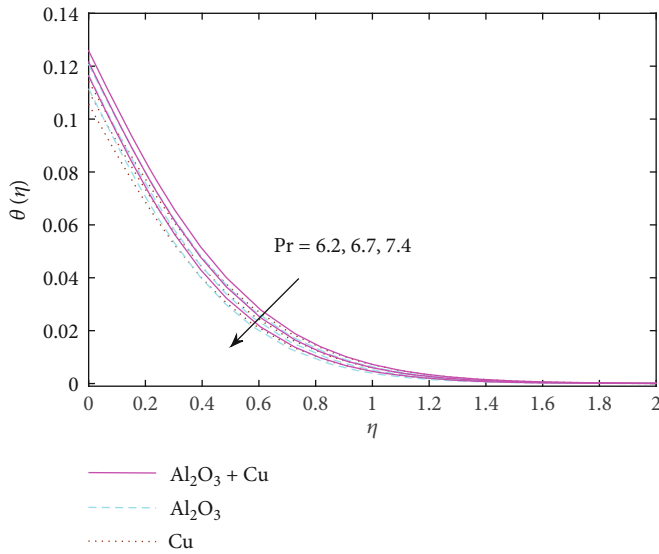


FIGURE 7:  $\theta(\eta)$  versus Pr.

### 3. Entropy Generation

The appearance of entropy production for Cross hybrid nanoliquid over a stretching sheet is defined as [46, 47]:

$$E_G = \frac{k_f}{T_\infty^2} \left[ \frac{k_{hnf}}{k_f} + \frac{16\sigma * T_\infty^2}{3k_f k^*} \left( \frac{\partial T}{\partial y} \right)^2 \right] + \mu_{hnf} \frac{1}{T_\infty} \left( \frac{\partial u}{\partial y} \right)^2 \left( \frac{1}{1 + \Gamma(\partial u / \partial y)^n} \right). \quad (12)$$

The characteristics entropy generation is described below:

$$E_0''' = \frac{k_{hnf}(T_f - T_\infty)}{xT_\infty^2}. \quad (13)$$

The dimensionless form of entropy generation is  $Ns = N_h + N_v$ .

$N_h = \Pi_5[1 + Rd](\theta')^2$  is the entropy generation due to heat transfer, and  $N_v = \Pi_4[1 + (1/(We f''^n))]f''^2$  is the entropy generation due to fluid friction.

$$Ns = \frac{E_G}{E_0'''} = \Pi_5[1 + Rd](\theta')^2 + Br\Pi_4 \left[ 1 + \frac{1}{(We f''^n)} \right] f''^2. \quad (14)$$

The Bejan number is defined by

$$Be = \frac{\Pi_5[1 + Rd](\theta')^2}{\Pi_5[1 + Rd](\theta')^2 + Br\Pi_4 \left[ 1 + \frac{1}{(We f''^n)} \right] f''^2}. \quad (15)$$

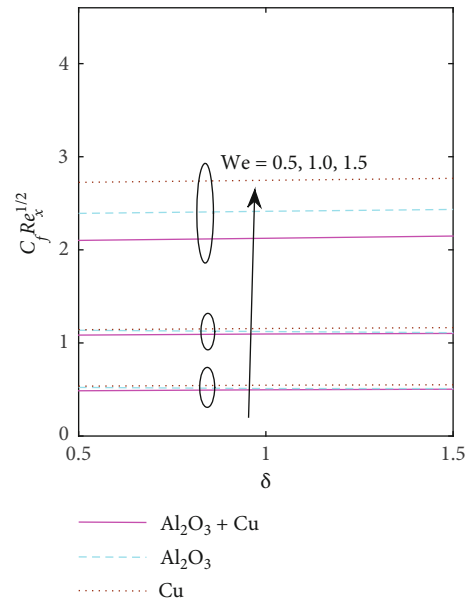


FIGURE 8: The influence of We and  $\delta$  on  $C_f Re_x^{1/2}$ .

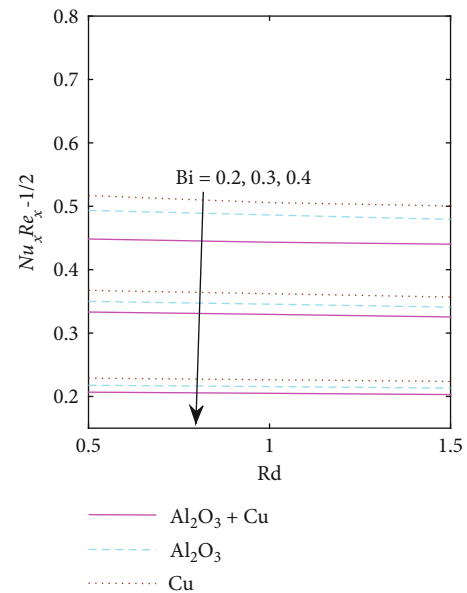


FIGURE 9: The influence of Rd and Bi on  $Nu_x Re_x^{-1/2}$ .

### 4. Numerical Investigation

The set of an altered system of highly nonlinear ODE's equations (6)–(7) with subject to the boundary condition (8) has been numerically computed with aid of the BVP4c method. For this purpose, first, we converted the higher order derivative into first order.

$$f = \Lambda_1, f' = \Lambda_2, f'' = \Lambda_3, f''' = \Lambda_3', \theta = \Lambda_4, \theta' = \Lambda_5, \theta'' = \Lambda_5', \quad (16)$$

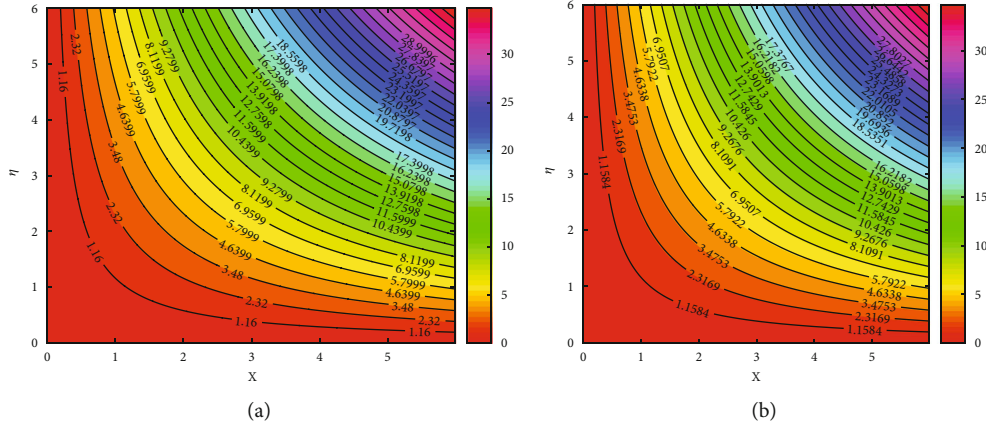


FIGURE 10: Stream line pattern for various values  $\phi_1 = 0, \phi_2 = 0$  and  $\phi_1 = 0.02, \phi_2 = 0$ .

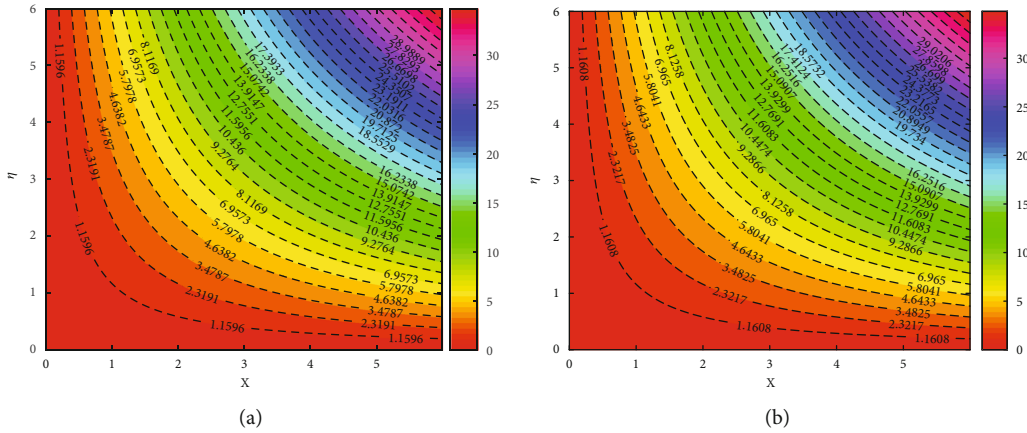


FIGURE 11: Stream line pattern for (a) unsteady flow and (b) steady flow.

$$\Lambda_3' = \frac{-\Pi_2[\Lambda_1\Lambda_3 - \delta(\Lambda_2 + (\eta/2)\Lambda_3) - (\Lambda_2)^2]\{1 + (We\Lambda_3)^n\}^2 - \Pi_3\lambda\Lambda_4\{1 + (We\Lambda_3)^n\}^2}{\Pi_1[1 + (1-n)(We\Lambda_3)^n]}, \tag{17}$$

$$\theta'' \left(1 + \Pi_4 \frac{4}{3} Rd\right) - \frac{\eta}{2} \delta \frac{\Pi_3}{\Pi_4} Pr \theta' + Pr \Pi_5 f \theta' = 0, \tag{18}$$

$$\Lambda_5' = \frac{-Pr \Pi_5 \Lambda_1 \Lambda_5 + (\eta/2) \delta (\Pi_3 / \Pi_4) Pr \Lambda_4}{(1 + \Pi_4 Rd)}$$

Converted boundary conditions are as follows:

$$\begin{aligned} \Lambda_1(0) = 0, \Lambda_2(0) = 1, \Lambda_5(0) = -Bi(1 - \Lambda_4(0)), \Lambda_2(\infty) \\ = 0, \Lambda_4(\infty) = 0. \end{aligned} \tag{19}$$

The iterative process has been used, and the accuracy of the solution is obtained to  $10^{-6}$ .

### 5. Result and Discussion

In this segment, we examine the variations of  $f'(\eta)$ ,  $\theta(\eta)$ ,  $Ns(\eta)$ , and  $Be(\eta)$  for different flow variables, such as Weissenberg number ( $We$ ), Biot number ( $Bi$ ), Prandtl

number ( $Pr$ ), thermal radiation ( $Rd$ ), nanoparticle volume fraction ( $\phi_1, \phi_2$ ), and mixed convection parameter ( $\lambda$ ). For performing graphical study, single variable varies, whereas all the physical variables were kept in constant values such as  $We = 0.5, n = 0.4, Bi = -0.3, \lambda = 1.0, Pr = 6.2, \delta = 0.3, Rd = 1.7$ . Table 1 demonstrates the thermophysical properties of Cu,  $Al_2O_3$ , and  $Cu+Al_2O_3$ . Tables 2 and 3 show the comparison outcome of  $-\theta(0)$  against  $Pr$  and  $f''(0)$  against  $\delta$  with the limiting case  $n = We = \lambda = 0$ . From these tables, it is found that our computations are optimum one. Table 4 shows the impact of  $We, \lambda, \delta, Bi, Pr$ , and  $Rd$  on skin friction coefficient for Cu,  $Al_2O_3$ , and  $Cu+Al_2O_3$ .

Figures 2(a)–2(d) display the fluctuation of Weissenberg ( $We$ ) on velocity distribution  $f'(\eta)$ , temperature field  $\theta(\eta)$ , entropy production  $Ns(\eta)$ , and Bejan number  $Be(\eta)$  for nanofluids ( $Cu+Al_2O_3$ ) and hybrid nanofluid ( $Cu + Al_2O_3$ ). The fluid velocity and entropy generation reduce when  $We$  augments. However, fluid temperature and Bejan number enhance when enhancing the quantity of  $We$ . Physically, the Weissenberg number means shear rate time which helps to rise the fluid thickness, and this causes to depreciate fluid velocity. The variations of  $\delta$  on  $f'(\eta)$ ,  $\theta(\eta)$ ,  $Ns(\eta)$ , and  $Be(\eta)$  are illustrated in Figures 3(a)–3(d) for nanofluids and hybrid nanofluid. It is seen from these figures that the fluid velocity,

fluid temperature, and entropy production decline when increasing the magnitude of  $\delta$ , and Bejan number raises when rising the values of  $\delta$ . Figures 4(a) and 4(b) present the consequences of  $\phi_1$  and  $\phi_2$  on  $f'(\eta)$  and  $\theta(\eta)$  for nanofluids and hybrid nanofluid for nanofluids and hybrid nanofluid. It is seen that the fluid velocity and fluid temperature upsurge when mounting the quantity of  $\phi_1$  and  $\phi_2$ . The impact of radiation on  $\theta(\eta)$ ,  $Ns(\eta)$ , and  $Be(\eta)$  was portrayed in Figures 5(a)–5(c) for nanofluids and hybrid nanofluid. It is concluded that the fluid temperature, entropy production, and Bejan number are increasing function of radiation parameter. Physically radiation parameter enhances the rate energy transport to the fluid and thereby enriching the fluid temperature and thicken the thermal boundary layer. Figures 6(a) and 6(b) provide the changes of  $f'(\eta)$  on  $\lambda$  and  $\theta(\eta)$  on Bi for nanofluids and hybrid nanofluid. It is detected that the momentum boundary layer thickness escalates when enriching the  $\lambda$  values, see Figure 6(a). The fluid temperature raises when raising the Biot number, see Figure 6(b). Physically, Biot number leads to enrich the heat transfer coefficient, this leads to enhance the fluid thermal state, and this causes to improve the fluid temperature and thicker the thermal boundary layer thickness. Figure 7 displays the effect of Pr on  $\theta(\eta)$  for nanofluids and hybrid nanofluid. It is found that the fluid temperature and its associated boundary layer thickness downturn when strengthening the Prandtl number.

Figure 8 shows the influence of  $\delta$  and We on skin friction coefficient for nanofluids and hybrid nanofluid. It is proved from this figure that the skin friction coefficient enriches when strengthening the We values, and it is almost fixed when changing the  $\delta$  values. Further, the skin friction coefficient is low in hybrid nanofluid than the nanofluids case. The local Nusselt number for various values of Rd and Bi for nanofluids and hybrid nanofluid is plotted in Figure 9. It is seen that the heat transfer gradient depresses when enriching the Rd and Bi for all cases. In addition, the less local Nusselt number is attained in hybrid nanofluid than the nanofluids case. Finally, Figures 10 and 11 present the streamline pattern for numerous values of nanoparticle volume fraction, Steady and unsteady flows.

## 6. Final Remarks

The two-dimensional mixed convection flow of Cross fluid is based on CMC-water with nanoparticles Cu and  $Al_2O_3$  with thermal radiation over a stretching sheet. The second law analysis has been made. The physical model is computed via the MATLAB BVP4c function. The numerical and graphical results for flow and energy transfer are produced for diverse values of dimensionless variables. Moreover, skin friction and Nusselt number have been computed. The main findings of this work are as follows:

- (i) Momentum boundary layer thickness of Cu,  $Al_2O_3$ , and Cu+ $Al_2O_3$  reduces as the Weissenberg number We is enhanced.
- (ii) The temperature profile Cu,  $Al_2O_3$ , and Cu+ $Al_2O_3$  is reduced for both  $\delta$  and We.

- (iii) Entropy generation and Bejan number of Cu,  $Al_2O_3$ , and Cu+ $Al_2O_3$  are quite similar trends for We and  $\delta$ .
- (iv) Temperature distribution, entropy generation, and Bejan number Cu,  $Al_2O_3$ , and Cu+ $Al_2O_3$  are enhanced as increases the value of thermal radiation Rd.
- (v) Both Biot number and mixed convection are enhanced for temperature and velocity distribution of Cu,  $Al_2O_3$ , and Cu+ $Al_2O_3$ .
- (vi) The drag friction and Nusselt number have an increasing effect for nanofluid and hybrid nanofluid.

## Nomenclature

a:	Stretching rate
t:	Time
$\lambda$ :	Mixed convection parameter
$k_{nf}$ :	Effective thermal conductivity
$\rho_f$ :	Reference density of fluid
$\rho_s$ :	Reference density of solid
Pr:	Prandtl number
Bi:	Biot number
Be:	Bejan number
Ns:	Total entropy generation
$\mu_f$ :	Viscosity of fluid
We:	Weissenberg number
$\delta$ :	Unsteady parameter
n:	Power-law index
k:	Thermal conductivity of base fluid
u:	Velocity along the x-axis
v:	Velocity along the y-axis
$\rho_{nf}$ :	Density of fluid
$\mu_{nf}$ :	Effective viscosity of nanofluid
$Nu_x$ :	Nusselt number
$k_f$ :	Thermal conductivity of fluid
$k_s$ :	Thermal conductivity of solid
$Re_x$ :	Local Reynolds number
T:	Fluid temperature
$T_f$ :	Temperature of the hot fluid

## Abbreviations

Cu:	Copper
PDE:	Partial differential equations
ODE:	Ordinary differential equations
CMC:	Carboxymethyl cellulose.

## Data Availability

The raw data supporting the conclusions of this article will be made available by the corresponding author without undue reservation.

## Conflicts of Interest

The authors declare that they have no conflicts of interest.

## Authors' Contributions

All authors listed have made a substantial, direct, and intellectual contribution to the work and approved it for publication.

## References

- [1] I. H. Mondal, *Carboxymethyl cellulose: synthesis and characterization*, Nova Science Publishers, Hauppauge, NY, USA, 2019.
- [2] A. Benchabane and K. Bekkour, "Rheological properties of carboxymethyl cellulose (CMC) solutions," *Colloid & Polymer Science*, vol. 286, no. 10, pp. 1173–1180, 2008.
- [3] K. Bekkour, D. Sun-Waterhouse, and S. S. Wadhwa, "Rheological properties and cloud point of aqueous carboxymethyl cellulose dispersions as modified by high or low methoxyl pectin," *Food Research International*, vol. 66, pp. 247–256, 2014.
- [4] I. H. Mondal, *Carboxymethyl Cellulose: Pharmaceutical and Industrial Applications*, Nova Science Publishers, Hauppauge, NY, USA, 2019.
- [5] E. Grzadka, J. Matusiak, A. Bastrzyk, and I. Polowczyk, "CMC as a stabiliser of metal oxide suspensions," *Cellulose*, vol. 27, no. 4, pp. 2225–2236, 2020.
- [6] J. Chen, H. Li, C. Fang, Y. Cheng, T. Tan, and H. Han, "Synthesis and structure of carboxymethylcellulose with a high degree of substitution derived from waste disposable paper cups," *Carbohydrate Polymers*, vol. 237, article 116040, 2020.
- [7] M. Saqib, I. Khan, and S. Shafie, "Natural convection channel flow of CMC-based CNTs nanofluid," *European Physical Journal Plus*, vol. 133, no. 12, p. 549, 2018.
- [8] A. R. Rahmati, O. A. Akbari, A. Marzban, D. Toghraie, R. Karimi, and F. Pourfattah, "Simultaneous investigations the effects of non-Newtonian nanofluid flow in different volume fractions of solid nanoparticles with slip and no-slip boundary conditions," *Thermal Science and Engineering Progress*, vol. 5, pp. 263–277, 2018.
- [9] F. O. Akinpelu, R. M. Alabison, and O. A. Olaleye, "Thermophysical properties of nanoparticles in carboxymethyl cellulose water mixture for heat enhancement applications," *IOP Conference Series Mater Science Engineering*, vol. 805, no. 1, article 012025, 2020.
- [10] F. A. Alwawi, H. T. Alkasasbeh, A. M. Rashad, and R. A. Idris, "A Numerical approach for the heat transfer flow of Carboxymethyl cellulose-water based Casson nanofluid from a solid sphere generated by mixed convection under the influence of Lorentz force," *Mathematics*, vol. 8, no. 7, p. 1094, 2020.
- [11] S. U. Choi and J. A. Eastman, *Enhancing Thermal Conductivity of Fluids with Nanoparticles; Technical Report*, Argonne National Lab, Argonne, IL, USA, 1995.
- [12] J. Buongiorno, "Convective transport in nanofluids," *Journal of Heat Transfer*, vol. 128, no. 3, pp. 240–250, 2006.
- [13] R. K. Tiwari and M. K. Das, "Heat transfer augmentation in a two-sided lid-driven differentially heated square cavity utilizing nanofluids," *International Journal of Heat and Mass Transfer*, vol. 50, no. 9–10, pp. 2002–2018, 2007.
- [14] S. A. Devi and S. S. U. Devi, "Numerical investigation of hydromagnetic hybrid Cu – Al<sub>2</sub>O<sub>3</sub>/water nanofluid flow over a permeable stretching sheet with suction," *International Journal of Nonlinear Science Numerical Simulation*, vol. 17, no. 5, pp. 249–257, 2016.
- [15] M. I. Afridi, M. Qasim, N. A. Khan, and M. Hamdani, "Heat transfer analysis of cu–Al<sub>2</sub>O<sub>3</sub>–water and cu– Al<sub>2</sub>O<sub>3</sub>–kerosene oil hybrid nanofluids in the presence of frictional heating: using 3-stage Lobatto IIIA formula," *Journal of Nanofluids*, vol. 8, no. 4, pp. 885–891, 2019.
- [16] U. Farooq, M. Afridi, M. Qasim, and D. Lu, "Transpiration and viscous dissipation effects on entropy generation in hybrid nanofluid flow over a nonlinear radially stretching disk," *Entropy*, vol. 20, no. 9, p. 668, 2018.
- [17] S. U. Devi and S. A. Devi, "Heat transfer enhancement of cu–Al<sub>2</sub>O<sub>3</sub>/water hybrid Nanofluid flow over a stretching sheet," *Journal of the Nigerian Mathematical Society*, vol. 36, pp. 419–433, 2017.
- [18] S. S. U. Devi and S. P. A. Devi, "Numerical investigation of three-dimensional hybrid Cu–Al<sub>2</sub>O<sub>3</sub>/water nanofluid flow over a stretching sheet with effecting Lorentz force subject to Newtonian heating," *Canadian Journal of Physics*, vol. 94, no. 5, pp. 490–496, 2016.
- [19] R. S. R. Gorla, S. Siddiqua, M. A. Mansour, A. M. Rashad, and T. Salah, "Heat source/sink effects on a hybrid nanofluid-filled porous cavity," *Journal of Thermophysics and Heat Transfer*, vol. 31, no. 4, pp. 847–857, 2017.
- [20] J. Chamkha, I. V. Miroshnichenko, and M. A. Sheremet, "Numerical analysis of unsteady conjugate natural convection of hybrid water-based nanofluid in a semicircular cavity," *Journal of Thermal Science and Engineering Applications*, vol. 9, no. 4, article 41004, 2017.
- [21] N. A. Zainal, R. Nazar, K. Naganthran, and I. Pop, "Unsteady three-dimensional MHD non-axisymmetric Homann stagnation point flow of a hybrid Nanofluid with stability analysis," *Mathematics*, vol. 8, no. 5, p. 784, 2020.
- [22] K. Loganathan, K. Mohana, M. Mohanraj, P. Sakthivel, and S. Rajan, "Impact of third-grade nanofluid flow across a convective surface in the presence of inclined Lorentz force: an approach to entropy optimization," *Journal of Thermal Analysis and Calorimetry*, vol. 144, no. 5, pp. 1935–1947, 2021.
- [23] M. Ramzan, A. Dawar, A. Saeed, P. Kumam, W. Watthayu, and W. Kumam, "Heat transfer analysis of the mixed convective flow of magnetohydrodynamic hybrid nanofluid past a stretching sheet with velocity and thermal slip conditions," *PLoS One*, vol. 16, no. 12, 2021.
- [24] I. Ahmad, M. Faisal, Q. Zan-Ul-Abadin, T. Javed, and L. Karuppusamy, "Unsteady 3D heat transport in hybrid nanofluid containing brick shaped ceria and zinc-oxide nanocomposites with heat source/sink," *Nanocomposites*, vol. 8, no. 1, pp. 1–12, 2022.
- [25] A. Dawar, E. Bonyah, S. Islam, A. Alshehri, and Z. Shah, "Theoretical analysis of Cu-H<sub>2</sub>O, Al<sub>2</sub>O<sub>3</sub>-H<sub>2</sub>O, and TiO<sub>2</sub>-H<sub>2</sub>O nanofluid flow past a rotating disk with velocity slip and convective conditions," *Journal of Nanomaterials*, vol. 2021, Article ID 5471813, 10 pages, 2021.
- [26] S. Eswaramoorthi, S. Divya, M. Faisal, N. Namgyel, M. Faisal, and N. Namgyel, "Entropy and Heat Transfer Analysis for MHD Flow of Cu/Ag-Water-Based Nanofluid on a Heated 3D Plate with Nonlinear Radiation," *Mathematical Problems in Engineering*, vol. 2022, Article ID 7319988, 14 pages, 2022.
- [27] A. Dawar, Z. Shah, A. Tassaddiq, P. Kumam, S. Islam, and W. Khan, "A convective flow of Williamson nanofluid through cone and wedge with non- isothermal and non-isosolutal conditions: a revised Buongiorno model," *Case Studies in Thermal Engineering*, vol. 24, article 100869, 2021.

- [28] K. Loganathan, N. Alessa, and S. Kayikci, "Heat transfer analysis of 3-D viscoelastic nanofluid flow over a convectively heated porous Riga plate with Cattaneo-Christov double flux," *Frontiers of Physics*, vol. 9, article 641645, 2021.
- [29] A. Bejan, "Second-law analysis in heat transfer and thermal design," *Advances in Heat Transfer*, vol. 15, pp. 1–58, 1982.
- [30] M. Ijaz Khana, M. U. Hafeez, T. Hayat, M. Imran Khan, and A. Alsaedi, "Magneto rotating flow of hybrid nanofluid with entropy generation," *Computer Methods and Programs in Biomedicine*, vol. 183, article 105093, 2020.
- [31] S. Ahmad, S. Nadeem, and N. Ullah, "Entropy generation and temperature-dependent viscosity in the study of SWCNT-MWCNT hybrid nanofluid," *Applied Nanoscience*, vol. 10, no. 12, pp. 5107–5119, 2020.
- [32] A. S. Butt, M. N. Tufail, A. Ali, and A. Dar, "Theoretical investigation of entropy generation effects in nanofluid flow over an inclined stretching cylinder," *International Journal of Exergy*, vol. 28, no. 2, pp. 126–157, 2019.
- [33] M. M. Rashidi, S. Bagheri, E. Momoniat, and N. Freidoonimehr, "Entropy analysis of convective MHD flow of third grade non-Newtonian fluid over a stretching sheet," *Ain Shams Engineering Journal*, vol. 8, no. 1, pp. 77–85, 2017.
- [34] O. D. Makinde and A. S. Eegunjobi, "Entropy generation in a couple stress fluid flow through a vertical channel filled with saturated porous media," *Entropy*, vol. 15, no. 12, pp. 4589–4606, 2013.
- [35] Z. H. Khan, O. D. Makinde, R. Ahmad, and W. A. Khan, "Numerical study of unsteady MHD flow and entropy generation in a rotating permeable channel with slip and hall effects," *Communications in Theoretical Physics*, vol. 70, no. 5, p. 641, 2018.
- [36] M. I. Afridi, I. Tlili, M. Goodarzi, M. Osman, and N. A. Khan, "Irreversibility analysis of hybrid nanofluid flow over a thin needle with effects of energy dissipation," *Symmetry*, vol. 11, no. 5, p. 663, 2019.
- [37] C. Srinivas Reddy, F. Ali, B. Mahanthesh, and K. Naikoti, "Irreversibility analysis of radiative heat transport of Williamson material over a lubricated surface with viscous heating and internal heat source," *Heat Transfer*, vol. 51, pp. 395–412, 2022.
- [38] M. M. Cross, "Rheology of non-Newtonian fluids: a new flow equation for pseudoplastic systems," *Journal of Colloid Science*, vol. 20, no. 5, pp. 417–437, 1965.
- [39] R. Ponalagusamy, R. T. Selvi, and A. K. Banerjee, "Mathematical model of pulsatile flow of non-Newtonian fluid in tubes of varying cross-sections and its implications to blood flow," *Journal of Franklin Institute*, vol. 349, no. 5, pp. 1681–1698, 2012.
- [40] A. R. Haghghi, N. Pirhadi, and M. Shahbazi Asl, "A Mathematical modeling for the study of blood flow as a cross fluid through a tapered artery," *Journal of New Researches in Mathematics*, vol. 5, no. 20, pp. 15–30, 2019.
- [41] M. Nazeer, "Numerical and perturbation solutions of cross flow of an Eyring-Powell fluid," *SN Applied Science*, vol. 3, no. 2, pp. 1–11, 2021.
- [42] Z. Sabir, A. Imran, M. Umar, M. Zeb, M. Shoaib, and M. A. Z. Raja, "A numerical approach for 2-D Sutterby fluid-flow bounded at a stagnation point with an inclined magnetic field and thermal radiation impacts," *Thermal Science*, vol. 25, no. 3 Part A, pp. 1975–1987, 2021.
- [43] L. Yao, A. Grishaev, G. Cornilescu, and A. Bax, "The impact of hydrogen bonding on amide 1H chemical shift anisotropy studied by cross-correlated relaxation and liquid crystal NMR spectroscopy," *Journal of the American Chemical Society*, vol. 132, no. 31, pp. 10866–10875, 2010.
- [44] M. I. Khan, T. Hayat, M. I. Khan, and A. Alsaedi, "Activation energy impact in nonlinear radiative stagnation point flow of Cross nanofluid," *International Communication of Heat Mass Transfer*, vol. 91, pp. 216–224, 2018.
- [45] C. S. Reddy and F. Ali, "Cattaneo-Christov double diffusion theory for MHD cross nanofluid flow towards a vertical stretching sheet with activation energy," *International Journal of Ambient Energy*, pp. 1–10, 2021.
- [46] S. Z. Abbas, W. A. Khan, H. Sun et al., "Mathematical modeling and analysis of Cross nanofluid flow subjected to entropy generation," *Applied Nanoscience*, vol. 10, no. 8, pp. 3149–3160, 2020.
- [47] M. Ali, W. A. Khan, M. Irfan, F. Sultan, M. Shahzed, and M. Khan, "Computational analysis of entropy generation for Cross-nanofluid flow," *Applied Nanoscience*, vol. 10, no. 8, pp. 3045–3055, 2020.
- [48] A. Wakif, "A novel numerical procedure for simulating steady MHD convective flows of radiative Casson fluids over a horizontal stretching sheet with irregular geometry under the combined influence of temperature-dependent viscosity and thermal conductivity," *Mathematical Problems in Engineering*, vol. 2020, Article ID 1675350, 20 pages, 2020.
- [49] F. Ali and A. Zaib, "Unsteady flow of an Eyring-Powell nanofluid near stagnation point past a convectively heated stretching sheet," *Arab Journal of Basic and Applied Science*, vol. 26, no. 1, pp. 215–224, 2019.

## Research Article

# A Novel Analysis of Generalized Perturbed Zakharov–Kuznetsov Equation of Fractional-Order Arising in Dusty Plasma by Natural Transform Decomposition Method

Sharifah E. Alhazmi,<sup>1</sup> Shaimaa A. M. Abdelmohsen,<sup>2</sup> Maryam Ahmed Alyami,<sup>3</sup> Aatif Ali ,<sup>4</sup> and Joshua Kiddy K. Asamoah <sup>5</sup>

<sup>1</sup>Mathematics Department, Al-Qunfudah University College, Umm Al-Qura University, Mecca, Saudi Arabia

<sup>2</sup>Department of Physics, College of Science, Princess Nourah bint Abdulrahman University, P.O. Box 84428, Riyadh 11681, Saudi Arabia

<sup>3</sup>Department of Mathematics, Faculty of Sciences, University of Jeddah, Jeddah, Saudi Arabia

<sup>4</sup>Department of Mathematics, Abdul Wali Khan University Mardan, Khyber Pakhtunkhwa 23200, Pakistan

<sup>5</sup>Department of Mathematics, Kwame Nkrumah University of Science and Technology, Kumasi, Ghana

Correspondence should be addressed to Joshua Kiddy K. Asamoah; [jkkasamoah@knust.edu.gh](mailto:jkkasamoah@knust.edu.gh)

Received 4 January 2022; Revised 2 February 2022; Accepted 13 May 2022; Published 1 June 2022

Academic Editor: Taza Gul

Copyright © 2022 Sharifah E. Alhazmi et al. This is an open access article distributed under the Creative Commons Attribution License, which permits unrestricted use, distribution, and reproduction in any medium, provided the original work is properly cited.

The natural transform decomposition method (NTDM) is a relatively new transformation method for finding an approximate differential equation solution. In the current study, the NTDM has been used for obtaining an approximate solution of the fractional-order generalized perturbed Zakharov–Kuznetsov (GPZK) equation. The method has been tested for three nonlinear cases of the fractional-order GPZK equation. The absolute errors are analyzed by the proposed method and the q-homotopy analysis transform method (q-HATM). 3D and 2D graphs have shown the proposed method's accuracy and effectiveness. NTDM gives a much-closed solution after a few terms.

## 1. Introduction

The power of applying fractional calculus to physical problems is that, when dealing with the integer order of derivative, which depends on the function's behavior, the fractional derivative produces the whole story of this function. For this reason, studying the behavior of the function fractionally is sometimes called the memory effect. This effect leads to many applications of differential equations. The importance of fractional differential equations (FDEs) cannot be denied in the recent advancement of the real world. There are models which provide a better way of managing the systems through fractional differential equations. These equations may arise in electronic circuits, physics, engineering [1, 2], bioscience, etc. [3, 4]. Finance also deals with the fractional-order differential equations to handle clients in more suitable and affordable

packages for dealing with financial crises [5, 6]. Other differential equation (DE) applications are image processing and signal processing [7, 8]. These equations may be linear or nonlinear, depending upon the geometry of the problem. Simple problems can be demonstrated by ordinary differential equations (ODEs), while complex problems can be demonstrated through partial differential equations (PDEs). Most linear problems have the exact solution, but it is hard to find the exact solution to complex nonlinear problems. To handle these problems, the researchers used numerical, analytical, and some homotopy-based methods to approximate such a nonlinear problem. Some famous methods which handle the DEs of fractional and integer order are the residual power series method [9, 10], Laplace decomposition method (LDM) [11], q-homotopy analysis method (q-HAM) [12], Adomian decomposition method (ADM) [13], reduced



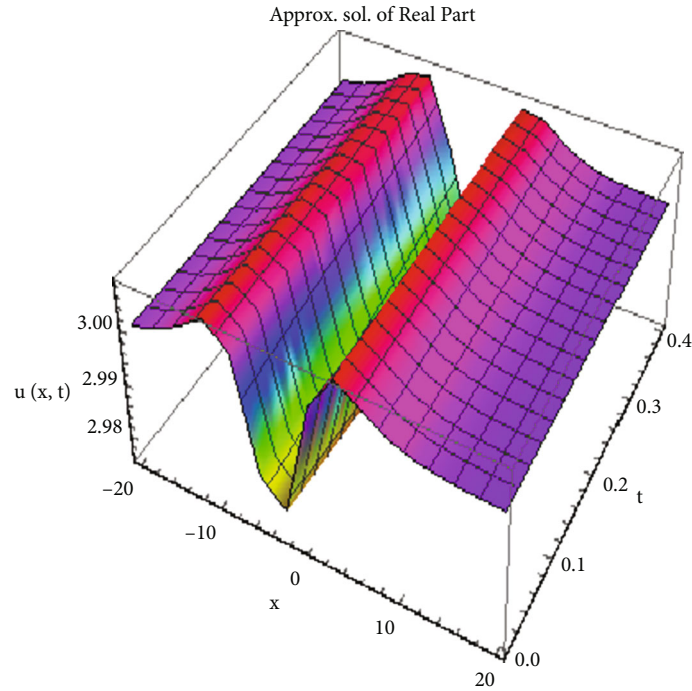


FIGURE 1: NTDM solution of the real part of problem 1.

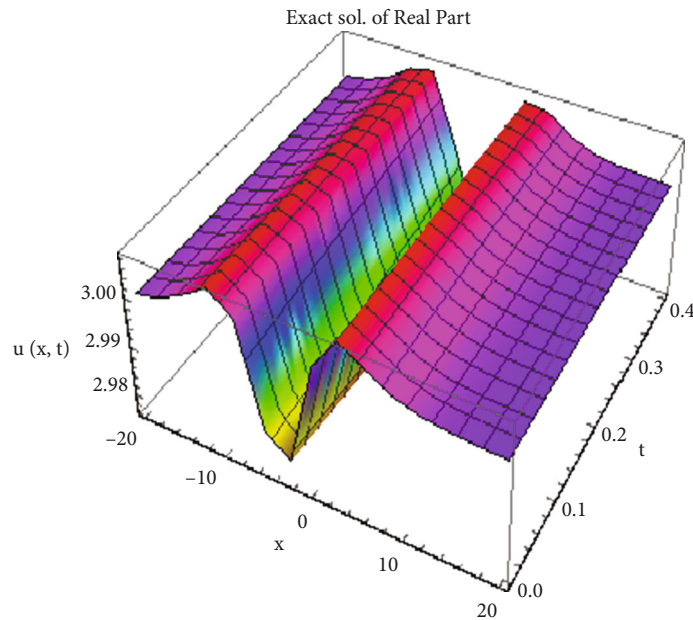


FIGURE 2: Exact solution of the real part of problem 1.

differential transform method (RDTM) [14], variational iteration method (VIM) [15], optimal homotopy asymptotic method (OHAM) [16, 17], homotopy perturbation method (HPM) [18], homotopy analysis method (HAM) [19], etc. Besides these methods, many researchers have introduced many numerical methods to handle differential equations [20]. Transformations also help for the solution approximation of DEs. In the present study, we apply a relatively new method named the natural transform decomposition method (NTDM). We decompose the nonlinear terms with the help of

Adomian polynomials and then apply the natural transformation to obtain the solution to the problem. Many researchers have applied NTDM to handle DEs of fractional order [21, 22]. The time-fractional GPZK equation (3 + 1) dimension with the following form is taken to analyze NTDM [23].

$$D_t^\alpha q + \beta_1 q^\lambda q_x + \beta_2 q_{xxx} + \beta_3 q_{xyy} + \beta_3 q_{xzz} + \zeta q_{xxxxx} = 0, 0 < \alpha \leq 1, t > 0, \quad (1)$$

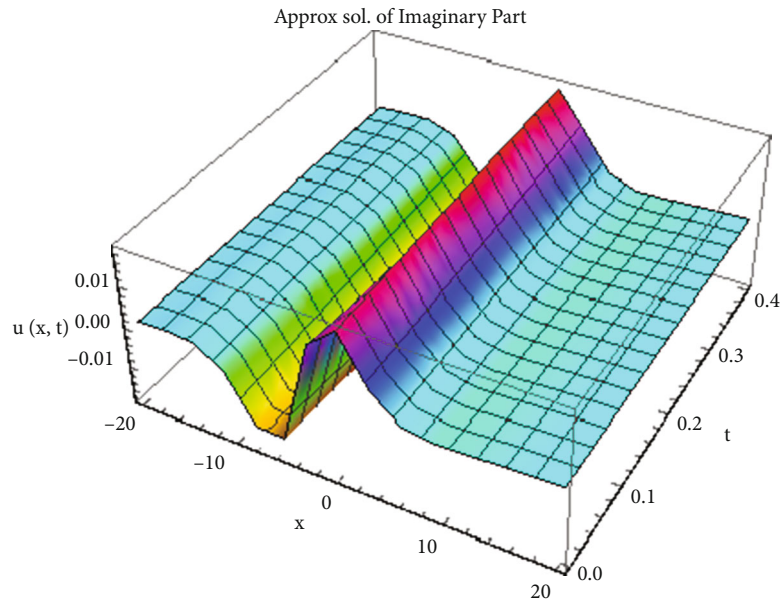


FIGURE 3: NTDM solution of the imaginary part of problem 1.

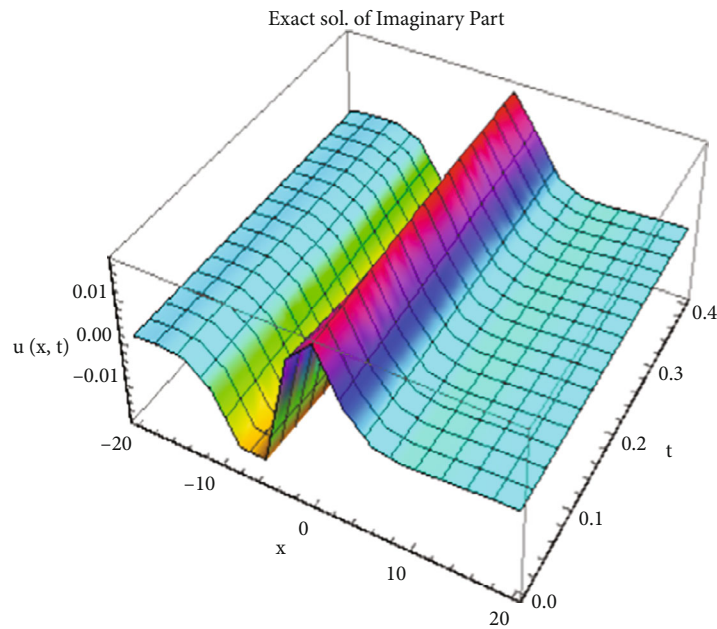


FIGURE 4: Exact solution of the imaginary part of problem 1.

where  $\alpha$  is the fractional-order of the Caputo's derivative,  $q$  is the electrostatic potential,  $\zeta$  represents the smallness parameter,  $\lambda$  is a positive number, and  $\beta_1$ ,  $\beta_2$ , and  $\beta_3$  are constants. Equation (1) describes the nonlinear dust-ion-acoustic waves in the magnetized plasmas [23]. The study of ion-acoustic waves and structures in dense quantum plasmas has sparked much interest in recent years.

The remaining paper is organized as follows: The preliminary definitions are given in Section 2 contains. Section 3 introduces the core concept of NTDM. In Section 4, NTDM is applied to three fractional-order ZK equations.

There is a conclusion to the method applications, and in the end, the bibliography is given.

## 2. Preliminaries

This section introduces some basic definition including the fractional Caputo's definition, the fractional order Riemann-Liouville (R-L) integral and some basic definitions of transformation regarding derivative and integration.

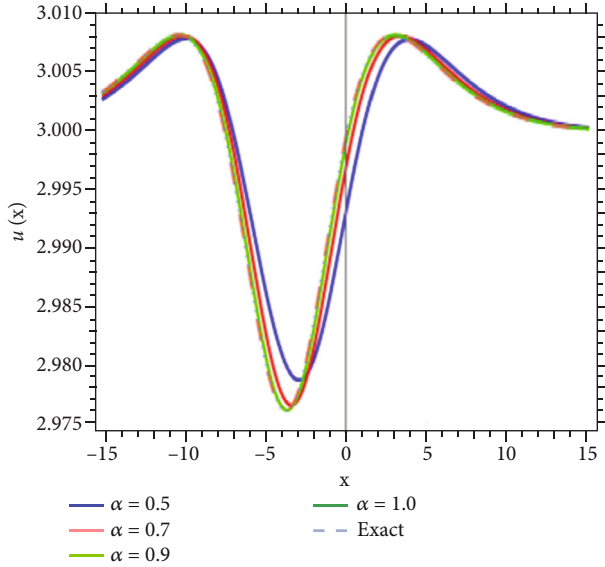


FIGURE 5: Real part solution comparison for fractional values of  $\alpha$  for problem 1.

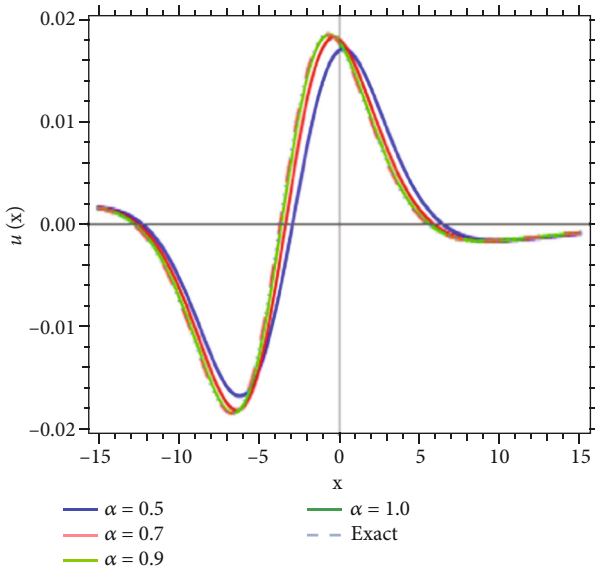


FIGURE 6: Imaginary part solution comparison for fractional values of  $\alpha$  for problem 1.

**Definition 1.** The R-L fractional integral ( $I_t^\alpha$ ) of order  $\alpha \geq 0$ ,  $f(t)$  is defined as follows:

$$I_t^\alpha f(t) = \frac{1}{\Gamma(\alpha)} \int_0^t (t-\eta)^{\alpha-1} f(\eta) d\eta, \quad (\alpha > 0, t > 0), \quad (2)$$

$$I_t^0 f(t) = f(t).$$

**Definition 2.** Caputo's fractional derivative of order  $\alpha > 0$  is

defined as follows:

$$D_t^\alpha q(x, t) = \frac{\partial^\alpha q(\varrho, t)}{\partial t^\alpha} = \begin{cases} \frac{1}{\Gamma(n-\alpha)} \int_0^t (t-\eta)^{n-\alpha-1} \frac{\partial^n q(\varrho, \eta)}{\partial \eta^n}, & \text{if } n-1 < \alpha < n, \\ \frac{\partial^n q(\varrho, t)}{\partial t^n}, & \text{if } \alpha = n \in \mathbb{N}. \end{cases} \quad (3)$$

**Definition 3.** Natural transform of  $q(t)$  is given as [17]

$$\mathbb{N}^+(q(t)) = \mathbb{R}(s, \nu) = \frac{1}{\nu} \int_0^\infty e^{-st/\nu} (q(t)) dt; \quad s, \nu > 0, \quad (4)$$

$s$  and  $\nu$  are the transform variables.

**Definition 4.** Inverse natural transform of  $\mathbb{R}(s, \nu)$  is written as follows:

$$\mathbb{N}^-(\mathbb{R}(s, \nu)) = q(t) = \frac{1}{2\pi i} \int_{c-i\infty}^{c+i\infty} e^{st/\nu} (\mathbb{R}(s, \nu)) ds, \quad (5)$$

the integral is along the complex plane.

**Definition 5.** If  $q^n(t)$  is the  $n$ th derivative of the function  $q(t)$ , then its natural transform is as follows:

$$\mathbb{N}^+(q^n(t)) = \mathbb{R}_n(s, \nu) = \frac{s^n}{\nu^n} \mathbb{R}(s, \nu) - \sum_{k=0}^{n-1} \frac{s^{n-(k+1)}}{\nu^{n-k}} (q^n(0)), \quad n \geq 1. \quad (6)$$

**Theorem 6.** If natural transform of  $g(t)$  and  $k(t)$  are, respectively,  $G(s, \nu)$  and  $K(s, \nu)$  and are defined in set  $A$ , then

$$\mathbb{N}[g * k] = \nu G(s, \nu) K(s, \nu), \quad (7)$$

where  $[g * k]$  is a convolution of  $g$  and  $k$ .

### 3. Basic Idea of NTDM

Consider the fractional order PDE of the form

$$D_t^\alpha (q(\varrho, t)) = f(\varrho, t) + Lq(\varrho, t) + \mathfrak{N}q(\varrho, t), \quad 0 < t \leq 1, \quad m-1 < \alpha < m, \quad m \in \mathbb{N}, \quad (8)$$

where  $\alpha$  is fractional derivative,  $L$  represents linear,  $\mathfrak{N}$  shows the nonlinear operator, and  $f(\varrho, t)$  is known function. The initial condition is given as follows:

$$u(\varrho, 0) = g(\varrho). \quad (9)$$

When we use the natural transform on Equation (8), we

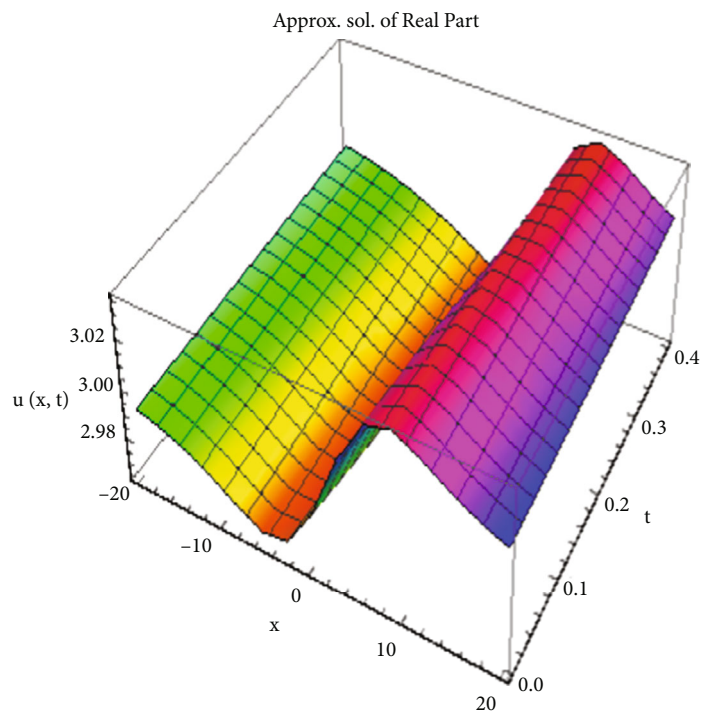


FIGURE 7: NTDM solution of the real part of problem 2.

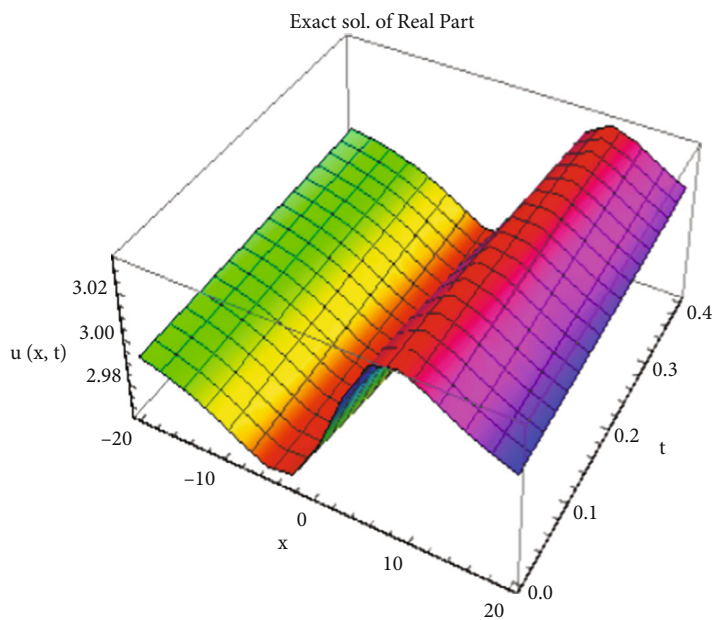


FIGURE 8: Exact solution of the real part of problem 2.

get

$$\mathbb{N}^+[D_t^\alpha(q(\varrho, t))] = \mathbb{N}^+[f(\varrho, t)] + \mathbb{N}^+[L(q(\varrho, t)) + \mathfrak{N}(q(\varrho, t))]. \tag{10}$$

Using the natural transform's differentiation characteristic

to Equation (10), we have

$$\begin{aligned} \frac{s^\alpha}{v^\alpha} \mathbb{N}^+[q(\varrho, t)] - \frac{s^{\alpha-1}}{v^\alpha} q(\varrho, 0) \\ = \mathbb{N}^+[f(\varrho, t)] + \mathbb{N}^+[Lq(\varrho, t) + \mathfrak{N}q(\varrho, t)]. \end{aligned} \tag{11}$$

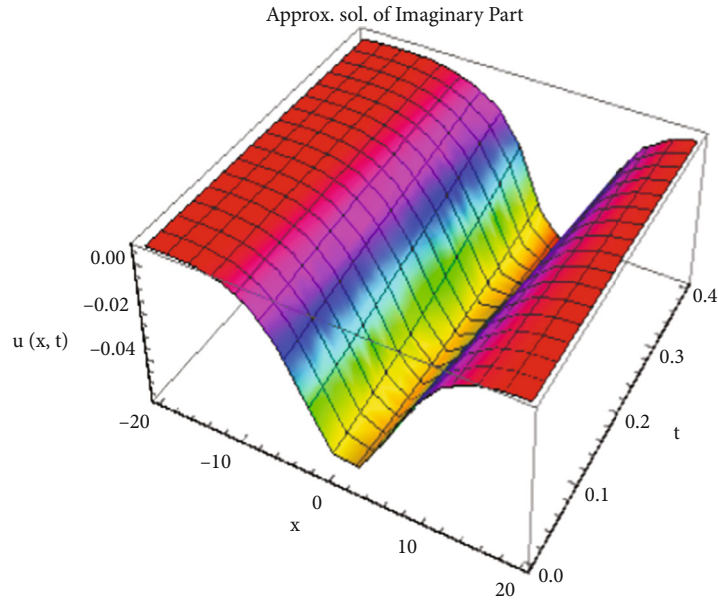


FIGURE 9: NTDM solution of the imaginary part of problem 2.

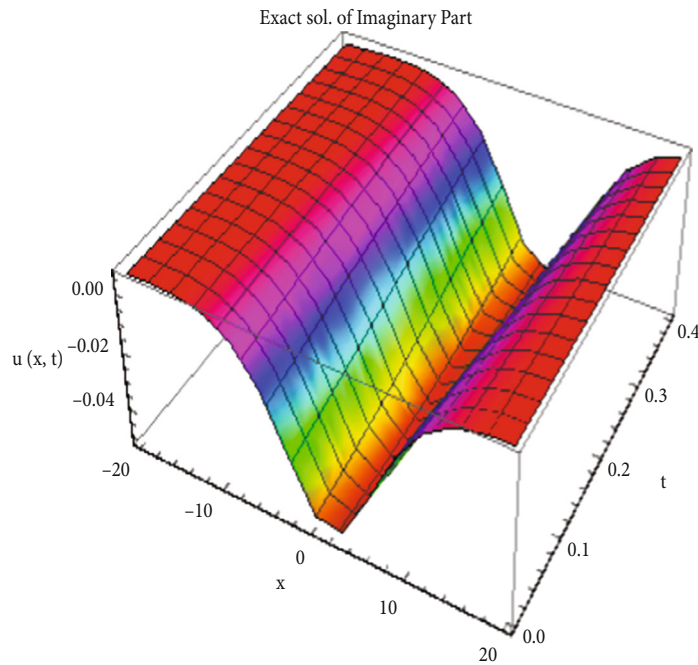


FIGURE 10: Exact solution of the imaginary part of problem 2.

Equation (11), after rearranging, is

$$\mathbb{N}^+[q(\wp, t)] = \frac{g(\wp)}{s} + \frac{v^\alpha}{s^\alpha} (\mathbb{N}^+[f(\wp, t)]) + \frac{v^\alpha}{s^\alpha} (\mathbb{N}^+[L(q(\wp, t)) + \mathbb{N}(q(\wp, t))]). \tag{12}$$

For the NTDM solution,  $q(\wp, t)$  expands as the infinite series

$$q(\wp, t) = \sum_{i=0}^{\infty} q_i(\wp, t). \tag{13}$$

The infinite series defines the nonlinear terms as follows:

$$\mathbb{N}q(\wp, t) = \sum_{i=0}^{\infty} A_i, \tag{14}$$

$$A_i = \frac{1}{i!} \left[ \frac{d^i}{d\lambda^i} \left[ \mathbb{N} \left( \sum_{i=0}^{\infty} \lambda^i q_i \right) \right] \right]_{\lambda=0}, \quad i = 0, 1, 2 \dots \tag{15}$$

The Adomian polynomials are represented by  $A_i$ . Equation (12) is modified by substituting Equations (13) and

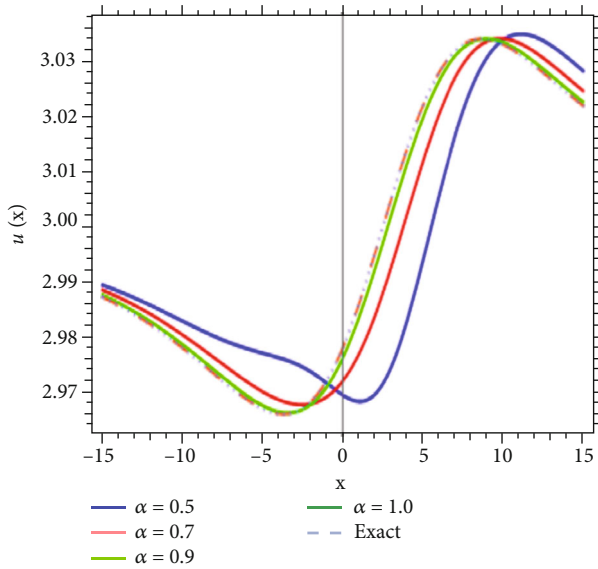


FIGURE 11: Real part solution comparison for fractional values of  $\alpha$  for problem 2.

(14).

$$\mathbb{N}^+ \left[ \sum_{i=0}^{\infty} q(\varrho, t) \right] = \frac{g(\varrho)}{s} + \frac{\nu^\alpha}{s^\alpha} \mathbb{N}^+ [f(\varrho, t)] + \frac{\nu^\alpha}{s^\alpha} \mathbb{N}^+ \left[ L \left( \sum_{i=0}^{\infty} q(\varrho, t) \right) + \sum_{i=0}^{\infty} A_i \right], \quad (16)$$

using the natural transform's linearity as follows:

$$\begin{aligned} \mathbb{N}^+ [q_0(\varrho, t)] &= \frac{g(\varrho, 0)}{s} + \frac{\nu^\alpha}{s^\alpha} \mathbb{N}^+ [f(\varrho, t)], \\ \mathbb{N}^+ [q_1(\varrho, t)] &= \frac{\nu^\alpha}{s^\alpha} \mathbb{N}^+ [L(q_0(\varrho, t)) + A_0], \\ &\vdots \\ \mathbb{N}^+ [q_{i+1}(\varrho, t)] &= \frac{\nu^\alpha}{s^\alpha} \mathbb{N}^+ [Lq_i(\varrho, t) + A_i], \quad i \geq 0. \end{aligned} \quad (17)$$

The solution components of Equation (28) are obtained by taking the inverse natural transform as follows:

$$\begin{aligned} q_0(\varrho, t) &= g(\varrho, t), \\ q_{i+1}(\varrho, t) &= \mathbb{N}^- \left[ \frac{\nu^\alpha}{s^\alpha} \mathbb{N}^+ [Lq_i(\varrho, t) + A_i] \right], \end{aligned} \quad (18)$$

where the term  $g(\varrho, t)$  is derived from the specified source term and initial condition.

The approximate  $m$ -term solution of Equations (8) and (9) is

$$q(\varrho, t) = q_0(\varrho, t) + q_1(\varrho, t) + q_2(\varrho, t) + \dots + q_{m-1}(\varrho, t). \quad (19)$$

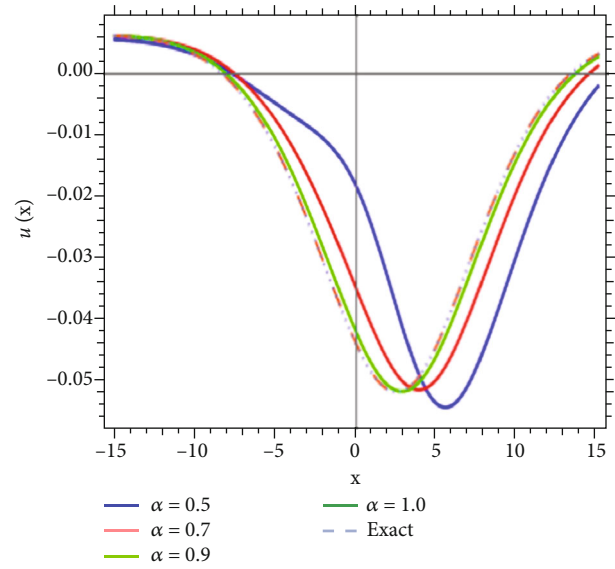


FIGURE 12: Imaginary part solution comparison for fractional values of  $\alpha$  for problem 2.

#### 4. Convergence Analysis of NTDM

**Theorem 7.** Let  $H$  be the Hilbert space defined by  $H = L^2((\alpha, \beta)X[0, T])$  the set of applications

$$q = (\alpha, \beta)X[0, T] \longrightarrow R \text{ with } \int_{(\alpha, \beta)X[0, T]} q^2(x, s) ds d\vartheta < +\infty. \quad (20)$$

In light of the above assumptions, we now consider the GPZK equation of fractional order and denote

$$L(q) = \frac{\partial^\alpha}{\partial t^\alpha} (q). \quad (21)$$

The GPZK equation is then written in operator form

$$L(q) = -\beta_1 q^k u_x - \beta_2 q_{xxx} - \beta_3 q_{xyy} - \beta_3 q_{xzz} - \zeta q_{xxxxx}. \quad (22)$$

If the following hypotheses are true, the NTDM is convergent:

$$(H1) (L(q) - L(\eta), q - \eta) \geq k \|q - \eta\|^2; \quad k > 0, \forall q, \eta \in H. \quad (23)$$

$H(2)$  whatever maybe  $M > 0$ , there exists a constant  $C(M) > 0$ , such that for  $q, \eta \in H$  with  $\|q\| \leq M, \|\eta\| \leq M$ , we have for every  $(L(q) - L(\eta), q - \eta) \leq C(M) \|q - \eta\| \|w\|$  for every  $w \in H$ .

#### 5. Applications of NTDM

5.1. Problem 1. Consider the following (3 + 1) dimension GPZK equation [23]

$$D_t^\alpha q + \beta_1 q q_{xx} + \beta_2 q_{xxx} + \beta_3 q_{xyy} + \beta_3 q_{xzz} + \zeta q_{xxxxx} = 0, \quad (24)$$

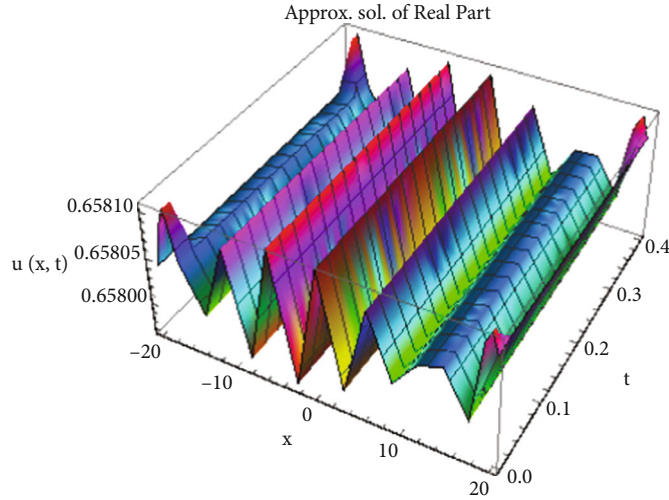


FIGURE 13: NTDM solution of the real part of problem 3.

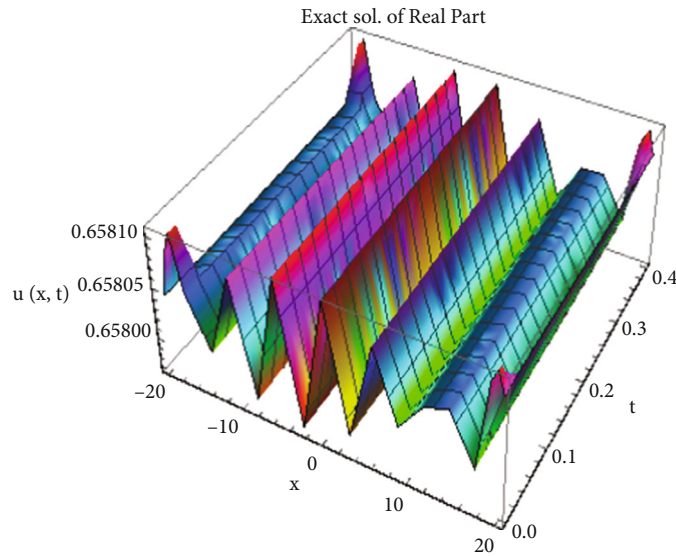


FIGURE 14: Exact solution of the real part of problem 3.

where  $q = q(\chi, y, z, t)$  together with initial conditions

$$q(\chi, y, z, 0) = e_0 - \frac{1680\zeta\rho^4}{\beta_1 \left( -z\sqrt{-(\beta_2\rho^2/\beta_3)} - \kappa^2 + \rho\chi + \kappa y + \phi \right)^4}. \tag{25}$$

The exact solution is given as [23]

$$q(\chi, y, z, t) = e_0 - \frac{1680\zeta\rho^4}{\beta_1 \left( -z\sqrt{-(\beta_2\rho^2/\beta_3)} - \kappa^2 + \rho\chi + \kappa y - \beta_1 e_0 \rho t + \phi \right)^4}. \tag{26}$$

The (24) is rearranged as follows:

$$D_t^\alpha q = -\beta_1 q q_\chi - \beta_2 q_{\chi\chi\chi} - \beta_3 q_{\chi y y} - \beta_3 q_{\chi z z} - \zeta q_{\chi\chi\chi\chi\chi}. \tag{27}$$

Apply natural transform to Equation (27), we have

$$\mathbb{N}^+[D_t^\alpha q] = \mathbb{N}^+ \left[ -\beta_1 q q_\chi - \beta_2 q_{\chi\chi\chi} - \beta_3 q_{\chi y y} - \beta_3 q_{\chi z z} - \zeta q_{\chi\chi\chi\chi\chi} \right]. \tag{28}$$

Use the natural transform's differentiation characteristic to Equation (28), we have

$$\begin{aligned} \frac{s^\alpha}{v^\alpha} q(\chi, y, z, t) - \frac{v^{\alpha-1}}{s^\alpha} q(\chi, y, z, 0) \\ = \mathbb{N}^+ \left[ -\beta_1 q q_\chi - \beta_2 q_{\chi\chi\chi} - \beta_3 q_{\chi y y} - \beta_3 q_{\chi z z} - \zeta q_{\chi\chi\chi\chi\chi} \right]. \end{aligned} \tag{29}$$

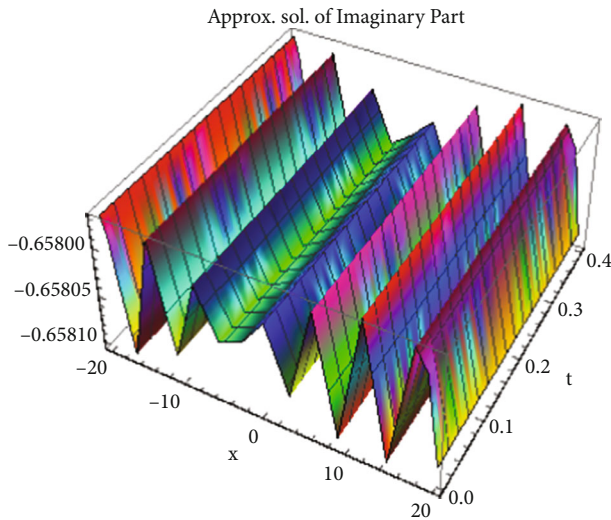


FIGURE 15: NTDM solution of the imaginary part of problem 3.

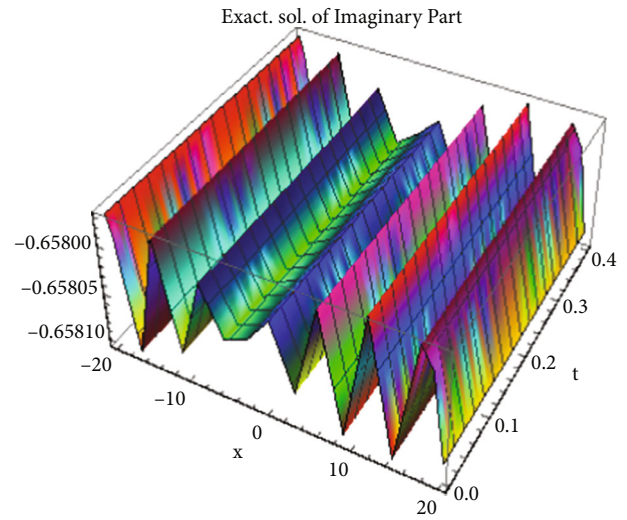


FIGURE 16: Exact solution of the imaginary part of problem 3.

After the application of inverse transform, we have

$$q(x, y, z, t) = \frac{q(x, y, z, 0)}{s} + \mathbb{N}^- \left[ \frac{v^\alpha}{s^\alpha} \mathbb{N}^+ \left[ -\beta_1 q q_x - \beta_2 q_{xxx} - \beta_3 q_{xyy} - \beta_3 q_{xzz} - \zeta q_{xxxxx} \right] \right]. \quad (30)$$

Using the recursive relation and replacing the nonlinear term  $qq_x$  by Adomian polynomials, Equation (30) yields

$$q(x, y, z, t) = \frac{q(x, y, z, 0)}{s} + \mathbb{N}^- \left[ \frac{v^\alpha}{s^\alpha} \mathbb{N}^+ \left[ -\beta_1 A_i - \beta_2 q_{xxx} - \beta_3 q_{xyy} - \beta_3 q_{xzz} - \zeta q_{xxxxx} \right] \right], i = 0, 1, 2, \dots \quad (31)$$

We got the solution components as follows by using the

NTDM concept

$$\left\{ \begin{aligned} q_0(x, y, z, t) &= \mathbb{N}^- \left[ \frac{q(x, y, z, 0)}{s} \right] \\ q_1(x, y, z, t) &= \mathbb{N}^- \left[ \frac{v^\alpha}{s^\alpha} \mathbb{N}^+ \left[ -\beta_1 A_0 - \beta_2 q_{0xxx} - \beta_3 q_{0xyy} - \beta_3 q_{0xzz} - \zeta q_{0xxxxx} \right] \right] \\ q_2(x, y, z, t) &= \mathbb{N}^- \left[ \frac{v^\alpha}{s^\alpha} \mathbb{N}^+ \left[ -\beta_1 A_1 - \beta_2 q_{1xxx} - \beta_3 q_{1xyy} - \beta_3 q_{1xzz} - \zeta q_{1xxxxx} \right] \right] \\ q_3(x, y, z, t) &= \mathbb{N}^- \left[ \frac{v^\alpha}{s^\alpha} \mathbb{N}^+ \left[ -\beta_1 A_2 - \beta_2 q_{2xxx} - \beta_3 q_{2xyy} - \beta_3 q_{2xzz} - \zeta q_{2xxxxx} \right] \right] \\ &\vdots \end{aligned} \right. \quad (32)$$

where  $A_0, A_1$ , and  $A_2$  are the Adomian polynomials and can be calculated using Equation (15). By solving, we get the solution as follows:

$$\left\{ \begin{aligned} q_0(x, y, z, t) &= e_0 - \frac{1680\zeta\rho^4}{\beta_1 \left( -z\sqrt{-(\beta_2\rho^2/\beta_3)} - \kappa^2 + \rho\chi + \kappa y + \phi \right)^4} \\ q_1(x, y, z, t) &= -\frac{6720e_0\zeta\rho^5 t^\alpha}{\Gamma(\alpha+1) \left( -z\sqrt{-(\beta_2\rho^2/\beta_3)} - \kappa^2 + \rho\chi + \kappa y + \phi \right)^5} \\ q_2(x, y, z, t) &= -\frac{33600\beta_1 e_0^2 \zeta \rho^6 t^{2\alpha}}{\Gamma(2\alpha+1) \left( -z\sqrt{-(\beta_2\rho^2/\beta_3)} - \kappa^2 + \rho\chi + \kappa y + \phi \right)^6} \\ q_3(x, y, z, t) &= \frac{201600\beta_1 e_0^3 \zeta \rho^7 \Gamma(2\alpha+1) t^{3\alpha} \left( -\left( \beta_1 e_0 \left( -z\sqrt{-(\beta_2\rho^2/\beta_3)} - \kappa^2 + \rho\chi + \kappa y + \phi \right)^4 \right) / \left( \Gamma(2\alpha+1) + \left( 1120\zeta\rho^4 / \Gamma(\alpha+1)^2 \right) - \left( 2240\zeta\rho^4 / \Gamma(2\alpha+1) \right) \right)}{\Gamma(3\alpha+1) \left( -z\sqrt{-(\beta_2\rho^2/\beta_3)} - \kappa^2 + \rho\chi + \kappa y + \phi \right)^{11}} \end{aligned} \right. \quad (33)$$



TABLE 1: Real part solution comparison for fractional values of  $\alpha$  for problem 1 at  $t = 0.01$ .

$x$	$\alpha = 0.5$	$\alpha = 0.7$	$\alpha = 0.9$	$\alpha = 1.0$	Exact	Abs. error NTDM	Abs. error [27]
-15	3.0034	3.0036	3.00369	3.00371	3.00371	$2.007727 \times 10^{-12}$	$2.007727 \times 10^{-12}$
-10	3.00812	3.00805	3.00798	3.00796	3.00796	$1.639577 \times 10^{-12}$	$1.639577 \times 10^{-12}$
-5	2.98107	2.97965	2.97917	2.97907	2.97907	$5.8479 \times 10^{-11}$	$5.8479 \times 10^{-11}$
0	2.99902	3.00045	3.00097	3.00108	3.00108	$4.721068 \times 10^{-11}$	$4.721068 \times 10^{-11}$
5	3.0066	3.00634	3.00623	3.00621	3.00621	$6.424195 \times 10^{-12}$	$6.424195 \times 10^{-12}$
10	3.00164	3.00152	3.00148	3.00147	3.00147	$5.728751 \times 10^{-14}$	$5.728751 \times 10^{-14}$
15	3.00023	3.0002	3.0002	3.00019	3.00019	$1.092459 \times 10^{-13}$	$1.092459 \times 10^{-13}$

TABLE 2: Imaginary part solution comparison for fractional values of  $\alpha$  for problem 1 at  $t = 0.01$ .

$x$	$\alpha = 0.5$	$\alpha = 0.7$	$\alpha = 0.9$	$\alpha = 1.0$	Exact	Abs. error NTDM	Abs. error [38]
-15	0.00151571	0.00146344	0.00143688	0.00143011	0.00143011	$1.789912 \times 10^{-12}$	$1.789912 \times 10^{-12}$
-10	-0.00722543	-0.00801857	-0.00835063	-0.0084304	-0.0084304	$2.285489 \times 10^{-11}$	$2.285489 \times 10^{-11}$
-5	-0.0123648	-0.0108878	-0.0102153	-0.0100505	-0.0100505	$6.996747 \times 10^{-11}$	$6.996747 \times 10^{-11}$
0	0.0175886	0.0171401	0.016905	0.0168458	0.0168458	$6.948674 \times 10^{-12}$	$6.948674 \times 10^{-12}$
5	0.000776644	0.000419639	0.000295525	0.000267266	0.000267266	$4.853387 \times 10^{-13}$	$4.853387 \times 10^{-13}$
10	-0.00160753	-0.00158678	-0.0015772	-0.00157485	-0.00157485	$7.746282 \times 10^{-13}$	$7.746282 \times 10^{-13}$
15	-0.000870554	-0.00084329	-0.000832837	-0.000830384	-0.000830384	$5.348467 \times 10^{-14}$	$5.348467 \times 10^{-14}$

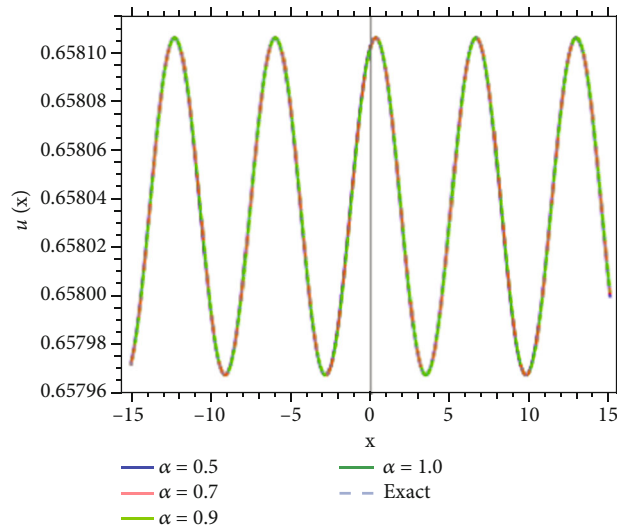


FIGURE 17: Real part solution comparison for fractional values of  $\alpha$  for problem 3.

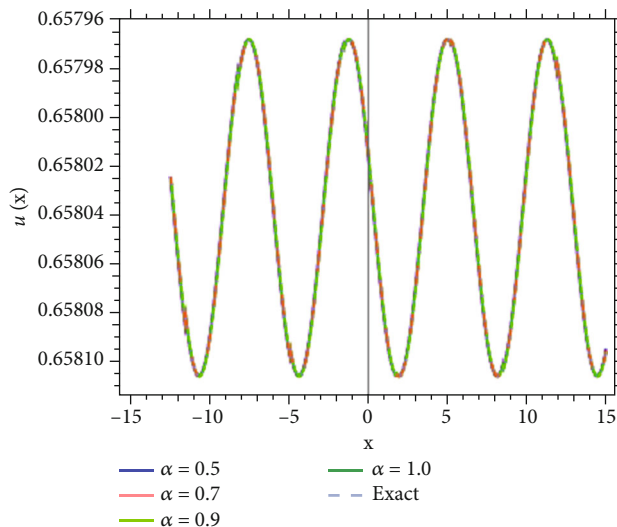


FIGURE 18: Imaginary part solution comparison for different fractional values of  $\alpha$  for problem 3.

TABLE 3: Real part solution comparison for fractional values of  $\alpha$  for problem 2 at  $t = 0.01$ .

$x$	$\alpha = 0.5$	$\alpha = 0.7$	$\alpha = 0.9$	$\alpha = 1.0$	Exact	Abs. error
-15	2.9874	2.98657	2.98621	2.98612	2.98612	$1.55851 \times 10^{-9}$
-10	2.97838	2.97696	2.97638	2.97624	2.97624	$9.833575 \times 10^{-9}$
-5	2.96771	2.96659	2.96637	2.96633	2.96633	$5.097527 \times 10^{-8}$
0	2.97778	2.98204	2.984	2.98448	2.98448	$8.531288 \times 10^{-8}$
5	3.02044	3.02508	3.02652	3.02683	3.02683	$4.077737 \times 10^{-9}$
10	3.03291	3.03204	3.03161	3.0315	3.0315	$3.67115 \times 10^{-8}$
15	3.02214	3.0207	3.02016	3.02003	3.02003	$2.767871 \times 10^{-9}$

TABLE 4: Imaginary part solution comparison for fractional values of  $\alpha$  for problem 2 at  $t = 0.01$ .

$x$	$\alpha = 0.5$	$\alpha = 0.7$	$\alpha = 0.9$	$\alpha = 1.0$	Exact	Abs. error
-15	0.00640835	0.00637269	0.00632898	0.0063165	0.0063165	$5.566582 \times 10^{-9}$
-10	0.00329588	0.00252435	0.00211105	0.00200535	0.00200536	$1.470755 \times 10^{-8}$
-5	-0.0117248	-0.0148465	-0.0162419	-0.0165841	-0.0165841	$2.044629 \times 10^{-8}$
0	-0.0429444	-0.0469602	-0.0481431	-0.0483942	-0.0483943	$7.870128 \times 10^{-8}$
5	-0.0448139	-0.0411819	-0.0396028	-0.0392184	-0.0392183	$9.6700550 \times 10^{-8}$
10	-0.0128468	-0.0095154	-0.00836997	-0.00811094	-0.00811095	$6.485631 \times 10^{-9}$
15	0.00309416	0.00400363	0.00429329	0.00435689	0.00435688	$1.14261 \times 10^{-8}$

Adding the components, we obtain the 3rd order solution as follows:

$$q(\chi, y, z, t) = q_0(\chi, y, z, t) + q_1(\chi, y, z, t) + q_2(\chi, y, z, t) + q_3(\chi, y, z, t)$$

$$\left\{ \begin{aligned} & - \frac{33600\beta_1 e_0^2 \zeta p^6 t^{2\alpha}}{\Gamma(2\alpha + 1) \left( -z\sqrt{-(\beta_2 p^2/\beta_3) - \kappa^2} + p\chi + \kappa y + \phi \right)^6 - \left( 6720e_0 \zeta p^5 t^\alpha / \left( \Gamma(\alpha + 1) \left( -z\sqrt{-(\beta_2 p^2/\beta_3) - \kappa^2} + p\chi + \kappa y + \phi \right)^5 \right) \right)} \\ & 201600\beta_1 e_0^2 \zeta p^7 \Gamma(2\alpha + 1) t^{3\alpha} \left( - \left( \left( \beta_1 e_0 \left( -z\sqrt{-(\beta_2 p^2/\beta_3) - \kappa^2} + p\chi + \kappa y + \phi \right)^4 \right) / \Gamma(2\alpha + 1) \right) \right) \\ & + \frac{\left( 1120\zeta p^4 / \Gamma(\alpha + 1)^2 \right) - \left( 2240\zeta p^4 / \Gamma(2\alpha + 1) \right)}{\Gamma(3\alpha + 1) \left( -z\sqrt{-(\beta_2 p^2/\beta_3) - \kappa^2} + p\chi + \kappa y + \phi \right)^{11} + e_0 - \left( 1680\zeta p^4 / \left( \beta_1 \left( -z\sqrt{-(\beta_2 p^2/\beta_3) - \kappa^2} + p\chi + \kappa y + \phi \right)^4 \right) \right)} \end{aligned} \right. \quad (34)$$

5.2. Problem 2. Consider the following (3 + 1) dimension GPZK equation [23]

$$D_t^\alpha q + \beta_1 q^2 q_\chi + \beta_2 q_{\chi\chi\chi} + \beta_3 q_{\chi\chi y} + \beta_3 q_{\chi z z} + \zeta q_{\chi\chi\chi\chi\chi} = 0, 0 < \alpha \leq 1, t > 0, \quad (35)$$

and initial condition as follows:

$$q(\chi, y, z, 0) = e_0 + \frac{6\sqrt{10}i\sqrt{\zeta}\rho^2}{\sqrt{\beta_1} \left( - \left( \sqrt{\sqrt{10}(-i)}\sqrt{\beta_1}e_0\sqrt{\zeta}\rho^2 - \beta_2\rho^2 - \beta_3\kappa^2/\sqrt{\beta_3} \right) z + \rho\chi + \kappa y + \phi \right)^2}. \quad (36)$$

The exact solution is given as [24]

$$q(\chi, y, z, t) = e_0 + \frac{6\sqrt{10}i\sqrt{\zeta}\rho^2}{\sqrt{\beta_1} \left( - \left( \sqrt{\sqrt{10}(-i)}\sqrt{\beta_1}e_0\sqrt{\zeta}\rho^2 - \beta_2\rho^2 - \beta_3\kappa^2/\sqrt{\beta_3} \right) z - \beta_1 e_0^2 \rho t + \rho\chi + \kappa y + \phi \right)^2}. \quad (37)$$

By using basics concepts of NTDM, the solution components obtained as follows:

$$\left\{ \begin{aligned} q_0(\chi, y, z, t) &= e_0 + \frac{6\sqrt{10}i\sqrt{\zeta}\rho^2}{\sqrt{\beta_1} \left( - \left( \sqrt{\sqrt{10}(-i)}\sqrt{\beta_1}e_0\sqrt{\zeta}\rho^2 - \beta_2\rho^2 - \beta_3\kappa^2/\sqrt{\beta_3} \right) z + \rho\chi + \kappa y + \phi \right)^2} \\ q_1(\chi, y, z, t) &= \frac{12i\sqrt{10}\sqrt{\beta_1}e_0^2\sqrt{\zeta}\rho^3 t^\alpha}{\Gamma(\alpha + 1) \left( - \left( \sqrt{\sqrt{10}(-i)}\sqrt{\beta_1}e_0\sqrt{\zeta}\rho^2 - \beta_2\rho^2 - \beta_3\kappa^2/\sqrt{\beta_3} \right) z + \rho\chi + \kappa y + \phi \right)^3} \\ q_2(\chi, y, z, t) &= \frac{36i\sqrt{10}\beta_1^{3/2}e_0^4\sqrt{\zeta}\rho^4 t^{2\alpha}}{\Gamma(2\alpha + 1) \left( - \left( z\sqrt{\sqrt{10}(-i)}\sqrt{\beta_1}e_0\sqrt{\zeta}\rho^2 - \beta_2\rho^2 - \beta_3\kappa^2/\sqrt{\beta_3} \right) + \rho\chi + \kappa y + \phi \right)^4} \end{aligned} \right. \quad (38)$$

TABLE 5: Real part solution comparison for fractional values of  $\alpha$  for problem 3 at  $t = 0.01$ .

$x$	$\alpha = 0.5$	$\alpha = 0.7$	$\alpha = 0.9$	$\alpha = 1.0$	Exact	Abs. error
-15	0.657972	0.6579720	0.6579720	0.6579720	0.6579720	$1.354472 \times 10^{-14}$
-10	0.657995	0.6579950	0.657996	0.6579960	0.657996	$3.119727 \times 10^{-14}$
-5	0.658078	0.658078	0.658078	0.658079	0.658079	$3.108624 \times 10^{-14}$
0	0.658102	0.658102	0.658102	0.658102	0.658102	$1.354472 \times 10^{-14}$
5	0.658033	0.658033	0.658032	0.658032	0.658032	$3.885781 \times 10^{-14}$
10	0.65797	0.657969	0.657969	0.657969	0.657969	$8.437695 \times 10^{-15}$
15	0.658002	0.658003	0.658003	0.658003	0.658003	$3.397282 \times 10^{-14}$

TABLE 6: Imaginary part solution comparison for fractional values of  $\alpha$  for problem 3 at  $t = 0.01$ .

$x$	$\alpha = 0.5$	$\alpha = 0.7$	$\alpha = 0.9$	$\alpha = 1.0$	Exact	Abs. error
-15	-0.658012	-0.6580130	-0.658013	-0.658013	-0.658013	$3.6526340 \times 10^{-14}$
-10	-0.658092	-0.6580920	-0.658093	-0.658093	-0.658093	$2.331468 \times 10^{-14}$
-5	-0.6580930	-0.6580930	-0.6580930	-0.6580930	-0.658093	$2.3425710 \times 10^{-14}$
0	-0.658014	-0.658013	-0.658013	-0.658013	-0.6580130	$3.663736 \times 10^{-14}$
5	-0.657968	-0.657968	-0.6579680	-0.657968	-0.657968	$2.775558 \times 10^{-15}$
10	-0.6580210	-0.6580220	-0.658022	-0.6580220	-0.658022	$3.808065 \times 10^{-14}$
15	-0.658097	-0.658097	-0.658098	-0.658098	-0.658098	$1.876277 \times 10^{-14}$

Adding the components, we get the solution as follows:

$$q(\chi, y, z, t) = q_0(\chi, y, z, t) + q_1(\chi, y, z, t) + q_2(\chi, y, z, t) = \left\{ \begin{aligned} & e_0 + \frac{6\sqrt{10}i\sqrt{\zeta}\rho^2}{\sqrt{\beta_1} \left( - \left( \sqrt{\sqrt{10}(-i)}\sqrt{\beta_1}e_0\sqrt{\zeta}\rho^2 - \beta_2\rho^2 - \beta_3\kappa^2/\sqrt{\beta_3} \right) z + \rho\chi + \kappa y + \phi \right)^2} \\ & + \frac{12i\sqrt{10}\sqrt{\beta_1}e_0^2\sqrt{\zeta}\rho^3t^\alpha}{\Gamma(\alpha+1) \left( - \left( \sqrt{\sqrt{10}(-i)}\sqrt{\beta_1}e_0\sqrt{\zeta}\rho^2 - \beta_2\rho^2 - \beta_3\kappa^2/\sqrt{\beta_3} \right) z + \rho\chi + \kappa y + \phi \right)^3} \\ & + \frac{36i\sqrt{10}\beta_1^{3/2}e_0^4\sqrt{\zeta}\rho^4t^{2\alpha}}{\Gamma(2\alpha+1) \left( - \left( z\sqrt{\sqrt{10}(-i)}\sqrt{\beta_1}e_0\sqrt{\zeta}\rho^2 - \beta_2\rho^2 - \beta_3\kappa^2/\sqrt{\beta_3} \right) + \rho\chi + \kappa y + \phi \right)^4} \end{aligned} \right\}. \tag{39}$$

5.3. Problem 3. Consider the following (3 + 1) dimension GPZK equation [23]

$$D_t^\alpha q + \beta_1 q^4 q_\chi + \beta_2 q_{\chi\chi\chi} + \beta_3 q_{\chi y y} + \beta_3 q_{\chi z z} + \zeta q_{\chi\chi\chi\chi} = 0, \tag{40}$$

and initial condition as follows:

$$q(\chi, y, z, 0) = \frac{(2^{3/4}\sqrt{-15}\sqrt{\zeta}\rho)}{\sqrt[4]{\beta_1}} \tan \left( \rho\chi + \kappa y - \frac{\sqrt{-20\zeta\rho^4 - \beta_2\rho^2 - \beta_3\kappa^2}}{\sqrt{\beta_3}} z \right). \tag{41}$$

The exact solution is given as [18]

$$q(\chi, y, z, t) = \frac{(2^{3/4}\sqrt{-15}\sqrt{\zeta}\rho)}{\sqrt[4]{\beta_1}} \tan \left( \rho\chi + \kappa y - \frac{\sqrt{-20\zeta\rho^4 - \beta_2\rho^2 - \beta_3\kappa^2}}{\sqrt{\beta_3}} z + 24\rho^5\zeta t \right). \tag{42}$$

Using NTDM concept, the solution components are obtained as follows:

$$\left\{ \begin{aligned} q_0(\chi, y, z, t) &= \frac{(2^{3/4} \sqrt[4]{-15} \sqrt[4]{\zeta} \rho)}{\sqrt[4]{\beta_1}} \tan \left( \rho\chi + \kappa y - \frac{\sqrt{-20\zeta\rho^4 - \beta_2\rho^2 - \beta_3\kappa^2}}{\sqrt{\beta_3}} z \right), q_1(\chi, y, z, t) = \frac{(24 + 24i) \sqrt[4]{30} \zeta^{5/4} \rho^6 t^\alpha \sec^2 \left( - \left( z \sqrt{-20\zeta\rho^4 - \beta_2\rho^2 - \beta_3\kappa^2} / \sqrt{\beta_3} \right) + \rho\chi + \kappa y \right)}{\sqrt[4]{\beta_1} \Gamma(\alpha + 1)} \\ q_2(\chi, y, z, t) &= \frac{(1152 + 1152i) \sqrt[4]{30} \zeta^{9/4} \rho^{11} t^{2\alpha}}{\sqrt[4]{\beta_1} \Gamma(2\alpha + 1)} \tan \left( - \frac{z \sqrt{-20\zeta\rho^4 - \beta_2\rho^2 - \beta_3\kappa^2}}{\sqrt{\beta_3}} + \rho\chi + \kappa y \right) \times \sec^2 \left( - \frac{z \sqrt{-20\zeta\rho^4 - \beta_2\rho^2 - \beta_3\kappa^2}}{\sqrt{\beta_3}} + \rho\chi + \kappa y \right) \end{aligned} \right\} \quad (43)$$

Adding the components, we get the solution as follows:

$$q(\chi, y, z, t) = q_0(\chi, y, z, t) + q_1(\chi, y, z, t) + q_2(\chi, y, z, t) = \left\{ \begin{aligned} &\frac{(2^{3/4} \sqrt[4]{-15} \sqrt[4]{\zeta} \rho)}{\sqrt[4]{\beta_1}} \tan \left( \rho\chi + \kappa y - \frac{\sqrt{-20\zeta\rho^4 - \beta_2\rho^2 - \beta_3\kappa^2}}{\sqrt{\beta_3}} z \right) + \\ &+ \frac{(24 + 24i) \sqrt[4]{30} \zeta^{5/4} \rho^6 t^\alpha \sec^2 \left( - \left( z \sqrt{-20\zeta\rho^4 - \beta_2\rho^2 - \beta_3\kappa^2} / \sqrt{\beta_3} \right) + \rho\chi + \kappa y \right)}{\sqrt[4]{\beta_1} \Gamma(\alpha + 1)} \\ &+ \frac{(1152 + 1152i) \sqrt[4]{30} \zeta^{9/4} \rho^{11} t^{2\alpha}}{\sqrt[4]{\beta_1} \Gamma(2\alpha + 1)} \tan \left( - \frac{z \sqrt{-20\zeta\rho^4 - \beta_2\rho^2 - \beta_3\kappa^2}}{\sqrt{\beta_3}} + \rho\chi + \kappa y \right) \times \\ &\sec^2 \left( - \frac{z \sqrt{-20\zeta\rho^4 - \beta_2\rho^2 - \beta_3\kappa^2}}{\sqrt{\beta_3}} + \rho\chi + \kappa y \right) \end{aligned} \right\} \quad (44)$$

### 6. Results and Discussion

This section presents the application of NTDM for solving fractional-order nonlinear GPZK equations. The values for the arbitrary constants have been taken as  $\beta_1 = 1, \beta_2 = 2, \beta_3 = 0.1, y = 2, z = 2, \zeta = 0.1, e_o = 3, \rho = 0.5, \varnothing = 0.5,$  and  $\phi = 1$  for problem 1-3. Problem 1 is approximated up to 3rd order. Problem 2 and problem 3 are approximated up to 2nd order by the NTDM algorithm. The approximate and exact real part of the solution is shown by Figures 1 and 2, respectively, by 3D plots for problem 1. The 3rd order approximate and exact solution of the imaginary part of problem 1 has been displayed by Figures 3 and 4, respectively. The solution obtained by NTDM has been compared by plots in Figures 5 and 6 for fractional values of  $\alpha$ . Figures 7 and 8 display the 3D plots of the 2nd order real part solution and exact solution, respectively, for problem 2. Figures 9 and 10 show the 2nd order imaginary part solution and exact solution, respectively, for problem 2. The solution gained by NTDM has been compared by 2D plots in Figures 11 and 12 for fractional values of  $\alpha$ .

Similarly, Figures 13 and 14 display the real part solution, and Figures 15 and 16 display the imaginary part solution for problem 3. In Tables 1 and 2, the absolute error is

compared with the q-HATM solution, which shows the convergence of NTDM. Figure 17 shows the real part solution comparison for fractional values of  $\alpha$  for problem 3. Figure 18 shows the imaginary part solution comparison for different fractional values of  $\alpha$  for problem 3. In Tables 1 and 2, the absolute error is compared with the q-HATM solution, which shows the convergence of NTDM. Similarly, Tables 3 and 4 are compared for problem 2, while Tables 5 and 6 show the comparison for problem 3.

The above conversation summarizes that NTDM is appropriate for solving DEs of fractional order.

### 7. Conclusion

The GPZK equation of fractional order has been solved by NTDM in the current study. Three nonlinear cases have been shown convergent by comparing the results with the exact solution and q-HATM solution. The effectiveness of NTDM has been shown by showing numerical results. The plots for different numerical values of  $\alpha$  confirm the convergence of NTDM as  $\alpha$  tend 1 the NTDM solution overlaps the exact solution. This discussion summarizes that the NTDM is suitable for approximating the complex nonlinear PDEs and ODEs of integer and fractional order.

## Data Availability

No data available for this study.

## Conflicts of Interest

The authors have declared no conflict of interest.

## Acknowledgments

The authors express their gratitude to the Princess Nourah bint Abdulrahman University Researchers Supporting Project (Grant No. PNURSP2022R61), Princess Nourah bint Abdulrahman University, Riyadh, Saudi Arabia.

## References

- [1] A. Khan, R. Zarin, U. W. Humphries, A. Akgül, A. Saeed, and T. Gul, "Fractional optimal control of COVID-19 pandemic model with generalized Mittag-Leffler function," *Advances in Difference Equations*, vol. 2021, no. 1, 2021.
- [2] A. Saeed, M. Bilal, T. Gul, P. Kumam, A. Khan, and M. Sohail, "Fractional order stagnation point flow of the hybrid nanofluid towards a stretching sheet," *Scientific Reports*, vol. 11, no. 1, pp. 1–15, 2021.
- [3] X.-H. Zhang, A. Ali, M. A. Khan, M. Y. Alshahrani, T. Muhammad, and S. Islam, "Mathematical analysis of the TB model with treatment via Caputo-type fractional derivative," *Discrete Dynamics in Nature and Society*, vol. 2021, Article ID 9512371, 15 pages, 2021.
- [4] Y.-M. Chu, A. Ali, M. A. Khan, S. Islam, and S. Ullah, "Dynamics of fractional order COVID-19 model with a case study of Saudi Arabia," *Results in Physics*, vol. 21, article 103787, 2021.
- [5] A. Ali, S. Islam, M. R. Khan et al., "Dynamics of a fractional-order Zika virus model with mutant," *Alexandria Engineering Journal*, vol. 2021, 2021.
- [6] W. Ma, M. Jin, Y. Liu, and X. Xu, "Empirical analysis of fractional differential equations model for relationship between enterprise management and financial performance," *Chaos, Solitons & Fractals*, vol. 125, pp. 17–23, 2019.
- [7] D. N. Tien, "Fractional stochastic differential equations with applications to finance," *Journal of Mathematical Analysis and Applications*, vol. 397, no. 1, pp. 334–348, 2013.
- [8] P. Ostalczyk, *Discrete Fractional Calculus: Applications in Control and Image Processing. Vol. 4*, World scientific, 2016.
- [9] G. Aubert, P. Kornprobst, and G. Aubert, *Mathematical Problems in Image Processing: Partial Differential Equations and the Calculus of Variations Vol. 147*, Springer, New York, 2006.
- [10] A. Kumar, S. Kumar, and S.-P. Yan, "Residual power series method for fractional diffusion equations," *Fundamenta Informaticae*, vol. 151, no. 1-4, pp. 213–230, 2017.
- [11] H. M. Jaradat, S. Al-Shara, Q. J. Khan, M. Alquran, and K. Al-Khaled, "Analytical solution of time-fractional Drinfeld-Sokolov-Wilson system using residual power series method," *IAENG International Journal of Applied Mathematics*, vol. 46, no. 1, pp. 64–70, 2016.
- [12] Y. Khan and F. Austin, "Application of the Laplace decomposition method to nonlinear homogeneous and non-homogenous advection equations," *Journal of Nature Research A*, vol. 65, no. 10, pp. 849–853, 2010.
- [13] M. A. El-Tawil and S. N. Huseen, "On convergence of q-homotopy analysis method," *International Journal of Contemporary Mathematical Sciences*, vol. 8, no. 10, pp. 481–497, 2013.
- [14] R. Rach, "On the Adomian (decomposition) method and comparisons with Picard's method," *Journal of Mathematical Analysis and Applications*, vol. 128, no. 2, pp. 480–483, 1987.
- [15] Y. Keskin and G. Oturanc, "Reduced differential transform method for partial differential equations," *International Journal of Nonlinear Sciences and Numerical Simulation*, vol. 10, no. 6, pp. 741–750, 2009.
- [16] Z. M. Odibat and S. Momani, "Application of variational iteration method to nonlinear differential equations of fractional order," *International Journal of Nonlinear Sciences and Numerical Simulation*, vol. 7, no. 1, pp. 27–34, 2006.
- [17] L. Zada and R. Nawaz, "Solution of time-fractional order RLW equation using optimal homotopy asymptotic method," *AIP Conference Proceedings*, vol. 2116, no. 1, 2019.
- [18] L. Zada, R. Nawaz, and S. S. Bushnaq, "An efficient approach for solution of fractional order differential-difference equations arising in nanotechnology," *Applied Mathematics E-Notes*, vol. 20, pp. 297–307, 2020.
- [19] S. Momani and Z. Odibat, "Homotopy perturbation method for nonlinear partial differential equations of fractional order," *Physics Letters A*, vol. 365, no. 5-6, pp. 345–350, 2007.
- [20] I. Hashim, O. Abdulaziz, and S. Momani, "Homotopy analysis method for fractional IVPs," *Communications in Nonlinear Science and Numerical Simulation*, vol. 14, no. 3, pp. 674–684, 2009.
- [21] A. K. Khalifa, K. R. Raslan, and H. M. Alzubaidi, "A collocation method with cubic B-splines for solving the MRLW equation," *Journal of Computational and Applied Mathematics*, vol. 212, no. 2, pp. 406–418, 2008.
- [22] L. Akinyemi, M. Şenol, and S. N. Huseen, "Modified homotopy methods for generalized fractional perturbed Zakharov-Kuznetsov equation in dusty plasma," *Advances in Difference Equations*, vol. 2021, no. 1, 2021.
- [23] H. Eltayeb, Y. Abdalla, I. Bachar, and M. Khabir, "Fractional telegraph equation and its solution by natural transform decomposition method," *Symmetry*, vol. 11, no. 3, p. 334, 2019.

## Research Article

# Cooling a Hot Semiannulus with Constant Heat Flux by Using $\text{Fe}_3\text{O}_4$ -Water Nanofluid and a Magnetic Field: Natural Convection Mechanism

Zhengqiang Yang,<sup>1</sup> S. M. Bouzgarrou,<sup>2,3</sup> Riadh Marzouki,<sup>4</sup> Fatma Aouaini,<sup>5</sup>  
M. A. El-Shorbagy ,<sup>6,7</sup> Mahidzal Dahari,<sup>8</sup> Said Anwar Shah,<sup>9</sup> and D. L. Suthar <sup>10</sup>

<sup>1</sup>School of Computer Science and Engineering, Xi'an Technological University, Xi'an 710021, China

<sup>2</sup>Civil Engineering Department, Faculty of Engineering, Jazan University, Saudi Arabia

<sup>3</sup>Higher Institute of Applied Sciences and Technologie of Sousse, Sousse University, Tunisia

<sup>4</sup>Department of Chemistry, College of Science, King Khalid University, Abha 61421, Saudi Arabia

<sup>5</sup>Department of Physics, College of Science, Princess Nourah bint Abdulrahman University, P.O. Box 84428, Riyadh 11671, Saudi Arabia

<sup>6</sup>Department of Mathematics, College of Science and Humanities in Al-Kharj, Prince Sattam Bin Abdulaziz University, Al-Kharj 11942, Saudi Arabia

<sup>7</sup>Department of Basic Engineering Science, Faculty of Engineering, Menoufia University, Shebin El-Kom 32511, Egypt

<sup>8</sup>Department of Electrical Engineering, Faculty of Engineering, University of Malaya, 50603 Kuala Lumpur, Malaysia

<sup>9</sup>Department of Basic Science and Islamiyat, University of Engineering and Technology, Peshawar, Pakistan

<sup>10</sup>Department of Mathematics, Wollo University, P.O. Box 1145, Dessie, Ethiopia

Correspondence should be addressed to D. L. Suthar; [dlsuthar@gmail.com](mailto:dlsuthar@gmail.com)

Received 13 January 2022; Revised 8 February 2022; Accepted 5 April 2022; Published 26 May 2022

Academic Editor: Taza Gul

Copyright © 2022 Zhengqiang Yang et al. This is an open access article distributed under the Creative Commons Attribution License, which permits unrestricted use, distribution, and reproduction in any medium, provided the original work is properly cited.

In this simulation, the nanoparticle distribution and entropy generation were studied using the Buongiorno's developed two-phase model and magnetic field inside a porous semiannulus cavity. The influence of three terms was considered in the Buongiorno's developed two-phase model such as Brownian motion, thermophoresis, and magnetophoresis effects. In addition, the entropy generation was assessed due to temperature and velocity gradient. The evidence showed that the effects of the magnetic field in high porosities and volume fraction of nanoparticles were remarkable on the Nusselt number and entropy generation. Also, irreversibility due to heat transfer is much greater than fluid friction.

## 1. Introduction

Nowadays, heat transfer processes have widely exerted for many applications such as cooling battery, CPU, forging, radiator in vehicles, heating the home, and powerplant [1–5]. One method that is popular between thermal engineering is injecting various nanoparticles such as metal, nonmetal, and oxide nanoparticles and nanoencapsulated phase change material (NEPCM) to host fluid [6–8], because mixing nanoparticles into host fluid can changed

the thermophysical properties, specifically, thermal conductivity of host fluid [9–11].

In recent years, the heat transfer rates by computational fluid dynamics (CFD) and entropy generation are significantly investigated by researchers and companies due to having accurate with experimental studies [12–15]. Moreover, owing to its large specific area and higher solid thermal conductivity, there has been growing interest in heat transfer inside the porous media. According to previous studies, porous structure improves thermal performance of

nanofluid [16–19]. A numerical investigation of heat transfer and fluid flow in a parabolic trough solar receiver with internal annular porous structure and synthetic oil- $\text{Al}_2\text{O}_3$  nanofluid was carried out by Bozorg et al. [20]. According to their results, utilization of porous structure and nanofluids enhances heat transfer coefficient 7% and 20%, respectively. Jamal-Abad et al. [21] experimentally studied the thermal efficiency of a solar parabolic trough collector filled with porous media; they illustrated an enhancement in efficiency of the collector by increasing the mass flow rate.

It is confirmed that in nanofluid simulation, two-phase approach provides better accuracy compared to single-phase approach [22–24]. A two-phase model presented by Buongiorno [25] has received significant attention; in this model, it is suggested that among seven slip mechanisms, Brownian motion and thermophoresis diffusion play vital role in nanofluid distribution. Natural convection of nanofluid in an inclined cavity and inside porous medium considering two-phase approach is studied by studies [6] and [15]. Their results demonstrate good agreement with experimental studies. Thermophoresis and Brownian motion effect on boundary layer flow of nanofluid in presence of thermal stratification due to solar energy is analyzed by Anbuechian et al. [26]. Their results highlighted that Brownian motion and thermophoresis distribution can affect the heat transfer properties; they reported a substantial impact on the boundary layer flow field by Brownian motion in the presence of thermal stratification. Kaloudis et al. [27] numerically investigated on parabolic trough solar collector with nanofluid using a two-phase model. They reported that two-phase simulation of nanofluids in solar studies shows better agreement with experimental studies. Also, the presence of nanoparticles improves collector's efficiency.

To obtain the optimal configuration of solar collectors, it is essential to analyze the entropy generation. Farshad and Sheikholeslami [28] scrutinize exergy loss and heat transfer of mixture of aluminum oxide and  $\text{H}_2\text{O}$  through a solar collector. Thermal performance and entropy generation analysis of a high concentration ratio parabolic trough solar collector was studied by Mwesigye et al. [29]. They reported a decrement in entropy generation with augmentation of nanofluid volume fraction for some ranges of Re number. Verma et al. [30] experimentally analyzed exergy efficiency and entropy generation in flat plate solar collectors for different types of nanofluids. They highlighted that rise of Bejan number towards unity illustrates the improvement of system performance due to efficient conversion of the available energy into useful functions. Also, Sheikholeslami et al. [31] scrutinized impact of Lorentz forces on magnetic nanofluid of  $\text{Fe}_3\text{O}_4$  with entropy and exergy analyzing inside a semiannulus. Afrand et al. [32] studied free convective heat transfer and entropy generation of  $\text{Al}_2\text{O}_3$ -water nanofluid in a triangular enclosure. They illustrated that the Bijan number increases by decreasing the Ra and increasing the Ha. The maximum heat transfer rate takes place at the enclosure angle of  $60^\circ$ .

To the best knowledge of the authors, there has been no detailed investigation of impacts of nonuniform magnetic fields on PTC thermal performance using nanofluid, consid-

ering Brownian motion and thermophoresis distribution as well as entropy generation. In the present work, a coil is wrapped around semiannulus to produce a variable magnetic field. Also, it focuses on the local distribution of nanoparticles, entropy generation due to fluid friction and heat transfer, and Nusselt number variation.

## 2. Physical Model

In the present study, 2-dimensional and steady-state natural convection is simulated in a semiannulus enclosure. Schematic presentation of the problem is presented in Figure 1. In Figure 1, two horizontal walls are thermally insulated, the inner semicircle wall at constant heat flux ( $q''$ ), and the outer semicircle wall is fixed at constant temperature ( $T_c$ ). The working fluid is  $\text{Fe}_3\text{O}_4$ -water nanofluid. Natural convection fluid flow is simulated based on Boussinesq's approximation. Also, heat transfer, nanoparticles distribution, and entropy generation in the presence of a nonuniform magnetic field are investigated. Therefore, it is assumed that nanoparticle distribution is based on Buongiorno two-phase model. According to the aforementioned assumption, the governing equations are presented in the next section.

## 3. Relations and Hypothesis

The nondimensional parameters are as follows:  $X = x/L$ ,  $Y = y/L$ ,  $T^* = k_f(T - T_c)/q''L$ ,  $\mathbf{V}^* = \mathbf{V}L/\nu_f$ ,  $P^* = PL^2/\rho_f\nu_f^2$ ,  $\mathbf{H}^* = \mathbf{H}/H_0$ ,  $\mathbf{M}^* = \mathbf{M}/M_0$ ,  $\phi^* = \phi/\phi_{\text{Ave}}$ ,

$$u^* = u/\alpha_f L, v^* = v/\alpha_f L, \nabla^* = L\nabla, \delta = k_f T_c/q''L, D_B^* = D_B/D_{B0}, D_T^* = D_T/D_{T0}, D_{T0} = \gamma\mu_f/\rho_f\phi_{\text{Ave}},$$

$$H_0 = I/2\pi\lambda, D_{B0} = K_B T_c/3\pi\mu_f d_{np}, \text{ and } M_0 = \chi(\phi_{\text{Ave}}, T_f)H_0 \text{ for } \phi_{\text{Ave}} = 0.02, \text{ and } T_m = T_c + q''L/2k_f.$$

The dimensionless forms of continuity equations, momentum, energy, and volume fraction are as follows:

Nondimensional continuity equation:

$$\nabla^* \cdot \mathbf{V}^* = 0. \quad (1)$$

Nondimensional momentum equation:

$$\left(\frac{1}{\varepsilon^2} \frac{\rho_{nf}}{\rho_f}\right) (\mathbf{V}^* \cdot \nabla^*) \mathbf{V}^* = -\nabla^* P^* - \left(\frac{\mu_{nf}}{\mu_f}\right) \frac{1}{Da} \mathbf{V}^* + \nabla^* \cdot \left(\frac{\mu_{nf}}{\mu_f} \nabla^* \mathbf{V}^*\right) + \left(\frac{(\rho\beta)_{nf}}{\rho_f \beta_f}\right) \frac{Ra_f}{Pr} T^* \cdot \hat{\mathbf{e}} + Mn (\mathbf{M}^* \cdot \nabla^*) \mathbf{H}^*. \quad (2)$$



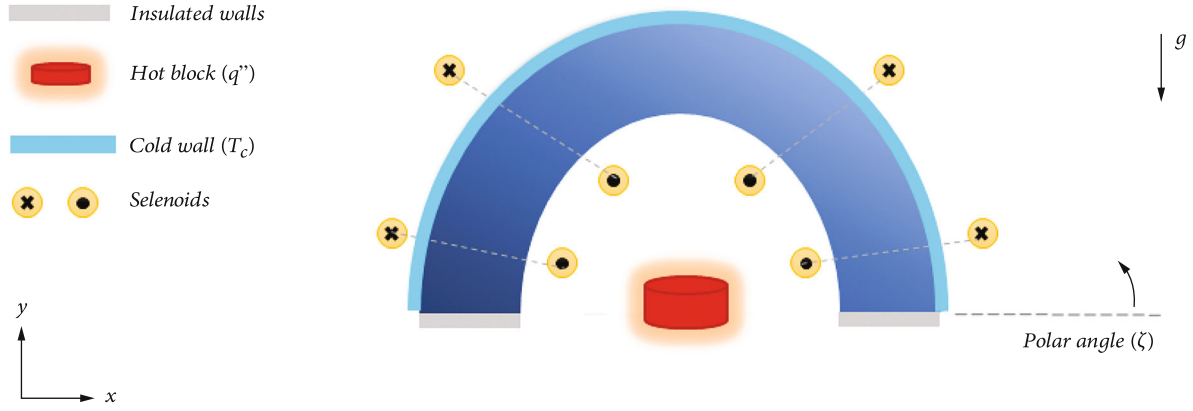


FIGURE 1: Schematic presentation of the problem.

Nondimensional heat transfer equation:

$$\frac{(\rho C_p)_{nf}}{(\rho C_p)_f} \mathbf{V}^* \cdot \nabla^* T^* = \frac{1}{Pr} \nabla^* \left( \frac{k_{eq}}{k_f} \nabla^* T^* \right) + \varepsilon \frac{1}{Pr Le} \left( D_B^* \nabla^* \varphi^* \cdot \nabla^* T^* + \frac{D_T^*}{N_{BT}} \frac{\nabla^* T^* \cdot \nabla^* T^*}{1 + (T^*/\delta)} - D_B^* \xi L(\xi) \varphi^* \frac{\nabla^* \mathbf{H}^* \cdot \nabla^* T^*}{\mathbf{H}^*} \right). \quad (3)$$

Nondimensional mass transfer equation:

$$\frac{1}{\varepsilon} \mathbf{V}^* \cdot \nabla^* \varphi^* = \frac{1}{Sc} \nabla^* \left( D_B^* \nabla^* \varphi^* + \frac{D_T^*}{N_{BT}} \frac{\nabla^* T^*}{1 + (T^*/\delta)} - D_B^* \xi L(\xi) \varphi^* \frac{\nabla^* \mathbf{H}^*}{\mathbf{H}^*} \right). \quad (4)$$

The dimensionless numbers in the above relationships are defined as:

$$\begin{aligned} Da &= \frac{K}{L^2}, Pr = \frac{\nu_f}{\alpha_f}, \alpha_f = \frac{k_f}{(\rho C_p)_f}, Ra_f = \frac{g B_f q' L^4}{k_f \alpha_f \nu_f}, Ra_p \\ &= Ra_f Da, \hat{\varepsilon} = \frac{g}{g}, Mn = \frac{\mu_0 H_0 M_0 L^2}{\rho_f \nu_f^2}, Le \\ &= \frac{k_f}{(\rho C_p)_{np} D_{B0} \varphi_{Ave}}, N_{BT} = \frac{\varphi_{Ave} D_{B0} \delta}{D_{T0}}, Sc = \frac{\nu_f}{D_{B0}}. \end{aligned} \quad (5)$$

$Mn$  is the magnetic number, which is defined as the ratio of the Kelvin force to the kinematic viscosity. Moreover,  $Da$ ,  $Ra$ ,  $Pr$ ,  $Le$ , and  $Sc$  denote the Darcy, Rayleigh, Prandtl, Lewis, and Schmitt numbers, respectively.

The average Nusselt on the constant heat flux wall (inner cylinder wall) is calculated as follows:

$$Nu_{loc} = \frac{k_{eq}}{k_{eff}} \frac{1}{T^*}, Nu_{ave} = \frac{1}{\pi} \int_0^\pi Nu_{loc}(\zeta) d\zeta. \quad (6)$$

In this study, the entropy generation is considered due to the irreversibility of the velocity gradients and temperature gradients. According to Shavik et al. [33], the entropy gener-

TABLE 1: Comparison of total entropy generation ( $S_{g,tot}$ ) and Bejan number ( $Be_{ave}$ ), for  $Pr = 0.71$  and irreversibility ( $X = 10^{-4}$ ).

	$Ra = 10^3$		$Ra = 10^5$	
	$S_{g,tot}$	$Be_{ave}$	$S_{g,tot}$	$Be_{ave}$
Present work	1.154	0.97	23.2	0.193
Shavik et al. [33]	1.15	0.97	23.27	0.194

ation is obtained as

$$\begin{aligned} s_s &= \frac{\mu_{nf}}{T_m} \left[ 2 \left( \frac{\partial u}{\partial x} \right)^2 + 2 \left( \frac{\partial v}{\partial y} \right)^2 + \left( \frac{\partial u}{\partial y} + \frac{\partial v}{\partial x} \right)^2 \right] \\ &+ \frac{k_{nf}}{T_m^2} \left[ \left( \frac{\partial T}{\partial x} \right)^2 + \left( \frac{\partial T}{\partial y} \right)^2 \right]. \end{aligned} \quad (7)$$

In the mentioned equation, the first and second terms are local entropy generation due to the fluid friction ( $S_{L,FF}$ ) and the heat transfer ( $S_{L,HT}$ ) irreversibility, respectively. Also, the dimensionless equation of entropy generation is as follows:

$$\begin{aligned} S_{L,HT} &= \frac{k_{nf}}{k_f} \left( \frac{\partial T^*}{\partial X} \right)^2 + \left( \frac{\partial T^*}{\partial Y} \right)^2, \\ S_{L,FF} &= X \frac{\mu_{nf}}{\mu_f} \left[ 2 \left[ \left( \frac{\partial u^*}{\partial X} \right)^2 + \left( \frac{\partial v^*}{\partial Y} \right)^2 \right] + \left( \frac{\partial u^*}{\partial Y} + \frac{\partial v^*}{\partial X} \right)^2 \right], X \\ &= \mu_f k_f T_m \left( \frac{\alpha_f}{L^2 q} \right)^2, \\ S_{L,s} &= s_s \times \frac{k_f T_m^2}{q} = S_{L,FF} + S_{L,HT}. \end{aligned} \quad (8)$$

Bejan number is the ratio of the entropy generation due to the heat transfer to the total entropy generation. This is as follows:

$$Be_L = \frac{S_{L,HT}}{S_{L,s}}. \quad (9)$$

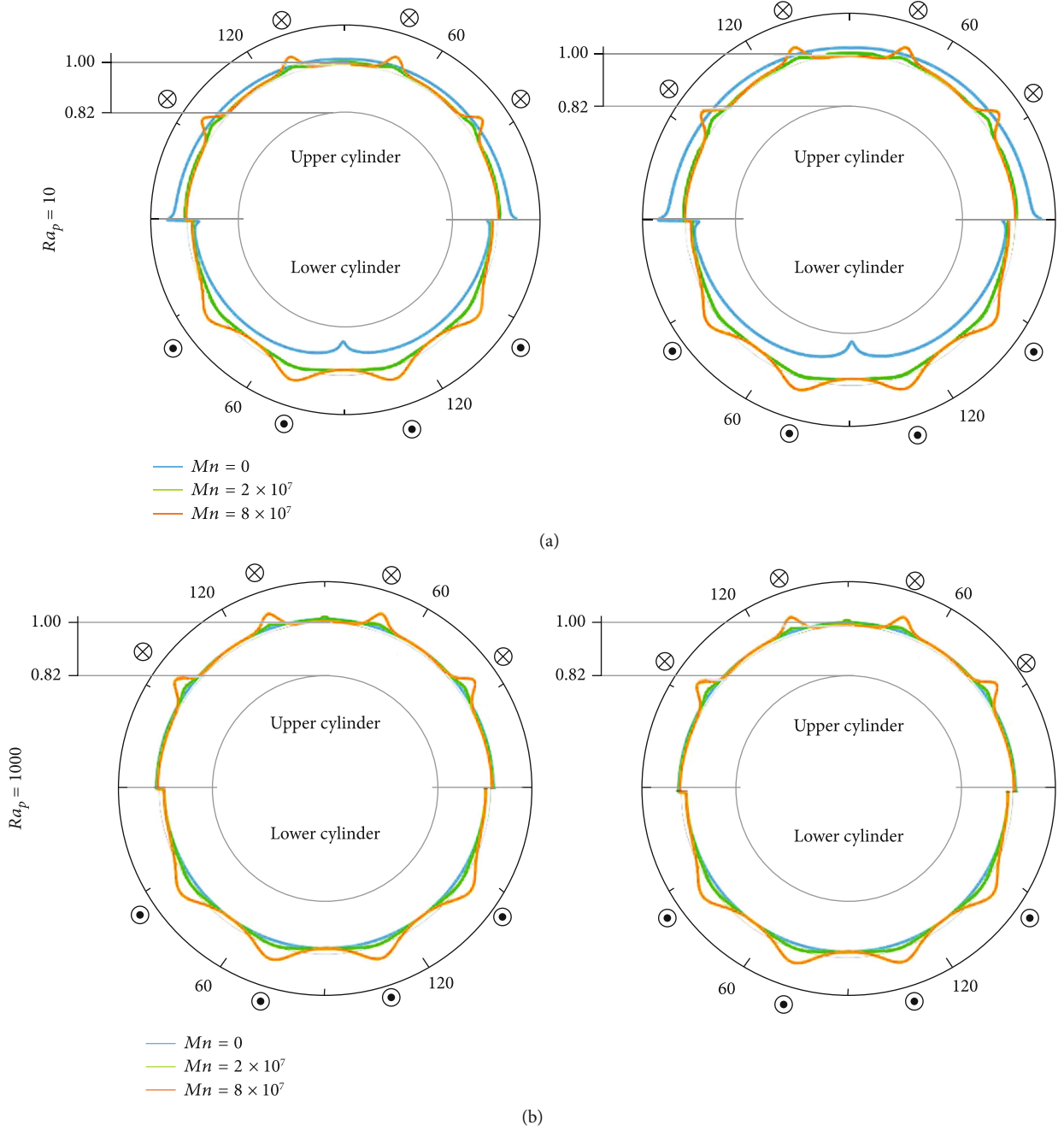


FIGURE 2: Nondimensional distribution of nanoparticles on the outer and inner cylinder walls for  $\varphi_{Ave} = 0.03$ ,  $Ra_p = 10$  and  $1000$ , and different magnetic numbers at (a)  $\varepsilon = 0.4$  and (b)  $\varepsilon = 0.7$ .

Total entropy generation and the total Bejan number are obtained by integrating the relations of local entropy generation and Bejan number.

$$\begin{aligned}
 S_{T,HT} &= \int_A S_{L,HT} dA, S_{T,FF} = \int_A S_{L,FF} dA, S_{T,s} \\
 &= \int_A S_{L,s} dA, Be_{ave} = \frac{\int_A Be_L dA}{\int_A dA}.
 \end{aligned} \quad (10)$$

#### 4. CFD Setting

The presented nonlinear governing PDE equations are solved based on finite volume method (FVM). The continuity and momentum equations are coupled and solved in an algorithm termed SIMPLE. The energy and concentration equations simultaneously solved. The advection terms in the governing equations are discretized based on first-order upwind schemes, and diffusion terms are solved based on second-order central schemes. The numerical convergence criterion was residual values. The

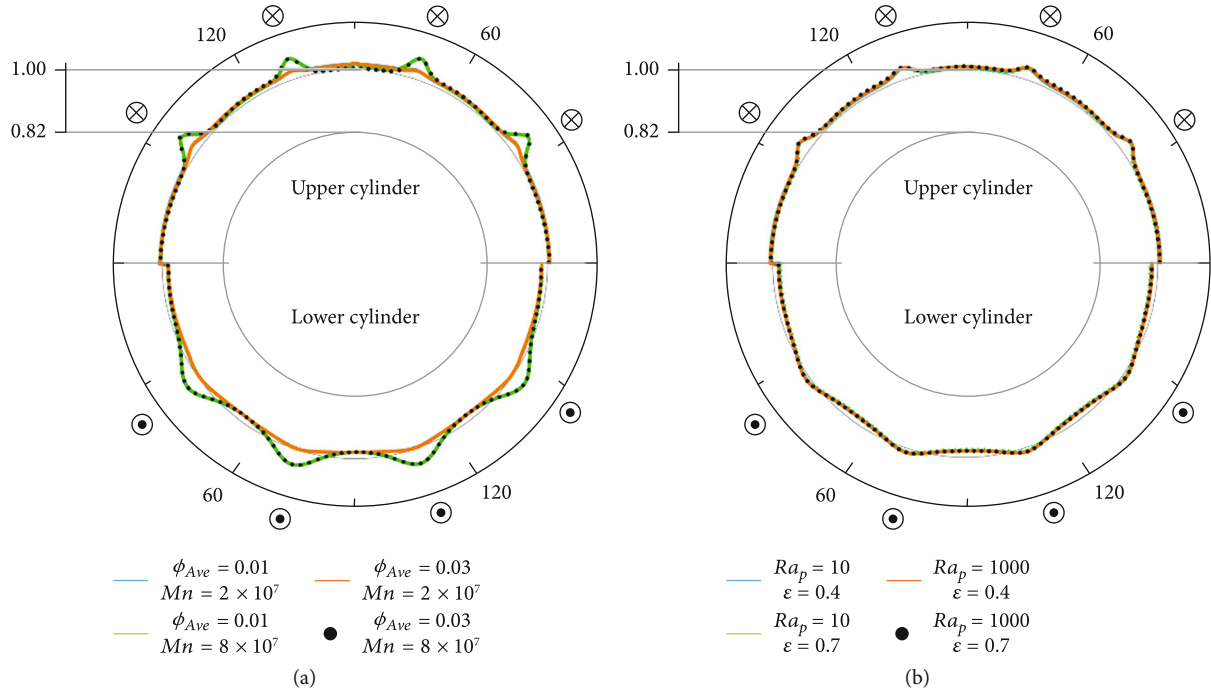


FIGURE 3: Nondimensional distribution of nanoparticles on inner and outer walls (with angle of  $\zeta$ ) for (a) different magnetic numbers and volume fraction at  $Ra_p = 1000$  and  $\epsilon = 0.7$ , (b) different porous Rayleigh number and porosity at  $\phi_{Ave} = 0.03$  and  $Mn = 8 \times 10^7$ .

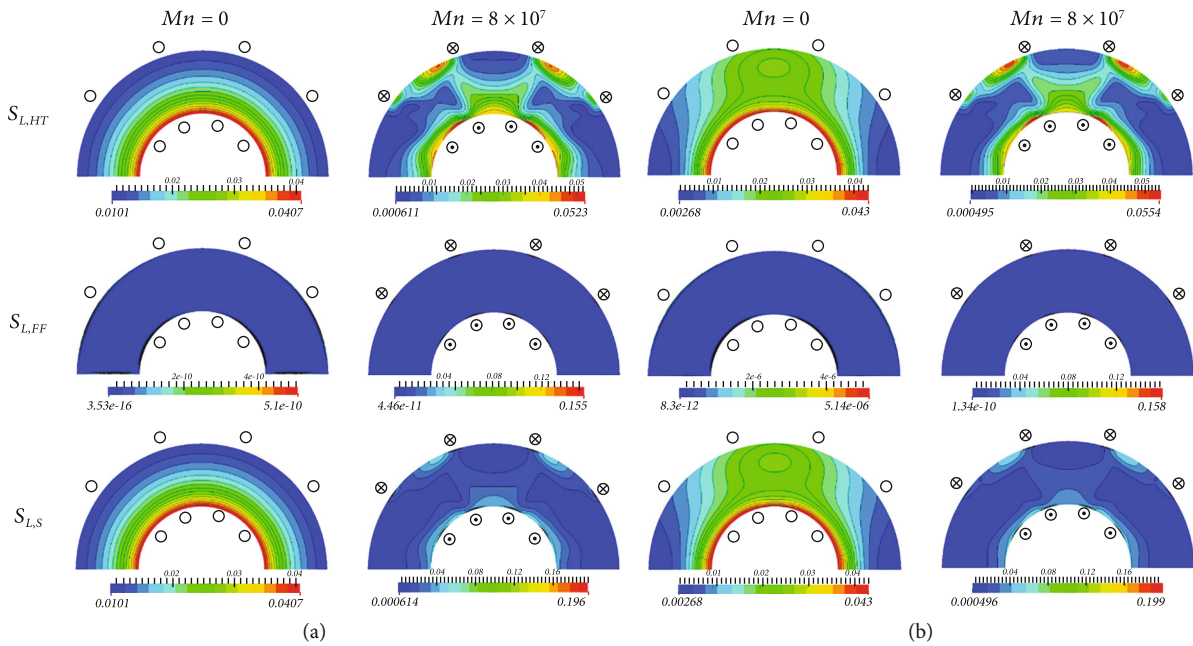


FIGURE 4: The dimensionless local entropy generation due to heat transfer ( $S_{L,HT}$ ), fluid friction ( $S_{L,FF}$ ) and summation ( $S_{L,S}$ ) for  $\phi_{Ave} = 0.03$ ,  $\epsilon = 0.7$ , and  $Mn = 0$  and  $8 \times 10^7$  at (a)  $Ra_p = 10$  and (b)  $Ra_p = 1000$ .

residual values at convergence for velocity and pressure fields were  $10^{-5}$ , and for temperature and  $\phi$  were  $10^{-6}$ . Under relaxation factors for velocity, pressure, temperature, and  $\phi$  were 0.4, 0.6, 0.2, and 0.01, respectively. Square uniform mesh is selected for presented study, based on nanoparticle distribu-

tion on the hot wall 40,000 ( $200 \times 200$ ) numbers of mesh selected. Moreover, for validation of the entropy generation, the results of the present study is compared with the work of Shavik et al. [33] (Table 1). In all cases, the results of this study are in good agreement.

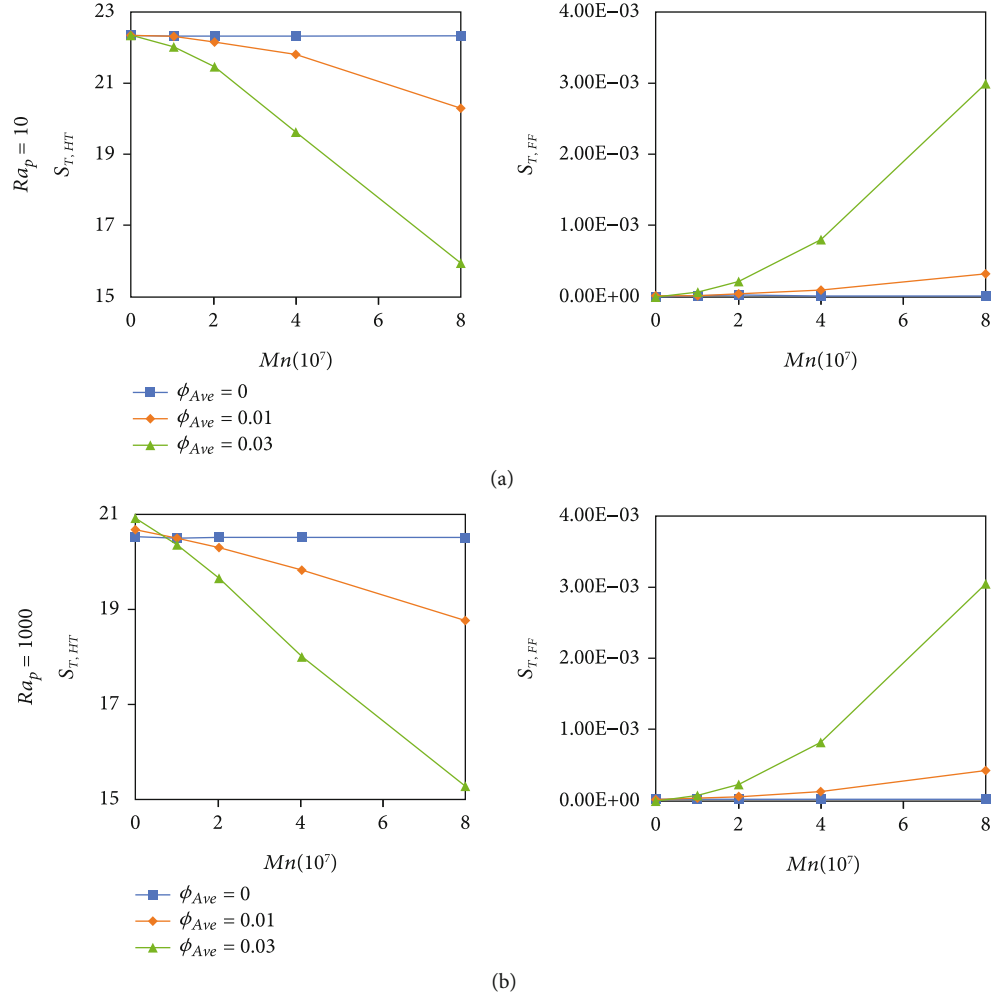


FIGURE 5: Dimensionless total entropy generation due to heat transfer ( $S_{T,HT}$ ) and fluid friction ( $S_{T,FF}$ ) for  $\varepsilon = 0.7$  and different volume fraction of nanoparticle.

## 5. Results and Discussion

Extended Buongiorno's two-phase model is considered for the distribution of nanoparticles. The numerical simulation has investigated for porous Rayleigh number ( $Ra_p = 10$  and  $1000$ ), the volume fraction of nanoparticles ( $\phi_{Ave} = 0, 0.01$  and  $0.03$ ), porosity number ( $\varepsilon = 0.4$  and  $0.7$ ), and magnetic number ( $0 \leq Mn \leq 8 \times 10^7$ ). Constant values included  $Pr = 4.623$ ,  $Sc = 3.55 \times 10^4$ ,  $T_c = 310 K$ ,  $q'' = 48.01 (w/m^2)$ ,  $1.71 \times 10^5 < Le < 6.84 \times 10^5$ ,  $Da = 10^{-3} (K = 0.625 \times 10^{-6})$ ,  $\delta = 161$ ,  $N_{BT} = 0.245$ ,  $X = 3 \times 10^{-11}$ , and  $T_m = T_c + Lq''/2k_f = 310.96 K$ .

The effects of the mentioned parameters have studied the distribution of nanoparticles and the entropy generation contours due to fluid friction and heat transfer, and Bejan.

Figure 2 shows the nondimensional distribution of nanoparticles on the lower and upper cylinder walls in  $\phi_{Ave} = 0.03$  and  $Ra_p = 10$  and  $1000$  for the different magnetic numbers. In Figure 2(a) and porous Rayleigh number 10, the density of nanoparticles is higher on the top wall (cold) than the down wall (hot); that is due to the thermophoresis term in the volume fractional equation. With the rising of porous

Rayleigh number, the dimensional distribution of nanoparticles is almost identical due to the increasing flow velocity on the inner and outer walls. By increasing the magnetic number to  $Mn = 2 \times 10^7$  for all of the cases, the density of nanoparticles for both walls is almost equal to the unit value, and no change occurs. But with the increasing magnetic number to  $Mn = 8 \times 10^7$ , the peak of nanoparticle density appears near the wires, which is due to the absorption of nanoparticles by the magnetic field. The above arguments are also true for Figure 2(b), which the porosity has increased to  $0.7$ . Besides, in all graphs, the peak of nanoparticle density in the inner wall is wider than the outer wall.

Figure 3 shows a better comparison of the effect of different parameters on the dimensional distribution of nanoparticles. Figure 3(a) is shown for magnetic numbers and different volume fractions in  $Ra_p = 1000$  and  $\varepsilon = 0.7$ . The dimensionless nanoparticle density is the same for the volume fraction  $0.01$  and  $0.03$  in a constant magnetic number. Therefore, the volume fraction does not affect the dimensionless distribution of nanoparticles. Also, in a constant volume fraction, the density of nanoparticles increases near

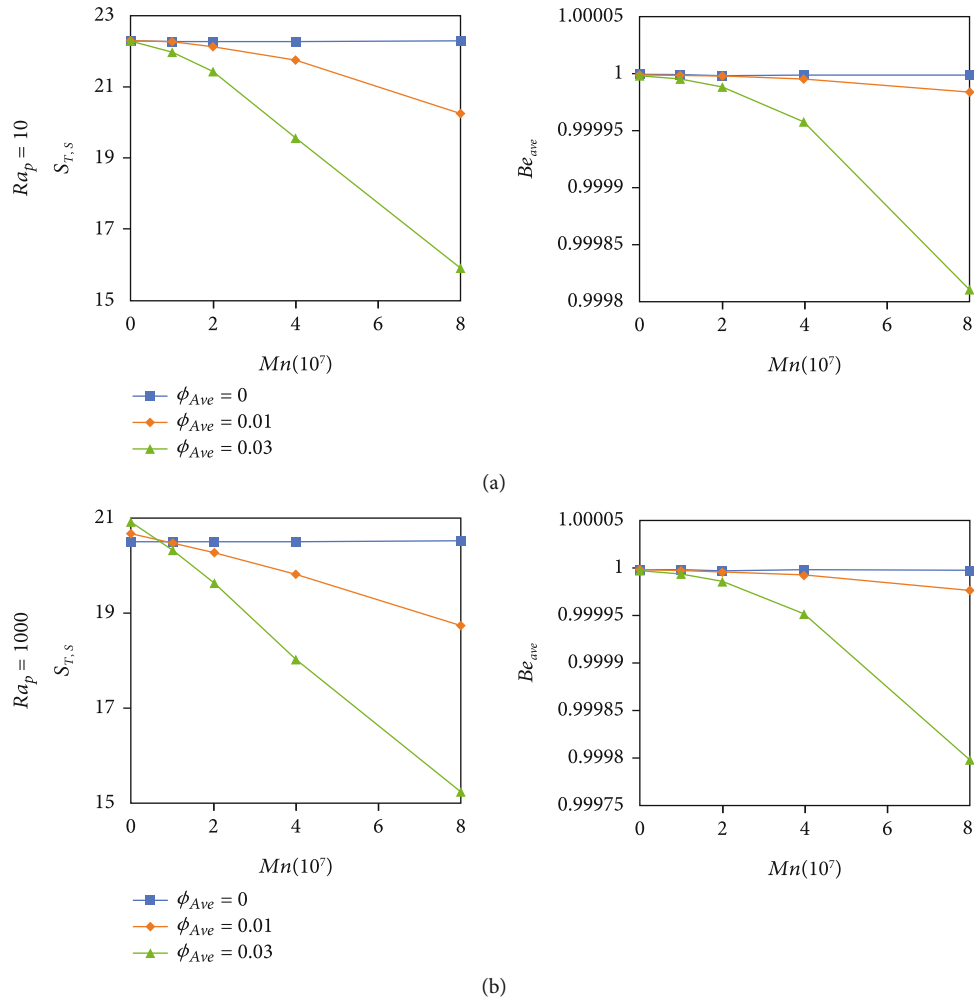


FIGURE 6: Dimensionless total entropy generation due to summation ( $S_{T,s}$ ) and Bijan number for  $\varepsilon = 0.7$  and different volume fraction of nanoparticle.

the wires due to increasing the magnetic number. Figure 3 (b) is plotted for different porosity and porous Rayleigh number in  $\phi_{Ave} = 0.03$  and  $Mn = 8 \times 10^7$ . Porosity and porous Rayleigh numbers do not affect on the dimensionless distribution of nanoparticles at the high magnetic field.

Figure 4 illustrates the dimensionless local entropy generation due to heat transfer ( $S_{L,HT}$ ) and fluid friction ( $S_{L,FF}$ ) and summation ( $S_{L,s}$ ) inside a semiannulus for  $\phi_{Ave} = 0.03$ ,  $\varepsilon = 0.7$ , and  $Mn = 0$  and  $8 \times 10^7$  for different porous Rayleigh number. In Figure 4(a) in the absence of a magnetic field and  $Ra_p = 10$ , the  $S_{L,HT}$  contours are similar to temperature contours. The highest value of  $S_{L,HT}$  is on the inner cylinder wall (hot) due to extreme temperature gradients. In Figure 4(b), as increasing porous Rayleigh number to 1000, the shape of the contours  $S_{L,HT}$  changes completely, in such a way that the densities of the contours increase near the inner cylinder wall and a core is created near the outer cylinder wall. By adding a magnetic field, the density of  $S_{L,HT}$  contours increase near the wires, and, with the rise of porous Rayleigh number, there is no change in the shape of the contours. In all cases, due to gradients of high velocity on the

walls and near the wires, the maximum value of  $S_{L,FF}$  are in these regions. By comparing the values of  $S_{L,HT}$  and  $S_{L,FF}$ , it can be seen that the effects of entropy generation due to heat transfer are much greater than the entropy generation due to fluid friction. As a result, the contours  $S_{L,s}$  are very similar to  $S_{L,HT}$  contours.

Figure 5 presents total entropy generation due to the heat transfer ( $S_{T,HT}$ ) and fluid friction ( $S_{T,FF}$ ) for the  $\varepsilon = 0.7$  and different volume fractions of nanoparticle in porous Rayleigh numbers 10 and 1000. According to Figure 5(a), by intensifying the magnetic field for both porous Rayleigh numbers,  $S_{T,HT}$  decreases linearly for the volume fraction of nanoparticles 0.01 and 0.03. In Figure 5(b), by intensifying the magnetic field at both porous Rayleigh numbers 10 and 1000,  $S_{T,FF}$  decreases linearly and nonlinearly for volume fractions 0.01 and 0.03, respectively. Also, in all cases and the absence of a magnetic field, the value of  $S_{T,FF}$  is almost zero. Figure 6(a) shows the dimensionless summation total entropy generation ( $S_{T,s}$ ) at  $\varepsilon = 0.7$  and different volume fraction of nanoparticles. According to the charts, the charts of  $S_{T,s}$  are similar to  $S_{T,HT}$  charts, because of the

values of  $S_{T,HT}$  dominates the values of  $S_{T,FF}$ . Also, according to Figure 6(b), with the increasing magnetic number for both porous Rayleigh numbers, Bejan number decreases linearly and nonlinearly for volume fractions 0.01 and 0.03, respectively.

## 6. Conclusion

In present work, effects of porous Rayleigh number, the volume fraction of nanoparticles, porosity, and magnetic number are investigated on nondimensional distribution of nanoparticles and entropy generation. The main findings can be condensed following point:

- (i) Adding a magnetic field increases the distribution of nanoparticles near the wires and causes the formation of vortices and increasing the flow velocity
- (ii) In the presence of the nonuniform magnetic field, with the increasing porosity and porous Rayleigh number, the distribution of nanoparticles becomes uniform. But, in the absence of a magnetic field, porosity and porous Rayleigh number do not affect the dimensionless distribution of nanoparticles
- (iii) By increasing magnetic number and volume fraction of nanoparticles, Bejan number, entropy generation due to heat transfer, and summation decrease but entropy generation due to fluid friction increases
- (iv) Entropy generation due to heat transfer is much greater than the entropy generation due to fluid friction
- (v) With increasing the magnetic number, entropy generation due to fluid friction increases near the wires

## Data Availability

No data were used to support this study.

## Conflicts of Interest

There is no conflict of interest regarding the publication of this article.

## Acknowledgments

The authors extend their appreciation to the Deanship of Scientific Research at King Khalid University for funding this work through research groups under grant number R.G.P.1/157/42. Also, this paper is supported by Shaanxi Key Research and Development Plan (Grant No. S2021-YF-YBGY-0708) and the authors extend their sincere appreciation to Princess Nourah bint Abdulrahman University Researchers Supporting Project number (PNURSP2022R46), Princess Nourah bint Abdulrahman University, Riyadh, Saudi Arabia.

## References

- [1] X. Zhang, Y. Tang, F. Zhang, and C. S. Lee, "A novel aluminum-graphite dual-ion battery," *Advanced Energy Materials*, vol. 6, no. 11, p. 1502588, 2016.
- [2] M. Wang, C. Jiang, S. Zhang, X. Song, Y. Tang, and H. M. Cheng, "Reversible calcium alloying enables a practical room-temperature rechargeable calcium-ion battery with a high discharge voltage," *Nature Chemistry*, vol. 10, no. 6, pp. 667–672, 2018.
- [3] S. Mu, Q. Liu, P. Kidkhunthod, X. Zhou, W. Wang, and Y. Tang, "Molecular grafting towards high-fraction active nanodots implanted in N-doped carbon for sodium dual-ion batteries," *National Science Review*, vol. 8, no. 7, p. nwa178, 2021.
- [4] X. Liu, G. Zhang, J. Li et al., "Deep learning for Feynman's path integral in strong-field time-dependent dynamics," *Physical Review Letters*, vol. 124, no. 11, article 113202, 2020.
- [5] W. Yang, Y. Lin, X. Chen et al., "Wave mixing and high-harmonic generation enhancement by a two-color field driven dielectric metasurface [invited]," *Chinese Optics Letters*, vol. 19, no. 12, article 123202, 2021.
- [6] S. Y. Motlagh, E. Golab, and A. N. Sadr, "Two-phase modeling of the free convection of nanofluid inside the inclined porous semi-annulus enclosure," *International Journal of Mechanical Sciences*, vol. 164, article 105183, 2019.
- [7] E. Golab, S. Goudarzi, H. Kazemi-Varnamkhasti et al., "Investigation of the effect of adding nano-encapsulated phase change material to water in natural convection inside a rectangular cavity," *Journal of Energy Storage*, vol. 40, article 102699, 2021.
- [8] A. N. Sadr, M. Shekaramiz, M. Zarinfar, A. Esmaily, H. Khoshtarash, and D. Toghraie, "Simulation of mixed-convection of water and nano-encapsulated phase change material inside a square cavity with a rotating hot cylinder," *Journal of Energy Storage*, vol. 47, article 103606, 2021.
- [9] B. Vahedi, E. Golab, A. N. Sadr, and K. Vafai, "Thermal, thermodynamic and exergoeconomic investigation of a parabolic trough collector utilizing nanofluids," *Applied Thermal Engineering*, vol. 206, article 118117, 2022.
- [10] Y. Cao, M. A. Abdous, S. G. Holagh, M. Shafiee, and M. Hashemian, "Entropy generation and sensitivity analysis of R134a flow condensation inside a helically coiled tube-in-tube heat exchanger," *International Journal of Refrigeration*, vol. 130, pp. 104–116, 2021.
- [11] C. Liu, M. Hashemian, A. Shawabkeh et al., "CFD-based irreversibility analysis of avant-garde semi-O/O-shape grooving fashions of solar pond heat trade-off unit," *Renewable Energy*, vol. 171, pp. 328–343, 2021.
- [12] Y. Cao, H. Ayed, S. Jafarmadar et al., "PEM fuel cell cathode-side flow field design optimization based on multi-criteria analysis of liquid-slug dynamics," *Journal of Industrial and Engineering Chemistry*, vol. 98, pp. 397–412, 2021.
- [13] M. Abbasi, A. N. Esfahani, E. Golab et al., "Effects of Brownian motions and thermophoresis diffusions on the hematocrit and LDL concentration/diameter of pulsatile non-Newtonian blood in abdominal aortic aneurysm," *Journal of Non-Newtonian Fluid Mechanics*, vol. 294, article 104576, 2021.
- [14] Y. Cao, H. Ayed, H. S. Dizaji, M. Hashemian, and M. Wae-hayee, "Entropic analysis of a double helical tube heat exchanger including circular depressions on both inner and outer tube," *Case Studies in Thermal Engineering*, vol. 26, article 101053, 2021.

- [15] S. Goudarzi, M. Shekaramiz, A. Omidvar, E. Golab, A. Karimipour, and A. Karimipour, "Nanoparticles migration due to thermophoresis and Brownian motion and its impact on Ag-MgO/water hybrid nanofluid natural convection," *Powder Technology*, vol. 375, pp. 493–503, 2020.
- [16] M. Aliakbari, "Numerical investigation of heat transfer of nanofluids in a channel under the influence of porous area," *Journal of Fundamental and Applied Sciences*, vol. 9, pp. 1175–1188, 2017.
- [17] M. Ahmadi, F. Dashti Ahangar, N. Astaraki, M. Abbasi, and B. Babaei, "FWNNNet: presentation of a new classifier of brain tumor diagnosis based on fuzzy logic and the wavelet-based neural network using machine-learning methods," *Computational Intelligence and Neuroscience*, vol. 2021, Article ID 8542637, 13 pages, 2021.
- [18] Y. Cao, H. Ayed, M. Hashemian, A. Issakhov, and M. Wae-hayee, "Thermal/frictional performance of spiral pipe with ring-shape depression used as in-pond heat exchanger," *Solar Energy*, vol. 224, pp. 742–756, 2021.
- [19] M. Siavashi, H. R. Talesh Bahrami, and H. Saffari, "Numerical investigation of flow characteristics, heat transfer and entropy generation of nanofluid flow inside an annular pipe partially or completely filled with porous media using two-phase mixture model," *Energy*, vol. 93, pp. 2451–2466, 2015.
- [20] M. V. Bozorg, M. Hossein Doranehgard, K. Hong, and Q. Xiong, "CFD study of heat transfer and fluid flow in a parabolic trough solar receiver with internal annular porous structure and synthetic oil-  $\text{Al}_2\text{O}_3$  nanofluid," *Renewable Energy*, vol. 145, pp. 2598–2614, 2020.
- [21] M. T. Jamal-Abad, S. Saedodin, and M. Aminy, "Experimental investigation on a solar parabolic trough collector for absorber tube filled with porous media," *Renewable Energy*, vol. 107, pp. 156–163, 2017.
- [22] M. Corcione, M. Cianfrini, and A. Quintino, "Two-phase mixture modeling of natural convection of nanofluids with temperature-dependent properties," *International Journal of Thermal Sciences*, vol. 71, pp. 182–195, 2013.
- [23] Y. A. Al-Turki, H. Moria, A. Shawabkeh, S. Pourhedayat, M. Hashemian, and H. S. Dizaji, "Thermal, frictional and exergetic analysis of non-parallel configurations for plate heat exchangers," *Chemical Engineering and Processing-Process Intensification*, vol. 161, article 108319, 2021.
- [24] S. Göktepe, K. Atalik, and H. Ertürk, "Comparison of single and two-phase models for nanofluid convection at the entrance of a uniformly heated tube," *International Journal of Thermal Sciences*, vol. 80, no. 1, pp. 83–92, 2014.
- [25] J. Buongiorno, "Convective transport in nanofluids," *Journal of Heat Transfer*, vol. 128, no. 3, pp. 240–250, 2006.
- [26] N. Anbuezhian, K. Srinivasan, K. Chandrasekaran, and R. Kandasamy, "Thermophoresis and Brownian motion effects on boundary layer flow of nanofluid in presence of thermal stratification due to solar energy," *Applied Mathematics and Mechanics*, vol. 33, no. 6, pp. 765–780, 2012.
- [27] E. Kaloudis, E. Papanicolaou, and V. Belessiotis, "Numerical simulations of a parabolic trough solar collector with nanofluid using a two-phase model," *Renewable Energy*, vol. 97, pp. 218–229, 2016.
- [28] S. A. Farshad and M. Sheikholeslami, "Nanofluid flow inside a solar collector utilizing twisted tape considering exergy and entropy analysis," *Renewable Energy*, vol. 141, pp. 246–258, 2019.
- [29] C. Ö. Vp-, A. Mwesigye, Z. Huan, and J. P. Meyer, "Thermal performance and entropy generation analysis of a high concentration ratio parabolic trough solar collector with Cu-Therminol®VP-1 nanofluid," *Energy Conversion and Management*, vol. 120, pp. 449–465, 2016.
- [30] S. K. Verma, A. K. Tiwari, and D. S. Chauhan, "Experimental evaluation of flat plate solar collector using nanofluids," *Energy Conversion and Management*, vol. 134, pp. 103–115, 2017.
- [31] M. Sheikholeslami, A. Arabkoohsar, I. Khan, A. Shafee, and Z. Li, "Impact of Lorentz forces on  $\text{Fe}_3\text{O}_4$ -water ferrofluid entropy and exergy treatment within a permeable semi annulus," *Journal of Cleaner Production*, vol. 221, pp. 885–898, 2019.
- [32] M. Afrand, A. Hajatzadeh, S. Aghakhani, and H. F. Oztop, "Free convection and entropy generation of a nanofluid in a tilted triangular cavity exposed to a magnetic field with sinusoidal wall temperature distribution considering radiation effects," *International Communications in Heat and Mass Transfer*, vol. 112, article 104507, 2020.
- [33] S. M. Shavik, M. N. Hassan, A. M. Morshed, and M. Q. Islam, "Natural convection and entropy generation in a square inclined cavity with differentially heated vertical walls," *Procedia Engineering*, vol. 90, pp. 557–562, 2014.

## Research Article

# Heat Transfer Analysis of the MHD Stagnation Point Flow of a Non-Newtonian Tangent Hyperbolic Hybrid Nanofluid past a Non-Isothermal Flat Plate with Thermal Radiation Effect

Abdullah Dawar <sup>1</sup>, Saeed Islam <sup>1</sup>, Ahmed Alshehri,<sup>2</sup> Ebenezer Bonyah <sup>3</sup>  
and Zahir Shah<sup>4</sup>

<sup>1</sup>Department of Mathematics, Abdul Wali Khan University, Mardan, 23200 Khyber Pakhtunkhwa, Pakistan

<sup>2</sup>Department of Mathematics, Faculty of Sciences, King Abdulaziz University, Jeddah 21589, Saudi Arabia

<sup>3</sup>Department of Mathematics Education, University of Education Winnebakumasi-(Kumasicampus), Kumasi 00233, Ghana

<sup>4</sup>Department of Mathematical Sciences, University of Lakki Marwat, Lakki Marwat, 28420 Khyber Pakhtunkhwa, Pakistan

Correspondence should be addressed to Ebenezer Bonyah; ebbonya@gmail.com

Received 21 December 2021; Accepted 9 May 2022; Published 25 May 2022

Academic Editor: Domenico Acierno

Copyright © 2022 Abdullah Dawar et al. This is an open access article distributed under the Creative Commons Attribution License, which permits unrestricted use, distribution, and reproduction in any medium, provided the original work is properly cited.

Heat transfer phenomena are used in a variety of industries, including chemical devices, shipbuilding, power plants, electronic devices, and medicinal plants. Propylene glycol, engine oil, water, and ethylene glycol are common single-phase heat transfer liquids used in a variety of industries, including chemical process industries and thermal power plants. Therefore, the authors are interested in investigating the magnetohydrodynamic flow of a water-based hybrid nanofluid containing ferrous and graphene oxide nanoparticles past a flat plate. The stagnation points, as well as the effects of magnetic field and thermal radiation are taken into account in this analysis. The non-Newtonian tangent hyperbolic flow, which is laminar and incompressible, is also considered to investigate the non-Newtonian behavior of the hybrid nanofluid flow. The proposed model has been solved analytically with the help of HAM. The convergence of HAM is shown with the help of figure. The hydrothermal characteristics of hybrid nanofluid flow past a nonisothermal flat plate at a stagnation point are affected by the necessary parameters. The results show that the boosting volume fractions of the ferrous and graphene oxide nanoparticles have significantly reduced the velocity field, while the thermal field has increased with the augmenting volume fractions of the ferrous and graphene oxide nanoparticles. The increasing power-law index has augmented the viscosity of the non-Newtonian hybrid nanofluid flow due to which the velocity field escalated. However, this impact is opposite for the thermal field. Due to the direct relation between the Weissenberg number and relaxation time, the greater Weissenberg number has reduced the velocity profile, while increased the thermal field.

## 1. Introduction

Because of various applications in healthcare and engineering, such as microelectronics, solar collectors, process industries, cancer therapy, heat exchangers, and power production, the mechanisms of heat exchange incorporating nanomaterials have piqued the interest of researchers. Regular liquids such as glycol mixtures, engine oil, and water had moderately poor thermal properties and inadequate capacity

to attain higher thermal efficiency. The use of nanoparticles to develop the thermal conductivity of various cooling fluids is a contemporary method. Nowadays, temperature distribution plays an essential function in a variety of scientific and technical disciplines. Heat transfer phenomena have a wide range of applications in sectors, shipbuilding, electronic devices, power plants, medicinal, and chemical devices. To design heat exchangers and discover the optimal geometry, radiators, condensers, evaporators, and boilers, heat transfer



analysis and the related cooling process become invaluable. Propylene glycol, engine oil, water, and ethylene glycol are common single-phase heat transfer liquids used in a variety of chemical process industries and thermal power plants. Due to its low thermal conductivity, the single-phase traditional liquids are acknowledged to have poor heat transmission ability. This improvement in working fluid heat transport is critical for achieving energy and cost reductions. In order to boost-up the thermal conductivity of the base fluids, many researchers have worked to resolve these issues and improve the thermal conductivity of the base fluids. Solid materials have higher thermal conductivity than those of liquids. As a result, dispersing microscopic solid particles into a base liquid is a novel technique to increase the thermal conductivity of the base fluids. Khan et al. [1] investigated the Casson nanofluid flow past a rotating disk. Shah et al. [2] addressed the applications of radius, heat flux, and mass flux of the water-based copper nanoparticles. Gul T et al. [3] investigated the flow of carbon nanotube nanofluid past a rotating cone and disk. Sowmya et al. [4] addressed the effects of convective condition and internal heat generation in a nanofluid flow past a porous fin. Ashraf et al. [5] analyzed the magnetohydrodynamic peristaltic flow of the blood-based magnetite nanoparticles. Dawar et al. [6] studied the unsteady flow of carbon nanotube nanofluid with the magnetic field impact. Rasool and Wakif [7] examined the electromagnetohydrodynamic second-grade nanofluid flow over a Riga plate. Alghamdi et al. [8] presented the magnetohydrodynamic flow of sodium alginate-based nanofluid bounded by slender surface with heat source impact. Rout et al. [9] analyzed the water- and kerosene-based nanofluid flow with viscous dissipation. Alshomrani and Gul [10] investigated the dissipative flow of water-based  $\text{Al}_2\text{O}_3$  and Cu nanoparticles past a stretching cylinder with convective condition. Further related analyses can be studied in [11–14].

Hybrid nanofluid is a class of nanofluids, developed by integrating a certain class of nanoparticles inside a functional fluid which has recently been used. Two different nanomaterials are suspended in a conventional fluid to create hybrid nanofluids. Hybrid nanofluids are widely used in a diversity of disciplines of engineering as well as refrigeration, space planes, biomedical, machining coolant, motor cooling, heat pipe reduction in medicine, and high-performance boats. Jana et al. [15] investigated the conductive nanomaterials like copper and gold nanoparticles and their hybrids. Khashi'ie et al. [16] analyzed heat transfer of a magnetohydrodynamic flow of a water-based hybrid nanofluid comprehending Cu and  $\text{Al}_2\text{O}_3$  nanoparticles. Their results show that the suction factor has a significant impact of heat transfer analysis. Additionally, they have computed the stability analysis as well. Nawaz and Nazir [17] studied the magnetohydrodynamic flow of an ethylene-based hybrid nanofluid flow containing  $\text{MoS}_2$  and  $\text{SiO}_2$  nanoparticles. They compared  $\text{MoS}_2$ /ethylene-based and  $\text{MoS}_2$ - $\text{SiO}_2$ /ethylene-based hybrid nanofluids. Their results showed that the thermal performance is greater for the  $\text{MoS}_2$ - $\text{SiO}_2$ /ethylene-based as compared to  $\text{MoS}_2$ /ethylene-based. Manjunatha et al. [18] presented the comparative analysis of the magnetohydrodynamic flows of Cu- $\text{H}_2\text{O}$  nanofluid and

Cu- $\text{Al}_2\text{O}_3$ / $\text{H}_2\text{O}$  hybrid nanofluid. They found that the nanoparticle volume fraction of the nanofluid and hybrid nanofluid has enhanced the velocity and thermal fields. Usman et al. [19] proposed the comparative analysis of the magnetohydrodynamic flow of a Cu/ $\text{H}_2\text{O}$  nanofluid,  $\text{Al}_2\text{O}_3$ / $\text{H}_2\text{O}$  nanofluid, and Cu- $\text{Al}_2\text{O}_3$ / $\text{H}_2\text{O}$  hybrid nanofluid. They claimed that the velocity fields of Cu- $\text{Al}_2\text{O}_3$ / $\text{H}_2\text{O}$  have dominant role on other nanofluids; however, this impact is reverse for thermal profile. Iqbal et al. [20] offered the comparative analysis of magnetohydrodynamic flows of  $\text{SiO}_2$ / $\text{H}_2\text{O}$  nanofluid and  $\text{MoS}_2$ - $\text{SiO}_2$ / $\text{H}_2\text{O}$  hybrid nanofluid considering different shapes of the nanoparticles. Their results showed that the nanofluid has slower flow as compared to hybrid nanofluid. Additionally, the lower temperature is observed for brick-shaped nanoparticles of the nanofluid, while the blade-shaped nanoparticle of the hybrid nanofluid has extreme temperature. Ghadikolaei et al. [21] offered the comparative investigation of magnetohydrodynamic flow of Cu/ $\text{H}_2\text{O}$  and hybrid nanofluid containing  $\text{TiO}_2$ -Cu/ $\text{H}_2\text{O}$  at a stagnation point. They also considered three different shapes of the nanoparticles named as platelets, bricks, and cylinders. It is clear from this research that using platelet-shaped nanoparticles is more effective. Gul et al. [22] addressed the magnetohydrodynamic flow of hybrid nanofluid containing Cu and  $\text{Fe}_3\text{O}_4$ . Their results showed that the nanoparticle volume fractions of Cu and  $\text{Fe}_3\text{O}_4$  have significantly improved the thermal transmission and velocity field. Alghamdi et al. [23] addressed the comparative analysis of the magnetohydrodynamic flows of blood-based Cu nanofluid and blood-based Cu-CuO hybrid nanofluid. It has been introduced that the hybrid nanofluid flow has more effective thermal conductivity in a contracting channels. Acharya [24] probed the application of solar energy toward a hybrid nanofluid flow containing alumina and copper nanoparticles. In another article, Acharya and Mabood [25] addressed the water-based hybrid nanofluid flow containing ferrous and graphene oxide nanoparticles. Thumma et al. [26] investigated the Cu-CuO nanoparticles past a porous extending surface. Acharya et al. [27, 28] analyzed the nanofluid and hybrid nanofluid flows under the impact of magnetic field.

According to the authors' knowledge, there is no study based on magnetohydrodynamic flow of water-based hybrid nanofluid containing ferrous and graphene oxide nanoparticles past a flat plate. The stagnation point along with the impacts of magnetic field and thermal radiation is taken in this consideration. The non-Newtonian tangent hyperbolic flow which is laminar and incompressible is also considered to investigate the non-Newtonian behavior of the hybrid nanofluid flow. The present analysis is composed of mathematical modeling which is shown in Section 2. HAM solution and convergence of HAM are presented in Sections 3 and 4, respectively. Section 5 is composed of results and discussion. In the last, the concluding remarks are shown in Section 6.

## 2. Model Formulation

Consider the stagnation point flow of a water-based hybrid nanofluid containing graphene oxide (GO) and ferrous

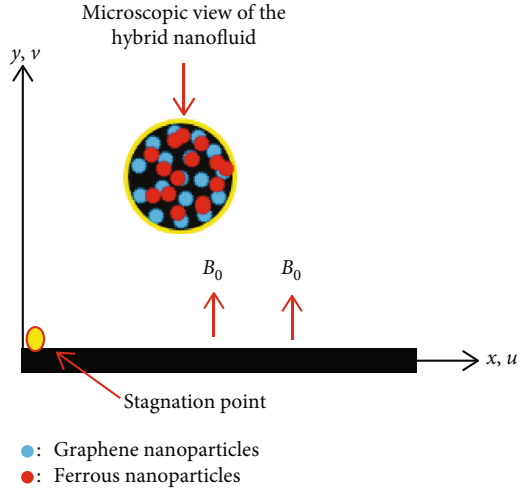


FIGURE 1: Geometry of the hybrid nanofluid flow.

( $\text{Fe}_3\text{O}_4$ ) nanoparticles past a flat plate. The flat plate is chosen to be a nonisothermal. The non-Newtonian tangent hyperbolic model is taken to be laminar and incompressible.  $u$  and  $v$  are the velocity components which are considered along  $x$ - and  $y$ -directions, respectively. A magnetic field  $B = (0, B_0, 0)$  is considered normal to the flow direction. The ambient velocity of the fluid flow along  $x$ -direction is  $u_e(x) = cx$ , where  $c$  is the positive constant. The wall temperature  $T_w(x) = T_\infty + bx$  varies linearly along  $x$ -direction in which  $b$  is the positive constant and  $T_\infty$  is the ambient temperature. Furthermore, the Hall current and thermal radiation effects are also considered. Following the above assumption, the leading equations are stated. Figure 1 shows the geometry of the hybrid nanofluid flow.

$$\frac{\partial u}{\partial x} + \frac{\partial v}{\partial y} = 0,$$

$$u \frac{\partial u}{\partial x} + v \frac{\partial u}{\partial y} = u_e \frac{du_e}{dx} + \frac{\mu_{hnf}}{\rho_{hnf}} \left[ (1-n) \frac{\partial^2 u}{\partial y^2} + \sqrt{2n}\Gamma \frac{\partial u}{\partial y} \frac{\partial^2 u}{\partial y^2} \right] - \frac{\sigma_{hnf} B_0^2}{\rho_{hnf}} (u - u_e),$$

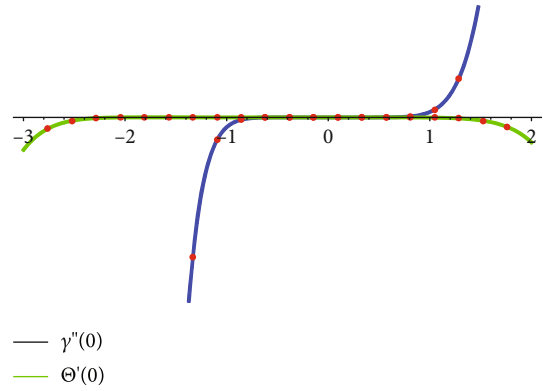
$$u \frac{\partial T}{\partial x} + v \frac{\partial T}{\partial y} = \alpha_{nf} \frac{\partial^2 T}{\partial y^2} - \frac{1}{(\rho C_p)_{hnf}} \frac{\partial q_r}{\partial y} + \frac{\sigma_{hnf} B_0^2}{(\rho C_p)_{hnf}} u^2 + \frac{\mu_{hnf}}{(\rho C_p)_{hnf}} \left[ (1-n) \left( \frac{\partial u}{\partial y} \right)^2 + \frac{n\Gamma}{\sqrt{2}} \left( \frac{\partial u}{\partial y} \right)^3 \right]. \quad (1)$$

The relevance boundary conditions are defined as

$$\left\{ \begin{array}{l} u = 0, v = 0, T = T_w \text{ at } y = 0, \\ u \rightarrow u_e, T \rightarrow T_\infty \text{ as } y \rightarrow \infty. \end{array} \right\} \quad (2)$$

TABLE 1: The numerical values of the thermophysical properties of base fluids and nanoparticles [29].

Base fluids/ nanoparticles	$\rho$ ( $\text{kg.m}^{-3}$ )	$C_p$ ( $\text{J.kg}^{-1}.\text{K}^{-1}$ )	$k$ [ $\text{W.m}^{-1}.\text{K}^{-1}$ ]	$\sigma$ (( $\Omega\text{m}$ ) $^{-1}$ )
$\text{H}_2\text{O}$	997	4180	0.6071	0.005
$\text{Fe}_3\text{O}_4$	5180	670	9.7	25000
GO	2250	2100	2500	$1 \times 10^7$

FIGURE 2:  $h$  - curves for velocity and temperature profiles.

The radiative heat flux  $q_r$  is defined as

$$q_r = -\frac{4\sigma^*}{3k^*} \frac{\partial T^4}{\partial y}. \quad (3)$$

By using the Taylor series expansion,  $T^4$  can be written as

$$T^4 \approx 4T_\infty^3 T - 3T_\infty^4. \quad (4)$$

For the simulation of hybrid nanofluid flow, the thermophysical properties are defined as

$$\left\{ \begin{array}{l} \frac{\mu_{hnf}}{\mu_f} = \frac{1}{(1-\phi_1-\phi_2)^{2.5}}, \quad \frac{\rho_{hnf}}{\rho_f} = (1-\phi_1-\phi_2) + \frac{\rho_{p1}\phi_1 + \rho_{p2}\phi_2}{\rho_f}, \\ \frac{(\rho C_p)_{hnf}}{(\rho C_p)_f} = (1-\phi_1-\phi_2) + \frac{(\rho C_p)_{p1}\phi_1 + (\rho C_p)_{p2}\phi_2}{(\rho C_p)_f}, \\ \frac{k_{hnf}}{k_f} = \frac{(k_{p1}\phi_1 + k_{p2}\phi_2/\phi_1 + \phi_2) + 2k_f + 2(k_{p1}\phi_1 + k_{p2}\phi_2) - 2(\phi_1 + \phi_2)k_f}{(k_{p1}\phi_1 + k_{p2}\phi_2/\phi_1 + \phi_2) + 2k_f - (k_{p1}\phi_1 + k_{p2}\phi_2) + (\phi_1 + \phi_2)k_f}, \\ \frac{\sigma_{hnf}}{\sigma_f} = 1 + \frac{3((\sigma_{p1}\phi_1 + \sigma_{p2}\phi_2/\sigma_f) - (\phi_1 + \phi_2))}{2 + (\sigma_{p1}\phi_1 + \sigma_{p2}\phi_2/(\phi_1 + \phi_2)\sigma_f) - (\sigma_{p1}\phi_1 + \sigma_{p2}\phi_2/\sigma_f) + (\phi_1 + \phi_2)}. \end{array} \right. \quad (5)$$

where  $p1$  and  $p2$  represent  $\text{Fe}_3\text{O}_4$  and GO nanoparticles, respectively, and  $\phi_1$  and  $\phi_2$  are the nanoparticle volume fractions of  $\text{Fe}_3\text{O}_4$  and GO, respectively. The numerical values of the thermophysical properties are defined in Table 1.

TABLE 2: Impacts of  $\phi_1, \phi_2, We, n,$  and  $M$  on  $\sqrt{Re_x}C_{fx}$ .

$\phi_1$	$\phi_2$	$We$	$n$	$M$	$\sqrt{Re_x}C_{fx}$
0.01					1.10639
0.02					1.10443
0.03					1.10381
	0.01				1.05003
	0.02				1.06374
	0.03				1.07768
		0.2			0.92856
		0.3			0.95661
		0.4			0.98308
			0.2		1.09048
			0.3		0.99856
			0.4		0.89890
				0.2	1.11986
				0.3	1.14266
				0.4	1.17459

The similarity transformations are defined as

$$\begin{aligned}
 u &= cxY'(\zeta), \\
 u &= -\sqrt{cv_f}Y(\zeta), \\
 \Theta(\zeta) &= \frac{T - T_\infty}{T_w - T_\infty}, \\
 \zeta &= y\sqrt{\frac{c}{v_f}}.
 \end{aligned}
 \tag{6}$$

Using the above similarity transformations, the leading equations are transformed as

$$\begin{aligned}
 &\frac{1}{(1 - \phi_1 - \phi_2)^{2.5}} \left[ (1 - n) + nWeY'' \right] Y''' \\
 &+ \left[ (1 - \phi_1 - \phi_2) + \frac{\rho_{p1}\phi_1 + \rho_{p2}\phi_2}{\rho_f} \right] \left( Y'Y'' + 1 - Y'^2 \right) - M^2 \\
 &\cdot \left[ 1 + \frac{3((\sigma_{p1}\phi_1 + \sigma_{p2}\phi_2/\sigma_f) - (\phi_1 + \phi_2))}{2 + (\sigma_{p1}\phi_1 + \sigma_{p2}\phi_2/(\phi_1 + \phi_2)\sigma_f) - (\sigma_{p1}\phi_1 + \sigma_{p2}\phi_2/\sigma_f) + (\phi_1 + \phi_2)} \right] \\
 &\cdot (Y' - 1) = 0, \\
 &\left[ \frac{(k_{p1}\phi_1 + k_{p2}\phi_2/\phi_1 + \phi_2) + 2k_f + 2(k_{p1}\phi_1 + k_{p2}\phi_2) - 2(\phi_1 + \phi_2)k_f}{(k_{p1}\phi_1 + k_{p2}\phi_2/\phi_1 + \phi_2) + 2k_f - (k_{p1}\phi_1 + k_{p2}\phi_2) + (\phi_1 + \phi_2)k_f} + \frac{4}{3}Rd \right] \Theta'' \\
 &+ Pr \left[ (1 - \phi_1 - \phi_2) + \frac{(\rho C_p)_{p1}\phi_1 + (\rho C_p)_{p2}\phi_2}{(\rho C_p)_f} \right] (Y'\Theta' - Y'\Theta) \\
 &+ \frac{EcPr}{(1 - \phi_1 - \phi_2)^{2.5}} \left( \frac{(1 - n)Y''^2}{2} + WeY''^3 \right) + PrM^2Ec \\
 &\cdot \left[ 1 + \frac{3((\sigma_{p1}\phi_1 + \sigma_{p2}\phi_2/\sigma_f) - (\phi_1 + \phi_2))}{2 + (\sigma_{p1}\phi_1 + \sigma_{p2}\phi_2/(\phi_1 + \phi_2)\sigma_f) - (\sigma_{p1}\phi_1 + \sigma_{p2}\phi_2/\sigma_f) + (\phi_1 + \phi_2)} \right] Y'^2 \\
 &= 0,
 \end{aligned}
 \tag{7}$$

TABLE 3: Impacts of  $\phi_1, \phi_2, We, n, Ec, Rd,$  and  $M$  on  $(1/\sqrt{Re_x})Nu_x$ .

$\phi_1$	$\phi_2$	$We$	$n$	$M$	$Ec$	$Rd$	$(1/\sqrt{Re_x})Nu_x$
0.01							0.42728
0.02							0.40796
0.03							0.38505
	0.01						0.42748
	0.02						0.40809
	0.03						0.38515
		0.2					0.60811
		0.3					0.60089
		0.4					0.59368
			0.2				0.32874
			0.3				0.37203
			0.4				0.41532
				0.2			0.32291
				0.3			0.31672
				0.4			0.30806
					0.2		-0.34687
					0.3		-0.77920
					0.4		-1.21753
						0.2	0.24689
						0.3	0.17259
						0.4	0.08544

with boundary conditions

$$\left\{ \begin{aligned}
 Y(0) &= 0, Y'(0) = 0, Y'(\infty) = 1, \\
 \Theta(0) &= 1, \Theta(\infty) = 0.
 \end{aligned} \right\}
 \tag{8}$$

The dimensionless parameters are defined as

$$\begin{aligned}
 Rd &= \frac{4\sigma^* T_\infty^3}{k^* k_f}, \\
 Pr &= \frac{\nu_f}{\alpha_f}, \\
 M &= \sqrt{\frac{\sigma_f B_0^2}{\rho_f c}}, \\
 We &= \sqrt{2c}\Gamma Re_x^{1/2}, \\
 Re_x &= \frac{xu_e(x)}{\nu_f}, \\
 Ec &= \frac{u_e^2}{(C_p)_f(T_w - T_\infty)}.
 \end{aligned}
 \tag{9}$$

Physical quantities of importance like skin friction  $C_{fx}$  and Nusselt number  $Nu_x$  are defined as

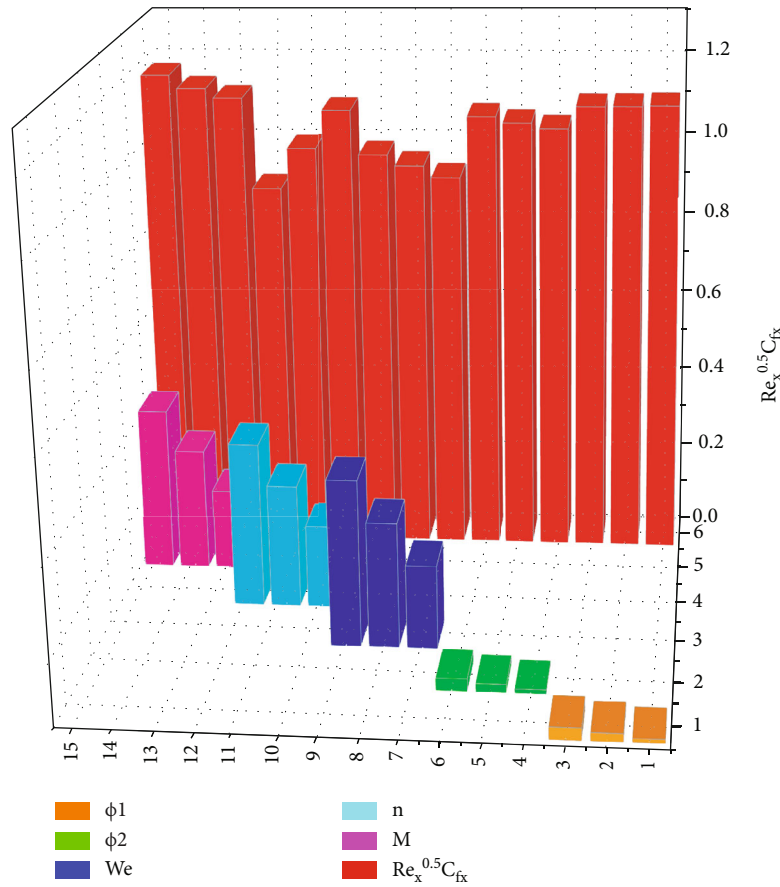


FIGURE 3: Impacts of  $\phi_1$ ,  $\phi_2$ ,  $We$ ,  $n$ , and  $M$  on  $\sqrt{Re_x}C_{fx}$ .

$$C_{fx} = \frac{\mu_{hnf}}{\rho_{hnf} u_e^2} \left[ (1-n) \frac{\partial u}{\partial y} + \frac{n\Gamma}{\sqrt{2}} \left( \frac{\partial u}{\partial y} \right)^2 \right] \Bigg|_{y=0},$$

$$Nu_x = -\frac{x}{(T_w - T_\infty)} \left[ \frac{k_{hnf}}{k_f} \frac{\partial T}{\partial y} + \frac{4\sigma^*}{3k^* k_f} \frac{\partial T^4}{\partial y} \right] \Bigg|_{y=0}. \tag{10}$$

Using the similarity transformations defined in equation (6), the above quantities are reduced to

$$Re_x^{1/2} C_{fx} = \frac{1}{(1 - \phi_1 - \phi_2)^{2.5} \left( (1 - \phi_1 - \phi_2) + (\rho_{p1}\phi_1 + \rho_{p2}\phi_2/\rho_f) \right)} \cdot \left[ (1-n) \Upsilon''(0) + \frac{nWe}{2} \Upsilon'''(0) \right],$$

$$Re_x^{-1/2} Nu_x = - \left[ \frac{(k_{p1}\phi_1 + k_{p2}\phi_2/\phi_1 + \phi_2) + 2k_f + 2(k_{p1}\phi_1 + k_{p2}\phi_2) - 2(\phi_1 + \phi_2)k_f}{(k_{p1}\phi_1 + k_{p2}\phi_2/\phi_1 + \phi_2) + 2k_f - 2(k_{p1}\phi_1 + k_{p2}\phi_2) + (\phi_1 + \phi_2)k_f} + \frac{4}{3} Rd \right] \Theta'(0). \tag{11}$$

### 3. HAM Solution

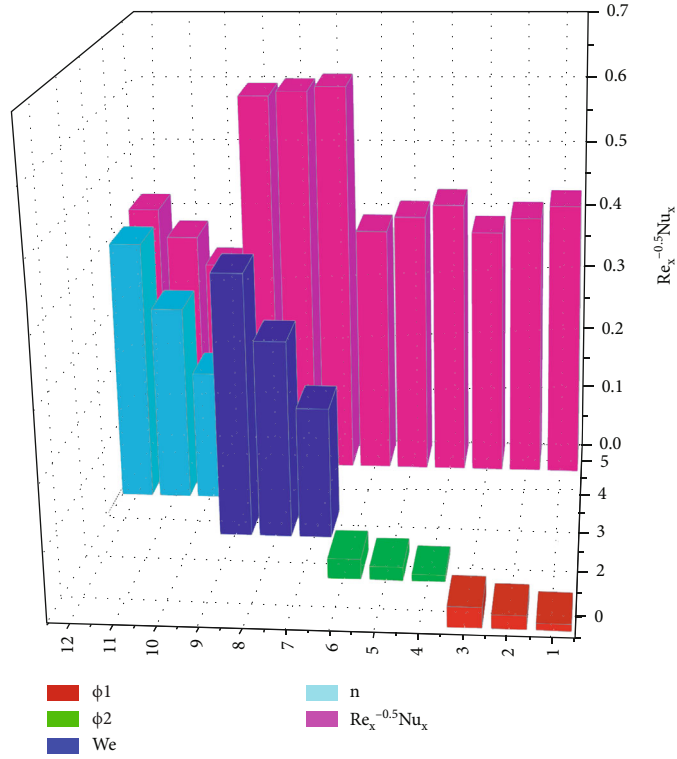
To attain the analytical solution of the proposed model along with the relevant boundary conditions, HAM method which was introduced by Liao [30] is applied. The initial guesses and linear operators are defined as

$$\begin{aligned} \Upsilon_0(\zeta) &= -1 + \zeta + e^{-\zeta}, \\ \Theta_0(\zeta) &= e^{-\zeta}, \\ L_\Upsilon &= \Upsilon''' - \Upsilon', \\ L_\Theta &= \Theta'' - \Theta, \end{aligned} \tag{12}$$

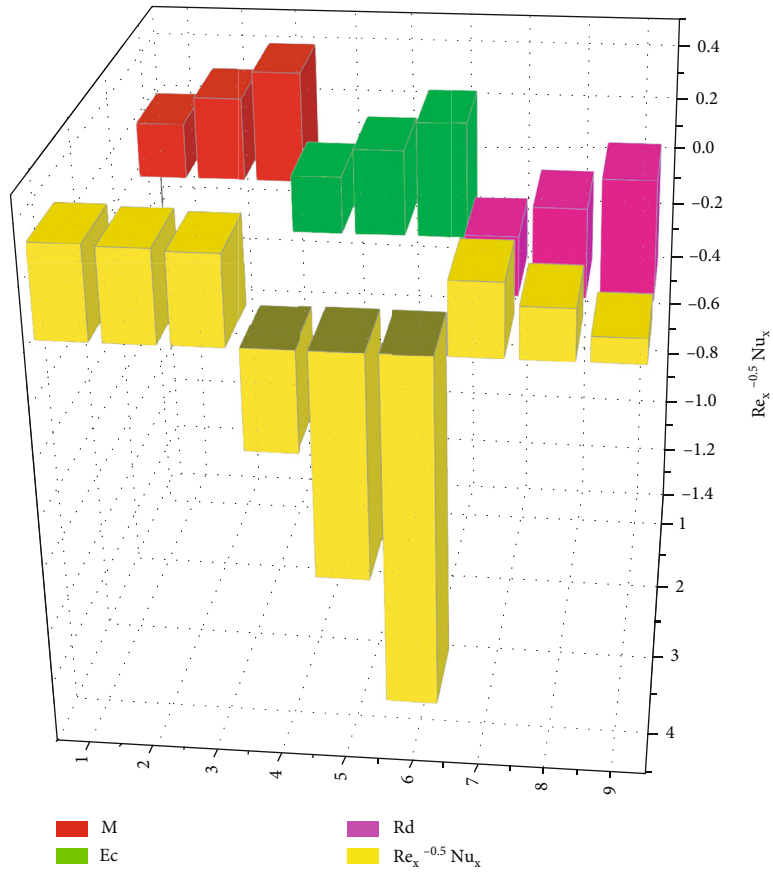
satisfying

$$\begin{aligned} L_\Upsilon \left[ \mathfrak{R}_1 + \mathfrak{R}_2 e^{-\zeta} + \mathfrak{R}_3 e^\zeta \right] &= 0, \\ L_\Theta \left[ \mathfrak{R}_4 e^{-\zeta} + \mathfrak{R}_5 e^\zeta \right] &= 0, \end{aligned} \tag{13}$$

where  $\mathfrak{R}_1 - \mathfrak{R}_5$  are constants.



(a)



(b)

FIGURE 4: (a) Impacts of  $\phi_1$ ,  $\phi_2$ ,  $We$ , and  $n$  on  $(1/\sqrt{Re_x})Nu_x$ . (b) Impacts of  $Ec$ ,  $Rd$ , and  $M$  on  $(1/\sqrt{Re_x})Nu_x$ .

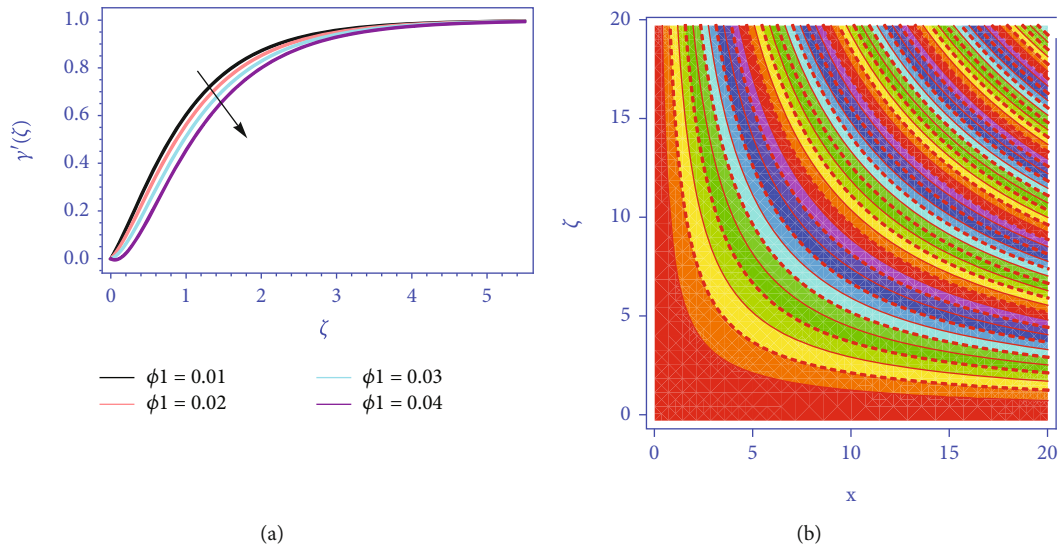


FIGURE 5: (a) Effect of  $\phi_1$  on  $\gamma'(\zeta)$ . (b) Streamline patterns for  $\phi_1$ .

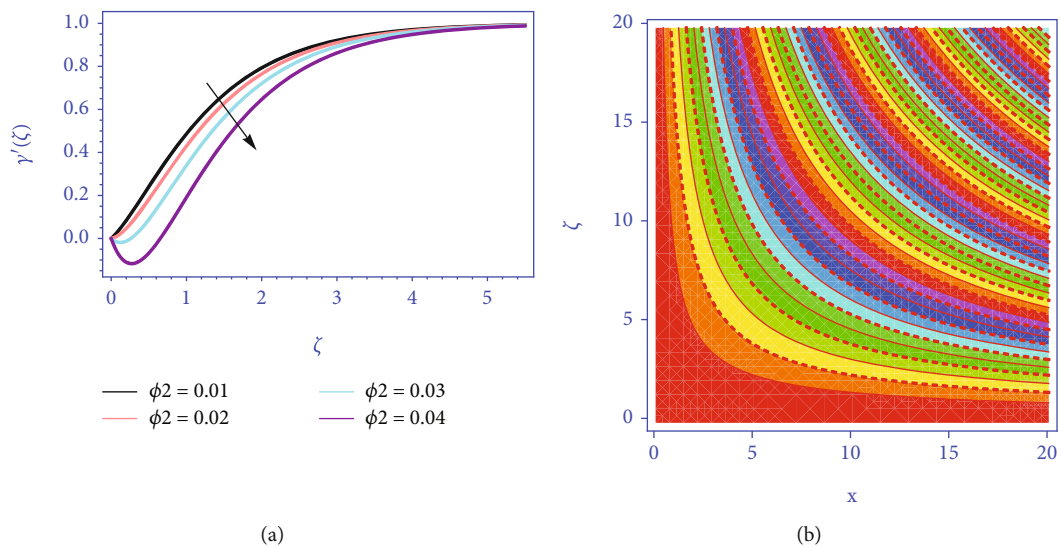


FIGURE 6: (a) Effect of  $\phi_2$  on  $\gamma'(\zeta)$ . (b) Streamline patterns for  $\phi_2$ .

#### 4. HAM Convergence

Homotopy analysis method guarantees the convergence analysis of the highly linear and nonlinear differential equations. The auxiliary parameter  $h$  insures the convergence area of the modeled problem. The convergence areas for velocity and temperature profiles are  $-1.0 \leq h_\gamma \leq 1.0$  and  $-2.5 \leq h_\theta \leq 1.5$ , respectively, as shown in Figure 2.

#### 5. Results and Discussion

This part explains how the hydrothermal characteristics of hybrid nanofluid flow past a nonisothermal flat plate at a stagnation point are affected by the necessary parameters. To demonstrate physically accurate effects, thermal radiation and magnetic field are added. The hybrid nanofluid

flow contains ferrous ( $\text{Fe}_3\text{O}_4$ ) and graphene oxide (GO) nanoparticles and water ( $\text{H}_2\text{O}$ ) is used as base fluid. In the present analysis, the default values are considered as  $M = 1.0$ ,  $n = 0.5$ ,  $We = 0.6$ ,  $Pr = 6.2$ ,  $\phi_1 = \phi_2 = 0.05$ ,  $Ec = 0.3$ , and  $Rd = 0.7$ .

The effects of the significant parameters on  $\sqrt{\text{Re}_x} C_{fx}$  and  $Nu_x/\sqrt{\text{Re}_x}$  are shown in Tables 2 and 3. The augmenting volume fraction of the  $\text{Fe}_3\text{O}_4$  nanoparticles declines the surface drag force, while the augmenting volume fraction of the GO nanoparticles boosts up the skin friction coefficient. The augmenting impacts of  $\text{Fe}_3\text{O}_4$  and GO nanoparticle volume fractions are found against heat transfer rate. The greater Weissenberg number  $We$  augments  $\sqrt{\text{Re}_x} C_{fx}$ ; however,  $Nu_x/\sqrt{\text{Re}_x}$  reduces with the higher  $We$ . A similar impact of  $n$  is found for  $\sqrt{\text{Re}_x} C_{fx}$  and  $Nu_x/\sqrt{\text{Re}_x}$ . The greater

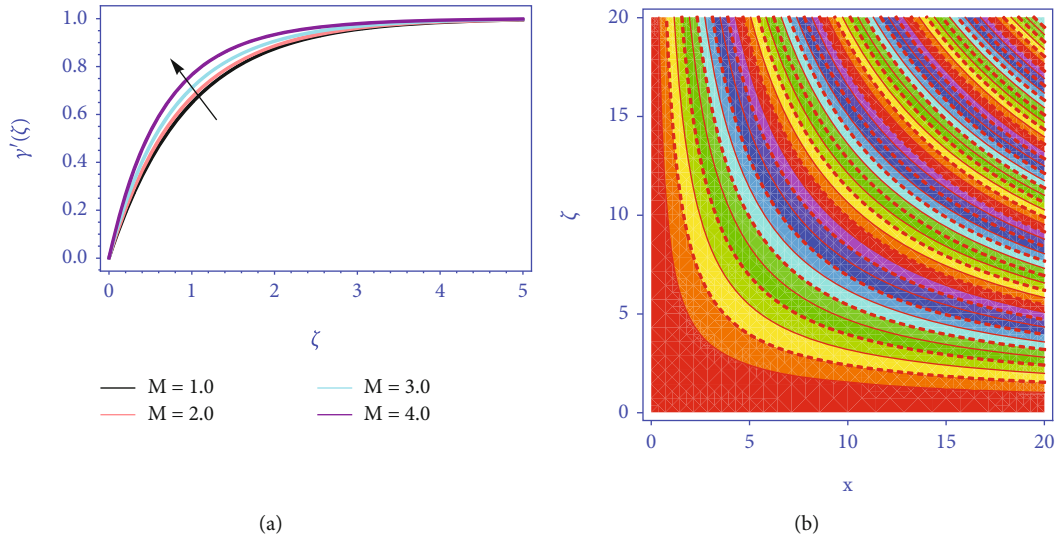


FIGURE 7: (a) Effect of  $M$  on  $Y'(\zeta)$ . (b) Streamline patterns for  $M$ .

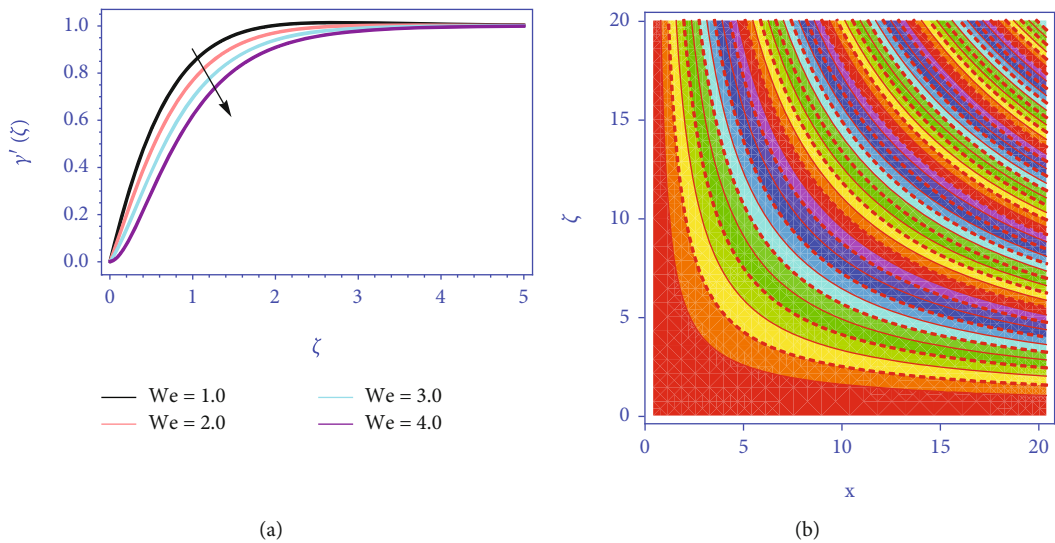


FIGURE 8: (a) Effect of  $We$  on  $Y'(\zeta)$ . (b) Streamline patterns for  $We$ .

magnetic parameter  $M$  augments  $\sqrt{Re_x}C_{fx}$ , while an opposite trend is observed for  $Nu_x/\sqrt{Re_x}$ . Also, the greater Eckert number  $Ec$  and thermal radiation parameter  $Rd$  have declining impacts on  $Nu_x/\sqrt{Re_x}$ . Figures 3 and 4 are displayed in order to clarify the variation in  $\sqrt{Re_x}C_{fx}$  and  $Nu_x/\sqrt{Re_x}$  via different embedded parameters. Figure 5(a) shows the impact of  $\phi_1$  on  $Y'(\zeta)$  when  $\phi_2 = 0.05$ . The augmenting  $\phi_1$  declines  $Y'(\zeta)$ . The increasing  $\phi_1$  declines the boundary layer thickness, which consequently reduces  $Y'(\zeta)$ . Figure 5(b) shows the streamline patterns for  $\phi_1$  when  $\phi_2 = 0.05$ . Figure 6(a) shows the impact of  $\phi_2$  on  $Y'(\zeta)$  when  $\phi_1 = 0.05$ . A similar impact as of  $Fe_3O_4$  nanoparticle is found here. Figure 6(b) shows the streamline patterns for  $\phi_2$  when  $\phi_1 = 0.05$ . Figure 7(a) signifies the consequence of  $M$  on  $Y'(\zeta)$ . The escalating magnetic parameter boosts up the veloc-

ity field. As the dynamic growth upsurges, the boundary layer of the velocity profile gets thinner, showing that the magnetic parameter augments the flow mobility near the heated plate. The present model is computed along with stagnation point flow, thus the augmenting impact of the magnetic parameter has been reported here. Figure 7(b) shows the streamline patterns for  $M$  when  $\phi_1 = \phi_2 = 0.05$ . Figure 8(a) signposts the effect of  $We$  on  $Y'(\zeta)$ . The augmenting  $We$  reduces  $Y'(\zeta)$ . The maximum value of the parameter  $We$  increases  $Y'(\zeta)$ , because  $We$  is directly related to the relaxation time  $\Gamma$ . The relaxation time of the examined non-Newtonian hybrid nanofluid has increased. As a result of this physical property, the water-based flow encounters extra barrier in developing easily across the flow boundary, lowering the hybrid nanofluid velocity. Figure 8(b) shows the streamline patterns for  $We$  when

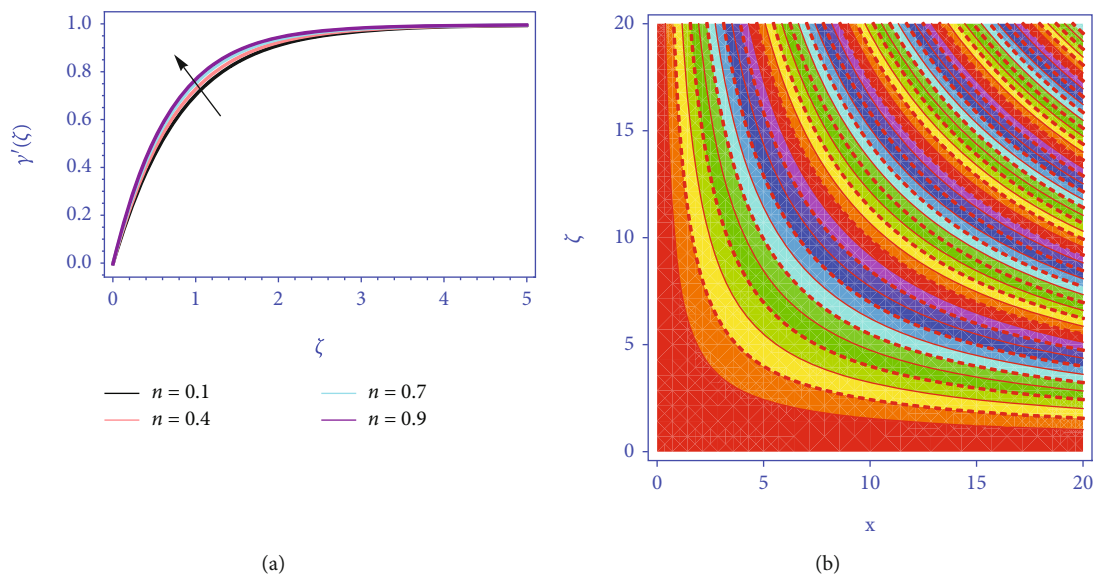


FIGURE 9: (a) Effect of  $n$  on  $\Upsilon'(\zeta)$ . (b) Streamline patterns for  $n$ .

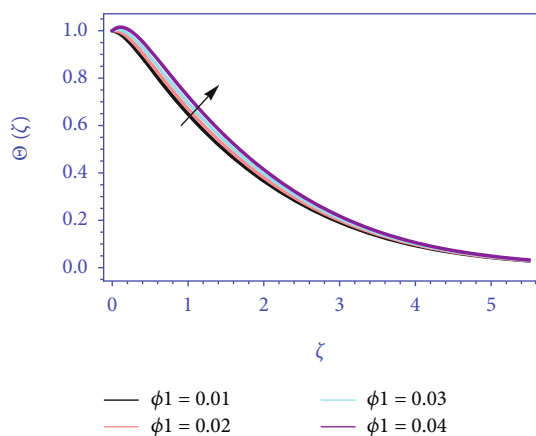


FIGURE 10: Effect of  $\phi_1$  on  $\Theta(\zeta)$ .

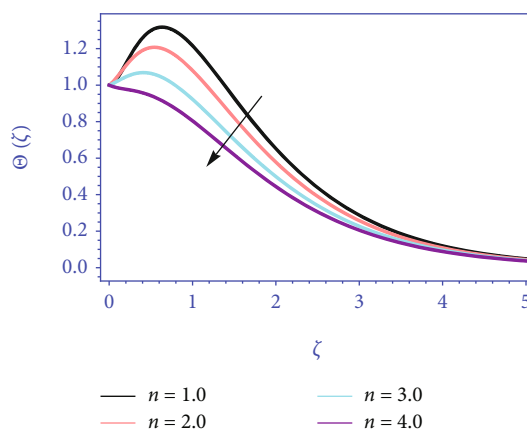


FIGURE 12: Effect of  $n$  on  $\Theta(\zeta)$ .

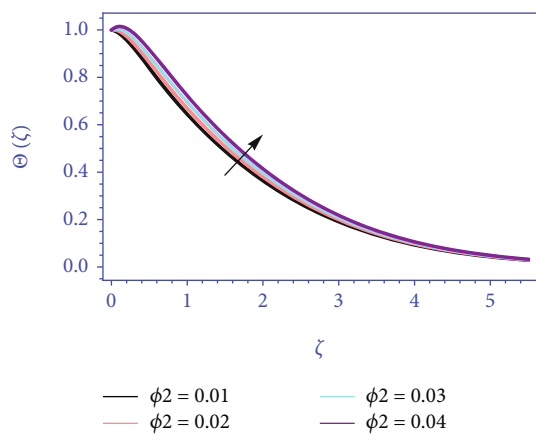


FIGURE 11: Effect of  $\phi_2$  on  $\Theta(\zeta)$ .

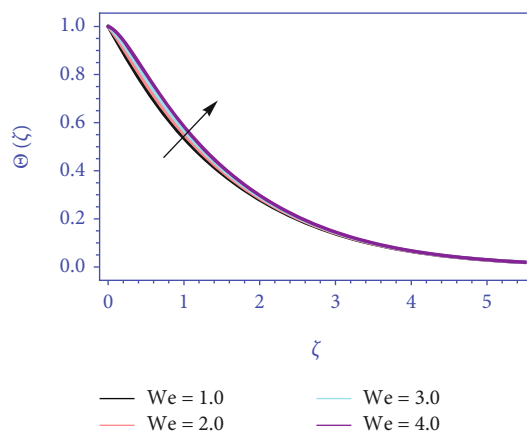


FIGURE 13: Effect of  $We$  on  $\Theta(\zeta)$ .



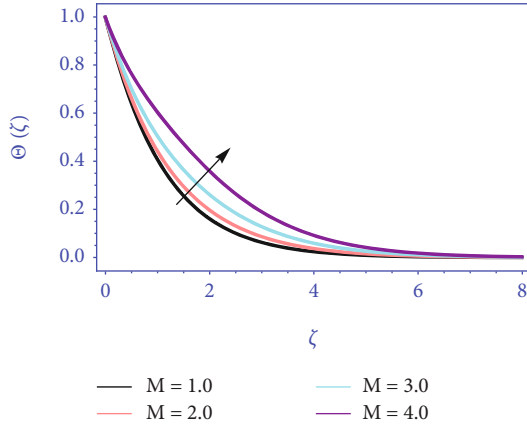


FIGURE 14: Effect of  $M$  on  $\Theta(\zeta)$ .

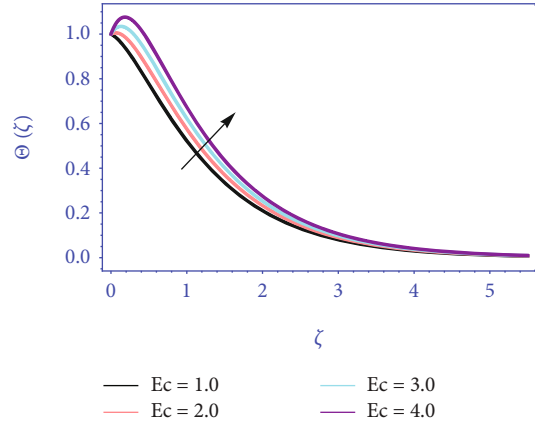


FIGURE 16: Effect of  $Ec$  on  $\Theta(\zeta)$ .

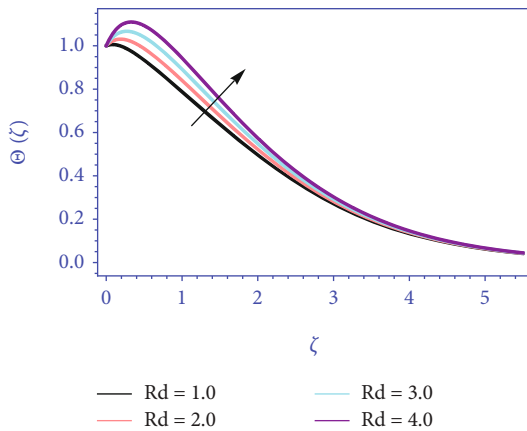


FIGURE 15: Effect of  $Rd$  on  $\Theta(\zeta)$ .

$\phi_1 = \phi_2 = 0.05$ . Figure 9(a) displays the effect of  $n$  on  $Y'(\zeta)$ . The escalating  $n$  shows augmenting conduct against  $Y'(\zeta)$ . The numerical value of the power-law index parameter is specified for two different fluids, namely, pseudoplastic ( $n < 1$ ) and dilatant ( $n > 1$ ). Physically, the escalating  $n$  interconnects an important augmentation in the viscosity of the non-Newtonian hybrid nanofluid flow. That is why the velocity boundary layer thickness is declined; as a result,  $Y'(\zeta)$  is augmented. Figure 9(b) shows the streamline patterns for  $n$  when  $\phi_1 = \phi_2 = 0.05$ . Figure 10 shows the effect of  $\phi_1$  on  $\Theta(\zeta)$  when  $\phi_2 = 0.05$ . The increasing  $\phi_1$  augments  $\Theta(\zeta)$ . Figure 11 shows the effect of volume fraction  $\phi_2$  on  $\Theta(\zeta)$  when  $\phi_1 = 0.05$ . The increasing  $\phi_2$  augments  $\Theta(\zeta)$ . Figure 12 shows the effect of power-law index  $n$  on  $\Theta(\zeta)$  when  $\phi_1 = \phi_2 = 0.05$ . The rising  $n$  declines  $\Theta(\zeta)$ . The increasing  $n$  thickens the temperature boundary layer which diminishes the temperature of the hybrid nanofluid flow. Thus, a declining impact is found here. Figure 13 exhibits the effect of  $We$  on  $\Theta(\zeta)$  when  $\phi_1 = \phi_2 = 0.05$ . The increasing  $We$  augments  $\Theta(\zeta)$ . The increasing  $We$  shows that the increased quantity of thermal energy provided to the nanofluidic system due to resistive nanofluid motion can explain this thermal behavior physically. Figure 14 displays the impact of  $M$  on  $\Theta(\zeta)$  when  $\phi_1 = \phi_2 = 0.05$ . The augmenting  $M$  escalates

$\Theta(\zeta)$  of the hybrid nanofluid flow. Physically, as the magnetic parameter increases, the movement of particles of hybrid nanofluid escalates. Thus, both the thermal boundary and temperature of the hybrid nanofluid augment. Figure 15 designates the effect of  $Rd$  on  $\Theta(\zeta)$  when  $\phi_1 = \phi_2 = 0.05$ . The increasing radiation parameter boosts up  $\Theta(\zeta)$ . Physically, the increasing radiation parameter augments the surface heat of the hybrid nanofluid flow which makes the hybrid nanofluid hotter. Thus, the escalating conduct is observed here. Figure 16 displays the effect of Eckert number  $Ec$  on  $\Theta(\zeta)$  when  $\phi_1 = \phi_2 = 0.05$ . The increasing Eckert number augments  $\Theta(\zeta)$ . The link between kinetic energy and enthalpy in a flow is described by the Eckert number. It denotes the effort expended in converting kinetic energy to internal energy in the face of viscous fluid forces. An increase in the Eckert number implies that the fluid has a high kinetic energy; consequently, the intermolecular collisions take place which enhances the particles vibration. So, the increased molecule collisions increase heat dissipation in the boundary layer region, causing  $\Theta(\zeta)$  to climb.

## 6. Conclusion

The magnetohydrodynamic flow of water-based hybrid nanofluid containing ferrous and graphene oxide nanoparticles past a flat plate has been studied in this article. The stagnation point along with the impacts of magnetic field and thermal radiation is taken in this consideration. The non-Newtonian tangent hyperbolic flow which is laminar and incompressible is also considered to investigate the non-Newtonian behavior of the hybrid nanofluid flow. The hydrothermal characteristics of the hybrid nanofluid flow past a nonisothermal flat plate at a stagnation point are affected by the necessary parameters. Key points of this analysis are as follows:

- (1) The increasing volume fractions of the ferrous and graphene oxide nanoparticles have significantly reduced the velocity field, while the thermal field has increased with the augmenting volume fractions of the ferrous and graphene oxide nanoparticles

- (2) The augmenting magnetic parameter has considerably enhanced the velocity and thermal fields
- (3) Due to the direct relation between the Weissenberg number and relaxation time, the greater Weissenberg number has reduced the velocity profile, while increased the thermal field
- (4) The increasing power-law index has augmented the viscosity of the non-Newtonian hybrid nanofluid flow due to which the velocity field escalated. However, this impact is opposite for the thermal field
- (5) The augmenting Eckert number and thermal radiation parameter have increased the thermal field

## Nomenclature

Constants:	$b, c$
Magnetic field strength:	$B_0$ (kg s <sup>-2</sup> A <sup>-1</sup> )
Skin friction coefficient:	$C_{fx}$
Specific heat:	$C_p$ (J kg <sup>-1</sup> K <sup>-1</sup> )
Eckert number:	$Ec$
Mean absorption coefficient:	$k^*$
Thermal conductivity:	$k$ (Wm <sup>-1</sup> K <sup>-1</sup> )
Magnetic parameter:	$M$
Power-law index:	$n$
Nusselt number:	$Nu_x$
Prandtl number:	$Pr$
Radiative heat flux:	$q_r$ (Wm <sup>-2</sup> )
Radiation parameter:	$Rd$
Local Reynolds number:	$Re$
Temperature:	$T$ (K)
Free-stream velocity:	$u_e(x)$ (ms <sup>-1</sup> )
Velocity components:	$(u, v)$ (ms <sup>-1</sup> )
Weissenberg number:	$We$
Cartesian coordinates:	$(x, y)$ (m).

## Greek Symbols

Kinetic viscosity:	$\nu$ (m <sup>2</sup> s <sup>-1</sup> )
Dimensionless temperature:	$\theta$
Nanoparticle volume fraction:	$\phi$
Dynamic viscosity:	$\mu$ (kgm <sup>-1</sup> s <sup>-1</sup> )
Time-dependent material:	$\Gamma$ (s)
Density:	$\rho$ (kgm <sup>-3</sup> )
Stefan–Boltzmann constant:	$\sigma^*$
Electrical conductivity:	$\sigma$ (Sm <sup>-1</sup> )
Similarity variable:	$\zeta$ .

## Subscripts

Base fluid:	$f$
Nanoparticles:	$p1, p2$
Wall boundary condition:	$w$
Free-stream condition:	$\infty$ .

## Data Availability

All the supporting data are within the manuscript.

## Conflicts of Interest

The authors declare that they have no conflict of interest.

## References

- [1] U. Khan, S. Bilal, A. Zaib, O. D. Makinde, and A. Wakif, “Numerical simulation of a nonlinear coupled differential system describing a convective flow of Casson gold–blood nanofluid through a stretched rotating rigid disk in the presence of Lorentz forces and nonlinear thermal radiation,” *Numerical Methods for Partial Differential Equations*, vol. 38, no. 3, pp. 308–328, 2020.
- [2] N. A. Shah, I. L. Animasaun, J. D. Chung, A. Wakif, F. I. Alao, and C. S. K. Raju, “Significance of nanoparticle’s radius, heat flux due to concentration gradient, and mass flux due to temperature gradient: the case of Water conveying copper nanoparticles,” *Scientific Reports*, vol. 11, no. 1, pp. 1–11, 2021.
- [3] T. Gul, R. S. Gul, W. Noman et al., “CNTs–nanofluid flow in a rotating system between the gap of a disk and cone,” *Physica Scripta*, vol. 95, no. 12, article 125202, 2020.
- [4] G. Sowmya, B. J. Gireesha, S. Sindhu, and B. C. Prasannakumara, “Investigation of Ti6Al4V and AA7075 alloy embedded nanofluid flow over longitudinal porous fin in the presence of internal heat generation and convective condition,” *Communications in Theoretical Physics*, vol. 72, no. 2, article 025004, 2020.
- [5] M. U. Ashraf, M. Qasim, A. Wakif, M. I. Afridi, and I. L. Animasaun, “A generalized differential quadrature algorithm for simulating magnetohydrodynamic peristaltic flow of blood-based nanofluid containing magnetite nanoparticles: a physiological application,” *Numerical Methods for Partial Differential Equations*, 2020.
- [6] A. Dawar, Z. Shah, W. Khan, M. Idrees, and S. Islam, “Unsteady squeezing flow of magnetohydrodynamic carbon nanotube nanofluid in rotating channels with entropy generation and viscous dissipation,” *Advances in Mechanical Engineering*, vol. 11, no. 1, Article ID 168781401882310, 2019.
- [7] G. Rasool and A. Wakif, “Numerical spectral examination of EMHD mixed convective flow of second-grade nanofluid towards a vertical Riga plate using an advanced version of the revised Buongiorno’s nanofluid model,” *Journal of Thermal Analysis and Calorimetry*, vol. 143, no. 3, pp. 2379–2393, 2021.
- [8] M. Alghamdi, A. Wakif, T. Thumma, U. Khan, D. Baleanu, and G. Rasool, “Significance of variability in magnetic field strength and heat source on the radiative-convective motion of sodium alginate-based nanofluid within a Darcy–Brinkman porous structure bounded vertically by an irregular slender surface,” *Case Studies in Thermal Engineering*, vol. 28, article 101428, 2021.
- [9] B. C. Rout, S. R. Mishra, and T. Thumma, “Effect of viscous dissipation on Cu–water and Cu–kerosene nanofluids of axisymmetric radiative squeezing flow,” *Heat Transfer—Asian Research*, vol. 48, no. 7, pp. 3039–3054, 2019.
- [10] A. S. Alshomrani and T. Gul, “A convective study of Al<sub>2</sub>O<sub>3</sub>–H<sub>2</sub>O and Cu–H<sub>2</sub>O nano-liquid films sprayed over a stretching cylinder with viscous dissipation,” *The European Physical Journal Plus*, vol. 132, no. 11, pp. 1–16, 2017.
- [11] M. Bilal, A. Saeed, T. Gul, I. Ali, W. Kumam, and P. Kumam, “Numerical approximation of microorganisms hybrid nanofluid flow induced by a wavy fluctuating spinning disc,” *Coatings*, vol. 11, p. 1032, 2021.

- [12] M. Jawad, A. Saeed, M. Bilal, T. Gul, A. Khan, and S. Nasir, "The impact of magnetohydrodynamic on bioconvection nanofluid flow with viscous dissipation and joule heating effects," *Engineering Research Express*, vol. 3, no. 1, article 015030, 2021.
- [13] T. Gul, J. U. Rahman, M. Bilal et al., "Viscous dissipated hybrid nanofluid flow with Darcy–Forchheimer and forced convection over a moving thin needle," *AIP Advances*, vol. 10, article 105308, 2020.
- [14] M. Bilal, T. Gul, A. Alsubie, and I. Ali, "Axisymmetric hybrid nanofluid flow with heat and mass transfer amongst the two gyrating plates," *ZAMM-Journal of Applied Mathematics and Mechanics/Zeitschrift für Angewandte Mathematik und Mechanik*, vol. 101, no. 11, article e202000146, 2021.
- [15] S. Jana, A. Salehi-Khojin, and W. H. Zhong, "Enhancement of fluid thermal conductivity by the addition of single and hybrid nano-additives," *Thermochimica Acta*, vol. 462, no. 1-2, pp. 45–55, 2007.
- [16] N. S. Khashi'ie, N. M. Arifin, R. Nazar, E. H. Hafidzuddin, N. Wahid, and I. Pop, "Magnetohydrodynamics (MHD) axisymmetric flow and heat transfer of a hybrid nanofluid past a radially permeable stretching/shrinking sheet with Joule heating," *Chinese Journal de Physique*, vol. 64, pp. 251–263, 2020.
- [17] M. Nawaz and U. Nazir, "An enhancement in thermal performance of partially ionized fluid due to hybrid nano-structures exposed to magnetic field," *AIP Advances*, vol. 9, no. 8, article 085024, 2019.
- [18] S. Manjunatha, B. Ammani Kuttan, S. Jayanthi, A. Chamkha, and B. J. Gireesha, "Heat transfer enhancement in the boundary layer flow of hybrid nanofluids due to variable viscosity and natural convection," *Heliyon*, vol. 5, no. 4, article e01469, 2019.
- [19] M. Usman, M. Hamid, T. Zubair, R. Ul Haq, and W. Wang, "Cu-Al<sub>2</sub>O<sub>3</sub>/water hybrid nanofluid through a permeable surface in the presence of nonlinear radiation and variable thermal conductivity via LSM," *International Journal of Heat and Mass Transfer*, vol. 126, pp. 1347–1356, 2018.
- [20] Z. Iqbal, E. N. Maraj, E. Azhar, and Z. Mehmood, "A novel development of hybrid (MoS<sub>2</sub>–SiO<sub>2</sub>/H<sub>2</sub>O) nanofluidic curvilinear transport and consequences for effectiveness of shape factors," *Journal of the Taiwan Institute of Chemical Engineers*, vol. 81, pp. 150–158, 2017.
- [21] S. S. Ghadikolaei, M. Yassari, H. Sadeghi, K. Hosseinzadeh, and D. D. Ganji, "Investigation on thermophysical properties of TiO<sub>2</sub>–Cu/H<sub>2</sub>O hybrid nanofluid transport dependent on shape factor in MHD stagnation point flow," *Powder Technology*, vol. 322, pp. 428–438, 2017.
- [22] T. Gul, M. Kashifullah, W. Bilal, M. I. Alghamdi, T. A. Asjad, and T. Abdeljawad, "Hybrid nanofluid flow within the conical gap between the cone and the surface of a rotating disk," *Scientific Reports*, vol. 11, no. 1, p. 1180, 2021.
- [23] W. Alghamdi, A. Alsubie, P. Kumam, A. Saeed, and T. Gul, "MHD hybrid nanofluid flow comprising the medication through a blood artery," *Scientific Reports*, vol. 11, no. 1, pp. 1–13, 2021.
- [24] N. Acharya, "On the flow patterns and thermal behaviour of hybrid nanofluid flow inside a microchannel in presence of radiative solar energy," *Journal of Thermal Analysis and Calorimetry*, vol. 141, no. 4, pp. 1425–1442, 2020.
- [25] N. Acharya and F. Mabood, "On the hydrothermal features of radiative Fe<sub>3</sub>O<sub>4</sub>–graphene hybrid nanofluid flow over a slippery bended surface with heat source/sink," *Journal of Thermal Analysis and Calorimetry*, vol. 143, no. 2, pp. 1273–1289, 2021.
- [26] T. Thumma, S. R. Mishra, and O. A. Bég, "ADM solution for Cu/CuO–water viscoplastic nanofluid transient slip flow from a porous stretching sheet with entropy generation, convective wall temperature and radiative effects," *Journal of Applied and Computational Mechanics*, pp. 1–15, 2021.
- [27] N. Acharya, K. Das, and P. K. Kundu, "Framing the effects of solar radiation on magneto-hydrodynamics bioconvection nanofluid flow in presence of gyrotactic microorganisms," *Journal of Molecular Liquids*, vol. 222, pp. 28–37, 2016.
- [28] N. Acharya, R. Bag, and P. K. Kundu, "On the impact of nonlinear thermal radiation on magnetized hybrid condensed nanofluid flow over a permeable texture," *Applied Nanoscience*, vol. 10, no. 5, pp. 1679–1691, 2020.
- [29] N. Acharya, "Spectral quasi linearization simulation on the hydrothermal behavior of hybrid nanofluid spraying on an inclined spinning disk," *Partial Differential Equations in Applied Mathematics*, vol. 4, article 100094, 2021.
- [30] S. Liao, "An optimal homotopy-analysis approach for strongly nonlinear differential equations," *Communications in Nonlinear Science and Numerical Simulation*, vol. 15, no. 8, pp. 2003–2016, 2010.

## Research Article

# Electro-Magnetohydrodynamic Fractional-Order Fluid Flow with New Similarity Transformations

Fuad S. Al-Duais <sup>1,2</sup>, Saeed Ahmed Asiri <sup>3</sup>, Anwar Saeed <sup>4</sup>, Jihen Majdoubi,<sup>5</sup>  
Mohammad Mahtab Alam <sup>6</sup> and Taza Gul <sup>7</sup>

<sup>1</sup>Mathematics Department, College of Humanities and Science in Al Aflaj, Prince Sattam Bin Abdulaziz University, Al Aflaj, Saudi Arabia

<sup>2</sup>Administration Department, Administrative Science College, Thamar University, Thamar, Yemen

<sup>3</sup>Mechanical Engineering Department, Engineering College, King Abdulaziz University, Jeddah, Saudi Arabia

<sup>4</sup>Center of Excellence in Theoretical and Computational Science (TaCS-CoE), Faculty of Science, King Mongkut's University of Technology Thonburi (KMUTT), 126 Pracha Uthit Rd., Bang Mod, Thung Khru, Bangkok 10140, Thailand

<sup>5</sup>Department of Computer Science, College of Science and Humanities at Alghat Majmmah University, Al-Majmaah 11952, Saudi Arabia

<sup>6</sup>Department of Basic Medical Sciences, College of Applied Medical Sciences, King Khalid University, Abha 61421, Saudi Arabia

<sup>7</sup>Department of Mathematics, City University of Science and Information Technology, Peshawar 25000, Pakistan

Correspondence should be addressed to Anwar Saeed; [anwar.sae@kmutt.ac.th](mailto:anwar.sae@kmutt.ac.th)

Received 3 January 2022; Revised 3 April 2022; Accepted 23 April 2022; Published 17 May 2022

Academic Editor: Filippo Giubileo

Copyright © 2022 Fuad S. Al-Duais et al. This is an open access article distributed under the Creative Commons Attribution License, which permits unrestricted use, distribution, and reproduction in any medium, provided the original work is properly cited.

The fractional-order differential equations that exist in the field of science and engineering have been studied in this paper. The 2D fluid flow problems are recommended for the classical- and fractional-order analysis. It has been found that the nonlinear fractional-order problems are more realistic than the classical models to describe the proposed flow problems since the behavior of the stress of the model problem is not linear. The similarity variable in this study has been used in fractional form to transform the modeled governing equations from partial PDEs. The acquired equations are the nonlinear ordinary differential equations (ODEs) in fractional form. The electromagnetic field has also been imposed into the fluid motion to calculate the embedded constraints in the case of classical and noninteger orders. The nonlinear problems are attempted using the FDE-12 technique. The important physical phenomena including Nusselt number and skin friction are also calculated in case of the integer- and noninteger-order problems. The electric and magnetic fields are examined and discussed in the case of fractional form and classical form.

## 1. Introduction

One of the demanding and competitive fields among researchers is the modeling of noninteger-order problems related to science and technology. The fractional models are more realistic than classical models to describe the nonlinear phenomena because the classical models do not completely represent all the requirements of the nonlinear problems. Moreover, the fractional models are more appropriate to calculate the actual influence of the parameters in the limited domain because the parameter impact in the

physical problems at small intervals is very necessary for the parameter range and limitations. In 1967, the concept of the noninteger-order derivative was introduced by Caputo [1] to discuss problems involving a fractional differential equation with initial conditions. That idea was further extended [2–4] to implement the noninteger-order derivative concept to the problems happening in the field of engineering, biomedical, and industry. The various noninteger-order operators were introduced and used by the scientists [5–14] to handle the more realistic physical problems. These problems include higher-order problems that occur in the

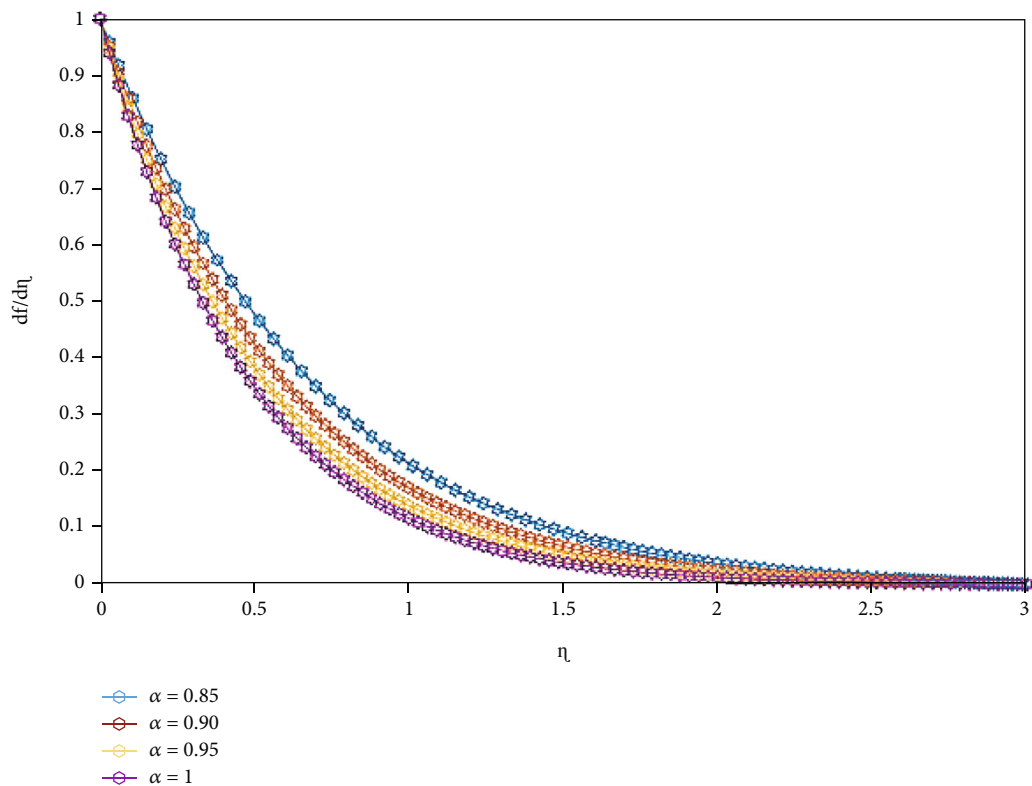


FIGURE 1: Impact of  $\alpha$  versus  $f'(\eta)$ . When  $M = 0.1$ ,  $E = 0.3$ , and  $Pr = 6.2$ .

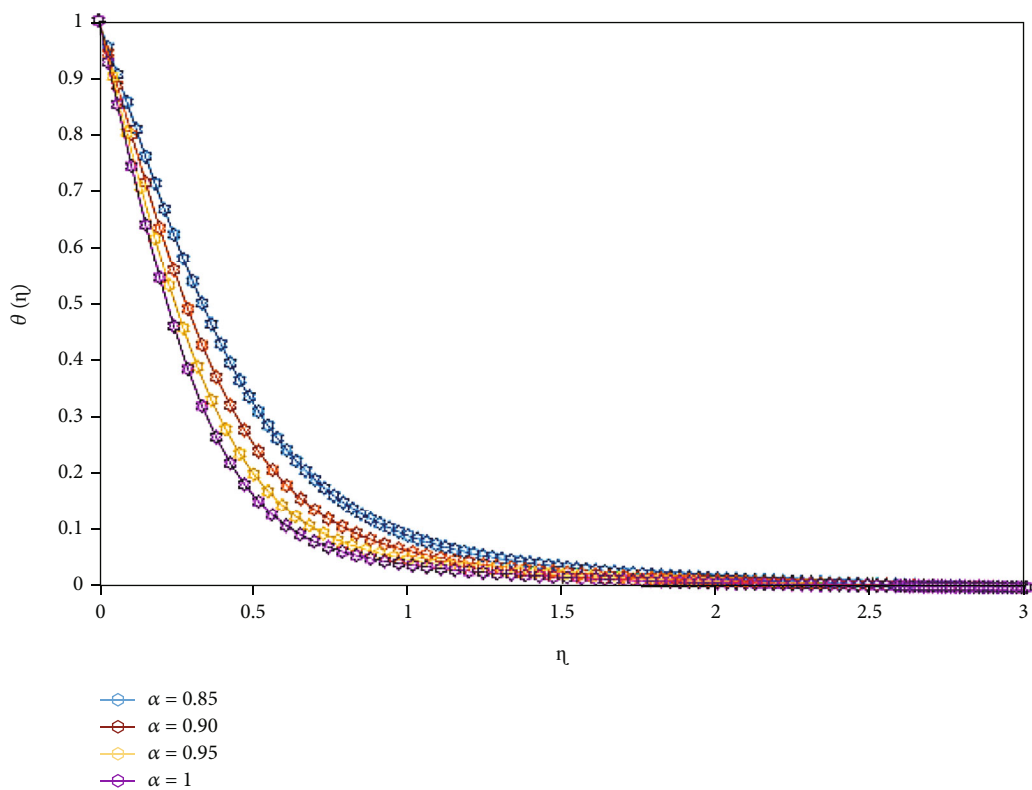


FIGURE 2: Impact of  $\alpha$  versus  $\theta(\eta)$ . When  $M = 0.1$ ,  $E = 0.3$ , and  $Pr = 6.2$ .

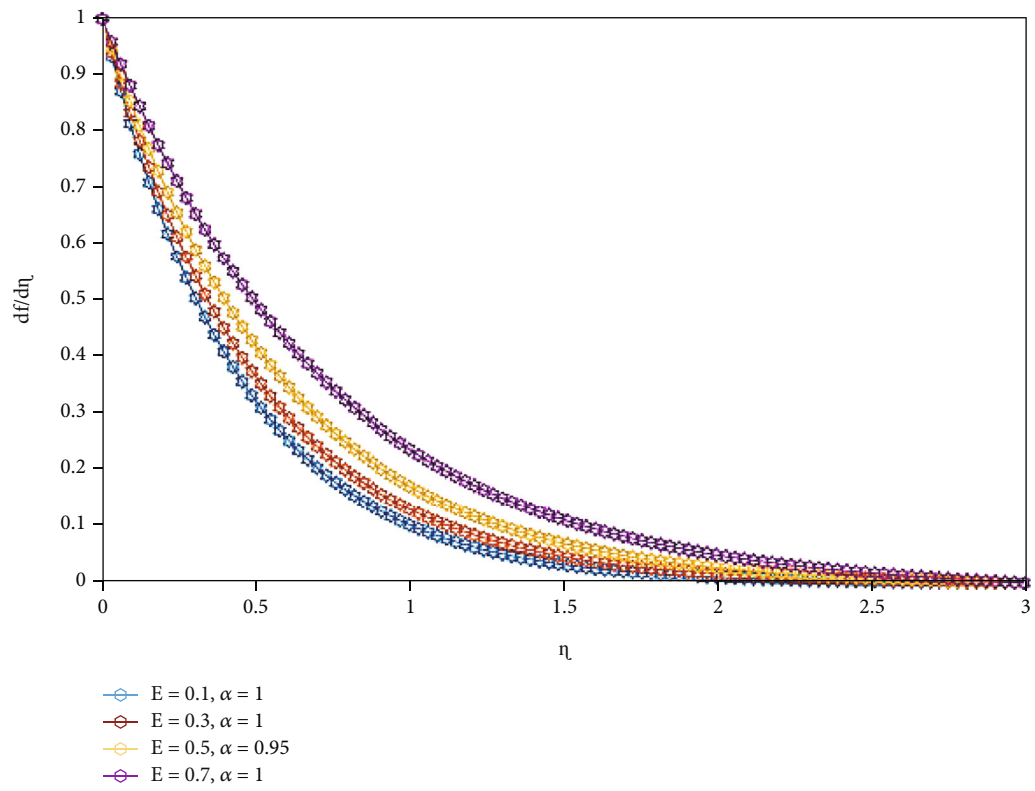


FIGURE 3: Impact of  $E$  versus  $f'(\eta)$ . When  $\alpha = 1, M = 0.3$ , and  $Pr = 6.2$ .

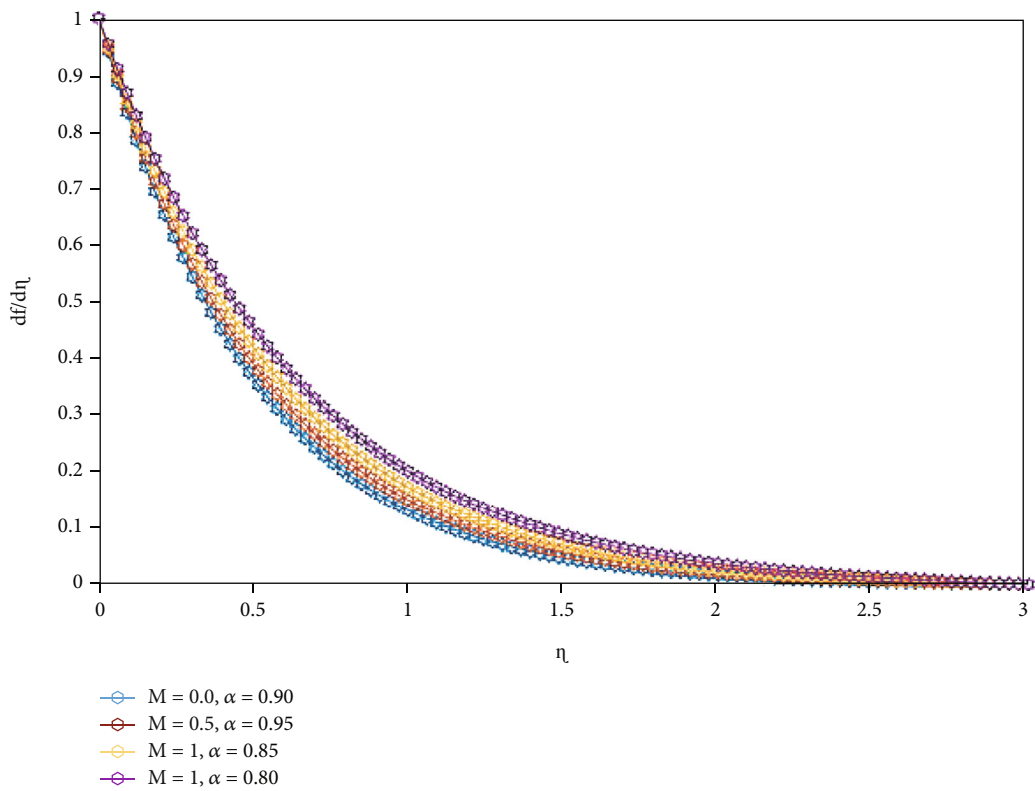


FIGURE 4: Impact of  $E$  versus  $f'(\eta)$ . When  $\alpha = 1, M = 0.3$ , and  $Pr = 6.2$ .

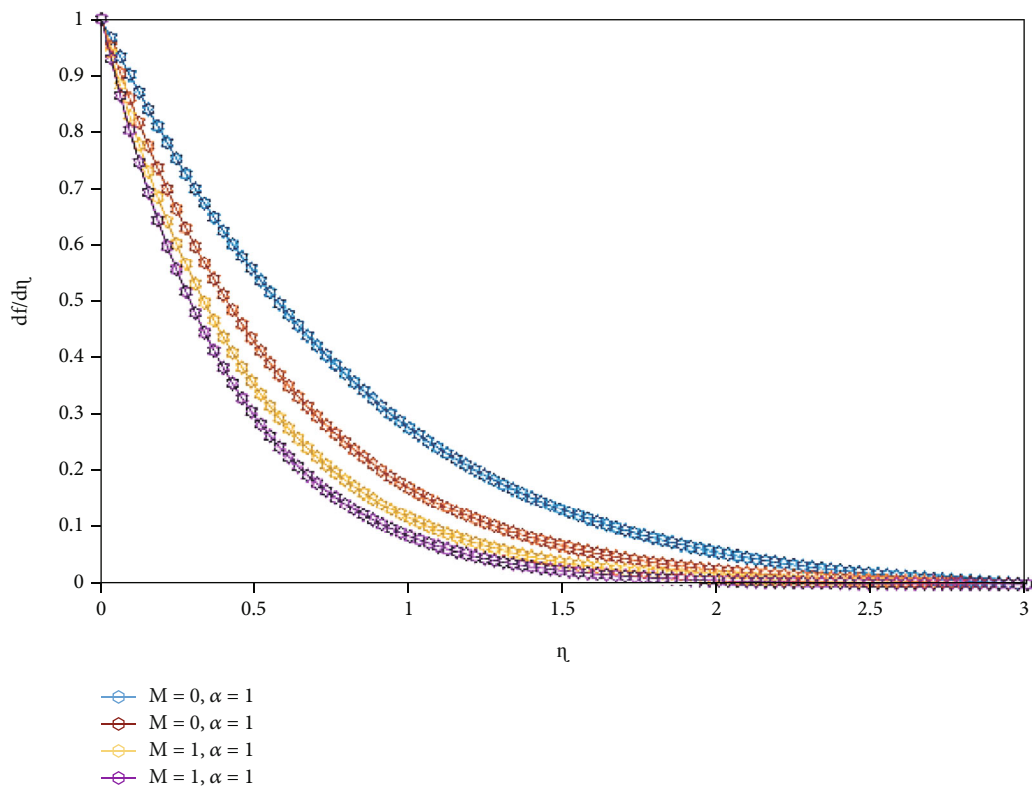


FIGURE 5: Impact of  $M$  versus  $f'(\eta)$ . When  $\alpha = 1, E = 0.3$ , and  $Pr = 6.2$ .

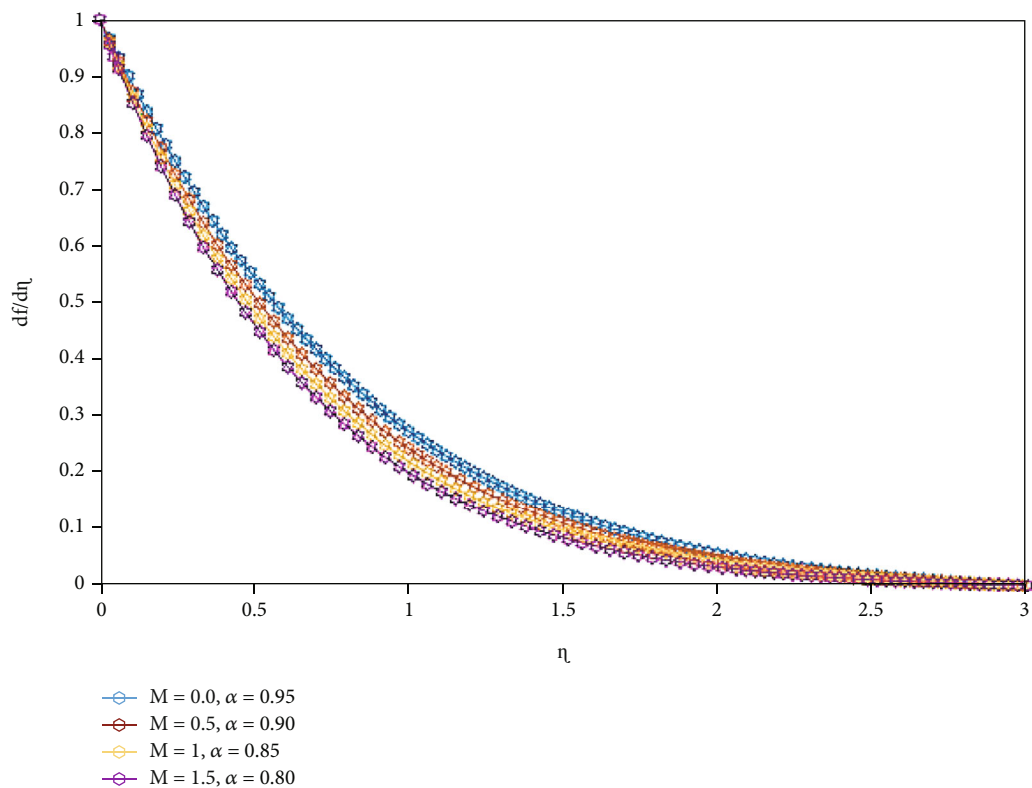


FIGURE 6: Impact of  $M$  versus  $f'(\eta)$ . When  $E = 0.3$  and  $Pr = 6.2$ .

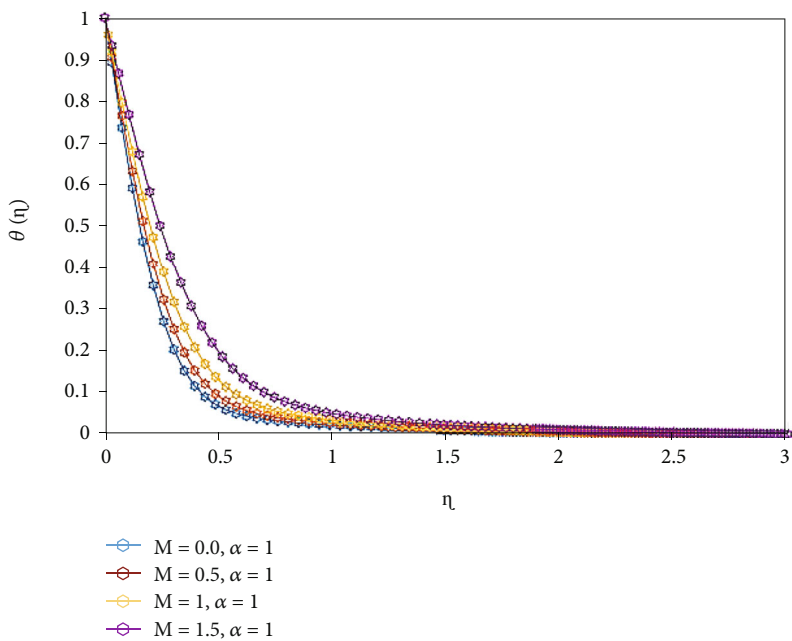


FIGURE 7: Impact of  $M$  versus  $\theta(\eta)$ . When  $\alpha = 1, E = 0.3,$  and  $Pr = 6.5.$

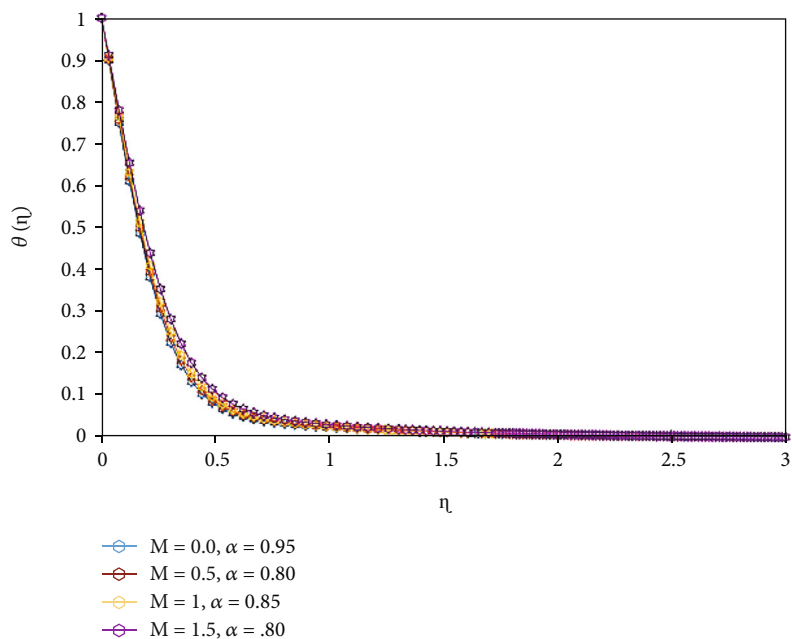


FIGURE 8: Impact of  $M$  versus  $\theta(\eta)$ . When  $\alpha = 1, E = 0.3,$  and  $Pr = 6.5.$

TABLE 1:  $(\alpha + 1)f''(0)$  and  $-\theta'(0)$ . When  $M = 0.1, E = 0.3,$  and  $Pr = 6.2.$

$\alpha$	$(\alpha + 1)f''(0)$	$-\theta'(0)$
1	0.732547	1.74584
0.95	0.710179	1.73294
0.90	0.691356	1.71865
0.85	0.67608	1.70272
0.80	0.664332	1.68486

field of science, wave equations and fraction hybrid differential operators, Mumps virus with optimal control,  $q$ -integro-differential equations, solution of the fractional Burgers equation, and solution of the fractional Allen–Cahn equations. However, the initial idea of the noninteger-order derivative was limited to the time-fractional derivative. Later, the idea of fractional-order derivative was further refined [15, 16] and the space variables have been introduced to handle the noninteger-order boundary value problems independent of time. The handling of nonlinear problems



TABLE 2:  $(\alpha + 1)f''(0)$  and  $-\theta'(0)$ . When  $E = 0.3$  and  $Pr = 6.2$ .

$\alpha, M$	$f''(0)$	$-\theta'(0)$	$\alpha, M$	$f''(0)$	$-\theta'(0)$
$\alpha = 1, M = 0.0, E = 0.1$	0.654686	1.68489	$\alpha = 0.95, E = 0.1, M = 0.0$	0.6966	1.73290
$M = 0.1$	0.726303	1.70721	$\alpha = 0.90, M = 0.1$	0.699356	1.71865
$M = 0.5$	0.739522	1.71849	$\alpha = 0.85, M = 0.5$	0.719129	1.70257
$M = 1$	0.82882	1.73258	$\alpha = 0.80, M = 1$	0.749324	1.68455
$\alpha = 1, M = 0.1, E = 0.1$	0.726303	1.70721	$\alpha = 0.90, M = 0.1$	0.699356	1.71865
$E = 0.3$	0.7141021	1.70721	$\alpha = 0.85, E = 0.3$	0.695231	1.71865
$E = 0.5$	0.7021202	1.70721	$\alpha = 0.80, E = 0.5$	0.691452	1.71865

TABLE 3:  $2f''(0)$  and  $-\theta'(0)$ . When  $\alpha = 1..$

$M$	$Pr$	$f''(0)$ (present)	$f''(0)$ [18]	$-\theta'(0)$ (present)	$-\theta'(0)$ [18]
0.0	6.2	0.717534	0.717984	1.74588	1.74598
	0.1	0.732547	0.732995	1.74584	1.74599
	0.5	0.791613	0.791874	1.74567	1.74589
	1	0.863306	0.863717	1.74546	1.74587
0.1	6.4	0.863306	0.863828	1.73482	1.73498
	6.6	0.863306	0.863897	1.72514	1.72568
	6.8	0.863306	0.863564	1.71554	1.71567

in the form of PDEs is not an easy job so the similarity transforms were implemented to convert the model PDEs into the nonlinear classical-order ODEs [17–21]. The noninteger-order similarity variables are used by El Rasouli et al. [22] to alter the classical PDEs into the noninteger-order ODEs for the gas flow model. Mohammadein et al. [23] used a similar idea for the boundary layer flow past an extending sheet.

The above idea is further improved in the recent study by using the same variable idea to alter the PDEs in the noninteger-order ODEs avoiding the separating of variable concepts. Considering the common parameters, the recent idea matches with the existing literature [17, 18] for the integer-order analysis. The acquired outcomes are also contrasted with the classical model. The results are obtained using the FDE-12 technique [24, 25].

Since in most of the problems the stress is not linear, that is why the fractional-order derivative approach is very essential to handle these kinds of problems.

The recent work is the generalized form of the 2D model, and one can easily get the existence model by putting  $n = 1$  as an integer case. Also, the electrical and magnetic fields are jointly used to improve the novelty.

## 2. Formulation of the Problem

The fluid flow is assumed in two-dimensional space considering the steady motion of the fluid towards the stretched surface. The electromagnetic field is imposed on the flow pattern in the vertical direction. All the assumptions are similar to the published work [17]. The elementary equations

are displayed as

$$\frac{\partial u}{\partial x} + \frac{\partial v}{\partial y} = 0, \tag{1}$$

$$\left( u \frac{\partial u}{\partial x} + v \frac{\partial u}{\partial y} \right) = \nu \frac{\partial^2 u}{\partial y^2} - \frac{1}{\rho} (\sigma B_0^2 u - E_0 B_0), \tag{2}$$

$$\left( u \frac{\partial T}{\partial x} + v \frac{\partial T}{\partial y} \right) = \frac{k}{\rho c_p} \frac{\partial T}{\partial y^2}. \tag{3}$$

The boundary conditions are

$$u = xb, v = 0, T = T_w \quad \text{at } y = 0, \tag{4}$$

$$u \longrightarrow 0, T \longrightarrow T_\infty, \quad \text{at } y \longrightarrow \infty. \tag{5}$$

Here,  $\nu, \rho, cp, E_0, k, \sigma, B_0$ , and  $T$  stand for kinematic viscosity, density, specific heat, electric conductivity, thermal conductivity, magnetic field, and temperature distribution, respectively. The similarity variable in fractional form with appropriate transformations is defined as [26, 27]

$$\psi = x(bv_f)^{1/2} f(\eta), \tag{6}$$

$$u = \frac{\partial \psi}{\partial y}, \tag{7}$$

$$v = -\frac{\partial \psi}{\partial x}, \tag{8}$$

$$\Theta(\eta) = \frac{(T - T_\infty)}{(T_w - T_\infty)}, \tag{9}$$

$$\eta^\alpha = \frac{y^\alpha}{\Gamma(\alpha + 1)} \sqrt{\frac{b}{v_f}} \Rightarrow \eta = y \sqrt{\frac{b}{v_f}}. \tag{10}$$

Upon using Equation (6) in Equations ((1)), ((2)), ((3)), ((4)), the noninteger-order ODEs are obtained as

$$\begin{aligned} &\alpha^2 \eta^{3\alpha-3} f^{\alpha+2} + \alpha^2 (\alpha - 1) (2\eta^{2\alpha-3} + \eta^{2\alpha-2}) f^{\alpha+1} \\ &+ \alpha (\alpha - 1)^2 \eta^{\alpha-2} f^\alpha + \alpha (\alpha - 1) \eta^{\alpha-1} f^\alpha f \\ &+ \alpha^2 \eta^{2\alpha-2} f^{\alpha+1} f - \alpha^2 \eta^{2\alpha-2} (f^\alpha)^2 + (EM - \alpha \eta^{\alpha-1} f^\alpha M) = 0, \end{aligned} \tag{11}$$

$$\alpha^2 \eta^{2\alpha-2} \Theta^{\alpha+1} + (\alpha-1) \eta^{\alpha-2} \Theta^\alpha + \text{Pr} \eta^{\alpha-2} f \Theta^\alpha = 0. \quad (12)$$

Reduced conditions are

$$f(0) = 0, \quad (13)$$

$$f^\alpha(0) = 1, \quad (14)$$

$$\theta(0) = 1, \quad (15)$$

$$f(\infty) = 0, \quad (16)$$

$$\theta(\infty) = 0. \quad (17)$$

$\alpha = 1$  reduce the above equations into the classical order as

$$f''' + ff'' - (f')^2 + ME - Mf' = 0, \quad (18)$$

$$\theta'' + \text{Pr}f\theta' = 0.$$

In Equations (11) and (12),  $\alpha$ ,  $M$ ,  $\text{Pr}$ , and  $E$  stand for the order exponent, magnetic field parameter, Prandtl number, and electric field as

$$M = \frac{\sigma B_0^2}{b \rho_f},$$

$$E = \frac{E_0}{B_0 u_w}, \quad (19)$$

$$\text{Pr} = \frac{\nu_f}{\alpha_f}.$$

**2.1. Physical Quantities of Interest.** The physical number is stated as

$$C_{fx} = \frac{\tau_w}{(1/2)\rho(u_w)^2}, \quad (20)$$

$$Nu_x = \frac{xq_w}{k(T_w - T_\infty)}. \quad (21)$$

The simplified form of Equation (20) using the similarity variable is

$$C_{fx} Re_x^{0.5} = (\alpha+1)f''(0), \quad (22)$$

$$Nu_x Re_x^{-0.5} = -\theta'(0).$$

### 3. Caputo Fractional Derivatives

The brief and basic theory of the Caputo is displayed as follows.

**3.1. Definition 1.** Let  $b, \alpha, t \in \mathbb{R}$ ,  $b > 0$ , and  $t > b$ . According to the Caputo fraction derivative, using  $\alpha$  as the fractional

order from the function  $g \in C^n$  is derived as

$${}_b^C D_t^\alpha g(t) = \frac{1}{\Gamma(n-\alpha)} \int_b^t \frac{g^{(n)}(\zeta)}{(t-\zeta)^{\alpha+1-n}} d\zeta, \quad n-1 < \alpha < n \in \mathbb{N}. \quad (23)$$

**3.2. Property.** Let  $g(t), h(t): [a, b] \rightarrow \mathfrak{R}$  be such that  ${}_b^C D_t^\alpha g(t)$  and  ${}_b^C D_t^\alpha h(t)$  exist almost everywhere, and let  $e_1, e_2 \in \mathfrak{R}$ . Then,  ${}_b^C D_t^\alpha \{e_1 g(t) + e_2 h(t)\}$  exists almost everywhere and

$${}_b^C D_t^\alpha \{e_1 g(t) + e_2 h(t)\} = e_1 {}_b^C D_t^\alpha g(t) + e_2 {}_b^C D_t^\alpha h(t). \quad (24)$$

### 4. Solution Methodology

Equations (11), (12), (13) are selected as

$$y_1 = f, y_2 = f', y_3 = f'', y_4 = \theta, y_5 = \theta', \quad (25)$$

$$y_1 = 0, y_2 - 1 = 0, y_3, y_4 - 1 = 0, y_5.$$

The above-selected functions are solved using the FDE-12 technique as mentioned in [24–27].

### 5. Results and Discussion

The two-dimensional flow on an extending surface is reflected. The electromagnetic term is considered vertically to the flow field including the momentum and energy equations. The main purpose of the research is to alter the modeled PDEs equations into noninteger-order ODEs by using similarity transformations. The fractional operator is used as  $\eta$  to alter the governing equations in the noninteger-order nonlinear ODEs. The nonlinear ODEs are then solved with the help of the FDE-12 method. The upshot of the constraints is observed using the classical- and noninteger-order systems. The noninteger-order exponent  $\alpha$  is exhibited in Figures 1 and 2 for the momentum and thermal boundary layers. The results obtained show that the noninteger-order results are compact in relation to conventional results. The electric field parameter improves the velocity profile in both classical- and fractional-order cases as shown in Figures 3 and 4. The result matches the existing literature in the case of the classical models. The noninteger-order improvement in the velocity field is comparatively compressed as displayed in Figure 4. The impact of the parameter  $M$  versus the fluid motion for its increasing value is shown in Figures 5 and 6. The fluid motion declines in both the classical shown in Figure 5 and fractional displayed in (Figure 6) for the rising values of  $M$ . The resistive forces existing in the magnetic field do not allow the fluid to flow freely, and the results are compacted via using the noninteger-order derivatives as shown in Figure 6. The resistance is accrued due to the existence of the Lorentz force. The rising credit of the Melevates the energy transference  $\theta(\eta)$  as shown in Figures 7 and 8. The impact of the parameter  $M$  is the same for both classical (Figure 7) and fractional (Figure 8). Again, the changes that occur in the temperature distribution are relatively compact in the noninteger case. Fractional-order

impact versus drag force and Nusselt number are shown in Table 1. The parameter  $M$  drops the fluid velocity for its larger values, and the impact is the same as shown in Table 2 taking the values of  $\alpha$  in both increasing and decreasing forms like  $\alpha = 0.95, 0.90, 0.85$ , and  $0.80$  or  $\alpha = 0.80, 0.85, 0.90$ , and  $0.95$ , while this retort is opposing in the case of Nusselt number. The electric field  $E$  declines the drag force in both classical and fractional cases as shown in Table 2. The decline rate is comparatively small using the noninteger form. The consequences of the parameters  $M$  and  $Pr$  versus energy transition are shown in Table 3. The larger magnitude of  $M$  enhances the heat transfer rate while the larger magnitude of  $Pr$  opposes the heat propagation rate. The variation of these parameters is also compared with the existing literature considering classical results. The comparison of the classical results authenticates the obtained results.

## 6. Conclusion

The fluid flow model in the form of boundary layer flow is considered in the two-dimensional space. The basic governing equations are transformed from the PDEs into the noninteger-order form of ODEs. The transform variable used in this transformation is in the noninteger order, and as a result, the high nonlinear ODE system is achieved. The influence of the physical parameters is obtained and shown graphically. The results obtained show that the influence of parameters is compact in comparison with conventional results. Moreover, it has been observed that fractional-order models are highly nonlinear. In very limited models, the stress is linear and in most of the fluid flow problems, the stress is nonlinear. Therefore, the fractional-order derivative is more essential and appropriate to deal the nonlinear problems.

The recent work is the generalized form of the 2D model, and  $n = 1$  becomes a special case for the classical model. Electric and magnetic field parameter results are obtained in both cases. The electric field improves the fluid motion while the magnetic field declines the fluid velocity.

## Data Availability

The relevant data exist in the article.

## Conflicts of Interest

No such interests exist.

## Acknowledgments

The authors extend their appreciation to the Deanship of Scientific Research at King Khalid University for funding this work through Group Research Project under grant number RGP. 2/160/43.

## References

- [1] M. Caputo, "Models of flux in porous media with memory," *Water Resources Research*, vol. 36, no. 3, pp. 693–705, 2000.

- [2] M. F. AminEl, A. G. Radwan, and S. Sun, "Analytical solution for fractional derivative gas-flow equation in porous media," *Results in Physics*, vol. 7, pp. 2432–2438, 2017.
- [3] A. Atangana and R. T. Alqahtani, "Numerical approximation of the space-time Caputo-Fabrizio fractional derivative and application to groundwater pollution equation," *Adv. Difference Equ.*, vol. 2016, no. 1, pp. 156–169, 2016.
- [4] B. S. T. Alkahtani, I. Koca, and A. Atangan, "A novel approach of variable order derivative: theory and methods," *Journal of Nonlinear Sciences and Applications*, vol. 9, no. 6, pp. 4867–4876, 2016.
- [5] M. E. Samei, V. Hedayati, and S. Rezapour, "Existence results for a fraction hybrid differential inclusion with Caputo–Hadamard type fractional derivative," *Advances in Difference Equations Adv. Difference Equ.*, vol. 2019, no. 1, pp. 1–15, 2019.
- [6] V. Hedayati and M. E. Samei, "Positive solutions of fractional differential equation with two pieces in chain interval and simultaneous Dirichlet boundary conditions," *Boundary Value Problems*, vol. 2019, no. 1, 23 pages, 2019.
- [7] H. Mohammadi, S. Kumar, S. Rezapour, and S. Etemad, "A theoretical study of the Caputo-Fabrizio fractional modeling for hearing loss due to mumps virus with optimal control," *Chaos, Solitons & Fractals*, vol. 144, p. 110668, 2021.
- [8] M. E. Samei and W. Yang, "Existence of solutions for  $k$ -dimensional system of multi-term fractional  $q$ -integro-differential equations under anti-periodic boundary conditions via quantum calculus," *Mathematical Methods in the Applied Sciences*, vol. 43, no. 7, pp. 4360–4382, 2020.
- [9] M. E. Samei and S. Rezapour, "On a system of fractional  $q$ -differential inclusions via sum of two multi-term functions on a time scale," *Boundary Value Problems*, vol. 2020, no. 1, 26 pages, 2020.
- [10] T. Akram, M. Abbas, M. B. Riaz, A. I. Ismail, and N. M. Ali, "An efficient numerical technique for solving time fractional Burgers equation," *Alexandria Engineering Journal*, vol. 59, no. 4, pp. 2201–2220, 2020.
- [11] N. Khalid, M. Abbas, M. K. Iqbal, and D. Baleanu, "A numerical investigation of Caputo time fractional Allen–Cahn equation using redefined cubic B-spline functions," *Advances in Difference Equations*, vol. 2020, no. 1, 22 pages, 2020.
- [12] A. Iqbal, M. J. Siddiqui, I. Muhi, M. Abbas, and T. Akram, "Nonlinear waves propagation and stability analysis for planar waves at far field using quintic B-spline collocation method," *Alexandria Engineering Journal*, vol. 59, no. 4, pp. 2695–2703, 2020.
- [13] N. Khalid, M. Abbas, M. K. Iqbal, J. Singh, and A. I. M. Ismail, "A computational approach for solving time fractional differential equation via spline functions," *Alexandria Engineering Journal*, vol. 59, no. 5, pp. 3061–3078, 2020.
- [14] M. Amin, M. Abbas, M. K. Iqbal, A. I. M. Ismail, and D. Baleanu, "A fourth order non-polynomial quintic spline collocation technique for solving time fractional superdiffusion equations," *Advances in Difference Equations*, vol. 2019, no. 1, 21 pages, 2019.
- [15] A. Ali, K. Shah, T. Abdeljawad, I. Mahariq, and M. Rashdan, "Mathematical analysis of nonlinear integral boundary value problem of proportional delay implicit fractional differential equations with impulsive conditions," *Boundary Value Problems*, vol. 7, 27 pages, 2021.
- [16] M. S. Abdo, T. Abdeljawad, S. M. Ali, and K. Shah, "On fractional boundary value problems involving fractional derivatives with Mittag-Leffler kernel and nonlinear integral

- conditions,” *Advances in Difference Equations*, vol. 37, 21 pages, 2021.
- [17] W. A. Khan and I. Pop, “Boundary-layer flow of a nanofluid past a stretching sheet,” *International journal of heat and mass transfer*, vol. 53, no. 11-12, pp. 2477–2483, 2010.
- [18] M. Z. Salleh, R. Nazar, and I. Pop, “Boundary layer flow and heat transfer over a stretching sheet with Newtonian heating,” *Journal of the Taiwan Institute of Chemical Engineers*, vol. 41, no. 6, pp. 651–655, 2010.
- [19] A. Khan, R. Zarin, S. Khan, A. Saeed, T. Gul, and U. W. Humphries, “Fractional dynamics and stability analysis of COVID-19 pandemic model under the harmonic mean type incidence rate,” *Computer Methods in Biomechanics and Biomedical Engineering*, vol. 25, no. 6, pp. 619–640, 2021.
- [20] N. Acharya, H. Mondal, and P. K. Kundu, “Spectral approach to study the entropy generation of radiative mixed convective couple stress fluid flow over a permeable stretching cylinder,” *Proceedings of the Institution of Mechanical Engineers, Part C: Journal of Mechanical Engineering Science*, vol. 235, no. 15, pp. 2692–2704, 2021.
- [21] N. Acharya, K. Das, and P. K. Kundu, “Framing the features of MHD boundary layer flow past an unsteady stretching cylinder in presence of non-uniform heat source,” *Journal of Molecular Liquids*, vol. 225, pp. 418–425, 2017.
- [22] A. Rasouli, A. Bafkar, and Z. Chaghakaboodi, “Kinetic and equilibrium studies of adsorptive removal of sodium-ion onto wheat straw and rice husk wastes,” *Central Asian Journal of Environmental Science and Technology Innovation*, vol. 1, no. 6, pp. 310–329, 2020.
- [23] A. S. Mohammadein, M. F. El-Amin, and H. M. Ali, “An approximate similarity solution for spatial fractional boundary-layer flow over an infinite vertical plate,” *Computational and Applied Mathematics*, vol. 39, no. 2, p. 114, 2020.
- [24] T. Gul, M. A. Khan, A. Khan, and M. Shuaib, “Fractional-order three-dimensional thin-film nanofluid flow on an inclined rotating disk,” *The European Physical Journal Plus*, vol. 133, no. 12, pp. 500–5011, 2018.
- [25] T. Gul, M. A. Khan, W. Noman, I. Khan, T. A. Alkanhal, and I. Tlili, “Fractional order forced convection carbon nanotubes nanofluid flow passing over a thin needle,” *Symmetry*, vol. 11, no. 3, p. 312, 2019.
- [26] T. Gul, W. Alghamdi, I. Khan, and I. Ali, “New similarity variable to transform the fluid flow from PDEs into fractional-order ODEs: numerical study,” *Physica Scripta*, vol. 96, no. 8, article 084009, 2021.
- [27] A. Saeed, M. Bilal, T. Gul, P. Kumam, A. Khan, and M. Sohail, “Fractional order stagnation point flow of the hybrid nanofluid towards a stretching sheet,” *Scientific Reports*, vol. 11, no. 1, pp. 1–15, 2021.

## Research Article

# Darcy-Forchheimer 3D Flow of Glycerin-Based Carbon Nanotubes on a Riga Plate with Nonlinear Thermal Radiation and Cattaneo-Christov Heat Flux

S. Eswaramoorthi <sup>1</sup>, K. Loganathan <sup>2,3</sup>, Reema Jain,<sup>2</sup> and Sonam Gyeltshen <sup>4</sup>

<sup>1</sup>Department of Mathematics, Dr. N.G.P. Arts and Science College, Coimbatore, Tamil Nadu, India

<sup>2</sup>Department of Mathematics and Statistics, Manipal University Jaipur, Jaipur, Rajasthan, India

<sup>3</sup>Research and Development Wing, Live4Research, Tiruppur-638106, Tamilnadu, India

<sup>4</sup>Department of Humanities and Management, Jigme Namgyel Engineering College, Royal University of Bhutan, Dewathang, Bhutan

Correspondence should be addressed to S. Eswaramoorthi; [eswaran.bharathiar@gmail.com](mailto:eswaran.bharathiar@gmail.com) and Sonam Gyeltshen; [sonamgyeltshen@jnec.edu.bt](mailto:sonamgyeltshen@jnec.edu.bt)

Received 7 January 2022; Revised 13 February 2022; Accepted 6 April 2022; Published 5 May 2022

Academic Editor: Taza Gul

Copyright © 2022 S. Eswaramoorthi et al. This is an open access article distributed under the Creative Commons Attribution License, which permits unrestricted use, distribution, and reproduction in any medium, provided the original work is properly cited.

The current investigation deliberates the consequence of the glycerin-based carbon nanotubes with velocity slip in Darcy-Forchheimer porous medium on a convectively heated Riga plate. The Fourier heat flux theory was replaced by the Cattaneo-Christov theory. Moreover, nonlinear facets of radiation are also included in the energy expression, and this creates the energy expression which becomes highly nonlinear. The governing flow problems are altered into an ODE model with the help of suitable variables. The reduced models are solved numerically by applying MATLAB bvp4c theory and analytically by HAM idea. The impact of diverse physical parameters on velocity, temperature, skin friction coefficients, local Nusselt number, entropy generation, and Bejan number are scrutinized through tables and graphs. It is seen that both directions of fluid motion elevate when raising the modified Hartmann number, and it diminishes when escalating the quantity of the Forchheimer number and porosity parameter. The fluid warmth grows when the higher magnitude of the Biot number and heat generation/consumption parameter, and it downturns when enriching the thermal relaxation time parameter. The entropy generation slumps when heightening the slip parameter, whereas it improves when rising the radiation parameter. The Bejan number upturns when upgrading the Biot number and heat generation/consumption parameter.

## 1. Introduction

The fluid thermal conductivity performs a significant role in many industrial and engineering procedures, especially in the cooling and heating of thermal systems. Conventional fluids like oil, ethylene glycol, and water transfer less heat due to weaker thermal conductivity. Nowadays, several scientists put more effort into upgrading the fluid thermal conductivity. The submersion of nanometer particles like oxide, carbides, metal oxides, carbon nanotubes (CNTs), and

graphite in conventional fluids is one of the easiest procedures for enhancing the fluid thermal conductivity. In particular, CNTs have superior power of enhancing thermal conductivity compared to other nanometer particles (see [1, 2]). The CNTs can be classified into SWCNTs and MWCNTs. Haq et al. [3] report the heat transfer analysis of an MHD viscous nanofluid flow on a stretching surface via carbon nanotubes. They noticed that the surface shear stress was high in engine oil-based CNTs than the ethylene glycol- and water-based CNTs. The outcome of nanofluid flow-

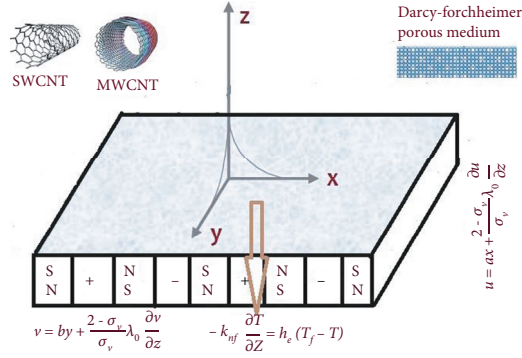


FIGURE 1: Physical configuration of the flow model.

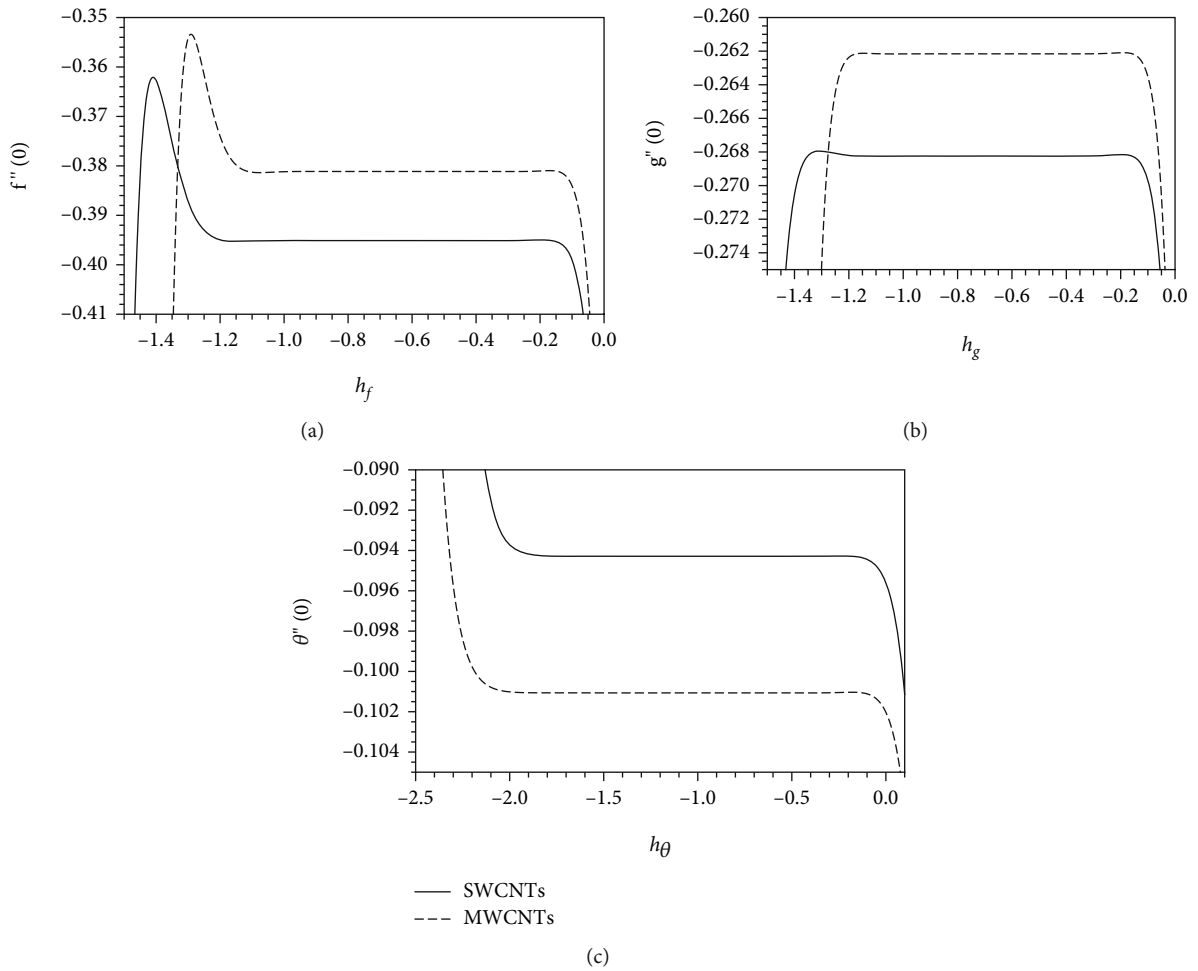


FIGURE 2:  $h$ -curves of (a)  $x$ -direction velocity, (b)  $y$ -direction velocity, and (c) nanomaterial volume fraction profiles for both nanotubes.

suspended CNTs with the presence of activation energy and binary chemical reaction on a non-Darcy porous medium was addressed by Lu et al. [4]. They exposed that the solid volume fraction of nanofluid enriches the fluid velocity. Rehman et al. [5] inspect the influence of SWCNTs on engine oil- and water-based 3D rotating fluid on a stretching sheet. They detected that engine oil-based fluid has a larger heat transfer gradient compared to water-based fluid.

TABLE 1: Physical properties.

Physical characteristics	SWCNTs	MWCNTs	Glycerin
$k$	6600	3000	0.286
$\rho$	2600	1600	1259.9
$c_p$	425	796	2427
Pr	—	—	6.78

TABLE 2: Order of approximations.

Order	SWCNTs			MWCNTs		
	$-f''(0)$	$-g''(0)$	$-\theta'(0)$	$-f''(0)$	$-g''(0)$	$-\theta'(0)$
1	0.391118	0.268199	0.093867	0.365128	0.259087	0.100429
5	0.395396	0.268234	0.094323	0.381107	0.262157	0.101120
10	0.395112	0.268247	0.094284	0.381126	0.262160	0.101061
14	0.395110	0.268247	0.094286	0.381132	0.262161	0.101066
15	0.395110	0.268247	0.094286	0.381132	0.262161	0.101066
20	0.395110	0.268247	0.094286	0.381132	0.262161	0.101066
25	0.395110	0.268247	0.094286	0.381132	0.262161	0.101066
30	0.395110	0.268247	0.094286	0.381132	0.262161	0.101066
35	0.395110	0.268247	0.094286	0.381132	0.262161	0.101066
40	0.395110	0.268247	0.094286	0.381132	0.262161	0.101066

TABLE 3: Comparison of  $-Cfx\sqrt{\text{Re}}$  and  $-Cfy\sqrt{\text{Re}}$  with Hayat et al. [56] with  $\phi = \text{Fr} = \lambda = \text{Ha} = 0$ .

$c$	$-Cfx\sqrt{\text{Re}}$		$-Cfy\sqrt{\text{Re}}$	
	Present	Ref. [56]	Present	Ref. [56]
0.0	1.00000	1.000000	0.00000	0.000000
0.3	1.05795	1.057955	0.243360	0.243360
0.5	1.09310	1.093094	0.465205	0.465205
0.8	1.14249	1.142488	0.866683	0.866680
1.0	1.17372	1.173722	1.173720	1.173723

MHD flow of SWCNTs and MWCNTs on a vertical cone with the convective heating condition was demonstrated by Sreedevi et al. [6]. They proved that the mass transfer gradient is lower in MWCNTs than in the SWCNTs for the varying values of nanoparticle volume fraction. Lu et al. [7] investigated the time-dependent squeezing flow of nanofluid suspended in CNTs with the Cattaneo-Christov theory. They have seen that the nanoparticle volume friction leads to slowing down the fluid temperature. The ferric oxide- and carbon nanotube water-based hybrid nanofluid on a wavy fluctuating rotating disk was discussed by Bilal et al. [8]. Their finding shows that both CNTs are enriching the fluid velocity. Gul et al. [9] discussed the impact of engine oil-based CNTs on a rotating disk with a magnetic field. They identified that the skin friction coefficient is high for MWCNTs than for the SWCNTs when changing the magnetic field parameter.

The fluid flow analysis through the porous medium is a salient feature in many industries, like porous bearings, crude oil production, fermentation processes, grain storage, and casting solidification. Many articles associated with porous space deal with implementing Darcy's law. The major demerit of this law is to apply only weaker porosity and lesser velocity problems. Most of the physical issues have uneven porosity and larger flow transportation. In this situation, Darcy's law is inadequate. Forchheimer [10] rectifies this difficulty by adding a square velocity term in the momentum expression. The forced convective flow of viscous fluid on a Darcy-Forchheimer porous shrinking sheet with multiple slip conditions was demonstrated by Bakar

et al. [11]. They proved that the fluid temperature declines in the first solution and increases in the second solution for changing the porosity parameter. Umavathi et al. [12] explored the Darcy-Forchheimer-Brinkman flow of a nanofluid in a rectangular duct. They discovered that the fluid temperature exalts for more quantity of the Brinkman number. The repercussion of heterogeneous/homogeneous reactions of a Darcy-Forchheimer flow of water-based carbon nanotubes on a rotating disk was studied by Hayat et al. [13]. Their decisions show that the Forchheimer number reinforces the skin friction coefficient. Ramzan and Shaheen [14] investigated the effects of the nanofluid flow through carbon nanotubes on a Darcy-Forchheimer stretching surface. They disclosed that the inertia coefficient leads to aggrandising the fluid velocity. The Darcy-Forchheimer flow of MHD nanofluid on a nonlinear stretching surface was evaluated by Rasool et al. [15]. They found that the surface shear stress jumps for a higher Forchheimer number. Nayak et al. [16] implemented the Darcy-Forchheimer law for investing the flow analysis of copper-water nanofluid on a disk. The 2D flow of MHD couple stress hybrid nanofluid on a Darcy-Forchheimer porous medium was inspected by Saeed et al. [17]. They proved that the inertia coefficient (Fr) decimates the fluid velocity. Darcy-Forchheimer flow of ethylene glycol-based nanofluid on a curved stretching surface with Arrhenius activation energy was presented by Maraj et al. [18].

Heat transfer through radiation plays a pivotal role in many manufacturing processes, like glass blowing, rubber sheet production, nuclear power plants, and tinning of copper wires. Keeping these usages in mind, several researchers scrutinized radiative heat transfer in different physical situations. Mehmood et al. [19] encountered the consequences of the radiative flow of viscoplastic fluid on a porous sheet. They detected that the thermal boundary layer thickened when raising the radiation parameter. Thermally radiative MHD flow nanofluid on a stretching sheet with second-order slip condition was inspected by Mabood and Das [20]. They observed that the fluid temperature upturns for increasing the radiation parameter. Ramzan et al. [21] deliberated the influence of nonlinear thermal radiation and chemical reaction of an MHD nanofluid on a heated plate.

TABLE 4: The HAM and numerical values of  $Cfx\sqrt{Re}$  and  $Cfy\sqrt{Re}$  of SWCNTs for diverse values of  $\lambda$ , Fr, Ha,  $c$ ,  $K$ , and  $\phi$ .

$\lambda$	Fr	Ha	$c$	$K$	$\phi$	SWCNTs			
						$Cfx\sqrt{Re}$		$Cfy\sqrt{Re}$	
						Numerical	Analytical	Numerical	Analytical
0	0.4	0.5	0.6	1	0.2	-0.628909	-0.628903	-0.927277	-0.92727
0.3						-0.717409	-0.717410	-1.042841	-1.042840
0.5						-0.765947	-0.765948	-1.102898	-1.102900
0.8						-0.827006	-0.827006	-1.176055	-1.176060
1						-0.861597	-0.861597	-1.216598	-1.216600
0.2	0	0.5	0.6	1	0.2	-0.654495	-0.654495	-0.987723	-0.987722
	0.5					-0.698291	-0.698291	-1.013220	-1.013222
	1					-0.734473	-0.734473	-1.036740	-1.036742
	1.5					-0.765175	-0.765175	-1.058400	-1.058405
	2					-0.791757	-0.791757	-1.078390	-1.078390
0.2	0.4	0	0.6	1	0.2	-0.811524	-0.811526	-0.995010	-0.995011
		0.3				-0.737372	-0.737372	-1.003201	-1.003200
		0.5				-0.690229	-0.690229	-1.008283	-1.008280
		0.8				-0.622351	-0.622351	-1.015440	-1.015440
		1				-0.578733	-0.578729	-1.019946	-1.019940
0.2	0.4	0.5	0.1	1	0.2	-0.673012	-0.673013	-2.161610	-2.161610
			0.3			-0.680479	-0.680478	-1.332389	-1.332390
			0.5			-0.687131	-0.687130	-1.082817	-1.082820
			0.8			-0.696063	-0.696063	-0.903290	-0.903291
			1			-0.701499	-0.701499	-0.830992	-0.830992
0.2	0.4	0.5	0.6	0	0.2	-1.689558	-1.689560	-2.237526	-2.237530
				1		-0.690229	-0.690229	-1.008283	-1.008280
				2		-0.444308	-0.444309	-0.672968	-0.672969
				3		-0.329252	-0.329232	-0.509501	-0.509500
0.2	0.4	0.5	0.6	1	0	-0.390100	-0.390100	-0.618400	-0.618399
					0.05	-0.446787	-0.446787	-0.692571	-0.692570
					0.1	-0.513787	-0.513787	-0.779871	-0.779870
					0.15	-0.593754	-0.593754	-0.883625	-0.883624
					0.2	-0.690229	-0.690229	-1.008283	-1.008280

They noticed that the heat transfer gradient escalates for enhancing the radiation parameter. The nonlinear thermal radiation effect on Cu-Al<sub>2</sub>O<sub>3</sub>-water-based hybrid nanofluid on the stretching surface was portrayed by Usman et al. [22]. They noticed that the local Nusselt number suppresses when there is more presence of nonlinear thermal radiation parameters. Waqas et al. [23] scrutinized the impact of nonlinear thermal radiation of a micropolar nanofluid with gyrotactic microorganisms. They uncovered that the fluid temperature grows for a high quantity of temperature ratio parameter. The series solution of time-dependent viscoelastic micropolar nanofluid with thermal radiation and Cattaneo-Christov heat/mass flux theory was derived by Khan et al. [24]. Li et al. [25] revealed the radiative flow of modified second-grade nanofluid with second-order slip conditions. They have seen that the temperature ratio parameter leads to the downfall of the heat transfer gradient.

Few progress about thermal radiative flow can be found in Refs. ([26–29]).

In the past few decades, many authors have examined entropy generation in fluid flow and heat transfer on a surface. Various factors, like viscous dissipation, chemical reactions, friction forces, and diffusion, are responsible for creating entropy. The entropy generation of the thermal system damages the effective work and suppresses the system efficiency. In this situation, Bejan [30] created a new model named as Entropy Generation Minimization (EGM), which is useful to reduce the energy losses in heat transfer processes and enrich the system efficiency. The entropy analysis of a forced convective flow of MHD Casson fluid in a microchannel with radiation was presented by Makinde and Eegunjobi [31]. They noticed that the Bejan number elevates for high magnitudes of magnetic field parameter. Bhatti et al. [32] derived the numerical



TABLE 5: The HAM and numerical values of  $Cfx\sqrt{Re}$  and  $Cfy\sqrt{Re}$  of MWCNTs for diverse values of  $\lambda$ , Fr, Ha,  $c$ ,  $K$ , and  $\phi$ .

$\lambda$	Fr	Ha	$c$	$K$	$\phi$	MWCNTs			
						$Cfx\sqrt{Re}$		$Cfy\sqrt{Re}$	
						Numerical	Analytical	Numerical	Analytical
0	0.4	0.5	0.6	1	0.2	-0.597692	-0.597688	-0.896045	-0.896037
0.3						-0.695638	-0.695639	-1.022917	-1.022920
0.5						-0.748363	-0.748363	-1.087344	-1.087340
0.8						-0.813778	-0.813779	-1.164709	-1.164710
1						-0.850433	-0.850433	-1.207141	-1.207150
0.2	0	0.5	0.6	1	0.2	-0.630797	-0.630796	-0.965518	-0.965518
	0.5					-0.673734	-0.673733	-0.990190	-0.990190
	1					-0.709390	-0.709390	-1.012999	-1.013000
	1.5					-0.739767	-0.739763	-1.034062	-1.034060
	2					-0.766154	-0.766163	-1.053545	-1.053550
0.2	0.4	0	0.6	1	0.2	-0.792587	-0.792588	-0.972431	-0.972433
		0.3				-0.715130	-0.715130	-0.980431	-0.980431
		0.5				-0.665811	-0.665810	-0.985407	-0.985407
		0.8				-0.594720	-0.594709	-0.992431	-0.992430
		1				-0.548995	-0.548938	-0.996860	-0.996859
0.2	0.4	0.5	0.1	1	0.2	-0.649036	-0.649035	-2.121875	-2.121870
			0.3			-0.656279	-0.656279	-1.304265	-1.304270
			0.5			-0.662776	-0.662775	-1.058626	-1.058630
			0.8			-0.671540	-0.671539	-0.882437	-0.882437
			1			-0.676890	-0.676889	-0.811676	-0.811676
0.2	0.4	0.5	0.6	0	0.2	-1.574918	-1.574920	-2.117896	-2.117900
				1		-0.665811	-0.665810	-0.985407	-0.985407
				2		-0.432015	-0.432023	-0.663082	-0.663083
				3		-0.321333	-0.321347	-0.503983	-0.503985
0.2	0.4	0.5	0.6	1	0	-0.390100	-0.390100	-0.618400	-0.618399
					0.05	-0.441792	-0.441791	-0.688175	-0.688175
					0.1	-0.503167	-0.503167	-0.770314	-0.770314
					0.15	-0.576723	-0.576723	-0.867974	-0.867974
					0.2	-0.665811	-0.665810	-0.985407	-0.985407

solution of radiative MHD Williamson nanofluid in a porous shrinking sheet with entropy generation. Rashidi et al. [33] deliberated the entropy analysis of MHD third-grade fluid on a stretching sheet. They found that the entropy generation exalts when escalating the Brinkman number. The 3D double-diffusive flow of power law fluid with entropy analysis was investigated by Zhu et al. [34]. Jain and Gupta [35] explored the 3D flow of water-based CNT nanofluid past a heated inclined porous stretching sheet with entropy generation. They exposed that the entropy generation number improves when growing the Biot and Reynolds numbers. The latest investigations for this concept are collected in Refs. [36–41].

The aforementioned literature studies divulge that none of them inspected the Darcy-Forchheimer flow of glycerin-based carbon nanotubes on a Riga plate subjected to heat absorption, slip, and convective heating condition. In addition,

our study includes entropy generation through different flow parameters inside the boundary layer flow. Our findings may find the applications in thermal extrusion phenomenon, cooling processes, oceanography, missile technology, and movement of biological fluids. Also, entropy generation plays a vital role in controlling the heat transfer rate in the proximity of a surface.

## 2. Mathematical Formulation

Let us contemplate the 3D Darcy-Forchheimer flow of glycerin-based carbon nanotubes over a Riga plate. There are two kinds of CNTs, like SWCNTs (single-wall carbon nanotubes) and MWCNTs (multiwall carbon nanotubes), which are considered. Let us choose  $x$ - and  $y$ -axes along with the plate, and  $z$  is perpendicular to the plate. Let  $u = ax$  and  $v = by$  be the velocity components in  $x$  and  $y$  directions. The

TABLE 6: The HAM and numerical values of local Nusselt number for diverse values of  $Ha$ ,  $c$ ,  $K$ ,  $\phi$ ,  $Hg$ ,  $R$ ,  $Bi$ ,  $\Gamma$ , and  $\Lambda$  for both CNTs.

Ha	c	K	$\phi$	Hg	R	Bi	$\Gamma$	$\Lambda$	$\frac{Nu}{\sqrt{Re}}$			
									SWCNTs		MWCNTs	
									Numerical	Analytical	Numerical	Analytical
0	0.6	1	0.2	-0.4	0.6	0.6	0.1	1.2	0.613593	0.613593	0.617908	0.617909
0.3									0.614827	0.614827	0.619235	0.619236
0.5									0.615577	0.615577	0.620041	0.620040
0.8									0.616613	0.616610	0.621154	0.621144
1									0.617254	0.617245	0.621841	0.621819
0.5	0.1	1	0.2	-0.4	0.6	0.6	0.1	1.2	0.611117	0.611118	0.615224	0.615225
	0.3								0.613118	0.613119	0.617379	0.617381
	0.5								0.614813	0.614814	0.619213	0.619214
	0.8								0.616973	0.616971	0.621556	0.621550
	1								0.618229	0.618225	0.622918	0.622906
0.5	0.6	0	0.2	-0.4	0.6	0.6	0.1	1.2	0.623712	0.623714	0.628428	0.628455
		1							0.615577	0.615577	0.620041	0.620040
		2							0.612416	0.612419	0.616674	0.616679
		3							0.610610	0.610612	0.614730	0.614735
0.5	0.6	1	0	-0.4	0.6	0.6	0.1	1.2	0.858530	0.858694	0.858530	0.858694
			0.05						0.713177	0.713261	0.720184	0.720290
			0.1						0.659079	0.659103	0.665538	0.665574
			0.15						0.631681	0.631685	0.637077	0.637084
0.5	0.6	1	0.2	-0.4	0.6	0.6	0.1	1.2	0.615577	0.615577	0.620040	0.620041
				-0.2					0.604723	0.604726	0.609498	0.609511
				-0.1					0.596760	0.596745	0.601962	0.601933
				0					0.585550	0.585552	0.591691	0.591621
				0.1					0.567896	0.567951	0.576447	0.576599
				0.2					0.532889	0.532766	0.550123	0.550314
0.5	0.6	1	0.2	-0.4	0	0.6	0.1	1.2	0.539505	0.539505	0.538442	0.538442
					0.3				0.577581	0.577581	0.579289	0.579288
					0.5				0.602920	0.602920	0.606467	0.606467
					0.8				0.640862	0.640863	0.647156	0.647155
					1				0.671718	0.666112	0.674229	0.674228
0.5	0.6	1	0.2	-0.4	0.6	-0.6	0.1	1.2	-0.769998	-0.769998	-0.778918	-0.778920
						-0.3			-0.362449	-0.362449	-0.366205	-0.366205
						0			0	0	0	0
						0.3			0.324160	0.324160	0.326820	0.326819
						0.6			0.615577	0.615577	0.620041	0.620040
0.5	0.6	1	0.2	-0.4	0.6	0.6	0	1.2	0.610956	0.610956	0.614983	0.614983
							0.2		0.617979	0.617979	0.622673	0.622672
							0.4		0.622974	0.622975	0.628155	0.628154
							0.6		0.630976	0.630976	0.636956	0.636956
							0.8		0.636674	0.636675	0.643239	0.643239
0.5	0.6	1	0.2	-0.4	0.6	0.6	0.1	1	0.615308	0.615309	0.619724	0.619721
								1.3	0.615858	0.615860	0.620374	0.620379
								1.5	0.616463	0.616472	0.621096	0.621122
								1.8	0.617147	0.617132	0.621896	0.621931
								2	0.617859	0.617839	0.622685	0.622704

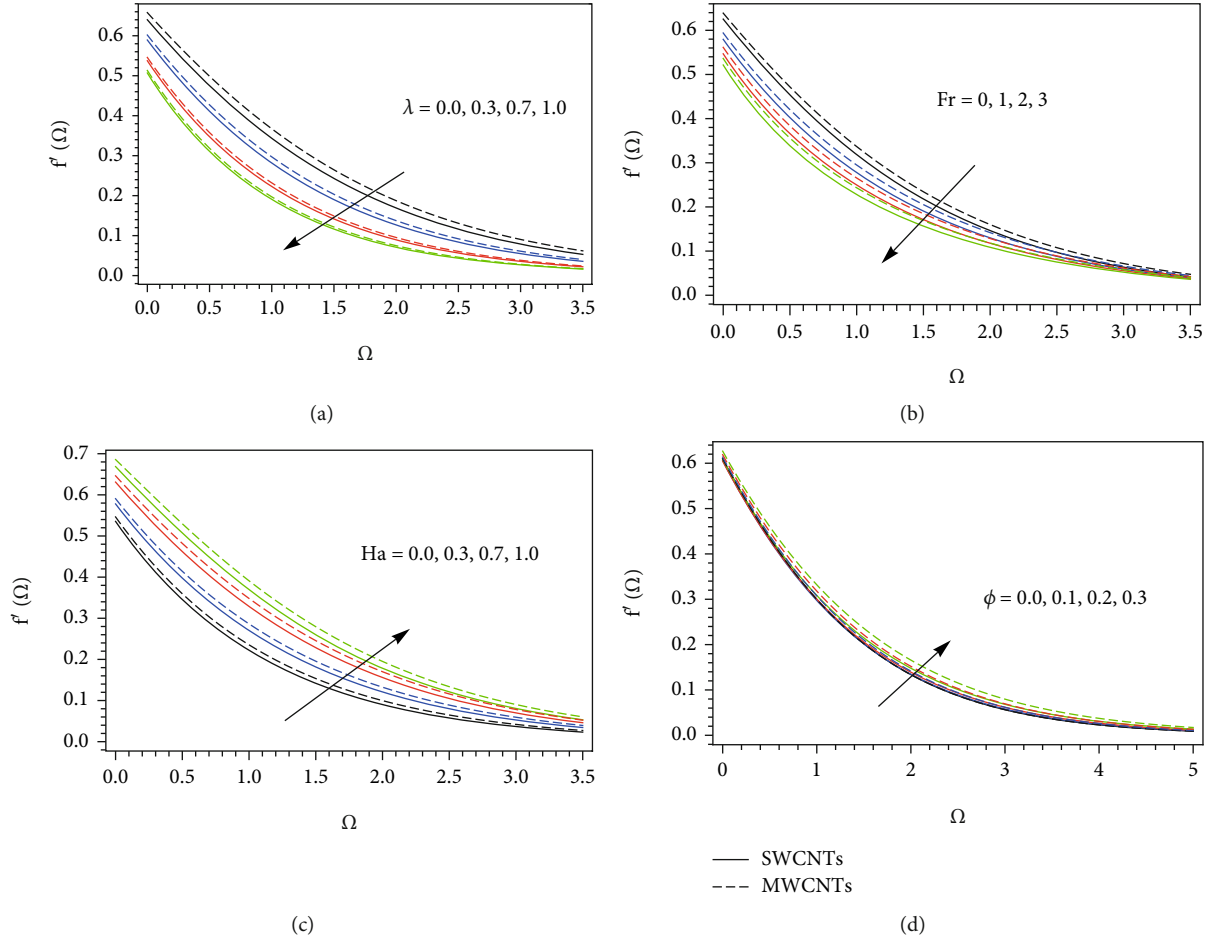


FIGURE 3: The  $x$ -direction velocity for distinct quantity of  $\lambda$  (a),  $Fr$  (b),  $Ha$  (c), and  $\phi$  (d).

fluid behaves heat consumption or generation (see Rana et al. [42]). The nonlinear thermal radiation is taken into account. The Fourier heat flux model was replaced by the Cattaneo-Christov model (see Punith Gowda et al. [43]). The underneath of the plate was convectively heated fluid by hot fluid with temperature  $T_f$ , and this generates heat transfer coefficient  $h_c$  (see Figure 1). Under the above considerations, the governing flow expression is as follows (see Hayat et al. [44–45] and Zeeshan et al. [46]):

$$\frac{\partial u}{\partial x} + \frac{\partial v}{\partial y} + \frac{\partial w}{\partial z} = 0, \quad (1)$$

$$u \frac{\partial u}{\partial x} + v \frac{\partial u}{\partial y} + w \frac{\partial u}{\partial z} = \nu_{nf} \frac{\partial^2 u}{\partial z^2} - \frac{\nu_{nf}}{k_1^*} u - Fu^2 + \frac{\pi J_0 M}{8 \rho_{nf}} \text{Exp} \left[ -\frac{\pi}{a_1} z \right], \quad (2)$$

$$u \frac{\partial v}{\partial x} + v \frac{\partial v}{\partial y} + w \frac{\partial v}{\partial z} = \nu_{nf} \frac{\partial^2 v}{\partial z^2} - \frac{\nu_{nf}}{k_1^*} v - Fv^2, \quad (3)$$

$$\begin{aligned} & u \frac{\partial T}{\partial x} + v \frac{\partial T}{\partial y} + w \frac{\partial T}{\partial z} \\ &= \alpha_{nf} \frac{\partial^2 T}{\partial z^2} + \frac{16\sigma^*}{3k^*(\rho c_p)_{nf}} \left[ T^3 \frac{\partial^2 T}{\partial y^2} + 3T^2 \left( \frac{\partial T}{\partial z} \right)^2 \right] \\ &+ \frac{Q}{(\rho c_p)_{nf}} (T - T_\infty) - \lambda \left[ u^2 \frac{\partial^2 T}{\partial x^2} + v^2 \frac{\partial^2 T}{\partial y^2} + w^2 \frac{\partial^2 T}{\partial z^2} \right. \\ &+ 2uv^2 \frac{\partial^2 T}{\partial x \partial y} + 2vw \frac{\partial^2 T}{\partial x \partial y} + 2wu \frac{\partial^2 T}{\partial z \partial x} \\ &+ \left( u \frac{\partial u}{\partial x} + v \frac{\partial u}{\partial y} + w \frac{\partial u}{\partial z} \right) \frac{\partial T}{\partial x} \\ &+ \left( u \frac{\partial v}{\partial x} + v \frac{\partial v}{\partial y} + w \frac{\partial v}{\partial z} \right) \frac{\partial T}{\partial y} \\ &+ \left. \left( u \frac{\partial w}{\partial x} + v \frac{\partial w}{\partial y} + w \frac{\partial w}{\partial z} \right) \frac{\partial T}{\partial x} \right], \end{aligned} \quad (4)$$

with interacted boundary conditions (see Hayat et al. [45])

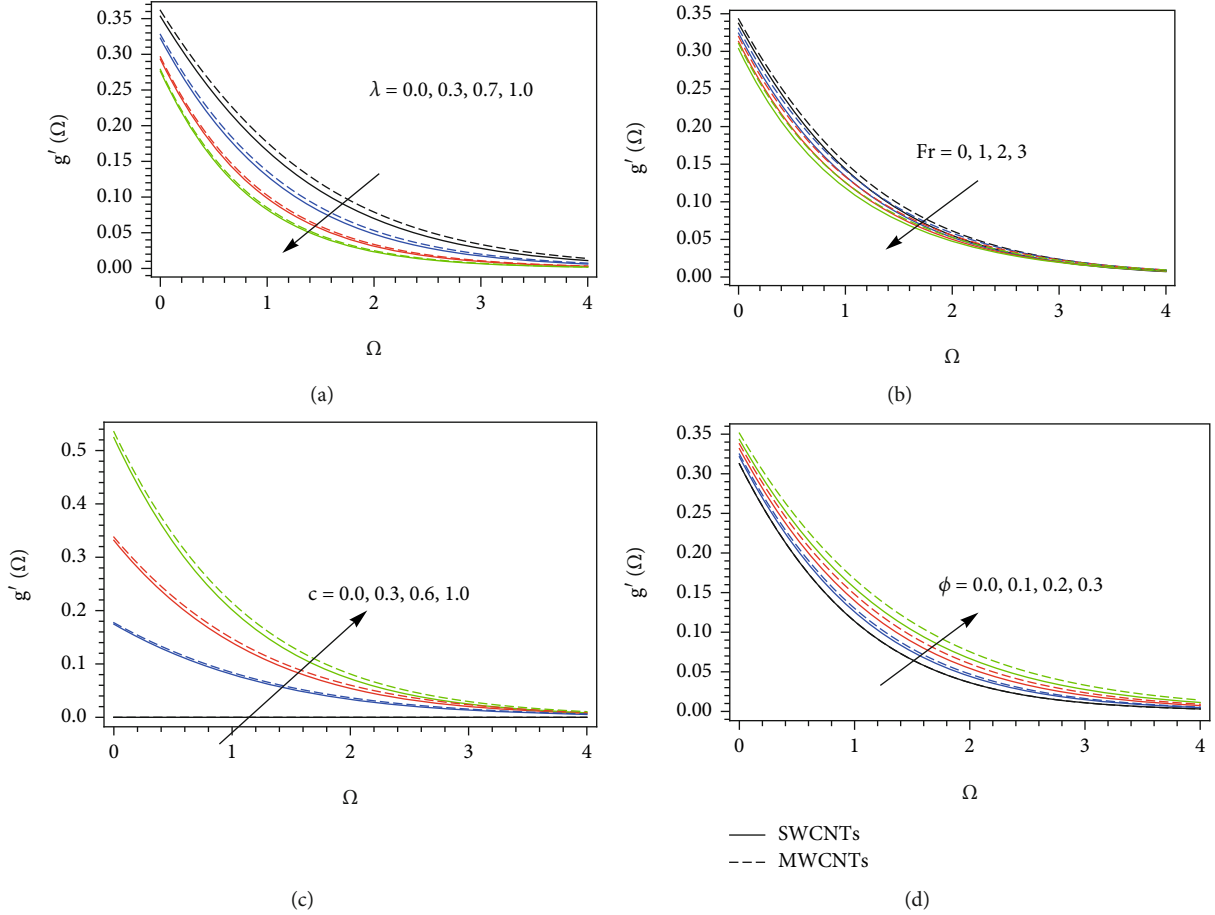


FIGURE 4: The  $y$ -direction velocity for distinct quantity of  $\lambda$  (a),  $Fr$  (b),  $c$  (c), and  $\phi$  (d).

and Subbarayudu et al. [47]):

$$u = U_w = ax + \frac{2 - \sigma_v}{\sigma_v} \lambda_0 \frac{\partial u}{\partial z}; v = V_w = by + \frac{2 - \sigma_v}{\sigma_v} \lambda_0 \frac{\partial v}{\partial z};$$

$$w = 0; -k_{nf} \frac{\partial T}{\partial z} = h_c [T_f - T] \text{ at } z = 0,$$

$$u \longrightarrow 0; v \longrightarrow 0; T \longrightarrow T_\infty \text{ as } z \longrightarrow \infty.$$

(5)

All notations are given in the nomenclature part.

The thermophysical properties of dynamic viscosity, density, heat capacitance of the nanofluid, thermal diffusivity, and thermal conductivity are mathematically expressed as

$$\frac{\mu_{nf}}{\mu_f} = \frac{1}{(1 - \phi)^{2.5}}; \frac{\rho_{nf}}{\rho_f} = 1 - \phi + \phi \frac{\rho_{CNT}}{\rho_f}; \frac{(\rho c_p)_{nf}}{(\rho c_p)_f} = 1 - \phi + \phi \frac{(\rho c_p)_{CNT}}{(\rho c_p)_f},$$

$$\alpha_{nf} = \frac{k_{nf}}{(\rho c_p)_{nf}}; \frac{k_{nf}}{k_f} = \frac{1 - \phi + 2\phi(k_{CNT}/(k_{CNT} - k_f)) \ln((k_{CNT} + k_f)/2k_f)}{1 - \phi + 2\phi(k_f/(k_{CNT} - k_f)) \ln((k_{CNT} + k_f)/2k_f)}.$$

(6)

Define

$$u = axf', v = ayg', w = -\sqrt{av_f}[f + g], \Omega = \sqrt{\frac{a}{v_f}}z, \theta = \frac{T - T_\infty}{T_f - T_\infty}.$$

(7)

Applying equation (7) in equations (2)–(4), we get

$$A_1 A_2 f'''' - f'^2 + [f + g]f'' - A_1 A_2 \lambda f' - Fr f'^2 + Ha A_2 \text{Exp}[-\beta \Omega] = 0,$$

(8)

$$A_1 A_2 g'''' - g'^2 + [f + g]g'' - A_1 A_2 \lambda g' - Fr g'^2 = 0,$$

(9)

$$\frac{A_3}{Pr A_4} \theta'' + [f + g]\theta' - \Gamma \left( [f + g]^2 \theta'' + [f + g] [f' + g'] \theta' \right) + \frac{Hg}{A_4} \theta + \frac{4}{3} R \frac{1}{A_4 Pr} \left[ (\Lambda - 1)^3 \theta^3 \theta'' + 3(\Lambda - 1)^3 \theta^2 \theta'^2 + 3(\Lambda - 1)^2 \theta^2 \theta'' + 6(\Lambda - 1)^2 \theta \theta'^2 + 3(\Lambda - 1) \theta \theta'' + 3(\Lambda - 1) \theta'^2 + \theta'^4 \right] = 0.$$

(10)

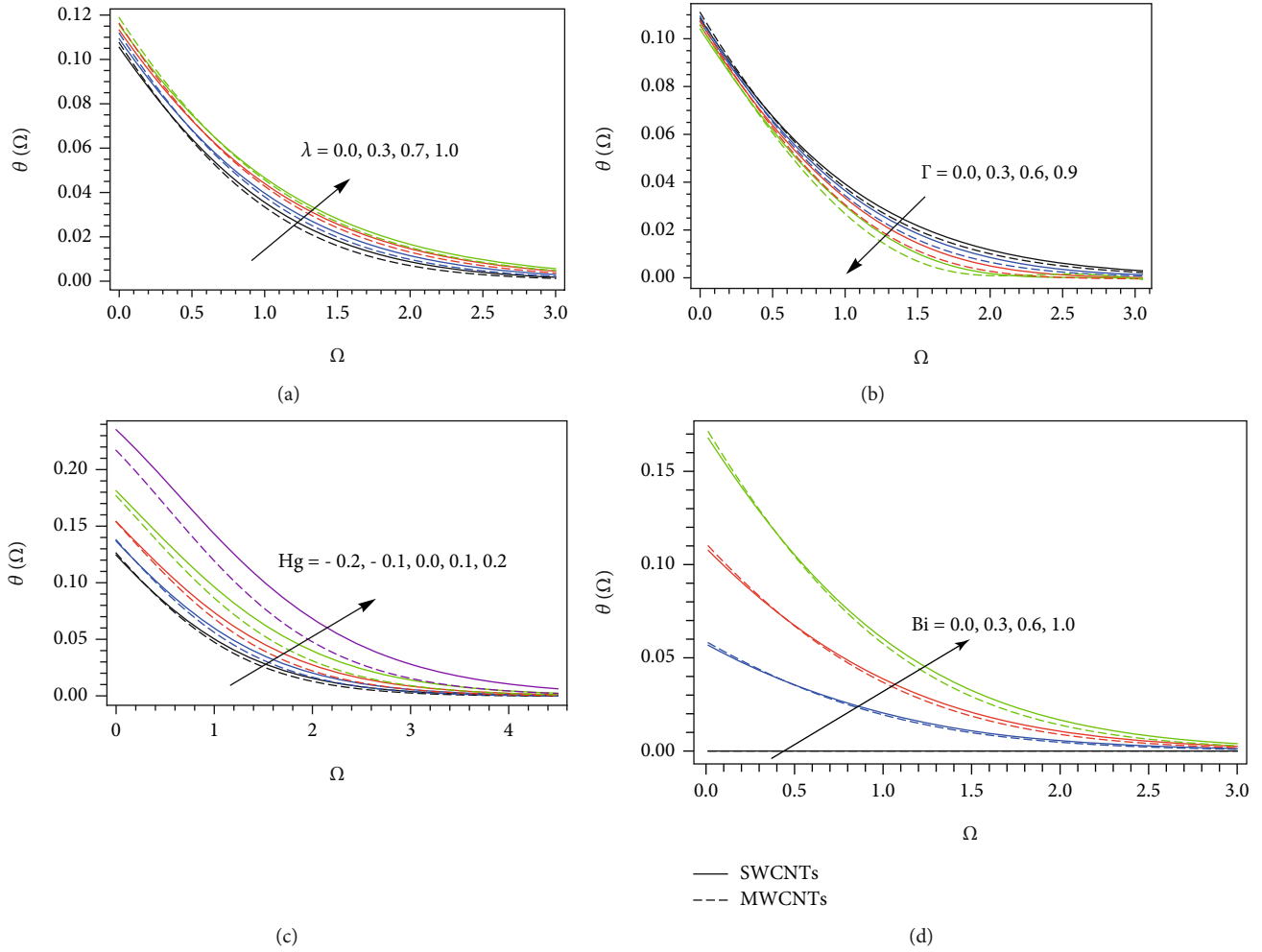


FIGURE 5: The temperature profile for distinct quantity of  $\lambda$  (a),  $\Gamma$  (b),  $Hg$  (c), and  $Bi$  (d).

The transferred boundary conditions are

$$f(0) = 0; f'(0) = 1 + Kf''(0); f'(\infty) = 0; g(0) = 0, \quad (11)$$

$$g'(0) = c + Kg''(0); g'(\infty) = 0; \theta'(0) = -\frac{Bi}{A_3} [1 - \theta(0)]; \theta(\infty) = 0. \quad (12)$$

All parameters are explained in Nomenclature. Here,

$$A_1 = \frac{1}{(1 - \phi)^{2.5}}; A_2 = \frac{1}{(1 - \phi) + \phi(\rho_{CNT}/\rho_f)},$$

$$A_3 = \frac{(1 - \phi) + 2\phi(k_{CNT}/(k_{CNT} - k_f)) \ln((k_{CNT} + k_f)/2k_f)}{(1 - \phi) + 2\phi(k_f/(k_{CNT} - k_f)) \ln((k_{CNT} + k_f)/2k_f)};$$

$$A_4 = (1 - \phi) + \phi \frac{(\rho c_p)_{CNT}}{(\rho c_p)_f}. \quad (13)$$

The skin friction coefficients and local Nusselt number are defined as follows:

$$Cf_x \sqrt{Re} = A_1 f''(0); Cf_y \sqrt{Re} = \frac{A_1}{c^{3/2}} g''(0); \frac{Nu}{\sqrt{Re}} = - \left[ A_3 + \frac{4}{3} R \{ 1 + (\Lambda - 1) \theta(0) \}^3 \right] \theta'(0). \quad (14)$$

### 3. Entropy Analysis

The entropy generation equation is expressed as (see Hayat et al. [44])

$$S_{gen} = \frac{k_f}{T_\infty^2} \left[ \frac{k_{nf}}{k_f} + \frac{16\sigma^* T^3}{3k_f k^*} \right] \left( \frac{\partial T}{\partial z} \right)^2 + \frac{\mu_{nf}}{T_\infty} (u^2 + v^2) + \frac{\mu_{nf}}{T_\infty} \left[ \left( \frac{\partial u}{\partial z} \right)^2 + \left( \frac{\partial v}{\partial z} \right)^2 \right]. \quad (15)$$

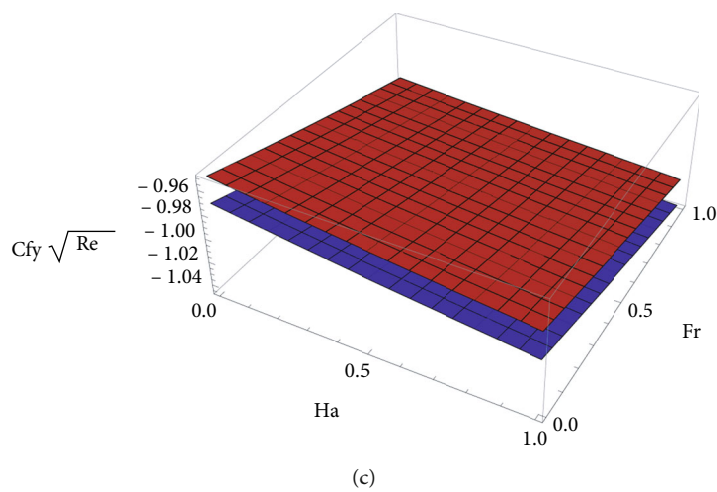
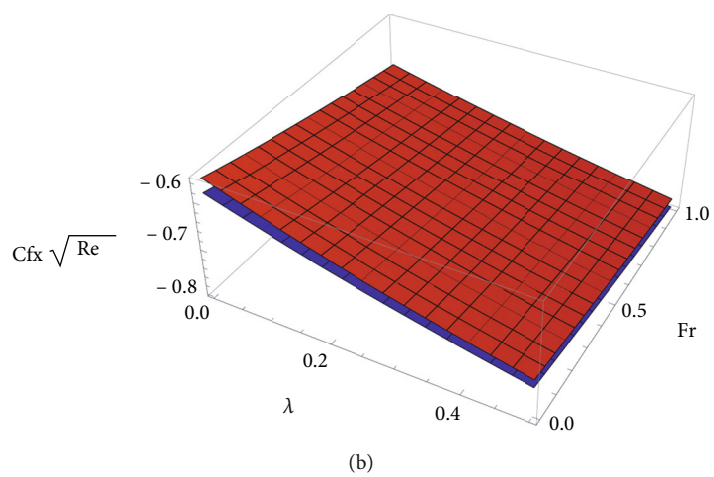
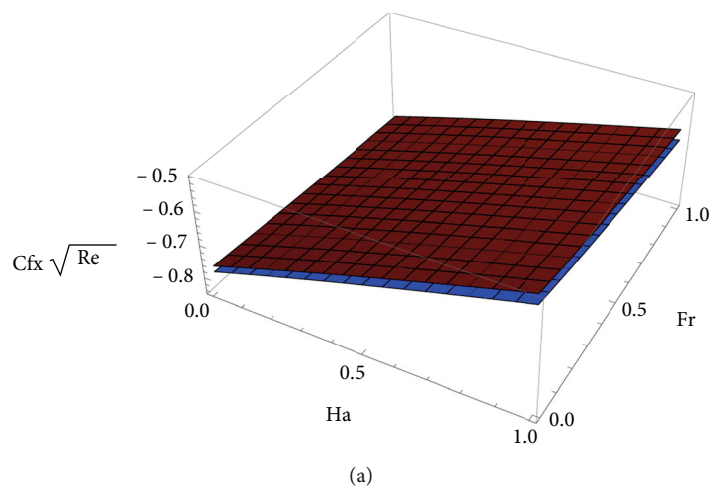


FIGURE 6: Continued.

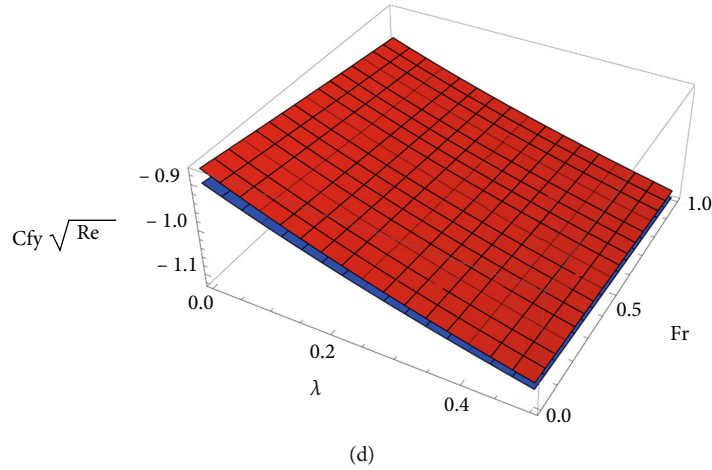


FIGURE 6: Skin friction coefficient (lower plate (SWCNTs) and upper plate (MWCNTs)) for different combinations of Ha, Fr, and  $\lambda$  on  $x$ -direction (a, b) and  $y$ -direction (c, d).

The converted EG equation is

$$\begin{aligned}
 EG = & A_3 \operatorname{Re} \theta'^2 + \frac{4}{3} R \operatorname{Re} \left[ (\Lambda - 1)^3 \theta^3 \theta'^2 + 3(\Lambda - 1)^2 \theta^2 \theta'^2 \right. \\
 & \left. + 3(\Lambda - 1) \theta \theta'^2 + \theta'^2 \right] + A_1 \operatorname{ReBr} \frac{\lambda}{\alpha_1} \left[ f'^2 + g'^2 \right] \\
 & + A_1 \operatorname{ReBr} \frac{1}{\alpha_1} \left[ f''^2 + g''^2 \right],
 \end{aligned}
 \tag{16}$$

where  $\operatorname{Re} = ax^2/\nu_f$  is the local Reynolds number,  $\operatorname{Br} = \mu_f a^2 x^2/k_f(T_f - T_\infty)$  is the Brinkman number, and  $\alpha_1 = (T_f - T_\infty)/T_\infty$  is the temperature difference parameter.

The Bejan number is expressed as

$$\begin{aligned}
 \operatorname{BN} = & \frac{\text{Entropy generation due to heat transfer}}{\text{Total entropy generation}}, \\
 \operatorname{BN} = & \frac{Z_1}{Z_2},
 \end{aligned}
 \tag{17}$$

where

$$\begin{aligned}
 Z_1 = & A_3 \operatorname{Re} \theta'^2 + \frac{4}{3} R \operatorname{Re} \left[ (\Lambda - 1)^3 \theta^3 \theta'^2 + 3(\Lambda - 1)^2 \theta^2 \theta'^2 \right. \\
 & \left. + 3(\Lambda - 1) \theta \theta'^2 + \theta'^2 \right], \\
 Z_2 = & A_3 \operatorname{Re} \theta'^2 + \frac{4}{3} R \operatorname{Re} \left[ (\Lambda - 1)^3 \theta^3 \theta'^2 + 3(\Lambda - 1)^2 \theta^2 \theta'^2 \right. \\
 & \left. + 3(\Lambda - 1) \theta \theta'^2 + \theta'^2 \right] + A_1 \operatorname{ReBr} \frac{\lambda}{\alpha_1} \left[ f'^2 + g'^2 \right] \\
 & + A_1 \operatorname{ReBr} \frac{1}{\alpha_1} \left[ f''^2 + g''^2 \right].
 \end{aligned}
 \tag{18}$$

### 4. Solutions

4.1. Numerical Solutions. The rechanged models ((8)-(10)) with the associated conditions (12) are numerically solved by applying the MATLAB `bvp4c` algorithm (see Rehman et al. [48] and Eswaramoorthi et al. [49]). To solve these equations, first, we convert higher ODE to first-order ODEs.

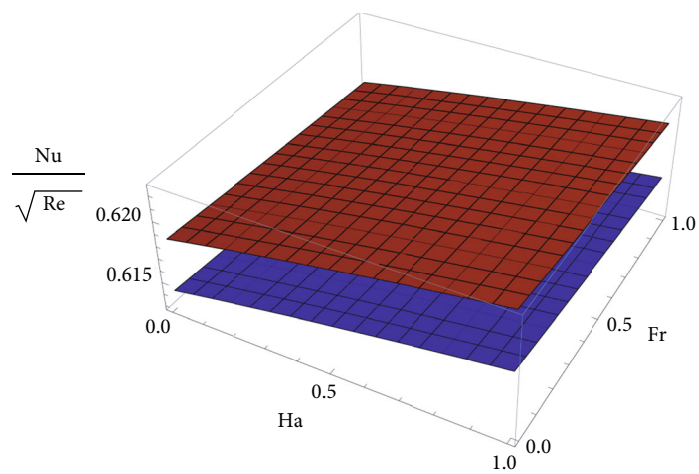
$$f = D_1, f' = D_2, f'' = D_3, g = D_4, g' = D_5, g'' = D_6, \theta = D_7, \theta' = D_8.
 \tag{19}$$

The systems of equations are

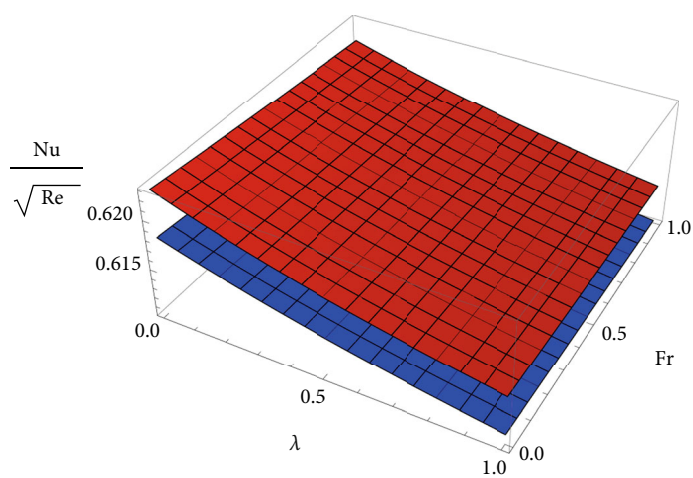
$$\begin{aligned}
 f' &= D_2, \\
 f'' &= D_3, \\
 f''' &= \frac{D_2^2 - (D_1 + D_4)D_3 - \operatorname{Ha}A_2 e^{-\beta\eta} + A_1A_2\lambda D_2 + \operatorname{Fr}D_2^2}{A_1A_2}, \\
 g' &= D_5, \\
 g'' &= D_6, \\
 g''' &= \frac{D_5^2 - (D_1 + D_4)D_6 + A_1A_2\lambda D_5 + \operatorname{Fr}D_5^2}{A_1A_2}, \\
 \theta' &= D_8, \\
 \theta'' &= \frac{P_1}{P_2},
 \end{aligned}
 \tag{20}$$

where

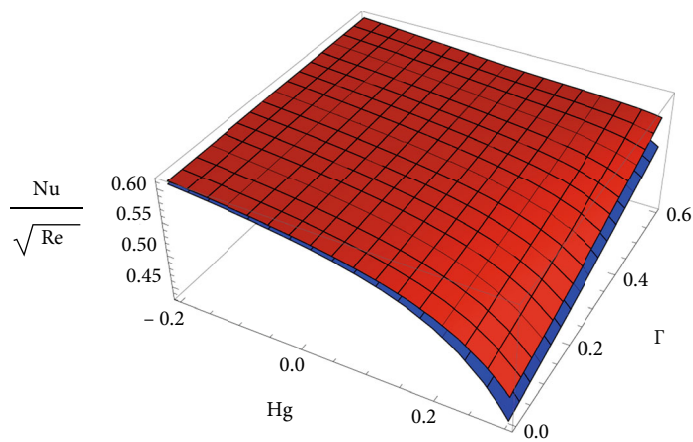
$$\begin{aligned}
 P_1 = & -\frac{1}{\operatorname{Pr}A_4} \frac{4}{3} R \left[ 3(\Lambda - 1)^3 D_7^2 D_8^2 + 6(\Lambda - 1)^2 D_7 D_8^2 + 3(\Lambda - 1) D_8^2 \right] \\
 & - (D_1 + D_4) D_8 + \Gamma(D_1 + D_4)(D_2 + D_5) D_8 - \frac{\operatorname{Hg}}{A_4} D_7, \\
 P_2 = & \frac{A_3}{\operatorname{Pr}A_4} - \Gamma(D_1 + D_4)^2 \\
 & + \frac{1}{\operatorname{Pr}A_4} \frac{4}{3} R \left[ (\Lambda - 1)^3 D_7^2 + 3(\Lambda - 1)^2 D_7^2 + 3(\Lambda - 1) D_7 + 1 \right].
 \end{aligned}
 \tag{21}$$



(a)



(b)



(c)

FIGURE 7: Continued.



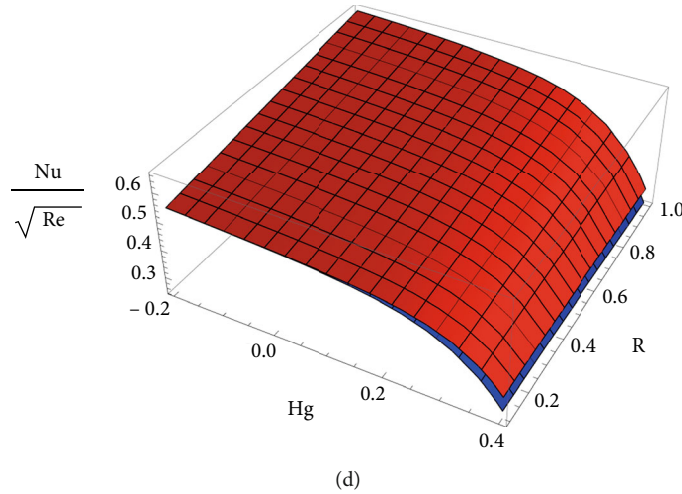


FIGURE 7: Local Nusselt number (lower plate (SWCNTs) and upper plate (MWCNTs)) for different combinations of Ha, Fr,  $\lambda$ , Hg,  $\Gamma$ , and R.

With the corresponding conditions,

$$\begin{aligned} D_1(0) = 0, D_2(0) = 1 + KD_3(0), D_2(\infty) = 0, \\ D_4(0) = 0, D_5(0) = c + KD_6(0), D_5(\infty) = 0, \\ D_8(0) = -\frac{Bi}{A_3}[1 - D_7(0)], D_7(\infty) = 0, \end{aligned} \quad (22)$$

**4.2. Analytical Solutions.** The nonlinear ODE models ((8)-(10)) with conditions (12) are analytically solved by implementing the HAM logic, because this method is a powerful tool for solving highly nonlinear problems (see Gul et al. [50], Islam et al. [51], Saeed et al. [52], and Khan et al. [53]). All computations are made by MATHEMATICA. Initially, we fix the initial approximation as  $f_0(\Omega) = (1/(1+K))(1 - (1/e^\Omega))$ ,  $g_0(\Omega) = (c/(1+K))(1 - (1/e^\Omega))$ , and  $\theta_0(\Omega) = Bi/(Bi + A_3)e^\Omega$ , and linear operators are  $L_f = D^3f - Df$ ,  $L_g = D^3g - Dg$ , and  $L_\theta = D^2\theta - \theta$ , where  $D$  is the differential operator, and the property  $L_f[X_1 + X_2e^\Omega + X_3(1/e^\Omega)] = 0 = L_g[X_4 + X_5e^\Omega + X_6(1/e^\Omega)] = L_\theta[X_7e^\Omega + X_8(1/e^\Omega)]$ , where  $X_k$  ( $k = 1 - 8$ ) are constants.

After substituting the  $M^{\text{th}}$ -order HAM, we have

$$\begin{aligned} f_M(\Omega) &= f_M^+(\Omega) + X_1 + X_2e^\Omega + X_3\frac{1}{e^\Omega}, \\ g_M(\Omega) &= g_M^+(\Omega) + X_4 + X_5e^\Omega + X_6\frac{1}{e^\Omega} \\ \theta_M(\Omega) &= \theta_M^+(\Omega) + X_7e^\Omega + X_8\frac{1}{e^\Omega}, \end{aligned} \quad (23)$$

where  $f_M^+(\Omega)$ ,  $\theta_M^+(\Omega)$ , and  $\phi_M^+(\Omega)$  are the particular solutions.

The HAM solutions contain the auxiliary parameters ( $h_f$ ,  $h_g$ , and  $h_\theta$ ), and these act as a key role for solution convergence (see Eswaramoorthi et al. [54] and Loganathan et al. [55]). In SWCNTs, the range values are  $-1.4 \leq h_f \leq -0.1$ ,  $-1.4 \leq h_g \leq -0.35$ , and  $-1.5 \leq h_\theta \leq -0.15$ , and MWCNTs are

$-1.3 \leq h_f \leq -0.1$ ,  $-1.15 \leq h_g \leq -0.1$ , and  $-1.35 \leq h_\theta \leq -0.25$  (see Figures 2(a)–2(c)). We fix  $h_f = h_g = h_\theta = -0.7$  for getting more accuracy in both CNTs.

## 5. Correlation Equations

The correlation equations are expressed using a recursion formula.

For SWCNTs,

$$Cfx\sqrt{\text{Re}} = -0.5751 - 1.7388\phi - 0.2239\lambda - 0.0653\text{Fr} \\ + 0.2325\text{Ha} - 0.0307c + 0.2032K,$$

$$Cfy\sqrt{\text{Re}} = -1.289 - 2.3097\phi - 0.2520\lambda - 0.0305\text{Fr} \\ - 0.0249\text{Ha} + 0.8516c + 0.2889K,$$

$$\begin{aligned} \frac{\text{Nu}}{\sqrt{\text{Re}}} &= -0.0276 - 0.7926\phi - 0.0124\lambda - 0.0045\text{Fr} + 0.0036\text{Ha} \\ &+ 0.0075c - 0.0052 - 0.1630\text{Hg} + 0.1238R + 1.1152\text{Bi}. \end{aligned} \quad (24)$$

For MWCNTs,

$$Cfx\sqrt{\text{Re}} = -0.5704 - 1.6028\phi - 0.243\lambda - 0.0646\text{Fr} \\ + 0.2433\text{Ha} - 0.03c + 0.1936K,$$

$$Cfy\sqrt{\text{Re}} = -1.2696 - 2.1782\phi - 0.2722\lambda - 0.0296\text{Fr} \\ - 0.0244\text{Ha} + 0.8372c + 0.2786K,$$

$$\begin{aligned} \frac{\text{Nu}}{\sqrt{\text{Re}}} &= 0.0299 - 0.8036\phi - 0.0084\lambda - 0.0020\text{Fr} + 0.0039\text{Ha} \\ &+ 0.0081c - 0.0034K - 0.1277\text{Hg} + 0.0443R + 1.1217\text{Bi}, \end{aligned} \quad (25)$$

where  $\phi \in [0, 0.3]$ ,  $\lambda, \text{Fr}, \text{Ha}, c \in [0, 1]$ ,  $K \in [0.5, 3]$ ,  $\text{Hg} \in [-0.6, 0.3]$ ,  $R \in [0, 2]$ , and  $\text{Bi} \in [-0.6, 0.6]$  with maximum error difference of 0.099.

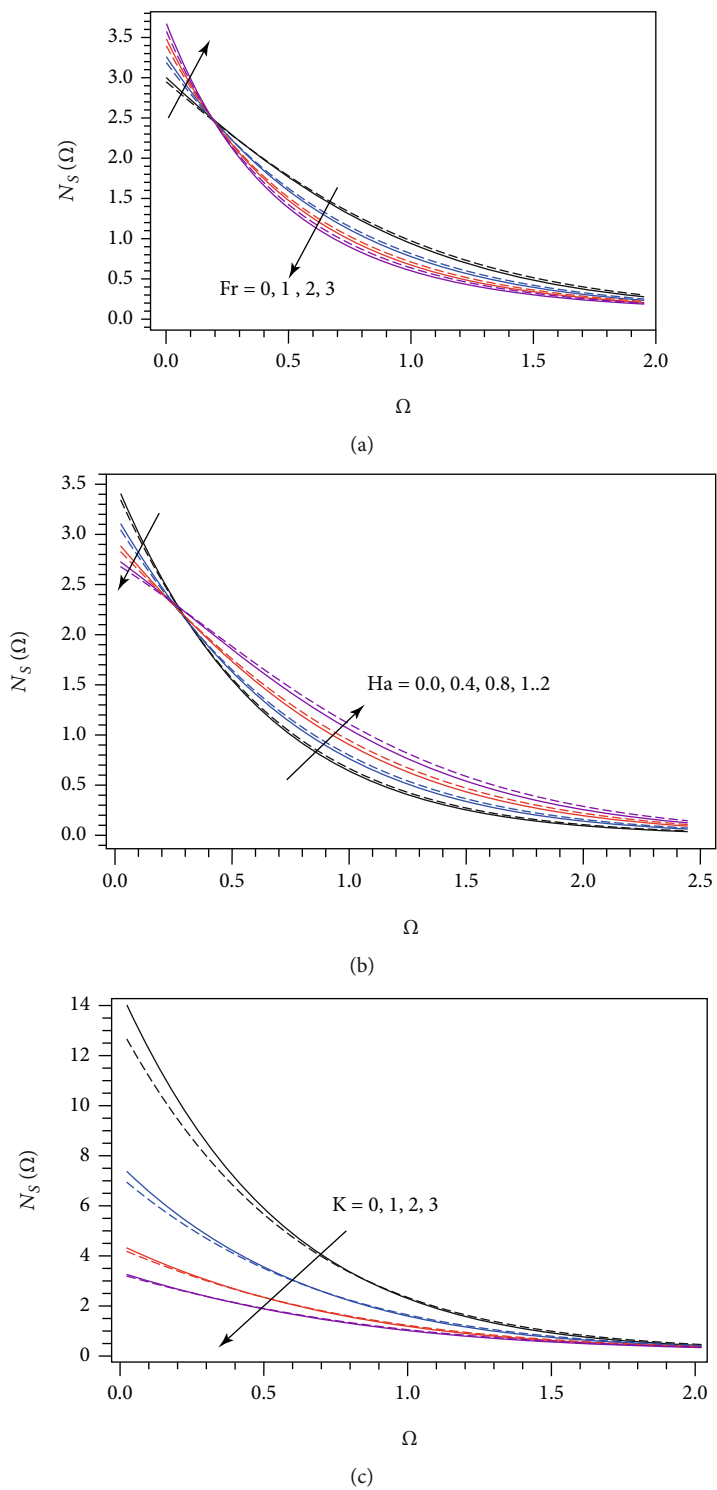


FIGURE 8: Continued.

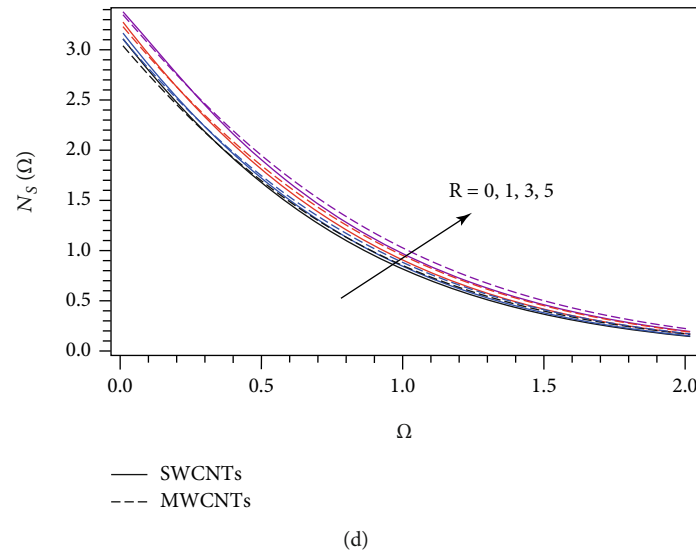


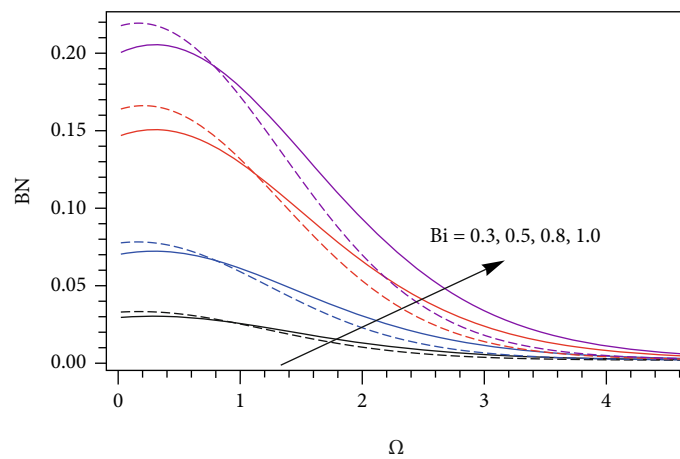
FIGURE 8: The entropy generation profile for distinct quantity of Fr (a), Ha (b),  $K$  (c), and  $R$  (d).

## 6. Results and Discussion

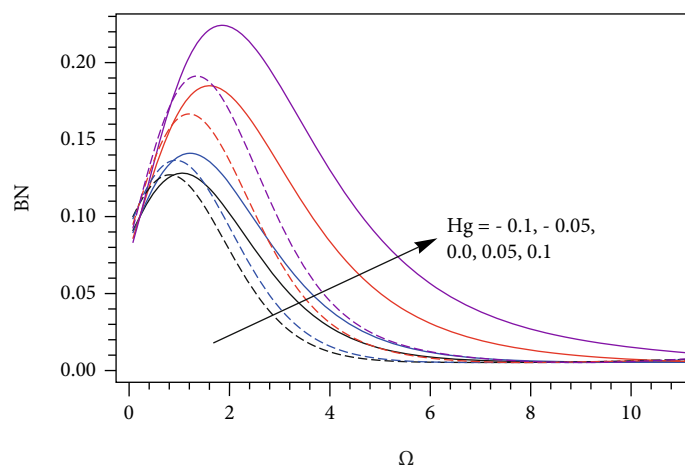
In this section, we explain the characteristics of flow parameters on velocity ( $f'(\Omega)$  and  $g'(\Omega)$ ), temperature ( $\theta(\Omega)$ ), skin friction coefficients ( $Cfx\sqrt{Re}$  and  $Cfy\sqrt{Re}$ ), local Nusselt number ( $Nu/\sqrt{Re}$ ), entropy generation ( $N_s(\Omega)$ ), and Bejan number (BN) through diagrams and tables. Table 1 provides the thermophysical properties of single-wall carbon nanotubes (SWCNTs), multiwall carbon nanotube (MWCNTs), and glycerin. The disparate order of HAM is presented in Table 2. From this table, we acknowledged that the 14<sup>th</sup> order is enough for all computations. The comparison of  $Cfx$  and  $Cfy$  with Hayat et al. [56] for different  $c$  values is illustrated in Table 3. It is seen that our numerical and HAM results are exactly matched with Hayat et al. [56] results. Tables 4 and 5 portrays the impact of  $\lambda$ , Fr, Ha,  $c$ ,  $K$ , and  $\phi$  on skin friction coefficients ( $Cfx\sqrt{Re}$  and  $Cfy\sqrt{Re}$ ) for both CNTs. It is detected that the surface drag force  $Cfx\sqrt{Re}$  decays when improving the quantity of  $\lambda$ , Fr,  $c$ , and  $\phi$ , and it enhances when raising the values of Ha and  $K$ . Also,  $Cfy\sqrt{Re}$  downfalls when strengthening the presence of  $\lambda$ , Fr, Ha, and  $\phi$ , and it improves when enriching the magnitude of  $c$  and  $K$  for both CNTs. The local Nusselt number for disparate values of Ha,  $c$ ,  $K$ ,  $\phi$ , Hg,  $R$ , Bi,  $\Gamma$ , and  $\Lambda$  for both CNTs is illustrated in Table 6. It proved that the heat transfer gradient upsurges for enlarging the Ha,  $c$ ,  $R$ ,  $\Gamma$ ,  $\Lambda$ , and Bi values, and it slumps when raising the values of  $K$ ,  $\phi$ , and Hg for both CNTs.

Figures 3(a)–3(d) display the consequences of  $\lambda$ , Fr, Ha, and  $\phi$  on the  $x$ -direction velocity profile. It is noticed that the  $x$ -direction velocity exalts when escalating the quantity of Ha and  $\phi$ , and its downfalls when raising the values of  $\lambda$  and Fr. The effectuates of  $\lambda$ , Fr,  $c$ , and  $\phi$  on the  $y$ -direction velocity profile are shown in Figures 4(a)–4(d). It is noted that the  $y$ -direction velocity surges when enhancing

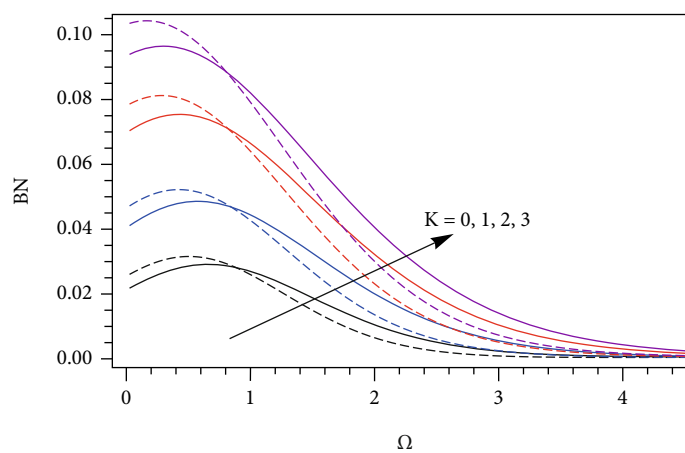
the amount of  $c$  and  $\phi$ , and it decays when raising the values of  $\lambda$  and Fr. Physically, the higher amount of porosity leads to enriching the fluid resistance, which suppresses the fluid motion and reduces the corresponding boundary layer thickness. From Figures 5(a)–5(d), it is concluded that the fluid temperature booms up when adding more quantities of  $\lambda$ , Hg, and Bi, and it weakens when strengthening the  $\Gamma$  values. The larger magnitude of the Biot number leads to enhancing the heat transfer coefficient, and this causes to reinforce the fluid warmth, which leads to the thickening of the thermal boundary layer. Figures 6(a)–6(d) illustrate the outcomes of Ha, Fr, and  $\lambda$  on skin friction coefficients ( $Cfx\sqrt{Re}$  and  $Cfy\sqrt{Re}$ ). It is seen that the  $Cfx\sqrt{Re}$  rises when raising the Ha values, and the opposite behavior was attained for more presence of Fr and  $\lambda$ . Also, Ha, Fr, and  $\lambda$  leads to suppressing the  $Cfy\sqrt{Re}$ . In addition, the surface shear stress is lower in SWCNTs than in MWCNTs. The local Nusselt number for different combinations of Ha, Fr,  $\lambda$ , Hg,  $\Gamma$ , and  $R$  is plotted in Figures 7(a)–7(d). It is proven that the heat transfer gradient ascents when enriching the Ha,  $\Gamma$ , and  $R$ , and it declines when increasing the  $\lambda$ , Fr, and Hg values. The larger values of the radiation parameter enhance the heat transfer rate from high-temperature places to low-temperature places, and this causes to rise in the heat transfer gradient. In addition, a higher heat transfer gradient occurs in MWCNTs compared to SWCNTs. Figures 8(a)–8(d) delineate the effects of Fr, Ha,  $K$ , and  $R$  on the entropy generation profile. It is noticed that the entropy generation profile increases (decreases) near the plate, and it diminishes (grows) away from the plate for changing the Fr (Ha) values. The entropy generation profile enhances when enriching the radiation parameter, and it weakens when raising the slip parameter. The variations of the Bejan number for disparate values of Bi, Hg,  $K$ , and  $R$  are presented in Figures 9(a)–9(d). It is exposed that the Bejan number progresses when upgrading the magnitude of Bi, Hg,  $K$ , and  $R$ .



(a)



(b)



(c)

FIGURE 9: Continued.

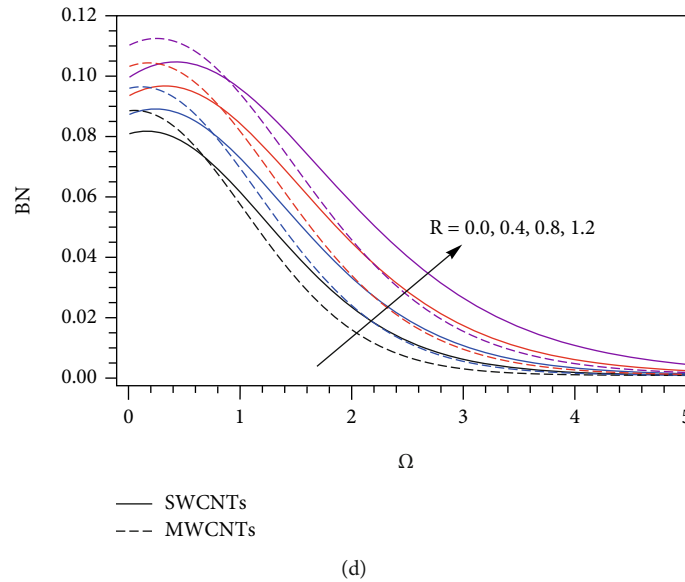


FIGURE 9: The Bejan number profile for distinct quantity of Bi (a), Hg (b), K (c), and R (d).

## 7. Conclusions

Here, we provide the impact of the Darcy-Forchheimer flow of glycerin-based carbon nanotubes with velocity slip over a heated Riga plate with heat absorption/generation. The Cattaneo-Christov heat flux theory is used to formulate the energy equation. In addition, nonlinear facets of radiation are also included in the energy expression. The obtained flow models are converted into an ODE model with the help of suitable variables. The ODE models are solved numerically and analytically by applying MATLAB bvp4c and HAM ideas, respectively. The main outputs of our investigation are summarized below:

- (i) The fluid motion in both directions is suppressed when adding more quantity of porosity parameter and Forchheimer number
- (ii) The fluid temperature aggravates when enriching the heat absorption/generation and convective heating parameters
- (iii) Both porosity parameter and Forchheimer number lead to curtailing the surface shear stress in both directions
- (iv) The thermal relaxation time parameter leads to exaggerating the heat transfer gradient, and heat absorption/generation parameters act opposite to the local Nusselt number
- (v) The thermal radiation parameter boosts up the entropy generation, and the slip parameter helps to cut down the entropy generation
- (vi) The Bejan number upgrades when there is more quantity of the Biot number and radiation parameter

## Nomenclature

$a, b:$	Positive constants ( $s^{-1}$ )
$\alpha:$	Thermal diffusivity ( $m^2 s^{-1}$ )
$a_1:$	Magnets positioned in the interval separating the electrodes (-)
$Cfx\sqrt{Re}$ & $Cfy\sqrt{Re}:$	Skin friction coefficients (-)
$c_p:$	Capacity of specific heat ( $m^2 s^{-2}$ ) $K^{-1}$
$F:$	Inertia coefficient of porous medium (-)
$h_c:$	Heat transfer coefficient (-)
$J_0:$	Current density applied to the electrodes ( $Am^{-2}$ )
$k^*:$	Thermal conductivity (-)
$M:$	Magnetic property of the permanent magnets that are organized on top of the plate surface ( $kg s^{-2} A^{-1}$ )
$nf, f:$	Subscript represents nanofluid and base fluid
$\nu:$	Kinematic viscosity ( $m^2 s^{-1}$ )
$\Omega:$	Dimensionless variable
$Q:$	Heat consumption/generation coefficient ( $Wm^{-3} K^{-1}$ )
$\rho:$	Fluid density ( $kg m^{-3}$ )
$T:$	Nondimensional temperature (K)
$T_f:$	Temperature of the hot fluid (K)
$T_w:$	Surface temperature (K)
$T_\infty:$	Ambient temperature (K)
$\tau_w:$	Surface shear stress
$\theta:$	Dimensionless temperature
$u, v, w:$	Velocity components
$U_w, V_w:$	Surface stretching velocities ( $m^2 s^{-1}$ )
$x, y, z:$	Cartesian coordinates (m)
$\alpha_1 (= T_f - T_\infty / T_\infty):$	Temperature difference parameter
$Bi (= (h_c / k_f) \sqrt{\nu_f / a}):$	Biot number

$\beta(= (\pi/a_1)\sqrt{v_f/a})$ :	Dimensionless parameter
$Br(= \mu_f a^2 x^2/k_f(T_f - T_\infty))$ :	Brinkman number
$Fr(= c_b/\sqrt{k_1^*})$ :	Forchheimer number
$\Gamma(= \lambda a)$ :	Thermal relaxation time parameter
$Ha(= \pi J_0 M/8\rho_f a^2 x)$ :	Modified Hartmann number
$Hg(= Q/(\rho c_p)_f a)$ :	Heat consumption/generation parameter
$\Lambda(= v_f/k_1^* a)$ :	Porosity parameter
$Pr(= (\mu c_p)_f/k_f)$ :	Prandtl number
$Re(= ax^2/v_f)$ :	Local Reynolds number.

### Abbreviations

HAM:	Homotopy analysis method
CNTs:	Carbon nanotubes
ODE:	Ordinary differential equations
MHD:	Magnetohydrodynamics
MWCNTs:	Multiwall carbon nanotubes
SWCNTs:	Single-wall carbon nanotubes.

### Data Availability

The raw data supporting the conclusions of this article will be made available by the corresponding author without undue reservation.

### Conflicts of Interest

The authors declare that they have no competing interests.

### Authors' Contributions

All authors contributed equally to this work. And all the authors have read and approved the final version manuscript.

### References

- [1] R. Kamali and A. R. Binesh, "Numerical investigation of heat transfer enhancement using carbon nanotube-based non-Newtonian nanofluids," *International Communications in Heat and Mass Transfer*, vol. 37, no. 8, pp. 1153–1157, 2010.
- [2] S. Harish, K. Ishikawa, E. Einarsson et al., "Enhanced thermal conductivity of ethylene glycol with single-walled carbon nanotube inclusions," *International Journal of Heat and Mass Transfer*, vol. 55, pp. 3885–3890, 2012.
- [3] R. U. Haq, S. Nadeem, Z. H. Khan, and N. F. M. Noor, "Convective heat transfer in MHD slip flow over a stretching surface in the presence of carbon nanotubes," *Physica B: Condensed Matter*, vol. 457, pp. 40–47, 2015.
- [4] D. Lu, M. Ramzan, S. Ahmad, J. D. Chung, and U. Farooq, "Upshot of binary chemical reaction and activation energy on carbon nanotubes with Cattaneo-Christov heat flux and buoyancy effects," *Physics of Fluids*, vol. 29, 2017.
- [5] A. U. Rehman, R. Mehmood, S. Nadeem, N. S. Akbar, and S. S. Motsa, "Effects of single and multi-walled carbon nanotubes on water and engine oil based rotating fluids with internal heating," *Advanced Powder Technology*, vol. 28, no. 9, pp. 1991–2002, 2017.
- [6] P. Sreedevi, P. S. Reddy, and A. J. Chamkha, "Magneto-hydrodynamics heat and mass transfer analysis of single and multi-wall carbon nanotubes over vertical cone with convective boundary condition," *International Journal of Mechanical Sciences*, vol. 135, pp. 646–655, 2018.
- [7] D. Lu, Z. Li, M. Ramzan, A. Shafee, and J. D. Chung, "Unsteady squeezing carbon nanotubes based nano-liquid flow with Cattaneo-Christov heat flux and homogeneous-heterogeneous reactions," *Applied Nanoscience*, vol. 9, no. 2, pp. 169–178, 2019.
- [8] M. Bilal, A. Saeed, T. Gul, I. Ali, W. Kumam, and P. Kumam, "Numerical approximation of microorganisms hybrid nano-fluid flow induced by a wavy fluctuating spinning disc," *Coatings*, vol. 11, no. 9, 2021.
- [9] T. Gul, M. Usman, I. Khan et al., "Magneto hydrodynamic and dissipated nanofluid flow over an unsteady turning disk," *Advances in Mechanical Engineering*, vol. 13, no. 7, 2021.
- [10] P. Forchheimer, "Wasserbewegung durch boden," *Zeitschrift für Acker und Pflanzenbau*, vol. 45, pp. 1782–1788, 1901.
- [11] S. A. Bakar, N. M. Arifin, R. Nazar, F. M. Ali, and I. Pop, "Forced convection boundary layer stagnation-point flow in Darcy-Forchheimer porous medium past a shrinking sheet," *Frontiers Heat and Mass Transfer*, vol. 7, no. 1, pp. 1–7, 2016.
- [12] J. C. Umavathi, O. Ojjela, and K. Vajravelu, "Numerical analysis of natural convective flow and heat transfer of nanofluids in a vertical rectangular duct using Darcy-Forchheimer-Brinkman model," *International Journal of Thermal Sciences*, vol. 111, pp. 511–524, 2017.
- [13] T. Hayat, F. Haider, T. Muhammad, and B. Ahmad, "Darcy-Forchheimer flow of carbon nanotubes due to a convectively heated rotating disk with homogeneous-heterogeneous reactions," *Journal of Thermal Analysis and Calorimetry*, vol. 137, no. 6, pp. 1939–1949, 2019.
- [14] M. Ramzan and N. Shaheen, "Thermally stratified Darcy Forchheimer nanofluid flow comprising carbon nanotubes with effects of Cattaneo-Christov heat flux and homogeneous-heterogeneous reactions," *Physica Scripta*, vol. 95, no. 1, 2020.
- [15] G. Rasool, A. Shafiq, M. S. Alqarni, A. Wakif, I. Khan, and M. S. Bhutta, "Numerical scrutinization of Darcy-Forchheimer relation in convective magnetohydrodynamic nanofluid flow bounded by nonlinear stretching surface in the perspective of heat and mass transfer," *Micromachines*, vol. 12, no. 4, p. 374, 2021.
- [16] M. K. Nayak, S. Shaw, M. I. Khan, V. S. Pandey, and M. Nazeer, "Flow and thermal analysis on Darcy-Forchheimer flow of copper-water nanofluid due to a rotating disk: a static and dynamic approach," *Journal of Materials Research and Technology*, vol. 9, no. 4, pp. 7387–7408, 2020.
- [17] A. Saeed, P. Kumam, T. Gul, W. Alghamdi, W. Kumam, and A. Khan, "Darcy-Forchheimer couple stress hybrid nanofluids flow with variable fluid properties," *Scientific Reports*, vol. 11, no. 1, pp. 1–13, 2021.
- [18] E. N. Maraj, Z. Khatoun, S. Ijaz, and R. Mehmood, "Effect of Arrhenius activation energy and medium porosity on mixed convective diluted ethylene glycol nanofluid flow towards a curved stretching surface," *International Communications in Heat and Mass Transfer*, vol. 129, pp. 1–9, 2021.
- [19] R. Mehmood, S. Khan, E. N. Maraj, S. Ijaz, and S. Rana, "Heat transport mechanism via ion-slip and hall current in

- viscoplastic flow along a porous elastic sheet,” *Proceedings of the Institution of Mechanical Engineers Part E: Journal of Process Mechanical Engineering*, 2021.
- [20] F. Mabood and K. Das, “Melting heat transfer on hydromagnetic flow of a nanofluid over a stretching sheet with radiation and second-order slip,” *The European Physical Journal Plus*, vol. 131, pp. 1–12, 2016.
- [21] M. Ramzan, J. Chung, and N. Ullah, “Radiative magnetohydrodynamic nanofluid flow due to gyrotactic microorganisms with chemical reaction and nonlinear thermal radiation,” *International Journal of Mechanical Sciences*, vol. 130, pp. 31–40, 2017.
- [22] M. Usman, M. Hamid, T. Zubair, R. U. Haq, and W. Wang, “Cu- $Al_2O_3$ /Water hybrid nanofluid through a permeable surface in the presence of nonlinear radiation and variable thermal conductivity via LSM,” *International Journal of Heat and Mass Transfer*, vol. 126, pp. 1347–1356, 2018.
- [23] H. Waqas, S. U. Khan, S. A. Shehzad, and M. Imran, “Significance of the nonlinear radiative flow of micropolar nanoparticles over porous surface with a gyrotactic microorganism, activation energy, and Nield’s condition,” *Heat Transfer-Asian Research*, vol. 48, no. 7, pp. 3230–3256, 2019.
- [24] S. U. Khan, S. A. Shehzad, A. Rauf, and Z. Abbas, “Thermally developed unsteady viscoelastic micropolar nanofluid with modified heat/mass fluxes: a generalized model,” *Physica A: Statistical Mechanics and its Applications*, vol. 550, article 123986, 2020.
- [25] Y. Li, H. Waqas, M. Imran, U. Farooq, F. Mallawi, and I. Tlili, “A numerical exploration of modified second-grade nanofluid with motile microorganisms, thermal radiation, and Wu’s slip,” *Symmetry*, vol. 12, no. 3, p. 393, 2020.
- [26] T. Muhammad, H. Waqas, S. A. Khan, R. Ellahi, and S. M. Sait, “Significance of nonlinear thermal radiation in 3D Eyring-Powell nanofluid flow with Arrhenius activation energy,” *Journal of Thermal Analysis and Calorimetry*, vol. 143, pp. 929–944, 2021.
- [27] M. I. Khan, H. Waqas, S. U. Khan et al., “Slip flow of micropolar nanofluid over a porous rotating disk with motile microorganisms, nonlinear thermal radiation and activation energy,” *International Communications in Heat and Mass Transfer*, vol. 122, article 105161, 2021.
- [28] U. Farooq, H. Waqas, M. I. Khan, S. U. Khan, Y. M. Chu, and S. Kadry, “Thermally radioactive bioconvection flow of Carreau nanofluid with modified Cattaneo-Christov expressions and exponential space-based heat source,” *Alexandria Engineering Journal*, vol. 60, no. 3, pp. 3073–3086, 2021.
- [29] Z. Shah, P. Kumam, and W. Deebani, “Radiative MHD Casson nanofluid flow with activation energy and chemical reaction over past nonlinearly stretching surface through entropy generation,” *Scientific Reports*, vol. 10, no. 1, pp. 1–14, 2020.
- [30] A. Bejan, “A study of entropy generation in fundamental convective heat transfer,” *Journal of Heat Transfer*, vol. 101, no. 4, pp. 718–725, 1979.
- [31] O. D. Makinde and A. S. Eegunjobi, “Entropy analysis of thermally radiating magneto-hydrodynamics slip flow of Casson fluid in a microchannel filled with saturated porous media,” *Journal of Porous Media*, vol. 19, no. 9, pp. 799–810, 2016.
- [32] M. M. Bhatti, T. Abbas, and M. M. Rashidi, “Numerical study of entropy generation with nonlinear thermal radiation on magnetohydrodynamics non-Newtonian nano fluid through a porous shrinking sheet,” *Journal of Magnetism*, vol. 21, pp. 468–475, 2016.
- [33] M. M. Rashidi, S. Bagheri, E. Momoniat, and N. Freidoonimehr, “Entropy analysis of convective MHD flow of third grade non-Newtonian fluid over a stretching sheet,” *Ain Shams Engineering Journal*, vol. 8, no. 1, pp. 77–85, 2017.
- [34] Q. Y. Zhu, Y. J. Zhuang, and H. Z. Yu, “Entropy generation due to three-dimensional double-diffusive convection of power-law fluids in heterogeneous porous media,” *International Journal of Heat and Mass Transfer*, vol. 106, pp. 61–82, 2017.
- [35] S. Jain and P. Gupta, “Entropy generation analysis of carbon nanotubes nanofluid 3D flow along a nonlinear inclined stretching sheet through porous media,” *International Journal of Heat and Technology*, vol. 37, no. 1, pp. 131–138, 2019.
- [36] M. Ramzan, M. Mohammad, F. Howari, and J. D. Chung, “Entropy analysis of carbon nanotubes based nanofluid flow past a vertical cone with thermal radiation,” *Entropy*, vol. 21, no. 7, p. 642, 2019.
- [37] M. Ramzan, M. Mohammad, and F. Howari, “Magnetized suspended carbon nanotubes based nanofluid flow with bioconvection and entropy generation past a vertical cone,” *Scientific Reports*, vol. 9, no. 1, pp. 1–15, 2019.
- [38] A. Khan, Z. Shah, E. Alzahrani, and S. Islam, “Entropy generation and thermal analysis for rotary motion of hydromagnetic Casson nanofluid past a rotating cylinder with Joule heating effect,” *International Communications in Heat and Mass Transfer*, vol. 119, article 104979, 2020.
- [39] S. Eswaramoorthi, S. Divya, M. Faisal, and N. Namgyel, “Entropy and Heat Transfer Analysis for MHD Flow of -Water-Based Nanofluid on a Heated 3D Plate with Nonlinear Radiation,” *Mathematical Problems in Engineering*, vol. 2022, Article ID 7319988, 14 pages, 2022.
- [40] K. Loganathan, K. Mohana, M. Mohanraj, P. Sakthivel, and S. Rajan, “Impact of third-grade nanofluid flow across a convective surface in the presence of inclined Lorentz force: an approach to entropy optimization,” *Journal of Thermal Analysis and Calorimetry*, vol. 144, no. 5, pp. 1935–1947, 2021.
- [41] P. Y. Xiong, Y. M. Chu, M. I. Khan, S. A. Khan, and S. Z. Abbas, “Entropy optimized Darcy-Forchheimer flow of Reiner-Philippoff fluid with chemical reaction,” *Computational and Theoretical Chemistry*, vol. 1200, article 113222, 2021.
- [42] S. Rana, R. Mehmood, and S. Nadeem, “Bioconvection through interaction of Lorentz force and gyrotactic microorganisms in transverse transportation of rheological fluid,” *Journal of Thermal Analysis and Calorimetry*, vol. 145, no. 5, pp. 2675–2689, 2021.
- [43] R. J. Punith Gowda, F. S. Al-Mubaddel, R. Naveen Kumar et al., “Computational modelling of nanofluid flow over a curved stretching sheet using Koo-Kleinstreuer and Li (KKL) correlation and modified Fourier heat flux model,” *Chaos, Solitons and Fractals*, vol. 145, article 110774, 2021.
- [44] T. Hayat, M. I. Khan, T. A. Khan, M. I. Khan, S. Ahmad, and A. Alsaedi, “Entropy generation in Darcy-Forchheimer bidirectional flow of water-based carbon nanotubes with convective boundary condition,” *Journal of Molecular Liquids*, vol. 265, pp. 629–638, 2018.
- [45] T. Hayat, M. Imtiaz, A. Alsaedi, and M. A. Kutbi, “MHD three-dimensional flow of nanofluid with velocity slip and nonlinear thermal radiation,” *Journal of Magnetism and Magnetic Materials*, vol. 396, no. 15, pp. 31–37, 2015.
- [46] A. Zeeshan, Z. Ali, M. R. Gorji, F. Hussain, and S. Nadeem, “Flow analysis of biconvective heat and mass transfer of two-dimensional couple stress fluid over a paraboloid of

- revolution,” *International Journal of Modern Physics B*, vol. 34, no. 11, 2020.
- [47] K. Subbarayudu, S. Suneetha, P. Bala Anki Reddy, and A. M. Rashad, “Framing the activation energy and binary chemical reaction on CNT’s with Cattaneo-Christov heat diffusion on Maxwell nanofluid in the presence of nonlinear thermal radiation,” *Arabian Journal for Science and Engineering*, vol. 44, no. 12, pp. 10313–10325, 2019.
- [48] A. Rehman, Z. Salleh, and T. Gul, “Heat transfer of thin film flow over an unsteady stretching sheet with dynamic viscosity,” *Journal of Advanced Research in Fluid Mechanics and Thermal Sciences*, vol. 81, no. 2, pp. 67–81, 2021.
- [49] S. Eswaramoorthi, N. Alessa, M. Sangeethavaanee, S. Kayikci, and N. Namgyel, “Mixed convection and thermally radiative flow of MHD Williamson nanofluid with Arrhenius activation energy and Cattaneo-Christov heat-mass flux,” *Journal of Mathematics*, vol. 2021, Article ID 2490524, 16 pages, 2021.
- [50] T. Gul, M. Rehman, A. Saeed et al., “Magnetohydrodynamic impact on Carreau thin film couple stress nanofluid flow over an unsteady stretching sheet,” *Mathematical Problems in Engineering*, vol. 2021, Article ID 8003805, 10 pages, 2021.
- [51] S. Islam, A. Khan, P. Kumam et al., “Radiative mixed convection flow of Maxwell nanofluid over a stretching cylinder with Joule heating and heat source/sink effects,” *Scientific Reports*, vol. 10, pp. 1–18, 2020.
- [52] A. Saeed, P. Kumam, S. Nasir, T. Gul, and W. Kumam, “Non-linear convective flow of the thin film nanofluid over an inclined stretching surface,” *Scientific Reports*, vol. 11, no. 1, pp. 1–15, 2021.
- [53] A. Khan, A. Saeed, A. Tassaddiq et al., “Bio-convective and chemically reactive hybrid nanofluid flow upon a thin stirring needle with viscous dissipation,” *Scientific Reports*, vol. 11, no. 1, 2021.
- [54] S. Eswaramoorthi, N. Alessa, M. Sangeethavaanee, and N. Namgyel, “Numerical and Analytical Investigation for Darcy-Forchheimer Flow of a Williamson Fluid over a Riga Plate with Double Stratification and Cattaneo-Christov Dual Flux,” *Advances in Mathematical Physics*, vol. 2021, Article ID 1867824, 15 pages, 2021.
- [55] K. Loganathan, N. Alessa, K. Tamilvanan, and F. S. Alshammari, “Significances of Darcy-Forchheimer porous medium in third-grade nanofluid flow with entropy features,” *The European Physical Journal Special Topics*, vol. 230, no. 5, pp. 1293–1305, 2021.
- [56] T. Hayat, F. Haider, T. Muhammad, and A. Alsaedi, “Darcy-Forchheimer three-dimensional flow of carbon nanotubes with nonlinear thermal radiation,” *Journal of Thermal Analysis and Calorimetry*, vol. 140, no. 6, pp. 2711–2720, 2020.



## Research Article

# Analysis of Natural Convection in Nanofluid Flow through a Channel with Source/Sink Effect

Imran Siddique <sup>1</sup>, Kashif Sadiq,<sup>1</sup> Fahd Jarad <sup>2,3,4</sup>, Mohammed K. Al Mesfer,<sup>5</sup> Mohd Danish,<sup>5</sup> and Sonia Yaqoob<sup>1</sup>

<sup>1</sup>Department of Mathematics, University of Management and Technology, Lahore 54770, Pakistan

<sup>2</sup>Department of Mathematics, Cankaya University, 06790, Etimesgut, Ankara, Turkey

<sup>3</sup>Department of Mathematics, King Abdulaziz University, Jeddah, Saudi Arabia

<sup>4</sup>Department of Medical Research, China Medical University Hospital, China Medical University, Taichung, Taiwan

<sup>5</sup>Chemical Engineering Department, College of Engineering, King Khalid University, Abha, Saudi Arabia

Correspondence should be addressed to Fahd Jarad; [fahd@cankaya.edu.tr](mailto:fahd@cankaya.edu.tr)

Received 9 November 2021; Revised 22 February 2022; Accepted 6 April 2022; Published 4 May 2022

Academic Editor: Taza Gul

Copyright © 2022 Imran Siddique et al. This is an open access article distributed under the Creative Commons Attribution License, which permits unrestricted use, distribution, and reproduction in any medium, provided the original work is properly cited.

In this study, the natural convection nanofluids flow through a channel formed by two vertical parallel plates having distance  $d$  between them has been examined under the influence of the ramped velocity. Sodium alginate is considered as base fluid, and nanoparticles of titania ( $\text{TiO}_2$ ) and alumina ( $\text{Al}_2\text{O}_3$ ) are added to it. Analytical and semianalytical results for temperature and velocity profiles are obtained with Laplace transform and inverse Laplace algorithms (Tzou, Stehfest, Talbot, Honig and Hirdes, and Fourier series), respectively. Furthermore, the impacts of nanoparticles, Prandtl number, heat absorption, and time on velocity and temperature are drawn graphically and discussed. The outcomes show that the high thermal conductivity of particles increases the temperatures, and the high density of particles decreases the velocities of the nanofluids. The current findings are compared to previous findings in the literature. In the tables, the effect of volume fraction on Nusselt numbers and skin frictions is explored.

## 1. Introduction

The study of viscous fluid between parallel plates is significant due to its vast applications in the science and engineering fields. Sahebi et al. [1] presented the analysis of the free convection non-Newtonian nanofluid flow in a vertical channel numerically and described its significance. Many engineers studied the flow of non-Newtonian fluids with constant physical properties and heat transport, manipulating problems related to fluid mechanics and heat transfer. Adesanya [2] studied the unsteady free convection flow with absorbing generation between two infinite parallel plates with a temperature jump and velocity slip in the slip flow regime. Boulama and Galanis [3] provided the exact results for mixed convection nanofluid flow between two plates with mass and heat transfer. Ajibade

and Bichi [4] studied an unsteady incompressible convective fluid flow that is optically dense through an upright channel due to the collective effect of thermal radiation and variable viscosity and concluded that by increasing the viscosity variation parameters and thermal radiation, the velocity of fluid increases and temperature also increases with a boost in thermal radiation. Rajkumar et al. [5] investigated the numerical results of the inner convection of heat sources in tandem planar. Nada [6] studied the heat transport rate of free convection flow in horizontally and vertically closed narrow heated finned base plates, and the outcomes confirmed that the fins increase the rate of heat exchange with fin array geometries. Usually, the concentration disparity in the mass transfer influences the rate of heat relocation. The buoyancy effects are the driving forces for natural convection.

Several researchers discussed their work on nanofluids. The idea of nanofluid was given by Eastman and Choi [7]. Nanofluid allocates the fluid in which the nanoparticles are hanging in the traditional fluid. Because of the rapid advancement of nanotechnology [8], various models of nanofluids are being implemented in the field of thermal engineering. So nanofluid shows more effective thermal conductivity as compared with the base fluid. Suspended components raise thermal conduction and heat conveyance processes as the solid bimetallic particles bear more calorific conductivity than the base fluid. High viscosity and more static with better diffusion, wetting, and propagation through solid aerofoils, even for minor nanoparticle addition, are significant features of nanofluids [9]. Nanofluids are comprised of super-fine nanoparticles (size < 100 nm) mixed in water or organic solvent [10].

Generally, nanoparticles of chemically stable materials like copper (Cu), gold (Au), silicon oxide ( $\text{SiO}_2$ ) or silica, zirconium oxide ( $\text{ZrO}_2$ ), titania ( $\text{TiO}_2$ ), copper oxide (CuO), alumina ( $\text{Al}_2\text{O}_3$ ), metallic nitrides (SiN, AlN), and carbon nanotubes (CNTs) are used. These solid-liquid specks quickly drop down, filled the flow ducts, serious pressure failure, and causing erosion of pipelines. Therefore because of these defects, ordinary solid-fluid fusions for heat change at micro levels are used instead of nanofluids. Nanofluids can increase critical temperatures and surfactants, or standard emulsifiers cannot increase thermal conductivity. Cooling plays important role in providing comfort for required functioning and well-founded results of developing products especially computers, electronic circuits, X-ray generators, automobile engines, high energy lasers, etc. Improvement of heat transfer characteristics of nanofluids stimulates the attainable development in the heating system or consignment and heat flows caused by power in small-scaled products elevated its applications in defensive structure, microelectronics, fabricating, transportation, metrology, and engine cooling system.

The researchers have conducted extensive studies in this field. Some investigations are experimental, while others are computational, and only a small amount of research has been undertaken on the analytical side. The efficacy of carbon nanostructures and water-based nanofluids as coolants was investigated by Halefadi et al. [11]. They looked at how low nanoparticle volume fractions (varying from 0.0055% to 0.278%) affected nanofluid density, thermal conductivity, and viscosity.

Solar thermal devices' efficiency and performance could be improved. The use of nanotechnology in solar collectors has been the subject of extensive research. Solar cells are heat engines that capture sunlight and transmit the heat to a liquid running past them. Tyagi et al. [12] discovered that adding nanoparticles to a collector improves its efficiency. His findings reveal that by changing the volume fraction from 0.1% to 2% and the size of the fraction, the efficiency increases dramatically. When compared to water, Yousefi et al. [13] discovered that nanofluid (with 0.2% wt.) had a higher efficiency. When they added surfactant to their trials, they saw a 15.63% improvement [14, 15], and the references therein include examples of nanoparticles in solar energy applications.

Fluid flow and linked mass and energy transmission through a channel have received less attention than the situation of a single plate. This design may be found in a wide range of fields, such as petroleum reservoirs, fire engineering, combustion modeling, and nuclear energy, to name a few. Many engineering systems show transport phenomena that combine the effects of concentration and thermal buoyancy. Modern thermal protection devices, chemical distilleries, building ventilation systems, solar panels, heat exchangers, and electric circuits all contain them [16, 17]. Gupta et al. [18] used Marangoni convection to study the flow of two separate nanofluids over a stretched surface in a porous medium. Gohar et al. [19] investigated a Darcy-Forchheimer flow of Casson hybrid nanofluid via a curved surface that was constantly growing. The viscous fluid flow in a porous medium is expressed by the Darcy-Forchheimer effect. Adnan et al. [20] investigated the flow of Cu-water and Cu-kerosene oil through two Riga plates, taking into account surface convection and radiation effects. Zaka Ullah et al. [21] studied the flow of a hybrid nanofluid in a diverging and a converging channel. The effects of ramped temperature, ramped concentration, chemical reaction, heat production, and magnetic force on Casson nanofluid flow via a conduit were studied by Sadiq et al. [22]. The influence of various fluid dynamical processes and flow geometry is the focus of the bulk of the study. In addition, the bulk of previous research was conducted using either experimental or numerical methods.

The energy storage devices are beneficial for regulating power and energy demand in concentrated solar power facilities. It is expected that increasing the capacity of materials used in total energy storage will increase their performance. As a result, the leading objective of this dissertation is to establish a solution to the problem of natural convection flow of two different nanofluids in a vertical channel under the influence of ramped velocity. Ramped wall velocity is useful to control the flow of the fluid. To the best of the author's knowledge, ramped velocity is not considered for this model. Sodium alginate (SA) is taken as a base fluid having nanoparticles of titania ( $\text{TiO}_2$ ) and alumina ( $\text{Al}_2\text{O}_3$ ) is studied. Analytical and semianalytical results for velocity field and temperature distribution are obtained by using the Laplace transform method and inverse numerical algorithms (Stehfest's [23], Tzou's [24], Talbot [25], Honig and Hirdes [26], and Fourier series [27]). Finally, the effects of nanoparticles, Prandtl number, heat absorption, and time on temperature and velocity profiles are graphically illustrated and discussed. The current findings are compared to previous findings in the literature. In the tables, the effect of volume fraction on Nusselt numbers and skin frictions is explored. The findings of this study are predicted to have a significant impact on solar thermal devices.

## 2. Mathematical Formulation

Consider the convective flow of two different nanofluids with ramped velocity in a vertical channel formed by two parallel infinite plates separated by a distance  $d$  in the presence of the source/sink effect. The left plate is considered

along the  $x'$ -axis as shown in Figure 1. At  $t' = 0$ , the nanofluid and plates are at rest at a moderate temperature  $T_0$ . At  $t' > 0$ , the right plate which is situated at  $y' = d$  begins to accelerate along  $x'$ -direction with  $A_0 t'$ , and temperatures of left and right plate are remained constant  $T_1$  and  $T_2$  ( $T_2 > T_1$ ), respectively. The slippage between nanoparticles and base fluid is neglected.

The heat and momentum are only the functions of  $y'$  and  $t'$  as the walls of the channel are extended infinitely. Sodium alginate (SA) is considered as a conventional base fluid having nanoparticles of titania ( $\text{TiO}_2$ ) and alumina ( $\text{Al}_2\text{O}_3$ ). The thermophysical characteristics of SA and nanoparticles are given in Table 1.

Under the above assumptions, the governing equations are [30]

$$\rho_{nf} \frac{\partial u'(y', t')}{\partial t'} = \mu_{nf} \frac{\partial^2 u'(y', t')}{\partial y'^2} + g(\rho\beta)_{nf} [T'(y', t') - T_1], \quad (1)$$

$$(\rho c_p)_{nf} \frac{\partial T'(y', t')}{\partial t'} = k_{nf} \frac{\partial^2 T'(y', t')}{\partial y'^2} - Q_0 [T'(y', t') - T_1], \quad (2)$$

with corresponding conditions

$$u'(y', 0) = 0, T'(y', 0) = T_1, 0 \leq y' \leq d, \quad (3)$$

$$u'(0, t') = 0, u'(d, t') = A_0 t', t' > 0, \quad (4)$$

$$T'(0, t') = T_1, T'(d, t') = T_2, t' > 0. \quad (5)$$

The thermal physical features of nanofluid are described by

$$\rho_{nf} = \varphi \rho_s + (1 - \varphi) \rho_f, \mu_{nf} (1 - \varphi)^{2.5} = \mu_f,$$

$$k_{nf} = \frac{(k_f - k_s)\varphi + 2k_f + k_s}{k_s - 2(k_f - k_s)\varphi + 2k_f} k_f,$$

$$\frac{(\rho\beta)_{nf}}{(\rho\beta)_f} = (1 - \varphi) + \varphi \frac{(\rho\beta)_s}{(\rho\beta)_f}, \frac{(\rho c_p)_{nf}}{(\rho c_p)_f} = (1 - \varphi) + \varphi \frac{(\rho c_p)_s}{(\rho c_p)_f}. \quad (6)$$

Introducing the following non-dimensional parameters into Eqs. (1)–(5).

$$u = \frac{u' v_f}{A_0 d^2}, y = \frac{y'}{d}, t = \frac{v_f}{d^2} t', T = \frac{T' - T_1}{T_2 - T_1}, \quad (7)$$

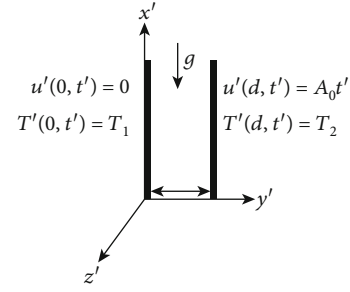


FIGURE 1: Flow geometry.

we get

$$\frac{\partial u(y, t)}{\partial t} = p_1 \frac{\partial^2 u(y, t)}{\partial y^2} + p_2 T(y, t), \quad (8)$$

$$\frac{\partial T(y, t)}{\partial t} = p_3 \frac{\partial^2 T(y, t)}{\partial y^2} - p_4 T(y, t), \quad (9)$$

with corresponding conditions,

$$T(y, 0) = 0, u(y, 0) = 0; 0 \leq y \leq 1, \quad (10)$$

$$T(0, t) = 0, u(0, t) = 0; t > 0, \quad (11)$$

$$T(1, t) = 1, u(1, t) = t; t > 0, \quad (12)$$

where

$$p_1 = \frac{\mu_{nf}}{\rho_{nf} v_f}, p_2 = Gr \frac{\beta_{nf}}{\beta_f}, p_3 = \frac{1}{Pr} \frac{k_{nf}}{k_f} \frac{(\rho c_p)_f}{(\rho c_p)_{nf}}, p_4 = Q \frac{(\rho c_p)_f}{(\rho c_p)_{nf}},$$

$$Gr = \frac{g(\beta)_f (T_2 - T_1)}{A_0}, Pr = \frac{v_f (\rho c_p)_f}{k_f}, Q = \frac{Q_0 d^2}{v_f (\rho c_p)_f}. \quad (13)$$

### 3. Solution of the Problem

3.1. Temperature Profile. Applying the Laplace transform into Eqs. (9), (11), and (12), using Eq. (10), we obtain

$$s \bar{T}(y, s) = p_3 \frac{\partial^2 \bar{T}(y, s)}{\partial y^2} - p_4 \bar{T}(y, s), \quad (14)$$

$$T(0, s) = 0, \bar{T}(1, s) = \frac{1}{s}. \quad (15)$$

Solution of Eq. (14) with the conditions in Eq. (15) is as

$$\bar{T}(y, s) = \frac{\sinh \sqrt{s + p_4/p_3} y}{s \sinh \sqrt{s + p_4/p_3}}, \quad (16)$$

TABLE 1: Thermophysical characteristics of nanoparticles and SA [28, 29].

Material	$k(\text{W/m.K})$	$\beta \times 10^5 (K^{-1})$	$C_p(\text{J/Kg.K})$	$\rho(\text{Kg/m}^3)$
Sodium alginate $\text{C}_6\text{H}_9\text{NaO}_7$ (SA)	0.6376	0.99	4175	989
Titania ( $\text{TiO}_2$ )	8.9538	0.90	686.2	4250
Alumina ( $\text{Al}_2\text{O}_3$ )	40	0.85	765	3970

TABLE 2: Variation of Nusselt numbers.

$\varphi$	$t$	$\text{TiO}_2$		$\text{Al}_2\text{O}_3$	
		$y=0$	$y=1$	$y=0$	$y=1$
0	0.5	-0.118	-2.989	-0.118	-2.989
0.01	0.5	-0.129	-3.024	-0.131	-3.031
0.05	0.5	-0.185	-3.164	-0.197	-3.198
0.10	0.5	-0.273	-3.344	-0.305	-3.413

or

$$\bar{T}(y, s) = \sum_{n=0}^{\infty} \left[ \frac{1}{s} \exp \left[ - \left( \frac{(2n+1)}{\sqrt{p_3}} - \frac{y}{\sqrt{p_3}} \right) \sqrt{s+p_4} \right] - \frac{1}{s} \exp \left[ - \left( \frac{(2n+1)}{\sqrt{p_3}} + \frac{y}{\sqrt{p_3}} \right) \sqrt{s+p_4} \right] \right]. \quad (17)$$

The inverse Laplace transform of Eq. (17) is

$$\begin{aligned} T(y, t) = & \frac{1}{2} \sum_{n=0}^{\infty} \exp \left( \frac{\sqrt{p_4}}{\sqrt{p_3}} (2n+1-y) \right) \\ & \cdot \left[ \operatorname{erfc} \left( \frac{2n+1-y}{2\sqrt{p_3 t}} + \sqrt{p_4 t} \right) \right. \\ & \left. + \operatorname{erfc} \left( \frac{2n+1-y}{2\sqrt{p_3 t}} + \sqrt{p_4 t} \right) \right] \\ & - \frac{1}{2} \sum_{n=0}^{\infty} \exp \left( \frac{\sqrt{p_4}}{\sqrt{p_3}} (2n+1+y) \right) \\ & \cdot \left[ \operatorname{erfc} \left( \frac{2n+1+y}{2\sqrt{p_3 t}} + \sqrt{p_4 t} \right) \right. \\ & \left. + \operatorname{erfc} \left( \frac{2n+1+y}{2\sqrt{p_3 t}} + \sqrt{p_4 t} \right) \right]. \end{aligned} \quad (18)$$

3.2. *Velocity Field.* Applying the Laplace transform to Eqs. (8), (11)<sub>2</sub>, and (12)<sub>2</sub>, using Eq. (10)<sub>2</sub>, we obtain

$$s\bar{u}(y, s) = p_1 \frac{\partial^2 \bar{u}(y, s)}{\partial y^2} + p_2 \bar{T}(y, s). \quad (19)$$

$$\bar{u}(0, s) = 0, \quad \bar{u}(1, s) = \frac{1}{s^2}. \quad (20)$$

Putting the value of  $\bar{T}(y, s)$  from Eq. (16) in Eq. (19), we have

$$s\bar{u}(y, s) = p_1 \frac{\partial^2 \bar{u}(y, s)}{\partial y^2} + p_2 \frac{\sinh \sqrt{s+p_4/p_3} y}{s \cdot \sinh \sqrt{s+p_4/p_3}}. \quad (21)$$

Solution of Eq. (21) with the conditions in Eq. (20) is as

$$\begin{aligned} \bar{u}(y, s) = & \frac{p_2 p_3 s + p_1 p_4 - (p_3 - p_1) s}{(p_1 p_4 - (p_3 - p_1) s) s^2} \frac{\sinh (y(\sqrt{s}/\sqrt{p_1}))}{\sinh (\sqrt{s}/\sqrt{p_1})} \\ & - \frac{p_2 p_3}{(p_1 p_4 - (p_3 - p_1) s) s} \frac{\sinh (y(\sqrt{s+p_4}/\sqrt{p_3}))}{\sinh (\sqrt{s+p_4}/\sqrt{p_3})}, \end{aligned} \quad (22)$$

or

$$\begin{aligned} \bar{u}(y, s) = & \frac{1}{s} \frac{\sinh ((y/\sqrt{p_1})\sqrt{s})}{s \cdot \sinh (\sqrt{s}/\sqrt{p_1})} - \frac{a_1}{s-a_2} \frac{\sinh ((y/\sqrt{p_1})\sqrt{s})}{s \cdot \sinh (\sqrt{s}/\sqrt{p_1})} \\ & + \frac{a_1}{s-a_2} \frac{\sinh ((\sqrt{s+p_4}/\sqrt{p_3})y)}{s \cdot \sinh (\sqrt{s+p_4}/\sqrt{p_3})}, \end{aligned} \quad (23)$$

where  $a_1 = p_2 p_3 / p_3 - p_1, a_2 = p_1 p_4 / p_3 - p_1$ .

The inverse Laplace transform of Eq. (23) is

$$\begin{aligned} u(y, t) = & (1 - a_1 e^{a_2 t}) * \sum_{n=0}^{\infty} \left[ \psi_n \left( \frac{y}{\sqrt{p_1}}, t, 0, \frac{1}{\sqrt{p_1}} \right) \right. \\ & \left. - \psi_n \left( -\frac{y}{\sqrt{p_1}}, t, 0, \frac{1}{\sqrt{p_1}} \right) \right] + (a_1 e^{a_2 t}) \\ & * \sum_{n=0}^{\infty} \left[ \psi_n \left( \frac{y}{\sqrt{p_3}}, t, p_4, \frac{1}{\sqrt{p_3}} \right) \right. \\ & \left. - \psi_n \left( -\frac{y}{\sqrt{p_3}}, t, p_4, \frac{1}{\sqrt{p_3}} \right) \right], \end{aligned} \quad (24)$$

where

$$\begin{aligned} \psi_n(x, \tau, y, z) = & \frac{1}{2} \left[ e^{-[(2n+1)z-x]\sqrt{\tau}} \operatorname{erfc} \left( \frac{(2n+1)z-x}{2\sqrt{\tau}} - \sqrt{y\tau} \right) \right. \\ & \left. + e^{[(2n+1)z-x]\sqrt{\tau}} \operatorname{erfc} \left( \frac{(2n+1)z-x}{2\sqrt{\tau}} + \sqrt{y\tau} \right) \right]. \end{aligned} \quad (25)$$

TABLE 3: Variation of skin frictions.

$\varphi$	$t$	TiO <sub>2</sub>		Al <sub>2</sub> O <sub>3</sub>	
		$y = 0$	$y = 1$	$y = 0$	$y = 1$
0	0.5	-0.52	-0.085	-0.52	-0.085
0.01	0.5	-0.53	-0.108	-0.532	-0.106
0.05	0.5	-0.576	-0.207	-0.583	-0.197
0.10	0.5	-0.647	-0.344	-0.659	-0.327

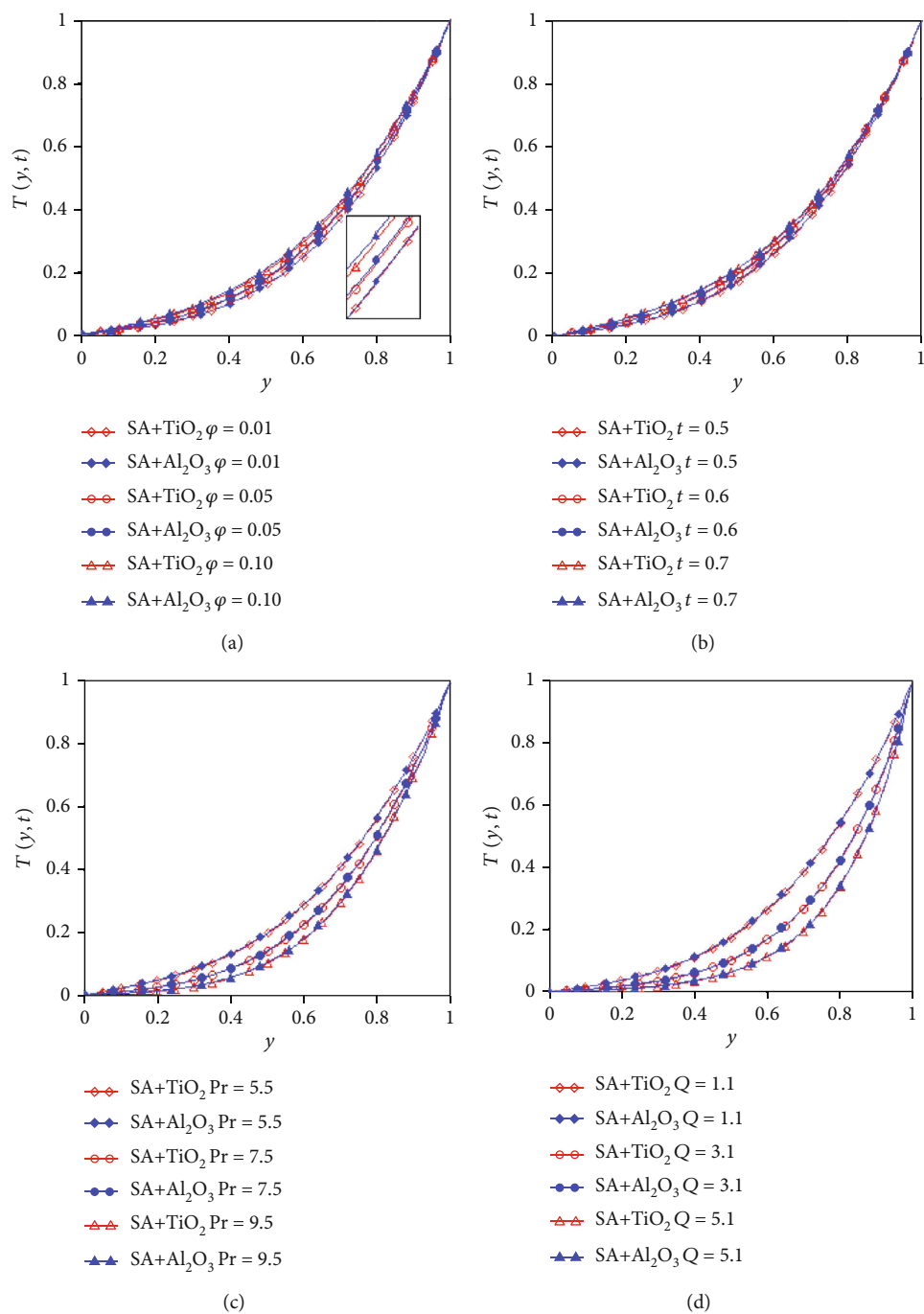


FIGURE 2: Variation of temperature fields.

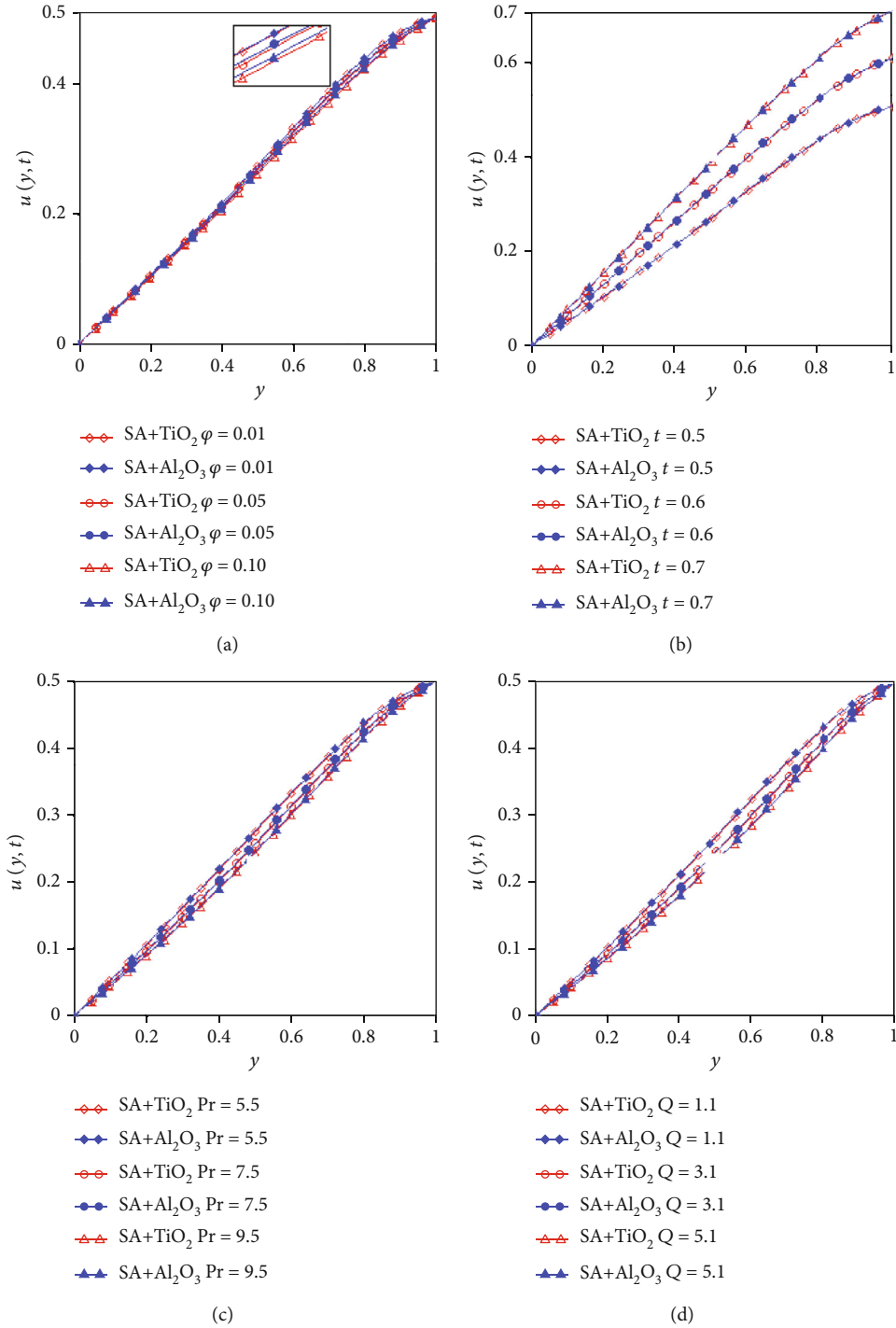


FIGURE 3: Variation of the velocity fields.

#### 4. Nusselt Numbers and Skin Frictions

The Nusselt numbers and skin frictions on both walls of the channel can express as

$$\text{Nusseltnumbers} = Nu_{0,1} = -\frac{k_{nf}}{k_f} L^{-1} \left\{ \frac{\partial \bar{\theta}(y, s)}{\partial y} \right\}_{y=0,1},$$

$$\text{skinfrictions} = Sk_{0,1} = -\frac{\mu_{nf}}{\mu_f} L^{-1} \left\{ \frac{\partial \bar{u}(y, s)}{\partial y} \right\}_{y=0,1}. \quad (26)$$

#### 5. Numerical Results and Discussions

The flow of two different SA-based nanofluids with natural convection and ramped velocity is compared in this section. The influence of volume fraction and time on flow and

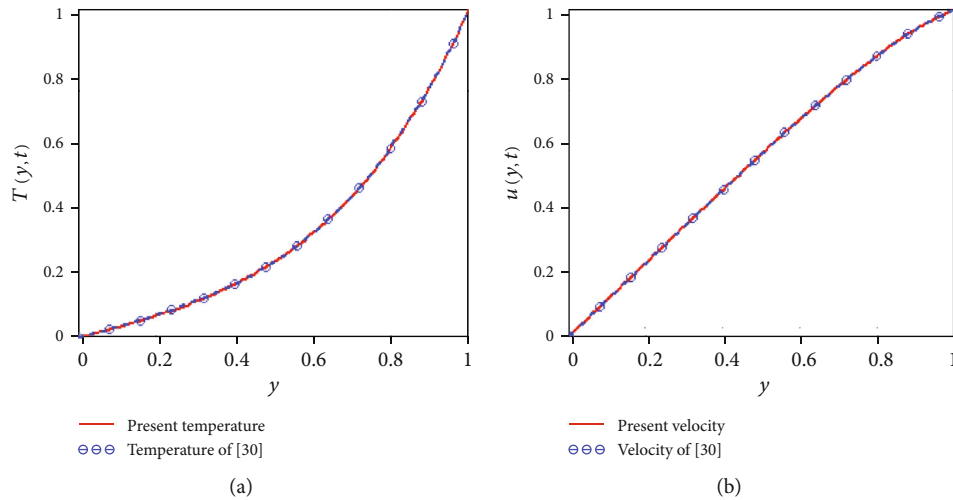


FIGURE 4: Comparison of results.

TABLE 4: Comparison of temperature profile with different Laplace inversion algorithms.

$y$	Results Eq. (18)	Stehfest's	Tzou's	Honing and Hirdes	Fourier series	Talbot
0	0	0	0	0	0	0
0.1	$3 \times 10^{-10}$	$5.2 \times 10^{-8}$	$2.4 \times 10^{-6}$	$1.1 \times 10^{-8}$	$3 \times 10^{-9}$	$3 \times 10^{-10}$
0.2	$1.1 \times 10^{-7}$	$3.3 \times 10^{-7}$	$6 \times 10^{-6}$	$1.59 \times 10^{-7}$	$1.3 \times 10^{-7}$	$1 \times 10^{-7}$
0.3	$4.1 \times 10^{-6}$	$4.6 \times 10^{-6}$	$1.8 \times 10^{-5}$	$4.06 \times 10^{-6}$	$4 \times 10^{-6}$	$4 \times 10^{-6}$
0.4	$7.7 \times 10^{-5}$	$9 \times 10^{-5}$	$1.1 \times 10^{-4}$	$7.75 \times 10^{-5}$	$7.7 \times 10^{-5}$	$7 \times 10^{-5}$
0.5	$9.9 \times 10^{-4}$	$9 \times 10^{-4}$	$1 \times 10^{-3}$	$9.1 \times 10^{-4}$	$9.8 \times 10^{-4}$	$9 \times 10^{-4}$
0.6	$9 \times 10^{-3}$	$8.4 \times 10^{-3}$	$8.5 \times 10^{-3}$	$8.41 \times 10^{-3}$	$8.4 \times 10^{-3}$	$9 \times 10^{-3}$
0.7	0.048	0.048	0.048	0.048	0.048	0.048
0.8	0.188	0.188	0.188	0.188	0.188	0.188
0.9	0.51	0.51	0.51	0.51	0.51	0.51
1	1	1.001	1.003	0.949	1	1

temperature is highlighted graphically and discussed. Furthermore, the results of this problem are compared by using different numerical inversion algorithms in Tables 2–3. In the graphical comparison, all parameters  $Q = 1.1$ ,  $Pr = 6.2$ ,  $\varphi = 0.04$ ,  $t = 0.5$ , and  $Gr = 3.8$  are fixed.

Figure 2(a) illustrates the variation and comparison of temperature profiles of two different nanofluids. The temperatures increase by increasing  $\varphi$ . The inclusion of nanoparticles increases the heat transport rate of nanofluids. Figure 2(b) depicts that the temperatures of nanofluids rise as time rises. The temperature of nanofluid-containing particles of  $Al_2O_3$  is higher due to greater thermal conductivity. Figures 2(c) and 2(d) show the influence of Prandtl number and heat absorption on temperatures. The temperature fields of the nanofluids are shown to be lower when  $Pr$  and  $Q$  are increased.

Figure 3(a) indicates that the thickness of nanofluids increases with an increase of  $\varphi$  due to the higher density of nanoparticles as a result velocities reduce. The velocity of SA +  $TiO_2$  is higher than SA +  $Al_2O_3$  due to the low density of  $TiO_2$ . Figure 3(b) illustrates that the velocities of both

fluids increase with increasing time. The influence of Prandtl number and heat absorption on the velocity profiles is seen in Figures 3(c) and 3(d). The velocities of nanofluids decrease with an increase in  $Pr$  and  $Q$ .

The authenticity of our results obtained for temperature and velocity is presented in Figure 4 by comparing them to the results of Hajizadeh et al. [30]. These figures show that for  $t = 1$ , our outcomes are equivalent to those found in [30]. The coinciding curves demonstrate the veracity of our findings.

Table 2 shows that when the volume fraction of nanoparticles rises, the heat transfer rate decreases on both plates. Table 3 displays the quantitative data of skin friction, which is decreased when the volume fraction values on both plates rise for two nanofluids.

Tables 4 and 5 show the comparison of our analytical solutions (18) and (24), with the semianalytical solutions obtained by different numerical inverse Laplace transform algorithms (Stehfest's [23], Tzou's [24], Fourier series [25], Talbot [26], and Honig and Hirdes [27]). From these figures and tables, it can be seen that all the numerical inverse

TABLE 5: Comparison of velocity profile with different Laplace inversion algorithms.

$y$	Results Eq. (24)	Stehfest's	Tzou's	Honing and Hirdes	Fourier series	Talbot
0	0	0	0	0	0	0
0.1	0.964	0.964	0.965	0.976	0.967	0.964
0.2	1.93	1.93	1.93	1.954	1.934	1.93
0.3	2.898	2.898	2.899	2.934	2.904	2.898
0.4	3.869	3.869	3.87	3.918	3.878	3.869
0.5	4.845	4.845	4.847	4.906	4.856	4.845
0.6	5.827	5.827	5.829	5.9	5.84	5.827
0.7	6.816	6.816	6.819	6.901	6.831	6.816
0.8	7.81	7.81	7.812	7.906	7.826	7.81
0.9	8.758	8.758	8.76	8.866	8.776	8.758
1	9.379	9.379	9.381	9.497	9.399	9.379

Laplace transform algorithms have good agreement with our obtained results.

## 6. Conclusion

The focus of this work is to examine the results of the convective flow of two nanofluids in an upright channel with ramped velocity. Analytical results of temperature and velocity fields are attained by using the Laplace transform technique. Sodium alginate is considered a base fluid, and nanoparticles of  $\text{TiO}_2$  and  $\text{Al}_2\text{O}_3$  are added to it. Analytical and semianalytical results are compared. The effects of time, Prandtl number, heat absorption, and volume fraction are discussed in detail. The current findings are compared to previous findings in the literature. In the tables, the effect of volume fraction on Nusselt numbers and skin frictions is explored. The main observations are as follows:

- (i) The temperature profiles increase for higher values of  $\varphi$  due to greater thermal conductivities
- (ii) The velocity fields decrease for greater values of  $\varphi$  due to high densities
- (iii) The velocity and temperature fields are increasing function of time  $t$
- (iv) The nanoparticles ( $\text{Al}_2\text{O}_3$ ) increase temperature much more than the nanoparticles ( $\text{TiO}_2$ )
- (v) The velocity is less when the nanoparticles alumina ( $\text{Al}_2\text{O}_3$ ) is added in base fluid than by adding the nanoparticles titania ( $\text{TiO}_2$ )
- (vi) The velocity can be controlled and predicted with ramped velocity conditions
- (vii) The thickness of nanofluids increases due to higher viscosity caused by greater values of  $Pr$  in return velocity and temperature reduces
- (viii) The momentum and energy of nanofluids are reduced for higher values of  $Q$

(ix) Nusselt numbers and skin frictions decrease on both walls of channel for both nanofluids by increasing  $\varphi$

(x) The solutions obtained by different methods are in good agreement

## Nomenclature

$u'$ :	Velocity
$T'$ :	Temperature
$g$ :	Gravitational acceleration
$\rho_{nf}$ :	Density
$Gr$ :	Grashof number
$\beta_{nf}$ :	Thermal expansion
$\mu_{nf}$ :	Dynamic viscosity
$Q_0$ :	Source/sink effect
$(c_p)_{nf}$ :	Specific heat
$Pr$ :	Prandtl number
$d$ :	Distance between plates
$Q$ :	Dimensionless source/sink effect
$\varphi$ :	Volume fraction
$Sk$ :	Skin friction
$Nu$ :	Nusselt number
$s$ :	Solid particles
$nf$ :	Nanofluid
$f$ :	Fluid.

## Data Availability

The data used to support the findings of this study are available from the corresponding author upon request.

## Conflicts of Interest

The authors declare that they have no conflicts of interest.

## Acknowledgments

This study was funded by Deanship of Scientific Research (Project no. RGP. 1/161/42), King Khalid University, Abha, Saudi Arabia.



## References

- [1] S. A. R. Sahebi, H. Pourziaei, A. R. Feizi, M. H. Taheri, Y. Rostamiyan, and D. D. Ganji, "Numerical analysis of natural convection for non-Newtonian fluid conveying nanoparticles between two vertical parallel plates," *The European Physical Journal*, vol. 1, no. 2, pp. 130–238, 2015.
- [2] S. O. Adesanya, "Free convective flow of heat generating fluid through a porous vertical channel with velocity slip and temperature jump," *Engineering Physics and Mathematics*, vol. 6, no. 3, pp. 1045–1052, 2015.
- [3] K. Boulama and N. Galanis, "Analytical solution for fully developed mixed convection between parallel vertical plates with heat and mass transfer," *ASME journal of heat transfer*, vol. 126, no. 3, pp. 381–388, 2004.
- [4] A. O. Ajibade and Y. A. Bichi, "Unsteady natural convection flow through a vertical channel due to the combined effects of variable viscosity and thermal radiation," *Journal of Applied and Computational Mathematics*, vol. 7, no. 3, p. 403, 2018.
- [5] M. R. Rajkumar, G. Venugopal, and S. A. Lal, "Natural convection from free standing tandem planar heat sources in a vertical channel," *Applied Thermal Engineering*, vol. 50, no. 1, pp. 1386–1395, 2013.
- [6] S. A. Nada, "Natural convection heat transfer in horizontal and vertical closed narrow enclosures with heated rectangular finned base plate," *International Journal of Heat and Mass Transfer*, vol. 50, no. 3-4, pp. 667–679, 2007.
- [7] S. U. S. Choi and J. A. Eastman, *Enhancing Thermal Conductivity of Fluids with Nanoparticles*, ASME IMECC, ASME-IMECC, San Francisco, USA, 1995.
- [8] Y. Xuan and Q. Li, "Investigation on convective heat transfer and flow features of nanofluids," *Journal of Heat Transfer*, vol. 125, no. 1, pp. 151–155, 2003.
- [9] S. Shateyi and J. Prakash, "A New Numerical Approach for MHD Laminar Boundary Layer Flow and Heat Transfer of Nanofluids over a Moving Surface in the Presence of Thermal Radiation," *Boundary value problems*, vol. 2014, no. 1, 2014.
- [10] S. U. S. Choi, "Nanofluids from vision to reality through research," *Journal of Heat Transfer*, vol. 131, pp. 1–9, 2009.
- [11] S. Halelfadl, T. Maré, and P. Estellé, "Efficiency of carbon nanotubes water based nanofluids as coolants," *Experimental Thermal and Fluid Science*, vol. 53, pp. 104–110, 2014.
- [12] H. Tyagi, P. Patrick, and R. Prasher, "Predicted efficiency of a low temperature nanofluidbased direct absorption solar collector," *Journal of Solar Energy Engineering*, vol. 131, no. 4, 2009.
- [13] T. Yousefi, F. Veysi, E. Shojaeizadeh, and S. Zinadini, "An experimental investigation on the effect of  $\text{Al}_2\text{O}_3\text{-H}_2\text{O}$  nanofluid on the efficiency of flat-plate solar collectors," *Renewable Energy*, vol. 39, no. 1, pp. 293–298, 2012.
- [14] H. Zamani, O. Mahian, I. Rashidi, G. Lorenzini, and S. Wongwises, "Exergy optimization of a double-exposure solar cooker by response surface method," *Journal of Thermal Science and Engineering Applications*, vol. 9, no. 1, article 011003, 2017.
- [15] O. Mahian, A. Kianifar, S. Z. Heris, D. Wen, A. Z. Sahin, and S. Wongwises, "Nanofluids effects on the evaporation rate in a solar still equipped with a heat exchanger," *Nano Energy*, vol. 36, pp. 134–155, 2017.
- [16] X. Qiang, I. Siddique, K. Sadiq, and N. A. Shah, "Double diffusive MHD convective flows of a viscous fluid under influence of the inclined magnetic field, source/sink and chemical reaction," *Alexandria Engineering Journal*, vol. 59, no. 6, pp. 4171–4181, 2020.
- [17] I. Siddique, K. Sadiq, I. Khan, and K. S. Nisar, "Nanomaterials in convection flow of nanofluid in upright channel with gradients," *Journal of Materials Research and Technology*, vol. 11, pp. 1411–1423, 2021.
- [18] R. Gupta, M. Gaur, Q. Al-Mdallal, S. D. Purohit, and D. L. Suthar, "Numerical study of the flow of two radiative nanofluids with Marangoni convection embedded in porous medium," *Journal of Nanomaterials*, vol. 2022, 7 pages, 2022.
- [19] T. Gohar, S. Khan, N. Sene, A. Mouldi, and A. Brahmia, "Heat and mass transfer of the Darcy-Forchheimer Casson hybrid nanofluid flow due to an extending curved surface," *Journal of Nanomaterials*, vol. 2022, 12 pages, 2022.
- [20] W. Ashraf, A. H. Alghtani, I. Khan, and M. Andualem, "Andualem. Thermal transport in radiative nanofluids by considering the influence of convective heat condition," *Journal of Nanomaterials*, vol. 2022, Article ID 1854381, 11 pages, 2022.
- [21] M. Zaka Ullah, D. Abuzaid, and M. Asma, "Abdul Bariq. Couple stress hybrid nanofluid flow through a converging-diverging channel," *Journal of Nanomaterials*, vol. 2021, Article ID 2355258, 13 pages, 2021.
- [22] K. Sadiq, I. Siddique, R. Ali, and F. Jarad, "Impact of ramped concentration and temperature on MHD Casson nanofluid flow through a vertical channel," *Journal of Nanomaterials*, vol. 2021, Article ID 3743876, 17 pages, 2021.
- [23] H. Stehfest, "Algorithm 368: numerical inversion of Laplace transforms [D5]," *Communications of the ACM*, vol. 13, no. 1, pp. 47–49, 1970.
- [24] D. Y. Tzou, *Macro to Microscale Heat Transfer, the Lagging Behavior*, Taylor and Francis, Washington, 1997.
- [25] A. Talbot, "The accurate numerical inversion of Laplace transforms," *IMA Journal of Applied Mathematics*, vol. 23, no. 1, pp. 97–120, 1979.
- [26] G. Honig and U. Hirdes, "A method for the numerical inversion of Laplace transforms," *Journal of Computational and Applied Mathematics*, vol. 10, no. 1, pp. 113–132, 1984.
- [27] B. Davies, "Integral transforms and their applications," *AMS*, vol. 25, 2005.
- [28] M. Turkyilmazoglu, "Exact analytical solutions for heat and mass transfer of MHD slip flow in nanofluids," *Chemical Engineering Science*, vol. 84, pp. 182–187, 2012.
- [29] M. Hatami and D. D. Ganji, "Natural convection of sodium alginate (SA) non-Newtonian nanofluid flow between two vertical flat plates by analytical and numerical methods," *Case studies in thermal engineering*, vol. 2, pp. 14–22, 2014.
- [30] A. Hajizadeh, N. A. Shah, F. D. Zaman, and I. L. Animasaun, "Analysis of natural convection bionanofluid between two vertical parallel plates," *Bionanosciences*, vol. 9, no. 4, pp. 930–936, 2019.

## Research Article

# Nonlinear Convective $\text{SiO}_2$ and $\text{TiO}_2$ Hybrid Nanofluid Flow over an Inclined Stretched Surface

Sehrish,<sup>1</sup> Said Anwar Shah,<sup>2</sup> Abir Mouldi,<sup>3</sup> and Ndolane Sene<sup>4</sup> 

<sup>1</sup>Department of Mathematics and Statistics, Bacha Khan University, Charsadda, Pakistan

<sup>2</sup>Department of Basic Sciences & Islamiat, University of Engineering and Technology, Peshawar, Pakistan

<sup>3</sup>Department of Industrial Engineering, College of Engineering, King Khalid University, Abha 61421, Saudi Arabia

<sup>4</sup>Laboratoire Lmdan, Departement de Mathematiques de Decision, Facultie des Sciences Economiques et Gestion, Universite Cheikh Anta Diop de Dakar, BP 5683 Dakar Fann, Senegal

Correspondence should be addressed to Ndolane Sene; [ndolanesene@yahoo.fr](mailto:ndolanesene@yahoo.fr)

Received 8 January 2022; Accepted 15 March 2022; Published 4 May 2022

Academic Editor: Amir Khan

Copyright © 2022 Sehrish et al. This is an open access article distributed under the Creative Commons Attribution License, which permits unrestricted use, distribution, and reproduction in any medium, provided the original work is properly cited.

The hybrid nanofluid is extensively used in manufacturing commercial applications due to its high exceptional capacity to increase the heat transfer rate. As a result, in the existence of nonlinear convection, the hybrid nanofluid is considered to flow on an inclined plane. The nonlinear convection has many applications in real life and is more relevant to the natural flow avoiding the flow restrictions. The focus has been executed on the thermal and mass Grashof numbers to analyse the fluid motion in the presence of these parameters for nonlinear nature. Moreover, the hybrid nanofluid flow analysis has been done to investigate the heat transfer analysis. The modelled equations are solved through an analytical approach. The heat and mass transfer rates and drag force are calculated under the influence of various physical parameters. The new parameter of the Grashof numbers improves the fluid motion for its larger values, and consequently, the fluid rapidly falls down from the inclined plane. The obtained outputs show that hybrid nanofluids are more effective in heat transfer analysis as compared to other conventional fluids.

## 1. Introduction

In the past few years, the utilization of thin-film liquid flow has fascinated researchers in the different area like engineering, technology, and industry; consequently, the study of thin-film liquid flow analysis regarding their application in many fields is necessary such as shipment through the flow in human lung and a lubricating process in the industry. These and a few more are considered to be the biggest subclass of thin-film liquid flow-related issues. The study of thin-film liquid flow in many active applications is a nice combination of structural mechanics, fluid mechanics, and theology. One of its main applications is the cable fiber undercoat. In addition, polymer and metal extrusion, food straightening, permanent formulation, elastic sheet drawing, and device fluidization, exchange, and chemical treatment apparatus are some of the well-known uses. Observing these applications, it became the principal subject for the investi-

gator to study and analyse the behaviour of thin-film liquid flow at stretching surfaces. The flow behaviour for the first time regarding thin-film was investigated through Newtonian liquids and then expanded to non-Newtonian liquids. The non-Newtonian thin-film flow of nanoliquids has been analysed by Sandeep et al. [1]. Wang [2] has examined the transient thin-film liquid flow at the stretching surface. The motion of thin-film finite fluid at the time-dependent stretching surface was analysed by Usha et al. [3]. Liu et al. [4] have studied the movement of thin-film liquid regarding heat transfer behaviours at a stretching surface. Aziz et al. [5] examined thermal generation within thin-film liquid flow at a stretching sheet. The thin-film liquid motion with heat radiation regarding the behaviour of heat transmission has been analysed by Tawade et al. [6]. They solved their proposed model using Runge-Kutta-Fehlberg and Newton method. The analysis of heat transfer through thin-film liquid flow at a stretching surface has been done by Anderssona

et al. [7]. Many researchers have worked independently on power-law liquid motion using thin-film time-dependent stretching sheets [8–11]. Megahe [12] has studied the flow of thin film of Casson liquid with heat transfer on a transient stretching sheet. In the proposed model, they also considered the slip velocity impact with heat flux and viscous dissipation. In the recent past, Tahir et al. [13] and Khan et al. [14] analysed the motion of thin-film nanoliquid through innovative approach. The growing interest in energy reserves is one of the most complicated issues for current researchers to fulfill the augmenting requirements for energy in modern scientific practices. Researchers are attempting to introduce new channel of energy that are convenient and reasonable for cooling and thermal applications. The most readily approachable means of renewable energy in the universe is solar energy. Solar energy is a good source of clean and renewable energy, so it will not cause environmental adulteration which is generated by conventional energy such as coal, oil during the process of use. The negative impacts of pollution on the earth cause global warming and lung and cancer disease. Solar energy is a good alternative to surmount this problem and reduce its detrimental impacts. Over the past 30 years, many developed and developing industrialized countries have focused on advancing solar technology. When there is oil, energy crisis, solar energy becomes more attractive. The oil crisis in general is a crisis of higher prices as OPEC countries raise fuel prices, so options include solar thermal, solar photovoltaic, wind energy, geothermal, marine, and wave energy. So scientists and researchers paid attention to all these things, and an interesting reality is that the energy that approaches the earth from 20 days of sunlight is equal to the energy stored in all the earth's storages of fossil fuels such as petroleum, coal, and natural gas. In this way, they play a prominent role in meeting the needs of the people in the world. Flat plates (solar collectors) use heat transfer liquids to transform solar energy into thermal energy. Rising energy needs around the world, including nonrenewable energy sources like fossil fuels, have minimal production of such resources, resulting in huge, detrimental effects on the environment, like global warming, climate change, and air pollution. To mitigate such losses, scientific approach has focused on improving the productivity of renewable energy processes, like solar energy. Solar energy is the cheapest and cleanest option of renewable energy, which converts solar energy into environmentally friendly electrical and thermal energy. For the conversion of solar energy into heat energy, a heat-changing liquid can be used in flat plate-type solar collectors [15]. Solar collectors receive solar rays through absorbing plates and converting such rays into a useful form of the energy (primarily water, water composition, and EG). Nevertheless, the major shortcomings are the low thermal properties of these conventional liquids, as they offer low thermal efficiency in the transformation process. Converting conventional working liquids into nanoliquids is one of the initiatives, which has received more attention over the past few years in enhancing the thermal efficiency of this technology. A stable synthesis of solids components between 1 nm and 100 nm is referred to nanoliquids [16]. Nanoliquid is also widely utilized in

solar energy depots [17, 18], heat exchangers [19], and freezing methods [20]. Mebarek-Oudina [21] studied nanofluid using various basic fluids. An analytical study of MHD nanoliquid motion, for heat transfer analysis, was done by Saeed and Gul [22]. Rehman et al. [23] analysed the motion of nanofluids by implementing the induced changeable magnetic field using the liquid film flow model. The motion of Darcy–Forchheimer nanoliquid through a mathematical model at the curved surfaces was analysed by Sajjad et al. [24]. Several recent analyses have been done in different energy and thermal environments using analytical and numerical methods, for handling heat exchanges and nanoliquid flow behaviour, by Sheikholeslami [25], Zhang et al. [26], and Gul et al. [27]. The magnetic properties of an electrically conducting liquid are referred to as MHD. In the natural and industrial spheres, we can notice that the behaviour of liquid motion is influenced by magnetic fields. The MHD phenomenon occurs when the velocity and magnetic field are combined. Instances of these kinds of fluids are liquid metals, electrolytes, plasma, etc. The concept of magnetohydrodynamic has been invented by Hannes Alfvén [28]. On this great success, he was given the Nobel Prize in Physics in 1970. MHD has many applications in engineering and technologies such as MHD generators, plasma, and nuclear reactors. The use of solar energy collectors also plays a significant role in medicine such as cancer therapy and MRI. This study is about the movements of ionized atoms or components and their liaison with the electric fields and neighbouring liquids. This safeguards against particle (atoms or molecules) and fluid transport phenomena such as electrorotation, dielectrophoresis, electro-osmosis, and electrokinesis. This has wide range of applications in many areas including gas pumps, drag reduction, increasing drying rate, and plasma actuators. At the outset, electrohydrodynamic fluid motion has been examined by Woodson and Melcher [29]. The impact of substitutive current and thermal transport on the dielectric viscous peristaltic fluid motion has been examined by Sayed et al. [30]. Khan et al. [31] investigated the irreversible behaviour of the electromagnetic hydrodynamic convective flow of viscous fluid. Rashid et al. [32] scrutinized the micro polar electromagnetohydrodynamic radiative fluid flow with convection state at a stretchable permeable sheet. In the recent past, scientists have focused on the fluids flowing at the permeable space and particles of various shapes inside the porous region. Their use can be understood in the multiple fields like nuclear engineering, environmental sciences, solar thermal engineering, bioinformatics, and construction engineering. Several processes that require the movement of fluids in a porous region include the utilization of geothermal energy, the flow of blood to lungs or veins, below-ground power lines, porous heating pipes, and chemically catalytic combiners. To understand the movements of fluid in porous space, Darcy's law is used frequently. Darcy's notion of high velocity and turbulent impacts in the porous space is wrong. Mebarek-Oudina et al. [21, 33–35] investigated the MHD hybrid nanofluid flow through various configuration and geometries in the presence of different nanomaterials.

Forchheimer [36] updated the momentum expression through the inclusion of second-order polynomial to adjust the impact of inertia on relative permeability. To analyse the impacts of inertia at relative permeability, a term of second-order polynomial in the momentum equation has been introduced by Forchheimer [36]. Muskat [37] pointed out that component as a Forchheimer component. Many researchers have investigated the fluid motion via porous media by utilizing the Darcy–Forchheimer idea in various geometries. Few of them are presented here. Saif et al. [24] explained the motion of nano-liquid in the porous gap and concluded that the fluctuation in the fluid flow forms the surface of the stretchable curve. The behaviour of nanofluid motion regarding Darcy–Forchheimer effects produced through a stretching sheet, as explored by Rasool et al. [38]. A Darcy–Forchheimer flow of liquid at a spinning disc has been explored by Sadiq et al. [39]. A non-Darcy liquid flow within a transparent gap is explained by Sheikholeslami et al. [40]. The impacts of Darcy–Forchheimer and EMHD on the movement of viscous liquid in the presence of Joule heating and heat flux at a stretching surface were scrutinized by Hayat et al. [41, 42]. In addition, they studied the process of entropy generation with the aid of the second law of thermodynamics. Kumar et al. [43] calculated the numerical outcomes of CNT nanofluids movement by the numerical scheme in divergent and convergent channels under the effects of thermal radiation. Akgül et al. [44–49] presented different novel technique for investigating fractional differential equations including the Atangana-Baleanu fractional derivative. The relevant and latest literature can be seen as [50–52].

The main objective of the ongoing research is to analyse the impact of electro-hydrodynamic Darcy–Forchheimer liquid movement and its use in augmenting the capacity of solar collectors through inclined plates. The energy equation has been developed under Joule heating, heat radiation, and viscous dissipation. The proposed model of the fluid flow has been formulated through PDEs and subsequently solved analytically in Mathematica using HAM technique. The analysis of different significant emerging parameters is elucidated in terms of temperature, velocity, and concentration. The numerical findings of the proposed model have been validated through findings in the literature. It reveals that the outcomes of the model are real and applicable in many fields of engineering and science.

The newness of the proposed model is as follows.

- (I) The inclined plane with nonlinear mixed convection is used for the first time
- (II) The nanoparticles  $\text{TiO}_2$  and  $\text{SiO}_2$  are used
- (III) The skin friction and Nusselt numbers are displayed through charts for the impact of different parameters
- (IV) HAM method has been used for the solution

## 2. Mathematical Formulation

A 2D steady fluid motion at a stretchable inclined plate is studied, which makes  $\theta$  angle along with vertical axis, as

shown in Figure 1, as a solar collector schematic outlook. The space is presumed as a porous Darcy–Forchheimer. In addition, the energy equation is updated through the inclusion of heat radiation, viscous dissipation, and Joule heating.

The term  $\vec{J} \times \vec{B}$  is referred to as Lorentz force, where  $\vec{B}$  and  $\vec{J}$  are the magnetic field and current density, respectively. Ohm's law can be stated as  $\vec{J} = \sigma(\vec{E} + \vec{V} \times \vec{B})$ ,  $E$  stands for electric field, and it is presumed that  $\vec{E} = 0$ . In addition,  $T_w$ ,  $T_\infty$ ,  $C_w$ , and  $C_\infty$  are wall's temperature, free-stream temperature, wall's concentration, and free-stream concentration, respectively. Using the above principles, the mathematical formulation of the proposed model is [21, 22, 25, 53]

$$\frac{\partial u}{\partial x} + \frac{\partial v}{\partial y} = 0, \quad (1)$$

$$\begin{aligned} \rho_{\text{hnf}} \left( u \frac{\partial u}{\partial x} + v \frac{\partial u}{\partial y} \right) &= \mu_{\text{hnf}} \left( \frac{\partial^2 u}{\partial y^2} \right) \\ &\pm g \cos \theta [(T - T_\infty)(\rho\beta_T)_{\text{hnf}} + (T - T_\infty)^2(\rho\beta_T)_{\text{hnf}}^2 \\ &+ (C - C_\infty)(\rho\beta_C)_{\text{hnf}} + (C - C_\infty)^2(\rho\beta_C)_{\text{hnf}}^2], \end{aligned} \quad (2)$$

$$(\rho c_p)_{\text{hnf}} \left( u \frac{\partial T}{\partial x} + v \frac{\partial T}{\partial y} \right) = k_{\text{hnf}} \frac{\partial T^2}{\partial y^2}, \quad (3)$$

$$\left( u \frac{\partial C}{\partial x} + v \frac{\partial C}{\partial y} \right) = D_{\text{hnf}} \frac{\partial C^2}{\partial y^2}. \quad (4)$$

Acceptable boundary conditions are

$$u = bx = u_w(x), v = 0, C = C_w, T = T_w, \text{ at } y = 0, \quad (5)$$

$$u = 0 = v, C \longrightarrow C_\infty, T \longrightarrow T_\infty, \text{ at } y \longrightarrow \infty, \quad (6)$$

where  $K$  represents the porous medium permeability and  $u$  and  $v$  denote the velocity components in the  $x$  and  $y$  direction.

Using the following pertinent transformation variables,

$$u = F'(\eta)bx, v = -\sqrt{bv_f}F(\eta), (T_w - T_\infty)\Theta(\eta) = T - T_\infty, \quad (7)$$

$$(C_w - C_\infty)\Phi(\eta) = C - C_\infty, \eta = y\sqrt{\frac{b}{v_f}}. \quad (8)$$

The reduced form of Equations (1),(2),(3),(4),(5) in the

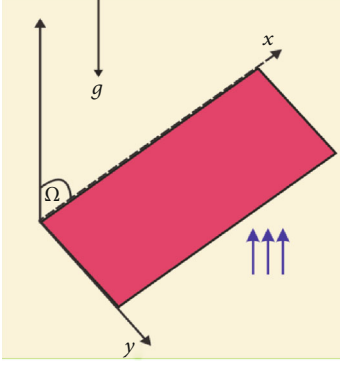


FIGURE 1: Geometry of the problem.

light of Equation (7) is as follows:

$$F''' + \frac{\rho_{\text{hnf}} \mu_f}{\rho_f \mu_{\text{hnf}}} [FF'' - F'^2] + \frac{\mu_f}{\mu_{\text{hnf}}} \cos \theta \left[ \begin{array}{l} \left[ \frac{(\rho\beta_T)_{\text{hnf}}}{(\rho\beta_T)_f} Gr\Theta + \left( \frac{(\rho\beta_T)_{\text{hnf}}}{(\rho\beta_T)_f} \right)^2 Gr^*\Theta^2 \right] \\ \pm \left[ \frac{(\rho\beta_C)_{\text{hnf}}}{(\rho\beta_C)_f} Gc\Phi + \left( \frac{(\rho\beta_C)_{\text{hnf}}}{(\rho\beta_C)_f} \right)^2 Gc^*\Phi^2 \right] \end{array} \right] = 0, \quad (9)$$

$$\frac{k_{\text{hnf}}}{k_f} \Theta'' + Pr \frac{(\rho Cp)_{\text{hnf}}}{(\rho Cp)_f} F\Theta' = 0, \quad (10)$$

$$\frac{\mu_f}{\mu_{\text{hnf}}} \Phi'' + Sc F\Phi' = 0. \quad (11)$$

With interrelated boundary conditions,

$$Gr = \frac{g\beta_{Tf}(T_w - T_\infty)}{bu_w}, \quad (12)$$

$$Gr^* = \frac{g\beta_{Tf}^2(T_w - T_\infty)^2}{bu_w}, \quad (13)$$

$$Gc = \frac{g\beta_{Cf}(C_w - C_\infty)}{bu_w}, \quad (14)$$

$$Gc^* = \frac{g\beta_{Cf}^2(C_w - C_\infty)^2}{bu_w}, \quad (15)$$

$$Pr = \frac{\nu_f}{\alpha_f}, \quad (16)$$

$$Sc = \frac{\nu_f}{D_B}. \quad (17)$$

The above physical quantities are Grashof number, Prandtl number, heat source/sink factor, and Schmidt number.

$$\nu_{\text{hnf}} = \frac{\mu_{\text{hnf}}}{\rho_{\text{hnf}}}, \quad (18)$$

$$\mu_{\text{hnf}} = \frac{\mu_f}{(1 - \phi_{\text{SiO}_2})^{5/2} (1 - \phi_{\text{TiO}_2})^{5/2}}, \quad (19)$$

$$\rho_{\text{hnf}} = (1 - \phi_{\text{TiO}_2}) \left\{ 1 - \left( 1 - \frac{\rho_{\text{TiO}_2}}{\rho_f} \right) \phi_{\text{SiO}_2} \right\} + \frac{\rho_{Ag}}{\rho_f} \phi_{\text{TiO}_2}, \quad (20)$$

$$(g\beta_T)_{\text{hnf}} = (1 - \phi_{\text{TiO}_2}) \left\{ 1 - \left( 1 - \frac{(\rho\beta_T)_{\text{SiO}_2}}{(\rho\beta_T)_f} \right) \phi_{\text{SiO}_2} \right\} + \frac{(\rho\beta_T)_{\text{TiO}_2}}{(\rho\beta_T)_f} \phi_{\text{TiO}_2}, \quad (21)$$

$$(g\beta_C)_{\text{hnf}} = (1 - \phi_{\text{TiO}_2}) \left\{ 1 - \left( 1 - \frac{(\rho\beta_C)_{\text{SiO}_2}}{(\rho\beta_C)_f} \right) \phi_{\text{SiO}_2} \right\} + \frac{(\rho\beta_C)_{\text{TiO}_2}}{(\rho\beta_C)_f} \phi_{\text{TiO}_2}, \quad (22)$$

$$\frac{(\rho Cp)_{\text{hnf}}}{(\rho Cp)_f} = (1 - \phi_{\text{TiO}_2}) \left\{ 1 - \left( 1 - \frac{(\rho Cp)_{\text{SiO}_2}}{(\rho Cp)_f} \right) \phi_{\text{SiO}_2} \right\} + \frac{(\rho Cp)_{\text{TiO}_2}}{(\rho Cp)_f} \phi_{\text{TiO}_2}, \quad (23)$$

$$\frac{k_{\text{hnf}}}{k_{\text{nf}}} = \left( \frac{k_{\text{TiO}_2} + 2k_{\text{nf}} - 2\phi_{\text{TiO}_2}(k_{\text{nf}} - k_{\text{TiO}_2})}{k_{\text{TiO}_2} + 2k_{\text{nf}} + \phi_{\text{TiO}_2}(k_{\text{nf}} - k_{\text{TiO}_2})} \right), \frac{k_{\text{nf}}}{k_f} = \left( \frac{k_{\text{SiO}_2} + 2k_f - 2\phi_{\text{SiO}_2}(k_f - k_{\text{SiO}_2})}{k_{\text{SiO}_2} + 2k_f + \phi_{\text{SiO}_2}(k_f - k_{\text{SiO}_2})} \right). \quad (24)$$

Furthermore, the additional most key physical number are skin friction coefficient ( $C_{fx}$ ), Nusselt number ( $Nu_x$ ), and Sherwood number written as

$$C_{fx} = \frac{\tau_w}{(1/2)\rho(u_w)^2}, \quad Nu_x = \frac{xq_w}{k(T_w - T_\infty)}, \quad Sh_x = \frac{xj_w}{D_B(T_w - T_\infty)}, \quad (25)$$

where  $\tau_w$  is the shear stress and  $q_w$  denotes heat flux near the surface. Utilizing Equation (7), Equation (18)

yields

$$\begin{aligned}
 C_{fx} \text{Re}_x^{0.5} &= 2 \frac{\mu_{\text{hnf}}}{\mu_f} F''(0), \\
 \text{Nu}_x \text{Re}_x^{-0.5} &= -\frac{k_{\text{hnf}}}{k_f} \Theta'(0), \\
 \text{Sh}_x \text{Re}_x^{-0.5} &= -\Phi'(0).
 \end{aligned}
 \tag{26}$$

### 3. Solution Methodology (HAM)

The optimal technique is used for the solution of the proposed model. The system of Equations (10),(11),(12) along with condition (18) is solved in Mathematica software via HAM. The method was first introduced by Liao [54, 55], and this method is frequently used in recent research [53, 56–62]. The HAM algorithm in Mathematica software is outlined as follows:

$$\widehat{F}(\eta) = 1 - e^{-\eta}, \widehat{\Theta}(\eta) = e^{-\eta}, \widehat{\Phi}(\eta) = e^{-\eta}, \tag{27}$$

Linear operators  $L_{\widehat{F}}$ ,  $L_{\widehat{\Theta}}$ , and  $L_{\widehat{\Phi}}$  are presumed as follows:  $L_{\widehat{F}}(\widehat{F}) = \widehat{F}'''$ ,  $L_{\widehat{\Theta}}(\widehat{\Theta}) = \widehat{\Theta}''$ ,  $L_{\widehat{\Phi}}(\widehat{\Phi}) = \widehat{\Phi}''$ .

$$\begin{aligned}
 L_{\widehat{F}}(\mathbb{N}_1 + \mathbb{N}_2\eta + \mathbb{N}_3\eta^2) &= 0, \\
 L_{\widehat{\Theta}}(\mathbb{N}_4 + \mathbb{N}_5\eta) &= 0, \\
 L_{\widehat{\Phi}}(\mathbb{N}_6 + \mathbb{N}_7\eta) &= 0.
 \end{aligned}
 \tag{28}$$

Here, we point out nonlinear terms that are specifically named as  $N_{\widehat{F}}$ ,  $N_{\widehat{\Theta}}$ , and  $N_{\widehat{\Phi}}$  in the algorithm:

$$\begin{aligned}
 N_{\widehat{F}}[\widehat{F}(\eta; \zeta)] &= \widehat{F}_{\eta\eta\eta} + \left[ \widehat{F}\widehat{F}_{\eta\eta} - \widehat{F}_{\eta\eta}^2 \right] \\
 &\quad + \cos \theta \left[ \text{Gr}\widehat{\Theta} + \text{Gr}^*(\widehat{\Theta})^2 + \text{Gc}\widehat{\Phi} + \text{Gc}^*(\widehat{\Phi})^2 \right], \\
 N_{\widehat{\Theta}}[\widehat{F}(\eta; \zeta), \widehat{\Theta}(\eta; \zeta)] &= \widehat{\Theta}_{\eta\eta} + \text{Pr}\widehat{F}\widehat{\Theta}_{\eta}, \\
 N_{\widehat{\Phi}}[\widehat{F}(\eta; \zeta), \widehat{\Phi}(\eta; \zeta)] &= \widehat{\Phi}_{\eta\eta} + \text{Sc}\widehat{F}\widehat{\Phi}_{\eta}.
 \end{aligned}
 \tag{29}$$

For Equations (1),(2),(3), the zero-order system is

$$\begin{aligned}
 (1 - \zeta)L_{\widehat{F}}[\widehat{F}(\eta; \zeta) - \widehat{F}_0(\eta)] &= p\hbar_{\widehat{F}}N_{\widehat{F}}[\widehat{F}(\eta; \zeta)], \\
 (1 - \zeta)L_{\widehat{\Theta}}[\widehat{\Theta}(\eta; \zeta) - \widehat{\Theta}_0(\eta)] &= p\hbar_{\widehat{\Theta}}N_{\widehat{\Theta}}[\widehat{F}(\eta; \zeta), \widehat{\Theta}(\eta; \zeta)], \\
 (1 - \zeta)L_{\widehat{\Phi}}[\widehat{\Phi}(\eta; \zeta) - \widehat{\Phi}_0(\eta)] &= p\hbar_{\widehat{\Phi}}N_{\widehat{\Phi}}[\widehat{F}(\eta; \zeta), \widehat{\Theta}(\eta; \zeta)],
 \end{aligned}
 \tag{30}$$

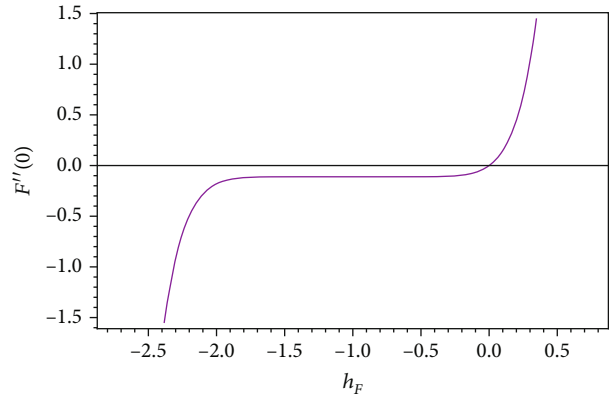


FIGURE 2: Velocity profile  $h$  curve.

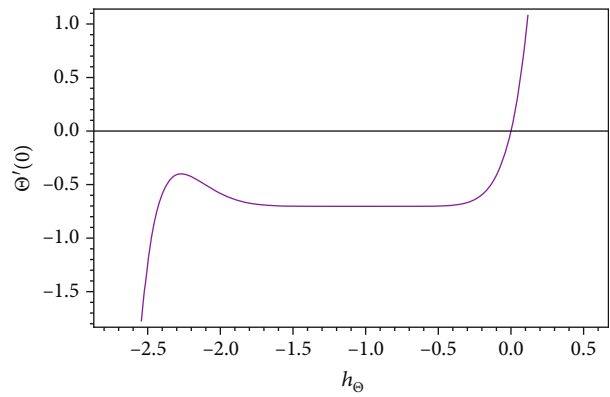


FIGURE 3: Temperature profile  $h$  curve.

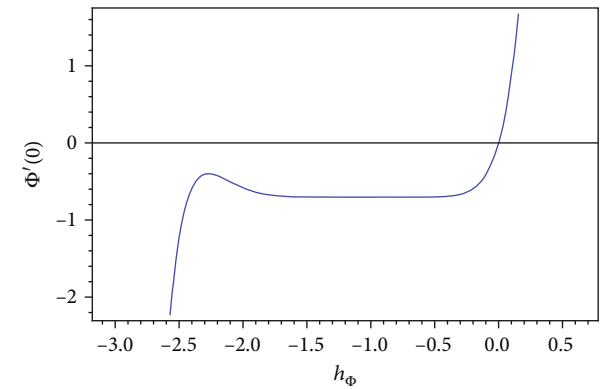


FIGURE 4: Concentration profile  $h$  curve.

while BCs are

$$\begin{aligned}
 \widehat{F}(\eta; \zeta) \Big|_{\eta=0} &= 0, \frac{\partial \widehat{F}(\eta; \zeta)}{\partial \eta} \Big|_{\eta=0} = 1, \\
 \widehat{\Theta}(\eta; \zeta) \Big|_{\eta=0} &= 1, \widehat{\Phi}(\eta; \zeta) \Big|_{\eta=0} = 1, \\
 \widehat{F}(\eta; \zeta) \Big|_{\eta=\infty} &\longrightarrow 0, \widehat{\Theta}(\eta; \zeta) \Big|_{\eta=\infty} \longrightarrow 0, \widehat{\Phi}(\eta; \zeta) \Big|_{\eta=\infty} \longrightarrow 0.
 \end{aligned}
 \tag{31}$$

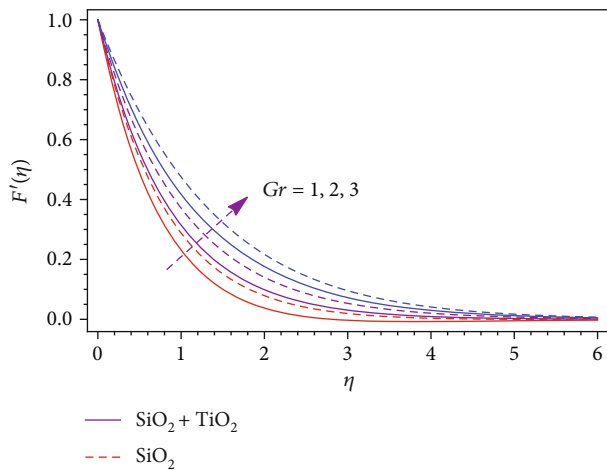


FIGURE 5: Effect of Grashof number on the velocity field.

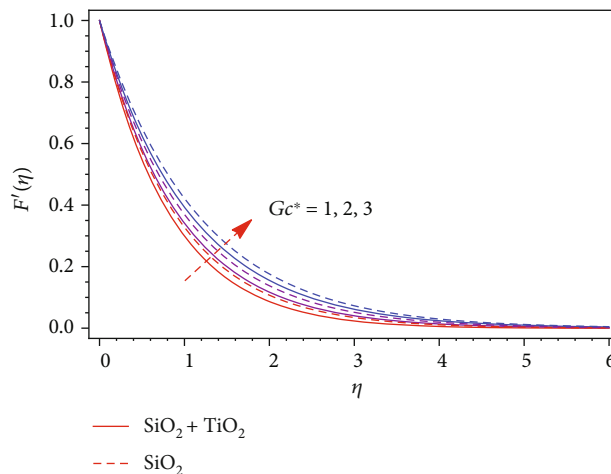


FIGURE 8: Effect of nonlinear mass Grashof number ( $Gc^*$ ) on the velocity field.

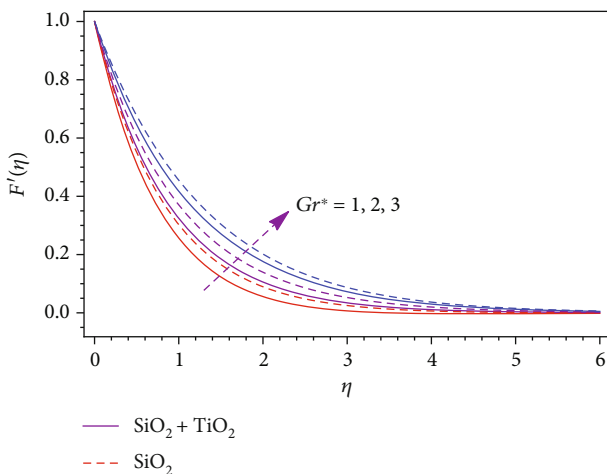


FIGURE 6: Impact of Grashof number ( $Gr^*$ ) at the velocity field.

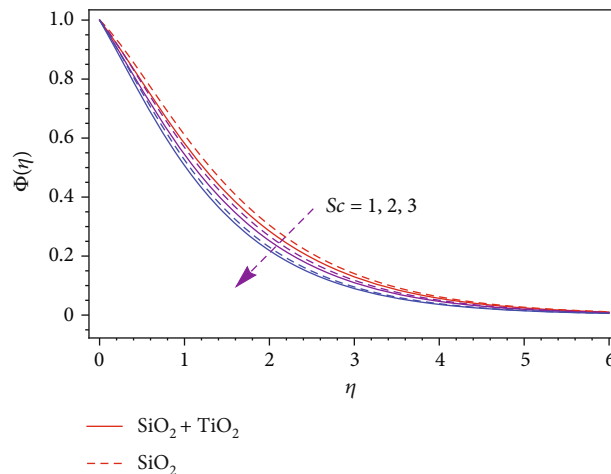


FIGURE 9: Influence of Schmidt number against concentration profile.

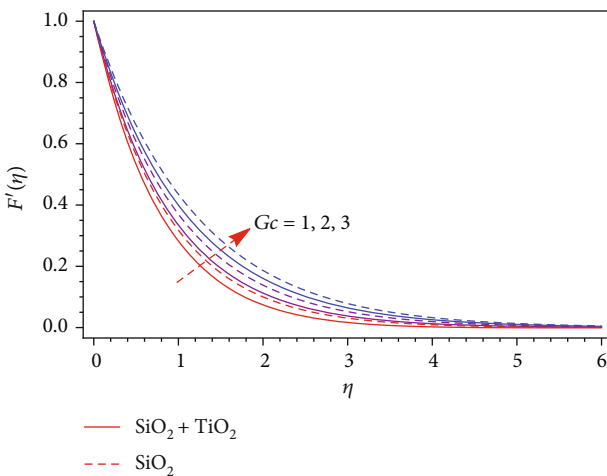


FIGURE 7: Impact of mass Grashof number ( $Gc$ ) at the velocity field.

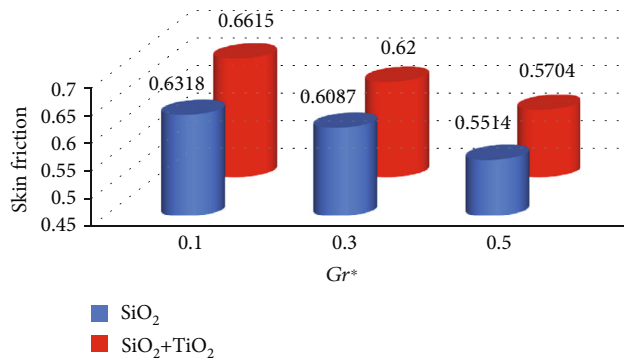


FIGURE 10: Skin friction versus thermal Grashof number.

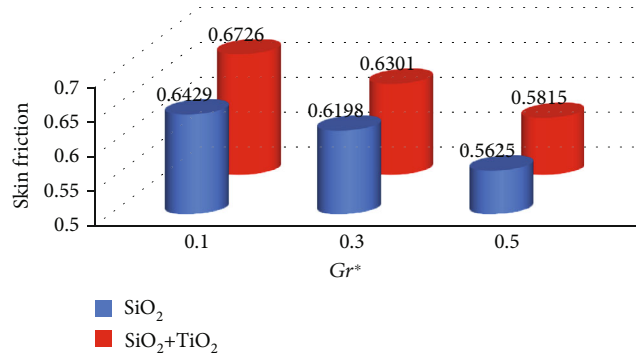


FIGURE 11: Skin friction versus nonlinear thermal Grashof number.

Now,

$$\begin{aligned} \mathfrak{R}_n^{\widehat{F}}(\eta) = & \widehat{F}'''_{n-1} + \left[ \sum_{j=0}^{w-1} \widehat{F}_{w-1-j} \widehat{F}''_j - \widehat{F}'^2_{n-1} \right] \\ & + \cos \theta \left[ \sum_{j=0}^{w-1} Gr \widehat{\Theta}_{w-1-j} + Gr^* (\widehat{\Theta}_{n-1})^2 \right. \\ & \left. + \sum_{j=0}^{w-1} Gc \widehat{\Phi}_{n-1} + \sum_{j=0}^{w-1} Gc^* (\widehat{\Phi}_{n-1})^2 \right] = 0, \end{aligned}$$

$$\mathfrak{R}_n^{\widehat{\Theta}}(\eta) = \widehat{\Theta}''_{n-1} + Pr \sum_{j=0}^{w-1} \widehat{F}_{w-1-j} \widehat{\Theta}'_j = 0,$$

$$\mathfrak{R}_n^{\widehat{\Phi}}(\eta) = \widehat{\Phi}''_{n-1} + Sc \sum_{j=0}^{w-1} \widehat{F}_{w-1-j} \widehat{\Phi}'_j = 0, \quad (32)$$

while

$$\chi_n = \begin{cases} 0, & \text{if } \zeta \leq 1, \\ 1, & \text{if } \zeta > 1. \end{cases} \quad (33)$$

**3.1. Convergence of HAM Solution.** The secondary conditions  $\tilde{h}_j$ ,  $\tilde{h}_\theta$ , and  $\tilde{h}_\phi$  totally become a source for the convergence of Equations (5),(7),(9); this is why the series solution has been chosen for controlling and merging. The probability sector of  $\tilde{h}$  is generated different  $\tilde{h}$  curves of  $\tilde{f}''(0)$ ,  $\tilde{\theta}'(0)$ , and  $\tilde{\phi}'(0)$  in the approximated 20<sup>th</sup> order HAM-based solution using Mathematica. The effective region of  $\tilde{h}$  is  $-1.5 < \tilde{h}_j < 0.0$ ,  $-1.5 < \tilde{h}_\theta < 0.0$ , and  $-2.5 < \tilde{h}_\phi < 0.0$ . The convergence of HAM algorithm via  $\tilde{h}$  curves for the three important profiles like temperature, velocity, and concentration has been sketched in various graphs (2-4), correspondingly. Figure 2 is the  $h$  curve for the velocity profile, Figure 3 is the  $h$  curve for the temperature field, and Figure 4 is the  $h$  curve for the concentration profile.

Figure 5 explains the behaviour of the proposed flow model through the various values of Grashof number (Gr). The sketch reveals that an increment in the value of Gr augments the liquid velocity. The reality furthers is, since (Ther-

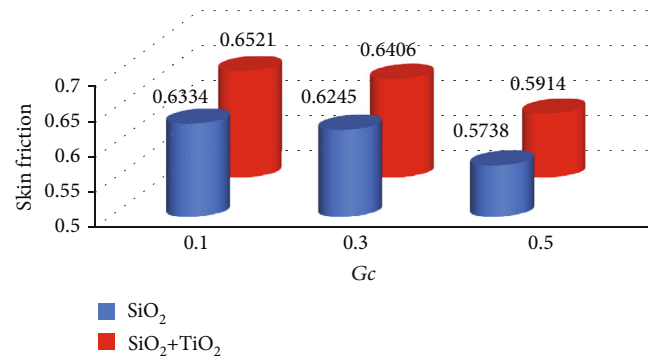


FIGURE 12: Skin friction versus mass Grashof number.

mal Grashof Number) integrates both hydrodynamic forces and the thermal buoyancy force, which occurs in the boundary layer due to variation in temperature. Therefore, increasing the thermal buoyancy effect of the liquid permits the specified fluid to cool the hot plate.

The impact of the Grashof number ( $Gr^*$ ) which is caused by nonlinear convection enhances the movement of fluid relatively larger and more related to natural phenomena and shown in Figure 6.

Figure 7 explains the flow properties at various values of mass Grashof number ( $Gc$ ). It reveals that a rise in the value of mass Grashof number increments the fluid velocity.

Figure 8 explains the flow properties at various values of mass Grashof number ( $Gc^*$ ). It reveals that a rise in the value of mass Grashof of number ( $Gc^*$ ) increments the velocity of the fluid.

The influence of  $Sc$  (Schmidt number) at the concentration profile is sketched in Figure 9, indicating that the enhancement of the value of  $Sc$  decrements the liquid concentration profile. The ratio of two properties such as momentum diffusion to mass diffusion is referred to as  $Sc$ . Therefore, for the larger value of  $Sc$ , the mass diffusion is due to momentum diffusion. While  $Sc$  increments, because of less mass diffusion and smaller  $D_B$ , the  $\Phi(\eta)$  profile diminishes.

The thermal Grashof number and nonlinear thermal Grashof enhance the fluid motion and consequently decline the skin friction as shown in Figures 10 and 11.



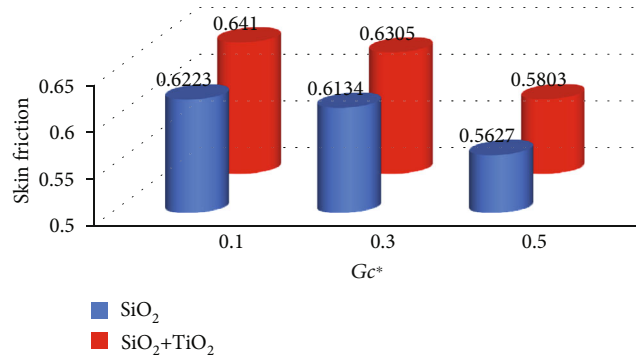


FIGURE 13: Skin friction versus nonlinear thermal Grashof number.

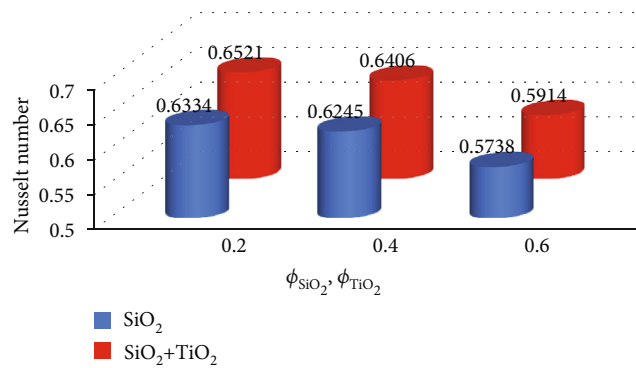


FIGURE 14: Heat transfer rate skin friction versus nanoparticle volume fraction.

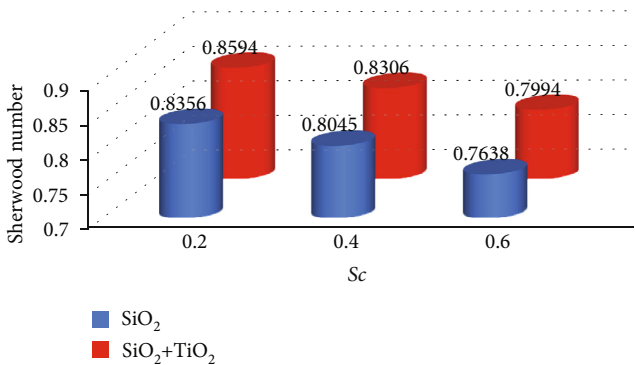


FIGURE 15: Mass transfer rate versus Schmidt number.

Furthermore, the effect is comparatively more impressible using the hybrid nanofluid.

The mass Grashof number and nonlinear mass Grashof strengthen the fluid velocity and consequently decline the skin friction as shown in Figures 12 and 13. Furthermore, the effect is comparatively more impressible using the hybrid nanofluid.

The hybrid nanofluids have the tendency to improve the thermal efficiency as shown in Figure 14. The heat transfer rate is comparatively more effective using the hybrid nanofluids. Physically, the thermal combined thermal conductivity of these nanoparticles is more reliable for the enhancement of heat transfer.

TABLE 1: Comparison of the present work with published work [63] considering  $-(k_{nf}/k_f)\Theta'(0)$ .

	$-(k_{nf}/k_f)\Theta'(0)$ [65]	$Pr - (k_{nf}/k_f)\Theta'(0)$ Present
6	0.789320421	0.789331322
7	0.77842876231	0.7784421573
8	0.76776543212	0.7677432641

The mass transfer declines with the increasing amount of  $Sc$  as shown in Figure 15. The Schmidt number also declines the concentration for its increasing values; that is why the mass transfer also declines.

The present work is compared with the published work [60] as shown in Table 1 by considering the common parameters. It is concluded that the obtained results closely agreed with the published work.

#### 4. Conclusion

In the present section, we evaluated the nonlinear convective fluid flow over an inclined plane considering heat and mass transfer analysis. The nonlinear convection is mainly focused to study the flow field down the inclined plane.

The highlights of the current work are as follows:

- (i) The nonlinear convection provides two Grashof numbers that represent linear and nonlinear phenomena. The greater values of both the thermal Grashof numbers increase the fluid motion for its larger values
- (ii) The mass Grashof numbers also used nonlinear and are more relevant to the natural phenomena. The increasing values of these parameters improve the fluid motion
- (iii) The obtained results illustrate that hybrid nanofluids are more affective for the heat transfer analysis
- (iv) The concentration field reduces with the greater value of  $Sc$

### Data Availability

All the relevant data exist in the manuscript.

### Conflicts of Interest

The authors declare that no such interest exists.

### Acknowledgments

The authors extend their appreciation to the Deanship of Scientific Research at King Khalid University for funding this work through research groups under grant number R.G.P.2/14/43.

### References

- [1] N. Sandeep and A. Malvandi, "Enhanced heat transfer in liquid thin film flow of non-Newtonian nanofluids embedded with graphene nanoparticles," *Advanced Powder Technology*, vol. 27, no. 6, pp. 2448–2456, 2016.
- [2] C. Y. Wang, "Liquid film on an unsteady stretching surface," *Quarterly of Applied Mathematics*, vol. 48, no. 4, pp. 601–610, 1990.
- [3] R. Usha and R. Sridharan, "On the motion of a liquid film on an unsteady stretching surface," *ASME Fluids Engineering*, vol. 150, pp. 43–48, 1993.
- [4] I. C. Liu and H. I. Andersson, "Heat transfer in a liquid film on an unsteady stretching sheet," *International Journal of Thermal Sciences*, vol. 47, no. 6, pp. 766–772, 2008.
- [5] R. C. Aziz, I. Hashim, and A. K. Alomari, "Thin film flow and heat transfer on an unsteady stretching sheet with internal heating," *Meccanica*, vol. 46, no. 2, pp. 349–357, 2011.
- [6] L. Tawade and M. Abel, "Thin film flow and heat transfer over an unsteady stretching sheet with thermal radiation, internal heating in presence of external magnetic field," *International journal of advances in applied mathematics and mechanics*, vol. 3, pp. 29–40, 2016.
- [7] H. I. Andersson, J. B. Aarseth, and B. S. Dandapatb, "Heat transfer in a liquid film on an unsteady stretching surface," *International Journal of Heat and Mass Transfer*, vol. 43, no. 1, pp. 69–74, 2000.
- [8] C. H. Chen, "Heat transfer in a power-law fluid film over a unsteady stretching sheet," *Heat and Mass Transfer*, vol. 39, no. 8-9, pp. 791–796, 2003.
- [9] C. H. Chen, "Effect of viscous dissipation on heat transfer in a non-Newtonian liquid film over an unsteady stretching sheet," *Journal of Non-Newtonian Fluid Mechanics*, vol. 135, no. 2-3, pp. 128–135, 2006.
- [10] C. Wang and L. Pop, "Analysis of the flow of a power-law fluid film on an unsteady stretching surface by means of homotopy analysis method," *Journal of Non-Newtonian Fluid Mechanics*, vol. 138, no. 2-3, pp. 161–172, 2006.
- [11] M. A. Mahmoud, "On flow and heat transfer in a thin liquid film over an unsteady stretching sheet with variable fluid properties and radiation," *Open Science journal of Mathematics and Application*, vol. 3, no. 1, pp. 14–18, 2015.
- [12] A. M. Megahe, "Effect of slip velocity on Casson thin film flow and heat transfer due to unsteady stretching sheet in presence of variable heat flux and viscous dissipation," *Applied Mathematics and Mechanics*, vol. 36, no. 10, pp. 1273–1284, 2015.
- [13] F. Tahir, T. Gul, S. Islam et al., "Flow of a nano-liquid film of Maxwell fluid with thermal radiation and magneto hydrodynamic properties on an unstable stretching sheet," *Journal of Nanofluids*, vol. 6, pp. 1–10, 2017.
- [14] N. S. Khan, T. Gul, S. Islam, A. Kha, and Z. Shah, "Brownian motion and thermophoresis effects on MHD mixed convective thin film second-grade nanofluid flow with Hall effect and heat transfer past a stretching sheet," *Journal of Nanofluids*, vol. 6, no. 5, pp. 812–829, 2017.
- [15] O. Rejeb, M. S. Yousef, C. Ghenai, H. Hassan, and M. Bettaye, "Investigation of a solar still behaviour using response surface methodology," *Case Studies in Thermal Engineering*, vol. 24, p. 100816, 2021.
- [16] U. S. Choi, "Enhancing thermal conductivity of fluids with nanoparticles," *AS-MEFED*, vol. 231, pp. 99–103, 1995.
- [17] K. Khanafer and K. Vafai, "A review on the applications of nanofluids in solar energy field," *Renewable Energy*, vol. 123, pp. 398–406, 2018.
- [18] H. T. Basha, R. Sivaraj, A. S. Reddy, and A. Chamkha, "SWCNH/diamond ethylene glycol nanofluid flow over a wedge, plate and stagnation point with induced magnetic field and nonlinear radiation-solar energy application," *The European Physical Journal Special Topics*, vol. 228, no. 12, pp. 2531–2551, 2019.
- [19] A. Izadi, M. Siavashi, and Q. Xiong, "Impingement jet hydrogen, air and CuH<sub>2</sub>O nanofluid cooling of a hot surface covered by porous media with non-uniform input jet velocity," *International Journal of Hydrogen Energy*, vol. 44, no. 30, pp. 15933–15948, 2019.
- [20] M. Siavashi and S. M. M. Joibary, "Numerical performance analysis of a counter-flow double-pipe heat exchanger with using nanofluid and both sides partly filled with porous media," *Journal of Thermal Analysis and Calorimetry*, vol. 135, no. 2, pp. 1595–1610, 2019.
- [21] F. Mebarek-Oudina, "Convective heat transfer of Titania nanofluids of different base fluids in cylindrical annulus with discrete heat source," *Heat Transfer—Asian Research*, vol. 48, no. 1, pp. 135–147, 2019.
- [22] A. Saeed and T. Gul, "Bioconvection Casson nanofluid flow together with Darcy-Forchheimer due to a rotating disk with thermal radiation and Arrhenius activation energy," *SN Applied Sciences*, vol. 3, no. 1, pp. 1–19, 2021.

- [23] S. Rehman, T. Gul, W. Khan, A. Khan, and Zeeshan, "Effects of chemical reaction, viscosity, thermal conductivity, heat source, radiation/absorption, on MHD mixed convection nano-fluids flow over an unsteady stretching sheet by HAM and numerical method," *Advances in Mechanical Engineering*, vol. 14, no. 1, 2022.
- [24] R. Sajjad, T. Hayat, R. Ellahi, T. Muhammad, and A. Alsaedi, "Darcy–Forchheimer flow of nanofluid due to a curved stretching surface," *International Journal of Numerical Methods for Heat & Fluid Flow*, vol. 29, no. 1, pp. 2–20, 2019.
- [25] M. Sheikholeslami, "Magnetic field influence on CuO-H<sub>2</sub>O nanofluid convective flow in a permeable cavity considering various shapes for nanoparticles," *International Journal of Hydrogen Energy*, vol. 42, no. 31, pp. 19611–19621, 2017.
- [26] L. Zhang, M. M. Bhatti, R. Ellahi, and E. M. Efstathios, "Oxytactic microorganism and thermo-bioconvection nanofluid flow over a porous Riga plate having Darcy-Brinkman-Forchheimer medium," *Journal of Non-Equilibrium Thermodynamics*, vol. 5, no. 3, pp. 257–268, 2020.
- [27] T. Gul, S. Nasir, S. Islam, Z. Shah, and M. A. Khan, "Effective Prandtl number model influences on the  $\gamma\text{Al}_2\text{O}_3\text{-H}_2\text{O}$  and  $\gamma\text{Al}_2\text{O}_3\text{-C}_2\text{H}_6\text{O}_2$  nanofluids spray along a stretching cylinder," *Arabian Journal for Science & Engineering*, vol. 44, no. 2, pp. 1–22, 2019.
- [28] H. Alfvén, "Existence of electromagnetohydrodynamic waves," *Nature*, vol. 150, no. 3805, pp. 405–406, 1942.
- [29] W. D. Jackson, J. H. Olsen, and A. T. Lewis, *Plasma magnetohydrodynamics and energy conversion*, Research Laboratory of Electronics (RLE) at the Massachusetts Institute of Technology (MIT), 1963.
- [30] M. M. Rashidi, S. Abelman, and N. F. Mehr, "Entropy generation in steady MHD flow due to a rotating porous disk in a nanofluid," *International Journal of Heat and Mass Transfer*, vol. 62, pp. 515–525, 2013.
- [31] W. A. Khan and I. Pop, "Boundary-layer flow of a nanofluid past a stretching sheet," *International Journal of Heat and Mass Transfer*, vol. 53, no. 11–12, pp. 2477–2483, 2010.
- [32] M. M. Rashidi and E. Erfani, "The modified differential transform method for investigating nano boundary-layers over stretching surfaces," *International Journal of Numerical Methods for Heat & Fluid Flow*, vol. 21, no. 7, pp. 864–883, 2011.
- [33] Z. Abdel-Nour, A. Aissa, F. Mebarek-Oudina et al., "Magneto-hydrodynamic natural convection of hybrid nanofluid in a porous enclosure: numerical analysis of the entropy generation," *Journal of Thermal Analysis and Calorimetry*, vol. 141, no. 5, pp. 1981–1992, 2020.
- [34] F. Mebarek-Oudina and R. Bessaih, "Oscillatory magnetohydrodynamic natural convection of liquid metal between vertical coaxial cylinders," *Journal of Applied Fluid Mechanics*, vol. 9, no. 6, pp. 1655–1665, 2016.
- [35] F. Mebarek-Oudina, A. Aissa, B. Mahanthesh, and H. F. Öztöp, "Heat transport of magnetized Newtonian nanoliquids in an annular space between porous vertical cylinders with discrete heat source," *International Communications in Heat and Mass Transfer*, vol. 117, p. 104737, 2020.
- [36] P. Forchheimer, "Wasserbewegung durch boden," *Zeitschrift des Vereins Deutscher Ingenieure*, vol. 45, pp. 1782–1788, 1901.
- [37] M. Muskat, *The Flow of Homogeneous Fluids through Porous Media*, McGraw-Hill, New York, 1946.
- [38] G. Rasool, A. Shafiq, C. M. Khaliq, and T. Zhang, "Magneto-hydrodynamic Darcy-Forchheimer nanofluid flow over a nonlinear stretching sheet," *Physica Scripta*, vol. 94, no. 10, article 105221, 2019.
- [39] M. A. Sadiq, F. Haider, T. Hayat, and A. Alsaedi, "Partial slip in Darcy-Forchheimer carbon nanotubes flow by rotating disk," *International Communications in Heat and Mass Transfer*, vol. 116, p. 104641, 2020.
- [40] M. Sheikholeslami, A. Arabkoohsar, and K. A. R. Ismail, "Entropy analysis for a nanofluid within a porous media with magnetic force impact using non-Darcy model," *International Communications in Heat and Mass Transfer*, vol. 112, p. 104488, 2020.
- [41] T. Hayat, S. A. Khan, A. Alsaedi, and H. M. Fardoun, "Heat transportation in electro-magnetohydrodynamic flow of Darcy-Forchheimer viscous fluid with irreversibility analysis," *Physica Scripta*, vol. 95, no. 10, p. 105214, 2020.
- [42] T. Hayat, F. Haider, and A. Alsaedi, "Darcy-Forchheimer flow with nonlinear mixed convection," *Applied Mathematics and Mechanics*, vol. 41, no. 11, pp. 1685–1696, 2020.
- [43] K. G. Kumar, M. Rahimi-Gorji, M. G. Reddy, A. J. Chamkha, and I. M. Alarifi, "Enhancement of heat transfer in a convergent/divergent channel by using carbon nanotubes in the presence of a Darcy–Forchheimer medium," *Microsystem Technologies*, vol. 26, no. 2, pp. 323–332, 2020.
- [44] M. Partoghghi, E. Karatas Akgül, G. W. Weber, G. Yao, and A. Akgül, "Recovering source term of the time-fractional diffusion equation," *Pramana*, vol. 95, no. 4, pp. 1–8, 2021.
- [45] A. Akgül, "A novel method for a fractional derivative with non-local and non-singular kernel," *Chaos, Solitons & Fractals*, vol. 114, pp. 478–482, 2018.
- [46] E. K. Akgül, A. Akgül, and M. Yavuz, "New illustrative applications of integral transforms to financial models with different fractional derivatives," *Chaos, Solitons & Fractals*, vol. 146, p. 110877, 2021.
- [47] E. Karatas Akgül, A. Akgül, and D. Baleanu, "Laplace transform method for economic models with constant proportional Caputo derivative," *Fractal and Fractional*, vol. 4, no. 3, p. 30, 2020.
- [48] S. Bilal, I. A. Shah, A. Akgül et al., "Finite difference simulations for magnetically effected swirling flow of Newtonian liquid induced by porous disk with inclusion of thermophoretic particles diffusion," *Alexandria Engineering Journal*, vol. 61, no. 6, pp. 4341–4358, 2022.
- [49] N. A. Shah, S. Saleem, A. Akgül, K. Nonlaopon, and J. D. Chung, "Numerical analysis of time-fractional diffusion equations via a novel approach," *Journal of Function Spaces*, vol. 2021, Article ID 9945364, 12 pages, 2021.
- [50] A. Dawar, E. Bonyah, S. Islam, A. Alshehri, and Z. Shah, "Theoretical analysis of Cu-H<sub>2</sub>O, Al<sub>2</sub>O<sub>3</sub>-H<sub>2</sub>O, and TiO<sub>2</sub>-H<sub>2</sub>O nanofluid flow past a rotating disk with velocity slip and convective conditions," *Journal of Nanomaterials*, vol. 2021, Article ID 5471813, 10 pages, 2021.
- [51] M. Z. Ullah, D. Abuzaid, M. Asma, and A. Bariq, "Couple stress hybrid nanofluid flow through a converging-diverging channel," *Journal of Nanomaterials*, vol. 2021, Article ID 2355258, 13 pages, 2021.
- [52] T. S. Khan, N. Sene, A. Mouldi, and A. Brahmia, "Heat and mass transfer of the Darcy-Forchheimer Casson hybrid nanofluid flow due to an extending curved surface," *Journal of Nanomaterials*, vol. 2022, 2022.

- [53] M. Jawad, A. Saeed, T. Gul, Z. Shah, and P. Kumam, "Unsteady thermal Maxwell power law nanofluid flow subject to forced thermal Marangoni convection," *Scientific Reports*, vol. 11, no. 1, pp. 1–14, 2021.
- [54] S. J. Liao, "An optimal homotopy-analysis approach for strongly nonlinear differential equations," *Communications in Nonlinear Science and Numerical Simulation*, vol. 15, no. 8, pp. 2003–2016, 2010.
- [55] S. J. Liao, Ed., *Advances in the Homotopy Analysis Method, chapter7*, World Scientific Press, 2014.
- [56] T. Gul and K. Ferdous, "The experimental study to examine the stable dispersion of the graphene nanoparticles and to look at the GO–H<sub>2</sub>O nanofluid flow between two rotating disks," *Nano*, vol. 8, no. 7, pp. 1711–1727, 2018.
- [57] M. Jawad, A. Saeed, T. Gul, and A. Bariq, "MHD Darcy-Forchheimer flow of Casson nanofluid due to a rotating disk with thermal radiation and Arrhenius activation energy," *Journal of Physics Communications*, vol. 5, no. 2, article 025008, 2021.
- [58] A. Rehman, Z. Salleh, and T. Gul, "Heat transfer of thin film flow over an unsteady stretching sheet with dynamic viscosity," *Journal of Advanced Research in Fluid Mechanics and Thermal Sciences*, vol. 81, no. 2, pp. 67–81, 2021.
- [59] A. Khan, W. Kumam, I. Khan et al., "Chemically reactive nanofluid flow past a thin moving needle with viscous dissipation, magnetic effects and hall current," *PLoS One*, vol. 16, no. 4, p. e0249264, 2021.
- [60] A. Khan, A. Saeed, A. Tassaddiq et al., "Bio-convective micropolar nanofluid flow over thin moving needle subject to Arrhenius activation energy, viscous dissipation and binary chemical reaction," *Case Studies in Thermal Engineering*, vol. 25, p. 100989, 2021.
- [61] M. Bilal, A. A. Gul, A. Alsubie, and I. Ali, "Axisymmetric hybrid nanofluid flow with heat and mass transfer amongst the two gyrating plates," *Zeitschrift für Angewandte Mathematik und Mechanik*, vol. 101, no. 11, 2021.
- [62] L. Ali, A. Tassaddiq, R. Ali et al., "A new analytical approach for the research of thin-film flow of magneto hydrodynamic fluid in the presence of thermal conductivity and variable viscosity," *ZAMM-Journal of Applied Mathematics and Mechanics/Zeitschrift für Angewandte Mathematik und Mechanik*, vol. 101, no. 2, 2021.
- [63] A. K. Alzahrani, M. Z. Ullah, A. S. Alshomrani, and T. Gul, "Hybrid nanofluid flow in a Darcy-Forchheimer permeable medium over a flat plate due to solar radiation," *Case Studies in Thermal Engineering*, vol. 26, p. 100955, 2021.

## Research Article

# Analytical Assessment of MHD Flow of Nanoliquid Subject to Thermal Radiation and Brownian Effect

Haroon Ur Rasheed <sup>1</sup>, Ebenezer Bonyah <sup>2</sup>, Soumaya Goudria,<sup>3</sup> Waris Khan <sup>4</sup>,  
Ahmed Alshehri <sup>5</sup> and Raees Khan<sup>6</sup>

<sup>1</sup>Department of Computer Science, Sarhad University of Science and Information Technology Peshawar, 25000 KP, Pakistan

<sup>2</sup>Department of Mathematics Education, Akenten Appiah Menka University of Skills Training and Entrepreneurial Development, (Kumasi Campus), Ghana

<sup>3</sup>Department of Physics, College of Science, Princess Nourah bint Abdulrahman University, P.O. Box 84428, Riyadh 11671, Saudi Arabia

<sup>4</sup>Department of Mathematics and Statistics, Hazara University Mansehra, 21120 KP, Pakistan

<sup>5</sup>Department of Mathematics, Faculty of Science, King Abdulaziz University, Jeddah 21589, Saudi Arabia

<sup>6</sup>Department of Mathematics, FATA University, Darra Adam Khel, FR Kohat, 26300 KP, Pakistan

Correspondence should be addressed to Ebenezer Bonyah; [ebbonya@gmail.com](mailto:ebbonya@gmail.com)

Received 19 October 2021; Accepted 28 March 2022; Published 28 April 2022

Academic Editor: Domenico Acierno

Copyright © 2022 Haroon Ur Rasheed et al. This is an open access article distributed under the Creative Commons Attribution License, which permits unrestricted use, distribution, and reproduction in any medium, provided the original work is properly cited.

This manuscript studies the impact of the heat and mass flow and chemical reaction with electromagnetic field and heat flow of non-Newtonian Walter-B nanofluid via the uniform magnetic field. A mathematical model is used to simulate the arisen nonlinear partial differential equations (PDEs). By employing the suitable transformations, the system of PDEs is then transformed to a nonlinear system of ordinary differential equations (ODEs). The impact of the pertinent parameters on the velocity profile, energy, and concentration distribution has been discussed. These nonlinear coupled equations were addressed analytically by implementing an efficient and validated analytical method, where Mathematica 11.0 programming code is established for simulating the flow system. Stability and convergence analysis have been performed in order to improve the accuracy of the flow system. In order to gain physical insight, the effects of dimensionless parameters on flow fields are investigated. In addition, the impression of system parameters on skin-friction, heat transfer coefficient, and mass flow rate profiles is also debated.

## 1. Introduction

Nanomaterials have been of great interest to engineers as well as to scientists during the previous decades. As a matter of fact, nanomaterials are known to enhance the thermal conductivity of base fluids. The first one who suggested the addition of carbon nanotubes and solid particles in base fluids was Maxwell [1]. The results achieved were motivational; however, some problems were raised such as pressure drop enhancement and pipe erosion. Then, Choi et al. [2] proposed the notion of carbon nanotubes and nanoscaled particles in base fluids and named them as nanofluids.

Metals, such as Ag and Cu, and metal oxides, such as  $\text{Al}_2\text{O}_3$  and CuO, are the most widely used nanoparticles. Improved nanofluids' thermal conductivity has important applications not only in domestic heating but also in heat exchangers and cooling systems. Nanofluids, discovered by Choi [3], are colloids composed of nanoparticles and base fluid. Nanoparticles have thermal conductivity, typically greater in magnitude than base fluids and significantly smaller in size than 100 nm. The work of nanoparticles greatly improves the heat transfer efficiency of the base fluids. Basic fluids can be water, synthetic liquids, fats, lubricants and blood. Nanoparticles are synthetic materials with

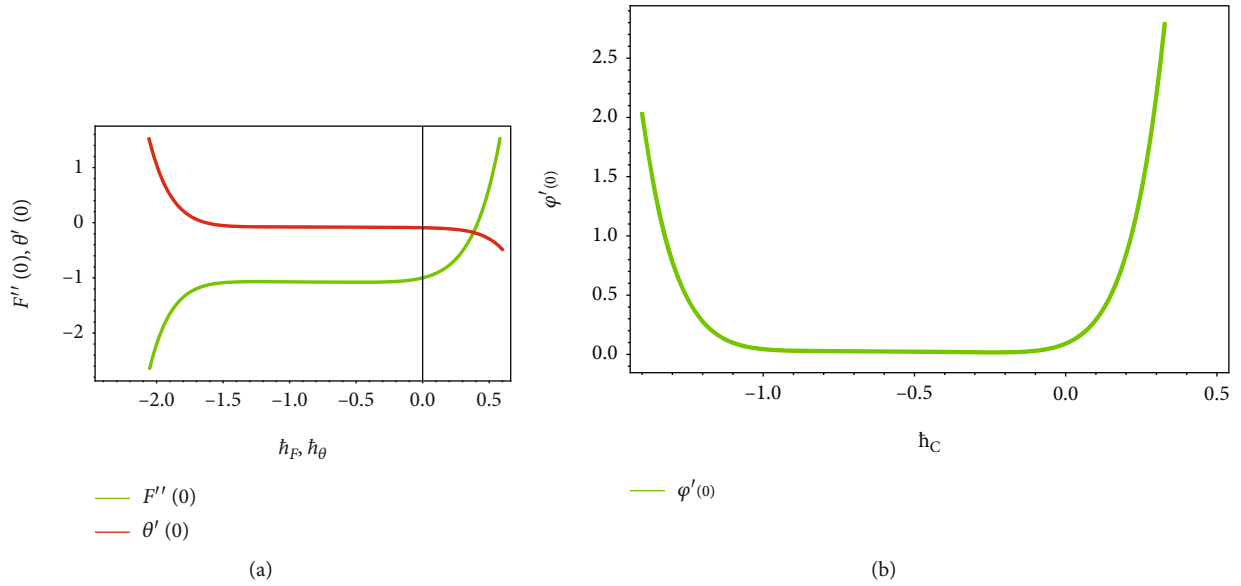


FIGURE 1: (a)  $\hbar$  - curves for  $F(\zeta)$  and  $\theta(\zeta)$  functions. (b)  $\hbar$  - curves for  $\varphi(\zeta)$  function.

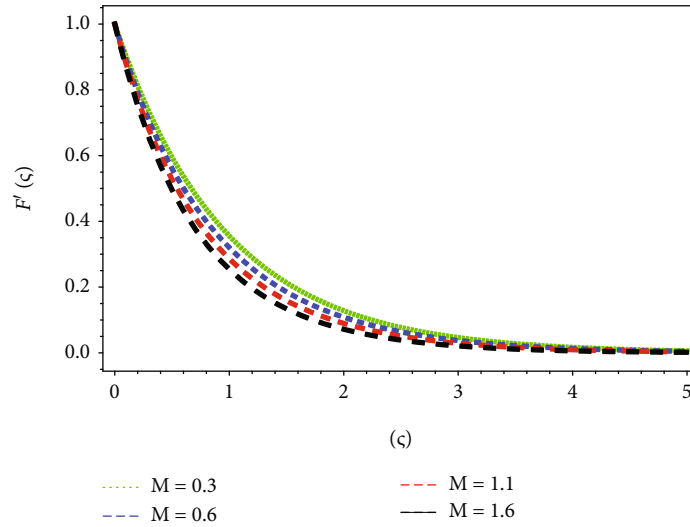
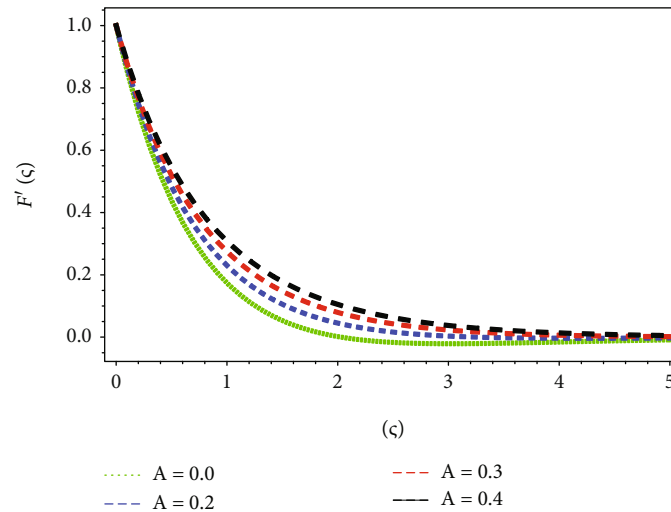
substantial use in biomedicine because of the special manner in which they interact with matter. Hybrid nanofluids are a particular type of nanofluid. Hybrid nanofluids are formed by the suspension in the base fluid of two or more kinds of nanoparticles with hybrid nanoparticles. Hybrid nanoparticle is a specific substance that integrates the physical and chemical characteristics of different materials at the same time and has been commonly used in the production of anti-tumor medicines. Some studies that discuss nanofluids and hybrid nanofluids are reported in the refs. [4–10]. Magnetic fluid flow due to the rotating body has potential applications in biomedical sciences, electronic devices, and aerodynamics [11]. Hafeez et al. investigated the flow of an Oldroyd-B fluid type's magnetic fluid in a rotating system using modified Fourier's law [12]. Reddy et al. reported the influence of hybrid nanoparticles in a swirling flow using an activation energy model [13]. Fluid flow investigation in biomicrofluidic systems is implemented by the electroosmosis process. The latter is the principal instrument for the stream activation in a wide scope of utilization. This electroosmotic transition takes place in such a way that, as long as the polar outer layer is connected to the electrolyte device, the counterparts of the electrolyte should be allowed to pass through the surface of the capacitor and ultimately to build a membrane with a high convergence of counteractors, which is commonly named after the Stern layer. In addition to the exterior diffuse coat, the Electric Double Layer (EDL) is produced in the area of the charged board. Applying the ambient electrical field to the electroosmotic flow (EOF), the functional particles in the dispersed area of the EOF are induced to travel and accomplish fluid displacement, which is typically known as the "EOF." Propelled by the monumental use of the stream of the electroassimilation, various experiments are investigated [14–18]. Christopher et al. [19] discussed the chemical reaction consequence on the flow of hybrid nanoliquid on an SS with Cattaneo–

TABLE 1: The allowable ranges for convergence solutions.

Approximate solutions	Auxiliary parameters	Convergent intervals
$F(\zeta)$	$\hbar_F$	$-1.4 \leq \hbar_F \leq -0.4$
$\theta(\zeta)$	$\hbar_\theta$	$-1.2 \leq \hbar_\theta \leq -0.5$
$\varphi(\zeta)$	$\hbar_\varphi$	$-0.7 \leq \hbar_\varphi \leq -0.3$

Christov heat flux. Gowda et al. [20] examined the convective stream of second grade fluid on a coiled SS with Dufour and Soret effects. Alhadhrami et al. [21] pondered the LTNE impact on the flow of Casson liquid on an SS with a porous medium. Recently, Ali et al. [22–26] conferred the flow of different fluid past stretching surfaces with several influencing factors by considering different nanoparticles' suspension. Another significant nonmechanical micropump is the electromagnetohydrodynamic (EMHD) which has different applications, some of which, fluid mixing and pumping along with flow control in microfluidic systems [27–29]. Lorentz force is generated because of an electric field force applied across the channel in the presence of a perpendicular magnetic field force. Reddy et al. reported the influence of hybrid nanoparticles in a swirling flow using an activation energy model [13]. Khan demonstrated the transportation of hybrid nanoparticles in convective flow due to a rotating plate [30]. Hayat et al. considered the viscous dissipation and Joule heating in the flow due to a rotating plate with variable thickness [31]. The following references [32–37] provide more about thermal radiation and activation energy.

In this study, we explored the nature of stagnation point flow of nanoliquid driven by stretching surface. The role of Brownian motion and thermophoresis is also considered in modeling the flow system. The mechanisms of heat and

FIGURE 2: Plot of  $F'(\zeta)$  via diverse  $M$ .FIGURE 3: Plot of  $F'(\zeta)$  via diverse  $A$ .

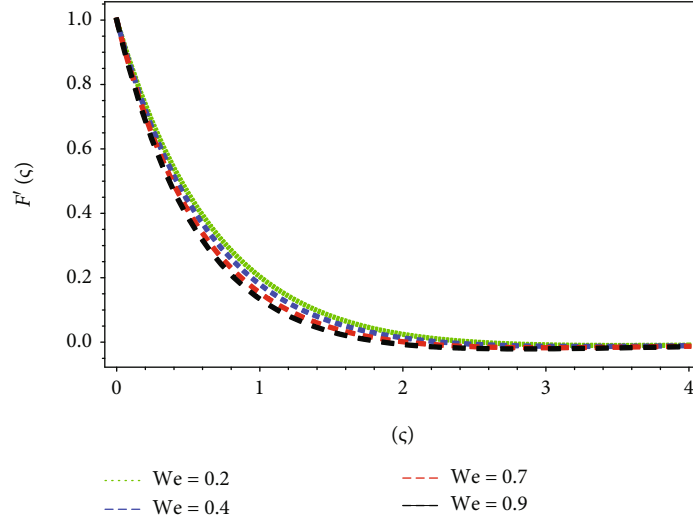
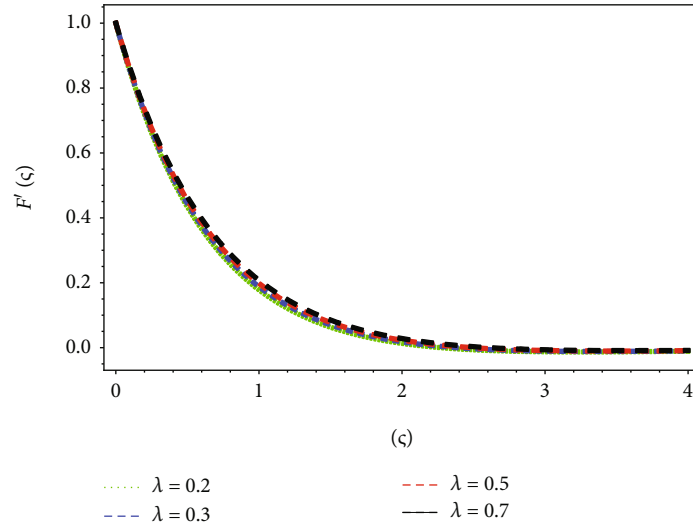
mass flow are also examined. The arisen nonlinear partial differential equations are altered to ODEs via transformations and then solved analytically [38–40]. Following are the key points of this investigation:

- (i) The main goal of this study is to examine the two-dimensional incompressible Walters-B nanofluid flow over a stretching sheet. Furthermore, the graphs are also used to discuss the variations in detailed profiles as a consequence of several dimensionless parameters
- (ii) To study time subservient Walter-B fluid flow resulting from the impression of heat and mass transfer
- (iii) Mathematical modeling of the fundamental flow equations comprises momentum, energy, and diffusion balances

## 2. Problem Formulation

Consider the magnetohydrodynamic MHD flow of a Walter-B non-Newtonian nanofluid with heat transfer transient through a two-dimensional conduit. The impact of Brownian and thermophoretic effects is considered into the account. Additionally, the thermal radiation, Joule heating, viscous dissipation, and heat generation/absorption characteristics are taken into consideration. The fluid is electrically conductive in nature along with uniform magnetic field  $B_0$  in normal direction. Based on these assumptions with the approximations of the boundary layer, the basic equations of Walter-B fluid reduced as follow [31]:

$$\frac{\partial \bar{u}}{\partial \bar{x}} + \frac{\partial \bar{v}}{\partial \bar{y}} = 0, \quad (1)$$

FIGURE 4: Plot of  $F'(\zeta)$  via diverse  $We$ .FIGURE 5: Plot of  $F'(\zeta)$  via diverse  $\lambda$ .

$$\begin{aligned} \bar{u} \frac{\partial \bar{u}}{\partial \bar{x}} + \bar{v} \frac{\partial \bar{u}}{\partial \bar{y}} = u_e \frac{\partial u_e}{\partial \bar{x}} + \nu \frac{\partial^2 \bar{u}}{\partial (\bar{y})^2} - \frac{k_0}{\rho_f} \left( \bar{u} \frac{\partial^3 \bar{u}}{\partial \bar{x} \partial (\bar{y})^2} + \bar{v} \frac{\partial^3 \bar{u}}{\partial (\bar{y})^3} \right. \\ \left. + \frac{\partial \bar{u}}{\partial \bar{x}} \frac{\partial^2 \bar{u}}{\partial (\bar{y})^2} - \frac{\partial \bar{u}}{\partial \bar{y}} \frac{\partial^2 \bar{u}}{\partial \bar{x} \partial \bar{y}} \right) + \frac{\sigma B_0^2 \bar{u}^2}{\rho_f} (u_e - \bar{u}) \\ + g \beta_T (\bar{T} - \bar{T}_\infty) - g \beta_C (\bar{C} - \bar{C}_\infty), \end{aligned} \quad (2)$$

$$\begin{aligned} \bar{u} \frac{\partial \bar{C}}{\partial \bar{x}} + \bar{v} \frac{\partial \bar{C}}{\partial \bar{y}} = D_B \left( \frac{\partial^2 \bar{C}}{\partial (\bar{y})^2} \right) + \frac{D_T}{\bar{T}_\infty} \left( \frac{\partial^2 \bar{T}}{\partial (\bar{y})^2} \right) \\ - k_r^2 e^{-E_a/kT^*} \left( \frac{\bar{T}}{\bar{T}_\infty} \right)^m (\bar{C} - \bar{C}_\infty), \end{aligned} \quad (4)$$

with boundary postulates [31]

$$\begin{aligned} \bar{u} \frac{\partial \bar{T}}{\partial \bar{x}} + \bar{v} \frac{\partial \bar{T}}{\partial \bar{y}} = \alpha \frac{\partial^2 \bar{T}}{\partial \bar{y}^2} - \frac{1}{(\rho c)_f} \frac{16\sigma^*}{3k^*} \frac{\partial}{\partial \bar{y}} \left( \bar{T}^3 \frac{\partial \bar{T}}{\partial \bar{y}} \right) + \frac{\sigma B_0^2 \bar{u}^2}{(\rho c)_f} \\ + \tau \left[ D_B \frac{\partial \bar{C}}{\partial \bar{y}} \frac{\partial \bar{T}}{\partial \bar{y}} + \frac{D_T}{\bar{T}_\infty} \left( \frac{\partial \bar{T}}{\partial \bar{y}} \right)^2 \right] \\ + \frac{Q_0}{(\rho c)_f} (\bar{T} - \bar{T}_\infty), \end{aligned} \quad (3)$$

$$\begin{aligned} \bar{u} = u_w(\bar{x}) = c_1 \bar{x}, \bar{v} = 0, -k \frac{\partial \bar{T}}{\partial \bar{y}} = (\bar{T}_s - \bar{T}) h_1, -D_B \frac{\partial \bar{C}}{\partial \bar{y}} = (\bar{C}_s - \bar{C}) h_2 : \bar{y} = 0 \\ \bar{u} = u_e = c_2 \bar{x}, \bar{T} \rightarrow \bar{T}_\infty, \bar{C} \rightarrow \bar{C}_\infty : \bar{y} \rightarrow \infty, \end{aligned} \quad (5)$$

whereas  $(\bar{u}, \bar{v})$  are velocity component in  $\bar{x}$ - and  $\bar{y}$ -direction,  $u_e$  is the free stream velocity,  $D_B$  Brownian motion,  $D_T$  thermophoretic coefficient,  $g$  gravitational acceleration,  $\bar{C}$  fluid concentration,  $\bar{T}$  temperature;  $\alpha = k/\rho c_f$  thermal



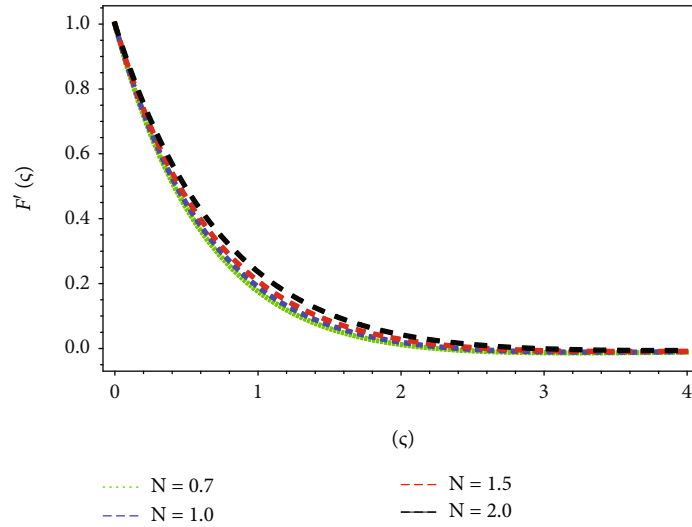


FIGURE 6: Plot of  $F'(\zeta)$  via diverse  $N$ .

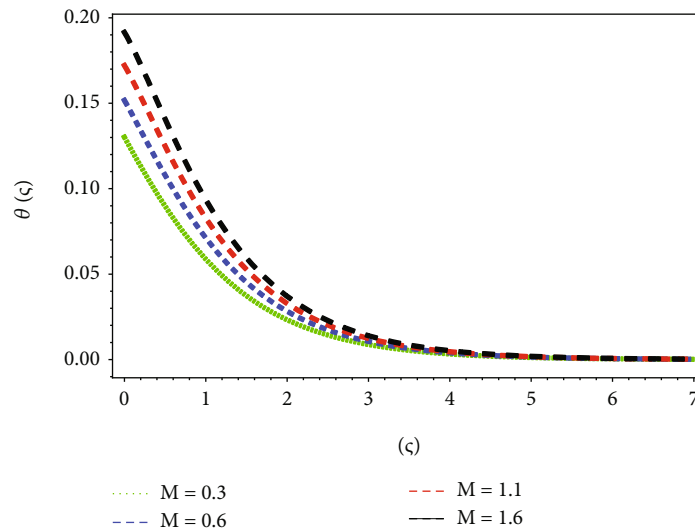


FIGURE 7: Impact of  $M$  on temperature field.

diffusion coefficient,  $\nu = \mu_0/\rho_f$  kinematic viscosity,  $\sigma^*$  is the Stefan-Boltzmann constant,  $k^*$  absorption coefficient,  $\beta_C$  denote the solutal expansion coefficient,  $\beta_T$  thermal expansion coefficient,  $\tau$  heat capacity ratio,  $\sigma$  electrical conductivity,  $Q_0$  heat generation/absorption,  $Ea$  activation energy,  $\bar{T}_s$  surface temperature,  $\bar{C}_s$  surface concentration,  $h_1$  heat transfer coefficient,  $h_2$  mass transfer coefficient,  $m$  fitted rate constant,  $kr$  reaction rate,  $\bar{T}_\infty$  ambient temperature,  $\bar{C}_\infty$  ambient concentration, and  $k_0$  short memory coefficient.

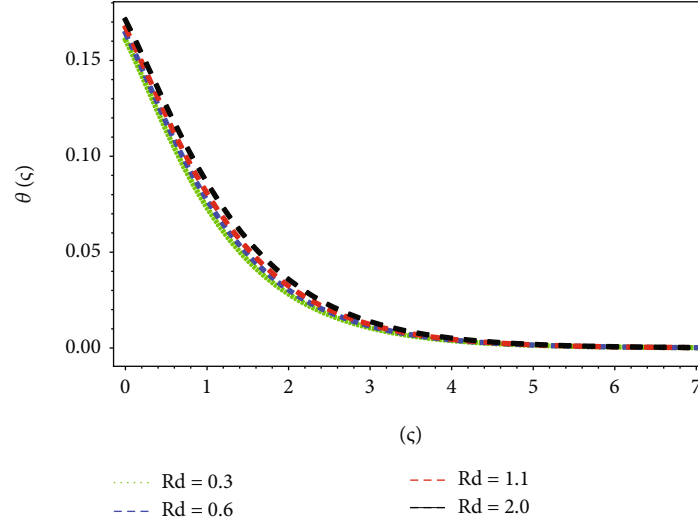
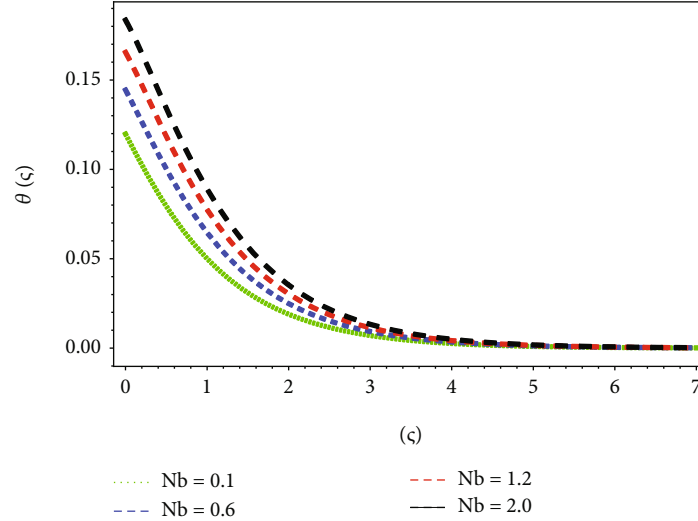
Adopting the local transformation similarity [31]:

$$\bar{u} = c_1 \bar{x} F'(\zeta), \bar{v} = -(c_1 \nu)^{1/2} F(\zeta), \zeta = \sqrt{\frac{c_1}{\nu}} \bar{y}, \theta = \frac{\bar{T} - \bar{T}_\infty}{\bar{T}_s - \bar{T}_\infty}, \varphi = \frac{\bar{C} - \bar{C}_\infty}{\bar{C}_s - \bar{C}_\infty}, \quad (6)$$

After incorporating Equation (6), one gets the dimensional Equations (2)–(5) into dimensionless form:

$$F''' - F'2 + FF'' + We(F''2 - 2F'F''' + FF'''' ) + M(A - F') + A^2 + \lambda(\theta + N\varphi) = 0, \quad (7)$$

$$\left( \left( 1 + \frac{3}{4}R(1 + (\theta_f - 1)\theta)^3 \right) \theta' \right)' + Pr(F\theta' + Nb\theta'\varphi' + Nt\theta'^2 + MEcF'^2 + S\theta) = 0, \quad (8)$$

FIGURE 8: Impact of  $R$  on temperature field.FIGURE 9: Impact of  $Nb$  on temperature field.

$$\varphi'' + ScF\varphi' + \left(\frac{Nt}{Nb}\right)\theta'' - Sc\sigma(1 + \delta_1\theta)^m \varphi \exp\left[\frac{-E_1}{1 + \delta_1\theta}\right] = 0, \quad (9)$$

$$F = 0, F' = 1, \theta' = -\alpha(1 - \theta), \varphi' = -\beta(1 - \varphi): \quad (10)$$

$$\zeta = 0 \text{ and } F' = A, \theta = 0, \varphi = 0 : \zeta = \infty$$

where  $We = k_0 c_1 / \mu_0$  is the Weissenberg number,  $\lambda = g\beta_T / c_1^2 \bar{x}(\bar{T}_s - \bar{T}_\infty)$  mixed convection parameter,  $M = \sigma B_0^2 / \rho_f c_1$  magnetic parameter,  $N = g\beta_C / c_1^2 \bar{x}(\bar{C}_s - \bar{C}_\infty)$  ratio of thermal to concentration buoyancy forces,  $Nt = \tau D_T / T_\infty^* \nu(\bar{T}_s - \bar{T}_\infty)$  thermophoresis force,  $Nb = \tau D_B / \nu(\bar{C}_s - \bar{C}_\infty)$  Brownian motion,  $\delta_1 = \bar{T}_s - \bar{T}_\infty / \bar{T}_\infty$  temperature difference,  $R = 4\sigma^* (\bar{T}_\infty)^3 / k k^*$  radiation factor,  $S = Q_0 / (\rho c)_f c_1$  heat generation factor,  $Ec = \bar{u}_w^2 / c_f(\bar{T}_s - \bar{T}_\infty)$  Eckert number,  $B_1 = h_1 / k\sqrt{\nu/y}$

thermal Biot number,  $B_2 = h_2 / D_B \sqrt{\nu/y}$  Biot number,  $Pr = \mu c_p / k$  Prandtl number,  $Sc = \nu / D_B$  Schmidt number,  $\sigma = k_r^2 / c_1$  dimensionless reaction rate,  $A = c_2 / c_1$  ratio of constants,  $\theta_F = \bar{T}_w / \bar{T}_\infty$  temperature ratio parameter, and  $E_1 = E_a / \kappa \bar{T}_\infty$  activation energy.

The physical quantities for the engineering practical and usefulness are the local skin friction, temperature gradient, and concentration gradient. The dimensionless form of these quantities is, respectively, expressed as follows

$$\sqrt{Re_x} C f_x = \left(1 - 3B \frac{dF}{d\zeta} \frac{d^2 F}{d\zeta^2}\right)_{\zeta=0}, \quad (11)$$

$$\frac{Nu_x}{\sqrt{Re_x}} = -\left(1 + \frac{4}{3}R(1 + (T_f - 1)T)^3\right) \frac{d\theta}{d\zeta} \Big|_{\zeta=0}, \quad (12)$$

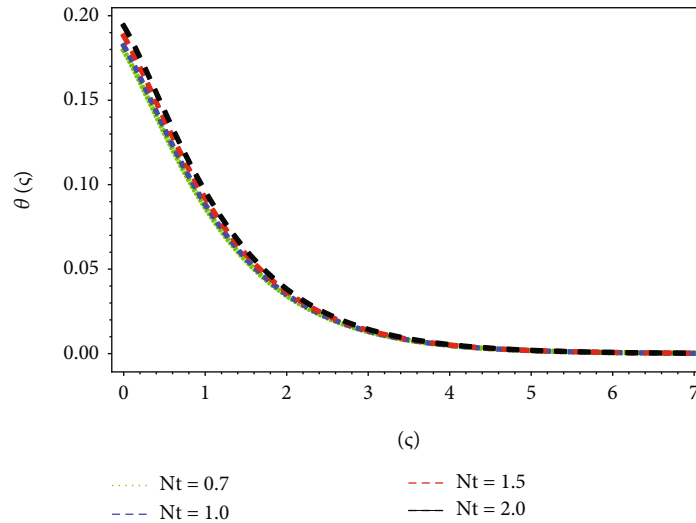


FIGURE 10: Impact of  $Nt$  on temperature field.

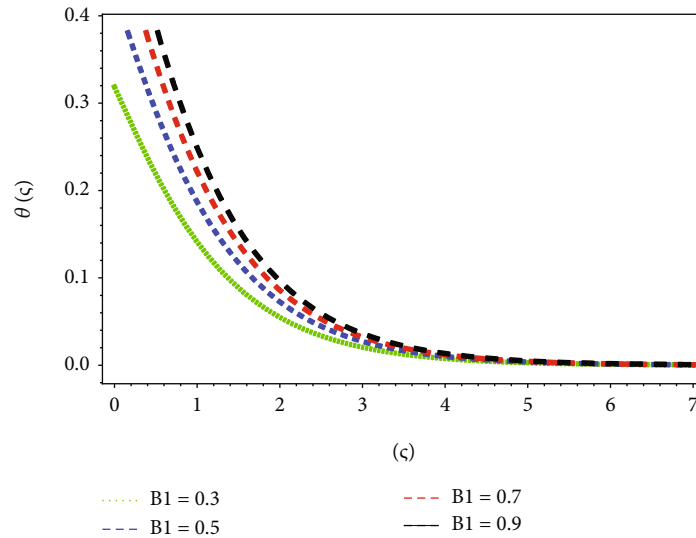


FIGURE 11: Impact of  $B_1$  on temperature field.

One can obtain the  $Cf_x$  in nondimensional form by substituting Equation (12) in Equation (12):

$$\frac{Sh_x}{\sqrt{Re_x}} = -\left. \frac{d\varphi}{d\zeta} \right|_{\zeta=0}, \tag{13}$$

$Re_x = c_1 x^2 / \nu$  is the local Reynold number.

### 3. Convergence and Stability Analysis

The series solutions developed by the homotopic analysis method (HAM) comprise the convergence control parameters  $\hbar_F, \hbar_\theta$  and  $\hbar_\varphi$  [36–38]. These convergence control parameters are effective at regulating and controlling the series solution convergence region. The admissible values are attained by the flat parts of the  $\hbar$  – curves. Figure 1 displays the acceptable ranges of  $\hbar_F, \hbar_\theta$  and  $\hbar_\varphi$  are  $-1.4 \leq$

$\hbar_F \leq -0.4, -1.2 \leq \hbar_\theta \leq -0.5$  and  $-0.7 \leq \hbar_\varphi \leq -0.3$ . Table 1 display the convergence region for the approximate solutions.

### 4. Discussions

This section discusses the graphical implications of the physical dimensionless quantities on the relevant profiles. By selecting appropriate similarity variables, the equations that reflect the specified flow are converted first into ODEs. To clearly understand the behavior of flow profiles, an analytical scheme is adopted, which is strategized and debated using graphs.

Figure 2 portrays the sway of  $M$  on velocity  $F'(\zeta)$  portraits of stagnation point flow of nanofluids. It is noticed that velocity distributions diminish with higher values of magnetic parameter  $M$ . In reality, the fluid viscosity increases as  $M$  apply to any fluid due to which magnetic field power

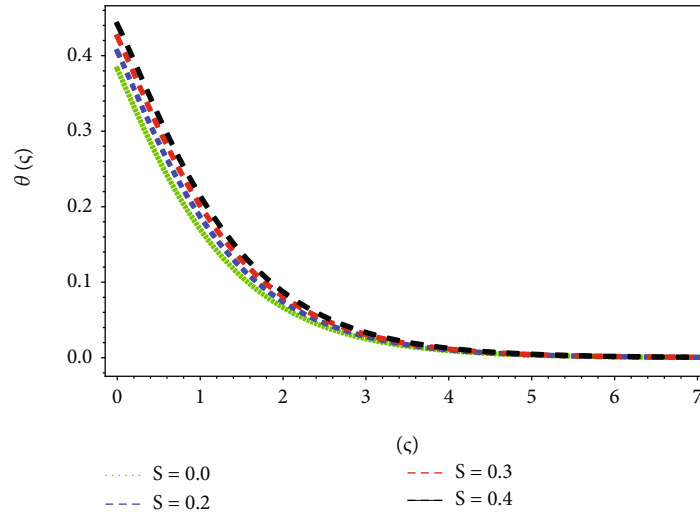


FIGURE 12: Impact of  $S$  on temperature field.

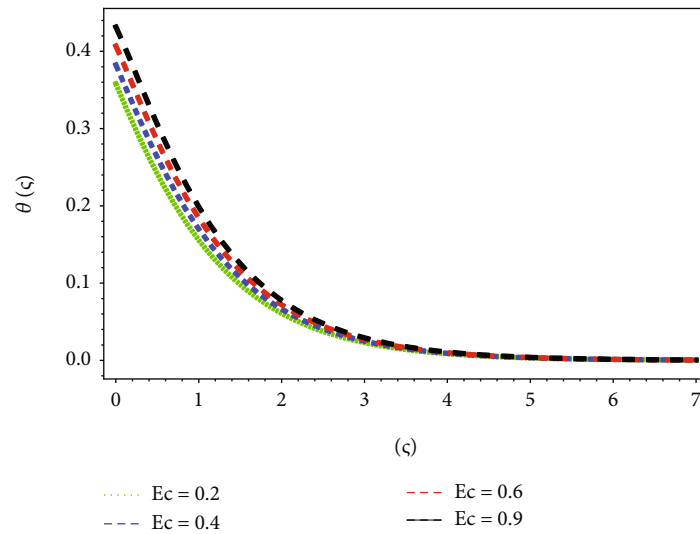


FIGURE 13: Impact of  $Ec$  on temperature field.

increase. In consequences, Lorentz force is produced which slows down the fluid flow significantly. It is observed from Figure 3 that the velocity sketches are enhance in the entire flow domain of nanofluid with the increasing values of ratio parameter  $A$ . Figure 4 reveals the sway of Weissenberg number  $We$  on velocity sketches of stagnation point flow of nanofluid. It is pointed out that in the intensification in  $F'(\zeta)$  field with step up values of  $We$  number. The sketches of velocity fields with augmented values of mixed convection parameter  $\lambda$  in the flow domain are illustrated through Figure 5. This is owing to the fact that the increasing values of  $\lambda$  increase the buoyancy force. Consequently,  $F'(\zeta)$  profiles increase. It is detected from Figure 6 that the  $F'(\zeta)$  profiles of the nanofluid intensify in the fluid region with higher estimation of ratio of thermal to concentration buoyancy forces  $N$ .

The distribution of  $\theta(\zeta)$  temperature of nanofluid with step up values of  $M$  is presented in Figure 7. It is observed

that boundary layer thickness improves with incrementing values of  $M$ . This is due to the fact that Lorentz force which acts against the fluid flow direction, hence the enhancement in  $\theta(\zeta)$  profiles with increasing values of  $M$  in the entire fluid flow. Attributes' features of radiation parameter  $R$  on  $\theta(\zeta)$  are exposed in Figure 8. It is perceived from this plot that the  $\theta(\zeta)$  sketches enhance in the entire flow of nanofluid with increasing data of  $R$ . The sketches of  $\theta(\zeta)$  field with augmented values of  $Nb$  in the flow region are describes through Figure 9. The energy sketches are enlarged with increasing data of  $Nb$ . This owes due to the motion of nanoparticles in the base fluid that is influenced by the motion of particles, and it moves from hot surface region and is related to the size and agglomeration of molecules. It is observed in Figure 10 that  $\theta(\zeta)$  intensify subject to increasing value of  $Nt$  parameter. In reality, the thermophoretic forces and the nanoscale solid particles in the base liquid produce warm surfaces in the boundary layer region. Thus,  $\theta(\zeta)$  of nanofluid in the entire fluid flow boosts. The effect of thermal

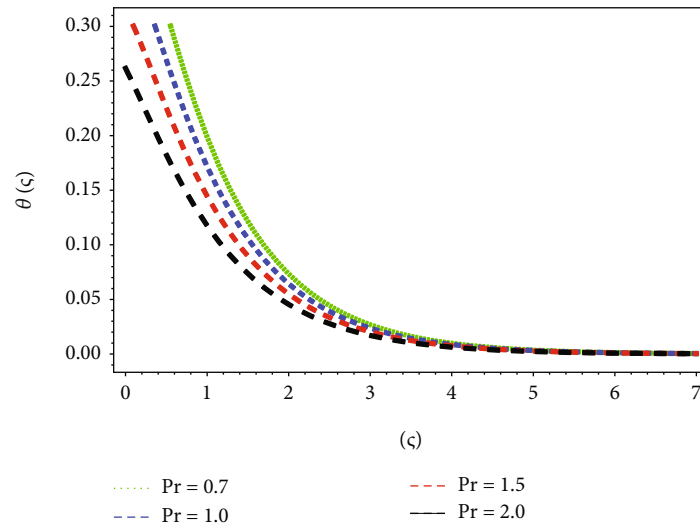


FIGURE 14: Impact of Pr on temperature field.

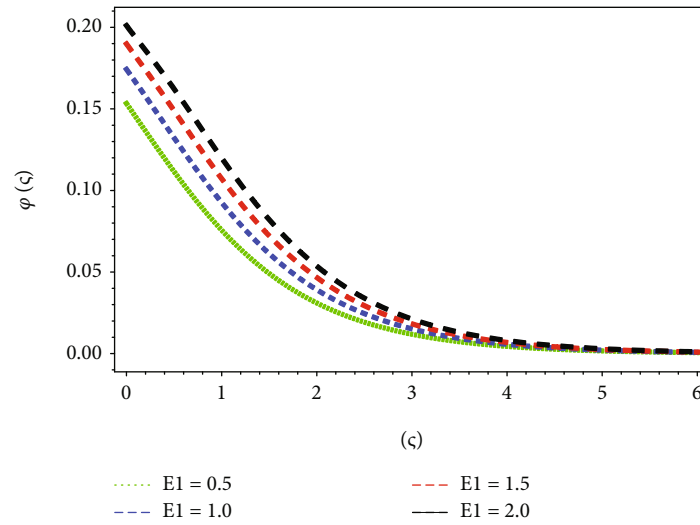


FIGURE 15: Nanoparticle volume fraction via  $E_1$ .

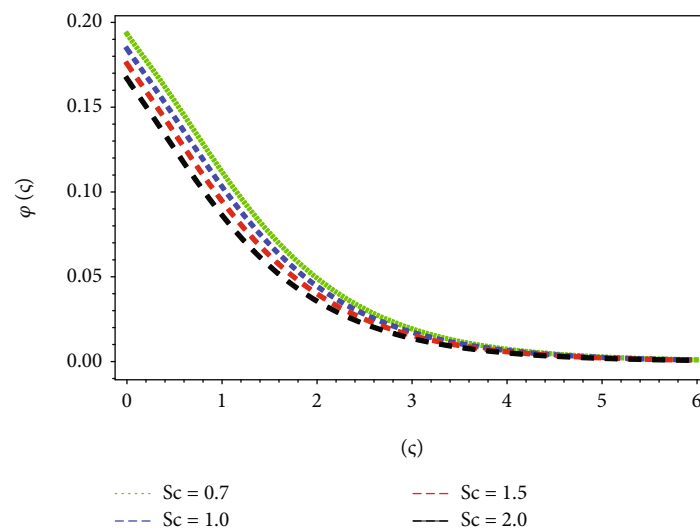


FIGURE 16: Nanoparticle volume fraction via Sc.

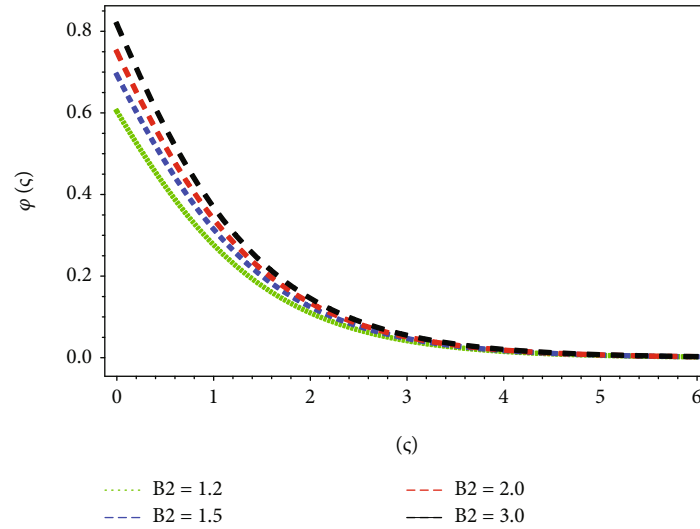


FIGURE 17: Nanoparticle volume fraction via  $B_2$ .

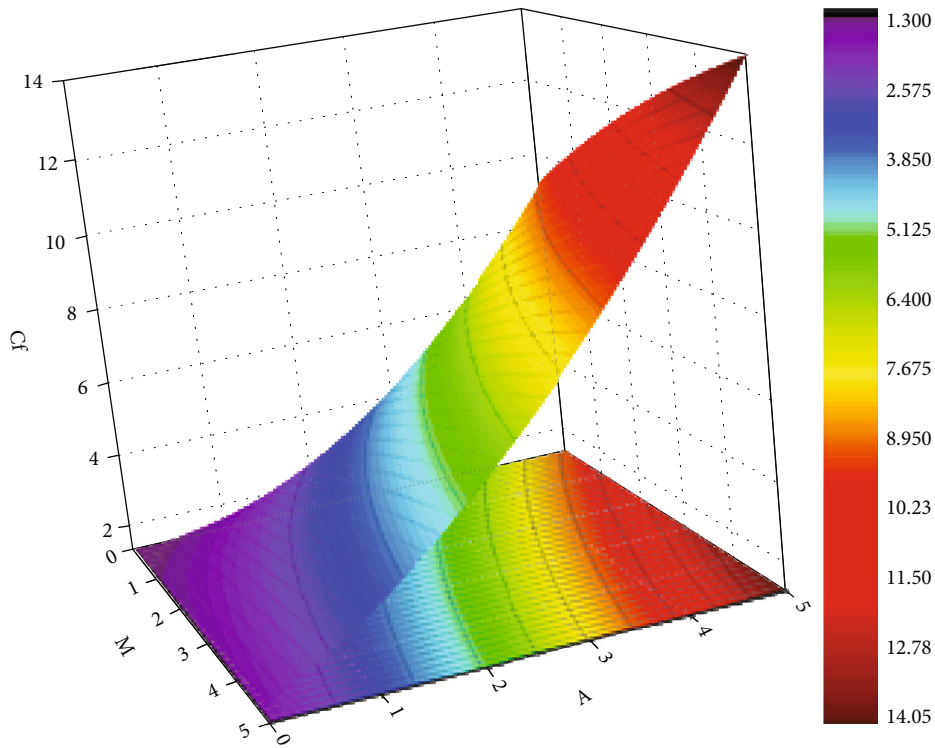


FIGURE 18: Results of  $M$  and  $A$  via  $Cf_x$ .

Biot number  $B_1$  on  $\theta(\zeta)$  is portrayed in Figure 11. It is cognized that temperature profiles of nanofluid increase with rising values of  $B_1$ . Figure 12 explains the effect of heat generation parameter  $S$  on  $\theta(\zeta)$  thermal curves. The energy field of the nanofluid increases with larger estimation of  $S$ . Physically, upsurgng values of  $S$  add extra thermal energy to the entire flow domain. Variation in  $\theta(\zeta)$  energy profiles is shown in Figure 13. The thermal field  $\theta(\zeta)$  sketches enhance in the entire flow of nanofluid with increasing data of  $Ec$ . Figure 14 discloses the sway of  $Pr$  on  $\theta(\zeta)$  sketches of

nanofluid. It is noticed that thermal diffusivity decreases with the incrementing values of  $Pr$ . Hence,  $\theta(\zeta)$  curves decline.

Figure 15 describes the power of  $E_1$  on  $\varphi(\zeta)$  concentration distribution nanofluids. It is pointed out that  $\varphi(\zeta)$  augmented with upsurgng values of  $E_1$ . Figure 16 shows the role of  $Sc$  on  $\varphi(\zeta)$ . The improving values of  $Sc$  diminish the concentration profiles. The lower values of  $Sc$  correspond to the uppermost  $\varphi(\zeta)$  of nanoscale materials. In an increment in the  $Sc$ , there is a decline in the  $\varphi(\zeta)$  due to the

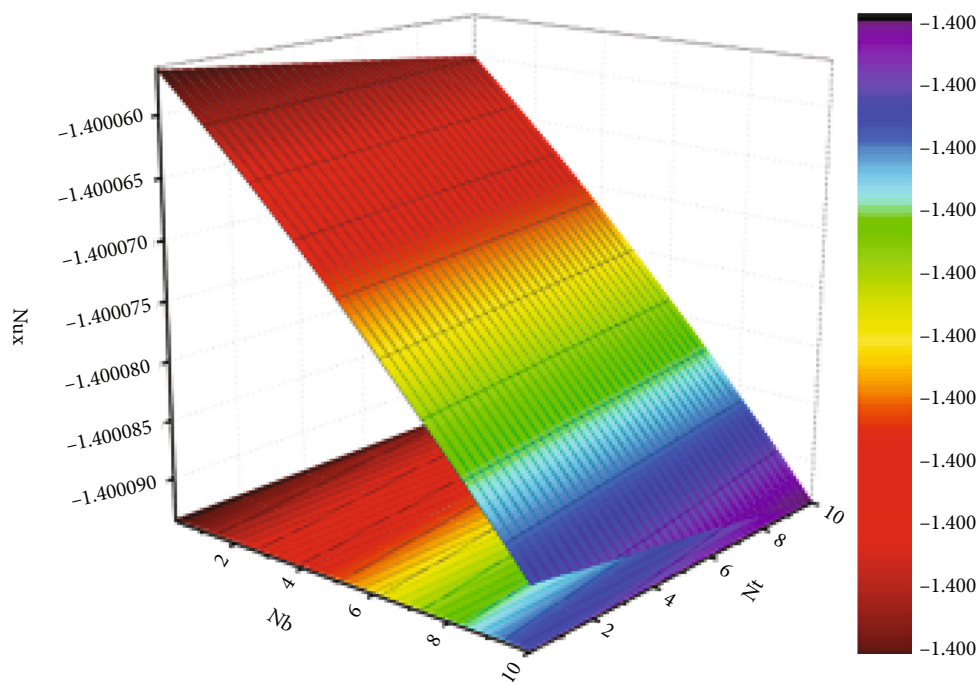


FIGURE 19: Results of  $Nb$  and  $Nt$  via  $Nu_x$ .

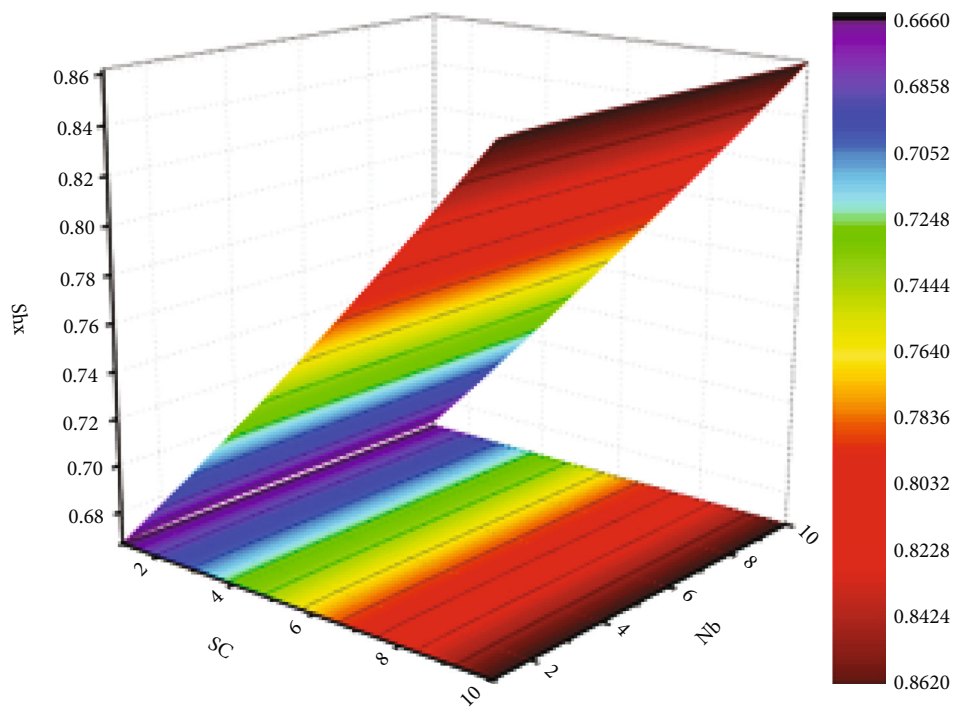


FIGURE 20: Results of  $Sc$  and  $Nb$  via  $Sh_x$ .

mass diffusion. The impression of  $B_2$  on  $\varphi(\zeta)$  is revealed in Figure 17. The increasing data of  $B_2$  enhances  $\varphi(\zeta)$  profiles. One can observe that  $\varphi(\zeta)$  is the increasing function of  $B_2$ . Figure 18 displays the variation of  $Cf_x$  for diverse values of  $M$  and  $A$ . As expected, both parameter the surface drag force with larger estimation of these factors.

Figure 19 shows the variation of  $Nu_x$  for unlike values of  $Nb$  and  $Nt$ . It has been detected from this plot that  $Nu_x$  gets dwindled for higher values of these parameters. Figure 20 shows the deviation in mass flow rate coefficient  $Sh_x$ . As witnessed, mass transfer rate increases for increasing data of  $Nb$  and  $Sc$ .

## 5. Conclusions

From this study, the following conclusions can be drawn:

- (i) It has been noticed that boundary layers in  $F'(\zeta)$  profiles diminish for incrementing data of  $M$  and  $We$ , whereas increasing the  $A$ ,  $N$ , and  $\lambda$  caused the  $F'(\zeta)$  profiles to upsurge
- (ii) The thermal field curves and heat transfer rates got boost due to augmentation in  $M$ ,  $R$ ,  $S$ , and  $Ec$  along with  $Nb$ ,  $Nt$ , and  $B_1$
- (iii) With the upsurge in the  $Pr$ , the fluid thermal energy and related thickness dwindle
- (iv) The fluid concentration curves increase owing to increase  $B_2$ ,  $E_1$ , and  $Nt$ . Moreover, increasing  $Nb$  and  $Sc$  caused the temperature profiles to diminish
- (v) The surface drag force coefficient  $Cf_x$  enhances with higher data of  $M$  and  $A$  parameters
- (vi) It has been found that the heat transfer coefficient  $Nu_x$  decays via increasing values of  $Nb$  and  $Nt$  parameters
- (vii) Uprising of mass flow rate  $Sh_x$  is detected for the increasing values of  $Sc$  and  $Nb$  parameters

## Data Availability

The data used to support the findings of this study are available from the corresponding author upon request.

## Conflicts of Interest

The authors declare no conflict of interest.

## Acknowledgments

This study was supported by the Princess Nourah bint Abdulrahman University Researchers Supporting Project number (PNURSP2022R184), Princess Nourah bint Abdulrahman University, Riyadh, Saudi Arabia.

## References

- [1] J. Maxwell, *A Treatise on Electricity and Magnetism*, Oxford University Press, Cambridge, UK, England, 1904.
- [2] S. U. S. Choi, Z. G. Zhang, W. Yu, F. E. Lockwood, and E. A. Grulke, "Anomalous thermal conductivity enhancement in nanotube suspensions," *Applied Physics Letters*, vol. 79, no. 14, pp. 2252–2254, 2001.
- [3] S. U. S. Choi, "Enhancing thermal conductivity of fluids with nanoparticles," *ASME International Mechanical Engineering Congress & Exposition*, pp. 99–105, 1995.
- [4] H. Sadaf and S. I. Abdelsalam, "Adverse effects of a hybrid nanofluid in a wavy non-uniform annulus with convective boundary conditions," *RSC Advances*, vol. 10, no. 26, pp. 15035–15043, 2020.
- [5] M. M. Bhatti, R. Ellahi, A. Zeeshan, M. Marin, and S. I. Abdelsalam, "Swimming of motile gyrotactic microorganisms and nanoparticles in blood flow through anisotropically tapered arteries," *Frontiers in Physics*, vol. 8, pp. 1–9, 2020.
- [6] S. I. Abdelsalam and M. M. Bhatti, "Anomalous reactivity of thermo-bioconvective nanofluid towards oxytactic microorganisms," *Applied Mathematics and Mechanics*, vol. 41, no. 5, pp. 711–724, 2020.
- [7] K. S. Mekheimer, W. M. Hasona, R. E. Abo-Elkhair, and A. Z. Zaher, "Peristaltic blood flow with gold nanoparticles as a third grade nanofluid in catheter: application of cancer therapy," *Physics Letters A*, vol. 382, no. 2–3, pp. 85–93, 2018.
- [8] M. Sohail, R. Naz, and S. I. Abdelsalam, "On the onset of entropy generation for a nanofluid with thermal radiation and gyrotactic microorganisms through 3D flows," *Physica Scripta*, vol. 95, no. 4, article 045206, 2020.
- [9] S. I. Abdelsalam and M. M. Bhatti, "The study of non-Newtonian nanofluid with hall and ion slip effects on peristaltically induced motion in a non-uniform channel," *RSC Advances*, vol. 8, no. 15, pp. 7904–7915, 2018.
- [10] S. I. Abdelsalam and M. M. Bhatti, "The impact of impinging TiO<sub>2</sub> nanoparticles in Prandtl nanofluid along with endoscopic and variable magnetic field effects on peristaltic blood flow," *Multidiscipline Modeling in Materials and Structures*, vol. 14, no. 3, pp. 530–548, 2018.
- [11] H. Rout, S. S. Mohapatra, S. Shaw, T. Muhammad, M. K. Nayak, and O. D. Makinde, "Entropy optimization for Darcy–Forchheimer electromagneto-hydrodynamic slip flow of ferronanofluid due to stretching/shrinking rotating disk," in *Waves in Random and Complex Media*.
- [12] A. Hafeez, M. Khan, and J. Ahmed, "Thermal aspects of chemically reactive Oldroyd-B fluid flow over a rotating disk with Cattaneo–Christov heat flux theory," *Journal of Thermal Analysis and Calorimetry*, vol. 144, no. 3, pp. 793–803, 2021.
- [13] M. G. Reddy, N. Kumar, B. C. Prasannakumara, N. G. Rudraswamy, and K. G. Kumar, "Magnetohydrodynamic flow and heat transfer of a hybrid nanofluid over a rotating disk by considering Arrhenius energy," *Communications in Theoretical Physics*, vol. 73, no. 4, p. 045002, 2021.
- [14] Y. Kang, C. Yang, and X. Huang, "Electroosmotic flow in a capillary annulus with high zeta potentials," *Journal of Colloid and Interface Science*, vol. 253, no. 2, pp. 285–294, 2002.
- [15] S. Ghosal, "Electrokinetic flow and dispersion in capillary electrophoresis," *Annual Review of Fluid Mechanics*, vol. 38, no. 1, pp. 309–338, 2006.
- [16] U. Ghosh and S. Chakraborty, "Electroosmosis of viscoelastic fluids over charge modulated surfaces in narrow confinements," *Physics of Fluids*, vol. 27, no. 6, article 062004, 2015.
- [17] K. S. Mekheimer, W. M. Hasona, A. A. El-Shehhy, and A. Z. Zaher, "Electrokinetics of dielectric non-Newtonian bio fluids with heat transfer through a flexible channel: numerical study," *Computational Methods in Science and Technology*, vol. 23, pp. 331–341, 2017.
- [18] H. Keramati, A. Sadeghi, M. H. Saidi, and S. Chakraborty, "Analytical solutions for thermo-fluidic transport in electroosmotic flow through rough microtubes," *International Journal of Heat and Mass Transfer*, vol. 92, pp. 244–251, 2016.
- [19] A. J. Christopher, N. Magesh, R. J. P. Gowda, R. N. Kumar, and R. S. V. Kumar, "Hybrid nanofluid flow over a stretched cylinder with the impact of homogeneous–heterogeneous reactions and Cattaneo–Christov heat flux: series solution and numerical simulation," *Heat Transfer*, vol. 50, no. 4, pp. 3800–3821, 2021.



- [20] R. J. P. Gowda, A. M. Jyothi, R. N. Kumar, B. C. Prasannakumara, and I. E. Sarris, "Convective flow of second grade fluid over a curved stretching sheet with Dufour and Soret effects," *International Journal of Applied and Computational Mathematics*, vol. 7, pp. 1–16, 2021.
- [21] A. Alhadhrami, C. Vishalakshi, B. Prasanna et al., "Numerical simulation of local thermal non-equilibrium effects on the flow and heat transfer of non-Newtonian Casson fluid in a porous media," *Case Studies in Thermal Engineering*, vol. 28, p. 101483, 2021.
- [22] B. Ali, S. Hussain, M. Shafique, D. Habib, and G. Rasool, "Analyzing the interaction of hybrid base liquid C<sub>2</sub>H<sub>6</sub>O<sub>2</sub>–H<sub>2</sub>O with hybrid nano-material Ag–MoS<sub>2</sub> for unsteady rotational flow referred to an elongated surface using modified Buongiorno's model: FEM simulation," *Mathematics and Computers in Simulation*, vol. 190, pp. 57–74, 2021.
- [23] B. Ali, R. A. Naqvi, D. Hussain, O. M. Aldossary, and S. Hussain, "Magnetic rotating flow of a hybrid nano-materials Ag–MoS<sub>2</sub> and Go–MoS<sub>2</sub> in C<sub>2</sub>H<sub>6</sub>O<sub>2</sub>–H<sub>2</sub>O hybrid base fluid over an extending surface involving activation energy: FE simulation," *Mathematics*, vol. 8, no. 10, p. 1730, 2020.
- [24] B. Ali, A. Shafiq, I. Siddique, Q. Al-Mdallal, and F. Jarad, "Significance of suction/injection, gravity modulation, thermal radiation, and magnetohydrodynamic on dynamics of micropolar fluid subject to an inclined sheet via finite element approach," *Case Studies in Thermal Engineering*, vol. 28, article ???, 2021.
- [25] B. Ali, T. Thumma, D. Habib, N. Salamat, and S. Riaz, "Finite element analysis on transient MHD 3D rotating flow of Maxwell and tangent hyperbolic nanofluid past a bidirectional stretching sheet with Cattaneo Christov heat flux model," *Thermal Science and Engineering Progress*, vol. 28, article 101089, 2022.
- [26] B. Ali, I. Siddique, A. Ahmadian, N. Senu, L. Ali, and A. Haider, "Significance of Lorentz and Coriolis forces on dynamics of water based silver tiny particles via finite element simulation," *Ain Shams Engineering Journal*, vol. 13, no. 2, p. 101572, 2022.
- [27] M. Buren and Y. Jian, "Electromagnetohydrodynamic (EMHD) flow between two transversely wavy microparallel plates," *Electrophoresis*, vol. 36, no. 14, pp. 1539–1548, 2015.
- [28] M. M. Bhatti, A. Zeeshan, N. Ijaz, O. Anwar Bég, and A. Kadir, "Mathematical modelling of nonlinear thermal radiation effects on EMHD peristaltic pumping of viscoelastic dusty fluid through a porous medium duct," *Engineering Science and Technology, an International Journal*, vol. 20, no. 3, pp. 1129–1139, 2017.
- [29] R. E. Abo-Elkhair, K. S. Mekheimer, and A. Z. Zaher, "Electromagnetohydrodynamic oscillatory flow of a dielectric fluid through a porous medium with heat transfer: Brinkman model," *Bio Nano Science*, vol. 8, no. 2, pp. 1–13, 2018.
- [30] M. I. Khan, "Transportation of hybrid nanoparticles in forced convective Darcy-Forchheimer flow by a rotating disk," *International Communications in Heat and Mass Transfer*, vol. 122, p. 105177, 2021.
- [31] T. Hayat, S. Qayyum, M. I. Khan, and A. Alsaedi, "Entropy generation in magnetohydrodynamic radiative flow due to rotating disk in presence of viscous dissipation and Joule heating," *Physics of Fluids*, vol. 30, no. 1, article 017101, 2018.
- [32] H. Ur Rasheed, A. AL-Zubaidi, S. Islam, S. Saleem, Z. Khan, and W. Khan, "Effects of joule heating and viscous dissipation on magnetohydrodynamic boundary layer flow of Jeffrey nanofluid over a vertically stretching cylinder," *Coatings*, vol. 11, no. 3, p. 353, 2021.
- [33] S. Islam, H. Ur Rasheed, K. S. Nisar, N. A. Alshehri, and M. Zakarya, "Numerical simulation of heat mass transfer effects on MHD flow of Williamson nanofluid by a stretching surface with thermal conductivity and variable thickness," *Coatings*, vol. 11, no. 6, p. 684, 2021.
- [34] H. U. Rasheed, S. Islam, Z. Khan et al., "Thermal radiation effects on unsteady stagnation point nanofluid flow in view of convective boundary conditions," *Mathematical Problems in Engineering*, vol. 2021, 13 pages, 2021.
- [35] H. U. Rasheed, S. Islam, Z. Khan, S. O. Alharbi, H. Alotaibi, and I. Khan, "Impact of nanofluid flow over an elongated moving surface with a uniform hydromagnetic field and nonlinear heat reservoir," *Complexity*, vol. 2021, Article ID 9951162, 9 pages, 2021.
- [36] A. Zaib, K. Bhattacharyya, and S. Shafie, "Unsteady boundary layer flow and heat transfer over an exponentially shrinking sheet with suction in a copper-water nanofluid," *Journal of Central South University*, vol. 22, no. 12, pp. 4856–4863, 2015.
- [37] A. K. Pandey, S. Rajput, K. Bhattacharyya, and P. Sibanda, "Impact of metal oxide nanoparticles on unsteady stagnation point flow of the hybrid base fluid along a flat surface," *Pramana*, vol. 95, no. 1, 2021.
- [38] S. J. Liao, *Homotopy analysis method in nonlinear differential equations*, Springer & Higher Education Press Heidelberg, Shanghai, China, 2012.
- [39] S. Liao, *Beyond Perturbation: Introduction to the Homotopy Analysis Method*, Chapman & Hall/CRC, Boca Raton, 2003.
- [40] S. J. Liao, "An optimal homotopy-analysis approach for strongly nonlinear differential equations," *Communications in Nonlinear Science and Numerical Simulation*, vol. 15, no. 8, pp. 2003–2016, 2010.

## Research Article

# Rheological Model for Generalized Energy and Mass Transfer through Hybrid Nanofluid Flow Comprised of Magnetized Cobalt Ferrite Nanoparticles

Fahad S. Al-Mubaddel,<sup>1,2</sup> F. M. Allehiany,<sup>3</sup> Taher A. Nofal,<sup>4</sup> Mohammad Mahtab Alam ,<sup>5</sup> Atif Ali ,<sup>6</sup> and Joshua Kiddy K. Asamoah <sup>7</sup>

<sup>1</sup>Department of Chemical Engineering, College of Engineering, King Saud University, Riyadh 11421, Saudi Arabia

<sup>2</sup>King Abdullah City for Renewable and Atomic Energy: Energy Research and Innovation Center, (ERIC), Riyadh 11451, Saudi Arabia

<sup>3</sup>Department of Mathematical Sciences, College of Applied Sciences, Umm Al-Qura University, P.O. Box 715, Makkah 21955, Saudi Arabia

<sup>4</sup>Department of Mathematics and Statistics, College of Science, Taif University, P.O. Box 11099, Taif 21944, Saudi Arabia

<sup>5</sup>Department of Basic Medical Sciences, College of Applied Medical Science, King Khalid University, Abha 61421, Saudi Arabia

<sup>6</sup>Department of Mathematics, Abdul Wali Khan University Mardan, KP 23200, Pakistan

<sup>7</sup>Department of Mathematics, Kwame Nkrumah University of Science and Technology, Kumasi, Ghana

Correspondence should be addressed to Joshua Kiddy K. Asamoah; [topeljoshua@gmail.com](mailto:topeljoshua@gmail.com)

Received 12 January 2022; Revised 18 February 2022; Accepted 5 April 2022; Published 22 April 2022

Academic Editor: Taza Gul

Copyright © 2022 Fahad S. Al-Mubaddel et al. This is an open access article distributed under the Creative Commons Attribution License, which permits unrestricted use, distribution, and reproduction in any medium, provided the original work is properly cited.

The goal of the current research is to evaluate a 3D stagnation point flow of Darcy Forchheimer's hybrid nanofluid (NF) through a heated wavy flexible cylinder under the influence of slip conditions and varying thickness. A numerical model is developed for the purpose to magnify the energy and mass transmission rate and maximize the efficiency and performance of thermal energy conduction for a variety of commercial and biological purposes through methanol-based hybrid NF flow consisting of cobalt ferrite and copper nanoparticles. Due to their inclusive range of applications, copper and cobalt iron oxide nanoparticles are gaining a lot of attention in medical and technical research. The model has been articulated in the form of a set of PDEs, which are reduced by the resemblance substitutions to the system of ODEs. The obtained 1<sup>st</sup>-order differential equations are further processed by the computational strategy PCM. For the sake of accuracy and credibility, the values are verified with the *bvp4c* package. The findings are physically exhibited and analyzed. It has been observed that the induced magnetic field lessens with the upshot of the magnetic term and enhances under the action of magnetic Prandtl number  $M$ . The energy profile declines due to the variation of thermal jump constraint and boosts with the absorption and generation term.

## 1. Introduction

The flow around convex and concave bodies have been studied extensively in order to ensure the safety of the buildings by minimizing vortex-flaking, which causes a substantial amount of drag, noise, and vibration. Shape alteration is used as a flow control strategy as geometric interruptions [1]. Flow within a circular cylinder is used in many engineering mechanisms, but far less study has been conducted on

flow over a cylinder in a constrained domain, such as flow in a horizontal channel or pipe flow. Many circumstances, such as blood flow via surgical supplies in veins and flow through cylindrical items near walls, necessitate consideration of wall effects while scaling a problem. Furthermore, whereas unstructured and random forms of external roughness, such as those seen in nature, have been studied, other types of organized roughness have not. A 3D printed solid with regular sinusoidal ridges may take curliness on its

exterior [2]. When heat generation is created, Salahuddin et al. [3] investigated the differently designed nanomaterials that influenced the thermodynamic effectiveness and flow performance of nanoliquid flow owing to rigid and sinusoidal barriers. To assess the aerodynamic workloads of a 5 : 1 rectangular sinusoidal radius cylinder, Wu et al. [4] used a wind tunnel with numerous active mechanisms. Changing the amplitude and frequency results in a streamwise sequence that is completely coherent, Bilal et al. [5] investigated a nonuniform Maxwell nanoliquid flow across a stretched cylinder accompanied by a nonfluctuating suction/injection. It has been shown that the angular momentum of mass propagation grows considerably when the thermophoresis ratio is increased, but radial and angular velocity declines as the viscosity element is improved. Seo et al. [6] demonstrated a numerical estimation of a 3D flow through a rectangular enclosure. In comparison to a circular cylinder, the sinusoidal cylinder was tested to see if it might enhance total heat conduction efficiency. The influence of the cylinder shape on heat transition was noticeable, with performance improving by up to 27%. Bilal et al. [7] use up an angled extendable tube to explore the iron oxide  $\text{Fe}_3\text{O}_4$  and carbon nanotube (CNT) hybrid nanofluid (HNF). The conclusions reveal that hybrid NF is the best heat enhancer and may be used for both heat transmission and cooling purposes. Some further applications, uses, and flow models can be found in [8–10].

In comparison to common fluids like gasoline, freshwater, solo nanoparticle nanofluids, and acetylene, HNF is a revolutionary type of fluid that excels at energy conversions. HNFs can be used for a variety of thermal applications, as well as freezing in high-heat environments [11]. Hybrid NFs are used in solar energy, heat pumps, heat converters, air conditioners, automobile industry, electrical coolers, generators, radioactive systems, transmitters, ships, and bioscience. In this work, we are focusing on copper (Cu) and cobalt ferrite ( $\text{CoFe}_2\text{O}_4$ ) NPs in the universal solvent water. Copper NPs in plant water extracts may be generated using a “green” chemical method called electrodeposition. Copper nanoparticles are being used as carriers for new antitubercular drugs [12]. Copper acts as an antifungal, antibiotic, and antimicrobial agent when it is added to freshwater for coatings, polymers, and textiles. Dietary supplements containing copper have a high absorptivity. Copper alloys and metals have high tensile strength [13]. Cobalt (Co) and iron (Fe) are metals. Fe lowers interstitial resistance, allowing for charge/ion mobility on the surface and a considerable increase in specific capacitance [14]. The use of imaging techniques like MRI, PET, and CT scan, among others, has proved crucial in detecting diseases efficiently. MRI is the most versatile of them all since it can provide both functional and morphological information while keeping excellent image quality. To make it more functional, bimagnetic particles are used. Bimagnetic core-shell cobalt ferrite NPs have emerged as a feasible option for generating new MRI contrast agents with improved magnetization. Bimagnetic NPs may also be used for drug transport and photothermal treatment, making them suitable entrants for the progress of novel nanotheragnostic drugs. Magnetic hydrotherapy is

used to treat tumors because cancer cells are more sensitive to tiny temperature variations than healthy tissue. As a result, a rise in local temperature generated by the accumulation of magnetic NPs can kill cancer cells in the tumor while having little effect on normal tissues [15].

Several mathematicians and researchers address the mathematical approach to the abovementioned applications and challenges. Bilal et al. [16], for example, looked at the effects of electric and magnetic forces on the flow of water-based ferrous oxides and carbon nanotubes hybrid NFs over two revolving surfaces. The electric factor boosts the momentum boundary layer while lowering the thermal factor. Ramesh et al. [17] performed the covalent bonding reaction and activation energy characteristics in the flow of HNF through a stream-wise location using  $\text{CoFe}_2\text{O}_4$  and  $\text{Fe}_3\text{O}_4$  in EG+water. Wang et al. [18] employed an MWCNT- $\text{Fe}_3\text{O}_4$  hybrid nanoliquid to model the effects of metallic foam and nanomaterial on a typical solid heat sink's thermal efficiency. Ibrahim et al. [19] assessed the effect of turbulators on enhancing energy efficiency, as well as the hydraulic efficiency of Cu water HNF in a solar accumulator, using numerical simulations and ANSYS software. The influence of concave and convex shape on the flow of a radiative hybrid NF ( $\text{SiO}_2$ - $\text{MoS}_2$ /water) was investigated by Yaseen et al. [20]. The thermal efficiency boosts by 15.47 percent for flow over convex-shaped sheets and 14.28 percent for flow over beveled edge sheets when the volume percentage of  $\text{SiO}_2$  nanocrystals is raised from 1% to 5%. Wang et al. [21] experimentally and technically assessed the  $\text{FeZn}_4\text{Co}$ /CNF electrocatalyst and discovered these nanomaterials. References [22–25] contain some relevant literature and applications of Cu and  $\text{CoFe}_2\text{O}_4$  NPs in water for biomedical and engineering objectives.

Magnetization is among the most essential factors in manufacturing and engineering, with numerous uses. The interplay of fluid nanomaterials with magnetic fields affects the quality of various industrial items such as heat exchangers, gearboxes, and compressors. The impact of magnetic fields can regulate and make accessible the rate of cooling of numerous industrial devices. Magnetic fields are vital in interplanetary and astronomical magnetosphere applications, as well as aeronautic technologies and chemical science. The strength and distribution of the administered magnetics have a significant impact on the flow properties. Many academics submitted research articles in fluid mechanics that described the flow features under the influence of MHD. Hayat and Noreen [26] explored the role of thermal expansion and a generated MHD on the oscillatory transport of a 4th-order fluid across a vertical tunnel. Raju et al. [27] considered the cumulative implications of heat exchange and the exponential component on MHD flow across a semiplate. Some recent literature related to MHD hybrid nanofluid exists in [28–30].

The objective of this study is to build on a concept proposed by Salahuddin et al. [31] by investigating the effects of methanol-based hybrid NFs consisting of Cu and  $\text{CoFe}_2\text{O}_4$  nanoparticles on heat and mass transmission. The fluid flow has been examined in a heated wavy flexible cylinder under the upshot of slip condition, variable thickness, Darcy

Forchheimer, heat absorption/generation, and chemical reaction. The second intention is to improve thermal energy conduction productivity and performance for a variety of commercial and biological applications. The PCM approach is used to simulate the problem, and the results are compared to those obtained using the Matlab software bvp4c.

## 2. Mathematical Formulation

We supposed the steady 3D stagnation point flow of HNF flow over a heated stretchy wavy cylinder. The hybrid NF is a solution of copper Cu and cobalt ferrite  $\text{CoFe}_2\text{O}_4$  nanomaterial in methanol fluid. The cylinder is located on  $xy$ -surface where the fluid is considered at  $z > 0$ . We suppose that the cylinder radius is extreme at point A called the nodule point through which fluid flow passes. Along the  $y$ -axis the wavy side of the cylinder is fixed, where the  $z$ -axis and  $x$ -axis are normal and upright to the wavy cylinder surface. Functions  $u_e = ax$  and  $v_e = bx$  epitomize the component of velocity at the stagnation point A. Here  $a$  and  $b$  are constants, in such a way  $|b| \leq |a|$ ,  $0 < a$  (see Figure 1).

Furthermore, we are analyzing the comportment of hybrid NF flow under the act of persistent magnetic field partaking uniform strength  $M_0$ . We suppose that  $M_1$ ,  $M_2$ , and  $M_3$  are the magnetic field components in the directions of  $x$ ,  $y$ , and  $z$ , respectively. At the cylinder surface,  $M_1$  and  $M_2$  approach to  $M_e(x)$  and  $M_e(y)$ , where  $M_3$  has vanished. Here,  $T_1$  and  $T_w$  are the surface and wall temperatures of the cylinder. The fundamental calculations that regulate the fluid flow are defined as follows [31]:

$$\frac{\partial u}{\partial x} + \frac{\partial v}{\partial y} + \frac{\partial w}{\partial z} = 0, \quad (1)$$

$$\frac{\partial M_1}{\partial x} + \frac{\partial M_2}{\partial y} + \frac{\partial M_3}{\partial z} = 0, \quad (2)$$

$$\begin{aligned} u \frac{\partial u}{\partial x} + v \frac{\partial u}{\partial y} + w \frac{\partial u}{\partial z} - \frac{\mu_e}{4\pi\rho_{\text{hnf}}} \left( M_1 \frac{\partial M_1}{\partial x} + M_2 \frac{\partial M_1}{\partial y} + M_3 \frac{\partial M_1}{\partial z} \right) \\ = \rho_{\text{hnf}} \frac{\partial^2 u}{\partial z^2} + a^2 x - \frac{\mu_e}{4\pi\rho_{\text{hnf}}} \\ M_e(x) \frac{dM_e(x)}{dx} - \frac{\nu}{k^*} u - Fu^2, \end{aligned} \quad (3)$$

$$\begin{aligned} u \frac{\partial v}{\partial x} + v \frac{\partial v}{\partial y} + w \frac{\partial v}{\partial z} - \frac{\mu_e}{4\pi\rho_{\text{hnf}}} \left( M_1 \frac{\partial M_2}{\partial x} + M_2 \frac{\partial M_2}{\partial y} + M_3 \frac{\partial M_2}{\partial z} \right) \\ = \rho_{\text{hnf}} \frac{\partial^2 v}{\partial z^2} + b^2 y - \frac{\mu_e}{4\pi\rho_{\text{hnf}}} \\ M_e(y) \frac{dM_e(y)}{dx} - \frac{\nu}{k^*} v - Fv^2, \end{aligned} \quad (4)$$

$$u \frac{\partial M_1}{\partial x} + v \frac{\partial M_1}{\partial y} + w \frac{\partial M_1}{\partial z} - \left( M_1 \frac{\partial u}{\partial x} + M_2 \frac{\partial u}{\partial y} + M_3 \frac{\partial u}{\partial z} \right) = \eta_0 \frac{\partial^2 M_1}{\partial z^2}, \quad (5)$$

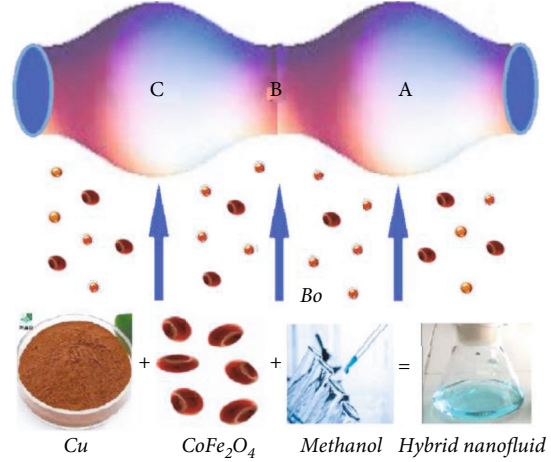


FIGURE 1: The hybrid nanofluid flows in a wavy heat cylinder.

$$u \frac{\partial M_2}{\partial x} + v \frac{\partial M_2}{\partial y} + w \frac{\partial M_2}{\partial z} - \left( M_1 \frac{\partial v}{\partial x} + M_2 \frac{\partial v}{\partial y} + M_3 \frac{\partial v}{\partial z} \right) = \eta_0 \frac{\partial^2 M_2}{\partial z^2}, \quad (6)$$

$$\left( u \frac{\partial T}{\partial x} + v \frac{\partial T}{\partial y} + w \frac{\partial T}{\partial z} \right) = \alpha_{\text{hnf}} \left( \frac{\partial^2 T}{\partial z^2} \right) + \frac{Q_0(T - T_\infty)}{\rho C_p}, \quad (7)$$

$$\left( u \frac{\partial C}{\partial x} + v \frac{\partial C}{\partial y} + w \frac{\partial C}{\partial z} \right) = D_{\text{hnf}} \left( \frac{\partial^2 C}{\partial z^2} \right) - Kc(C - C_\infty). \quad (8)$$

Here,  $Kr$  is chemical reaction rate,  $R_1$  and  $R_2$  are the slip terms,  $Q_0$  is the heat source term,  $k^*$  is the porosity term,  $M_e(x) = xM_0$  and  $M_e(y) = yM_0$  show the magnetic strength in  $x$ ,  $y$  direction, and  $F = xC_b/rk^{*1/2}$  is the nonuniform inertia factor constant.

Here Equation (1) describes the conservation of mass. Equation (2) shows the magnetic flux. Equations (3) and (4) are the momentum equations that pronounce the conduct of fluid flow. Equations (5) and (6) represent magnetic induction. Equations (7) and (8) are the energy and mass equations that describe the energy and mass transference around and near the wavy surface of the cylinder.

The initial and boundary conditions are as follows:

$$\begin{aligned} u = u_w + \mu_{\text{hnf}} R_1 \frac{\partial u}{\partial z}, v = v_w + \mu_{\text{hnf}} R_1 \frac{\partial v}{\partial z}, w = 0, M_1 = M_2 \\ = M_3 = 0, T = T_w + k_{\text{hnf}} R_2 \frac{\partial T}{\partial z}, C = C_0 \text{ at } z = 0 \end{aligned}$$

$$\begin{aligned} u \longrightarrow u_e, v \longrightarrow v_e, M_1 \longrightarrow M_e(x), M_2 \longrightarrow M_e(y), \\ T \longrightarrow T_\infty, C \longrightarrow C_\infty \text{ at } z \longrightarrow \infty. \end{aligned}$$

(9)

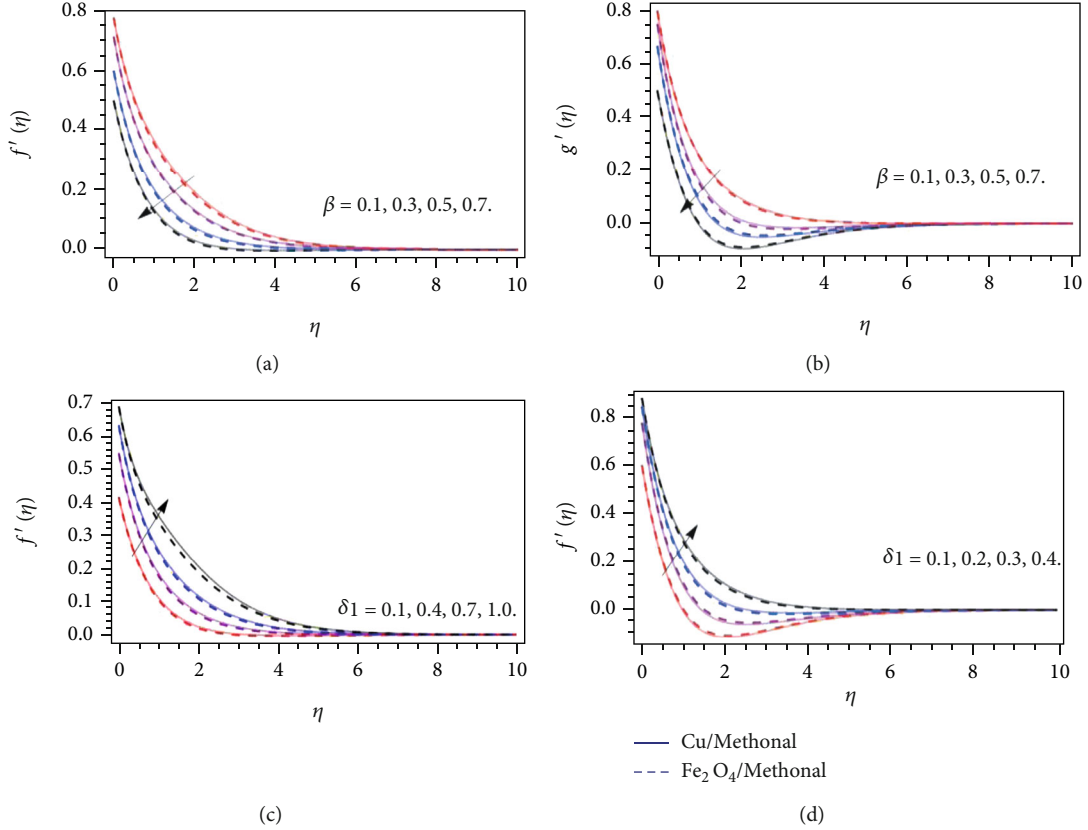


FIGURE 2: The presentation of velocity ( $f(\eta), g(\eta)$ ) profile versus (a, b) magnetic parameter  $\beta$  and (c, d) velocity slip parameter  $\delta_1$ .

The transformation variables are as follows:

$$\begin{aligned}
 u &= axf'(\eta), v = byg'(\eta), w + (f(\eta) + cg(\eta))\sqrt{av} = 0, \\
 M_1 &= xM_0h_1(\eta) = 0, M_2 = yM_0h_2(\eta) = 0, \\
 M_3 + \left(\frac{v_f}{a}\right)^{1/2} (h_1 + h_2)M_0 &= 0, \eta = \sqrt{\frac{a}{v_f}}z, T = T_\infty \\
 &+ (T_w - T_\infty)\Theta(\eta), C = C_\infty + (C_w - C_\infty)\Phi(\eta)
 \end{aligned} \quad (10)$$

By incorporating Equation (10), we get the following:

$$\frac{\hbar_1}{\hbar_2}(1 + cg + f)f'' - \frac{\beta}{\hbar_2}(h_1h_1'' + h_2h_1'' + 1) + 1 - Frf'^2 = 0, \quad (11)$$

$$\frac{\hbar_1}{\hbar_2}(1 + cg + f)g'' - \frac{\beta}{\hbar_2}(h_2h_2'' + h_1h_2'' + 1) + c - Frcg'^2 = 0, \quad (12)$$

$$h_1'' + (h_1'f - f''h_1 - f''h_2 + ch_1'g)M = 0, \quad (13)$$

$$h_2'' + (h_2'f - cg''h_1 - cg''h_2 + ch_2'g)M = 0, \quad (14)$$

$$\frac{\hbar_4}{\hbar_3}\Theta''(\eta) + \Theta'(\eta) + c\Theta'(\eta)g + Q_0\Theta(\eta) = 0, \quad (15)$$

$$\hbar_6\varphi''(\eta) + \varphi'(\eta) + c\varphi'(\eta)g + Kr\varphi(\eta) = 0. \quad (16)$$

The transform conditions are as follows:

$$\left. \begin{aligned}
 f(0) = 0, f'(0) = \delta_1 h_1 f''(\eta)_{\eta=0}, g(0) = 0, g'(0) = \hbar_1 \delta_1 g''(\eta)_{\eta=0}, h_1(0) = 0, h_2(0) = 0 \\
 \Theta(0) = \delta_2 \hbar_4, \Phi(0) = 1 \text{ at } \eta = 0 \\
 f'(\eta) \rightarrow 0, g'(\eta) \rightarrow 0, h_1(\eta) \rightarrow 1, h_2(\eta) \rightarrow 1, \Theta(\eta) \rightarrow 0, \Phi(\eta) \rightarrow 0 \text{ as } \eta \rightarrow \infty
 \end{aligned} \right\} \quad (17)$$

Here,  $\hbar_1 = \mu_{\text{hnf}}/\mu_{\text{bf}}$ ,  $\hbar_2 = \rho_{\text{hnf}}/\rho_{\text{bf}}$ ,  $\hbar_3 = (\rho C_p)_{\text{hnf}}/(\rho C_p)_{\text{bf}}$ ,  $\hbar_4 = k_{\text{hnf}}/k_{\text{bf}}$ ,  $\hbar_5 = \sigma_{\text{hnf}}/\sigma_{\text{bf}}$ ,  $\hbar_6 = D_{\text{hnf}}/D_{\text{bf}}$ .

Here,  $h_1$  and  $h_2$  are magnetic field dimensionless terms.  $\delta_1$  and  $\delta_2$  are the velocity and thermal slip coefficient, where  $\beta$  is the magnetic parameters,  $Kr$  is the chemical reaction term,  $\lambda$  is the porosity term,  $Fr$  is the Forchheimer number, and  $Q_1$  is the heat absorption and generation term defined as follows:

$$\beta = \frac{\mu_e}{4\pi\rho_f} \left(\frac{M_0}{a}\right)^2, M = \frac{v_f}{\eta_0}, Kr = \frac{K_c(1-\lambda t)}{c}, \lambda = \frac{v}{k^* \Omega}, Fr = \frac{C_b}{k^{*1/2}}, Q_1 = \frac{xQ_0}{\rho C_p}. \quad (18)$$

Here,  $\mu_e$  and  $\eta_0$  are the magnetic absorptivity and diffusivity.

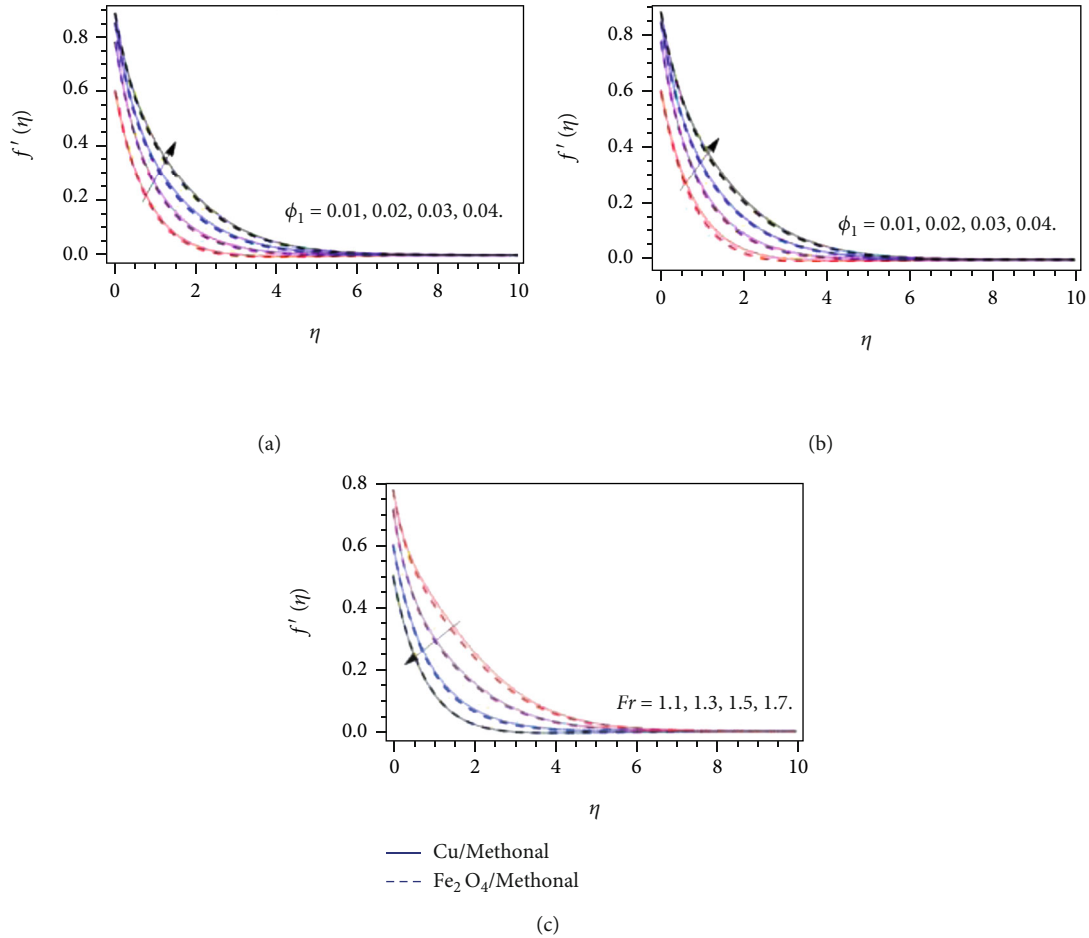


FIGURE 3: The performance of velocity  $f(\eta)$  profile versus (a) copper  $\phi_1$  nanoparticles, (b) cobalt ferrite  $\phi_2$  nanoparticles, and (c) Darcy Forchheimer  $Fr$ .

The interest physical quantities are as follows:

$$C_{f_x} = \frac{\tau_{wx}|_{z=0}}{u_w^2 \rho_f}, C_{f_y} = \frac{\tau_{wy}|_{z=0}}{v_w^2 \rho_f}, Nu = \frac{q_w x}{(T_w - T_\infty) k_f}, Sh = \frac{j_w x}{(C_w - C_\infty) D_f}, \quad (19)$$

where

$$\begin{aligned} \tau_{wx} &= \mu_{hnf} \left( \frac{\partial u}{\partial z} \right)_{z=0}, \tau_{wy} = \mu_{hnf} \left( \frac{\partial v}{\partial z} \right)_{z=0}, \\ q_w &= -k_{hnf} \left( \frac{dT}{dz} \right)_{z=0}, j_w = -D_{hnf} \left( \frac{dC}{dz} \right)_{z=0}. \end{aligned} \quad (20)$$

The dimensionless form of Equation (19) is as follows:

$$\begin{aligned} Re^{1/2} C_{f_x} &= \frac{cy}{x \tilde{h}_1} f''(0), C_{f_y} = \frac{cy}{x \tilde{h}_1} g''(0), Re^{1/2} Nu_x \\ &= -\frac{k_{hnf}}{k_f} \Theta'(0), Re^{-1/2} Sh = -\Phi'(0). \end{aligned} \quad (21)$$

### 3. Numerical Solution

The main phases, while employing the parametric methodology, are as follows [34–38]:

Step 1. Simplifying the modeled equations

$$\left. \begin{aligned} \vartheta_1 &= f(\eta), \vartheta_2 = f'(\eta), \vartheta_3 = g(\eta), \vartheta_4 = g'(\eta), \vartheta_5 = h_1(\eta), \vartheta_6 = h_1'(\eta), \\ \vartheta_7 &= h_2(\eta), \vartheta_8 = h_2'(\eta), \vartheta_9(\eta) = \Theta(\eta), \vartheta_{10} = \Theta'(\eta), \vartheta_{11} = \Phi(\eta), \vartheta_{12} = \Phi'(\eta) \end{aligned} \right\} \quad (22)$$

By putting (22) in (11)–(16) and (17), we get the following:

$$\frac{\tilde{h}_1}{\tilde{h}_2} (1 + c\vartheta_3 + \vartheta_1)\vartheta_2' - \frac{\beta}{\tilde{h}_2} (\vartheta_5\vartheta_6'^2 + \vartheta_7\vartheta_1' + 1) + 1 - Fr\vartheta_2^2 = 0, \quad (23)$$

$$\frac{\tilde{h}_1}{\tilde{h}_2} (1 + c\vartheta_3 + \vartheta_1)\vartheta_4' - \frac{\beta}{\tilde{h}_2} (\vartheta_7\vartheta_8'^2 + \vartheta_5\vartheta_7 + 1) + c - Fr c\vartheta_4^2 = 0, \quad (24)$$

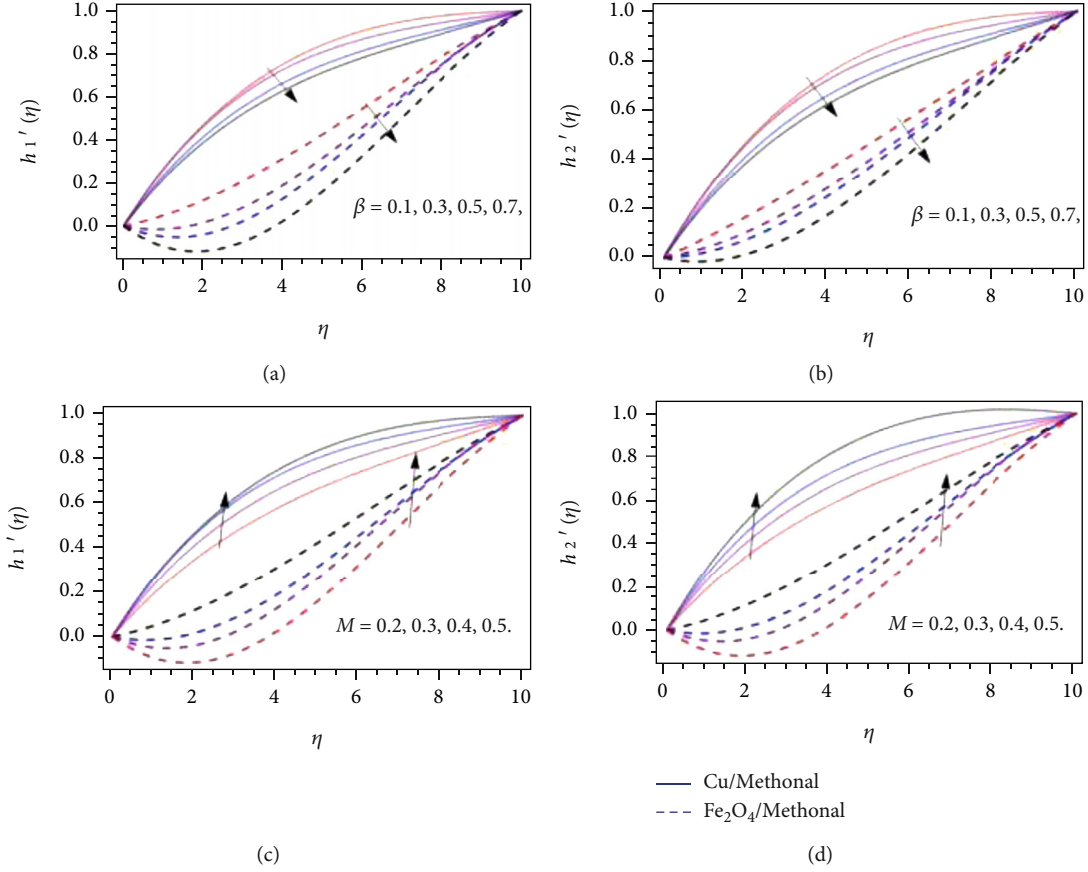


FIGURE 4: The performance of induced magnetic field ( $h_1'(\eta), h_2'(\eta)$ ) profile versus (a, b) magnetic parameter  $\beta$  and (c, d) magnetic Prandtl number  $M$ .

$$\vartheta_6' + \left( \vartheta_6 \vartheta_1 - \vartheta_2' \vartheta_5 - \vartheta_2' \vartheta_7 + c \vartheta_6 \vartheta_3 \right) M = 0, \quad (25)$$

$$\vartheta_8' + \left( \vartheta_8 \vartheta_1 - c \vartheta_4' \vartheta_5 - c \vartheta_4' \vartheta_7 + ch \vartheta_8 \vartheta_3 \right) M = 0, \quad (26)$$

$$\frac{\hbar_4}{\hbar_3} \vartheta_{10}'(\eta) + \vartheta_{10}(\eta) + c \vartheta_{10}(\eta) g + Q_0 \vartheta_9(\eta) = 0, \quad (27)$$

$$\hbar_6 \vartheta_{12}'(\eta) + \vartheta_{12}(\eta) + c \vartheta_{12}(\eta) \vartheta_3 + Kr \vartheta_{11}(\eta) = 0, \quad (28)$$

and the transform conditions are as follows:

$$\left. \begin{aligned} \vartheta_1(0) = 0, \vartheta_2(0) = \delta_1, \hbar_1 \vartheta_2'(\eta)_{\eta=0}, \vartheta_3(0) = 0, \vartheta_4(0) = \delta_1, \hbar_1 \vartheta_4'(\eta)_{\eta=0}, \vartheta_5(0) = 0, \vartheta_7(0) = 0, \\ \vartheta_9(0) = \delta_2, \hbar_4, \vartheta_{11}(0) = 1 \text{ at } \eta = 0, \\ \vartheta_2(\eta) \rightarrow 0, \vartheta_4(\eta) \rightarrow 0, \vartheta_5(\eta) \rightarrow 1, \vartheta_7(\eta) \rightarrow 1, \vartheta_9(\eta) \rightarrow 0, \vartheta_{11}(\eta) \rightarrow 0 \text{ as } \eta \rightarrow \infty \end{aligned} \right\} \quad (29)$$

Step 2. Introducing parameter  $p$

$$\frac{\hbar_1}{\hbar_2} (1 + c \vartheta_3 + \vartheta_1) \vartheta_2' - \frac{\beta}{\hbar_2} (\vartheta_5 \vartheta_6'^2 + \vartheta_7 \vartheta_1' + 1) + 1 - Fr (\vartheta_2^2 - 1) p = 0, \quad (30)$$

$$\vartheta_6' + \left( \vartheta_1 (\vartheta_6 = 1) p - \vartheta_2' \vartheta_5 - \vartheta_2' \vartheta_7 + c \vartheta_6 \vartheta_3 \right) M = 0, \quad (31)$$

$$\vartheta_8' + \left( \vartheta_1 (\vartheta_8 = 1) p - c \vartheta_4' \vartheta_5 - c \vartheta_4' \vartheta_7 + ch \vartheta_8 \vartheta_3 \right) M = 0, \quad (32)$$

$$\frac{\hbar_4}{\hbar_3} \vartheta_{10}'(\eta) + (\vartheta_{10}(\eta) - ) p + c \vartheta_{10}(\eta) g + Q_0 \vartheta_9(\eta) = 0, \quad (33)$$

$$\hbar_6 \vartheta_{12}'(\eta) + (\vartheta_{12}(\eta) - 1) p + c \vartheta_{12}(\eta) \vartheta_3 + Kr \vartheta_{11}(\eta) = 0. \quad (34)$$

Step 3. Differentiating by parameter “ $p$ ”

By differentiating Equations (30)–(34) w. r. t parameter  $p$ , we get the following:

$$V' = AV + R, \quad (35)$$

$$\frac{d\zeta_i}{d\tau}, \quad (36)$$

where  $i = 1, 2, \dots \dots \dots 11$ .

Step 4. Applying the superposition principle

$$V = aU + W. \quad (37)$$

For each element, resolve the two Cauchy problems listed below.

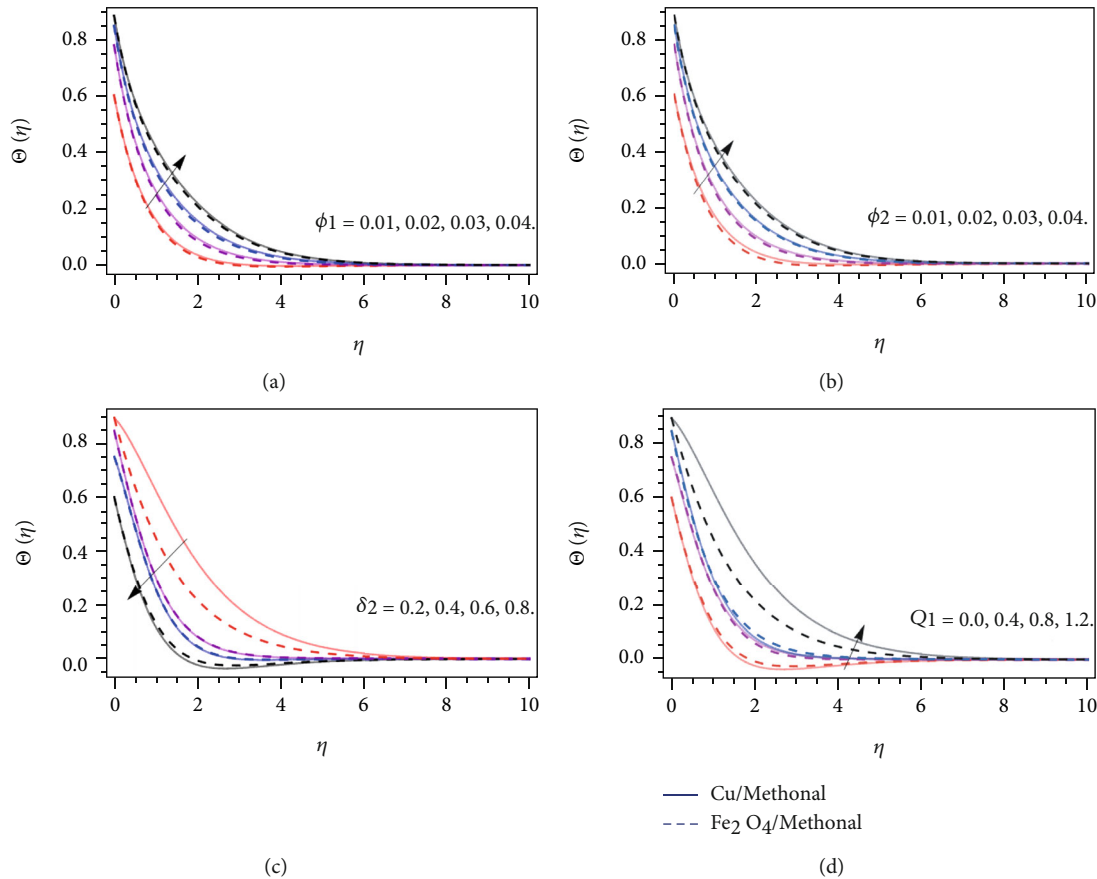


FIGURE 5: The performance of energy  $\Theta(\eta)$  profile versus (a) copper  $\phi_1$  nanoparticles, (b) cobalt ferrite  $\phi_2$  nanoparticles, (c) thermal jump parameter  $\delta_2$ , (d) heat source term  $Q_1$ .

$$U = aU, \tag{38}$$

$$W' = AW + R. \tag{39}$$

By putting Equation (39) in Equation (37), we get

$$(aU + W)' = A(aU + W) + R. \tag{40}$$

Step 5. Solving the Cauchy problems

By utilizing implicit scheme,

$$\frac{U^{i+1} - U^i}{\Delta\eta} = AU^{i+1}, \quad \frac{W^{i+1} - W^i}{\Delta\eta} = AW^{i+1}. \tag{41}$$

The final iterative form is as follows:

$$U^{i+1} = \frac{U^i}{(I - \Delta\eta A)}, \quad W^{i+1} = \frac{(W^i + \Delta\eta R)}{(I - \Delta\eta A)}. \tag{42}$$

#### 4. Result and Discussion

The preceding is some of the findings that have been noticed:

Velocity profile  $(f(\eta), g(\eta))$

Figures 2(a)–2(d) particularize the presentation of velocity  $(f(\eta), g(\eta))$  profile against the variation of magnetic parameter  $\beta$  and velocity slip term  $\delta_1$ , respectively. Figures 2(a) and 2(b) reveal that the fluid velocity profile reduces under the upshot of the magnetic term  $\beta$ . Physically, it is clear that the magnetic field creates resistive force around its self, which provides hurdles (Lorentz force) to the flow field, and as a result, fluid flow declines. Figures 2(c) and 2(d) show that the fluid velocity diminishes with the varying effect of velocity slip term  $\delta_1$ .

Figures 3(a)–3(c) illustrate the performance of velocity  $f(\eta)$  profile against the variation of copper  $\phi_1$  nanoparticles, cobalt ferrite  $\phi_2$  nanoparticles, and Darcy Forchheimer  $Fr$ , respectively. Figures 3(a) and 3(b) expose that the velocity field substantially boosts with the action of copper  $\phi_1$  and cobalt ferrite  $\phi_2$  nanoparticles. The specific heat capacity of methanol is remarkably greater, while the thermal conductivity is less than the copper and cobalt ferrite nanomaterials, that is why the inclusion of hybrid nanoparticles, especially copper, reduces its average heat-absorbing efficiency, which results in the enhancement of velocity field. The upshot of Darcy Forchheimer's number degenerates the velocity distribution as shown in Figure 3(c).

Induced magnetic field  $(h'_1(\eta), h'_2(\eta))$



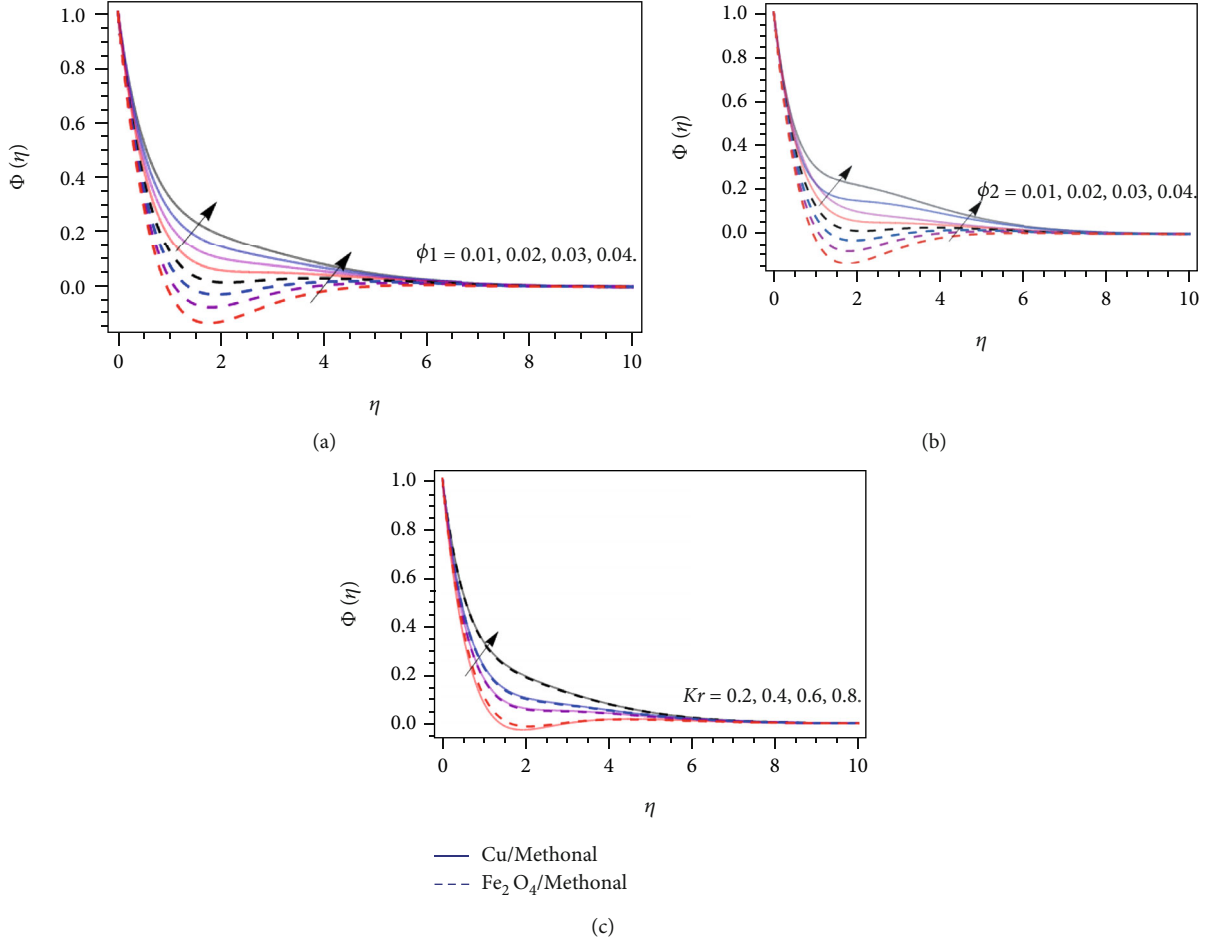


FIGURE 6: The performance of concentration  $\Phi(\eta)$  profile versus (a) copper  $\phi_1$  nanoparticles, (b) cobalt ferrite  $\phi_2$  nanoparticles, and (c) chemical reaction term  $Kr$ .

TABLE 1: The statistical properties of copper, cobalt iron oxide, and methanol [32, 33].

	$\rho$ (kg/m <sup>3</sup> )	$C_p$ (j/kgK)	$k$ (W/mK)	$\sigma$ (S/m)
Methanol	792	2545	0.2035	$0.5 \times 10^{-6}$
Copper (Cu)	8933	385	401	$5.96 \times 10^7$
CoFe <sub>2</sub> O <sub>4</sub>	4907	700	3.7	$5.51 \times 10^9$

Figures 4(a)–4(d) highlight the presentation of  $(h'_1(\eta), h'_2(\eta))$  profiles versus  $\beta$  (magnetic constraint) and  $M$ . Figures 4(a) and 4(b) show that the induced magnetic field profile decreases with the effect of the magnetic parameter  $\beta$ . Actually, the improving values of magnetic term suppressed the induced magnetic field which indicates deteriorating conduct of the induced magnetic field. Figures 4(c) and 4(d) report that the positive influence of  $M$  encourages the  $(h'_1(\eta), h'_2(\eta))$  profiles. The fundamental reason for this is that multiplying the ratios of  $M$  corresponds to a reduced magnetic diffusive, resulting in a loss of magnetic field strength. It improves the curve. Hence, the rising credit of  $M$  improves the induced magnetic field profile.

#### Temperature profile $\Theta(\eta)$

Figures 5(a)–5(d) illustrate the performance of energy  $\Theta(\eta)$  profile against the variation of copper  $\phi_1$  nanoparticles, cobalt ferrite  $\phi_2$  nanoparticles, thermal jump parameter  $\delta_2$ , and heat source term  $Q_1$ . Figures 5(a) and 5(b) explain that the energy  $\Theta(\eta)$  profile boosts with the positive variation of copper  $\phi_1$  and cobalt ferrite  $\phi_2$  nanoparticles. We have discussed before that the thermal conductivity of fluid enhances, while specific heat capacity is condensed under the action of copper  $\phi_1$  and cobalt ferrite  $\phi_2$  nanoparticles. That is why such a situation has been noticed in Figures 5 (a) and 5(b). Figures 5(c) and 5(d) show an opposite behavior of energy profile versus thermal jump parameter  $\delta_2$  and heat source term  $Q_1$ . The energy profile declines due to the variation of thermal jump constraint. To put it another way, the energy field is a diminishing function  $\delta_2$ . Logically, increasing  $\delta_2$  enables the wavy cylinder to expand. As a result of this, the thickness of the cylinder rises, reducing the energy field curvature. Heat is emitted as energy by nanosized particles in practice. The more the input of micro-particles, the greater the heat production as energy. The heat absorption and generation term  $Q_1$  boost the temperature field because its effect generates heat, which causes the rises in energy profile as shown in Figure 5(d).

TABLE 2: The thermal properties of the hybrid nanofluid ( $\phi_1 = \phi_{Cu}$ ,  $\phi_2 = \phi_{CoFe_2O_4}$ ) [32, 33].

Properties	
Viscosity	$\mu_{hnf}/\mu_{bf} = 1/(1 - \phi_{Cu} - \phi_{CoFe_2O_4})^2$
Density	$\rho_{hnf}/\rho_{bf} = \phi_{Cu}(\rho_{Cu}/\rho_{bf}) + \phi_{CoFe_2O_4}(\rho_{CoFe_2O_4}/\rho_{bf}) + (1 - \phi_{Cu} - \phi_{CoFe_2O_4})\rho_{bf}$
Thermal capacity	$(\rho C_p)_{hnf}/(\rho C_p)_{bf} = \phi_{Cu}((\rho C_p)_{Cu}/(\rho C_p)_{bf}) + \phi_{CoFe_2O_4}((\rho C_p)_{CoFe_2O_4}/(\rho C_p)_{bf}) + (1 - \phi_{Cu} - \phi_{CoFe_2O_4})\rho_{bf} C_{p,bf}$
Thermal conductivity	$k_{hnf}/k_{bf} = [(\phi_{Cu}k_{Cu} + \phi_{CoFe_2O_4}k_{CoFe_2O_4}/\phi_{Cu} + \phi_{CoFe_2O_4}) + 2k_{bf} + 2(\phi_{Cu}k_{Cu} + \phi_{CoFe_2O_4}k_{CoFe_2O_4}) - 2(\phi_{Cu} + \phi_{CoFe_2O_4})k_{bf}] / [(\phi_{Cu}k_{Cu} + \phi_{CoFe_2O_4}k_{CoFe_2O_4}/\phi_{Cu} + \phi_{CoFe_2O_4}) + 2k_{bf} - 2(k_{Cu}\phi_{Cu} + k_{CoFe_2O_4}\phi_{CoFe_2O_4}) + (\phi_{Cu} + \phi_{CoFe_2O_4})2k_{bf}]$
Electrical conductivity	$\sigma_{hnf}/\sigma_{bf} = [(\phi_{Cu}\sigma_{Cu} + \phi_{CoFe_2O_4}\sigma_{CoFe_2O_4}/\phi_{Cu} + \phi_{CoFe_2O_4}) + 2\sigma_{bf} + 2(\phi_{Cu}\sigma_{Cu} + \phi_{CoFe_2O_4}\sigma_{CoFe_2O_4}) - 2(\phi_{Cu} + \phi_{CoFe_2O_4})\sigma_{bf}] / [(\phi_{Cu}\sigma_{Cu} + \phi_{CoFe_2O_4}\sigma_{CoFe_2O_4}/\phi_{Cu} + \phi_{CoFe_2O_4}) + 2\sigma_{bf} - (\phi_{Cu}\sigma_{Cu} + \phi_{CoFe_2O_4}\sigma_{CoFe_2O_4}) + (\phi_{Cu} + \phi_{CoFe_2O_4})\sigma_{bf}]$

TABLE 3: Statistical results for Nusselt number.

$\delta_2$	$Q_1$	$\phi_1, \phi_2$	PCM ( $k_{nf}/k_f$ ) $\Theta'(0)$	bvp4c ( $k_{nf}/k_f$ ) $\Theta'(0)$	PCM ( $k_{hnf}/k_f$ ) $\Theta'(0)$	bvp4c ( $k_{hnf}/k_f$ ) $\Theta'(0)$
0.2			0.0475535	0.0474435	0.0484531	0.0484431
0.4			0.0355123	0.0354042	0.0366122	0.0366023
0.6			0.0365852	0.0364743	0.0369853	0.0369752
0.8			0.0292107	0.0291003	0.0271407	0.0271323
	0.0		0.0565588	0.0564476	0.0554555	0.0554456
	0.4		0.0575760	0.0574652	0.0575961	0.0575854
	0.8		0.0579962	0.0578861	0.0589965	0.0589846
	1.2	0.01	0.0674420	0.06734310	0.0683460	0.0683350
		0.02	0.0684241	0.0683220	0.0693271	0.0693160
		0.03	0.0691324	0.0690313	0.0713142	0.0713041
		0.04	0.0722419	0.0723407	0.0743319	0.0743217

TABLE 4: Numerical outcomes for Sherwood number.

$Kr$	$\phi_1, \phi_2$	PCM ( $D_{nf}/D_f$ ) $\Phi'(0)$	bvp4c ( $D_{nf}/D_f$ ) $\Phi'(0)$	PCM ( $D_{hnf}/D_f$ ) $\Phi'(0)$	bvp4c ( $D_{hnf}/D_f$ ) $\Phi'(0)$
0.2		0.0632428	0.0632228	0.0642421	0.0642220
0.4		0.0629422	0.0629210	0.0639437	0.0639234
0.6		0.0615944	0.0615742	0.0614946	0.0614743
0.8		0.5930362	0.5930160	0.5910341	0.5910141
	0.01	0.0627713	0.0627511	0.0677736	0.0677634
	0.02	0.0638833	0.0638631	0.0728855	0.0728651
	0.03	0.6687551	0.6687340	0.7774605	0.7774402
	0.04	0.7026619	0.7026617	0.7906815	0.7906613

### Concentration profile $\Phi(\eta)$

Figures 6(a)–6(c) report the performance of concentration  $\Phi(\eta)$  profile versus copper  $\phi_1$  nanoparticles, cobalt ferrite  $\phi_2$  nanoparticles, and chemical reaction term  $Kr$ , respectively. Figures 6(a) and 6(b) describe that the mass transfer  $\Phi(\eta)$  profile improves with the positive deviation of copper  $\phi_1$  and cobalt ferrite  $\phi_2$  nanoparticulate. We have reviewed earlier that the thermal conductivity of fluid enhances, while specific

heat capacity is condensed under the action of copper  $\phi_1$  and cobalt ferrite  $\phi_2$  nanoparticles. That is why such a situation has been noticed in Figures 6(a) and 6(b). The chemical reaction coefficient positively affects the mass transfer, because it also encourages fluid particles to move fast, which results in the positive variation as elaborated in Figure 6(c).

Tables 1 and 2 exemplify the thermochemical possessions and model of base fluid, copper, and cobalt iron oxide

individually. Tables 3 and 4 report the statistical assessment of PCM and bvp4c techniques, to confirm the legality of the current report. The energy field and mass transition profile are associated with the determination. Tables 3 and 4 also reveal the comparative assessments between simple and hybrid NF. It has been clearly perceived that the mass and heat transfer ratio of hybrid NF as compared to simple NF or ordinary fluid is greater.

## 5. Conclusion

The objective of this research is to build a computational model to investigate the effects of methanol-based hybrid NFs consisting of Cu and  $\text{CoFe}_2\text{O}_4$  nanoparticles on heat and mass communication. The fluid flow has been examined in a heated wavy flexible cylinder under the impact of slip condition, variable thickness, Darcy Forchheimer, heat absorption/generation, and chemical reaction. The PCM approach is used to simulate the problem, and the results are compared to those obtained using the Matlab software bvp4c. The key observations are as follows:

- (i) The velocity profile reduces with the effect of the magnetic parameter  $\beta$ , velocity slip constant  $\delta_1$ , and Darcy Forchheimer's number  $Fr$
- (ii) The velocity and energy field significantly boosts with the inclusion of copper  $\phi_1$  and cobalt ferrite  $\phi_2$  nanoparticulates in the base fluid methanol
- (iii) The  $(h'_1(\eta), h'_2(\eta))$  profile decreases with the effect of the  $\beta$ , while enhances under the action of parameter  $M$
- (iv) The energy profile declines due to the variation of thermal jump constraint and boosts with the absorption and generation term  $Q_1$
- (v) The mass propagation rate can be significantly enhancing with the effect of chemical reaction parameter  $Kr$
- (vi) The hybrid NF has greater tendency to enhance the energy and velocity of base fluid as compared to the ordinary NF

## Data Availability

No data were used to support this study.

## Conflicts of Interest

The authors have declared no conflict of interest.

## Acknowledgments

The authors are thankful to the Deanship of Scientific Research, King Khalid University, Abha, Saudi Arabia, for financially supporting this work through the General Research Project under Grant no. R.G.P.2/160/43. Taif Uni-

versity Researchers Supporting Project number (TURSP-2020/31), Taif University, Taif, Saudi Arabia.

## References

- [1] S. H. Nam and H. S. Yoon, "Effect of the wavy geometric disturbance on the flow over elliptic cylinders with different aspect ratios," *Ocean Engineering*, vol. 243, p. 110287, 2022.
- [2] K. Cavanagh and R. Wulandana, "2D flow past a confined circular cylinder with sinusoidal ridges," 2019.
- [3] T. Salahuddin, A. M. Bashir, M. Khan, and W. F. Xia, "Multiple shaped nano-particles influence on thermal conductivity of fluid flow between inflexible and sinusoidal walls," *Case studies in thermal engineering*, vol. 25, p. 100930, 2021.
- [4] B. Wu, S. Li, L. Zhang, and K. Li, "Experimental determination of the two-dimensional aerodynamic admittances of a 5: 1 rectangular cylinder in streamwise sinusoidal flows," *Journal of Wind Engineering and Industrial Aerodynamics*, vol. 210, p. 104525, 2021.
- [5] M. Bilal, A. Saeed, M. M. Selim, T. Gul, I. Ali, and P. Kumam, "Comparative numerical analysis of Maxwell's time-dependent thermo-diffusive flow through a stretching cylinder," *Case Studies in Thermal Engineering*, vol. 27, p. 101301, 2021.
- [6] Y. M. Seo, K. Luo, M. Y. Ha, and Y. G. Park, "Direct numerical simulation and artificial neural network modeling of heat transfer characteristics on natural convection with a sinusoidal cylinder in a long rectangular enclosure," *International Journal of Heat and Mass Transfer*, vol. 152, p. 119564, 2020.
- [7] M. Bilal, I. Khan, T. Gul et al., "Darcy-forchheimer hybrid nano fluid flow with mixed convection past an inclined cylinder," *CMC-Computers Materials & Continua*, vol. 66, no. 2, pp. 2025–2039, 2021.
- [8] A. Sarchami, M. Najafi, A. Imam, and E. Houshfar, "Experimental study of thermal management system for cylindrical Li-ion battery pack based on nanofluid cooling and copper sheath," *International Journal of Thermal Sciences*, vol. 171, p. 107244, 2022.
- [9] I. Ullah, T. Hayat, A. Alsaedi, and S. Asghar, "Dissipative flow of hybrid nanoliquid (H<sub>2</sub>O-aluminum alloy nanoparticles) with thermal radiation," *Physica Scripta*, vol. 94, no. 12, p. 125708, 2019.
- [10] M. Shuaib, A. Ali, M. A. Khan, and A. Ali, "Numerical investigation of an unsteady nanofluid flow with magnetic and suction effects to the moving upper plate," *Advances in Mechanical Engineering*, vol. 12, no. 2, 2020.
- [11] H. Waqas, M. Imran, T. Muhammad, S. M. Sait, and R. Ellahi, "Numerical investigation on bioconvection flow of Oldroyd-B nanofluid with nonlinear thermal radiation and motile microorganisms over rotating disk," *Journal of Thermal Analysis & Calorimetry*, vol. 145, no. 2, pp. 523–539, 2021.
- [12] B. Mussabayeva, K. Murzagulova, Z. Aripzhanova, and A. Klivenko, "Preparation of silver and copper nanoparticles for biomedical application," in *2017 IEEE 7th International Conference Nanomaterials: Application & Properties*, Zatocha, Ukraine, Sep 2017.
- [13] H. H. Kart, H. Yildirim, S. O. Kart, and T. Çağın, "Physical properties of Cu nanoparticles: a molecular dynamics study," *Materials Chemistry and Physics*, vol. 147, no. 1-2, pp. 204–212, 2014.

- [14] S. Munjal, N. Khare, C. Nehate, and V. Koul, "Water dispersible CoFe<sub>2</sub>O<sub>4</sub> nanoparticles with improved colloidal stability for biomedical applications," *Journal of Magnetism and Magnetic Materials*, vol. 404, pp. 166–169, 2016.
- [15] V. Nica, C. Caro, J. M. Páez-Muñoz, M. P. Leal, and M. L. Garcia-Martin, "Bi-magnetic core-shell CoFe<sub>2</sub>O<sub>4</sub>@ MnFe<sub>2</sub>O<sub>4</sub> nanoparticles for in vivo theranostics," *Nanomaterials*, vol. 10, no. 5, p. 907, 2020.
- [16] M. Bilal, T. Gul, A. Alsubie, and I. Ali, "Axisymmetric hybrid nanofluid flow with heat and mass transfer amongst the two gyrating plates," *ZAMM-Journal of Applied Mathematics and Mechanics/Zeitschrift für Angewandte Mathematik und Mechanik*, vol. 101, no. 11, article e202000146, 2021.
- [17] G. K. Ramesh, J. K. Madhukesh, B. C. Prasannakumara, S. A. Shehzad, and F. M. Abbasi, "Thermodynamics examination of Fe<sub>3</sub>O<sub>4</sub>-CoFe<sub>2</sub>O<sub>4</sub>/water+ EG nanofluid in a heated plate: crosswise and stream-wise aspects," *Arabian Journal for Science and Engineering*, pp. 1–10, 2021.
- [18] J. Wang, Y. P. Xu, R. Qahiti et al., "Simulation of hybrid nanofluid flow within a microchannel heat sink considering porous media analyzing CPU stability," *Journal of Petroleum Science and Engineering*, vol. 208, p. 109734, 2022.
- [19] M. Ibrahim, A. Abidi, E. A. Algehyne, T. Saeed, G. Cheraghian, and M. Sharifpur, "Improvement of the energy and exergy efficiencies of the parabolic solar collector equipped with a twisted turbulator using SWCNT-Cu/water two-phase hybrid nanofluid," *Sustainable Energy Technologies and Assessments*, vol. 49, p. 101705, 2022.
- [20] M. Yaseen, S. K. Rawat, and M. Kumar, "Hybrid nanofluid (MoS<sub>2</sub>-SiO<sub>2</sub>/water) flow with viscous dissipation and Ohmic heating on an irregular variably thick convex/concave-shaped sheet in a porous medium," *Heat Transfer*, vol. 51, no. 1, pp. 789–817, 2022.
- [21] F. Wang, Z. Xiao, X. Liu et al., "Strategic design of cellulose nanofibers@ zeolitic imidazolate frameworks derived mesoporous carbon-supported nanoscale CoFe<sub>2</sub>O<sub>4</sub>/CoFe hybrid composition as trifunctional electrocatalyst for Zn-air battery and self-powered overall water-splitting," *Journal of Power Sources*, vol. 521, p. 230925, 2022.
- [22] I. Ullah, R. Ali, I. Khan, and K. S. Nisar, "Insight into kerosene conveying CNTs and Fe<sub>3</sub>O<sub>4</sub> nanoparticles through a porous medium: significance of Coriolis force and entropy generation," *Physica Scripta*, vol. 96, no. 5, article 055705, 2021.
- [23] I. Ullah, T. Hayat, A. Alsaedi, and H. M. Fardoun, "Numerical treatment of melting heat transfer and entropy generation in stagnation point flow of hybrid nanomaterials (SWCNT-MWCNT/engine oil)," *Modern Physics Letters B*, vol. 35, no. 6, p. 2150102, 2021.
- [24] T. Hayat, I. Ullah, T. Muhammad, and A. Alsaedi, "Hydro-magnetic squeezed flow of second-grade nanomaterials between two parallel disks," *Journal of Thermal Analysis and Calorimetry*, vol. 139, no. 3, pp. 2067–2077, 2020.
- [25] I. Ullah, T. Hayat, and A. Alsaedi, "Nonlinear radiative squeezed flow of nanofluid subject to chemical reaction and activation energy," *Journal of Heat Transfer*, vol. 142, no. 8, 2020.
- [26] T. Hayat and S. Noreen, "Peristaltic transport of fourth grade fluid with heat transfer and induced magnetic field," *Comptes Rendus Mécanique*, vol. 338, no. 9, pp. 518–528, 2010.
- [27] M. C. Raju, S. V. K. Varma, and B. Seshaiiah, "Heat transfer effects on a viscous dissipative fluid flow past a vertical plate in the presence of induced magnetic field," *Ain Shams Engineering Journal*, vol. 6, no. 1, pp. 333–339, 2015.
- [28] N. S. Khashi'ie, N. M. Arifin, and I. Pop, "Magnetohydrodynamics (MHD) boundary layer flow of hybrid nanofluid over a moving plate with Joule heating," *Alexandria Engineering Journal*, vol. 61, no. 3, pp. 1938–1945, 2022.
- [29] M. Khazayinejad and S. S. Nourazar, "On the effect of spatial fractional heat conduction in MHD boundary layer flow using Gr-Fe<sub>3</sub>O<sub>4</sub>-H<sub>2</sub>O hybrid nanofluid," *International Journal of Thermal Sciences*, vol. 172, p. 107265, 2022.
- [30] I. Ullah, "Activation energy with exothermic/endothemic reaction and Coriolis force effects on magnetized nanomaterials flow through Darcy–Forchheimer porous space with variable features," *Waves in Random and Complex Media*, pp. 1–14, 2022.
- [31] T. Salahuddin, N. Siddique, M. Khan, and Y. M. Chu, "A hybrid nanofluid flow near a highly magnetized heated wavy cylinder," *Alexandria Engineering Journal*, vol. 61, no. 2, p. 1297–1308, 2022.
- [32] P. B. A. Reddy, "Biomedical aspects of entropy generation on electromagnetohydrodynamic blood flow of hybrid nanofluid with nonlinear thermal radiation and non-uniform heat source/sink," *The European Physical Journal Plus*, vol. 135, no. 10, pp. 1–30, 2020.
- [33] C. Sulochana, S. R. Aparna, and N. Sandeep, "Impact of linear/nonlinear radiation on incessantly moving thin needle in MHD quiescent Al-Cu/methanol hybrid nanofluid," *International Journal of Ambient Energy*, pp. 1–7, 2020.
- [34] M. Shuaib, R. A. Shah, I. Durrani, and M. Bilal, "Electrokinetic viscous rotating disk flow of Poisson-Nernst-Planck equation for ion transport," *Journal of Molecular Liquids*, vol. 313, p. 113412, 2020.
- [35] M. Shuaib, R. A. Shah, and M. Bilal, "Von-Karman rotating flow in variable magnetic field with variable physical properties," *Advances in Mechanical Engineering*, vol. 13, no. 2, 2021.
- [36] H. Alrabaiah, M. Bilal, M. A. Khan, T. Muhammad, and E. Y. Legas, "Parametric estimation of gyrotactic microorganism hybrid nanofluid flow between the conical gap of spinning disk-cone apparatus," *Scientific Reports*, vol. 12, no. 1, pp. 1–14, 2022.
- [37] A. Ahmadian, M. Bilal, M. A. Khan, and M. I. Asjad, "Numerical analysis of thermal conductive hybrid nanofluid flow over the surface of a wavy spinning disk," *Scientific Reports*, vol. 10, no. 1, pp. 1–13, 2020.
- [38] Y. P. Lv, E. A. Algehyne, M. G. Alshehri et al., "Numerical approach towards gyrotactic microorganisms hybrid nanofluid flow with the hall current and magnetic field over a spinning disk," *Scientific Reports*, vol. 11, no. 1, pp. 1–13, 2021.

## Research Article

# New Iterative Method for Solving a Coupled System of Fractional-Order Drinfeld–Sokolov–Wilson (FDSW) and Fractional Shallow Water (FSW) Equations

Nasir Ali <sup>1</sup>, Mansour F. Yassen,<sup>2,3</sup> Saeed Ahmed Asiri <sup>4</sup>, Rashid Nawaz <sup>1</sup>, Laiq Zada,<sup>1</sup> Mohammad Mahtab Alam <sup>5</sup> and Ndolane Sene <sup>6</sup>

<sup>1</sup>Department of Mathematics, Abdul Wali Khan University Mardan, KP, Pakistan

<sup>2</sup>Department of Mathematics, College of Science and Humanities in Al-Aflaj, Prince Sattam Bin Abdulaziz University, Al-Aflaj 11912, Saudi Arabia

<sup>3</sup>Department of Mathematics, Faculty of Science, Damietta University, New Damietta 34517 Damietta, Egypt

<sup>4</sup>Mechanical Engineering Department, Engineering College, King Abdulaziz University, Jeddah, Saudi Arabia

<sup>5</sup>Department of Basic Medical Sciences, College of Applied Medical Science, King Khalid University, Abha 61421, Saudi Arabia

<sup>6</sup>Laboratoire Lmdan, Departement De Mathematiques De Decision, Faculté des Sciences Economiques et Gestion, Université Cheikh Anta Diop De Dakar, BP 5683 Dakar Fann, Senegal

Correspondence should be addressed to Nasir Ali; [nasirali988@gmail.com](mailto:nasirali988@gmail.com)

Received 14 January 2022; Accepted 17 March 2022; Published 7 April 2022

Academic Editor: Amir Khan

Copyright © 2022 Nasir Ali et al. This is an open access article distributed under the Creative Commons Attribution License, which permits unrestricted use, distribution, and reproduction in any medium, provided the original work is properly cited.

In this study, the new iterative method has been applied to a coupled system of fractional-order Drinfeld–Sokolov–Wilson (FDSW) and fractional shallow water (FSW) equations. The fractional-order derivatives are taken in the Caputo sense whose order is between 0 and 1. The suggested method is capable to handle the FDEs without any transformation and discretization. The obtained results have been compared with the exact solution and with the q-homotopy analysis transform method. The outcomes show the efficiency and effectiveness of NIM by comparing through tables and graphs.

## 1. Introduction

Differential equations (DEs) can be used to model the majority of physical occurrences on the planet. The DEs are divided into many categories. They may be in the form of ordinary differential equations (ODEs) or partial differential equations (PDEs). Due to significant advancements in mathematics, a new discipline known as fractional calculus was introduced which has new concepts and operations for handling derivatives and integrations. Fractional calculus deals with the DEs of noninteger order known as fractional-order differential equations (FDEs). Linear differential equations model the simple phenomenon while nonlinear equations are used in a variety of research and engineering applications including plasma physics, hydrodynamics, fluid dynamics, solid-state physics, acoustics, and

optical fibers. In many fields of engineering and biosciences, the DEs occur in the form of coupled systems. The solution of a differential equation may depend on the linearity of the DE. The coupled systems in linear cases may be solved using basic analytical methods. However, due to the higher degree of nonlinearity, solving nonlinear differential equations by simple methods is not always practicable. As a result of the complexity for obtaining a solution of nonlinear DEs, researchers initiated some new approaches for approximating the solution of nonlinear DEs. They may be perturbation methods [1, 2], numerical methods [3, 4], iterative methods [5, 6], etc. Sometimes these techniques apply some transformation to reduce the equations into more simple equations or even a system of equations while some other techniques offer the solution in the form of series that converges to the exact solution [7, 8]. Besides, some other techniques

which employ a trial function in an iterative scheme converge quickly. The concept of homotopy from topology and conventional perturbation methods introduced new methods such as the optimal homotopy asymptotic method, homotopy perturbation method, homotopy analysis method suggest a general analytic solution [9–11]. Therefore, these techniques are independent of the availability of a small parameter. On the other hand, a relatively new method known as the new iterative method (NIM) [12, 13] is a modified form of the Adomian decomposition method (ADM) [14] in which the Adomian polynomials are replaced by DJ polynomials in the nonlinear terms.

In the present work, coupled system of fractional-order differential equations will be solved using NIM. FDEs have been solved using NIM with the help of fractional derivative and integral operators [13, 15–17]. In this paper, we will find the solution of the Fractional Drinfeld–Sokolov–Wilson (FDSW) coupled system and fractional shallow water (FSW) coupled system. The fractional-order DSW equation is used to add memory effects and genetic consequences into the system, and these features let us grasp important physical properties of complex issues. The fractional DSW coupled system is of the form [18]

$$D_t^\beta \varphi(x, t) + 3\psi(x, t)\psi(x, t)_x = 0, \quad (1)$$

$$D_t^\beta \psi(x, t) + 2\psi(x, t)_{xxx} + 2\varphi(x, t)\psi(x, t)_x + \varphi(x, t)_x\psi(x, t) = 0, \quad (2)$$

where  $0 < \beta \leq 1$  is the fractional order of derivative of the system and is defined with Caputo's fractional derivative operator.

The second coupled system presented in this paper is the fractional-order shallow water (FSW) equation which describes a thin layer of fluid in hydrostatic equilibrium with a constant density. The equivalent wave motion is the coupled SW equation. The time-fractional SW coupled system is of the form [19]

$$D_t^\beta \varphi(x, t) = -\psi(x, t)\varphi(x, t)_x - \varphi(x, t)\psi(x, t)_x, \quad (3)$$

$$D_t^\beta \psi(x, t) = -\psi(x, t)\psi(x, t)_x - \varphi(x, t)_x, \quad (4)$$

where  $\varphi(x, t)$  and  $\psi(x, t)$  denote the free surface and the horizontal velocity component.

Many researchers pay attention to fractional DSW and fractional SW equations by using different approaches [20–23].

The remaining article is planned as follows: Section 2 contains some basics from fractional calculus relevant to our study. The essential concepts of the NIM are presented in Section 3. The proposed approach is used to solve the fractional DSW and fractional SW coupled systems in Section 4. The numerical results by NIM are presented in Section 5 with the help of graphs and Tables 1–4. The final paragraph contains the conclusion.

## 2. Fractional Calculus

We will present some essential definitions from fractional calculus that are relevant to our work [24].

*Definition 1.* The fractional integral operator in Riemann–Liouville (R-L) sense is defined as

$$I_t^\beta = \begin{cases} \frac{1}{\Gamma(\beta)} \int_0^t (t-\gamma)^{\beta-1} f(\gamma) d\gamma & \text{if } \beta > 0, t > 0, \\ f(\gamma) & \text{if } \beta = 0, \end{cases} \quad (5)$$

where  $\Gamma$  is the gamma function.

*Definition 2.* The Caputo fractional derivative operator of order  $\beta$  is described as follows:

$$D_t^\beta \varphi(t) = \frac{1}{\Gamma(n-\beta)} \left[ \int_0^t (t-\gamma)^{n-\beta-1} f^n(\gamma) d\gamma \right] \text{ if } n-1 < \beta \leq n, n \in \mathbb{N}. \quad (6)$$

*Definition 3.* Relationship of the Caputo's fractional derivative and the R-L integral is defined as follows:

If  $m-1 < \beta \leq m, m \in \mathbb{N}$ , then

$$I_t^\beta \left[ D_t^\beta \varphi(t) \right] = \varphi(t) + \sum_{j=0}^{m-1} \varphi^{(j)}(\gamma) \frac{(t-\gamma)^j}{\Gamma(j+1)}, t > 0, \varphi \in C_{\beta}^{\mu}, \mu \geq -1. \quad (7)$$

## 3. New Iterative Method

Assume a nonlinear equation of the form [12]

$$\psi(\underline{\chi}, t) = h(\underline{\chi}, t) + L\psi(\underline{\chi}, t) + \aleph\psi(\underline{\chi}, t), \quad (8)$$

where  $\underline{\chi} = \chi_1, \chi_2, \dots, \chi_n$ ,  $h(\underline{\chi}, t)$ ,  $L$ , and  $\aleph$  indicate the source term, linear operator, and nonlinear operator, respectively. The solution of Equation (8), according to NIM, can be expanded as follows:

$$\psi(\underline{\chi}, t) = \sum_{m=0}^{\infty} \psi_m(\underline{\chi}, t). \quad (9)$$

Due to the linearity of  $L$ ,  $\psi(\underline{\chi}, t)$  is expressed as

$$L \left( \sum_{m=0}^{\infty} \psi_m(\underline{\chi}, t) \right) = \sum_{m=0}^{\infty} L(\psi_m(\underline{\chi}, t)). \quad (10)$$

The nonlinear operator  $N$  presented by Daftardar-Gejji and Jaffari is expressed as

$$\aleph \left( \sum_{m=0}^{\infty} \psi_m(\underline{\chi}, t) \right) = \aleph(\psi_0(\underline{\chi}, t)) + \sum_{m=1}^{\infty} \left\{ \aleph \left( \sum_{j=0}^i \psi_j(\underline{\chi}, t) \right) - \aleph \left( \sum_{j=0}^{m-1} \psi_j(\underline{\chi}, t) \right) \right\}. \quad (11)$$

TABLE 1: The absolute error of the 2<sup>nd</sup>-order NIM and 2<sup>nd</sup>-order q-HATM solution for  $\varphi(x, t)$  the FDSW coupled system.

$x$	$t$	$\beta = 0.5$	$\beta = 0.7$	$\beta = 0.9$	$\beta = 1.0$	Exact sol.	NIM error	Error [18]
2.5	0.025	0.0880367	0.0880367	0.0880367	0.0880367	0.0880429	$6.13333 \times 10^{-6}$	$1.23436 \times 10^{-5}$
	0.05	0.0971	0.0971	0.0971	0.0971	0.0971513	$5.13081 \times 10^{-5}$	$1.00990 \times 10^{-4}$
	0.075	0.107004	0.107004	0.107004	0.107004	0.107185	$1.809556 \times 10^{-4}$	$3.48632 \times 10^{-4}$
	0.1	0.117785	0.117785	0.117785	0.117785	0.118233	$4.479405 \times 10^{-4}$	$8.45395 \times 10^{-4}$
5	0.025	0.0880367	0.0880367	0.0880367	0.0880367	0.0880429	$6.13333 \times 10^{-6}$	$9.30466 \times 10^{-8}$
	0.05	0.0971	0.0971	0.0971	0.0971	0.0971513	$5.13081 \times 10^{-5}$	$7.63637 \times 10^{-7}$
	0.075	0.107004	0.107004	0.107004	0.107004	0.107185	$1.809556 \times 10^{-4}$	$2.64499 \times 10^{-6}$
	0.1	0.117785	0.117785	0.117785	0.117785	0.118233	$4.479405 \times 10^{-4}$	$6.43687 \times 10^{-6}$
7.5	0.025	$4.05657 \times 10^{-6}$	$4.05657 \times 10^{-6}$	$4.05657 \times 10^{-6}$	$4.05657 \times 10^{-6}$	$4.05689 \times 10^{-6}$	$3.215065 \times 10^{-10}$	$6.27408 \times 10^{-10}$
	0.05	$4.48085 \times 10^{-6}$	$4.48085 \times 10^{-6}$	$4.48085 \times 10^{-6}$	$4.48085 \times 10^{-6}$	$4.48356 \times 10^{-6}$	$2.702048 \times 10^{-9}$	$5.14926 \times 10^{-9}$
	0.075	$4.94552 \times 10^{-6}$	$4.94552 \times 10^{-6}$	$4.94552 \times 10^{-6}$	$4.94552 \times 10^{-6}$	$4.95510 \times 10^{-6}$	$9.576419 \times 10^{-9}$	$1.78358 \times 10^{-8}$
	0.1	$5.45240 \times 10^{-6}$	$5.4524 \times 10^{-6}$	$5.4524 \times 10^{-6}$	$5.45240 \times 10^{-6}$	$5.47623 \times 10^{-6}$	$2.382852 \times 10^{-8}$	$4.34062 \times 10^{-8}$
10	0.025	$5.37770 \times 10^{-8}$	$3.49043 \times 10^{-8}$	$2.87695 \times 10^{-8}$	$2.7333 \times 10^{-8}$	$2.73351 \times 10^{-8}$	$2.166307 \times 10^{-12}$	$4.22746 \times 10^{-12}$
	0.05	$7.37214 \times 10^{-8}$	$4.34152 \times 10^{-8}$	$3.28010 \times 10^{-8}$	$3.01918 \times 10^{-8}$	$3.02100 \times 10^{-8}$	$1.820637 \times 10^{-11}$	$3.46956 \times 10^{-11}$
	0.075	$9.27727 \times 10^{-8}$	$5.2151 \times 10^{-8}$	$3.71170 \times 10^{-8}$	$3.33227 \times 10^{-8}$	$3.33872 \times 10^{-8}$	$6.452584 \times 10^{-11}$	$1.20177 \times 10^{-10}$
	0.1	$1.11597 \times 10^{-7}$	$6.12942 \times 10^{-8}$	$4.17686 \times 10^{-8}$	$3.67380 \times 10^{-8}$	$3.68986 \times 10^{-8}$	$1.605564 \times 10^{-10}$	$2.92470 \times 10^{-10}$

TABLE 2: The absolute error of the 2<sup>nd</sup>-order NIM and 2<sup>nd</sup>-order q-HATM solution for  $\psi(x, t)$  the FDSW coupled system.

$x$	$t$	$\beta = 0.5$	$\beta = 0.7$	$\beta = 0.9$	$\beta = 1.0$	Exact sol.	NIM error	Error [18]
2.5	0.025	0.474805	0.385607	0.351313	0.342621	0.342623	$1.595560 \times 10^{-6}$	$5.67484 \times 10^{-6}$
	0.05	0.558666	0.429127	0.374743	0.359897	0.35991	$1.308247 \times 10^{-5}$	$4.57167 \times 10^{-5}$
	0.075	0.63306	0.470474	0.398436	0.377993	0.378038	$4.519525 \times 10^{-5}$	$1.55336 \times 10^{-4}$
	0.1	0.703019	0.511305	0.422738	0.396935	0.397044	$1.095138 \times 10^{-4}$	$3.70588 \times 10^{-4}$
5	0.025	0.0392622	0.0319312	0.0290606	0.0283316	0.0283322	$5.654244 \times 10^{-7}$	$5.67870 \times 10^{-7}$
	0.05	0.0459425	0.0355452	0.0310238	0.0297801	0.0297847	$4.581037 \times 10^{-6}$	$4.60060 \times 10^{-6}$
	0.075	0.051697	0.038937	0.0330033	0.0312959	0.0313116	$1.565947 \times 10^{-5}$	$1.57255 \times 10^{-5}$
	0.1	0.0569726	0.0422418	0.0350246	0.0328792	0.0329168	$3.759878 \times 10^{-5}$	$3.77553 \times 10^{-5}$
7.5	0.025	0.00322299	0.00262123	0.00238556	0.00232572	0.00232577	$4.667055 \times 10^{-8}$	$4.66719 \times 10^{-8}$
	0.05	0.00377121	0.0029179	0.00254673	0.00244463	0.00244501	$3.781143 \times 10^{-7}$	$3.78125 \times 10^{-7}$
	0.075	0.00424335	0.00319632	0.00270924	0.00256908	0.00257037	$1.292494 \times 10^{-6}$	$1.29253 \times 10^{-6}$
	0.1	0.00467611	0.00346756	0.00287517	0.00269905	0.00270215	$3.103259 \times 10^{-6}$	$3.10335 \times 10^{-6}$
10	0.025	0.000264559	0.000215164	0.000195819	0.000190907	0.000190911	$3.831095 \times 10^{-9}$	$3.83110 \times 10^{-9}$
	0.05	0.00030956	0.000239516	0.000209049	0.000200668	0.000200699	$3.103867 \times 10^{-8}$	$3.10387 \times 10^{-8}$
	0.075	0.000348315	0.00026237	0.000222388	0.000210883	0.000210989	$1.060983 \times 10^{-7}$	$1.06098 \times 10^{-7}$
	0.1	0.000383838	0.000284635	0.000236009	0.000221552	0.000221806	$2.547404 \times 10^{-7}$	$2.54740 \times 10^{-7}$

TABLE 3: Numerical comparison of different values of  $\beta$  and absolute error of the 2<sup>nd</sup>-order NIM solution of  $\varphi(x, t)$  for the FSW system.

$x$	$t$	$\beta = 0.5$	$\beta = 0.7$	$\beta = 0.9$	$\beta = 1.0$	Exact sol.	NIM error
2.5	0.025	0.380492	0.298803	0.269985	0.262974	0.262985	$1.092004 \times 10^{-5}$
	0.05	0.461865	0.337071	0.289279	0.276917	0.277008	$9.164358 \times 10^{-5}$
	0.075	0.536682	0.374877	0.309367	0.291859	0.292184	$3.24701 \times 10^{-4}$
	0.1	0.608701	0.413306	0.330496	0.307833	0.308642	$8.08642 \times 10^{-4}$
5	0.025	2.70572	2.12482	1.91989	1.87004	1.87011	$7.765359 \times 10^{-5}$
	0.05	3.28437	2.39695	2.05709	1.96919	1.96984	$6.516877 \times 10^{-4}$
	0.075	3.81641	2.66579	2.19994	2.07544	2.07775	$2.308985 \times 10^{-3}$
	0.1	4.32854	2.93907	2.3502	2.18904	2.19479	$5.750343 \times 10^{-3}$
7.5	0.025	7.1448	5.61085	5.06972	4.93807	4.93827	$2.05054 \times 10^{-4}$
	0.05	8.6728	6.32945	5.43201	5.19988	5.2016	$1.720863 \times 10^{-3}$
	0.075	10.0777	7.03935	5.80922	5.48047	5.48657	$6.097163 \times 10^{-3}$
	0.1	11.43	7.76097	6.20598	5.78043	5.79561	$1.51845 \times 10^{-2}$
10	0.025	13.6977	10.7569	9.71947	9.46706	9.46746	$3.931213 \times 10^{-4}$
	0.05	16.6271	12.1346	10.414	9.969	9.9723	$3.299169 \times 10^{-3}$
	0.075	19.3206	13.4956	11.1372	10.5069	10.5186	$1.168923 \times 10^{-2}$
	0.1	21.9132	14.879	11.8979	11.082	11.1111	$2.911111 \times 10^{-2}$

TABLE 4: Numerical comparison of different values of  $\beta$  and absolute error of the 2<sup>nd</sup>-order NIM solution of  $\psi(x, t)$  for the FSW system.

$x$	$t$	$\beta = 0.5$	$\beta = 0.7$	$\beta = 0.9$	$\beta = 1.0$	Exact sol.	NIM error
2.5	0.025	-1.23094	-1.09261	-1.03916	-1.02563	-1.02564	$1.255342 \times 10^{-5}$
	0.05	-1.35945	-1.16031	-1.07566	-1.05253	-1.05263	$1.038012 \times 10^{-4}$
	0.075	-1.47213	-1.22437	-1.11257	-1.08072	-1.08108	$3.623311 \times 10^{-4}$
	0.1	-1.57702	-1.28731	-1.15038	-1.11022	-1.11111	$8.888889 \times 10^{-4}$
5	0.025	-3.2825	-2.91362	-2.7711	-2.73501	-2.73504	$3.347578 \times 10^{-5}$
	0.05	-3.62521	-3.09415	-2.86844	-2.80674	-2.80702	$2.768031 \times 10^{-4}$
	0.075	-3.92569	-3.26498	-2.96685	-2.88192	-2.88288	$9.662162 \times 10^{-4}$
	0.1	-4.20538	-3.43283	-3.06769	-2.96059	-2.96296	$2.37037 \times 10^{-3}$
7.5	0.025	-5.33406	-4.73464	-4.50304	-4.44439	-4.44444	$5.439815 \times 10^{-5}$
	0.05	-5.89096	-5.028	-4.66121	-4.56095	-4.5614	$4.498051 \times 10^{-4}$
	0.075	-6.37925	-5.30559	-4.82113	-4.68311	-4.68468	$1.570101 \times 10^{-3}$
	0.1	-6.83374	-5.57835	-4.98499	-4.81096	-4.81481	$3.851852 \times 10^{-3}$
10	0.025	-7.38562	-6.55566	-6.23498	-6.15377	-6.15385	$7.532051 \times 10^{-5}$
	0.05	-8.15671	-6.96184	-6.45399	-6.31517	-6.31579	$6.22807 \times 10^{-4}$
	0.075	-8.83281	-7.3462	-6.67542	-6.48431	-6.48649	$2.173986 \times 10^{-3}$
	0.1	-9.4621	-7.72387	-6.9023	-6.66133	-6.66667	$5.333333 \times 10^{-3}$



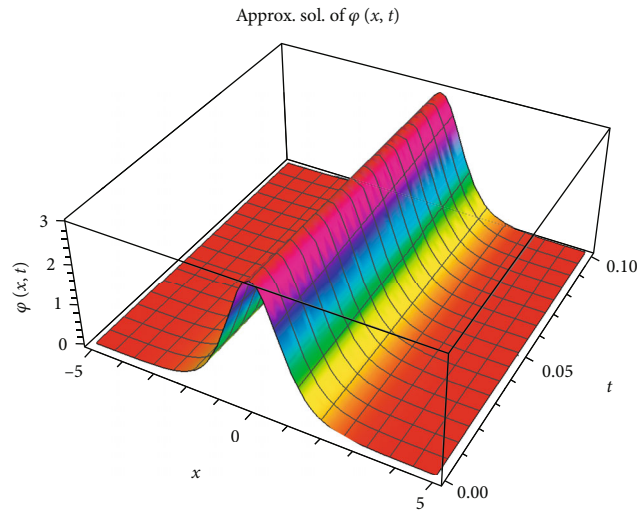


FIGURE 1: 2<sup>nd</sup>-order NIM solution of  $\varphi(x, t)$  FDSW system.

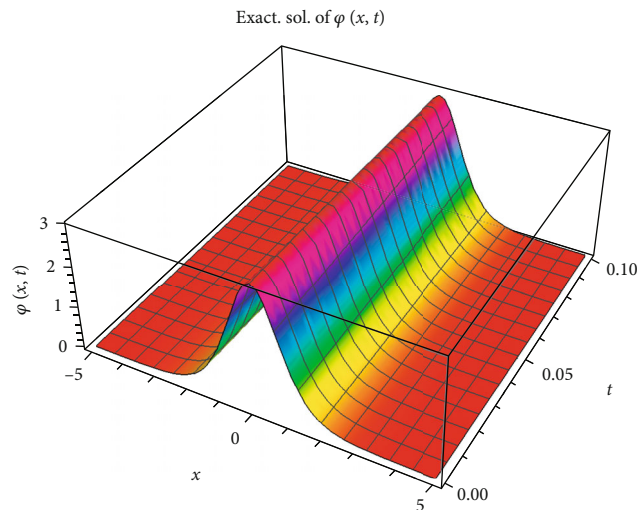


FIGURE 2: Exact solution of  $\varphi(x, t)$  FDSW system.

Equations (9)–(11) are substituted in Equation (8) to obtain and then,

$$\sum_{i=1}^{\infty} \psi_i = h + \sum_{m=0}^{\infty} L(\psi_m) + \mathcal{N}(\psi_0) + \sum_{m=1}^{\infty} \left\{ \mathcal{N} \left( \sum_{j=0}^m \psi_j \right) - \mathcal{N} \left( \sum_{j=0}^{m-1} \psi_j \right) \right\}. \quad (12)$$

We define the recursive relation as follows:

$$\begin{cases} \psi_0(\underline{\chi}, t) = h, \\ \psi_1(\underline{\chi}, t) = L(\psi_0) + \mathcal{N}(\psi_0), \\ \psi_2(\underline{\chi}, t) = L(\psi_1) + \mathcal{N}(\psi_0 + \psi_1) - \mathcal{N}(\psi_0), \\ \vdots \\ \psi_m(\underline{\chi}, t) = L(\psi_{m-1}) + \mathcal{N}(\psi_0 + \psi_1 + \dots + \psi_{m-1}) - \mathcal{N}(\psi_0 + \psi_1 + \dots + \psi_{m-2}), \\ m = 1, 2, 3, \dots, \end{cases} \quad (13)$$

$$\psi_m(\underline{\chi}, t) = L(\psi_0 + \psi_1 + \dots + \psi_{m-1}) + \mathcal{N}(\psi_0 + \psi_1 + \dots + \psi_{m-1}), \quad m = 1, 2, 3, \dots,$$

$$\sum_{m=0}^{\infty} \psi_m(\underline{\chi}, t) = h(\underline{\chi}, t) + L \left( \sum_{m=0}^{\infty} \psi_m(\underline{\chi}, t) \right) + \mathcal{N} \left( \sum_{m=0}^{\infty} \psi_m(\underline{\chi}, t) \right). \quad (14)$$

The  $n$ -term NIM solution of Equations (8) and (9) is

$$\psi(\underline{\chi}, t) = \psi_0 + \psi_1 + \dots + \psi_{n-1}. \quad (15)$$

**3.1. NIM Convergence.** In this section, the conditions for the convergence of NIM are given in the following theorems for the series  $\sum_{m=0}^{\infty} \psi_m(\underline{\chi}, t)$ .

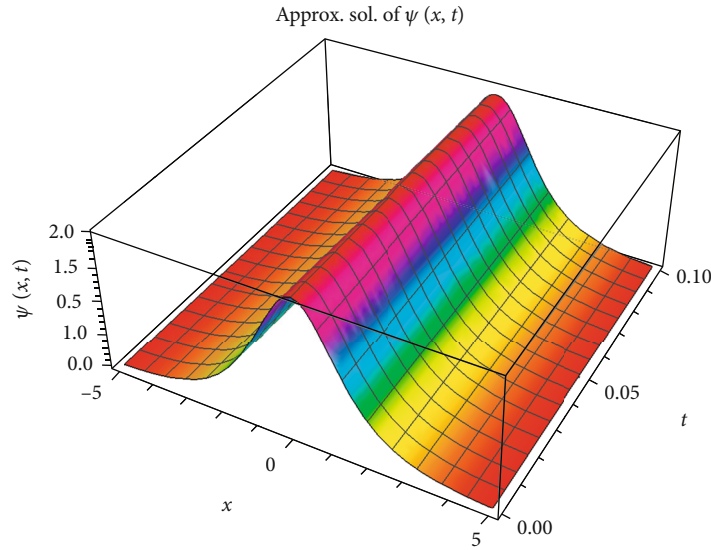


FIGURE 3: 2<sup>nd</sup>-order NIM solution of  $\psi(x, t)$  FDSW system at  $c = 2$ .

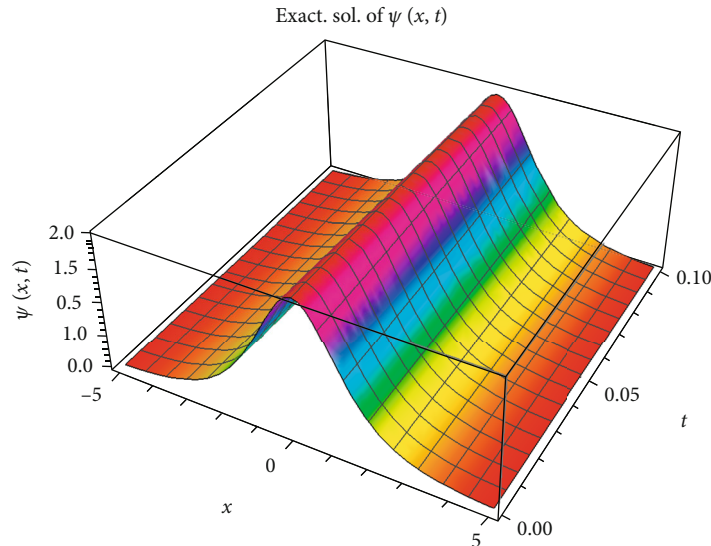


FIGURE 4: Exact solution of  $\psi(x, t)$  FDSW system at  $c = 2$ .

**Theorem 4.** If  $\aleph$  is  $C^{(\infty)}$  in a neighborhood of  $\psi_0$  and  $\|\aleph^n(\psi_0)\| \leq L$ , for some real  $L > 0$  and any  $n$   $\|\psi_j\| \leq M < 1/e, j = 1, 2, \dots$ , then the series  $\sum_{n=0}^{\infty} G_n$  is convergent, and moreover,  $\|G_n\| \leq LM^n e^{n-1}(e-1), n = 1, 2, \dots$ .

**Theorem 5.** If  $\aleph$  is  $C^\infty$  and  $\|\aleph^n(\psi_0)\| \leq M \leq e^{-1} \forall n$ , then the series  $\sum_{n=0}^{\infty} G_n$  is convergent. The detail of NIM convergence can be seen in article written by Bhalekar and Daftardar-Geiji in [25].

#### 4. Implementation of NIM

In this section, we implement NIM firstly to the fractional Drinfeld–Sokolov–Wilson coupled system and then to the fractional shallow water coupled system. The implementation is done by considering the fractional derivative in Capu-

to's sense, and the R-L integral is applied to the equations. The method is applied directly for obtaining an approximate solution.

**4.1. Fractional Drinfeld–Sokolov–Wilson (FDSW) Coupled System.** Consider the FDSW system of the form by rearranging Equation (1), and we write [18]

$$D_t^\beta \varphi(x, t) = -3\psi(x, t)\psi(x, t)_x, \quad (16)$$

$$D_t^\beta \psi(x, t) = -2\psi(x, t)_{xxx} - 2\varphi(x, t)\psi(x, t)_x - \varphi(x, t)_x \psi(x, t), \quad (17)$$

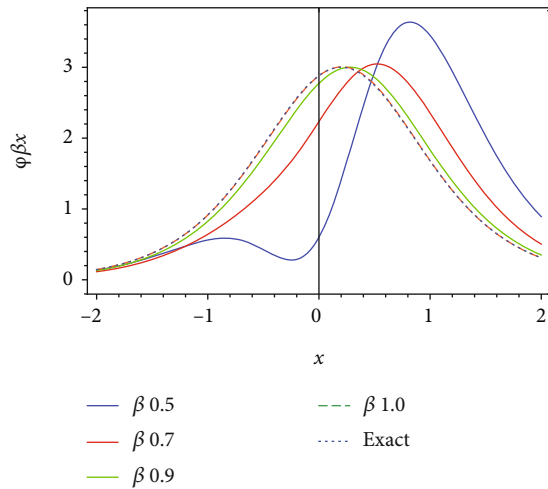


FIGURE 5: 2<sup>nd</sup>-order NIM and exact solution of  $\varphi(x, t)$  at  $t = 0.1$  of FDSW equation and for fractional values of  $\beta$ .

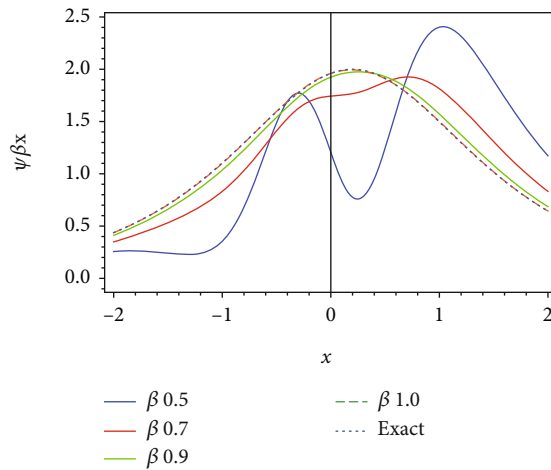


FIGURE 6: 2<sup>nd</sup>-order NIM and exact solution of  $\psi(x, t)$  at  $t = 0.1$  of FDSW equation and for fractional values of  $\beta$ .

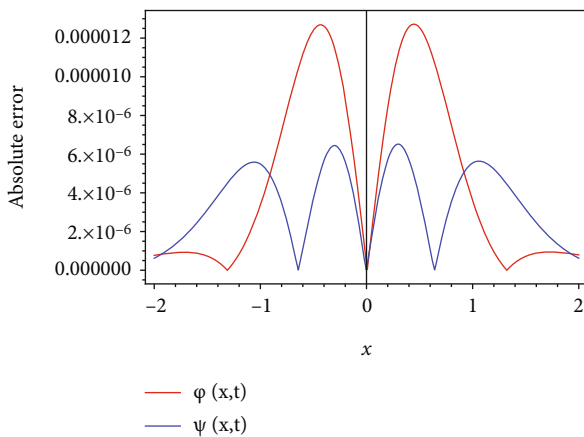


FIGURE 7: Comparison of the absolute error of the 2<sup>nd</sup>-order NIM solution for  $\varphi(x, t)$  and  $\psi(x, t)$  at  $t = 0.01$  for the fractional DSW equations.

together with the initial condition

$$\varphi(x, 0) = \frac{1}{2}(3c) \operatorname{sech}^2\left(\sqrt{\frac{c}{2}}x\right), \tag{18}$$

$$\psi(x, 0) = c \operatorname{sech}\left(\sqrt{\frac{c}{2}}x\right).$$

Equation (16) has the exact solution for  $\beta = 1$  as

$$\varphi(x, t) = \frac{1}{2}(3c) \operatorname{sech}^2\left(\sqrt{\frac{c}{2}}(x - ct)\right), \tag{19}$$

$$\psi(x, t) = c \operatorname{sech}\left(\sqrt{\frac{c}{2}}(x - ct)\right).$$

Applying  $I_t^\beta$  to Equation (16), we have

$$\begin{aligned} I_t^\beta D_t^\beta \varphi(x, t) &= \varphi(x, 0) + I_t^\beta \{-3\psi(x, t)\psi(x, t)_x\}, \\ I_t^\beta D_t^\beta \psi(x, t) &= \psi(x, 0) + I_t^\beta \{-2\psi(x, t)_{xxx} - 2\varphi(x, t)\psi(x, t)_x - \varphi(x, t)_x\psi(x, t)\}. \end{aligned} \tag{20}$$

By substituting the initial condition, we get

$$\begin{aligned} \varphi(x, t) &= \frac{1}{2}(3c) \operatorname{sech}^2\left(\sqrt{\frac{c}{2}}(x - ct)\right) + I_t^\beta \{-3\psi(x, t)\psi(x, t)_x\}, \\ \psi(x, t) &= c \operatorname{sech}\left(\sqrt{\frac{c}{2}}(x - ct)\right) + I_t^\beta \{-2\psi(x, t)_{xxx} - 2\varphi(x, t)\psi(x, t)_x - \varphi(x, t)_x\psi(x, t)\}. \end{aligned} \tag{21}$$

By NIM algorithm, the zeroth-order component of  $\varphi(x, t)$  and  $\psi(x, t)$  solution is as follows:

$$\left\{ \begin{aligned} \varphi_0(x, t) &= \frac{1}{2}(3c) \operatorname{sech}^2\left(\sqrt{\frac{c}{2}}x\right) \\ \psi_0(x, t) &= c \operatorname{sech}\left(\sqrt{\frac{c}{2}}x\right) \end{aligned} \right\}. \tag{22}$$

The first-order component of solution is as follows:

$$\left\{ \begin{aligned} \varphi_1(x, t) &= \frac{3c^{5/2}t^\beta \tanh\left(\sqrt{cx}/\sqrt{2}\right) \operatorname{sech}^2\left(\sqrt{cx}/\sqrt{2}\right)}{\sqrt{2}\Gamma(\beta + 1)} \\ \psi_1(x, t) &= \frac{c^{5/2}t^\beta \tanh\left(\sqrt{cx}/\sqrt{2}\right) \operatorname{sech}\left(\sqrt{cx}/\sqrt{2}\right)}{\sqrt{2}\Gamma(\beta + 1)} \end{aligned} \right\}. \tag{23}$$

The second-order component of solution is as follows:

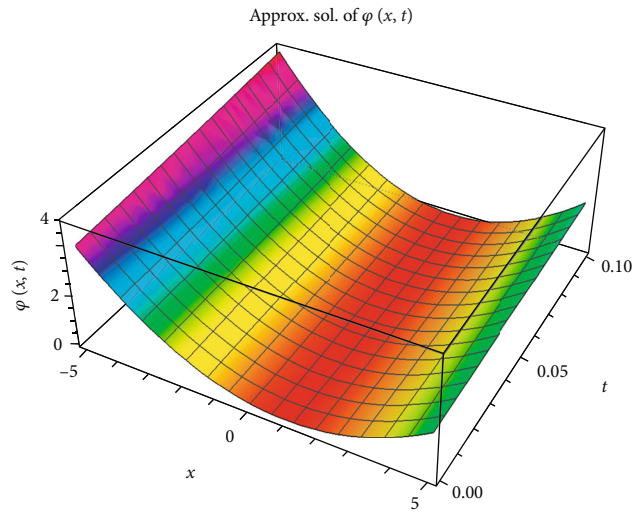


FIGURE 8: 2<sup>nd</sup>-order NIM solution of  $\varphi(x, t)$  FSW system.

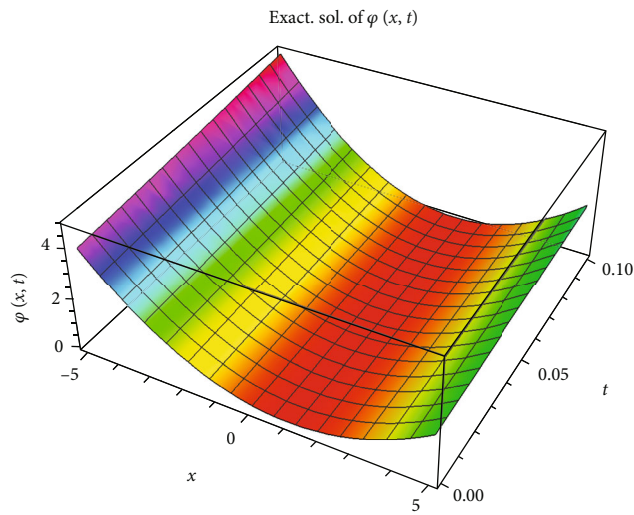


FIGURE 9: Exact solution of  $\varphi(x, t)$  DSW system.

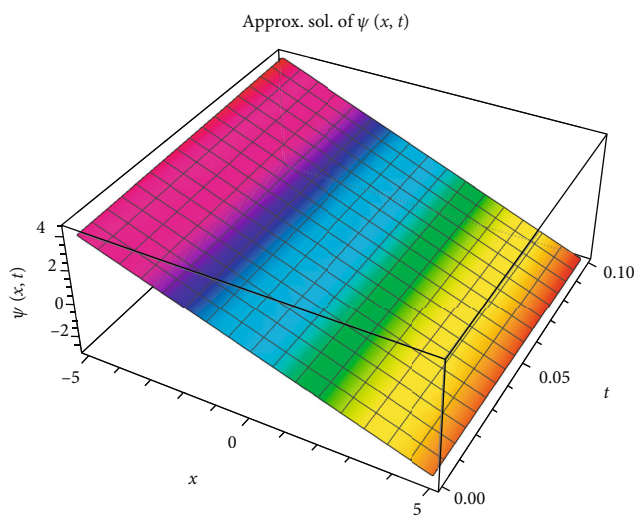


FIGURE 10: 2<sup>nd</sup>-order NIM solution of  $\varphi(x, t)$  DSW system.

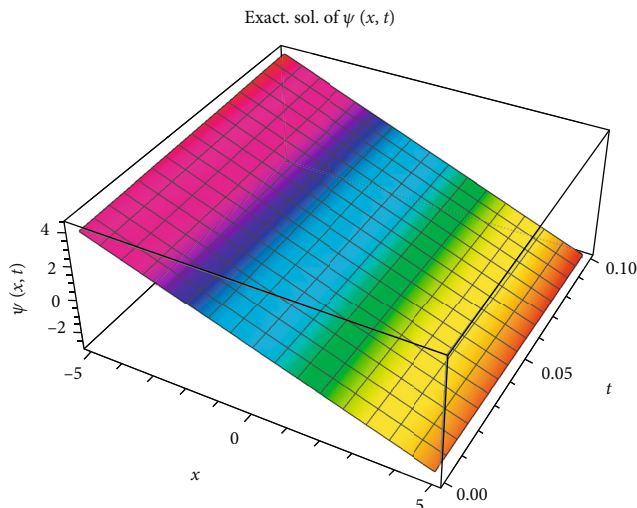


FIGURE 11: Exact solution of  $\psi(x, t)$  DSW system.

$$\left\{ \begin{array}{l} \varphi_2(x, t) = \frac{3c^4 \operatorname{sech}^5(\sqrt{cx}/\sqrt{2})}{16\Gamma(\beta + 1)^2} \left( \frac{\sqrt{2}c^{3/2}\Gamma(2\beta + 1)t^{3\beta} \begin{pmatrix} \sinh(3\sqrt{cx}/\sqrt{2}) \\ -7 \sinh(\sqrt{cx}/\sqrt{2}) \end{pmatrix}}{\Gamma(3\beta + 1)} + \frac{4\Gamma(\beta + 1)^2 t^{2\beta} (\cosh(3\sqrt{cx}/\sqrt{2}) - 3 \cosh(\sqrt{cx}/\sqrt{2}))}{\Gamma(2\beta + 1)} \right) \\ \psi_2(x, t) = \frac{c^4 \operatorname{sech}^3(\sqrt{cx}/\sqrt{2})}{4\Gamma(\beta + 1)^2} \left( \frac{3\sqrt{2}c^{3/2}\Gamma(2\beta + 1)t^{3\beta} \begin{pmatrix} \sinh(3\sqrt{cx}/\sqrt{2}) \\ -6 \sinh(\sqrt{cx}/\sqrt{2}) \end{pmatrix} \operatorname{sech}^3(\sqrt{cx}/\sqrt{2})}{\Gamma(3\beta + 1)} + \frac{\Gamma(\beta + 1)^2 t^{2\beta} (\cosh(\sqrt{2}\sqrt{cx}) - 3)}{\Gamma(2\beta + 1)} \right) \end{array} \right. \quad (24)$$

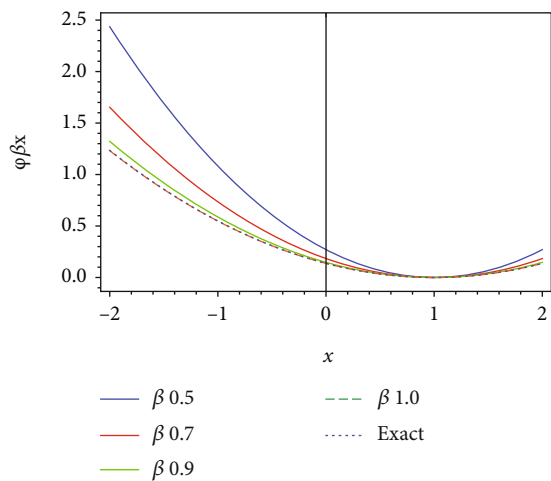


FIGURE 12: 2<sup>nd</sup>-order NIM solution and exact solution of  $\varphi(x, t)$  at  $t = 0.1$  of FSW equation and for fractional values of  $\beta$ .

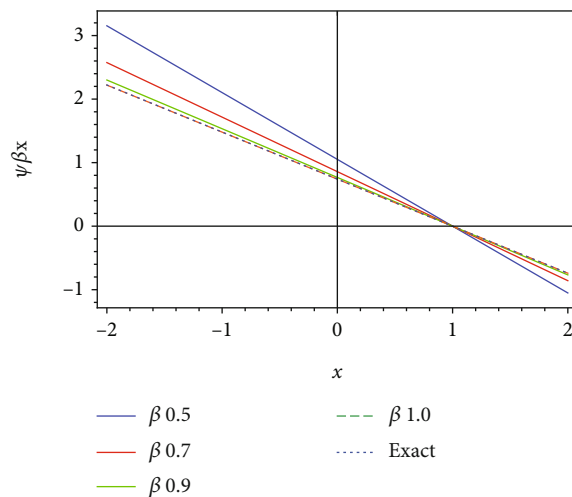


FIGURE 13: 2<sup>nd</sup>-order NIM solution and exact solution of  $\psi(x, t)$  at  $t = 0.1$  of FSW equation and for fractional values of  $\beta$ .

$$\left. \begin{aligned} \varphi(x, t) = \varphi_0 + \varphi_1 + \varphi_2 = & \left\{ \begin{aligned} & \frac{3}{2}c \operatorname{sech}^2\left(\frac{\sqrt{cx}}{\sqrt{2}}\right) + \frac{3c^{5/2}t^\beta \tanh\left(\frac{\sqrt{cx}}{\sqrt{2}}\right) \operatorname{sech}^2\left(\frac{\sqrt{cx}}{\sqrt{2}}\right)}{\sqrt{2}\Gamma(\beta+1)} \\ & + \frac{3c^4 \operatorname{sech}^5\left(\frac{\sqrt{cx}}{\sqrt{2}}\right)}{16\Gamma(\beta+1)^2} \left( \begin{aligned} & \frac{\sqrt{2}c^{3/2}\Gamma(2\beta+1)t^{3\beta} \left( \begin{aligned} & \sinh\left(3\sqrt{cx}/\sqrt{2}\right) \\ & -7 \sinh\left(\sqrt{cx}/\sqrt{2}\right) \end{aligned} \right)}{\Gamma(3\beta+1)} \\ & + \frac{4\Gamma(\beta+1)^2 t^{2\beta} \left( \cosh\left(3\sqrt{cx}/\sqrt{2}\right) - 3 \cosh\left(\sqrt{cx}/\sqrt{2}\right) \right)}{\Gamma(2\beta+1)} \end{aligned} \right) \end{aligned} \right\} \\ \psi(x, t) = \psi_0 + \psi_1 + \psi_2 = & \left\{ \begin{aligned} & c \operatorname{sech}\left(\frac{\sqrt{cx}}{\sqrt{2}}\right) + \frac{c^{5/2}t^\beta \tanh\left(\frac{\sqrt{cx}}{\sqrt{2}}\right) \operatorname{sech}\left(\frac{\sqrt{cx}}{\sqrt{2}}\right)}{\sqrt{2}\Gamma(\beta+1)} \\ & + \frac{c^4 \operatorname{sech}^3\left(\frac{\sqrt{cx}}{\sqrt{2}}\right)}{4\Gamma(\beta+1)^2} \left( \begin{aligned} & \frac{3\sqrt{2}c^{3/2}\Gamma(2\beta+1)t^{3\beta} \left( \begin{aligned} & \sinh\left(3\sqrt{cx}/\sqrt{2}\right) \\ & -6 \sinh\left(\sqrt{cx}/\sqrt{2}\right) \end{aligned} \right) \operatorname{sech}^3\left(\frac{\sqrt{cx}}{\sqrt{2}}\right)}{\Gamma(3\beta+1)} \\ & + \frac{\Gamma(\beta+1)^2 t^{2\beta} \left( \cosh\left(\sqrt{2}\sqrt{cx}\right) - 3 \right)}{\Gamma(2\beta+1)} \end{aligned} \right) \end{aligned} \right\}. \end{aligned} \quad (25)$$

By combining the zeroth, first, and second-order components of  $\varphi(x, t)$  and  $\psi(x, t)$  the solution, we obtain the 2<sup>nd</sup>-order NIM solution as

4.2. *Fractional Shallow Water (FSW) Coupled System.* Consider the nonlinear FSW coupled system by rearranging Equation (3), and we have [19]

$$D_t^\beta \varphi(x, t) = -\psi(x, t)\varphi(x, t)_x - \varphi(x, t)\psi(x, t)_x, \quad (26)$$

$$D_t^\beta \psi(x, t) = -\psi(x, t)\psi(x, t)_x - \varphi(x, t)_x, \quad (27)$$

together with the initial condition

$$\begin{aligned} \varphi(x, 0) &= \frac{1}{9}(x^2 - 2x + 1), \\ \psi(x, 0) &= \frac{2(1-x)}{3}, \end{aligned} \quad (28)$$

where  $c$  is the wave front's velocity. The exact solution of Equation (26) is given as

$$\begin{aligned} \varphi(x, t) &= \frac{(x-1)^2}{9(t-1)^2}, \\ \psi(x, t) &= \frac{2(x-1)}{3(t-1)}. \end{aligned} \quad (29)$$

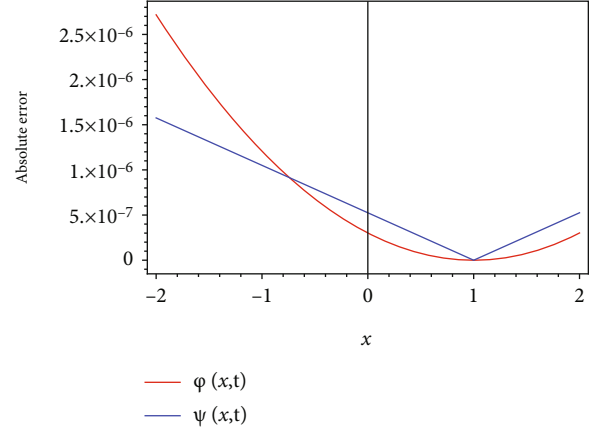


FIGURE 14: Comparison of the absolute error of the 2<sup>nd</sup>-order NIM solution for  $\varphi(x, t)$  and  $\psi(x, t)$  at  $t = 0.01$  for the fractional SW equations.

Applying  $I_t^\beta$  to Equation (30), we have

$$I_t^\beta D_t^\beta \varphi(x, t) = \varphi(x, 0) + I_t^\beta \{-\psi(x, t)\varphi(x, t)_x - \varphi(x, t)\psi(x, t)_x\}, \quad (30)$$

$$I_t^\beta D_t^\beta \psi(x, t) = \psi(x, 0) + I_t^\beta \{-\psi(x, t)\psi(x, t)_x - \varphi(x, t)_x\}. \quad (31)$$

By substituting the initial condition, we get

$$\begin{aligned}\varphi(x, t) &= \frac{1}{9}(x^2 - 2x + 1) + I_t^\beta \{-\psi(x, t)\varphi(x, t)_x - \varphi(x, t)\psi(x, t)_x\}, \\ \psi(x, t) &= \frac{2(1-x)}{3} + I_t^\beta \{-\psi(x, t)\psi(x, t)_x - \varphi(x, t)_x\}.\end{aligned}\quad (32)$$

Using the procedure of NIM, we have the zeroth-order component of the solution as

$$\left\{ \begin{aligned}\varphi_0(x, t) &= \frac{1}{9}(x^2 - 2x + 1) \\ \psi_0(x, t) &= \frac{2(1-x)}{3}\end{aligned} \right\}.\quad (33)$$

The first-order component of solution is as follows:

$$\left\{ \begin{aligned}\varphi_1(x, t) &= \frac{2(x-1)^2 t^\beta}{9\Gamma(\beta+1)} \\ \psi_1(x, t) &= -\frac{2(x-1)t^\beta}{3\Gamma(\beta+1)}\end{aligned} \right\}.\quad (34)$$

The second-order component of solution is as follows:

$$\left\{ \begin{aligned}\varphi_2(x, t) &= \frac{2(x-1)^2(3\Gamma(\beta+1)t^{2\beta}/\Gamma(2\beta+1) + 2\Gamma(2\beta+1)t^{3\beta}/\Gamma(3\beta+1))}{9\Gamma(\beta+1)^2} \\ \psi_2(x, t) &= -\frac{4(x-1)(3\Gamma(\beta+1)t^{2\beta}/\Gamma(2\beta+1) + \Gamma(2\beta+1)t^{3\beta}/\Gamma(3\beta+1))}{9\Gamma(\beta+1)^2}\end{aligned} \right\}.\quad (35)$$

By NIM algorithm, the zeroth-order component of  $\varphi(x, t)$  and  $\psi(x, t)$  solution is as follows:

$$\left\{ \begin{aligned}\varphi(x, t) &= \varphi_0 + \varphi_1 + \varphi_2 = \left\{ \frac{1}{9}(x^2 - 2x + 1) + \frac{2(x-1)^2 t^\beta}{9\Gamma(\beta+1)} + \frac{2(x-1)^2(3\Gamma(\beta+1)t^{2\beta}/\Gamma(2\beta+1) + 2\Gamma(2\beta+1)t^{3\beta}/\Gamma(3\beta+1))}{9\Gamma(\beta+1)^2} \right\} \\ \psi(x, t) &= \psi_0 + \psi_1 + \psi_2 = \left\{ \frac{2(1-x)}{3} - \frac{2(x-1)t^\beta}{3\Gamma(\beta+1)} - \frac{4(x-1)(3\Gamma(\beta+1)t^{2\beta}/\Gamma(2\beta+1) + \Gamma(2\beta+1)t^{3\beta}/\Gamma(3\beta+1))}{9\Gamma(\beta+1)^2} \right\}\end{aligned} \right\}.\quad (36)$$

## 5. Numerical Results and Discussion

The fractional DSW and fractional SW coupled systems of PDEs have been solved by NIM. We calculated the approximate solution up to 2<sup>nd</sup> order and observed the convergence of the method. The results have been plotted with the help of 2D and 3D graphs and also shown in the tables through a numerical comparison for different values. The following discussion shows the detail of figures and tables.

Figures 1 and 2 show the 2<sup>nd</sup>-order NIM and the exact solution, respectively, in 3D plots  $\varphi(x, t)$  while Figures 3 and 4 show the 2<sup>nd</sup>-order NIM and the exact solution, respectively,  $\psi(x, t)$  for the fractional DSW equations. In Figures 5 and 6, the different fractional values of  $\beta$  of the 2<sup>nd</sup>-order NIM solution are compared for  $\varphi(x, t)$  and  $\psi(x,$

$t)$ , respectively. In Figure 7, the 2D plot shows the absolute error for the 2<sup>nd</sup>-order NIM solution for both  $\varphi(x, t)$  and  $\psi(x, t)$  of the fractional DSW equation. Similarly, the fractional SW coupled system of equations is discussed in Figures 8–14. The 3D plots of Figures 8 and 9 represent the 2<sup>nd</sup>-order NIM solution and the exact solution, respectively,  $\varphi(x, t)$ . Figures 10 and 11 show the 2<sup>nd</sup>-order approximate solution and exact solution for  $\psi(x, t)$  of the fractional SW equations. The 2D plots in Figures 12 and 13 compare the different fractional values of  $\beta$  for the 2<sup>nd</sup>-order approximate solution of  $\varphi(x, t)$  and  $\psi(x, t)$ , respectively. In Figure 14, the absolute errors are compared for the 2<sup>nd</sup>-order NIM solution of the fractional SW equations. In all these figures, we noted that as the fractional order of differential equation tends to 1, the approximate solution converges to

exact solution and for  $\beta = 1$ , the approximate solution overlaps the exact solution which verifies the accuracy of our proposed method.

## 6. Conclusion

We implemented new iterative method (NIM) for the solution of the fractional Drinfeld–Sokolov–Wilson equations and fractional-order shallow water equations. The numerical comparison is made with the q-homotopy analysis transform method. The results show that NIM is conveniently convergent and provides an accurate approximate solution. The tables and figures show that as the value of  $\beta$  approaches the classical value (1 for these systems) of the differential equation, the approximate solution converges to the exact solution. Comparisons in tables and graphs verify that NIM converges more rapidly and is widely useful for obtaining the approximate solution of differential equations.

## Data Availability

Data will be available on reasonable statement.

## Conflicts of Interest

The authors declare that they have no conflicts of interest.

## Acknowledgments

The authors are thankful to the Deanship of Scientific Research, King Khalid University, Abha, Saudi Arabia, for financially supporting this work through the General Research Project under Grant no. R.G.P.2/160/43.

## References

- [1] A. H. Nayfeh, *Introduction to perturbation techniques*, John Wiley & Sons, 2011.
- [2] P. A. Lagerstrom and R. G. Casten, “Basic concepts underlying singular perturbation techniques,” *SIAM Review*, vol. 14, no. 1, pp. 63–120, 1972.
- [3] K. J. Bathe, *Finite element method*, Wiley Encyclopedia of Computer Science and Engineering, 2007.
- [4] R. J. LeVeque, “Finite difference methods for differential equations,” *Draft Version for Use in a Math*, vol. 585, no. 6, p. 112, 1998.
- [5] A. M. Wazwaz, “A study on linear and nonlinear Schrodinger equations by the variational iteration method,” *Chaos, Solitons & Fractals*, vol. 37, no. 4, pp. 1136–1142, 2008.
- [6] R. Lyons, A. S. Vatsala, and R. A. Chiquet, “Picard’s iterative method for Caputo fractional differential equations with numerical results,” *Mathematics*, vol. 5, no. 4, p. 65, 2017.
- [7] “New integral transform: Shehu transform a generalization of Sumudu and Laplace transform for solving differential equations,” <https://arxiv.org/abs/1904.11370>.
- [8] J. S. Chen, C. W. Liu, and C. M. Liao, “Two-dimensional Laplace-transformed power series solution for solute transport in a radially convergent flow field,” *Advances in Water Resources*, vol. 26, no. 10, pp. 1113–1124, 2003.
- [9] R. Nawaz and L. Zada, “Solving time fractional Sharma-Tasso-Olver equation by optimal homotopy asymptotic method,” *AIP Conference Proceedings*, vol. 1978, no. 1, article 310002, 2018.
- [10] L. Zada and R. Nawaz, “Solution of time-fractional order RLW equation using optimal homotopy asymptotic method,” *AIP Conference Proceedings*, vol. 2116, no. 1, article 300005, 2019.
- [11] S. Liao, “Comparison between the homotopy analysis method and homotopy perturbation method,” *Applied Mathematics and Computation*, vol. 169, no. 2, pp. 1186–1194, 2005.
- [12] S. Bhalekar and V. Daftardar-Gejji, “New iterative method: application to partial differential equations,” *Applied Mathematics and Computation*, vol. 203, no. 2, pp. 778–783, 2008.
- [13] S. Bhalekar and V. Daftardar-Gejji, “Solving evolution equations using a new iterative method,” *Numerical Methods for Partial Differential Equations: An International Journal*, vol. 26, no. 4, pp. 906–916, 2010.
- [14] D. J. Evans and K. R. Raslan, “The Adomian decomposition method for solving delay differential equation,” *International Journal of Computer Mathematics*, vol. 82, no. 1, pp. 49–54, 2005.
- [15] L. Zada, R. Nawaz, S. Ahsan, K. S. Nisar, and D. Baleanu, “New iterative approach for the solutions of fractional order inhomogeneous partial differential equations,” *AIMS Mathematics*, vol. 6, no. 2, pp. 1348–1365, 2021.
- [16] R. Nawaz, N. Ali, L. Zada, Z. Shah, A. Tassaddiq, and N. A. Alreshidi, “Comparative analysis of natural transform decomposition method and new iterative method for fractional foam drainage problem and fractional order modified regularized long-wave equation,” *Fractals*, vol. 28, no. 7, article 2050124, 2020.
- [17] M. J. Khan, R. Nawaz, S. Farid, and J. Iqbal, “New iterative method for the solution of fractional damped burger and fractional Sharma-Tasso-Olver equations,” *Complexity*, vol. 2018, Article ID 3249720, 7 pages, 2018.
- [18] W. Gao, P. Veerasha, D. G. Prakasha, H. M. Baskonus, and G. Yel, “A powerful approach for fractional Drinfeld–Sokolov–Wilson equation with Mittag-Leffler law,” *Alexandria Engineering Journal*, vol. 58, no. 4, pp. 1301–1311, 2019.
- [19] S. Kumar, A. Kumar, Z. Odibat, M. Aldhaifallah, and K. S. Nisar, “A comparison study of two modified analytical approach for the solution of nonlinear fractional shallow water equations in fluid flow,” *AIMS Mathematics*, vol. 5, no. 4, pp. 3035–3055, 2020.
- [20] S. Bhattar, A. Mathur, D. Kumar, and J. Singh, “A new analysis of fractional Drinfeld–Sokolov–Wilson model with exponential memory,” *Physica A: Statistical Mechanics and its Applications*, vol. 537, article 122578, 2020.
- [21] J. Singh, D. Kumar, D. Baleanu, and S. Rathore, “An efficient numerical algorithm for the fractional Drinfeld–Sokolov–Wilson equation,” *Applied Mathematics and Computation*, vol. 335, pp. 12–24, 2018.
- [22] S. Kumar, “A numerical study for the solution of time fractional nonlinear shallow water equation in oceans,” *Zeitschrift für Naturforschung A*, vol. 68, no. 8-9, pp. 547–553, 2013.
- [23] D. H. Kim, Y. S. Cho, and W. G. Kim, “Weighted average flux-type scheme for shallow-water equations with fractional step method,” *Journal of Engineering Mechanics*, vol. 130, no. 2, pp. 152–160, 2004.



- [24] R. Gorenflo and F. Mainardi, "Fractional Calculus," in *Fractals and Fractional Calculus in Continuum Mechanics*, Springer, Vienna, 1997.
- [25] S. Bhalekar and V. Daftardar-Gejji, "Convergence of the new iterative method," *International Journal of Differential Equations*, vol. 2011, Article ID 989065, 10 pages, 2011.

## Research Article

# Fractional Analysis of Dissipative Viscous Fluid Flow with Mixed Convection and Variable Viscosity

Abir Mouldi,<sup>1</sup> Riadh Marzouki,<sup>2</sup> Mohamed Hechmi El Ouni,<sup>3</sup> and Abdul Bariq<sup>4</sup> 

<sup>1</sup>Department of Industrial Engineering, College of Engineering, King Khalid University, Abha-61421, Saudi Arabia

<sup>2</sup>Department of Chemistry, College of Science, King Khalid University, Abha-61421, Saudi Arabia

<sup>3</sup>Department of Civil Engineering, College of Engineering, King Khalid University, Abha-61421, Saudi Arabia

<sup>4</sup>Department of Mathematics, Laghman University, Mehterlam, 2701 Laghman, Afghanistan

Correspondence should be addressed to Abdul Bariq; [abdulbariq.maths@lu.edu.af](mailto:abdulbariq.maths@lu.edu.af)

Received 29 September 2021; Accepted 21 February 2022; Published 6 April 2022

Academic Editor: Hui Yao

Copyright © 2022 Abir Mouldi et al. This is an open access article distributed under the Creative Commons Attribution License, which permits unrestricted use, distribution, and reproduction in any medium, provided the original work is properly cited.

Time-dependent viscosity and thermal conductivity have been studied in relation to flow and thermal energy propagation along a vertical turning cone. Except the density variance, the other fluid's properties are assumed to be constant. Using the similarities procedure, the nonlinear system of differential equations is simplified to dimensionless ODEs. The resultant nonlinear ODEs system is computed while using fractional code FDE12, and the findings are quantitatively examined using the *bvp4c* approach for accuracy and consistency. In form of figures and tables, the behavior of momentum, energy, and mass is interpreted versus the physical constraints. The axial and radial velocity, both declines with the variation of unsteadiness parameter *S*. The axial velocity of the fluid is considerably increased when the mixed convection parameter is elevated, but the radial velocity is reduced. Similarly, when the variable viscosity increases, the velocity profile develops.

## 1. Introduction

The results of this study show that disk-cone appliances are used in a variety of technical applications, including determining the viscosity of a fluid (viscosimetry), convective diffusion, medical devices, and biomedicine for oxygen measurement [1]. The heat transfer through a spinning cone is also addressed in this research. Many academics are drawn to this sort of study to investigate its properties, behavior, and applications. Turkilmazoglu [2] investigated a steady Newtonian viscous fluid over a rotating cone using the homotopy analysis technique. The mixed convective simulation with momentum and heat distribution across a perforated upward spinning cone in an ambient liquid was numerically calculated by Chamkha and Al-Mudhaf [3]. They hypothesized that when cone angular velocity varies, axial, and tangential velocity increases considerably. Garrett et al. [4] investigated the fluid flow across a turning cone (half angle) in axial direction. The MHD (magnetohydrody-

namics) nanoliquid flow with Brownian motion and thermophoresis influence over a revolving cone was deled by Nadeem and Saleem [5] and Towers and Garrett [6]. It is worth noting that surface temperature and Mach number destabilise the system, whereas suction stabilises it. Hayat et al. [7] used a shooting method to emphasize the MHD chemical reactivity of an unsteady viscous fluid over a turning cone. Chamkha et al. [8] evaluated the influence of a rotating cone on a 3D CNT hybrid nanofluid in a trapezoid permeable cavity, considering MHD interactions.

The upshot of unsteady viscosity on viscous fluid characteristics causes some variation. The viscosity of liquids, for example, decreases as temperature goes up, but the viscosity of gases improves. The rises in thermal energy cause friction in oily fluids, which affects fluid viscosity, and the viscosity no longer holds consistent. In light of this deficiency, a growing number of researchers are focusing their efforts on demonstrating the impact of changing viscosity phenomena under various situations. The effects of fluctuating viscosity

of third-grade dispersed fluid flow via a conduit have been explored by Christie and Massoudi [9]. The numerical outputs were discovered using the finite difference method. Seddeek [10] investigated unstable free convection MHD flow across an infinite plate under the influence of a magnetic field and changing viscosity. The computational solution of the simulated equations is done using the finite difference method. MHD boundary layer flow over an extending heated surface with variable viscosity is reported by Pantokratoras [11]. Their analysis also included a graphical representation of viscosity variations. Mukhopadhyay and Layek [12] looked studied heat exchange across a stretched vertical porous surface with changing fluid viscosity. They discovered that increasing the viscosity, enhances the velocity while decreasing the energy field. Using a discrete variant of HAM known as spectral homotopy evaluation over a stretched surface, Dada and Onwubuoya [13] addressed mass and energy distribution through fluid flow with changing viscosity and activation energy. Hazarika et al. [14] evaluated the upshots of changing viscosity, thermal radiation, and MHD on fluid flow through a vertical cone.

The thermal transition rates are affected by viscous dissipation, which acts as an energy source. The relevance of viscous dissipation is determined by whether the cone is freezing or warmed. Reddy et al. [15] estimated MHD flow and energy propagation across a stretched substrate as a function of heat source and viscous dissipation. Mabood et al. [16] evaluated the MHD flow, energy transport, and chemical reaction of a nanofluid containing copper Cu and aluminium oxide particulates in a porous media under the viscous dissipation influence. Deebani et al. [17] assessed the role of viscous dissipation and MHD across a revolving cone. Gayatri et al. [18] studied viscous dissipation in 2D fluid flow with varying thickness and slip coefficients across a stretched surface. They discovered that the slip parameters increase friction while lowering fluid velocity. Using the Atangana-Baleanu fractional method, Saqib et al. [19] investigated electro-osmotic nanofluid flow.

Fractional calculus, which is an extension of regular calculus, has a 300-year history. This field has exploded in popularity in recent years. Almost all activities in applied sciences are described by signal processing, fluid flow in permeable substances, wave transference in mechanical properties, finance theory, and biological system electric conductance [20, 21]. Many definitions exist for the fractional derivative; however, the Caputo and Riemann Liouville fractional derivatives are particularly important in terms of applicability [22]. We know that the kernel was single in both fractional definitions. To overcome this difficulty, Caputo and Fabrizio presented a new point of view of non-integer order derivative with nonsingular kernel [23] in 2016, which is highly beneficial for a variety of physical problems. Manzoor et al. [24] analyzed the uniqueness and existence of solutions of fractional order differential equations with Caputo derivatives. They came up with a set of requirements to assure solution validity while maintaining Hyers-Ulam stability. The fractional assessments for Darcy hybrid nanoliquid flow over a perforated spinning disc were elaborated by Li et al. [25]. The proposed model has been put up

using Matlab fractional code Fde12 to produce the fractional solution. The outputs are compared to the fast-approaching numerical Matlab scheme boundary value solver for correctness and validity of the resultant framework.

We generalized the approach of [26] based on the aforementioned literature and its application in the actual world. The goal of this study is to assess the upshots of time-dependent viscosity on flow, thermal energy, and mass transfer in a vertical rotating cone. The spinning phenomenon is arranged in the format of a system of PDEs for this reason. Which are solved using the fractional code FDE12, and the results are checked for validity and correctness using the Matlab numerical software boundary value solver (bvp4c). The findings are depicted graphically and shortly reviewed.

## 2. Mathematical Formulation

We considered axisymmetric, an incompressible and unsteady fluid flow with an angular velocity  $\Omega$  across a rotating cone. The  $u$ ,  $v$ , and  $w$  are the velocity component has been considered along  $x$ ,  $y$ ,  $z$  direction. The gravity  $g$  impact is downward, and the buoyancy force exist due to the temperature variation. The tangential direction influences temperature  $T_w$  variability near the cone's edge, while temperature  $T_\infty$  away from the cone kept fixed. Fluid flow mechanism over a rotating cone is depicted through Figure 1. Furthermore, the variable thermal conductivity and viscosity are expressed as [26]: the variable viscosity model used here is the Reynold's model. The Taylor series expansion has been used to obtain.

$$\begin{aligned}\mu &= \mu_0(1 - A\theta), \mu = \mu_0 e^{-\eta(T-T_\infty)}, \\ k &= k_0 e^{-c(T-T_\infty)}, k = k_0(1 - \varepsilon\theta).\end{aligned}\quad (1)$$

Where

$$A = (T_w - T_\infty)\eta \text{ and } \varepsilon = -(T_w - T_\infty)c. \quad (2)$$

Here,  $k_0$  and  $\mu_0$  is the fluid conductivity and dynamic viscosity.

The governing system of nonlinear PDEs for momentum, mass, and energy may be written as by utilising Boussinesq approximation boundary layer theory and the aforementioned assumption [26]:

$$\frac{\partial(xu)}{\partial x} + \frac{\partial(xv)}{\partial z} = 0. \quad (3)$$

$$\frac{\partial u}{\partial t} + u \frac{\partial u}{\partial x} + w \frac{\partial u}{\partial z} - \frac{v^2}{x} = \frac{1}{\rho} \frac{\partial}{\partial z} \left( \mu \frac{\partial u}{\partial z} \right) + g(T - T_\infty) \beta \cos \alpha^*, \quad (4)$$

$$\frac{\partial v}{\partial t} + u \frac{\partial v}{\partial x} + w \frac{\partial v}{\partial z} + \frac{uv}{x} = \frac{1}{\rho} \frac{\partial}{\partial z} \left( \mu \frac{\partial v}{\partial z} \right), \quad (5)$$

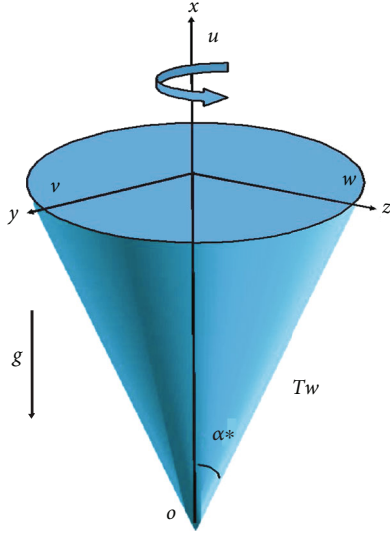


FIGURE 1: Fluid flow mechanism over a rotating cone.

$$\frac{\partial T}{\partial t} + u \frac{\partial T}{\partial x} + w \frac{\partial T}{\partial z} = \frac{1}{\rho C_p} \frac{\partial}{\partial z} \left( k \frac{\partial T}{\partial z} \right) + \frac{\mu}{\rho C_p} \left[ \left( \frac{\partial u}{\partial z} \right)^2 + \left( \frac{\partial v}{\partial z} \right)^2 \right]. \quad (6)$$

$$\frac{\partial C}{\partial t} + u \frac{\partial C}{\partial x} + w \frac{\partial C}{\partial z} = D \frac{\partial^2 C}{\partial z^2}. \quad (7)$$

Where  $\alpha^*$ ,  $\beta$ ,  $k$ ,  $\rho$ , and  $g$  are the cone vertical angle, thermal expansion, thermal conductivity, density, and gravity, respectively.

The boundary conditions are:

$$\begin{aligned} u(0) = 0, v(0) &= \frac{1}{(1-st^*)} \Omega x \sin \alpha^*, T(0) = T_w, C(0) = C_w, \\ u(\infty) &\longrightarrow 0, v(\infty) \longrightarrow 0, T(\infty) \longrightarrow T_\infty, C(\infty) \longrightarrow C_\infty. \end{aligned} \quad (8)$$

To simplify the PDEs to ODES, we commence the preceding similarity variables [26]:

$$\begin{aligned} u &= \frac{1}{2(1-st^*)} \Omega x \sin \alpha^* f'(\eta), \\ w &= \left( \frac{1}{(1-st^*)} \Omega x \sin \alpha^* \right)^{\frac{1}{2}} f(\eta), \eta = \left( \frac{\Omega \sin \alpha^*}{v_0(1-st^*)} \right)^{\frac{1}{2}} z, \\ T &= T_\infty + (T_w - T_\infty) \theta(\eta), T_w - T_\infty = \frac{(T_0 - T_\infty) x}{(1-st^*)^2 l}, \\ v &= \frac{1}{(1-st^*)} \Omega x \sin \alpha^* g(\eta), \\ C &= C_\infty + (C_w - C_\infty) \phi(\eta), \text{ where } t^* = (\Omega \sin \alpha^*) t, \end{aligned} \quad (9)$$

By plunking Equation (9) in Equation (3)–(8), we track down:

TABLE 1: Comparative analysis with [26]  $\alpha = 1$ .

$\eta$	Ref. [26]			Present work		
	$f''(\eta)$	$g'(\eta)$	$\theta'(\eta)$	$f''(\eta)$	$g'(\eta)$	$\theta'(\eta)$
1.0	0.5666	1.2994	1.5036	0.5667	1.2996	1.5039
4.0	0.6616	1.3526	1.3883	0.6635	1.3740	1.3911
8.0	0.6633	1.3738	1.3909	0.6642	1.3761	1.3909
12	0.6642	1.3758	1.3903	0.6645	1.3761	1.3899
16	0.6645	1.3761	1.3899	0.6645	1.3761	1.3899
20	0.6645	1.3761	1.3899	0.6645	1.3761	1.3899

TABLE 2: Comparative analysis between fractional and numerical outcomes.

$Pr$	Numerical (bvp4c)			Fractional (FDE12)	
	$\lambda$	$C_{fx} Re_x^{1/2}$	$0.5 C_{fy} Re_x^{1/2}$	$C_{fx} Re_x^{1/2}$	$0.5 C_{fy} Re_x^{1/2}$
1.7	0	1.1254	0.7153	1.1256	0.7155
	1	2.3008	0.9492	2.3009	0.9494
	10	8.6042	1.4990	8.6045	1.4993
9	0	1.1256	0.7157	1.1257	0.7161
	1	1.5627	0.7835	1.5630	0.7845
	10	5.1821	0.9941	5.1823	0.9950

TABLE 3: Comparative analysis between fractional and numerical outcomes.

$Pr$	Numerical (bvp4c)			Fractional (FDE12)	
	$\lambda$	$Nu Re_x^{-1/2}$	$Re^{-1/2} Sh_r$	$Nu Re_x^{-1/2}$	$Re^{-1/2} Sh_r$
1.7	0	0.3255	0.5276	0.3257	0.5278
	1	0.6121	0.7123	0.6126	0.7127
	10	1.0097	1.2099	1.0099	1.2102
9	0	1.4110	1.5112	1.4121	1.5121
	1	1.5660	1.6662	1.5678	1.6671
	10	2.3581	2.5583	2.3593	2.5592

$$\begin{aligned} f''''(1-A\theta) - f''A\theta' + \frac{1}{2}(f')^2 - 2g^2 - ff'' \\ - 2\lambda\theta - s \left( \frac{\eta}{2} f'' + f' \right) = 0, \end{aligned} \quad (10)$$

$$\begin{aligned} g''(1-A\theta) - Ag'\theta' + gf' - fg' - s((\eta/2)g' + g) = 0, \\ (11) (1/Pr) (\epsilon(\theta')^2 + (1+\epsilon\theta)\theta'') - f\theta' + 1/2 f'\theta - s((\eta/2)\theta + 2\theta) + Ec((g')^2 + 1/4(f'')^2)(1-A\theta) = 0, (12) \end{aligned}$$

$$\left( \phi'' - Sc(g\phi') \right) = 0. \quad (11)$$

The reduced conditions are:

$$\begin{aligned} f(0) = 0, g(0) = 1, f'(0) = \phi(0) = 0, \theta(0) = 0, \\ f'(\infty) \longrightarrow 0, g(\infty) \longrightarrow 0, \phi(\infty) \longrightarrow 0, \theta(\infty) \longrightarrow 0, \end{aligned} \quad (12)$$

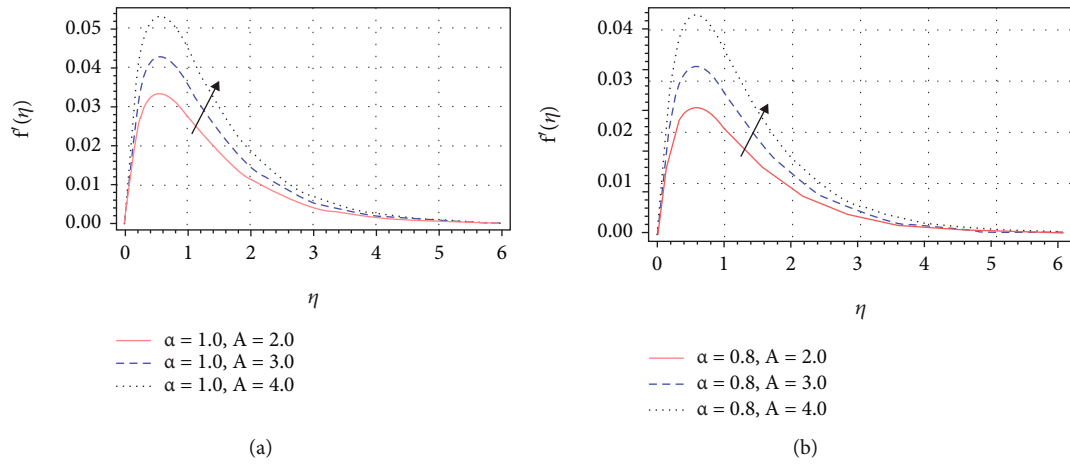


FIGURE 2: Viscosity parameter  $A$  effect on axial velocity profile  $f'(\eta)$ .

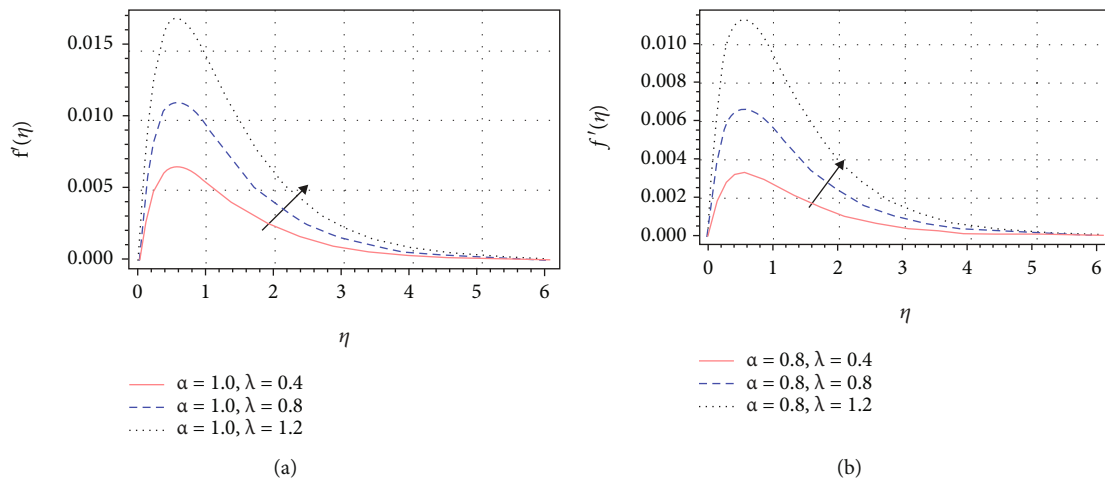


FIGURE 3: Mixed convection parameter  $\lambda$  effect on axial velocity profile  $f'(\eta)$ .

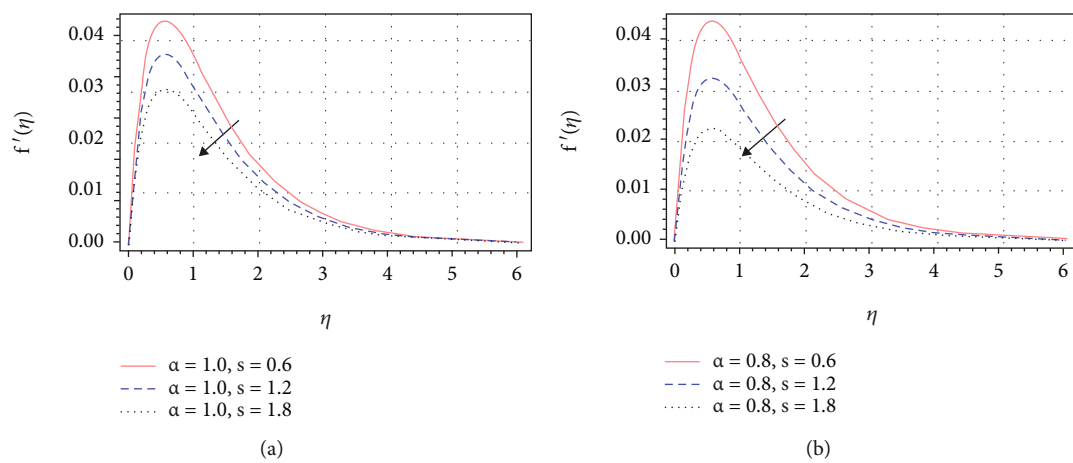
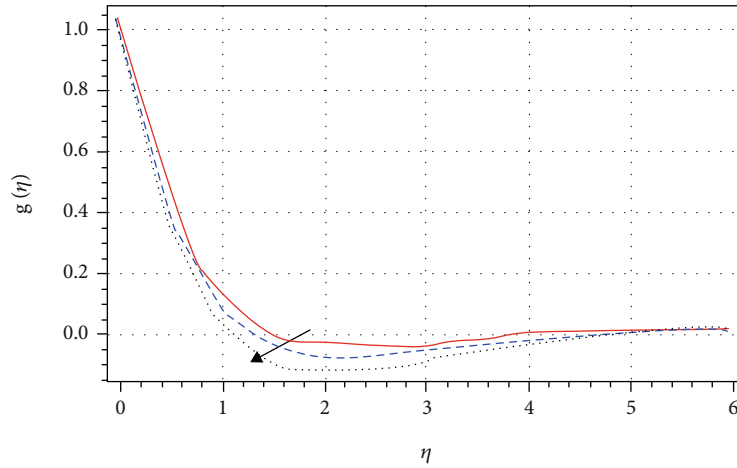
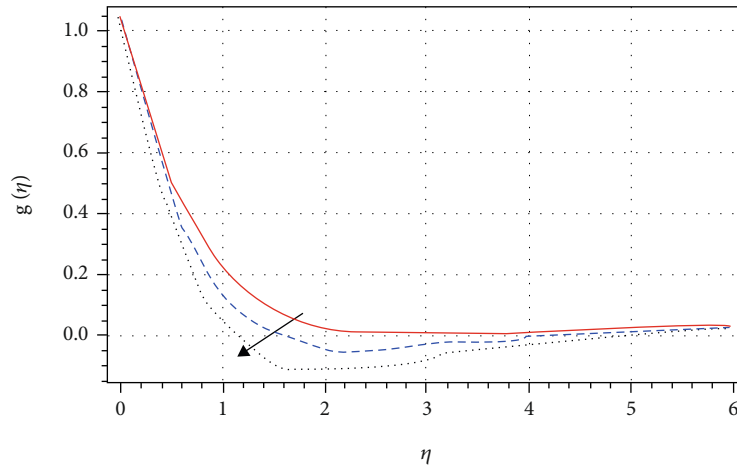


FIGURE 4: Unsteadiness parameter  $S$  effect on axial velocity profile  $f'(\eta)$ .



—  $\alpha = 1.0, A = 2.0$   
 - -  $\alpha = 1.0, A = 3.0$   
 ...  $\alpha = 1.0, A = 4.0$

(a)



—  $\alpha = 0.8, A = 2.0$   
 - -  $\alpha = 0.8, A = 3.0$   
 ...  $\alpha = 0.8, A = 4.0$

(b)

FIGURE 5: Viscosity parameter  $A$  effect on radial velocity profile  $g(\eta)$ .

The parameters generated are rebound as:

$$\text{Pr} = \frac{\nu}{\alpha}, \text{Re}_L = \Omega \sin \alpha^* \frac{L^2}{\nu_0}, \text{Gr} = g(T_0 - T_\infty) \frac{L^3}{\nu_0^2} \beta \cos \alpha^*,$$

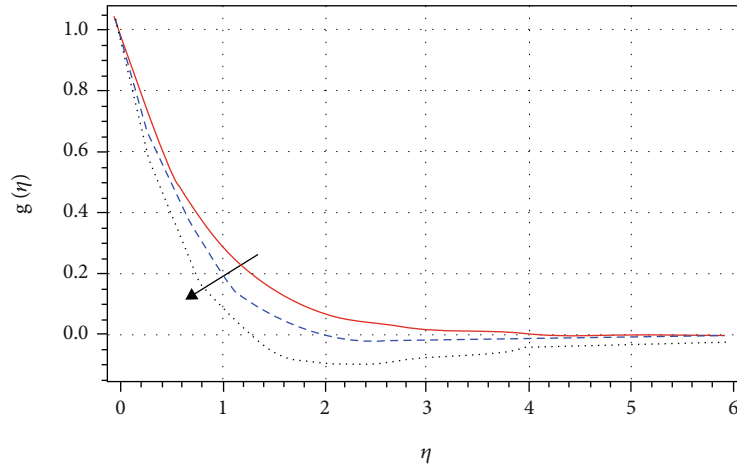
$$\lambda = \frac{\text{Gr}}{\text{Re}_L}, \text{Ec} = \frac{xL(\Omega \sin \alpha^*)^2}{C_p(T_0 - T_w)}, \text{Sc} = \frac{\nu_f}{D_f}. \tag{13}$$

Where  $\text{Pr}$ ,  $\text{Sc}$ , and  $\text{Ec}$  are the Prandtl, Schmidt, and Eckert number, respectively. While  $S$  is the unsteadiness and  $\lambda$  is the mixed convection coefficient.

The skin friction, mass transfer, and Nusselt number are written as:

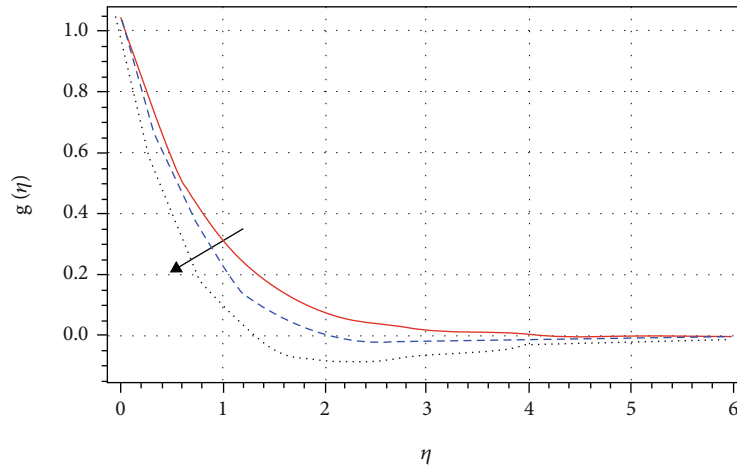
$$C_{fx} = \frac{2\tau_{xz}|_{z=0}}{\rho[\Omega \sin \alpha^*/(1 - st^*)]^2}, C_{fy} = \frac{-2\tau_{yz}|_{z=0}}{\rho[\Omega \sin \alpha^*/(1 - st^*)]^2}, \tag{14}$$

$$\text{Sh}_r = -\frac{x(\partial C/\partial z)|_{z=0}}{(C_w - C_\infty)}, \text{Nu}_x = \frac{x(\partial T/\partial z)|_{z=0}}{(T_w - T_\infty)}. \tag{15}$$



—  $\alpha = 1.0, \lambda = 0.4$   
 - -  $\alpha = 1.0, \lambda = 0.8$   
 ...  $\alpha = 1.0, \lambda = 1.2$

(a)



—  $\alpha = 0.8, \lambda = 0.4$   
 - -  $\alpha = 0.8, \lambda = 0.8$   
 ...  $\alpha = 0.8, \lambda = 1.2$

(b)

FIGURE 6: Mixed convection parameter  $\lambda$  effect on radial velocity profile  $g(\eta)$ .

Equations (14) and (15) dimensionless set up are:

$$C_{fx} \text{Re}_x^{\frac{1}{2}} = \left[ -(1 - A\theta)f'(\eta) \right]_{\eta=0},$$

$$C_{fy} \text{Re}_x^{\frac{1}{2}} = \left[ -(1 - A\theta)g'(\eta) \right]_{\eta=0},$$

$$Nu_x \text{Re}_x^{-1/2} = -\theta'(\eta)_{\eta=0}, \quad \text{Re}^{-1/2} Sh_r = -\phi'(0). \quad (16)$$

Where

$$\text{Re}_x = \frac{1}{\nu_0(1 - st^*)} \Omega x^2 \sin \alpha^*. \quad (17)$$

### 3. Preliminaries

*Definition 1.* For a function  $g : \mathfrak{R}^+ \rightarrow \mathfrak{R}$ , the fractional integral of order  $\alpha > 0$  is defined as:

$$I_t^\alpha(g(t)) = \frac{1}{\Gamma(\alpha)} \int (t - \chi)^{\alpha-1} g(\chi) d\chi. \quad (18)$$

*Definition 2.* For function  $g \in C^n$ , the Caputo noninteger order derivative is defined as:

$${}^c D_t^\alpha(g(t)) = I^{n-\alpha} D^n g(t) = \frac{1}{\Gamma(n-\alpha)} \int_0^t \frac{g^n(\chi)}{(t-\chi)^{\alpha+n-1}} d\chi. \quad (19)$$

Clearly  ${}^c D_t^\alpha(g(t))$  tends to  $g'(t)$  as  $\alpha \rightarrow 1$ .

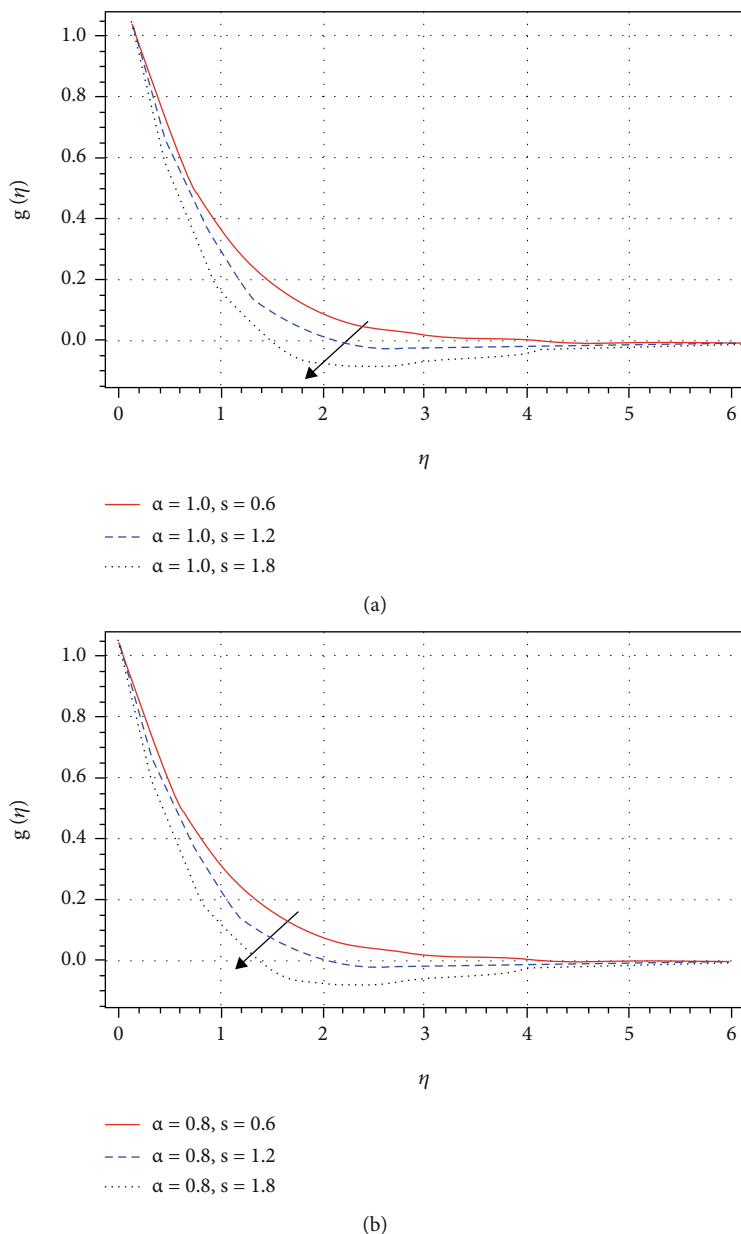


FIGURE 7: Unsteadiness parameter S effect on radial velocity profile  $g(\eta)$ .

#### 4. Problem Solution

By defining the preceding variables, the system of ODEs (10)–(13) and (14) are reduced to a dimensionless first order differential equations (DE):

$$\left. \begin{aligned}
 \eta = \gamma_1, f = \gamma_2, f' = \gamma_3, f'' = \gamma_4, g = \gamma_5, g' = \gamma_6, \theta = \gamma_7, \theta' = \gamma_8, \phi = \gamma_9, \phi' = \gamma_{10} \} \\
 \left\{ \begin{aligned}
 &\gamma_1 = 1, \gamma_2 = \gamma_3, \gamma_3 = \gamma_4 \\
 &\gamma_4 = \frac{1}{1 - A\gamma_7} \left\{ A\gamma_8\gamma_4 - \frac{1}{2}(\gamma_3)^2 + \gamma_2\gamma_4 + 2(\gamma_5)^2 + 2\lambda\gamma_7 + S\left(\gamma_3 + \frac{\eta}{2}\gamma_4\right) \right\}, \\
 &\gamma_5 = \gamma_6, D_t^\alpha \gamma_6 = \frac{1}{1 - A\gamma_7} \left\{ A\gamma_8\gamma_6 + \gamma_2\gamma_6 - \gamma_5\gamma_3 + S\left(\gamma_5 + \frac{\eta}{2}\gamma_6\right) \right\}, \gamma_7 = \gamma_8, \\
 &\gamma_8 = \frac{1}{1 + \epsilon\gamma_7} \left\{ \text{Pr} \left[ \gamma_2\gamma_8 - \frac{1}{2}\gamma_3\gamma_7 + S\left(\frac{\eta}{2}\gamma_7 + 2\gamma_7\right) \right] - \text{Ec} \left( \frac{1}{4}(\gamma_4)^2 + (\gamma_6)^2 \right) (1 - A\gamma_7) \right\} - \epsilon(\gamma_8)^2, \\
 &\gamma_9 = \gamma_{10}, \gamma_{10} = \text{Sc}(\gamma_5\gamma_{10}).
 \end{aligned} \right\} \tag{20}$$



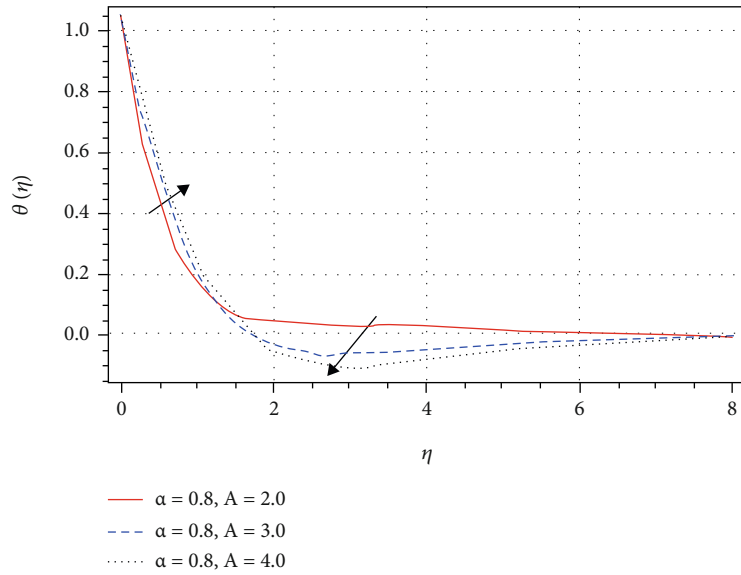
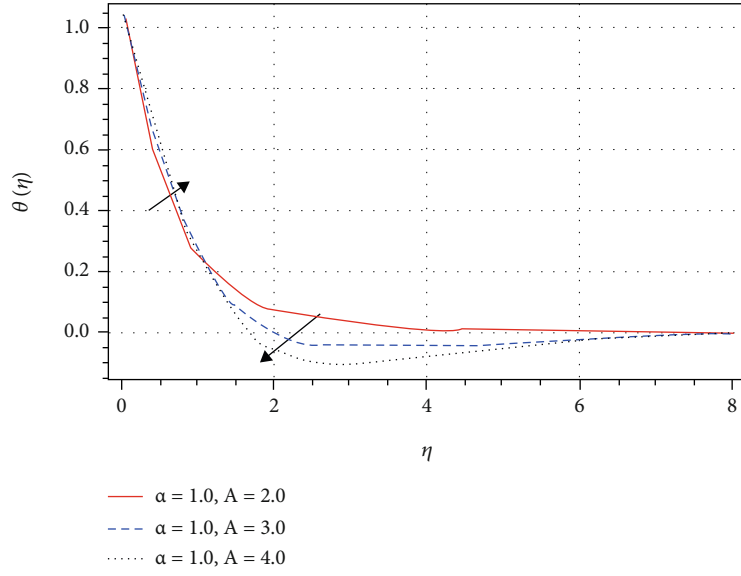


FIGURE 8: Viscosity parameter  $A$  effect on energy profile  $\theta(\eta)$ .

We now use the Caputo fractional derivative to extend the previous system of first order DEs to noninteger order:

$$\begin{cases} D_t^\alpha \gamma_4 = \frac{1}{1 - A\gamma_7} \left\{ A\gamma_8\gamma_4 - \frac{1}{2}(\gamma_3)^2 + \gamma_2\gamma_4 + 2\lambda\gamma_7 + 2(\gamma_5)^2 + S\left(\frac{\eta}{2}\gamma_4 + \gamma_3\right) \right\}, \\ D_t^\alpha \gamma_6 = \frac{1}{1 - A\gamma_7} \left\{ A\gamma_8\gamma_6 - \gamma_5\gamma_3 + \gamma_2\gamma_6 + S\left(\frac{\eta}{2}\gamma_6 + \gamma_5\right) \right\}, D_t^\alpha \gamma_{10} = Sc(\gamma_{10}\gamma_5), \\ D_t^\alpha \gamma_8 = \frac{1}{1 + \varepsilon\gamma_7} \left\{ Pr \left[ \gamma_8\gamma_2 - \frac{1}{2}\gamma_3\gamma_7 + S\left(\frac{\eta}{2}\gamma_7 + 2\gamma_7\right) - Ec \left( (\gamma_6)^2 + \frac{1}{4}(\gamma_4)^2 \right) (1 - A\gamma_7) \right] - \varepsilon(\gamma_8)^2 \right\}. \end{cases} \quad (21)$$

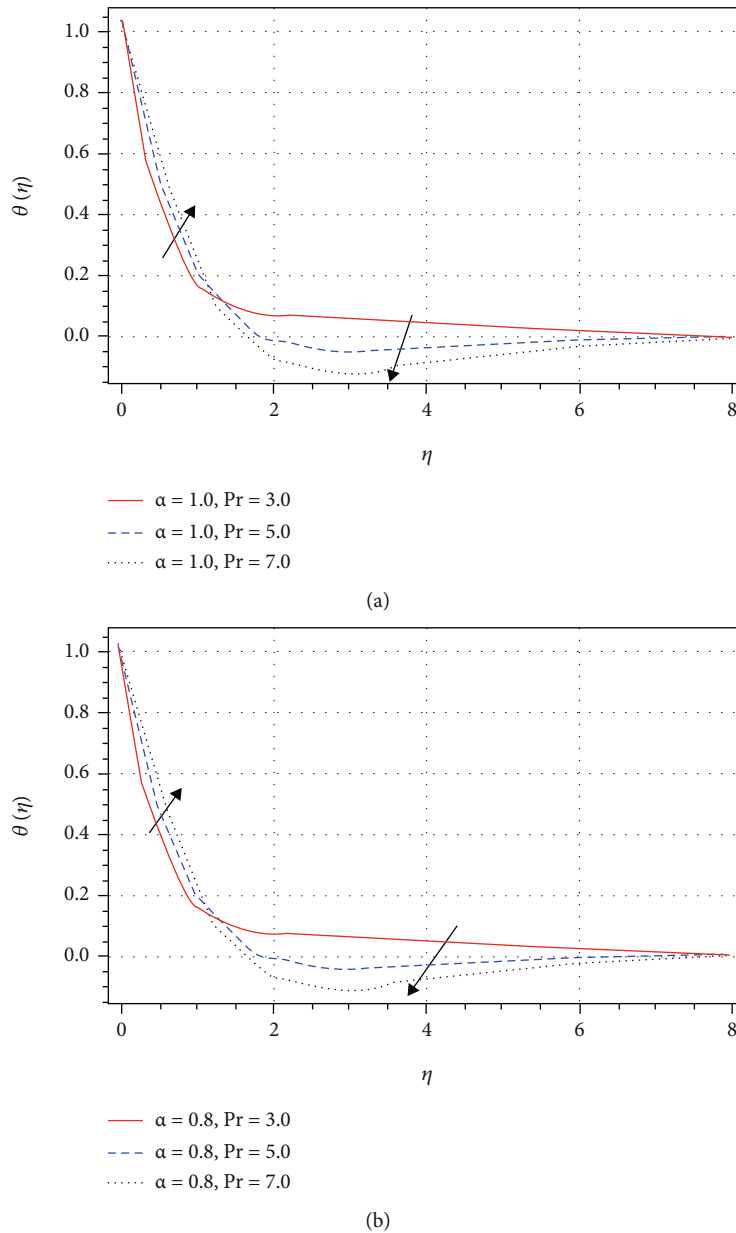


FIGURE 9: Prandtl number  $Pr$  effect on energy profile  $\theta(\eta)$ .

## 5. Result and Discussion

The purpose of this section is to quantify and compare the functionality of energy and mass transition rate based on various physical factors. The findings are produced using Matlab fractional package (fde12), and a fast-approaching numerical technique `bvp4c`, has been applied to ensure the validity and correctness of the outcomes.

Table 1 shows the adequacy of the current study when compared to [26]. While the fractional and numerical methods have been compared in Tables 2 and 3, respectively. For mixed convection and Prandtl number  $Pr$ , the numerical out-

comes of tangential and azimuthal skin friction is shown in Table 2. For mixed convection and Prandtl number, Table 3 shows the quantitative results of Sherwood Nusselt number.

The schematic drawing of a revolving cone is depicted in Figure 1. Figures 2–12(a) depict the behavior of various flow entities when  $\alpha = 1$ , whereas Figures 2–12(b) describe the fractional behavior of basic constraints when  $\alpha = 0.8$ .

The upshot of  $A$  (variable viscosity) on the velocity field is noticed in Figure 2. At  $t = 0$ , the velocity at the cone surface is assumed to be zero, and with increasing credit of viscosity variation, the fluid velocity rises in both Figures 2(a) and 2(b).

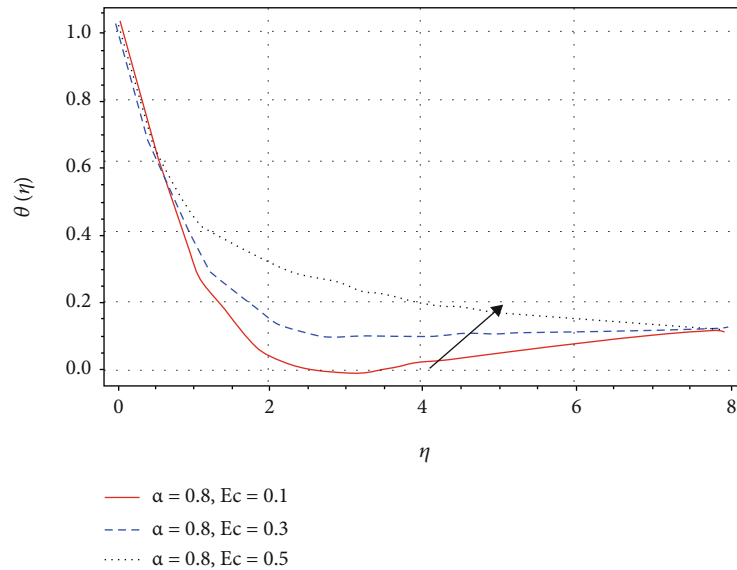
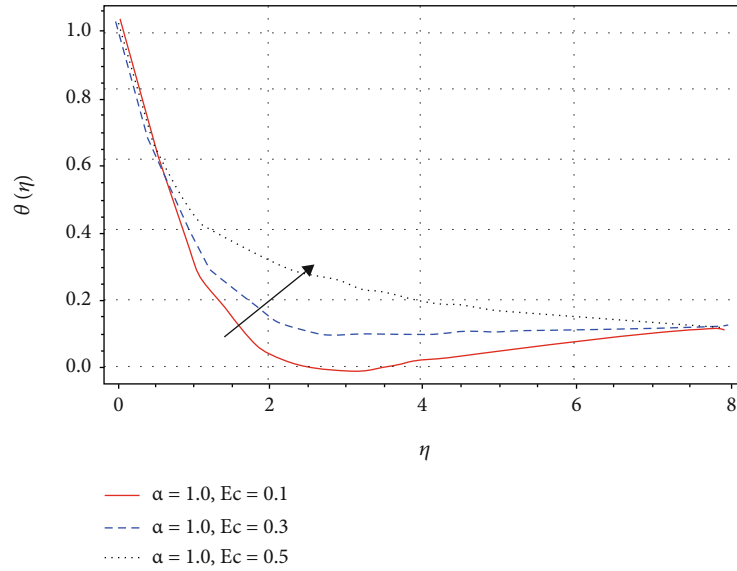


FIGURE 10: Eckert number  $Ec$  effect on energy profile  $\theta(\eta)$ .

Figures 3(a) and 3(b) demonstrate the distribution of the mixed convection  $\lambda$  vs the axial velocity profile  $f'(\eta)$ . Physically, mixed convection has a beneficial influence on boundary layer thickness, resulting in an increase in fluid axial velocity. Convection decreases fluid density, causing fluid particles to move as a result of forces and pressure.

Figures 4(a) and 4(b) show that increasing the value of the unsteadiness parameter  $S$  lowers fluid velocity. Figures 5(a) and 5(b) exhibit the radial velocity features versus the variable viscosity coefficient  $A$ . It has been discovered that when the variable viscosity  $A$  increases, the fluid's radial velocity decreases. Figures 6(a) and 6(b) depict the effect of the convection component on radial velocity. The convection component has a significant impact on fluid motion, and as a result, the velocity drops. In the presence

of the unsteadiness parameter  $S$ , the radial velocity responds similar as an axial velocity. The radial velocity decreases with the increment in  $S$  as elaborated through Figures 7(a) and 7(b).

Figures 8(a) and 8(b) show a reduction in thermal gradient when the variable viscosity factor is increased. The interaction forces within fluid molecules grow as the amount of variable viscosity rises, which results in the lowering fluid energy profile. It is self-evident that when the Prandtl number  $Pr$  increases, the fluid temperature significantly reduces. Because a fluid with a higher Prandtl number has a lower thermal diffusivity (Figures 9(a) and 9(b)).

In Figures 10(a) and 10(b), an increase in energy profile is observed against the Eckert number  $Ec$ . The Eckert number describes a fluid's self-rising thermal rate as a result of

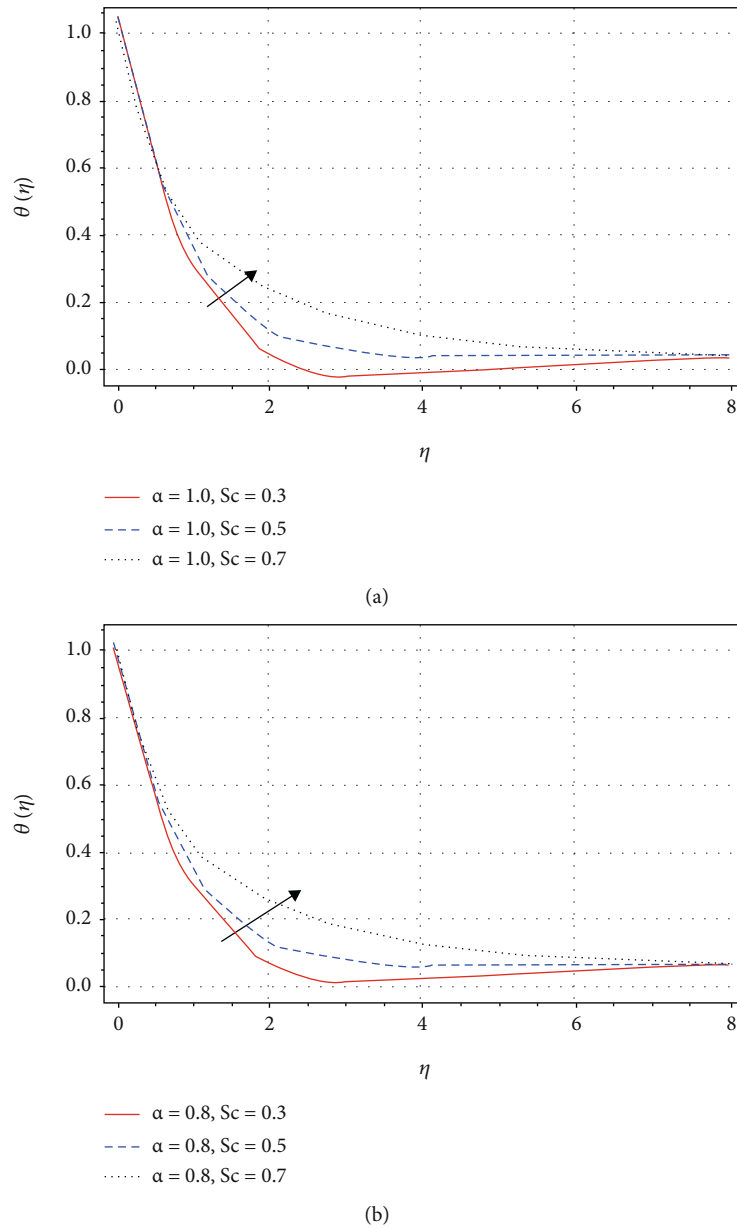


FIGURE 11: Variable thermal conductivity  $\varepsilon$  effect on energy profile  $\theta(\eta)$ .

viscous dissipation. The fluid temperature is efficiently increased using a variable thermal conductivity as revealed through Figures 11(a) and 11(b). The result of Schmidt number vs mass transmission rate is shown in Figures 12(a) and 12(b). The fluid's mass transfer rate is reduced as the Schmidt number is increased.

## 6. Conclusion

The rotating flow of a viscous fluid with time-dependent viscosity and thermal conductivity across a vertical cone is evaluated in this study. A comparison of the numerical `bvp4c` method and `fractional fde12` package is also emphasized. The study's compelling observations are listed below:

- (i) With a positive increase in unsteadiness entity  $S$ , both the axial and radial velocity declines
- (ii) As the value of the mixed convection component improves, the fluid axial velocity  $f'(\eta)$  appears to increase substantially, but the secondary velocity  $g(\eta)$  gradient decreases
- (iii) Similarly, the main velocity  $f'(\eta)$  increases as the viscosity variability component  $A$  grows, while the radial velocity  $g(\eta)$  operates transversely as  $A$  increases
- (iv) Improvements in thermal conductivity, Eckert number  $Ec$  and viscosity constraint  $A$ , limit the rate of thermal energy transference  $NuRe_x^{-1/2}$

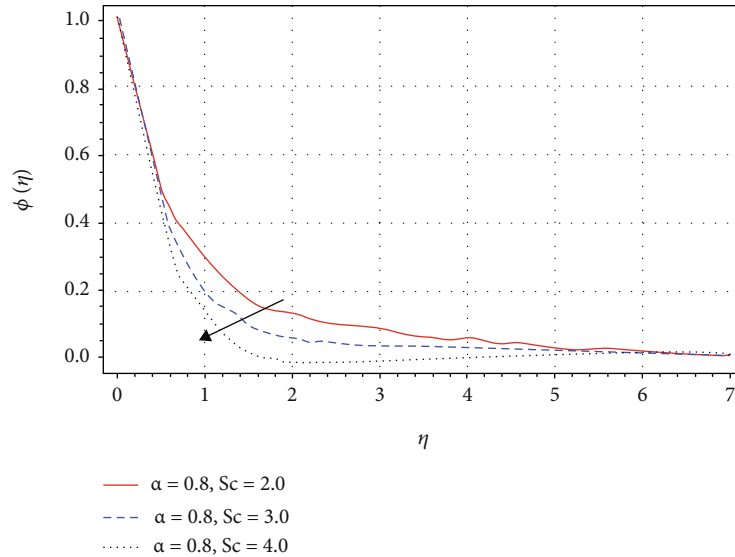
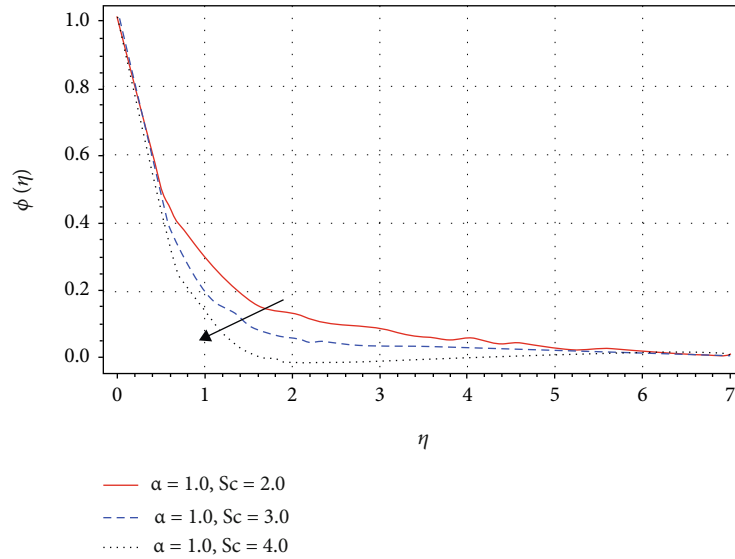


FIGURE 12: Schmidt number effect on mass profile  $\phi(\eta)$ .

(v) Mixed convection has a beneficial influence on boundary layer thickness, resulting in an increase in fluid primary velocity. Convection reduces the density of the fluid, causing fluid particles to flow owing to forces and pressure

## Nomenclature

$S$ : Unsteadiness parameter  
 $\alpha^*$ : Semi vertical angle of cone  
 $T$ : Fluid temperature (K)  
 $T_\infty$ : Temperature away from cone surface  
 $\varepsilon$ : Variable thermal conductivity coefficient  
 $\eta$ : Similarity variable  
 $\mu_0$ : Dynamic viscosity  
 $\nu_0$ : Kinematic viscosity

$Pr$ : Prandtl number  
 $\theta$ : Dimensionless temperature  
 $\rho$ : Density  
 $c_p$ : Specific heat  
 $z$ -axis: Axial or normal to cone  
 $C_{fx}$ : Skin friction  
 $Nu_x$ : Nusselt number  
 $Bvp4c$ : Boundary value solver  
 $u, v, w$ : Velocity component  
 $\alpha$ : Fractional order  
 $T_w$ : Wall temperature  
 $\beta$ : Temperature expansion coefficient  
 $g$ : Gravity  
 $\lambda$ : Mixed convection  
 $t^*$ : Dimensionless time  
 $k$ : Thermal conductivity

$\Omega$ : Angular velocity of disk ( $\text{r s}^{-1}$ )  
 $\phi$ : Dimensionless concentration  
 $k_0$ : Fluid conductivity  
 $Ec$ : Eckert number  
 $A$ : Variable viscosity coefficient  
 $C_{fy}$ : Skin friction  
 $Sh_x$ : Sherwood number  
 FDE12: Matlab fractional package.

## Data Availability

All the data exist in the manuscript.

## Conflicts of Interest

The authors declare that they have no conflicts of interest.

## Acknowledgments

The authors extend their appreciation to the Deanship of Scientific Research at King Khalid University for funding this work through research groups under grant number R.G.P.1/154/42.

## References

- [1] C. Spruell and A. B. Baker, "Analysis of a high-throughput cone-and-plate apparatus for the application of defined spatio-temporal flow to cultured cells," *Biotechnology and Bioengineering*, vol. 110, no. 6, pp. 1782–1793, 2013.
- [2] M. Turkyilmazoglu, "On the purely analytic computation of laminar boundary layer flow over a rotating cone," *International Journal of Engineering Science*, vol. 47, no. 9, pp. 875–882, 2009.
- [3] A. J. Chamkha and A. Al-Mudhaf, "Unsteady heat and mass transfer from a rotating vertical cone with a magnetic field and heat generation or absorption effects," *International Journal of Thermal Sciences*, vol. 44, no. 3, pp. 267–276, 2005.
- [4] S. J. Garrett, Z. Hussain, and S. O. Stephen, "Boundary-layer transition on broad cones rotating in an imposed axial flow," *AIAA Journal*, vol. 48, no. 6, pp. 1184–1194, 2010.
- [5] S. Nadeem and S. Saleem, "Theoretical investigation of MHD nanofluid flow over a rotating cone: An optimal solutions," *Information Sciences Letters*, vol. 3, no. 2, pp. 55–62, 2014.
- [6] P. D. Towers and S. J. Garrett, "Similarity solutions of compressible flow over a rotating cone with surface suction," *Thermal Science*, vol. 20, no. 2, pp. 517–528, 2016.
- [7] T. Hayat, S. A. Khan, M. I. Khan, and A. Alsaedi, "Irreversibility characterization and investigation of mixed convective reactive flow over a rotating cone," *Computer Methods and Programs in Biomedicine*, vol. 185, no. 185, article 105168, 2020.
- [8] A. J. Chamkha, F. Selimefendigil, and H. F. Oztop, "Effects of a rotating cone on the mixed convection in a double lid-driven 3D porous trapezoidal nanofluid filled cavity under the impact of magnetic field," *Nanomaterials*, vol. 10, no. 3, p. 449, 2020.
- [9] Massoudi and Christie, "Effects of variable viscosity and viscous dissipation on the flow of a third grade fluid in a pipe," *International Journal of Non-Linear Mechanics*, vol. 30, no. 5, pp. 687–699, 1995.
- [10] M. A. Seddeek, "Effects of radiation and variable viscosity on a MHD free convection flow past a semi-infinite flat plate with an aligned magnetic field in the case of unsteady flow," *International Journal of Heat and Mass Transfer*, vol. 45, no. 4, pp. 931–935, 2002.
- [11] A. Pantokratoras, "Study of MHD boundary layer flow over a heated stretching sheet with variable viscosity: a numerical reinvestigation," *International Journal of Heat and Mass Transfer*, vol. 51, no. 1-2, pp. 104–110, 2008.
- [12] S. Mukhopadhyay and G. C. Layek, "Effects of thermal radiation and variable fluid viscosity on free convective flow and heat transfer past a porous stretching surface," *International Journal of Heat and Mass Transfer*, vol. 51, no. 9-10, pp. 2167–2178, 2008.
- [13] M. S. Dada and C. Onwubuoya, "Variable viscosity and thermal conductivity effects on Williamson fluid flow over a slendering stretching sheet," *Journal of Engineering*, vol. 17, no. 3, 371 pages, 2020.
- [14] G. C. Hazarika, B. Phukan, and S. Ahmed, "Effect of variable viscosity and thermal conductivity on unsteady free convective flow of a micropolar fluid past a vertical cone," *Journal of Engineering Physics and Thermophysics*, vol. 93, no. 1, pp. 178–185, 2020.
- [15] M. G. Reddy, P. Padma, and S. Bandari, "Effects of viscous dissipation and heat source on unsteady MHD flow over a stretching sheet," *Ain Shams Engineering Journal*, vol. 6, no. 4, pp. 1195–1201, 2015.
- [16] F. Mabood, S. Shateyi, M. M. Rashidi, E. Momoniat, and N. Freidoonimehr, "MHD stagnation point flow heat and mass transfer of nanofluids in porous medium with radiation, viscous dissipation and chemical reaction," *Advanced Powder Technology*, vol. 27, no. 2, pp. 742–749, 2016.
- [17] W. Deebani, A. Tassaddiq, Z. Shah, A. Dawar, and F. Ali, "Hall effect on radiative casson fluid flow with chemical reaction on a rotating cone through entropy optimization," *Entropy*, vol. 22, no. 4, p. 480, 2020.
- [18] M. Gayatri, K. J. Reddy, and M. J. Babu, "Slip flow of Carreau fluid over a slendering stretching sheet with viscous dissipation and Joule heating," *SN Applied Sciences*, vol. 2, no. 3, pp. 1–1, 2020.
- [19] S. Murtaza, M. Iftekhhar, F. Ali, and I. Khan, "Exact analysis of non-linear Electro-Osmotic flow of generalized maxwell nanofluid: applications in concrete based nano-materials," *IEEE Access*, vol. 8, no. 8, pp. 96738–96747, 2020.
- [20] A. A. A. Kilbas, H. M. Srivastava, and J. J. Trujillo, *Theory and Applications of Fractional Differential Equations*, vol. 204, Elsevier Science Limited, 2006.
- [21] F. Mainardi, *Fractional Calculus and Waves in Linear Viscoelasticity: An Introduction to Mathematical Models*, World Scientific, 2010.
- [22] Z. M. Odibat, "Computing eigenlements of boundary value problems with fractional derivatives," *Mathematics of Computation*, vol. 215, no. 8, pp. 3017–3028, 2009.
- [23] M. Caputo and M. Fabrizio, "A new definition of fractional derivative without singular kernel," *Progress in Fractional Differentiation and Applications*, vol. 1, no. 2, pp. 1–13, 2016.
- [24] M. Ahmad, J. Jiang, A. Zada, S. O. Shah, and J. Xu, "Analysis of coupled system of implicit fractional differential equations involving Katugampola–Caputo fractional derivative," *Complexity*, vol. 2020, 11 pages, 2020.

- [25] Y. X. Li, T. Muhammad, M. Bilal, M. A. Khan, A. Ahmadian, and B. A. Pansera, "Fractional simulation for Darcy-Forchheimer hybrid nanoliquid flow with partial slip over a spinning disk," *Alexandria Engineering Journal*, vol. 60, no. 5, pp. 4787–4796, 2021.
- [26] M. Y. Malik, H. Jamil, T. Salahuddin, S. Bilal, K. U. Rehman, and Z. Mustafa, "Mixed convection dissipative viscous fluid flow over a rotating cone by way of variable viscosity and thermal conductivity," *Results in Physics*, vol. 6, no. 6, pp. 1126–1135, 2016.

## Research Article

# Impact of Ferromagnetic Nanoparticles Submerged in Chemically Reactive Viscoelastic Fluid Transport Influenced by Double Magnetic Dipole

N. Kousar <sup>1</sup>, Taher A. Nofal,<sup>2</sup> W. Tahir,<sup>1</sup> S. M. Bilal,<sup>1</sup> and Ndolane Sene <sup>3</sup>

<sup>1</sup>Department of Mathematics, Air University, E-9 Islamabad 44000, Pakistan

<sup>2</sup>Department of Mathematics and Statistics, College of Science, Taif University, P.O. Box 11099, Taif 21944, Saudi Arabia

<sup>3</sup>Laboratoire Lmdan, Departement De Mathematiques De Decision, Facultè Des Sciences Economiques Et Gestion, Universite Cheikh Anta Diop De Dakar, BP 5683 Dakar Fann, Senegal

Correspondence should be addressed to Ndolane Sene; ndolanesene@yahoo.fr

Received 13 January 2022; Revised 20 February 2022; Accepted 1 March 2022; Published 1 April 2022

Academic Editor: Taza Gul

Copyright © 2022 N. Kousar et al. This is an open access article distributed under the Creative Commons Attribution License, which permits unrestricted use, distribution, and reproduction in any medium, provided the original work is properly cited.

The present article summarized the effects of double magnetic dipole for chemically reactive viscoelastic fluid in the presence of two different ferromagnetic particles, namely, nickel zinc ferrite ( $NiZnFe_2O_4$ ) and magnetite ferrite ( $Fe_3O_4$ ). Due to double magnetic dipole, an external magnetic field is applied normal to the flow. Blood is used as base fluid due to its viscoelastic fluid properties. The Cattaneo-Christov heat flux model is used for heat transport phenomena. The physical model is formulated in the form of partial differential equations which are then converted into ordinary differential equations using the suitable transformations. The system is solved numerically using shooting method along with Runge-Kutta-Fehlberg method. The characteristics of different parameters like the strength of homogeneous-heterogeneous reactions ( $k_1$  and  $k_2$ ), ferrohydrodynamic interaction ( $\beta_1$ ), Schmidt number ( $S_c$ ), Deborah number ( $\alpha_{1a}$ ), and thermal relaxation time ( $\alpha_{1c}$ ) on velocity, temperature, and concentration profiles are analyzed through graphs and in tabular form. It has been observed that as magnetic dipole creates a force which attracts the ferrite particles, hence, it slows down the velocity profile. Concentration field depresses due to the presence of strength of heterogeneous reaction parameter  $k_2$ . It is also noted that by expanding values of thermal relaxation time ( $\alpha_{1c}$ ), the temperature profile shows a reverse behavior.

## 1. Introduction

Ferrofluids lie in the category of smart materials those consist of micron-sized colloidal magnetic nanoparticles that are saturated in a nonmagnetic base fluid. The most fascinating feature of these fluids is its highly magnetizing ability when an external magnetic field is applied. Pappell [1] initially highlighted the characteristic of ferrofluid in 1963. He utilized ferrofluid in a weightless atmosphere in terms of liquid rocket fuel, which is pinched near a pump inlet by applying an external magnetic field. Ferrofluids have many appealing applications in electrical instruments such as in hard disk, rotating X-ray tubes, shafts, and rods. The role of ferrofluids in biomedical equipment's is no doubt incredible, which is helpful in the process of wound treat-

ment, asthma treatment, removal of cancer with hyperthermia, and many more. For these kinds of procedures, the homogeneous and heterogeneous have great importance. The homogenous and heterogeneous reactions take places in the bulk and occur on the catalyst surface, respectively. Whether the process is homogeneous or heterogeneous depends upon the situation that they exist in the absolute majority of the fluid or a part of catalytic surfaces. In essence, the homogeneous process is continuously intact within the given phase, whereas heterogeneous reactions have restricted boundaries. There are also a variety of chemically reacting structures that involve both h-h reactions termed as such as catalysis, burning, and biochemical reacting systems. In this flow, due to an external flow applied on the outer region of boundary layer, there exists a reaction in



that region as explained by [2, 3]. Initially, Andersson and Valnes [4] studied the viscous ferrofluid with magnetic dipole effects on the stretching surface. They examined the influence of magnetothermomechanical coupling on the fluid. Numerical studies related to ferrofluid inside a channel with cold walls focusing on a line source dipole delineated by Ganguly et al. [5]. In a porous medium, Sharma et al. [6] specified the attributes of convection by focusing dust particles on a ferromagnetic fluid. The results corresponding to characteristics of heat transfer in a Darcy number ferrofluid flow with porous wall is analyzed by Strek [7]. The dipole effects in a ferrofluid flow origin below the channel with isothermal wall were studied by Strek and Jopek [8]. They focused on time dependent heat transfer and analyzed the spatial alteration creating magnetization because of gradient effects, depending temperature magnetic susceptibility for ferrofluids. Sadiq et al. [9] studied the Casson fluid model to study the thermal performance under the Brownian and thermoheteric effects of hybrid nanoparticles. The dipole's magnetization in the series flow of ferrofluid taking elongated surface highlighting thermal radiation is explored by Makinde and Aziz [10]. Aminfar et al. [11] implement a non-acting magnetic field inside a vertical tube during the numerical studies of mixed convection of ferrofluid. During his studies, he used both + and - types of magnetic gradients; the (-) gradient of magnetic field reacts the same as the buoyancy forces and boosts the Nusselt number, whereas the magnetic field with a (+) gradient decelerates it. A stagnation point flow along elongated sheet in the presence of heterogeneous-homogeneous reactions that is analyzed by Bachok et al. [12] analyzed a chemically reactive stagnation point flow over the elongated sheet. In his paper, he discussed the case of fluid having less kinetic viscosity in which he observed that when the extending velocity is low as compared to free stream velocity, a boundary layer is achieved, whereas the inverted boundary layer attains in the case when stretching the velocity exceeds the free stream velocity. Affixing 2-phase mixture model and effecting control volume method, Aminfar et al. [13] executed the transversal non acting magnetic field accomplishing electric current during the inspection of flowing ferrofluid inside a duct. They showed the flourishing behavior of average heat transfer coefficient. The shrinking surface is taken by Kameswaran et al. [14] during the investigation of homogeneous-heterogeneous reaction in a porous medium. By taking into account the radiation effect in an extended sheet, Titus and Abraham [15] used ferrofluid. It also concludes that due to magnetic field local vortex vary the advection energy transport also boosting heat transfer ability. Sheikholeslami et al. [16] conferred the aspects of non-uniform magneto hydrodynamic flow of ferrofluid utilizing convective heat transport. Hayat et al. [17] also detailed the effects of MHD nanofluid with heterogeneous-homogeneous reaction and velocity slip condition. It is concluded that in the case of concentration, both homogeneous and heterogeneous parameters show a reverse behavior. Imtiaz et al. [18] reflected the

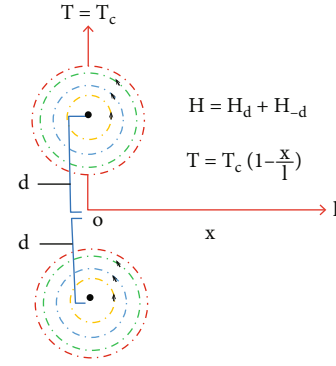


FIGURE 1: Geometry of flow model.

impact of homogeneous and heterogeneous reactions in the examination of MHD flow in a curved stretchable surface. He depicted the increasing behavior between curvature parameter and fluid velocity. Due to many applications, the boundary layer flow of non-Newtonian fluids with different effects has added an enormous attraction in the recent years [19–33].

The ultimate goal of this research is to scrutinize the effects of magnetic double dipole in the examination of Maxwell ferrofluid which is composed of base fluid blood, whereas ferrite particles were used as ( $NiZnFe_2O_4$  and  $Fe_3O_4$ ) under the high lightening impact of homogeneous and heterogeneous reaction. Also, the concentration levels of these particles are about 20% into the base fluid. The basic theme of including these ferrite particles is to enhance the strength of heat transferring phenomena which is the inspiration of this research. Brief literature survey is summarized in Section 1. Section 2 is focused on the mathematical formulation of problem. In Section 3, the computational procedure is discussed in details. The possible outcomes of the current study are deliberated in Section 4. Section 5 presents the key features of this article.

## 2. Mathematical Formulation

Consider a steady 2D flow of an incompressible non-Newtonian Maxwell electrically conducting a ferromagnetic fluid running on a flat surface in  $x$  direction as shown in Figure 1. The location of dipole is set in theydirection as the displacement between the dipole and surface is taken as  $d$ , while the magnetic field ( $H$ ) generated with the presence of magnetic dipole directions as  $x$ -axis. The scalar potential of permanent magnetic dipole which influences ferrofluid defined in [2] is

$$\delta_a = -\frac{I_0}{2\pi} \left[ \text{Tan}^{-1} \left( \frac{y+d}{x} \right) + \text{Tan}^{-1} \left( \frac{y-d}{x} \right) \right], \quad (1)$$

where  $I_0$  is the representation of dipole moment per unit length. The relation between gradient of magnetic scalar potential  $\delta_a$  and applied magnetic field is held as  $H_1 = -\nabla$

$\delta_a$ . The components of  $H_1$  are

$$H_x = -\frac{\partial \delta_a}{\partial x} = -\frac{I_0}{2\pi} \left[ \frac{y+d}{x^2+(y+d)^2} + \frac{y-d}{x^2+(y-d)^2} \right], \quad (2)$$

$$H_y = -\frac{\partial \delta_a}{\partial y} = -\frac{I_0}{2\pi} \left[ \frac{x}{x^2+(y-d)^2} + \frac{x}{x^2+(y+d)^2} \right].$$

The force field strength has a resultant magnitude  $H$ , with their element forms that are termed as

$$H = \left[ \left( \frac{\partial \delta_a}{\partial x} \right)^2 + \left( \frac{\partial \delta_a}{\partial y} \right)^2 \right]^{\frac{1}{2}}, \quad (3)$$

$$(\nabla H)_x = \frac{\partial \delta_a / \partial x (\partial^2 \delta_a / \partial x^2) + (\partial \delta_a / \partial y) (\partial^2 \delta_a / \partial x \partial y)}{[(\partial \delta_a / \partial x)^2 + (\partial \delta_a / \partial y)^2]^{1/2}}, \quad (4)$$

$$(\nabla H)_y = \frac{\partial \delta_a / \partial x (\partial^2 \delta_a / \partial x \partial y) + (\partial \delta_a / \partial y) (\partial^2 \delta_a / \partial y^2)}{[(\partial \delta_a / \partial x)^2 + (\partial \delta_a / \partial y)^2]^{1/2}}. \quad (5)$$

Experiencing Equation (1) in Equations (4)-(5), we get the following form by expanding up to order  $x^2$ :

$$(\nabla H)_y = 0. \quad (6)$$

The assuming effects of surface's wall is  $(\partial \delta_a / \partial x)_{y=0} =$

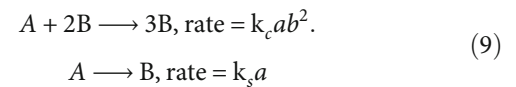
$(\partial^2 \delta_a / \partial y^2)_{y=0} = 0$ , with including assumption that  $x \gg d$ . We get the transformed form of equation (4)

$$(\nabla H)_x = -\frac{I_0}{\pi} \frac{1}{x^2}. \quad (7)$$

The change in magnetization  $M$  can be expressed as

$$M = K_1(T_c - T). \quad (8)$$

**2.1. Analysis of Flow.** We have considered a viscoelastic fluid flow over a flat surface with double magnetic dipoles, which are placing at a space ( $d$ ) from the wall and perpendicular to the surface. Consider  $l$  as the length of plate ( $l \gg d$ ) with the wall. The temperature changes linearly with the plate length that is defined as  $T_w = T_c(1 - x/l)$ . In the boundary layer flow, the connection between homogeneous and heterogeneous reactions adding 2-species chemically, named, A and B, are taken following Chaudhary and Merkin [2] as



Concentrations A and B are represented by  $a$  and  $b$ , and  $k_i$  ( $i = c, s$ ) are termed as rate constants. The process is considered to be isothermal for both reactions.

The corresponding flow equations in the presence of magnetic dipole are

$$\frac{\partial u}{\partial x} + \frac{\partial v}{\partial y} = 0,$$

$$\left( u \frac{\partial u}{\partial x} + v \frac{\partial u}{\partial y} \right) + \lambda_a \left( u^2 \frac{\partial^2 u}{\partial x^2} + v^2 \frac{\partial^2 u}{\partial y^2} + 2uv \right) = \frac{\mu_0}{\rho_{nf}} M \frac{\partial H}{\partial x} + \frac{\mu_{nf}}{\rho_{nf}} \frac{\partial^2 u}{\partial y^2},$$

$$\left( u \frac{\partial T}{\partial x} + v \frac{\partial T}{\partial y} \right) + \lambda_c \left( u \frac{\partial u}{\partial x} \frac{\partial T}{\partial x} + v \frac{\partial v}{\partial y} \frac{\partial T}{\partial y} + u \frac{\partial v}{\partial x} \frac{\partial T}{\partial y} + v \frac{\partial u}{\partial y} \frac{\partial T}{\partial x} + 2uv \frac{\partial^2 T}{\partial x \partial y} + u^2 \frac{\partial^2 T}{\partial x^2} + v^2 \frac{\partial^2 T}{\partial y^2} \right) = \frac{k_{nf}}{(\rho c_p)_{nf}} \frac{\partial^2 T}{\partial y^2}, \quad (10)$$

$$u \frac{\partial a}{\partial x} + v \frac{\partial a}{\partial y} = D_A \frac{\partial^2 a}{\partial y^2} - k_c ab^2,$$

$$u \frac{\partial b}{\partial x} + v \frac{\partial b}{\partial y} = D_B \frac{\partial^2 b}{\partial y^2} + k_c ab^2.$$

The admissible flow conditions are

$$u|_{y=0} = 0, v|_{y=0} = 0, T|_{y=0} = T_c \left( 1 - \frac{x}{l} \right), D_A \frac{\partial a}{\partial y} \Big|_{y=0} = k_s a(0), D_B \frac{\partial a}{\partial y} \Big|_{y=0} = -k_s a(0),$$

$$u|_{y \rightarrow \infty} = u_0, T|_{y \rightarrow \infty} = T_c, a|_{y \rightarrow \infty} \rightarrow a_0, b|_{y \rightarrow \infty} \rightarrow 0. \quad (11)$$

where  $(u, v)$  is the velocity components along  $x$  and  $y$  directions,  $(\mu_0)$  is the magnetic permeability,  $(\mu_{nf})$  is the dynamic viscosity,  $(\nu_{nf})$  is the kinematic viscosity of nanofluid,  $(\rho_{nf})$  is the nanofluid density,  $(\rho c_p)_{nf}$  is the specific heat,  $(k_{nf})$  represented as thermal conductivity of the nanofluid,  $(\lambda_a)$  is the relaxation time of fluid, and  $(\lambda_c)$  identifies as the relaxation time of heat flux.

TABLE 1: Thermophysical properties of blood, nickel zinc ferrite, and magnetite ferrite.

	$\rho(\text{kg/m}^3)$	$C_p(\text{J/kgK})$	$k(\text{W/mK})$
Blood	1060.0	3770	0.52
Nickel zinc ferrite	4800	710	6.3
Magnetite ferrite	5180	670	9.7

TABLE 2: Grid independence for Nusselt number and skin friction for  $\beta = 0.1$ ,  $\lambda = 0.01$ ,  $\gamma = 1.0$ ,  $\text{Pr} = 6.0$ .

$\zeta$	Nusselt number	Skin friction
$10^{-2}$	3.9475	2.5523
$10^{-4}$	3.9471	2.5514
$10^{-6}$	3.9471	2.5514

2.2. *Thermophysical Properties.* Using similarity transform as defined by [23],

$$\eta = \left(\frac{u_0}{\nu x}\right)^{\frac{1}{2}} y, T = T_c \left(1 - \frac{x}{l} \theta(\eta)\right),$$

$$u = u_0 f'(\eta), v = \left(\frac{\nu u_0}{x}\right)^{\frac{1}{2}} \left(\frac{\eta f'(\eta)}{2} - \frac{f(\eta)}{2}\right), \quad (12)$$

$$a = a_0 g(\eta), b = a_0 h(\eta).$$

By implementing similarity variables express in Eq. (12), our modified equations take the subsequent form:

$$\left(\frac{1}{(1-\phi)^{2.5} (1-\phi + \phi(\rho_s/\rho_f))} - \frac{\alpha_{1a} f^2}{4}\right) f''' + \frac{ff''}{2} - \frac{\alpha_{1a}}{4} (f'^2 f'' \eta + 2ff' f'') - \frac{\beta_1 \theta}{(1-\phi + \phi(\rho_s/\rho_f))} = 0, \quad (13)$$

$$\left(\frac{k_{nf}/k_f}{(1-\phi + \phi((\rho C_p)_s/(\rho C_p)_f))} - \frac{\alpha_{1c} \text{Pr} f^2}{4}\right) \theta_1'' + \text{Pr} \left(\frac{f\theta'}{2} - f'\theta + \frac{\alpha_{1c}}{4} (2ff'' + 2ff'\theta')\right) = 0, \quad (14)$$

$$\frac{1}{S_c} g'' + fg' - k_1 gh^2 = 0, \quad (15)$$

$$\frac{\delta}{S_c} h'' + fh' + k_1 gh^2 = 0, \quad (16)$$

with nondimensional boundary conditions:

$$f(\eta) = f'(\eta) = 0, \theta(\eta) = 1, g'(\eta) = k_2 g(\eta), \delta h'(\eta) = -k_2 g(\eta) \text{ at } \eta = 0,$$

$$f'(\eta) \rightarrow 1, \theta(\eta) \rightarrow 0, g(\eta) = 1, h(\eta) = 0 \text{ as } \eta \rightarrow \infty. \quad (17)$$

TABLE 3: Obtained values of  $-\theta'(\theta)$  by altering values of  $\beta$  and  $\text{Pr}$ .

$\beta$	$\text{Pr}$	$-\theta'(\theta)$
<b>(NiZnFe<sub>2</sub>O<sub>4</sub>)</b>		
0.0		3.0554
1.0	5	3.0180
2.0		3.0074
	4	3.0000
1.0	5	3.0180
	6	3.1079
<b>(Fe<sub>3</sub>O<sub>4</sub>)</b>		
0.0		3.0904
1.0	5	3.0489
2.0		3.0093
	4	3.0060
1.0	5	3.0489
	6	3.1479

TABLE 4: Obtained values of  $g'(0)$  by altering values of  $k_1, k_2$  and  $S_c$ .

$k_1$	$k_2$	$S_c$	$g'(0)$
<b>(NiZnFe<sub>2</sub>O<sub>4</sub>)</b>			
0.1			1.3726
0.3		0.1	1.3931
0.5			1.4145
		0.1	1.3726
0.1		0.2	1.1121
		0.3	0.8977
	0.1		1.3726
	0.3	0.1	2.0805
	0.5		2.5090
		0.1	1.3726
	0.1	0.2	1.1121
		0.3	0.8977
<b>(Fe<sub>3</sub>O<sub>4</sub>)</b>			
0.1			1.2858
0.3		0.1	1.3051
0.5			1.3253
		0.1	1.2858
0.1		0.2	1.0510
		0.3	0.8555
	0.1		1.2858
	0.3	0.1	1.9481
	0.5		2.3486
		0.1	1.2858
	0.1	0.2	1.0510
		0.3	0.8555

In Eqs. (13)-(16),  $\beta_1$  is the ferrohydrodynamic interaction,  $\text{Pr}$  defines the Prandtl number,  $\alpha_{1a}$  mean the Deborah number,  $\alpha_{1c}$  is represented here as a

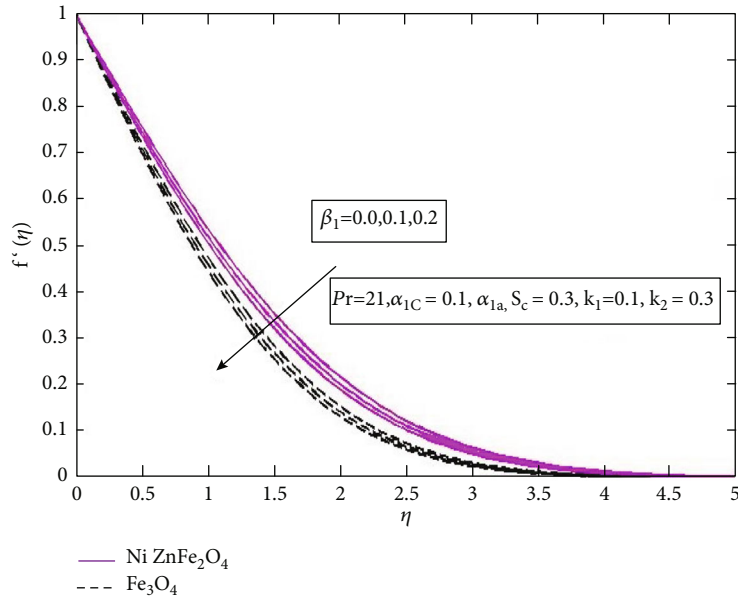


FIGURE 2: Velocity profile with fluctuation in  $\beta_1$ .

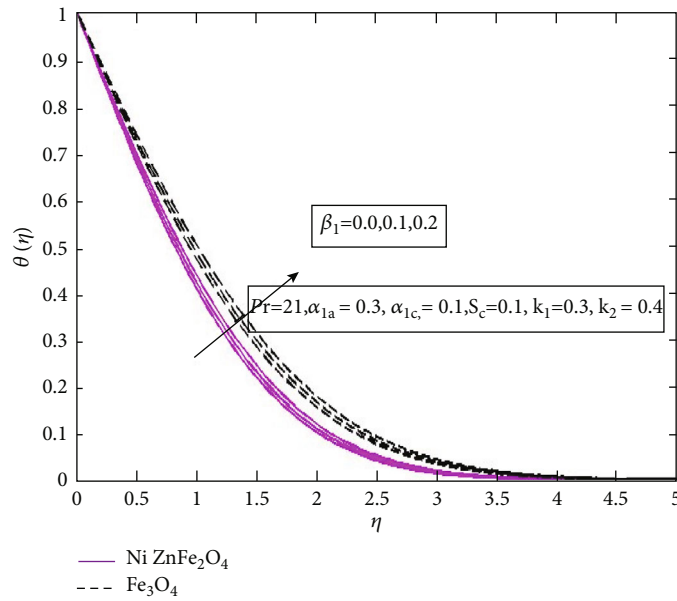


FIGURE 3: Temperature profile with fluctuation in  $\beta_1$ .

nondimensional thermal relaxation time,  $S_c$  the shows Schmidt number, and  $k_1$  and  $k_2$  describe the strength of homogeneous and heterogeneous reaction parameters, which are defined here as

$$\beta_1 = \frac{I_0 \mu_0 K T_c}{\pi \rho \mu_0^2}, Pr = \frac{\rho c_p \nu}{k}, \alpha_{1a} = \lambda_{1a} u_0 x_{-1}, \alpha_{1c} = \lambda_{1c} u_0 x$$

$$S_c = \frac{\nu_f}{D_A}, k_1 = \frac{k_c a_0^2}{S}, k_2 = \frac{k_s}{D_A} \sqrt{\frac{\nu_f}{S}}. \tag{18}$$

$D_A$  and  $D_B$  are equivalent, i.e.,  $\delta = 1$ ; then, we can write as

$$g(\eta) + h(\eta) = 1. \tag{19}$$

Utilizing Eqs. (15)-(16), we get the equation as

$$\frac{1}{S_c} g'' + f g' - k_1 g(1-g)^2 = 0. \tag{20}$$

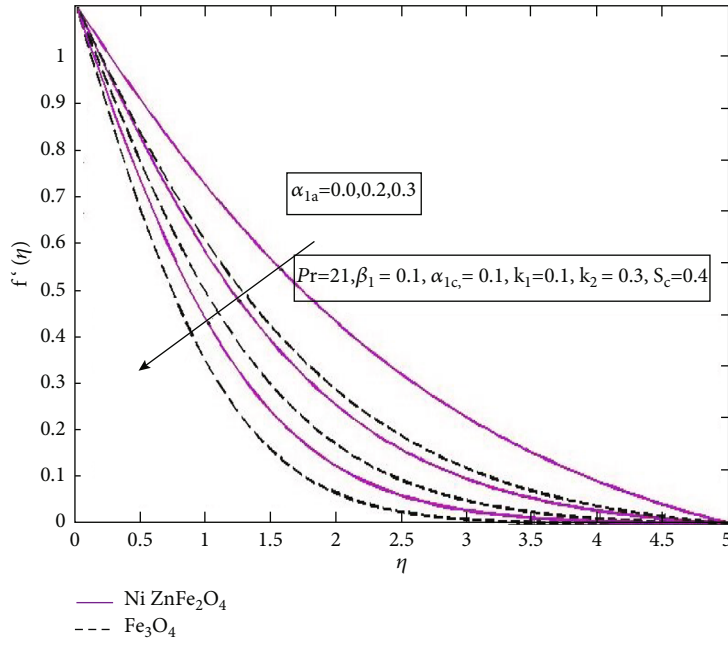


FIGURE 4: Velocity profile with fluctuation in  $\alpha_{1a}$ .

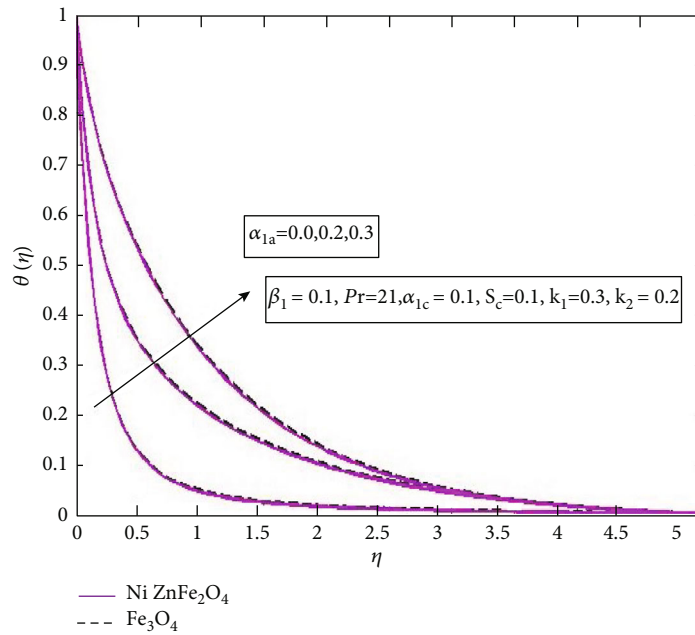


FIGURE 5: Temperature profile with fluctuation in  $\alpha_{1a}$ .

The corresponding boundary equation of the concentration field yields the following form:

$$g'(\eta) = k_2 g(\eta), \eta \rightarrow 0, g(\eta) = 1, \eta \rightarrow \infty. \quad (21)$$

The conversions of the wall drag and convective heat

transfer into a nondimensional form are scaled as

$$C_f = \frac{-2\tau_w}{\rho_{nf} u_0^2}, Nu = \frac{x k_{nf}}{k_f (T_c - T_w)} \frac{\partial T}{\partial y} \Big|_{y=0}. \quad (22)$$

The wall shear stress is termed as

$$\tau_w = \mu_{nf} \left( \frac{\partial u}{\partial y} \right) \Big|_{y=0}, q_w = -k_{nf} \left( \frac{\partial T}{\partial y} \right) \Big|_{y=0}. \quad (23)$$

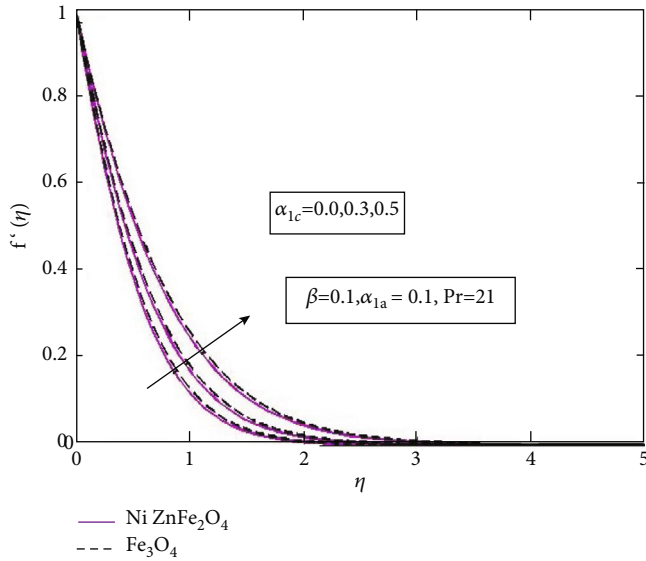


FIGURE 6: Velocity profile with fluctuation in  $\alpha_{1c}$ .

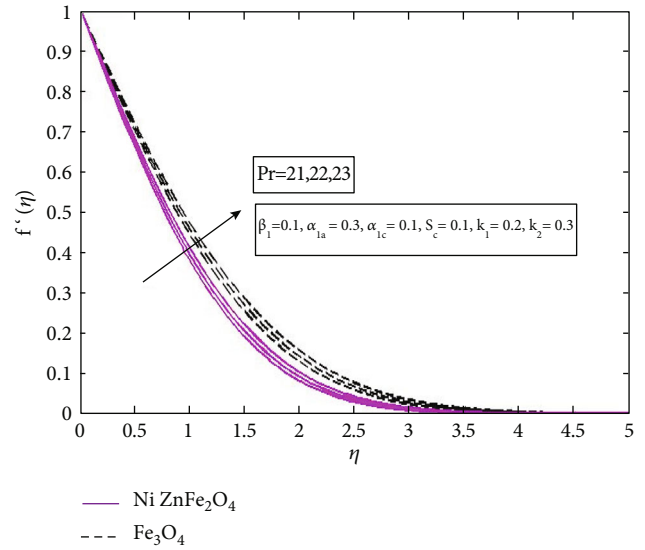


FIGURE 8: Velocity profile with fluctuation in Pr.

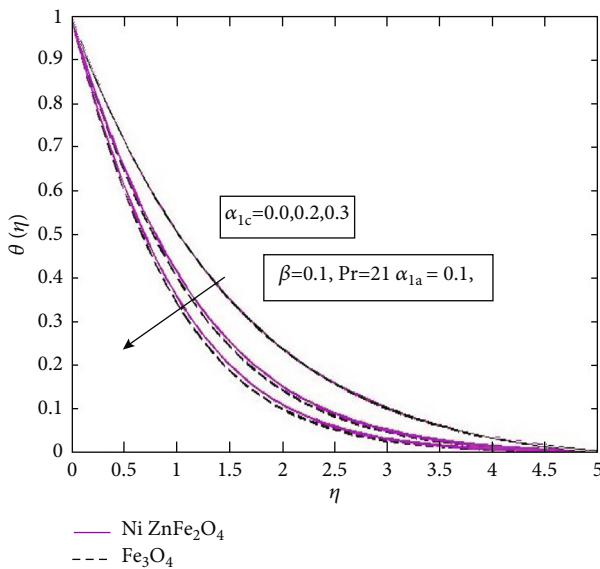


FIGURE 7: Temperature profile with fluctuation in  $\alpha_{1c}$ .

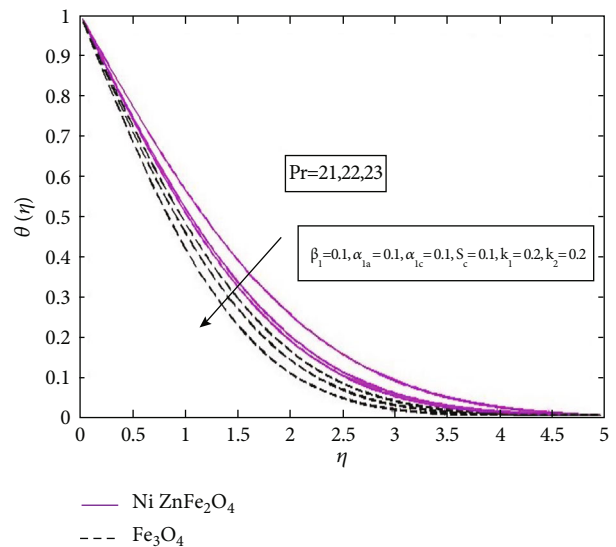


FIGURE 9: Temperature profile with fluctuation in Pr.

The dimensionless expressions of Eq. (22) are attained:

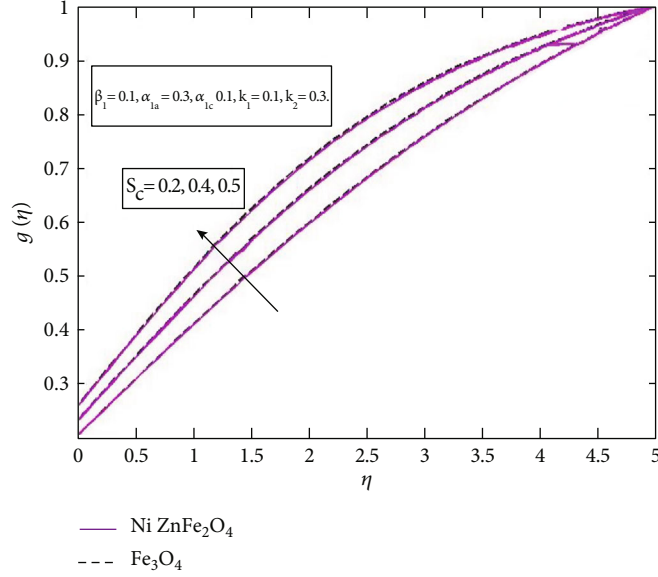
$$\frac{1}{2} \text{Re}_x^{\frac{1}{2}} C_f = \frac{1}{(1-\phi)^{-2.5}} f''(0), \text{Re}_x^{\frac{1}{2}} N_{ux} = -\frac{k_{nf}}{k_f} \theta_1'(0), \quad (24)$$

where,

$$\text{Re}_x = \frac{\rho_{nf} u_0 x}{\mu_{nf}}. \quad (25)$$

### 3. Numerical Methodology

The saturation of two ferrite particles into Maxwell fluid under the action of a double magnetic dipole is examined with homogeneous and heterogeneous reactions. The transformed nonlinear systems of ODEs are solved numerically using the shooting method along with the RK-45 algorithm. For the implementation of the shooting method, one should convert the boundary value problem into an initial value problem. The reduce initial value problem is further converted into a system of first order differential equations and then solved by choosing the missing conditions as an initial guess. Therefore, the suitable transformations are used to obtain initial value problem. The new set of variables for

FIGURE 10: Concentration profile with fluctuation in  $S_c$ .

first order system of equations is defined as

$$\left( y_1, y_2, y_3, y_4, y_5, y_6, y_7 = f, f', f'', \theta, \theta', g, g' \right). \quad (26)$$

This substitution yields

$$y_1' = y_2, y_1' = y_2, \quad (27)$$

$$y_2' = y_3, \quad (28)$$

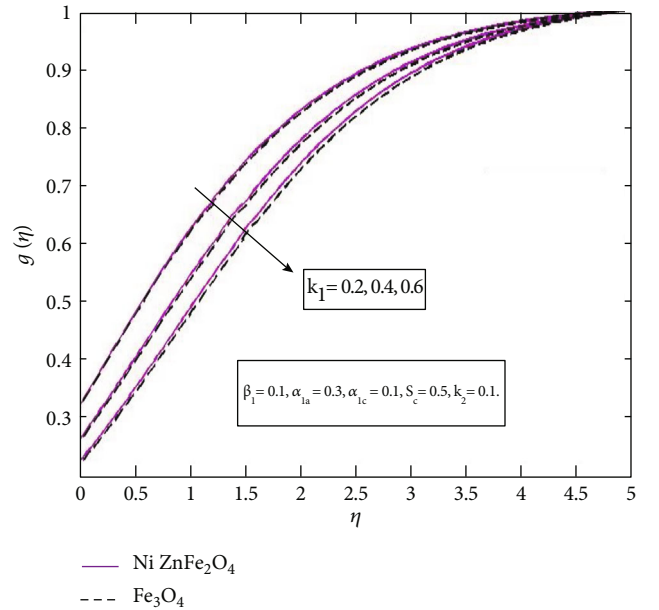
$$y_3' = \left( \frac{1}{(1-\phi)^{2.5}(1-\phi+\phi(\rho_s/\rho_f))} - \frac{\alpha_{1a}y_1^2}{4} \right) * \left( -\frac{y_1y_3}{2} + \frac{\alpha_{1a}}{4}(y_2^2y_3\eta + 2y_1y_2y_3) + \frac{\beta y_4}{(1-\phi+\phi(\rho_s/\rho_f))} \right), \quad (29)$$

$$y_4' = y_5 \quad (30)$$

$$y_5' = \left( \frac{1}{1-\phi+\phi^*((\rho C p)s/(\rho C p)f)} - \frac{\alpha_{1c} \text{Pr} f^2}{4} \right) * \left( \text{Pr}^* \left( -\frac{y_1y_5}{2} + y_2y_4 - \frac{\alpha_{1c}}{4}(2y_1y_3 + 2y_3y_2y_5) \right) \right), \quad (31)$$

$$y_6' = y_7 \quad (32)$$

$$y_6' = -S_c(y_1y_7 - k_1(y_6(1-y_7^2)^2)). \quad (33)$$

FIGURE 11: Concentration profile with fluctuation in  $k_1$ .

which are subject to the following conditions:

$$\begin{aligned} y_1(0) = 0, y_2(0) = 0, y_3(0) = \omega_1 \text{ (unknown initial condition),} \\ y_4(0) = 1, y_5(0) = \omega_2 \text{ (unknown initial condition),} \\ y_7(0) = k_2y_6(0), y_8(0) = \omega_3 \text{ (unknown initial condition).} \end{aligned} \quad (34)$$

To solve the above system of Eqs. (27)-(33), the values of  $\omega_1$ ,  $\omega_2$ , and  $\omega_3$  are unknown, so by taking a suitable initial guess, the convergent numerical solution is obtained. It is important to note that if the boundary residuals are fewer than the tolerance error  $10^{-6}$ , the calculated solution

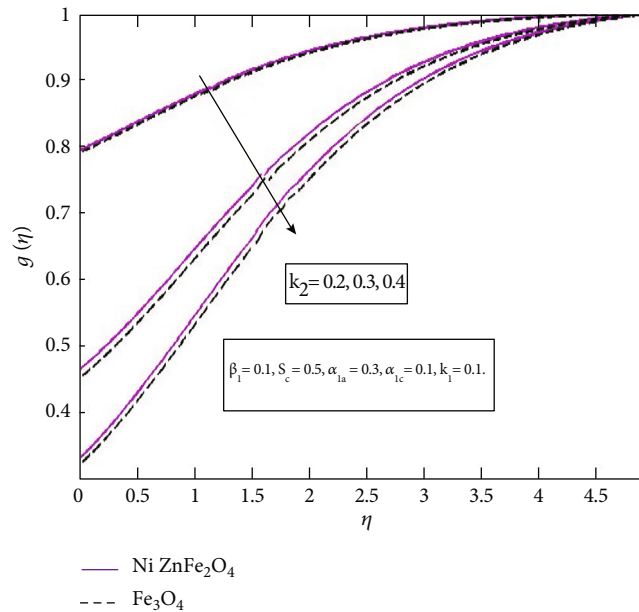


FIGURE 12: Concentration profile with fluctuation in  $k_2$ .

converges. If the computed results do not satisfy this requirement, the initial estimates are changed by using Newton's technique, and the procedure is repeated until the solution fulfills the specified convergence threshold. The thermophysical properties of the base fluid and ferrite particles for numerical procedure are defined in Table 1.

#### 4. Results and Discussion

The mathematical model of chemically reactive viscoelastic fluid over the stretching surface is solved numerically. The numerical solutions are checked by applying the grid independence test. The analysis is performed at different tolerance levels for Nusselt number and skin friction coefficient. The numerical values of Nusselt number and skin friction are presented in Table 2.

Table 3 represents the performance of quantity of engineering interest (Nusselt number) against ferrohydrodynamic interaction ( $\beta$ ) and Prandtl number (Pr) in both cases nickel zinc ferrite ( $NiZnFe_2O_4$ ) and magnetite ferrite ( $Fe_3O_4$ ). It is depicted that the increment occurs in the Nusselt number due to the increasing values of Pr, with better results of magnetite ferrite ( $Fe_3O_4$ ) as compared to nickel zinc ferrite ( $NiZnFe_2O_4$ ). Table 4 displays the response of mass flux coefficient against the strength of homogeneous and heterogeneous parameters and Schmidt number. It is perceived that the mass flux coefficient shows a positive trend towards the strength of homogeneous ( $k_1$ ) and heterogeneous parameters ( $k_2$ ) while an opposite behavior seen in the case of the Schmidt number ( $S_c$ ). The higher magnitude was observed in the case of nickel zinc ferrite.

The analysis of ferrohydrodynamic interaction ( $\beta_1$ ) on velocity field is seen in Figure 2. It is depicted that the velocity decreases due to the increasing values of ferrohydrodynamic interaction parameter ( $\beta_1$ ). This opposite behavior

is due to the action of Lorentz forces which resist the flow and provide more resistance to transportation phenomena. From the graph, it is cleared that the magnetite ferrite offers more resistance due to which the velocity profile decreases in the case of magnetite ferrite ( $Fe_3O_4$ ). Figure 3 results an inclination in temperature with altering values of  $\beta_1$ . It is detected that the temperature profile boosts up as soon as the ferrohydrodynamic interaction parameter ( $\beta_1$ ) enhances. Reasoned is that Lorentz forces which produces under the action of magnetic field have the potential to produce resistance which in term produce heating among the layers of fluids hence thermal boundary layer thickness rises. It is also perceived that the magnetite ferrite ( $Fe_3O_4$ ) offers more resistance due to which the rapid temperature enhancement occurred in the case of the magnetite ferrite ( $Fe_3O_4$ ). The sketch of velocity with augmenting values of Deborah number ( $\alpha_{1a}$ ) is displayed in Figure 4. It is detected that the increasing Deborah number results in a decreasing velocity profile. As ( $\alpha_{1a}$ ) precisely relate to relaxation time of fluid, immediately ( $\alpha_{1a}$ ) increasing fluid relaxation time shot up and provide extra blocking to the fluid motion which results in thinning momentum boundary layer thickness. The maximum velocity is depicted in the case of nickel zinc ferrite ( $NiZnFe_2O_4$ ). The graph of Deborah number ( $\alpha_{1a}$ ) against the temperature field is seen in Figure 5. It is perceived that the augmented values of the Deborah number ( $\alpha_{1a}$ ) amplifies the temperature field. This phenomena can be depicted as the enlarging Deborah number ( $\alpha_{1a}$ ) tends to have a larger relaxation time of fluid which directly means to offer resistance and generates heat which enhances the temperature profile. The effects of the thermal relaxation parameter ( $\alpha_{1c}$ ) upon the velocity profile is observed in Figure 6. It is clear from the figure that the increasing thermal relaxation parameter ( $\alpha_{1c}$ ) is responsible for the increasing velocity profile. This fact is explained as by up surging



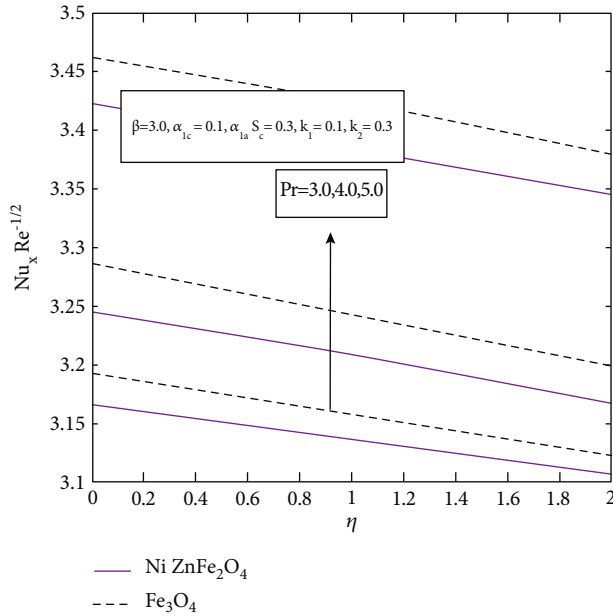


FIGURE 13: Nusselt number with mutation of  $\beta$  and Pr..

thermal relaxation parameter ( $\alpha_{1c}$ ) momentum of fluid particles also enhances which in term increase kinetic energy and velocity profile. Figure 7 enlightened the conduct of thermal relaxation time ( $\alpha_{1c}$ ) on the temperature field. By expanding values of ( $\alpha_{1c}$ ) temperature profile show reverse behavior, because enlarging thermal relaxation time implies materials particles demand extra pace to exchanging energy to their connecting particles, thus cause reduction in temperature profile. The impression of Prandtl number on velocity is realized in Figure 8. The increasing behavior of velocity is observed by the altering values of the Prandtl number, which is due to straight forward relation between the Prandtl number and momentum diffusivity. As soon as the Prandtl increases, the momentum diffusivity also increases; thus, in the result, fluid motion and momentum boundary layer thickness also boost up. Association between Prandtl number and temperature field clearly delineated in Figure 9, the contrary response of temperature towards Prandtl number, actually Prandtl number exhibit inverse relation to thermal diffusivity of fluid, So by enhancing Prandtl number directly means to lessen diffused heat betwixt fluid layers hence reduces temperature profile. The response of Schmidt number ( $S_c$ ) towards the concentration field is characterized in Figure 10. The increase in Schmidt number ( $S_c$ ) consequently increases the concentration field because the concentration field relates with a viscous diffusion rate to molecular diffusion rate, so when the Schmidt number ( $S_c$ ) magnifies the viscous diffusion rate, it also magnifies which in turn enhances the concentration field. Figure 11 shows the connection between the strength of homogeneous reaction parameter ( $k_1$ ) and concentration field. It is observed by enhancing the strength of homogeneous parameter( $k_1$ )concentration field that is going to shrink. This conduct is explained as reactants are consumed

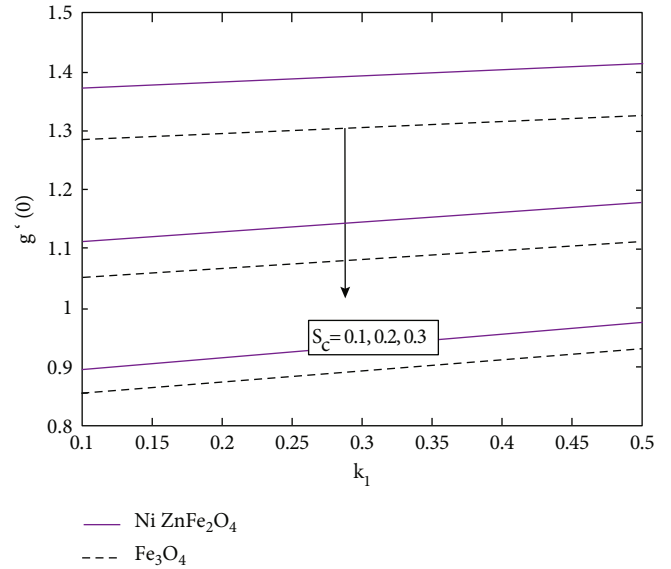


FIGURE 14: Mass flux coefficient with mutation of  $k_1$  and  $S_c$ ..

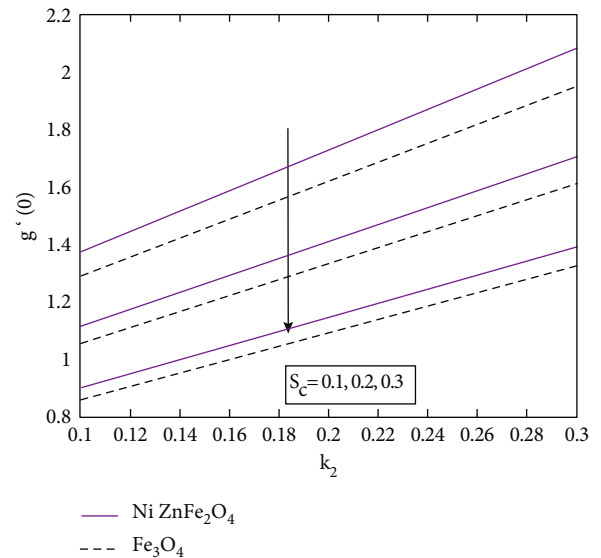


FIGURE 15: Mass flux coefficient with mutation of  $k_2$  and  $S_c$ ..

during the process of homogeneous reaction which depresses concentration profile. Also, the minimum concentration was observed in case of magnetite ferrite ( $Fe_3O_4$ ). The graph of concentration field against the altering values of strength of heterogeneous reaction parameter ( $k_2$ ) is displayed in Figure 12. An increase in ( $k_2$ ) causes a reduction in concentration field, while higher concentration is found in the case of nickel zinc ferrite ( $NiZnFe_2O_4$ ). Figure 13 shows the impact of Pr number upon a heat transfer rate. As we increase the Prandtl number, the Nusselt number also increases because by increasing Prandtl number rate of momentum, the diffusivity also increases which gives rise to the kinetic energy and also the heat transfer through convection. The impact of strength of homogeneous parameter ( $k_1$ ) and Schmidt number ( $S_c$ ) in the mass flux coefficient

$g'(0)$  is carried out in Figure 14. It is seen that  $(S_c)$  shows a negative response, while  $(k_1)$  displays an augmented amplitude against  $(g'(0))$ . Figure 15 depicts the trend of  $(g'(0))$  that relates with the strength of the heterogeneous parameter and Schmidt number  $(S_c)$ . As it is remarked because of the amplification in  $(k_2)$ , the mass flux coefficient  $(g'(0))$  magnifies due to the accumulation of particles by the generation of the heterogeneous mixture. Also in the case of  $(S_c)$ , we observed that as soon as  $(S_c)$  increases, the Sherwood number  $(g'(0))$  reduces by reducing the mass diffusivity.

## 5. Concluding Remarks

In this article, we have examined the response of double magnetic dipole in a chemically reactive viscoelastic fluid over a flat sheet by considering the two nanomagnetic ferrite particles. For heat transfer rate, we used the Cattaneo-Christov heat flux model which is the generalization of Fourier law by including thermal relaxation term. The thermal relaxation time converts the energy transport in form of thermal waves with finite speed. The modeled PDEs are converted into the system of ODEs and then solved numerically by shooting method. The results are depicted graphically with the impact of important parameters. The major outcomes of this study are as follows:

- (i) Due to the force generated by magnetic dipoles, the velocity of the fluid reduces, and the temperature increases by increasing the ferrohydrodynamic interaction parameter  $\beta_1$
- (ii) For the large value of Deborah number  $(\alpha_{1a})$ , the velocity profile decreases
- (iii) The thermal relaxation parameter  $(\alpha_{1c})$  shows a positive response towards velocity while the negative response towards temperature because particles take a surplus time to shifting energy
- (iv) The strength of homogeneous reaction parameter  $k_1$  undermines concentration
- (v) The concentration field depresses due to the presence of strength of heterogeneous reaction parameter  $k_2$
- (vi) It has been observed that heat transfer rate increases in the presence of magnetite ferrite ( $NiZnFe_2O_4$ ) as compared to nickel zinc ferrite ( $NiZnFe_2O_4$ ) by increasing Pr
- (vii) From physical point of view, Pr is the proportion of momentum diffusivity to thermal diffusivity. The contrary response of temperature towards the Prandtl number is observed; actually, the Prandtl number exhibits an inverse relation to thermal diffusivity of the fluid, so by enhancing Prandtl number directly means to lessen the diffused heat between fluid layers and hence reduce the temperature profile

## Nomenclature

$u, v$ :	Velocity components
$l$ :	Length of plate
$T_w$ :	Surface temperature
$T_c$ :	Curie temperature
$\mu_0$ :	Magnetic permeability
$\mu_{nf}$ :	Dynamic viscosity of nanofluid
$\mu_f$ :	Dynamic viscosity of base fluid
$k_{nf}$ :	Thermal conductivity of nanofluid
$\rho_{nf}$ :	Density of nanofluid
$(\rho c_p)_f$ :	Heat capacitance of fluid
$(\rho c_p)_s$ :	Heat capacitance of solid particle
$(\rho c_p)_{nf}$ :	Heat capacitance of nanofluid
$H_x$ :	Magnetic field intensity along $x$ direction
$H_y$ :	Magnetic field intensity along $y$ direction
$M$ :	Magnetization
$\nu$ :	Kinematic viscosity
$\tau_w$ :	Wall shear stress
$\lambda_{1a}$ :	Relaxation time of fluid
$\lambda_{1c}$ :	Relaxation time of heat flux
$\alpha_{1a}$ :	Deborah number in case of double dipole
$\alpha_{1c}$ :	Thermal relaxation in case of double dipole
$S_c$ :	Schmidt number
$k_1$ :	Strength of homogeneous reaction
$k_2$ :	Strength of heterogeneous reaction
$\zeta$ :	Tolerance rate
$\delta$ :	Ratio of mass diffusion coefficients
$\delta_a$ :	Magnetic scalar potential.

## Data Availability

Data are available within the article.

## Conflicts of Interest

The authors declare no conflict of interest.

## Acknowledgments

This study is supported by the Taif University Researchers Supporting Project number (TURSP-2020/31), Taif University, Taif, Saud Arabia.

## References

- [1] S. S. Papell, *United States Patent Office Filed Ser*, 1963.
- [2] M. A. Chaudhary and J. H. Merkin, "A simple isothermal model for homogeneous-heterogeneous reactions in boundary-layer flow. II Different diffusivities for reactant and autocatalyst," *Fluid Dynamics Research*, vol. 16, no. 6, pp. 335–359, 1995.
- [3] J. H. Merkin, "A model for isothermal homogeneous-heterogeneous reactions in boundary-layer flow," *Mathematical and Computer Modelling*, vol. 24, no. 8, pp. 125–136, 1996.
- [4] H. I. Andersson and O. A. Valnes, "Flow of a heated ferrofluid over a stretching sheet in the presence of a magnetic dipole," *Acta Mechanica*, vol. 128, no. 1-2, pp. 39–47, 1998.

- [5] R. Ganguly, S. Sen, and I. K. Puri, "Heat transfer augmentation using a magnetic fluid under the influence of a line dipole," *Journal of Magnetism and Magnetic Materials*, vol. 271, no. 1, pp. 63–73, 2004.
- [6] A. Sharma, D. Sharma, and R. C. Sharma, "Effect of dust particles on thermal convection in a ferromagnetic fluid," *Zeitschrift für Naturforschung A*, vol. 60, pp. 7494–7502, 2005.
- [7] T. Strek, "Heat Transfer in Ferrofluid in Channel with Porous Walls," in *Proceedings of the COMSOL Users Conference*, pp. 1–12, Prague, Czech Republic, 2006.
- [8] T. Strek and H. Jopek, "Computer simulation of heat transfer through a ferrofluid," *Physica status solidi*, vol. 244, no. 3, pp. 1027–1037, 2007.
- [9] M. A. Sadiq and H. M. S. Bahaidarah, "Numerical study on generalized heat and mass in Casson fluid with hybrid nanostructures," *Journal of Nanometers*, vol. 11, no. 10, p. 2675, 2021.
- [10] O. D. Makinde and A. Aziz, "Boundary layer flow of nanofluid past a stretching sheet with a convective boundary condition," *International Journal of Thermal Sciences*, vol. 50, no. 7, pp. 1326–1332, 2011.
- [11] H. Aminfar, M. Mohammadpourfard, Y. Narmani Kahnamouei, M. M. Pourfard, and Y. N. Kahnamouei, "A3D numerical simulation of mixed convection of a magnetic nanofluid in the presence of non-uniform magnetic field in a vertical tube using two phase mixture model," *Journal of Magnetism and Magnetic Materials*, vol. 323, no. 15, pp. 1963–1972, 2011.
- [12] N. Bachok, A. Ishak, and I. Pop, "On the stagnation-point flow towards a stretching sheet with homogeneous-heterogeneous reactions effects," *Communications in Nonlinear Science and Numerical Simulation*, vol. 16, no. 11, pp. 4296–4302, 2011.
- [13] H. Aminfar, M. M. Pourfard, and S. A. Zonouzi, "Numerical study of the ferrofluid flow and heat transfer through a rectangular duct in the presence of non-uniform transverse magnetic field," *Journal of Magnetism and Magnetic Materials*, vol. 327, pp. 31–42, 2013.
- [14] P. K. Kameswaran, S. Shaw, P. Sibanda, and P. V. S. N. Murthy, "Homogeneous-heterogeneous reactions in a nanofluid flow due to porous stretching sheet," *International Journal of Heat and Mass Transfer*, vol. 57, no. 2, pp. 465–472, 2013.
- [15] L. S. R. Titus and A. Abraham, "Heat transfer in ferrofluid flow over a stretching sheet with radiation," *International Journal of Engineering Research & Technology*, vol. 3, 2014.
- [16] M. Shekholeslami, M. M. Rashidi, and D. D. Ganji, "Effect of non-uniform magnetic field on forced convection heat transfer of Fe<sub>3</sub>O<sub>4</sub>-water nanofluid," *Computer Methods in Applied Mechanics and Engineering*, vol. 294, pp. 299–312, 2015.
- [17] T. Hayat, M. Imtiaz, and A. Alsaedi, "MHD flow of nanofluid with homogeneous-heterogeneous reactions and velocity slip," *Thermal Science*, vol. 67, 2015.
- [18] M. Imtiaz, T. Hayat, A. Alsaedi, and A. Hobiny, "Homogeneous-heterogeneous reactions in MHD flow due to an unsteady curved stretching surface," *Journal of Molecular Liquids*, vol. 221, pp. 245–253, 2016.
- [19] A. Majeed, A. Zeeshan, and R. Ellahi, "Unsteady ferromagnetic liquid flow and heat transfer analysis over a stretching sheet with the effect of dipole and prescribed heat flux," *Journal of Molecular Liquids*, vol. 223, pp. 528–533, 2016.
- [20] T. Hayat, M. Waqas, S. A. Shehzad, and A. Alsaedi, "On 2D stratified flow of an Oldroyd-B fluid with chemical reaction: an application of non-Fourier heat flux theory," *Journal of Molecular Liquids*, vol. 223, pp. 566–571, 2016.
- [21] T. Hayat, M. I. Khan, M. Farooq, A. Alsaedi, M. Waqas, and T. Yasmeen, "Impact of Cattaneo-Christov heat flux model in flow of variable thermal conductivity fluid over a variable thicked surface," *International Journal of Heat and Mass Transfer*, vol. 99, pp. 702–710, 2016.
- [22] M. Sajid, S. A. Iqbal, M. Naveed, and Z. Abbas, "Effect of homogeneous-heterogeneous reactions and magnetohydrodynamics on Fe<sub>3</sub>O<sub>4</sub> nanofluid for the Blasius flow with thermal radiations," *Journal of Molecular Liquids*, vol. 233, pp. 115–121, 2017.
- [23] S. U. Rehman, A. Zeeshan, A. Majeed, and M. B. Arain, "Impact of Cattaneo-Christov heat flux model on the flow of Maxwell ferromagnetic liquid along a cold flat plate embedded with two equal magnetic dipoles," *Journal of Magnetic*, vol. 22, no. 3, pp. 472–477, 2017.
- [24] U. Nazir, M. A. Sadiq, and M. Nawaz, "Non-Fourier thermal and mass transport in hybrid nano-Williamson fluid under chemical reaction in Forchheimer porous medium," *International Communication in Heat and Mass Transfer*, vol. 127, article 105536, 2021.
- [25] M. A. Qureshi, S. Hussain, and M. A. Sadiq, "Numerical simulation of MHD mixed convection of hybrid nano fluid flow in a horizontal channel with cavity impact on heat transfer and hydro nano forces," *Journal of Case Studies in Thermal Engineering*, vol. 27, article 101321, 2021.
- [26] W. Tahir, S. Bilal, N. Kousar, I. A. Shah, and A. S. Alqahtani, "Analysis about enhancement in thermal characteristics of viscous fluid flow with induction of ferrite particles by using cattaneo christov theory," *Proceedings of the Institution of Mechanical Engineers, Part C: Journal of Mechanical Engineering Science*, vol. 236, no. 1, pp. 208–218, 2022.
- [27] M. A. Sadiq, "Non-Fourier heat transfer enhancement in Power law fluid with mono and hybrid nano particles," *Journal in Research Square*, vol. 11, 2021.
- [28] M. A. Sadiq, "Heat transfer of a nanoliquid thin film over a stretching sheet with surface temperature and internal heat generation," *Journal of Thermal Analysis and Calorimetry*, vol. 143, no. 3, pp. 2075–2083, 2021.
- [29] A. Saeed, P. Kumam, T. Gul, W. Alghamdi, W. Kumam, and A. Khan, "Darcy-Forchheimer couple stress hybrid nanofluids flow with variable fluid properties," *Scientific Reports*, vol. 11, no. 1, pp. 1–13, 2021.
- [30] T. Gul, M. Rehman, A. Saeed et al., "Magnetohydrodynamic impact on Carreau thin film couple stress nanofluid flow over an unsteady stretching sheet," *Mathematical Problems in Engineering*, vol. 2021, 10 pages, 2021.
- [31] A. Saeed, P. Kumam, S. Nasir, T. Gul, and W. Kumam, "Non-linear convective flow of the thin film nanofluid over an inclined stretching surface," *Scientific Reports*, vol. 11, no. 1, pp. 1–15, 2021.
- [32] M. Bilal, A. Saeed, T. Gul, I. Ali, W. Kumam, and P. Kumam, "Numerical approximation of microorganisms hybrid nanofluid flow induced by a wavy fluctuating spinning disc," *Coatings*, vol. 11, no. 9, p. 1032, 2021.
- [33] T. Gul, M. Usman, I. Khan et al., "Magneto hydrodynamic and dissipated nanofluid flow over an unsteady turning disk," *Advances in Mechanical Engineering*, vol. 13, no. 7, 2021.
- [34] A. Rehman, Z. Salleh, and T. Gul, "Heat transfer of thin film flow over an unsteady stretching sheet with dynamic viscosity," *Journal of Advanced Research in Fluid Mechanics and Thermal Sciences*, vol. 81, no. 2, pp. 67–81, 2021.

## Research Article

# Analytical and Numerical Analysis of the Squeezed Unsteady MHD Nanofluid Flow in the Presence of Thermal Radiation

Hakeem Ullah <sup>1</sup>, Muhammad Arif Khan,<sup>1</sup> Mehreen Fiza,<sup>1</sup> Kashif Ullah,<sup>1</sup> Muhammad Ayaz,<sup>1</sup> and Seham M. Al-Mekhlafi <sup>2</sup>

<sup>1</sup>Department of Mathematics, Abdul Wali Khan University, Mardan, KP, Pakistan

<sup>2</sup>Department of Mathematics, Sanna University, Yemen

Correspondence should be addressed to Seham M. Al-Mekhlafi; [smdk100@gmail.com](mailto:smdk100@gmail.com)

Received 29 December 2021; Revised 9 March 2022; Accepted 14 March 2022; Published 31 March 2022

Academic Editor: Anwar Saeed

Copyright © 2022 Hakeem Ullah et al. This is an open access article distributed under the Creative Commons Attribution License, which permits unrestricted use, distribution, and reproduction in any medium, provided the original work is properly cited.

In this study, the unsteady squeezing nanofluid flow between two plates with thermal radiation has been investigated. The governing equations of the flow model have been transformed to a set of nonlinear ordinary differential equations (ODEs) from a set of partial differential equations (PDEs) using a suitable similarity variable. The optimal auxiliary function method (OAFM) and Runge–Kutta method of order 4 (RK method of order 4) are used for the solution of the modeled problem. The variation of the squeezing number, Prandtl number, Eckert number, and thermal radiation has been presented. The magnetic field resists the flow velocity, and the Prandtl number resists the temperature distribution. The increase in volume fraction decreases the velocity profile whereas increases the temperature profile. The skin friction coefficient and the Nusselt number are inversely proportional to  $S$ . The effect of increasing values of  $E_c$  is to decrease the skin friction coefficient  $C_f$  and the heat transfer rate  $Nu_x$ . The increasing value of  $\phi$  increases the skin friction coefficient and decreases the heat transfer rate.

## 1. Introduction

The nanofluid consists of the nanometer particle size of the fluid having less than  $10^9$  nm, such as copper, aluminum, silver, silicon, aluminum oxides, and graphite. The base fluids are water, oil, and ethylene glycol. Choi et al. [1] introduced the term nanofluid and heat transfer features of the fluids, such as thermal conductivity is enriched by the addition of nanoparticles into it [2, 3]. The study of heat and mass transfer for squeezing unsteady viscous flow between two parallel plates has a wide range of physical applications, including lubrication systems, polymer processing, food processing, hydrodynamical machines, compression, and crop damage due to freezing, formation, and dispersion. Squeeze flow, also known as squeezing flow, squeezing film flow, or squeeze flow theory, is a flow in which a material is squeezed out between two parallel plates. Josef Stefan studied it in 1874 for the first time. There are several squeeze flow models that may be used to explain Newtonian and non-Newtonian fluids that are squeezed under various geometries and condi-

tions. Squeeze flow is used in a variety of scientific and engineering areas, including welding engineering, and materials science, to name a few. Sheikholeslami et al. [4] used heat line analysis to simulate a two-phase simulation of nanofluid flow and heat transfer. Moreover, Sheikholeslami et al. [5] investigated the unsteady flow of a nanofluid squeezing between two parallel plates using the Adomian decomposition method (ADM). Also, the problem of squeezing flow between rotating disks has been studied by Hamza [6] and Bhattacharyya [7]. Magnetohydrodynamics (MHD) is the information of the magnetic assets of electrically conducting fluids. Plasmas, electrolytes, water, and liquid metals are examples of magneto fluids. Hannes Alfvén [8] was the first who introduced the field of MHD. MHD has several applications in the field of industries and engineering such as plasma, crystal growth, MHD sensors, liquid-metal cooling of MHD casting, MHD power generation, and magnetic drug targeting. MHD depends on the strength of the magnetic field; the stronger the magnetic field, the greater is MHD effects and vice versa. MHD includes plasmas, molten

metals, saltwater, and electrolytes. [9–13]. Seddiqui, Domairy, and Aziz et al. [14, 15] explored two-dimensional MHD squeezing flow between parallel plates and parallel disc. Magnetic nanofluid is a one-of-a-kind material that combines the qualities of a liquid with a magnetic material [16]. Magneto-optical wavelength filters [17, 18], optical modulators, [19], nonlinear optical materials [20], tunable optical fiber filters [21], optical gratings, and optical switches have all been discovered to use such fluids [22]. Changing the magnetic field can change a lot of the physical features of these fluids. They also served as an excellent model system for fundamental investigations. Manipulation of nanoparticles with carbon nanotubes has recently been shown to result in increased thermal conductivity. The thermal characteristics of nanofluids are the parameters that are critical to the performance of nanofluids. Thermal conductivity, specific heat, viscosity, and heat transfer coefficient are the four variables. Solar collector thermal performance is mostly determined by how thermal characteristics behave under various operating situations. Temperature, environmental conditions, type of base fluid, particle size and form of the nanoparticle, and volume concentration are all operating parameters. Taking into account all of these factors, choosing the right nanofluid is critical for optimum performance. Based on this idea, scientist studies many important flow models for various physical aspects [23–26]. Explicit Runge–Kutta techniques have become popular for wave simulations due to their great accuracy and low memory requirements [27]. The traditional fourth-order Runge–Kutta technique requires three memory places per dependent variable [28]; however, low-storage approaches may be constructed that only require two memory sites per dependent variable [29]. A third-order Runge–Kutta technique can readily accomplish this characteristic, while a fourth-order approach requires an additional stage [30]. Because the evaluation of the derivative function is the fundamental cost of integration, and each level necessitates a function evaluation, the new stage implies a large rise in cost. Some of the recent development in the related field can be seen in [26, 31–42]. In this paper, we propose the OAFM [43, 44] for the squeezed unsteady MHD nanofluid flow in the presence of thermal radiation. The validity of OAFM is based on the auxiliary function which optimally controls the convergence of the solution. The efficiency of OAFM is proved in comparison to the numerical solutions obtained by Runge–Kutta method of order 4. In the present work, we show how solutions to the modeled problem can be obtained using OAFM, without the need for complex and complicated calculations with low specification of computer with high accuracy. Moreover, OAFM presented here is less computational work and simple in applications at the first iteration. Up to now, the squeezed unsteady MHD nanofluid flow in the presence of thermal radiation has not been studied. The purpose of this study is to provide an analytical solution of the squeezed unsteady MHD nanofluid flow in the presence of thermal radiation by using the newly developed method OAFM. In the above-mentioned problem, analytical and numerical methods are used for the solution of the problem. The numerical methods required the linearization and discretiza-

tion techniques and huge computer memory with operating time; we show how solutions to the boundary value problem can be obtained using OAFM, without the need for complex and involved mathematical algorithms, and at a relatively low computing memory and easy approach with high accuracy at the first iteration.

## 2. Basic Mathematical Theory of OAFM [43, 44]

Let us look at the OAFM for the differential equation

$$L(f(\eta)) + s(\eta) + N(f(\eta)) = 0, \quad (1)$$

where  $L, N$  denotes the linear and nonlinear operators;  $s$  denotes the source function,  $f(\kappa)$ , and is an unknown function at this stage; the initial/boundary conditions are

$$B\left(f(\eta), \frac{df(\eta)}{d\eta}\right) = 0. \quad (2)$$

Because finding an accurate solution to severely nonlinear equations is extremely difficult, the proposed approximation is as follows:

$$f(\eta, E_k) = f_u(\eta) + f_1(\eta, E_k), k = 1, 2, \dots, s. \quad (3)$$

Using Equation (3) in Equation (1), we have

$$L(f_0(\eta)) + L(f_1(\eta, E_k)) + s(\eta) + N(f_0(\eta) + f_1(\eta, E_k)) = 0, \quad (4)$$

where  $E_k, k = 1, 2, \dots, s$  are control convergence parameters to be determined.

The initial approximation is determined as

$$L(f_0(\eta)) + s(\eta) = 0, \quad B\left(f_0(\eta), \frac{df_0(\eta)}{d\eta}\right) = 0. \quad (5)$$

The first approximation is obtained as

$$L(f_1(\eta, E_k)) + N(f_0(\eta) + f_1(\eta, E_k)) = 0, \quad B\left(f_1(\eta), \frac{df_1(\eta)}{d\eta}\right) = 0. \quad (6)$$

The nonlinear term is expressed as

$$D_1, D_2 N(f_0(\eta) + f_1(\eta, E_k)) = N(f_0(\eta)) + \sum_{i=1}^{\infty} u(t, E_k) N(f_0(\eta)). \quad (7)$$

The last term in Equation (7) seems difficult to solve, so to avoid this difficulty and to fast the convergence of the

solution. Equation (6) can be written as

$$L(f_1(\eta, E_k)) + D_1((f_0(\eta), E_m)F(N(f_0(\eta)))) + D_2(f_0(\eta), E_n) = 0,$$

$$B\left(f_1(\eta, E_k) \frac{df_1(\eta, E_k)}{d\eta}\right) = 0, n = 1, 2 \dots q, m = q + 1, q + 2, \dots, s,$$
(8)

where  $D_1, D_2$  are optimal auxiliary which depends on  $f_0(\kappa)$  and  $E_n, E_m$  and  $F(N(f_0(\kappa)))$  is a function which depends on the expression appearing within the nonlinear term of  $N(f_0(\kappa))$ . The optimal auxiliary function should be expressed in the sum form of  $f_0(\kappa)$  such as if  $f_0(\kappa)$  are polynomial. Exponential and trigonometric then  $D_1, D_2$  would be the sum of polynomial, exponential, and trigonometric, respectively. Also  $f_0(\kappa)$  would be the exact solution of the original problem, if  $N(f_0(\kappa)) = 0$ . The optimal auxiliary functions can be obtained from method of least square, collocation method Galerkin Ritz methods.

**2.1. Convergence of the Method.** In order to obtain the convergent solution, we calculate the optimal constants also known as control convergence constant by method of least squares: These optimal constants are resubmitted into original equation to get the series solution.

$$J(E_1, E_2, \dots, E_s) = \int_1 R^2(\eta, E_1, E_2, \dots, E_s) d\eta, \quad (9)$$

where  $I$  is equation domain.

The unknown constants are established as

$$\frac{\partial J}{\partial E_1} = \frac{\partial J}{\partial E_2} = \dots = \frac{\partial J}{\partial E_n} = 0. \quad (10)$$

The  $m$ th order approximate solution can be obtained by these constants so obtained.

### 3. Formulation of the Problem

The flow and heat transfer of two-dimensional unsteady squeezing nanofluid via the lateral plates is observed in this study, as shown in Figure 1.

At any nondimensional time  $t$ , the distance between the two plates is given as

$$z = \pm l(1 - at)^{\frac{1}{2}} = \pm h(t), \text{ for } a > 0. \quad (11)$$

The two plates are squeezed until they touch each other at  $1/\alpha$ , whereas at  $\alpha < 0$ , the two plates are separated. Here,  $\alpha$  is a constant,  $l$  is the initial position (at  $t = 0$ ), and  $z$  is the axial coordinate, which is obviously zero from the flow zone, with the flow model evaluated along the  $x$  and  $y$  axes. The nondimensional time throughout the flow is represented by the variable  $t$ . The heat source and viscous dissipation effect as a result of friction caused by fluid flow shear are

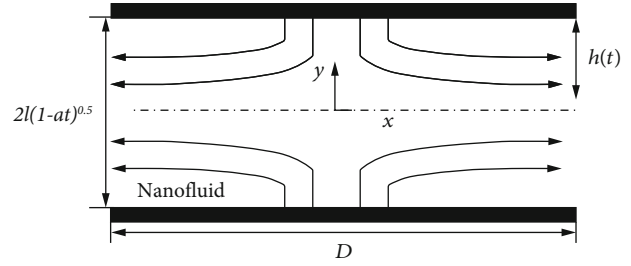


FIGURE 1: Geometry of the flow problem.

both protected. As a result, this behavior occurs when the Eckert number is very high. Meanwhile, the copper material was enclosed in a nanofluid. A uniform magnet is used perpendicular to the flow. The following are the governing equations:

$$\frac{\partial u}{\partial x} + \frac{\partial v}{\partial y} = 0, \quad (12)$$

$$\frac{\partial u}{\partial x} + u \frac{\partial v}{\partial y} + v \frac{\partial u}{\partial y} = -\frac{1}{\rho_{nf}} \frac{\partial p}{\partial y} + \frac{\mu_{nf}}{\rho_{nf}} \left( \frac{\partial^2 v}{\partial x^2} + \frac{\partial^2 u}{\partial y^2} \right) - \frac{\sigma B_0^2}{\rho_{nf}} u, \quad (13)$$

$$\frac{\partial v}{\partial t} + u \frac{\partial v}{\partial x} + v \frac{\partial v}{\partial y} = -\frac{1}{\rho_{nf}} \frac{\partial p}{\partial y} + \frac{\mu_{nf}}{\rho_{nf}} \left( \frac{\partial^2 v}{\partial x^2} + \frac{\partial^2 v}{\partial y^2} \right), \quad (14)$$

$$\frac{\partial T}{\partial t} + u \frac{\partial T}{\partial x} + v \frac{\partial T}{\partial y} = \frac{k_{nf}}{(\rho C_p)_{nf}} \left( \frac{\partial^2 T}{\partial x^2} + \frac{\partial^2 T}{\partial y^2} \right) + \frac{\mu_{nf}}{(\rho C_p)_{nf}} \left( 4 \left( \frac{\partial u}{\partial y} \right)^2 \right) - \frac{1}{\rho C_p} \frac{\partial q_r}{\partial y}. \quad (15)$$

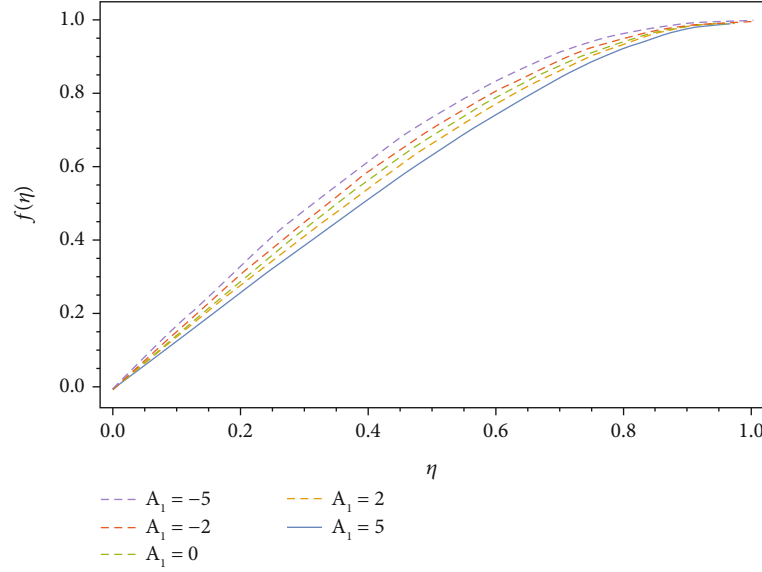
The velocities in the  $x$  and  $y$  directions are represented by  $u$  and  $v$ , respectively. While  $p, T, T_\infty, f$ , and  $k_{nf}$  are the effective density, dynamic viscosity, heat capacity, and thermal conductivity of the nanofluid;  $\rho_{nf}, \mu_{nf}, (\rho C_p)$ , and  $k_{nf}$  are the effective density, dynamic viscosity, heat capacity, and thermal conductivity of the nanofluid, respectively.

$$\rho_{nf} = (1 - \phi)\rho_f + \phi\rho_p, \quad (16)$$

$$(\rho C_p)_{nf} = (1 - \phi)(\rho C_p)_f + \phi(\rho C_p)_p, \quad (17)$$

$$\mu_{nf} = \frac{\mu_f}{(1 - \phi)^{2.5t}} \text{ (Brinkman)}, \quad (18)$$

$$\frac{k_{nf}}{k_f} = \frac{k_s + 2k_f - 2\phi(k_f - k_s)}{k_s + 2k_f + 2\phi(k_f - k_s)} \text{ (Maxwell-Garnett)}. \quad (19)$$

FIGURE 2: Effect of the  $A_1$  on the  $f$ .

Subject to the following boundary conditions

$$v = v_w = \frac{dh}{dt} T = T_H \text{ at } y = h(t), v = \frac{\partial u}{\partial y} = \frac{\partial T}{\partial y} = 0 \text{ at } y = 0. \quad (20)$$

The radiative heat flux in Equation (4) is given by the Rosseland formula as

$$q_r = -\frac{4\sigma^* \partial T^4}{3k^* \partial y}. \quad (21)$$

The Stefan-Boltzmann constant and the mean absorption number, respectively, are  $\sigma^*$  and  $k^*$ . We assume that the temperature variation among the flow is greatly constrained, and that the expression  $T^4$  may be regarded a linear function of temperature, based on various research, As a result,  $T^4$  is enlarged by disregarding the higher-order terms and utilizing Taylor series expansion about  $T$ .

$$T^4 = 4T_\infty^3 - 3T_\infty^4. \quad (22)$$

Substituting Equations (21) and (22) into Equation (15), we obtain

$$\begin{aligned} \frac{\partial T}{\partial t} + u \frac{\partial T}{\partial x} + v \frac{\partial T}{\partial y} &= \frac{k_{nf}}{(\rho C_p)_{nf}} \left( \frac{\partial^2 T}{\partial x^2} + \frac{\partial^2 T}{\partial y^2} \right) \\ &+ \frac{\mu_{nf}}{(\rho C_p)_{nf}} \left( 4 \left( \frac{\partial u}{\partial x} \right)^2 \right) + \frac{32\sigma^* T_\infty^3 \partial^2 T}{3\rho C_p k^* \partial y^2}. \end{aligned} \quad (23)$$

To begin, introduce the following quantities:

$$\eta = \frac{y}{[l(1-\alpha t)^{1/2}]}, u = \frac{ax}{[2(1-\alpha t)]} f'(\eta), \quad (24)$$

$$v = -\frac{al}{[2(1-\alpha t)]} f(\eta), \theta = \frac{T}{T_H},$$

$$A_1 = (1-\phi) + \phi \frac{\rho_s}{\rho_f}, N = \frac{4\sigma^* T_\infty^3}{k_{fp} C_p k^*},$$

$$f^{iv} - SA_1(1-\phi)^{2.5} (\eta f'''' + 3f'' + f'f'' - ff''') - M^2 f' = 0, \quad (25)$$

$$\begin{aligned} (12A_3 + 16A_2N)\theta'' + 3 \text{Pr} SA_2 (f\theta' - \eta\theta') \\ + \frac{3 \text{Pr} E_c}{(1-\phi)^{2.5}} (f'^2 + 4\delta^2 f'^2) = 0. \end{aligned} \quad (26)$$

where  $N$  denotes heat/thermal radiation as defined by Equation (10), and  $A_2$  and  $A_3$  denote dimensionless constants as defined by

$$A_2 = (1-\phi) + \phi \frac{(\rho C_p)_s}{(\rho C_p)_f}, A_3 = \frac{k_{nf}}{k_f}. \quad (27)$$

Equations (25) and (26) must now be solved in the context of

$$f(0) = 0, f(1) = 1, f'(1) = 0, \theta'(0) = 0, \theta(1) = 1. \quad (28)$$

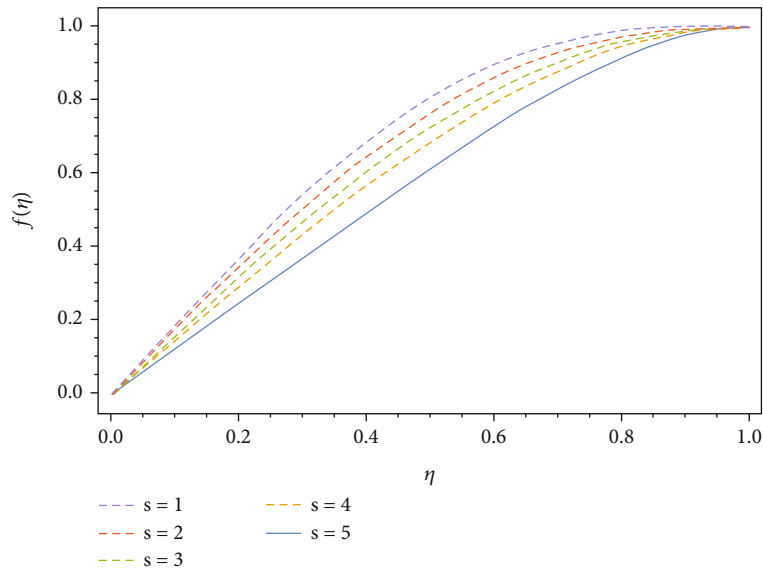


FIGURE 3: Effect of  $s$  on  $f$ .

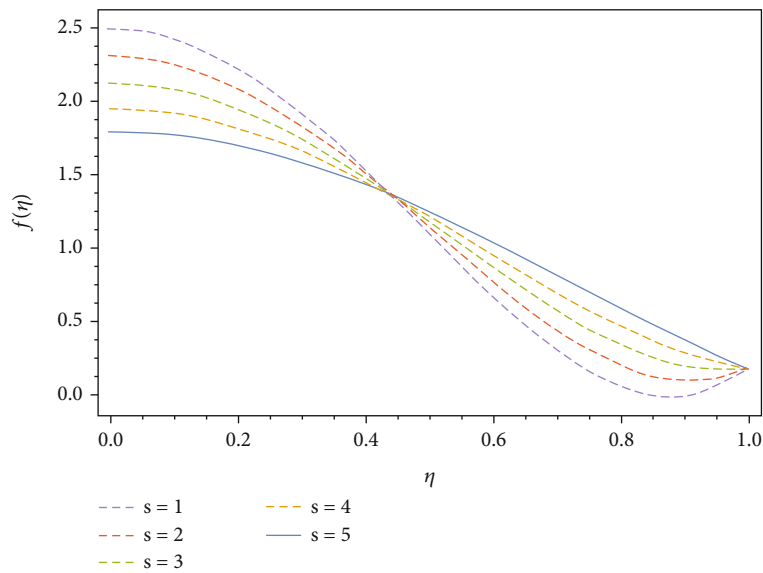


FIGURE 4: Effect of  $S$  on  $f'$ .

Here,  $S$  is the squeezing integer;  $P_r$  and  $Ec$  are the Prandtl and Eckert numbers, respectively.

$$S = \frac{al}{2v_f}, P_r = \frac{\mu_f(\rho C_p)_f}{\rho_f k_f}, E_c = \frac{\rho_f}{(\rho C_p)_f} \left( \frac{ax}{2(1-\alpha t)} \right)^2, \quad (29)$$

$$\delta = \frac{1}{x} \cdot M^2 = \frac{\sigma B_0^2}{\rho_{nf}} \left( \frac{ax}{2(1-\alpha t)} \right), f''(0) = 0,$$

The following quantities are categorically used for practical interest as defined

$$C_f = \frac{\mu_{nf}(\partial u/\partial y)_{y=h(t)}}{\rho_{nf} v_w^2}, N_u = \frac{-lk_{nf}(\partial T/\partial y)_{y=h(t)}}{kT_H}. \quad (30)$$

Equation (24) provides the following result:

$$C_f = \frac{l^2}{x^2(1-\alpha t) \text{Re}_x C_f} = A_1(1-\phi)^{2.5} f''(1), \quad (31)$$

$$Nu^* = \sqrt{1-\alpha t} Nu = -A_3 \theta'(1).$$

The linear and nonlinear operators of Equations (11) and (12) are

$$L(f(\kappa)) = f^{iv}(\kappa) \quad (32)$$

$$L(\theta(\kappa)) = \theta'''(\kappa) \quad (33)$$



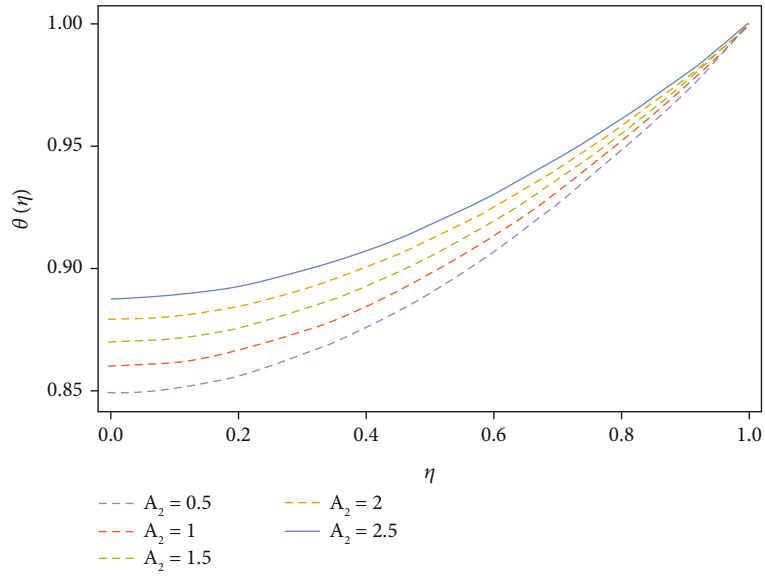


FIGURE 5: Effect of  $A_2$  on  $\Theta$ .

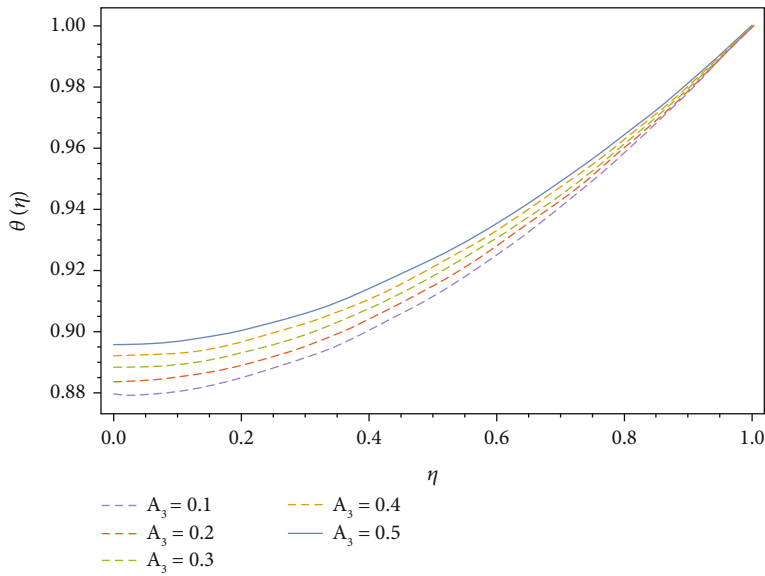


FIGURE 6: Effect of  $A_3$  on  $\Theta$ .

$N(f(\kappa)) = -SA(1 - \phi)^{2.5} (\eta f'''' + 3f'' + f'f'' - ff''') - M^2f'$  has solution as

(34)

$N(\theta(\kappa)) = 3 \text{ Pr } SA_2 (f\theta' - \eta\theta') + \frac{3 \text{ Pr } Ec}{(1 - \phi)^{2.5}} (f''^2 + 4\delta^2 f'^2)$

(35)

$f_0(\kappa) = \frac{1}{2} (3\kappa - \kappa^3),$

$\theta_0(\kappa) = 1.$

(37)

From Equation (5), we have

$f^{iv}(\kappa) = 0, f(0) = 0, f'(0) = 0, f(1) = 1, f'(1) = 0,$

$\theta''(\kappa) = 0, \theta'(0) = 0, \theta(1) = 1,$

(36)

Based on Equation (23), we get

$N(f_o(\kappa)) = -SA_1(1 - \phi)^{2.5} (18\kappa^2 - 18\kappa - 6\eta),$

$N(\theta_o(\kappa)) = \frac{3 \text{ Pr } Ec}{(1 - \phi)^{2.5}} (36\delta\kappa^4 + 36\kappa^2 + 9\delta).$

(38)

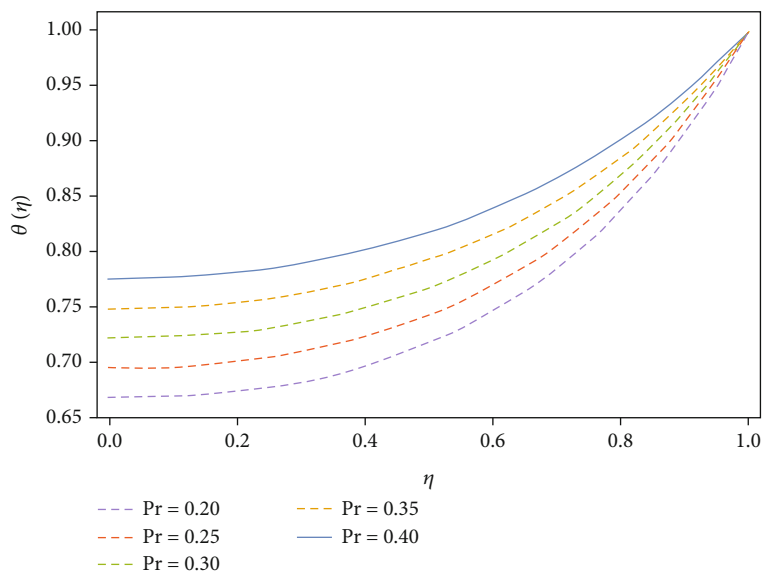


FIGURE 7: Effect of Pr on  $\Theta$ .

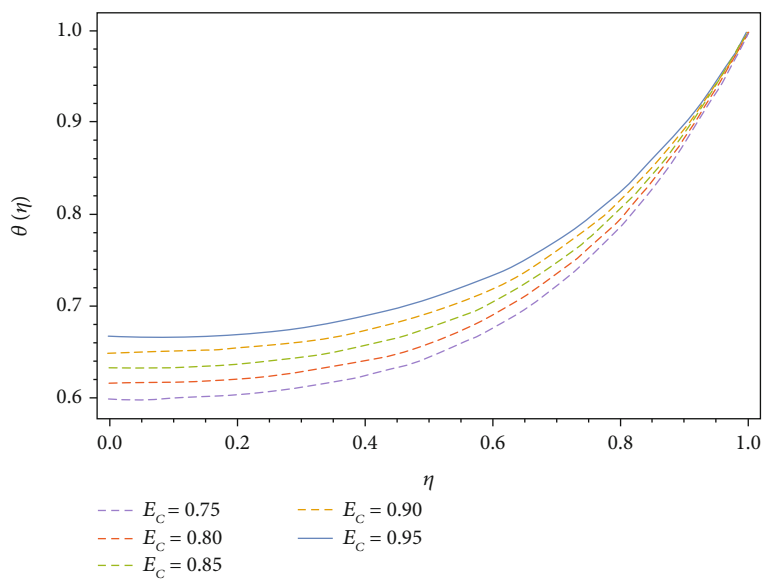


FIGURE 8: Effect of  $E_c$  on  $\Theta$ .

In the first approximation based on Equations (8), (32), (33), and (24), we get

$$\begin{aligned}
 & f^{iv}(\kappa) + D_1(\kappa, \kappa^2, \kappa^3, E_m) (-SA_1(1 - \phi)^{2.5}(18\kappa^2 - 18\kappa - 6\eta)) \\
 & + D_2(\kappa, \kappa^2, \kappa^3, E_n) = 0, \\
 & \theta''(\kappa) + D_3(\kappa, \kappa^2, \kappa^3, E_p) \left( \frac{3 \text{Pr} E_c}{(1 - \phi)^{2.5}} (36\delta\kappa^4 + 36\kappa^2 + 9\delta) \right) \\
 & + D_4(\kappa, \kappa^2, \kappa^3, E_r) = 0.
 \end{aligned}$$

(39)

with boundary conditions

$$\begin{aligned}
 & f(0) = 0, f'(0) = 0, f(1) = 1, f'(1) = 0, \\
 & \theta'(0) = 0, \theta(1) = 1.
 \end{aligned}$$

(40)

The OAF can be chosen freely as

$$D_1(f_o(\kappa), E_m) = -(E_1 + E_2\kappa),$$

$$D_2(f_o(\kappa), E_n) = -(E_1 + E_2\kappa)\kappa - (E_5 + E_6\kappa + E_7\kappa^2)\kappa^2,$$

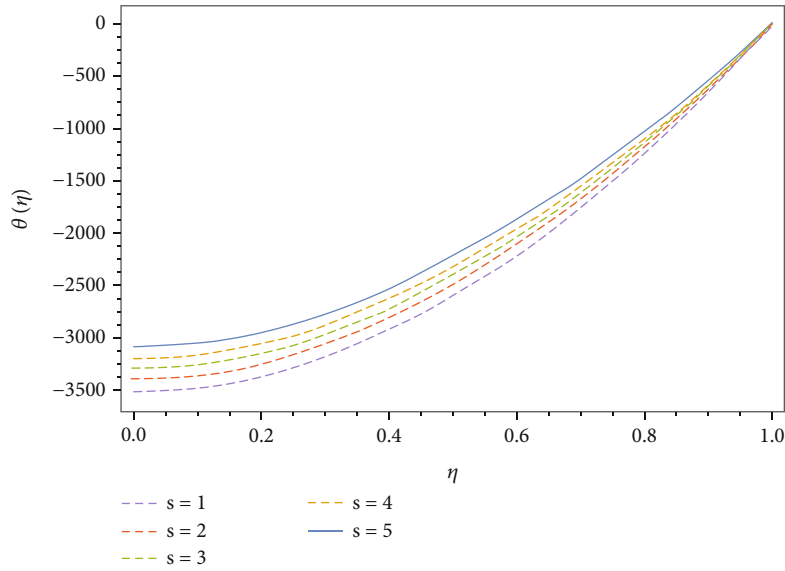


FIGURE 9: Effect of  $s$  on  $\Theta$ .

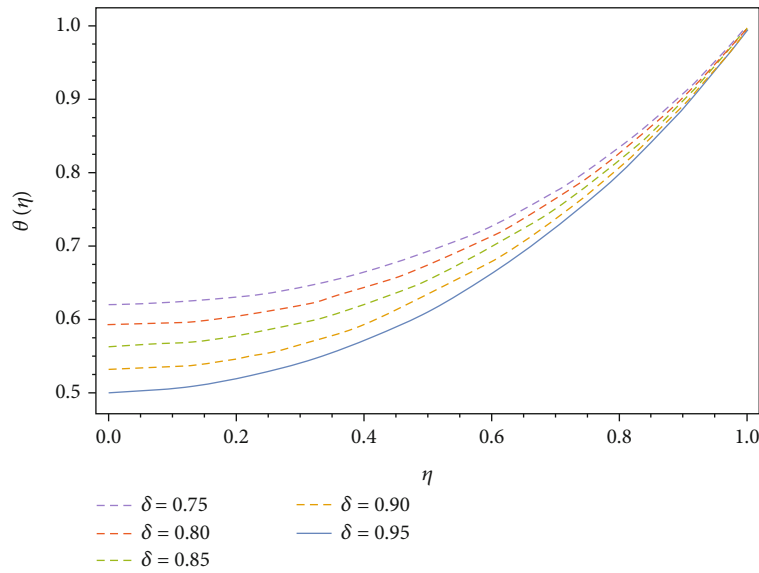


FIGURE 10: Effect of  $\delta$  on  $\Theta$ .

$$D_3(f_o(\kappa), E_p) = 0,$$

$$D_4(f_o(\kappa), E_r) = -(E_8 + E_9\kappa) - (E_{10} + E_{11}\kappa + E_{12}\kappa^2)\kappa^2.$$

(41)

$$\theta''(\kappa) + D_3(\kappa, \kappa^2, \kappa^3, E_p) \left( \frac{3 \text{Pr} E_c}{(1-\phi)^{2.5}} (36\delta\kappa^4 + 36\kappa^2 + 9\delta) \right) + D_4(\kappa, \kappa^2, \kappa^3, E_r) = 0.$$

(42)

We obtained the first approximate solution

$$f^{iv}(\kappa) + D_1(\kappa, \kappa^2, \kappa^3, E_m) (-SA_1(1-\phi)^{2.5}(18\kappa^2 - 18\kappa - 6\eta)) + D_2(\kappa, \kappa^2, \kappa^3, E_n) = 0,$$

And its solution is given as by putting the values of the optimal constants obtained from the method of least square.

$$f(\kappa) = -\frac{1}{280} \kappa \left( 140(-3 + \kappa^2) + \text{chst}(-26 + \kappa^2)(-1 + \kappa^2)^2 \right),$$

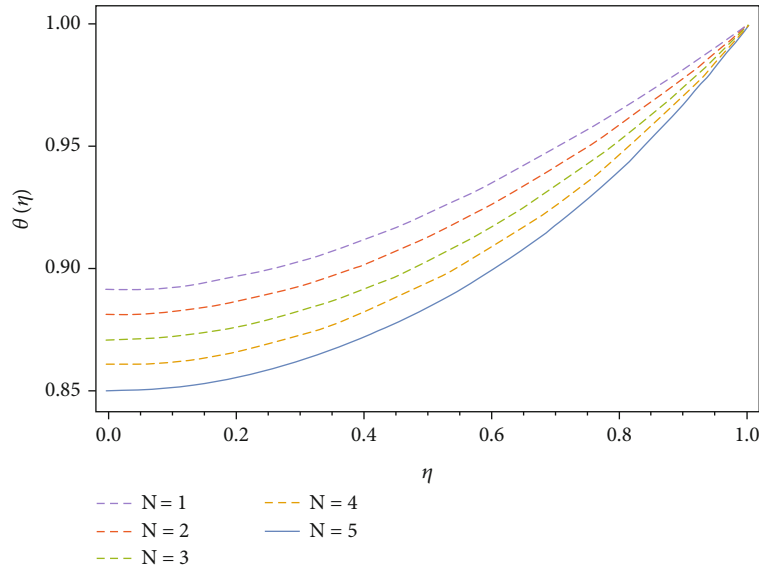


FIGURE 11: Effect of  $N$  on  $\Theta$ .

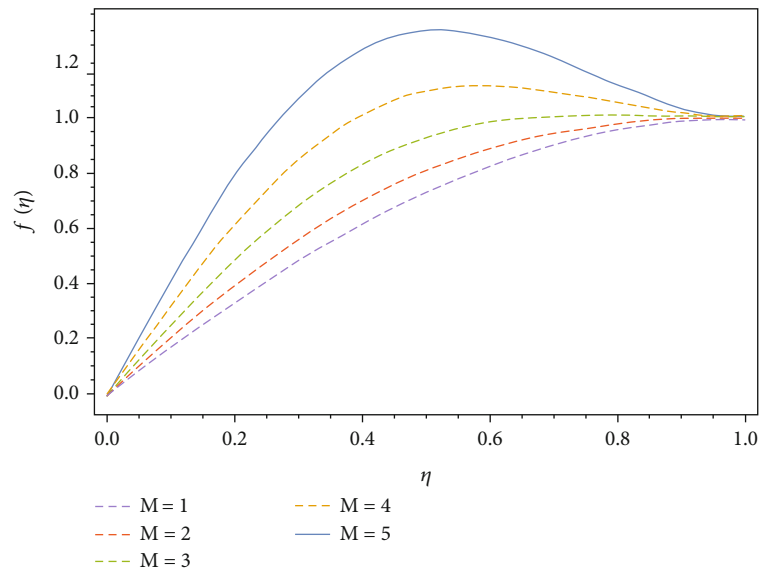


FIGURE 12: Effect of  $M$  on  $f(\eta)$ .

$$\theta(\kappa) = \frac{20t + 3h(-1 + \kappa^2)(15 \text{ Pr } Q(1 + \kappa^2) + 2t(11 - 4\kappa^2 + \kappa^4)\delta^2)}{20t} \tag{43}$$

#### 4. Numerical Method of Solution

The differential Equations (25) and (26) along with the side condition (28) have been solved using the fourth-order Runge–Kutta method (FORKM) along with the shooting technique. The nonlinear Equations (25) and (26) of fourth and second order are reduced to a set of six first-order simultaneous equations as follows:

$$f_1 = f, f_2 = f', f_3 = f'', f_4 = f''', f_5 = \theta, f_6 = \theta', f_4' = f''''', f_6' = \theta''', \tag{44}$$

$$f_4' = SA_1(1 - \phi)^{2.5}(\eta f_4 + 3f_3 + f_2 f_3 - f_1 f_4) - M^2 f', \tag{45}$$

$$f_6' = -3 \text{ Pr } SA_2(f_1 f_6 - \eta f_6) - \frac{3 \text{ Pr } Ec}{(1 - \phi)^{2.5}} \frac{(f_3^2 + 4\delta^2 f_2^2)}{12A_3 + 16A_2 N}. \tag{46}$$

The boundary condition now became

$$f_1(0) = 0, f_3(0) = 0, f_1(1) = 0, f_2(1) = 0, f_4(1) = 1, f_3(0) = 0. \tag{47}$$

Solving of this system, six initial conditions are needed, while only three conditions are available. Some initial conditions are not given in the problem. Here, the values of  $f, f'$

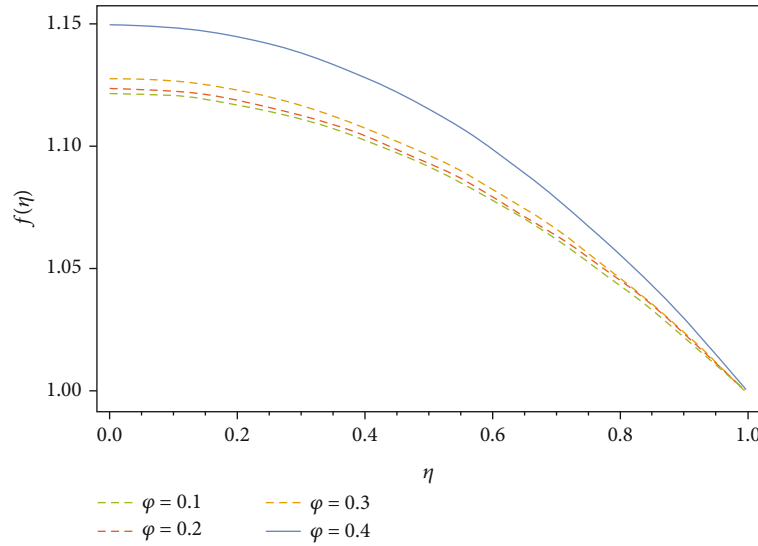


FIGURE 13: Effect of volume friction  $\phi$  on  $f(\eta)$ .ss

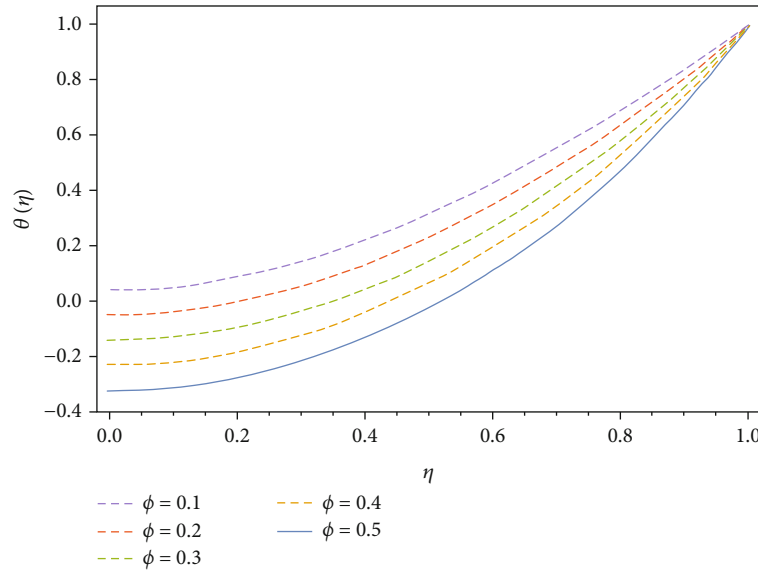


FIGURE 14: Effect of volume friction  $\phi$  on  $\theta(\eta)$ .

and  $f'''$  are known as  $\eta \rightarrow 1$ . These three-end conditions are used to produce the three unknown initial conditions by applying the shooting technique.

### 5. Results and Discussion

**5.1. Graphical Discussion.** The main focus of the study is to develop a mathematical model of an unstable nanofluid flow squeezed between parallel plates, as illustrated in Figure 1. Figure 2 shows the effect of  $A_1$  on the velocity profile  $f$ . An increase in  $A_1$  causes to increase the velocity profile  $f$ . Figures 3 and 4 demonstrate the influence of the squeeze number on the velocity profile. The motion of the plates represented by squeezing flow is indicated by the squeeze number  $S$ . When  $S > 0$ , the plates are moving separately, but when  $S < 0$ , the plates are moving collectively. Positive and

negative squeezing values have distinct effects on the velocity profile. The velocity rises when the absolute value of the squeeze number is 0.5, but drops when it is  $>0.5$ . An increase in the stretching parameter causes to increase the velocity profile. The stretching parameter assists the flow velocity. Figure 5 shows the effect of  $A_2$  on the temperature profile  $\theta(\eta)$ . The temperature profile increases by increasing  $A_2$ . Also, the effect of  $A_3$  on the temperature profile  $\theta(\eta)$  is given in Figure 6. By increasing the values of  $A_3$ , a reverse effect as compared to  $A_2$  has been observed. The influence of the Prandtl number  $P_r$  on temperature distributions is seen in Figure 7. With a large number of  $P_r$ , the temperature distribution obviously decreases, whereas with a small number of  $P_r$ , it grows. Fluids with a low Prandtl number have a higher thermal diffusivity than fluids with a high Prandtl number. A high  $P_r$  causes the thermal boundary layer to

TABLE 1: Comparison of the value of rate of velocity profile  $f(\eta)$  for different value of  $\eta$  when  $S = 0.90$ ,  $Pr = 0.3$ ,  $Ec = 0.5$ ,  $A_1 = 0.1$ ,  $A_2 = 0.5$ ,  $A_3 = 0.7$ ,  $\delta = 0.6$ ,  $M = 1$ .

$\eta$	OAFM	4th RKM	Absolute error
0	0.	0.	0.00000000
0.1	0.119482	0.119482	$1.245789 \times 10^{-17}$
0.2	0.241044	0.241044	$1.02145 \times 10^{-17}$
0.3	0.365079	0.365079	$3.21458 \times 10^{-17}$
0.4	0.490248	0.490248	$2.01245 \times 10^{-17}$
0.5	0.613586	0.613586	$1.02158 \times 10^{-17}$
0.6	0.730601	0.730601	$3.12458 \times 10^{-17}$
0.7	0.835395	0.835395	$2.32489 \times 10^{-17}$
0.8	0.920813	0.920813	$2.87963 \times 10^{-17}$
0.9	0.97866	0.97866	$1.98756 \times 10^{-17}$
1	1.	1.	$1.05896 \times 10^{-16}$

decrease as a result. The impact is much more noticeable for a small number of  $P_r$  because the thermal boundary layer thickness is so high. The impact of Eckert number and Prandtl number on the temperature profile is shown in Figure 8. It is observed that the temperature rises substantially with rising  $E_c$ . The effect of  $s$  and  $\delta$  on the temperature profile is given in Figures 9 and 10. Again, an increase in  $s$  and  $\delta$  causes to decrease the temperature profile. The effect of the thermal radiation  $N$  on the temperature profile is given in Figure 11. The increase in thermal radiations causes to increase the temperature profile, since the thermal radiations increase the kinetic energy of the particles and their collision is caused to rise the temperature profile. The effect of magnetic field on the velocity profile is presented in Figure 12. The increase in magnetic field  $M$  reduces the velocity profile, since the magnetic field is applied perpendicular to the flow, and hence the conducting fluid particles feel the opposite force of magnetic field and hence reduce the velocity profile. The effect of volume fraction of nanofluid on the velocity and temperature profiles is given in Figures 13 and 14, respectively. The increase in volume fraction  $\phi$  decreases the velocity profile whereas increases the temperature profile.

**5.2. Tables' Discussion.** The results of OAFM are validated in comparison with the results obtained from the Runge–Kutta method of order 4 along with absolute errors as given in Tables 1 and 2. The OAFM results obtained at just one iteration provide us a simple way to control the convergence and nearly identical to the results obtained from RKM fourth-order method. The effects of the squeeze number  $S$  on the skin friction coefficient,  $C_f$ , and the Nusselt number,  $Nu_x$ , are given in Table 3. From Table 3, it is obvious that the skin friction coefficient and the Nusselt number are inversely proportional to  $S$ . Table 4 displays the effects of the skin friction coefficient and the Nusselt number for different values of the Eckert number. It is noticed from the table that the effect of increasing values of  $Ec$  is to decrease the skin friction coefficient,  $C_f$ , and the heat transfer rate  $Nu_x$ . Fur-

TABLE 2: Comparison of the value of rate of velocity profile  $\phi(\eta)$  for different value of  $\eta$  when  $S = 0.90$ ,  $Pr = 0.3$ ,  $Ec = 0.5$ ,  $A_1 = 0.1$ ,  $A_2 = 0.5$ ,  $A_3 = 0.7$ ,  $\delta = 0.6$ ,  $M = 1$ .

$\eta$	OAFM	4th RKM	Absolute error
0	0	0	0
0.1	0.14866782146738375	0.14866782146738370	$5.3241 \times 10^{-17}$
0.2	0.29447924328271025	0.29447924328271020	$5.3243 \times 10^{-17}$
0.3	0.4345297029288129	0.4345297029288122	$5.3246 \times 10^{-17}$
0.4	0.5658641096465703	0.5658641096465697	$5.3247 \times 10^{-17}$
0.5	0.6854800169389675	0.6854800169389669	$5.3249 \times 10^{-17}$
0.6	0.7903318397285185	0.7903318397285178	$5.3253 \times 10^{-17}$
0.7	0.8773361110067814	0.8773361110067808	$5.3256 \times 10^{-17}$
0.8	0.9433777722643691	0.9433777722643686	$5.3259 \times 10^{-17}$
0.9	0.9853174912829916	0.9853174912829909	$5.3262 \times 10^{-17}$
1	1.0000000000000002	1.0000000000000007	$1.3263 \times 10^{-16}$

TABLE 3: Comparison of skin friction and Nusselt numbers for various values of  $s$ .

$s$	$C_f$	$Nu_x$
1	-1.24578	0.145875
2	-2.65862	0.0254863
3	-3.54879	0.0354856
4	-3.998547	0.0421586
5	-4.214585	0.0015482

TABLE 4: Comparison of skin friction and Nusselt numbers for various values of  $Ec$ .

$Ec$	$C_f$	$Nu_x$
1	-1.56896	0.025486
2	-2.48523	0.052463
3	-2.012458	0.078563
4	-2.000458	0.0965482

TABLE 5: Comparison of skin friction and Nusselt numbers for various values of  $M$ .

$M$	$C_f$	$Nu_x$
1	-1.53624	0.0215463
2	-1.68459	0.0020012
3	-1.89654	0.015362
4	-2.12546	0.012156

ther, from Table 5, it is concluded that the increasing value of  $M$  decreases the skin friction coefficient and increases the heat rate. The effects of the nanoparticle volume fraction  $\phi$  on the skin friction coefficient  $C_f$  Nusselt number (the

TABLE 6: Comparison of skin friction and Nusselt numbers for various values of  $\varphi$ .

$\varphi$	$C_f$	$Nu_x$
0.10	-1.214655	0.045236
0.20	-1.284562	0.041256
0.30	-1.2954632	0.031256
0.40	-2.59632	0.021548

heat transfer rate)  $Nu$  are given in Table 6. From this table, it is concluded that the increasing value of  $\varphi$  increases the skin friction coefficient and decreases the heat transfer rate.

## 6. Conclusions

In this study, a new analytical method is suggested for the solution of the model problem. We obtain the first-order series solution for the governing equations of the model problem and achieved the first-order solution with high accuracy. For the accuracy and validity of OAFM, results are compared with numerical method. For comparison, it is concluded that the OAFM is very accurate and simple in application. OAFM is very easy in applicable to high nonlinear initial and boundary value problems even if the nonlinear initial/boundary value problem does not contain the small parameter. In comparison with other analytical methods, OAFM is very easy in applicability and provides us good results of more complex nonlinear initial/boundary value problems. OAFM contains the optimal auxiliary constants through which we can control the convergence as OAFM contains the auxiliary functions  $D_1, D_2, D_3, E_4$  in which the optimal constants  $E_m, E_n, E_r, E_p$  and the control convergence parameters exist to play an important role to get the convergent solution which is obtained rigorously. The computational work in OAFM is less when compared to other methods, and even a low specification computer can do the computational work easily. The less computational work and rapid convergent solution at just the first iteration enable us to implement this efficient method in our future work for more complex models arising from real-world problems. The numerical method required maximum space and time as compared to OAFM is the short method and is very rapidly convergent. Numerical methods required to have large computational work and required the latest computer for computational work.

Based on the results and discussion, some points are presented here:

- (i) The motion of the plates represented by squeezing flow is indicated by the squeeze number  $S$ . When  $S > 0$ , the plates are moving separately, but when  $S < 0$ , the plates are moving collectively. Positive and negative squeezing values have distinct effects on the velocity profile. The velocity rises when the absolute value of the squeeze number is 0.5, but drops when it is  $> 0.5$

- (ii) With a large number of  $P_r$ , the temperature distribution obviously decreases, whereas with a small number of  $P_r$ , it grows. Fluids with a low Prandtl number have a higher thermal diffusivity than fluids with a high Prandtl number. A high  $P_r$  causes the thermal boundary layer to decrease as a result. The impact is much more noticeable for a small number of  $P_r$  because the thermal boundary layer thickness is so high
- (iii) The increase in magnetic field  $M$  reduces the velocity profile, since the magnetic field is applied perpendicular to the flow, and hence, the conducting fluid particles feel the opposite force of magnetic field and hence reduce the velocity profile
- (iv) The increase in volume fraction  $\phi$  decreases the velocity profile whereas increases the temperature profile
- (v) An increase in  $s$  and  $\delta$  causes to decrease the temperature profile
- (vi) The skin friction coefficient and the Nusselt number are inversely proportional to  $S$
- (vii) The effect of increasing values of  $E_c$  is to decrease the skin friction coefficient,  $C_f$ , and the heat transfer rate,  $ssNu_x$
- (viii) The increasing value of  $\varphi$  increases the skin friction coefficient and decreases the heat transfer rate

## Abbreviations

- $a, b, c$ : Constants  
 $\tilde{B}$ : Magnetic field ( $NmA^{-1}$ )  
 $C$ : Fluid concentration  
 $c_p$ : Specific heat ( $J/kgK$ )  
 $C_f$ : Skin friction coefficient  
 $D_B$ : Brownian diffusion of nanofluids  
 $D_T$ : Thermophoretic diffusion of nanofluids  
 $\tilde{E}$ : Electric field intensity ( $NC^{-1}$ )  
 $\widehat{F}_1, \widehat{F}_2$ : Homotopic functions  
 $h$ : Distance between the plates  
 $J_w$ : Mass flux  
 $k$ : Thermal conductivity ( $Wm^{-1}K^{-1}$ )  
 $Kr$ : Rotation parameter  
 $k$ : The boundary parameter  
 $M$ : Magnetic parameter  
 $m$ : Hall parameter  
 $n_e$ : Number density of electron  
 $Nb$ : Brownian motion  
 $Nt$ : Thermophoretic parameter  
 $Nu$ : Nusselt number  
 $O$ : Origen  
 $P$ : Fluid pressure ( $Pa$ )  
 $Pr$ : Prandtl number  
 $Q_w$ : Heat flux ( $Wm^{-2}$ )

$q_r$ : Radioactive heat flux ( $J$ )  
 $Re$ : Viscosity parameter  
 $Rd$ : Radiation parameter  
 $R_{ex}$ : Local Reynolds number  
 $S$ : Cauchy stress tensor  
 $Sc$ : Schmidt number  
 $Sh$ : Sherwood number  
 $t_e$ : Flow time ( $s$ )  
 $T$ : Fluid temperature ( $K$ )  
 $u, vw$ : Velocities components ( $ms^{-1}$ )  
 $u_w$ : Stretching velocity ( $ms^{-1}$ )  
 $x, y, z$ : Coordinates  
 $X, Y$ : Topological space

#### Greek Letters:

$\alpha$ : Thermal diffusivity ( $m^2s^{-1}$ )  
 $\eta$ : Similarity variable  
 $\widehat{\kappa}$ : Vertex viscosity ( $mPa$ )  
 $\kappa_m$ : Constants where  $m = 1, 2, ..$   
 $\mu$ : Dynamic viscosity ( $mPa$ )  
 $\nu$ : Kinematic coefficient of viscosity  
 $\rho_f$ : Base fluid density ( $Kgm^{-3}$ )  
 $\rho_b$ : Density of the particles ( $Kgm^{-3}$ )  
 $\sigma_{nf}$ : Electrical conductivity of nanofluid ( $Sm^{-1}$ )  
 $\tau^*$ : Ratio of nanoparticles and heat capacity  
 $\varphi$ : Stefan Boltzmann constant  
 $h$ : Assisting parameter  
 $\Phi$ : Dimensional concentration profile  
 $\omega_e$ : Oscillating frequency of the electron ( $S^{-1}$ )  
 $\Omega$ : Angular velocity ( $ms^{-1}$ ).

#### Data Availability

All the relevant data is available in the manuscript.

#### Conflicts of Interest

All the authors declare that there is no conflict of interest regarding the publication of this paper.

#### References

- [1] S. U. S. Choi and J. A. Estman, "Enhancing thermal conductivity of fluids with nanoparticles," in *1995 International mechanical engineering congress and exhibition*, San Francisco, CA, USA, 1995.
- [2] T. Hayat, M. Khurshed, M. Farooq, and A. Alsaedi, "Squeezed flow subject to Cattaneo-Christov heat flux and rotating frame," *Journal of Molecular Liquids*, vol. 220, pp. 216–222, 2016.
- [3] T. Hayat, M. Waqas, S. A. Shehzad, and A. Alsaedi, "MHD stagnation point flow of Jeffrey fluid by a radially stretching surface with viscous dissipation and Joule heating," *Journal of Hydrology and Hydromechanics*, vol. 63, no. 4, pp. 311–317, 2015.
- [4] M. Sheikholeslami, M. Gorji Bandpy, and S. Soleimani, "Two phase simulation of nanofluid flow and heat transfer using heatline analysis," *International Communications in Heat and Mass Transfer*, vol. 47, pp. 73–81, 2013.
- [5] M. Sheikholeslami, D. D. Ganji, and H. R. Ashorynejad, "Investigation of squeezing unsteady nanofluid flow using ADM," *Powder Technology*, vol. 239, pp. 259–265, 2013.
- [6] E. A. Hamza, "The magneto hydrodynamic effects on a fluid film squeezed between two rotating surfaces," *Journal of Physics D: Applied Physics*, vol. 24, no. 4, pp. 547–554, 1991.
- [7] S. Bhattacharyya and A. Pal, "Unsteady MHD squeezing flow between two parallel rotating discs," *Mechanics Research Communications*, vol. 24, no. 6, pp. 615–623, 1997.
- [8] H. Alfven, "Existence of electromagnetic-hydrodynamic waves," *Nature*, vol. 150, no. 3805, pp. 405–406, 1942.
- [9] M. Abd-El Aziz, "Unsteady fluid and heat flow induced by a stretching sheet with mass transfer and chemical reaction," *Chemical Engineering Communications*, vol. 197, no. 10, pp. 1261–1272, 2010.
- [10] T. Hayat, M. Qasim, and Z. Abbas, "Radiation and mass transfer effects on the magnetohydrodynamic unsteady flow induced by a Stretching sheet," *Zeitschrift für Naturforschung*, vol. 65, no. 3, pp. 231–239, 2010.
- [11] M. Sheikholeslami, M. Hatami, and G. Domairry, "Numerical simulation of two phase unsteady nanofluid flow and heat transfer between parallel plates in presence of time dependent magnetic field," *Journal of the Taiwan Institute of Chemical Engineers*, vol. 46, pp. 43–50, 2015.
- [12] M. A. Sheremet, T. Grosan, and I. Pop, "Free convection in a square cavity filled with a porous medium saturated by nanofluid using Tiwari and Das' nanofluid model," *Transport in Porous Media*, vol. 106, no. 3, pp. 595–610, 2015.
- [13] M. A. Sheremet, I. Pop, and M. M. Rahman, "Three-dimensional natural convection in a porous enclosure filled with a nanofluid using Buongiorno's mathematical model," *International Journal of Heat and Mass Transfer*, vol. 82, pp. 396–405, 2015.
- [14] M. A. Sheremet, I. Pop, and N. C. Rosca, "Magnetic field effect on the unsteady natural convection in a wavy-walled cavity filled with a nanofluid: Buongiorno's mathematical model," *Journal of the Taiwan Institute of Chemical Engineers*, vol. 61, pp. 211–222, 2016.
- [15] N. S. Bondareva, M. A. Sheremet, and I. Pop, "Magnetic field effect on the unsteady natural convection in a right-angle trapezoidal cavity filled with a nanofluid," *International Journal of Numerical Methods for Heat and Fluid Flow*, vol. 25, no. 8, pp. 1924–1946, 2015.
- [16] M. Sheikholeslami and D. D. Ganji, "Nanofluid flow and heat transfer between parallel plates considering Brownian motion using DTM," *Computer Methods in Applied Mechanics and Engineering*, vol. 283, pp. 651–663, 2015.
- [17] M. Sheikholeslami, D. D. Ganji, M. Younus Javed, and R. Ellahi, "Effect of thermal radiation on magnetohydrodynamics nanofluid flow and heat transfer by means of two phase model," *Journal of Magnetism and Magnetic Materials*, vol. 374, pp. 36–43, 2015.
- [18] M. Sheikholeslami, M. M. Rashidi, and D. D. Ganji, "Ferrofluid flow and heat transfer in a semi annulus enclosure in the presence of magnetic source considering thermal radiation," *Journal of the Taiwan Institute of Chemical Engineers*, vol. 47, pp. 6–17, 2015.
- [19] M. Barzegar Gerdroodbary, M. Rahimi Takami, and D. D. Ganji, "Investigation of Thermal Radiation on Traditional Jeffery-Hamel flow to stretchable convergent/divergent channels," *Case Studies in Thermal Engineering*, vol. 6, pp. 28–39, 2015.



- [20] S. G. Martyushev and M. A. Sheremet, "Characteristics of Rosseland and P-1 approximations in modeling nonstationary conditions of convection-radiation heat transfer in an enclosure with a local energy source," *Journal of Engineering Thermophysics*, vol. 21, no. 2, pp. 111–118, 2012.
- [21] A. Y. Bakier, "Thermal radiation effect on mixed convection from vertical surface in saturated porous media," *International Communications in Heat and Mass Transfer*, vol. 28, no. 1, pp. 119–126, 2001.
- [22] R. A. Damseh, "Magnetohydrodynamics-mixed convection from radiate vertical isothermal surface embedded in a saturated porous media," *Journal of Applied Mechanics*, vol. 73, no. 1, pp. 54–59, 2006.
- [23] A. Saeed, P. Kumam, T. Gul, W. Alghamdi, W. Kumam, and A. Khan, "Darcy-Forchheimer couple stress hybrid nanofluids flow with variable fluid properties," *Scientific Reports*, vol. 11, no. 1, pp. 1–13, 2021.
- [24] A. Saeed, P. Kumam, S. Nasir, T. Gul, and W. Kumam, "Non-linear convective flow of the thin film nanofluid over an inclined stretching surface," *Scientific Reports*, vol. 11, no. 1, pp. 1–15, 2021.
- [25] A. Rehman, Z. Salleh, and T. Gul, "Heat transfer of thin film flow over an unsteady stretching sheet with dynamic viscosity," *Journal of Advanced Research in Fluid Mechanics and Thermal Sciences*, vol. 81, no. 2, pp. 67–81, 2021.
- [26] M. Bilal, A. Saeed, T. Gul, I. Ali, W. Kumam, and P. Kumam, "Numerical approximation of microorganisms hybrid nanofluid flow induced by a wavy fluctuating spinning disc," *Coatings*, vol. 11, no. 9, p. 1032, 2021.
- [27] E. K. Blum, "A modification of the Runge–Kutta fourth-order method," *Mathematics of Computation*, vol. 16, no. 78, pp. 176–187, 1962.
- [28] J. C. Butcher, "The non-existence of ten stage eighth order explicit Runge–Kutta methods," *BIT*, vol. 25, no. 3, pp. 521–540, 1985.
- [29] J. C. Butcher, *The Numerical Analysis of Ordinary Differential Equations*, Wiley, New York, 1987.
- [30] M. H. Carpenter and C. A. Kennedy, *Fourth-Order 2N-Storage Runge–Kutta Schemes*, no. article 109112, 1994NASA TM, 1994.
- [31] M. Bilal, A. Saeed, M. M. Selim, T. Gul, I. Ali, and P. Kumam, "Comparative numerical analysis of Maxwell's time-dependent thermo-diffusive flow through a stretching cylinder," *Case studies in Thermal Engineering*, vol. 27, article 101301, 2021.
- [32] Z. Shah, P. Kumam, A. Dawar, and P. Thounthong, "Study of the couple stress convective micropolar fluid flow in a hall MHD generator system," *Frontiers in Physics*, vol. 7, p. 171, 2019.
- [33] A. Dawar, Z. Shah, and P. Kumam, "Chemically reactive MHD micropolar nanofluid flow with velocity slips and variable heat source/sink," *Scientific Reports*, vol. 10, no. 1, pp. 1–23, 2020.
- [34] A. Dawar, Z. Shah, and S. Islam, "A comparative analysis of MHD Casson and Maxwell flows past a stretching sheet with mixed convection and chemical reaction," *Waves in Random and Complex Media*, vol. 25, 2021.
- [35] S. G. Bejawada, Y. D. Reddy, W. Jamshed, K. S. Nisar, A. N. Alharbi, and R. Chouikh, "Radiation effect on MHD Casson fluid flow over an inclined non-linear surface with chemical reaction in a Forchheimer porous medium," *Alexandria Engineering Journal*, vol. 61, no. 10, pp. 8207–8220, 2022.
- [36] T. C. Sun, I. Uddin, M. A. Zahoor Raja et al., "Numerical investigation of thin-film flow over a rotating disk subject to the heat source and nonlinear radiation: Lobatto IIIA approach," *Waves in Random and Complex Media*, vol. 10, pp. 1–15, 2022.
- [37] W. Jamshed, R. Safdar, A. Brahmia, A. K. Alanazi, H. M. Abo-Dief, and M. R. Eid, "Numerical simulations of environmental energy features in solar pump application by using hybrid nanofluid flow: Prandtl-Eyring case," *Energy & Environment*, vol. 15, pp. 1–44, 2022.
- [38] F. Shahzad, W. Jamshed, A. Koulali et al., "Computational examination of Jeffrey nanofluid through a stretchable surface employing Tiwari and Das model," *Open Physics*, vol. 19, no. 1, pp. 897–911, 2021.
- [39] W. Jamshed, A. K. Alanazi, S. S. P. Mohamed Isa et al., "Thermal efficiency enhancement of solar aircraft by utilizing unsteady hybrid nanofluid: a single-phase optimized entropy analysis," *Sustainable Energy Technologies and Assessments*, vol. 52, article 101898, 2021.
- [40] S. G. Bejawada, W. Jamshed, R. Safdar et al., "Chemical reactive and viscous dissipative flow of magneto nanofluid via natural convection by employing Galerkin finite element technique," *Coatings*, vol. 12, p. 151, 2022.
- [41] S. E. Alhazmi, F. Wang, U. Nazir et al., "Utilization of modified fluxes on thermal and mass transportation in Williamson material," *Advances in Mechanical Engineering*, vol. 14, no. 1, 2022.
- [42] M. Ouni, L. M. Ladhar, M. Omri, W. Jamshed, and M. R. Eid, "Solar water-pump thermal analysis utilizing copper–gold/engine oil hybrid nanofluid flowing in parabolic trough solar collector: thermal case study," *Case Studies in Thermal Engineering*, vol. 30, p. 101756, 2022.
- [43] N. Herisanu and V. Marinca, "An efficient analytical approach to investigate the dynamics of a misaligned multirotor system," *Mathematics*, vol. 8, no. 7, p. 1083, 2020.
- [44] N. Herisanu, V. Marinca, G. Madescu, and F. Dragan, "Dynamic response of a permanent magnet synchronous generator to a wind gust," *Energies*, vol. 12, no. 5, p. 915, 2019.

## Research Article

# Analytical Approximate Solution of the Fractional Order Biological Population Model by Using Natural Transform

Nasir Ali,<sup>1</sup> Rashid Nawaz ,<sup>1</sup> Laiq Zada ,<sup>1</sup> Abir Mouldi,<sup>2</sup> Souhail Mohamed Bouzgarrou,<sup>3</sup> and Ndolane Sene <sup>4</sup>

<sup>1</sup>Department of Mathematics, Abdul Wali Khan University, Mardan, KP, Pakistan

<sup>2</sup>Department of Industrial Engineering, College of Engineering, King Khalid University, Abha 61421, Saudi Arabia

<sup>3</sup>Department of Civil Engineering, Faculty of Engineering, Jazan University, Saudi Arabia

<sup>4</sup>Laboratoire Lmdan, Departement De Mathematiques De Decision, Facultie des Sciences Economiques et Gestion, Universite Cheikh Anta Diop De Dakar, Fann, BP 5683 Dakar, Senegal

Correspondence should be addressed to Ndolane Sene; [ndolanesene@yahoo.fr](mailto:ndolanesene@yahoo.fr)

Received 14 January 2022; Revised 6 February 2022; Accepted 24 February 2022; Published 19 March 2022

Academic Editor: Taza Gul

Copyright © 2022 Nasir Ali et al. This is an open access article distributed under the Creative Commons Attribution License, which permits unrestricted use, distribution, and reproduction in any medium, provided the original work is properly cited.

In the present work, the natural transform iterative method (NTIM) is implemented to solve the biological population model (BPM) of fractional order. The method is tested for three nonlinear examples. The NTIM is a combination of a new iterative method and natural transform. We see that the solution pattern converges to the exact solution in a few iterations. The method handles an extensive range of differential equations of both fractional and integer order. The fractional order derivative is considered in Caputo's sense. For mathematical computation, Mathematica 10 is used.

## 1. Introduction

The globe and our everyday lives have been revolutionized by modern technologies. Technology is being used in a wide range of engineering applications, including aerodynamics, fluid dynamics, medical sciences, and finance. The essence of technology is influenced and designed by mathematical modeling. The modeling might take the form of mathematical models that can be described using differential equations. These differential equations may have been used to represent the transmission of electromagnetic waves, which is at the root of many present technologies. A variety of applications ranging from wireless communications to radar, medical imaging, and remote sensing have played a great role in our life [1, 2]. Mathematics and biosciences have also numerous practical applications related to real life [3, 4]. Several diseases can be modeled through mathematical calculations and can be controlled by collecting data and making precise analysis [5]. There is a strong and interesting relationship between biology and mathematics utilizing differential equations. The noninteger order differential equations are termed as fractional order

differential equations (FDEs) [32–35]. The branch of mathematics dealing with FDEs is known as fractional calculus [6]. Depending on the nature of the problem, differential equations can be linear or nonlinear. Simple analytical methods may be used to analyze linear differential equations, but investigators have developed several ways for solving nonlinear differential equations as their exact solutions are not always feasible. The importance of the FDEs can be discussed in many fields of sciences [7, 23–27]. Many operators for fractional derivatives have been given by several researchers. The most famous is Caputo's fractional derivative operator [8]. Li et al. introduced the fractional order integral operator for handling differential equations [9]. Recently, many transformations have been used to solve fractional order differential equations. Some of them are the Laplace transform, Sumudu transform, Elzaki transform, etc. [10–12, 28–31]. In this work, we will deal with the natural transform iterative method (NTIM), a combination of the natural transform and the new iterative method (NIM). The proposed techniques have been recently applied by Nawaz et al. for solving noninteger order differential equations [13]. Many other researchers have applied NIM

and natural transform for handling the FDEs [14–17]. In this article, we will consider fractional biological population model (FBPM) as [18]

$$\begin{cases} D_t^\beta \phi = (\phi^2)_{xx} + (\phi^2)_{yy} + f(\phi) = 0, 0 < \beta \leq 1, t > 0, (x, y) \in R^2, \\ f(\phi) = h\phi^a(1 - r\phi^b), \end{cases} \quad \phi(x, y, 0) = g(x, y). \quad (1)$$

In Equation (1),  $\phi = \phi(x, y, t)$  is the population density and  $f$  is the supply of population due to births and deaths. The  $h, a, b,$  and  $r$  are the real numbers and  $g(x, y)$  is the initial condition. The detailed solution of Equation (1) can be found in [19, 20]. FBPM is a mathematical model of biology which will be thoroughly investigated in this paper. FBPM aids in the understanding of the dynamical procedure of population changes in biological population models, as well as providing useful predictions.

The remaining paper is structured as follows: Preliminary definitions from fractional calculus are contained in Section 2. The notion of NTIM is introduced in Section 3. The NTIM is used to solve three FBPM in Section 4. In Section 5, some results have been discussed. Lastly, a concrete conclusion is given.

## 2. Preliminaries

*Definition 1.* Riemann-Liouville (R-L) fractional integral is defined as

$$\begin{aligned} J_t^\beta f(t) &= \frac{1}{\Gamma(\beta)} \int_0^t (t - \tau)^{\beta-1} f(\tau) d\tau, (\beta > 0, t > 0), \\ J_t^0 f(t) &= f(t), \end{aligned} \quad (2)$$

where  $\Gamma(\cdot)$  is the gamma function.

*Definition 2.* Caputo's time-fractional derivative operator of order  $\beta > 0$  is defined as

$$D_t^\beta \phi(\varrho, t) = \frac{\partial^\beta \phi(\varrho, t)}{\partial t^\beta} = \begin{cases} \frac{1}{\Gamma(n - \beta)} \int_0^t (t - \tau)^{n-\beta-1} \frac{\partial^n \phi(\varrho, \tau)}{\partial \tau^n}, & \text{if } n - 1 < \beta < n, \\ \frac{\partial^n \phi(\varrho, t)}{\partial t^n}, & \text{if } \beta = n \in N. \end{cases} \quad (3)$$

*Definition 3.* Natural transform of  $\phi(t)$  is defined as [21]

$$\mathbb{N}^+(\theta(t)) = R(s, \nu) = \frac{1}{\nu} \int_0^\infty e^{-\frac{st}{\nu}} (\phi(t)) dt; \quad s, \nu > 0, \quad (4)$$

where  $s$  and  $\nu$  are the transform variables.

*Definition 4.* The inverse of natural transform of  $R(s, \nu)$  is defined as

$$\mathbb{N}^-(R(s, \nu)) = \phi(t) = \frac{1}{2\pi i} \int_{c-i\infty}^{c+i\infty} e^{\frac{st}{\nu}} (R(s, \nu)) ds, \quad (5)$$

where  $c \in R$  and the integral are taken in the complex plane  $s = a + bi$  along  $s = c$ .

*Definition 5.* If the  $n$ th derivative of  $\phi(t)$  is  $\phi^n(t)$ , then its natural transform is given as

$$\mathbb{N}^+(\phi^n(t)) = R_n(s, \nu) = \frac{s^n}{\nu^n} R(s, \nu) - \sum_{k=0}^{n-1} \frac{s^{n-(k+1)}}{\nu^{n-k}} (\phi^n(0)), \quad n \geq 1. \quad (6)$$

**Theorem 6.** If the natural transform of  $h(t)$  and  $k(t)$  are  $h(s, \nu)$  and  $k(s, \nu)$  respectively, defined on set  $A$ , then

$$\mathbb{N}[h * k] = \nu H(s, \nu) K(s, \nu), \quad (7)$$

where  $\mathbb{N}[h * k]$  is convolution the functions  $h$  and  $k$ .

## 3. Natural Transform Iterative Method (NTIM) [13]

Consider FDE of the form

$$D_t^\beta (\phi(\varrho, t)) = f(\varrho, t) + L\phi(\varrho, t) + \mathbb{N}\phi(\varrho, t), 0\varrho, t > 0, m - 1 < \alpha < m, \quad (8)$$

where  $\varrho = x_1, x_2, \dots, x_n$  and  $m \in N$ . The linear operator, non-linear operator, and the source term are  $L, \mathbb{N}$ , and  $f$ , respectively. The initial condition is given as

$$\phi(\varrho, 0) = g(\varrho). \quad (9)$$

By applying the natural transform to Equation (8), we have

$$\mathbb{N}^+ \left[ D_t^\beta (\phi(\varrho, t)) \right] = \mathbb{N}^+ [f(\varrho, t)] + \mathbb{N}^+ [L(\phi(\varrho, t)) + \mathbb{N}(\phi(\varrho, t))]. \quad (10)$$

Using the natural transform differentiation property, Equation (10) can be written as

$$\frac{s^\beta}{\nu^\beta} \mathbb{N}^+ [\phi(\varrho, t)] - \frac{s^{\beta-1}}{\nu^\beta} \phi(\varrho, 0) = \mathbb{N}^+ [f(\varrho, t)] + \mathbb{N}^+ [L(\phi(\varrho, t)) + \mathbb{N}(\phi(\varrho, t))]. \quad (11)$$

By rearranging Equation (11), we have

$$\mathbb{N}^+ [\phi(\varrho, t)] = \frac{g(\varrho)}{s} + \frac{\nu^\beta}{s^\beta} (\mathbb{N}^+ [f(\varrho, t)]) + \frac{\nu^\beta}{s^\beta} (\mathbb{N}^+ [L(\phi(\varrho, t)) + \mathbb{N}(\phi(\varrho, t))]). \quad (12)$$

For the NTIM solution,  $\phi(\varrho, t)$  is expanded as

$$u(\varrho, t) = \sum_{i=0}^{\infty} \phi_i(\varrho, t), \quad (13)$$

and  $\aleph(\phi(\varrho, t))$ , the nonlinear term, is defined as

$$\aleph\left(\sum_{m=0}^{\infty} \phi_m(\varrho, t)\right) = \aleph(\phi_0(\varrho, t)) + \sum_{m=1}^{\infty} \left\{ \aleph\left(\sum_{j=0}^m \phi_j(\varrho, t)\right) - \aleph\left(\sum_{j=0}^{m-1} \phi_j(\varrho, t)\right) \right\}. \quad (14)$$

Using Equation (13) and Equation (14) in Equation (12), we obtain

$$\begin{aligned} \mathbb{N}^+ \left[ \sum_{i=1}^{\infty} \phi_i \right] &= \frac{g(\varrho)}{s} + \frac{\nu^\beta}{s^\beta} (\mathbb{N}^+[f(\varrho, t)]) \\ &+ \frac{\nu^\beta}{s^\beta} \left[ \mathbb{N}^+ \left[ \sum_{m=0}^{\infty} L(\phi_m) + \aleph(\phi_0) + \sum_{m=1}^{\infty} \left\{ \aleph\left(\sum_{j=0}^m \phi_j\right) - \aleph\left(\sum_{j=0}^{m-1} \phi_j\right) \right\} \right] \right]. \end{aligned} \quad (15)$$

Using the recursive relation,

$$\begin{aligned} \mathbb{N}^+[\phi_0(\varrho, t)] &= \frac{g(\varrho)}{s} + \frac{\nu^\beta}{s^\beta} \mathbb{N}^+[f(\varrho, t)], \\ \mathbb{N}^+[\phi_1(\varrho, t)] &= \frac{\nu^\beta}{s^\beta} \mathbb{N}^+[L(\phi_0) + \aleph(\phi_0)], \\ \mathbb{N}^+[\phi_2(\varrho, t)] &= \frac{\nu^\beta}{s^\beta} \mathbb{N}^+[L(\phi_1 + \phi_0) + \aleph(\phi_0 + \phi_1) - \aleph(\phi_0)] \\ &\vdots \\ \mathbb{N}^+[\phi_{i+1}(\varrho, t)] &= \frac{\nu^\beta}{s^\beta} \mathbb{N}^+[L(\phi_i) + \aleph(\phi_0 + \phi_1 + \dots + \phi_i) - \aleph(\phi_0 + \phi_1 + \dots + \phi_{i-1})], i \geq 0. \end{aligned} \quad (16)$$

Now by taking the inverse natural transform of Equation (16), we have

$$\begin{aligned} \phi_0(\varrho, t) &= \mathbb{N}^- \left[ \frac{g(\varrho)}{s} + \frac{\nu^\beta}{s^\beta} \mathbb{N}^+[f] \right], \\ \phi_1(\varrho, t) &= \mathbb{N}^- \left[ \frac{\nu^\beta}{s^\beta} \mathbb{N}^+[L(\phi_0) + \aleph(\phi_0)] \right], \\ \phi_2(\varrho, t) &= \mathbb{N}^- \left[ \frac{\nu^\beta}{s^\beta} \mathbb{N}^+[L(\phi_1) + \aleph(\phi_0 + \phi_1) - \aleph(\phi_0)] \right], \\ &\vdots \\ \phi_{i+1}(\varrho, t) &= \mathbb{N}^- \left[ \frac{\nu^\beta}{s^\beta} \mathbb{N}^+[L(\phi_i) + \aleph(\phi_0 + \phi_1 + \dots + \phi_i) - \aleph(\phi_0 + \phi_1 + \dots + \phi_{i-1})] \right], i \geq 0. \end{aligned} \quad (17)$$

Then by adding the components, the approximate solution of Equations (8) and (9) by NITM is given as

$$\phi(\varrho, t) = \phi_0(\varrho, t) + \phi_1(\varrho, t) + \dots + \phi_{m-1}(\varrho, t), m \in \mathbb{N}. \quad (18)$$

Convergence of NTIM is as a convergence of NIM and is proved by Bhalekar and Daftardar-Gejji [22].

#### 4. Applications of NTIM

In this section, we apply the natural transform iterative method NTIM for handling the three nonlinear cases of FBPM. The method is applied directly to the problems without any discretization by using the given initial conditions. Then, the comparison is made with the help of plots and numerical tables

with the existing methods which shows the effectiveness of the proposed method [18].

*Problem 7.* Consider the population model as [18]

$$D_t^\beta \phi = (\phi^2)_{xx} + (\phi^2)_{yy} + h\phi, \quad t > 0, 0 < \beta \leq 1, \quad (19)$$

where  $\phi = \phi(x, y, t)$  together with initial conditions

$$\phi(x, y, 0) = \sqrt{xy}, \quad (20)$$

and the exact solution is

$$\phi(x, y, z, t) = \sqrt{xy} e^{ht}. \quad (21)$$

Taking natural transformation of Equation (19), we have

$$\mathbb{N}^+ [D_t^\beta \phi] = \mathbb{N}^+ [(\phi^2)_{xx} + (\phi^2)_{yy} + h\phi]. \quad (22)$$

Applying the natural transform differentiation property to Equation (22), we get

$$\frac{s^\beta}{\nu^\beta} \phi(x, y, t) - \frac{\nu^{\beta-1}}{s^\beta} \phi(x, y, 0) = \mathbb{N}^+ [(\phi^2)_{xx} + (\phi^2)_{yy} + h\phi]. \quad (23)$$

Taking the inverse natural transform of Equation (23), we have

$$\phi(x, y, t) = \frac{\phi(x, y, 0)}{s} + \mathbb{N}^- \left[ \frac{\nu^\beta}{s^\beta} \mathbb{N}^+ [(\phi^2)_{xx} + (\phi^2)_{yy} + h\phi] \right]. \quad (24)$$

Using the idea of NTIM and the recursive relation of Equation (16), we obtained the solution components as

$$\left\{ \begin{aligned} \phi_0(x, y, t) &= \mathbb{N}^- \left[ \frac{\phi(x, y, 0)}{s} \right], \\ \phi_1(x, y, t) &= \mathbb{N}^- \left[ \frac{\nu^\alpha}{s^\alpha} \mathbb{N}^+ [(\phi_0^2)_{xx} + (\phi_0^2)_{yy} + h\phi_0] \right], \\ \phi_2(x, y, t) &= \mathbb{N}^- \left[ \frac{\nu^\alpha}{s^\alpha} \mathbb{N}^+ [(\phi_0 + \phi_1)^2_{xx} + (\phi_0 + \phi_1)^2_{yy} + h\phi_1 - ((\phi_0^2)_{xx} + (\phi_0^2)_{yy})] \right], \\ \phi_3(x, y, t) &= \mathbb{N}^- \left[ \frac{\nu^\alpha}{s^\alpha} \mathbb{N}^+ \left[ (\phi_0 + \phi_1 + \phi_2)^2_{xx} + (\phi_0 + \phi_1 + \phi_2)^2_{yy} + h\phi_2 \right. \right. \\ &\quad \left. \left. - (\phi_0 + \phi_1)^2_{xx} + (\phi_0 + \phi_1)^2_{yy} \right] \right], \\ &\vdots \end{aligned} \right. \quad (25)$$

By using the software package, the solution components are obtained as

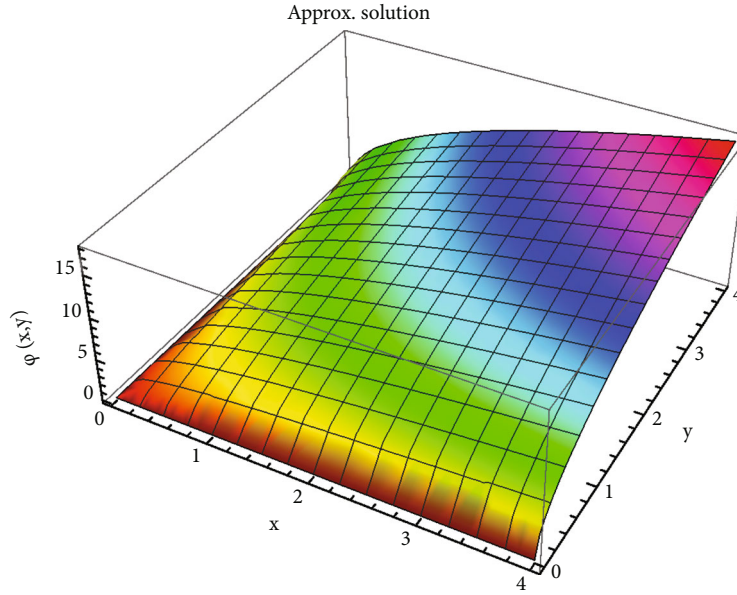


FIGURE 1: NTIM solution of problem 1 at  $h = 1$ ,  $t = 1.5$ , and  $\beta = 1$ .

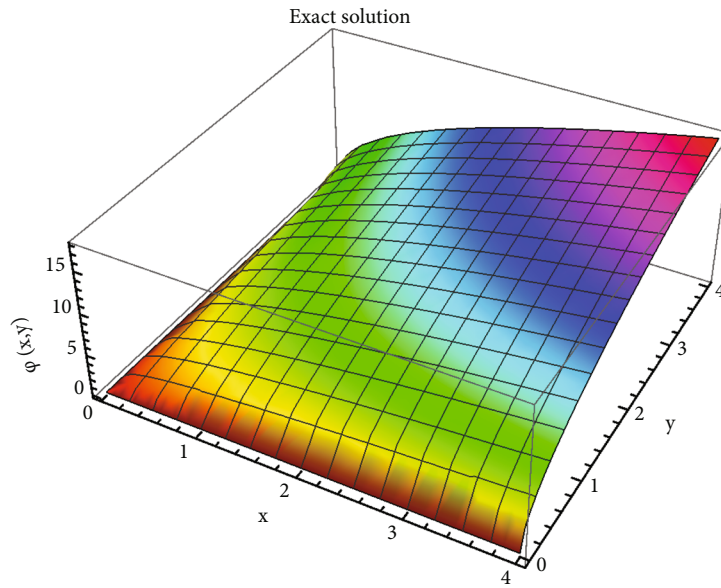


FIGURE 2: Exact solution of problem 1 at  $h = 1$ ,  $t = 1.5$ , and  $\beta = 1$ .

$$\left\{ \begin{array}{l} \phi_0(x, y, t) = \sqrt{xy}, \phi_1(x, y, t) = \frac{ht^\beta \sqrt{xy}}{\Gamma(\beta + 1)}, \\ \phi_2(x, y, t) = \frac{h^2 t^{2\beta} \sqrt{xy}}{\Gamma(2\beta + 1)}, \phi_3(x, y, t) = \frac{h^3 t^{3\beta} \sqrt{xy}}{\Gamma(3\beta + 1)}, \\ \phi_4(x, y, t) = \frac{h^4 t^{4\beta} \sqrt{xy}}{\Gamma(4\beta + 1)}, \\ \vdots \end{array} \right. \quad (26)$$

$$\begin{aligned} \phi(x, y, t) &= \phi_0 + \phi_1 + \phi_2 + \phi_3 + \phi_4 + \dots \\ &= \dots \left\{ \sqrt{xy} + \frac{ht^\beta \sqrt{xy}}{\Gamma(\beta + 1)} + \frac{h^2 t^{2\beta} \sqrt{xy}}{\Gamma(2\beta + 1)} + \frac{h^3 t^{3\beta} \sqrt{xy}}{\Gamma(3\beta + 1)} + \frac{h^4 t^{4\beta} \sqrt{xy}}{\Gamma(4\beta + 1)} + \dots \right\}. \end{aligned} \quad (27)$$

Equation (27) can be simplified as

$$\phi(x, y, t) = \sqrt{xy} \left( \frac{ht^\beta}{\Gamma(\beta + 1)} + \frac{h^2 t^{2\beta}}{\Gamma(2\beta + 1)} + \frac{h^3 t^{3\beta}}{\Gamma(3\beta + 1)} + \frac{h^4 t^{4\beta}}{\Gamma(4\beta + 1)} + \dots \right). \quad (28)$$

Combining the components, the 4<sup>th</sup> order approximate solution is given as

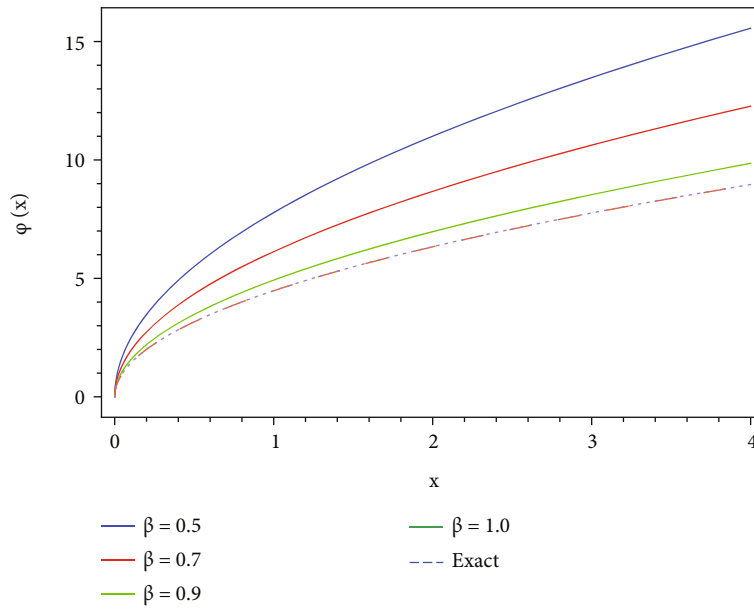


FIGURE 3: Comparison of an approximate solution by NTIM for different values of  $\beta$  at  $h = 1, t = 1.5,$  and  $y = 1$  for Problem 7.

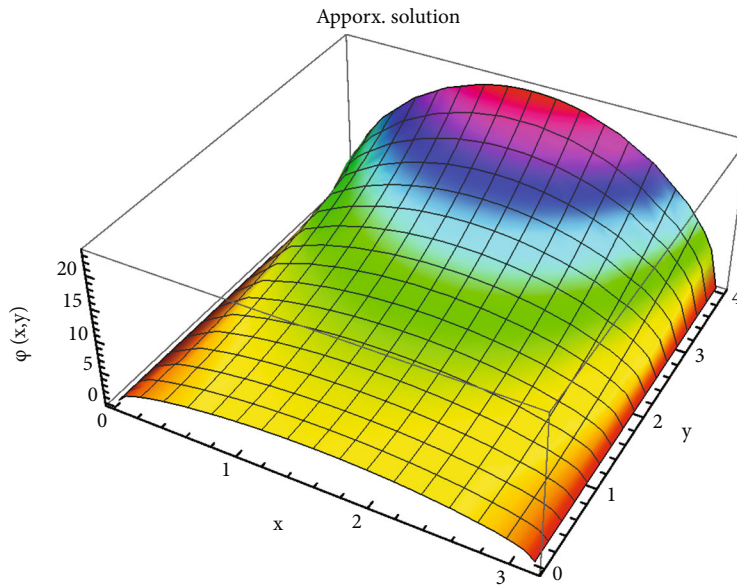


FIGURE 4: NTIM Solution of problem 1 at  $t = 1.5$  and  $\beta = 1.$

For  $\beta = 1,$  Equation (28) converges as

$$\phi(x, y, t) = \sqrt{xy} \left( 1 + ht + \frac{(ht)^2}{2!} + \frac{(ht)^3}{3!} + \frac{(ht)^4}{4!} + \dots \right), \quad (29)$$

which converges to the exact solution given by Equation (21).

*Problem 8.* Consider the biological population model as [18]

$$D_t^\beta \phi = (\phi^2)_{xx} + (\phi^2)_{yy} + \phi, \quad t > 0, 0 < \beta \leq 1, \quad (30)$$

where  $\phi = \phi(x, y, t)$  together with initial conditions

$$\phi(x, y, 0) = \sqrt{\sin(x) \cosh(y)}, \quad (31)$$

and the exact solution is

$$\phi(x, y, t) = \sqrt{\sin(x) \cosh(y)} e^t. \quad (32)$$

Taking natural transform of Equation (30), we have

$$\mathbb{N}^+ [D_t^\beta \phi] = \mathbb{N}^+ [(\phi^2)_{xx} + (\phi^2)_{yy} + \phi]. \quad (33)$$

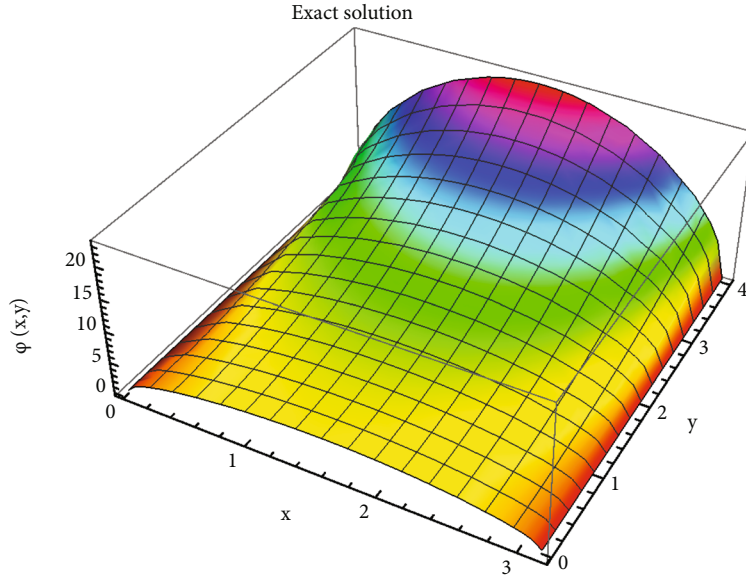


FIGURE 5: Exact solution of problem 1 at  $t = 1.5$  and  $\beta = 1$ .

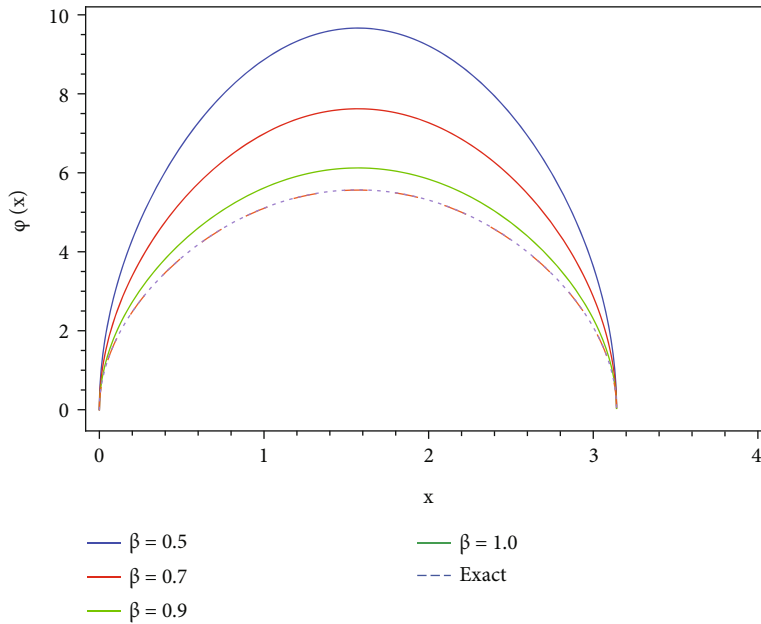


FIGURE 6: Comparison of the approximate solution by NTIM for different values of  $\beta$  at  $t = 1.5$  and  $y = 1$  for Problem 8.

Using the natural transform differentiation property, we obtain

$$\frac{s^\beta}{\nu^\beta} \phi(x, y, t) - \frac{\nu^{\beta-1}}{s^\beta} \phi(x, y, 0) = \mathbb{N}^+ \left[ (\phi^2)_{xx} + (\phi^2)_{yy} + \phi \right]. \tag{34}$$

Taking the inverse natural transform, we have

$$\phi(x, y, t) = \frac{\phi(x, y, 0)}{s} + \mathbb{N}^- \left[ \frac{\nu^\beta}{s^\beta} \mathbb{N}^+ \left[ (\phi^2)_{xx} + (\phi^2)_{yy} + \phi \right] \right]. \tag{35}$$

Using the recursive relation, the solution components can be obtained as

$$\left\{ \begin{aligned} \phi_0(x, y, t) &= \mathbb{N}^- \left[ \frac{\phi(x, y, 0)}{s} \right], \\ \phi_1(x, y, t) &= \mathbb{N}^- \left[ \frac{\nu^\alpha}{s^\alpha} \mathbb{N}^+ \left[ (\phi_0^2)_{xx} + (\phi_0^2)_{yy} + \phi_0 \right] \right], \\ \phi_2(x, y, t) &= \mathbb{N}^- \left[ \frac{\nu^\alpha}{s^\alpha} \mathbb{N}^+ \left[ (\phi_0 + \phi_1)^2_{xx} + (\phi_0 + \phi_1)^2_{yy} + \phi_1 - \left( (\phi_0^2)_{xx} + (\phi_0^2)_{yy} \right) \right] \right], \\ \phi_3(x, y, t) &= \mathbb{N}^- \left[ \frac{\nu^\alpha}{s^\alpha} \mathbb{N}^+ \left[ (\phi_0 + \phi_1 + \phi_2)^2_{xx} + (\phi_0 + \phi_1 + \phi_2)^2_{yy} + \phi_2 \right. \right. \\ &\quad \left. \left. - (\phi_0 + \phi_1)^2_{xx} - (\phi_0 + \phi_1)^2_{yy} \right] \right], \\ &\vdots \end{aligned} \right. \tag{36}$$

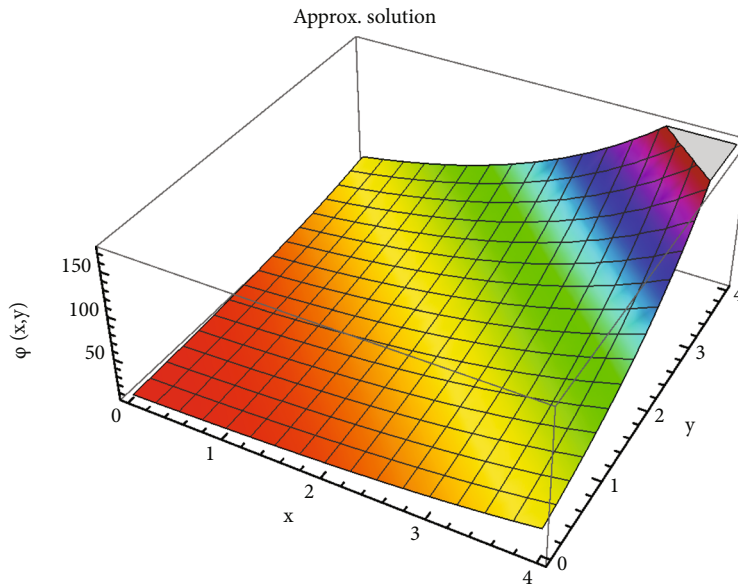


FIGURE 7: NTIM solution of Problem 7 at  $h = 1$ ,  $t = 1.5$ , and  $\beta = 1$ .

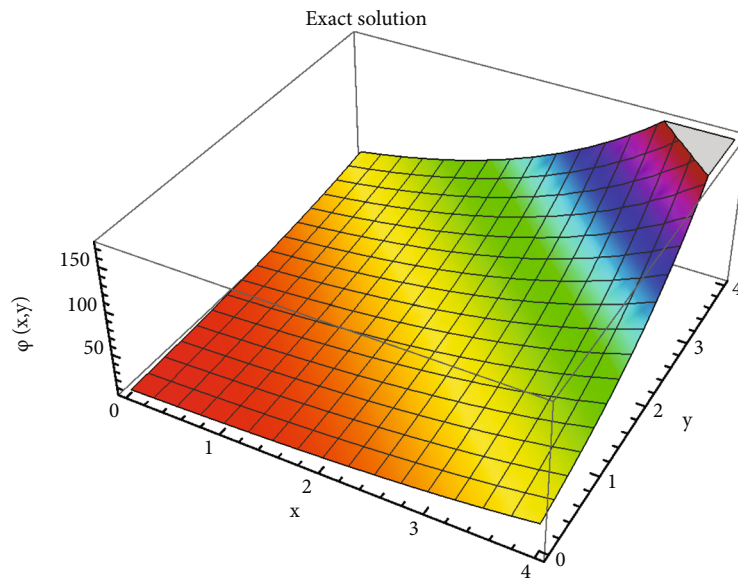


FIGURE 8: Exact solution of Problem 7 at  $h = 1$ ,  $t = 1.5$ , and  $\beta = 1$ .

By using the software package, the solution components are obtained as

$$\left\{ \begin{array}{l} \phi_0(x, y, t) = \sqrt{\sin(x) \cosh(y)}, \phi_1(x, y, t) = \frac{t^\beta \sqrt{\sin(x) \cosh(y)}}{\Gamma(\beta + 1)}, \\ \phi_2(x, y, t) = \frac{t^{2\beta} \sqrt{\sin(x) \cosh(y)}}{\Gamma(2\beta + 1)}, \phi_3(x, y, t) = \frac{t^{3\beta} \sqrt{\sin(x) \cosh(y)}}{\Gamma(3\beta + 1)}, \\ \phi_4(x, y, t) = \frac{t^{4\beta} \sqrt{\sin(x) \cosh(y)}}{\Gamma(4\beta + 1)}, \\ \vdots \end{array} \right. \quad (37)$$

Combining the components, the 4<sup>th</sup> order approximate solution is given as

$$\phi(x, y, t) = \phi_0 + \phi_1 + \phi_2 + \phi_3 + \phi_4 + \dots$$

$$= \left\{ \begin{array}{l} \sqrt{\sin(x) \cosh(y)} + \frac{t^\beta \sqrt{\sin(x) \cosh(y)}}{\Gamma(\beta + 1)} + \frac{t^{2\beta} \sqrt{\sin(x) \cosh(y)}}{\Gamma(2\beta + 1)} \\ + \frac{t^{3\beta} \sqrt{\sin(x) \cosh(y)}}{\Gamma(3\beta + 1)} + \frac{t^{4\beta} \sqrt{\sin(x) \cosh(y)}}{\Gamma(4\beta + 1)} + \dots \end{array} \right. \quad (38)$$

Equation (38) can be simplified as

$$\phi(x, y, t) = \sqrt{\sin(x) \cosh(y)} \left( \frac{t^\beta}{\Gamma(\beta + 1)} + \frac{t^{2\beta}}{\Gamma(2\beta + 1)} + \frac{t^{3\beta}}{\Gamma(3\beta + 1)} + \frac{t^{4\beta}}{\Gamma(4\beta + 1)} + \dots \right). \quad (39)$$



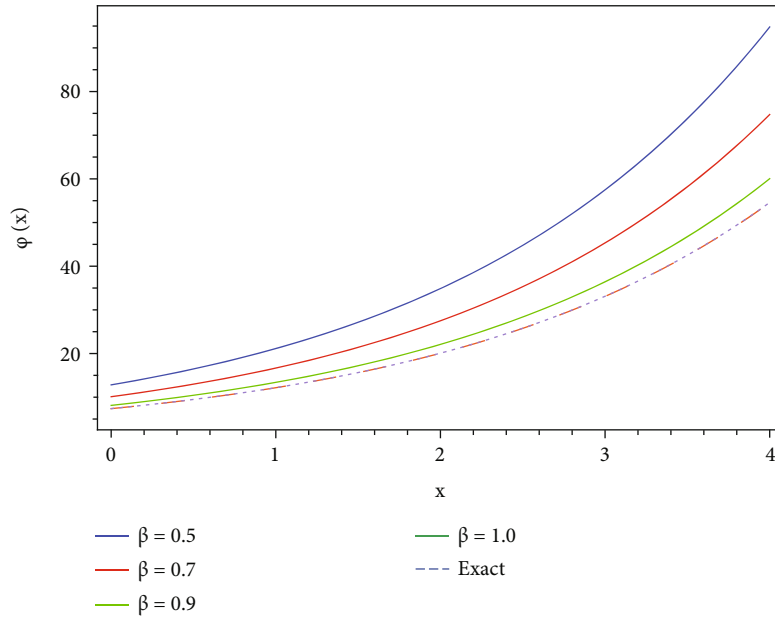


FIGURE 9: Comparison of the approximate solution by NTIM for different values of  $\beta$  at  $h = 1, t = 1.5,$  and  $y = 1$  for Problem 9.

TABLE 1: Comparison of the different values of  $\beta$  and the absolute error of the 6<sup>th</sup> order NTIM solution with the 6<sup>th</sup> order MGTFSM solution for Problem 7.

$x, y$	$t$	$\beta = 0.5$	$\beta = 0.7$	$\beta = 0.9$	$\beta = 1.0$	Exact	NTIM error	Error [18]
0.1	0.1	0.778064	0.6135	0.492898	0.110517	0.110517	$2.009212 \times 10^{-12}$	$1.4090 \times 10^{-10}$
	0.3	0.778064	0.6135	0.492898	0.134986	0.134986	$4.507600 \times 10^{-9}$	$1.0576 \times 10^{-7}$
	0.5	0.778064	0.6135	0.492898	0.164872	0.164872	$1.652645 \times 10^{-7}$	$2.3354 \times 10^{-6}$
	0.7	0.778064	0.6135	0.492898	0.201373	0.201375	$1.788941 \times 10^{-6}$	$1.8129 \times 10^{-5}$
	0.9	0.778064	0.6135	0.492898	0.24595	0.24596	$1.067487 \times 10^{-5}$	$8.4486 \times 10^{-5}$
0.3	0.1	2.33419	1.8405	1.47869	0.331551	0.331551	$6.027678 \times 10^{-12}$	$4.2269 \times 10^{-10}$
	0.3	2.33419	1.8405	1.47869	0.404958	0.404958	$1.352280 \times 10^{-8}$	$3.1727 \times 10^{-7}$
	0.5	2.33419	1.8405	1.47869	0.494616	0.494616	$4.957934 \times 10^{-7}$	$7.0062 \times 10^{-6}$
	0.7	2.33419	1.8405	1.47869	0.60412	0.604126	$5.366824 \times 10^{-6}$	$5.4387 \times 10^{-5}$
	0.9	2.33419	1.8405	1.47869	0.737849	0.737881	$3.202460 \times 10^{-5}$	$2.5346 \times 10^{-4}$
0.5	0.1	3.89032	3.0675	2.46449	0.552585	0.552585	$1.004596 \times 10^{-11}$	$7.0449 \times 10^{-10}$
	0.3	3.89032	3.0675	2.46449	0.674929	0.674929	$2.253800 \times 10^{-8}$	$5.2879 \times 10^{-7}$
	0.5	3.89032	3.0675	2.46449	0.82436	0.824361	$8.263223 \times 10^{-7}$	$1.1677 \times 10^{-5}$
	0.7	3.89032	3.0675	2.46449	1.00687	1.00688	$8.944707 \times 10^{-6}$	$9.0645 \times 10^{-5}$
	0.9	3.89032	3.0675	2.46449	1.22975	1.2298	$5.337433 \times 10^{-5}$	$4.2243 \times 10^{-4}$

For  $\beta = 1,$  Equation (39) converges as

$$\phi(x, y, t) = \sqrt{\sin(x) \cosh(y)} \left( 1 + t + \frac{t^2}{2!} + \frac{t^3}{3!} + \frac{t^4}{4!} + \dots \right), \tag{40}$$

which yields the exact solution given by Equation (32).

Problem 9. Consider the biological population model as [18]

$$D_t^\beta \phi = (\phi^2)_{xx} + (\phi^2)_{yy} + h \phi (1 - r \phi), t > 0, 0 < \beta \leq 1, \tag{41}$$

where  $\phi = \phi(x, y, t)$  subject to the initial condition

$$\phi(x, y, 0) = e^{(\sqrt{hr/\beta})(x+y)}, \tag{42}$$

and the exact solution is

TABLE 2: Comparison of the different values of  $\beta$  and the absolute error of the 6<sup>th</sup> order NTIM solution with the 6<sup>th</sup> order MGTFSM solution for Problem 8.

$x, y$	$t$	$\beta = 0.5$	$\beta = 0.7$	$\beta = 0.9$	$\beta = 1.0$	Exact	NTIM error	Error [18]
0.1	0.1	2.46455	1.94329	1.56127	0.350067	0.350067	$6.364298 \times 10^{-12}$	$1.4090 \times 10^{-10}$
	0.3	2.46455	1.94329	1.56127	0.427573	0.427573	$1.427800 \times 10^{-8}$	$1.0576 \times 10^{-7}$
	0.5	2.46455	1.94329	1.56127	0.522238	0.522239	$5.234815 \times 10^{-7}$	$2.3354 \times 10^{-6}$
	0.7	2.46455	1.94329	1.56127	0.637858	0.637864	$5.666541 \times 10^{-6}$	$1.8129 \times 10^{-5}$
	0.9	2.46455	1.94329	1.56127	0.779055	0.779089	$3.381305 \times 10^{-5}$	$8.4486 \times 10^{-5}$
0.3	0.1	4.32451	3.40986	2.73955	0.614259	0.614259	$1.116729 \times 10^{-11}$	$4.2268 \times 10^{-10}$
	0.3	4.32451	3.40986	2.73955	0.750258	0.750258	$2.505345 \times 10^{-8}$	$3.1726 \times 10^{-7}$
	0.5	4.32451	3.40986	2.73955	0.916366	0.916367	$9.185473 \times 10^{-7}$	$7.0059 \times 10^{-6}$
	0.7	4.32451	3.40986	2.73955	1.11924	1.11925	$9.943018 \times 10^{-6}$	$5.4385 \times 10^{-5}$
	0.9	4.32451	3.40986	2.73955	1.367	1.36706	$5.933139 \times 10^{-5}$	$2.5345 \times 10^{-4}$
0.5	0.1	5.72082	4.51084	3.6241	0.812592	0.812592	$1.477307 \times 10^{-11}$	$7.0425 \times 10^{-10}$
	0.3	5.72082	4.51084	3.6241	0.992502	0.992502	$3.314275 \times 10^{-8}$	$5.2860 \times 10^{-7}$
	0.5	5.72082	4.51084	3.6241	1.21224	1.21224	$1.21513 \times 10^{-6}$	$1.1673 \times 10^{-5}$
	0.7	5.72082	4.51084	3.6241	1.48063	1.48064	$1.315344 \times 10^{-5}$	$9.0614 \times 10^{-5}$
	0.9	5.72082	4.51084	3.6241	1.80838	1.80846	$7.848841 \times 10^{-5}$	$4.2228 \times 10^{-4}$

TABLE 3: Comparison of the different values of  $\beta$  and the absolute error of the 6<sup>th</sup> order NTIM solution with the 6<sup>th</sup> order MGTFSM solution for Example 1.

$x, y$	$t$	$\beta = 0.5$	$\beta = 0.7$	$\beta = 0.9$	$\beta = 1.0$	Exact	NTIM error	Error [18]
0.1	0.1	8.59894	6.78023	5.44736	1.2214	1.2214	$2.220490 \times 10^{-11}$	$1.5572 \times 10^{-9}$
	0.3	8.59894	6.78023	5.44736	1.49182	1.49182	$4.981669 \times 10^{-8}$	$1.1688 \times 10^{-6}$
	0.5	8.59894	6.78023	5.44736	1.82212	1.82212	$1.826455 \times 10^{-6}$	$2.5810 \times 10^{-5}$
	0.7	8.59894	6.78023	5.44736	2.22552	2.22554	$1.977086 \times 10^{-5}$	$2.0036 \times 10^{-4}$
	0.9	8.59894	6.78023	5.44736	2.71816	2.71828	$1.179755 \times 10^{-4}$	$9.3372 \times 10^{-4}$
0.3	0.1	10.5028	8.28139	6.65342	1.49182	1.49182	$2.712142 \times 10^{-11}$	$1.9019 \times 10^{-9}$
	0.3	10.5028	8.28139	6.65342	1.82212	1.82212	$6.084624 \times 10^{-8}$	$1.4276 \times 10^{-6}$
	0.5	10.5028	8.28139	6.65342	2.22554	2.22554	$2.230837 \times 10^{-6}$	$3.1525 \times 10^{-5}$
	0.7	10.5028	8.28139	6.65342	2.71826	2.71828	$2.414818 \times 10^{-5}$	$2.4472 \times 10^{-4}$
	0.9	10.5028	8.28139	6.65342	3.31997	3.32012	$1.440956 \times 10^{-4}$	$1.1404 \times 10^{-3}$
0.5	0.1	12.8281	10.1149	8.12651	1.82212	1.82212	$3.312617 \times 10^{-11}$	$2.3230 \times 10^{-9}$
	0.3	12.8281	10.1149	8.12651	2.22554	2.22554	$7.431777 \times 10^{-8}$	$1.7436 \times 10^{-6}$
	0.5	12.8281	10.1149	8.12651	2.71828	2.71828	$2.724750 \times 10^{-6}$	$3.8504 \times 10^{-5}$
	0.7	12.8281	10.1149	8.12651	3.32009	3.32012	$2.949466 \times 10^{-5}$	$2.9890 \times 10^{-4}$
	0.9	12.8281	10.1149	8.12651	4.05502	4.0552	$1.759988 \times 10^{-4}$	$1.3929 \times 10^{-3}$

$$\phi(x, y, z, t) = e^{(\sqrt{hr/8})(x+y)+ht}. \quad (43)$$

Using the same procedure as for Problems 7 and 8, we obtain the solution as

$$\left\{ \begin{array}{l} \phi_0(x, y, t) = e^{\frac{\sqrt{hr}}{8}(x+y)}, \phi_1(x, y, t) = \frac{ht^\beta e^{\sqrt{hr}(x+y)/2\sqrt{2}}}{\Gamma(\beta+1)}, \\ \phi_2(x, y, t) = \frac{h^2 t^{2\beta} e^{\sqrt{hr}(x+y)/2\sqrt{2}}}{\Gamma(2\beta+1)}, \phi_3(x, y, t) = \frac{h^3 t^{3\beta} e^{\sqrt{hr}(x+y)/2\sqrt{2}}}{\Gamma(3\beta+1)}, \\ \phi_4(x, y, t) = \frac{h^4 t^{4\beta} e^{\sqrt{hr}(x+y)/2\sqrt{2}}}{\Gamma(4\beta+1)}, \\ \vdots \end{array} \right. \quad (44)$$

Combining the components, the 3<sup>rd</sup> order approximate solution is given as

$$\phi(x, y, t) = \phi_0 + \phi_1 + \phi_2 + \phi_3 + \phi_4 + \dots \\ = \left\{ e^{\frac{\sqrt{hr}}{8}(x+y)} + \frac{ht^\beta e^{\sqrt{hr}(x+y)/2\sqrt{2}}}{\Gamma(\beta+1)} + \frac{h^2 t^{2\beta} e^{\sqrt{hr}(x+y)/2\sqrt{2}}}{\Gamma(2\beta+1)} + \frac{h^3 t^{3\beta} e^{\sqrt{hr}(x+y)/2\sqrt{2}}}{\Gamma(3\beta+1)} + \frac{h^4 t^{4\beta} e^{\sqrt{hr}(x+y)/2\sqrt{2}}}{\Gamma(4\beta+1)} + \dots \right\}. \quad (45)$$

Equation (27) can be simplified as

$$\phi(x, y, t) = e^{\frac{\sqrt{hr}(x+y)}{2\sqrt{2}}} \left( \frac{ht^\beta}{\Gamma(\beta+1)} + \frac{h^2 t^{2\beta}}{\Gamma(2\beta+1)} + \frac{h^3 t^{3\beta}}{\Gamma(3\beta+1)} + \frac{h^4 t^{4\beta}}{\Gamma(4\beta+1)} + \dots \right). \quad (46)$$

For  $\beta = 1$ , Equation (29) converges as

$$\phi(x, y, t) = e^{(\sqrt{hr}(x+y))/(2\sqrt{2})} \left( 1 + ht + \frac{(ht)^2}{2!} + \frac{(ht)^3}{3!} + \frac{(ht)^4}{4!} + \dots \right), \quad (47)$$

which converges to the exact solution given by Equation (43).

## 5. Results and Discussions

The biological population model of fractional order has been investigated in the present work. We observe that the solution pattern for Examples 1-3 converges very rapidly to the exact solution in a few iterations. The results have been compared through graphs and tables which confirms the convergence of NTIM. Figure 1 is the NTIM approximate solution, and Figure 2 is the exact solution for  $\beta = 1$  of Example 1. The 6<sup>th</sup> order approximate solution for different fractional values of  $\beta$  for Example 1 is depicted in Figure 3. Furthermore, Figures 4 and 5 show the 6<sup>th</sup> order NTIM solution and the exact solution, respectively, for Example 2 by mean of 3D plots. The comparison for different fractional values of  $\beta$  and exact solution is made in Figure 6 for Example 2. Similarly Figures 7 and 8 show, respectively, the 6<sup>th</sup> order NTIM solution and exact solution for Example 3. Figure 9 is the

comparison of fractional values of  $\beta$  and exact solution for Example 3. In Table 1–3, the approximate solution has been compared in tabular form for  $\beta = 0.5$ ,  $\beta = 0.7$ ,  $\beta = 0.9$ , and  $\beta = 1.0$ , with the exact solution. The value  $\beta = 1.0$  converts the FDE to the classical PDE. The absolute error by the proposed NTIM in Tables 1–3 has been compared with the absolute error obtained by the modified generalized Taylor fractional series method (MGTFSM) for Examples 1-3. It is concluded from the results of Examples 1-3 that as the fractional value of  $\beta$  reaches 1, the NTIM approximate solution meets with the exact solution. We also observe that NTIM yields an excellent approximate solution.

## 6. Conclusion

Three nonlinear problems of fractional order biological population model have been investigated by the natural transform iterative method in the current study. The method is applied to nonlinear problems without any discretization. We found that NTIM converges very rapidly to the exact solution. The advantage of the method is that it is free of any large or small parameter assumptions or to find any constant at the end of the solution. The obtained results of the FBPM have been compared through 3D and 2D plots, and also, the numerical values have been compared in tabular form for different values of  $\beta$ . The comparison between absolute errors of the NTIM approximate solution and modified generalized Taylor fractional series method solution is done with the help of tables. In each case, NTIM reveals an efficient approximate solution as compared with other methods in the literature.

## Data Availability

No data were generated or analyzed during the study.

## Conflicts of Interest

The authors declare that they have no conflicts of interest.

## Acknowledgments

The authors extend their appreciation to the Deanship of Scientific Research at King Khalid University for funding this work through research groups under grant number R.G.P.2/14/43.

## References

- [1] T. Rabczuk, H. Ren, and X. Zhuang, "A nonlocal operator method for partial differential equations with application to electromagnetic waveguide problem," *Computers, Materials & Continua*, vol. 59, no. 1, pp. 31–55, 2019.
- [2] D. H. Staelin, A. W. Morgenthaler, and J. A. Kong, *Electromagnetic Waves*, Pearson Education, India, 1994.
- [3] D. Tripathi and O. A. Bég, "Mathematical modelling of peristaltic propulsion of viscoplastic bio-fluids," *Proceedings of the Institution of Mechanical Engineers, Part H: Journal of Engineering in Medicine*, vol. 228, no. 1, pp. 67–88, 2014.

- [4] A. Dumas, J. Dijkstra, and J. France, "Mathematical modelling in animal nutrition: a centenary review," *The Journal of Agricultural Science*, vol. 146, no. 2, pp. 123–142, 2008.
- [5] D. Baleanu, H. Mohammadi, and S. Rezapour, "A mathematical theoretical study of a particular system of Caputo–Fabrizio fractional differential equations for the Rubella disease model," *Advances in Difference Equations*, vol. 2020, no. 1, 2020.
- [6] R. Hilfer, *Applications of Fractional Calculus in Physics*, World scientific, Covent Garden, London, 2000.
- [7] R. Almeida, "A Caputo fractional derivative of a function with respect to another function," *Communications in Non-linear Science and Numerical Simulation*, vol. 44, pp. 460–481, 2017.
- [8] N. H. Tuan, H. Mohammadi, and S. Rezapour, "A mathematical model for COVID-19 transmission by using the Caputo fractional derivative," *Chaos, Solitons & Fractals*, vol. 140, article 110107, 2020.
- [9] C. Li, D. Qian, and Y. Chen, "On Riemann-Liouville and Caputo derivatives," *Discrete Dynamics in Nature and Society*, vol. 2011, 15 pages, 2011.
- [10] L. Kexue and P. Jigen, "Laplace transform and fractional differential equations," *Applied Mathematics Letters*, vol. 24, no. 12, pp. 2019–2023, 2011.
- [11] D. S. Bodkhe and S. K. Panchal, "On Sumudu transform of fractional derivatives and its applications to fractional differential equations," *Asian Journal of Mathematics and Computer Research*, vol. 11, no. 1, pp. 69–77, 2016.
- [12] Y. Singh, V. Gill, S. Kundu, and D. Kumar, "On the Elzaki transform and its applications in fractional free electron laser equation," *Acta Universitatis Sapientiae, Mathematica*, vol. 11, no. 2, pp. 419–429, 2019.
- [13] R. Nawaz, N. Ali, L. Zada, K. S. Nisar, M. R. Alharthi, and W. Jamshed, "Extension of natural transform method with Daftardar-Jafari polynomials for fractional order differential equations," *Alexandria Engineering Journal*, vol. 60, no. 3, pp. 3205–3217, 2021.
- [14] R. Nawaz, N. Ali, L. Zada, Z. Shah, A. Tassaddiq, and N. A. Alreshidi, "Comparative analysis of natural transform decomposition method and new iterative method for fractional foam drainage problem and fractional order modified regularized long-wave equation," *Fractals*, vol. 28, no. 7, article 2050124, 2020.
- [15] L. Zada, R. Nawaz, S. Ahsan et al., "New iterative approach for the solutions of fractional order inhomogeneous partial differential equations," *AIMS Mathematics*, vol. 6, no. 2, pp. 1348–1365, 2021.
- [16] S. Bhalekar and V. Daftardar-Gejji, "New iterative method: application to partial differential equations," *Applied Mathematics and Computation*, vol. 203, no. 2, pp. 778–783, 2008.
- [17] H. Eltayeb, Y. T. Abdalla, I. Bachar, and M. H. Khabir, "Fractional telegraph equation and its solution by natural transform decomposition method," *Symmetry*, vol. 11, no. 3, p. 334, 2019.
- [18] A. Khalouta, A. Kadem, and Laboratory of Fundamental and Numerical Mathematics, Department of Mathematics, Faculty of Sciences, Ferhat Abbas University of Setif 1, Sétif 19000, Algeria, "A new numerical technique for solving Caputo time-fractional biological population equation," *AIMS Mathematics*, vol. 4, no. 5, pp. 1307–1319, 2019.
- [19] M. Zellal and K. Belghaba, "An accurate algorithm for solving biological population model by the variational iteration method using He's polynomials," *Arab Journal of Basic and Applied Sciences*, vol. 25, no. 3, pp. 142–149, 2018.
- [20] A. M. A. El-Sayed, S. Z. Rida, and A. A. M. Arafa, "Exact solutions of fractional-order biological population model," *Communications in Theoretical Physics*, vol. 52, no. 6, pp. 992–996, 2009.
- [21] R. Shah, H. Khan, S. Mustafa, P. Kumam, and M. Arif, "Analytical solutions of fractional-order diffusion equations by natural transform decomposition method," *Entropy*, vol. 21, no. 6, p. 557, 2019.
- [22] S. Bhalekar and V. Daftardar-Gejji, "Convergence of the new iterative method," *International journal of differential equations*, vol. 2011, 10 pages, 2011.
- [23] A. Khan, R. Zarin, U. W. Humphries, A. Akgül, A. Saeed, and T. Gul, "Fractional optimal control of COVID-19 pandemic model with generalized Mittag-Leffler function," *Advances in Difference Equations*, vol. 2021, no. 1, 2021.
- [24] A. Saeed, M. Bilal, T. Gul, P. Kumam, A. Khan, and M. Sohail, "Fractional order stagnation point flow of the hybrid nanofluid towards a stretching sheet," *Scientific Reports*, vol. 11, no. 1, pp. 1–15, 2021.
- [25] T. Gul, M. Altaf Khan, A. Khan, and M. Shuaib, "Fractional-order three-dimensional thin-film nanofluid flow on an inclined rotating disk," *The European Physical Journal Plus*, vol. 133, no. 12, article 500, 2018.
- [26] T. Gul, H. Anwar, M. A. Khan, I. Khan, and P. Kumam, "Integer and non-integer order study of the GO-W/GO-EG nanofluids flow by means of Marangoni convection," *Symmetry*, vol. 11, no. 5, p. 640, 2019.
- [27] T. Gul, M. Khan, W. Noman, I. Khan, T. Abdullah Alkanhal, and I. Tlili, "Fractional order forced convection carbon nanotube nanofluid flow passing over a thin needle," *Symmetry*, vol. 11, no. 3, p. 312, 2019.
- [28] W. Jamshed, N. A. A. M. Nasir, S. S. P. M. Isa et al., "Thermal growth in solar water pump using Prandtl-Eyring hybrid nanofluid: a solar energy application," *Scientific Reports*, vol. 11, no. 1, pp. 1–21, 2021.
- [29] W. Jamshed, K. S. Nisar, R. W. Ibrahim, F. Shahzad, and M. R. Eid, "Thermal expansion optimization in solar aircraft using tangent hyperbolic hybrid nanofluid: a solar thermal application," *Journal of Materials Research and Technology*, vol. 14, pp. 985–1006, 2021.
- [30] W. Jamshed, S. U. Devi, and K. S. Nisar, "Single phase based study of ag-cu/EO Williamson hybrid nanofluid flow over a stretching surface with shape factor," *Physica Scripta*, vol. 96, no. 6, article 065202, 2021.
- [31] W. Jamshed, K. S. Nisar, R. W. Ibrahim, F. Shahzad, and M. R. Eid, "Thermal expansion optimization in solar aircraft using tangent hyperbolic hybrid nanofluid: a solar thermal application," *Journal of Materials Research and Technology*, vol. 14, pp. 985–1006, 2021.
- [32] X.-H. Zhang, A. Ali, M. A. Khan, M. Y. Alshahrani, T. Muhammad, and S. Islam, "Mathematical analysis of the TB model with treatment via Caputo-type fractional derivative," *Discrete Dynamics in Nature and Society* 2021, vol. 2021, pp. 1–15, 2021.
- [33] A. Ali, F. S. Alshammari, S. Islam, M. A. Khan, and S. Ullah, "Modeling and analysis of the dynamics of novel coronavirus (COVID-19) with Caputo fractional derivative," *Results in Physics*, vol. 20, article 103669, 2021.

- [34] A. Ali, Q. Iqbal, J. K. K. Asamoah, and S. Islam, "Mathematical modeling for the transmission potential of Zika virus with optimal control strategies," *The European Physical Journal Plus*, vol. 137, no. 1, pp. 1–30, 2022.
- [35] Y. M. Chu, A. Ali, M. A. Khan, S. Islam, and S. Ullah, "Dynamics of fractional order COVID-19 model with a case study of Saudi Arabia," *Results in Physics*, vol. 21, article 103787, 2021.

## Research Article

# Evaluating the Higher-Order Slip Consequence in Bioconvection Nanofluid Flow Configured by a Variable Thick Surface of Disk

Hassan Waqas <sup>1</sup>, Sumeira Yasmin,<sup>1</sup> Nesreen Althobaiti,<sup>2</sup> Ebenezer Bonyah <sup>3</sup>,  
Ahmed Alshehri <sup>4</sup> and Zahir Shah <sup>5</sup>

<sup>1</sup>Department of Mathematics, Government College University Faisalabad, Layyah Campus 31200, Pakistan

<sup>2</sup>Department of Mathematics and Statistics, College of Sciences, Taif University, P.O. Box 11099, Taif 21944, Saudi Arabia

<sup>3</sup>Department of Mathematics Education, University of Education Winneba Kumasi Campus, Kumasi 00233, Ghana

<sup>4</sup>Department of Mathematics, Faculty of Sciences, King Abdulaziz University, Jeddah 21589, Saudi Arabia

<sup>5</sup>Department of Mathematical Sciences, University of Lakki Marwat, Lakki Marwat, 28420 Khyber Pakhtunkhwa, Pakistan

Correspondence should be addressed to Ebenezer Bonyah; [ebonyah@gmail.com](mailto:ebonyah@gmail.com)

Received 2 October 2021; Accepted 24 January 2022; Published 14 February 2022

Academic Editor: Amir Khan

Copyright © 2022 Hassan Waqas et al. This is an open access article distributed under the Creative Commons Attribution License, which permits unrestricted use, distribution, and reproduction in any medium, provided the original work is properly cited.

For innovations in manufacturing and engineering scientific fields, the devices (electrical and computer systems) with large thermal effectiveness are needed. As a result, their thermal efficiency has become a very hot problem for many canvassers. With the novelty of this analysis, a mathematical study is performed to estimate the Darcy-Forchheimer flow of viscous magnetized fluid with Arrhenius activation energy and bioconvection effects through a variable thick surface of a rotating disk. The impact of thermal conductivity, heat source, and nonlinear thermal radiation is considered. The higher-order velocity slip impacts are also scrutinized. The system of partial differential equations (PDEs) and specific boundary restrictions is altered into a system of ODEs by adopting the suitable similarity transformations. The reduced ODE's system is tackled with the aid of shooting scheme under (bvp4c) built-in tool commercial software MATLAB. Moreover, the effects of different parameters over velocity components, thermal conductivity, concentration, and microorganism's fields are also examined. The confirmation of our findings is also explained through tables and graphical results. The results revealed that the radial velocity increases with the growing estimations of mixed convection parameter. The second-order velocity slip in radial direction causes a decrement in the estimation of axial velocity. Temperature distribution increases with a larger temperature ratio parameter. The concentration field of species and microorganism profile is reduced via a Brownian motion parameter and Peclet number, respectively.

## 1. Introduction

**1.1. Literature Survey.** Nanofluid is a fluid constructed with nanosized (1 to 100 nm) materials or molecules, named “nanomaterials” and otherwise “nanoparticles.” Such substances are designed colloidal suspension of nanopowders in a continuous phase fluid. Nanoparticles utilized in nanofluids are constructed with oxidations, metals, and carbon nanotubes including carbides. Continuous phase fluids include ethanol glycol oil as well as water. Nanofluids have novel characteristics that build them potentially helpful in a broad range of heat transformation applications such as fuel cells, microprocessors, hybrid powered engines, phar-

macological mechanisms, cooling equipment, chillers, refrigerators, and heat radiators in grinding, among others. Nanofluids are combinations of nanoparticles and the base fluids that can generate numerous heterogeneous nanofluids that are described for their thermophysical characteristics (thermal diffusivity and thermal conductivity, as well as viscosity) as a cooling system in heat transmission in comparison to base fluid, which increased with growing volumetric fraction of nanomaterials. Choi and Eastman [1] were firstly introduced to the basic idea of nanoparticles in constant phase fluids. Buongiorno [2] addressed nanoparticle study by developing a model to evaluate the thermal properties of continuous phase fluids. He predicted that the increased

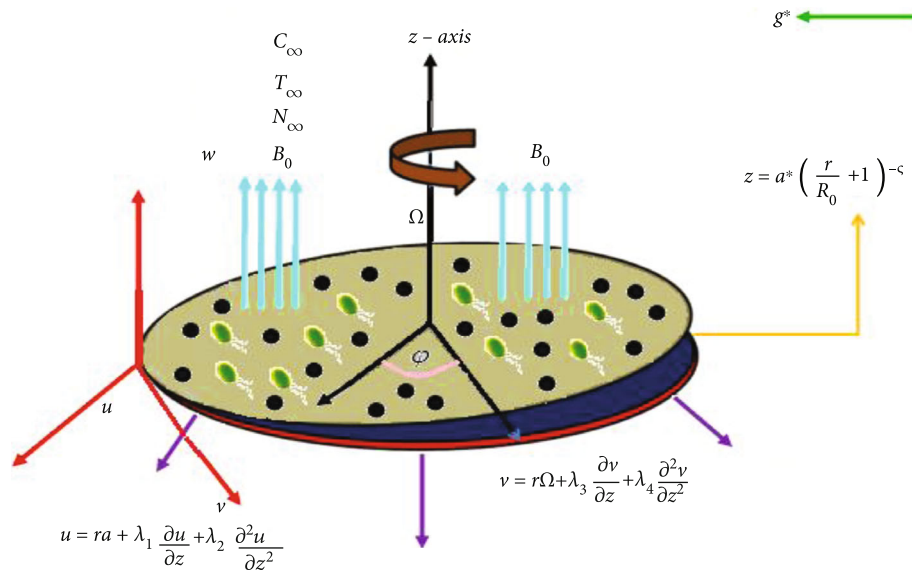


FIGURE 1: Schematic configuration of the flow problem.

conductance of constant phase fluid would be caused by the tiny-sized and lower volume fraction of supporting nanoelements. Nanotechnology is extremely important in numerous fields including chemical as well as metallurgical operating systems, transportation, macroscopic objects, cancer treatment, and electricity generation. Eid and Mabood [3] reported the suspending magnetohydrodynamic (MHD) flowing of micropolar dusty nanoparticles impinging on a permeability expanding sheet. Umar et al. [4] studied numerically the 3-dimensional incompressible Eyring-Powell nanofluid flow across a stretched surface including velocity slip as well as activation energy. Muhammad et al. [5] explored numerical simulations for 3-D Eyring-Powell (EP) nanoliquid under the nonlinear thermal radiation with changed heat and solutal fluxes. Rasool et al. [6] researched the Marangoni convective Casson-type flow of nanofluid impacted by the existence of Lorentz forces introduced into the modeling by an organized arrangement of magnets in the shape of the Riga configuration. Mahanthesh et al. [7] described the effect of quadratic thermal radiation as well as convection on the boundary layer 2-phase flowing of a dusty flow of nanoliquid through a vertical surface. Aaiza et al. [8] evaluate the magneto-nanoliquid flow across a channel in the presence of different nanoparticle shape factors. Hussanan et al. [9] investigate the thermal transportation phenomenon in micropolar water-based fluid. Khalid et al. [10] scrutinized the exact solution of nanofluid flow. Ali et al. [11] discussed the Brinkman-type nanofluid flow through vertical surface. Zin et al. [12] introduced the free convection behavior in Jeffery fluid through vertical porous surface.

The word activation energy plays a significant role in chemical reactions. The scientist Svante Arrhenius was the principal who initiated the description on activation energy in 1889 and that it is the minimum amount of energy required to initiate chemical reactions to a state in which they could experience material change. The application includes compound construction, food processing, transpor-

tation structures, a geothermal stored, and businesses. Heat and mass distribution aspects manage various mechanisms that were reacting synthetically which include the species composite reactions as well as codification strength having application in oil production and geothermal configuration. In actuality, it is the least amount of energy required to transform the reactants into substances. Activation energy can take the shape of kinetic and potential energy. It is essential to generate theoretical observations in addition to experimental contributions to measure the flow influence of activation energy. There have been very several theoretical efforts on this discussion. Indeed, the relationship between mass transfer and chemical reaction becomes tiresome. Such interactions can be observed both within the fluid and in mass transmission during the production process and employ of reactants at various levels. Bestman [13] clarified that viscoelastic fluid flow of thermal and mass moved in which restricts divider movements in its own plane utilizing a simplistic scientific theory of twofold material reaction with Arrhenius actuation energy. In this inspection, he obtained an analytical curriculum of action for the problem by employing an irritation method. Guo et al. [14] examined the kinetic model and thermodynamic of oxidant pyrolysis of microalgae wastes using a double distribution activation energy concept and simulating annealing. Hayat et al. [15] evaluated the effect of activation energy on entropy generation (EG) in a 3-dimensional magnetohydrodynamic (MHD) rotational flowing of nanofluids containing a binary chemical process. Araújo et al. [16] scrutinized the kinetic modeling and Arrhenius activation energy distributions in complicated systems with Hopfield Neural Network-based system. Elangovan and Natarajan [17] reported the primary treatment influences on qualitative characteristics, hydration diffusivity, and Arrhenius activation energy of solar drying gourd. The numerical analysis of unsteady Maxwell nanofluid is simulated by Bilal et al. [18]. The effect of magneto nanofluid flow over disk with viscous dissipation is analyzed by Saeed et al. [19].

TABLE 1: Dimensionless prominent parameters.

Reynolds number	$Re = \Omega R_0^2 \rho_f / \mu_f$
Mixed convection variable	$\lambda = \beta^{**} g * (1 - C_{\infty}) (T_f - T_{\infty}) / \tau \Omega^2$
Buoyancy ratio parameter	$Nr = (\rho_p - \rho_f) (C_f - C_{\infty}) / \rho_f (1 - C_{\infty}) (T_f - T_{\infty}) \beta^{**}$
Bioconvection Rayleigh number	$Nc = \gamma * (\rho_m - \rho_f) (N_f - N_{\infty}) / \rho_f (1 - C_{\infty}) (T_f - T_{\infty}) \beta^{**}$
Dimensionless constants	$(r^* = r/R_0^2, \varepsilon = r^*/(1 + r^*))$
Magnetic parameter	$M = \sigma_f \beta_0^2 / \rho_f \Omega$
Local porosity parameter	$K_1^* = \nu_f / k^* \Omega$
Forchheimer number	$F_r = Fr, Fr = C_b^* / \sqrt{k^*}$
Eckert number	$Ec = r^2 \Omega^2 / c_p (T_f - T_{\infty})$
Brownian motion parameter	$Nb = \tau D_B (C_f - C_{\infty}) / \nu_f$
Prandtl number	$Pr = (\rho c_p \nu_f) / k_f$
Thermal source parameter	$Q (= Q^* / (\rho c_p)_f \Omega)$
Nonlinear thermal radiation parameter	$Rd = 4\sigma^* T_{\infty}^3 / k^*$
Thermophoretic parameter	$Nt = \tau D_T (T_f - T_{\infty}) / \nu_f T_{\infty}$
Activation energy parameter	$E_1 = E_a / \kappa T_{\infty}$
Schmidt number	$Sc = \nu_f / D_B$
Stretching rate to angular frequency	$A_1 = a / \Omega$
First-order slip parameters in radial direction	$L_1 = (\lambda_1 / R_0) (1 + r^*)^{\zeta} (\Omega R_0^2 \rho_f / \mu_f)^{1/(n+1)} > 0,$ $L_3 = (\lambda_3 / R_0) (1 + r^*)^{\zeta} (\Omega R_0^2 \rho_f / \mu_f)^{1/(n+1)} > 0$
Tangential directional second-order slip parameters	$L_2 = (\lambda_2 / R_0^2) (1 + r^*)^{2\zeta} (\Omega R_0^2 \rho_f / \mu_f)^{2/(n+1)} < 0,$ $L_4 = (\lambda_4 / R_0^2) (1 + r^*)^{2\zeta} (\Omega R_0^2 \rho_f / \mu_f)^{2/(n+1)} < 0$
Thermal Biot number	$\Omega_1 = (h_1 / k_f) (R_0 / (1 + r^*)^{\zeta}) (\mu_f / \Omega R_0^2 \rho_f)^{1/(n+1)}$
Solutal Biot number	$\Omega_2 = (h_2 / D_m) (R_0 / (1 + r^*)^{\zeta}) (\mu_f / \Omega R_0^2 \rho_f)^{1/(n+1)}$
Microorganism Biot number	$\Omega_3 = (h_3 / D_m) (R_0 / (1 + r^*)^{\zeta}) (\mu_f / \Omega R_0^2 \rho_f)^{1/(n+1)}$
Chemical reaction parameter	$K_1 = k_r^2 / \Omega$
Temperature ratio parameter	$\alpha_1 = (T_f - T_{\infty}) / T_{\infty}$
Disk thickness coefficient	$\alpha = (a / R_0^2) (\Omega R_0^2 \rho_f / \mu_f)^{-1/(n+1)}$
Bioconvective Lewis number	$Lb = \nu / D_m$
Peclet number	$Pe = b W_c / D_m$
Microorganism difference number	$\Omega_0 = N_{\infty} / N_f - N_{\infty}$

Microorganism molecules have been widely used in the production of manufacturing and industrial products such as ethanol, waste-derived biofuel, and fertilizers. They are also utilized in water therapeutic facilities. These microorganisms generate hydrogen gas and biofuel, a favorable dispatchable energy source. As a result, we must investigate the swimming structures and mass transmission properties of

microorganisms in order to make their applications more successful, profitable, and widespread for the benefit of humanity. Bioconvection is the production of various types of irregular fluid structures at the microscopic level therefore of the unexpected swimming of self-propelled microorganisms found in water or those certain denser fluids. Natural hypotheses such as searching for nutrients, oxygen for



breathing, and improving light absorption for photosynthesis influence the swimming of such microorganisms. Platt in 1961 [20] introduced the term “bioconvection” to illustrate the methodology of improvement of manners in depth suspensions of motile microorganisms at constant temperatures, in comparison to those reported under convective conditions. Kuznetsov [21] proposed the concept of biothermal convection caused by temperature gradients as well as microorganism swimming. Tlili et al. [22] scrutinized the effect of bioconvection micropolar nanoliquid flow including gyrotactic motile microorganisms on thermal and solutal stratifications at the boundary layer. Al-Mubaddel et al. [23] examined Sisko-based nanofluid under the bioconvection radiation flow with specific thermal and solutal fluxes. Abbasi et al. [24] illustrated the flow of viscoelastic nanoparticles containing gyrotactic motile microorganisms across a rotating stretched disk under convective and zero mass flux conditions. Shehzad et al. [25] scrutinized the bioconvection of a Maxwell-based nanoliquid above an isolated rotational disk under the effect of double diffusional Cattaneo–Christov (C-C) concepts. Aziz et al. [26] evaluated the effects of motile microorganisms on unstable Williamson nanoliquid caused by a bidirectional accelerating surface. Alizadeh and Ganji [27] analyzed the two-phase thermosyphon utilizing RSM. The thermal transportation features and thermal resistance are discussed by Alizadeh and Ganji [28]. Some important research work about fluid flow and heat transfer can be studied in [29–31].

Taking the higher-order velocity slip consider, this communication extends the bioconvection nanofluid flow through a stretching disk. The Darcy-Forchheimer porous medium is considered. The heat transfer is incorporated in the presence of nonlinear thermal radiation, joule heating, thermophoresis, and Brownian diffusion. The significance of Arrhenius activation energy is considered. The dimensionless system is tackled by utilizing a shooting scheme with the `bvp4c` function of MATLAB. The effects of flow controlling parameters are analyzed.

## 2. Mathematical Description

**2.1. Flow Analysis.** Here, our main purpose is to scrutinize the steady three-dimensional, incompressible, and axially symmetric laminar flow of nanofluid including bioconvection with motile microorganism over a stretching disk surface. The schematic view of flow problem and the system of coordinates is depicted in Figure 1; here, the surface of the disk is stretchable through the rate of  $\alpha$  and moving along own axis under an angular frequency  $\Omega$ . Due to the stretchable and angular frequency as well as electrical conduction in the presence of electromagnetic field, the flow is produced. The suitable boundary conditions are applied at the disk surface. Here, no suction/injection is present at the disk surface, that is,  $w = 0$ . The velocity components denoted as  $(u, v, \text{ and } w)$  are along the  $(r, \varphi, \text{ and } z)$  axis, respectively. The temperature of fluid  $T_f$ , nanoparticle concentration of fluid  $C_f$ , bioconvection fluid  $N_f$ , ambient temperature  $T_\infty$ , and ambient volumetric concentration  $C_\infty$  as

well as ambient swimming organisms  $N_\infty$  are also presented at the surface of a stretching disk.

The governing partial differential equations are expressed as [32, 33]

$$u_r + \frac{u}{r} + w_z = 0, \quad (1)$$

$$u\partial_r(u) - \frac{v^2}{r} + w_z(u) = \nu_f u_{zz} - \frac{\sigma_f \beta_0^2}{\rho_f} u - \frac{\nu_f}{k^*} u - Fu^2 + \frac{1}{\rho_f} \begin{bmatrix} (1-C_f)\rho_f \beta^{**} g^* (T - T_\infty) \\ -(\rho_p - \rho_f) g^* (C - C_\infty) \\ -(N - N_\infty) g^* \gamma (\rho_m - \rho_f) \end{bmatrix}, \quad (2)$$

$$uv_r + \frac{uv}{r} + w_z(v) = \nu_f v_{zz} - \frac{\sigma_f \beta_0^2}{\rho_f} v - \frac{\nu_f}{k^*} v - Fv^2, \quad (3)$$

$$u_r(T) + w(T_z) = \frac{1}{\rho c_p} [K(T_z)T_{zz}] + \frac{k_f}{(\rho c_p)_f} T_{zz} + \frac{\sigma_f \beta_0^2}{(\rho c_p)_f} (u^2 + v^2) + \frac{H_f}{(\rho c_p)_f} \{((u_z)^2 + (v_z)^2)\} + \tau \left( D_B(T_z) \partial_z(C) + \frac{D_T}{T_\infty} (T_z)^2 \right) + \frac{16\sigma^*}{3k^*(\rho c)_f} (T_z)^3 T_{zz} + \frac{Q^*}{(\rho c_p)_f} (T - T_\infty), \quad (4)$$

$$uC_r + wC_z = D_B[C_{zz}] + \frac{D_T}{T_\infty} [T_{zz}] - kr^2(C - C_\infty) \left( \frac{T}{T_\infty} \right)^m \exp\left(\frac{-E_a}{\kappa T}\right), \quad (5)$$

$$uN_r + wN_z + [(N_z(C_{zz}))] \frac{bW_c}{(C_w - C_\infty)} = D_m(N_{zz}). \quad (6)$$

### 2.2. With Boundary Restrictions.

$$\begin{aligned} u &= ra + \lambda_1(u_z) + \lambda_2(u_{zz}), \\ v &= r\Omega + \lambda_3(v_z) + \lambda_4(v_{zz}), \\ w &= 0, \\ -k(T_z) &= h_1(T_f - T), \\ -D_B(C_z) &= h_2(C_f - C), \\ -D_m(N_z) &= h_3(N_f - N), \\ \text{at } z &= a^* \left( \frac{r}{R_0} + 1 \right)^{-\zeta}, \\ u &\longrightarrow 0, \\ v &\longrightarrow 0, \\ T &\longrightarrow T_\infty, \\ C &\longrightarrow C_\infty, \\ N &\longrightarrow N_\infty, \end{aligned} \quad (7)$$

when  $z \longrightarrow \infty$ .

In the above governing equations, the velocity components are  $u, v, \text{ and } w$  along  $r, \varphi, \text{ and } z$  directions,  $\nu_f$  represent the kinematic viscosity;  $\sigma_f$  is the electrical

conductivity of momentum;  $\rho_f$  is the fluid density of microorganism;  $K^*$  demonstrate the porous space permeability;  $\beta_0$  is the magnetic field strength;  $F(=C_b^*/r\sqrt{K^*})$  illustrate the coefficient of nonuniform inertia;  $g$  is the gravity; volume expansion coefficient is indicated by  $\beta^{**}$ ;  $D_m$  represents the microorganism diffusion parameter;  $m$  exemplify the power law index; chemotaxis constant is expressed as  $b$ ; the cell swimming speed is identified as  $W_e$ ;  $C_b^*$  display the drag coefficient;  $T, C,$  and  $N$  are the basic temperature, volumetric concentration, and swimming bioconvection of fluid;  $k_f$  signify the thermal conductivity;  $c_p$  represents specific heat capacity; the heat capacitance ratio is symbolized by  $\tau = (\rho c_p)_p / (\rho c_p)_f$ ;  $D_T$  represents thermophoresis diffusion coefficient;  $T_\infty$  stand for ambient temperature;  $m$  is the fitted rate constant;  $D_B$  represent the Brownian motion coefficient; the dynamic viscosity is  $\mu_f$ ,  $C_\infty$  and  $N_\infty$  are ambient concentration and ambient density microorganism, respectively; the rate of chemical reaction is  $k_r^2$ ;  $\beta_1, \beta_2, \beta_3,$  and  $\beta_4$  are linear/nonlinear thermal-based and nanoparticle concentration expansions; the exponential function is  $\exp$ ; the angular frequency is  $\Omega$ ; the activation energy is symbolized by  $E_a$ ; the stretching constant is  $a$ ;  $\kappa = 8.61 \times 10^{-5}$  eV/K expressed the Stefan Boltzmann constant;  $\lambda_1 (\lambda_2 < 0)$  and  $\lambda_3 (\lambda_4 < 0)$  are the first- and second-order slip coefficients, respectively; and  $h_1$  and  $h_2$  are the heat mass transfer coefficient and the mass transfer coefficient, respectively.

2.3. *Similarities.* The similarity variables are

$$\begin{aligned} u &= r^* R_0 \Omega F(\eta), \\ v &= r^* R_0 \Omega G(\eta), \\ w &= R_0 \Omega (1+r^*)^{-\zeta} \left( \frac{\Omega R_0^2 \rho_f}{\mu_f} \right)^{-1/(n+1)} H(\eta), \\ \Theta &= \frac{T - T_\infty}{T_f - T_\infty}, \\ \Phi &= \frac{C - C_\infty}{C_f - C_\infty}, \\ X &= \frac{N - N_\infty}{N_f - N_\infty}, \\ \eta &= \frac{z}{R_0} (1+r^*)^\zeta \left( \frac{\Omega R_0^2 \rho_f}{\mu_f} \right)^{1/(n+1)}. \end{aligned} \tag{9}$$

In above transformations, radius is  $R_0$ ; the power law index is  $n$ ; the thickness power law index is  $\zeta$ ; the components of velocity (radial, tangential, and axial) are symbolized by  $F, G,$  and  $H$ ; and  $r^*$  is the constant of nondimensional radius. The temperature variable conductivity is addressed as

$$K(T) = k_\infty \left[ 1 + \epsilon_1 \left( \frac{T - T_\infty}{\Delta T} \right) \right]. \tag{10}$$

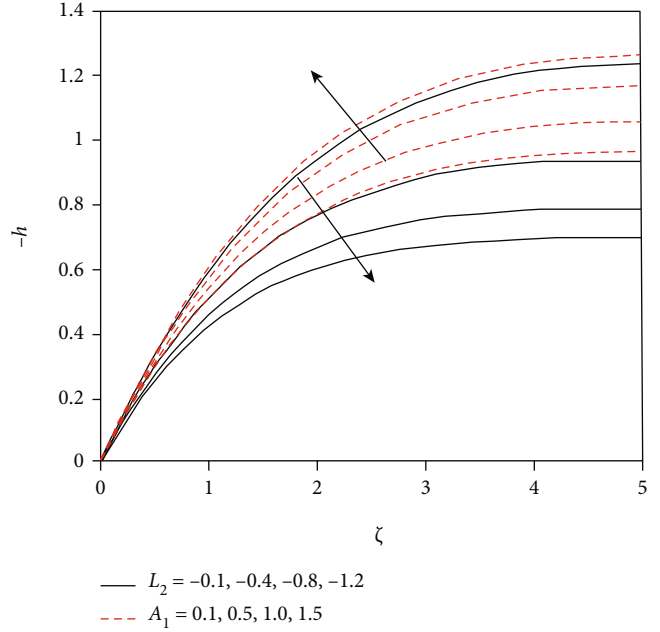


FIGURE 2: Fluctuation in axial velocity component against two different parameters.

2.4. *Reduced Equations.* The governing dimensionless equations after applying the suitable similarity transformation are expressed as

$$2F + H_\eta + \eta \epsilon \zeta F_\eta = 0, \tag{11}$$

$$\begin{aligned} (\text{Re})^{(1-n)/(1+n)} (1+r^*)^{2\zeta} F_{\eta\eta} - 2F_\eta^2 + G^2 - HF - FF_\eta \zeta \eta \epsilon - MF \\ - K_1^* F - F_r F^2 + \lambda(\Theta - \text{Nr}\Phi - \text{Nc}X) = 0, \end{aligned} \tag{12}$$

$$(\text{Re})^{(1-n)/(1+n)} (1+r^*)^{2\zeta} G_{\eta\eta} - 2FG - HG_\eta - FG_\eta \zeta \eta \epsilon - MG - K_1^* G - F_r G^2 = 0, \tag{13}$$

$$\begin{aligned} \frac{1}{\text{Pr}} (\text{Re})^{(1-n)/(1+n)} (1+r^*)^{2\zeta} (1 + \epsilon_1) \Theta_{\eta\eta} + \epsilon_1 \Theta_\eta^2 \\ + \frac{4}{3} \text{Rd} \left[ \begin{aligned} &\Theta_{\eta\eta} + (\theta_w - 1)^3 (3\Theta^2 \Theta_\eta^2 + \Theta^3 \Theta_{\eta\eta}) \\ &+ 3(\Theta_w - 1)^2 (2\Theta \Theta_\eta^2 + \Theta^2 \Theta_{\eta\eta}) \\ &+ 3(\Theta_w - 1) (\Theta_\eta^2 + \Theta \Theta_{\eta\eta}) \end{aligned} \right] - H\Theta_\eta \\ - F\Theta_\eta \zeta \eta \epsilon + \text{Nt} (\text{Re})^{(1-n)/(1+n)} (1+r^*)^{2\zeta} \Theta_\eta^2 \\ + \text{Nb} (\text{Re})^{(1-n)/(1+n)} \Theta_\eta \Phi_\eta + \text{MEc} (F^2 + G^2) \\ + \text{Ec} (\text{Re})^{(1-n)/(1+n)} (1+r^*)^\zeta (F_\eta^2 + G_\eta^2) + Q\Theta = 0, \end{aligned} \tag{14}$$

$$\begin{aligned} \left( \frac{\text{Nt}}{\text{Nb}} \right) (\text{Re})^{(1-n)/(1+n)} (1+r^*)^{2\zeta} \Theta_{\eta\eta} + (\text{Re})^{(1-n)/(1+n)} (1+r^*)^{2\zeta} \Phi_{\eta\eta} \\ - \text{Sc} \zeta \eta \epsilon F \Theta_\eta - \text{Sc} H \Phi_\eta - K_1 \Phi (1 + \alpha_1 \Theta)^m \exp \left[ \frac{-E_1}{(1 + \alpha_1 \Theta)} \right] = 0, \end{aligned} \tag{15}$$

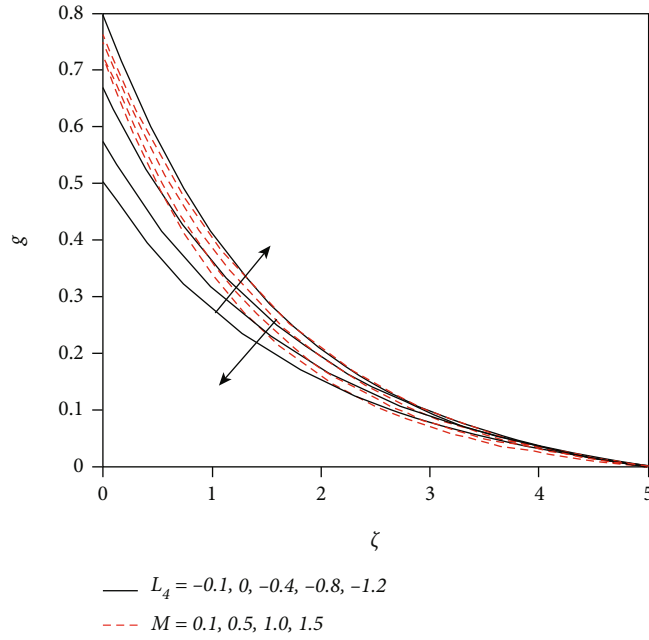


FIGURE 3: Fluctuation in tangential velocity component against two different parameters.

$$(\text{Re})^{(1-n)/(1+n)}(1+r^*)^{2c}X_{\zeta\zeta} - \text{LbHX}_{\zeta} + \text{Lbc}\eta\epsilon FX_{\eta} - \text{Pe}(\Phi_{\eta\eta}(X + \Omega_0) + X_{\eta}\Phi_{\eta}) = 0, \tag{16}$$

with

$$\begin{aligned} F(\alpha) &= A + L_1 F_{\eta}(\alpha) + L_2 F_{\eta\eta}(\alpha), \\ G(\alpha) &= 1 + L_3 G_{\eta}(\alpha) + L_4 G_{\eta\eta}(\alpha), \\ H(\alpha) &= 0, \\ \Theta_{\eta}(\alpha) &= -\Omega_1(1 - \Theta(\alpha)), \\ \Phi_{\eta}(\alpha) &= -\Omega_2(1 - \Phi(\alpha)), \\ X_{\eta}(\alpha) &= -\Omega_3(1 - X(\alpha)), \end{aligned} \tag{17}$$

$$\begin{aligned} F(\infty) &\longrightarrow 0, \\ G(\infty) &\longrightarrow 0, \\ \Theta(\infty) &\longrightarrow 0, \\ \Phi(\infty) &\longrightarrow 0, \\ X(\infty) &\longrightarrow 0. \end{aligned} \tag{18}$$

The following are currently considered for introducing the innovative similarity transformation to modify the origin

from  $\alpha$  to 0, that is,

$$\begin{aligned} H(\eta) &= h(\eta - \alpha) = h(\zeta), \\ F(\eta) &= f(\eta - \alpha) = f(\zeta), \\ G(\eta) &= g(\eta - \alpha) = g(\zeta), \\ \Theta(\eta) &= \theta(\eta - \alpha) = \theta(\zeta), \\ \Phi(\eta) &= \phi(\eta - \alpha) = \phi(\zeta), \\ X(\eta) &= \chi(\eta - \alpha) = \chi(\zeta). \end{aligned} \tag{19}$$

We get

$$2f + h_{\zeta} + (\zeta + \alpha)\zeta\epsilon F_{\zeta} = 0, \tag{20}$$

$$\begin{aligned} (\text{Re})^{(1-n)/(1+n)}(1+r^*)^{2c}f_{\zeta\zeta} - 2f_{\zeta}^2 + g^2 - hf - ff_{\zeta}\zeta(\eta + \alpha)\epsilon - Mf - K_1^*f - F_r f^2 \\ + \lambda(\theta - \text{Nr}\phi - \text{Nc}\chi) = 0, \end{aligned} \tag{21}$$

$$(\text{Re})^{(1-n)/(1+n)}(1+r^*)^{2c}g_{\zeta\zeta} - 2fg - hg_{\zeta} - fg_{\zeta}\zeta(\eta + \alpha)\epsilon - Mg - K_1^*g - F_r g^2 = 0, \tag{22}$$

$$\begin{aligned} \frac{1}{pr}(\text{Re})^{(1-n)/(1+n)}(1+r^*)^{2c}(1 + \epsilon_1)\theta_{\zeta\zeta} + \epsilon_1\theta_{\zeta}^2 + \frac{4}{3}\text{Rd} \left[ \begin{aligned} &\theta_{\zeta\zeta} + (\theta_w - 1)^3(3\theta^2\theta_{\zeta}^2 + \theta^3\theta_{\zeta\zeta}) \\ &+ 3(\theta_w - 1)^2(2\theta\theta_{\zeta}^2 + \theta^2\theta_{\zeta\zeta}) \\ &+ 3(\theta_w - 1)(\theta_{\zeta}^2 + \theta\theta_{\zeta\zeta}) \end{aligned} \right] \\ - h\theta_{\zeta} - f\theta_{\zeta}\zeta(\zeta + \alpha)\epsilon + \text{Nt}(\text{Re})^{(1-n)/(1+n)}(1+r^*)^{2c}\theta_{\zeta}^2 + \text{Nb}(\text{Re})^{(1-n)/(1+n)}\theta_{\zeta}\phi_{\zeta} \\ + \text{MEc}(f^2 + g^2) + \text{Ec}(\text{Re})^{(1-n)/(1+n)}(1+r^*)^c(f_{\zeta}^2 + g_{\zeta}^2) + Q\theta = 0, \end{aligned} \tag{23}$$

$$\begin{aligned} & \left(\frac{Nt}{Nb}\right) (\text{Re})^{(1-n)/(1+n)} (1+r^*)^{2c} \theta_{\zeta\zeta} + (\text{Re})^{(1-n)/(1+n)} (1+r^*)^{2c} \phi_{\zeta\zeta} - \text{Sc}_c(\zeta + \alpha) \epsilon f \theta_{\zeta} \\ & - \text{Sch} \phi_{\zeta} - K_1 \phi (1 + \alpha_1 \theta)^m \exp \left[ \frac{-E_1}{(1 + \alpha_1 \theta)} \right] = 0, \end{aligned} \quad (24)$$

$$(\text{Re})^{(1-n)/(1+n)} (1+r^*)^{2c} \chi_{\zeta\zeta} - \text{Lb} h \chi_{\zeta} + \text{Lb} c (\zeta + \alpha) \epsilon f \chi_{\zeta} - \text{Pe} (\phi_{\zeta\zeta} (\chi + \Omega) + \chi_{\zeta} \phi_{\zeta}) = 0, \quad (25)$$

through boundary conditions

$$\begin{aligned} f(0) &= A_1 + L_1 f_{\zeta}(0) + L_2 f_{\zeta\zeta}(0), \\ g(0) &= 1 + L_3 g_{\zeta}(0) + L_4 g_{\zeta\zeta}(0), \\ h(0) &= 0, \\ \theta_{\zeta}(0) &= -\Omega_1 (1 - \theta(0)), \\ \phi_{\zeta}(0) &= -\Omega_2 (1 - \phi(0)), \\ \chi_{\zeta}(0) &= -\Omega_3 (1 - \chi(0)), \end{aligned} \quad (26)$$

$$\begin{aligned} f(\infty) &\longrightarrow 0, \\ g(\infty) &\longrightarrow 0, \\ \theta(\infty) &\longrightarrow 0, \\ \phi(\infty) &\longrightarrow 0, \\ \chi(\infty) &\longrightarrow 0. \end{aligned} \quad (27)$$

**2.5. Dimensionless Prominent Parameters.** Now, the dimensionless prominent parameters are given in Table 1.

**2.6. Physical Quantities.** Here, the local skin friction coefficient (LSF)  $C_f$ , local Nusselt number (LNN)  $\text{Nu}_x$ , local Sherwood number (LSW)  $\text{Sh}_x$ , and density motile microorganism (LMN)  $\text{Sn}_x$  are represented as follows:

Local skin friction coefficient

$$C_f = \frac{\sqrt{\tau_{zr}^2 + \tau_{z\theta}^2}}{\rho_f (\Omega r)^2}. \quad (28)$$

Here,  $\tau_{zr}$  and  $\tau_{z\theta}$  are expressed as

$$\tau_{zr} = \mu_f (u_z) \Big|_{z=0} = \mu_f r^* \Omega_1 (1+r^*)^c \left( \frac{\Omega R_0^2 \rho_f}{\mu_f} \right)^{1/(n+1)} f_{\zeta}(0), \quad (29)$$

$$\tau_{z\theta} = \mu_f (v_z) \Big|_{z=0} = \mu_f r^* \Omega_1 (1+r^*)^c \left( \frac{\Omega R_0^2 \rho_f}{\mu_f} \right)^{1/n+1} g_{\zeta}(0). \quad (30)$$

Here,  $\tau_w$  is identified as

$$\tau_w = \sqrt{\tau_{zr}^2 + \tau_{z\theta}^2}. \quad (31)$$

Finally, local skin friction coefficient

$$C_{fx} \text{Re}^{(n-1)/(n+1)} = \frac{\tau_w|_{z=0}}{\rho_f (r\Omega)^2} = \frac{1}{r^*} (1+r^*)^c \left[ (f_{\zeta}(0))^2 + (g_{\zeta}(0))^2 \right]^{1/2}. \quad (32)$$

Here,  $\tau_{zr}$  denoted the shear stress along the radial direction,  $\tau_{z\theta}$  represent the shear stress along the direction of tangential, and  $\tau_w$  denoted the shear stress.

Local Nusselt number

$$\text{Nu}_x = \frac{R_0 q_w}{k_f (T_f - T_{\infty})} \Big|_{z=0}. \quad (33)$$

Here,  $q_w$  is symbolized as

$$q_w|_{z=0} = -k_f (T_z)|_{z=0} = -k_f (T_f - T_{\infty}) (1+r^*)^c \left( \frac{\Omega R_0^2 \rho_f}{\mu_f} \right)^{1/(n+1)} \theta_{\zeta}(0). \quad (34)$$

Finally, the local Nusselt number

$$\text{Re}^{-1/(n+1)} \text{Nu}_x = -(1+r^*)^c \theta_{\zeta}(0). \quad (35)$$

Local Sherwood number

$$\text{Sh}_x = \frac{R_0 q_m}{D_B (C_f - C_{\infty})} \Big|_{z=0}. \quad (36)$$

Here,  $q_m$  is denoted as

$$q_m = -D_B (C_z)|_{z=0}. \quad (37)$$

Finally, the local Sherwood number

$$\text{Sh}_x \text{Re}^{-1/(n+1)} = -(1+r^*)^c \phi_{\zeta}(0). \quad (38)$$

Density motile microorganism number

$$\text{Sn}_x = \frac{R_0 q_n}{D_m (N_f - N_{\infty})} \Big|_{z=0}. \quad (39)$$

Here,  $q_n$  is identified as

$$q_n = -D_m (N_z)|_{z=0}. \quad (40)$$

Finally, the density motile microorganism number

$$\text{Sn}_x \text{Re}^{-1/(n+1)} = -(1+r^*)^c \chi_{\zeta}(0). \quad (41)$$

### 3. Numerical Scheme

Significantly, the method of finding the exact solution for momentum, temperature, nanoparticle concentration, and bioconvection equations through corresponding initial

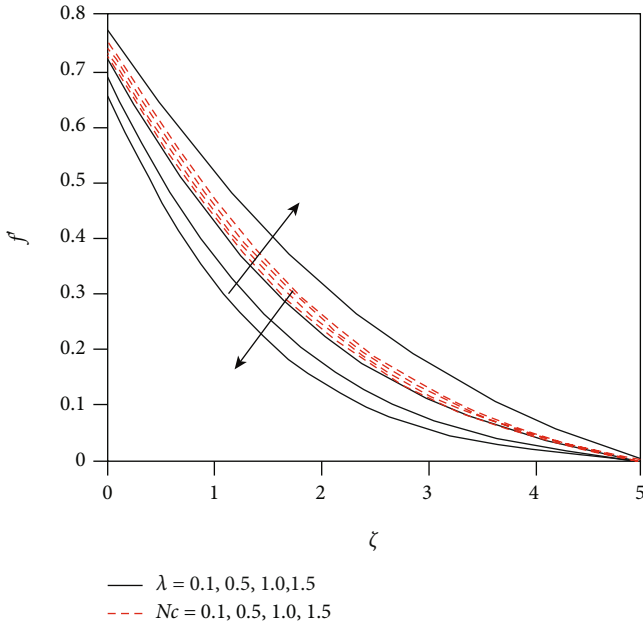


FIGURE 4: Fluctuation in radial velocity component against two different parameters.

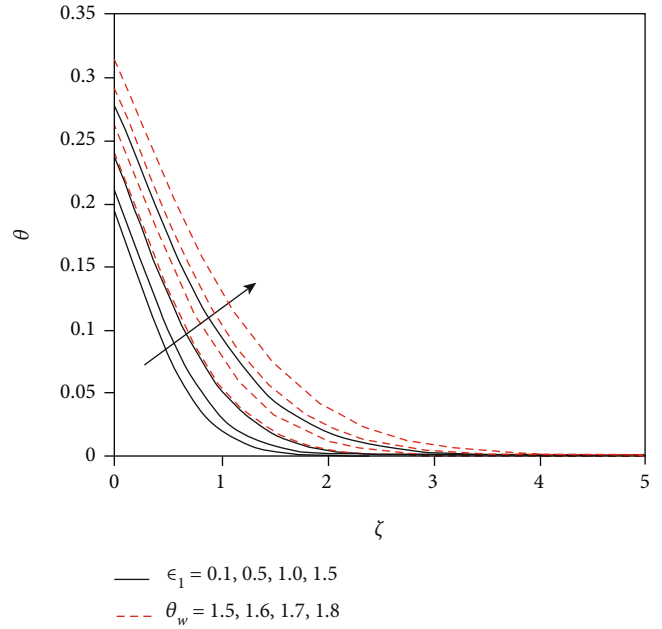


FIGURE 6: Fluctuation in thermal field against two different parameters.

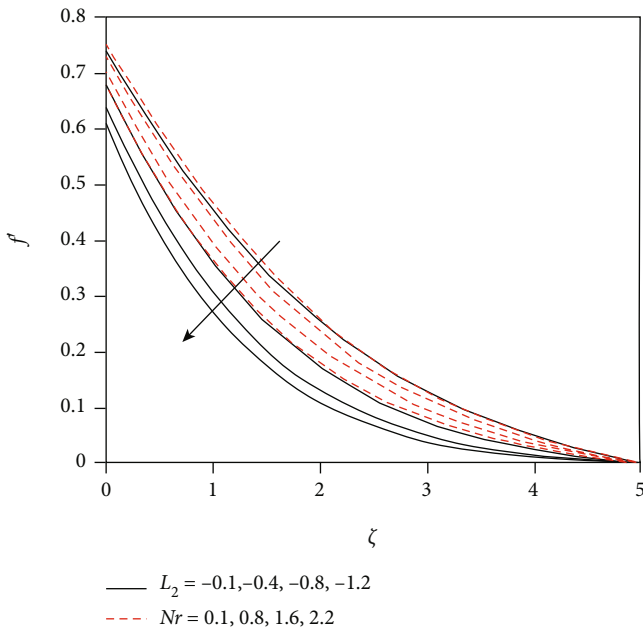


FIGURE 5: Fluctuation in radial velocity component against two different parameters.

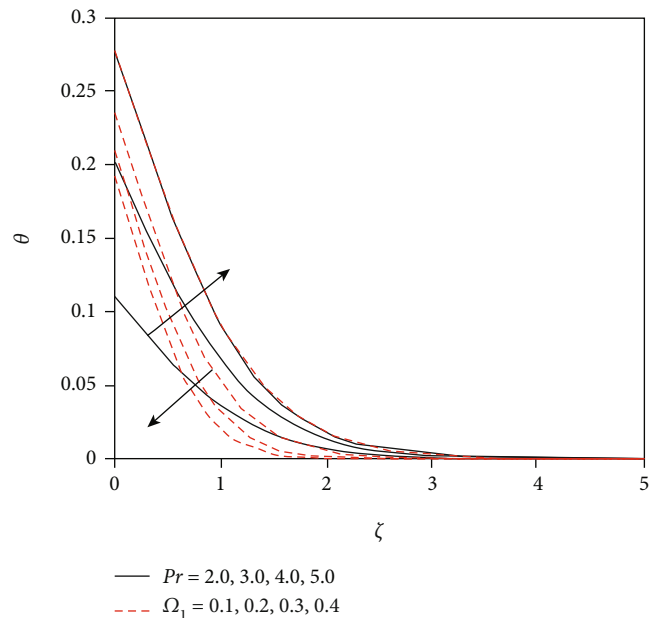


FIGURE 7: Fluctuation in thermal field against two different parameters.

conditions is very complicated and doubtful about the significance of results. Researchers have attempted to mathematically research the nanoliquid flowing past the stretching disk. Chemical processes, including activation energy, are also used to research the characteristics of mass transformation. Choose the initial guesses, and the dimensionless highly linear governing equations ((20))–((25)) with the related boundary conditions ((26))–((27)) are numeri-

cally integrated by utilizing the computational software MATLAB through built-in rule bvp4c (shooting method). The bvp4c method is a powerful way of resolving an initial value problem and a well-known methodology to find more than one solution. In order to solve these equations, first, we converted the higher-order differential equation into a first-order system by using the following technique.

We identify new variables as

$$\begin{aligned}
 h &= r_1, \\
 h_\zeta &= r_1', \\
 f &= r_2, \\
 f_\zeta &= r_3, \\
 f_{\zeta\zeta} &= r_3', \\
 g &= r_4, \\
 g_\zeta &= r_5, \\
 g_{\zeta\zeta} &= r_5', \\
 \theta &= r_6, \\
 \theta_\zeta &= r_7, \\
 \theta_{\zeta\zeta} &= r_7', \\
 \phi &= r_8, \\
 \phi_\zeta &= r_9, \\
 \phi_{\zeta\zeta} &= r_9', \\
 \chi &= r_{10}, \\
 \chi_\zeta &= r_{11}, \\
 \chi_{\zeta\zeta} &= r_{11}',
 \end{aligned} \tag{42}$$

$$r_1' = -2r_2 - (\zeta + \alpha)\zeta\epsilon r_3, \tag{43}$$

$$r_3' = \frac{2r_3^2 - r_4^2 + r_1r_2 + r_2r_3\zeta(\zeta + \alpha)\epsilon + Mr_2 + K_1^*r_2 + F_r r_2^2 - \lambda(r_6 - Nrr_8 - Ncr_{10})}{(\text{Re})^{(1-n)/(1+n)}(1+r^*)^{2\zeta}}, \tag{44}$$

$$r_5' = \frac{2r_2r_4 + r_1r_5 + r_2r_5\zeta(\zeta + \alpha)\epsilon + Mr_4 + K_1^*r_4 + F_r r_4^2}{(\text{Re})^{(1-n)/(1+n)}(1+r^*)^{2\zeta}}, \tag{45}$$

$$r_7' = \frac{r_1r_7 - \epsilon_1r_7^2 + r_2r_7\zeta(\zeta + \alpha)\epsilon - \text{Nt}(\text{Re})^{(1-n)/(1+n)}(1+r^*)^{2\zeta}r_7^2 - \text{Nb}(\text{Re})^{(1-n)/(1+n)}r_7r_9 - \text{MEc}(r_2^2 + r_4^2) - \text{Ec}(\text{Re})^{(1-n)/(1+n)}(1+r^*)^\zeta(r_3^2 + r_5^2) - (4/3)\text{Rd}[(\theta_w - 1)^3(3r_6^2r_7^2) + 3(\theta_w - 1)^2(2r_6r_7\zeta^2) + 3(\theta_w - 1)(r_7^2)] - Qr_6}{(1)/pr(\text{Re})^{(1-n)/(1+n)}(1+r^*)^{2\zeta}(1+\epsilon_1) + (4/3)\text{Rd}(1 + (\theta_w - 1)^3r_6^3 + 3(\theta_w - 1)^2r_6^2 + 3(\theta_w - 1)r_6)}, \tag{46}$$

$$r_9' = \frac{-(\text{Nt}/\text{Nb})(\text{Re})^{(1-n)/(1+n)}(1+r^*)^{2\zeta}r_7' + \text{Sc}\zeta(\zeta + \alpha)\epsilon r_2r_7 + \text{Scr}_1r_9 + K_1r_8(1 + \alpha_1r_6)^m \exp[-E_1/(1 + \alpha_1r_6)]}{(\text{Re})^{(1-n)/(1+n)}(1+r^*)^{2\zeta}}, \tag{47}$$

$$r_{11}' = \frac{\text{Lbr}_1r_{11} - \text{Lbc}\zeta(\zeta + \alpha)\epsilon r_2r_{11} + \text{Pe}(r_9'(r_{10} + \Omega) + r_{11}r_9)}{(\text{Re})^{(1-n)/(1+n)}(1+r^*)^{2\zeta}}, \tag{48}$$

$$r_2(0) = A_1 + L_1r_3(0) + L_2r_3'(0), r_4(0) = 1 + L_3r_5(0) + L_4r_5'(0), r_1(0) = 0, r_7(0) = -\Omega_1(1 - r_6(0)), r_9(0) = -\Omega_2(1 - r_8(0)), r_{11}(0) = -\Omega_3(1 - r_{10}(0)), \tag{49}$$

$$r_2(\infty) \longrightarrow 0, r_4(\infty) \longrightarrow 0, r_6(\infty) \longrightarrow 0, r_8(\infty) \longrightarrow 0, r_{10}(\infty) \longrightarrow 0. \tag{50}$$

## 4. Result and Discussion

The aim of this portion is to envisage variations in velocity components, thermal field, concentration of nanoparticles, and microorganism profile due to interesting involved parameters introduced during the flow of bioconvective nanofluid that are demonstrated in Figures 2–10. Figure 2 explains the effects of second-order slip parameter and stretching rate to angular frequency. The escalating estima-

tions of stretching rate to frequency exaggerate the axial velocity component. From this scenario, it can be detected that axial velocity of nanofluid decays via larger variations in second-order velocity slip parameter. Figure 3 communicates the impacts of second-order velocity slip as well as magnetic parameter versus tangential velocity. It can be observed that tangential velocity boosts up via larger second-order velocity slip parameter. Here, we also observe that the larger estimations in magnetic parameter diminishes

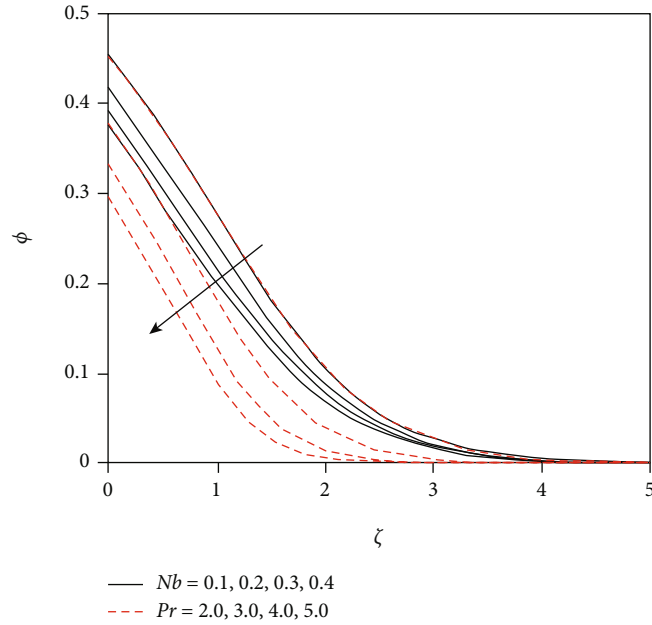


FIGURE 8: Fluctuation in concentration field against two different parameters.

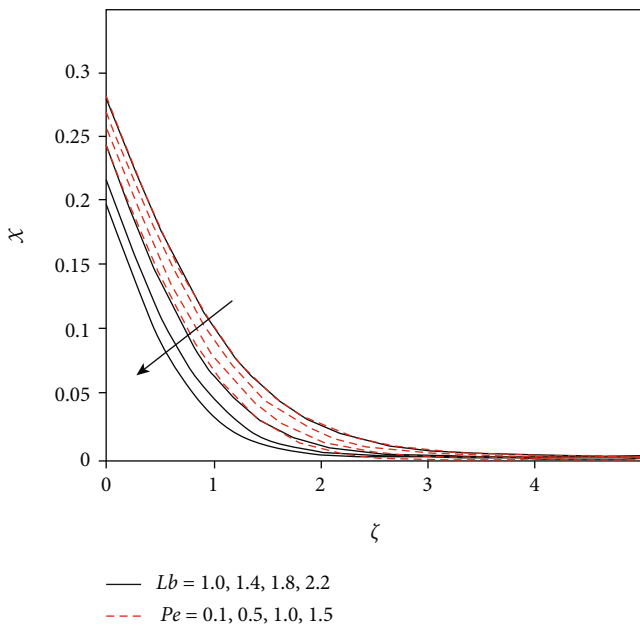


FIGURE 9: Fluctuation in the microorganism's field against two different parameters.

the tangential velocity of nanofluid flow. In terms of physics, the magnetic parameter is associated to the Lorentz force, which is a resistive force to the fluid flow. As the magnetic parameter increases, the resistance forces increase, and the velocity decreases. Figure 4 demonstrates the features of mixed convection parameter as well as bioconvection Rayleigh number over a radial velocity component. It is noticed that velocity is improved by growing the estimations of mixed convection parameter while it depresses via a greater bioconvection Rayleigh number. The features of buoyancy

ratio parameter and second-order velocity slip parameter versus radial component of velocity are elaborated through Figure 5. The radial velocity is a decreasing function of second-order velocity slip parameter and buoyancy ratio parameter. Physically, for a given buoyancy impact, bioconvection inhibits the up movement of solid particles that arise in nanofluid; however, for a higher buoyancy impact, the fluid resists the fluid, resulting in fluid movement decline.

Figure 6 examines the behavior of thermal conductivity and temperature ratio parameter via thermal distribution of nanomaterials. It is witnessed that temperature field upsurges due to an increment in thermal conductivity and temperature ratio parameter. Figure 7 portrays the impression of Prandtl number and thermal Biot number versus temperature field. It is mentioned that improving Prandtl number reduces the temperature distribution. From this communication, we analyzed that enhancing the thermal Biot number escalates thermal field. Physically, when the Prandtl number rises, the thermal diffusivity diminishes. Fluid temperature drops as a result of the lower thermal diffusivity. Figure 8 presents the trend of the Brownian motion coefficient and Prandtl number against solutal field. Here, concentration reduces via a greater amount of Brownian motion coefficient as well as Prandtl number. Micromixing and heat conduction in the nanofluid are aided by enhancing the Brownian motion parameter, causing the temperature to rise and the nanoparticles to scatter more widely.

Figure 9 shows the nature of bioconvection Lewis number and Peclet number over a microorganism's field. It is concluded that the microorganism field diminishes by increasing the variations of bioconvection Lewis number and Peclet number. The bioconvection Lewis number has an converse relationship with microorganism diffusivity. As the bioconvection Lewis number rises, the diffusivity decreases, and the microorganism profile drops. The features

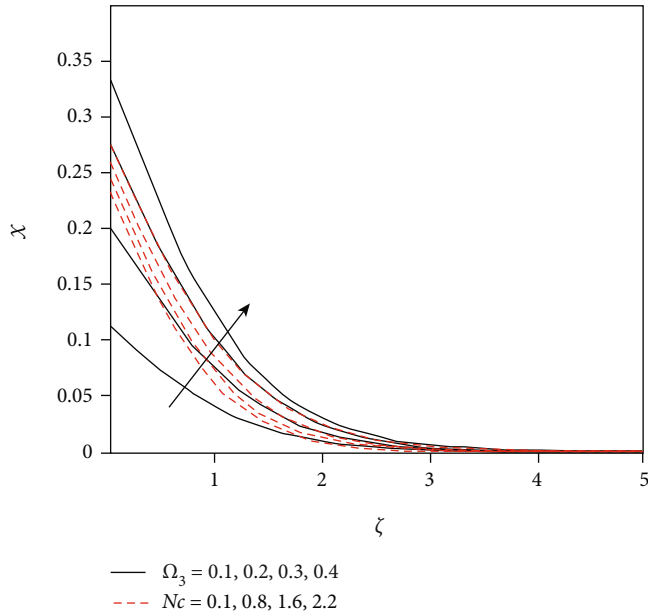


FIGURE 10: Fluctuation in the microorganism's field against two different parameters.

TABLE 2: Validation in results between published literature and current outcomes are present.

	$f''(0)$	$g'(0)$	$\theta'(0)$
Xun et al. [29]	0.51023	0.61592	0.39627
Anderson et al. [30]	0.510	0.616	0.3963
Ming et al. [31]	0.51021	0.61591	0.39632
Khan et al. [33]	0.51082	0.61595	0.3958
Current results	0.51084	0.61598	0.3958

of microorganism Biot number and bioconvection Rayleigh number are mentioned in Figure 10. It is noted that larger magnitudes of microorganism Biot number and bioconvection Rayleigh number increases the microorganism's profile. Here, it was analyzed that good validation in results between published literature and current outcomes is presented in Table 2.

## 5. Conclusion

Computational analysis is conducted on bioconvective viscous nanofluid flow past a stretching disk with higher-order slips and nonlinear thermal radiation. The main outcomes are listed as follows:

- (i) Axial velocity component escalates versus a larger amount of stretching rate to angular frequency
- (ii) Tangential velocity is increases against a second-order slip parameter
- (iii) The increment in radial velocity has been analyzed along with increments in mixed convection parameter

- (iv) The larger slip parameter and buoyancy ratio parameter reduce the radial velocity of nanofluid
- (v) Thermal field of species rises against temperature-dependent thermal conductivity
- (vi) Temperature distribution is increased via the temperature ratio parameter
- (vii) Greater values of the thermal Biot number boost the temperature field
- (viii) Concentration is reduced against the Brownian motion parameter
- (ix) The microorganism's profile boosts via the microorganism's Biot number while it diminishes against the Peclet number
- (x) The microorganism's field is depressed against the bioconvection Lewis number

## Nomenclature

- $(u, v, w)$ : Velocity components ( $\text{m}\cdot\text{s}^{-1}$ )  
 $(r, \varphi, z)$ : Coordinates of system (m)  
 $\nu_f$ : Kinematic viscosity  
 $F$ : Inertia coefficient  
 $k^*$ : Porous permeability  
 $b$ : Chemotaxis constant  
 $\sigma_f$ : Electrical conductivity  
 $g^*$ : Gravitational acceleration  
 $\beta^{**}$ : Volume expansion coefficient  
 $D_T$ : Thermophoretic diffusion coefficient  
 $D_m$ : Microorganism coefficient  
 $\tau$ : Capacity ratio  
 $\sigma^*$ : Stefan Boltzmann number  
 $kr^2$ : Chemical reaction coefficient  
 $E_a$ : Coefficient of activation energy  
 $N_\infty$ : Ambient microorganisms  
 $W_c$ : Cell swimming speed  
 $N_f$ : Surface microorganisms  
 $K_1^*$ : Chemical reaction parameter  
 $K_1$ : Chemical reaction parameter  
 $F_r$ : Darcy Forchheimer parameter  
 $\lambda$ : Mixed convection parameter  
 $M$ : Magnetic parameter  
 $Nr$ : Buoyancy ratio parameter  
 $Nc$ : Bioconvection Rayleigh number  
 $Lb$ : Bioconvection Lewis number  
 $\alpha_1$ : Temperature ratio parameter  
 $\tau_{zr}$ : Radial directional shear stress  
 $\tau_{z\theta}$ : Tangential directional shear stress  
 $Pe$ : Peclet number  
 $\Omega_0$ : Microorganism difference parameter  
 $A$ : Stretching ratio to angular frequency  
 $L_1$ : Radial direction first-order velocity slip  
 $Sh_x$ : LSN  
 $Sn_x$ : LMN  
 $\rho_f$ : Fluid density ( $\text{kg}/\text{m}^3$ )



$\rho_p$ :	Nanoparticle density
$\rho_m$ :	Microorganism density
$k_f$ :	Thermal conductivity ( $\text{Wm}^{-1}\text{K}^{-1}$ )
$c_p$ :	Specific heat (J/K)
$(\rho c_p)_f$ :	Heat capacity ( $\text{Jm}^{-3}\text{K}^{-1}$ )
$T_\infty$ :	Ambient temperature
$\beta_0$ :	Magnetic field strength ( $\text{N}\cdot\text{m}^{-1}\cdot\text{A}^{-1}$ )
$D_B$ :	Brownian diffusion coefficient
$k^*$ :	Mean absorption coefficient
$\lambda_3, \lambda_4$ :	Coefficient of velocity slips
$h_1, h_2, h_3$ :	Heat, mass, microorganism transfer coefficient
Nb:	Brownian motion parameter
$C_\infty$ :	Ambient concentration
$T_f$ :	Surface temperature
$C_f$ :	Surface concentration
Re:	Reynolds number
Pr:	Prandtl number
Rd:	Thermal radiation parameter
$\theta_w$ :	Temperature difference parameter
$E_1$ :	Activation energy parameter
Nt:	Thermophoresis parameter
Ec:	Eckert number
Sc:	Schmidt number
$L_2$ :	Radial direction second-order velocity slip
$L_3$ :	Tangential direction first-order velocity slip
$L_4$ :	Tangential direction second-order velocity slip
$\Omega_1$ :	Thermal Biot number
$\Omega_2$ :	Mass Biot number
$\Omega_3$ :	Microorganism Biot number
$C_f$ :	Skin friction coefficient
$\text{Nu}_x$ :	LNN
$\text{Nu}_x$ :	Nusselt number
$\tau_w$ :	Shear stress

## Data Availability

The data that support the findings of this study are available from the corresponding author upon reasonable request.

## Conflicts of Interest

The authors proclaim that they have no competing interests.




## References

- [1] S. U. S. Choi and J. A. Eastman, "Enhancing thermal conductivity of fluids with nanoparticles," in *1995 International mechanical engineering congress and exhibition*, United States, 1995.
- [2] J. Buongiorno, "Convective transport in nanofluids," *Journal of Heat Transfer*, vol. 128, pp. 240–250, 2006.
- [3] M. R. Eid and F. Mabood, "Entropy analysis of a hydromagnetic micropolar dusty carbon NTs-kerosene nanofluid with heat generation: Darcy–Forchheimer scheme," *Journal of Thermal Analysis and Calorimetry*, vol. 143, no. 3, pp. 2419–2436, 2021.
- [4] M. Umar, R. Akhtar, Z. Sabir et al., "Numerical treatment for the three-dimensional Eyring–Powell fluid flow over a stretching sheet with velocity slip and activation energy," *Advances in Mathematical Physics*, vol. 2019, 2019.
- [5] T. Muhammad, H. Waqas, S. A. Khan, R. Ellahi, and S. M. Sait, "Significance of nonlinear thermal radiation in 3D Eyring–Powell nanofluid flow with Arrhenius activation energy," *Journal of Thermal Analysis and Calorimetry*, vol. 143, no. 2, pp. 929–944, 2021.
- [6] G. Rasool, A. Shafiq, and C. M. Khalique, "Marangoni forced convective Casson type nanofluid flow in the presence of Lorentz force generated by Riga plate," *Discrete & Continuous Dynamical Systems-S.*, vol. 14, no. 7, pp. 2517–2533, 2021.
- [7] B. Mahanthesh, J. Mackolil, M. Radhika, and W. Al-Kouz, "Significance of quadratic thermal radiation and quadratic convection on boundary layer two-phase flow of a dusty nanofluid past a vertical plate," *International Communications in Heat and Mass Transfer*, vol. 120, article 105029, 2021.
- [8] G. Aaiza, I. Khan, and S. Shafie, "Energy transfer in mixed convection MHD flow of nanofluid containing different shapes of nanoparticles in a channel filled with saturated porous medium," *Nanoscale Research Letters*, vol. 10, no. 1, pp. 1–14, 2015.
- [9] A. Hussanan, M. Z. Salleh, I. Khan, and S. Shafie, "Convection heat transfer in micropolar nanofluids with oxide nanoparticles in water, kerosene and engine oil," *Journal of Molecular Liquids*, vol. 229, pp. 482–488, 2017.
- [10] A. Khalid, I. Khan, and S. Shafie, "Exact solutions for free convection flow of nanofluids with ramped wall temperature," *The European Physical Journal Plus*, vol. 130, no. 4, pp. 1–14, 2015.
- [11] F. Ali, M. Gohar, and I. Khan, "MHD flow of water-based Brinkman type nanofluid over a vertical plate embedded in a porous medium with variable surface velocity, temperature and concentration," *Journal of Molecular Liquids*, vol. 223, pp. 412–419, 2016.
- [12] N. A. M. Zin, I. Khan, and S. Shafie, "The impact silver nanoparticles on MHD free convection flow of Jeffrey fluid over an oscillating vertical plate embedded in a porous medium," *Journal of Molecular Liquids*, vol. 222, pp. 138–150, 2016.
- [13] A. R. Bestman, "Natural convection boundary layer with suction and mass transfer in a porous medium," *International Journal of Energy Research*, vol. 14, pp. 389–396, 1990.
- [14] X. Guo, J. Cai, and X. Yu, "Kinetics and thermodynamics of microalgae residue oxidative pyrolysis based on double distributed activation energy model with simulated annealing method," *Journal of Analytical and Applied Pyrolysis*, vol. 154, 2021.
- [15] T. Hayat, A. Aziz, and A. Alsaedi, "Analysis of entropy production and activation energy in hydromagnetic rotating flow of nanofluid with velocity slip and convective conditions," *Journal of Thermal Analysis and Calorimetry*, vol. 146, no. 6, pp. 2561–2576, 2021.
- [16] N. R. Araújo, Á. C. Duarte, F. J. Pujatti, M. B. Freitas-Marques, and R. C. Sebastião, "Kinetic models and distribution of activation energy in complex systems using Hopfield neural network," *Thermochimica Acta*, vol. 697, article 178847, 2021.
- [17] E. Elangovan and S. K. Natarajan, "Effects of pretreatments on quality attributes, moisture diffusivity, and activation energy of solar dried ivy gourd," *Journal of Food Process Engineering*, vol. 44, no. 4, 2021.
- [18] M. Bilal, A. Saeed, M. M. Selim, T. Gul, I. Ali, and P. Kumam, "Comparative numerical analysis of Maxwell's time-dependent thermo-diffusive flow through a stretching

- cylinder,” *Case Studies in Thermal Engineering*, vol. 27, article 101301, 2021.
- [19] A. Saeed, A. Alsubie, P. Kumam, S. Nasir, T. Gul, and W. Kumam, “Blood based hybrid nanofluid flow together with electromagnetic field and couple stresses,” *Scientific Reports*, vol. 11, no. 1, pp. 1–18, 2021.
- [20] J. R. Platt, “Bioconvection patterns in cultures of free-swimming organisms,” *Science*, vol. 133, no. 3466, pp. 1766–1767, 1961.
- [21] A. V. Kuznetsov, “Thermo-bioconvection in a suspension of oxytactic bacteria,” *International Communications in Heat and Mass Transfer*, vol. 32, no. 8, pp. 991–999, 2005.
- [22] I. Tlili, M. Ramzan, H. U. Nisa, M. Shutaywi, Z. Shah, and P. Kumam, “Onset of gyrotactic microorganisms in MHD micropolar nanofluid flow with partial slip and double stratification,” *Journal of King Saud University-Science*, vol. 32, no. 6, pp. 2741–2751, 2020.
- [23] F. S. Al-Mubaddel, U. Farooq, K. Al-Khaled et al., “Double stratified analysis for bioconvection radiative flow of Sisko nanofluid with generalized heat/mass fluxes,” *Physica Scripta*, vol. 96, no. 5, article 055004, 2021.
- [24] A. Abbasi, F. Mabood, W. Farooq, and M. Batool, “Bioconvective flow of viscoelastic nanofluid over a convective rotating stretching disk,” *International Communications in Heat and Mass Transfer*, vol. 119, 2020.
- [25] S. A. Shehzad, M. G. Reddy, A. Rauf, and Z. Abbas, “Bioconvection of Maxwell nanofluid under the influence of double diffusive Cattaneo–Christov theories over isolated rotating disk,” *Physica Scripta*, vol. 95, no. 4, article 045207, 2020.
- [26] S. Aziz, I. Ahmad, S. U. Khan, and N. Ali, “A three-dimensional bioconvection Williamson nanofluid flow over bidirectional accelerated surface with activation energy and heat generation,” *International Journal of Modern Physics B*, vol. 35, no. 9, article 2150132, 2021.
- [27] M. Alizadeh and D. D. Ganji, “Multi-objective optimization of an externally finned two-phase closed thermosyphon using response surface methodology,” *Applied Thermal Engineering*, vol. 171, article 115008, 2020.
- [28] M. Alizadeh and D. D. Ganji, “Heat transfer characteristics and optimization of the efficiency and thermal resistance of a finned thermosyphon,” *Applied Thermal Engineering*, vol. 183, article 116136, 2021.
- [29] S. Xun, J. Zhao, L. Zheng, X. Chen, and X. Zhang, “Flow and heat transfer of Ostwald-de Waele fluid over a variable thickness rotating disk with index decreasing,” *International Journal of Heat and Mass Transfer*, vol. 103, pp. 1214–1224, 2016.
- [30] H. I. Andersson, E. D. Korte, and R. Meland, “Flow of a power-law fluid over a rotating disk revisited,” *Fluid Dynamics Research*, vol. 28, no. 2, pp. 75–88, 2001.
- [31] C. Y. Ming, L. C. Zheng, and X. X. Zhang, “Steady flow and heat transfer of the power-law fluid over a rotating disk,” *Communications in Heat and Mass Transfer*, vol. 38, no. 3, pp. 280–284, 2011.
- [32] S. Z. Abbas, M. I. Khan, S. Kadry, W. A. Khan, M. Israr-Ur-Rehman, and M. Waqas, “Fully developed entropy optimized second order velocity slip MHD nanofluid flow with activation energy,” *Computer Methods and Programs in Biomedicine*, vol. 190, article 105362, 2020.
- [33] M. I. Khan, F. Alzahrani, A. Hobiny, and Z. Ali, “Fully developed second order velocity slip Darcy-Forchheimer flow by a variable thicked surface of disk with entropy generation,” *International Communications in Heat and Mass Transfer*, vol. 117, article 104778, 2020.

## Research Article

# Numerical Investigation of Fractional-Order Kawahara and Modified Kawahara Equations by a Semianalytical Method

Weaam Alhejaili,<sup>1</sup> Sharifah E. Alhazmi,<sup>2</sup> Rashid Nawaz ,<sup>3</sup> Aatif Ali ,<sup>3</sup> Joshua Kiddy Kwasi Asamoah ,<sup>4</sup> and Laiq Zada<sup>3</sup>

<sup>1</sup>Department of Mathematical Sciences, College of Science, Princess Nourah bint Abdulrahman University, P.O. Box 84428, Riyadh 11671, Saudi Arabia

<sup>2</sup>Umm Al-Qura University, College of Education for Girls at Al-Qunfudah, Mathematics Department, Mecca, Saudi Arabia

<sup>3</sup>Department of Mathematics, Abdul Wali Khan University Mardan, Khyber Pakhtunkhwa 23200, Pakistan

<sup>4</sup>Department of Mathematics, Kwame Nkrumah University of Science and Technology, Kumasi, Ghana

Correspondence should be addressed to Joshua Kiddy Kwasi Asamoah; [topeljoshua@gmail.com](mailto:topeljoshua@gmail.com)

Received 22 December 2021; Revised 8 January 2022; Accepted 17 January 2022; Published 3 February 2022

Academic Editor: Anwar Saeed

Copyright © 2022 Weaam Alhejaili et al. This is an open access article distributed under the Creative Commons Attribution License, which permits unrestricted use, distribution, and reproduction in any medium, provided the original work is properly cited.

In this work, the optimal homotopy asymptotic method (OHAM) has been used to find approximate solutions to the nonlinear fractional-order Kawahara and modified Kawahara equations. The method convergence is controlled by a flexible function known as the auxiliary function. The values of the unknown arbitrary constants in the auxiliary function are computed using the Caputo derivative fractional-order and the well-known approach of least squares. Fractional-order derivatives are taken in the Caputo sense with numerical values in the closed interval  $[0, 1]$ . The suggested method is directly applied to fractional-order Kawahara and modified Kawahara equations, with no need for small or large parameter assumptions. The numerical results obtained by the proposed method are compared to the new iterative method (NIM). Results reveal that the proposed method converges faster to the exact solution than other methods in the literature.

## 1. Introduction

Fractional computation was established as an important subject of mathematics in 1695. Fractional calculus ideas have recently been successfully expanded to numerous sectors, and academics have increasingly realized that fractional calculus may well reflect many nonlocal occurrences in the fields of natural science and architecture. Rheology, liquid flow, dispersion diffusion transport, dynamic cycles in self-compatible and porous materials, viscoelasticity, and optics are some of the key areas of fractional calculation today. Very few researchers have drawn on the successful use of fractional systems in these fields to examine their mathematical approximation methods, since diagnostic frameworks are usually difficult to obtain. A variety of real-world problems can be modeled using fractional-order differential equations. These equations have many applications in fluid

mechanics, electromagnetic theory, electric grids, diffuse transport, groundwater problems, biological sciences, etc. [1–9]. The exact solution for nonlinear problems is very hard to obtain, and an alternative way is to find the approximate solution. Some familiar approximation methods are used in the series of papers [9–21], etc. Similarly, we extend the well-known optimal homotopy asymptotic method (OHAM) to fractional-order Kawahara and modified Kawahara equations.

The proposed approach was presented by Marinca and Herisanu and applied to resolve nonlinear differential equations in the literature series [22–26]. Recently, Sarwar et al. extended the idea of OHAM fractional-order partial differential equations and used them for different problems having fractional-order derivatives [27, 28]. Nawaz et al. applied the suggested approach to the fractional-order Zakharov-Kuznetsov equations [29]. Likewise, Zada et al.

applied the proposed approach to various fractional PDEs in the series of articles [30, 31]. In this article, the application of OHAM is extended to the modified Kawahara and Kawahara equations together with initial conditions:

$$\frac{\partial^\alpha Y(\xi, \tau)}{\partial \tau^\alpha} + Y(\xi, \tau) \frac{\partial Y(\xi, \tau)}{\partial \xi} + Y(\xi, \tau) - \frac{\partial^5 Y(\xi, \tau)}{\partial \xi^5} = 0, 0 < \alpha \leq 1,$$

$$Y(\xi, 0) = \frac{105}{169} \sec h^4 \left( \frac{\xi}{2\sqrt{13}} \right), \tag{1}$$

$$\frac{\partial^\alpha Y(\xi, \tau)}{\partial \tau^\alpha} + Y^2(\xi, \tau) \frac{\partial Y(\xi, \tau)}{\partial \xi} + \rho \frac{\partial^3 Y(\xi, \tau)}{\partial \xi^3} + \mu \frac{\partial^5 Y(\xi, \tau)}{\partial \xi^5} = 0, 0 < \alpha \leq 1, \tag{2}$$

$$Y(\xi, 0) = \frac{3\rho}{\sqrt{-10\mu}} \sec h^2(k\xi), k = \frac{1}{2} \sqrt{\frac{-\rho}{2\mu}}.$$

Here,  $\rho$  and  $\mu$  are constants. Equations (1) and (2) have become the subject of active and wide research topics in recent times [32–34].

### 2. Preliminaries

*Definition 1.* The Riemann-Liouville fractional integral operator of an order  $\alpha \geq 0$  of a function  $G \in C_\mu, \mu \geq -1$  is presented by

$$\begin{cases} I_a^\alpha G(\xi) = \frac{1}{\Gamma(\alpha)} \int_a^\xi (\xi - \mu)^{\alpha-1} G(\mu) d\mu, \alpha > 0, \xi > 0, \\ I_a^0 G(\xi) = G(\xi). \end{cases} \tag{3}$$

*Definition 2.* The fractional derivative  $G(\xi)$  according to Caputo is presented by

$$\begin{cases} D_a^\alpha G(\xi) = I_a^{m-\alpha} D^m G(\xi) = \frac{1}{\Gamma(m-\alpha)} \int_a^\xi (\xi - \mu)^{m-\alpha-1} G^m(\mu) d\mu, \\ m-1 < \alpha \leq m, m \in N, \xi > 0, G \in C_{-1}^m. \end{cases} \tag{4}$$

*Definition 3.* If  $m-1 < \alpha \leq m, m \in N$ , and  $G \in C_\mu^m, \mu \geq -1$ , then  $D_a^\alpha I_a^\alpha G(\xi) = G(\xi)$  and  $D_a^\alpha I_a^\alpha G(\xi) = G(\xi) - \sum_{k=0}^{m-1} G^{(k)}(\xi - a)/k!, \xi > 0$ .

The properties of operator  $I^\alpha$  are found in [3, 11]. We introduce the subsequent.

For  $G \in C_\mu^m, \alpha, \beta > 0, \mu \geq -1$ , and  $\gamma \geq -1$ ,

- (1)  $I_a^\alpha G(\xi)$  exist for almost every  $\xi \in [a, b]$
- (2)  $I_a^\alpha I_a^\beta G(\xi) = I_a^{\alpha+\beta} G(\xi)$
- (3)  $I_a^\alpha I_a^\beta G(\xi) = I_a^\beta I_a^\alpha G(\xi)$
- (4)  $I_a^\alpha (\xi - a)^\gamma = (\Gamma(\gamma + 1)/\Gamma(\alpha + \gamma + 1))(\xi - a)^{\alpha+\gamma}$

### 3. OHAM Methodology to Fractional-Order PDEs [27, 28]

To extend the basic theory of OHAM for fractional-order PDEs, we assume that the subsequent general fractional differential system

$$\frac{\partial^\alpha Y(\xi, \tau)}{\partial \tau^\alpha} = A(Y(\xi, \tau) + F(\xi, \tau))\alpha > 0, \tag{5}$$

with initial condition

$$\begin{aligned} D_0^{\alpha-\kappa} Y(\xi, 0) &= h_\kappa(r), (\kappa = 0, 1, 2, \dots, n-1), D_0^{\alpha-n} Y(\xi, 0) = 0, n = [\alpha], \\ D_0^\kappa Y(\xi, 0) &= g_\kappa(r), (\kappa = 0, 1, 2, \dots, n-1), D_0^n Y(\xi, 0) = 0, n = [\alpha]. \end{aligned} \tag{6}$$

In the above equation,  $\partial^\alpha/\partial \tau^\alpha$  represents the Caputo fractional derivative operator,  $A$  stands for the differential operator, and  $Y(\xi, \tau)$  represents an unknown function.  $F(\xi, \tau)$  is a function that serves as an analytical function.

The homotopy using OHAM for equation (5) is  $\phi(\xi, \tau; p): \Omega \times [0, 1] \rightarrow R$  which is satisfied:

$$\begin{aligned} (1-p) \left( \frac{\partial^\alpha \phi(\xi, \tau)}{\partial \tau^\alpha} - F(\xi, \tau) \right) - H(\xi, p) \\ \cdot \left( \frac{\partial^\alpha \phi(\xi, \tau)}{\partial \tau^\alpha} - (A(\phi(\xi, \tau)) + F(\xi, \tau)) \right) = 0. \end{aligned} \tag{7}$$

Hence,  $p \in [0, 1]$  which is an embedding parameter and  $H(\xi, \tau)$  shows the auxiliary function such that

$$H(\xi, \tau) \neq 0 \text{ for } p \neq 0 \text{ and } H(\xi, 0) = 0. \tag{8}$$

*Remark 4.* The approximate solution  $\phi(\xi, \tau)$  approaches to the closed solution when the numerical values of  $p$  varies for 0 to 1 in the closed interval  $[0, 1]$ . The convergence of the OHAM purely depends on the auxiliary function.

The auxiliary function  $H(\xi, p)$  is set out below:

$$H(\xi, p) = pk_1(\xi, C_i) + p^2k_2(\xi, C_i) + p^3k_3(\xi, C_i) + \dots + p^mk_m(\xi, C_i). \tag{9}$$

In equation (9),  $C_i, i = 1, 2, \dots$ , convergence control parameters  $k_i(\xi), i = 1, 2, \dots$ , is a function of  $\xi$ .

By extending  $\phi(\xi, \tau; p, C_i)$  in Taylor's series about  $p$ , one can obtain

$$\phi(\xi, \tau; C_i) = Y_0(\xi, \tau) + \sum_{k=1}^m Y_k(\xi, \tau; C_i)p^k, i = 1, 2, 3, \dots. \tag{10}$$

Putting  $p = 1$ , in the above equation, we have

$$Y(\xi, \tau; C_i) = Y_0(\xi, \tau) + \sum_{k=1}^{\infty} Y_k(\xi, \tau; C_i), i = 1, 2, 3, \dots \quad (11)$$

By substituting equation (10) in equation (7) and equating the coefficient of the same powers of  $p$ , we acquire the series of problems:

$$\begin{aligned} p^0 &: \frac{\partial^\alpha Y_0(\xi, \tau)}{\partial \tau^\alpha} - F = 0, \\ p^1 &: \frac{\partial^\alpha Y_1(\xi, \tau, C_1)}{\partial \tau^\alpha} - (1 + C_1) \frac{\partial^\alpha Y_0(\xi, \tau)}{\partial \tau^\alpha} \\ &\quad + (1 + C_1)F + C_1 A(Y_0(\xi, \tau)) = 0, \\ p^2 &: \frac{\partial^\alpha Y_2(\xi, \tau, C_1, C_2)}{\partial \tau^\alpha} - (1 + C_1) \frac{\partial^\alpha Y_1(\xi, \tau, C_1)}{\partial \tau^\alpha} - C_2 \frac{\partial^\alpha Y_0(\xi, \tau)}{\partial \tau^\alpha} \\ &\quad + C_1 A(Y_1(\xi, \tau, C_1)) + C_2(F + A(Y_0(\xi, \tau))) = 0 \dots \end{aligned} \quad (12)$$

The above problems contain fractional-order derivatives. So, we apply the inverse of the operator  $I^\alpha$  on both sides of the above problems:

$$\begin{aligned} Y_0(\xi, \tau) &= I^\alpha[F], \\ Y_1(\xi, \tau; C_1) &= I^\alpha \left[ (1 + C_1) \frac{\partial^\alpha Y_0(\xi, \tau)}{\partial \tau^\alpha} - (1 + C_1)F - C_1 A(Y_0(\xi, \tau)) \right], \\ Y_2(\xi, \tau; C_1, C_2) &= I^\alpha \left[ (1 + C_1) \frac{\partial^\alpha Y_1(\xi, \tau; C_1)}{\partial \tau^\alpha} + C_2 \frac{\partial^\alpha Y_0(\xi, \tau)}{\partial \tau^\alpha} \right. \\ &\quad \left. - C_1 A(Y_1(\xi, \tau; C_1)) - C_2(F + A(Y_0(\xi, \tau))) \right] \dots \end{aligned} \quad (13)$$

By using these solutions in equation (11), we obtain the approximate solution:

$$\tilde{Y}(\xi, \tau; C_i) = Y_0(\xi, \tau) + Y_1(\xi, \tau; C_1) + Y_2(\xi, \tau; C_1, C_2) + \dots \quad (14)$$

The residual  $R(\xi, \tau; C_i)$  is acquired by using equation (14) into equation (5).

$C_1, C_2, \dots$  can be found by using either the Ritz method, the least squared method, the collocation method, or Galerkin's method. The least-square approach is used here. Here, we introduce the functional

$$\chi(C_i) = \int_0^t \int_{\Omega} R^2(\xi, \tau; C_i) d\xi d\tau, \quad (15)$$

then calculate the optimal values for auxiliary constants  $C_i$  by solving the following equation system:

$$\frac{\partial \chi}{\partial C_1} = \frac{\partial \chi}{\partial C_2} = \dots = \frac{\partial \chi}{\partial C_m} = 0. \quad (16)$$

**3.1. Convergence Theorem.** If the series (11) converge to

$Y(\xi, \tau)$ , where  $Y_k(\xi, \tau) \in L(R^+)$  is generated by the zero-order system and the  $K$ -order deformation, then  $Y(\xi, \tau)$  is the exact solution of (5).

*Proof.* The following series

$$\sum_{k=1}^{\infty} Y_{i,k}(\xi, \tau; C_1, C_2, \dots, C_k) \quad (17)$$

converges and is presented by

$$\psi_i(\xi, \tau) = \sum_{k=1}^{\infty} Y_{i,k}(\xi, \tau; C_1, C_2, \dots, C_k), \quad (18)$$

which satisfies the following:

$$\lim_{k \rightarrow \infty} Y_{i,k}(\xi, \tau; C_1, C_2, \dots, C_k) = 0. \quad (19)$$

Indeed, the subsequent equation is fulfilled:

$$\begin{aligned} Y_{i,i}(\xi, \tau; C_1) + \sum_{k=2}^n Y_{i,k}(\xi, \tau; \vec{C}_k) - \sum_{k=2}^n Y_{i,k-1} \\ \cdot (\xi, \tau; \vec{C}_{k-1}) = Y_{i,2}(\xi, \tau; \vec{C}_2) \\ - Y_{i,1}(\xi, \tau; C_1) + \dots + Y_{i,n}(\xi, \tau; \vec{C}_n) \\ - Y_{i,n-1}(\xi, \tau; \vec{C}_{n-1}) = Y_{i,n}(\xi, \tau; \vec{C}_n). \end{aligned} \quad (20)$$

Now, we have

$$\begin{aligned} L_{i,1}(Y_{i,1}(\xi, \tau; C_1) + \sum_{k=2}^{\infty} L_1(Y_{i,k}(\xi, \tau; \vec{C}_k))) \\ - \sum_{k=2}^{\infty} L_i(Y_{i,k-1}(\xi, \tau; \vec{C}_{k-1})) \\ = L_i(Y_{i,1}(\xi, \tau; C_1)) + \sum_{k=2}^{\infty} L_i(Y_{i,k}(\xi, \tau; \vec{C}_k)) \\ - \sum_{k=2}^{\infty} L_i(Y_{i,k-1}(\xi, \tau; \vec{C}_{k-1})) = 0, \end{aligned} \quad (21)$$

which satisfies

$$\begin{aligned} L_{i,1}(Y_{i,1}(\xi, \tau; C_1) + L_i \sum_{k=2}^{\infty} (Y_{i,k}(\xi, \tau; \vec{C}_k))) \\ - L_i \sum_{k=2}^{\infty} (Y_{i,k-1}(\xi, \tau; \vec{C}_{k-1})) \\ = \sum_{k=2}^{\infty} C_m [L_i((Y_{i,k-m}(\xi, \tau; \vec{C}_{k-m}))) \\ + N_{i,k-m}(Y_{i,k-1}(\xi, \tau; C_{k-1}))] + g_i(\xi, \tau) = 0. \end{aligned} \quad (22)$$

TABLE 1: Numerical values of  $C_1, C_2$  for time-fractional Kawahara equation for several values of  $\alpha$ .

$\alpha$	$C_1$	$C_2$
1.0	-0.9999983031706354	0.000002.417505787703306
$\frac{2}{3}$	-0.9999609966319342	0.000030849221963805824

TABLE 2: Numerical values of  $C_1$  for time-fractional modified Kawahara equations for several values of  $\alpha$ .

$\alpha$	$C_1$
1.0	-0.4647234979611254
$\frac{2}{3}$	-0.9999609966319342

TABLE 3: Comparison of second-order OHAM solution with third-order NIM solution for time-fractional Kawahara equation for different values of  $\alpha$ .

$\xi$	$\tau$	OHAM $\alpha = 2/3$	OHAM $\alpha = 1$	Exact $\alpha = 1$
-5	0.02	0.252877	0.253985	0.253985
	0.04	0.252017	0.253625	0.253625
	0.06	0.251298	0.253265	0.253265
	0.08	0.250657	0.252905	0.252905
	0.1	0.250069	0.252546	0.252546
0	0.02	0.621292	0.621301	0.621301
	0.04	0.621277	0.6213	0.6213
	0.06	0.621259	0.621298	0.621298
	0.08	0.621239	0.621295	0.621295
	0.1	0.621217	0.621291	0.621291
5	0.02	0.255821	0.254707	0.254707
	0.04	0.256691	0.255068	0.255068
	0.06	0.257422	0.255429	0.255429
	0.08	0.258076	0.255791	0.255791
	0.1	0.258678	0.256153	0.256153

Now, if  $C_m, m = 1, 2, 3, \dots$ , is correctly selected, then the equation leading to

$$L_i(Y_i(\xi, \tau) + A) = 0 \tag{23}$$

is the exact solution. □

### 4. Main Results

We test our adopted procedure OHAM for finding the approximate solution of the fractional-order Kawahara equation. For most of the computational work, we used MathType and Mathematica 10.

4.1. Numerical Solution of Fractional Kawahara Equation. First, we assume that the time-fractional Kawahara equation is given in [35]:

TABLE 4: Comparison absolute errors of 2<sup>nd</sup>-order OHAM solution with 3<sup>rd</sup>-order NIM solution for time-fractional Kawahara equations for different values of  $\alpha$ .

$\xi$	$\tau$	Residual $\alpha = 0.5$	NIM [35] $\alpha = 1$	OHAM $\alpha = 1$
-5	0.02	$-1.31504 \times 10^{-6}$	$2.27500 \times 10^{-10}$	$8.04633 \times 10^{-10}$
	0.04	$-3.18365 \times 10^{-6}$	$1.81933 \times 10^{-9}$	$1.20722 \times 10^{-9}$
	0.06	$-5.04947 \times 10^{-6}$	$6.13795 \times 10^{-9}$	$8.08547 \times 10^{-10}$
	0.08	$-6.91298 \times 10^{-6}$	$1.45438 \times 10^{-8}$	$7.88584 \times 10^{-10}$
	0.1	$-8.77447 \times 10^{-6}$	$2.83953 \times 10^{-8}$	$3.97934 \times 10^{-9}$
0	0.02	$-8.08613 \times 10^{-8}$	$1.76636 \times 10^{-13}$	$1.29552 \times 10^{-12}$
	0.04	$-2.14003 \times 10^{-7}$	$2.82618 \times 10^{-12}$	$3.06177 \times 10^{-12}$
	0.06	$-3.84142 \times 10^{-7}$	$1.43068 \times 10^{-11}$	$1.05937 \times 10^{-12}$
	0.08	$-5.84492 \times 10^{-7}$	$4.52161 \times 10^{-11}$	$2.1665 \times 10^{-11}$
	0.1	$-8.11039 \times 10^{-7}$	$1.10391 \times 10^{-10}$	$7.35924 \times 10^{-11}$
5	0.02	$1.33389 \times 10^{-6}$	$2.27670 \times 10^{-10}$	$8.05429 \times 10^{-10}$
	0.04	$3.22731 \times 10^{-6}$	$1.82204 \times 10^{-9}$	$1.20837 \times 10^{-9}$
	0.06	$5.12378 \times 10^{-6}$	$6.15166 \times 10^{-9}$	$8.03524 \times 10^{-10}$
	0.08	$7.02284 \times 10^{-6}$	$1.45871 \times 10^{-8}$	$8.16471 \times 10^{-10}$
	0.1	$8.92419 \times 10^{-6}$	$2.85011 \times 10^{-8}$	$4.061 \times 10^{-9}$

$$\frac{\partial^\alpha Y(\xi, \tau)}{\partial \tau^\alpha} + Y(\xi, \tau) \frac{\partial Y(\xi, \tau)}{\partial \xi} + \frac{\partial^3 Y(\xi, \tau)}{\partial \xi^3} - \frac{\partial^5 Y(\xi, \tau)}{\partial \xi^5} = 0, 0 < \alpha \leq 1. \tag{24}$$

Subject to I.C.,

$$Y(\xi, 0) = \frac{105}{169} \operatorname{sech}^4\left(\frac{\xi}{2\sqrt{13}}\right). \tag{25}$$

For  $\alpha = 1$ , an exact solution for equation (24) is found by [35] as

$$Y(\xi, \tau) = \frac{105}{169} \operatorname{sech}^4\left(\frac{1}{2\sqrt{13}}\left(\xi - \frac{36\tau}{169}\right)\right). \tag{26}$$

Recall the OHAM preparation given in Section 3, we obtain the subsequent problems:

Zero-order problem:

$$\frac{\partial^\alpha Y_0(\xi, \tau)}{\partial \tau^\alpha} = 0, Y_0(\xi, \tau) = \frac{105}{169} \operatorname{sech}^4\left(\frac{\xi}{2\sqrt{13}}\right). \tag{27}$$

First-order problem:

$$\begin{aligned} \frac{\partial^\alpha Y_1(\xi, \tau)}{\partial \tau^\alpha} = & \frac{\partial^\alpha Y_0(\xi, \tau)}{\partial \tau^\alpha} + C_1 \frac{\partial^\alpha Y_0(\xi, \tau)}{\partial \tau^\alpha} - C_1 Y_0 \frac{\partial Y_0(\xi, \tau)}{\partial \xi} \\ & + C_1 \frac{\partial^3 Y_0(\xi, \tau)}{\partial \xi^3} - C_1 \frac{\partial^5 Y_0(\xi, \tau)}{\partial \xi^5}. \end{aligned} \tag{28}$$

TABLE 5: Comparison of 1<sup>st</sup>-order OHAM solution with 3<sup>rd</sup>-order NIM solution for time-fractional modified Kawahara equations For different values of  $\alpha$ .

$\xi$	$\tau$	Exact solution	OHAM solution	Absolute error NIM for [35] $\alpha = 1$	Absolute error OHAM for $\alpha = 1$
-5	0.02	$9.474889415 \times 10^{-4}$	$9.474984314 \times 10^{-4}$	$9.48992 \times 10^{-9}$	$9.48992 \times 10^{-9}$
	0.04	$9.474794138 \times 10^{-4}$	$9.474984314 \times 10^{-4}$	$1.90176 \times 10^{-8}$	$1.90176 \times 10^{-8}$
	0.06	$9.474698483 \times 10^{-4}$	$9.474984314 \times 10^{-4}$	$2.8583 \times 10^{-8}$	$2.8583 \times 10^{-8}$
	0.08	$9.474602454 \times 10^{-4}$	$9.474984314 \times 10^{-4}$	$3.81862 \times 10^{-8}$	$3.81862 \times 10^{-8}$
	0.1	$9.474506042 \times 10^{-4}$	$9.474984314 \times 10^{-4}$	$4.78271 \times 10^{-8}$	$4.78271 \times 10^{-8}$
0	0.02	$9.486832790 \times 10^{-4}$	$9.486832980 \times 10^{-4}$	$1.89737 \times 10^{-11}$	$1.89737 \times 10^{-11}$
	0.04	$9.486832221 \times 10^{-4}$	$9.486832980 \times 10^{-4}$	$7.58947 \times 10^{-11}$	$7.58947 \times 10^{-11}$
	0.06	$9.486831272 \times 10^{-4}$	$9.486832980 \times 10^{-4}$	$1.70763 \times 10^{-10}$	$1.70763 \times 10^{-10}$
	0.08	$9.486829944 \times 10^{-4}$	$9.486832980 \times 10^{-4}$	$3.03579 \times 10^{-10}$	$3.03579 \times 10^{-10}$
	0.1	$9.486828237 \times 10^{-4}$	$9.486832980 \times 10^{-4}$	$4.74342 \times 10^{-10}$	$4.74342 \times 10^{-10}$
5	0.02	$9.475078835 \times 10^{-4}$	$9.474984314 \times 10^{-4}$	$9.45216 \times 10^{-9}$	$9.45216 \times 10^{-9}$
	0.04	$9.475172979 \times 10^{-4}$	$9.474984314 \times 10^{-4}$	$1.88666 \times 10^{-8}$	$1.88666 \times 10^{-8}$
	0.06	$9.475266744 \times 10^{-4}$	$9.474984314 \times 10^{-4}$	$2.82432 \times 10^{-8}$	$2.82432 \times 10^{-8}$
	0.08	$9.475360132 \times 10^{-4}$	$9.474984314 \times 10^{-4}$	$3.75821 \times 10^{-8}$	$3.75821 \times 10^{-8}$
	0.1	$9.475453144 \times 10^{-4}$	$9.474984314 \times 10^{-4}$	$4.68832 \times 10^{-8}$	$4.68832 \times 10^{-8}$

Second-order problem:

$$\begin{aligned}
 \frac{\partial^\alpha Y_2(\xi, \tau)}{\partial \tau^\alpha} &= C_2 \frac{\partial^\alpha Y_0(\xi, \tau)}{\partial \tau^\alpha} + \frac{\partial^\alpha Y_0(\xi, \tau)}{\partial \tau^\alpha} + C_1 \frac{\partial^\alpha Y_1(\xi, \tau)}{\partial \tau^\alpha} \\
 &+ C_2 Y_0(\xi, \tau) \frac{\partial Y_0(\xi, \tau)}{\partial x} \xi + C_1 Y_0(\xi, \tau) \frac{\partial Y_0(\xi, \tau)}{\partial \xi} \\
 &+ C_1 Y_0(\xi, \tau) \frac{\partial Y_1(\xi, \tau)}{\partial \xi} + C_2 \frac{\partial^3 Y_0(\xi, \tau)}{\partial \xi^3} \\
 &+ C_1 \frac{\partial^3 Y_1(\xi, \tau)}{\partial \xi^3} - C_2 \frac{\partial^5 Y_1(\xi, \tau)}{\partial \xi^5}.
 \end{aligned}
 \tag{29}$$

Apply the inverse operator  $I^\alpha$ , the solution of the above problems is given as follows:

$$\begin{aligned}
 Y_0(\xi, \tau) &= \frac{105}{169} \operatorname{sech}^4\left(\frac{\xi}{2\sqrt{13}}\right), \\
 Y_1(\xi, \tau, C_1) &= \frac{-7560C_1\tau^\alpha \operatorname{sech}^4\left(\frac{\xi/2\sqrt{13}}{\tau}\right) \tan\left(\frac{\xi/2\sqrt{13}}{\tau}\right)}{28561\sqrt{13}\Gamma(1+\alpha)}, \\
 Y_2(\xi, \tau, C_1, C_2) &= \frac{1}{62748517\Gamma(1+\alpha)} \\
 &\cdot \left(1890e^{-\xi/\sqrt{13}}\tau^\alpha \left(-169\sqrt{13}(C_1 + C_2^2 + C_2)(-1 + e^{2\xi/\sqrt{13}})\right)\right. \\
 &\left. + \frac{92^{3-2\alpha}C_1^2(1 - 3e^{\xi/\sqrt{13}} + e^{2\xi/\sqrt{13}})\sqrt{\pi}\tau^\alpha}{\sqrt{13}\Gamma(1+\alpha)}\right) \operatorname{sech}^6\left(\frac{\xi}{2\sqrt{13}}\right).
 \end{aligned}
 \tag{30}$$

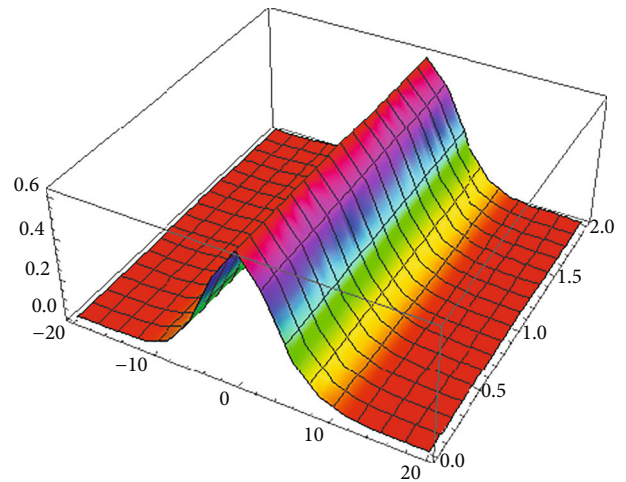


FIGURE 1: 3D surface obtained by OHAM solution for fractional Kawahara equation at  $\alpha = 0.5$ .

The second-order OHAM solution is presented as follows:

$$\tilde{Y}(\xi, \tau, C_i) = Y_0(\xi, \tau) + Y_1(\xi, \tau, C_1) + Y_2(\xi, \tau, C_1, C_2).
 \tag{31}$$

For  $\alpha = 1$ , second-order OHAM solution for Kawahara equation is

$$\tilde{Y}(\xi, \tau) = \frac{105 \operatorname{sech}^4\left(\xi/2\sqrt{13}\right) \left(371293 + 72\tau(-9C_1^2\tau(-4 + 5 \operatorname{sech}^2\left(\xi/2\sqrt{13}\right)) - 169\sqrt{13}(C_1(2 + C_1) + C_2) \tanh\left(\xi/2\sqrt{13}\right))\right)}{62748517}. \quad (32)$$

For  $\alpha = 2/3$ , second-order OHAM solution for Kawahara equation is

$$\tilde{Y}(\xi, \tau) = \frac{105 \operatorname{sech}^4\left(\xi/2\sqrt{13}\right) \left(371293 + 72\tau^{2/3}(-18C_1^2\tau^{2/3}(-4 + 5 \operatorname{sech}^2\left(\xi/2\sqrt{13}\right)))/\Gamma(7/3) - 169\sqrt{13}(C_1(2 + C_2) \tanh\left(\xi/2\sqrt{13}\right))/\Gamma(5/3)\right)}{62748517}. \quad (33)$$

**4.2. Numerical Solution of Fractional Modified Kawahara Equation.** Assume the following time-fractional modified Kawahara system presented by

$$\frac{\partial^\alpha Y(\xi, \tau)}{\partial \tau^\alpha} + Y^2(\xi, \tau) \frac{\partial Y(\xi, \tau)}{\partial \xi} + p \frac{\partial^3 Y(\xi, \tau)}{\partial \xi^3} + q \frac{\partial^5 Y(\xi, \tau)}{\partial \xi^5} = 0, 0 < \alpha \leq 1, \quad (34)$$

with I.C.,

$$Y(\xi, 0) = \frac{3\rho}{\sqrt{-10\mu}} \operatorname{sech}^2(k\xi), k = \frac{1}{2} \sqrt{\frac{-\rho}{2\mu}}. \quad (35)$$

When  $\alpha = 1$ , the exact solution is given by [35] as

$$Y(\xi, \tau) = \frac{3\rho}{\sqrt{-10\mu}} \operatorname{sech}^2(k(\xi - \psi t)), \psi = \frac{25\mu - 4\rho^2}{25\mu}. \quad (36)$$

Following the OHAM procedure, we have the following.

$$Y_0(\xi, \tau) = \frac{3\rho}{\sqrt{-10\mu}} \operatorname{sech}^2\left(\left(\frac{1}{2} \sqrt{\frac{-\rho}{2\mu}}\right) \xi\right),$$

$$Y_1(\xi, \tau, C_1) = \frac{3C_1\rho^7/2\tau^\alpha \operatorname{sech}^5\left(\sqrt{\rho}\xi/2\sqrt{5}\sqrt{\mu}\right) \left(-59 \sin\left(\sqrt{\rho}\xi/2\sqrt{5}\sqrt{\mu}\right) + \sin\left(\sqrt{\rho}\xi/2\sqrt{5}\sqrt{\mu}\right)\right) \tan\left(\xi/2\sqrt{13}\right)}{500\sqrt{-\mu}\mu^{3/2}\sqrt{2}\alpha\Gamma\alpha}. \quad (39)$$

The 1<sup>st</sup>-order OHAM solution is given by the following expression:

$$\tilde{Y}(\xi, \tau, C_i) = Y_0(\xi, \tau) + Y_1(\xi, \tau, C_1). \quad (40)$$

## 5. Results and Discussion

We implemented OHAM to provide approximate numerical solutions to fractional and modified Kawahara equations.

Zero-order problem:

$$\frac{\partial^\alpha Y_0(\xi, \tau)}{\partial \tau^\alpha} = 0, Y_0(\xi, 0) = \frac{3\rho}{\sqrt{-10\mu}} \operatorname{sech}^2(k\xi), k = \frac{1}{2} \sqrt{\frac{-\rho}{2\mu}}. \quad (37)$$

First-order problem:

$$\frac{\partial^\alpha Y_1(\xi, \tau)}{\partial \tau^\alpha} = \frac{\partial^\alpha Y_0(\xi, \tau)}{\partial \tau^\alpha} + C_1 \frac{\partial^\alpha Y_0(\xi, \tau)}{\partial \tau^\alpha} - C_1 Y_0 \frac{\partial Y_0(\xi, \tau)}{\partial \xi} + C_1 \frac{\partial^3 Y_0(\xi, \tau)}{\partial \xi^3} - C_1 \frac{\partial^5 Y_0(\xi, \tau)}{\partial \xi^5}.$$

Apply the inverse operator  $I^\alpha$ , the solution of the above problems is given as follows:

Numerical values are tabulated for the auxiliary constants in Tables 1 and 2 for Kawahara and modified Kawahara equations at various values of  $\alpha$ . Table 3 gives the estimation of the second-order OHAM solution and the third-order NIM solution for the Kawahara fractional equation. Table 4 compares the absolute errors of the second-order OHAM solution for various  $\alpha$  values. Table 4 presents the values of the first-order OHAM solution and the third-order NIM solution for the various values of  $\alpha$ . Table 5



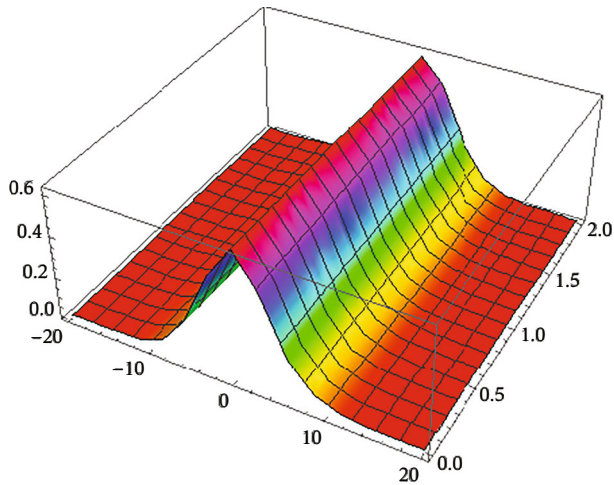


FIGURE 2: 3D surface obtained by OHAM solution for fractional Kawahara equation at  $\alpha = 1$ .

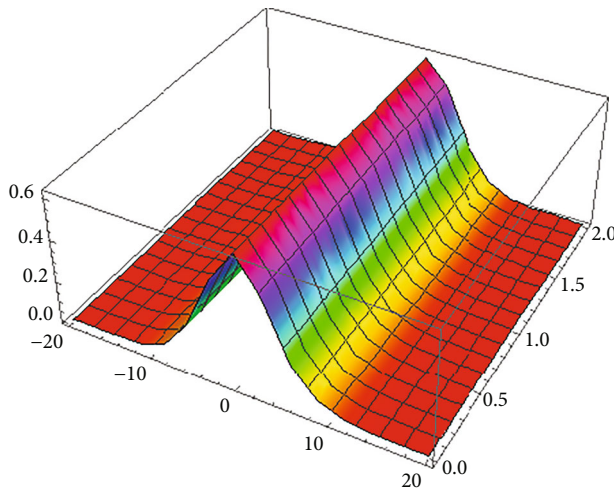


FIGURE 3: 3D surface obtained by exact solution for fractional Kawahara equation at  $\alpha = 1$ .

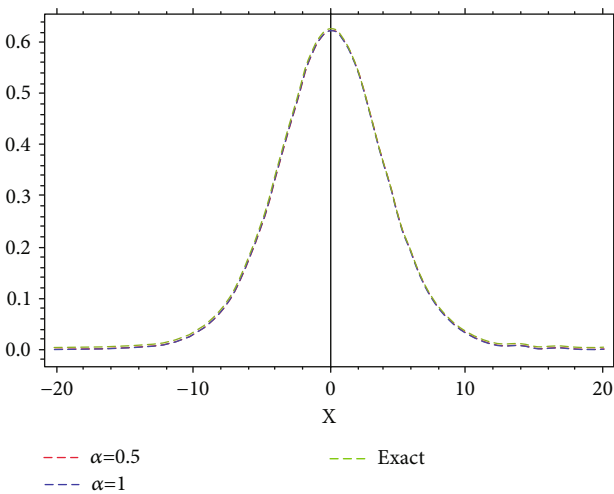


FIGURE 4: The curves show the comparison between exact solution and approximate solution for different values of  $\alpha$  at  $\tau = 0.5$  for Kawahara equation.

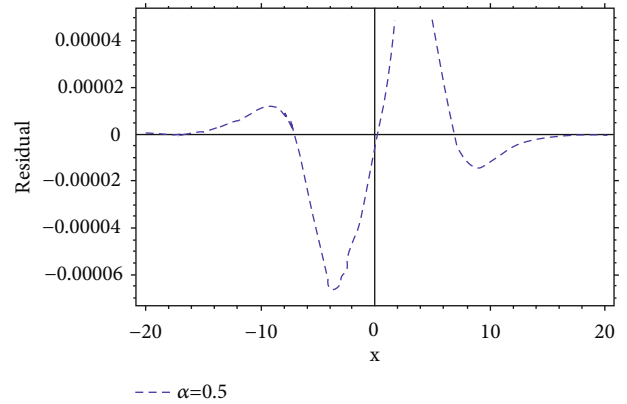


FIGURE 5: Residual obtained by OHAM for  $\alpha = 0.5$  at  $\tau = 0.5$ , for Kawahara equation.

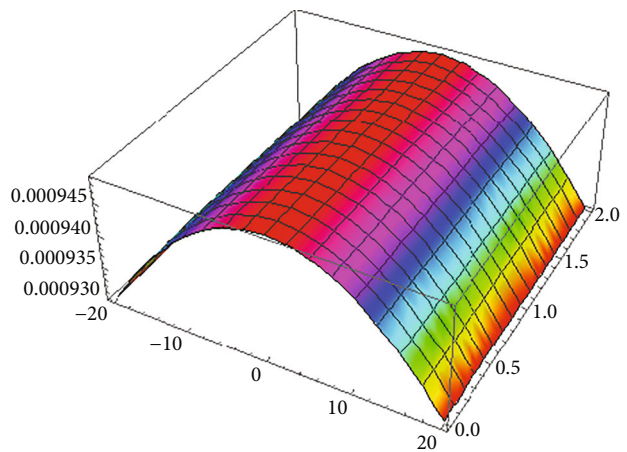


FIGURE 6: 3D plot of OHAM solution for fractional modified Kawahara equation at  $\alpha = 0.5$ .

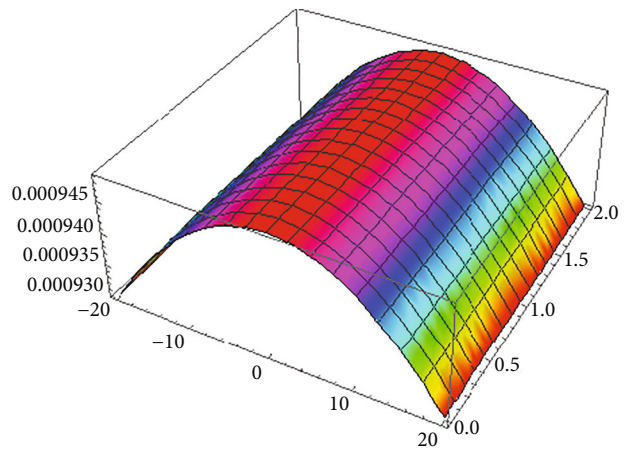


FIGURE 7: 3D surface obtained by OHAM solution for fractional modified Kawahara equation at  $\alpha = 1$ .

compares first-order OHAM solution with third-order NIM solution for time-fractional modified Kawahara equations for different values of  $\alpha$ .

Figures 1–3 depict the 3D surfaces obtained by second-order OHAM as well as the accurate solutions to fractional

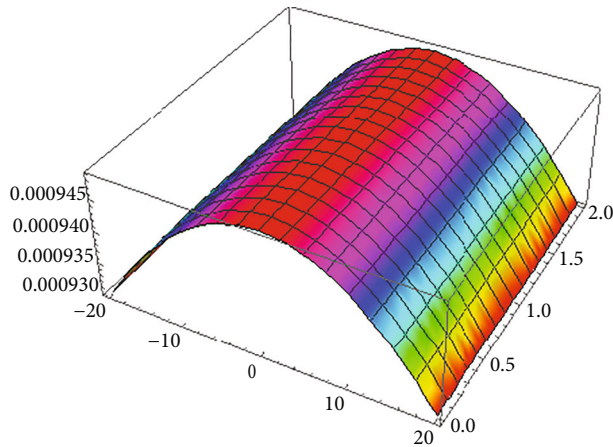


FIGURE 8: 3D surface obtained by exact solution for fractional modified Kawahara equation at  $\alpha = 1$ .

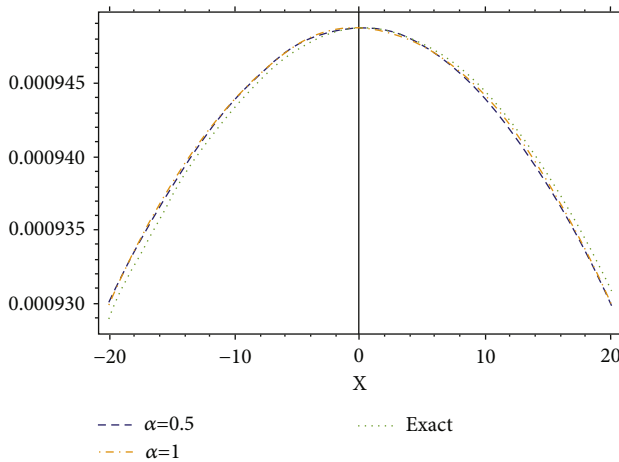


FIGURE 9: The curves show the comparison between exact solution and approximate solution for different values of  $\alpha$  at  $\tau = 0.5$  for modified Kawahara equation.

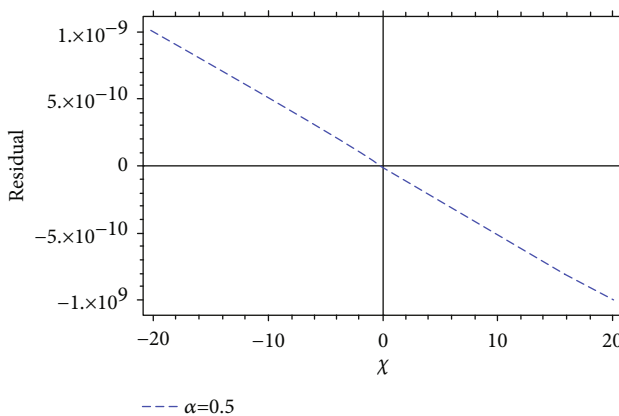


FIGURE 10: Residual obtained by OHAM for  $\alpha = 0.5$  at  $\tau = 0.5$ , for modified Kawahara equation.

Kawahara equation at  $\alpha = 0.5$  and 1. Figure 4 shows the residual for  $\alpha = 0.5$ , whereas Figure 5 shows the 2D surface of the second-order OHAM solution for various values of  $\alpha$ . Figures 6–8 show the 3D plots for the first-order OHAM solution and exact solution for the fractional modified Kawahara equation at  $\alpha = 0.5$  and 1. Figure 9 depicts a two-dimensional graph of the first-order OHAM solution for different values of  $\alpha$ . The residual for  $\alpha = 0.5$  is shown in Figure 10.

The results obtained by the second-order OHAM solution for the Kawahara fractional equation agree with both the closed and the NIM solution. Similarly, for fractional modified Kawahara equation, the results achieved by the first-order OHAM solutions are exactly the same as for the third-order NIM solutions.

## 6. Conclusions

We observe that OHAM converges rapidly towards the closed solution with a lower sequence of approximation of fractional orders of the Kawahara equations and modified Kawahara equations based on the calculated results. The results achieved with the proposed approach are highly encouraging compared to the new iterative method (NIM). This proposed approach is capable of providing the greatest accuracy within the lowest approximation sequence. This approach does not require choices between small and large parameter assumptions in problems. The results are analyzed and explained with the help of graphs by considering different values of parameters. Results reveal that as the value of fractional-order derivatives approaches to 1, the approximate solution converges to the exact solution. The convergence of this approach is independent of initial assumptions. The precision of the proposed approach can be improved by assuming high approximations, and therefore, it may be highly attractive for researchers to use our approach to solve fractional-order systems emerging in the science of technology.

## Data Availability

There is no data for this study.

## Conflicts of Interest

The authors have declared no conflict of interest.

## Acknowledgments

This research was funded by Princess Nourah bint Abdulrahman University Researchers Supporting Project number (PNURSP2022R229), Princess Nourah bint Abdulrahman University, Riyadh, Saudi Arabia.

## References

- [1] I. Podlubny, *Fractional Differential Equations: An Introduction to Fractional Derivatives, Fractional Differential Equations, to Methods of Their Solution and Some of Their Applications*, Elsevier, 1998.

- [2] L. Debnath, "Recent applications of fractional calculus to science and engineering," *International Journal of Mathematics and Mathematical Sciences*, vol. 2003, no. 54, pp. 3413–3442, 2003.
- [3] K. S. Miller and B. Ross, *An Introduction to the Fractional Calculus and Fractional Differential Equations*, Wiley, 1993.
- [4] F. Calculus, *Integrations and Differentiations of Arbitrary Order*, K. Nishimoto, 1989.
- [5] A. Ali, S. Islam, M. R. Khan et al., "Dynamics of a fractional order Zika virus model with mutant," *Alexandria Engineering Journal*, vol. 61, no. 6, pp. 4821–4836, 2022.
- [6] X.-H. Zhang, A. Ali, M. A. Khan, M. Y. Alshahrani, T. Muhammad, and S. Islam, "Mathematical analysis of the TB model with treatment via Caputo-type fractional derivative," *Discrete Dynamics in Nature and Society*, vol. 2021, 15 pages, 2021.
- [7] A. Ali, F. S. Alshammari, S. Islam, M. A. Khan, and S. Ullah, "Modeling and analysis of the dynamics of novel coronavirus (COVID-19) with Caputo fractional derivative," *Results in Physics*, vol. 20, article 103669, 2021.
- [8] M. A. Aba Oud, A. Ali, H. Alrabaiah, S. Ullah, M. A. Khan, and S. Islam, "A fractional order mathematical model for COVID-19 dynamics with quarantine, isolation, and environmental viral load," *Advances in Difference Equations*, vol. 2021, no. 1, pp. 106–119, 2021.
- [9] A. Rehman, Z. Salleh, and T. Gul, "Soot formation characteristics of homogeneous supercritical fuel spray of diesel/ethanol blend," *Journal of Advanced Research in Fluid Mechanics and Thermal Sciences*, vol. 81, no. 2, pp. 67–81, 2021.
- [10] G. Adomian, *Solving Frontier Problems of Physics: The Decomposition Method*, vol. 60, Springer Science & Business Media, 2013.
- [11] G. Adomian and R. Rach, "Modified Adomian polynomials," *Mathematical and Computer Modelling*, vol. 24, no. 11, pp. 39–46, 1996.
- [12] J. H. He, "Variational iteration method - a kind of non-linear analytical technique: some examples," *International Journal of Non-Linear Mechanics*, vol. 34, no. 4, pp. 699–708, 1999.
- [13] N. H. Sweilam and M. M. Khader, "Variational iteration method for one dimensional nonlinear thermoelasticity," *Chaos, Solitons & Fractals*, vol. 32, no. 1, pp. 145–149, 2007.
- [14] J. H. He, "Homotopy perturbation technique," *Computer Methods in Applied Mechanics and Engineering*, vol. 178, no. 3-4, pp. 257–262, 1999.
- [15] S. Abbasbandy, "The application of homotopy analysis method to nonlinear equations arising in heat transfer," *Physics Letters A*, vol. 360, no. 1, pp. 109–113, 2006.
- [16] W. Deng, "Finite Element Method for the Space and Time Fractional Fokker-Planck Equation," *SIAM Journal on Numerical Analysis*, vol. 47, no. 1, pp. 204–226, 2009.
- [17] V. Daftardar-Gejji and H. Jafari, "An iterative method for solving nonlinear functional equations," *Journal of Mathematical Analysis and Applications*, vol. 316, no. 2, pp. 753–763, 2006.
- [18] V. Daftardar-Gejji and S. Bhalekar, "Solving multi-term linear and non-linear diffusion-wave equations of fractional order by Adomian decomposition method," *Fractional Calculus and Applied Analysis*, vol. 202, no. 1, pp. 113–120, 2008.
- [19] A. Saeed, P. Kumam, T. Gul, W. Alghamdi, W. Kumam, and A. Khan, "Darcy-Forchheimer couple stress hybrid nanofluids flow with variable fluid properties," *Scientific Reports*, vol. 11, no. 1, pp. 1–13, 2021.
- [20] Y. Cao, H. Aayed, T. Abdulrazzaq, T. Gul, A. Bariq, and B. Bouallegue, "Effect of the number of nozzles of swirl flow generator utilized in flat plate solar collector: an entropic analysis," *International Journal of Photoenergy*, vol. 2021, 10 pages, 2021.
- [21] A. Saeed, P. Kumam, S. Nasir, T. Gul, and W. Kumam, "Non-linear convective flow of the thin film nanofluid over an inclined stretching surface," *Scientific Reports*, vol. 11, no. 1, pp. 1–15, 2021.
- [22] V. Marinca, N. Herişanu, and I. Nemeş, "Optimal homotopy asymptotic method with application to thin film flow," *Open Physics*, vol. 6, no. 3, pp. 648–653, 2008.
- [23] V. Marinca and N. Herişanu, "The optimal homotopy asymptotic method for solving Blasius equation," *Applied Mathematics and Computation*, vol. 231, pp. 134–139, 2014.
- [24] N. Herişanu, V. Marinca, and G. Madescu, "An analytical approach to non-linear dynamical model of a permanent magnet synchronous generator," *Wind Energy*, vol. 18, no. 9, pp. 1657–1670, 2015.
- [25] V. Marinca and N. Herişanu, "Application of optimal homotopy asymptotic method for solving nonlinear equations arising in heat transfer," *International Communications in Heat and Mass Transfer*, vol. 35, no. 6, pp. 710–715, 2008.
- [26] V. Marinca, N. Herişanu, C. Bota, and B. Marinca, "An optimal homotopy asymptotic method applied to the steady flow of a fourth-grade fluid past a porous plate," *Applied Mathematics Letters*, vol. 22, no. 2, pp. 245–251, 2009.
- [27] S. Sarwar, S. Alkhalaf, S. Iqbal, and M. A. Zahid, "A note on optimal homotopy asymptotic method for the solutions of fractional order heat- and wave-like partial differential equations," *Computers & Mathematics with Applications*, vol. 70, no. 5, pp. 942–953, 2015.
- [28] S. Sarwar and M. M. Rashidi, "Approximate solution of two-term fractional-order diffusion, wave-diffusion, and telegraph models arising in mathematical physics using optimal homotopy asymptotic method," *Waves in Random and Complex Media*, vol. 26, no. 3, pp. 365–382, 2016.
- [29] R. Nawaz, L. Zada, A. Khattak, M. Jibrán, and A. Khan, "Optimum solutions of fractional order Zakhharov-Kuznetsov equations," *Complexity*, vol. 2019, 9 pages, 2019.
- [30] L. Zada, R. Nawaz, and S. S. Bushnaq, "An efficient approach for solution of fractional order differential-difference equations arising in nanotechnology," *Applied Mathematics E-Notes*, vol. 20, pp. 297–307, 2020.
- [31] L. Zada and R. Nawaz, "Solution of time-fractional order RLW equation using optimal homotopy asymptotic method," *AIP Conference Proceedings*, vol. 2116, no. 1, p. 300005, 2019.
- [32] N. A. Kudryashov, "A note on new exact solutions for the Kawahara equation using Exp-function method," *Journal of Computational and Applied Mathematics*, vol. 234, no. 12, pp. 3511–3512, 2010.
- [33] D. Kaya and K. Al-Khaled, "A numerical comparison of a Kawahara equation," *Physics Letters A*, vol. 363, no. 5-6, pp. 433–439, 2007.
- [34] J. Lu, "Analytical approach to Kawahara equation using variational iteration method and homotopy perturbation method," *Topological Methods in Nonlinear Analysis*, vol. 31, no. 2, pp. 287–293, 2008.
- [35] B. R. Sontakke and A. Shaikh, "Approximate solutions of time fractional Kawahara and modified Kawahara equations by fractional complex transform," *Communications in numerical analysis*, vol. 2016, no. 2, pp. 218–229, 2016.

## Research Article

# Heat and Mass Transfer of the Darcy-Forchheimer Casson Hybrid Nanofluid Flow due to an Extending Curved Surface

Gohar,<sup>1</sup> Tahir Saeed Khan,<sup>1</sup> Ndolane Sene ,<sup>2</sup> Abir Mouldi,<sup>3</sup> and Ameni Brahmia<sup>4</sup>

<sup>1</sup>Mathematics Department, University of Peshawar, Peshawar, Pakistan

<sup>2</sup>Laboratoire Lmdan, Departement De Mathematiques De Decision, Faculté des Sciences Economiques et Gestion, Université Cheikh Anta Diop De Dakar, BP 5683 Dakar Fann, Senegal

<sup>3</sup>Department of Industrial Engineering, College of Engineering, King Khalid University, Abha 61421, Saudi Arabia

<sup>4</sup>Chemistry Department, College of Science, King Khalid University, Abha 61413, Saudi Arabia

Correspondence should be addressed to Ndolane Sene; ndolanesene@yahoo.fr

Received 11 October 2021; Revised 7 December 2021; Accepted 10 December 2021; Published 18 January 2022

Academic Editor: Amir Khan

Copyright © 2022 Gohar et al. This is an open access article distributed under the Creative Commons Attribution License, which permits unrestricted use, distribution, and reproduction in any medium, provided the original work is properly cited.

The current paper describes a Darcy-Forchheimer flow of Casson hybrid nanofluid through an incessantly expanding curved surface. Darcy-Forchheimer influence expresses the viscous fluid flow in the porous medium. Carbon nanotubes (CNTs) with a cylindrical form and iron-oxide are utilized to make hybrid nanofluids. Using Karman's scaling, the principal equations are rearranged to nondimensional ordinary differential equations. The "Homotopy analysis method" is used to further build up the analytic arrangement of modeled equations. The impact of flow variables on the velocity and temperature profiles has been tabulated and explained. The flow velocity is raised when both the curvature and volume fraction parameters are elevated. The temperature and velocity profiles exhibit the opposite tendency when the Forchheimer number is increased, since the fluid velocity decreases while the energy profile grows. The addition of CNTs and iron nanocomposites improves the thermophysical characteristics of the base fluid significantly. The obtained consequences show that hybrid nanofluids are more efficient to improve the heat transfer rate. Using CNTs and nanomaterials in the base fluid to control the coolant level in industrial equipment is a wonderful idea.

## 1. Introduction

The flow over an extending surface has received much importance due to its significant role in several sectors of industry and engineering, such as condensation process, spinning of fiber and continuous casting of fiber, plastic sheet extraction, paper production, and many others. Crane [1] was the first to study the flow over an expanding planar surface. Many researchers have since followed the concept of the crane [2–5], expanding the sheets to investigate various aspects of this form of flow. Sajid et al. [6] addressed boundary layer flow and micropolar fluid, concluding that the curvature effect leads to a reduction in boundary layer size. Gul et al. [7] have investigated the flow of the boundary layer on the stretching surface using the Fractional Order Derivatives

Scheme. Imtiaz et al. [8] demonstrated the fluid flow under the upshots of the magnetic field over an extending curved surface. It has been noticed that with the action of curvature coefficient, the energy profile is enhanced. Rosca et al. [9] have analyzed the flow caused by contracting and expanding sheets. Saeed et al. [10] offered a complete investigation of the Darcy hybrid nanofluid flow through a curved surface that is exponentially expanding. The outcomes signify using SWCNTs, MWCNTs, and Fe<sub>3</sub>O<sub>4</sub> nanomaterials for the increase in the nusselt number. Ali et al. [11] analyzed the hydrological importance of wave propagation of hybrid nanofluid over a warmed extended curved surface with the impacts of a magnetic field using bvp4c. The suspension of carbon nanotubes in a magnetite nanofluid promotes local surface drag but reduces local heat flow. Kumar et al. [12]

have reported the radiation impact on the Casson fluid across the exponentially curved sheet. Hayat et al. [13] explored ferroliquid flow with the mass and heat transition across a curved stretching surface. Hussain et al. [14] reported the findings of their investigation on hybrid nanofluid flow across a curved sheet. The outcomes of the survey revealed that the energy transference efficiency in hybrid nanocrystals is higher than that in nanofluids for large frequencies of the curvature index. Qian et al. [15] and Khan evaluated that how heat transmission and radiation were affected by the conducting flow over a curved extending surface. Their study was found to be in good accord with a previously published finding.

The heat transmission in carbon nanofluids has gotten a lot of interest from researchers in a variety of fields in the last few years. CNTs are carbon nanotubes with a fundamental chemical structure and a carbon atom formation wrapped in a cylindrical shape. CNTs have superior chemical, thermophysical, and mechanical characteristics, making them ideal for usage as a particulate in a base fluid. They offer various advantages over other nanomaterials due to their tiny size, structure, configuration, dimension, and hardness. Haq et al. [16] evaluated the computational findings for conductive fluid using carbon nanomaterials along an extensive surface. Ahmadian et al. [17] addressed a 3D model of an unsustainable hybrid nanofluid flow with fluid and momentum transmission caused by surface accelerating displacement. The use of hybrid nanoparticles is thought to have enhanced the carrier fluid's thermal properties substantially. Because of the C-C link, CNTs are more effective than other forms of nanoparticles in the carrier fluid. CNTs nanofluid may be further functionalized to get the desired result, which may be used in a range of applications through noncovalent and covalent manipulation [18]. Saeed et al. [19] have considered the nanofluid containing CNTs and iron oxide nanomaterials using the flow of fluid over a curved surface. Gul et al. [20, 21] studied the flow of nanofluids to enhance heat transfer and thermal applications. Alghamdi et al. [22] have observed the flow of hybrid nanofluid through a blood artery for medications. Using the *bvp4c* tool, Li et al. [23], and Ding et al. [24] used (MWCNTs) in the base liquid to evaluate heat transmission. Akbar et al. [25] described the influence of a magnetic field on the flow of CNT nanofluids through a moving permeable channel. Gul et al. [26] and Bilal et al. [27] used an inclined extending cylinder to examine the Darcy-Forchheimer hybrid nanoliquid flow. They examined the carbon nanotubes (CNTs) and iron oxide  $\text{Fe}_3\text{O}_4$  as two distinct nanomaterials. Ahmed et al. [28] represented temperature propagation in a wavy-wall impermeable enclosure through nanofluids. It was discovered that increasing the waviness of the sheet boosts both the heat transmission rate. Yarmand et al. [29] investigated how graphene nanoplatelets/platinum hybrid nanofluids with diverse properties may improve heat transfer rates. Sajid et al. [30] examined the thermophysical characteristics of hybrid and single-form nanotubes using numerical methods. They determined that the size, type, concentra-

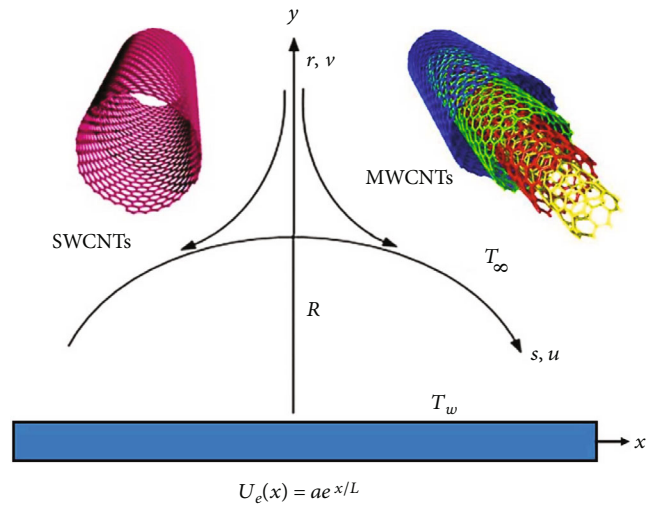


FIGURE 1: Physical sketch.

tion, and temperature fluctuation of nanoparticles had a significant impact on the thermophysical characteristics of nanofluid. Kumar et al. [31] examined the solar radiation impact on the flow of ferromagnetic hybrid nanofluid. Gowda et al. [32] studied the flow of nanofluid over the stretched and curved surface using (KKL) relation. Kumar et al. [33] have used the concept of the magnetic dipole for the flow of nanofluid over a cylinder. Zeeshan et al. [34] have studied the couple stress nanofluid flow using the paraboloid model.

The curved surface for the fluid flow has many applications in the mechanical and automotive industry. Sanni et al. [35], Jawad et al. [36], and Saeed et al. [37] have studied the fluid flow on a curved surface using various kinds of nanofluids for the heat transfer enhancement. Hayat et al. [9, 38], Rosca, and Pop [39] have explained the homogeneous-heterogeneous reaction phenomena using the curved surface for the flow pattern. Okechi et al. [40], Asghar et al. [41], and Hayat et al. [42] have used the non-Newtonian fluid flow over the curved surface with various extensions considering Darcy-Forchheimer flow medium. The related work to the proposed model can be seen in the References [9, 35, 43–45].

The inertia effect is taken into account by incorporating a squared component to the momentum equation, called Forchheimer's modification [46]. Muskat [47] used the term "Forchheimer factor" to describe this new concept. It is critical to include non-Darcy consequences in convective transport analysis to properly represent real-world challenges. The novelty of the model has been presented as

- (i) For the hybrid nanofluid flow, heat and mass transmission is examined simultaneously
- (ii) The (CNTs +  $\text{Fe}_3\text{O}_4/\text{H}_2\text{O}$ ) hybrid nanoliquid flow across a stretching surface with the mass and heat transition has been addressed

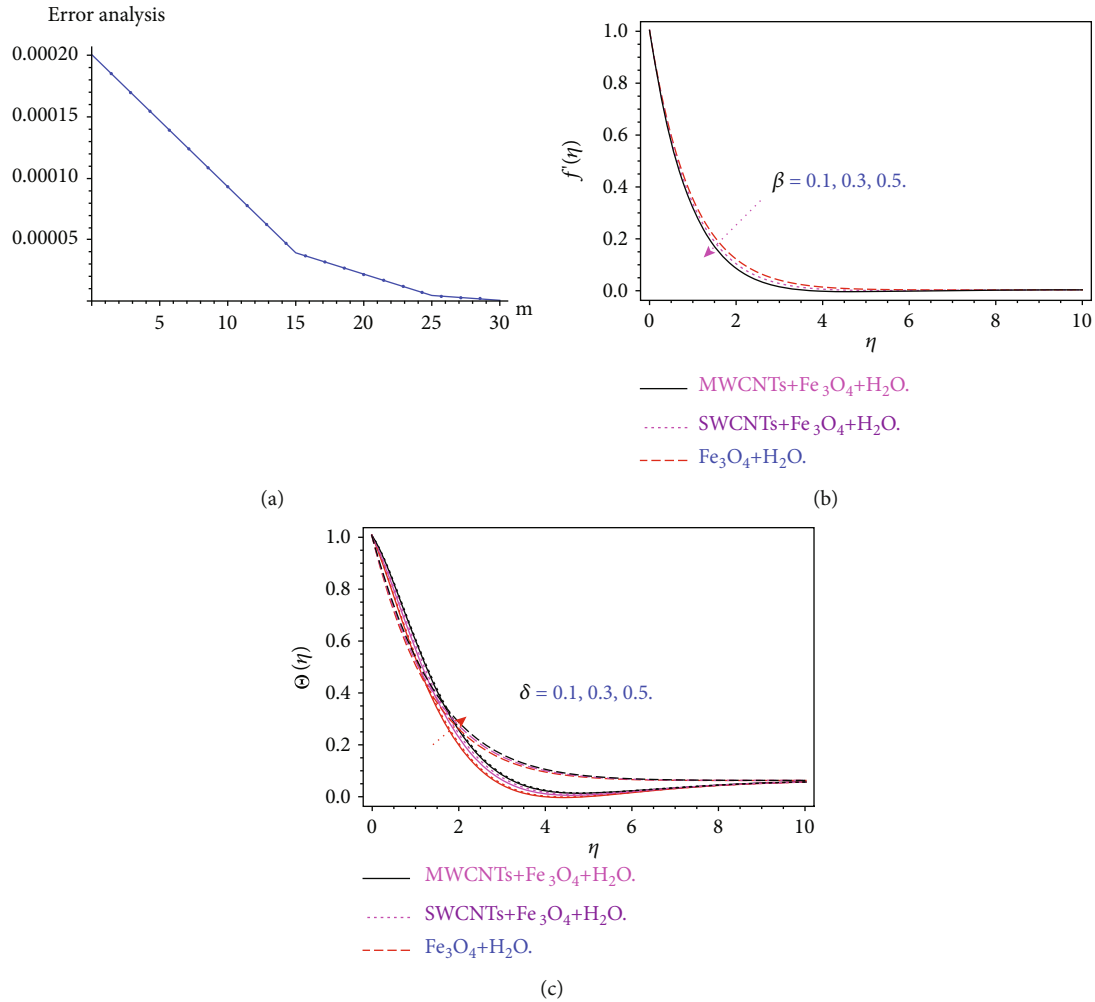


FIGURE 2: (a)–(c) HAM solution, Casson parameter, and heat absorption\omission parameter influence.

- (iii) The non-Newtonian Casson hybrid nanofluid has been used as another extension in the existing literature
- (iv) Heat absorption\omission has also been considered in the flow regime
- (v) This study intends to evaluate and simulate the Darcy-Forchheimer water-based hybrid nanoliquid flow induced by a curved surface that extends
- (vi) The second priority is to modify the Saba et al. [48] and Xue [49] model for hybrid nanofluid flow
- (vii) The proposed model has been solved by the homotopy analysis method

term  $(r, s)$  is taken as the space coordinate and  $(u, v)$  is the velocity component. Here,  $U_w(s) = ae^{s/L}$  is the exponential stretching velocity,  $T_w$  is the curved surface, and  $T_\infty$  is the ambient temperature. Keeping in view, the above superposition, the energy, and momentum equations along with their boundary conditions are expressed as [9, 36–39, 46]

$$\frac{\partial}{\partial r}((r+R)v) + R \frac{\partial u}{\partial s} = 0, \tag{1}$$

$$\frac{u^2}{r+R} = \frac{1}{\rho_{\text{hnf}}} \frac{\partial p}{\partial r}, \tag{2}$$

## 2. Mathematical Formulation

The Darcy-Forchheimer flow considers CNTs and  $Fe_3O_4$  nanomaterials across an expanding curved sheet. The viscous fluid flow has been expressed in the permeable space by the Darcy-Forchheimer effect. The flow is assumed across the stretching sheet, with radius  $R$ , as depicted in Figure 1. The

$$\begin{aligned} v \frac{\partial u}{\partial r} + \frac{R}{r+R} u \frac{\partial u}{\partial s} + \frac{uv}{r+R} = & -\frac{1}{\rho_{\text{hnf}}} \frac{R}{r+R} \frac{\partial p}{\partial s} \\ & + v_{\text{hnf}} \left(1 + \frac{1}{\beta}\right) \left(\frac{\partial^2 u}{\partial r^2} - \frac{u}{(r+R)^2} + \frac{1}{r+R} \frac{\partial u}{\partial r}\right) \\ & - \frac{v_{\text{hnf}}}{K^*} u - \frac{1}{\rho_{\text{hnf}}} F u^2, \end{aligned} \tag{3}$$

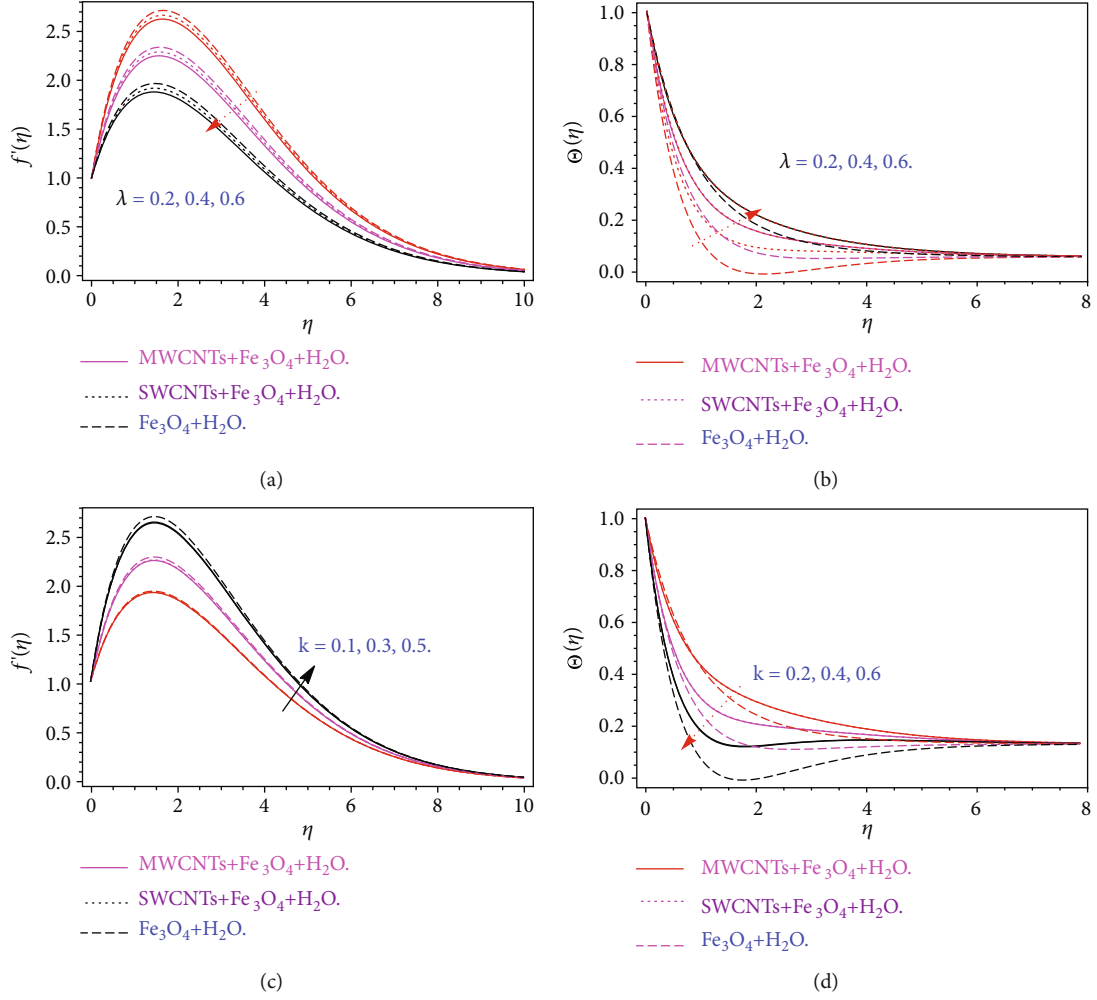


FIGURE 3: (a, b) Porosity parameter  $\lambda$  impact on the velocity  $f'(\eta)$  and temperature profile  $\theta(\eta)$ . (c, d) Curvature parameter  $k$  effect on velocity  $f'(\eta)$  and temperature profile, respectively.

$$\left[ v \frac{\partial T}{\partial r} + u \frac{\partial T}{\partial s} \frac{R}{r+R} \right] = \alpha_{\text{hnf}} \left( \frac{\partial^2 T}{\partial r^2} + \frac{1}{r+R} \frac{\partial T}{\partial r} \right) + \frac{Q}{(\rho c_p)_{\text{hnf}}} (T - T_{\infty}), \quad (4)$$

$$\left[ v \frac{\partial C}{\partial r} + u \frac{\partial C}{\partial s} \frac{R}{r+R} \right] = D_{\text{hnf}} \left( \frac{\partial^2 C}{\partial r^2} + \frac{1}{r+R} \frac{\partial C}{\partial r} \right). \quad (5)$$

The basic flow conditions are

$$v = 0, \quad u = U_w(s) = ae^{s/L}, \quad T = T_{\infty} + T_0 e^{As/2L} = T_w,$$

$$C = C_{\infty} + C_0 e^{As/2L} = C_w, \quad \text{at } r = 0,$$

$$u \longrightarrow 0, \quad \frac{\partial u}{\partial r}, T \longrightarrow T_{\infty}, \quad C \longrightarrow C_{\infty}, \quad \text{at } r \longrightarrow \infty. \quad (6)$$

Here,  $K^*$  and  $F = C_b/sK^{*1/2}$ , are the permeability and iner-

tia factors.

$$\begin{aligned} v_{\text{hnf}} &= \frac{\mu_{\text{hnf}}}{\rho_{\text{hnf}}}, \quad \frac{\mu_{\text{hnf}}}{\mu_f} = (1 - \phi_1)^{-5/2} (1 - \phi_2)^{-5/2}, \quad \frac{(\rho)}{(\rho)_f} \\ &= (1 - \phi_2) \left\{ 1 - \left( 1 - \frac{(\rho)Ms}{(\rho)_f} \right) \phi_1 \right\} + \frac{(\rho)_{\text{CNT}}}{(\rho)_f} \phi_2, \\ \frac{k_{\text{hnf}}}{k_{\text{bf}}} &= \left[ 2\phi_2 \frac{k_{\text{CNT}}}{(k_{\text{CNT}} - k_{\text{bf}})} + (1 - \phi_2) - \ln \frac{k_{\text{CNT}} + k_{\text{bf}}}{2k_{\text{bf}}} \right] \\ &\cdot \left[ 2\phi_2 \frac{k_{\text{bf}}}{(k_{\text{CNT}} - k_{\text{bf}})} + (1 - \phi_2) - \ln \frac{k_{\text{CNT}} + k_{\text{bf}}}{2k_{\text{bf}}} \right]^{-1}, \\ \frac{k_{\text{bf}}}{k_f} &= (k_{\text{MS}} + (m-1)_{\text{kf}} - \phi_1 (k_f - k_{\text{MS}}))^{-1} \\ &\cdot (k_{\text{MS}} + (m-1)_{\text{kf}} - (m-1)\phi_1 (k_f - k_{\text{MS}})), \\ \frac{(\rho C_p)_{\text{hnf}}}{(\rho C_p)_f} &= \frac{(\rho C_p)_{\text{CNT}}}{(\rho C_p)_f} \phi_2 + (1 - \phi_2) \left\{ 1 - \left( 1 - \frac{(\rho C_p)Ms}{(\rho C_p)_f} \right) \phi_1 \right\}. \end{aligned} \quad (7)$$

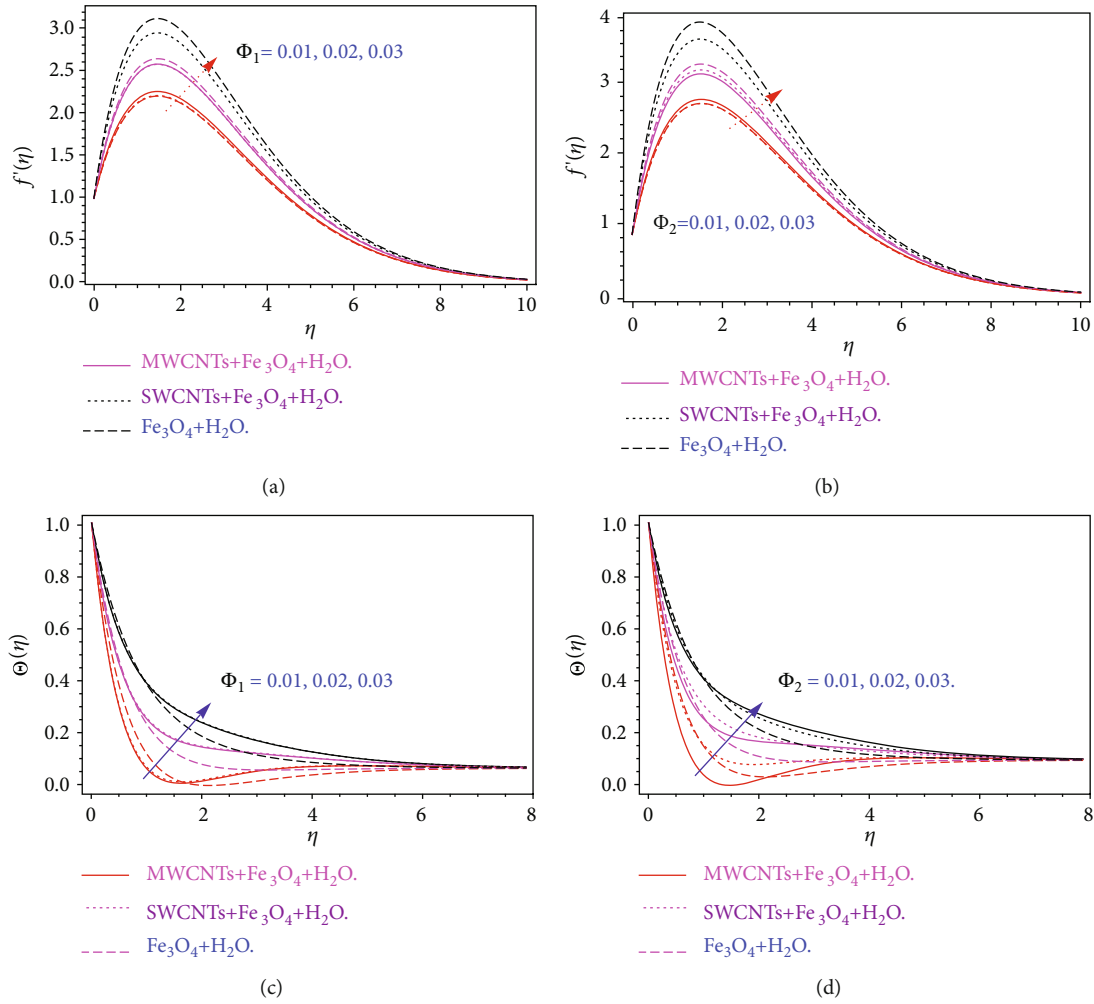


FIGURE 4: (a)–(d) Volume friction parameters  $\phi_1$  and  $\phi_2$  impact on the velocity  $f'(\eta)$  and temperature profiles  $\theta(\eta)$ , respectively.

The  $k_{\text{hnf}}$  is the thermal conductivity,  $\phi_1$  and  $\phi_2$  are the volume friction parameters,  $(C_p)_{\text{MS}}$  is the specific heat capacity,  $\rho_{\text{MS}}$  and  $\rho_{\text{CNT}}$  are specified densities of Fe<sub>3</sub>O<sub>4</sub> and CNTs, and  $Sc$  is the Schmidt number, respectively.

The transformation variables are [50]

$$\eta = \left( \frac{ae^{s/L}}{2v_f L} \right)^{1/2} r, \quad v = -\frac{R}{r+R} \sqrt{\frac{av_f e^{s/L}}{2L}} (f(\eta) + \eta f'(\eta)),$$

$$u = U_w = ae^{s/L} f'(\eta),$$

$$p = \rho_f a^2 e^{2s/L} H(\eta), \quad T = T_\infty + T_0 e^{\frac{As}{2L}} \Theta(\eta), \quad C = C_\infty + C_0 e^{\frac{As}{2L}} \Phi(\eta). \quad (8)$$

Thus, by using Eq. (8), Eqs. (2)–(7) yield

$$H' = \left( \frac{(\rho)_{\text{hnf}}}{(\rho)_f} \right) \frac{1}{\eta + K} f'^2, \quad (9)$$

$$\left( 1 + \frac{1}{\beta} \right) \left( f''' + \frac{1}{\eta + K} f'' - \frac{1}{(\eta + K)^2} f' - 2\lambda f' \right)$$

$$- (1 - \phi_1)^{2.5} (1 - \phi_2)^{2.5} \left( \frac{(\rho)_{\text{hnf}}}{(\rho)_f} \right)$$

$$\left( \frac{\eta + 2K}{(\eta + K)^2} K (f')^2 - \frac{K}{\eta + K} f f'' - \frac{K}{(\eta + K)^2} + 2Fr f'^2 \right)$$

$$= (1 - \phi_1)^{2.5} (1 - \phi_2)^{2.5} \frac{K}{\eta + K} (4H + \eta H), \quad (10)$$

$$\frac{k_{\text{hnf}}}{k_f} \left( \Theta'' + \frac{1}{\eta + K} \Theta' \right) + \left( \frac{(\rho C_p)_{\text{hnf}}}{(\rho C_p)_f} \right)$$

$$\cdot \text{Pr} \left[ \frac{K}{\eta + K} (f \Theta' - A f' \Theta) + \delta \Theta \right] = 0, \quad (11)$$

$$(1 - \phi_1)(1 - \phi_2) \left( \Phi'' + \frac{1}{\eta + K} \Phi' \right) + Sc \left( \frac{K}{\eta + K} f \Phi' \right) = 0. \quad (12)$$



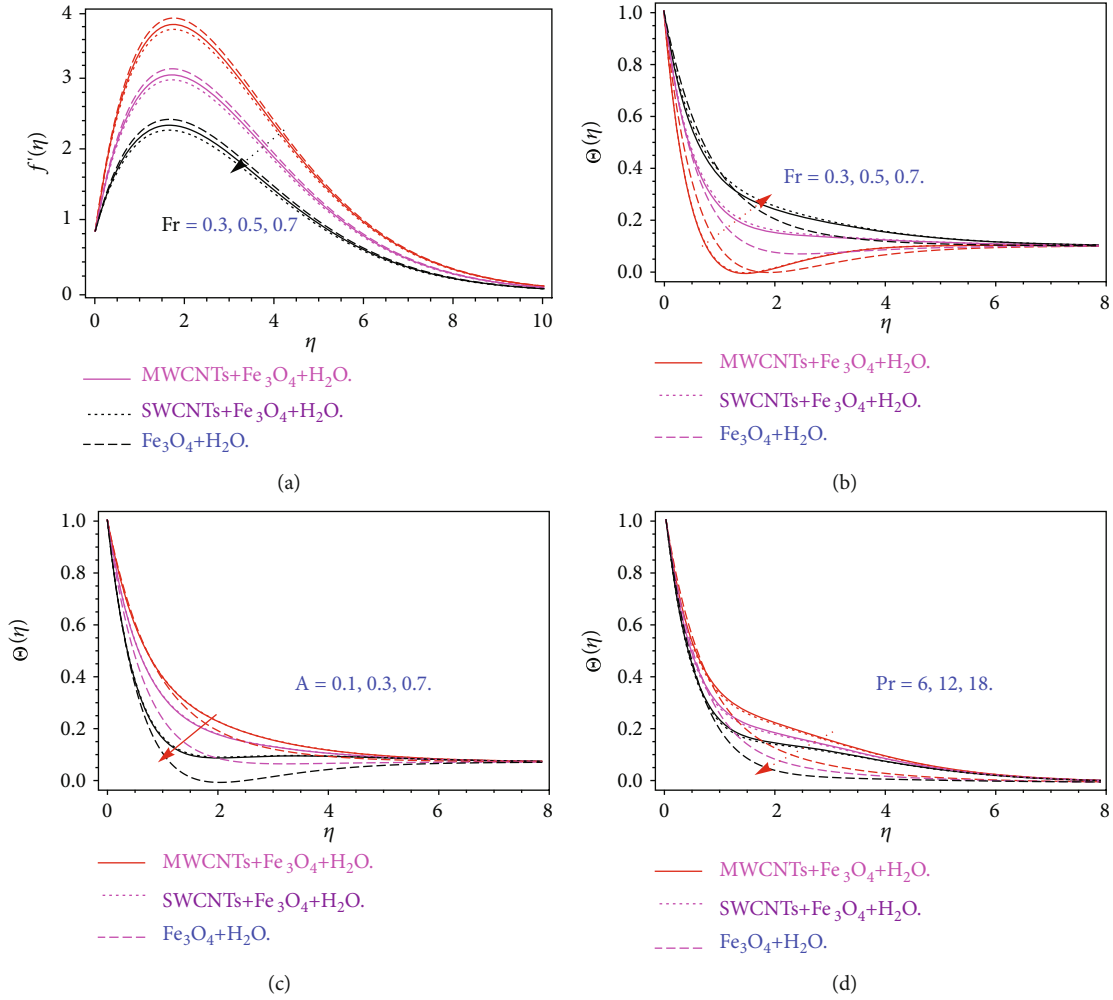


FIGURE 5: (a, b) Forchheimer parameter  $Fr$  impact on the velocity  $f'(\eta)$  and temperature profiles  $\theta(\eta)$ , (c) temperature exponent coefficient, and (d) Prandtl number  $Pr$  effects on temperature.

By eliminating  $H$  from Eqs. (9) and (10), we get

$$\begin{aligned} & \left(1 + \frac{1}{\beta}\right) \left[ f^{iv} + \frac{2}{\eta+K} f''' - \frac{1}{(\eta+K)^2} f'' + \frac{1}{(\eta+K)^3} \right. \\ & \cdot f' - 2\lambda \left( f'' + \frac{1}{(\eta+K)} f' \right) \left. \right] \\ & + \frac{(\rho)_{hnf}}{(\rho)_f} \left[ \frac{K}{(\eta+K)^2} f f'' + \frac{K}{(\eta+K)} f f''' - \frac{K}{(\eta+K)^3} \right. \\ & \cdot f f' - \frac{3K}{(\eta+K)^2 f'^2} - \frac{3K}{(\eta+K)} \\ & \cdot f' f'' - 2Fr \left( 2f' f'' + \frac{1}{\eta+K} f'^2 \right) \left. \right] = 0. \end{aligned} \quad (13)$$

The transform conditions are

$$\begin{aligned} f = 0, f' = 1, \Phi = 1, \Theta = 1 \text{ at } \eta = 0, \\ f' \rightarrow 0, f'' \rightarrow 0, \Phi \rightarrow 0, \Theta \rightarrow 0 \text{ at } \eta \rightarrow \infty, \end{aligned} \quad (14)$$

where  $Fr$ ,  $\lambda$ , and  $k$  are the Forchheimer, porosity, and curvature parameters, respectively, which can be rebound as

$$\begin{aligned} Fr = \frac{C_b}{K^{*1/2}}, Pr = \frac{\nu_f}{\alpha_f}, \delta = \frac{2QL}{U_w(\rho c_p)}, k = \left( \frac{ae^{s/L}}{2\nu_f L} \right), \\ \lambda = \frac{\nu_f L}{K^* U_w}, Sc = \frac{\nu_f}{D_f}. \end{aligned} \quad (15)$$

The local Nusselt number, Sherwood Number, and Skin friction are expressed as

$$\begin{aligned} \frac{L}{S} \left( \frac{Re}{2} \right)^{\frac{1}{2}} Nu_x = -\frac{k_{hnf}}{k_{bf}} \Theta'(0), \frac{L}{S} \left( \frac{Re}{2} \right)^{\frac{1}{2}} Sh_x = -\Phi'(0), \\ \sqrt{\frac{Re}{2}} C_{fx} = \frac{1}{(1-\phi_1)^{2.5} (1-\phi_2)^{2.5}} \left( 1 + \frac{1}{\beta} \right) f''(0), \end{aligned} \quad (16)$$

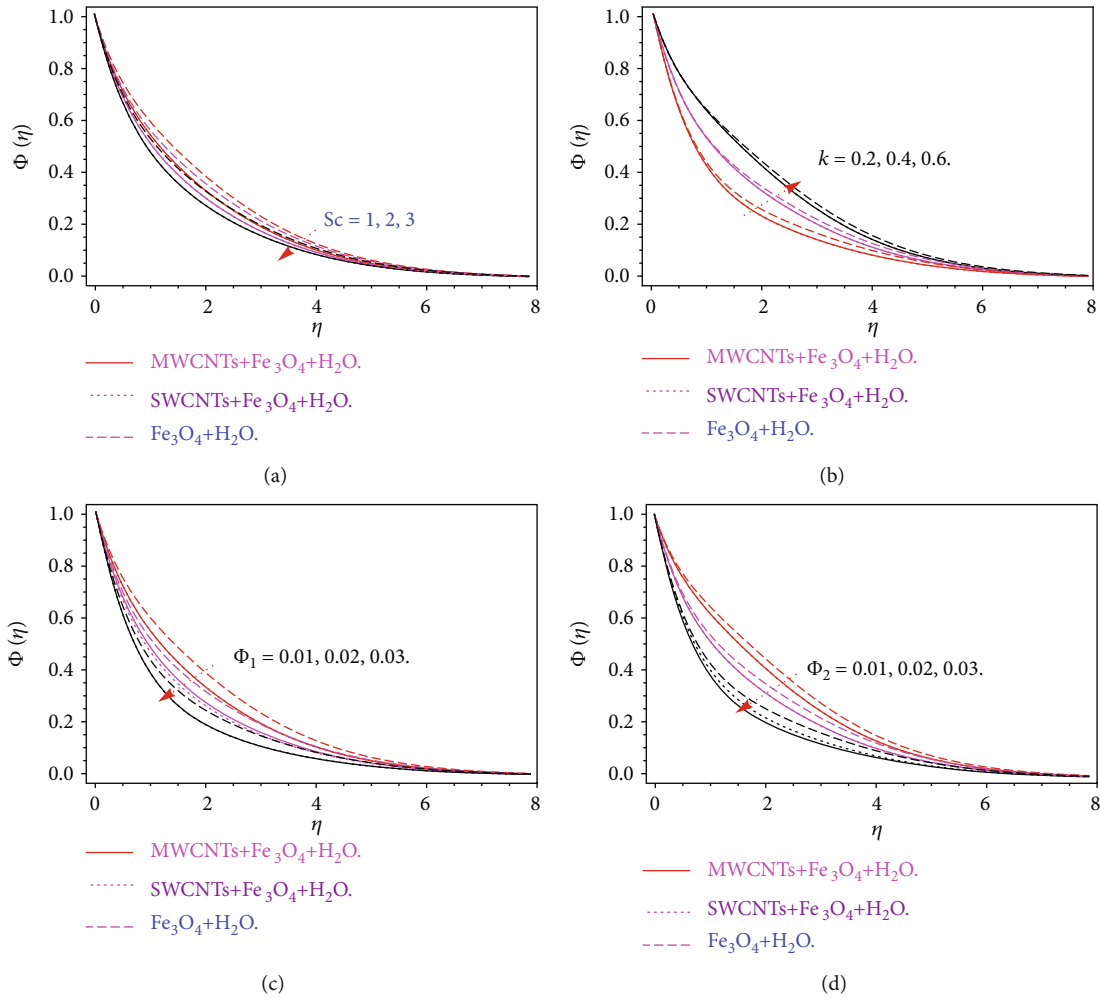


FIGURE 6: (a) Schmidt number  $Sc$ , (b) curvature parameter, and (c, d) volume friction parameters effects on mass transfer profile, respectively.

where local Reynolds number is

$$Re_x = \frac{u_0 x^2}{\nu l}. \quad (17)$$

### 3. Problem Solution

For analytical findings, the HAM approach has been utilized to solve the modeled equations, which was firstly introduced by Liao [51–53]. The initial guesses for velocity  $f_0$  and temperature  $\Theta_0$  are given as

$$f_0(\eta) = e^{-\eta} - e^{-2\eta}, \Theta_0(\eta) = e^{-\eta}, \Phi_0(\eta) = e^{-\eta}. \quad (18)$$

The linear terms are

$$\mathcal{L}_f(f) = f^{l\nu} \quad \text{and} \quad \mathcal{L}_\Theta(\Theta) = \Theta^l. \quad (19)$$

The expanded form of  $\mathcal{L}_f$ ,  $\mathcal{L}_\Theta$  and  $\mathcal{L}_\Phi$  is

$$\begin{aligned} \mathcal{L}_f[\chi_1 + \chi_2\eta + \chi_3\eta^2 + \chi_4\eta^3] &= 0, \\ \mathcal{L}_\Theta[\chi_5 + \chi_6\eta] &= 0, \quad \mathcal{L}_\Phi[\chi_7 + \chi_8\eta] = 0. \end{aligned} \quad (20)$$

3.1. OHAM Convergence. The converging of the OHAM approach was achieved employing Liao's concept [51–61].

$$\varepsilon_m^f = \frac{1}{l+1} \sum_{j=1}^l \left[ N_f \left( \sum_{k=1}^m f(\eta) \right)_{\eta=j\delta\eta} \right]^2, \quad (21)$$

$$\varepsilon_m^\Theta = \frac{1}{l+1} \sum_{j=1}^l \left[ N_\Theta \left( \sum_{k=1}^m f(\eta), \sum_{k=1}^m \Theta(\eta) \right)_{\eta=j\delta\eta} \right]^2, \quad (22)$$

$$\varepsilon_m^\Phi = \frac{1}{l+1} \sum_{j=1}^l \left[ N_\Phi \left( \sum_{k=1}^m \Phi(\eta) \right)_{\eta=j\delta\eta} \right]^2. \quad (23)$$

The sum of residual error is  $\varepsilon_m^t = \varepsilon_m^f + \varepsilon_m^\Theta + \varepsilon_m^\Phi$ .

### 4. Results and Discussion

The goal of this portion is forward to see how the temperature and velocity profiles function under the effect of the predicted factors. The flow configuration is shown in Figure 1. The OHAM technique's progress has been

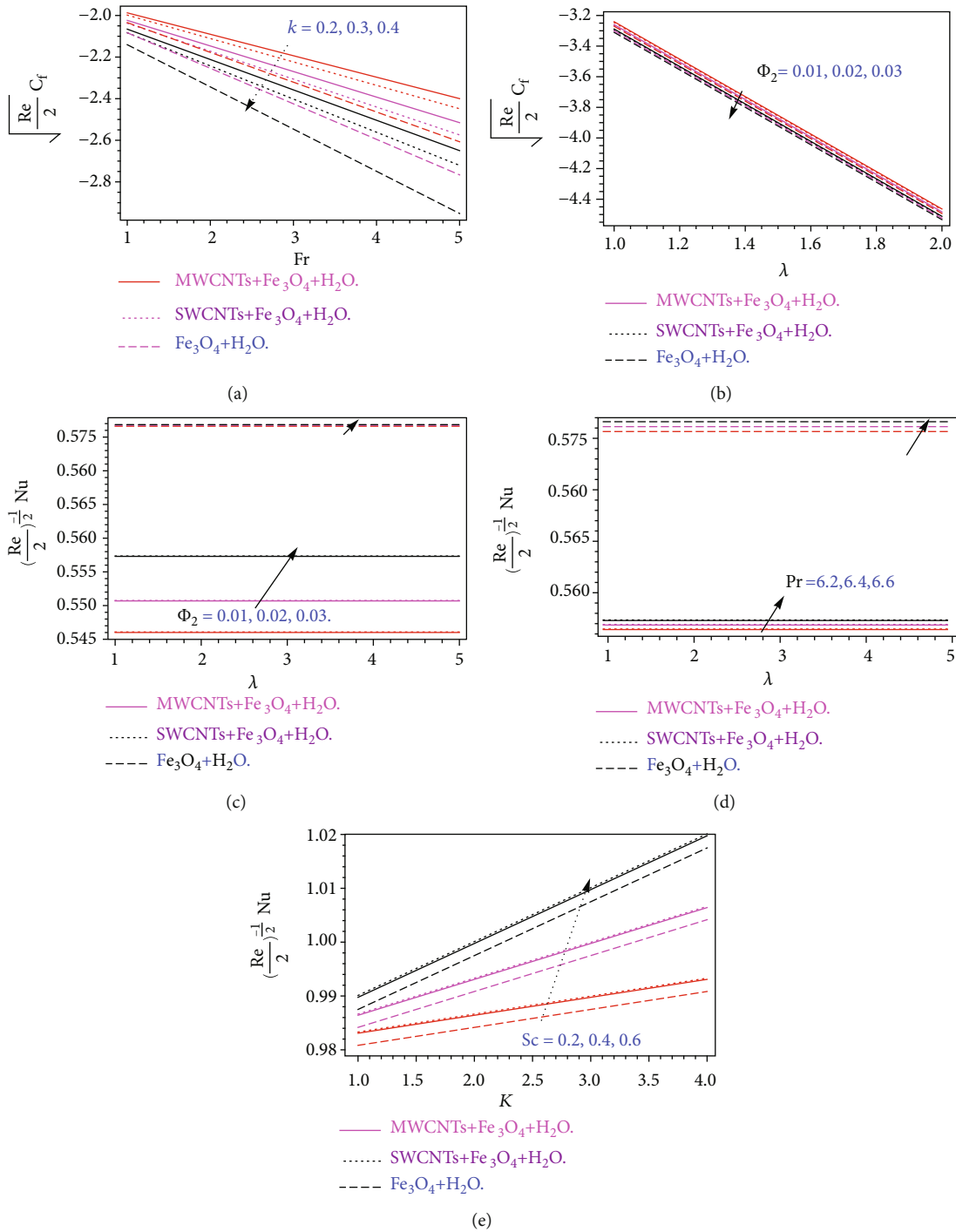


FIGURE 7: (a) Skin friction  $\sqrt{Re/2}C_{fx}$  for Fr and  $k$ , (b) skin friction  $\sqrt{Re/2}C_{fx}$  for  $\lambda$  and  $\phi_2$ , (c) Nusselt number  $(L/S)(Re/2)^{-1/2}Nu_x$  for  $\lambda$  and  $\phi_2$ , (d) Nusselt number  $(L/S)(Re/2)^{-1/2}Nu_x$  for  $\lambda$  and Pr, and (e) Sherwood number  $(L/S)(Re/2)^{-1/2}Sh_x$  for  $k$  and Sc.

computed and is depicted in Figure 2(a). Figure 2(b) displays the influence of velocity field versus  $M$ . The Lorentz force augments the resistance against the fluid motion and as a result, the velocity reduces with the greater value of the magnetic parameter. The augmentation in the Casson parameter declines the velocity profile. The Casson parameter at the infinity tends to the Newtonian fluid. The larger value of

the heat absorption and omission parameter improves the temperature distribution as shown in Figure 2(c). The greater value of the parameter  $\delta$  improves the temperature distribution. Figure 3 illustrates the effects of the (porosity term) and  $k$  on velocity and temperature. This conclusion can be drawn that the velocity  $f'(\eta)$  decrease, while the temperature field is increased versus rising values of porosity

TABLE 1: The numerical properties of nanomaterials and base fluid [27].

	$\rho(\text{kg/m}^3)$	$C_p(\text{J/kgK})$	$k(\text{W/mK})$
Pure water	997.1	4179	0.613
$\text{Fe}_3\text{O}_4$	5200	670	6
SWCNTs	2600	425	6600
MWCNTs	1600	796	300

TABLE 2: The total residual errors, when  $Fr = k = 0.6$ ,  $\phi_1 = 0.02$ ,  $\phi_2 = 0.2$ ,  $\lambda = 0.2$ ,  $Pr = 6.3$ , and  $A = 0.4$ .

$m$	$\epsilon_m^t$ SWCNTs	$\epsilon_m^t$ MWCNTs	$\epsilon_m^t$ $\text{Fe}_3\text{O}_4$
5	$1.8168 \times 10^{-4}$	$1.9479 \times 10^{-4}$	$1.4257 \times 10^{-4}$
13	$1.1223 \times 10^{-5}$	$1.2354 \times 10^{-5}$	$1.18312 \times 10^{-5}$
23	$1.3599 \times 10^{-6}$	$0.4698 \times 10^{-6}$	$0.4489 \times 10^{-6}$
30	$3.2578 \times 10^{-7}$	$4.3689 \times 10^{-7}$	$4.1464 \times 10^{-7}$

TABLE 3: The comparative analysis with the published work, when  $\phi_1 = \phi_2$ ,  $Fr = k = 0.6$ ,  $\lambda = 0.2$ ,  $Pr = 6.3$ , and  $A = 0.4$ .

	Hayat et al. [35]	Present
$f''(0)$	0.735	0.7352130
$-\Theta'(0)$	-1.375	-1.3752410
$-\Phi'(0)$	.....	-1.3620189

parameter  $\lambda$  as illustrated in Figures 3(a) and 3(b). Practically, the kinetic viscosity and length of the extending surface are enhanced with the action of the porosity parameter; therefore, such a phenomenon has been observed. On the other hand, the action of curvature parameter  $k$  enhances the velocity field and declines the temperature propagation as illustrated in Figures 3(c) and 3(d).

Figures 4(a)–4(d) are sketched to illustrate the consequences of volume friction coefficients  $\phi_{\text{CNT}}$  and  $\phi_{\text{Fe}_3\text{O}_4}$  on velocity and energy propagation. The specific heat capacity of  $\text{H}_2\text{O}$  is greater than much iron and carbon nanoparticles. The addition of nanoparticles in the water reduces its heat-absorbing capacity, which results in an excessive amount of heat in the fluid. These factors cause the enhancement of fluid velocity and thermal energy transition.

Figures 5(a) and 5(b) revealed the influence of Forchheimer number  $Fr$  on velocity and temperature profiles, respectively. The increment in the Forchheimer term reduces the fluid velocity and enhances the thermal energy profile. Because the permeability of fluid reduces by the action of the Forchheimer term, therefore, such a phenomenon has been observed. The energy profile declines with the effect of temperature exponent coefficient  $A$  and Prandtl number  $Pr$  as displayed in Figures 5(c) and 5(d). The thermal diffusivity of fluid rises with the increasing credit of Prandtl number, which results in declination of fluid temperature  $\theta(\eta)$  as shown in Figure 5(d). The thickness of the boundary layer improved with the increasing value of  $Pr$

and consequently, the temperature profile reduces. Figures 6(a) and 6(b) illustrate to elaborate the consequences of curvature parameter  $k$  and Schmidt number  $Sc$  on mass transport  $\Phi(\eta)$  profile. The mass transition rate reduces with the influence of Schmidt number while enhancing with the positive effects of curvature term, because the fluid mean viscosity becomes thick as the number of carbon and iron oxide particulates continues to increase.

The surface drag force  $\sqrt{Re/2}C_{fx}$  for carbon nanoliquid and  $\text{Fe}_3\text{O}_4$  is declared via Figures 7(a) and 7(b). It is been evidenced that as the curvature and the volumetric parameters are increased, the skin friction drops. Figures 7(c) and 7(d) demonstrate the numerical results for the Nusselt number  $(L/S)(Re/2)^{-1/2}Nu_x$ . It has been discovered that the heat conversion rate accelerated as the number of carbon nanomaterials in the conventional fluids and the Prandtl number expanded. Figure 7(e) indicates that the Sherwood number  $(L/S)(Re/2)^{-1/2}Sh_x$  is an enhancing factor of the Schmidt number. Table 1 displays the thermophysical properties of solid substrates and basic fluids. The OHAM technique's consolidation has been computed up to the 30th iteration and is reported in Table 2. Table 3 offers a comparative analysis of the current study to the existing literature.

## 5. Conclusion

We addressed the Darcy-Forchheimer flow of Casson hybrid nanoliquid induced by an extended curved surface in this problem. The momentum and energy equations are included in the flow model, which is set up as a system of partial differential equations. The ‘‘Homotopy analysis method’’ is used to further build up the analytic arrangement of modeled equations. This mathematical model attempts to highlight the dominance of nanofluid in heat and mass transmission in advanced technologies and industries. The following are the core findings:

- (i) The velocity and temperature fields both show positive behaviors against the increasing values of  $\phi_1$  and  $\phi_2$  (volume fraction parameters) of CNTs and  $\text{Fe}_3\text{O}_4$

The accumulative values of the Casson parameter decline the hybrid nanofluid motion.

- (ii) The employment of CNT and  $\text{Fe}_3\text{O}_4$  nanomaterials in the base fluid, to regulate the coolant level in industrial equipment, is quite beneficial
- (iii) The thermal energy profile shows a reducing trend versus larger values of temperature exponent coefficient  $A$
- (iv) High fluid velocity is achieved by increasing the value of  $k$  (curvature parameter), while the fluid temperature drops
- (v) The temperature and velocity profiles exhibit the opposite tendency when the Forchheimer number

is elevated since the fluid velocity decreases, whereas the temperature profile improves

- (vi) The temperature distribution increases for the larger values of the absorption parameter
- (vii) The comparison of the recent work with the published work authenticates the obtained results

### Data Availability

Data are available in the manuscript.

### Conflicts of Interest

No such interest exists.

### Acknowledgments

The authors extend their appreciation to the Deanship of Scientific Research at King Khalid University for funding this work through research groups under grant number RGP. 1/260/42.

### References

- [1] L. J. Crane, "Flow past a stretching plate," *Journal for Applied Mathematics and Physics*, vol. 21, no. 4, pp. 645–647, 1970.
- [2] I. A. Hassanien, "Similarity solutions for flow and heat transfer of a viscoelastic fluid over a stretching sheet extruded in a Cross Cooling stream," *ZAMM-Journal of Applied Mathematics and Mechanics/Zeitschrift für Angewandte Mathematik und Mechanik: Applied Mathematics and Mechanics*, vol. 82, no. 6, pp. 409–419, 2002.
- [3] T. C. Chiam, "Micropolar fluid flow over a stretching sheet," *ZAMM-Journal of Applied Mathematics and Mechanics/Zeitschrift für Angewandte Mathematik und Mechanik*, vol. 62, no. 10, pp. 565–568, 1982.
- [4] P. D. Ariel, "Generalized three-dimensional flow due to a stretching sheet," *ZAMM-Journal of Applied Mathematics and Mechanics/Zeitschrift für Angewandte Mathematik und Mechanik: Applied Mathematics and Mechanics*, vol. 83, no. 12, pp. 844–852, 2003.
- [5] K. Bhattacharyya, T. Hayat, and A. Alsaedi, "Exact solution for boundary layer flow of Casson fluid over a permeable stretching/shrinking sheet," *ZAMM-Journal of Applied Mathematics and Mechanics/Zeitschrift für Angewandte Mathematik und Mechanik*, vol. 94, no. 6, pp. 522–528, 2014.
- [6] M. Sajid, N. Ali, T. Javed, and Z. Abbas, "Stretching a curved surface in a viscous fluid," *Chinese Physics Letters*, vol. 27, article 024703, 2010.
- [7] T. Gul, W. Alghamdi, I. Khan, and I. Ali, "New similarity variable to transform the fluid flow from PDEs into fractional-order ODEs: numerical study," *Physica Scripta*, vol. 96, no. 8, 2021.
- [8] M. Imtiaz, T. Hayat, A. Alsaedi, and A. Hobiny, "Homogeneous-heterogeneous reactions in MHD flow due to an unsteady curved stretching surface," *Journal of Molecular Liquids*, vol. 221, pp. 245–253, 2016.
- [9] N. C. Rosca and I. Pop, "Unsteady boundary layer flow over a permeable curved stretching/shrinking surface," *European Journal of Mechanics - B/Fluids*, vol. 51, pp. 61–67, 2015.
- [10] A. Saeed, W. Alghamdi, S. Mukhtar et al., "Darcy-Forchheimer hybrid nanofluid flow over a stretching curved surface with heat and mass transfer," *PLoS One*, vol. 16, no. 5, article e0249434, 2021.
- [11] A. Ali, R. N. Jana, and S. Das, "Radiative CNT-based hybrid magneto-nanoliquid flow over an extending curved surface with slippage and convective heating," *Heat Transfer*, vol. 50, no. 3, pp. 2997–3020, 2021.
- [12] K. A. Kumar, V. Sugunamma, and N. Sandeep, "Effect of thermal radiation on MHD Casson fluid flow over an exponentially stretching curved sheet," *Journal of Thermal Analysis and Calorimetry*, vol. 140, no. 5, pp. 2377–2385, 2020.
- [13] M. Imtiaz, T. Hayat, and A. Alsaedi, "Convective flow of ferrofluid due to a curved stretching surface with homogeneous-heterogeneous reactions," *Powder Technology*, vol. 310, pp. 154–162, 2017.
- [14] Z. Hussain, S. Muhammad, and M. S. Anwar, "Effects of first-order chemical reaction and melting heat on hybrid nanoliquid flow over a nonlinear stretched curved surface with shape factors," *Advances in Mechanical Engineering*, vol. 13, no. 4, Article ID 168781402199952, 2021.
- [15] W. M. Qian, M. I. Khan, F. Shah et al., "Mathematical modeling and MHD flow of micropolar fluid toward an exponential curved surface: heat analysis via ohmic heating and heat source/sink," *Arabian Journal for Science and Engineering*, vol. 2021, pp. 1–12, 2021.
- [16] R. U. Haq, Z. H. Khan, and W. A. Khan, "Thermophysical effects of carbon nanotubes on MHD flow over a stretching surface," *Physica E: Low-dimensional Systems and Nanostructures*, vol. 63, pp. 215–222, 2014.
- [17] A. Ahmadian, M. Bilal, M. A. Khan, and M. I. Asjad, "Numerical analysis of thermal conductive hybrid nanofluid flow over the surface of a wavy spinning disk," *Scientific Reports*, vol. 10, no. 1, pp. 1–13, 2020.
- [18] Y. P. Lv, E. A. Algehyne, M. G. Alshehri et al., "Numerical approach towards gyrotactic microorganisms hybrid nanoliquid flow with the hall current and magnetic field over a spinning disk," *Scientific Reports*, vol. 11, no. 1, pp. 1–13, 2021.
- [19] A. Saeed, P. Kumam, T. Gul, W. Alghamdi, W. Kumam, and A. Khan, "Darcy-Forchheimer couple stress hybrid nanofluids flow with variable fluid properties," *Scientific Reports*, vol. 11, no. 1, pp. 1–13, 2021.
- [20] T. Gul, A. Qadeer, W. Alghamdi, A. Saeed, S. M. Mukhtar, and M. Jawad, "Irreversibility analysis of the couple stress hybrid nanofluid flow under the effect of electromagnetic field," *International Journal of Numerical Methods for Heat & Fluid Flow*, vol. 2021, 2021.
- [21] T. Gul, Z. Ahmed, M. Jawad, A. Saeed, and W. Alghamdi, "Bio-convectational nanofluid flow due to the thermophoresis and gyrotactic microorganism between the gap of a disk and cone," *Brazilian Journal of Physics*, vol. 51, no. 3, pp. 687–697, 2021.
- [22] W. Alghamdi, A. Alsubie, P. Kumam, A. Saeed, and T. Gul, "MHD hybrid nanofluid flow comprising the medication through a blood artery," *Scientific Reports*, vol. 11, no. 1, pp. 1–13, 2021.
- [23] Y. X. Li, T. Muhammad, M. Bilal, M. A. Khan, A. Ahmadian, and B. A. Pansera, "Fractional simulation for Darcy-Forchheimer hybrid nanoliquid flow with partial slip over a spinning disk," *Alexandria Engineering Journal*, vol. 60, no. 5, pp. 4787–4796, 2021.

- [24] Y. Ding, H. Alias, D. Wen, and R. A. Williams, "Heat transfer of aqueous suspensions of carbon nanotubes (CNT nanofluids)," *International Journal of Heat and Mass Transfer*, vol. 49, no. 1-2, pp. 240–250, 2006.
- [25] N. S. Akbar, M. Raza, and R. Ellahi, "Influence of induced magnetic field and heat flux with the suspension of carbon nanotubes for the peristaltic flow in a permeable channel," *Journal of Magnetism and Magnetic Materials*, vol. 381, article 405415, pp. 405–415, 2015.
- [26] T. Gul, A. Khan, M. Bilal et al., "Magnetic dipole impact on the hybrid nanofluid flow over an extending surface," *Scientific Reports*, vol. 10, no. 1, pp. 1–13, 2020.
- [27] M. Bilal, I. Khan, T. Gul et al., "Darcy-Forchheimer hybrid Nano fluid flow with mixed convection past an inclined cylinder," *CMC-Computers Materials & Continua*, vol. 66, no. 2, pp. 2025–2039, 2021.
- [28] S. E. Ahmed, "Effect of fractional derivatives on natural convection in a complex-wavy-wall surrounded enclosure filled with porous media using nanofluids," *ZAMM-Journal of Applied Mathematics and Mechanics/Zeitschrift für Angewandte Mathematik und Mechanik*, vol. 100, no. 1, article e201800323, 2020.
- [29] H. Yarmand, S. Gharekhani, S. F. S. Shirazi et al., "Study of synthesis, stability and thermo-physical properties of graphene nanoplatelet/platinum hybrid nanofluid," *International Communications in Heat and Mass Transfer*, vol. 77, pp. 15–21, 2016.
- [30] M. U. Sajid and H. M. Ali, "Thermal conductivity of hybrid nanofluids: a critical review," *International Journal of Heat and Mass Transfer*, vol. 126, pp. 211–234, 2018.
- [31] K. G. Kumar, E. H. B. Hani, M. E. H. Assad, M. Rahimi-Gorji, and S. Nadeem, "A novel approach for investigation of heat transfer enhancement with ferromagnetic hybrid nanofluid by considering solar radiation," *Microsystem Technologies*, vol. 27, no. 1, pp. 97–104, 2021.
- [32] R. P. Gowda, F. S. Al-Mubaddel, R. N. Kumar et al., "Computational modelling of nanofluid flow over a curved stretching sheet using Koo-Kleinstreuer and Li (KKL) correlation and modified Fourier heat flux model," *Chaos, Solitons & Fractals*, vol. 145, 2021.
- [33] R. N. Kumar, R. P. Gowda, A. M. Abusorrah et al., "Impact of magnetic dipole on ferromagnetic hybrid nanofluid flow over a stretching cylinder," *Physica Scripta*, vol. 96, no. 4, article 045215, 2021.
- [34] A. Zeeshan, Z. Ali, M. R. Gorji, F. Hussain, and S. Nadeem, "Flow analysis of biconvective heat and mass transfer of two-dimensional couple stress fluid over a paraboloid of revolution," *International Journal of Modern Physics B*, vol. 34, no. 11, p. 2050110, 2020.
- [35] K. M. Sanni, S. Asghar, M. Jalil, and N. F. Okechi, "Flow of viscous fluid along a nonlinearly stretching curved surface," *Results in Physics*, vol. 7, pp. 1–4, 2017.
- [36] M. Jawad, A. Saeed, T. Gul, and A. Khan, "The magnetohydrodynamic flow of a nanofluid over a curved exponentially stretching surface," *Heat Transfer*, vol. 50, no. 6, pp. 5356–5379, 2021.
- [37] A. Saeed, P. Kumam, S. Nasir, T. Gul, and W. Kumam, "Non-linear convective flow of the thin film nanofluid over an inclined stretching surface," *Scientific Reports*, vol. 11, no. 1, pp. 1–15, 2021.
- [38] T. Hayat, M. Rashid, M. Imtiaz, and A. Alsaedi, "MHD convective flow due to a curved surface with thermal radiation and chemical reaction," *Journal of Molecular Liquids*, vol. 225, p. 482, 2017.
- [39] T. Hayat, R. Sajjad, R. Ellahi, A. Alsaedi, and T. Muhammad, "Homogeneous-heterogeneous reactions in MHD flow of micropolar fluid by a curved stretching surface," *Journal of Molecular Liquids*, vol. 240, p. 209, 2017.
- [40] N. F. Okechi, M. Jalil, and S. Asghar, "Flow of viscous fluid along an exponentially stretching curved surface," *Results in Physics*, vol. 7, pp. 2851–2854, 2017.
- [41] Z. Asghar, N. Ali, R. Ahmed, M. Waqas, and W. A. Khan, "A mathematical framework for peristaltic flow analysis of non-Newtonian Sisko fluid in an undulating porous curved channel with heat and mass transfer effects," *Computer Methods and Programs in Biomedicine*, vol. 182, 2019.
- [42] T. Hayat, R. S. Saif, R. Ellahi, T. Muhammad, and B. Ahmad, "Numerical study for Darcy-Forchheimer flow due to a curved stretching surface with Cattaneo-Christov heat flux and homogeneous-heterogeneous reactions," *Results in Physics*, vol. 7, pp. 2886–2892, 2017.
- [43] Z. Abbas, M. Naveed, and M. Sajid, "Hydromagnetic slip flow of nanofluid over a curved stretching surface with heat generation and thermal radiation," *Journal of Molecular Liquids*, vol. 215, pp. 756–762, 2016.
- [44] Z. Mehmood, Z. Iqbal, E. Azhar, and E. N. Maraj, "Nanofluidic transport over a curved surface with viscous dissipation and convective mass flux," *Zeitschrift für Naturforschung A*, vol. 72, no. 3, pp. 223–229, 2017.
- [45] N. Acharya, "Active-passive controls of liquid di-hydrogen mono-oxide based nanofluidic transport over a bended surface," *International Journal of Hydrogen Energy*, vol. 44, no. 50, pp. 27600–27614, 2019.
- [46] P. Forchheimer, "Water movement through ground," *Journal of the Association of German Engineers.*, vol. 45, pp. 1782–1788, 1901.
- [47] M. Muskat, "The flow of homogeneous fluids through porous media," *Soil Science*, vol. 46, no. 2, p. 169, 1938.
- [48] F. Saba, N. Ahmed, U. Khan, and S. T. Mohyud-Din, "A novel coupling of (CNT-Fe<sub>3</sub>O<sub>4</sub>/H<sub>2</sub>O) hybrid nanofluid for improvements in heat transfer for flow in an asymmetric channel with dilating/squeezing walls," *International Journal of Heat and Mass Transfer*, vol. 136, pp. 186–195, 2019.
- [49] Q. Z. Xue, "Model for thermal conductivity of carbon nanotube-based composites," *Physica B: Condensed Matter*, vol. 368, pp. 302–307, 2005.
- [50] T. Hayat, F. Haider, T. Muhammad, and A. Alsaedi, "Numerical treatment for Darcy-Forchheimer flow of carbon nanotubes due to an exponentially stretching curved surface," *Journal of Central South University*, vol. 26, no. 4, pp. 865–872, 2019.
- [51] T. Hayat, F. Haider, T. Muhammad, and A. Alsaedi, "Numerical study for Darcy-Forchheimer flow of nanofluid due to an exponentially stretching curved surface," *Results in Physics*, vol. 8, pp. 764–771, 2018.
- [52] S. J. Liao, "An optimal homotopy-analysis approach for strongly nonlinear differential equations," *Communications in Nonlinear Science and Numerical Simulation*, vol. 15, no. 8, pp. 2003–2016, 2010.
- [53] S. J. Liao, Ed., *Advances in the Homotopy Analysis Method, Chapter 7*, World Scientific Press, 2013.
- [54] T. Gul and K. Ferdous, "The experimental study to examine the stable dispersion of the graphene nanoparticles and to look

- at the GO–H<sub>2</sub>O nanofluid flow between two rotating disks,” *Nano*, vol. 8, no. 7, pp. 1711–1727, 2018.
- [55] M. Jawad, A. Saeed, T. Gul, and A. Bariq, “MHD Darcy-Forchheimer flow of Casson nanofluid due to a rotating disk with thermal radiation and Arrhenius activation energy,” *Journal of Physics Communications*, vol. 5, no. 2, article 025008, 2021.
- [56] A. Rehman, Z. Salleh, and T. Gul, “Heat transfer of thin film flow over an unsteady stretching sheet with dynamic viscosity,” *Journal of Advanced Research in Fluid Mechanics and Thermal Sciences*, vol. 81, no. 2, pp. 67–81, 2021.
- [57] M. Jawad, A. Saeed, T. Gul, Z. Shah, and P. Kumam, “Unsteady thermal Maxwell power law nanofluid flow subject to forced thermal Marangoni convection,” *Scientific Reports*, vol. 11, no. 1, pp. 1–14, 2021.
- [58] A. Khan, W. Kumam, I. Khan et al., “Chemically reactive nanofluid flow past a thin moving needle with viscous dissipation, magnetic effects and hall current,” *PLoS One*, vol. 16, no. 4, article e0249264, 2021.
- [59] A. Khan, A. Saeed, A. Tassaddiq et al., “Bio-convective micropolar nanofluid flow over thin moving needle subject to Arrhenius activation energy, viscous dissipation and binary chemical reaction,” *Case Studies in Thermal Engineering*, vol. 25, 2021.
- [60] M. Bilal, T. Gul, A. Alsubie, and I. Ali, “Axisymmetric hybrid nanofluid flow with heat and mass transfer amongst the two gyrating plates,” *Zeitschrift für Angewandte Mathematik und Mechanik*, vol. 101, no. 11, 2021.
- [61] L. Ali, A. Tassaddiq, R. Ali et al., “A new analytical approach for the research of thin-film flow of magneto hydrodynamic fluid in the presence of thermal conductivity and variable viscosity,” *ZAMM-Journal of Applied Mathematics and Mechanics/Zeitschrift für Angewandte Mathematik und Mechanik*, vol. 101, no. 2, 2021.

## Research Article

# Numerical Study of the Flow of Two Radiative Nanofluids with Marangoni Convection Embedded in Porous Medium

Ravi Gupta <sup>1</sup>, Manish Gaur <sup>2</sup>, Qasem Al-Mdallal <sup>3</sup>, Sunil Dutt Purohit <sup>4</sup>,  
and Daya Lal Suthar <sup>5</sup>

<sup>1</sup>School of Science and Technology, Vardhman Mahaveer Open University, Kota, India

<sup>2</sup>Department of Mathematics, Government PG College, Kota, India

<sup>3</sup>Department of Mathematical Sciences, UAE University, P.O. Box 15551, Al Ain, UAE

<sup>4</sup>Department of HEAS (Mathematics), Rajasthan Technical University, Kota 324010, India

<sup>5</sup>Department of Mathematics, Wollo University, P.O. Box 1145, Dessie, Ethiopia

Correspondence should be addressed to Daya Lal Suthar; [dlsuthar@gmail.com](mailto:dlsuthar@gmail.com)

Received 19 October 2021; Revised 28 December 2021; Accepted 30 December 2021; Published 17 January 2022

Academic Editor: Taza Gul

Copyright © 2022 Ravi Gupta et al. This is an open access article distributed under the Creative Commons Attribution License, which permits unrestricted use, distribution, and reproduction in any medium, provided the original work is properly cited.

The aim of this study is to investigate the flow of two distinct nanofluids over a stretching surface in a porous medium with Marangoni convection. This investigation is studied under the effect of thermal radiation. Here, we have considered  $\text{Fe}_3\text{O}_4$  and  $\text{ZrO}_2$  nanosized particles suspended in engine oil (EO) base fluid. For the numerical simulation of the flow, the fourth-order Runge-Kutta method and suitable similarity solutions were used. Numerical solutions with graphical representation are presented.  $\text{Fe}_3\text{O}_4/\text{EO}$  nanofluid is more significant in the cooling process in comparison to  $\text{ZrO}_2/\text{EO}$  nanofluid. With increased radiation and temperature ratio parameters, a decrement in the temperature field has been noticed for both nanofluids. For increased values of volume friction parameter, a decrement is noticed for velocity profile and increment is noted for temperature profiles for both nanofluids. Also, a reduced velocity profile can be obtained with increased porosity parameter.

## 1. Introduction

In the past two decades, nanofluids got the vast attention of researchers due to their proven efficiency in thermal conductivity. A base fluid with suspended nanometer-sized particles with different shapes and sizes is called nanofluids. These nanoparticles can be metallic or nonmetallic or oxidic, for example, Al, Cu, Ag,  $\text{SiO}_2$ ,  $\text{Al}_2\text{O}_3$ ,  $\text{Fe}_3\text{O}_4$ , and  $\text{ZrO}_2$ , and base fluids can be  $\text{H}_2\text{O}$ ,  $\text{C}_2\text{H}_6\text{O}_2$ , and engine oil. Initially, Choi [1] investigated this phenomenon and named these fluids as “nanofluids.” Afterward, Xuan and Roetzel [2] studied the correlation between heat transfer and nanofluids and presented a numerical model. The heat transfer capacity of nanofluids is much higher than that of conventional fluid because the thermal conductivity of a fluid can be optimized by adding nanosized particles; a number of studies have been presented by researchers proving this concept for the nanofluids using different sizes, shapes, and concentrations

of nanoparticles with different base liquids, on different geometries [3–13]. Some key applications of nanofluids are in the field of nuclear plants, micropolymer films, heat exchangers, electronic devices, space technology, and production of heat pipes.

The convection characterized by the surface tension differences at the interface is defined as Marangoni convection. This interface dissipative flow can be relevant where different surface tension exists at interfaces, and by changing the temperature or concentration, this difference can be created. Marangoni convective boundary layer flows of nanofluids have their applications in various fields like thin film, melting of crystals, welding, semiconductors, vapor bubbles, material sciences, soap films, silicon wafers, and microgravity conditions. Napolitano [14] was the first who gave this phenomenon and named it. Christopher and Wang [15] studied the Prandtl number effects for Marangoni convective flow through a flat surface. Furthermore, Aly and Ebaid [16]



investigated radiative Marangoni convective flow of three different hybrid nanofluids with porosity and MHD effects. The thermal performance of glycerol/water mixture in the microchannel with Marangoni convection is studied by Yang et al. [17]. Afterward, this phenomenon is studied with different parameters, nanofluids, and geometries by some researchers [18–20].

Although nanofluids have been studied by many researchers with different nanoparticles suspended in different base fluids, in this study, engine oil base fluid is considered which is rare in the literature. Marangoni convection is an important aspect of determining fluid motion and material processing, particularly in low-gravity hydrodynamics, for analyzing heat transfer interactions, and nanoparticles can improve the flow's thermal performance. As per the best knowledge of the authors, the present study of Marangoni convective radiative flow of nanosized particles suspended in engine oil (EO) base fluid is novel. A comparative analysis for both nanofluids is also presented by the graphs and discussed and obtained a strong agreement with the existing literature.

## 2. Mathematical Model

Marangoni convective boundary layer flow of two different viscous, compressible nanofluids with thermal radiation, along the stretched surface, is studied in 2D. Engine oil is considered the base fluid with suspension of  $\text{Fe}_3\text{O}_4$  and  $\text{ZrO}_2$  nanoparticles. Base fluid and nanosized particles of laminar flow are assumed to be thermally stable. The fluid flow is considered at  $y \geq 0$ ; here, the  $x$ -axis is chosen parallel to the surface, and the  $y$ -axis is considered perpendicular to the stretching surface.  $T_w$  is the temperature at the surface, and  $T_\infty$  is the ambient temperature. Likewise, as Marangoni convection is considered, a linear relation of surface tension with temperature is given by [19]

$$\gamma = \gamma_0[1 - \bar{\gamma}(T - T_\infty)]. \quad (1)$$

Here,  $\gamma_0$  is the surface tension and  $\bar{\gamma}$  is the rate of change of surface tension along  $T$  (temperature). Taking these assumptions, the equation of the governing convective flows of the nanofluid is described as follows [19]:

$$\frac{\partial u}{\partial x} + \frac{\partial v}{\partial y} = 0, \quad (2)$$

$$u \frac{\partial u}{\partial x} + v \frac{\partial v}{\partial y} = \frac{\mu_{\text{nf}}}{\rho_{\text{nf}}} \frac{\partial^2 u}{\partial y^2} - \frac{\mu_{\text{nf}}}{\rho_{\text{nf}} k} u, \quad (3)$$

$$u \frac{\partial T}{\partial x} + v \frac{\partial T}{\partial y} = \frac{k_{\text{nf}}}{(\rho C_p)_{\text{nf}}} \frac{\partial^2 T}{\partial y^2} - \frac{1}{(\rho C_p)_{\text{nf}}} \left( \frac{\partial q_r}{\partial y} \right), \quad (4)$$

with the boundary condition:

$$\begin{aligned} v = 0, T = T_\infty + ax^2, \mu_{\text{nf}} \left( \frac{\partial u}{\partial y} \right) &= \frac{\partial \sigma}{\partial T} \frac{\partial T}{\partial x} \text{ at } y = 0, \\ u \longrightarrow 0, T \longrightarrow T_\infty \text{ as } y \longrightarrow \infty. \end{aligned} \quad (5)$$

Here, velocity notations in  $x$  and  $y$  directions are chosen as  $u$  and  $v$  accordingly. Radiative heat flux is represented by  $q_r$ . The Rosseland approximation takes into account radiative heat flux which is reported by [20]

$$q_r = -\frac{4\sigma^*}{3k^*} \frac{\partial T^4}{\partial y} = -\frac{16\sigma^*}{3k^*} T^3 \frac{\partial T}{\partial y}. \quad (6)$$

In the above equation, the mean absorption coefficient is denoted by  $k^*$  and  $\sigma^*$  denotes the Stefan-Boltzmann constant. After substituting this  $q_r$  into equation (4), the reduced equation is given as follows:

$$u \frac{\partial T}{\partial x} + v \frac{\partial T}{\partial y} = \frac{k_{\text{nf}}}{(\rho C_p)_{\text{nf}}} \frac{\partial^2 T}{\partial y^2} + \frac{16\sigma^*}{3(\rho C_p)_{\text{nf}} k^*} \frac{\partial}{\partial y} \left( T^3 \frac{\partial T}{\partial y} \right). \quad (7)$$

Here,  $\mu_{\text{nf}}$  is the viscosity,  $\rho_{\text{nf}}$  is the density,  $\kappa_{\text{nf}}$  is the thermal conductivity, and  $(\rho C_p)_{\text{nf}}$  is the heat capacity of nanofluids. Subscripts f and nf are used to denote base fluids and nanofluids accordingly. Also, the volume fraction is  $\phi$ ; also,  $m = 3$  is chosen for spherical-type nanoparticles. Physical constraints and thermophysical value of nanoliquids and base fluid are reported in Tables 1 and 2, respectively.

## 3. Similarity Solutions

The following similarity transformation is used to solve our model [19]:

$$\eta = \zeta_1 y, \varphi = \zeta_2 x f(\eta), \theta(\eta) = \frac{T - T_\infty}{T_w - T_\infty}, \quad (8)$$

where  $\zeta_1 = (\gamma_0 \bar{\gamma} a \rho_f / \mu_f^2)^{1/3}$ ,  $\zeta_2 = (\gamma_0 \bar{\gamma} a \mu_f / \rho_f^2)^{1/3}$ ,  $u = \partial \varphi / \partial y$ , and  $v = -\partial \varphi / \partial x$ .

Following the foregoing transformations, equations (3) and (7) are turned into nonlinear ordinary differential equations as follows:

$$f''' + \left( 1 - \phi + \phi \frac{\rho_s}{\rho_f} \right) (1 - \phi)^{2.5} (ff'' - f'^2) - Kf' = 0, \quad (9)$$

$$\begin{aligned} \theta'' [1 + R_d A (\theta(\theta_w - 1) + 1)^3] \\ + R_d A [3\theta'^2 (\theta_w - 1) \{ \theta(\theta_w - 1) + 1 \}^2] \\ + B (f\theta' - 2\theta f') = 0. \end{aligned} \quad (10)$$

Here,  $A = \kappa_f / \kappa_{\text{nf}} = \{ (\kappa_s + (m - 1)\kappa_f + (\kappa_f - \kappa_s)\phi) / (\kappa_s + (m - 1)\kappa_f - (m - 1)(\kappa_f - \kappa_s)\phi) \}$ ,  $B = \text{Pr}_f (1 - \phi + \phi(\rho_s / \rho_f)) (1 - \phi)^{2.5}$ , and  $C = (1 - \phi)^{2.5}$ .

TABLE 1: Table of physical constraints of nanofluids used.

$\mu_{\text{nf}} = \mu_f / (1 - \phi)^{2.5}$	Effective dynamic viscosity
$\rho_{\text{nf}} = (1 - \phi)\rho_f + \phi\rho_s$	Effective density
$\kappa_{\text{nf}} = \{\kappa_s + (m - 1)\kappa_f - (m - 1)(\kappa_f - \kappa_s)\phi / \kappa_s + (m - 1)\kappa_f + (\kappa_f - \kappa_s)\phi\} \kappa_f$	Thermal conductivity
$(\rho C_p)_{\text{nf}} = (\rho C_p)_s \phi + (\rho C_p)_f (1 - \phi)$	Heat capacitance

The above equations are with the modified boundary conditions:

$$\theta(0) = 1, f(0) = 0, f''(0) = -2C, \theta(\infty) = 0, f'(\infty) = 0, \quad (11)$$

where  $R_d = 16\sigma^* T_\infty^3 / 3k^* k_f$  is the radiation parameter,  $\text{Pr} = (\rho C_p)_f \nu_f / \kappa_f$  is the Prandtl number,  $K = 1/\psi_1^2 k$  is the permeability parameter, and  $\theta_w = T_w / T_\infty$  is the temperature ratio parameter.

#### 4. Numerical Solution

With the help of the above-described similarity transformation, the governing equation of the flows has been converted into a set of the ordinary differential equations. Moreover, in order to tackle these equations using the Runge-Kutta method with a shooting technique, equations (9) and (10) together with the boundary conditions (11) turned into an initial value problem, as shown below.

$$f = h_1, f' = h_2, f'' = h_3, \theta = h_4, \text{ and } \theta' = h_5, \text{ where } h_3' = (1 - \phi)^{2.5} (1 - \phi + \phi(\rho_s / \rho_f)) (h_2^2 - h_1 h_3) + K h_2 \text{ and } h_5' = (-R_d A [3h_5^2 (\theta_w - 1) \{h_4 (\theta_w - 1) + 1\}^2] - B (h_1 h_5 - 2h_4 h_2)) / (1 + R_d A \{h_4 (\theta_w - 1) + 1\}^3).$$

The above equations are with the following transformed boundary conditions,  $h_1(0) = 0$ ,  $h_3(0) = -2C$ , and  $h_4(0) = 1$ . The best approximated numerical results are obtained by some initial guesses with the shooting method. To get exact results up to  $10^{-7}$  accuracy, an iterated approach is used in this method. The Prandtl number for EO is 6450, and the step size  $\Delta\eta = 0.01$  is considered.

#### 5. Results and Discussion

The comparative investigation of Marangoni convection of  $\text{Fe}_3\text{O}_4$  and  $\text{ZrO}_2$  nanofluid flow is studied. This investigation is studied under the effect of thermal radiation over the stretching surface. Numerical simulation is performed with the above-described method, and results are presented graphically to illustrate the impacts of several nondimensional physical parameters for  $f'(\eta)$  (temperature profile) and  $\theta(\eta)$  (velocity profile).

The impact of  $K$  on  $f'(\eta)$  for  $\text{Fe}_3\text{O}_4/\text{EO}$  and  $\text{ZrO}_2/\text{EO}$  nanofluids, respectively, is depicted in Figure 1. It is observed that with increased  $K$ , a decrement in  $f'(\eta)$  is seen for both nanofluids. With the fact  $K \propto 1/k$ , hence if we raise the coefficient of porosity, the permeability of the porous media decreases, resulting in a drop in fluid velocity.

TABLE 2: Thermophysical properties [19, 20].

	$\rho(\text{kg m}^{-3})$	$C_p(\text{J kg}^{-1} \text{K}^{-1})$	$k(\text{W m}^{-1} \text{K}^{-1})$	Pr
EO	884	1910	0.144	6450
$\text{Fe}_3\text{O}_4$	5810	670	6	—
$\text{ZrO}_2$	5680	502	1.7	—

The effect of volume friction  $\phi$  on  $f'(\eta)$  is depicted in Figure 2. It is noticed that with increased  $\phi$ , we get a decreased velocity profile. With rising  $\phi$ , there is a significant influence of  $\phi$  on the velocity profiles, with the speed of fluid being reduced at the vicinity of the surface and the reverse effect being visible further from the surface. It is also worth noting that the  $\text{ZrO}_2/\text{EO}$  nanofluid has a larger velocity than the  $\text{Fe}_3\text{O}_4/\text{EO}$  nanofluid. This is due to the fact that density of  $\text{ZrO}_2$  is lower than that of  $\text{Fe}_3\text{O}_4$ , implying that  $\text{ZrO}_2$  is lighter in motion than  $\text{Fe}_3\text{O}_4$ .

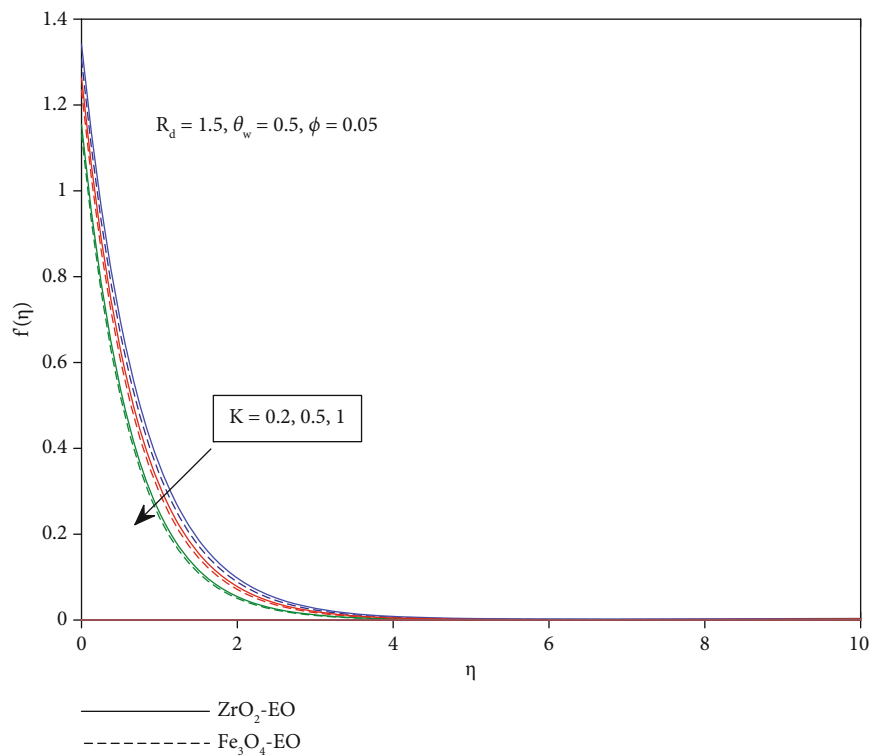
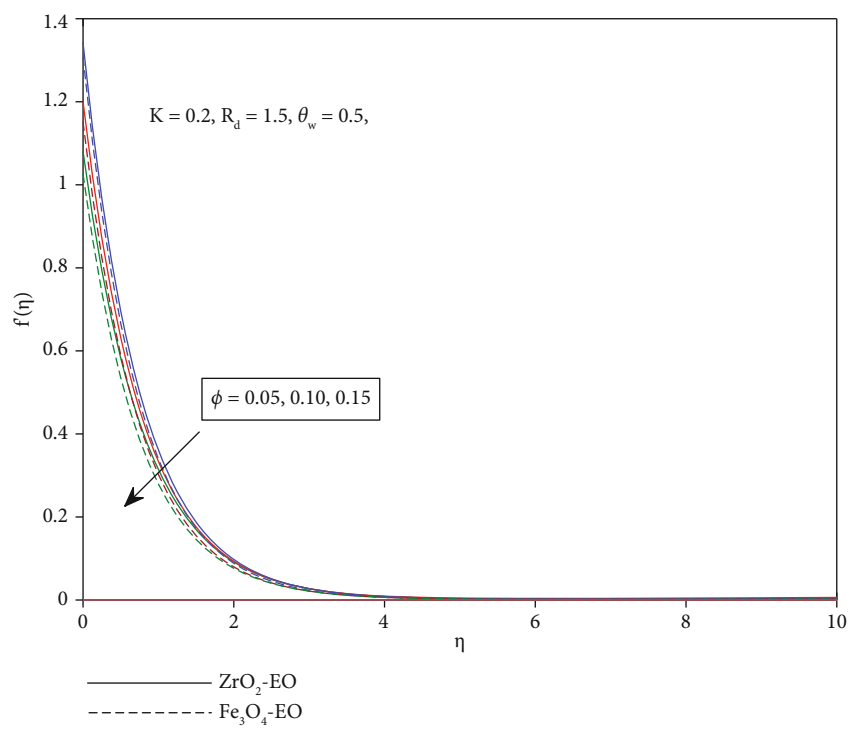
The impact of  $\phi$  on  $\theta(\eta)$  is depicted in Figure 3. It is observed that with increased  $\phi$ , an increased temperature profile for both nanofluids is seen. With increased nanoparticles of both nanofluids, the temperature of fluid is increased; as a result, the temperature field may rise.

The impact of  $R_d$  on  $\theta(\eta)$  is depicted in Figure 4. It is concluded that with increased  $R_d$  along with  $\theta(\eta)$ , an increased temperature profile is observed. Radiations create additional heat within the fluids, which results in higher temperature fields. Furthermore,  $R_d$  has no substantial effect on the velocity fields. The radiation parameter, which is the inverse of the Stephan number, is used to determine the relative significance of thermal radiation versus conductive heat transmission. As a result of the thermal radiation's dominance over conduction, it may be employed to regulate the thermal boundary layers rather well.

The impact of the temperature ratio parameter  $\theta_w$  on  $\theta(\eta)$  is depicted in Figure 5. It is concluded that with increased  $\theta_w$  along with  $\theta(\eta)$ , an increased temperature profile is observed. As a recognizable outcome, it is likewise seen that the temperature profile of the  $\text{Fe}_3\text{O}_4/\text{EO}$  nanofluid remains consistently greater than that of the  $\text{ZrO}_2/\text{EO}$  nanofluid.

#### 6. Code of Verification

For the validation of this research, comparison with Das et al. [21] and Jamshed et al. [4] was made for local Nusselt numbers using several values of Pr as shown in Table 3. To do this, the remaining parameters in our simulation approach are set to zero ( $R_d = K = \phi = \theta_w = 0$ ). The calculated findings are found to be in good match with the previous results.

FIGURE 1: Velocity profile for  $K$ .FIGURE 2: Velocity profile for  $\phi$ .

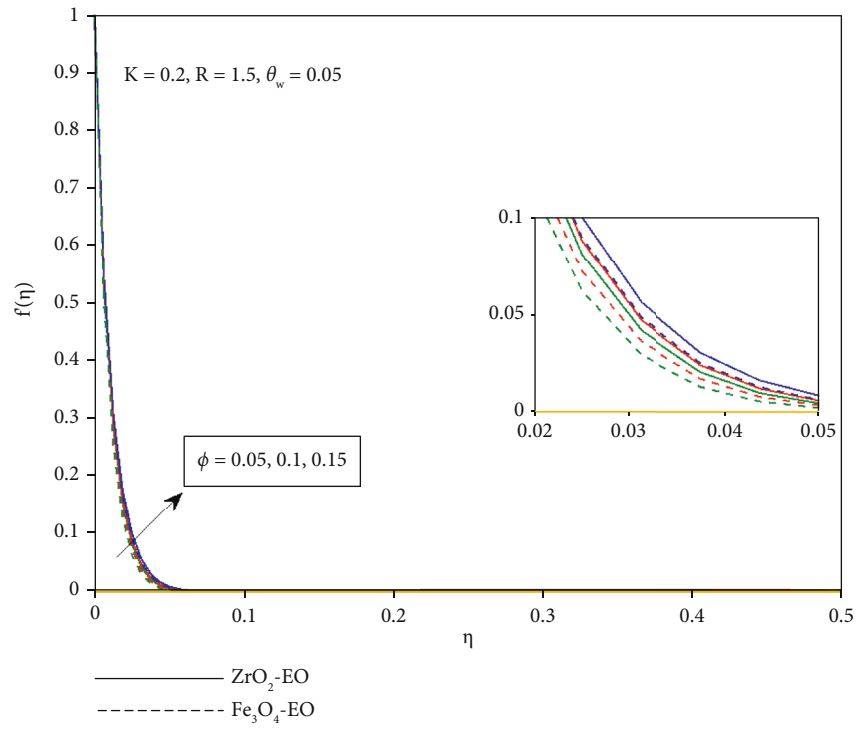


FIGURE 3: Temperature profile for  $\phi$ .

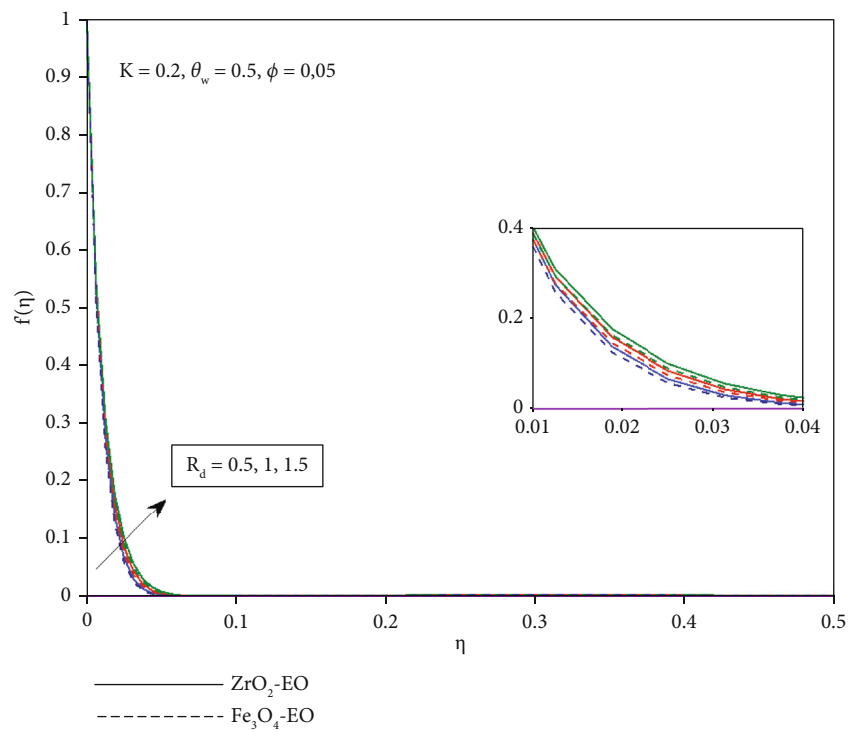
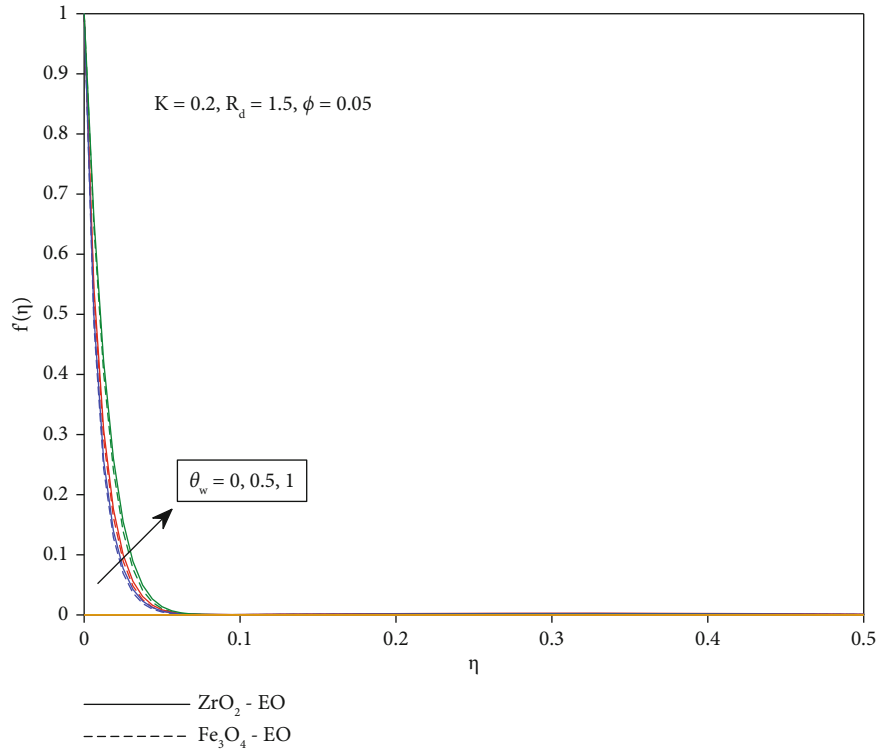


FIGURE 4: Temperature profile for  $R_d$ .

FIGURE 5: Temperature profile for  $\theta_w$ .TABLE 3: Comparison for different values of the Prandtl number for  $-\theta'(0)$  assuming  $R_d = K = \phi = \theta_w = 0$ .

Pr	Jamshed et al. [4]	Das et al. [21]	Present study
0.72	0.80876181	0.80876122	0.80876183
1	1	1	1
3	1.92357420	1.92357431	1.92357424
7	3.07314651	3.07314679	3.07314652
10	3.72055429	3.72055436	3.72055430

## 7. Conclusions

Marangoni convection of  $\text{Fe}_3\text{O}_4$  and  $\text{ZrO}_2$  nanofluid flow past a stretching surface with thermal radiation embedded in porous media is considered. The flow's governing model is encountered with the Runge-Kutta fourth-order technique and suitable similarity transformations. These results can be used to study the thermal performance with other boundary conditions.

The following important outcomes are obtained.

- (i) The  $\text{Fe}_3\text{O}_4/\text{EO}$  nanofluid is more significant in the cooling process in comparison to the  $\text{ZrO}_2/\text{EO}$  nanofluid
- (ii) With increased porosity parameter  $K$ , a decrement in the velocity field has been noticed for both nanofluids

(iii) With increased  $R_d$  and  $\theta_w$  parameters, a decrement in the temperature field has been noticed for both nanofluids

(iv) For the increased values of  $\phi$ , a decrement is noticed for the velocity profile and opposite behavior is observed for temperature profiles for  $\text{Fe}_3\text{O}_4/\text{EO}$  and  $\text{ZrO}_2/\text{EO}$  nanofluids

## Data Availability

No data were used to support this study.

## Conflicts of Interest

There is no conflict of interest regarding the publication of this article.

## References

- [1] S. U. S. Choi, "Enhancing thermal conductivity of fluids with nanoparticles," in *The Proceedings of the 1995 ASME International Mechanical Engineering Congress and Exposition*, pp. 99–105, San Francisco, ASME, FED 231/MD66, USA, 1995.
- [2] Y. M. Xuan and W. Roetzel, "Conceptions of heat transfer correlation of nanofluids," *International Journal Communications of Heat and Mass Transfer*, vol. 43, pp. 3701–3707, 2020.
- [3] L. A. Khan, M. Raza, N. A. Mir, and R. Ellahi, "Effects of different shapes of nanoparticles on peristaltic flow of MHD

- nanofluids filled in an asymmetric channel,” *Journal of Thermal Analysis and Calorimetry*, vol. 140, pp. 879–890, 2020.
- [4] W. Jamshed, K. S. Nisar, R. W. Ibrahim, T. Mukhtar, V. Vijayakumar, and F. Ahmad, “Computational frame work of Cattaneo-Christov heat flux effects on engine oil based Williamson hybrid nanofluids: a thermal case study,” *Case Studies in Thermal Engineering*, vol. 26, 2021.
- [5] P. K. Dadheech, P. Agrawal, F. Mebarek-Oudina, N. Abu-Hamdeh, and A. Sharma, “Comparative heat transfer analysis of MoS<sub>2</sub>/C<sub>2</sub>H<sub>6</sub>O<sub>2</sub> and SiO<sub>2</sub>-MoS<sub>2</sub>/C<sub>2</sub>H<sub>6</sub>O<sub>2</sub> Nanofluids with natural convection and inclined magnetic field,” *Journal of Nanofluids*, vol. 9, no. 3, pp. 161–167, 2020.
- [6] A. Mourad, A. Aissa, F. Mebarek-Oudina et al., “Galerkin finite element analysis of thermal aspects of Fe<sub>3</sub>O<sub>4</sub>-MWCNT/water hybrid nanofluid filled in wavy enclosure with uniform magnetic field effect,” *International Communications in Heat and Mass Transfer*, vol. 126, 2021.
- [7] A. Saeed, P. Kumam, S. Nasir, T. Gul, and W. Kumam, “Non-linear convective flow of the thin film nanofluid over an inclined stretching surface,” *Scientific Reports*, vol. 11, no. 1, 2021.
- [8] M. Bilal, A. Saeed, T. Gul, I. Ali, W. Kumam, and P. Kumam, “Numerical approximation of microorganisms hybrid nanofluid flow induced by a wavy fluctuating spinning disc,” *Coatings*, vol. 11, no. 9, p. 1032, 2021.
- [9] A. Saeed, P. Kumam, T. Gul, W. Alghamdi, W. Kumam, and A. Khan, “Darcy-Forchheimer couple stress hybrid nanofluids flow with variable fluid properties,” *Scientific Reports*, vol. 11, no. 1, 2021.
- [10] R. Ellahi, F. Hussain, S. Asad Abbas, M. M. Sarafraz, M. Goodarzi, and M. S. Shadloo, “Study of two-phase Newtonian nanofluid flow hybrid with hafnium particles under the effects of slip,” *Inventions*, vol. 5, no. 1, p. 6, 2020.
- [11] M. Raza, R. Ellahi, S. M. Sait et al., “Enhancement of heat transfer in peristaltic flow in a permeable channel under induced magnetic field using different CNTs,” *Journal of Thermal Analysis and Calorimetry*, vol. 140, pp. 1277–1291, 2020.
- [12] P. K. Dadheech, P. Agrawal, A. Sharma, A. Dadheech, Q. al-Mdallal, and S. D. Purohit, “Entropy analysis for radiative inclined MHD slip flow with heat source in porous medium for two different fluids,” *Case Studies in Thermal Engineering*, vol. 28, 2021.
- [13] K. S. Nisar, U. Khan, A. Zaib, I. Khan, and D. Baleanu, “Numerical Simulation of Mixed Convection Squeezing Flow of a Hybrid Nanofluid Containing Magnetized Ferroparticles in 50%:50% of Ethylene Glycol–Water Mixture Base Fluids Between Two Disks With the Presence of a Non-linear Thermal Radiation Heat Flux,” *Frontiers in Chemistry*, vol. 8, p. 792, 2020.
- [14] L. G. Napolitano, “Marangoni boundary layers,” in *Proceedings 3rd European Symposium on Material Science in Space*, Grenoble, 1979.
- [15] D. M. Christopher and B. X. Wang, “Prandtl number effects for Marangoni convection over a flat surface,” *International Journal of Thermal Sciences*, vol. 40, no. 6, pp. 564–570, 2001.
- [16] E. H. Aly and A. Ebaid, “Exact analysis for the effect of heat transfer on MHD and radiation Marangoni boundary layer nanofluid flow pasta surface embedded in a porous medium,” *Journal of Molecular Liquids*, vol. 215, 2016.
- [17] B. Yang, M. M. Sarafraz, and M. Arjomandi, “Marangoni effect on the thermal performance of glycerol/water mixture in microchannel,” *Applied Thermal Engineering*, vol. 161, 2019.
- [18] Q. M. Al-Mdallal, N. Indumathi, B. Ganga, and A. K. Abdul Hakeem, “Marangoni radiative effects of hybrid-nanofluids flow past a permeable surface with inclined magnetic field,” *Case Studies in Thermal Engineering*, vol. 17, 2020.
- [19] P. K. Dadheech, P. Agrawal, A. Sharma, K. S. Nisar, and S. D. Purohit, “Marangoni convection flow of  $\gamma$ -Al<sub>2</sub>O<sub>3</sub> nanofluids past a porous stretching surface with thermal radiation effect in the presence of an inclined magnetic field,” *Heat Transfer*, vol. 51, no. 1, pp. 534–550, 2022.
- [20] P. Agrawal, P. K. Dadheech, R. N. Jat, K. S. Nisar, M. Bohra, and S. D. Purohit, “Magneto Marangoni flow of  $\gamma$ -AL<sub>2</sub>O<sub>3</sub> nanofluids with thermal radiation and heat source/sink effects over a stretching surface embedded in porous medium,” *Case Studies in Thermal Engineering*, vol. 23, 2021.
- [21] S. Das, S. Chakraborty, R. N. Jana, and O. D. Makinde, “Entropy analysis of unsteady magneto-nanofluid flow past accelerating stretching sheet with convective boundary condition,” *Applied Mathematics and Mechanics*, vol. 36, no. 12, pp. 1593–1610, 2015.

## Research Article

# Thermal Transport in Radiative Nanofluids by Considering the Influence of Convective Heat Condition

Adnan <sup>1</sup>, Waqas Ashraf,<sup>2</sup> Abdulaziz H. Alghtani,<sup>3</sup> Ilyas Khan <sup>4</sup> and M. Andualem <sup>5</sup>

<sup>1</sup>Department of Mathematics, Mohi-ud-Din Islamic University, Nerian Sharif, AJ&K 12080, Pakistan

<sup>2</sup>Department of Applied Mathematics and Statistics (AM&S), Institute of Space Technology (IST), Islamabad 44000, Pakistan

<sup>3</sup>Mechanical Engineering Department at Taif University, P.O. Box 11099, Taif 21944, Saudi Arabia

<sup>4</sup>Department of Mathematics, College of Science Al-Zulfi, Majmaah University, Al-Majmaah 11952, Saudi Arabia

<sup>5</sup>Department of Mathematics, Bonga University, Bonga, Ethiopia

Correspondence should be addressed to Adnan; [adnan\\_abbasi89@yahoo.com](mailto:adnan_abbasi89@yahoo.com)  
and M. Andualem; [mulugetaandualem4@gmail.com](mailto:mulugetaandualem4@gmail.com)

Received 18 October 2021; Revised 27 November 2021; Accepted 13 December 2021; Published 5 January 2022

Academic Editor: Taza Gul

Copyright © 2022 Adnan et al. This is an open access article distributed under the Creative Commons Attribution License, which permits unrestricted use, distribution, and reproduction in any medium, provided the original work is properly cited.

The analysis of nanofluid dynamics in a bounded domain attained much attention of the researchers, engineers, and industrialists. These fluids became much popular in the researcher's community due to their broad uses regarding the heat transfer in various industries and fluid flowing in engine and in aerodynamics as well. Therefore, the analysis of Cu-kerosene oil and Cu-water is organized between two Riga plates with the novel effects of thermal radiations and surface convection. The problem reduced in the form of dimensionless system and then solved by employing variational iteration and variation of parameter methods. For the sake of validity, the results checked with numerical scheme and found to be excellent. Further, it is examined that the nanofluids move slowly by strengthen Cu fraction factor. The temperature of Cu-kerosene oil and Cu-water significantly rises due to inducing thermal radiations and surface convection. The behaviour of shear stresses is in reverse proportion with the primitive parameters, and local Nusselt number increases due to varying thermal radiations, Biot number, and fraction factor, respectively.

## 1. Introduction

The heat transfer caused troubles for industrialists and engineers because reasonable amount of it required to cope many industrial and engineering processes. Therefore, a second generation of the fluid was developed called nanofluids [1]. These fluids are the composition of two or more than two nanoscaled particles in the host liquid. Due to reasonable thermal performance of these fluids, researchers focused on the study of nanofluids and its advancements. The applications of these fluids fall in the field medical sciences, electronic devices, paint industries, drug delivery system, the study of bionanofluids in human veins and arteries, the reaction of nanomaterials by taking blood as a host fluid, coating of various aircraft parts, and in many other potential fields of interest. Therefore, it is imperative to address the comparative heat transfer analysis in different nanofluids.

To improve the heat transport in nanofluids, many theoretical models have been suggested; some of them are Hamilton and Crossers model, Maxwell Garnett model, KKL model, Buongiorno's model, etc. By utilizing aforementioned thermal conductivity models, many researchers explored the problems of nanofluids in various geometries and studied their dynamics under various conditions. In 2016, Mohyud-Din et al. [2] discussed the mass and heat transfer analysis in opening (diverging) and narrowing (converging) channel. They assumed that walls of the channel capable to stretching and shrinking. The investigation of heat transfer over a stretchable surface by inducing an MHD and thermal radiation examined by Khan et al. [3] in 2016.

Sheikholeslami [4] explored the behaviour of nanofluid under the governing parameters and Lorentz forces. The effect of Lorentz forces on the nanoliquid past a porous

cylinder with the help of Darcy model was reported in [5]. Adnan et al. [6] explored the second-grade fluid problem between opening/narrowing walls by inducing cross diffusion effects in the constitutive model. Also, they demonstrated the effects of other flow parameters ingrained in the flow model on the velocity, temperature, and concentration fields. The analysis of two phase nanoliquid model by plugging the effects of Lorentz forces is presented in [7]. Another imperative inspection of the nanoliquid dynamics is reported in [8]. For thermal enhancement, they induced KKL correlation in the model.

Influence of thermal radiation between oblique walls was reported by Adnan et al. [9]. They assumed that the boundaries of the channel are capable to stretching and shrinking. Furthermore, they solved the model and explored the effects of various flow parameters in the flow field. The significant analysis regarding the heat transfer in nanoliquids under multiple flow scenarios is reported in [10, 11]. The dynamics of radiative nanoliquid by considering combined convection is reported by Gul et al. [12]. The important analysis of the nanoliquids under imposed magnetic field and other governing quantities is conducted in [13, 14], respectively.

The analysis of the squeezing flow has great significance in the light of its applications in different industries. These applications comprised in the field of biomechanics, mechanical engineering, chemical engineering, and in the food industries. The earlier work in this era was done by Stefan [15]. The behaviour of squeezed fluid was investigated by Rashidi et al. [16]. Another analysis related to squeezed flow is done by Khan et al. [17]. Gailitis and Lielausis [18] presented the study of fluid flowing between Riga plates. The model is solved via suitable technique and then explained the physical results deeply.

The dynamics of bioconvection nanoliquid regarding the heat transfer are examined in [19]. They organized the study in 3D, and the problem is developed by Buongiorno nanoliquid model and then found the solution analytically. In 2019, Shamshuddin et al. [20] reported the novel influences of ohmic heating and magnetic field in the flow of nanoliquid between two Riga sheets. They analyzed the model analytically and provided pictorial results against the pertinent flow quantities. The investigation of local heat transport mechanism in the nanoliquid and transportation of the shears stresses at the walls are also reported in their study. The effect of partial slip in the nanoliquid flow over a spinning geometry is reported in [21]. They used the nanoliquid composed by MgO and discussed the heat transport properties. Another imperative heat transfer treatment in bioconvection nanoliquid under the influences of Lorentz forces and internal heat source is explored in [22]. Some significant investigations related to nanoliquids under multiple conditions are reported in [23–25].

Thermal diffusion and heat generation are very important physical phenomena that play significant role in the nanofluid heat transport performance. In this regard, a potential study is reported in [26] past through porous oscillating plate placed in vertical plane. The authors computed the results and for the shear stresses, Nusselt number and furnished graphical results for the velocity and temperature

distribution. Another potential work for the heat transfer in the nanofluid under the effects of imposed Lorentz forces is discussed in [27]. Thin film flows attained much attention of the industrialists due to their broad applications in many industries. The analysis of heat transport in the nanofluids over a thin film is very prominent. Therefore, a recent study in this regard is reported in [28]. Theoretical study of the flow models under varying flow conditions has its own importance, and researchers paved their attentions to analyze the dynamics of fluids through theoretical approaches. In this regard, a study is reported in [29] by considering the flow inside the cavity filled with nanoliquid. The authors treated the model numerically and authenticate their results with previously published work. The study of different flow parameters and their impacts on the heat transfer is organized in [30]. It is reported that the temperature drops due higher thermophoresis effects.

From the available science literature, it is noted that the analytical heat transport mechanism in water and kerosene oil saturated by Cu nanomaterials is not investigated so far. Therefore, the analysis is organized to examine the nanofluid characteristics between Riga plates. The model is obtained via similarity transforms, and then for solution purpose, two different analytical techniques (VIM and VPM) are implemented. The solutions are tabulated successfully and discussed the graphical results comprehensively within desired domain.

## 2. Modelling of the Flow Configuration

In this study, we consider the squeezed flow of copper nanofluids between Riga plates. The plates are situated at  $y = 0$  (lower plate) and  $y = h(t) = (a/v_f(1 - \gamma t))^{-1/2}$  (upper plate). The lower Riga plate is capable to stretching with velocity  $U_w = ax(1 - \gamma t)^{-1}$ . The base liquids diluted with Cu nanoparticles flow with velocity  $v_h = dh/dt$  between Riga plates. Furthermore, thermal radiation effects are under consideration. Figure 1 demonstrates flow scenario for the nanofluids between Riga plates.

The squeezing flow of nanofluids past a Riga plate described by the following system [31]:

$$\frac{\partial u}{\partial x} + \frac{\partial v}{\partial y} = 0, \quad (1)$$

$$\frac{\partial u}{\partial t} + u \frac{\partial u}{\partial x} + v \frac{\partial u}{\partial y} = \frac{1}{\rho_{nf}} \left[ -\frac{\partial p}{\partial x} + \mu_{nf} \left( \frac{\partial^2 u}{\partial x^2} + \frac{\partial^2 u}{\partial y^2} \right) \right] + \frac{\pi j_0 M_0 e^{(-\pi y/b)}}{8 \rho_{nf}}, \quad (2)$$

$$\frac{\partial v}{\partial t} + u \frac{\partial v}{\partial x} + v \frac{\partial v}{\partial y} = \frac{1}{\rho_{nf}} \left[ -\frac{\partial p}{\partial y} + \mu_{nf} \left( \frac{\partial^2 v}{\partial x^2} + \frac{\partial^2 v}{\partial y^2} \right) \right], \quad (3)$$

$$\frac{\partial T}{\partial t} + u \frac{\partial T}{\partial x} + v \frac{\partial T}{\partial y} = \frac{k_{nf}}{(\rho C_p)_{nf}} \left[ \frac{\partial^2 T}{\partial x^2} + \frac{\partial^2 T}{\partial y^2} \right] - \frac{1}{(\rho C_p)_{nf}} \frac{\partial}{\partial y} (q_r). \quad (4)$$

Equation (1) is the mathematical expression for



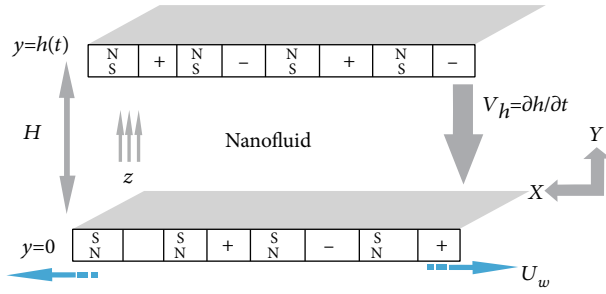


FIGURE 1: The flow scenario between Riga plates.

conservation of mass. Equations (2) and (3) presenting the  $x$  and  $y$  components of the momentum equation and energy equation are described by Equation (4). The term  $q_r$  comprised in energy equation is defined as:

$$q_r = -\frac{4\sigma^*}{3k^*} \frac{\partial}{\partial y} (T^4). \quad (5)$$

Here,  $\sigma^*$  denotes the Stefan-Boltzmann constant, and  $q_r$  denotes the radiative heat flux. By expanding  $T^4$  in well-known Taylor series centered at  $T_h$ , we arrived with the following form:

$$T^4 = \sim 4T_h^3 - 3T_h^4. \quad (6)$$

By utilizing above expressions, updated version of energy equation is as follows:

$$\frac{\partial T}{\partial t} + u \frac{\partial T}{\partial x} + v \frac{\partial T}{\partial y} = \frac{k_{nf}}{(\rho C_p)_{nf}} \left[ \frac{\partial^2 T}{\partial x^2} + \frac{\partial^2 T}{\partial y^2} \right] - \frac{1}{(\rho C_p)_{nf}} \frac{16\sigma^*}{3k^*} T_h^3 \frac{\partial^2 T}{\partial y^2}. \quad (7)$$

For under consideration flow model of nanofluid, the flow conditions are as follows [31]:

$$u = U_w(x) = (1 - \gamma t)^{-1} ax, \quad (8)$$

$$v = 0, -\frac{k\partial T}{\partial y} = \frac{k_1}{(T_f - T)^{-1}}, \quad (9)$$

$$u = 0, v = \frac{dh}{dt} = -\frac{\gamma}{2} \left( \frac{a(1 - \gamma t)}{v_f} \right)^{-1/2}, T = T_h. \quad (10)$$

In Equations (8) and (10),  $\rho_{nf}$  represents the nanofluid density,  $\mu_{nf}$  represents the effective dynamic viscosity, and  $(\rho C_p)_{nf}$  represents the effective heat capacity. Here, we used Brinkman and Maxwell Garnett model for effective dynamic viscosity and thermal for the thermal conductivity of the nanofluid [32]:

$$\begin{aligned} \rho_{nf} &= \frac{(1 - \phi)}{\rho_f^{-1}} + \frac{\phi}{\rho_s^{-1}}, \\ \mu_{nf} &= \frac{\mu_f}{(1 - \phi)^{2.5}}, \\ (\rho C_p)_{nf} &= \frac{(1 - \phi)}{(\rho C_p)_f^{-1}} + \frac{\phi}{(\rho C_p)_s^{-1}}, \\ k_{nf} &= k_f \left[ \frac{k_s + 2k_f - 2\phi(k_f - k_s)}{k_s + 2k_f + \phi(k_f - k_s)} \right]. \end{aligned} \quad (11)$$

In above expressions,  $\phi$  is called the nanoparticle volume fraction.

The dimensionless feasible transformations for the flow model are given by the following expressions:

$$\begin{aligned} \psi &= \left( \frac{av_f}{1 - \gamma t} \right)^{1/2} x F(\eta), \eta = \frac{y}{h(t)}, \\ u &= U_w F'(\eta), \\ v &= -\left( \frac{av_f}{1 - \gamma t} \right)^{1/2}, \\ \theta(\eta) &= \left( \frac{T - T_f}{T_h - T_f} \right). \end{aligned} \quad (12)$$

Applying these transformations and suitable differentiation in Equations (2)–(7), the following system is attained:

$$\begin{aligned} F''''(\eta) + \left[ (1 - \phi) + \phi \left\{ \frac{\rho_s}{\rho_f} \right\} \right] (1 - \phi)^{2.5} \left[ -F'(\eta)F''(\eta) + F(\eta)F'''(\eta) - \frac{\beta}{2} (3F''(\eta) + \eta F'''(\eta)) \right] - (1 - \phi)^{2.5} Z^* B^* \text{Exp}(-B^* \eta) &= 0, \\ \left[ 1 + Rd \left[ \frac{k_s + 2k_f - 2\phi(k_f - k_s)}{k_s + 2k_f + \phi(k_f - k_s)} \right]^{-1} \right] \theta''(\eta) + \left[ \frac{k_s + 2k_f - 2\phi(k_f - k_s)}{k_s + 2k_f + \phi(k_f - k_s)} \right]^{-1} \left[ \left\{ (1 - \phi) + \phi \left\{ \frac{(\rho C_p)_s}{(\rho C_p)_f} \right\} \right\} \text{Pr} \left\{ F(\eta)\theta'(\eta) - \frac{\beta\eta}{2}\theta'(\eta) \right\} \right] &= 0. \end{aligned} \quad (13)$$

Supporting boundary conditions for above flow model in dimensionless form is given in Equations (14) and (15) for upper and lower Riga plates:

$$F'(\eta=0) = 1, F(\eta=1) = \frac{\beta}{2}, F'(\eta=1) = 0, F(\eta=0) = 0, \quad (14)$$

$$\theta(\eta=1) = 0, \theta'(\eta=0) = -B_i(1 - \theta(\eta=0)). \quad (15)$$

Also, squeeze number  $\beta$ , Prandtl number  $Pr$ , and radiation parameter  $Rd$  are described by the following expressions:

$$\beta = \frac{\gamma}{a}, \quad Pr = \frac{\mu_f(C_p)_f}{k_f}, \quad Rd = \frac{16\sigma^* T_h^3}{3k^* k_f}, \quad B_i = -\frac{h_1}{k} \sqrt{v_f(1 - \gamma t)/a}. \quad (16)$$

The dimensional expressions for local heat transport rate and walls shear stresses are

$$C_F = \frac{\tau_w}{\rho_{nf} U_w^2}, \quad Nu_x = \frac{xq_w}{k_f(T - T_h)} + q_r. \quad (17)$$

Here,  $\tau_w = \mu_{nf}(\partial u/\partial y)|_{y=h(t)}$  and  $q_w = -k_{nf}(\partial T/\partial y)|_{y=h(t)}$ .

Finally got the following version:

$$C_F \sqrt{Re_x} = \frac{1}{A_1(1 - \phi)^{2.5}} F''(\eta=1). \quad (18)$$

$$Nu_x \sqrt{\frac{(1 - \gamma t)}{Re_x}} = -(A_3 + Rd)\theta'(\eta=1).$$

where  $Re_x$  is called the local Reynolds number and is  $Re_x = xU_w/\nu_f$ . Furthermore,  $A_1$  and  $A_3$  are as follows:

$$A_1 = (1 - \phi) + \frac{\phi}{(\rho_s/\rho_f)^{-1}}, \quad (19)$$

$$A_3 = \left[ \frac{(k_s + 2k_f) - 2\phi(k_f - k_s)}{(k_s + 2k_f) + \phi(k_f - k_s)} \right].$$

### 3. Solution of the Model

In this section, solutions for the model are performed. For said purpose, we employed analytical and numerical methods. First subsection deals with the study of solutions found by variation of parameters method, and the second one deals with the study of solutions found by variational iteration method. Numerical solution and error analysis are also tabulated.

**3.1. Solution Using VPM.** The solution for the model by utilizing VPM is performed in this subsection. The procedure is adopted by the following steps:

$$F_{n+1}(\eta) = F(0) + \eta F'(0) + \frac{\eta^2}{2!} F''(0) + \frac{\eta^3}{3!} F'''(0) - \int_0^\eta \frac{(s\eta - s + (-\eta s + \eta))^3}{3!} \left[ \left[ (1 - \phi) + \phi \left\{ \frac{\rho_s}{\rho_f} \right\} \right] (1 - \phi)^{2.5} \cdot \left[ F'_n(s)F'_n(s) - F_n(s)F''_n(s) - \frac{\beta}{2} (3F'_n(s) + sF''_n(s)) \right] - (1 - \phi)^{2.5} Z^* B^* \text{Exp}(-B^* \eta) \right] ds, n \geq 0,$$

$$\theta_{n+1}(\eta) = \theta(0) + \eta \theta'(0) - \frac{1}{(1 + Rd/A_3)} \int_0^\eta \frac{(\eta^2 s - s + (\eta - s\eta^2))}{1!} \cdot \left[ \frac{A^*}{A_3} Pr \left\{ F_n(s)\theta'_n(s) - \frac{\beta s}{2} \theta''_n(s) \right\} \right] ds, n \geq 0, \quad (20)$$

where  $A^* = \{(1 - \phi) + \phi\{(\rho C_p)_s/(\rho C_p)_f\}\}$

By using the conditions ( $\eta=0$ ) and putting  $F''(0) = \alpha_1^*$ ,  $F'''(0) = \alpha_2^*$ , and  $\theta(0) = \alpha_3^*$ , above recursive relation takes the following form:

$$F_{n+1}(\eta) = F_0(\eta) + \frac{\eta^2}{2!} \alpha_1^* + \frac{\eta^3}{3!} \alpha_2^* - \int_0^\eta \frac{(s\eta - s + (-\eta s + \eta))^3}{3!} \left[ \left[ (1 - \phi) + \phi \left\{ \frac{\rho_s}{\rho_f} \right\} \right] (1 - \phi)^{2.5} \cdot \left[ F'_n(s)F'_n(s) - F_n(s)F''_n(s) - \frac{\beta}{2} (3F'_n(s) + sF''_n(s)) \right] \right] - (1 - \phi)^{2.5} Z^* B^* \text{Exp}(-B^* \eta) ds, n \geq 0, \quad (21)$$

$$\theta_{n+1}(\eta) = \alpha_3^* + \eta(-B_i(1 - \theta(0))) - \frac{1}{(1 + Rd/A_3)} \int_0^\eta \frac{(\eta^2 s - s + (\eta - s\eta^2))}{1!} \cdot \left[ \frac{A^*}{A_3} Pr \left\{ F_n(s)\theta'_n(s) - \frac{\beta s}{2} \theta''_n(s) \right\} \right] ds, n \geq 0. \quad (22)$$

In more comprehensive form, Equations (21) and (22) become:

$$F_{n+1}(\eta) = F_0(\eta) - \int_0^\eta \frac{(s\eta - s + (-\eta s + \eta))^3}{3!} \cdot \left[ \left[ (1 - \phi) + \phi \left\{ \frac{\rho_s}{\rho_f} \right\} \right] (1 - \phi)^{2.5} \cdot \left[ F'_n(s)F'_n(s) - F_n(s)F''_n(s) - \frac{\beta}{2} (3F'_n(s) + sF''_n(s)) \right] \right] - (1 - \phi)^{2.5} Z^* B^* \text{Exp}(-B^* \eta) ds, n \geq 0,$$

$$\theta_{n+1}(\eta) = \theta_0(\eta) - \frac{1}{(1 + \text{Rd}/A_3)} \int_0^\eta \frac{(\eta^2 s - s + (\eta - s\eta^2))}{1!} \cdot \left[ \frac{A^*}{A_3} \text{Pr} \left\{ F_n(s)\theta'_n(s) - \frac{\beta s}{2}\theta'_n(s) \right\} \right] ds, n \geq 0. \quad (23)$$

Here,

$$F_0(\eta) = \eta + \frac{\eta^2}{2!}\alpha_1^* + \frac{\eta^3}{3!}\alpha_2^*, \quad (24)$$

$$\theta_0(\eta) = \alpha_3^* + \eta(-B_i(1 - \theta(0))), \quad (25)$$

and  $\alpha_1^*$ ,  $\alpha_2^*$ , and  $\alpha_3^*$  are unknown constant and can be determined by utilizing remaining boundary conditions. Other approximations of the solution can be calculated for varying  $n$ .

**3.2. Solution Using VIM.** The solution procedure by using VIM is followed as follows:

$$F_{n+1}(\eta) = F_n(\eta) + \int_0^\eta (-1)^4 \frac{(s\eta + s + (-\eta s - \eta))^3}{3!} \cdot \left[ F_n''(s) + \left[ (1 - \phi) + \phi \left\{ \frac{\rho_s}{\rho_f} \right\} \right] (1 - \phi)^{2.5} \cdot \left[ F_n'(s)F_n'(s) - F_n(s)F_n''(s) - \frac{\beta}{2}(3F_n'(s) + sF_n''(s)) \right] \right] - (1 - \phi)^{2.5} Z^* B^* \text{Exp}(-B^* \eta) ds, n \geq 0,$$

$$\theta_{n+1}(\eta) = \theta_n(\eta) + \int_0^\eta \frac{(\eta^2 s + s + (-\eta - s\eta^2))}{1!} \cdot \left[ \left( 1 + \frac{\text{Rd}}{A_3} \right) \theta'_n(s) + \frac{A^*}{A_3} \text{Pr} \left\{ F_n(s)\theta'_n(s) - \frac{\beta s}{2}\theta'_n(s) \right\} \right] ds, n \geq 0. \quad (26)$$

In order to initiate the recursive relation for variational iteration method, we need initial guesses  $F_0(\eta)$  and  $\theta_0(\eta)$ . These initial trials are same as given in Equations (24) and (25) for velocity and temperature, respectively.

Tables 1 and 2 show the comparative analysis among the solutions calculated by adopting variation of parameters and variational iteration methods. Furthermore, these solutions are compared with numerical solutions to check the validity of the both applied methods (VPM and VIM). It is easy to see that both analytical solutions are in magnificent agreement with numerical solutions. The error for VPM and VIM is also discussed and given by Tables 3 and 4 for velocity and temperature fields, respectively.

#### 4. Results with Comprehensive Discussion

This subsection is organized to investigate the behaviour of the nanoliquid motion, temperature, shear stresses, and local thermal performance rate over the region of interest. The results are captured by altering the governing parameter

TABLE 1: Comparison of the solution for the velocity field.

$\eta$	Cu/water			Cu/kerosene oil		
	VPM	VIM	Num	VPM	VIM	Num
0.0	0	0	0	0	0	0
0.1	0.084124	0.084124	0.084124	0.089562	0.089562	0.089562
0.2	0.139400	0.139400	0.139400	0.159755	0.159755	0.159755
0.3	0.170301	0.170301	0.170301	0.212844	0.212844	0.212844
0.4	0.181418	0.181418	0.181418	0.251099	0.251099	0.251099
0.5	0.177425	0.177425	0.177425	0.276795	0.276795	0.276795
0.6	0.163070	0.163070	0.163070	0.292230	0.292230	0.292230
0.7	0.143176	0.143176	0.143176	0.299751	0.299751	0.299751
0.8	0.122658	0.122658	0.122658	0.301797	0.301797	0.301797
0.9	0.106544	0.106544	0.106544	0.300949	0.300949	0.300949
1.0	0.100000	0.100000	0.100000	0.299999	0.299999	0.299999

within physical domain. These results are plotted for both sort of nanoliquids.

Figure 2 elaborates the behaviour of Cu-kerosene oil and Cu-water against the squeeze number  $\beta$  and Cu fraction factor  $\phi$ . It is examined that the fluid motion rises due to higher  $\beta$ . Physically, the acceleration of the plates exerts pressure force on the fluid particles due to which these particles move rapidly in the region of interest. The rapid increment in the motion is observed in the locality of the upper Riga plate. On the other hand, higher fraction factor opposes the fluid velocity in Figure 2(b). The core reason behind this behaviour is the density of the nanofluid. By increasing the strength of  $\phi$ , the nanofluid becomes more thicker, and ultimately, the internal fluid forces become dominant which resists the motion.

The effects of thermal radiation, Cu fraction factor, and Biot number on the thermal performance of Cu-water and Cu-kerosene oil are furnished in Figures 3 and 4, respectively. The results plotted in Figure 3(a) ensure that the thermal performance of Cu-water and Cu-kerosene oil can be augmented by imposing thermal radiation effects. Physically, thermal radiation provides the heat energy to the fluid particles which leads to increment in the temperature. Similarly, the higher volumetric fraction also favors the nanofluid temperature, and these effects are pictured in Figure 3(b).

Convectively heated surface is a big source of heat transfer augmentation in the nanofluid. Therefore, the temperature alterations due to convective surface (Biot number) are decorated in Figure 4. It can be that augmentations in the heat transfer are more rapid due convectively heated surface. Near the surface, these effects are very prominent because of maximum amount of heat transfer at the surface. The particles attached to the surface transfer the energy to rest of the particles; as a result, the fluid temperature goes up.

The study of shear stresses in Cu-water and Cu-kerosene oil is imperative for industrial and engineering applications. Therefore, Figure 5 is designed to explore the trends of shear stresses for varying  $\beta$  and  $\phi$ . From the results, it is

TABLE 2: Comparison of the solutions for the temperature.

$\eta$	Cu/water			Cu/kerosene oil		
	VPM	VIM	Num	VPM	VIM	Num
0.0	0.137213	0.137213	0.137213	0.289725	0.289725	0.289725
0.1	0.120072	0.120072	0.120072	0.247533	0.247533	0.247533
0.2	0.103522	0.103522	0.103522	0.207552	0.207552	0.207552
0.3	0.087895	0.087895	0.087895	0.171065	0.171065	0.171065
0.4	0.073295	0.073295	0.073295	0.138484	0.138484	0.138484
0.5	0.059663	0.059663	0.059663	0.109623	0.109623	0.109623
0.6	0.046852	0.046852	0.046852	0.083962	0.083962	0.083962
0.7	0.034670	0.034670	0.034670	0.060841	0.060841	0.060841
0.8	0.022917	0.022917	0.022917	0.039574	0.039574	0.039574
0.9	0.011409	0.011409	0.011409	0.019499	0.019499	0.019499
1.0	-1.60000e-10	-1.60000e-10	0	4.3e-09	0	0

TABLE 3: Error analysis between VPM and VIM for velocity.

$\eta$	Cu-water		Cu-kerosene oil	
	Error VPM	Error VIM	Error VPM	Error VIM
0.0	0	0	0	0
0.1	4.053854336e-010	3.553854294e-010	07.56226369e-009	7.522263687e-009
0.2	1.140821326e-009	1.040821318e-009	2.681196706e-008	2.681196706e-008
0.3	2.15307891e-009	2.053078901e-009	5.202073416e-008	5.222073418e-008
0.4	3.044108965e-009	3.044108965e-009	7.806090879e-008	7.81609088e-008
0.5	3.994240744e-009	3.694240719e-009	9.931656803e-008	9.961656799e-008
0.6	4.081787769e-009	3.981787761e-009	1.094292154e-007	1.095292154e-007
0.7	3.710801472e-009	3.410801475e-009	1.033390067e-007	1.034390067e-007
0.8	2.277394731e-009	2.477394734e-009	7.577738309e-008	7.58773831e-008
0.9	3.673078369e-010	3.269216842e-011	3.079392602e-008	3.139392601e-008
1.0	9.999999717e-010	5.999999664e-010	1.000002303e-010	2.000002386e-010

TABLE 4: Error analysis between VPM and VIM for temperature.

$\eta$	Cu-water		Cu-kerosene oil	
	Error VPM	Error VIM	Error VPM	Error VIM
0.0	2.917453946e-007	2.916453946e-007	2.270226419e-005	2.269216419e-005
0.1	2.9763384e-007	2.9753384e-007	2.405097907e-005	2.404027907e-005
0.2	3.030928012e-007	3.029928012e-007	2.532916947e-005	2.531796947e-005
0.3	3.084416274e-007	3.083416274e-007	2.649541049e-005	2.648381049e-005
0.4	3.128298272e-007	3.127198272e-007	2.751250899e-005	2.750040899e-005
0.5	3.131458008e-007	3.130458008e-007	2.821819169e-005	2.820559169e-005
0.6	3.011267026e-007	3.009967026e-007	2.804527177e-005	2.803227177e-005
0.7	2.650793188e-007	2.649293188e-007	2.586572549e-005	2.585322549e-005
0.8	1.982127418e-007	1.980027418e-007	2.043576037e-005	2.042346037e-005
0.9	1.054550512e-007	1.050350512e-007	1.140035168e-005	1.139085168e-005
1.0	1.600000001e-010	6.94690402e-010	4.3e-009	5.4e-009

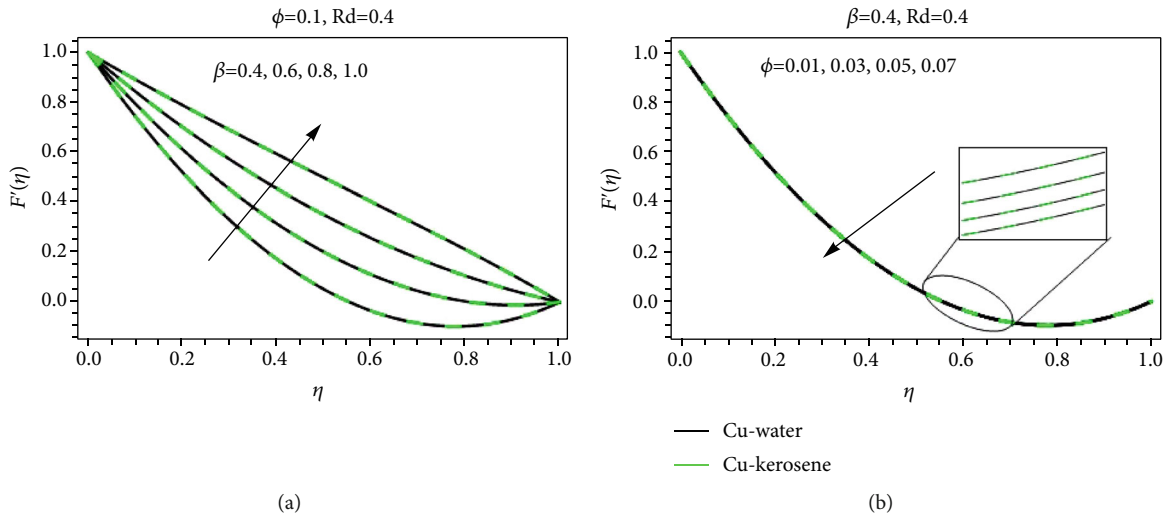


FIGURE 2: Impact of (a)  $Rd$  and (b)  $\beta$  on  $F'(\eta)$ .

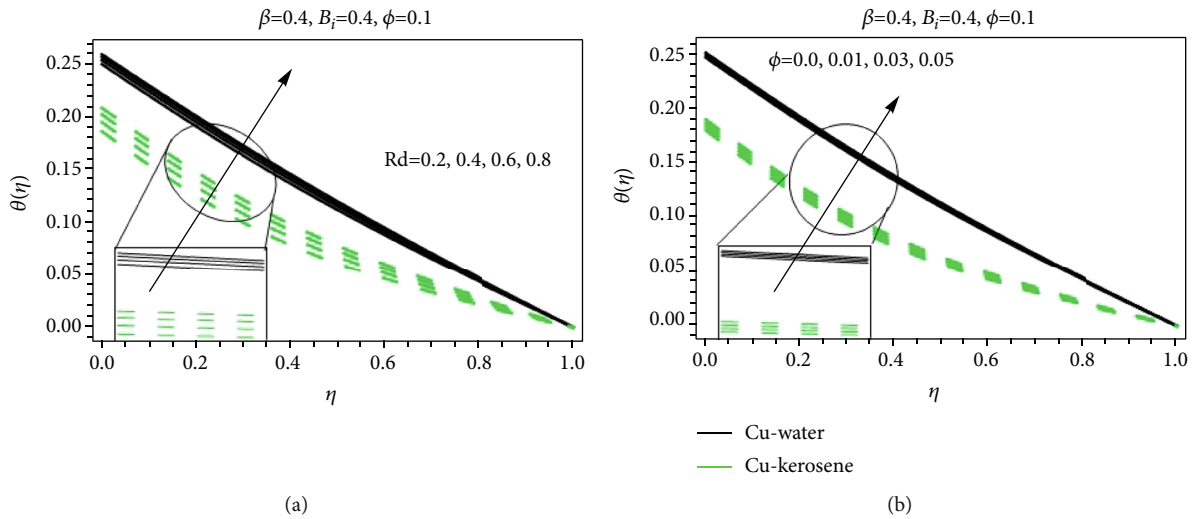


FIGURE 3: Impact of (a)  $Rd$  and (b)  $\phi$  on  $\theta(\eta)$ .

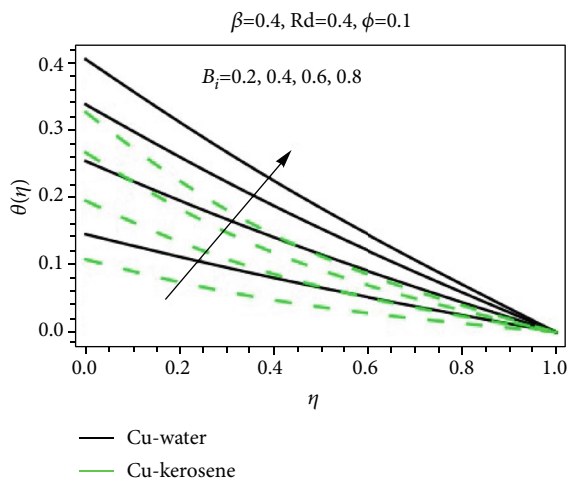


FIGURE 4: Impact of  $B_i$  on  $\theta(\eta)$ .

noteworthy that the shear stresses drop against the stronger  $\beta$ . For Cu-kerosene oil, these are very rapid than Cu-water in which thermophysical values of the base liquid and guest nanoparticles playing significant role. The slow decline in the shear stresses can be examined from Figure 5(b).

The local thermal performance in the nanofluids is of much interest due to their broad applications in the modern world. For this purpose, Figures 6–8 are decorated by considering different values of the pertinent flow parameters. It is investigated that the Biot number and thermal radiation are very beneficial for thermal performance in Cu-water and Cu-kerosene oil. The nanofluids gained much energy from Biot and thermal radiation parameters due to which the heat transfer rate rises. Furthermore,  $\beta$  and volumetric fraction are playing important role in thermal rate of Cu-water and Cu-kerosene oil. Thermophysical values of the guest nanoparticles and host liquid are described in Table 5.

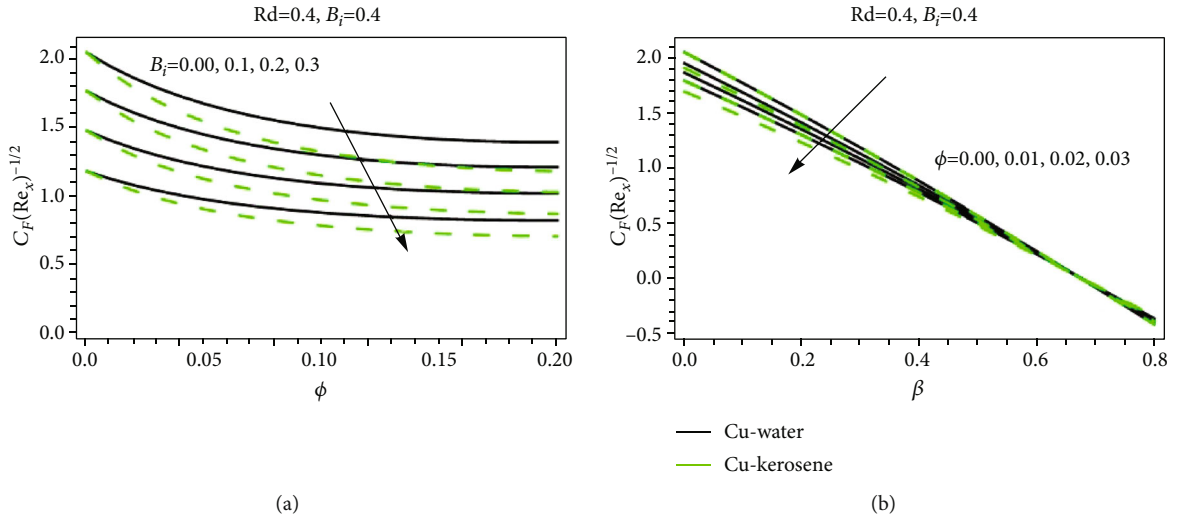


FIGURE 5: Impact of (a)  $\beta$  and (b)  $\phi$  on shear stresses.

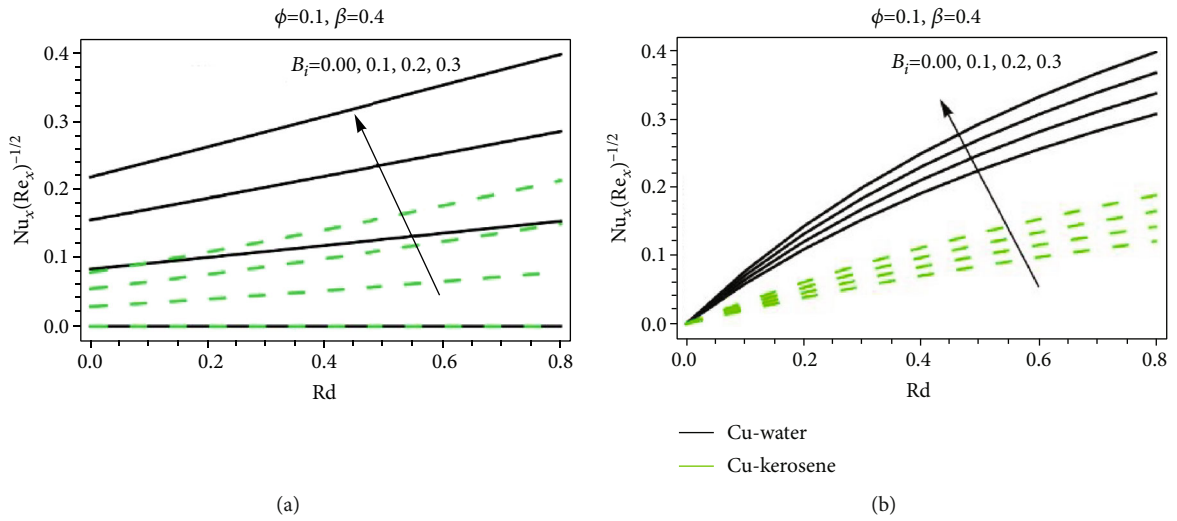


FIGURE 6: Impact of (a)  $B_i$  and (b)  $Rd$  on Nusselt number.

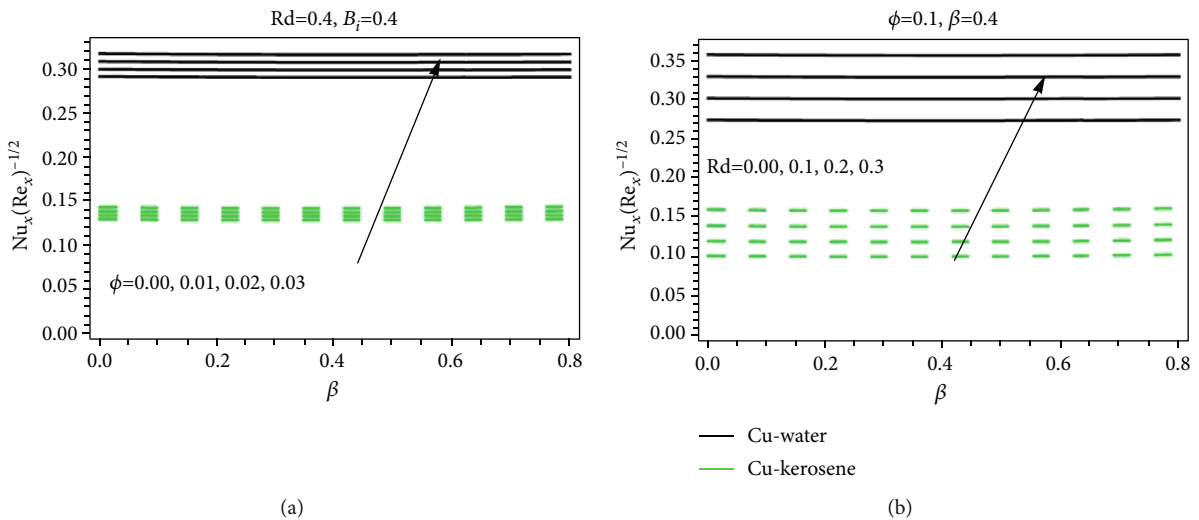


FIGURE 7: Impact of (a)  $\phi$  and (b)  $Rd$  on Nusselt number.

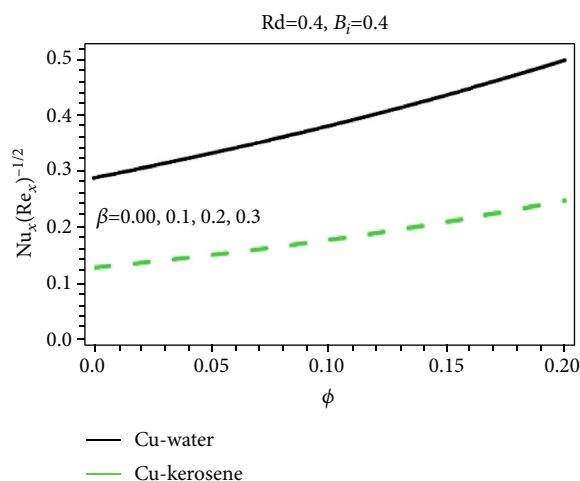
FIGURE 8: Impact of  $\beta$  and  $\phi$  on local Nusselt number.

TABLE 5: Thermo-physical values of carbon nanotubes and the regular liquids [33].

	$\rho$ (kg/m <sup>3</sup> )	$C_p$ (J/kgK)	$k$ (W/mK)	Pr
Pure water	997.1	4179	0.613	6.2
Kerosene oil	783	2090	0.145	21
Copper	8933	385	401	—

TABLE 6: Comparison with existing literature.

$\beta$	$F''(1)$	
	Present	Hayat et al. [31]
0.1	1.69208	1.69635
0.3	1.08117	1.08543
0.5	0.46327	0.467511

## 5. Comparison with Existing Literature

It is very imperative to authenticate the present analysis with previously published work. Therefore, a useful comparison is made by taking  $\phi = 0$ ,  $Z = 1.5$ . The computed results are then compared with the results reported in [31]. From Table 6, it is noted that the results reported in the study are valid under aforementioned assumption which is evidence of the reliability of the study.

## 6. Conclusions

The study of nanofluids synthesized by water and kerosene oil in the presence of Cu guest nanoparticles is organized between two Riga plates. The similarity relations are used for the conversion of dimensional model into dimensionless form and then performed mathematical analysis. Two well-known effective analytical techniques are adopted for the solution purpose and then decorated the results against the flow parameters over the desired region. From the study, it is concluded as follows:

- (i) The velocity reduces by increasing the volumetric fraction of the nanoparticles
- (ii) The temperature significantly rises for stringer thermal radiations and fraction factor  $\phi$  for both Cu-H<sub>2</sub>O and Cu-kerosene oil nanofluids
- (iii) The convectively heated plate produces extra heat to the nanofluid particles due to which it enhances rapidly
- (iv) The decreasing trends in the shear stresses are rapid for Cu-kerosene oil than Cu-H<sub>2</sub>O
- (v) The local Nusselt number increases against thermal radiations,  $B_i$  and  $\phi$
- (vi) The VPM is more effective than VIM for such non-linear nanofluid models

## Nomenclature

- ( $u, v$ ): Velocity components  
 $p$ : Pressure  
 $T$ : Temperature  
 $\mu_{nf}$ : Nanoliquid dynamic viscosity  
 $k_{nf}$ : Nanoliquid thermal conductivity  
 $\sigma^*$ : Stefan Boltzmann constant  
 $k^*$ : Mean absorption coefficient  
 $\phi$ : Fraction factor of Cu  
 $\rho_f$ : Fluids density  
 $\rho_s$ : Cu density  
 $\Psi$ : Stream function  
 $\eta$ : Self-similar variable  
 $nf$ : Stands for nanoliquid  
 $F(\eta)$ : Dimensionless velocity  
 $\theta$ : Dimensionless temperature  
 $Rd$ : Radiation number  
 $Pr$ : Prandtl number  
 $B_i$ : Biot number.

## Data Availability

The study based on numerical technique and no data is used in findings of the study.

## Conflicts of Interest

The authors declare no financial/competing interest regarding this work.

## Authors' Contributions

A. and W.A. wrote the original draft. Problem formulation was done by A.H.A., I.K., and A. M.A., A., I.K., and A.H.A. contributed to the results and discussion. Validity of the study was done by A. and W.A. Software was done by M.A. and I.K. Language correction was done by A., A.H.A., and M.A.

## References

- [1] S. Choi, "Enhancing thermal conductivity of fluids with nanoparticles in developments and applications of non-Newtonian flows," *ASME*, vol. 66, pp. 99–105, 1995.
- [2] S. T. Mohyud-Din, U. Khan, N. Ahmed, and B. Bin-Mohsin, "Heat and mass transfer analysis for MHD flow of nanofluid convergent/divergent channels with stretchable walls using Buongiorno's model," *Neural Computing and Applications*, vol. 28, no. 12, pp. 4079–4092, 2017.
- [3] U. Khan, N. Ahmed, S. T. Mohyud-Din, and B. Bin-Mohsin, "Nonlinear radiation effects on MHD flow of nanofluid over a nonlinearly stretching/shrinking wedge," *Neural Computing and Applications*, vol. 28, no. 8, pp. 2041–2050, 2017.
- [4] M. Sheikholeslami, "CVFEM for magnetic nanofluid convective heat transfer in a porous curved enclosure," *The European Physical Journal Plus*, vol. 131, no. 11, pp. 131–413, 2016.
- [5] M. Sheikholeslami, "Influence of Lorentz forces on nanofluid flow in a porous cylinder considering Darcy model," *Journal of Molecular Liquids*, vol. 225, pp. 903–912, 2017.
- [6] K. U. Adnan, U. Khan, N. Ahmed, and S. T. Mohyud-Din, "Thermo-diffusion and diffusion-thermo effects on flow of second grade fluid between two inclined plane walls," *Journal of Molecular Liquids*, vol. 224, pp. 1074–1082, 2016.
- [7] M. Sheikholeslami and H. B. Rokni, "Nanofluid two phase model analysis in existence of induced magnetic field," *International Journal of Heat and Mass Transfer*, vol. 107, pp. 288–299, 2017.
- [8] M. S. Kandelous, "KKL correlation for simulation of nanofluid flow and heat transfer in a permeable channel," *Physics Letters A*, vol. 378, no. 45, pp. 3331–3339, 2014.
- [9] A. M. Adnan, M. Asadullah, U. Khan, N. Ahmed, and S. T. Mohyud-Din, "Analytical and numerical investigation of thermal radiation effects on flow of viscous incompressible fluid with stretchable convergent/divergent channels," *Journal of Molecular Liquids*, vol. 224, pp. 768–775, 2016.
- [10] A. Saeed, P. Kumam, S. Nasir, T. Gul, and W. Kumam, "Non-linear convective flow of the thin film nanofluid over an inclined stretching surface," *Scientific Reports*, vol. 11, no. 1, article 97576, 2021.
- [11] A. Gul, I. Khan, and S. Shafie, "Energy transfer in mixed convection MHD flow of nanofluid containing different shapes of nanoparticles in a channel filled with saturated porous medium nanoscale," *Nanoscale Research Letters*, vol. 10, 2015.
- [12] A. Gul, I. Khan, and S. Shafie, "Radiation and heat generation effects in MHD mixed convection flow of nanofluids," *Thermal Science*, vol. 22, 2018.
- [13] N. A. Mohd Zin, I. Khan, and S. Shafie, "The impact silver nanoparticles on MHD free convection flow of Jeffrey fluid over an oscillating vertical plate embedded in a porous medium," *Journal of Molecular Liquids*, vol. 222, pp. 138–150, 2016.
- [14] A. Khalid, I. Khan, and S. Shafie, "Heat transfer in ferrofluid with cylindrical shape nanoparticles past a vertical plate with ramped wall temperature embedded in a porous medium," *Journal of Molecular Liquids*, vol. 221, pp. 1175–1183, 2016.
- [15] M. J. Stefan, "Versuch uber die scheinbare Adhasion, sitzungsb., Abt II Osterr.," *Annalen der Physik*, vol. 69, pp. 316–318, 1874.
- [16] M. M. Rashidi, H. Shahmohamadi, and S. Dinarvand, "Analytic Approximate Solutions for Unsteady Two-Dimensional and Axisymmetric Squeezing Flows between Parallel Plates," *Mathematical Problems in Engineering*, vol. 2008, Article ID 935095, 13 pages, 2008.
- [17] U. Khan, N. Ahmed, M. Asadullah, and S. Tauseef Mohyud-din, "Effects of viscous dissipation and slip velocity on two-dimensional and axisymmetric squeezing flow of Cu-water and Cu-kerosene nanofluids," *Propulsion and Power Research*, vol. 4, no. 1, pp. 40–49, 2015.
- [18] A. Gailitis and O. Lielausis, "On a possibility to reduce the hydrodynamic resistance of a plate in an electrolyte," *Applied Magnetohydrodynamics*, vol. 12, pp. 143–146, 1961.
- [19] M. D. Shamshuddin, S. R. Mishra, O. Anwar Beg, and A. Kadir, "Adomian decomposition method simulation of von Kármán swirling bioconvection nanofluid flow," *Journal of Central South University*, vol. 26, no. 10, pp. 2797–2813, 2019.
- [20] M. D. Shamshuddin, S. R. Mishra, O. A. Bég, and A. Kadir, "Viscous dissipation and joule heating effects in non-Fourier MHD squeezing flow, heat and mass transfer between Riga plates with thermal radiation: variational parameter method solutions," *Arabian Journal for Science and Engineering*, vol. 44, no. 9, pp. 8053–8066, 2019.
- [21] Y. X. Li, T. Muhammad, M. Bilal, M. A. Khan, A. Ahmadian, and B. A. Pansera, "Fractional simulation for Darcy-Forchheimer hybrid nanofluid flow with partial slip over a spinning disk," *Alexandria Engineering Journal*, vol. 60, no. 5, pp. 4787–4796, 2021.
- [22] M. Bilal, A. Saeed, T. Gul, I. Ali, W. Kumam, and P. Kumam, "Numerical approximation of microorganisms hybrid nanofluid flow induced by a wavy fluctuating spinning disc," *Coatings*, vol. 11, no. 9, p. 1032, 2021.
- [23] A. R. Ehman, Z. Salleh, and T. Gul, "Heat transfer of thin film flow over an unsteady stretching sheet with dynamic viscosity," *Journal of Advanced Research in Fluid Mechanics and Thermal Sciences*, vol. 81, no. 2, pp. 67–81, 2021.
- [24] H. R. Kataria and A. S. Mittal, "Velocity, mass and temperature analysis of gravity-driven convection nanofluid flow past an oscillating vertical plate in the presence of magnetic field in a porous medium," *Applied Thermal Engineering*, vol. 110, pp. 864–874, 2017.
- [25] H. R. Kataria and A. S. Mittal, "Mathematical model for velocity and temperature of gravity-driven convective optically thick nanofluid flow past an oscillating vertical plate in presence of magnetic field and radiation," *Journal of the Nigerian Mathematical Society*, vol. 34, no. 3, pp. 303–317, 2015.
- [26] M. Sheikholeslami, H. R. Kataria, and A. Mittal, "Effect of thermal diffusion and heat-generation on MHD nanofluid flow past an oscillating vertical plate through porous medium," *Journal of Molecular Liquids*, vol. 257, pp. 12–25, 2018.
- [27] N. Ahmed, Adnan, U. Khan, and S. T. Mohyud-Din, "Influence of shape factor on flow of magneto-nanofluid squeezed between parallel disks," *Alexandria Engineering Journal*, vol. 57, no. 3, pp. 1893–1903, 2018.
- [28] M. Turkyilmazoglu, "Nanoliquid film flow due to a moving substrate and heat transfer," *European Physical Journal Plus*, vol. 135, no. 10, 2020.
- [29] A. A. Siddiqui and M. Turkyilmazoglu, "A new theoretical approach of wall transpiration in the cavity flow of the ferrofluids," *Micromechanics*, vol. 10, no. 6, p. 373, 2019.
- [30] J. A. Khan, M. Mustafa, T. Hayat, M. Turkyilmazoglu, and A. Alsaedi, "Numerical study of nanofluid flow and heat



- transfer over a rotating disk using Buongiorno's model," *International Journal of Numerical Methods for Heat & Fluid Flow*, vol. 27, no. 1, pp. 221–234, 2017.
- [31] T. Hayat, M. Khan, M. Imtiaz, and A. Alsaedi, "Squeezing flow past a Riga plate with chemical reaction and convective conditions," *Journal of Molecular Liquids*, vol. 96, 2017.
- [32] M. Sheikholeslami, T. Hayat, and A. Alsaedi, "MHD free convection of  $\text{Al}_2\text{O}_3$ -water nanofluid considering thermal radiation: A numerical study," *International Journal of Heat and Mass Transfer*, vol. 96, pp. 513–524, 2016.
- [33] U. Khan, N. Ahmed, and S. T. Mohyud-Din, "Numerical investigation for three dimensional squeezing flow of nanofluid in a rotating channel with lower stretching wall suspended by carbon nanotubes," *Applied Thermal Engineering*, vol. 113, pp. 1107–1117, 2017.

## Research Article

# Theoretical Analysis of Cu-H<sub>2</sub>O, Al<sub>2</sub>O<sub>3</sub>-H<sub>2</sub>O, and TiO<sub>2</sub>-H<sub>2</sub>O Nanofluid Flow Past a Rotating Disk with Velocity Slip and Convective Conditions

Abdullah Dawar,<sup>1</sup> Ebenezer Bonyah ,<sup>2</sup> Saeed Islam ,<sup>1</sup> Ahmed Alshehri,<sup>3</sup> and Zahir Shah<sup>4</sup>

<sup>1</sup>Department of Mathematics, Abdul Wali Khan University, Mardan, Mardan, 23200 Khyber Pakhtunkhwa, Pakistan

<sup>2</sup>Department of Mathematics Education, University of Education Winnebakumasi-(Kumasicompus), Kumasi 00233, Ghana

<sup>3</sup>Department of Mathematics, Faculty of Sciences, King Abdulaziz University, Jeddah 21589, Saudi Arabia

<sup>4</sup>Department of Mathematical Sciences, University of Lakki Marwat, Lakki Marwat, 28420 Khyber Pakhtunkhwa, Pakistan

Correspondence should be addressed to Ebenezer Bonyah; ebbonya@gmail.com

Received 2 September 2021; Accepted 11 November 2021; Published 26 November 2021

Academic Editor: Vincenzo Baglio

Copyright © 2021 Abdullah Dawar et al. This is an open access article distributed under the Creative Commons Attribution License, which permits unrestricted use, distribution, and reproduction in any medium, provided the original work is properly cited.

The nanofluids can be used in the subsequent precise areas like chemical nanofluids, environmental nanofluids, heat transfer nanofluids, pharmaceutical nanofluids, drug delivery nanofluids, and process/extraction nanofluids. In short, the number of engineering and industrial applications of nanofluid technologies, as well as their emphasis on particular industrial applications, has been increased recently. Therefore, this exploration is carried out to analyze the nanofluid flow past a rotating disk with velocity slip and convective conditions. The water-based spherical-shaped nanoparticles of copper, alumina, and titanium have been considered in this analysis. The modeled problem has been solved with the help of homotopic technique. Convergence of the homotopic technique is shown with the help of the figure. The role of the physical factors on radial and tangential velocities, temperature, surface drag force, and heat transfer rate are displayed through figures and tables. The outcomes demonstrate that the surface drag force of the water-based spherical-shaped nanoparticles of Cu, Al<sub>2</sub>O<sub>3</sub>, and TiO<sub>2</sub> has been reduced with a greater magnetic field. The radial and tangential velocities of the water-based spherical-shaped nanoparticles of Cu, Al<sub>2</sub>O<sub>3</sub>, and TiO<sub>2</sub>, and pure water have been augmented via magnetic parameter. The radial velocity of the water-based spherical-shaped nanoparticle of Cu has been augmented via nanoparticle volume fraction, whereas reduced for the Al<sub>2</sub>O<sub>3</sub> and TiO<sub>2</sub> nanoparticles. The tangential velocity of the water-based spherical-shaped nanoparticles of Cu, Al<sub>2</sub>O<sub>3</sub>, and TiO<sub>2</sub> has reduced via nanoparticle volume fraction. Also, the variations in radial and tangential velocities are greater for slip conditions as compared to no-slip conditions.

## 1. Introduction

The suspension of nanosized (between 1 nm and 100 nm) material into conventional fluids such as oil, ethylene glycol, water, and sodium alginate is called nanofluids. Nanofluids with their innovative and advanced ideas have intriguing thermal transfer properties as opposed to traditional heat transfer fluids. There has been a great deal of research into nanofluids' dominant heat transfer properties, especially convective heat transfer and thermal conductivity. With these properties, nanofluid implementations in industries like heat exchange

systems look promising. The nanofluids can be used in the subsequent precise areas like chemical nanofluids, environmental nanofluids, heat transfer nanofluids, pharmaceutical nanofluids, drug delivery nanofluids, and process/extraction nanofluids. In short, the number of engineering and industrial applications of nanofluids technologies, as well as their emphasis on particular industrial applications, has been increased recently [1–7]. The capability of thermal transmission of nanofluids can be quantified by their properties like specific heat, density, viscosity, and thermal conductivity. The thermal properties are contingent on the shape, base fluid,

particle size, material, and concentration. To utilize the applications towards engineering and industries, researchers are working on the evaluation and characterization of the thermo-physical properties of nanofluids for heat transfer analysis [8]. Sheikholeslami [9] analyzed the different shapes of aluminum oxide using the Darcy porous medium with thermal radiation. Hayat et al. [10] investigated the nanofluid flow with Hall and Ohmic influences. They deliberated the thermal convective and velocity slip boundary conditions. The Hall and Ohmic parameters have reduced the velocity and heat transfer rate. Sheikholeslami [11] presented the analysis different shapes of nanoparticles of copper oxide water with Brownian motion. It has been introduced that the platelet shape nanoparticles has leading impression as associated to other shapes of nanoparticles. Thumma et al. [12] investigated the non-Newtonian nanofluid flow containing water-based CuO and Cu nanoparticles past porous extending sheet with entropy optimization and velocity condition. A non-Fourier has been implemented to analyze the heat transfer rate. Hayat et al. [13] examined the Cu, Fe<sub>2</sub>O<sub>3</sub>, and Au nanoparticles with Hall and Ohmic effects using constant and variable viscosities. Sheikholeslami et al. [14] addressed the Al<sub>2</sub>O<sub>3</sub>-water nanoparticles through a channel with Brownian motion impact. Thumma et al. [15] deliberated the radiative boundary layer nanofluid flow past a nonlinear extending surface with viscous dissipation. Rout et al. [16] analyzed the water-based Cu and kerosene oil-based Cu between two parallel plates with thermal radiation. Further studies related to nanofluids are mentioned in [17–26].

The flow behavior of a flowing conducting liquid is described by magnetohydrodynamic (MHD), which polarizes it. In industrial activities such as nuclear power plants, crystal manufacture, electric generators, and fuel industry, the impact of magnetic fields is assessed. Tamim et al. [27] addressed the MHD mixed convective flow of nanofluid on a vertical plate. They studied both opposing and assisting flows. The water-based Cu, Al<sub>2</sub>O<sub>3</sub>, and TiO<sub>2</sub> are examined. Ghadikolaei et al. [28] implemented the induced magnetic field on hybrid nanofluid flow through an extending surface. Hayat et al. [29] explore the unsteady MHD viscous fluid flow with Joule heating, thermal radiation, and thermal stratification influences. Ahmad et al. [30] expressed the MHD flow of ferrofluid past an exponentially extending surface. Singh et al. [31] investigated the MHD flow of water-based alumina nanofluid past a flat plate with slip condition. Mliki et al. [32] evaluated the convective nanofluid flow with MHD effect. Upreti et al. [33] presented the CNT nanofluids past an extending surface with nonuniform heat source/sink and Ohmic heating. Pandey et al. [34] presented the MHD water-based copper nanofluid flow inside a convergent/divergent channel. Upreti et al. examined the MHD Ag-kerosene oil nanofluid with suction/injection roles. Turkeyilmazoglu [35] presented the viscous fluid flow with magnetic field impact past a spinning disk. The MHD viscous fluid flow considering wall slip conditions has been investigated by Hussain et al. [36]. Dawar et al. [19] presented the highly magnetized and nonmagnetized non-Newtonian fluid flow past an extending cylinder. Further related results can be seen in [18, 37–45].

Magnetic nanoparticles pique the researchers' interest in various fields, including homogeneous and heterogeneous

catalysis, magnetic fluids, environmental remediation, biomedicine, data storage, and magnetic resonance imaging (MRI) for instance purification of water. The literature proves that the nanoparticles of size less than the critical value (i.e., 10–20 nm) perform best [46]. Nanoparticles' magnetic properties effectively monopolize at such a small scale, rendering them beneficial and helpful in a wide range of applications [46–49]. In light of the abovementioned applications, we have considered a mathematical model for the flow of nanofluid containing the nanoparticles of Cu-H<sub>2</sub>O, Al<sub>2</sub>O<sub>3</sub>-H<sub>2</sub>O, and TiO<sub>2</sub>-H<sub>2</sub>O, and pure water with a strong magnetic field. According to the authors knowledge, there is no study based on spherical-shaped nanoparticles of the Cu, Al<sub>2</sub>O<sub>3</sub>, and TiO<sub>2</sub> using water as a based fluid past a rotating disk. Furthermore, the velocity slip and convective conditions are considered to analyze the flow behavior in the presence and absence of slip conditions. The mathematical model is solved with the help of the homotopic approach.

## 2. Physical Model

We consider the water-based nanomaterials (Cu, Al<sub>2</sub>O<sub>3</sub>, and TiO<sub>2</sub>) past a rotating disk. The velocity components  $\tilde{u}_1, \tilde{u}_2$ , and  $\tilde{u}_3$  are taken along  $\tilde{r}, \phi$ , and  $\tilde{z}$  directions, respectively. The disk rotates with an angular velocity  $\Omega$  at  $\tilde{z} = 0$  (see Figure 1). A magnetic field of strength  $B_0$  is applied normal to the fluid flow. The flow is subjected to velocity slip and thermal convective conditions. The leading equations are defined as follows [35]:

$$\frac{\partial \tilde{u}_1}{\partial \tilde{r}} + \frac{\tilde{u}_1}{\tilde{r}} + \frac{\partial \tilde{u}_3}{\partial \tilde{z}} = 0,$$

$$\begin{aligned} \tilde{u}_1 \frac{\partial \tilde{u}_1}{\partial \tilde{r}} - \frac{\tilde{u}_2^2}{\tilde{r}} + \tilde{u}_3 \frac{\partial \tilde{u}_1}{\partial \tilde{z}} = & -\frac{1}{\rho_{\text{nf}}} \frac{\partial \tilde{p}}{\partial \tilde{r}} + \frac{\mu_{\text{nf}}}{\rho_{\text{nf}}} \\ & \cdot \left( \frac{\partial^2 \tilde{u}_1}{\partial \tilde{r}^2} + \frac{1}{\tilde{r}} \frac{\partial \tilde{u}_1}{\partial \tilde{r}} - \frac{\tilde{u}_1}{\tilde{r}^2} + \frac{\partial^2 \tilde{u}_1}{\partial \tilde{z}^2} \right) \\ & - \frac{\sigma_{\text{nf}}}{\rho_{\text{nf}}} B_0^2 \tilde{u}_1, \end{aligned}$$

$$\begin{aligned} \tilde{u}_1 \frac{\partial \tilde{u}_2}{\partial \tilde{r}} + \frac{\tilde{u}_1 \tilde{u}_2}{\tilde{r}} + \tilde{u}_3 \frac{\partial \tilde{u}_2}{\partial \tilde{z}} = & \frac{\mu_{\text{nf}}}{\rho_{\text{nf}}} \left( \frac{\partial^2 \tilde{u}_2}{\partial \tilde{r}^2} + \frac{1}{\tilde{r}} \frac{\partial \tilde{u}_2}{\partial \tilde{r}} - \frac{\tilde{u}_2}{\tilde{r}^2} + \frac{\partial^2 \tilde{u}_2}{\partial \tilde{z}^2} \right) \\ & - \frac{\sigma_{\text{nf}}}{\rho_{\text{nf}}} B_0^2 \tilde{u}_2, \end{aligned}$$

$$\tilde{u}_1 \frac{\partial \tilde{u}_3}{\partial \tilde{r}} + \tilde{u}_3 \frac{\partial \tilde{u}_3}{\partial \tilde{z}} = -\frac{1}{\rho_{\text{nf}}} \frac{\partial \tilde{p}}{\partial \tilde{z}} + \frac{\mu_{\text{nf}}}{\rho_{\text{nf}}} \left( \frac{\partial^2 \tilde{u}_3}{\partial \tilde{r}^2} + \frac{1}{\tilde{r}} \frac{\partial \tilde{u}_3}{\partial \tilde{r}} + \frac{\partial^2 \tilde{u}_3}{\partial \tilde{z}^2} \right),$$

$$\tilde{u}_1 \frac{\partial \tilde{T}}{\partial \tilde{r}} + \tilde{u}_3 \frac{\partial \tilde{T}}{\partial \tilde{z}} = \frac{k_{\text{nf}}}{(\rho c_p)_{\text{nf}}} \left( \frac{\partial^2 \tilde{T}}{\partial \tilde{r}^2} + \frac{1}{\tilde{r}} \frac{\partial \tilde{T}}{\partial \tilde{r}} + \frac{\partial^2 \tilde{T}}{\partial \tilde{z}^2} \right), \quad (1)$$

with boundary conditions:

$$\left\{ \begin{aligned} \tilde{u}_1 = L \frac{\partial \tilde{u}_1}{\partial \tilde{z}}, \tilde{u}_2 = L \frac{\partial \tilde{u}_2}{\partial \tilde{z}} + \Omega \cdot \tilde{r}, \tilde{u}_3 = 0, -k_{\text{nf}} \frac{\partial \tilde{T}}{\partial \tilde{z}} = h_f (\tilde{T}_f - \tilde{T}) \text{ at } \tilde{z} = 0 \\ \tilde{u}_1 \longrightarrow 0, \tilde{u}_2 \longrightarrow 0, \tilde{T} \longrightarrow \tilde{T}_\infty \text{ as } \tilde{z} \longrightarrow \infty \end{aligned} \right\}. \quad (2)$$

The thermophysical properties of the nanofluids are defined as [50]

$$\left\{ \begin{array}{l} \frac{\mu_{nf}}{\mu_f} = \frac{1}{(1-\varphi)^{2.5}}, \frac{\rho_{nf}}{\rho_f} = (1-\varphi) + \varphi \frac{\rho_{np}}{\rho_f}, \frac{(\rho c_p)_{nf}}{(\rho c_p)_f} = (1-\varphi) + \varphi \frac{(\rho c_p)_{np}}{(\rho c_p)_f} \\ \frac{\sigma_{nf}}{\sigma_f} = 1 + \frac{3((\sigma_{np}/\sigma_f) - 1)\varphi}{((\sigma_{np}/\sigma_f) + 2) - ((\sigma_{np}/\sigma_f) - 1)\varphi}, \frac{k_{nf}}{k_f} = \frac{k_{np} + (n-1)k_f - (n-1)(k_f - k_{np})\varphi}{k_{np} + (n-1)k_f + (k_f - k_{np})\varphi} \end{array} \right\}. \quad (3)$$

In the above equations,  $\mu$  is the dynamic viscosity,  $\rho$  is the density,  $c_p$  is the heat capacitance,  $L$  is the wall slip parameter,  $\tilde{p}$  is the pressure,  $k$  is the thermal conductivity, and  $\varphi$  represents the volume fraction of the nanoparticles. Furthermore, the subscript  $f$  indicates the base fluid,  $nf$  shows the nanofluids, and  $np$  is used for nanoparticles.

The correspondence variables are defined as [53–55]

$$\left\{ \begin{array}{l} \tilde{u}_1 = \tilde{r}\Omega f(\eta), \tilde{u}_2 = \tilde{r}\Omega g(\eta), \tilde{u}_3 = \sqrt{\Omega\nu_f}h(\eta) \\ \tilde{p} = \tilde{p}_\infty + 2\Omega\mu_f\tilde{P}(\eta), \tilde{T} = \tilde{T}_\infty + (\tilde{T}_f - \tilde{T}_\infty)\theta(\eta), \eta = \sqrt{\frac{\Omega}{\nu_f}}\tilde{z} \end{array} \right\}. \quad (4)$$

The above system is transformed as

$$\begin{aligned} h' + 2f &= 0, \\ f'' + \frac{\bar{M}_2}{\bar{M}_1} [hf' - f^2 + g^2] - \frac{\bar{M}_3}{\bar{M}_1} Mf &= 0, \\ g'' - \frac{\bar{M}_2}{\bar{M}_1} [2gf + g'h] - \frac{\bar{M}_3}{\bar{M}_1} Mg &= 0, \\ \theta'' - \frac{\bar{M}_5}{\bar{M}_4} \text{Pr} \theta'h &= 0, \end{aligned} \quad (5)$$

where

$$\left\{ \bar{M}_1 = \frac{\mu_{nf}}{\mu_f}, \bar{M}_2 = \frac{\rho_{nf}}{\rho_f}, \bar{M}_3 = \frac{\sigma_{nf}}{\sigma_f}, \bar{M}_4 = \frac{k_{nf}}{k_f}, \bar{M}_5 = \frac{(\rho c_p)_{nf}}{(\rho c_p)_f} \right\}. \quad (6)$$

with

$$\left\{ \begin{array}{l} f(0) = \alpha f'(0), g(0) = 1 + \alpha g'(0), h(0) = 0, \frac{k_{nf}}{k_f} \theta'(0) = \text{Bi}(\theta(0) - 1) \\ f(\eta \rightarrow \infty) \rightarrow 0, g(\eta \rightarrow \infty) \rightarrow 0, \theta(\eta \rightarrow \infty) \rightarrow 0 \end{array} \right\}. \quad (7)$$

Here,  $M = \sigma_f B_0^2 / \rho_f \Omega$  is the magnetic parameter,  $\text{Pr} = \nu_f / \alpha_f$  is the Prandtl number,  $\alpha = L\tilde{r}\sqrt{\Omega/\nu_f}$  is the wall slip

parameter, and  $\text{Bi} = (h_f/k_f)\sqrt{\Omega/\nu_f}$  is the thermal Biot number.

The surface drag force  $C_{f\tilde{r}}$  and heat transfer rate  $\text{Nu}_r$  are defined as [53, 55]

$$C_{f\tilde{r}} = \frac{1}{\rho_f \tilde{r}^2 \Omega^2} \sqrt{\tau_r^2 + \tau_\phi^2}, \text{Nu}_r = \frac{\tilde{r}q_w}{k_f(T_f - T_w)}, \quad (8)$$

where  $\tau_r$ ,  $\tau_\phi$ , and  $q_w$  are defined as

$$\begin{aligned} \tau_r &= \mu_{nf} \left( \frac{\partial \tilde{u}_1}{\partial \tilde{z}} + \frac{\partial \tilde{u}_3}{\partial \tilde{r}} \right) \Big|_{\tilde{z}=0}, \\ \tau_\phi &= \mu_{nf} \left( \frac{\partial \tilde{u}_2}{\partial \tilde{z}} + \frac{1}{\tilde{r}} \frac{\partial \tilde{u}_3}{\partial \phi} \right) \Big|_{\tilde{z}=0}, \\ q_w &= -k_{nf} \frac{\partial \tilde{T}}{\partial \tilde{z}} \Big|_{\tilde{z}=0}. \end{aligned} \quad (9)$$

The dimensionless form of Equation (7) is:

$$\sqrt{\text{Re}} C_{f\tilde{r}} = \bar{M}_1 \sqrt{f'^2(0) + g'^2(0)}, \frac{\text{Nu}_r}{\sqrt{\text{Re}}} = -\bar{M}_4 \theta'(0), \quad (10)$$

where  $\text{Re} = \Omega \tilde{r}^2 / \nu_f$  is the local Reynolds number.

### 3. HAM Solution

The initial guesses and linear operators are defined as

$$f_0(\eta) = 0, g_0(\eta) = \frac{1}{1+\alpha} e^{-\eta}, \theta_0(\eta) = \frac{k_f}{k_{nf}} \frac{\text{Bi}}{1+\text{Bi}} e^{-\eta}, \quad (11)$$

$$L_f = f'' - f, L_g = g'' - g, L_\theta = \theta'' - \theta,$$

with the following properties:

$$L_f[c_1 e^{-\eta} + c_2 e^{\eta}] = 0, L_g[c_3 e^{-\eta} + c_4 e^{\eta}] = 0, L_\theta[c_5 e^{-\eta} + c_6 e^{\eta}] = 0, \quad (12)$$

where  $c_i (i = 1 - 6)$  are called arbitrary constants.

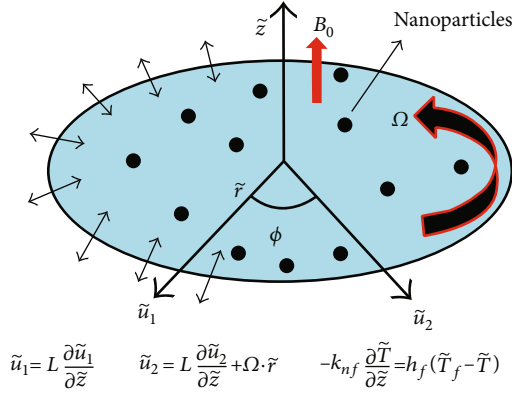


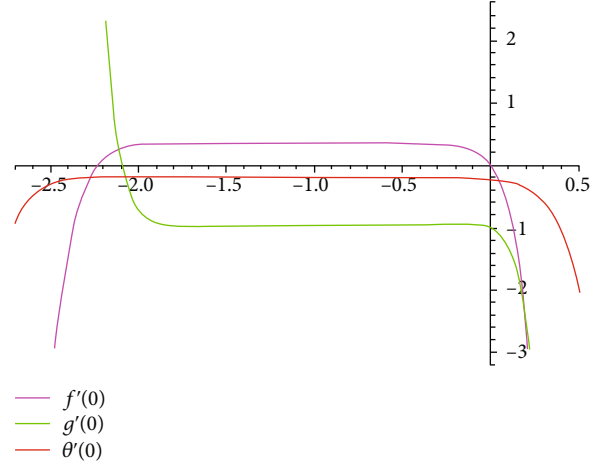
FIGURE 1: Geometrical representation of the flow problem.

#### 4. HAM Convergence

Figure 2 is displayed for the convergence of series solutions. The auxiliary parameters  $\tilde{h}_f$ ,  $\tilde{h}_g$ , and  $\tilde{h}_\theta$  are responsible for the adjustment and controlling of the series solutions. Therefore, the acceptable values for velocities and thermal profiles are  $-2.1 \leq \tilde{h}_f \leq -0.1$ ,  $-1.9 \leq \tilde{h}_g \leq 0.0$ , and  $-2.5 \leq \tilde{h}_\theta \leq 0.2$ .

#### 5. Results and Discussion

This segment compacts with the impressions of different embedded factors on velocities and temperature, surface drag force and heat transfer rate. We have considered the spherical-shaped three different nanoparticles like Cu,  $\text{Al}_2\text{O}_3$ , and  $\text{TiO}_2$  with a base fluid  $\text{H}_2\text{O}$ . Since water is used as a base fluid, therefore,  $\text{Pr} = 6.2$ . The thermophysical properties of Cu,  $\text{Al}_2\text{O}_3$ ,  $\text{TiO}_2$ , and  $\text{H}_2\text{O}$  are presented in Table 1. The shape factor and sphericity of the different nanoparticles are presented in Table 2. In Table 3, we have presented the numerical values of skin friction via magnetic parameter for different water-based spherical-shaped nanoparticles and pure water. Both slip and no-slip conditions are considered here. The greater magnetic parameter augments the skin friction coefficient. Actually, the magnetic parameter drops off the velocity function due to Lorentz force. The heightening Lorentz force means the skin friction coefficient augments which has been seen for the spherical-shaped Cu,  $\text{Al}_2\text{O}_3$ , and  $\text{TiO}_2$  nanoparticles and pure water for the case of no-slip condition. For the case of slip condition, interesting results have been introduced here. Physically, the presence of slip parameter reduces the velocity of the fluid due augmenting skin friction coefficient as occurs which allow more fluid to past the disk as found for pure water. However, for the spherical-shaped Cu,  $\text{Al}_2\text{O}_3$ , and  $\text{TiO}_2$  nanoparticles, the presence of slip and magnetic parameters have diverse impact on surface drag force. In addition, the greater impact of magnetic parameter occurs in the absence of slip effect. Table 4 shows the numerical values of surface drag force via spherical-shaped nanoparticle volume fraction for the different water-based nanoparticles. Physically, the increasing nanoparticle volume fraction means that the nanoparti-

FIGURE 2:  $h$ -curves for  $f'(0)$ ,  $g'(0)$ , and  $\theta'(0)$ .TABLE 1: Numerical values of the thermophysical properties of  $\text{H}_2\text{O}$ , Cu,  $\text{Al}_2\text{O}_3$ , and  $\text{TiO}_2$  [13, 51, 52].

Base fluid and nanoparticles	$\rho$ (kg/m <sup>3</sup> )	$c_p$ (J/kgK)	$k$ (W/mK)	$\sigma$ (1/ $\Omega\text{m}$ )
$\text{H}_2\text{O}$	997.1	4179	0.613	0.05
$\text{Al}_2\text{O}_3$	3970	765	40	$1 \times 10^{-10}$
Cu	8933	385	401	$5.96 \times 10^7$
$\text{TiO}_2$	4250	685.2	8.9539	$2.6 \times 10^6$

TABLE 2: Shape factor and sphericity of different particle shapes [56, 57].

Shape of the nanoparticle	Sphericity	Shape factor
Sphere	1.0	3.00
Cylinder	0.62	4.84
Blade	0.36	8.33
Platelet	0.52	5.77
Brick	0.81	3.70

cles and the base fluid collide with each other which accelerates the fluid motion; consequently, the momentum boundary layer thickness decreases and upsurges the surface drag force. Also, the impact of spherical-shaped nanoparticles volume fraction is the same for the local Nusselt number as portrayed in Table 5. Additionally, the surface drag force is greater for the case of no-slip condition. The increasing thermal Biot number augments the heat transfer rate. Tables 6–8 show the comparison of analytical and numerical techniques for  $f(\eta)$ ,  $g(\eta)$ , and  $\theta(\eta)$ . Here, a close agreement between both techniques is found. Figure 3 shows the impact of nanoparticle volume fraction on spherical-shaped Cu,  $\text{Al}_2\text{O}_3$ , and  $\text{TiO}_2$  nanoparticles. Figure 4 shows the variation in radial velocity of the spherical-shaped Cu,  $\text{Al}_2\text{O}_3$ , and  $\text{TiO}_2$  nanoparticles and pure water ( $\text{H}_2\text{O}$ ) via a magnetic parameter for the case of no-slip condition. The greater magnetic factor diminishes the radial velocity of the spherical-shaped Cu,  $\text{Al}_2\text{O}_3$ , and  $\text{TiO}_2$  nanoparticles and

TABLE 3: Numerical values of the skin friction via magnetic parameter for different water-based spherical-shaped nanoparticles and pure water.

Magnetic parameter	Values	No-slip condition	Cu	Al <sub>2</sub> O <sub>3</sub>	TiO <sub>2</sub>	Pure water	
<i>M</i>	1.0	$\alpha = 0.0$	0.97455	0.95901	0.97484	0.94904	
	2.0		1.33931	1.30845	1.34076	1.30432	
	3.0		1.70971	1.66292	1.71184	1.66454	
		Slip condition					
	1.0		$\alpha = 0.5$	0.69813	0.69369	0.69740	0.82172
	2.0		0.78174	0.77365	0.78104	0.57823	
	3.0	0.86542	0.85368	0.86475	0.33615		

TABLE 4: Numerical values of the skin friction via spherical-shaped nanoparticle volume fraction for different water-based nanoparticles.

Nanoparticles volume fraction	Values	No-slip condition	Cu	Al <sub>2</sub> O <sub>3</sub>	TiO <sub>2</sub>	
$\varphi$	0.1	$\alpha = 0.0$	0.97455	0.95901	0.97484	
	0.2		1.00105	0.96960	1.00142	
	0.3		1.02854	0.98086	1.02879	
		Slip condition				
	0.1		$\alpha = 0.5$	0.69813	0.69369	0.69740
	0.2		0.71727	0.70832	0.71578	
	0.3	0.73702	0.72352	0.73397		

TABLE 5: Numerical values of the local Nusselt number via the Biot number and spherical-shaped nanoparticle volume fraction for different water-based nanoparticles and pure water.

Parameters	Values	Cu	Al <sub>2</sub> O <sub>3</sub>	TiO <sub>2</sub>	Pure water
Bi	0.1	0.08433	0.08449	0.08504	0.08787
	0.2	0.15021	0.15050	0.15146	0.15648
	0.3	0.20882	0.20321	0.20450	0.21124
$\varphi$	0.1	0.16124	0.15782	0.14667	—
	0.2	0.29520	0.28292	0.24451	—
	0.3	0.54998	0.51512	0.41199	—

TABLE 6: Analytical and numerical solutions for  $f(\eta)$ .

$\eta$	HAM	Shooting	Absolute error
0.0	$1.277200 \times 10^{-17}$	0.048458	0.048458
0.5	0.079926	0.157846	0.077921
1.0	0.092998	0.199663	0.106666
1.5	0.083715	0.203372	0.119657
2.0	0.068544	0.186409	0.117866
2.5	0.053523	0.159724	0.106202
3.0	0.040535	0.129866	0.089330
3.5	0.029738	0.100012	0.070274
4.0	0.020472	0.070470	0.049998
4.5	0.011394	0.038415	0.027021
5.0	$8.673620 \times 10^{-19}$	-0.004014	0.004014

pure water (H<sub>2</sub>O). Physically, the applied magnetic field creates Lorentz force during the fluid flow which opposes the motion of the flow nanoparticles; consequently, a reducing impact is observed. For the case of slip condition, a similar impact of magnetic parameter is observed for radial velocity of the spherical-shaped Cu, Al<sub>2</sub>O<sub>3</sub>, and TiO<sub>2</sub> nanoparticles and pure water (H<sub>2</sub>O) as displayed in Figure 5. Furthermore, the presence of a slip parameter reduces the velocity of the fluid due to augmenting skin friction coefficient occurring which allows more fluid to past the disk. So, the combination of magnetic and slip parameters has greater impact on velocity profile of the spherical-shaped Cu, Al<sub>2</sub>O<sub>3</sub>, and TiO<sub>2</sub> nanoparticles and pure water (H<sub>2</sub>O) as compared to no-slip condition. Figure 6 displays the variation in radial velocity  $f(\eta)$  of the spherical-shaped Cu, Al<sub>2</sub>O<sub>3</sub>, and TiO<sub>2</sub> nanoparticles via  $\varphi$  for the case of no-slip condition. The greater  $\varphi$  augments the radial velocity of the spherical-shaped Cu nanoparticle, while it reduces the radial velocity of the spherical-shaped Al<sub>2</sub>O<sub>3</sub> and TiO<sub>2</sub> nanoparticles. Physically, the greater  $\varphi$  opposes the motion of the spherical-shaped Al<sub>2</sub>O<sub>3</sub> and TiO<sub>2</sub> nanoparticles which augments the boundary layer thickness and slows down the velocity profile, while this impact is opposite for Cu nanoparticle. For the case of slip condition, the greater  $\varphi$  augments the radial velocity of the spherical-shaped Cu nanoparticle, while it reduces the velocity profile for Al<sub>2</sub>O<sub>3</sub> and TiO<sub>2</sub> nanoparticles next to the surface of the rotating disk and moderates the increasing effect as  $\eta \rightarrow \infty$  (see Figure 7). Figures 8 and 9 portray the variation in  $g(\eta)$  of the spherical-shaped Cu, Al<sub>2</sub>O<sub>3</sub>, and TiO<sub>2</sub> nanoparticles via a magnetic parameter for the case of no-slip and slip conditions, respectively. For both no-

TABLE 7: Analytical and numerical solutions for  $g(\eta)$ .

$\eta$	HAM	Shooting	Absolute error
0.0	1.000000	0.918880	0.081120
0.5	0.622565	0.730215	0.107650
1.0	0.401548	0.588991	0.187443
1.5	0.263876	0.474205	0.210329
2.0	0.175398	0.377681	0.202282
2.5	0.117530	0.296126	0.178596
3.0	0.079169	0.227544	0.148375
3.5	0.053275	0.169557	0.116282
4.0	0.035073	0.118368	0.083296
4.5	0.020845	0.067299	0.046454
5.0	0.006738	0.003395	0.003343

TABLE 8: Analytical and numerical solutions for  $\theta(\eta)$ .

$\eta$	HAM	Shooting	Absolute error
0.0	0.520728	0.514973	0.005755
0.5	0.407258	0.303778	0.103477
1.0	0.316987	0.170961	0.146029
1.5	0.248884	0.098508	0.150376
2.0	0.196218	0.059782	0.136436
2.5	0.153566	0.038072	0.115494
3.0	0.117379	0.024878	0.092501
3.5	0.085413	0.016085	0.069328
4.0	0.056215	0.009652	0.046563
4.5	0.028772	0.004487	0.024285
5.0	0.002246	-0.000105	0.002351

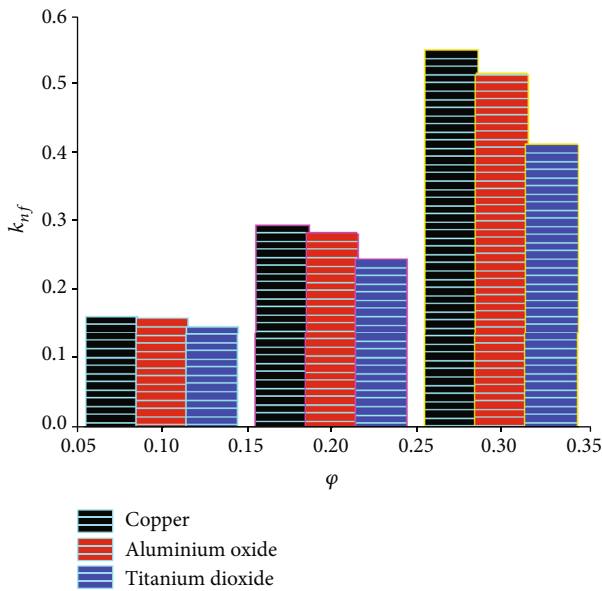


FIGURE 3: Impact of nanoparticle volume fraction on spherical-shaped nanoparticles of water-based Cu,  $Al_2O_3$ , and  $TiO_2$ .

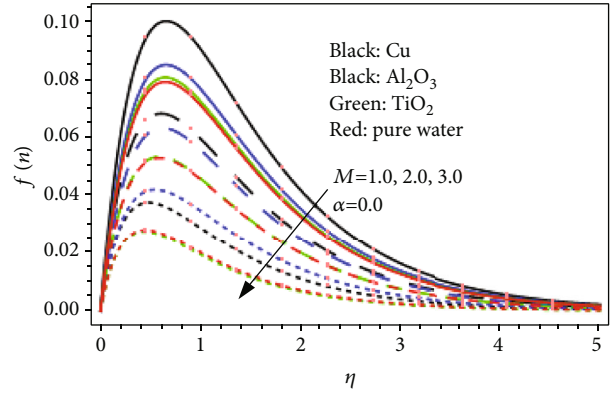


FIGURE 4: Variation in  $f(\eta)$  via  $M$  when  $\alpha = 0.0$ .

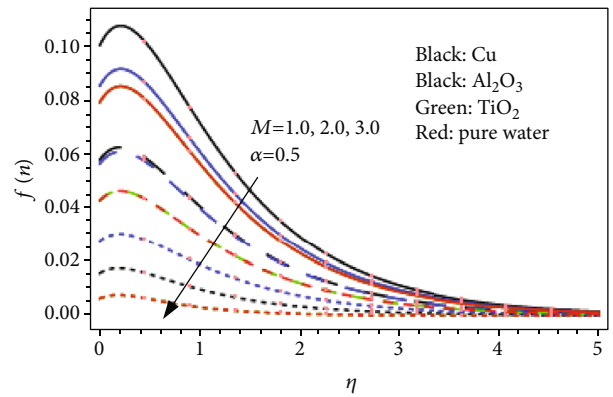


FIGURE 5: Variation in  $f(\eta)$  via  $M$  when  $\alpha = 0.5$ .

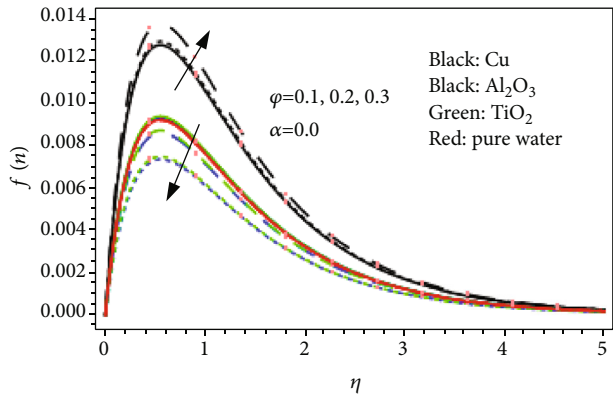


FIGURE 6: Variation in  $f(\eta)$  via  $\phi$  when  $\alpha = 0.0$ .

slip and slip conditions, similar impacts are found here as seen in Figures 4 and 5. However, the impact of slip condition is greater for  $f(\eta)$  as compared to  $g(\eta)$ . Figure 10 shows the variation in velocity profile  $g(\eta)$  of the spherical-shaped Cu,  $Al_2O_3$ , and  $TiO_2$  nanoparticles via  $\phi$  for the case when  $\alpha = 0.0$ . The greater  $\phi$  augments the velocity profile  $g(\eta)$  of the spherical-shaped Cu,  $Al_2O_3$ , and  $TiO_2$  nanoparticles. Physically, the greater  $\phi$  opposes the motion of the spherical-shaped Cu,  $Al_2O_3$ , and  $TiO_2$  nanoparticles which augments the boundary layer thickness and slows down the velocity profile. For the case when  $\alpha = 0.5$ , the greater

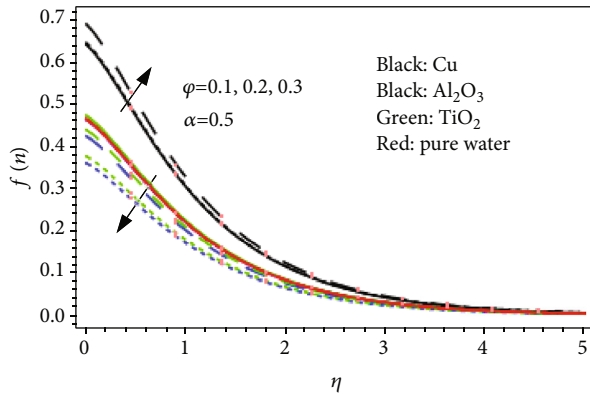


FIGURE 7: Variation in  $f(\eta)$  via  $\phi$  when  $\alpha = 0.5$ .

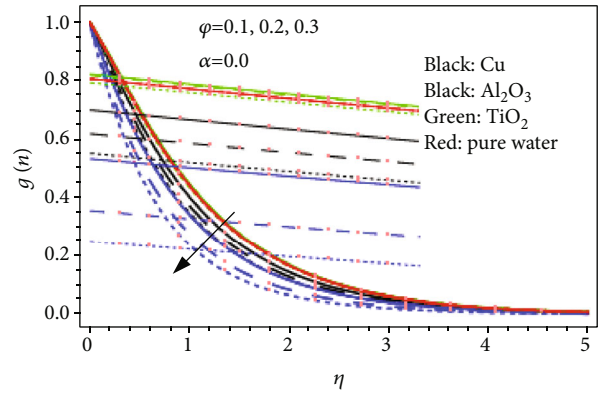


FIGURE 10: Variation in  $g(\eta)$  via  $\phi$  when  $\alpha = 0.0$ .

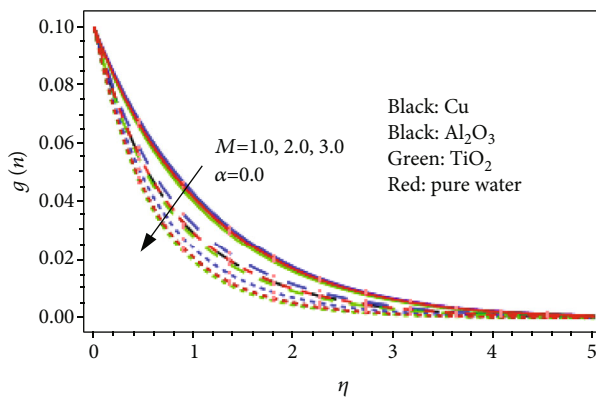


FIGURE 8: Variation in  $g(\eta)$  via  $M$  when  $\alpha = 0.0$ .

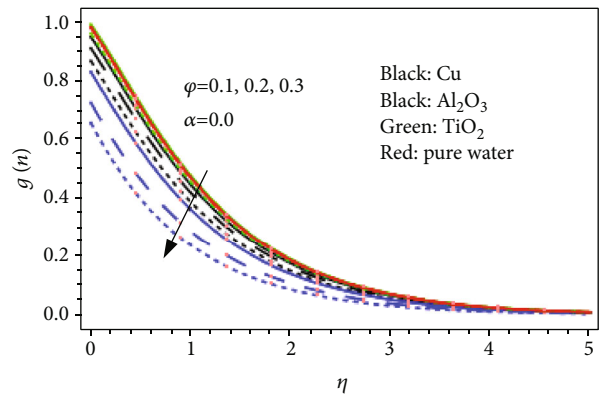


FIGURE 11: Variation in  $g(\eta)$  via  $\phi$  when  $\alpha = 0.5$ .

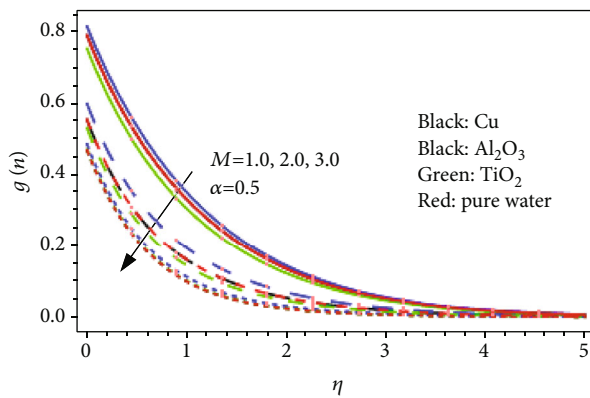


FIGURE 9: Variation in  $g(\eta)$  via  $M$  when  $\alpha = 0.5$ .

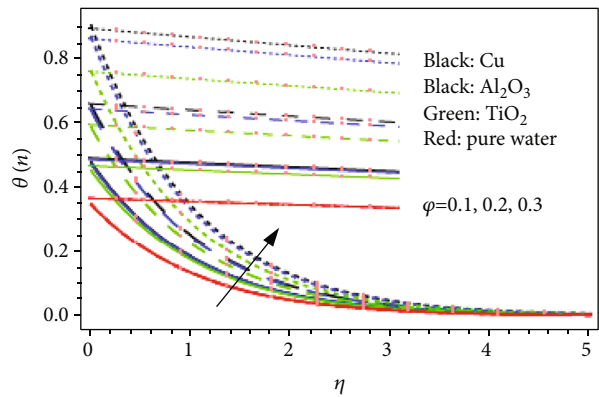


FIGURE 12: Variation in  $\theta(\eta)$  via  $\phi$ .

$\phi$  reduces the velocity profile  $g(\eta)$  of the spherical-shaped Cu,  $\text{Al}_2\text{O}_3$ , and  $\text{TiO}_2$  nanoparticles (see Figure 11). Additionally, the reducing impact of  $\phi$  is greater for  $\alpha = 0.5$  as compared to  $\alpha = 0.0$ . Figure 12 shows the variation in temperature profile  $\theta(\eta)$  of the spherical-shaped Cu,  $\text{Al}_2\text{O}_3$ , and  $\text{TiO}_2$  nanoparticles via  $\phi$ . The greater  $\phi$  augments the temperature profile. Physically, the greater  $\phi$  upsurges the thermal conductivity of the Cu,  $\text{Al}_2\text{O}_3$ , and  $\text{TiO}_2$  nanoparticles and thermal transfer rate. Therefore, the nanoparticle which has high thermal conductivity has the dominant impact on temperature profile and heat transfer rate as

shown in Figure 3 and Table 5. Here, Cu nanoparticle has greater thermal conductivity than  $\text{Al}_2\text{O}_3$  nanoparticle, and  $\text{Al}_2\text{O}_3$  nanoparticle has greater thermal conductivity than  $\text{TiO}_2$  nanoparticle. So, the greatest impact of Cu nanoparticle is found here. Figure 13 shows the variation in temperature profile  $\theta(\eta)$  of the spherical-shaped Cu,  $\text{Al}_2\text{O}_3$ , and  $\text{TiO}_2$  nanoparticles via the thermal Biot number. The greater Biot number augments the thermal profile  $\theta(\eta)$  of the spherical-shaped Cu,  $\text{Al}_2\text{O}_3$ , and  $\text{TiO}_2$  nanoparticles. Physically, the heat transfer coefficient caused by the hot fluid is directly related to the Biot number. Therefore, the greater



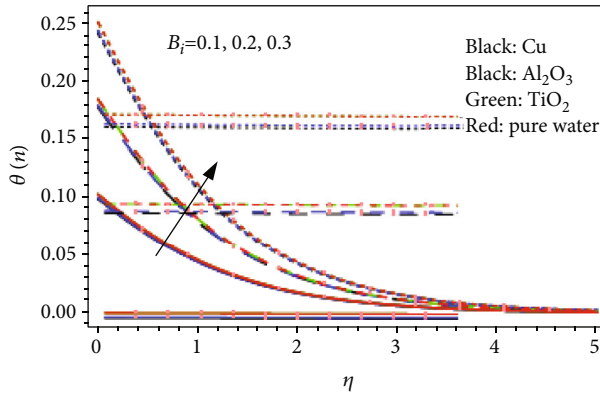


FIGURE 13: Variation in  $\theta(\eta)$  via Bi.

Biot number raises the convection and thermal profile significantly. Additionally, the spherical-shaped Cu nanoparticle has greater impact on thermal profile as compared to  $\text{Al}_2\text{O}_3$  and  $\text{TiO}_2$  nanoparticles.

## 6. Conclusion

In this work, we have examined the water-based spherical-shaped nanoparticles of copper-water, aluminum oxide-water, titanium dioxide-water, and pure water past a rotating disk. Slip and no-slip conditions are considered in order to examine the variations in radial and tangential velocities due to the magnetic field, nanoparticle volume fraction, and thermal Biot number. The final points are mentioned below:

- For  $\alpha = 0.5$ , the surface drag force of Cu,  $\text{Al}_2\text{O}_3$ , and  $\text{TiO}_2$  have reduced with the increasing magnetic parameter, while for  $\alpha = 0.0$ , the surface drag force of the Cu,  $\text{Al}_2\text{O}_3$ , and  $\text{TiO}_2$  nanoparticles have augmented with the increasing magnetic parameter. Additionally, the greater impact of magnetic parameter occurs when  $\alpha = 0.5$
- The surface drag force and heat transfer rate of spherical-shaped nanoparticles of Cu,  $\text{Al}_2\text{O}_3$ , and  $\text{TiO}_2$  is augmented via nanoparticle volume fraction
- For  $\alpha = 0.5$  and  $\alpha = 0.0$ , the radial and tangential velocities of the spherical-shaped nanoparticles of Cu,  $\text{Al}_2\text{O}_3$ , and  $\text{TiO}_2$  and pure water have augmented via a magnetic parameter. Additionally, the impact of magnetic field is greater for radial velocity as compared to tangential velocity
- For  $\alpha = 0.5$  and  $\alpha = 0.0$ , the tangential velocity of the spherical-shaped nanoparticle of Cu,  $\text{Al}_2\text{O}_3$ , and  $\text{TiO}_2$  has reduced via nanoparticle volume fraction. Additionally, the reducing impact of nanoparticle volume fraction is greater for  $\alpha = 0.5$  as compared to  $\alpha = 0.0$
- The greater nanoparticle volume fraction and thermal Biot number have increased the temperature

profile of the spherical-shaped nanoparticles of Cu,  $\text{Al}_2\text{O}_3$ , and  $\text{TiO}_2$

## Nomenclature

$B_0$ :	Strength of magnetic field
Bi:	Thermal Biot number
$C_f$ :	Skin friction coefficient
$c_i (i = 1 - 6)$ :	Arbitrary constants
$c_p$ :	Heat capacitance
$f_0, \theta_0, g_0$ :	Initial guesses
$k$ :	Thermal conductivity
$L$ :	Wall slip parameter
$L_f, L_g, L_\theta$ :	Linear operators
$M$ :	Magnetic parameter
Nu:	Nusselt number
$\tilde{p}$ :	Pressure
Re:	Reynolds number
Pr:	Prandtl number
$\tilde{r}, \phi, \tilde{z}$ :	Coordinates
$\tilde{u}_1, \tilde{u}_2, \tilde{u}_3$ :	Velocity components

### Greek Letters

$\Omega$ :	Angular velocity
$\sigma$ :	Electrical conductivity
$\rho$ :	Density
$\mu$ :	Dynamic viscosity
$\alpha$ :	Dimensionless wall slip parameter
$\varphi$ :	Volume fraction of the nanoparticles

### Subscripts

f:	Fluid
nf:	Nanofluids
np:	Nanoparticles.

## Data Availability

All the supporting data are within the manuscript.

## Conflicts of Interest

The authors declare that they have no conflict of interest.

## References

- H. Upreti and M. Kumar, "Influence of non-linear radiation, Joule heating and viscous dissipation on the boundary layer flow of MHD nanofluid flow over a thin moving needle," *Multidiscipline Modeling in Materials and Structures*, vol. 16, no. 1, pp. 208–224, 2020.
- J. Raza, F. Mebarek-Oudina, and A. J. Chamkha, "Magnetohydrodynamic flow of molybdenum disulfide nanofluid in a channel with shape effects," *Multidiscipline Modeling in Materials and Structures*, vol. 15, no. 4, pp. 737–757, 2019.
- J. Raza, F. Mebarek-Oudina, and B. Mahanthesh, "Magnetohydrodynamic flow of nano Williamson fluid generated by stretching plate with multiple slips," *Multidiscipline Modeling in Materials and Structures*, vol. 15, no. 5, pp. 871–894, 2019.

- [4] J. Raza, M. Farooq, F. Mebarek-Oudina, and B. Mahanthesh, "Multiple slip effects on MHD non-Newtonian nanofluid flow over a nonlinear permeable elongated sheet," *Multidiscipline Modeling in Materials and Structures*, vol. 15, no. 5, pp. 913–931, 2019.
- [5] C. Sulochana and S. R. Aparna, "Unsteady magnetohydrodynamic radiative liquid thin film flow of hybrid nanofluid with thermophoresis and Brownian motion," *Multidiscipline Modeling in Materials and Structures*, vol. 16, no. 4, pp. 811–834, 2020.
- [6] S. S. Giri, K. Das, and P. K. Kundu, "Inclined magnetic field effects on unsteady nanofluid flow and heat transfer in a finite thin film with non-uniform heat source/sink," *Multidiscipline Modeling in Materials and Structures*, vol. 15, no. 1, pp. 265–282, 2019.
- [7] A. Kumar, V. Sugunamma, N. Sandeep et al., "Impact of Brownian motion and thermophoresis on bioconvective flow of nanoliquids past a variable thickness surface with slip effects," *Multidiscipline Modeling in Materials and Structures*, vol. 15, no. 1, pp. 103–132, 2019.
- [8] A. A. Minea, *Advances in New Heat Transfer Fluids: From Numerical to Experimental Techniques*, CRC Press, 2017.
- [9] M. Sheikholeslami, "Numerical approach for MHD  $Al_2O_3$ -water nanofluid transportation inside a permeable medium using innovative computer method," *Computer Methods in Applied Mechanics and Engineering*, vol. 344, pp. 306–318, 2019.
- [10] T. Hayat, B. Ahmed, F. M. Abbasi, and A. Alsaedi, "Peristalsis of nanofluid through curved channel with Hall and Ohmic heating effects," *Journal of Central South University*, vol. 26, no. 9, pp. 2543–2553, 2019.
- [11] M. Sheikholeslami, "Finite element method for PCM solidification in existence of  $CuO$  nanoparticles," *Journal of Molecular Liquids*, vol. 265, pp. 347–355, 2018.
- [12] T. Thumma, S. R. Mishra, and O. A. Bég, "ADM solution for  $Cu/CuO$ -water viscoplastic nanofluid transient slip flow from a porous stretching sheet with entropy generation, convective wall temperature and radiative effects," *Journal of Applied and Computational Mechanics*, vol. 7, no. 3, pp. 1291–1305, 2021.
- [13] T. Hayat, B. Ahmed, F. M. Abbasi, and A. Alsaedi, "Hydro-magnetic peristalsis of water based nanofluids with temperature dependent viscosity: a comparative study," *Journal of Molecular Liquids*, vol. 234, pp. 324–329, 2017.
- [14] M. Sheikholeslami, M. B. Gerdroodbary, R. Moradi, A. Shafee, and Z. Li, "Application of neural network for estimation of heat transfer treatment of  $Al_2O_3$ - $H_2O$  nanofluid through a channel," *Computer Methods in Applied Mechanics and Engineering*, vol. 344, pp. 1–12, 2019.
- [15] T. Thumma, O. Anwar Bég, and A. Kadir, "Numerical study of heat source/sink effects on dissipative magnetic nanofluid flow from a non-linear inclined stretching/shrinking sheet," *Journal of Molecular Liquids*, vol. 232, pp. 159–173, 2017.
- [16] B. C. Rout, S. R. Mishra, and T. Thumma, "Effect of viscous dissipation on  $Cu$ -water and  $Cu$ -kerosene nanofluids of axisymmetric radiative squeezing flow," *Heat Transfer—Asian Research*, vol. 48, no. 7, pp. 3039–3054, 2019.
- [17] T. Gul, S. Nasir, S. Islam, Z. Shah, and M. A. Khan, "Effective Prandtl number model influences on the  $\gamma Al_2O_3$ - $H_2O$  and  $\gamma Al_2O_3$ - $C_2H_6O_2$  nanofluids spray along a stretching cylinder," *Arabian Journal for Science and Engineering*, vol. 44, 2019.
- [18] T. Gul and K. Firdous, "The experimental study to examine the stable dispersion of the graphene nanoparticles and to look at the  $GO$ - $H_2O$  nanofluid flow between two rotating disks," *Applied Nanoscience*, vol. 8, no. 7, pp. 1711–1727, 2018.
- [19] H. Štorkánová, S. Oreská, M. Špiritović et al., "Plasma Hsp90 levels in patients with systemic sclerosis and relation to lung and skin involvement: a cross-sectional and longitudinal study," *Scientific Reports*, vol. 11, no. 1, pp. 1–15, 2021.
- [20] W. Alghamdi, A. Alsubie, P. Kumam, A. Saeed, and T. Gul, "MHD hybrid nanofluid flow comprising the medication through a blood artery," *Scientific Reports*, vol. 11, no. 1, pp. 1–13, 2021.
- [21] Z. Boulahia, A. Wakif, and R. Sehaqui, "Finite volume analysis of free convection heat transfer in a square enclosure filled by a  $Cu$ -water nanofluid containing different shapes of heating cylinder," *Journal of Nanofluids*, vol. 6, no. 4, pp. 761–768, 2017.
- [22] Z. Boulahia, A. Wakif, and R. Sehaqui, "Numerical modeling of natural convection heat transfer in a wavy wall enclosure filled by a  $Cu$ -water nanofluid with a square cooler," *Journal of Nanofluids*, vol. 6, no. 2, pp. 324–333, 2017.
- [23] A. Shafiq, G. Rasool, H. Alotaibi et al., "Thermally enhanced Darcy-Forchheimer Casson-water/glycerine rotating nanofluid flow with uniform magnetic field," *Micromachines*, vol. 12, no. 6, p. 605, 2021.
- [24] A. Wakif, Z. Boulahia, S. R. Mishra, M. Mehdi Rashidi, and R. Sehaqui, "Influence of a uniform transverse magnetic field on the thermo-hydrodynamic stability in water-based nanofluids with metallic nanoparticles using the generalized Buongiorno's mathematical model," *The European Physical Journal Plus*, vol. 133, no. 5, p. 181, 2018.
- [25] Z. Boulahia, A. Wakif, A. J. Chamkha, and R. Sehaqui, "Numerical study of natural and mixed convection in a square cavity filled by a  $Cu$ -water nanofluid with circular heating and cooling cylinders," *Mechanics & Industry*, vol. 18, no. 5, p. 502, 2017.
- [26] A. Dawar, Z. Shah, W. Khan, M. Idrees, and S. Islam, "Unsteady squeezing flow of magnetohydrodynamic carbon nanotube nanofluid in rotating channels with entropy generation and viscous dissipation," *Advances in Mechanical Engineering*, vol. 11, no. 1, Article ID 168781401882310, 2019.
- [27] H. Tamim, S. Dinarvand, R. Hosseini, and I. Pop, "MHD mixed convection stagnation-point flow of a nanofluid over a vertical permeable surface: a comprehensive report of dual solutions," *Heat and Mass Transfer*, vol. 50, no. 5, pp. 639–650, 2014.
- [28] S. S. Ghadikolaei, M. Yassari, H. Sadeghi, K. Hosseinzadeh, and D. D. Ganji, "Investigation on thermophysical properties of  $TiO_2$ - $Cu/H_2O$  hybrid nanofluid transport dependent on shape factor in MHD stagnation point flow," *Powder Technology*, vol. 322, pp. 428–438, 2017.
- [29] T. Hayat, S. Qayyum, M. Imtiaz, and A. Alsaedi, "MHD flow and heat transfer between coaxial rotating stretchable disks in a thermally stratified medium," *PLoS One*, vol. 11, no. 5, article e0155899, 2016.
- [30] R. Ahmad, M. Mustafa, T. Hayat, and A. Alsaedi, "Numerical study of MHD nanofluid flow and heat transfer past a bidirectional exponentially stretching sheet," *Journal of Magnetism and Magnetic Materials*, vol. 407, pp. 69–74, 2016.
- [31] P. Singh, A. K. Pandey, and M. Kumar, "Forced convection in MHD slip flow of alumina-water nanofluid over a flat plate," *Journal of Enhanced Heat Transfer*, vol. 23, no. 6, pp. 487–497, 2016.

- [32] B. Mliki, M. A. Abbassi, A. Omri, and B. Zeghami, "Effects of nanoparticles Brownian motion in a linearly/sinusoidally heated cavity with MHD natural convection in the presence of uniform heat generation/absorption," *Powder Technology*, vol. 295, pp. 69–83, 2016.
- [33] H. Upreti, A. K. Pandey, M. Kumar, and O. D. Makinde, "Ohmic heating and non-uniform heat source/sink roles on 3D Darcy–Forchheimer flow of CNTs nanofluids over a stretching surface," *Arabian Journal for Science and Engineering*, vol. 45, no. 9, pp. 7705–7717, 2020.
- [34] A. K. Pandey and M. Kumar, "MHD flow inside a stretching/shrinking convergent/divergent channel with heat generation/absorption and viscous-ohmic dissipation utilizing CU-WATER nanofluid," *Computational Thermal Sciences: An International Journal*, vol. 10, no. 5, pp. 457–471, 2018.
- [35] M. Turkyilmazoglu, "Nanofluid flow and heat transfer due to a rotating disk," *Computers and Fluids*, vol. 94, pp. 139–146, 2014.
- [36] A. Hussain, S. T. Mohyud-Din, and T. A. Cheema, "Analytical and numerical approaches to squeezing flow and heat transfer between two parallel disks with velocity slip and temperature jump," *Chinese Physics Letters*, vol. 29, no. 11, article 114705, 2012.
- [37] N. A. Alreshidi, Z. Shah, A. Dawar, P. Kumam, M. Shutaywi, and W. Watthayu, "Brownian motion and thermophoresis effects on MHD three dimensional nanofluid flow with slip conditions and joule dissipation due to porous rotating disk," *Molecules*, vol. 25, no. 3, p. 729, 2020.
- [38] A. Dawar, Z. Shah, P. Kumam et al., "Chemically reactive MHD micropolar nanofluid flow with velocity slips and variable heat source/sink," *Scientific Reports*, vol. 10, no. 1, pp. 1–23, 2020.
- [39] M. W. Ahmad, P. Kumam, Z. Shah et al., "Darcy-Forchheimer MHD couple stress 3D nanofluid over an exponentially stretching sheet through Cattaneo-Christov convective heat flux with zero nanoparticles mass flux conditions," *Entropy*, vol. 21, no. 9, p. 867, 2019.
- [40] I. Waini, A. Ishak, and I. Pop, "MHD flow and heat transfer of a hybrid nanofluid past a permeable stretching/shrinking wedge," *Applied Mathematics and Mechanics*, vol. 41, no. 3, pp. 507–520, 2020.
- [41] K. Vajravelu, K. V. Prasad, C.-O. Ng, and H. Vaidya, "MHD squeeze flow and heat transfer of a nanofluid between parallel disks with variable fluid properties and transpiration," *International Journal of Mechanical and Materials Engineering*, vol. 12, no. 1, pp. 1–14, 2017.
- [42] T. Gul, R. A. Shah, S. Islam, and M. Arif, "MHD thin film flows of a third grade fluid on a vertical belt with slip boundary conditions," *Journal of Applied Mathematics*, vol. 2013, Article ID 707286, 14 pages, 2013.
- [43] A. S. Alshomrani and T. Gul, "A convective study of  $\text{Al}_2\text{O}_3$ - $\text{H}_2\text{O}$  and Cu- $\text{H}_2\text{O}$  nano-liquid films sprayed over a stretching cylinder with viscous dissipation," *International Journal of Mechanical and Materials Engineering*, vol. 132, no. 11, pp. 1–16, 2017.
- [44] T. Gul, Kashifullah, M. Bilal, W. Alghamdi, M. I. Asjad, and T. Abdeljawad, "Hybrid nanofluid flow within the conical gap between the cone and the surface of a rotating disk," *Scientific Reports*, vol. 11, no. 1, p. 1180, 2021.
- [45] T. Gul, H. Anwar, M. A. Khan, I. Khan, and P. Kumam, "Integer and non-integer order study of the GO-W/GO-EG nanofluids flow by means of Marangoni convection," *Symmetry*, vol. 11, no. 5, p. 640, 2019.
- [46] G. Reiss and A. Hütten, "Applications beyond data storage," *Nature Materials*, vol. 4, no. 10, pp. 725–726, 2005.
- [47] D. Faivre and M. Bennet, "Magnetic nanoparticles line up," *Nature*, vol. 535, no. 7611, pp. 235–236, 2016.
- [48] G. Priyadarshana, N. Kottegoda, A. Senaratne, A. De Alwis, and V. Karunaratne, "Synthesis of magnetite nanoparticles by top-down approach from a high purity ore," *Journal of Nanomaterials*, vol. 2015, 8 pages, 2015.
- [49] Y. Zhou, C.-K. Dong, L. L. Han, J. Yang, and X. W. du, "Top-down preparation of active cobalt oxide catalyst," *ACS Catalysis*, vol. 6, no. 10, pp. 6699–6703, 2016.
- [50] U. Rashid, D. Baleanu, A. Iqbal, and M. Abbas, "Shape effect of nanosize particles on magnetohydrodynamic nanofluid flow and heat transfer over a stretching sheet with entropy generation," *Entropy*, vol. 22, no. 10, p. 1171, 2020.
- [51] H. F. Oztop and E. Abu-Nada, "Numerical study of natural convection in partially heated rectangular enclosures filled with nanofluids," *International Journal of Heat and Fluid Flow*, vol. 29, no. 5, pp. 1326–1336, 2008.
- [52] M. Sheikholeslami, M. Gorji-Bandpy, and D. D. Ganji, "Numerical investigation of MHD effects on  $\text{Al}_2\text{O}_3$ -water nanofluid flow and heat transfer in a semi-annulus enclosure using LBM," *Energy*, vol. 60, pp. 501–510, 2013.
- [53] P. Ragupathi, T. Muhammad, S. Islam, and A. Wakif, "Application of Arrhenius kinetics on MHD radiative Von Kármán Casson nanofluid flow occurring in a Darcy-Forchheimer porous medium in the presence of an adjustable heat source," *Physica Scripta*, vol. 96, article 125228, 2021.
- [54] T. V. Kármán, "Über laminare und turbulente Reibung," *ZAMM-Journal of Applied Mathematics and Mechanics/Zeitschrift für Angewandte Mathematik und Mechanik*, vol. 1, pp. 233–252, 1921.
- [55] U. Khan, S. Bilal, A. Zaib, O. D. Makinde, and A. Wakif, "Numerical simulation of a nonlinear coupled differential system describing a convective flow of Casson gold–blood nanofluid through a stretched rotating rigid disk in the presence of Lorentz forces and nonlinear thermal radiation," *Numerical Methods for Partial Differential Equations*, 2020.
- [56] R. L. Hamilton and O. K. Crosser, "Thermal conductivity of heterogeneous two-component systems," *Industrial and Engineering Chemistry Fundamentals*, vol. 1, no. 3, pp. 187–191, 1962.
- [57] E. V. Timofeeva, J. L. Routbort, and D. Singh, "Particle shape effects on thermophysical properties of alumina nanofluids," *Journal of Applied Physics*, vol. 106, no. 1, article 14304, 2009.

## Research Article

# Couple Stress Hybrid Nanofluid Flow through a Converging-Diverging Channel

Malik Zaka Ullah,<sup>1</sup> Dina Abuzaid,<sup>1</sup> M. Asma,<sup>2</sup> and Abdul Bariq <sup>3</sup>

<sup>1</sup>Department of Mathematics, Faculty of Science, King Abdulaziz University, Jeddah 21589, Saudi Arabia

<sup>2</sup>Institute of Mathematical Sciences, Faculty of Science, University of Malaya, 50603 Kuala Lumpur, Malaysia

<sup>3</sup>Department of Mathematics, Laghman University, Mehtarlam 2701, Laghman, Afghanistan

Correspondence should be addressed to Abdul Bariq; [abdulbariq.maths@lu.edu.af](mailto:abdulbariq.maths@lu.edu.af)

Received 4 September 2021; Revised 29 September 2021; Accepted 30 September 2021; Published 10 November 2021

Academic Editor: Amir Khan

Copyright © 2021 Malik Zaka Ullah et al. This is an open access article distributed under the Creative Commons Attribution License, which permits unrestricted use, distribution, and reproduction in any medium, provided the original work is properly cited.

This research work is aimed at scrutinizing the mathematical model for the hybrid nanofluid flow in a converging and diverging channel. Titanium dioxide and silver are considered solid nanoparticles while blood is considered as a base solvent. The couple stress fluid model is essentially used to describe the blood flow. The radiation terminology is also included in the energy equation for the sustainability of drug delivery. The aim is to link the recent study with the applications of drug delivery. It is well-known from the available literature that the combination of  $\text{TiO}_2$  with any other metal can vanish more cancer cells than  $\text{TiO}_2$  separately. Governing equations are altered into the system of nonlinear coupled equations the similarity variables. The Homotopy Analysis Method (HAM) analytical approach is applied to obtain the preferred solution. The influence of the modeled parameters has been calculated and displayed. The confrontation to wall shear stress and hybrid nanofluid flow growth as the couple stress parameter rises which improves the stability of the base fluid (blood). The percentage (%) increase in the heat transfer rate with the variation of nanoparticle volume fraction is also calculated numerically and discussed.

## 1. Introduction

The flow of fluids in converging/diverging channels has particularly significant applications in science and technology, such as flows in cavities and channels. The converging/divergent channels also relate to the blood flow in the arteries and capillaries. The stretching converging and diverging channels are also very significant to the blood flow due to the occurrence of stress effects. The researcher has worked in the same model for other industrial applications. Sheikholeslami et al. [1] demonstrated the effect of nanoparticles considering Jeffery fluid. Turkyilmazoglu [2], Dogonchi and Ganji [3], Xia et al. [4], and Mishra et al. [5] have considered the same model for the fluid flow using the concept of shrinking/stretching in converging/diverging channels.

Nanotechnology has refined and expanded the horizons of today's scientific world owing to its unpredicted results occurring in the field of energy, biotechnology, drugs, and therapeutics. It has also been demonstrated that stenosis is

a damaging and potentially fatal disease, so researchers attempted to eliminate the problem using nanotechnology. Researchers believe that nanotechnology can deliver innovation in treating these kinds of problems since nanoparticles can pass through tissues and cells. Following that, there is a noticeable increase in research related to the advanced progress of nanoparticles in drugs [6–9].

Shahzadi and Bilal [10] pioneered nanoparticles by revealing their dynamic and abnormal properties. Nadeem and Ijaz [11] described the use of nanoparticles to transport blood through a stenosis artery with a permeable wall. Ellahi et al. [12] reported blood flow to arteries consisting of the composite when nanoparticles were used. Nadeem and Ijaz [13] studied the effect of nanoparticles on stenotic artery hemodynamics and found them to be very helpful in reducing wall pressure with a shear rate.

There is dispersion of more nanoparticles with different thermophysical properties from hybrid nanofluids that have attracted researchers because they are widely used in the

fields of energy and medicine [14]. The case of bionanotechnology, which is a renovation and an open and innovative horizon in medicine, is one of the most auspicious applications of hybrid fluids. Numerous studies have demonstrated the effectiveness of nanoparticles in tumor targeting, therapy, and diagnosis process. Many studies have shown how effective nanoparticles are in tumor targeting, diagnosis, and treatment. It should be noted that nanoparticles have eliminated some of the shortcomings of traditional chemotherapy [15]. Liu et al. [16] investigated the use of Pt/TiO<sub>2</sub> and Au/TiO<sub>2</sub> nanocomposites, which are useful for cancer cell treatment. It was observed that the combination of TiO<sub>2</sub> with any other metal can vanish more cancer cells than TiO<sub>2</sub> separately. Silver has a wide range of biomedical uses due to its exclusive properties. The product containing silver is usually used for antimicrobial activity versus a broad spectrum of microorganisms. Moreover, experimental data suggest that Ag nanoparticles are a more ecological and biocompatible substitute to standard anti-cancer medicines [17].

Blood, the most important biological fluid, is a liquid composed of various cell types suspended in a matrix of aqueous fluid (the plasma). It should be noted that red blood cells in plasma contribute to rotary motion in the occurrence of a velocity gradient. Body tissues have an angular gyration moment as well as an angular orbital moment. As a result, blood may be assumed a non-Newtonian fluid with a constant density. Stokes' theory is one of several polar fluid theories that take into consideration [18].

Couple stress fluid applications in biological problems are gaining popularity, and they are critical from both a theoretical and practical standpoint. Blood flow can be controlled with adequate couple stress. The theory of couple stress is first time introduced by Stokes [19] in the blood flow and claimed that blood is very reasonably flowing in the vessels due to the occurrence of the couple stresses. Devakar and Iyengar [20] suggested using a couple-stress term to regulate blood flow through the human system. Similarly, the idea was further extended by Devakar and Iyengar using the isothermal conditions and have found the exact solution. Recently, Saeed et al. [21], Ahmad et al. [22], and Gul et al. [23, 24] have used the couple stress fluid terminology in the hybrid nanofluids for drug transport and medication. They have also studied the heat transfer enhancement effect on the blood flow in various geometries.

In the light of the above discussion, the novelty of this study is highlighted as follows:

- (i) According to the best of the author's knowledge, no one has tried to investigate the flow through a converging/diverging stretchable/shrinkable channel with blood as the base fluid and TiO<sub>2</sub>-Ag as nanoparticles
- (ii) This article examines a suitable background of couple stress hybrid nanofluid flow through converging/diverging stretchable/shrinkable channels
- (iii) Heat absorption/omission and thermal radiation terminologies also strengthen the novelty of the work

(iv) The system of equations is then analytically solved by HAM

(v) The statistical analysis is also performed and presented through bar charts

## 2. Formulation

Assume the steady, laminar, incompressible, and couple stress (TiO<sub>2</sub>-Ag) hybrid nanofluid, while the fluid motion is caused by the thermal radiation and a source or sink among the binary contracting/expanding channel, such that  $2\alpha$  is the angle between them. The walls of the channel are also assumed to be stretchable along the radial direction.

$$u = \frac{s}{r} = u_w. \quad (1)$$

Here,  $u = u(r, \theta)$ ,  $s$  stands for the velocity of the hybrid nanofluids and extending/contracting phenomena, respectively. The conditions ( $\alpha > 0$ ,  $\alpha < 0$ ) are used to show that the channels are divergent and convergent correspondingly. The velocity for the fluid motion is the function of both ( $r, \theta$ ). The couple stress terminology is imposed to the flow field whereas the other assumptions of [3–5] are used; the basic constituent dimensional equations of the hybrid nanofluid are taken into account.

$$\rho_{\text{hnf}} \left( \frac{u}{r} + \frac{\partial u}{\partial r} \right) = 0, \quad (2)$$

$$\rho_{\text{hnf}} \left( u \frac{\partial u}{\partial r} \right) + \left( \frac{\partial P}{\partial r} \right) = \mu_{\text{hnf}} \left( \frac{\partial}{\partial r} \left( \frac{u}{r} + \frac{\partial u}{\partial r} \right) + \frac{1}{r^2} \frac{\partial^2 u}{\partial \theta^2} \right) - \eta_0 \frac{\partial^4 u}{\partial r^4}, \quad (3)$$

$$\frac{\partial P}{\partial \theta} - 2\mu_{\text{hnf}} \frac{1}{r^2} \frac{\partial u}{\partial \theta} = 0, \quad (4)$$

$$\begin{aligned} (\rho C_p)_{\text{hnf}} \left( u \frac{\partial T}{\partial r} \right) &= k_{\text{hnf}} \left( \frac{1}{r} \frac{\partial}{\partial r} \left( r \frac{\partial T}{\partial r} \right) + \frac{1}{r^2} \frac{\partial^2 T}{\partial \theta^2} \right) \\ &\quad - \frac{1}{r} \left( \frac{1}{r} \frac{\partial}{\partial \theta} (q_{\theta, \text{rad}}) + \frac{\partial}{\partial r} (r q_{r, \text{rad}}) \right). \end{aligned} \quad (5)$$

The pressure of fluid, electromagnetic field, and radiative heat flux are presented by  $P, B_0, q_{r, \text{rad}}, q_{\theta, \text{rad}}$ .

The radiation terms are further written as

$$q_{\theta, \text{rad}} = \left( \frac{-16\sigma^* T_0^3}{3k_{f^*}} \right) \frac{\partial T}{\partial \theta}, \quad (6)$$

$$q_{r, \text{rad}} = \left( \frac{-16\sigma^* T_0^3}{3k_{f^*}} \right) \frac{\partial T}{\partial r}. \quad (7)$$

Here,  $k_{f^*}$  and  $\sigma^*$  are the absorption term and Stefan-Boltzmann constants.

TABLE 1: Properties of TiO<sub>2</sub> and blood nanofluid [18].

Viscosity	$\mu_{nf} = \mu_f / (1 - \phi_1)^{2.5}$
Density	$\rho_{nf} = \left\{ \rho_f (1 - \phi_1) + \rho_f \phi_1 (\rho_{TiO_2}) \right\}$
Specific heat	$(\rho C_p)_{nf} = \left[ (\rho C_p)_f (1 - \phi_1) + \phi_1 (\rho C_p)_{TiO_2} \right]$
Thermal conductivity	$k_{nf} = k_f (k_{TiO_2} + 2k_f + 2\phi_1 (k_f - k_{TiO_2}))^{-1} (k_{TiO_2} + 2k_f - 2\phi_1 (k_f - k_{TiO_2}))$

TABLE 2: Various thermophysical properties of TiO<sub>2</sub>-Ag are stated as [18].

Viscosity	$\mu_{hnf} = \mu_f (1 - \phi_1)^{-2.5} (1 - \phi_2)^{-2.5}$
Density	$\rho_{hnf} = (1 - \phi_2) \left\{ \phi_1 \rho_{TiO_2} + (1 - \phi_1) \rho_f \right\} + \phi_2 \rho_{TiO_2}$
Specific heat	$(\rho C_p)_{hnf} = (\rho C_p)_f (1 - \phi_2) (1 - \phi_1) + \phi_1 (\rho C_p)_{TiO_2} + \phi_2 (\rho C_p)_{Ag}$
Thermal conductivity	$k_{hnf} = k_f \left\{ (k_{TiO_2} + 2k_{nf} + 2\phi_2 (k_{nf} - k_{TiO_2}))^{-1} (k_{TiO_2} + 2k_{nf} - 2\phi_2 (k_{nf} - k_{TiO_2})) \right\} \times$ $\left\{ (k_{Ag} + 2k_f - 2\phi_1 (k_f - k_{Ag}))^{-1} (k_{Ag} + 2k_f - 2\phi_1 (k_f - k_{Ag})) \right\}$

Putting the values of equation (7) into equation (5), we have

$$(\rho C_p)_{hnf} \left( u \frac{\partial T}{\partial r} \right) = \left( k_{hnf} + \frac{16\sigma^* T_\infty^3}{3k_f^*} \right) \left[ \frac{1}{r} \frac{\partial}{\partial r} \left( r \frac{\partial T}{\partial r} \right) + \frac{1}{r^2} \frac{\partial^2 T}{\partial \theta^2} \right]. \quad (8)$$

In the above equations,  $\eta_0$  is the couple stress term; also,  $\rho_{hnf}$ ,  $\mu_{hnf}$ ,  $(\rho C_p)_{hnf}$ , and  $k_{hnf}$  represent density, viscosity, density, and specific heat; the thermal conductivity of the hybrid nanofluids such that hnf stands for hybrid nanofluid.

**2.1. Properties of the Materials.** Initially, nanoparticles (titanium) are dispersed in the bloodstream (base fluid) to produce one (mono-nano fluid). (Silver) is then distributed as an additional nanoparticle to form the (hybrid nanofluid). On this occasion, TiO<sub>2</sub> represents (titanium dioxide nanomaterial) and silver (Ag nanoparticles) and subscript  $f$  describes blood (base fluid). In Tables 1 and 2,  $\phi_1$  and  $\phi_2$  state the volume fraction of TiO<sub>2</sub> and Ag nanoparticles, where  $\phi_1 = \phi_2 = 0$  refers to the base fluid.

**2.2. Initial and Boundary Conditions.** The auxiliary conditions at boundaries are

$$\left. \begin{aligned} u = r^{-1} u_c, \quad \frac{\partial T}{\partial \theta} = u \frac{\partial T}{\partial r} = 0, \text{ at } \theta \longrightarrow 0, r \neq 0 \\ u = r^{-1} s = u_w, T = r^{-2} T_w \text{ as } \theta \longrightarrow \pm \alpha \end{aligned} \right\}. \quad (9)$$

**2.3. Introduction of Nondimensional Variables.** In the case of the radial flow, equation (1) reduced to

$$F(\theta) = ru(r, \theta). \quad (10)$$

The nondimensional transformation is defined as

$$F(\eta) = (u_c)^{-1} F(\theta), \Theta(\eta) = (r^2 T) T_w^{-1}, \quad \eta = \theta \alpha^{-1}. \quad (11)$$

The use of (10) and (11) and thermophysical properties alter equations (3)–(5) in the simplified form as

$$F''' + 2\alpha \text{Re} \frac{\rho_{hnf} \mu_f}{\rho_f \mu_{hnf}} FF' + 4\alpha^2 F' - 24\alpha^2 k^* F' = 0, \quad (12)$$

$$\left( \frac{k_{hnf}}{k_f} + Rd \right) \Theta'' + \alpha^2 \left[ \frac{(\rho C_p)_{hnf}}{(\rho C_p)_f} 2 \text{Pr} F\Theta + 4 + 4Rd\Theta \right] = 0. \quad (13)$$

The simplified form of the physical conditions are stated as

$$\left. \begin{aligned} F = 1, \Theta' = F' = 0, \text{ at } \eta = 0 \\ F = \lambda, \Theta = 1, \text{ at } \eta = \pm 1 \end{aligned} \right\}. \quad (14)$$

Here,  $\lambda = s/u_c > 0$  is the stretching parameter,  $\lambda = s/u_c < 0$  is a shrinking parameter,  $Rd = 16\sigma^* T_\infty^3 / 3k_f k_f^*$  is radiation parameter,  $\text{Re} = \rho \alpha u_c / \nu_f$  is the Reynolds number,  $\text{Pr} = (\mu C_p)_f / k_f$  is the Prandtl number, and  $k^* = \eta_0 / \mu r^2$  is the couple stress parameter.

**2.4. Drag Force and Heat Transfer Rate.** The significant parameters of curiosity are defined as

$$u_c^2 \rho_f C_f = \mu_{hnf} \left( \frac{1}{r} \frac{\partial u}{\partial \theta} \right) \Big|_{\theta=\pm\alpha}, \quad (15)$$

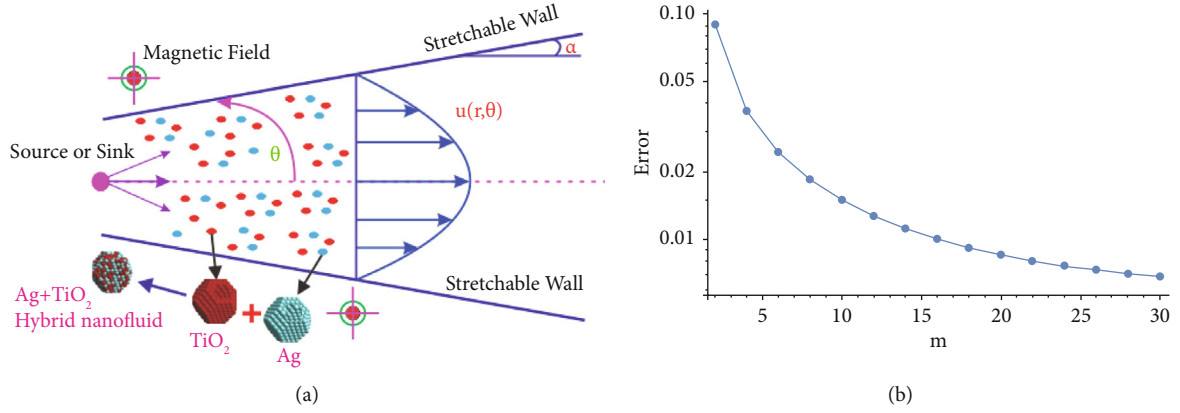


FIGURE 1: (a) The geometry of the problem and (b) the HAM method.

$$T_w \text{Nu} = \left( \frac{16\sigma^* T_\infty^3}{3k_f k_f^*} + \frac{k_{\text{hnf}}}{k_f} \right) \frac{\partial T}{\partial \theta} \Big|_{\theta=\pm\alpha}. \quad (16)$$

The alteration used for equation (16) and the simplified form is attained as

$$C_f = \frac{1}{\text{Re}} \frac{\mu_{\text{hnf}}}{\mu_f} |f'(\pm 1)|, \quad (17)$$

$$\text{Nu} = \frac{1}{\alpha} \left| \left( Rd + \frac{k_{\text{hnf}}}{k_f} \right) \Theta'(\pm 1) \right|.$$

### 3. Solution Methodology

The series solution is one of the valued methods to handle nonlinear problems. Nonlinear problems usually arise in the field of science and engineering. HAM is one of the latest and fast convergence techniques and is frequently used in the solution of nonlinear and coupled equations. The BVPh 1.0 and BVPh 2.0 are the latest packages of HAM that enhance the convergence of the proposed problems. These packages are very helpful in the rapid convergence, and one can use the BVPh 2.0 package up to the 100th iterations easily. The idea of HAM was first introduced by Liao [25]. The idea is further improved by the same author by introducing the new packages [26]. These packages are frequently used like [27–32].

The feedback problem (12)–(18) was resolved by the HAM-BVPh 2.0 technique. The estimate of the iterations is utilized up to the 30th order. The trial solution or initial solution is required for the HAM solution. The zeroth-order solution is obtained as

$$F_0(\eta) = 1 - \eta^2(1 - \lambda) \text{ and } \Theta_0(\eta) = 1. \quad (18)$$

Equations (12)–(14) are set under the planned packaging and presented as

TABLE 3: Numerous thermophysical properties are defined as [18].

Solid material and base fluid	$c_p$ (J/kgK)	$k$ (W/mK)	$\rho$ (Kg/m <sup>3</sup> )
TiO <sub>2</sub> (titanium dioxide)	686.2	8.954	4250
Silver: Ag	235	429	10500
Blood	3594	0.492	1063

$$\lambda_p^F = \frac{1}{p+1} \sum_{k=1}^p \left[ \Phi_F \left( \sum_{j=1}^l F(\eta) \right)_{\eta=kjp} \right]^2,$$

$$\lambda_p^\Theta = \frac{1}{p+1} \sum_{k=1}^p \left[ \left( \sum_{j=1}^l F(\eta) \right)_{\eta=kjp} \Phi_\Theta \left( \sum_{j=1}^l \Theta(\eta) \right)_{\eta=kjp} \right]^2. \quad (19)$$

The sum of the two components in the form of square residual errors is displayed as

$$\lambda_p^{\text{Total}} = \lambda_p^F + \lambda_p^\Theta. \quad (20)$$

The numerical results of the converging parameter are obtained as

$$0.130021 \leq h_f \leq -1.203417, \quad (21)$$

$$0.120432 \leq h_\theta \leq -0.8992310.$$

The range of convergence control parameters is used to find out the physical and numeric results.

### 4. Results and Discussion

The flow of the blood-based hybrid nanofluent consisting of TiO<sub>2</sub> and Ag has been considered in the converging and diverging channel. The heat transfer mechanism and medication are the main purposes of the proposed model. The main finding of the obtained results is shown physically and numerically. The geometry of the problem and convergence controlling sketches are demonstrated in Figures 1(a)

TABLE 4: Comparison between the present work with previous work considering common parameters only.

Re	$F''(\pm 1),$ $(\alpha = 5^0)$ [3]	$F''(\pm 1)$ $(\alpha = 5^0)$ [4]	$F''(\pm 1)$ $(\alpha = 5^0)$ [5]	$F''(\pm 1)$ $(\alpha = 5^0)$ [Present]	$F''(\pm 1),$ $(\alpha = -5^0)$ [3]	$F''(\pm 1)$ $(\alpha = -5^0)$ [4]	$F''(\pm 1)$ $(\alpha = -5^0)$ [5]	$F''(\pm 1)$ $(\alpha = -5^0)$ [Present]
1	1.86420	1.86431	1.86412	1.86701	0.77420	0.77432	0.77411	0.77703
2	1.88644	1.88652	1.88631	1.88912	0.79531	0.79542	0.79520	0.79821
3	1.90422	1.90434	1.90412	1.907	0.80214	0.80223	0.80205	0.80501

TABLE 5: Influence of parameter versus  $-Re C_f$ .

$\phi_1, \phi_2$	Re	$k^*$	$-Re C_f$	$F(\eta)$	$-Re C_f$	$-Re C_f$
			$(\alpha > 0)$		$(\alpha < 0)$	$(\alpha < 0)$
			TiO <sub>2</sub> + Ag		TiO <sub>2</sub> + Ag	TiO <sub>2</sub>
0.00	0.1	0.1	0.39586	0.37369	1.29495	1.27531
0.01			0.41871	0.40651	1.27122	1.24531
0.01			0.434932	0.413731	1.28712	1.2661
	0.2		0.49638	0.47416	1.38542	1.36321
	0.4		0.597493	0.575294	1.49615	1.42402
		0.2	0.46735	0.44513	1.35621	1.13032
		0.4	0.515401	0.504021	1.40487	1.38612

TABLE 6: Nusselt number  $Nu_x$  versus physical parameters.

Rd	$\phi_1, \phi_2$	$-Nu$	$-Nu$	$-Nu$	$-Nu$
		TiO <sub>2</sub> &Ag	TiO <sub>2</sub>	TiO <sub>2</sub> &Ag	TiO <sub>2</sub>
		$\alpha > 0$	$\alpha < 0$	$\alpha > 0$	$\alpha < 0$
0.2	0.01	9.41571	9.33102	11.39253	11.29123
0.4		9.47321	9.37321	11.50320	11.32134
0.6		9.53631	9.41241	11.63103	11.53161
	0.02	9.44645	9.24609	11.45708	11.38163
	0.03	9.65435	9.58479	11.78790	11.67849

and 1(b). The thermophysical properties of the materials are presented in Tables 1–3.

Table 4 shows the assessment of the current work with the available literature and the closed agreement to authenticate the validation of the problem. The drag force on the upper and lower walls is calculated for the embedding parameters and demonstrated in Table 5. The accumulative growth in the values of the constraints is used to keep the convergent range of the proposed problem. The drag force rises with the increment in these parameters ( $\phi_1, \phi_2, Re,$  and  $k^*$ ) for both nanofluids and hybrid nanofluids. The calculated increase shows that the resistive force is more effective by using the hybrid nanofluid TiO<sub>2</sub> + Ag at both the lower and upper walls of the channels. Furthermore, the friction force is efficiently working in the converging channel as compared to the other one.

The heat transfer rate is calculated numerically using the embedded parameters, and the results are exhibited in Table 6. The augmentation in the values of the parameters  $Rd, \phi_1,$  and  $\phi_2$  progresses the heat transfer rate ultimately. The attained results show that the heat transfer rate is more

immediate by using the (TiO<sub>2</sub> + Ag) hybrid nanofluids. The heat transfer rate stimulates fluid motion by controlling the viscous effect. The TiO<sub>2</sub> material works as the treatment material in cancer therapy while the stability in the blood is controlled through silver. The (%) wise increase in the heat transfer rate versus the nanoparticle volume fraction has been calculated and displayed in Table 7. The hybrid nanofluid improves the heat transfer analysis as compared to the other traditional fluids.

Figures 1–4 describe the influence of the physical parameters ( $\phi_1, \phi_2, Re, k^*$ ), on the velocity  $F(\eta)$  considering both converging and divergent channels. The parts (a, b) and (c, d) of each figure show the same effect in 2D and 3D expressions. The parameters ( $\phi_1, \phi_2$ ) decline the fluid motion  $F(\eta)$  for its higher values using the extending/convergent and contracting/divergent channels as revealed in Figures 2(a)–2(d). The nanoparticle dispersion in the base fluid enhances the viscous effect of the base solvent and improves the cohesive forces among the fluid molecules to resist the fluid motion.



TABLE 7: % analysis versus  $Nu_x$ .

$\phi_1, \phi_2$	-Nu ( $\alpha > 0$ )		-Nu ( $\alpha > 0$ )		-Nu ( $\alpha < 0$ )	% ( $\alpha < 0$ )	-Nu ( $\alpha < 0$ )	% ( $\alpha < 0$ )
	(TiO <sub>2</sub> &Ag)	%( $\alpha > 0$ )	TiO <sub>2</sub>	%( $\alpha > 0$ )	TiO <sub>2</sub> &Ag	( $\alpha < 0$ )	TiO <sub>2</sub>	( $\alpha < 0$ )
0.0	9.23445	.....	9.23445	.....	11.14515	.....	11.14515	.....
0.01	9.41871	1.997	9.33402	0.909	11.39553	2.249	11.30423	1.429
0.02	9.52403	3.138	9.4261	2.078	11.54584	3.598	11.44363	2.68
0.03	9.63442	4.334	9.50511	2.933	11.68721	4.866	11.57623	3.87
0.04	9.74832	5.568	9.61612	4.136	11.80628	5.935	11.68198	4.82

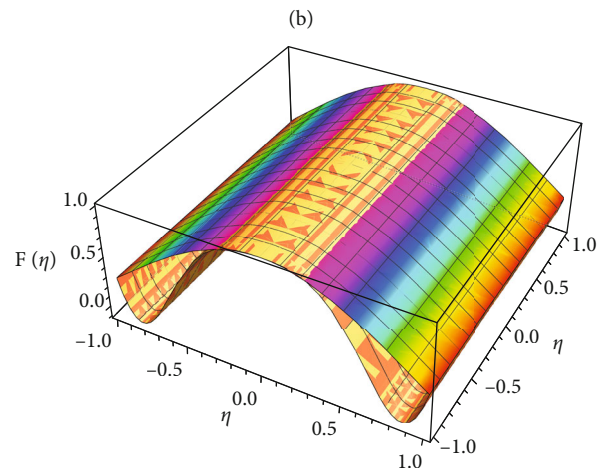
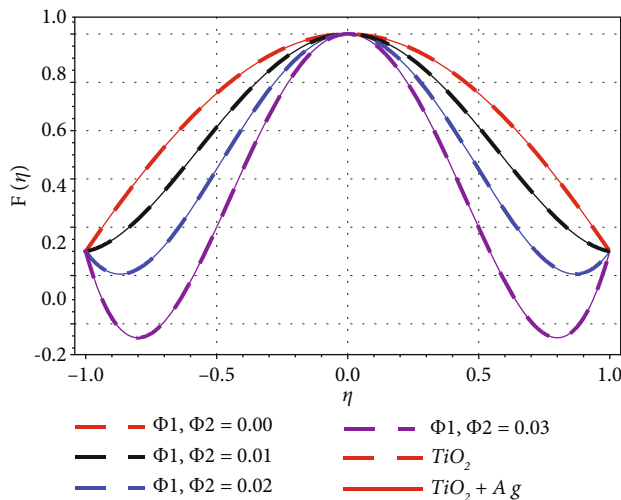
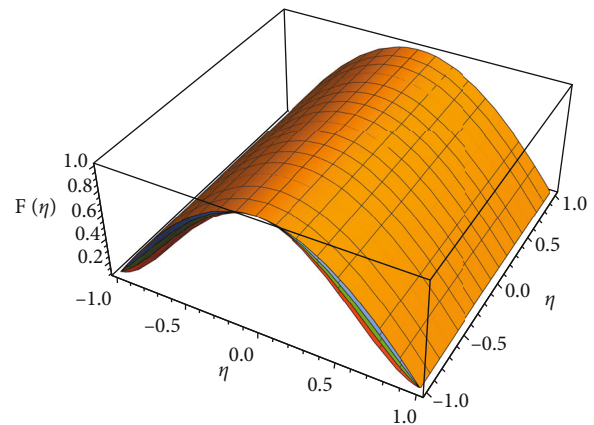
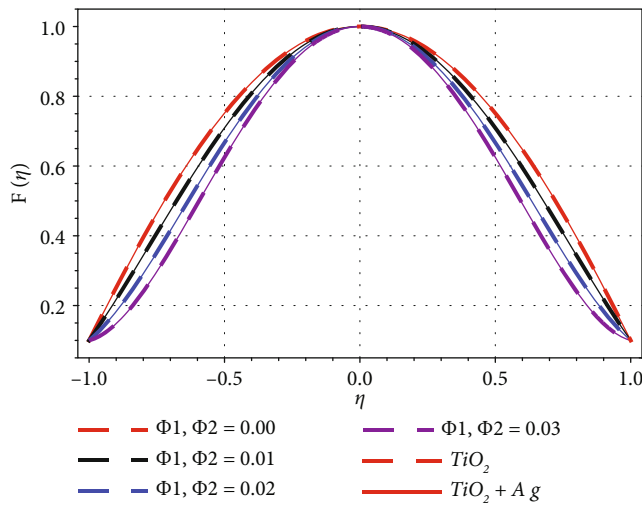


FIGURE 2:  $F(\eta)$  versus  $\phi_1, \phi_2$  in stretching/convergent circumstance with  $\alpha = -5^\circ, 5^\circ$ .

Figures 3(a)–3(d) show the effect of  $Re$  on  $F(\eta)$  in the case of extending/convergence and narrowing/diverging. It can be witnessed that the increases in Reynolds number cause an increase in extending/convergent case, which can be observed from Figures 3(a) and 3(b) while a reverse result is obtained in the contracting/divergent case because the

growth in Reynolds number causes a decline in the fluid motion, in this case, that can be seen in Figures 3(c) and 3(d). Figures 3(a)–3(d) show the effect of  $Re$  on  $F(\eta)$  in the case of extending/convergence and narrowing/diverging. It can be witnessed that the increases in Reynolds number cause an increase in extending/convergent case, which can

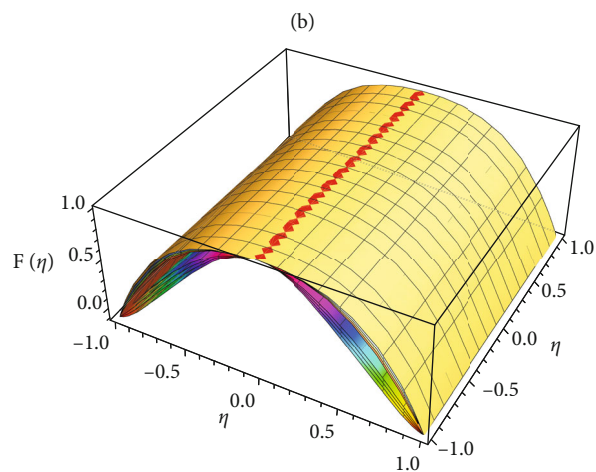
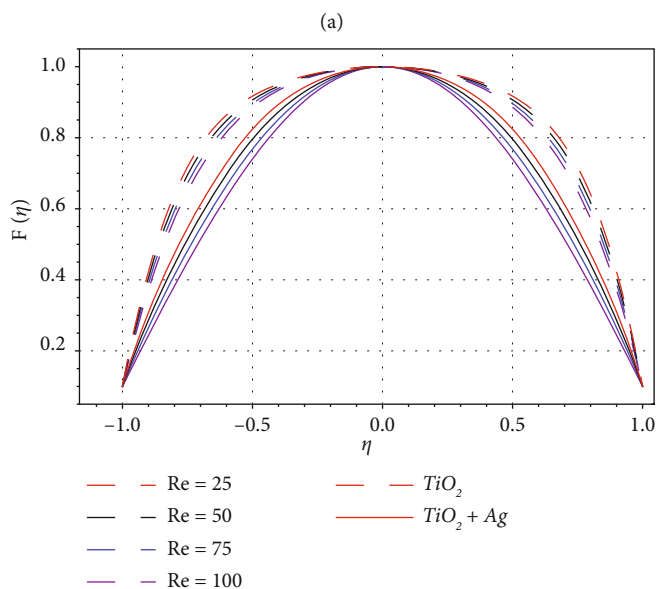
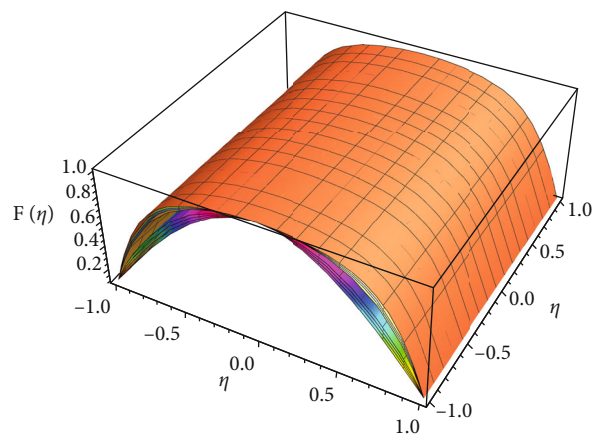
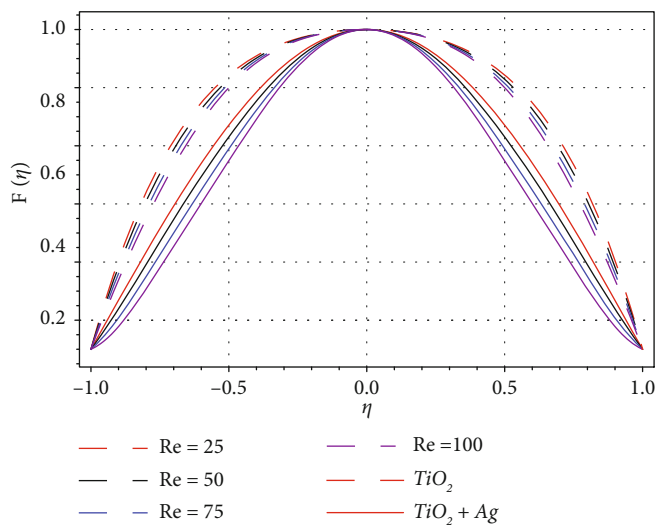


FIGURE 3: (a–d)  $F(\eta)$  versus Re stretching/convergent circumstance with  $\alpha = -5^\circ, 5^\circ$ .

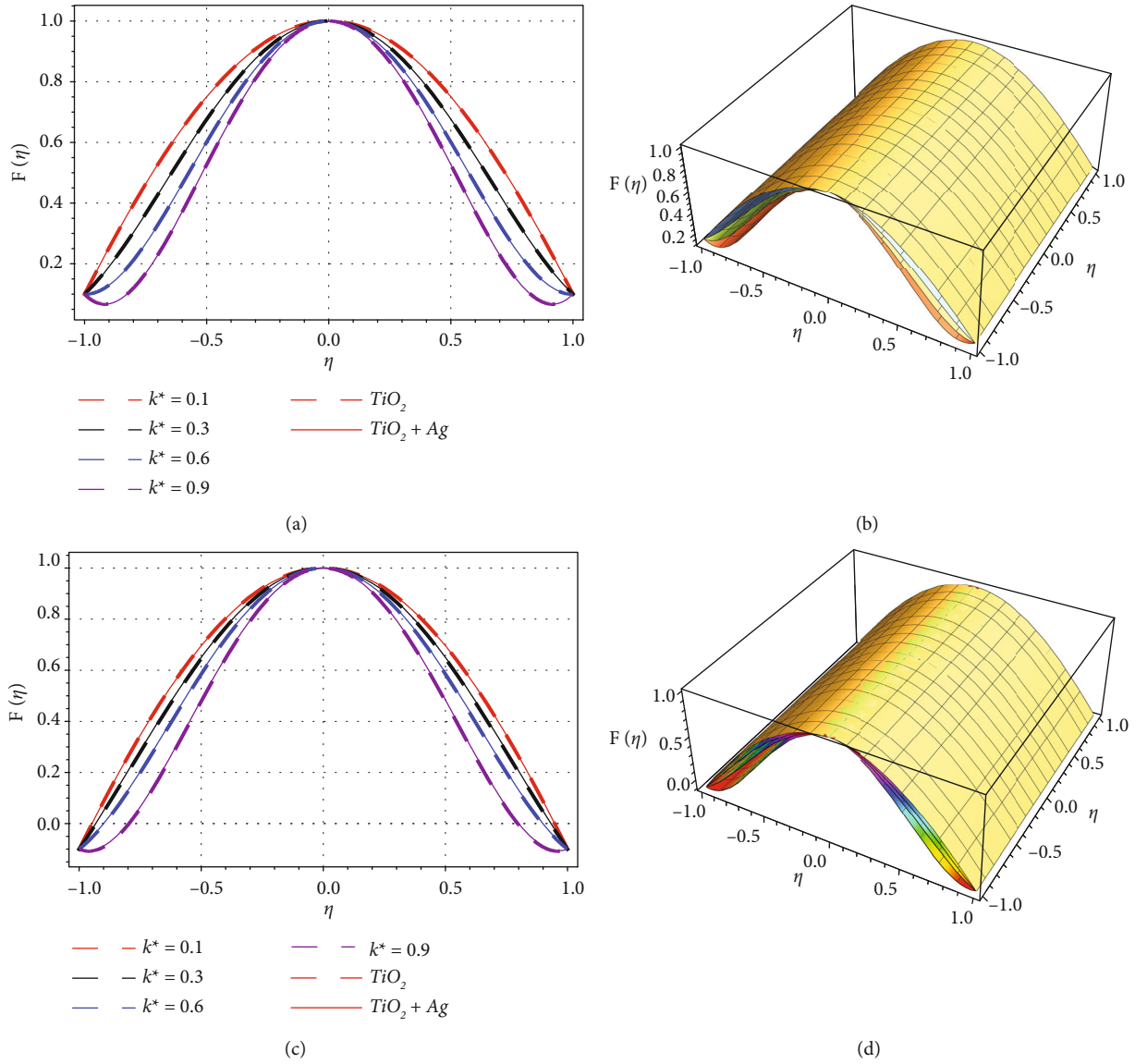
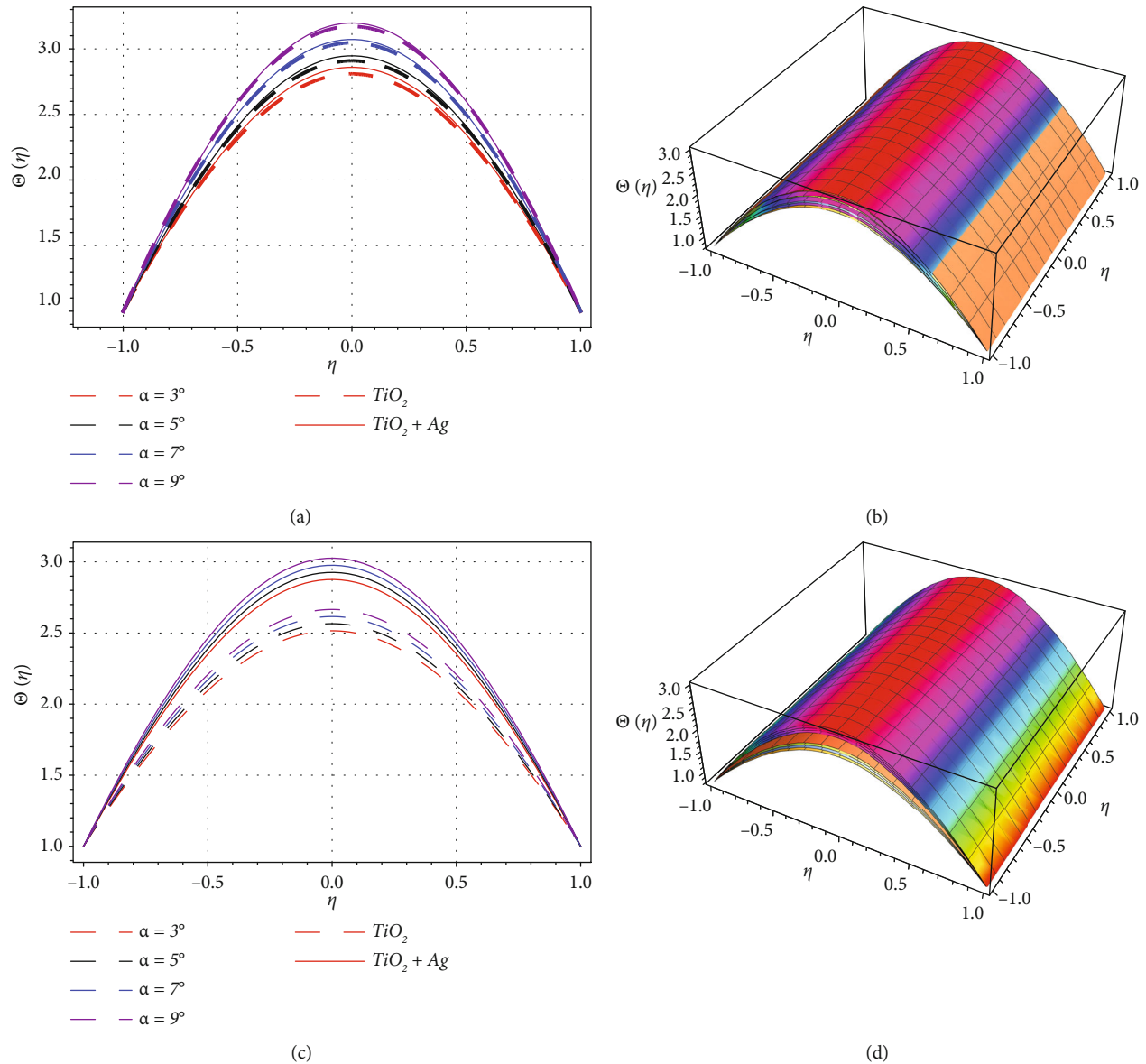


FIGURE 4: (a–d)  $F(\eta)$  versus  $k^*$  in stretching/convergent circumstance with  $\alpha = -5^\circ, 5^\circ$ .

FIGURE 5: (a–d)  $\Theta(\eta)$  versus  $\alpha$ .

be observed from Figures 3(a) and 3(b) while a reverse result is obtained in the contracting/divergent case because the growth in Reynolds number causes a decline in the fluid motion, in this case, that can be seen in Figures 3(c) and 3(d).

Figures 4(a)–4(d) indicate the influence of  $(k^*)$  on  $F(\eta)$  in extending/convergent and contracting/divergent cases. The fluid motion decays as increasing the value of  $(k^*)$ , that is, fluid motion decline with the improvement in the values of  $(k^*)$ .

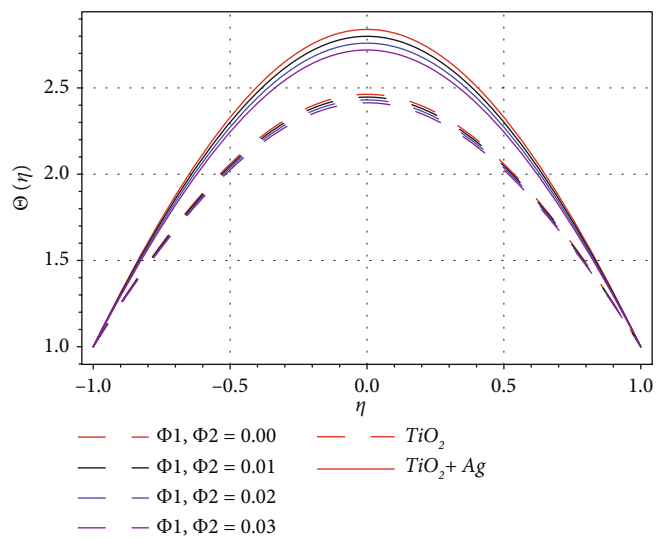
Figures 5(a)–5(d) and 6(a)–6(d) represent the special effects of  $\alpha$  and  $(\phi_1, \phi_2)$  temperature distribution  $\Theta(\eta)$  for extending/convergent and contracting/divergent cases.

The larger values of  $\alpha$  augmented the temperature distribution in each case as shown in Figures 5(a)–5(d). The enlarging values of the parameters  $\phi_1$  and  $\phi_2$  in the specific

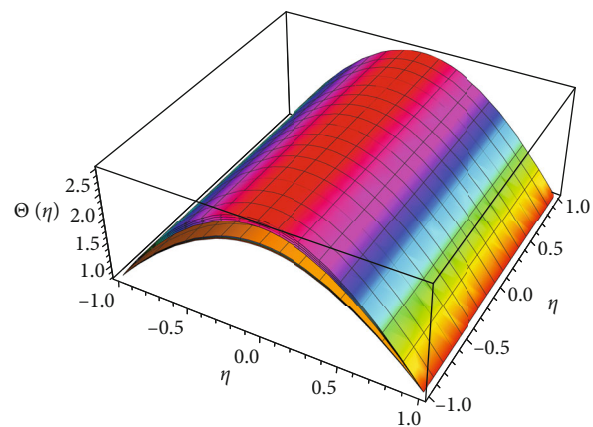
domain enhance the temperature distribution and are revealed in Figures 6(a)–6(d). In each case, the accumulative growth provides the increasing effect, and this improvement is more effective using the hybrid nanofluids.

The comparison of the obtained results is compared with the available literature [3–5] and displayed in Figures 7(a) and 7(b) considering diverging and converging cases of the channel. The closed agreement has been achieved while choosing the common parameter  $Re$ . The influence of the nanoparticle volume fraction versus the skin friction has been shown in Figures 7(c) and 7(d) for both cases. The augmentation in the values of  $\phi_1, \phi_2$  improves the resistive force to rise the drag force at the upper and lower walls. The influence is relatively strong using the hybrid nanofluids.

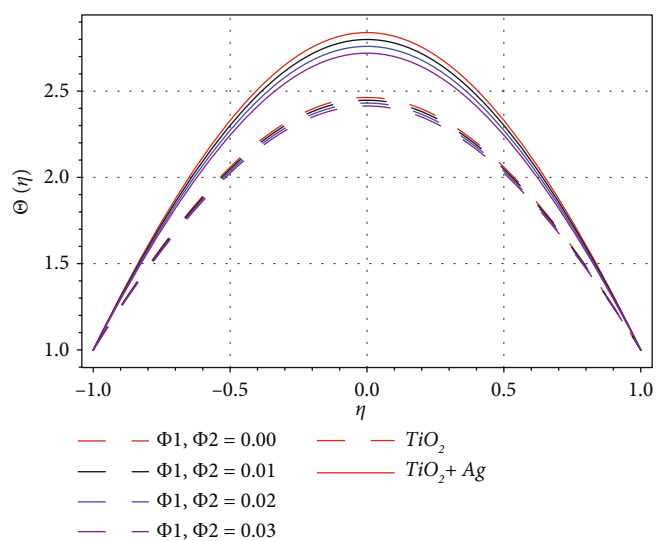
The percentage increase in the heat transfer rate has been revealed in Figures 8(a)–8(d). The values of the



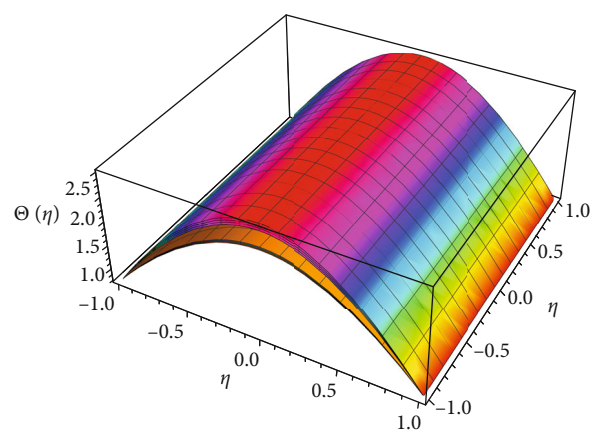
(a)



(b)



(c)



(d)

FIGURE 6: (a-d)  $\Theta(\eta)$  versus  $\phi_1, \phi_2$ .

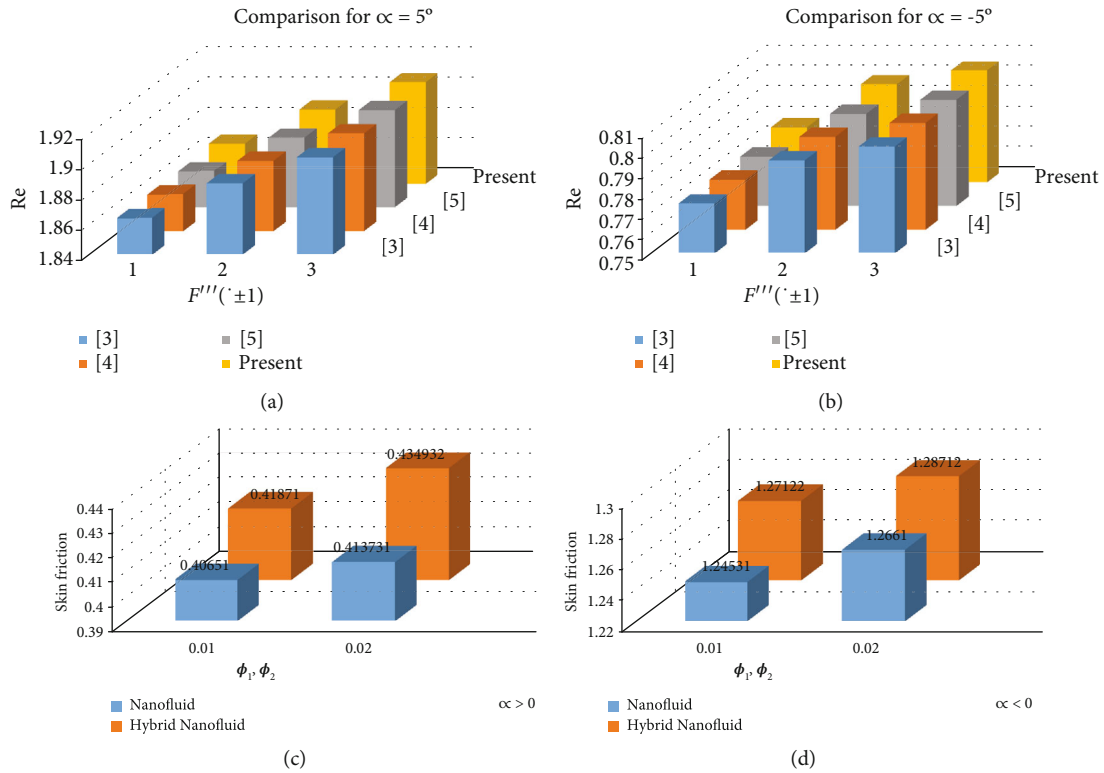


FIGURE 7: (a-d) Matching of the current work with published literature [3-5] and  $C_f$  versus  $\phi_1, \phi_2$ .

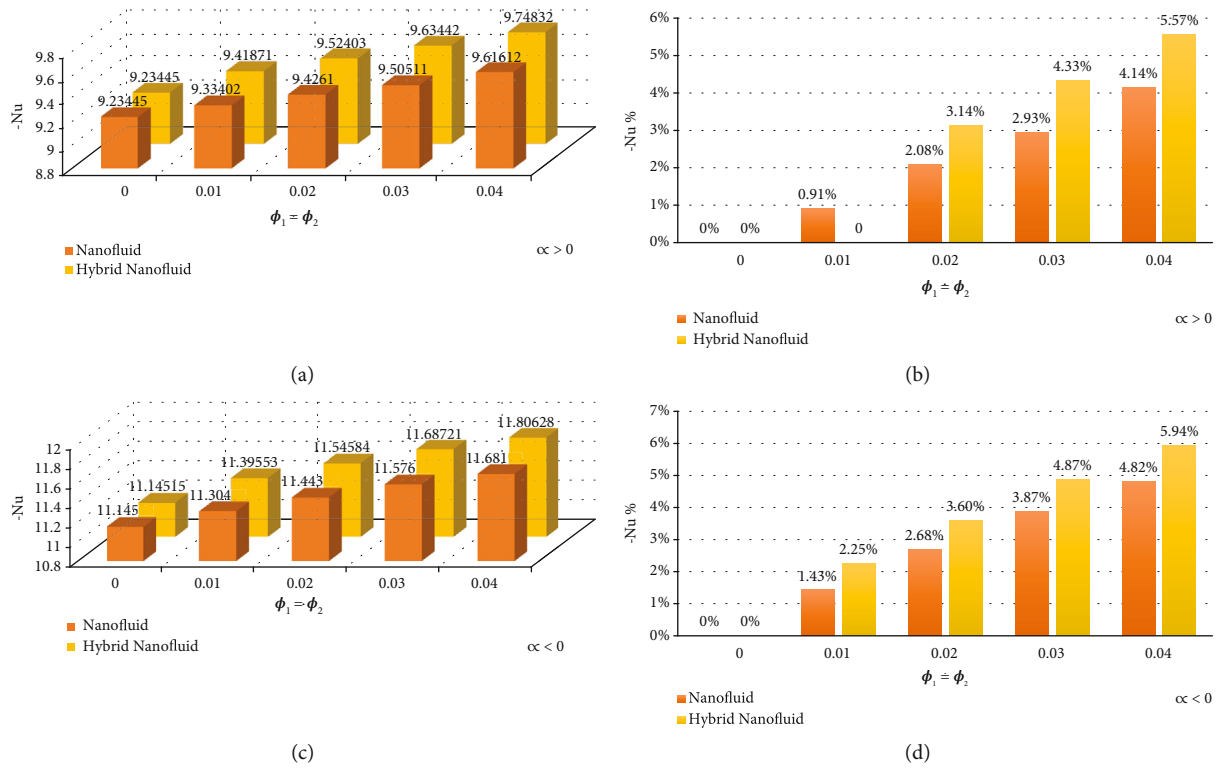


FIGURE 8: (a-d) Matching of the current work with published literature [3-5] and  $C_f$  versus  $\phi_1, \phi_2$ .

nanoparticle volume fraction are used up to 3% as ( $\phi_1, \phi_2 = 0.0, 0.01, 0.02, 0.03$ ). The comparative analysis of the nanofluid and hybrid nanofluid is shown in Figures 8(a) and 8(c) for the diverging and converging cases of the channel, while the % analysis has been performed in Figures 8(b) and 8(d) for the same cases, respectively. The % increase is more appropriate by using the hybrid nanofluids in both  $\alpha > 0$  and  $\alpha < 0$ .

## 5. Conclusions

The current article explores the blood flow across a converging/diverging channel with stretchable/shrinkable walls with couple stress for the application of drug delivery. The consequences of the converging/diverging parameter, couple stress parameter, and solid nanoparticles are incorporated.

To the best of our knowledge and belief, the converging/diverging channel including blood as a base fluid does not exist in the existing literature. Furthermore, the work also extended using the Ag and TiO<sub>2</sub> hybrid nanofluid. Couple stress terminologies are also used as a novelty in the current problem.

The key conclusions of the existing study are as follows:

- (i) The rising values of solid nanoparticles  $\phi_1, \phi_2$  enhance the energy transmission rate, and the impact is relatively larger in the case of hybrid nanofluid
- (ii) The velocity field declines with the accumulative values of the parameters  $\phi_1, \phi_2$ , and Re
- (iii) The couple stress parameter  $k^*$  has a significant role in blood flow analysis and declines the hybrid nanofluid motion
- (iv) TiO<sub>2</sub> + Ag hybrid nanofluids have an important role in the Escherichia coli culture to evaluate their antibacterial strength
- (v) The % analysis shows that hybrid nanofluids are more efficient for heat transfer analysis
- (vi) The pH values improve with the increment in heat transfer. That is why the purpose of the recent study is to use the TiO<sub>2</sub> + Ag hybrid nanofluids for medication

## Data Availability

All the relevant data exist in the manuscript.

## Conflicts of Interest

The authors declare that they have no conflict of interest.

## Acknowledgments

The Deanship of Scientific Research (DSR) at King Abdulaziz University, Jeddah, Saudi Arabia, has funded this project, under grant no. KEP-37-130-42.

## References

- [1] M. Sheikholeslami, D. D. Ganji, H. R. Ashorynejad, and H. B. Rokni, "Analytical investigation of Jeffery-Hamel flow with high magnetic field and nanoparticle by Adomian decomposition method," *Applied Mathematics and Mechanics*, vol. 33, no. 1, pp. 25–36, 2012.
- [2] M. Turkyilmazoglu, "Extending the traditional Jeffery-Hamel flow to stretchable convergent/divergent channels," *Computers and Fluids*, vol. 100, pp. 196–203, 2014.
- [3] A. S. Dogonchi and D. D. Ganji, "Investigation of MHD nanofluid flow and heat transfer in a stretching/shrinking convergent/divergent channel considering thermal radiation," *Journal of Molecular Liquids*, vol. 220, pp. 592–603, 2016.
- [4] W. F. Xia, M. I. Khan, S. U. Khan, F. Shah, and M. I. Khan, "Dynamics of unsteady reactive flow of viscous nanomaterial subject to Ohmic heating, heat source and viscous dissipation," *Ain Shams Engineering Journal*, vol. 2021, 2021.
- [5] A. Mishra, A. K. Pandey, A. J. Chamkha, and M. Kumar, "Roles of nanoparticles and heat generation/absorption on MHD flow of Ag-H<sub>2</sub>O nanofluid via porous stretching/shrinking convergent/divergent channel," *Journal of the Egyptian Mathematical Society*, vol. 28, no. 1, 2020.
- [6] S. Zuhra, N. S. Khan, Z. Shah, S. Islam, and E. Bonyah, "Simulation of bioconvection in the suspension of second grade nanofluid containing nanoparticles and gyrotactic microorganisms," *AIP Advances*, vol. 8, no. 10, p. 105210, 2018.
- [7] S. M. Moghimi, A. C. Hunter, and J. C. Murray, "Nanomedicine: current status and future prospects," *The FASEB Journal*, vol. 19, pp. 311–330, 2005.
- [8] Z. Shah, M. Sheikholeslami, Ikramullah, and P. Kumam, "Influence of nanoparticles inclusion into water on convective magneto hydrodynamic flow with heat transfer and entropy generation through permeable domain," *Case Studies in Thermal Engineering*, vol. 21, p. 100732, 2020.
- [9] M. G. Reddy and O. D. Makinde, "Magneto hydrodynamic peristaltic transport of Jeffrey nanofluid in an asymmetric channel," *Journal of Molecular Liquids*, vol. 223, pp. 1242–1248, 2016.
- [10] I. Shahzadi and S. Bilal, "A significant role of permeability on blood flow for hybrid nanofluid through bifurcated stenosed artery: drug delivery application," *Computer Methods and Programs in Biomedicine*, vol. 187, p. 105248, 2020.
- [11] S. Nadeem and S. Ijaz, "Theoretical analysis of metallic nanoparticles on blood flow through stenosed artery with permeable walls," *Physics Letters A*, vol. 379, pp. 542–554, 2015.
- [12] R. Ellahi, S. U. Rahman, S. Nadeem, and N. S. Akbar, "Blood flow of nanofluid through an artery with composite stenosis and permeable walls," *Applied Nanoscience*, vol. 48, no. 4, pp. 919–926, 2013.
- [13] S. Nadeem and S. Ijaz, "Theoretical examination of nanoparticles as a drug carrier with slip effects on the wall of stenosed arteries," *International Journal of Heat and Mass Transfer*, vol. 93, pp. 1137–1149, 2016.
- [14] S. Dinarvand, M. Nademi Rostami, R. Dinarvand, and I. Pop, "Improvement of drug delivery micro-circulatory system with a novel pattern of CuO-Cu/blood hybrid nanofluid flow towards a porous stretching sheet," *International Journal of Numerical Methods for Heat & Fluid Flow*, vol. 29, no. 11, pp. 4408–4429, 2019.
- [15] B. Bahrami, M. Hojjat-Farsangi, H. Mohammadi et al., "Nanoparticles and targeted drug delivery in cancer therapy," *Immunology Letters*, vol. 190, pp. 64–83, 2017.

- [16] L. Liu, P. Miao, Y. Xu, Z. Tian, Z. Zou, and G. Li, "Study of Pt/TiO<sub>2</sub> nanocomposite for cancer-cell treatment," *Journal of Photochemistry and Photobiology B: Biology*, vol. 98, no. 3, pp. 207–210, 2010.
- [17] H. Shojaie Chahregh and S. Dinarvand, "TiO<sub>2</sub>-Ag/blood hybrid nanofluid flow through an artery with applications of drug delivery and blood circulation in the respiratory system," *International Journal of Numerical Methods for Heat & Fluid Flow*, vol. 30, no. 11, pp. 4775–4796, 2020.
- [18] V. K. Stokes, "Couple Stresses in Fluids," in *Theories of Fluids with Microstructure*, pp. 34–80, Springer, Berlin, Heidelberg, 1984.
- [19] L. M. Srivastava, "Flow of couple stress fluid through stenotic blood vessels," *Journal of Biomechanics*, vol. 18, no. 7, pp. 479–485, 1985.
- [20] M. Devakar and T. K. V. Iyengar, "Stokes' problems for an incompressible couple stress fluid," *Nonlinear Analysis: Modelling and Control*, vol. 13, no. 2, pp. 181–190, 2008.
- [21] A. Saeed, A. Alsubie, P. Kumam, S. Nasir, T. Gul, and W. Kumam, "Blood based hybrid nanofluid flow together with electromagnetic field and couple stresses," *Scientific Reports*, vol. 11, no. 1, pp. 1–18, 2021.
- [22] M. W. Ahmad, P. Kumam, Z. Shah et al., "Darcy–Forchheimer MHD couple stress 3D nanofluid over an exponentially stretching sheet through Cattaneo–Christov convective heat flux with zero nanoparticles mass flux conditions," *Entropy*, vol. 21, no. 9, p. 867, 2019.
- [23] T. Gul, A. Qadeer, W. Alghamdi, A. Saeed, S. M. Mukhtar, and M. Jawad, "Irreversibility analysis of the couple stress hybrid nanofluid flow under the effect of electromagnetic field," *International Journal of Numerical Methods for Heat & Fluid Flow*, vol. ahead-of-print, 2021.
- [24] T. Gul, B. Ali, W. Alghamdi et al., "Mixed convection stagnation point flow of the blood based hybrid nanofluid around a rotating sphere," *Scientific Reports*, vol. 11, no. 1, 2021.
- [25] S. J. Liao, "An explicit, totally analytic approximate solution for Blasius' viscous flow problems," *International Journal of Non-Linear Mechanics*, vol. 34, no. 4, pp. 759–778, 1999.
- [26] S. Liao, "An optimal homotopy-analysis approach for strongly nonlinear differential equations," *Communications in Nonlinear Science and Numerical Simulation*, vol. 15, no. 8, pp. 2003–2016, 2010.
- [27] T. Gul, R. S. Gul, W. Noman et al., "CNTs-Nanofluid flow in a rotating system between the gap of a disk and cone," *Physica Scripta*, vol. 95, no. 12, p. 125202, 2020.
- [28] T. Gul, M. Z. Ullah, A. K. Alzahrani, Z. Zaheer, and I. S. Amiri, "MHD thin film flow of kerosene oil based CNTs nanofluid under the influence of Marangoni convection," *Physica Scripta*, vol. 95, no. 1, article 015702, 2020.
- [29] A. Saeed and T. Gul, "Bioconvection Casson nanofluid flow together with Darcy-Forchheimer due to a rotating disk with thermal radiation and Arrhenius activation energy," *SN Applied Sciences*, vol. 3, no. 1, 2021.
- [30] A. Khan, A. Saeed, A. Tassaddiq et al., "Bio-convective micro-polar nanofluid flow over thin moving needle subject to Arrhenius activation energy, viscous dissipation and binary chemical reaction," *Case Studies in Thermal Engineering*, vol. 25, p. 100989, 2021.
- [31] F. Ahmad, T. Gul, I. Khan et al., "MHD thin film flow of the Oldroyd-B fluid together with bioconvection and activation energy," *Case Studies in Thermal Engineering*, vol. 27, article 101218, 2021.
- [32] A. K. Alzahrani, M. Z. Ullah, A. S. Alshomrani, and T. Gul, "Hybrid nanofluid flow in a Darcy-Forchheimer permeable medium over a flat plate due to solar radiation," *Case Studies in Thermal Engineering*, vol. 26, article 100955, 2021.



## Research Article

# Numerical Investigation of Chemical Schnakenberg Mathematical Model

Faiz Muhammad Khan,<sup>1</sup> Amjad Ali,<sup>1</sup> Nawaf Hamadneh ,<sup>2</sup> Abdullah,<sup>1</sup> and Md Nur Alam <sup>3</sup>

<sup>1</sup>Department of Mathematics and Statistics, University of Swat, Pakhtunkhwa, Pakistan

<sup>2</sup>Department of Basic Sciences, College of Science and Theoretical Studies, Saudi Electronic University, Riyadh 11673, Saudi Arabia

<sup>3</sup>Department of Mathematics, Pabna University of Science and Technology, Pabna 6600, Bangladesh

Correspondence should be addressed to Nawaf Hamadneh; nhamadneh@seu.edu.sa and Md Nur Alam; nuralam.pstu23@gmail.com

Received 20 September 2021; Accepted 19 October 2021; Published 9 November 2021

Academic Editor: Taza Gul

Copyright © 2021 Faiz Muhammad Khan et al. This is an open access article distributed under the Creative Commons Attribution License, which permits unrestricted use, distribution, and reproduction in any medium, provided the original work is properly cited.

Schnakenberg model is known as one of the influential model used in several biological processes. The proposed model is an autocatalytic reaction in nature that arises in various biological models. In such kind of reactions, the rate of reaction speeds up as the reaction proceeds. It is because when a product itself acts as a catalyst. In fact, model endows fractional derivatives that got great advancement in the investigation of mathematical modeling with memory effect. Therefore, in the present paper, the authors develop a scheme for the solution of fractional order Schnakenberg model. The proposed model describes an auto chemical reaction with possible oscillatory behavior which may have several applications in biological and biochemical processes. In this work, the authors generalized the concept of integer order Schnakenberg model to fractional order Schnakenberg model. We provided the approximate solution for the underlying generalized nonlinear Schnakenberg model in the sense of Caputo differential operator via Laplace Adomian decomposition method (LADM). Furthermore, we established the general scheme for the considered model in the form of infinite series by the aforementioned technique. The consequent results obtained by the proposed technique ensure that LADM is an effective and accurate techniques to handle nonlinear partial differential equations as compared to the other available numerical techniques. Finally, the obtained numerical solution is visualized graphically by MATLAB to describe the dynamics of desired solution.

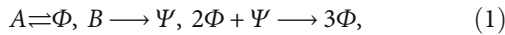
## 1. Introduction

Since the biological processes are not linear systems by nature, which happen at various time scales, therefore, several complex problems arise as a result of fast or slow responds with following interventions or treatment. Thus, to capture an appropriate individual trajectories, the study underconsideration depends on a sequential sample over in appropriate time course. Although various classical methods give a significant insight for the better understanding of a variety of biological processes, but due to some properties like localizing, quantifying and pressibility of measuring revolutionized our thoughts and motivated the researchers and

scientists to construct some dynamical methods to tackle various biological phenomena. Most of dynamical and biological phenomena that are involved in the study of chemical theory, fluid dynamics, and mathematical biology have more importance due to explaining the processes related to real life. Such phenomena are usually modulated by linear or nonlinear partial differential equations (PDEs). DEs have ability to predict about the dynamical phenomena around the globe and also used to describe the exponential growth and decay over the time. DEs are having a diverse range of applications in several field, such as physics, engineering, and biology. The researchers use the tool of differential equation, to modulate aforesaid phenomena. Furthermore,

some useful applications of DEs to modulate the engineering and chemical phenomena can be found in some recent articles (see [1–5]). PDEs often model multidimensional dynamical system, i.e., it can be used to formulate natural phenomena, such as sound, heat, electrostatics, electrodynamics, quantum mechanics, and flow of fluid (see [6, 7]).

It is important to note that reaction-diffusion systems have been used over decades to study the deep insights of biological systems. More precisely, these models have been used in several biological, physical, environmental, and chemical processes of real life. In reaction-diffusion systems, Brusselator, Lengyel-Epstein, and Schnakenberg models are the most famous due to its applicability and reliable results. These models are used for generating patterns for both biological and chemical systems and so called turning type models. The Schnakenberg model is one of the well-known chemical reaction-diffusion model which was introduced by Schnakenberg in 1979. It is important to note that an auto chemical reaction having oscillatory behavior is precisely described by Schnakenberg model with a verity of the biological and biochemical processes like pattern formations in skin analysis and embryogenesis. Further in biology, it also models the spatial distribution of a morphogen. Science in several biological systems, these types of models involve auto catalytic reactions which natural arises. Therefore, in such reactions, the rate of reaction boost with the reaction proceeds, due to the role of a product acts as catalysts. In tri-molecular reaction, the reaction under consideration plays a role of two species models. Such types of reaction between chemical sources  $A$  and  $B$  and products  $\Phi$  and  $\Psi$  are described as:



where  $A$  and  $B$  are two chemical sources and  $\Phi$  and  $\Psi$  are products. A system of reaction-diffusion equations is obtained by using law of mass of action, for the concentrations  $\phi(x, t)$  and  $\psi(x, t)$  of the products  $\Phi$  and  $\Psi$  described in (1). The derived nondimensional form of the system [8, 9] is given by

$$\begin{cases} \frac{\partial \phi(x, t)}{\partial t} = \alpha - \phi(x, t) + \phi^2(x, t)\psi(x, t) + D_1 \frac{\partial^2 \phi(x, t)}{\partial x^2}, \\ \frac{\partial \psi(x, t)}{\partial t} = \beta - \phi^2(x, t)\psi(x, t) + D_2 \frac{\partial^2 \psi(x, t)}{\partial x^2}, \end{cases} \quad (2)$$

where  $\phi = \phi(x, t)$  and  $\psi = \psi(x, t)$  represent the concentration and  $\alpha$  and  $\beta$  are positive arbitrary constants and represent the concentration of  $A$  and  $B$ .  $D_1$  and  $D_2$  are the diffusion coefficients of the chemicals  $\Phi$  and  $\Psi$ , for detail study (see [8–11]).

In modern era, the researchers paid keen interest to investigate nonlinear PDEs due to its wide range of applications in physics, engineering, and modern sciences. In last two decades, a considerable number of efforts have been made to investigate field of the fractional order partial differential equations (FOPDEs) in all aspects, such as theoretical, numerical, and applications. These equations provide the

hereditary properties and description of memory effect of different phenomena. Fractional order differential operator has the advantage of being a nonlocal operator and possesses greater degree of freedom as compared to conventional differential operator. Fractional calculus has got the consideration of researchers, due to its extensive applications in the aforesaid fields. The mathematical models involving fractional order derivatives are more reliable and great degree of freedom and accuracy as compared to traditional derivatives. In some situation, a mathematical model involving integer order derivative does not describe the real situation. In such circumstances, fractional order derivatives are more reliable to describe these real word problems, (see [12–19]). In this regard, the proposed model has been studied by various researchers from both analytical and numerical points of view (see [11, 20, 21]).

After the comprehensive literature review, it was found that mathematical models consist of Caputo fractional order operators that are more accurate and reliable instead of integer order model. Keeping the aforementioned applications of FDEs, the researchers investigated different aspects of various mathematical models. In this continuation, the researchers well explored different aspects of mathematical modeling and published variety of articles (see [2, 22, 23]). Therefore, the researchers investigated different features of aforementioned model. An important class of biochemical model known as Schnakenberg model represents a chemical process, where sudden fluctuation occurs during the reaction. The considered model can be well described by Caputo fractional differential operator instead of integer order derivatives. Therefore, the author used the idea of Caputo fractional order derivatives to generalize the concept of model (2) into Caputo fractional order Schnakenberg model given by

$$\begin{cases} \frac{\partial^\sigma \phi(x, t)}{\partial t^\sigma} = \alpha - \beta\phi(x, t) + \phi^2(x, t)\psi(x, t) + D_1 \frac{\partial^{2\eta} \phi(x, t)}{\partial x^{2\eta}}, \\ \frac{\partial^\sigma \psi(x, t)}{\partial t^\sigma} = \gamma - \phi^2(x, t)\psi(x, t) + D_2 \frac{\partial^{2\eta} \psi(x, t)}{\partial x^{2\eta}}, \\ 0 < \sigma, \eta \leq 1, \end{cases} \quad (3)$$

subjected to the initial conditions (ICs)

$$\begin{aligned} \phi(x, 0) &= h(x), \\ \psi(x, 0) &= g(x). \end{aligned} \quad (4)$$

We have established the numerical scheme for aforementioned model with the help of well-known numerical technique called LADM. The proposed technique consists of special polynomial known as Adomian polynomial. The specific class of this polynomial decomposes the nonlinear term involving in the model in the form of series. With the help of Adomian polynomial, the nonlinear term is decomposes as

$$H(w(x, t)) = \sum_{m=0}^{\infty} A_m, \quad (5)$$

where  $A_m$ 's are called Adomian polynomials introduced by Adomian and defined as

$$A_m = \frac{1}{\Gamma(m+1)} \frac{d^m}{d\lambda^m} \left[ H \sum_{i=0}^m \lambda^i w_i(x, t) \right]_{\lambda=0}. \quad (6)$$

The technique of Laplace Adomian decomposition is the tool to obtain the approximate solution of nonlinear PDEs. LADM is the combination of two powerful techniques, i.e., Adomian decomposition method and Laplace transform. The main advantage of LADM is that it can provide both analytic and numerical solution to a class of nonlinear differential equations (DEs). The considered technique is more superior as compared to the other available techniques, because it gives us particular solutions without finding general solution for DEs. Furthermore, it does not require predefined size declaration like Runge-Kutta method, possess less parameters, and requires no discretization and linearization. In comparison with other analytical techniques, the proposed technique is an efficient and simple tool to investigate numerical solution of nonlinear fractional partial differential equations. The results obtained by this method, ensure the capability and reliability of the proposed method for nonlinear fractional partial differential equations (for detail, see [16, 24, 25]).

In present paper, the authors have generalized the idea of integral order Schnakenberg model to fractional order model in the terms of singular kernel operator. Moreover, we have developed the scheme for the considered fractional model via LADM in the form of infinite series. We have obtained the semianalytical solution for the considered nonlinear model with the help of proposed techniques. The results obtained by the proposed technique ensure that the consider technique is very effective and easy to implement. The numerical simulation is visualized graphically via MATLAB to explain the dynamical behavior of aforementioned model.

## 2. Preliminaries

The concerned section is devoted to the well-known definitions related to fractional calculus and semianalytic techniques, which are helpful in further corresponding in this work.

*Definition 1* (see [25]). The LT of a function  $g(x, t)$ , defined  $\forall t \geq 0$ , is denoted by  $G(x, s) = \mathcal{L}\{g(x, t)\}$  and is given as

$$G(x, s) = \mathcal{L}\{g(x, t)\} = \int_0^{\infty} e^{-st} g(x, t) dt, \quad (7)$$

where “ $\mathcal{L}$ ” is called LT operator or Laplace transformation and “ $s$ ” is the transformed variable.

*Definition 2* (see [25]). The noninteger order derivative for the function  $\psi$  on the interval  $(0, \infty) \times (0, \infty)$  in Caputo

sense is defined such as

$${}^c \mathcal{D}^\alpha \psi(x, t) = \frac{1}{\Gamma(m-\alpha)} \int_0^t (t-s)^{m-\alpha-1} \psi^m(x, s) ds, \quad (8)$$

$$\alpha \in (m-1, m), m \in \mathbb{N},$$

where  $m = [\alpha] + 1$ ,  $[\alpha]$  is the integral part of  $\alpha$ , and  $\alpha$  denotes real number. Now, for  $\alpha \rightarrow m$ , the Caputo fractional derivative becomes conventional  $n$ th order derivative of the function.

Particularly for  $\alpha \in (0, 1)$ ,

$${}^c \mathcal{D}^\alpha \psi(x, t) = \frac{1}{\Gamma(m-1)} \int_0^t \frac{1}{(t-s)^\alpha} \frac{\partial}{\partial s} \psi(x, s) ds. \quad (9)$$

*Definition 3* (see [25]). The LT of Caputo derivatives is given by

$$\mathcal{L}\{{}^c \mathcal{D}^\alpha \psi(x, t)\} = s^\alpha \psi(x, s) - \sum_{k=0}^{m-1} s^{\alpha-k-1} \psi^k(x, 0), \quad (10)$$

$$\alpha \in (m-1, m), m \in \mathbb{N},$$

where  $m = [\alpha] + 1$  and  $[\alpha]$  denote the nonfractional part of  $\alpha$ .

## 3. General Scheme for the Solution Schnakenberg Model

This section is committed to the general scheme for the solution of fractional order Schnakenberg model via LADM. The fractional order nondimensional Schnakenberg model is given by

$$\begin{cases} \frac{\partial^\sigma \phi(x, t)}{\partial t^\sigma} = \alpha - \phi(x, t) + \phi^2(x, t) \psi(x, t) + D_1 \frac{\partial^{2\eta} \phi(x, t)}{\partial x^{2\eta}}, \\ \frac{\partial^\sigma \psi(x, t)}{\partial t^\sigma} = \beta - \phi^2(x, t) \psi(x, t) + D_2 \frac{\partial^{2\eta} \psi(x, t)}{\partial x^{2\eta}}, \\ 0 < \sigma, \eta \leq 1, \end{cases} \quad (11)$$

subjected to ICs:

$$\begin{cases} \phi(x, 0) = h(x), \\ \psi(x, 0) = g(x), \end{cases} \quad (12)$$

where  $\phi = \phi(x, t)$  and  $\psi = \psi(x, t)$  represent the concentrations,  $\alpha$  and  $\beta$  that are positive arbitrary constants and  $D_1$  and  $D_2$  are the diffusion coefficients of the substances.

Applying Laplace transform on (11), we have

$$\begin{cases} \mathcal{L}\left\{\frac{\partial^\sigma \phi(x,t)}{\partial t^\sigma}\right\} = \mathcal{L}\left\{\alpha - \phi(x,t) + \phi^2(x,t)\psi(x,t) + D_1 \frac{\partial^{2\eta} \phi(x,t)}{\partial x^{2\eta}}\right\}, \\ \mathcal{L}\left\{\frac{\partial^\sigma \psi(x,t)}{\partial t^\sigma}\right\} = \mathcal{L}\left\{\beta - \phi^2(x,t)\psi(x,t) + D_2 \frac{\partial^{2\eta} \psi(x,t)}{\partial x^{2\eta}}\right\}. \end{cases} \quad (13)$$

By using properties of Laplace transform, (13) becomes

$$\begin{cases} \Phi(x,s) - \frac{1}{s}\phi(x,0) = \frac{1}{s^\sigma} \mathcal{L}\left\{\alpha - \phi(x,t) + \phi^2(x,t)\psi(x,t) + D_1 \frac{\partial^{2\eta} \phi(x,t)}{\partial x^{2\eta}}\right\}, \\ \Psi(x,s) - \frac{1}{s}\psi(x,0) = \frac{1}{s^\sigma} \mathcal{L}\left\{\beta - \phi^2(x,t)\psi(x,t) + D_2 \frac{\partial^{2\eta} \psi(x,t)}{\partial x^{2\eta}}\right\}. \end{cases} \quad (14)$$

Now applying inverse Laplace transform on (14) and using ICs, we get

$$\begin{cases} \phi(x,t) = h(x) + \mathcal{L}^{-1}\left[\frac{1}{s^\sigma} \mathcal{L}\left\{\alpha - \phi(x,t) + \phi^2(x,t)\psi(x,t) + D_1 \frac{\partial^{2\eta} \phi(x,t)}{\partial x^{2\eta}}\right\}\right], \\ \psi(x,t) = g(x) + \mathcal{L}^{-1}\left[\frac{1}{s^\sigma} \mathcal{L}\left\{\beta - \phi^2(x,t)\psi(x,t) + D_2 \frac{\partial^{2\eta} \psi(x,t)}{\partial x^{2\eta}}\right\}\right]. \end{cases} \quad (15)$$

The nonlinear term  $\phi^2(x,t)\psi(x,t)$  presenting in (15) is decomposed as

$$\phi^2(x,t)\psi(x,t) = \sum_{n=0}^{\infty} A_m, \quad (16)$$

where  $A_m$  is called Adomian polynomial and defined as

$$A_m = \frac{1}{\Gamma(m+1)} \frac{d^m}{d\lambda^m} \left[ \left( \sum_{i=0}^m \lambda^i \phi_i(x,t) \right)^2 \left( \sum_{i=0}^m \lambda^i \psi_i(x,t) \right) \right]_{\lambda=0}. \quad (17)$$

For  $m = 0$

$$A_0 = \phi_0^2(x,t)\psi_0(x,t). \quad (18)$$

For  $m = 1$

$$A_1 = \phi_0^2(x,t)\psi_1(x,t) + 2\phi_0(x,t)\psi_0(x,t)\phi_1(x,t). \quad (19)$$

The assumed solutions  $\phi(x,t)$  and  $\psi_i(x,t)$  are in the form of

$$\begin{aligned} \phi(x,t) &= \sum_{i=0}^{\infty} \phi_i(x,t), \\ \psi(x,t) &= \sum_{i=0}^{\infty} \psi_i(x,t). \end{aligned} \quad (20)$$

Plugging these values in system (15), we have

$$\begin{cases} \sum_{i=0}^{\infty} \phi_i(x,t) = h(x) + \mathcal{L}^{-1}\left[\frac{1}{s^\sigma} \mathcal{L}\left\{\alpha - \sum_{i=0}^{\infty} \phi_i(x,t) + \sum_{n=0}^{\infty} A_n + D_1 \frac{\partial^{2\eta}}{\partial x^{2\eta}} \sum_{i=0}^{\infty} \phi_i(x,t)\right\}\right], \\ \sum_{i=0}^{\infty} \psi_i(x,t) = g(x) + \mathcal{L}^{-1}\left[\frac{1}{s^\sigma} \mathcal{L}\left\{\beta - \sum_{n=0}^{\infty} A_n + D_2 \frac{\partial^{2\eta}}{\partial x^{2\eta}} \sum_{i=0}^{\infty} \psi_i(x,t)\right\}\right]. \end{cases} \quad (21)$$

Comparing both sides of system (21), we have

$$\begin{cases} \phi_0(x,t) = h(x), \\ \psi_0(x,t) = g(x), \\ \phi_1(x,t) = \mathcal{L}^{-1}\left[\frac{1}{s^\sigma} \mathcal{L}\left\{\alpha - \phi_0(x,t) + A_0 + D_1 \frac{\partial^{2\eta}}{\partial x^{2\eta}} \phi_0(x,t)\right\}\right], \\ \psi_1(x,t) = \mathcal{L}^{-1}\left[\frac{1}{s^\sigma} \mathcal{L}\left\{\beta - A_0 + D_2 \frac{\partial^{2\eta}}{\partial x^{2\eta}} \psi_0(x,t)\right\}\right], \\ \phi_n(x,t) = \mathcal{L}^{-1}\left[\frac{1}{s^\sigma} \mathcal{L}\left\{\alpha - \phi_{n-1}(x,t) + A_{n-1} + D_1 \frac{\partial^{2\eta}}{\partial x^{2\eta}} \phi_{n-1}(x,t)\right\}\right], \\ \psi_n(x,t) = \mathcal{L}^{-1}\left[\frac{1}{s^\sigma} \mathcal{L}\left\{\beta - A_{n-1} + D_2 \frac{\partial^{2\eta}}{\partial x^{2\eta}} \psi_{n-1}(x,t)\right\}\right]. \end{cases} \quad (22)$$

In this manner, we obtain the desired solution given by

$$\begin{cases} \phi(x,t) = \sum_{i=0}^{\infty} \phi_i(x,t), \\ \psi(x,t) = \sum_{i=0}^{\infty} \psi_i(x,t). \end{cases} \quad (23)$$

By simple computational work, we get

$$\begin{cases} \phi_0(x,t) = h(x), \\ \psi_0(x,t) = g(x), \\ \phi_1(x,t) = \left(\alpha - \phi_0(x,t) + \phi_0^2(x,t)\psi_0(x,t) + D_1 \frac{\partial^{2\eta}}{\partial x^{2\eta}} \phi_0(x,t)\right) \frac{t^\sigma}{\Gamma(\sigma+1)}, \\ \psi_1(x,t) = \left(\beta - \phi_0^2(x,t)\psi_0(x,t) + D_2 \frac{\partial^{2\eta}}{\partial x^{2\eta}} \psi_0(x,t)\right) \frac{t^\sigma}{\Gamma(\sigma+1)}, \\ \phi_2(x,t) = \alpha \frac{t^{2\sigma}}{\Gamma(2\sigma+1)} - \left(\xi - \phi_0^2(x,t)\zeta - 2\phi_0(x,t)\psi_0(x,t)\xi - D_1 \frac{\partial^{2\eta}}{\partial x^{2\eta}} \xi\right) \frac{t^{2\sigma}}{\Gamma(2\sigma+1)}, \\ \psi_2(x,t) = \beta \frac{t^{2\sigma}}{\Gamma(2\sigma+1)} - \left(\phi_0^2(x,t)\zeta + 2\phi_0(x,t)\psi_0(x,t)\xi - D_2 \frac{\partial^{2\eta}}{\partial x^{2\eta}} \zeta\right) \frac{t^{2\sigma}}{\Gamma(2\sigma+1)}, \end{cases} \quad (24)$$

where

$$\begin{aligned} \xi &= \alpha - \phi_0(x,t) + \phi_0^2(x,t)\psi_0(x,t) + D_1 \frac{\partial^{2\eta}}{\partial x^{2\eta}} \phi_0(x,t), \\ \zeta &= \beta - \phi_0^2(x,t)\psi_0(x,t) + D_2 \frac{\partial^{2\eta}}{\partial x^{2\eta}} \psi_0(x,t). \end{aligned} \quad (25)$$

Thus, the three term solutions are given by

$$\begin{cases} \phi(x, t) = h(x) + \left( 2\alpha - \phi_0(x, t) + \phi_0^2(x, t)\psi_0(x, t) + D_1 \frac{\partial^{2\eta}}{\partial x^{2\eta}} \phi_0(x, t) \right) \frac{t^\sigma}{\Gamma(\sigma + 1)} - \left( \xi - \phi_0^2(x, t)\zeta - 2\phi_0(x, t)\psi_0(x, t)\xi - D_1 \frac{\partial^{2\eta}}{\partial x^{2\eta}} \xi \right) \frac{t^{2\sigma}}{\Gamma(2\sigma + 1)} + \dots \\ \psi(x, t) = g(x) + \left( 2\beta - \phi_0^2(x, t)\psi_0(x, t) + D_2 \frac{\partial^{2\eta}}{\partial x^{2\eta}} \psi_0(x, t) \right) \frac{t^\sigma}{\Gamma(\sigma + 1)} - \left( \phi_0^2(x, t)\zeta + 2\phi_0(x, t)\psi_0(x, t)\xi - D_2 \frac{\partial^{2\eta}}{\partial x^{2\eta}} \zeta \right) \frac{t^{2\sigma}}{\Gamma(2\sigma + 1)} + \dots \end{cases} \quad (26)$$

### 4. Numerical Discussion

In this section of research work, we provide some numerical example to illustrate the main work.

*Example 1.* Let  $\alpha = \beta = \eta = 1$  and  $D_1 = D_2 = 2$ , so the proposed model becomes

$$\begin{cases} \frac{\partial^\sigma \phi(x, t)}{\partial t^\sigma} = 1 - \phi(x, t) + \phi^2(x, t)\psi(x, t) + 2 \frac{\partial^2}{\partial x^2} \phi(x, t), \\ \frac{\partial^\sigma \psi(x, t)}{\partial t^\sigma} = 1 - \phi^2(x, t)\psi(x, t) + 2 \frac{\partial^2}{\partial x^2} \psi(x, t), \\ 0 < \sigma \leq 1, \end{cases} \quad (27)$$

subjected to ICs:

$$\begin{cases} \phi(x, 0) = e^x \sin x, \\ \psi(x, 0) = xe^x. \end{cases} \quad (28)$$

Applying Laplace transform to system (27), we get

$$\begin{cases} \mathcal{L} \left\{ \frac{\partial^\sigma \phi(x, t)}{\partial t^\sigma} \right\} = \mathcal{L} \left\{ 1 - \phi(x, t) + \phi^2(x, t)\psi(x, t) + 2 \frac{\partial^2 \phi(x, t)}{\partial x^2} \right\}, \\ \mathcal{L} \left\{ \frac{\partial^\sigma \psi(x, t)}{\partial t^\sigma} \right\} = \mathcal{L} \left\{ 1 - \phi^2(x, t)\psi(x, t) + 2 \frac{\partial^2 \psi(x, t)}{\partial x^2} \right\}. \end{cases} \quad (29)$$

By using properties of Laplace transform, system (29) becomes

$$\begin{cases} \Phi(x, s) - \frac{1}{s} u(x, 0) = \frac{1}{s^\sigma} \mathcal{L} \left\{ 1 - \phi(x, t) + \phi^2(x, t)\psi(x, t) + 2 \frac{\partial^2 \phi(x, t)}{\partial x^2} \right\}, \\ \Psi(x, s) - \frac{1}{s} v(x, 0) = \frac{1}{s^\sigma} \mathcal{L} \left\{ 1 - \phi^2(x, t)\psi(x, t) + 2 \frac{\partial^2 \psi(x, t)}{\partial x^2} \right\}. \end{cases} \quad (30)$$

Now applying inverse Laplace transform on (30) and using ICs, we obtain

$$\begin{cases} \phi(x, t) = e^x \sin x + \mathcal{L}^{-1} \left[ \frac{1}{s^\sigma} \mathcal{L} \left\{ 1 - \phi(x, t) + \phi^2(x, t)\psi(x, t) + 2 \frac{\partial^2 \phi(x, t)}{\partial x^2} \right\} \right], \\ \psi(x, t) = xe^x + \mathcal{L}^{-1} \left[ \frac{1}{s^\sigma} \mathcal{L} \left\{ 1 - \phi^2(x, t)\psi(x, t) + 2 \frac{\partial^2 \psi(x, t)}{\partial x^2} \right\} \right]. \end{cases} \quad (31)$$

The nonlinear term  $\phi^2(x, t)\psi(x, t)$  involved in (31) is decomposed by Adomian polynomial

$$\phi^2(x, t)\psi(x, t) = \sum_{n=0}^{\infty} A_n. \quad (32)$$

Plugging these values in system (31), we have

$$\begin{cases} \sum_{i=0}^{\infty} \phi_i(x, t) = e^x \sin x + \mathcal{L}^{-1} \left[ \frac{1}{s^\sigma} \mathcal{L} \left\{ 1 - \sum_{i=0}^{\infty} \phi_i(x, t) + \sum_{m=0}^{\infty} A_m + 2 \frac{\partial^2}{\partial x^2} \sum_{i=0}^{\infty} \phi_i(x, t) \right\} \right], \\ \sum_{i=0}^{\infty} \psi_i(x, t) = xe^x + \mathcal{L}^{-1} \left[ \frac{1}{s^\sigma} \mathcal{L} \left\{ 1 - \sum_{m=0}^{\infty} A_m + 2 \frac{\partial^2}{\partial x^2} \sum_{i=0}^{\infty} \psi_i(x, t) \right\} \right]. \end{cases} \quad (33)$$

Comparing both sides of system (33), we have

$$\begin{cases} \phi_0(x, t) = e^x \sin x, \\ \psi_0(x, t) = xe^x, \\ \phi_1(x, t) = \mathcal{L}^{-1} \left[ \frac{1}{s^\sigma} \mathcal{L} \left\{ 1 - \phi_0(x, t) + A_0 + 2 \frac{\partial^2}{\partial x^2} \phi_0(x, t) \right\} \right], \\ \psi_1(x, t) = \mathcal{L}^{-1} \left[ \frac{1}{s^\sigma} \mathcal{L} \left\{ 1 - A_0 + 2 \frac{\partial^2}{\partial x^2} \psi_0(x, t) \right\} \right], \\ \phi_n(x, t) = \mathcal{L}^{-1} \left[ \frac{1}{s^\sigma} \mathcal{L} \left\{ 1 - u_{n-1}(x, t) + R_{n-1} + 2 \frac{\partial^2}{\partial x^2} \phi_{n-1}(x, t) \right\} \right], \\ \psi_n(x, t) = \mathcal{L}^{-1} \left[ \frac{1}{s^\sigma} \mathcal{L} \left\{ 1 - R_{n-1} + 2 \frac{\partial^2}{\partial x^2} \psi_{n-1}(x, t) \right\} \right]. \end{cases} \quad (34)$$

Assume the solution in the form of

$$\begin{cases} \phi(x, t) = \sum_{i=0}^{\infty} \phi_i(x, t), \\ \psi(x, t) = \sum_{i=0}^{\infty} \psi_i(x, t). \end{cases} \quad (35)$$

By simple computational work, we obtain

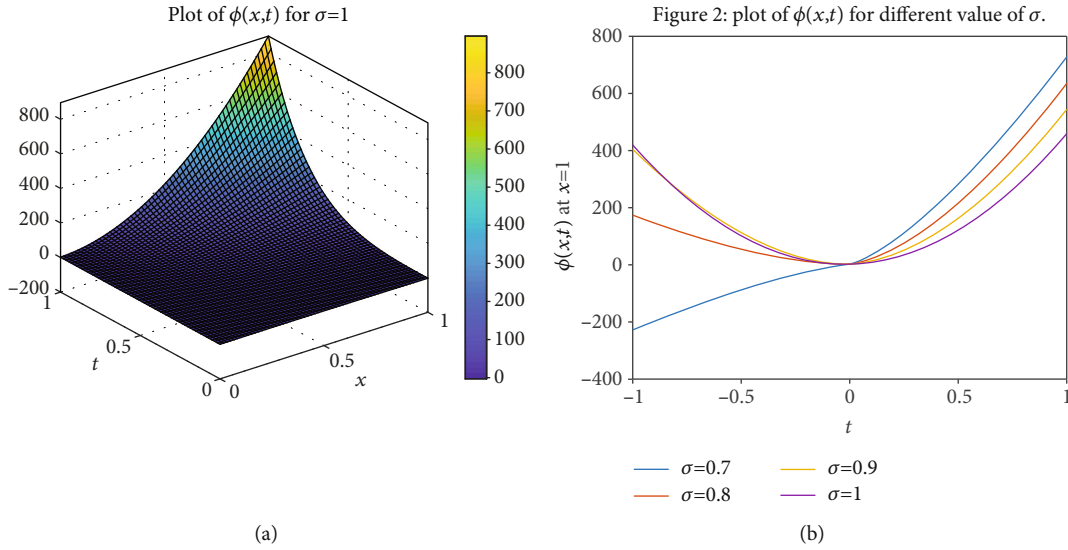


FIGURE 1: (a, b) Spatial numerical solution of  $\psi(x, t)$  in 3D and 2D, respectively.

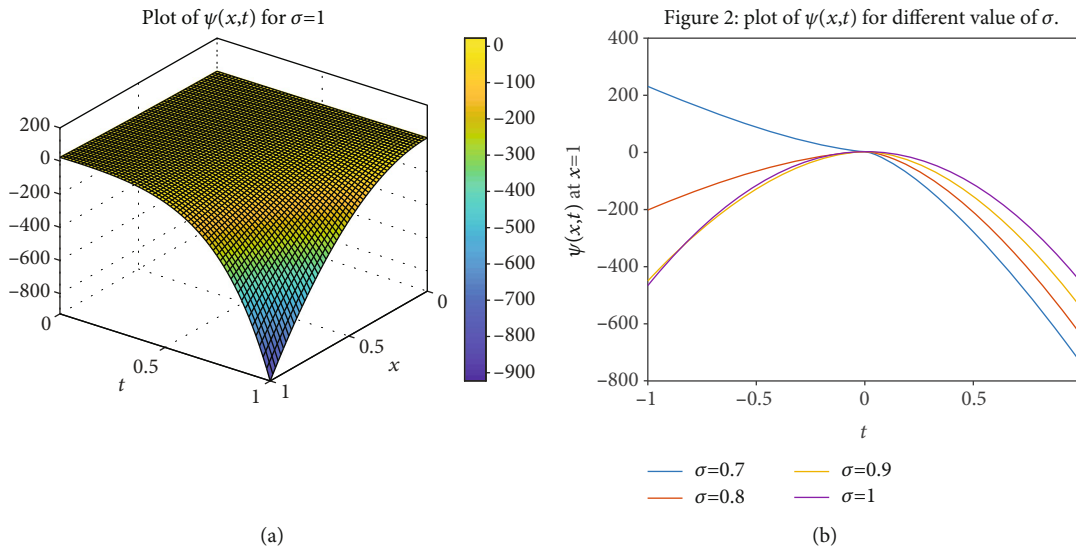


FIGURE 2: (a, b) Spatial numerical solution of  $\phi(x, t)$  in 3D and 2D, respectively.

$$\begin{cases} \phi_1(x, t) = (1 - e^x \sin x + xe^{3x} \sin^2 x + 4e^x \cos x) \frac{t^\sigma}{\Gamma(\sigma + 1)}, \\ \psi_1(x, t) = (1 - xe^{3x} \sin^2 x + 2xe^x + 4e^x) \frac{t^\sigma}{\Gamma(\sigma + 1)}, \end{cases}$$

$$\begin{cases} \phi_2(x, t) = \frac{t^\sigma}{\Gamma(\sigma + 1)} + (17xe^{3x} \sin^2 x - 1 - 15e^x \sin x - 8e^x \cos x + e^{2x} \sin^2 x - xe^{5x} \sin^4 x + 16e^{3x} \sin^2 x + 2xe^{2x} \sin x + 2x^2 e^{5x} \sin^3 x + 16xe^{3x} \sin 2x + 4xe^{3x} \cos 2x + 4e^{3x} \sin 2x) \frac{t^{2\sigma}}{\Gamma(2\sigma + 1)}, \\ \psi_2(x, t) = \frac{t^\sigma}{\Gamma(\sigma + 1)} - (e^{2x} \sin^2 x - xe^{5x} \sin^4 x + 16e^{3x} \sin^2 x + 2xe^{2x} \sin x + 2x^2 e^{5x} \sin^3 x + 4xe^{3x} \cos 2x + 16xe^{3x} \sin 2x + 4e^{3x} \sin 2x + 18xe^{3x} \sin x - 4xe^x - 16e^x) \frac{t^{2\sigma}}{\Gamma(2\sigma + 1)}. \end{cases}$$

(36)

Continuing the similar fashion, the solution terminated after three terms is given by

$$\begin{cases} \phi(x, t) = e^x \sin x + (2 - e^x \sin x + xe^{3x} \sin^2 x + 4e^x \cos x) \frac{t^\sigma}{\Gamma(\sigma+1)} + (17xe^{3x} \sin^2 x - 1 - 15e^x \sin x - 8e^x \cos x + e^{2x} \sin^2 x - xe^{5x} \sin^4 x + 16e^{3x} \sin^2 x + 2xe^{2x} \sin x + 2x^2 e^{5x} \sin^3 x + 16xe^{3x} \sin 2x + 4xe^{3x} \cos 2x + 4e^{3x} \sin 2x) \frac{t^{2\sigma}}{\Gamma(2\sigma+1)}, \\ \psi(x, t) = xe^x + (2 - xe^{3x} \sin^2 x + 2xe^x + 4e^x) \frac{t^\sigma}{\Gamma(\sigma+1)} - (e^{2x} \sin^2 x - xe^{5x} \sin^4 x + 16e^{3x} \sin^2 x + 2xe^{2x} \sin x + 2x^2 e^{5x} \sin^3 x + 4xe^{3x} \cos 2x + 16xe^{3x} \sin 2x + 4e^{3x} \sin 2x + 18xe^{3x} \sin x - 4xe^x - 16e^x) \frac{t^{2\sigma}}{\Gamma(2\sigma+1)}. \end{cases} \quad (37)$$

For classical order  $\sigma = 1$ , the solution become

$$\begin{cases} \phi(x, t) = e^x \sin x + (2 - e^x \sin x + xe^{3x} \sin^2 x + 4e^x \cos x)t + (17xe^{3x} \sin^2 x - 1 - 15e^x \sin x - 8e^x \cos x + e^{2x} \sin^2 x - xe^{5x} \sin^4 x + 16e^{3x} \sin^2 x + 2xe^{2x} \sin x + 2x^2 e^{5x} \sin^3 x + 16xe^{3x} \sin 2x + 4xe^{3x} \cos 2x + 4e^{3x} \sin 2x)t^2, \\ \psi(x, t) = xe^x + (2 - xe^{3x} \sin^2 x + 2xe^x + 4e^x)t - (e^{2x} \sin^2 x - xe^{5x} \sin^4 x + 16e^{3x} \sin^2 x + 2xe^{2x} \sin x + 2x^2 e^{5x} \sin^3 x + 4xe^{3x} \cos 2x + 16xe^{3x} \sin 2x + 4e^{3x} \sin 2x + 18xe^{3x} \sin x - 4xe^x - 16e^x)t^2. \end{cases} \quad (38)$$

The Schnakenberg mathematical model actually represents the three steps biochemical processes. In such process, the final product is in the form of  $\phi(x, t)$ , whose details are given in the introduction of this work. As evident form, the graphical solution of Figures 1(a) and 1(b) shows that the concentration of  $\psi(x, t)$  increases and then decreases. While from Figures 2(a) and 2(b), the graph shows that the concentration of  $\phi(x, t)$  decreases and then increases. This is a clear evidence that the final product will be obtained in terms of  $\phi(x, t)$  with the passage of times which justify the aforementioned three-step process.

## 5. Conclusion

The authors have successfully established the numerical scheme for the generalized fractional order Schnakenberg biochemical model. In order to obtain the desired results, we utilized the tools of well-known numerical technique called Laplace Adomian decomposition method. We have obtained the semianalytic solution for the nonlinear Schnakenberg model in the sense of Caputo differential operator with the help of proposed method. To elaborate our main results, we have provided a numerical example to illustrate our main work. The numerical simulation has been visualized graphically via MATLAB to explain the model's dynamical behavior.

## Data Availability

The data will be available for public after publication.

## Conflicts of Interest

The authors declare that they have no conflicts of interest.

## References

- [1] L. Perko, *Differential Equations and Dynamical Systems*, Springer, New York, NY, USA, 2008.
- [2] K. M. Owolabi, "Modelling and simulation of a dynamical system with the Atangana-Baleanu fractional derivative," *The European Physical Journal Plus*, vol. 133, no. 1, 2018.
- [3] K. Alligood, T. Sauer, and C. J. Yorke, *An Introduction to Dynamical Systems*, Springer-Verlag, New York, NY, USA, 1997.
- [4] M. W. Hirsch and S. Smale, *Differential Equations, Dynamical Systems, and Linear Algebra*, Academic Press, San Diego, CA, USA, 1989.
- [5] A. Katok and B. Hasselblatt, *Introduction to the Modern Theory of Dynamical Systems*, Cambridge University Press, Cambridge, UK, 1995.
- [6] E. L. Ince, *Ordinary Differential Equations*, Dover Public, New York, NY, USA, 1956.
- [7] C. Chicone, *Ordinary Differential Equations with Applications*, Springer, New York, NY, USA, 2006.
- [8] J. Schnakenberg, "Simple chemical reaction systems with limit cycle behaviour," *Journal of Theoretical Biology*, vol. 81, no. 3, pp. 389–400, 1979.
- [9] Y. Li, "Steady-state solution for a general Schnakenberg model," *Nonlinear Analysis: Real World Applications*, vol. 12, pp. 1985–1990, 2011.
- [10] C. Xu and J. Wei, "Hopf bifurcation analysis in a one-dimensional Schnakenberg reaction-diffusion model," *Nonlinear Analysis: Real World Applications*, vol. 13, no. 4, pp. 1961–1977, 2012.
- [11] K. S. Al Noufaey, "Semi-analytical solutions of the Schnakenberg model of a reaction-diffusion cell with feedback," *Results in Physics*, vol. 9, pp. 609–614, 2018.
- [12] S. Saravi and M. Saravi, "A short survey in application of ordinary differential equations on cancer research," *American Journal of Computational and Applied Mathematics*, vol. 10, pp. 1–5, 2020.
- [13] K. L. WANG, K. J. WANG, and C. H. HE, "Physical insight of local fractional calculus and its application to fractional KdV-Burgers-Kuramoto equation," *Fractals*, vol. 27, no. 7, article 1950122, 2019.
- [14] D. Baleanu, A. Fernandez, and A. Akgül, "On a fractional operator combining proportional and classical Differintegrals," *Mathematics*, vol. 8, no. 3, p. 360, 2020.

- [15] A. Ali, B. Samet, K. Shah, and R. A. Khan, *Existence and Stability of Solution to a Topped System of Differential Equations of Non-Integer Order*, Springer, 2017.
- [16] A. Ali, K. Shah, and R. A. Khan, "Numerical treatment for traveling wave solutions of fractional Whitham-Broer- Kaup equations," *Alexandria Engineering Journal*, vol. 57, no. 3, pp. 1991–1998, 2018.
- [17] K. S. Miller and B. Ross, *An Introduction to the Fractional Calculus and Fractional Differential Equations*, A Wiley-Interscience Publications, John Wiley and Sons, Inc., New York, NY, USA, 1993.
- [18] B. Ross, *Fractional Calculus and its Applications*, Springer Verlag, 1975.
- [19] R. Hilfer, *Applications of Fractional Calculus in Physics*, World Scientific, Singapore, 2000.
- [20] M. Ghergu and V. D. Radulescu, *Nonlinear PDEs: Mathematical Models in Biology, Chemistry and Population Genetics*, Springer, 2012.
- [21] M. R. Ricard and S. Mischler, "Turing instabilities at hopf bifurcation," *Journal of Nonlinear Science*, vol. 19, no. 5, pp. 467–496, 2009.
- [22] D. Baleanu, H. Mohammadi, and S. Rezapour, "A fractional differential equation model for the COVID-19 transmission by using the Caputo-Fabrizio derivative," *Advances in Difference Equations*, vol. 2020, no. 1, 2020.
- [23] H. Alrabaiah, A. Ali, F. Haq, and K. Shah, "Existence of fractional order semianalytical results for enzyme kinetics model," *Advances in Difference Equations*, vol. 2020, no. 1, 2020.
- [24] A. Ali, A. Zeb, V. E. Turk, and R. A. Khan, "Numerical solution of fractional order immunology and AIDS via Laplace transform adomian decomposition method," *Journal of Fractional Calculus and Applications*, vol. 10, no. 1, 2019.
- [25] A. Ali, Abdullah, and A. Ahmad, "The solution of Poisson partial differential equations via Double Laplace Transform Method," *Partial Differential Equations in Applied Mathematics*, vol. 4, p. 100058, 2021.



## Research Article

# Impact of Ramped Concentration and Temperature on MHD Casson Nanofluid Flow through a Vertical Channel

Kashif Sadiq,<sup>1</sup> Imran Siddique <sup>1</sup>, Rifaqat Ali <sup>2</sup>, and Fahd Jarad <sup>3,4</sup>

<sup>1</sup>Department of Mathematics, University of Management and Technology, Lahore 54770, Pakistan

<sup>2</sup>Department of Mathematics, College of Science and Arts, King Khalid University, Muhayil, Abha 61413, Saudi Arabia

<sup>3</sup>Department of Mathematics, Cankaya University, Etimesgut, Ankara, Turkey

<sup>4</sup>Department of Medical Research, China Medical University Hospital, China Medical University, Taichung, Taiwan

Correspondence should be addressed to Imran Siddique; [imransmsrazi@gmail.com](mailto:imransmsrazi@gmail.com) and Fahd Jarad; [fahd@cankaya.edu.tr](mailto:fahd@cankaya.edu.tr)

Received 10 September 2021; Accepted 8 October 2021; Published 31 October 2021

Academic Editor: Taza Gul

Copyright © 2021 Kashif Sadiq et al. This is an open access article distributed under the Creative Commons Attribution License, which permits unrestricted use, distribution, and reproduction in any medium, provided the original work is properly cited.

The mass and heat transport of Casson nanofluid flow in a channel under the influence of the magnetic field, heat generation, chemical reaction, ramped concentration, and ramped temperature is studied. Nanoparticles of copper (Cu) are inserted in sodium alginate (SA) to make nanofluid. The definition of time-fractional Caputo derivative is applied to have the fractional model. The analytical results of concentration, temperature, velocity, skin friction, Sherwood numbers, and Nusselt numbers for ramped and isothermal boundary conditions are obtained in the form of summation after applying the Laplace inverse transform. The effects of the fractional parameter ( $\xi$ ) and physical parameters are depicted graphically. For higher values of  $\xi$  the velocity, concentration and temperature reduce. The fractional model is a better choice to control velocity, concentration, and temperature profiles. The energy enhances by increasing volume fraction ( $\phi$ ), whereas mass and flow of nanofluid reduce. The Sherwood and Nusselt numbers for both isothermal and ramped conditions increase by increasing  $\phi$ . Ramped conditions can control the flow, mass, and heat of the nanofluid.

## 1. Introduction

Non-Newtonian fluids have attracted several scientists and researchers due to their industrial applications such as cosmetics, synthetic lubricants, clay coating, certain oils, paint, synthetic lubricants, certain oils, biological fluids, pharmaceuticals, and drilling muds. The flow features of non-Newtonian cannot be defined briefly by the Navier-Stokes equation due to the complex formulation of the problem. Thus, according to qualities, different models of non-Newtonian fluids are categorized such as Seely, Bulky, Jeffrey, Eyring-Powell, Oldroyd-B, Burger, Oldroyd-A, Carreau, Maxwell, and Casson. For the expectancy of flow tendency of balanced pigment oil, Casson [1] introduced the model of Casson fluid in 1959. Casson fluid is a shear-thinning fluid with endless and zero viscosity at zero and infinite shear, respectively [2]. Tomato sauce, jelly, human blood, soup, and honey are examples of Casson fluids.

Many researchers and scientists are investigating nanofluids due to their common uses in industrial and engineering fields. They have revealed the significant thermal characteristics and ways to boost the thermal conductivity of nanofluids. The addition of nanofluids and biotechnological apparatus may give proficient applications in agriculture, pharmaceuticals, and biosensors. Several nanomaterials are used in biotechnology, for instance, nanowires, nanostructures, nanoparticles, and nanofibers. The significance of microfluidics and nanofluids is unquestionable in biomedical devices. MHD nanofluids have magnetic and liquid characteristics; it has several applications, for instance, optical controls, modulators, and adjustable fiber filters. Magnetic nanoparticles are very significant for the treatment of cancer in medicine. The researchers are using nanofluids to improve the efficiency of and thermal conductivity of conventional fluids [3–6]. Zari et al. [7] numerically investigated Casson nanofluid flow on an

inclined plate with double stratification. Ali et al. [8] discussed the numerical results of Carreau flow of Casson nanofluid with magnetohydrodynamics. Shafiq et al. [9] analyzed Casson nanofluid flow on a rotating disk.

Daily life problems frequently have arbitrary wall conditions. It is practical to study such problems in which wall temperature changes step-wise. Researchers are making a lot of efforts to investigate such problems. The flow of heat in fluids demonstrates a vital role in extensive engineering and industrial procedures, such as nuclear operations, gas turbines, processes of heating and cooling, scheming of devices, and supervision of high-tech thermal systems. The studies of the flow of MHD nanofluid with ramped concentration and temperature conditions in the literature currently are not discussed analytically in detail due to its complicated relations. Hayday et al. [10], Schetz [11], and Malhotra et al. [12] have established the idea of ramped temperature. The most significant use of ramped heat is to raze cancer cells during thermal therapy. Ramped conditions help to control the temperature rise caused by natural conditions [13]. The impact of ramped heating on an incompressible visually thin fluid flow above a plate was examined by Das et al. [14]. Nandkeolyar et al. [15] evaluated and compared MHD natural convection flow and diverse movements of the plate having uniform velocity, periodic acceleration, and single acceleration due to ramped and constant boundary conditions. Seth et al. [16–19] investigated mass and heat transport in the existence of various parameters like chemical reaction, heat absorption, Darcy's law, thermal radiation, porous medium, and Hall current with ramped concentration and temperature on a vertical plate. Zin et al. [20] analyzed the effects of ramped temperature, thermal radiation, and magnetic field on the natural convection Jeffrey fluid flow.

Narahari [21] investigated the effects of ramped heating and thermal radiation through a channel. Khalid et al. [22] compared the ramped and isothermal boundary conditions of convective nanofluid flow. Mahanthesh et al. [23] evaluated the analytical results of nanofluid flow over a plate in the existence of heat generation and magnetic field. Jha and Gambo [24] examined mass and heat transport of transient free convective flow affected by the Dufour and Soret effect through a channel with ramped temperature and concentration. Arif et al. [25] studied fractionalized Casson fluid flow on a plate with ramped concentration and temperature. Anwer et al. [26] discussed MHD Oldroyd-B convective flow of nanofluid with ramped velocity and ramped temperature. The MHD Casson nanofluid flow with ramped concentration and temperature through a channel is not investigated in literature yet.

The mathematical models described by fractional differential equations are useful because such models include the memory effects, therefore offering more information regarding the complex diffusive processes. Also, for some experiments, the adequate fractional model could be chosen that gives the best agreement between analytical results and those experimental. Therefore, researchers are using fractional models instead of classical ones to meet the growing demand of modern technology. Fractional calculus is very effective in

diffusion, electrochemistry, relaxation processes, and viscoelasticity. Fractional models help to understand memory and hereditary properties that were not possible with integral models. Fractional models are applicable in modern sciences like mathematical biology, applied sciences, physics, and fractals. Various definitions of fractional derivatives are available in the literature. Riemann-Liouville defined Caputo derivative [27] for physical problems like viscoelasticity, electrohysteresis, and damage and fatigue. Riemann-Liouville [28] used fractional derivatives to solve complex problems. For example, the nonzero result fractional derivative of constant.

Motivated by the above literature focus of this work is to scrutinize the results of chemical reaction, heat generation, and magnetic force with ramped concentration and temperature unsteady flow of Casson nanofluid. The nanofluid is prepared by adding nanoparticles of Cu into SA. The analytical results of velocity, skin friction, temperature, Nusselt numbers, concentration, and Sherwood numbers for isothermal and ramped wall boundary conditions are calculated by using the Laplace transform. The significant results are illustrated graphically and discussed in detail.

## 2. Mathematical Model

Consider the Casson nanofluid flow through a vertical channel with heat and mass transport under the effect of magnetic force, chemical reaction, and heat generation. The nanoparticles of Cu are suspended uniformly into SA. Initially, the walls of the channel and nanofluid are at rest at fixed temperature  $\widetilde{T}_l$  and concentration  $\widetilde{C}_l$  at  $\tilde{t} = 0$ . At time  $\tilde{t} = 0^+$ , the concentration and temperature of the left wall rise momentarily to  $\widetilde{C}_l + (\widetilde{C}_0 - \widetilde{C}_l)\tilde{t}/\tilde{t}_0$  and  $\widetilde{T}_l + (\widetilde{T}_0 - \widetilde{T}_l)\tilde{t}/\tilde{t}_0$ , respectively, for  $0 < \tilde{t} < \tilde{t}_0$ ; the concentration and temperature are maintained at  $C_0$  and  $T_0$  when  $\tilde{t} > \tilde{t}_0$ . The initial concentration  $\widetilde{C}_l$  and temperature  $\widetilde{T}_l$  will remain unchanged on the right wall at  $\tilde{y} = l$ . A constant magnetic force  $B_0$  is applied perpendicularly on the left wall externally (see Figure 1).

Thermophysical characteristics SA and Cu are assumed constant and shown in Table 1. The slippage between SA and Cu is negligible due to thermal equilibrium. The addition of nanoparticles of Cu in SA makes the fluid thick and reduces the flow.

By the above assumptions, the governing equations of unsteady flow are [31, 32]

$$\rho_{nf} \frac{\partial \tilde{u}(\tilde{y}, \tilde{t})}{\partial \tilde{t}} = \mu_{nf} \left( 1 + \frac{1}{\gamma} \right) \frac{\partial^2 \tilde{u}(\tilde{y}, \tilde{t})}{\partial \tilde{y}^2} + g(\rho\beta_C)_{nf} \left( \tilde{C}(\tilde{y}, \tilde{t}) - \widetilde{C}_l \right) + g(\rho\beta_T)_{nf} \left( \tilde{T}(\tilde{y}, \tilde{t}) - \widetilde{T}_l \right) - \sigma_{nf} B_0^2 \tilde{u}(\tilde{y}, \tilde{t}), \quad (1)$$

$$(\rho c_p)_{nf} \frac{\partial \tilde{T}(\tilde{y}, \tilde{t})}{\partial \tilde{t}} = k_{nf} \frac{\partial^2 \tilde{T}(\tilde{y}, \tilde{t})}{\partial \tilde{y}^2} + Q_0 \left( \tilde{T}(\tilde{y}, \tilde{t}) - \widetilde{T}_l \right), \quad (2)$$

$$\frac{\partial \tilde{C}(\tilde{y}, \tilde{t})}{\partial \tilde{t}} = D_{nf} \frac{\partial^2 \tilde{C}}{\partial \tilde{y}^2} - K_C \left( \tilde{C}(\tilde{y}, \tilde{t}) - \widetilde{C}_l \right), \quad (3)$$

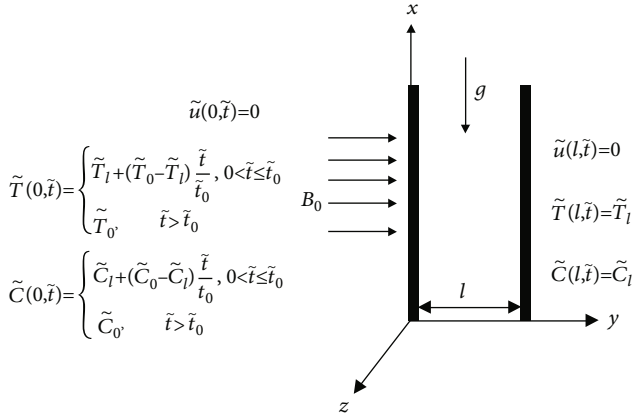


FIGURE 1: Flow geometry.

with corresponding initial and boundary conditions

$$\tilde{u}(\tilde{y}, 0) = 0, \quad (4)$$

$$\tilde{T}(\tilde{y}, 0) = \tilde{T}_l, \quad (5)$$

$$\tilde{C}(\tilde{y}, 0) = \tilde{C}_l, \quad (6)$$

$$0 \leq \tilde{y} \leq l, \quad (7)$$

$$\tilde{u}(0, \tilde{t}) = 0, \quad \tilde{T}(0, \tilde{t}) = \begin{cases} \tilde{T}_l + (\tilde{T}_0 - \tilde{T}_l) \frac{\tilde{t}}{\tilde{t}_0}, & 0 < \tilde{t} \leq \tilde{t}_0, \\ \tilde{T}_0, & \tilde{t} > \tilde{t}_0, \end{cases} \quad (8)$$

$$\tilde{C}(0, \tilde{t}) = \begin{cases} \tilde{C}_l + (\tilde{C}_0 - \tilde{C}_l) \frac{\tilde{t}}{\tilde{t}_0}, & 0 < \tilde{t} \leq \tilde{t}_0, \\ \tilde{C}_0, & \tilde{t} > \tilde{t}_0, \end{cases} \quad (9)$$

$$\tilde{u}(l, \tilde{t}) = 0, \quad (10)$$

$$\tilde{T}(l, \tilde{t}) = \tilde{T}_l, \quad (11)$$

$$\tilde{C}(l, \tilde{t}) = \tilde{C}_l. \quad (12)$$

The expressions of nanofluid are defined by [33, 34].

$$\begin{aligned} \frac{\mu_{nf}}{\mu_f} &= \frac{1}{(1-\phi)^{2.5}}, \\ \frac{\rho_{nf}}{\rho_f} &= (1-\phi) + \phi \frac{\rho_s}{\rho_f}, \\ \frac{(\rho c_p)_{nf}}{(\rho c_p)_f} &= (1-\phi) + \phi \frac{(\rho c_p)_s}{(\rho c_p)_f}, \\ \frac{(\rho \beta_T)_{nf}}{(\rho \beta_T)_f} &= (1-\phi) + \phi \frac{(\rho \beta_T)_s}{(\rho \beta_T)_f}, \end{aligned}$$

$$\frac{(\rho \beta_C)_{nf}}{(\rho \beta_C)_f} = (1-\phi) + \phi \frac{(\rho \beta_C)_s}{(\rho \beta_C)_f},$$

$$D_{nf} = (1-\phi)D_f,$$

$$\frac{\sigma_{nf}}{\sigma_f} = \left[ 1 + \frac{3((\sigma_s/\sigma_f) - 1)\phi}{((\sigma_s/\sigma_f) + 2) - ((\sigma_s/\sigma_f) - 1)\phi} \right],$$

$$\frac{k_{nf}}{k_f} = \left[ \frac{k_s + 2k_f - 2\phi(k_f - k_s)}{k_s + 2k_f + \phi(k_f - k_s)} \right]. \quad (13)$$

Introducing the dimensionless parameters, functions, and variables,

$$u = \frac{\tilde{u}}{U_0}, \quad (14)$$

$$t = \frac{\tilde{t}}{\tilde{t}_0},$$

$$\tilde{t}_0 = \frac{l^2}{\nu_f},$$

$$y = \frac{\tilde{y}}{l},$$

$$\theta = \frac{\tilde{T} - \tilde{T}_l}{\tilde{T}_0 - \tilde{T}_l},$$

$$C = \frac{\tilde{C} - \tilde{C}_l}{\tilde{C}_0 - \tilde{C}_l},$$

$$\psi_1 = \frac{1}{(1-\phi)^{2.5}} \frac{\rho_f}{\rho_{nf}} \left( 1 + \frac{1}{\beta} \right),$$

$$\psi_2 = Gr \frac{(\beta_C)_{nf}}{(\beta_C)_f},$$

$$\psi_3 = Gr \frac{(\beta_T)_{nf}}{(\beta_T)_f},$$

$$\psi_4 = M \frac{\sigma_{nf} \rho_f}{\sigma_f \rho_{nf}},$$

$$\psi_5 = \frac{1}{Pr} \frac{k_{nf} (\rho c_p)_f}{k_f (\rho c_p)_{nf}},$$

$$\psi_6 = Q \frac{(\rho c_p)_f}{(\rho c_p)_{nf}},$$

$$\psi_7 = \frac{1-\phi}{Sc},$$

$$\psi_8 = K = \frac{K_C l^2}{\nu_f},$$

$$Gm = \frac{g(\beta_C)_f (C_0 - C_l) d^2}{U_0 \nu_f},$$

TABLE 1: Thermophysical characteristics of Cu and SA [29, 30].

Material	$\rho$ (kg/m <sup>3</sup> )	$C_p$ (J/kg·K)	$k$ (W/m·K)	$\beta \times 10^5$ (K <sup>-1</sup> )	$\sigma$ ( $\Omega\text{m}$ ) <sup>-1</sup>
Sodium alginate C <sub>6</sub> H <sub>9</sub> NaO <sub>7</sub> (SA)	989	4175	0.6376	0.99	$5.5 \times 10^{-6}$
Copper (Cu)	8933	385	401	1.67	$59.6 \times 10^6$

$$Gr = \frac{g(\beta_T)_f(T_0 - T_1)d^2}{U_0\nu_f},$$

$$M = \frac{\sigma_f B_0^2 l^2}{\mu_f},$$

$$Q = \frac{Q_0 l^2}{(\rho c_p)_f \nu_f},$$

$$Pr = \frac{(\rho c_p)_f \nu_f}{k_f}, Sc = \frac{\nu_f}{D_f}. \quad (15)$$

By substituting equation (15) to equations (1)–(12), we get

$$\frac{\partial u(y, t)}{\partial t} = \psi_1 \frac{\partial^2 u(y, t)}{\partial y^2} + \psi_2 C(y, t) + \psi_3 \theta(y, t) - \psi_4 u(y, t), \quad (16)$$

$$\frac{\partial \theta(y, t)}{\partial t} = \psi_5 \frac{\partial^2 \theta(y, t)}{\partial y^2} + \psi_6 \theta(y, t), \quad (17)$$

$$\frac{\partial C(y, t)}{\partial t} = \psi_7 \frac{\partial^2 C(y, t)}{\partial y^2} - \psi_8 C(y, t). \quad (18)$$

$$u(y, 0) = 0, \theta(y, 0) = 0, C(y, 0) = 0, \quad 0 \leq y \leq 1, \quad (19)$$

$$u(0, t) = 0,$$

$$\theta(0, t) = C(0, t) = \begin{cases} t, & 0 < t \leq 1, \\ 1, & t > 1, \end{cases} = H(t)t - H(t-1)(t-1), \quad (20)$$

$$u(1, t) = 0,$$

$$\theta(1, t) = 0, \quad (21)$$

$$C(1, t) = 0.$$

The researchers used Caputo time-fractional derivatives of order  $\xi$  to develop fractional models in equations (16)–(18).

$$D_t^\xi u(y, t) = \psi_1 \frac{\partial^2 u(y, t)}{\partial y^2} + \psi_2 C(y, t) + \psi_3 \theta(y, t) - \psi_4 u(y, t), \quad (22)$$

$$D_t^\xi \theta(y, t) = \psi_5 \frac{\partial^2 \theta(y, t)}{\partial y^2} + \psi_6 \theta(y, t), \quad (23)$$

$$D_t^\xi C(y, t) = \psi_7 \frac{\partial^2 C(y, t)}{\partial y^2} - \psi_8 C(y, t). \quad (24)$$

Where  $D_t^\xi u(y, t)$  represents the time-fractional Caputo derivative,

$$D_t^\xi u(\eta, \tau) = \begin{cases} \frac{1}{\Gamma(1-\xi)} \int_0^\tau (\tau-w)^\xi \frac{\partial u(\eta, w)}{\partial w} dw, & 0 \leq \xi < 1; \\ \frac{\partial u(\eta, \tau)}{\partial \tau}, & \xi = 1. \end{cases} \quad (25)$$

### 3. Solution of the Problem

3.1. Concentration. Applying Laplace transform (LT) to equations (24), (20)<sub>3</sub>, and (21)<sub>3</sub> and using (19)<sub>3</sub>, we obtain

$$\psi_7 \frac{\partial^2 \bar{C}(y, s)}{\partial y^2} - (s^\xi + \psi_8) \bar{C}(y, s) = 0, \quad (26)$$

$$\bar{C}(0, s) = s^{-2}(1 - e^{-s}), \quad (27)$$

$$\bar{C}(1, s) = 0.$$

The solution of equation (26) subject to equation (27) gives

$$\bar{C}(y, s) = (1 - e^{-s}) \frac{\sinh \left[ (1-y) \sqrt{(s^\xi + \psi_8)/\psi_7} \right]}{s^2 \sinh \left[ \sqrt{(s^\xi + \psi_8)/\psi_7} \right]}. \quad (28)$$

This expression can be written as

$$\bar{C}(y, s) = (1 - e^{-s}) \left( \frac{1}{s^{2-\xi}} + \frac{\psi_8}{s^2} \right) \cdot \sum_{k=0}^{\infty} \left[ \frac{e^{-(2k+y)\sqrt{(s^\xi + \psi_8)/\psi_7}}}{s^\xi + \psi_8} - \frac{e^{-(2k+2-y)\sqrt{(s^\xi + \psi_8)/\psi_7}}}{s^\xi + \psi_8} \right]. \quad (29)$$

Taking inverse LT of equation (29), we get

$$C(y, t) = C_0(y, t) - H(t-1)C_0(y, t-1), \quad (30)$$

where

$$C_0(y, t) = \sum_{k=0}^{\infty} \int_0^t \left( \frac{(t-p)^{1-\xi}}{\Gamma(2-\xi)} + \psi_8(t-p) \right) \cdot \left( g \left( \frac{2k+y}{\sqrt{\psi_7}}, \psi_8, p \right) - g \left( \frac{2k+2-y}{\sqrt{\psi_7}}, \psi_8, p \right) \right) dp, \quad (31)$$

$$g(a, b, p) = \int_0^\infty e^{-bu} \operatorname{erfc} \left( \frac{a}{2\sqrt{u}} \right) \frac{1}{p} \Phi(0, -\xi, -up^{-\xi}) du.$$

3.2. *Temperature Distribution.* Applying LT to equations (23), (20)<sub>2</sub>, and (21)<sub>2</sub> and using (19)<sub>2</sub>, we obtain

$$\psi_5 \frac{\partial^2 \bar{\theta}(y, s)}{\partial y^2} - (s^\xi - \psi_6) \bar{\theta}(y, s) = 0, \quad (32)$$

$$\begin{aligned} \bar{\theta}(0, s) &= s^{-2}(1 - e^{-s}), \\ \bar{\theta}(1, s) &= 0. \end{aligned} \quad (33)$$

The solution of equation (32) subject to equation (33) gives

$$\bar{\theta}(y, s) = (1 - e^{-s}) \frac{\sinh \left[ (1-y) \sqrt{(s^\xi - \psi_6)/\psi_5} \right]}{s^2 \sinh \left[ \sqrt{(s^\xi - \psi_6)/\psi_5} \right]}. \quad (34)$$

This expression can be written as

$$\begin{aligned} \bar{\theta}(y, s) &= (1 - e^{-s}) \left( \frac{1}{s^{2-\xi}} - \frac{\psi_6}{s^2} \right) \\ &\cdot \sum_{k=0}^{\infty} \left[ \frac{e^{-(2k+y) \sqrt{(s^\xi - \psi_6)/\psi_5}}}{s^\xi - \psi_6} - \frac{e^{-(2k+2-y) \sqrt{(s^\xi - \psi_6)/\psi_5}}}{s^\xi - \psi_6} \right]. \end{aligned} \quad (35)$$

Taking inverse LT of equation (35), we get

$$\theta(y, t) = \theta_0(y, t) - H(t-1)\theta_0(y, t-1), \quad (36)$$

where

$$\begin{aligned} \theta_0(y, t) &= \sum_{k=0}^{\infty} \int_0^t \left( \frac{(t-p)^{1-\xi}}{\Gamma(2-\xi)} - \psi_6(t-p) \right) \\ &\cdot \left( g \left( \frac{2k+y}{\sqrt{\psi_5}}, -\psi_6, p \right) - g \left( \frac{2k+2-y}{\sqrt{\psi_5}}, -\psi_6, p \right) \right) dp. \end{aligned} \quad (37)$$

3.3. *Velocity Field.* Applying LT to equations (22), (20)<sub>1</sub>, and (21)<sub>1</sub> and using (19)<sub>1</sub>, we obtain

$$\psi_1 \frac{\partial^2 \bar{u}(y, s)}{\partial y^2} - (s^\xi + \psi_4) \bar{u}(y, s) = -\psi_2 \bar{C}(y, s) - \psi_3 \bar{\theta}(y, s), \quad (38)$$

$$\begin{aligned} \bar{u}(0, s) &= 0, \\ \bar{u}(1, s) &= 0. \end{aligned} \quad (39)$$

The solution of equation (38) subject to equation (39) gives

$$\begin{aligned} \bar{u}(y, s) &= (1 - e^{-s}) \left( \frac{a_1}{s^\xi + a_2} + \frac{a_3}{s^\xi + a_4} \right) \frac{\sinh \left[ (1-y) \sqrt{(s^\xi + \psi_4)/\psi_1} \right]}{s^2 \sinh \left[ \sqrt{(s^\xi + \psi_4)/\psi_1} \right]} \\ &- (1 - e^{-s}) \left( \frac{a_1}{s^\xi + a_2} \right) \frac{\sinh \left[ (1-y) \sqrt{(s^\xi + \psi_8)/\psi_7} \right]}{s^2 \sinh \left[ \sqrt{(s^\xi + \psi_8)/\psi_7} \right]} \\ &- (1 - e^{-s}) \left( \frac{a_3}{s^\xi + a_4} \right) \frac{\sinh \left[ (1-y) \sqrt{(s^\xi + \psi_6)/\psi_5} \right]}{s^2 \sinh \left[ \sqrt{(s^\xi + \psi_6)/\psi_5} \right]}. \end{aligned} \quad (40)$$

This expression can be as

$$\begin{aligned} \bar{u}(y, s) &= (1 - e^{-s}) \left[ \left( \frac{a_1 + a_3}{s^2} + \frac{a_1(\psi_4 - a_2)}{s^2(s^\xi + a_2)} + \frac{a_3(\psi_4 - a_4)}{s^2(s^\xi + a_4)} \right) \right. \\ &\cdot \sum_{k=0}^{\infty} \left( \frac{e^{-(2k+y) \sqrt{(s^\xi + \psi_4)/\psi_1}}}{s^\xi + \psi_4} - \frac{e^{-(2k+2-y) \sqrt{(s^\xi + \psi_4)/\psi_1}}}{s^\xi + \psi_4} \right) \\ &- \left( \frac{a_1}{s^2} + \frac{a_1(\psi_8 - a_2)}{s^2(s^\xi + a_2)} \right) \sum_{k=0}^{\infty} \left( \frac{e^{-(2k+y) \sqrt{(s^\xi + \psi_8)/\psi_7}}}{s^\xi + \psi_8} \right. \\ &- \frac{e^{-(2k+2-y) \sqrt{(s^\xi + \psi_8)/\psi_7}}}{s^\xi + \psi_8} \left. \right) - \left( \frac{a_3}{s^2} - \frac{a_3(\psi_6 + a_4)}{s^2(s^\xi + a_4)} \right) \\ &\cdot \sum_{k=0}^{\infty} \left( \frac{e^{-(2k+y) \sqrt{(s^\xi + \psi_6)/\psi_5}}}{s^\xi - \psi_6} - \frac{e^{-(2k+2-y) \sqrt{(s^\xi + \psi_6)/\psi_5}}}{s^\xi - \psi_6} \right) \left. \right]. \end{aligned} \quad (41)$$

Taking inverse LT of equation (41), we get

$$u(y, t) = u_0(y, t) - H(t-1)u_0(y, t-1), \quad (42)$$

where

$$\begin{aligned} u_0(y, t) &= \sum_{k=0}^{\infty} \int_0^t \left( (a_1 + a_3)(t-p) + a_1(\psi_4 - a_2)f_1(t-p) \right. \\ &+ a_3(\psi_4 - a_4)f_2(t-p) \left. \right) \left( g \left( \frac{2k+y}{\sqrt{\psi_1}}, \psi_4, p \right) \right. \\ &- \left. g \left( \frac{2k+2-y}{\sqrt{\psi_1}}, \psi_4, p \right) \right) dp - \sum_{k=0}^{\infty} \int_0^t (a_1(t-p) \\ &+ a_1(\psi_8 - a_2)f_1(t-p)) \left( g \left( \frac{2k+y}{\sqrt{\psi_7}}, \psi_8, p \right) \right. \\ &- \left. g \left( \frac{2k+2-y}{\sqrt{\psi_7}}, \psi_8, p \right) \right) dp - \sum_{k=0}^{\infty} \int_0^t (a_3(t-p) \\ &- a_3(\psi_6 + a_4)f_2(t-p)) \left( g \left( \frac{2k+y}{\sqrt{\psi_5}}, -\psi_6, p \right) \right. \\ &- \left. g \left( \frac{2k+2-y}{\sqrt{\psi_5}}, -\psi_6, p \right) \right) dp, \end{aligned}$$

$$\begin{aligned}
 f_1(t) &= \int_0^t w^\xi E_{\xi, \xi+1}(-a_2 w^\xi) dw, \\
 f_2(t) &= \int_0^t w^\xi E_{\xi, \xi+1}(-a_4 w^\xi) dw.
 \end{aligned}
 \tag{43}$$

3.4. Sherwood Numbers, Skin Friction, and Nusselt Numbers. Skin friction at  $y = 0$  is defined as

$$C_{f_0} = - \left. \frac{\mu_{nf}}{\mu_f} \frac{\partial u(y, t)}{\partial y} \right|_{y=0} = -(1-\phi)^{-2.5} L^{-1} \left\{ \left. \frac{\partial \bar{u}(y, s)}{\partial y} \right|_{y=0} \right\}.
 \tag{44}$$

By using equation (41) in equation (44),

$$C_{f_0} = \frac{1}{(1-\phi)^{2.5}} [u_1(t) - H(t-1)u_1(t-1)],
 \tag{45}$$

where

$$\begin{aligned}
 u_1(t) &= \frac{1}{\sqrt{\psi_1}} \sum_{k=0}^{\infty} \int_0^t ((a_1 + a_3)(t-p) + a_1(\psi_4 - a_2)f_1(t-p) \\
 &+ a_3(\psi_4 - a_4)f_2(t-p)) \left( L' \left( \frac{k}{\sqrt{\psi_1}}, \psi_4, p \right) \right. \\
 &+ \left. L' \left( \frac{k+1}{\sqrt{\psi_1}}, \psi_4, p \right) \right) dp - \frac{1}{\sqrt{\psi_7}} \sum_{k=0}^{\infty} \int_0^t (a_1(t-p) \\
 &+ a_1(\psi_8 - a_2)f_1(t-p)) \left( L' \left( \frac{k}{\sqrt{\psi_7}}, \psi_8, p \right) \right. \\
 &+ \left. L' \left( \frac{k+1}{\sqrt{\psi_7}}, \psi_8, p \right) \right) dp - \frac{1}{\sqrt{\psi_5}} \sum_{k=0}^{\infty} \int_0^t (a_3(t-p) \\
 &- a_3(\psi_6 + a_4)f_2(t-p)) \left( L' \left( \frac{k}{\sqrt{\psi_5}}, -\psi_6, p \right) \right. \\
 &+ \left. L' \left( \frac{k+1}{\sqrt{\psi_5}}, -\psi_6, p \right) \right) dp,
 \end{aligned}$$

$$L'(a, b, p) = \int_0^{\infty} \frac{1}{\sqrt{\pi w}} e^{-((a^2/4w)+bw)} \frac{1}{p} \Phi(0, -\xi, -wp^{-\xi}) dw.
 \tag{46}$$

Skin friction at  $y = 1$  is defined as

$$C_{f_1} = - \left. \frac{\mu_{nf}}{\mu_f} \frac{\partial u(y, t)}{\partial y} \right|_{y=1} = -(1-\phi)^{-2.5} L^{-1} \left\{ \left. \frac{\partial \bar{u}(y, s)}{\partial y} \right|_{y=1} \right\}.
 \tag{47}$$

By using equation (41) in equation (47),

$$C_{f_1} = \frac{1}{(1-\phi)^{2.5}} [u_2(t) - H(t-1)u_2(t-1)],
 \tag{48}$$

where

$$\begin{aligned}
 u_2(t) &= \frac{1}{\sqrt{\psi_1}} \sum_{k=0}^{\infty} \int_0^t ((a_1 + a_3)(t-p) + a_1(\psi_4 - a_2)f_1(t-p) \\
 &+ a_3(\psi_4 - a_4)f_2(t-p)) \left( 2L' \left( \frac{2k+1}{\sqrt{\psi_1}}, \psi_4, p \right) \right) dp \\
 &- \frac{1}{\sqrt{\psi_7}} \sum_{k=0}^{\infty} \int_0^t (a_1(t-p) + a_1(\psi_8 - a_2)f_1(t-p)) \\
 &\cdot \left( 2L' \left( \frac{2k+1}{\sqrt{\psi_7}}, \psi_8, p \right) \right) dp - \frac{1}{\sqrt{\psi_5}} \\
 &\cdot \sum_{k=0}^{\infty} \int_0^t (a_3(t-p) - a_3(\psi_6 + a_4)f_2(t-p)) \\
 &\cdot \left( 2L' \left( \frac{2k+1}{\sqrt{\psi_5}}, -\psi_6, p \right) \right) dp.
 \end{aligned}
 \tag{49}$$

Nusselt numbers

$$Nu_0 = - \left. \frac{k_{nf}}{k_f} \frac{\partial \theta}{\partial y} \right|_{y=0} = - \frac{k_{nf}}{k_f} L^{-1} \left\{ \left. \frac{\partial \bar{\theta}}{\partial y} \right|_{y=0} \right\}.
 \tag{50}$$

By using equation (36) in equation (50),

$$Nu_0 = \frac{k_{nf}}{k_f} [\theta_1(t) - H(t-1)\theta_1(t-1)],
 \tag{51}$$

where

$$\begin{aligned}
 \theta_1(t) &= \frac{1}{\sqrt{\psi_5}} \sum_{k=0}^{\infty} \int_0^t \left( \frac{(t-p)^{1-\xi}}{\Gamma(2-\xi)} - \psi_6(t-p) \right) \\
 &\cdot \left( L' \left( \frac{k}{\sqrt{\psi_5}}, -\psi_6, p \right) + L' \left( \frac{k+1}{\sqrt{\psi_5}}, -\psi_6, p \right) \right) dp,
 \end{aligned}
 \tag{52}$$

$$Nu_1 = - \left. \frac{k_{nf}}{k_f} \frac{\partial \theta}{\partial y} \right|_{y=1} = - \frac{k_{nf}}{k_f} L^{-1} \left\{ \left. \frac{\partial \bar{\theta}}{\partial y} \right|_{y=1} \right\},
 \tag{53}$$

By using equation (36) in equation (53),

$$Nu_1 = \frac{k_{nf}}{k_f} [\theta_2(t) - H(t-1)\theta_2(t-1)],
 \tag{54}$$

where

$$\theta_2(t) = \frac{1}{\sqrt{\psi_5}} \sum_{k=0}^{\infty} \int_0^t \left( \frac{(t-p)^{1-\xi}}{\Gamma(2-\xi)} - \psi_6(t-p) \right) \cdot \left( 2L' \left( \frac{2k+1}{\sqrt{\psi_5}}, -\psi_6, p \right) \right) dp, \quad (55)$$

$$Sh_0 = -\frac{D_{nf}}{D_f} \frac{\partial C}{\partial y} \Big|_{y=0} = -\frac{D_{nf}}{D_f} L^{-1} \left\{ \frac{\partial \bar{C}}{\partial y} \Big|_{y=0} \right\}. \quad (56)$$

By using equation (29) in equation (56),

$$Sh_0 = \frac{D_{nf}}{D_f} [C_1(t) - H(t-1)C_1(t-1)], \quad (57)$$

where

$$C_1(t) = \frac{1}{\sqrt{\psi_7}} \sum_{k=0}^{\infty} \int_0^t \left( \frac{(t-p)^{1-\xi}}{\Gamma(2-\xi)} + \psi_8(t-p) \right) \cdot \left( L' \left( \frac{k}{\sqrt{\psi_7}}, \psi_8, p \right) + L' \left( \frac{k+1}{\sqrt{\psi_7}}, \psi_8, p \right) \right) dp, \quad (58)$$

$$Sh_1 = -\frac{D_{nf}}{D_f} \frac{\partial C}{\partial y} \Big|_{y=1} = -\frac{D_{nf}}{D_f} L^{-1} \left\{ \frac{\partial \bar{C}}{\partial y} \Big|_{y=1} \right\}. \quad (59)$$

By using equation (29) in equation (59),

$$Sh_1 = \frac{D_{nf}}{D_f} [C_2(t) - H(t-1)C_2(t-1)], \quad (60)$$

where

$$C_2(t) = \frac{1}{\sqrt{\psi_7}} \sum_{k=0}^{\infty} \int_0^t \left( \frac{(t-p)^{1-\xi}}{\Gamma(2-\xi)} + \psi_8(t-p) \right) \cdot \left( 2L' \left( \frac{2k+1}{\sqrt{\psi_7}}, \psi_8, p \right) \right) dp. \quad (61)$$

**3.5. Solution of Problem for Isothermal Conditions.** For isothermal conditions equation (20) becomes  $\theta(0, t) = C(0, t) = 1$ ,  $u(0, t) = 0$ .

$$C(y, t) = \sum_{k=0}^{\infty} \int_0^t \left( \frac{(t-p)^{-\xi}}{\Gamma(1-\xi)} + \psi_8 \right) \left( g \left( \frac{2k+y}{\sqrt{\psi_7}}, \psi_8, p \right) - g \left( \frac{2k+2-y}{\sqrt{\psi_7}}, \psi_8, p \right) \right) dp,$$

$$\theta(y, t) = \sum_{k=0}^{\infty} \int_0^t \left( \frac{(t-p)^{-\xi}}{\Gamma(1-\xi)} - \psi_6 \right) \left( g \left( \frac{2k+y}{\sqrt{\psi_5}}, -\psi_6, p \right) - g \left( \frac{2k+2-y}{\sqrt{\psi_5}}, -\psi_6, p \right) \right) dp,$$

$$u(y, t) = \sum_{k=0}^{\infty} \int_0^t \left( (a_1 + a_3) + \frac{a_1(\psi_4 - a_2)}{a_2} f_3(t-p) + \frac{a_3(\psi_4 - a_4)}{a_4} f_4(t-p) \right) \left( g \left( \frac{2k+y}{\sqrt{\psi_1}}, \psi_4, p \right) - g \left( \frac{2k+2-y}{\sqrt{\psi_1}}, \psi_4, p \right) \right) dp - \sum_{k=0}^{\infty} \int_0^t \left( a_1 + \frac{a_1(\psi_8 - a_2)}{a_2} f_3(t-p) \right) \cdot \left( g \left( \frac{2k+y}{\sqrt{\psi_7}}, \psi_8, p \right) - g \left( \frac{2k+2-y}{\sqrt{\psi_7}}, \psi_8, p \right) \right) dp - \sum_{k=0}^{\infty} \int_0^t \left( a_3 - \frac{a_3(\psi_6 + a_4)}{a_4} f_4(t-p) \right) \cdot \left( g \left( \frac{2k+y}{\sqrt{\psi_5}}, -\psi_6, p \right) - g \left( \frac{2k+2-y}{\sqrt{\psi_5}}, -\psi_6, p \right) \right) dp, \quad (62)$$

where

$$f_3(t) = a_2 t^\xi E_{\xi, \xi+1}(-a_2 w^\xi), \quad (63)$$

$$f_4(t) = a_4 t^\xi E_{\xi, \xi+1}(-a_4 w^\xi).$$

**3.6. Sherwood Numbers, Skin Friction, and Nusselt Numbers (for Isothermal).** Skin friction at  $y = 0$  is defined as

$$C_{f_0} = \frac{1}{(1-\phi)^{2.5} \sqrt{\psi_1}} \sum_{k=0}^{\infty} \int_0^t \left( (a_1 + a_3) + \frac{a_1(\psi_4 - a_2)}{a_2} f_3(t-p) + \frac{a_3(\psi_4 - a_4)}{a_4} f_4(t-p) \right) \left( L' \left( \frac{k}{\sqrt{\psi_1}}, \psi_4, p \right) + L' \left( \frac{k+1}{\sqrt{\psi_1}}, \psi_4, p \right) \right) dp - \frac{1}{(1-\phi)^{2.5} \sqrt{\psi_7}} \cdot \sum_{k=0}^{\infty} \int_0^t \left( a_1 + \frac{a_1(\psi_8 - a_2)}{a_2} f_3(t-p) \right) \cdot \left( L' \left( \frac{k}{\sqrt{\psi_7}}, \psi_8, p \right) + L' \left( \frac{k+1}{\sqrt{\psi_7}}, \psi_8, p \right) \right) dp - \frac{1}{(1-\phi)^{2.5} \sqrt{\psi_5}} \sum_{k=0}^{\infty} \int_0^t \left( a_3 - \frac{a_3(\psi_6 + a_4)}{a_4} f_4(t-p) \right) \cdot \left( L' \left( \frac{k}{\sqrt{\psi_5}}, -\psi_6, p \right) + L' \left( \frac{k+1}{\sqrt{\psi_5}}, -\psi_6, p \right) \right) dp. \quad (64)$$

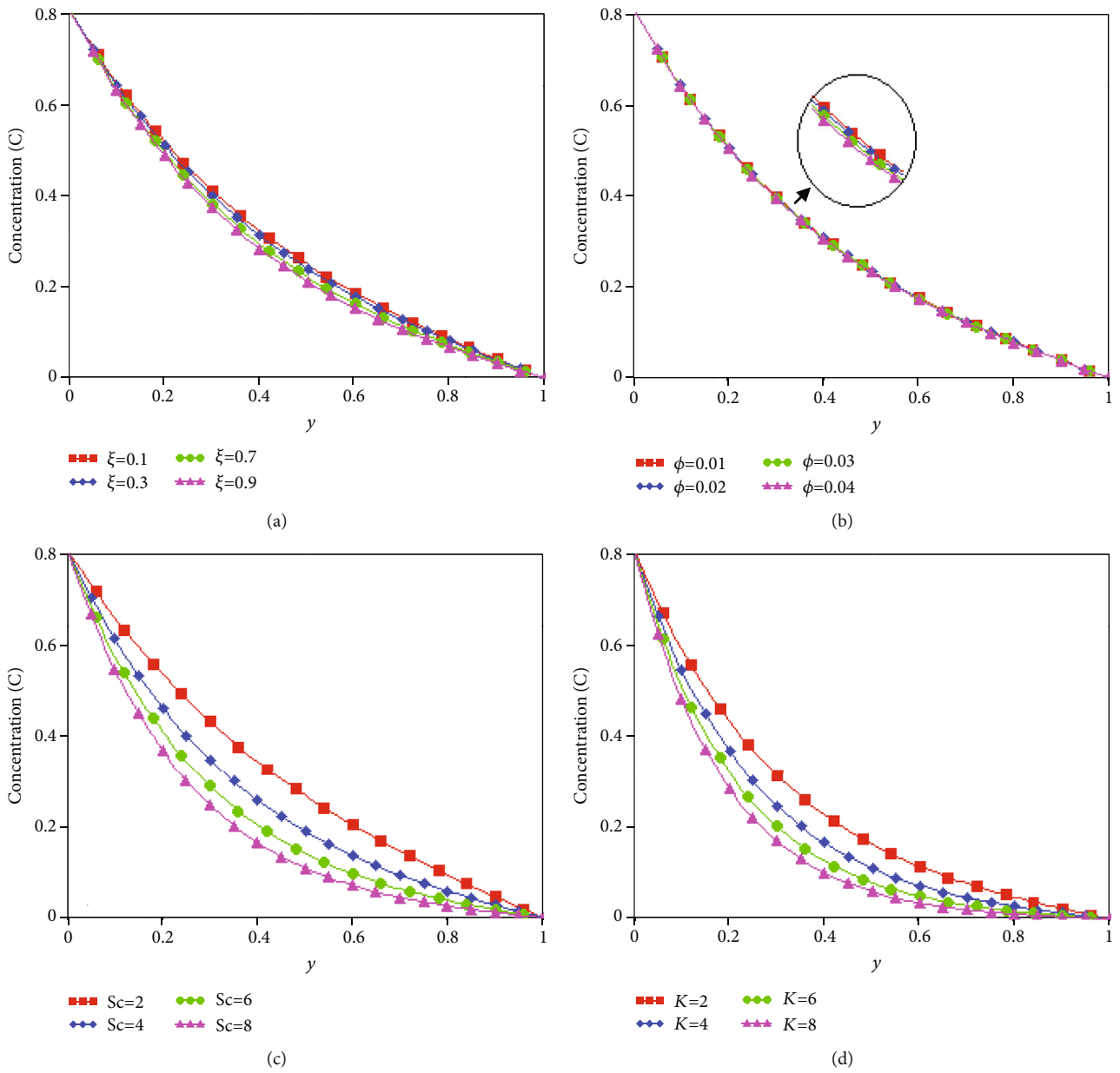


FIGURE 2: Variation of concentration.



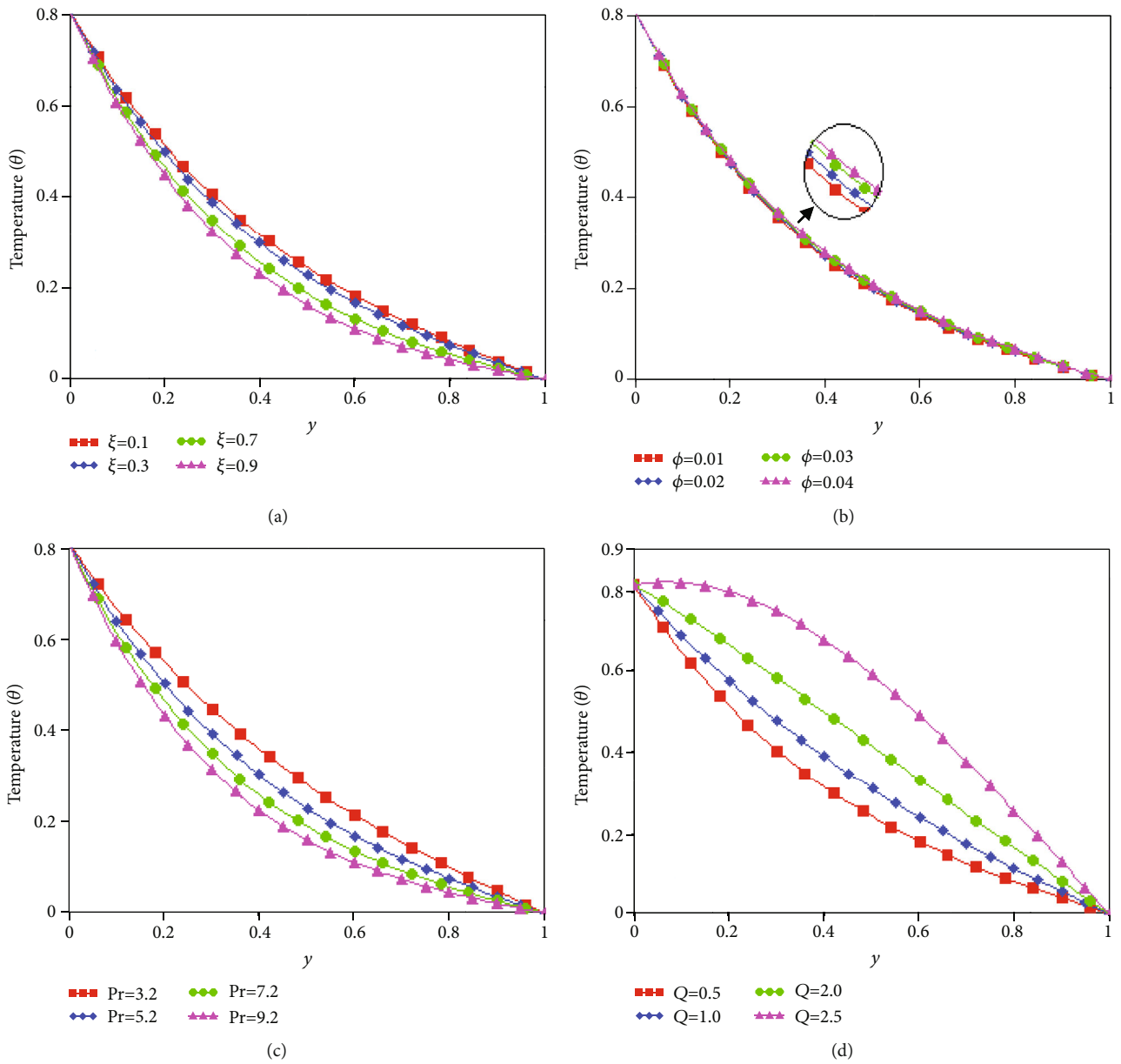
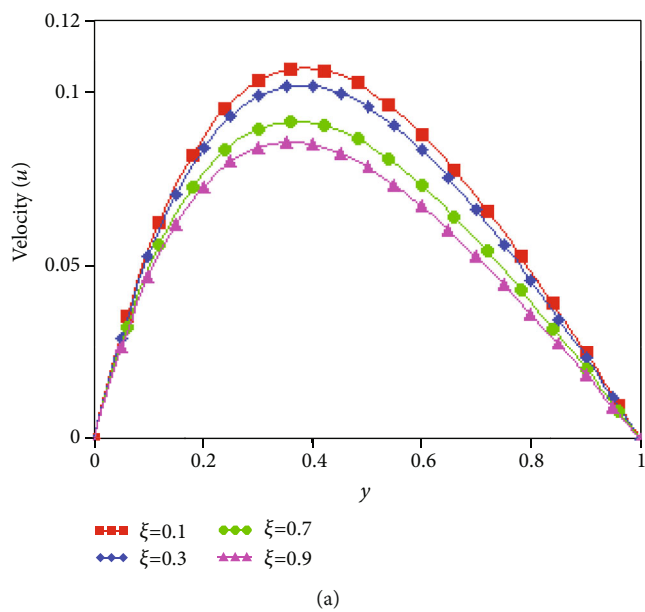
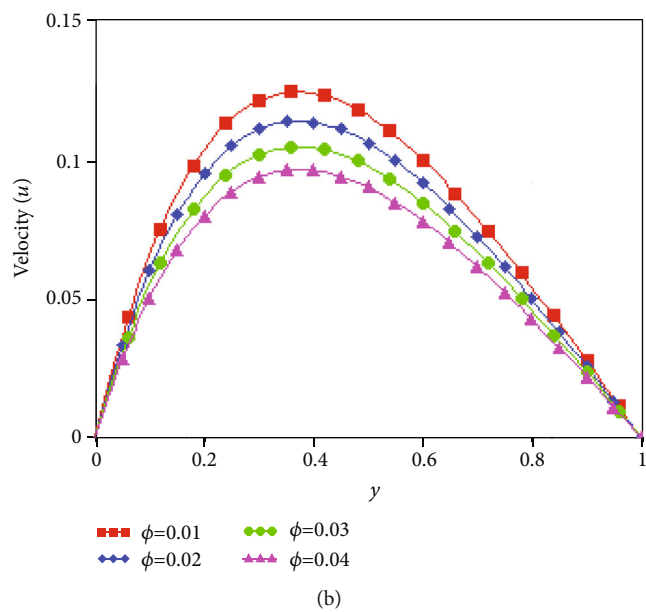


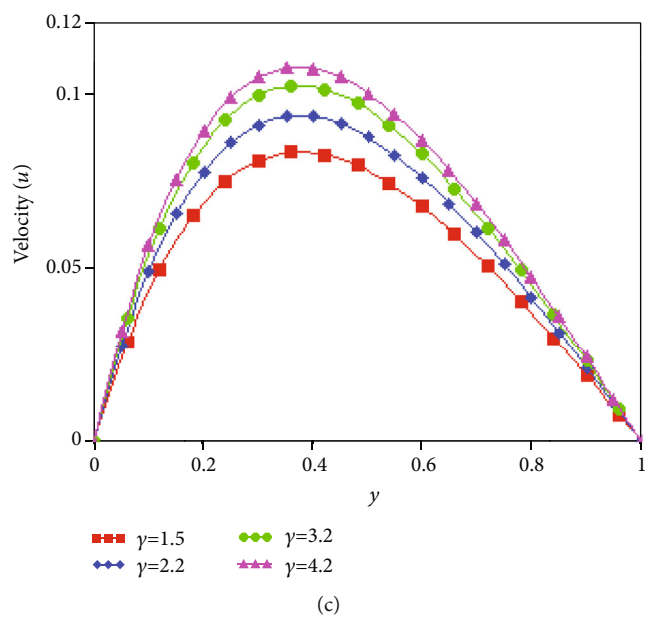
FIGURE 3: Variation of temperature.



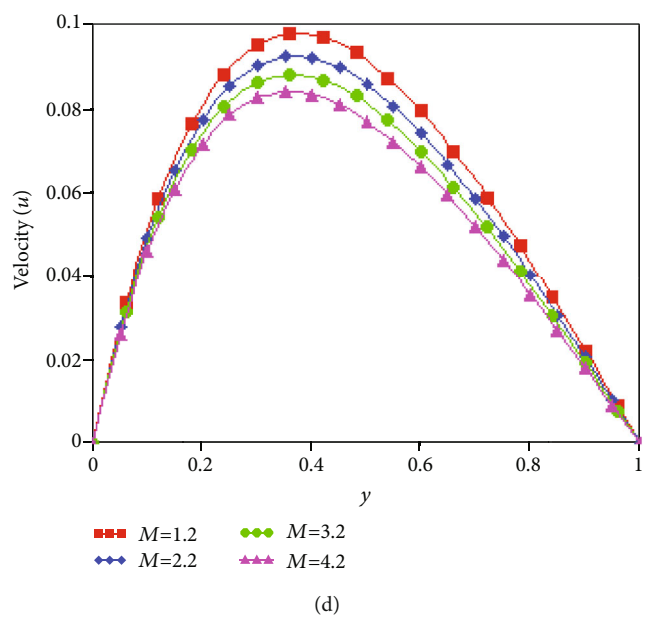
(a)



(b)



(c)



(d)

FIGURE 4: Continued.

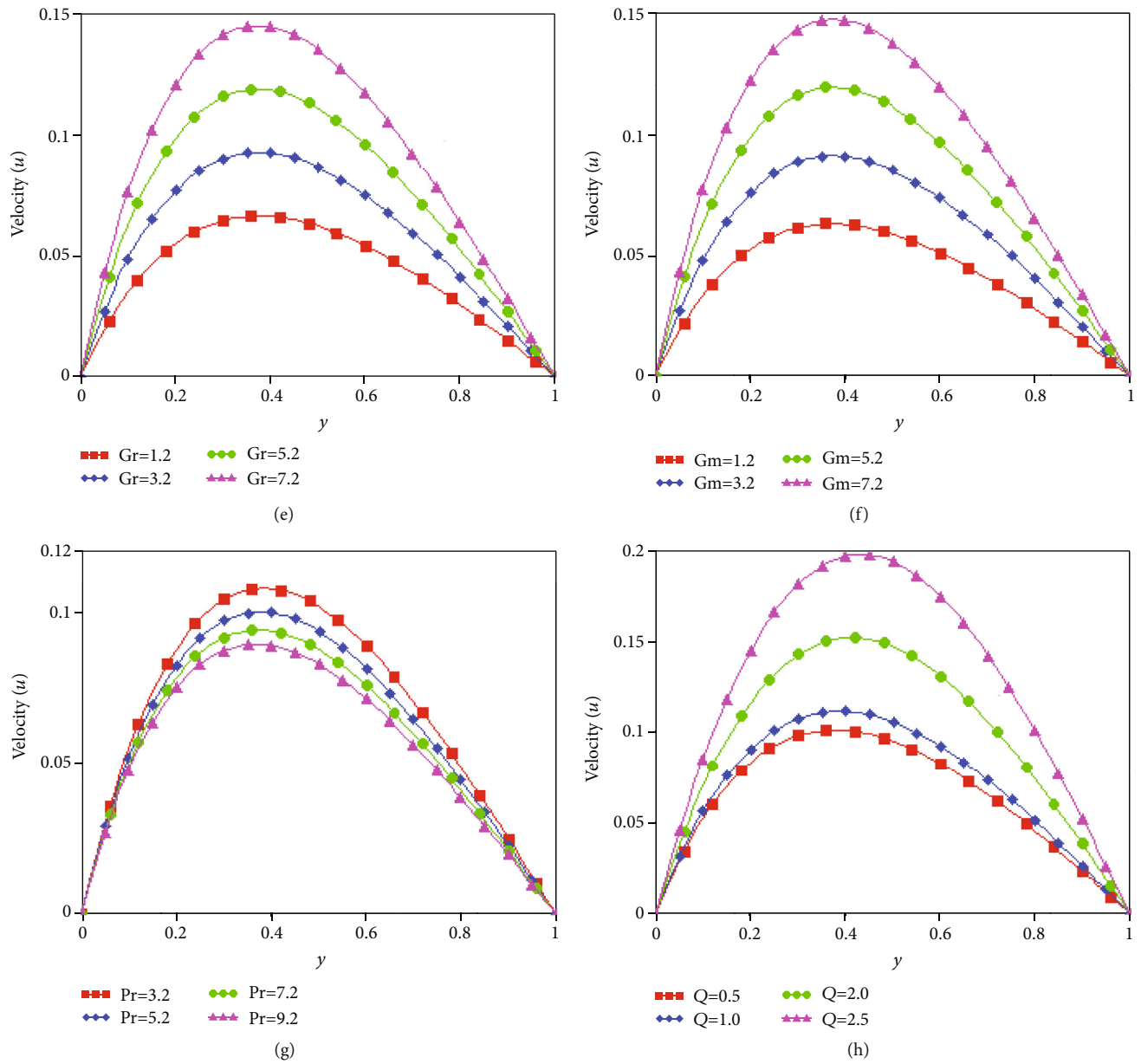


FIGURE 4: Continued.

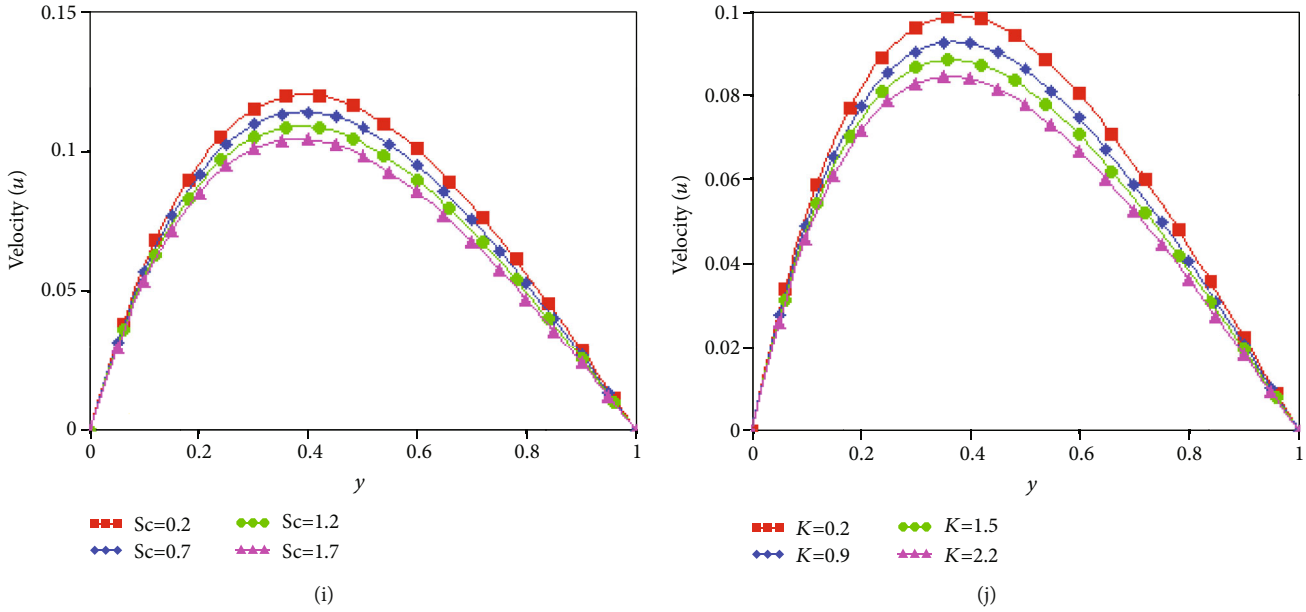


FIGURE 4: Variation of velocity.

Skin friction at  $y = 1$  is defined as

$$\begin{aligned}
 C_{f_1} = & \frac{1}{(1-\phi)^{2.5} \sqrt{\psi_1}} \sum_{k=0}^{\infty} \int_0^t \left( (a_1 + a_3) + \frac{a_1(\psi_4 - a_2)}{a_2} f_3(t-p) \right. \\
 & + \frac{a_3(\psi_4 - a_4)}{a_4} f_4(t-p) \left. \right) \left( 2L' \left( \frac{2k+1}{\sqrt{\psi_1}}, \psi_4, p \right) \right) dp \\
 & - \frac{1}{(1-\phi)^{2.5} \sqrt{\psi_7}} \sum_{k=0}^{\infty} \int_0^t \left( a_1 + \frac{a_1(\psi_8 - a_2)}{a_2} f_3(t-p) \right) \\
 & \cdot \left( 2L' \left( \frac{2k+1}{\sqrt{\psi_7}}, \psi_8, p \right) \right) dp - \frac{1}{(1-\phi)^{2.5} \sqrt{\psi_5}} \\
 & \cdot \sum_{k=0}^{\infty} \int_0^t \left( a_3 - \frac{a_3(\psi_6 + a_4)}{a_4} f_4(t-p) \right) \\
 & \cdot \left( 2L' \left( \frac{2k+1}{\sqrt{\psi_5}}, -\psi_6, p \right) \right) dp.
 \end{aligned}
 \tag{65}$$

Nusselt numbers

$$\begin{aligned}
 Nu_0 = & \frac{1}{\sqrt{\psi_5}} \frac{k_{nf}}{k_f} \sum_{k=0}^{\infty} \int_0^t \left( \frac{(t-p)^{-\xi}}{\Gamma(1-\xi)} - \psi_6 \right) \\
 & \cdot \left( L' \left( \frac{k}{\sqrt{\psi_5}}, -\psi_6, p \right) + L' \left( \frac{k+1}{\sqrt{\psi_5}}, -\psi_6, p \right) \right) dp, \\
 Nu_1 = & \frac{1}{\sqrt{\psi_5}} \frac{k_{nf}}{k_f} \sum_{k=0}^{\infty} \int_0^t \left( \frac{(t-p)^{-\xi}}{\Gamma(1-\xi)} - \psi_6 \right) \\
 & \cdot \left( 2L' \left( \frac{2k+1}{\sqrt{\psi_5}}, -\psi_6, p \right) \right) dp.
 \end{aligned}
 \tag{66}$$

Sherwood numbers

$$\begin{aligned}
 Sh_0 = & \frac{1-\phi}{\sqrt{\psi_7}} \sum_{k=0}^{\infty} \int_0^t \left( \frac{(t-p)^{-\xi}}{\Gamma(1-\xi)} + \psi_8 \right) \\
 & \cdot \left( L' \left( \frac{k}{\sqrt{\psi_7}}, \psi_8, p \right) + L' \left( \frac{k+1}{\sqrt{\psi_7}}, \psi_8, p \right) \right) dp, \\
 Sh_1 = & \frac{1-\phi}{\sqrt{\psi_7}} \sum_{k=0}^{\infty} \int_0^t \left( \frac{(t-p)^{-\xi}}{\Gamma(1-\xi)} + \psi_8 \right) \left( 2L' \left( \frac{2k+1}{\sqrt{\psi_7}}, \psi_8, p \right) \right) dp.
 \end{aligned}
 \tag{67}$$

#### 4. Graphical Results and Discussions

In this section, the influences of dimensionless parameters on fluid flow are discussed. The impact of ramped temperature, ramped concentration and volume fraction, and fractional and physical parameters on Casson nanofluid in a channel is analyzed.

For comparison, the graphs of nondimensional concentration, temperature, and velocity profiles corresponding to Casson parameter ( $\gamma$ ), magnetic parameter ( $M$ ), nanoparticle volume parameter ( $\phi$ ), Grashof numbers ( $Gr$  and  $Gr$ ), Schmidt number ( $Sc$ ), Prandtl number ( $Pr$ ), heat generation ( $Q$ ), chemical reaction ( $K$ ), and fractional parameters ( $\xi$ ) are shown in Figures 2–4. In the entire comparison all Casson parameter,  $\gamma = 2.5$ ,  $\phi = 0.04$ ,  $\xi = 0.5$ ,  $t = 0.8$ ,  $Pr = 6.2$ ,  $Gm = 3.6$ ,  $Gr = 3.5$ ,  $Q = 0.2$ ,  $M = 1.5$ , and  $K = 0.5$  are fixed except the deviation in the respective figures.

Figures 2(a), 3(a), and 4(a) show the influence of  $\xi$  on concentration, temperature, and velocity fields. Velocity, concentration, and temperature obtained with derivatives are the better choice to have controlled results. The concentration, temperature, and velocity profiles reduce for higher values of  $\xi$  with ramped boundary conditions. Figures 2(b),

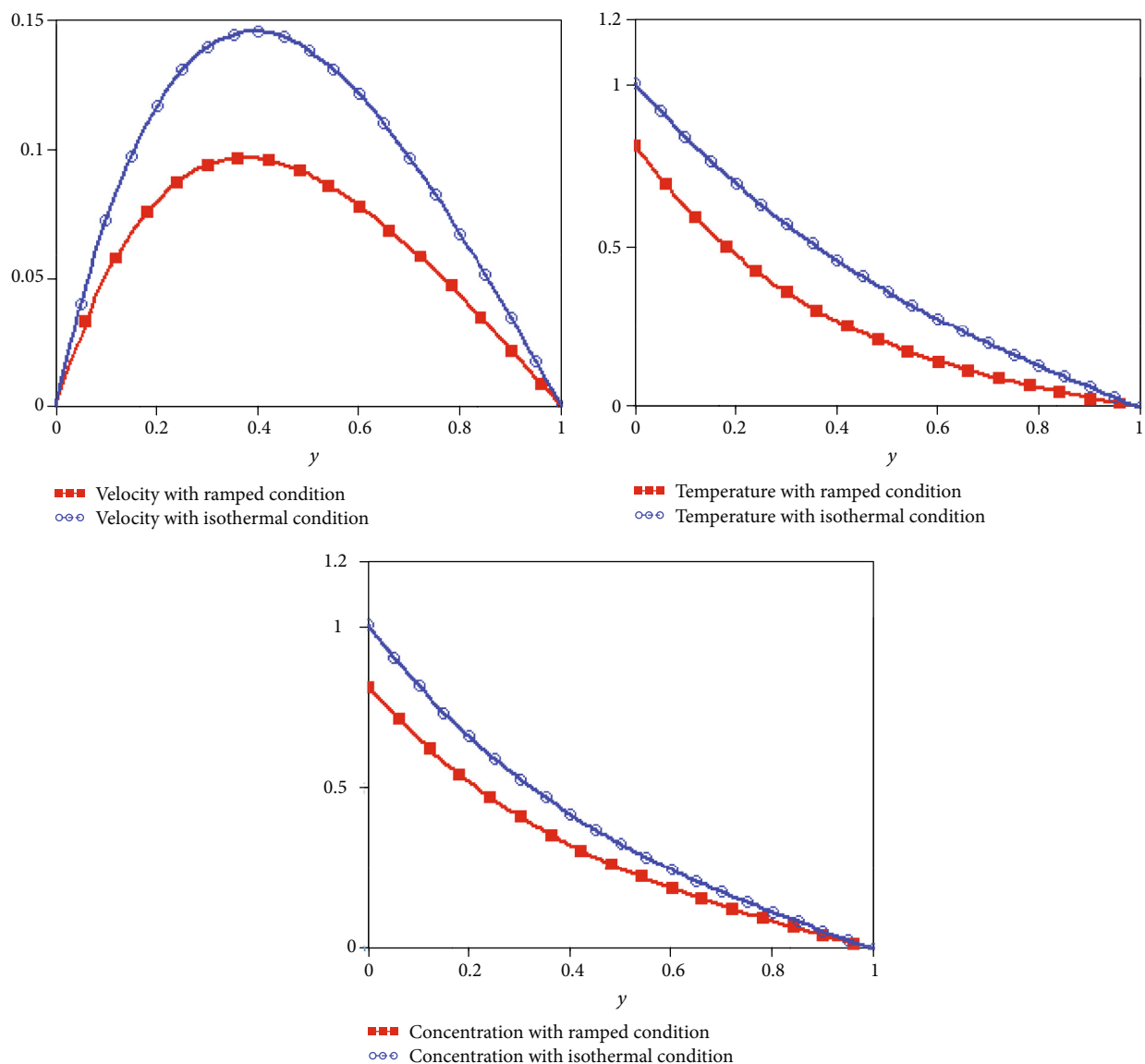


FIGURE 5: Comparison for velocity, temperature, and concentration fields with isothermal and ramped conditions.

3(b), and 4(b) depict the influence of  $\phi$  on concentration, temperature, and velocity profiles. From Figures 2(b) and 4(b), it is noticed that the concentration and velocity of nanofluid decreases for higher values of  $\phi$ . The increasing values of  $\phi$  enhance the thickness and dynamic viscosity that reduce concentration and velocity of the nanofluid. Figure 3(b) illustrates that the temperature field of nanofluid increases due to the collision of nanoparticles for greater values of volume fraction. Also, the temperature increases due to the higher thermal conductivity of Cu nanoparticles.

Figures 2(c) and 4(i) demonstrate that the rise in  $Sc$  is similar to a poor solute diffusion which lets shallower dispersion of solute outcome. Consequently, the concentration and velocity reduce. Thus, the larger of  $Sc$  reduces the thickness

of the boundary layer. Figures 2(d) and 4(g) indicate that the concentration and velocity fields reduce rapidly as  $K$  increases. The solute molecules increase under the influence of chemical reaction parameter.

Figures 3(c) and 4(g) show the impact of  $Pr$  on temperature and velocity. The higher values of  $Pr$  increase the viscosity of the nanofluid and reduce the heat transport rate of the nanofluid that reduces velocity and temperature. Figures 3(d) and 4(h) illustrate that by increasing  $Q > 0$ , the heat is discharged due to which temperature and velocity increase.

Figure 4(c) demonstrates the impact of the Casson parameter on velocity. The flow increases by increasing  $\gamma$ . Figure 4(d) reflects the influence of magnetic parameter ( $M$ ) on the velocity field. An increase in  $M$  reduces the

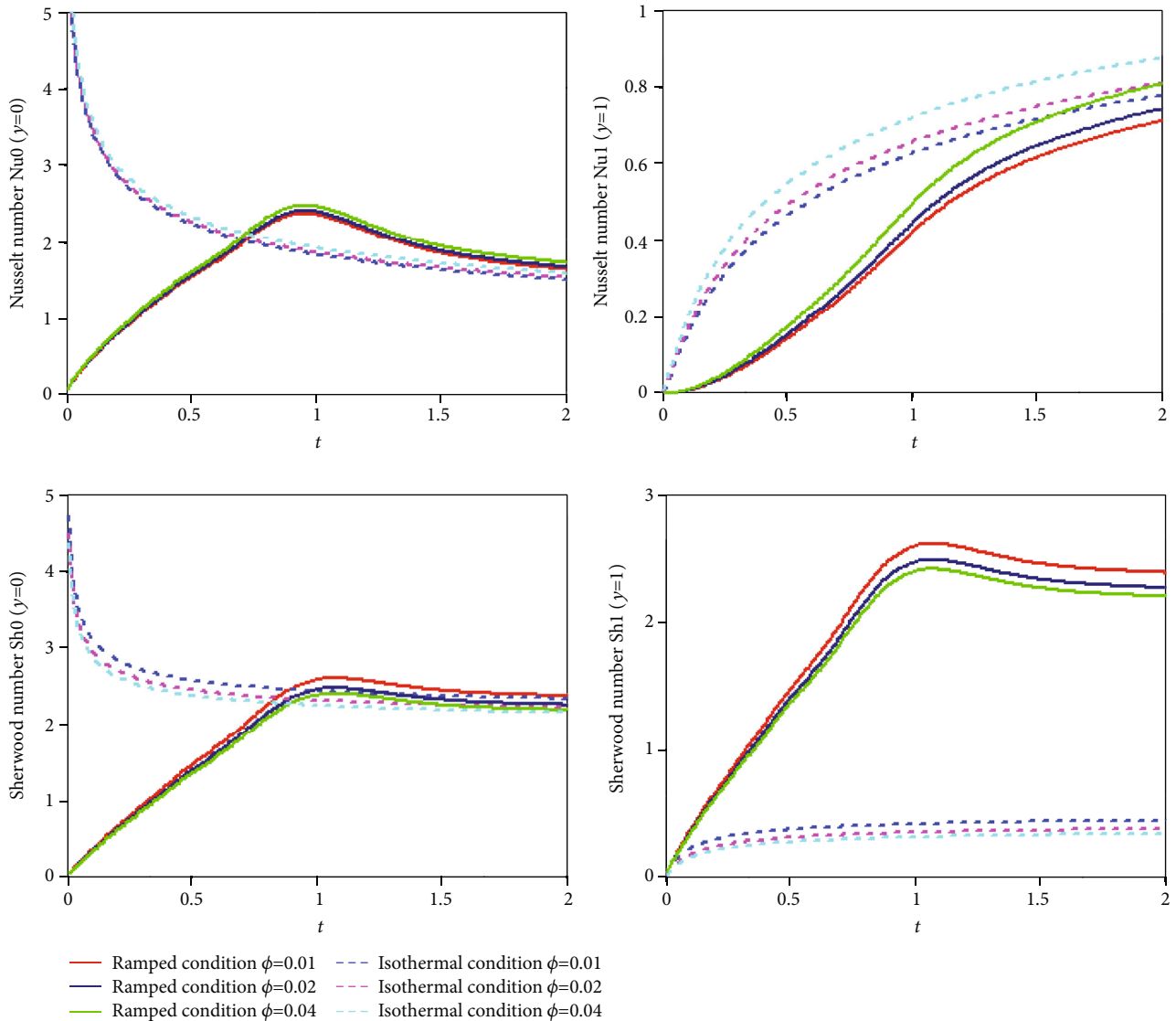


FIGURE 6: Effects of  $\phi$  on Nusselt and Sherwood numbers.

thickness of the flow boundary and decreases the velocity. Figures 4(e) and 4(f) show that the velocity increases for increasing Grashof numbers ( $Gr$  and  $Gm$ ). Grashof numbers indicate the relative significance of viscous force to buoyancy force. The viscous effect in velocity reduces by large Grashof numbers.

Figure 5 illustrates the comparison of velocity, concentration, and temperature with constant and ramped boundary conditions. It established that ramped velocity, concentration, and temperature are lower than acquired by isothermal conditions. Thus, the ramped boundary conditions are more stable.

Figure 6 shows the variations in Nusselt and Sherwood numbers on both plates with ramped and isothermal conditions. The Sherwood numbers decrease and Nusselt numbers increase by increasing volume fraction.

Figure 7 illustrates the comparison of present results with existing results of Ramzan et al. [31]. It is concluded that in the absence of  $\phi$ , porosity and Dufour effects the results are identical.

## 5. Conclusions

An unsteady Casson nanofluid flow within a channel with ramped concentration and temperature is investigated. Furthermore, chemical reaction, heat generation, and magnetic effects are considered. The problem is generalized by Caputo time-fractional derivative, and Laplace transform is used to find analytical results of ramped and isothermal boundary conditions. In this work, SA is considered as a base fluid containing the nanoparticles of Cu. The significant results for velocity, concentration, temperature, Nusselt numbers,

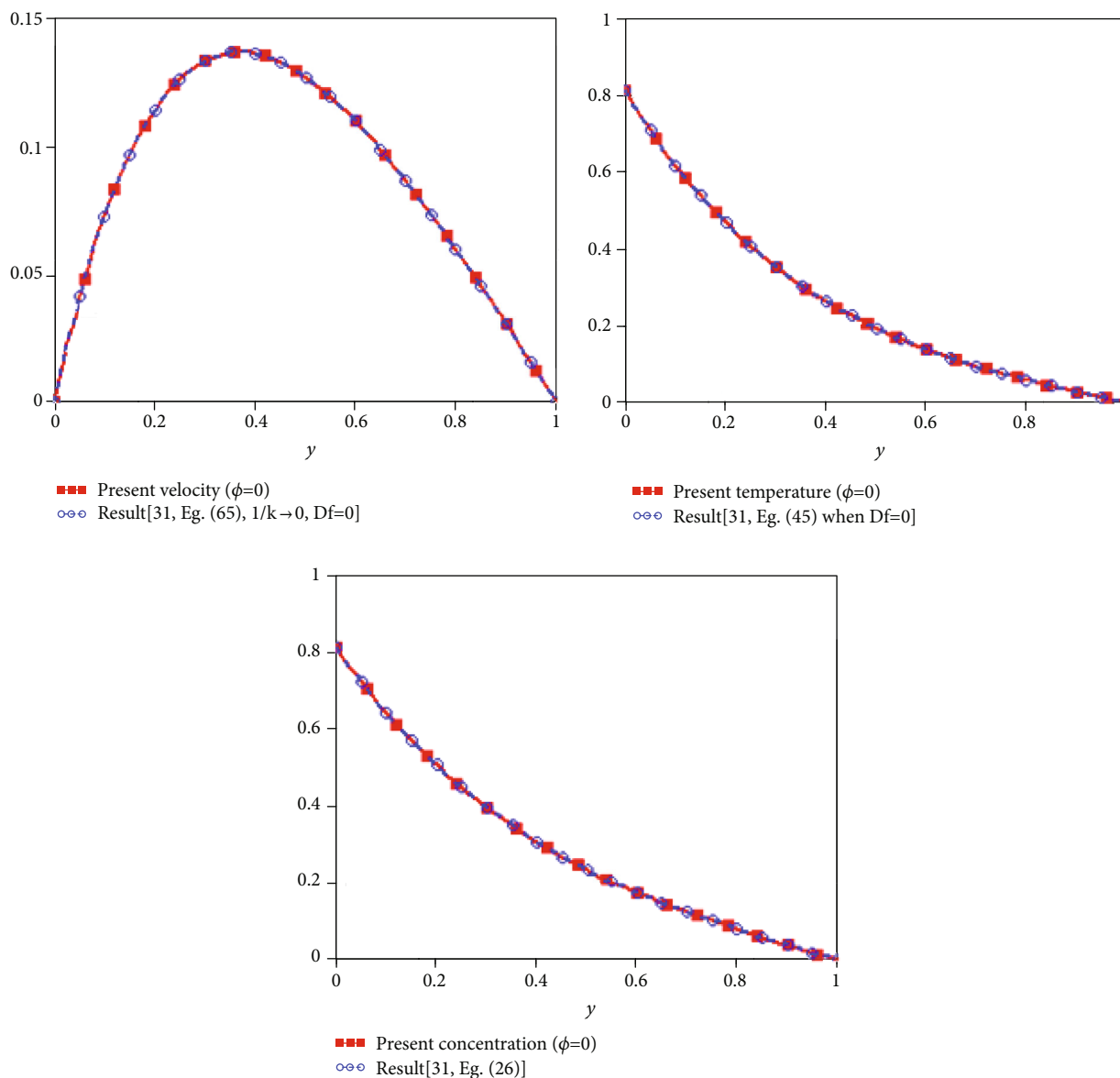


FIGURE 7: Comparison of results.

and Sherwood numbers are graphically underlined and discussed in detail.

The major points of this work are as follows:

- (i) Velocity, concentration, and temperature are lesser for ramped boundary conditions than isothermal
- (ii) Ramped wall velocity is increasing for greater values of  $\gamma$ ,  $Gr$ ,  $Gm$ , and  $Q$  and decreasing for higher values of  $\xi$ ,  $\phi$ ,  $M$ ,  $Pr$ ,  $Sc$ , and  $K$
- (iii) Ramped wall temperature is decreasing for higher values of  $\xi$  and  $Pr$  and decreasing for growing values of  $\phi$  and  $Q$
- (iv) Ramped wall concentration is decreasing for increasing values of  $\xi$ ,  $\phi$ ,  $Sc$ , and  $K$
- (v) Sherwood and Nusselt numbers both are increasing function of  $\phi$  for both isothermal and ramped conditions
- (vi) Velocity, concentration, and temperature obtained with ordinary derivatives are higher than that obtained by fractional derivatives. Thus, the fractional derivative is a better choice to have controlled results
- (vii) Ramped boundary conditions are useful to manage velocity, concentration, and temperature profiles

## Appendix

$$\begin{aligned}
 L^{-1} \left\{ \frac{e^{-a\sqrt{s^{\xi}+b}}}{\sqrt{s^{\xi}+b}} \right\} &= \int_0^{\infty} \frac{1}{\sqrt{\pi w}} e^{\left(\frac{-a^2}{4w}-bw\right)} t^{-1} \Phi\left(0, -\xi, -wt^{-\xi}\right) dw, \\
 L^{-1} \left\{ \frac{e^{-a\sqrt{s^{\xi}+b}}}{s^{\xi}+b} \right\} &= \int_0^{\infty} e^{-bw} \operatorname{erfc}\left(\frac{a}{2\sqrt{w}}\right) t^{-1} \Phi\left(0, -\xi, -wt^{-\xi}\right) dw, \\
 L^{-1} \left\{ \frac{1}{(s^{\xi}+a)s^2} \right\} &= \int_0^t w^{\xi-1} E_{\xi, \xi+1}(-aw^{\xi}) dw, \\
 L^{-1} \left\{ \frac{a}{(s^{\xi}+a)s} \right\} &= at^{\xi} E_{\xi, \xi+1}(-aw^{\xi}), \\
 L^{-1} \left\{ \frac{1}{s^{\xi}} \right\} &= \frac{t^{\xi-1}}{\Gamma(\xi)}.
 \end{aligned}
 \tag{A1}$$

## Nomenclature

$\tilde{u}(\tilde{y}, \tilde{t})$ : Velocity ( $\text{m s}^{-1}$ )  
 $\tilde{C}(\tilde{y}, \tilde{t})$ : Concentration ( $\text{kg m}^{-3}$ )  
 $\tilde{T}(\tilde{y}, \tilde{t})$ : Temperature (K)  
 $Q_0$ : Heat generation coefficient ( $\text{W m}^{-3} \text{K}^{-1}$ )  
 $k$ : Thermal conductivity ( $\text{W m}^{-1} \text{K}^{-1}$ )  
 $g$ : Gravitational acceleration ( $\text{m s}^{-2}$ )  
 $Q$ : Dimensionless heat generation  
 $D$ : Mass diffusivity ( $\text{m}^2 \text{s}^{-1}$ )  
 $R$ : Chemical reaction coefficient ( $\text{s}^{-1}$ )  
 $Gm$ : Mass Grashof number  
 $c_p$ : Specific heat ( $\text{J kg}^{-1} \text{K}^{-1}$ )  
 $K$ : Dimensionless chemical reaction  
 $Gr$ : Thermal Grashof number  
 $Sc$ : Schmidt number  
 $Pr$ : Prandtl number  
 $C_f$ : Skin friction  
 $Sh$ : Sherwood number  
 $Nu$ : Nusselt number.

## Greek Symbols

$\gamma$ : Casson parameter  
 $\rho$ : Density ( $\text{kg m}^{-3}$ )  
 $\beta_C$ : Mass volumetric coefficient ( $\text{m}^3 \text{kg}^{-1}$ )  
 $\nu$ : Kinematic viscosity ( $\text{m}^2 \text{s}^{-1}$ )  
 $\beta_T$ : Thermal expansion coefficient ( $\text{K}^{-1}$ )  
 $\theta$ : Dimensionless temperature  
 $\mu$ : Dynamic viscosity ( $\text{kg m}^{-1} \text{s}^{-1}$ )  
 $\phi$ : Nanoparticle volume fraction  
 $\sigma$ : Electric conductivity ( $\Omega \text{m}$ ) $^{-1}$ .

## Subscript

$nf$ : Fluid  
 $nf$ : Nanofluid  
 $s$ : Solid particles.

## Data Availability

No data were used in this manuscript.

## Conflicts of Interest

The authors declare that they have no conflicts of interest.

## Acknowledgments

The author Rifaqat Ali would like to express his gratitude to the Deanship of Scientific Research at King Khalid University, Saudi Arabia, for providing funding research groups under the research grant no. R. G. P. 1/162/42.

## References

- [1] N. Casson, *A Flow Equation for Pigment-Oil Suspensions of the Printing Ink Type, Rheology of Disperse Systems*, Pergamon Press, London, UK, 1959.
- [2] R. K. Dash, K. N. Mehta, and G. Jayaraman, "Casson fluid flow in a pipe filled with a homogenous porous medium," *International Journal of Engineering Science*, vol. 34, no. 10, pp. 1145–1156, 1996.
- [3] M. Usman, T. Gul, A. Khan, A. Alsubie, and M. Z. Ullah, "Electromagnetic couple stress film flow of hybrid nanofluid over an unsteady rotating disc," *International Communications in Heat and Mass Transfer*, vol. 127, article 105562, 2021.
- [4] A. Saeed, M. Jawad, W. Alghamdi, S. Nasir, T. Gul, and P. Kumam, "Hybrid nanofluid flow through a spinning Darcy-Forchheimer porous space with thermal radiation," *Scientific Reports*, vol. 11, no. 1, article 16708, 2021.
- [5] M. Bilal, A. Saeed, M. M. Selim, T. Gul, I. Ali, and P. Kumam, "Comparative numerical analysis of Maxwell's time-dependent thermo-diffusive flow through a stretching cylinder," *Case Studies in Thermal Engineering*, vol. 27, article 101301, 2021.
- [6] A. Saeed, W. Alghamdi, S. Mukhtar et al., "Darcy-Forchheimer hybrid nanofluid flow over a stretching curved surface with heat and mass transfer," *PLoS One*, vol. 16, no. 5, article e0249434, 2021.
- [7] I. Zari, A. Shafiq, G. Rasool, T. N. Sindhu, and T. S. Khan, "Double-stratified Marangoni boundary layer flow of Casson nanoliquid: probable error application," *Journal of Thermal Analysis and Calorimetry*, 2021.
- [8] B. Ali, G. Rasool, S. Hussain, D. Baleanu, and S. Bano, "Finite element study of magnetohydrodynamics (MHD) and activation energy in Darcy-Forchheimer rotating flow of Casson Carreau nanofluid," *PRO*, vol. 8, no. 9, p. 1185, 2020.
- [9] A. Shafiq, G. Rasool, H. Alotaibi et al., "Thermally enhanced Darcy-Forchheimer Casson-water/glycerine rotating nanofluid flow with uniform magnetic field," *Micromachines*, vol. 12, no. 6, p. 605, 2021.
- [10] A. A. Hayday, D. A. Bowlus, and R. A. McGraw, "Free convection from a vertical flat plate with step discontinuities in surface temperature," *Journal of Heat Transfer*, vol. 89, no. 3, pp. 244–249, 1967.
- [11] J. A. Schetz, "On the approximate solution of viscous-flow problems," *Journal of Applied Mechanics*, vol. 30, no. 2, pp. 263–268, 1963.



- [12] C. P. Malhotra, R. L. Mahajan, W. S. Sampath, K. L. Barth, and R. A. Enzenroth, "Control of temperature uniformity during the manufacture of stable thin-film photovoltaic devices," *International Journal of Heat and Mass Transfer*, vol. 49, no. 17–18, pp. 2840–2850, 2006.
- [13] R. McIntosh and S. Waldram, "Obtaining more, and better, information from simple ramped temperature screening tests," *Journal of Thermal Analysis and Calorimetry*, vol. 73, no. 1, pp. 35–52, 2003.
- [14] S. Das, M. Jana, and R. N. Jana, "Radiation effect on natural convection near a vertical plate embedded in porous medium with ramped wall temperature," *Open Journal of Fluid Dynamics*, vol. 1, no. 1, pp. 1–11, 2011.
- [15] R. Nandkeolyar, M. Das, and P. Sibanda, "Exact solutions of unsteady MHD free convection in a heat absorbing fluid flow past a flat plate with ramped wall temperature," *Boundary Value Problems*, vol. 2013, no. 1, 2013.
- [16] G. S. Seth, S. M. Hussain, and S. Sarkar, "Hydromagnetic natural convection flow with heat and mass transfer of a chemically reacting and heat absorbing fluid past an accelerated moving vertical plate with ramped temperature and ramped surface concentration through a porous medium," *Journal of the Egyptian Mathematical Society*, vol. 23, no. 1, pp. 197–207, 2015.
- [17] G. S. Seth, R. Sharma, and S. Sarkar, "Natural convection heat and mass transfer flow with hall current, rotation, radiation and heat absorption past an accelerated moving vertical plate with ramped temperature," *Journal of Applied Fluid Mechanics*, vol. 8, no. 1, pp. 7–20, 2015.
- [18] G. S. Seth, S. Sarkar, S. M. Hussain, and G. K. Mahato, "Effects of hall current and rotation on hydromagnetic natural convection flow with heat and mass transfer of a heat absorbing fluid past an impulsively moving vertical plate with ramped temperature," *Journal of Applied Fluid Mechanics*, vol. 8, no. 1, pp. 159–171, 2015.
- [19] G. S. Seth, M. S. Ansari, and R. Nandkeolyar, "MHD natural convection flow with radiative heat transfer past an impulsively moving plate with ramped wall temperature," *Heat and Mass Transfer*, vol. 47, no. 5, pp. 551–561, 2011.
- [20] N. A. Mohd Zin, I. Khan, and S. Shafie, "Influence of thermal radiation on unsteady MHD free convection flow of Jeffrey fluid over a vertical plate with ramped wall temperature," *Mathematical Problems in Engineering*, vol. 2016, 12 pages, 2016.
- [21] M. Narahari, "Transient free convection flow between long vertical parallel plates with ramped wall temperature at one boundary in the presence of thermal radiation and constant mass diffusion," *Meccanica*, vol. 47, no. 8, pp. 1961–1976, 2012.
- [22] A. Khalid, I. Khan, and S. Shafie, "Exact solutions for free convection flow of nanofluids with ramped wall temperature," *European Physical Journal Plus*, vol. 130, no. 4, p. 4, 2015.
- [23] B. Mahanthesh, B. J. Gireesha, and R. S. R. Gorla, "Heat and mass transfer effects on the mixed convective flow of chemically reacting nanofluid past a moving/stationary vertical plate," *Alexandria Engineering Journal*, vol. 55, no. 1, pp. 569–581, 2016.
- [24] B. K. Jha and Y. Y. Gambo, "Soret and Dufour effects on transient free convection heat and mass transfer flow in a vertical channel with ramped wall temperature and specie concentration: an analytical approach," *Arab Journal of Basic and Applied Sciences*, vol. 27, no. 1, pp. 344–357, 2020.
- [25] M. Arif, P. Kumam, W. Kumam, I. Khan, and M. Ramzan, "A fractional model of Casson fluid with ramped wall temperature: engineering applications of engine oil," *Computational and Mathematical Methods*, no. article e1162, 2021.
- [26] T. Anwar, P. Kumam, I. Khan, and W. Watthayu, "Heat transfer enhancement in unsteady MHD natural convective flow of CNTs Oldroyd-B nanofluid under ramped wall velocity and ramped wall temperature," *Entropy*, vol. 22, no. 4, p. 401, 2020.
- [27] C. Li, D. Qian, and Y. Chen, "On Riemann-Liouville and caputo derivatives," *Discrete Dynamics in Nature and Society*, vol. 2011, 15 pages, 2011.
- [28] N. Heymans and I. Podlubny, "Physical interpretation of initial conditions for fractional differential equations with Riemann-Liouville fractional derivatives," *Rheologica Acta*, vol. 45, no. 5, pp. 765–771, 2006.
- [29] M. Turkyilmazoglu, "Exact analytical solutions for heat and mass transfer of MHD slip flow in nanofluids," *Chemical Engineering Science*, vol. 84, pp. 182–187, 2012.
- [30] M. Hatami and D. D. Ganji, "Natural convection of sodium alginate (SA) non-Newtonian nanofluid flow between two vertical flat plates by analytical and numerical methods," *Case Studies in Thermal Engineering*, vol. 2, pp. 14–22, 2014.
- [31] M. Ramzan, M. Nazar, Z. Un Nisa, M. Ahmad, and N. Ali Shah, "Unsteady free convective magnetohydrodynamics flow of a Casson fluid through a channel with double diffusion and ramp temperature and concentration," *Mathematical Methods in Applied Sciences*, pp. 1–20, 2021.
- [32] I. Siddique, K. Sadiq, I. Khan, and K. S. Nisar, "Nanomaterials in convection flow of nanofluid in upright channel with gradients," *Journal of Materials Research and Technology*, vol. 11, pp. 1411–1423, 2021.
- [33] S. Kakaç and A. Pramuanjaroenkij, "Review of convective heat transfer enhancement with nanofluids," *International Journal of Heat and Mass Transfer*, vol. 52, no. 13–14, pp. 3187–3196, 2009.
- [34] H. F. Oztop and E. Abu-Nada, "Numerical study of natural convection in partially heated rectangular enclosures filled with nanofluids," *International Journal of Heat and Fluid flow*, vol. 29, no. 5, pp. 1326–1336, 2008.